Gas Lasers

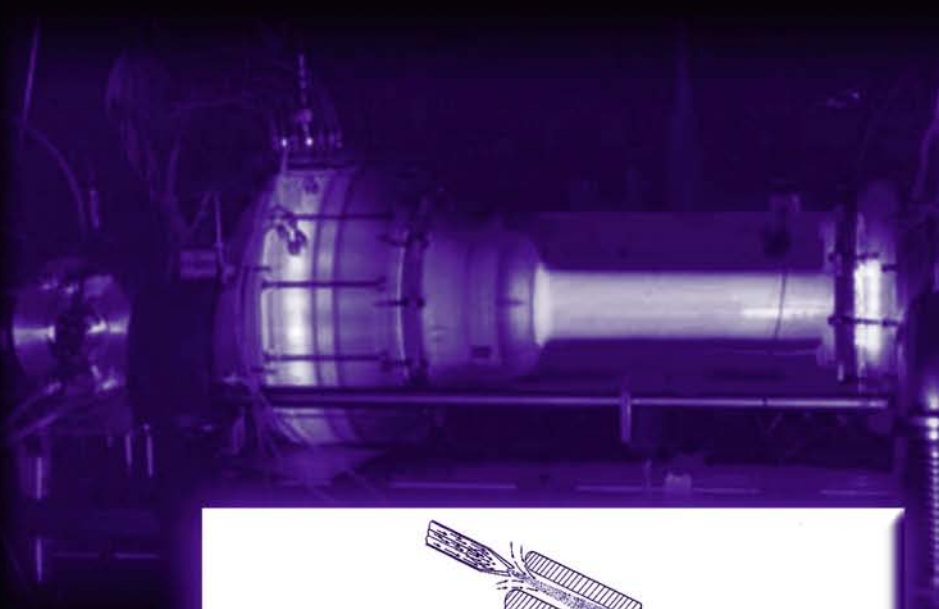

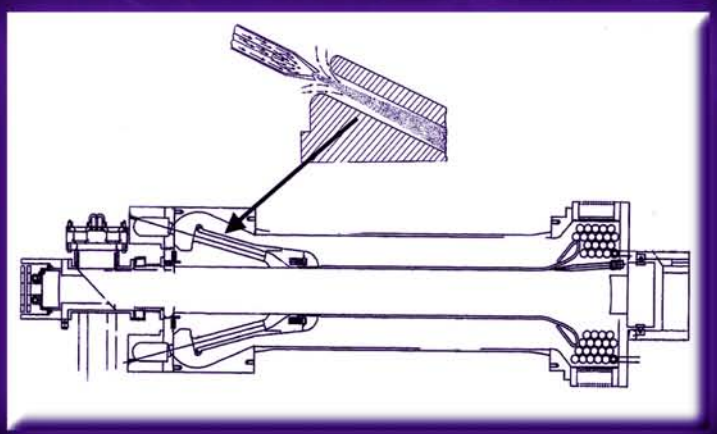

edited by

Masamori Endo
Robert F. Walter

CRC Press
Taylor & Francis Group

GasLasers

OPTICAL SCIENCE AND ENGINEERING

Founding Editor
Brian J. Thompson
University of Rochester
Rochester, New York

1. Electron and Ion Microscopy and Microanalysis: Principles and Applications, *Lawrence E. Murr*
2. Acousto-Optic Signal Processing: Theory and Implementation, *edited by Norman J. Berg and John N. Lee*
3. Electro-Optic and Acousto-Optic Scanning and Deflection, *Milton Gottlieb, Clive L. M. Ireland, and John Martin Ley*
4. Single-Mode Fiber Optics: Principles and Applications, *Luc B. Jeunhomme*
5. Pulse Code Formats for Fiber Optical Data Communication: Basic Principles and Applications, *David J. Morris*
6. Optical Materials: An Introduction to Selection and Application, *Solomon Musikant*
7. Infrared Methods for Gaseous Measurements: Theory and Practice, *edited by Joda Wormhoudt*
8. Laser Beam Scanning: Opto-Mechanical Devices, Systems, and Data Storage Optics, *edited by Gerald F. Marshall*
9. Opto-Mechanical Systems Design, *Paul R. Yoder, Jr.*
10. Optical Fiber Splices and Connectors: Theory and Methods, *Calvin M. Miller with Stephen C. Mettler and Ian A. White*
11. Laser Spectroscopy and Its Applications, *edited by Leon J. Radziemski, Richard W. Solarz, and Jeffrey A. Paisner*
12. Infrared Optoelectronics: Devices and Applications, *William Nunley and J. Scott Bechtel*
13. Integrated Optical Circuits and Components: Design and Applications, *edited by Lynn D. Hutcheson*
14. Handbook of Molecular Lasers, *edited by Peter K. Cheo*
15. Handbook of Optical Fibers and Cables, *Hiroshi Murata*
16. Acousto-Optics, *Adrian Korpel*
17. Procedures in Applied Optics, *John Strong*
18. Handbook of Solid-State Lasers, *edited by Peter K. Cheo*
19. Optical Computing: Digital and Symbolic, *edited by Raymond Arrathoon*
20. Laser Applications in Physical Chemistry, *edited by D. K. Evans*
21. Laser-Induced Plasmas and Applications, *edited by Leon J. Radziemski and David A. Cremers*
22. Infrared Technology Fundamentals, *Irving J. Spiro and Monroe Schlessinger*
23. Single-Mode Fiber Optics: Principles and Applications, Second Edition, Revised and Expanded, *Luc B. Jeunhomme*
24. Image Analysis Applications, *edited by Rangachar Kasturi and Mohan M. Trivedi*
25. Photoconductivity: Art, Science, and Technology, *N. V. Joshi*
26. Principles of Optical Circuit Engineering, *Mark A. Mentzer*
27. Lens Design, *Milton Laikin*

28. Optical Components, Systems, and Measurement Techniques, *Rajpal S. Sirohi and M. P. Kothiyal*
29. Electron and Ion Microscopy and Microanalysis: Principles and Applications, Second Edition, Revised and Expanded, *Lawrence E. Murr*
30. Handbook of Infrared Optical Materials, *edited by Paul Klocek*
31. Optical Scanning, *edited by Gerald F. Marshall*
32. Polymers for Lightwave and Integrated Optics: Technology and Applications, *edited by Lawrence A. Hornak*
33. Electro-Optical Displays, *edited by Mohammad A. Karim*
34. Mathematical Morphology in Image Processing, *edited by Edward R. Dougherty*
35. Opto-Mechanical Systems Design: Second Edition, Revised and Expanded, *Paul R. Yoder, Jr.*
36. Polarized Light: Fundamentals and Applications, *Edward Collett*
37. Rare Earth Doped Fiber Lasers and Amplifiers, *edited by Michel J. F. Digonnet*
38. Speckle Metrology, *edited by Rajpal S. Sirohi*
39. Organic Photoreceptors for Imaging Systems, *Paul M. Borsenberger and David S. Weiss*
40. Photonic Switching and Interconnects, *edited by Abdellatif Marrakchi*
41. Design and Fabrication of Acousto-Optic Devices, *edited by Akis P. Goutzoulis and Dennis R. Pape*
42. Digital Image Processing Methods, *edited by Edward R. Dougherty*
43. Visual Science and Engineering: Models and Applications, *edited by D. H. Kelly*
44. Handbook of Lens Design, *Daniel Malacara and Zacarias Malacara*
45. Photonic Devices and Systems, *edited by Robert G. Hunsberger*
46. Infrared Technology Fundamentals: Second Edition, Revised and Expanded, *edited by Monroe Schlessinger*
47. Spatial Light Modulator Technology: Materials, Devices, and Applications, *edited by Uzi Efron*
48. Lens Design: Second Edition, Revised and Expanded, *Milton Laikin*
49. Thin Films for Optical Systems, *edited by Francoise R. Flory*
50. Tunable Laser Applications, *edited by F. J. Duarte*
51. Acousto-Optic Signal Processing: Theory and Implementation, Second Edition, *edited by Norman J. Berg and John M. Pellegrino*
52. Handbook of Nonlinear Optics, *Richard L. Sutherland*
53. Handbook of Optical Fibers and Cables: Second Edition, *Hiroshi Murata*
54. Optical Storage and Retrieval: Memory, Neural Networks, and Fractals, *edited by Francis T. S. Yu and Suganda Jutamulia*
55. Devices for Optoelectronics, *Wallace B. Leigh*
56. Practical Design and Production of Optical Thin Films, *Ronald R. Willey*
57. Acousto-Optics: Second Edition, *Adrian Korpel*
58. Diffraction Gratings and Applications, *Erwin G. Loewen and Evgeny Popov*
59. Organic Photoreceptors for Xerography, *Paul M. Borsenberger and David S. Weiss*
60. Characterization Techniques and Tabulations for Organic Nonlinear Optical Materials, *edited by Mark G. Kuzyk and Carl W. Dirk*
61. Interferogram Analysis for Optical Testing, *Daniel Malacara, Manuel Servin, and Zacarias Malacara*
62. Computational Modeling of Vision: The Role of Combination, *William R. Uttal, Ramakrishna Kakarala, Spiram Dayanand, Thomas Shepherd, Jagadeesh Kalki, Charles F. Lunskis, Jr., and Ning Liu*
63. Microoptics Technology: Fabrication and Applications of Lens Arrays and Devices, *Nicholas Borrelli*
64. Visual Information Representation, Communication, and Image Processing, *edited by Chang Wen Chen and Ya-Qin Zhang*
65. Optical Methods of Measurement, *Rajpal S. Sirohi and F. S. Chau*

66. Integrated Optical Circuits and Components: Design and Applications, *edited by Edmond J. Murphy*
67. Adaptive Optics Engineering Handbook, *edited by Robert K. Tyson*
68. Entropy and Information Optics, *Francis T. S. Yu*
69. Computational Methods for Electromagnetic and Optical Systems, *John M. Jarem and Partha P. Banerjee*
70. Laser Beam Shaping, *Fred M. Dickey and Scott C. Holswade*
71. Rare-Earth-Doped Fiber Lasers and Amplifiers: Second Edition, Revised and Expanded, *edited by Michel J. F. Digonnet*
72. Lens Design: Third Edition, Revised and Expanded, *Milton Laikin*
73. Handbook of Optical Engineering, *edited by Daniel Malacara and Brian J. Thompson*
74. Handbook of Imaging Materials: Second Edition, Revised and Expanded, *edited by Arthur S. Diamond and David S. Weiss*
75. Handbook of Image Quality: Characterization and Prediction, *Brian W. Keelan*
76. Fiber Optic Sensors, *edited by Francis T. S. Yu and Shizhuo Yin*
77. Optical Switching/Networking and Computing for Multimedia Systems, *edited by Mohsen Guizani and Abdella Battou*
78. Image Recognition and Classification: Algorithms, Systems, and Applications, *edited by Bahram Javidi*
79. Practical Design and Production of Optical Thin Films: Second Edition, Revised and Expanded, *Ronald R. Willey*
80. Ultrafast Lasers: Technology and Applications, *edited by Martin E. Fermann, Almantas Galvanauskas, and Gregg Sucha*
81. Light Propagation in Periodic Media: Differential Theory and Design, *Michel Nevière and Evgeny Popov*
82. Handbook of Nonlinear Optics, Second Edition, Revised and Expanded, *Richard L. Sutherland*
83. Polarized Light: Second Edition, Revised and Expanded, *Dennis Goldstein*
84. Optical Remote Sensing: Science and Technology, *Walter Egan*
85. Handbook of Optical Design: Second Edition, *Daniel Malacara and Zacarias Malacara*
86. Nonlinear Optics: Theory, Numerical Modeling, and Applications, *Partha P. Banerjee*
87. Semiconductor and Metal Nanocrystals: Synthesis and Electronic and Optical Properties, edited by *Victor I. Klimov*
88. High-Performance Backbone Network Technology, *edited by Naoaki Yamanaka*
89. Semiconductor Laser Fundamentals, *Toshiaki Suhara*
90. Handbook of Optical and Laser Scanning, *edited by Gerald F. Marshall*
91. Organic Light-Emitting Diodes: Principles, Characteristics, and Processes, *Jan Kalinowski*
92. Micro-Optomechatronics, *Hiroshi Hosaka, Yoshitada Katagiri, Terunao Hirota, and Kiyoshi Itao*
93. Microoptics Technology: Second Edition, *Nicholas F. Borrelli*
94. Organic Electroluminescence, *edited by Zakya Kafafi*
95. Engineering Thin Films and Nanostructures with Ion Beams, *Emile Knystautas*
96. Interferogram Analysis for Optical Testing, Second Edition, *Daniel Malacara, Manuel Sercin, and Zacarias Malacara*
97. Laser Remote Sensing, *edited by Takashi Fujii and Tetsuo Fukuchi*
98. Passive Micro-Optical Alignment Methods, *edited by Robert A. Boudreau and Sharon M. Boudreau*
99. Organic Photovoltaics: Mechanism, Materials, and Devices, *edited by Sam-Shajing Sun and Niyazi Serdar Saracftci*
100. Handbook of Optical Interconnects, *edited by Shigeru Kawai*
101. GMPLS Technologies: Broadband Backbone Networks and Systems, *Naoaki Yamanaka, Kohei Shiomoto, and Eiji Oki*

102. Laser Beam Shaping Applications, *edited by Fred M. Dickey, Scott C. Holswade and David L. Shealy*
103. Electromagnetic Theory and Applications for Photonic Crystals, *Kiyotoshi Yasumoto*
104. Physics of Optoelectronics, *Michael A. Parker*
105. Opto-Mechanical Systems Design: Third Edition, *Paul R. Yoder, Jr.*
106. Color Desktop Printer Technology, *edited by Mitchell Rosen and Noboru Ohta*
107. Laser Safety Management, *Ken Barat*
108. Optics in Magnetic Multilayers and Nanostructures, *Štefan Višňovský*
109. Optical Inspection of Microsystems, *edited by Wolfgang Osten*
110. Applied Microphotonics, *edited by Wes R. Jamroz, Roman Kruzelecky, and Emile I. Haddad*
111. Organic Light-Emitting Materials and Devices, *edited by Zhigang Li and Hong Meng*
112. Silicon Nanoelectronics, *edited by Shunri Oda and David Ferry*
113. Image Sensors and Signal Processor for Digital Still Cameras, *Junichi Nakamura*
114. Encyclopedic Handbook of Integrated Circuits, *edited by Kenichi Iga and Yasuo Kokubun*
115. Quantum Communications and Cryptography, *edited by Alexander V. Sergienko*
116. Optical Code Division Multiple Access: Fundamentals and Applications, *edited by Paul R. Prucnal*
117. Polymer Fiber Optics: Materials, Physics, and Applications, *Mark G. Kuzyk*
118. Smart Biosensor Technology, *edited by George K. Knopf and Amarjeet S. Bassi*
119. Solid-State Lasers and Applications, *edited by Alphan Sennaroglu*
120. Optical Waveguides: From Theory to Applied Technologies, *edited by Maria L. Calvo and Vasudevan Lakshiminarayanan*
121. Gas Lasers, *edited by Masamori Endo and Robert F. Walter*
122. Lens Design, Fourth Edition, *Milton Laikin*
123. Photonics: Principles and Practices, *Abdul Al-Azzawi*
124. Microwave Photonics, *edited by Chi H. Lee*

Gas Lasers

edited by

Masamori Endo

Robert F. Walter

CRC Press
Taylor & Francis Group
Boca Raton London New York

CRC Press is an imprint of the
Taylor & Francis Group, an informa business

CRC Press
Taylor & Francis Group
6000 Broken Sound Parkway NW, Suite 300
Boca Raton, FL 33487-2742

Printed in the United States of America on acid-free paper
10 9 8 7 6 5 4 3 2 1

International Standard Book Number-10: 0-8493-3553-1 (Hardcover)
International Standard Book Number-13: 978-0-8493-3553-2 (Hardcover)

Library of Congress Cataloging-in-Publication Data

Gas lasers / edited by Masamori Endo and Robert F. Walter.
p. cm. -- (Optical science and engineering ; 121)
Includes bibliographical references and index.
ISBN 0-8493-3553-1 (978-0-8493-3553-2 : alk. paper)
1. Gas lasers. I. Endo, Masamori, 1965- II. Walter, Robert F., 1950- III. Title. IV. Series.

TA1695.G3385 2006
621.36'63--dc22 2006030226

Visit the Taylor & Francis Web site at
http://www.taylorandfrancis.com

and the CRC Press Web site at
http://www.crcpress.com

Preface

More than 40 years have passed since the first demonstration of the laser. Lasers are the only coherent electromagnetic waves at the optical frequency, and they never existed on earth until 1960, when T.H. Maiman* demonstrated the first "atomic lamp."** Now lasers have become indispensable tools in our modern life. In particular, the application of laser technology to communication and information processing is so successful that more than a billon laser diodes are manufactured annually. It should be mentioned that lasers involve in some way in most of the innovative advances in every other area of science as well.

This book deals with a special kind of laser. The book focuses on the laser whose active medium is gaseous. Today, the number of gas lasers manufactured is significantly greater than the number of semiconductor lasers; however, the contribution of gas lasers to our life is just as important as that of semiconductor lasers.

The variety of laser media makes it possible for gas lasers to extend their oscillating wavelength range from far infrared to vacuum ultraviolet. Today's revolution in microelectronics is largely due to the sophisticated UV excimer laser lithography technology. The CO_2 laser has dominated the machine tool market for almost 30 years. The substitution of the laser source to the solid-state ones has just started recently owing to the recent advances in high-power diode lasers. However, the CO_2 laser is still more cost-effectiveness, has better beam quality, and better output power scalability.

Currently, the interests of research in laser devices seem to be shifting to solid-state lasers. However, solid-state lasers are not almighty, and one should know about other laser sources before starting something. In this context, the editors thought that it is worth publishing a book devoted to gas lasers that contains not only their basics, but also their up-to-date research.

The target of this book is not undergraduate students who have just started studying laser physics. Instead, this book is devoted to graduate students, scientists, and engineers who are or will be involved in gas lasers. The latest and most comprehensive information on the most popular gas lasers will be found in this book.

The properties of this book may be summarized as follows:

1. Information on the state-of-art technology of each laser is featured.
2. The first chapter begins with the properties of gas lasers in general, and then goes on to discuss the general aspects of gas lasers, namely, gas dynamics, electric circuits for excitation, and optical resonators.
3. The basic physics of each laser are especially emphasized in this book, which is comparable with books devoted to those specific lasers.
4. Application of gas lasers, especially their potential applications to modern engineering, are described.

In summary, this book is devoted to readers who are working with or interested in gas lasers, from basic research to novel applications. The authors are experts of specific laser physics from all over the word. Each chapter includes the basic physics, characteristics, applications, and current research tasks of specific lasers. The types of lasers chosen to be included in the

*Maiman, T.H., *Nature*, 493, 1960.
**Headline of *Asahi Shinbun*, daily newspaper, Japan, July 7, 1960.

book were made on the basis of their importance in today's science and engineering. We selected the authors carefully; however, the selection may be biased by our personal relationships and the authors' availability.

Chapter 1 provides a definition of gaseous media and is followed by a description of the rovibrational spectral characteristics of gaseous media without the requirement of knowledge of advanced quantum mechanics. Then, a description of spectral broadening, especially Doppler broadening caused by translational movement and pressure broadening caused by the collision of atoms, is discussed. From Chapter 2 to Chapter 4, fluid dynamics, electric excitation circuits, and optical resonators of gas lasers in general are discussed. As the excitation of gaseous media is much more diverse than solid-state lasers, it must be classified. Though fluid dynamics are important for gas lasers, optical resonators need to be considered specially in a discussion on energy extraction from gaseous media.

From Chapter 5 to Chapter 10, selected specific laser devices are featured. These are classified by the laser medium and subclassified in terms of the excitation scheme and kinds of atoms or molecules, when necessary. Chapter 11 discusses other gas lasers that are not discussed in the previous chapters. We hope this book serves as a comprehensive encyclopedia for gas laser scientists and engineers.

Masamori Endo

Editors

Masamori Endo was born in Tokyo, Japan, in 1965. He received the BA and PhD degrees from Keio University in 1988 and 1993, respectively. After that, he worked for Mitsubishi Heavy Industries, Ltd. for 3 years. He studied microwave heating and complex dielectric properties of materials. Since 1996, he has been at Tokai University, where he has worked with chemical oxygen iodine lasers (COIL), laser material processing, and theoretical modeling of optical resonators. Since 2004, he has also been an associate professor at the Department of Physics, School of Science of Tokai University. He is a member of the International Society for Optical Engineering (SPIE), the American Institute of Aeronautics and Astronautics, the Applied Physics Society of Japan, and the Laser Society of Japan.

Robert F. Walter is Group Leader for Directed Energy Systems at the Schafer Corporation, Albuquerque, New Mexico. He was born in Conyngham, Pennsylvania, in 1950. He received the SB, SM, and PhD degrees in aeronautics and astronautics from Massachusetts Institute of Technology (MIT) in 1972, 1973, and 1978, respectively. Before joining the Schafer Corporation in 1982, Dr. Walter worked as a high-energy laser gas-dynamics specialist at the Air Force Weapons Laboratory. He has over 30 years of experience with high-power gas lasers. He has made significant contributions in the modeling and simulation of a wide variety of high-power gas lasers, including the COIL, the electric oxygen iodine laser (EOIL), the CO_2 gas-dynamic and electric discharge laser, excimer lasers (XeF, XeCl, and KrF), and Raman lasers. He is a member of the Plasmadynamics and Laser Technical Committee of the American Institute of Aeronautics and Astronautics, which he chaired from 1922 to 1994. Dr. Walter is also a member of the International Advisory Committee of the Gas Flow and Chemical Laser Symposium and editor of the volume *High Power Laser: Science and Engineering*, published in 1996 for NATO.

Contributors

Krzysztof M. Abramski
Wrocław University of Technology
Wrocław, Poland

Wilhelm H. Behrens
Fluid & Thermophysics Department
Northrop Grumman Space Technology (NGST)
Redondo Beach
California

Anatoly S. Boreysho
Baltic State Technical University
Laser Systems Inc.
St. Petersburgh
Russia

Steven J. Davis
Applied Sciences Department
Physical Sciences Inc.
Andover
Massachusetts

Michael C. Heaven
Department of Chemistry
Emory University
Atlanta
Georgia

Alan E. Hill
Plasmatronics Inc.
Albuquerque, New Mexico
and
Texas A&M University
College Station, Texas

Andrey A. Ionin
P.N. Lebedev Physical Institute of Russian Academy of Sciences
Moscow
Russia

Vladimir V. Khukharev
D.V. Efremov Scientific Research Institute of Electrophysical Apparatus
St. Petersburgh
Russia

Peter D. Lohn
Retired from Fluid & Thermophysics Department
Northrop Grumman Space Technology (NGST)
Redondo Beach
California

Victor M. Malkov
Baltic State Technical University
Laser Systems Inc.
St. Petersburgh
Russia

William E. McDermott
University of Denver Research Institute
Denver
Colorado

Anatoly P. Napartovich
Troitsk Institute for Innovation and Fusion Research
Troitsk
Russia

Edward F. Plinski
Wrocław University of Technology
Wrocław, Poland

Nikola V. Sabotinov
Institute of Solid State Physics
Bulgarian Academy of Sciences
Sofia
Bulgaria

Andrey V. Savin
Baltic State Technical University
Laser Systems Inc.
St. Petersburgh
Russia

Robert F. Walter
Schafer Corporation
Albuquerque
New Mexico

Sergey I. Yakovlenko
General Physics Institute
Moscow
Russia

Table of Contents

1 Principles of Gas Lasers

Krzysztof M. Abramski and Edward F. Plinski

CONTENTS

The year 1960 witnessed the beginning of a new revolution in optics. The effect of stimulated emission, predicted in 1917 by Albert Einstein, was finally implemented in practice. The

discovery of the new optical device, called laser, was preceded by several theoretical works of Ch. Towns, N.G. Basov, and A.N. Prokhorov, who won a Nobel Prize in 1964. The man, who first admired a coherent radiation from his ruby laser was T.H. Maiman; however, he was not a Nobel Prize Laureate. In fact, the revolution in optics was rather calm, and it would be much better to call it "a velvet revolution." Nobody expected any practical use for the new, sophisticated toy of scientists. At that time, the laser was called "the device waiting for a job." The year 1960 brought a new device—a helium–neon (He–Ne) laser elaborated by A. Javan. The He–Ne laser operating on a 1.15 μm wave initiated a new branch in optics—gas lasers. Soon, the next milestone was reached in 1964 by C.K.N. Patel, who invented a laser operating on carbon dioxide (CO_2) molecules. After a few modifications such as the addition of nitrogen (N_2) and He, the laser gave an output of 100 watts. It was a big breakthrough in laser physics, and it kindled the imagination of scientists and engineers. Applications of lasers in different branches of science and technology became a reality. Even today, gas lasers fulfill leading roles in research, technology, techniques, and many unexpected branches of human activity.

1.1 INTRODUCTION

What does the term *Laser* mean?

The acronym LASER (light amplification by stimulated emission of radiation) suggests that the device is an amplifier. However, it is not true; it is an oscillator. Moreover, replacing amplification by oscillation could bring funny associations. Let us leave it as it is.

What adjectives usually precede the word laser?

The terms "gas," "solid state," and "liquid" give the most general description of lasers. This systematics is very natural, taken from the names of media, which occur in nature surrounding us. In practice, more precise adjectives describing the types of a laser can be met. Adjectives "He–Ne," "carbon monoxide" (CO), "CO_2", and N_2 are examples of names, which directly describe the laser medium. In that case, they are gas lasers. They can be divided into atomic or molecular lasers. Nd–YAG, fiber and diode lasers belong to a group of solid-state lasers. Words like rare-gas, copper, gold vapor, ion, and free electron indicate specific laser media. The adjective chemical refers to lasers governed by chemical reactions, and they are also gas lasers. The adjective excimer describes the specific medium existing only in an excited state like XeF*. X-ray or e-beam indicates the mechanism of the excitation. Sometimes an acronym is used as an adjective like SSDPL (solid-state diode pumped laser); of course, the device belongs to solid-state lasers. A similar example is a COIL (chemical oxygen iodine laser) or TEA laser (transverse excited atmospheric laser)—certainly gas lasers. Dye lasers belong to the liquid laser group. More systematic description of gas lasers is given in Chapter 11.

Why was gas laser development so dynamic?

Since the 1960s, gas laser technology has demonstrated a very rapid rate of development. Gas lasers hit an extremely favorable historical period. Flourishing investigations on gases, high vacuum technology, discharges, and plasma were the factors that accelerated the development of gas lasers at that time. Additionally, well-developed spectroscopy brought significant information about energy structures of different gas media—the base to discover new laser transitions. We should also remember the new technologies of low-loss laser dielectric optics and infrared (IR) components, like ZnSe or ZnS (irtrans).

Why are gas lasers so interesting?

– The well-developed technique of gas discharges allows exciting gas media in reasonable, easyily formable, laser cavities.

– According to its nature, gas adopts shapes limited by a laser cavity.
– Gas lasers can be easily scaled in length, area, and volume without a significant increase in the cost of the device.
– Long lifetime has been achieved for gas laser devices because of well-developed high-vacuum technologies. For instance, many who work in the laboratory or industry can use a He–Ne laser even a few decades old without any noticeable degradation.
– In many lasers, recycling of the gas sufficiently increases their lifetime.
– Only gas media have the possibility of flowing fast through the laser device. In that way, refreshing and heat removal can be easily achieved.
– A huge advantage of gases is their ability to mix in different ratios and at different pressures to form highly homogeneous media.
– A relatively low density of gas medium demonstrates narrow and well-defined spectral emission lines, which makes them stable sources of optical radiation (in output power and frequency).
– The other advantage is the possibility of using isotopes to shift the spectrum of laser radiation.
– Gas laser output covers all optical spectra from far infrared (FIR) radiation to x-ray. Some representative examples are shown in Figure 1.1.

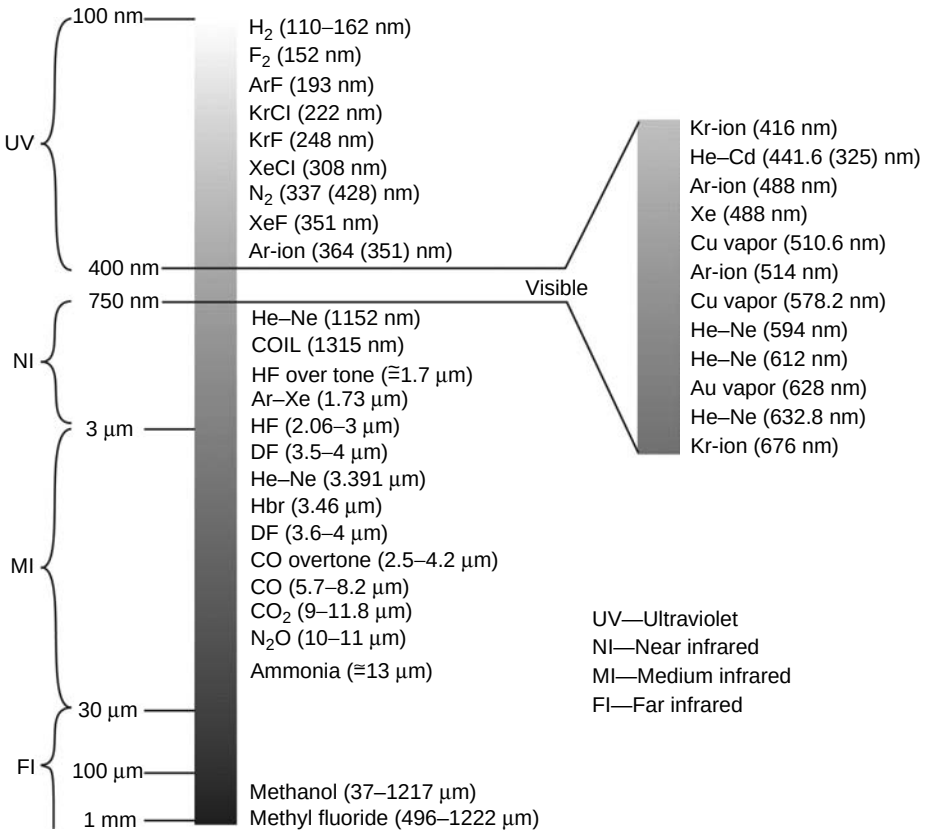

FIGURE 1.1 The spectral map of popular gas laser radiation.

What to Read?

This chapter gives some elementary knowledge about gas laser operation. It includes a description of properties of neutral and weakly ionized gases. Next, it introduces gas spectroscopy and optical gain conditions. The simple model of a laser action is presented, and different kinds of laser excitation are reviewed. A systematic description of different gas lasers is given. However, the basic knowledge given in this chapter is limited. The reader who wants to extend his basic knowledge about lasers as such can find it in well-known and reliable handbooks written by famous authors. We encourage to reach for books by Siegman [1], Verdeyen [2], Svelto [3], Milloni [4], and two books by Yariv [5,6]. We would also like to recommend an important book edited by Eden [7] which contains a set of the most significant publications that are the milestones in gas laser science and technology.

In the successive chapters of this book, the reader will find detailed information about: fluid dynamics (Chapter 2), optical resonators (Chapter 3), electric circuits (Chapter 4), molecular CO and CO_2 lasers (Chapter 5 and Chapter 6), chemical HF lasers (Chapter 7), excimer lasers (Chapter 8), iodine lasers (Chapter 9), metal vapor lasers (Chapter 10), and the other gas lasers (Chapter 11).

1.2 GAS MEDIA

Gas media were the first to be recognized as laser media. There is, of course, one exception—ruby, which was the first operating laser, but it is the exception proving the rule that random character of science development has its own charm. Irrespective of the competitions between different kinds of media, the gas lasers were the first and fastest developing devices at the beginning of their history, which was in the late fifties of the twentieth century. Gas medium, treated as a chaotic assembly of species (atoms, molecules) that have no volume and forces between them, can be described by an ideal gas equation:

$$pV = RT, \tag{1.1}$$

where p is the absolute pressure, V the specific volume, T the absolute temperature, and R is the gas constant.

Equation 1.1 can be rewritten in a different form:

$$pV = NkT, \tag{1.2}$$

where k is the Boltzmann constant and N is Avogadro's number ($6.0248 \cdot 10^{23}$).

The specific property of the gas medium is the so-called Avogadro law, which states: equal volumes of ideal gases at the same temperature and pressure contain the same number of species (atoms or molecules). The equations considered here are valid for diluted gases. In practice, the gas at atmospheric pressure can be still considered as diluted. Most gas lasers operate at pressures equal or below one atmosphere. Hence, the ideal gas equation can be applied for most gas laser media. The neutral gas considered here does not fulfill conditions for laser action. The medium has to be excited between the chosen internal energy levels of atoms or molecules for the appearance of population inversion. It can be achieved by different mechanisms of excitation. The main technique to obtain the population inversion in a gas medium is excitation by discharge. Experimental and theoretical researches on discharges together with the development of gas spectroscopy have been well elaborated since the middle of the twentieth century. All this knowledge had formed a very solid base to the fast and natural development of gas lasers from the beginning of laser history, which started just after the Second World War.

Gas as a laser medium is easily formable in length and shape—the reservoir and the excitation geometry determine the laser dimensions. The huge advantage of gas medium is the homogeneity and scalability. The researches dealing with gas lasers show that laser medium parameters can be controlled at a reasonably large scale by changing the pressure, excitation parameters (discharge current), and gas components.

Generally, neutral gas does not fulfill conditions for quantum gain and laser action. Although, there are cases, like FIR lasers (submillimeter lasers), when the neutral gas is excited via external pumping laser beam (no electrical species like free electrons or ions in the gas). Nevertheless, most gas lasers use gas discharge media obtained by different techniques.

1.2.1 Ionized Gas

Gas laser discharge can be considered as the so-called weakly ionized plasma, which contains some charged species (free electrons, ions) necessary to obtain excitation of the gas medium. Ionized gas is described by its basic parameter—free electron density n_e. For typical gas discharges, the electron density falls in the range $n_e = 10^{16}/10^{20}/\mathrm{m}^3$ [8], compared with the density of gas in normal conditions (atmospheric pressure at 0°C) $N = 2.7 \cdot 10^{25}/\mathrm{m}^3$.

A weakly ionized gas discharge can be still considered as a neutral gas. Such a gas discharge forms the so-called quasineutral plasma, where strong electric fields do not appear. From a physical point of view, it means that the next net charge density of free electrons n_i, positive n_i^+, and negative n_i^- ions produced in the plasma is close to zero:

$$n_e + n_i^- \approx n_i^+. \tag{1.3}$$

For ionized media, apart from free electrons there are several species of ions, which can give quite a complicated picture of discharge, particularly in the case of molecular gases.

1.2.2 Interactions

Atoms or molecules have two kinds of energy: internal and kinetic. The exchange of energy in the process of chaotic motions occurs via collision mechanisms. Two kinds of species collisions can be distinguished:

1. Inelastic collisions—when internal energy of species under collision is changed.
2. Elastic collision—when only the kinetic energy (not internal) of species under collision exchanges (billard ball collision analogy).

There are different processes in a plasma to obtain population inversion, necessary to achieve the lasing condition. Table 1.1 summarizes some of the most important interactions that occur in gas discharges [8].

Electrical properties of plasma are mainly determined by inelastic collisions responsible for creating free electrons and ionized species. Nevertheless, elastic collisions also contribute substantially to electrical properties of discharge (see Table 1.2).

1.2.3 Free Electrons

Electrons play the most important role in inelastic collisions. They are responsible for ionization and excitation of atoms and molecules. There are two basic parameters characterizing electrons: the electron density n_e and electron temperature T_e. The electron density is directly related to the electrical current discharge (DC or RF excitation). Free electrons in

TABLE 1.1
List of Important Inelastic Interactions in Gas Discharges

1	$e + X \rightarrow X^* + e$ $e + X^* \rightarrow X^{**} + e$	Collisional excitation of an atom or molecule by an electron
2	$e + X^* \rightarrow X + e$	Deexcitation of an atom and producing a fast electron via superelastic collision of an excited atom and an electron
3	$e + X \rightarrow X^+ + e + e$ $e + X^* \rightarrow X^+ + e + e$	Electron collisional ionization
4	$X^+ + e + e \rightarrow X + e$	Collisional recombination
5	$e + YZ \rightarrow e + X^+ + Z^-$ $e + YZ \rightarrow e + Y + Z$ $e + YZ \rightarrow Y + Z^-$	Dissociations and ionizations of molecules
6	$e + X \rightarrow X^- + h\nu$	Forming a negative ion by radiative attachment
7	$X^- + h\nu \rightarrow e + X$	Photodetachment
8	$e + YZ^+ \rightarrow Y + Z^*$	Dissociative recombination
		Ionic Processes
9	$X + Y^+ \rightarrow X^+ + Y$	Charge transfer
10	$X^- + Y^+ \rightarrow XY$	Ion–ion recombination
		Collisions with Neutrals
11	$X^* + Y \rightarrow X + Y^*$ $X^* + Y \rightarrow X + Y +$ kin. en.	Excitation exchange and collisional deexcitation
12	$X^* + Z \rightarrow X + Z^+ + e$	Penning ionization

Source: From Charrington, B.E., *Gaseous Electronic and Gas Lasers*, Pergamon Press, Oxford, New York, 1979.

discharge, as light particles, are most movable. Hence, kinetic temperature T_e can be much higher than the kinetic temperature T of much heavier species (molecules, atoms, and ions), according to the solution:

$$\frac{m\bar{v}^2}{2} = 3k\frac{T_e}{2}, \tag{1.4}$$

where m is the electron mass, $\bar{v}^2$ the mean square electron velocity, and k is Boltzmann's constant.

The electron temperature in discharge can reach a range of tens of thousand kelvin, when the temperature of the rest of species (ions, neutrals, and excited atoms or molecules) is much lower; that is, at the level of 300 K and higher. The temperature distribution inside plasma discharge is described by the heat transfer differential equation as follows:

$$\nabla(\lambda(T)\nabla(T)) = -w(x,y,z), \tag{1.5}$$

TABLE 1.2
List of Important Elastic Interactions in Gas Discharges

$e + X \rightarrow (e - \text{kin. en.}) + (X + \text{kin. en.})$
$e_1 + e_2 \rightarrow (e_1 - \text{kin. en.}) + (e_2 + \text{kin. en.})$
$X^+ + Y \rightarrow (X^+ - \text{kin. en.}) + (Y + \text{kin. en.})$

Source: From Charrington, B.E., *Gaseous Electronic and Gas Lasers*, Pergamon Press, Oxford, New York, 1979.

where $\lambda(T)$ is the thermal conductivity of the gas (gas mixture) and $w(x,y,z)$ is the power distribution per unit volume.

The movement of a free electron in a gas discharge is determined by the local electric $\overline{E}$ and magnetic $\overline{B}$ fields and its collisions with ions and neutrals. It can be described by Langevin equation:

$$\frac{\mathrm{d}}{\mathrm{d}t} m\overline{v} = -e\left[\overline{E} + \overline{v} \times \overline{B}\right] - m\overline{v}\nu_{\mathrm{c}}, \tag{1.6}$$

where e is the electron charge, v the electron velocity, and ν_{c} is the collision frequency for momentum transfer.

The electric field $\overline{E}$ plays a dominating role in creating plasma. Ignoring the magnetic field $\overline{B}$ in Equation (1.6), we have

$$m\frac{\mathrm{d}\overline{v}}{\mathrm{d}t} = -e\overline{E} - m\overline{v}\nu_{\mathrm{c}}. \tag{1.7}$$

It is convenient to consider DC discharge, where drift velocity $\overline{v} \approx \text{const}$. Hence,

$$\overline{v} = \frac{e\overline{E}}{m\nu_{\mathrm{c}}}. \tag{1.8}$$

Introducing a mean free time between collisions, $\tau = 1/\nu_{\mathrm{c}}$, the main parameter of discharge, mobility μ_{e}, can be defined as

$$\mu_{\mathrm{e}} = -\frac{v}{E} = \frac{e}{m\nu_{\mathrm{c}}} = \frac{e\tau}{m}. \tag{1.9}$$

The vector of a current density in discharge is given by

$$\overline{J} = n_{\mathrm{e}} e\overline{v}. \tag{1.10}$$

Taking into account Equation 1.9 and Equation 1.10, the conductivity σ can be introduced as

$$\sigma = \frac{J}{E} = \frac{n_{\mathrm{e}} e^2}{m\nu_{\mathrm{c}}}. \tag{1.11}$$

Power density lost in discharge, often called specific power, is given by

$$\rho_{\mathrm{e}} = \overline{E}\,\overline{J} = \frac{m_{\mathrm{e}} e^2}{m\nu_{\mathrm{c}}} E^2 \tag{1.12}$$

and it is the electrical power consumed by heating.

1.2.4 Electron Events in Discharge

The energy of electron in an electric field of a discharge changes in time and space, and it determines its behavior in plasma. The main source of the electron energy in an electric field, the electron gains energy from the field. However, in the meantime, it loses usually a small part of its kinetic energy in the process of an elastic collision. Much higher losses of the kinetic

energy of electrons can occur because of inelastic collision with atoms or molecules. In that process internal quantum energy of atom molecule increases. The slower electron is again accelerated in the electric field. Following the qualitative model presented by Verdeyen [2], the mean kinetic energy w_e of electron gas with n_e density changes with time: increasing (because of the field) and decreasing (because of both kinds of collisions):

$$\begin{aligned}\frac{dw_e}{dt} &= \text{electrical power} - \text{gas heating} - \text{excitation} \\ &= P_{el} - \nu_c \delta n_e \left(\frac{3}{2}\in_k - \frac{3}{2}\in_A\right) - \sum_j n_e \nu_{inel} \Delta w_j,\end{aligned} \tag{1.13}$$

where

$$w_e = n_e\left(\frac{3}{2}\in_k\right),$$

$\in_k$ is the characteristic energy of the electrons (kT_e), $\in_A$ the characteristic energy of the atom (kT_A), $\delta = 2m/M$ the fraction of the excess energy lost per elastic collision, ν_{inel} the inelastic collision rate, and Δw_j is the energy lost in an inelastic collision.

The excitation term in Equation 1.13 represents the elementary excitation mechanism [8] that is described in Table 1.1

$$e(W_{kin.}) + A = A^*(\Delta W) + e(W_{kin.} - \Delta W) \tag{1.14}$$

For the established conditions of discharge, $dw_e/dt = 0$ in Equation 1.13. Additionally, neglecting effects of inelastic excitation in Equation 1.13, the equation can be rewritten as

$$\frac{3}{2}(\in_k - \in_A) = \frac{2}{\delta}\frac{1}{2}m\left(\frac{eE}{m\nu_c}\right)^2. \tag{1.15}$$

Keeping in mind that the collision frequency ν_c of electrons is

$$\nu_c = N\sigma V, \tag{1.16}$$

where σ is the collision cross section and N is the neutral gas density; for many reasons, it is convenient to describe the right-hand side of Equation 1.15 as a function of practical ratio, the electrical field/gas density (E/N) parameter:

$$\frac{3}{2}(\in_k - \in_A) = \frac{2}{\delta}\frac{1}{2}m\left(\frac{e}{m\sigma V}\right)^2\frac{E}{N}. \tag{1.17}$$

It is clear that electron energy $\in_k = kT_e$ of the electron gas is an increasing function of E/N ratio. The E/N parameter plays a basic role in many calculations and descriptions of gas discharges:

- The characteristic energy of a free electron in plasma can be measured as a function of E/N.
- Ionization balance conditions control E/N of a discharge.
- E/N controls the performance of the laser.
- Drift electron velocity strongly depends on E/N ratio.

If the reader wants to gain more knowledge to that presented here, we recommend the classic book by Brown [9] and additionally, the book by Hirsh and Oskam [10].

1.3 SPECTROSCOPY OF GASES

The quantum nature of matter is particularly easy to observe in gases. Glowing discharge is a spectacular phenomenon, where this quantum nature appears. Generally, the gas matter consists of atoms, molecules, and their ions. Qualitatively gases can be distinguished into atomic gases or molecular ones. The main difference between atoms and molecules lies in their spectroscopic nature or their internal energy storage. The energetic state of the particles (atoms and molecules) is described by Schrödinger wave equation:

$$H\Psi(\bar{r},t) = i\hbar\frac{\partial}{\partial t}\Psi(\bar{r},t), \tag{1.18}$$

where $\Psi(\bar{r},t)$ is the wave function of the particle (according to Max Born, $\Psi(\bar{r},t) \cdot \Psi^*(\bar{r},t)$ provides the probability of observing the particle at the position $\bar{r}$, at time t),

$$H = \frac{\hbar^2}{2m}\nabla^2 + V(\bar{r}) \tag{1.19}$$

is the Hamiltonian operator and $V(\bar{r})$ is the potential energy operator of the particle of mass m.

The solution of a wave function is expected to be oscillating with angular frequency ω,

$$\Psi(\bar{r},t) = \Psi(r)e^{-i\omega t}, \tag{1.20}$$

and the time-independent Schrödinger equation takes the singular form:

$$H\Psi(\bar{r},t) = \hbar\omega\Psi(\bar{r}) = E\Psi(\bar{r}), \tag{1.21}$$

where E is the so-called eigenvalue (quantized energy) of wave function $\Psi(\bar{r},t)$.

1.3.1 Quantized States of Atoms

Let us consider the Schrödinger equation that describes the Bohr atom (single electron in the field of charge e). The potential energy $V(\bar{r})$ is the electrostatic potential in a Coulomb field:

$$V(\bar{r}) = -\frac{e^2}{4\pi\varepsilon_0 r}. \tag{1.22}$$

The solution gives the quantized energy (eigenvalues) of a hydrogen-like atom:

$$E_n = -\frac{1}{(4\pi\varepsilon_0)^2}\frac{e^4 m_e}{2\hbar^2}\left[\frac{1}{n^2}\right] = -\frac{13.6\ (\text{eV})}{n^2}, \tag{1.23}$$

where n is an integer. The solution for the wave function for spherical coordinates is

$$\Psi(r,\Theta,\phi) = \Psi_{n,l,m}(r,\Theta,\phi) = \Psi(n,l,m) \tag{1.24}$$

and depends on three n, l, m numbers, where: n is the principle quantum number ($n = 1, 2, \ldots, \infty$), l the azimuthal quantum number ($l = 0, 1, 2, \ldots, n-1$), and m is the magnetic quantum number ($m = 0, \pm 1, \ldots, \pm l$).

Adding two possible spin states of electrons, the number of states possessing E_n energy is

$$2 \times \sum_{l=0}^{n=l} (2l + 1) = 2n^2.$$

We call it $2n^2$-fold degenerated. The energy levels n with azimuthal levels l for the hydrogen atom are illustrated in Figure 1.2a. Figure 1.2b shows the energy levels of an nitrogen atom (heavier than a hydrogen one), for which the hydrogen-like rules are not fulfilled. Such a clear quantum model of energy levels can be described only for hydrogen (and possible for helium). The atoms with Z protons and Z electrons are much more complicated in finding the analytic solution for their quantum energy levels. There are possible radiative transitions (emissions and absorptions) between some levels. We call them optically allowed transitions between levels. The electron of the atom jumps from upper level E_2 to the lower level E_1 and emits photons with energy described by Bohr formula:

$$h\nu = E_2 - E_1. \tag{1.25}$$

The selection rule

$$\Delta l = \pm 1 \tag{1.26}$$

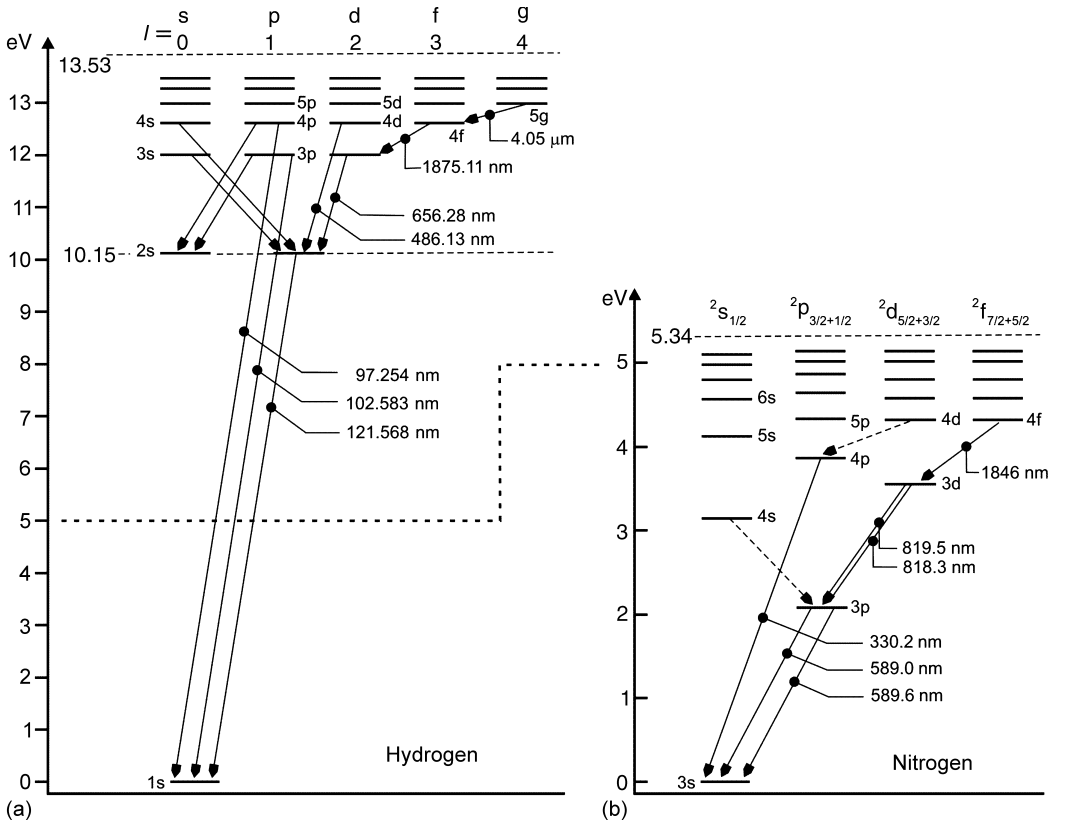

FIGURE 1.2 An energy-level diagram for hydrogen and nitrogen.

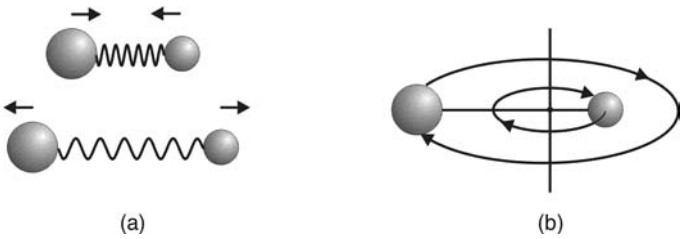

FIGURE 1.3 Simple demonstration of vibrational (a) and rotational (b) movements of a two-atom molecule.

says that only these transitions that differ in azimuthal quantum number l by unit are allowed. As can be seen from Figure 1.2, the typical transitions have energies in the range 1/10 eV and their spectra spread from near IR via visible to UV range.

1.3.2 Quantized States of Molecules

A molecule, which is a complex quantum structure of two or more atoms, is characterized by additional forms of internal energies: vibrational and rotational. A diatomic molecule (H_2, N_2, O_2, and CO), apart from its electronic states, has additional states associated with its vibrations and rotations (Figure 1.3), which are also quantized [11].

1.3.2.1 Vibrational States of Diatomic Molecules

Let us start with the phenomenon of vibrations. A two-atom molecule can be treated as the so-called harmonic oscillator. When the Schrödinger equation is applied to such a two-atom vibrating system with the parabolic potential function $V(r)$ of the oscillator:

$$V(r) = \frac{1}{2} k m_r^2, \tag{1.27}$$

where k is the restoring force constant and $m_r = m_1 m_2/(m_1 + m_2)$ is the reduced mass of nuclei, the solution for eigenvalues of vibrational energy also gives quantized values:

$$E_\nu = h\nu_{\text{osc}}\left(\nu + \frac{1}{2}\right), \tag{1.28}$$

where ν is the so-called vibrational quantum number and

$$\nu_{\text{osc}} = \frac{1}{2\pi}\sqrt{\frac{k}{m_r}} \tag{1.29}$$

is the frequency of harmonic oscillation.

The harmonic oscillations are illustrated in Figure 1.4a, where the parabolic shape of potential function $V(r)$ forms the envelope of equally separated oscillating levels. The quantum selection rule for the vibration transitions is $\Delta v = \pm 1$.

However, the parabolic shape of the oscillation potential operates well only for low quantum v numbers. When the internal vibrational energy increases, the amplitude of vibrations increases and the shape of the potential changes into anharmonic (the so-called Born-Oppenheimer approximation). This is demonstrated in Figure 1.4b.

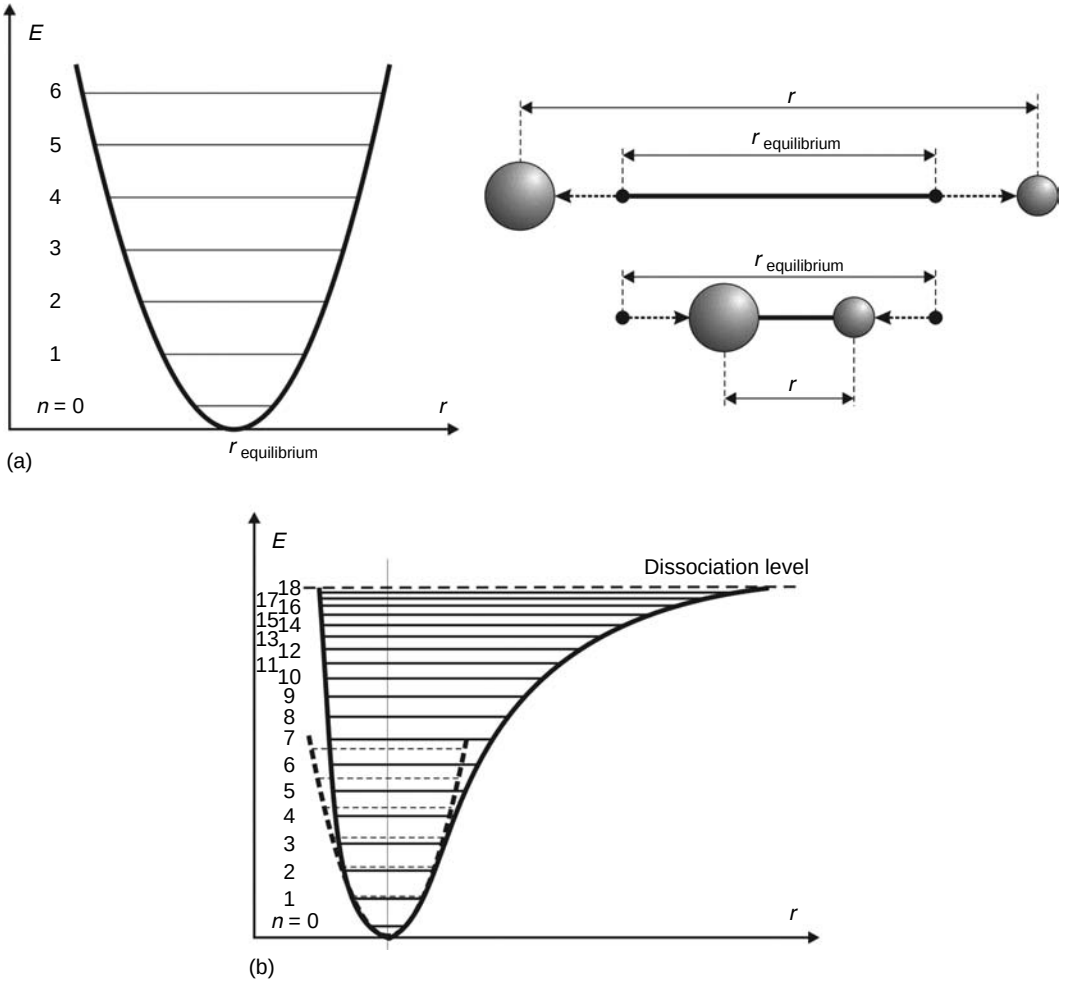

FIGURE 1.4 The illustration of harmonic (a) and anharmonic (b) vibrational levels.

The allowed vibrational energies for the two-atom anharmonic oscillator are modified and are given:

$$E_v = h\nu_{\text{osc}}\left(v + \frac{1}{2}\right) - h\nu_{\text{osc}}X_{\text{e}}\left(v + \frac{1}{2}\right)^2, \tag{1.30}$$

where X_{e} is the anharmonity parameter.

The energy distance between neighboring levels, ΔE, is no longer constant

$$\Delta E = E_{v+1} - E_v = h\nu_{\text{osc}}[1 - 2X_{\text{e}}(v+1)] \tag{1.31}$$

and it decreases when ν increases (Figure 1.3b).

When internal vibrational energy reaches the D_0 level, the molecule dissociates. A typical dissociation D_0 level has a value of a few electron volts for a diatomic molecule. It has to be

pointed that because of anharmonicity, quantum selection rule for vibrational levels is no longer so strong and it accepts transitions:

$$\Delta v = \pm 1,\ \pm 2, \ldots \tag{1.32}$$

Energetic differences between neighboring vibrational levels are typically equal to ten parts of electron volts and their typical spectra appear in the near- and mid-IR. However, it should be noted that for more complicated multiatom molecules, possessing permanent dipole moment (see chapter "Other Gas Lasers") the selection rule for vibrational levels can also be $\Delta v = 0$.

1.3.2.2 Rotational States of a Diatomic Molecule

A molecule can be considered as a rigid rotator as shown in Figure 1.2b, with fixed separation R_0 between atoms. The molecule rotates around its axis and the Schrödinger equation for that case has the form

$$-\frac{\hbar^2}{2m_r}\nabla^2\Psi = E_{\text{rot}}\Psi. \tag{1.33}$$

The rotation energy of a molecule is quantized and is given by

$$E_J = \frac{\hbar^2}{2m_r R^2}J(J+1) = B_{\text{e}}J(J+1), \tag{1.34}$$

where J is the rotational quantum number and can obtain any integer value and B_{e} is the rotational constant characterizing a molecule. The rotation energy increases quadratically with J. The quantum selection rule for radiative transition in a molecule is given by

$$\Delta J = \pm 1. \tag{1.35}$$

The energetic distance between two neighboring rotational levels J and $J+1$ is given by

$$\Delta E = B_{\text{e}}(J+1), \tag{1.36}$$

and the structure of rotational levels belonging to succeeding vibrational levels is illustrated in Figure 1.5.

However, the rotational constant B_{e} depends on the particular vibrational level ν of a molecule and can be replaced by the so-called effective rotational constant B_v:

$$B_\nu = B_{\text{e}} - \alpha_{\text{e}}\left(v + \frac{1}{2}\right), \tag{1.37}$$

where α_{e} is a small (compared with B_{e}) positive constant.

The total internal energy of the molecule is a sum of vibrational E_v (Equation 1.30) and rotational E_J energies (Equation 1.37):

$$E(v,J) = E_\nu + E_J = h\nu_{\text{osc}}\left(v + \frac{1}{2}\right) - h\nu_{\text{osc}}X_{\text{e}}\left(v + \frac{1}{2}\right)^2 + B_v J(J+1). \tag{1.38}$$

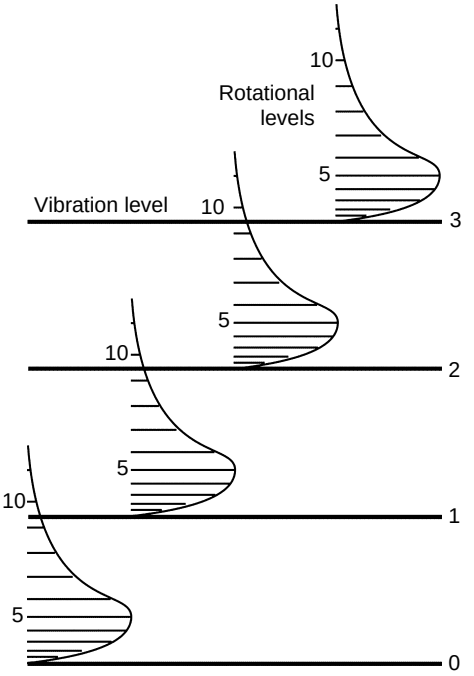

FIGURE 1.5 Vibrational and rotational levels, weighed by Maxwell distribution of population for thermodynamic equilibrium.

The schematic energy-level diagram for a vibrating–rotating model is shown in Figure 1.5.

The quantum selection rule for molecules with zero electron momentum about the internuclear axis is described by Equation 1.35 as $\Delta J = \pm 1$. However, for molecules possessing nonzero electron angular momentum, the quantum selection rule is given by

$$\Delta J = 0, \pm 1. \tag{1.39}$$

Combining the selection rules for vibrational and rotational levels ($\Delta v = \pm 1,\ \pm 2, \ldots$ and $\Delta J = \pm 1$), the allowed radiative transitions can be set into two branches:

1. R-branch formed by transitions $J \rightarrow (J-1)$
2. P-branch formed by transitions $J \rightarrow (J+1)$

This idea of forming the R- and P-branches is illustrated in Figure 1.6. For the rules $\Delta v = \pm 1$ and $\Delta J = 0$, transitions $J \rightarrow J$ form Q-line and they overlap into one strong line.

Each free electron has three degrees of freedom. According to statistical mechanics, each degree of freedom is represented by kT energy, where k is a Boltzmann constant and T is the absolute temperature. Hence, translation energy of the atom is $3/2kT$. A polyatomic N-atom molecule has $3N$ degrees of freedom. Three of them are occupied by the total translation motion of the molecule and two (for a linear molecule) or three (for a nonlinear molecule) are represented by free rotations of a molecule. Hence, we have $(3N - 6)$ possible vibrational modes in nonlinear molecules and $(3N - 5)$ modes in linear molecules.

Similar to an atom, a molecule also has its electronic levels. Therefore, three kinds of transitions can be distinguished in a molecule:

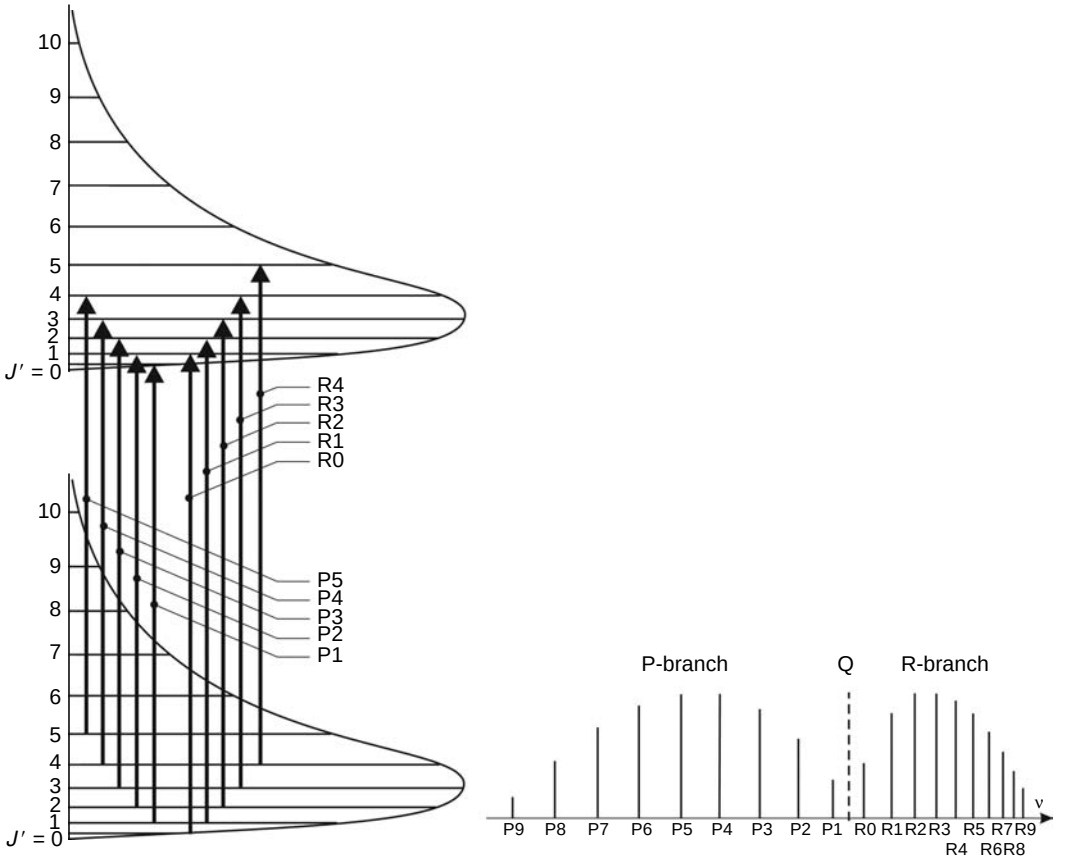

FIGURE 1.6 Model of rotational transitions: forming P-branch, Q-line, and R-branch.

1. Rotational transitions (when the vibrational quantum number and the electronic state do not change). Their typical spectra range in the FIR and submillimeter regions.
2. Vibrational–rotational transitions (when the electronic state does not change). The typical spectra range from near IR to FIR.
3. Electronic transitions (when all quantum numbers change). The typical spectral range: visible and near IR.

To spread further knowledge to the reader, we would like to direct the reader to good books about quantum mechanics [11–14].

1.4 SPECTRAL LINES

The quantum nature of atoms or molecules causes one of the mechanisms of changing their internal energy to be radiative transition—emission or absorption. The allowed radiative transition is possible between two levels E_2 and E_1 (Figure 1.7), when quantum selective rules accept it. According to the quantum theory, radiative transition between two levels can occur by the emission of a photon with energy $h\nu$:

$$E_2 - E_1 = h\nu \tag{1.40}$$

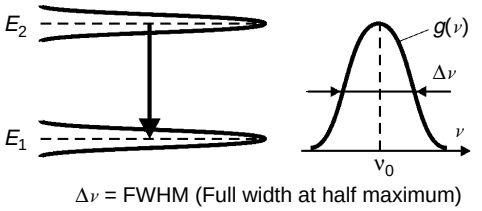

FIGURE 1.7 Line-broadening demonstration.

or by absorption of the photon with the same energy, demonstrated by a spectral line of radiation (emission or absorption) at the frequency υ. Although the levels are quantized, the term "line" does not mean the mathematical line (which for a reader familiar with mathematics means δ-Dirac function).

Because of different physical mechanisms the levels are broadened.

1.4.1 Natural Broadening

The finite lifetime of the level caused by spontaneous emission effect gives the so-called natural broadening. When we have an atom with two distinguished levels as is shown in Figure 1.7 and the atom is in state 2, it can radiate the photon spontaneously to state 1. This spontaneous transition 2−1 occurs statistically in τ_{21} time, which is called lifetime of 2−1 transition. For an assembly of atoms excited to level 2, the lifetime τ_{21} can be interpreted as the decay rate that decreases the population of level 2 and simultaneously increases the population of level 1. The spontaneous emission effect leads to the natural spectral broadening of a single radiative transition or single separated two-level atom.

The spectrum of the natural broadened line is given by the so-called Lorentzian shape and is described by the formula:

$$G_{\mathrm{L}}(\omega) = \frac{\left(\frac{1}{\tau_{21}}\right)^2}{(\omega - \omega_0)^2 + \left(\frac{1}{\tau_{21}}\right)^2}, \tag{1.41}$$

where ω_0 is the central angular frequency of the line.

From this equation one can see that the full width at half maximum $\Delta\omega_n$ can be easily calculated as

$$\Delta\omega_n = \frac{2}{\tau_{21}} \quad \text{or} \quad \Delta\nu_n = \frac{1}{\pi\tau_{21}}. \tag{1.42}$$

Typical lifetimes of radiative transitions are at 10^{-8}/sec. Hence, the natural lifewidth of typical radiative transitions are tens of MHz. However, there are lines in gases that have much longer lifetimes. They can be as long as 1 sec, 1 h, 1 day, and some lines can be particularly narrow.

1.4.2 Collisional (Pressure) Broadening

Different kinds of collisions of atoms or molecules in the gas environment are the source of extra perturbations leading to the broadening of transition lines. The collisions reduce the

lifetime of the excited state. They can also perturb the energy separation between two levels of the emitting or absorbing atom or molecule. The measure of collisional broadening is the collisional lifetime τ_c given by the formula

$$\frac{1}{\tau_c} = N\sigma v_{av} = Nf_c, \tag{1.43}$$

where N is the gas density, $f_c = \sigma v_{av}$ is the effective frequency of collisions, σ is the collision cross section of the atom or molecule, and v_{av} is the average velocity of the atom or molecule.

The nature of collisional broadening is similar to natural broadening and it has the same statistical character and the same Lorentzian shape:

$$G_L(\omega) = \frac{\left(\frac{1}{\tau}\right)^2}{(\omega - \omega_0)^2 + \left(\frac{1}{\tau}\right)^2}, \tag{1.44}$$

where

$$\frac{1}{\tau} = \frac{1}{\tau_{21}} + \frac{1}{\tau_c},$$

and $\tau \to \tau_{21}$ when the pressure of gas achieves zero.

In practice, collisional (pressure) broadening depends on atoms or molecules taking part in the collisions. Hence different lines are described by pressure broadening coefficients expressing frequency broadening by unit pressure (MHz/Torr). For example, typical laser transitions are: He–Ne (line 632.8 nm)—70MHz/Torr, CO_2 (CO_2, H_2, He mixture, 10.6 μm) ~5MHz/Torr, and they depend on the partial ratios of used species.

It is interesting to notice that at the pressure 1 bar of the mixture CO_2 laser the pressure-broadened spectral line has 40 GHz linewidth. The lines of the vibrational–rotational branch of a CO_2 molecule are separated at about 50 GHz, and at atmospheric pressure the lines overlap into one spectral branch. Depending on the partners under collisions, the broadenings can be distinguished into:

1. Holtzmark broadening (collisions between the same species)
2. van der Waals broadening (collisions between unlike species)

1.4.3 Doppler Broadening

When the radiating atom or molecule is in random movement among many species and its velocity component is v_z along the axis (chosen by an observer, Figure 1.8), as the result of Doppler effect, the frequency of a photon emitted toward the observer will be Doppler shifted:

$$v = v_0\left(1 + \frac{v_z}{c}\right), \tag{1.45}$$

where v_z can be positive or negative depending on the direction of the atom movement and c is the light velocity.

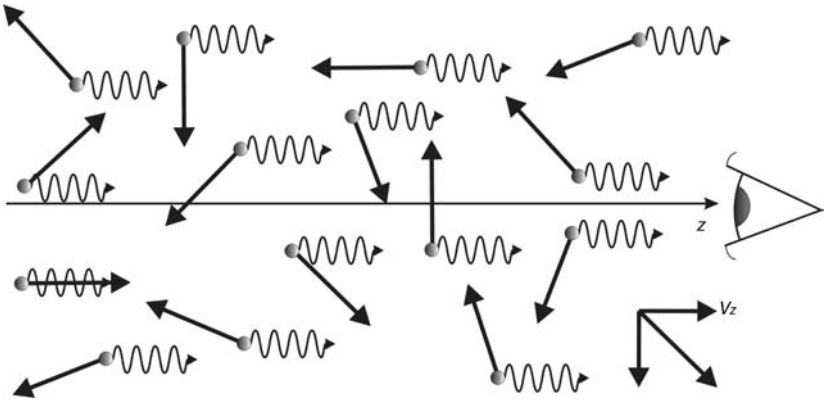

FIGURE 1.8 Radiation from random movement of species. Velocity component v_z is indicated.

The gas in the thermodynamic equilibrium is governed by Maxwellian velocity distribution $f(v_z)$ with the Gaussian shape:

$$f(v_z) = \frac{1}{\sqrt{\pi} v_p} \exp\left(-\frac{v_z}{v_p}\right)^2 = G_0 \exp\left(-\frac{v_z}{v_p}\right)^2, \tag{1.46}$$

where $v_p = (2kT/m)^{1/2}$ is the most probable velocity and m is the atomic mass of the emitter.

The Maxwellian distribution $f(v_z)$ in the velocity domain can be replaced by the frequency domain by simple transformation of Equation 1.45:

$$v_z = \frac{\nu - \nu_0}{\nu_0} c \tag{1.47}$$

and then we obtain the line shape $G_D(\nu)$ determined by a Doppler effect:

$$G_D(\nu) = G_0 \exp\left[-\frac{m}{2kT}\frac{c^2}{\nu_0}(\nu_0 - \nu)^2\right], \tag{1.48}$$

which still preserves the Gaussian shape. The elementary calculation allows establishing the full width at half maximum $\Delta\nu_D$ of a Doppler-broadened line:

$$\Delta\nu_D = \nu_0 \sqrt{8 \ln 2 \frac{kT}{mc^2}}. \tag{1.49}$$

It is clear from Equation 1.49 that Doppler broadening depends linearly on a transition frequency. It means that this type of broadening dominates strongly in UV and visible regions, less in near IR and mid-IR, and it is almost negligible in the FIR and submillimeter regions. The second factor increasing Doppler linewidth is the temperature (square root). A few examples of Doppler linewidths $\Delta\nu_D$ and pressure-broadened lines $\Delta\nu_{coll}$ for representative gas lasers are presented in Table 1.3.

TABLE 1.3
Doppler Linewidths $\Delta\nu_D$ and Pressure-Broadened Lines $\Delta\nu_{Coll}$ for Some Gas Lasers

Laser	λ	$\Delta\nu_D$	$\Delta\nu_{coll}$
Argon	514.5 nm (visible)	~3.5 GHz	~20 MHz
He–Ne	632.8 mm (visible)	~1.5 GHz	~20 MHz
He–Ne	3.39 μm (infrared)	~300 MHz	~50 MHz
CO_2 (10 Torr)	10.6 μm (infrared)	~60 MHz	~60 MHz
CO_2 (1 bar)	10.6 μm (infrared)	~60 MHz	~40 GHz

Depending on circumstances (pressure, temperature, gas ratio, and wavelengths), different kinds of broadening can determine the spectral linewidths. The collision and Doppler effects determine the shape of the spectral line, which is generally given by the convolution integral:

$$G(\nu) = \int_{-\infty}^{+\infty} G_D(\nu')G_L(\nu - \nu')\,d\nu', \tag{1.50}$$

where $G_L(\nu,\nu')$ is the Lorentzian shape of emission at frequency ν for the emitting atom with a central frequency ν' (see Figure 1.9), and $G_D(\nu')$ represents the Gaussian shape caused by Doppler effect. This is the situation when the Doppler broadening overshadows collision profiles, and it forms the Gaussian envelope of Doppler-shifted Lorentzian lines.

1.5 GAIN CONDITIONS

Following the famous analysis by Einstein, dealing with blackbody radiation presented in many books on laser [1–4], three elementary quantum mechanisms of radiation in a simple two-level model of an atom can be distinguished: absorption, spontaneous emission, and stimulated emission (Figure 1.10).

Introduced by Einstein, a coefficient of stimulated emission is very sufficient to explain the mechanism of the so-called black body radiation, but contribution of stimulated photons to all radiative effects like absorption and spontaneous emission in an excited medium is very poor. It explains why a laser was not invented immediately after Einstein's analysis was published. The picture of radiative processes is completely different when the excited medium is placed into an optical resonator. Very quickly (after a few hundred transitions along the

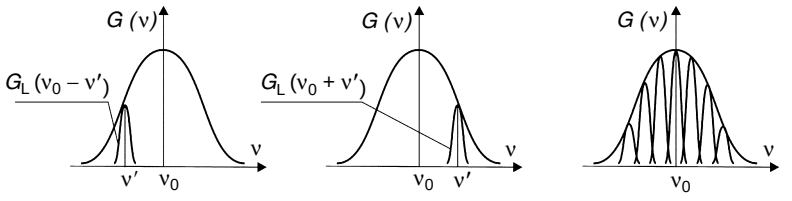

FIGURE 1.9 Creation of a Doppler-broadened line.

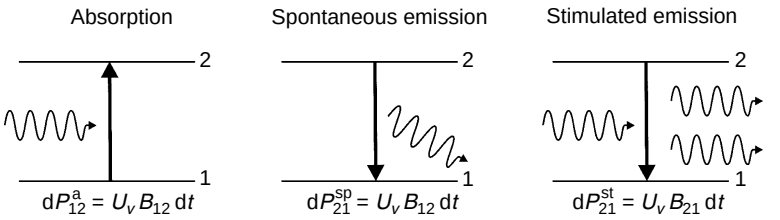

FIGURE 1.10 Three elementary quantum mechanisms of radiation: dP_{12}^{a}, dP_{21}^{sp}, dP_{21}^{st}—probability of absorption, spontaneous emission, and stimulated emission, respectively, B_{12}, B_{21}—Einstein coefficients of absorption and stimulated emission ($B_{12} = B_{21} = B$), A_{21}—Einstein coefficient of spontaneous emission, and U_ν—energy density of electromagnetic radiation.

resonator), as it was proved in a famous work by Fox and Li [15], stimulated photons become predominant in the laser cavity.

To find the amplification conditions, let us consider a reservoir with two-level atoms of density $n_1 + n_2 = n$, where n_1, n_2 are atom densities in states 1 and 2, respectively. The transparent reservoir is illuminated by the monochromatic wave of intensity $I(\nu)$ as presented in Figure 1.11.

When the frequency ν of external wave coincides with the broadened spectral line $G(\nu)$ of 2→1 transition, it causes the absorption of photons and emission as well. The number of emitting n_{em} and absorbing n_{ab} atoms is given by the following equations:

$$\frac{dn_{em}}{dt} = n_2[BI(\nu) + A], \tag{1.51}$$

$$\frac{dn_{ab}}{dt} = n_1 BI(\nu). \tag{1.52}$$

The difference of Equation 1.51 and Equation 1.52 in emitting and absorbing atoms is the measure of gain properties of the gas:

$$\left(\frac{dn_{em}}{dt} - \frac{dn_{ab}}{dt}\right) = n_2[BI(\nu) + A] - n_1 BI(\nu). \tag{1.53}$$

Because of the isotropic nature of spontaneous emission, it can be totally ignored in our considerations. Multiplying both sides of Equation 1.53 by dz and multiplying by photon energy $h\nu$ weighted by the shape line $G(\nu)$, we get the increase in $dI(\nu)$ over dz distance:

$$\frac{d(n_{em} - n_{ab})}{dt} h\nu\, dz = dI = I(\nu)(n_2 - n_1)h\nu G\, dz. \tag{1.54}$$

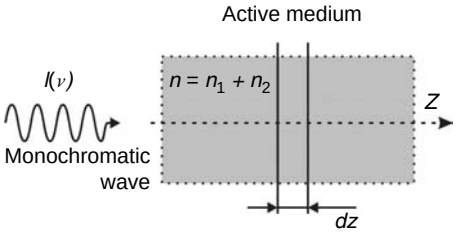

FIGURE 1.11 The plane wave penetrating the assembly of two-level atoms.

Transforming Equation 1.54 leads to the definition of differential equation for intensity:

$$\frac{\mathrm{d}I}{I} = g\,\mathrm{d}z, \tag{1.55}$$

where

$$g(\nu) = (n_2 - n_1)BhvG(\nu) \tag{1.56}$$

is the so-called differential gain of the medium and $(n_2 - n_1)$ is the difference in population of both levels. The solution of differential Equation 1.55 is

$$I(\nu) = I_0(\nu)e^{g(\nu)dz}. \tag{1.57}$$

It is clear that the necessary condition to obtain the amplification is

$$n_2 - n_1 > 0, \tag{1.58}$$

which is called population inversion. The gain $g(\nu)$ is not constant along the z axis. Because of saturation effect, the gain decreases when the intensity of the incident wave increases. This phenomenon is illustrated in Figure 1.12, which presents nonlinear behavior of gain with the intensity for two characteristic gain lines: collisional and Doppler broadened. This behavior distinguished two characters of lines: homogenously broadened line (all atoms interact with the monochromatic wave) and inhomogenously broadened line (only a part of the Doppler-shifted atoms interacts with the monochromatic wave).

The gain is the function of intensity and it depends on the character of the line. For homogenously broadened lines

$$g(I) = \frac{g_0}{1 + \frac{I}{I_s}}, \tag{1.59}$$

and for inhomogenously broadened lines

$$g(I) = \frac{g_0}{\sqrt{1 + \frac{I}{I_s}}} \tag{1.60}$$

The gas medium is characterized by two basic parameters: g_0—unsaturated differential gain (or small signal gain); I_s—saturation intensity. Saturation intensity is defined as the intensity at which the gain drops twice (homogenous case) or the gain drops $\sqrt{2}$ times (inhomogenous case). Table 1.4 gives some examples for saturation intensity I_s and unsaturated gain values.

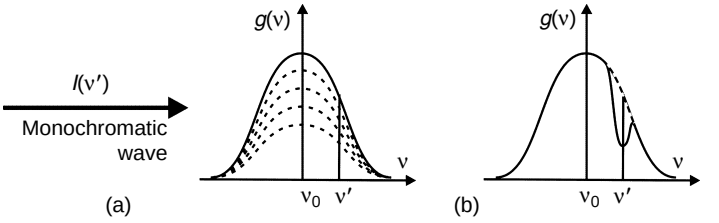

FIGURE 1.12 Saturation effect in (a) homogenously broadened line and (b) inhomogenously broadened line.

TABLE 1.4
Examples of Saturation Intensities and Small Signal Gains

Laser	λ	I_s	g_0
He–Ne	632.8 nm	~5 W/cm^2	0.02/m
He–Ne	3.39 μm (1 Torr)	~3 mW/cm^2	0.6/m
CO_2	10.6 μm (20 Torr)	~20 W/cm^2	~0.3/m
CO_2	10.6 μm (100 Torr)	~10 kW/cm^2	~0.6/m

1.6 LASER ACTION—A SIMPLE MODEL

A laser, as was said in the introduction, is an optical oscillator. Using an electronic analogy, the electronic oscillator consists of an amplifier with a specially formed feedback loop to enable such a system to obtain stable and periodic self-oscillations (Figure 1.13a).

To obtain self-oscillations, a part of the output signal has to be coupled back into the input of the amplifier. Two conditions have to be fulfilled; the amplitude of the feedback signal has to have enough value and the phase of this signal should have approximately the same phase as the input signal. These two conditions are called amplitude/phase conditions for self-oscillations.

The feedback analogy is even clearer in the optical case presented in Figure 1.13b, where the optical amplifier was set in the optical ring resonator forming the optical feedback running wave (signal). When amplitude/phase conditions are fulfilled, the running wave starts traveling inside the ring resonator. In practice we have two running waves, clockwise and anticlockwise, which can appear in the resonator.

The output beam leaves the resonator as a useful laser beam when the output mirror is partly transparent. The qualitative difference between electronic and optical oscillators relies on D/λ ratio of average physical dimension D of an oscillator to the oscillating electromagnetic wavelength λ. The D/λ ratio is much less than unity for typical electronic oscillators and it is much higher than unity for optical devices. Somewhere between these devices are located microwave oscillators, for which D/λ is comparable with unity.

Considering the ring system illustrated in Figure 1.13b, one can imagine the evolution of the ring resonator into the so-called linear resonator by parallel translation of two mirrors toward two left, forming a "corner cube" configuration into plane–plane or Fabry–Perot (F–P) resonator. The linear resonator is the most frequently used configuration and the laser with F–P resonator is the most representative. The running wave in a ring resonator becomes a standing wave (two waves traveling in opposite directions) in a linear F–P resonator (Figure 1.14).

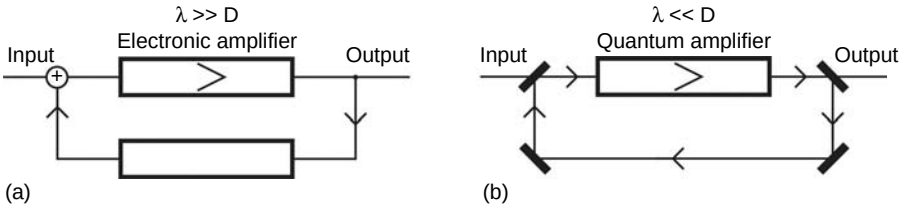

FIGURE 1.13 The block diagram of an electronic oscillator (a) and its optical analogy (b).

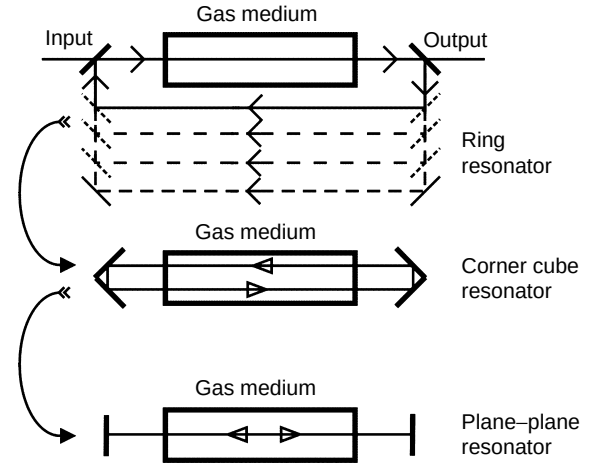

FIGURE 1.14 The evolution of a ring resonator into a linear resonator.

1.6.1 Empty Cavity Model

Let us consider, as it is done in many books dealing with lasers [1–5], the empty passive F–P resonator with its basic parameters: L—geometrical length, and R_1, R_2—reflectivities of F–P mirrors. The refractive index of gas media can be assumed as unity. The main parameter describing its selective properties is transmission $T(\nu)$ as a function of frequency (Figure 1.15a).

The transmission $T(\nu)$ of such a resonator is given by the formula

$$T(\nu) = \frac{I_{\mathrm{tr}}(\nu)}{I_{\mathrm{in}}(\nu)} = \frac{(1-R_1)(1-R_2)}{\left(1-\sqrt{R_1R_2}\right)^2 + 4R_1R_2\sin^2\left(\dfrac{2\pi\nu L}{c}\right)}. \tag{1.61}$$

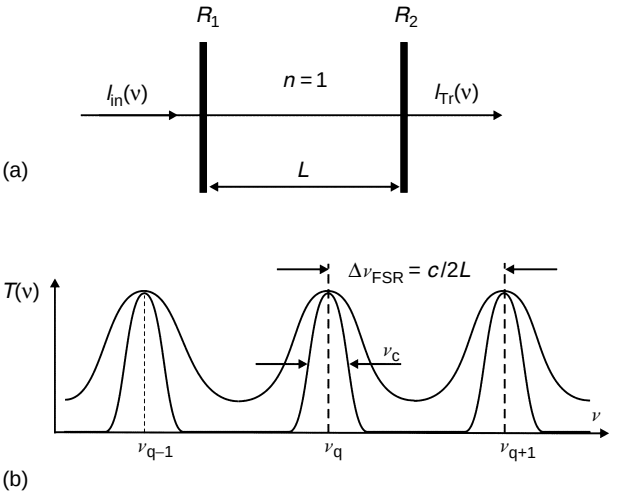

FIGURE 1.15 The Fabry–Perot resonator configuration (a) and its transmission characteristics (b).

The plot of the transmission coefficient $T(\nu)$ as a function of frequency is illustrated in Figure 1.15b as an array of resonances at resonant frequencies ν_q, where

$$q = \frac{L}{\frac{\lambda_q}{2}} \tag{1.62}$$

is the number of half wavelengths forming a standing wave between L-separated mirrors.

The resonances are separated by the so-called "free spectral range" $\Delta\nu_{FSR}$

$$\Delta\nu_{FSR} = \frac{c}{2L} \tag{1.63}$$

and the spectral width $\Delta\nu_c$ (empty cavity) of one resonance is

$$\Delta\nu_c = \frac{c}{2L}\left[\frac{1-(R_1R_2)^{\frac{1}{2}}}{\pi(R_1R_2)^{\frac{1}{4}}}\right] = \Delta\nu_{FSR}\left[\frac{1-(R_1R_2)^{\frac{1}{2}}}{\pi(R_1R_2)^{\frac{1}{4}}}\right]. \tag{1.64}$$

There are two important parameters of an empty cavity describing its selective properties: Q factor

$$Q = \frac{\nu_0}{\Delta\nu_c} \tag{1.65}$$

and finesse F

$$F = \frac{\Delta\nu_{FSR}}{\Delta\nu_c}. \tag{1.66}$$

1.6.2 Laser Action

Let us consider a case when the resonator is filled with a gaining medium that enables the amplification of the optical wave. The wave, which is weakened mainly by the output coupling and by internal losses inside the resonator, should be compensated to form a steady-state standing wave inside the resonator. The gain $g(I)$ according to Equation 1.59 and Equation 1.60 is a nonlinear function of the wave intensity. The net gain G per full round trip in the resonator is

$$G = e^{2L\overline{g(I)}}, \tag{1.67}$$

where $\overline{g(I)}$ is the differential average gain over full round trip. If only a medium is able to compensate losses, there is a chance of obtaining self-sustained oscillations. The balance between gain and losses requires the fulfillment of a simple condition:

$$GR_1R_2 = 1. \tag{1.68}$$

The main consequence of this assumption lies in the analysis of Equation 1.64. Formally replacing (R_1, R_2) product by (G, R_1, R_2) gives the linewidth $\Delta\nu_L$ of the resonator filled with the gain medium, and taking into account Equation 1.68 we obtain

$$\Delta\nu_L = 0. \tag{1.69}$$

TABLE 1.5
Some Representative Calculations of Intrinsic Linewidths of Gas Lasers

	He–Ne (λ = 632.8 nm)	CO_2 (λ = 10.6 μm)
P_{out}	2 mW	30 W
$\Delta\nu_c$	0.5 MHz	5 MHz
$\Delta\nu_i$	$2.5 \cdot 10^{-4}$ Hz	$1 \cdot 10^{-6}$Hz

What does it mean physically? It means that the linewidth of the laser radiation theoretically equals zero. This happens for an absolutely coherent signal with δ-Dirac spectrum. In practice, however, it is not possible to obtain such a narrow linewidth (*natura non facit saltum!* [Nature makes no leap]). It has some finite linewidth. Nevertheless, the laser action of the lasing signal means dramatic narrowing (many orders) of the laser line $\Delta\nu_L$ compared with the linewidth $\Delta\nu_c$ of the passive resonator.

1.6.3 Schawlow–Townes Formula

This problem was first noticed by A.L. Schawlow and Ch. Townes [16], and they gave the formula for the linewidth of laser radiation $\Delta\nu_i$ (intrinsic)

$$\Delta\nu_i = \frac{2\pi(\Delta\nu_c)^2 h\nu}{P_{out}}, \tag{1.70}$$

where h is the Planck constant, ν the frequency of the laser radiation, and P_{out} is the output power of the laser radiation. A few elementary data for some representative gas lasers are presented in Table 1.5.

1.6.4 Multimode Operation of Lasers

Because of the fact that spectral linewidth of the gain lines spans in the range of tens of megahertz to a few gigahertz, it can overlap (depending on the length L of the laser resonator) many resonances of longitudinal modes. This situation is illustrated in Figure 1.16.

Each laser resonator has its own level of losses. To obtain lasing, the gain has to compensate losses. Figure 1.16 shows the case when four longitudinal modes are able to compensate a virtual level of losses. For this case, the laser operates in four longitudinal modes weighed by the Doppler shape of inhomogenously broadened line. One can imagine a single-frequency operation, when free spectral range $\Delta\nu_{FSR}$ is large enough to coincide one node with the gain profile.

1.6.5 Pulse Operation

Two kinds of laser operations can be distinguished, continuous or pulse operations. Each laser medium can operate in pulse regime. To get continuous wave (CW) operation, the medium has to fulfill a basic condition, the population inversion, $\Delta n = n_2 - n_1$, has to be kept permanently in time. However, not all media are able to keep inversion continuously (like excimers, high-pressure CO_2). Such media are prepared only for pulse operation. The CW laser can always be adapted to pulse operation by internal Q-switching or mode-locking techniques.

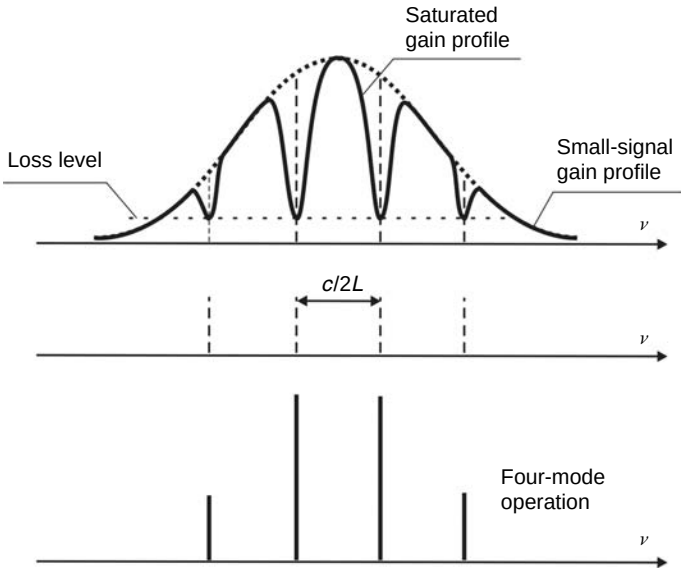

FIGURE 1.16 Multimode operation.

1.7 LASER RESONATORS

The F–P resonator with plane–plane mirrors considered in Section 1.6.1 is a good teaching example to explain a basic description of standing wave forming, optical resonances, or longitudinal modes. It has, however, a severe disadvantage—difficulties in controlling laser beam transverse distribution. The plane–plane resonator found limited applications, mainly for high-gain medium lasers like an excimer laser, TEA and waveguide CO_2 lasers, or semiconductor lasers. However, most gas lasers, particularly low-pressure lasers, do not accept a plane–plane configuration because of their high losses.

Struggles in the development of gas lasers in their early stages created the beautiful idea of Gaussian resonators based on curved mirrors. The configuration is presented in Figure 1.17. It allows to easily control laser beam transverse mode structure. In this case the laser beam is well defined as the so-called Gaussian beam. It determines basic optical parameters of the beam like a transverse mode structure, front wave radius, and divergence. This resonator allows us to get the most desirable basic TEM_{00} Gaussian mode of the highest quality ($M^2 = 1$, see Chapter 4). The same Gaussian beam can be created in different sets of the laser mirrors if they only match the wave fronts of the beam appropriately. This situation is illustrated in Figure 1.18. Although the resonator is open (no side walls), the Gaussian laser beam does not escape beyond a mirror aperture, (the so-called stable resonator).

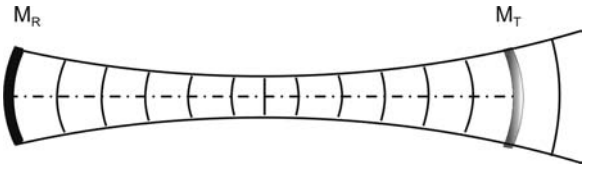

FIGURE 1.17 Basic idea of a Gaussian laser resonator: M_R—total reflecting mirror, M_T—transmitting mirror. Wave fronts are indicated.

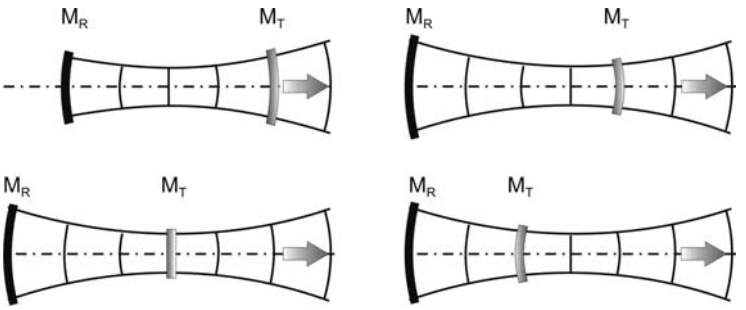

FIGURE 1.18 Examples of optical resonators blended into the same Gaussian beam.

Development of high-power laser systems with large volume gain media required efficient extraction of the power. This requirement forced new solutions. Unstable resonators fulfill the expectations. In fact, an unstable resonator is also created by curved mirrors, but here the laser beam that is opposite to the stable configuration leaves the lasing volume beyond an aperture of one mirror (see Figure 1.19.) In this case, both mirrors are fully reflected. As seen in the figure, the laser beam formed inside an unstable resonator is wide enough to fill all available gain volume.

Other concepts led to solutions based on special formation of the laser beam inside the resonator. Two techniques can be distinguished: the resonator with super-Gaussian mirrors and the resonator with diffractive mirrors (diffractive optical elements—DOE technique). Both techniques allow shaping the beam profile, for example, a "top-hat" profile of the output laser beam desired in material processing.

The reader interested in the subject can find much more information in the chapter on laser resonators. Recommended basic handbooks devoted to laser resonators are by Hodgson and Weber [17], Hall and Jackson [18], Anan'ev [19], Kossowski [20], and Siegman [1].

1.8 PUMPING TECHNIQUES

Gas lasers are usually excited by electrical current flowing through a gas medium. Three basic techniques of electrical excitation are distinguished: DC, RF, and pulse excitations. However, there are some lasers that can be pumped by mechanisms other than electrical discharge, such as gas dynamic expansion, chemical reaction, or optical pumping by another laser.

The atom or molecule in the excited state can decay to the lower states by four main mechanisms [3]:

– Collision between an electron and the excited atom or molecule (superelastic collision)
– Near-resonance collisions between excited species and the species in the ground state

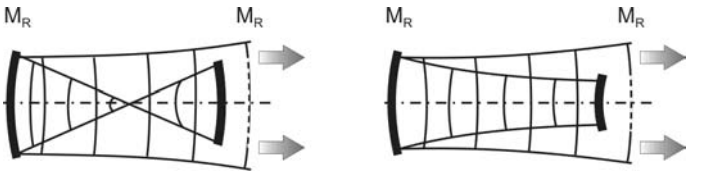

FIGURE 1.19 Possible configurations of unstable resonators.

– Collision with the wall of the reservoir
– Spontaneous emission

Distribution of energy level population is the result of excitation process. To obtain gaining properties of a medium, it is necessary to get population inversion between two energy levels with radiative transition allowed between them. The population inversion is determined by two basic conditions [3]: the excitation rate should be greater for the upper energy level 2 than for the lower energy level 1, and the decay of the upper level 2 should be slower than for lower level 1. The rate of transition 2→1 has to be less than the decay rate of level 1 to obtain CW laser operation. When this condition is not fulfilled, the laser operation is still possible, but only in pulse regime.

1.8.1 DC Discharge

DC gas discharge is usually described as the process of electron emission from the cathode as the result of collision of the cathode by ions, fast atoms, and photons from gas medium. In a tube with a cathode and anode (Figure 1.20) filled with gas under moderately high pressure (a few to couple of tens Torr), DC voltage E_s through a ballast resistor R_b is applied. Then, the typical voltage/current characteristic looks like that shown in Figure 1.21.

The voltage–current curve can be divided into five basic regions: I—Townsend discharge; II—corona discharge; III—normal discharge; IV—abnormal discharge and V—arc.

The normal discharge region is applied in continuous gas lasers. The positive column of the electrical discharge in a cylindrical tube forms the basic discharge configuration in many popular DC discharge lasers (He–Ne, CO_2, argon ion, and so on), as is shown in Figure 1.22.

DC discharge has negative dynamic resistance in the normal discharge region. Hence, to obtain stable flow of DC current in the discharge tube, the ballast resistor R_b should fulfill the simple condition

$$R_b \geq \frac{dU}{dI} \text{ at } I_{operation} = I_0. \tag{1.71}$$

The electrical field in the area of a positive column is constant. Owing to this, plasma properties along a tube are quite homogenous. It means that the total charge of positive ions n_i^+ and electron n_e per unit length of column is equal: $n_i^+ = n_e$. The drift current of the electrons can be separated into a current in the direction of the axis and a current normal to the axis [21]. Depending on the gas medium, the laser tube configuration, and the heat

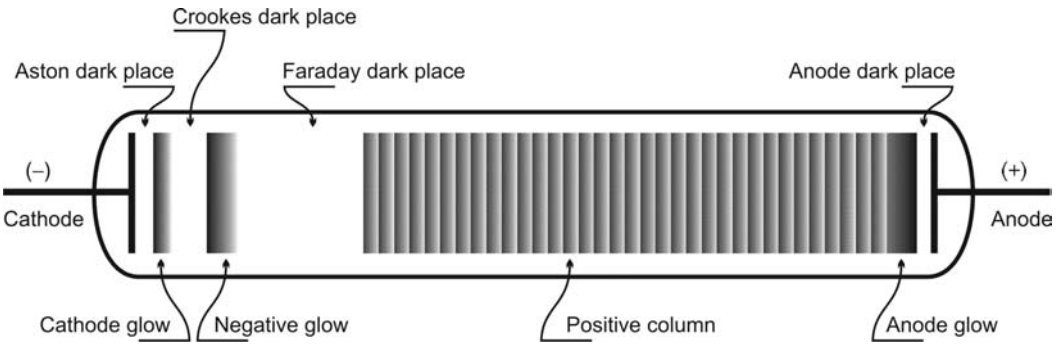

FIGURE 1.20 Schematic discharge tube showing distribution of emitted light areas.

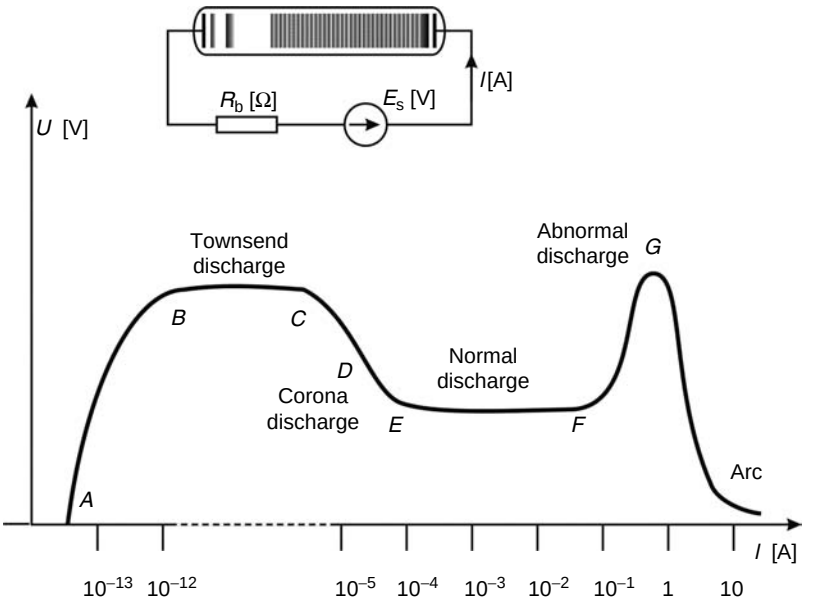

FIGURE 1.21 Schematic voltage–current curve of glow discharge.

extraction, it is necessary to add a water jacket to the tube to remove heating from the discharge (CO_2 lasers, argon-ion lasers).

The evolution of the DC discharges for different lasers established the configuration of hollow cathodes particularly useful in metal vapor lasers; they are metal vapor lasers (copper, silver, gold, and zinc) in noble gas buffers (He, Ne). Figure 1.23 shows some electrode configurations applied for these lasers.

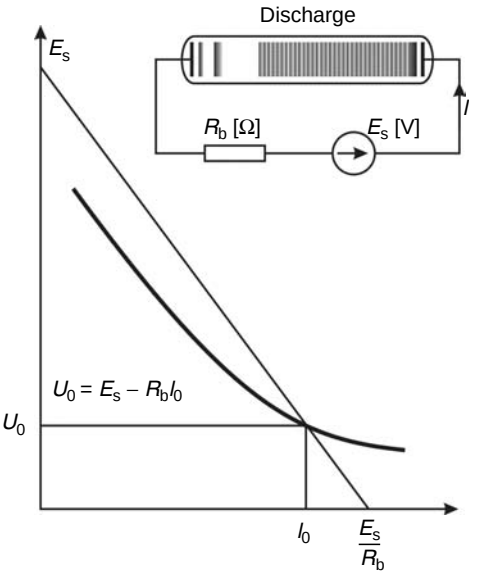

FIGURE 1.22 The general view of a DC discharge laser tube (a) and the fragment of its negative characteristics with operation condition U_0 and I_0 (b).

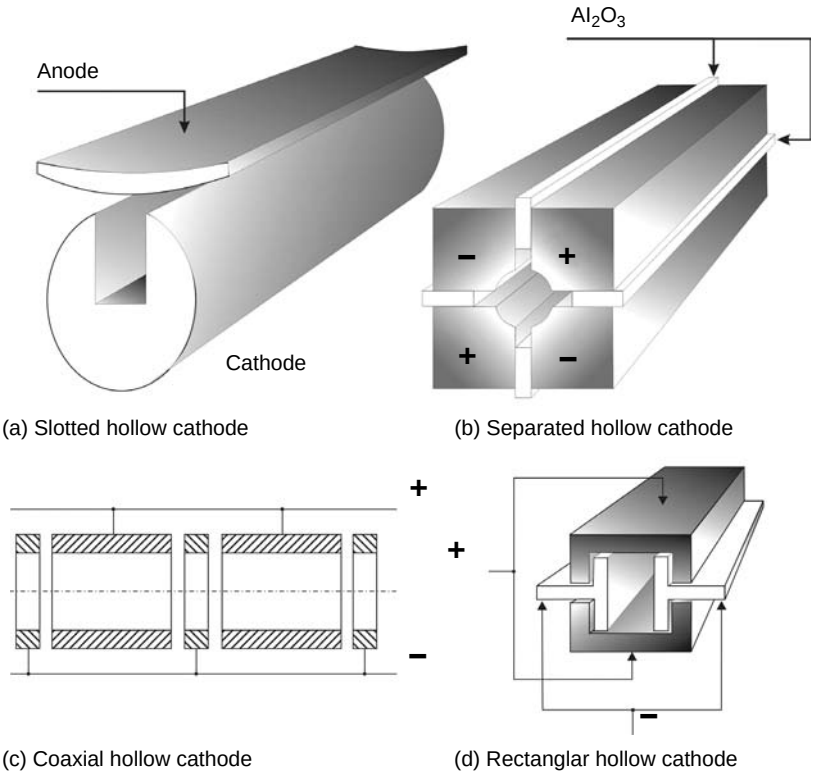

FIGURE 1.23 Some examples of hollow cathodes.

The voltage between electrodes can differ highly. For glass tubes with separated electrodes of a few tens of centimeters, the voltage applied can be as high as few kilovolts, while for hollow cathode configurations the voltage of a few hundred volts is applied. The shape of the hollow cathode system determines the resonator configuration of a laser. These configurations can be used for quasipulsed operations, when discharge is sustained by low DC current and high current pulses with controlled length and repetition. The transverse discharge can be also formed by means of multipin electrode arrays (see Figure 1.24).

The technique allows the formation of discharges in large volume areas that can be homogenized and stabilized by using an appropriately formed magnetic field.

1.8.2 Pulse Discharge Excitation

There are gas media for which it is not possible to obtain permanent population inversion. However, it is possible to reach inversion only for a short period (below 1 μsec). There are different reasons for this. Two kinds of gas lasers can be given as examples:

- High-pressure CO_2 lasers, in which high pressure destroys population inversion because of the short collisional time of the molecules.
- Excimer lasers, which are characterized by very short lifetime of so called excimers (unusual molecules, which can exist only in excited states).

The best way to obtain the population inversion for high-pressure media is high-energy pulse discharge excitation. It has developed completely different geometry of tranverse discharges.

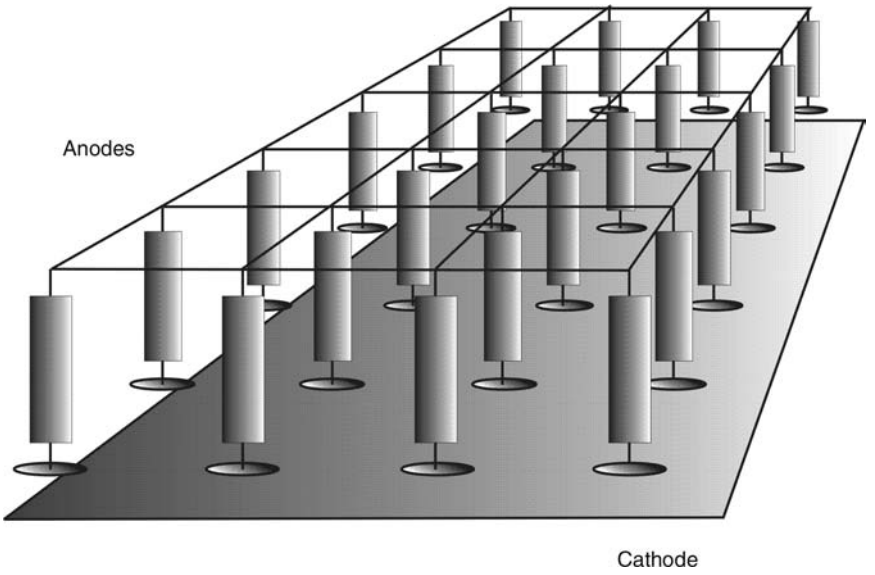

FIGURE 1.24 Schematic diagram of the multipin electrode discharge.

The lasers mentioned here (CO_2 or excimers) are the two basic ones that forced the sophisticated development of pulsed lasers in the past. The electrical and mechanical constructions for these lasers can often be common (only changing optics and gas mixture is necessary to get operational conditions). The idea of construction of TEA is shown in Figure 1.25.

Two specially profiled (Chang profile, Rogowski profile, Ernst profile) aluminum electrodes separated by a distance of a few centimeters are settled in a large chamber filled with lasing mixture (usually of atmospheric or higher pressure). Stable and homogenous plasma can be obtained when a short and high enough voltage pulse reaches the anode. To get a stable discharge, the space between electrodes should be preionized a little earlier (microseconds) by UV radiation from specially formed UV source (spark arrays) in order to initiate free electrons in this area.

Figure 1.26 illustrates a typical pulse electrical supply. The main idea is to settle multistage Marx generator, where the system of charged capacitors and spark gapes makes it possibile to add voltages to all charged capacitors.

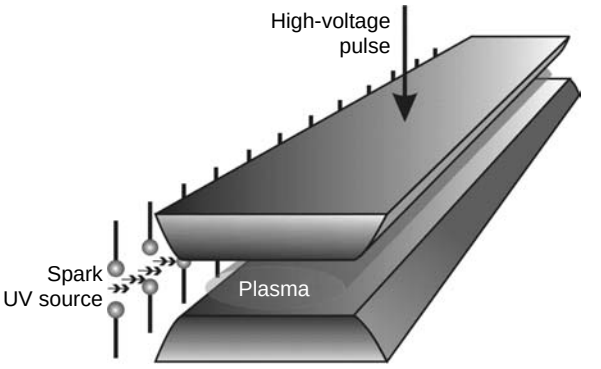

FIGURE 1.25 Schematic diagram of transverse pulse excitation.

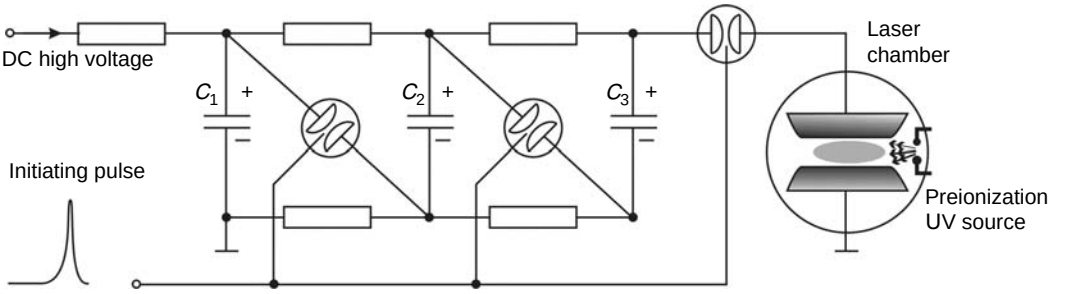

FIGURE 1.26 High-voltage pulse supply based on multistage Marx generator technique.

This is the simple idea of charging C_1, C_2, C_3 capacitors to the high-voltage level U_0 and then by forming short connections at the same time in the spark gapes S_1, S_2, S_3. The voltages of all three (of more, if necessary) capacitors are summed and a high-voltage pulse ($3\times U_0$) initiates plasma discharge between laser electrodes.

Quite popular is a system with dielectric corona preionization, where uniform preionization can be obtained from the same pulsing circuit as shown in Figure 1.27.

A high-voltage pulse appearing with a rapid rise between electrodes causes a strong electric field in dielectric plates. The key factor for obtaining substantial preionization is the use of high $\mathrm{d}U/\mathrm{d}t$ voltage pulses to initiate the corona discharge.

The ionization necessary to maintain discharge can also be obtained by injecting an external electron beam into a gas medium (Figure 1.28). It is rather sophisticated and quite an original construction and was developed mainly for high-pressure CO_2 lasers [7].

Short-pulse lasers require rapid change of current $\mathrm{d}I/\mathrm{d}t$ in a discharge. Such requirement determines low inductance L of the laser head because the change in current is inversely proportional to L,

$$\frac{\mathrm{d}I}{\mathrm{d}t} \sim \frac{1}{L}.$$

Hence, great efforts were made in TEA systems to solve this problem. Each construction of a laser head and a pulse supply system is a result of the individual experience of a designer and the simulation procedures.

There are two examples of constructions minimizing the length of pulses delivered to the transversely excited lasers. *Blumlein*-driven pulse-forming network (PFN) is one example. It is

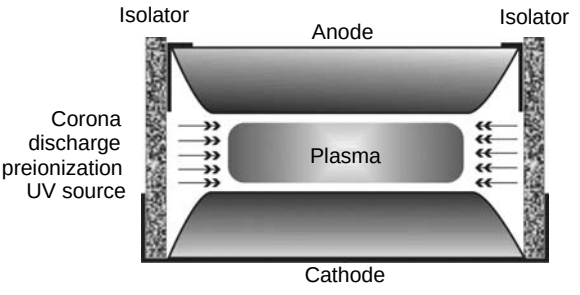

FIGURE 1.27 The idea of corona discharge preionization. (Taken from Witteman, W.J., *The CO_2 Laser*, Springer, New York, 1987.)

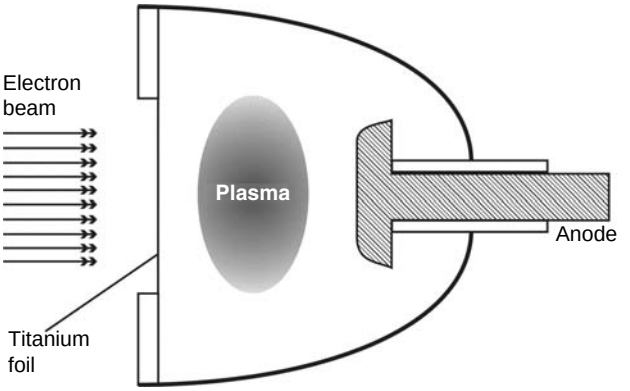

FIGURE 1.28 Schematic setup of an e-beam-controlled laser.

based on low-independence transmission line. The idea of this lies in storing energy in the PFN and in electrical matching of the low-resistance laser discharge to the wave impedance of the transmission line (Figure 1.29).

Another way of compressing the length of current pulse in discharge is using magnetic pulse compression in the supply setup, as shown in Figure 1.30.

The separate practical problem is the high repetition (multikilohertz) pulse operation of gas lasers, well developed for TEA CO_2 lasers and excimer lasers.

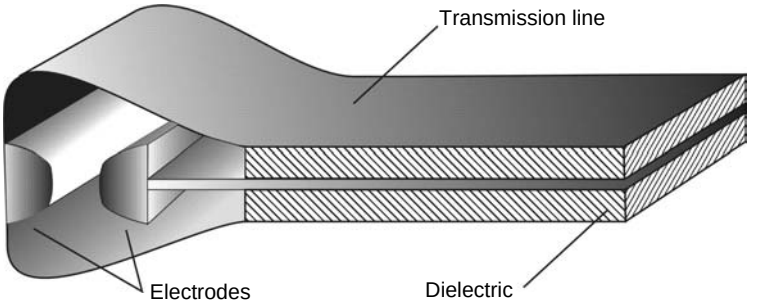

FIGURE 1.29 Blumlein-driven pulse-forming network (PFN).

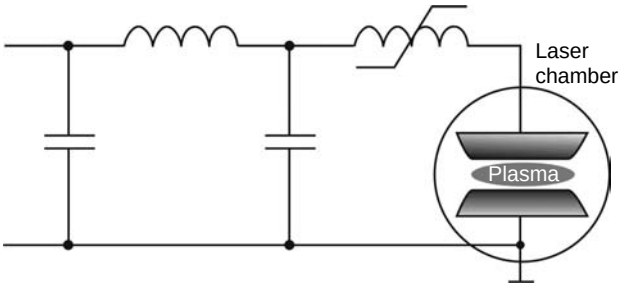

FIGURE 1.30 Magnetic pulse compression.

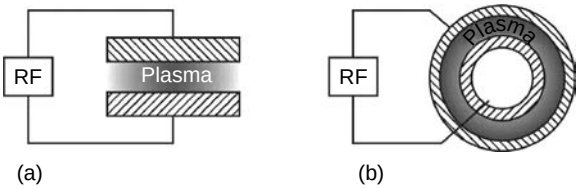

FIGURE 1.31 Two basic configurations of RF excitation: (a) planar and (b) annular.

1.8.3 RF Discharge Excitation

The first operating He–Ne laser consisted of a glass tube filled with He–Ne mixture, which was inductively coupled into RF resonant circuit allowing RF excitation of plasma inside the tube. However, it was quickly replaced by DC excitation technique, which was much efficient, at least for glass tube constructions. The RF technique of laser plasma excitation became popular in the 1980s, when the idea of a diffusion cooled molecular laser appeared in waveguide and slab configurations. The general idea is to form gas discharge between two electrodes formed in planar or annual configurations (Figure 1.31).

These configurations allow us to decrease an electrode separation to about 2 mm gap and as a result, to increase the pressure up to 100–150 Torr. This is the way to drastically increase CW power extraction from the unit value of laser discharge. A new practical parameter, the extraction of output power from unit area, can be introduced. For example, 20 kW/m^2 can be extracted from RF-excited CO_2 slab lasers. The RF excitation idea was applied mainly to molecular lasers. RF excitation technique enabled the development of new techniques of waveguide lasers (Figure 1.32), slab lasers, slab-waveguide lasers, and waveguide arrays. These techniques substantially minimize the dimensions of laser constructions at the kilowatt scale.

1.8.4 Microwave Excitation

The natural continuity of the RF excitation (from tens of megahertz to a few hundred megahertz) seems to use the microwaves as an efficient plasma excitation technique. Attempts have been made to get such excitations for CO_2 and excimer lasers. However, till today there are no practical ways of effective excitation of plasma. In our opinion, this kind of formation of laser plasma is quite attractive and prospective, but it requires some sophisticated and clever solutions which can push this idea ahead.

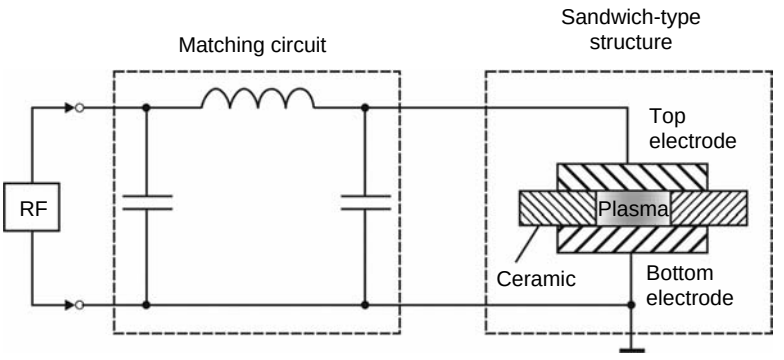

FIGURE 1.32 Schematic diagram of an RF-excited waveguide laser.

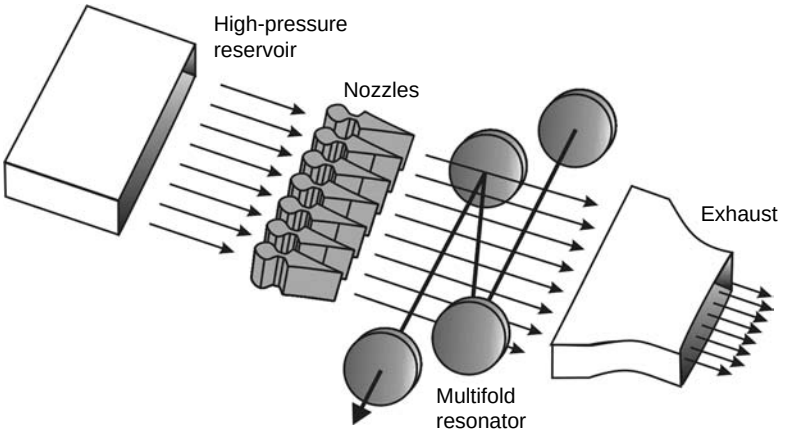

FIGURE 1.33 Schematic diagram of a gas-dynamic laser.

1.8.5 Gas-Dynamic Excitation

Population inversion can be obtained in a gas medium without any electrical discharge. It can happen for molecular CO_2–N_2 mixture called a gas-dynamic laser (Figure 1.33).

The gas mixture of CO_2 and N_2 is heated in high-pressure reservoir to about 2000 K under pressure of several tens of atmospheres. The hot gas from this high-pressure reservoir escapes through a special system of nozzles. A supersonic expansion dramatically decreases the translation temperature to the lowest room temperature and the pressure to about a few tens of Torr. Rotational energy of the molecules relaxes quickly and it reaches thermal equilibrium much faster than vibrational relaxations, which have large inertia like a ''frozen'' process. Such a gas in nonequilibrium flow exhibits a population inversion. The laser resonator is settled perpendicularly to the flow direction and it can extract high output power, to tens of kilowatts.

1.8.6 Optical Pumping

The optical pumping technique, which dominates solid-state laser technology currently, is also applied to one particular sort of gas lasers—FIR lasers. The multiatom molecules (like alcohols) have quite complicated vibrational–rotational spectra. For this kind of molecules, the rotational–rotational radiative transmission is allowed in the frame of the same vibrational state. This transmission corresponds to the submillimeter spectral range (10 μm $\rightarrow$ 3 mm). Their spectral lines are weakly broadened by Doppler effect and are quite narrow. For many of these gas media, their upper laser lines can absorb IR coherent radiation (e.g., from CO_2 laser). Hence, very good conditions for population inversion can be obtained by illuminating an FIR laser cavity with precisely tuned IR coherent radiation. The spectral scheme of FIR action is presented in Figure 1.34.

1.9 COOLING SYSTEMS

An important common problem that appears in gas laser technology is heat removal from laser discharge. Most gas lasers are not high-efficiency devices, with efficiency at the level of percent or below. Only molecular lasers can reach 10%–15% efficiency. Most of the power delivered to the laser plasma has to be removed from the discharge volume; otherwise, it is

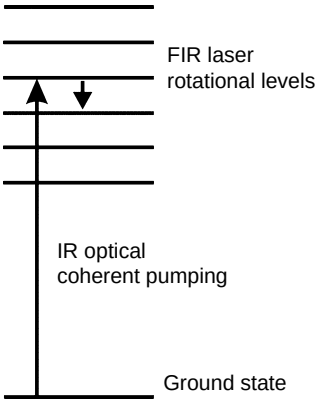

FIGURE 1.34 Quantum scheme of optical pumping.

difficult to keep the thermal conditions of discharge steady. Depending on the laser construction, overheated plasma can substantially decrease population inversion of the medium and can destroy the entire system. Particularly for molecular laser, overheating of the gas causes degradation of the population inversion by thermal population of the lower laser level (CO_2 lasers). Research dealing with water-cooled CW CO_2 lasers knows what happens when one forgets to turn off a cooling system after switching on the laser discharge. If this reaction is not quick enough, unexpected frustrating damages can happen. To demonstrate the influence of heating discharge on the output power, it is worth proving the practical finger rule for CO_2 CW lasers, that increasing the temperature of cooling water by 1°C causes a 0.5% decrease in output power.

Cooling systems can be divided into two categories:

1. Diffusion cooling system
2. Gas flow system

1.9.1 Diffusion Cooling

Diffusion cooling systems are most desirable because they ensure relatively small dimensions of a laser device. Natural air diffusion cooling used for low-power lasers (He–Ne lasers) can

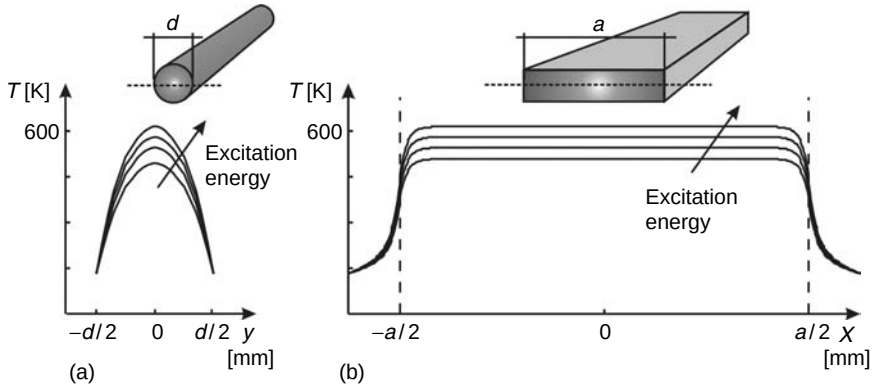

FIGURE 1.35 Examples of temperature distributions for molecular CO_2 lasers for two geometry plasma configurations: (a) cylindrical and (b) slab.

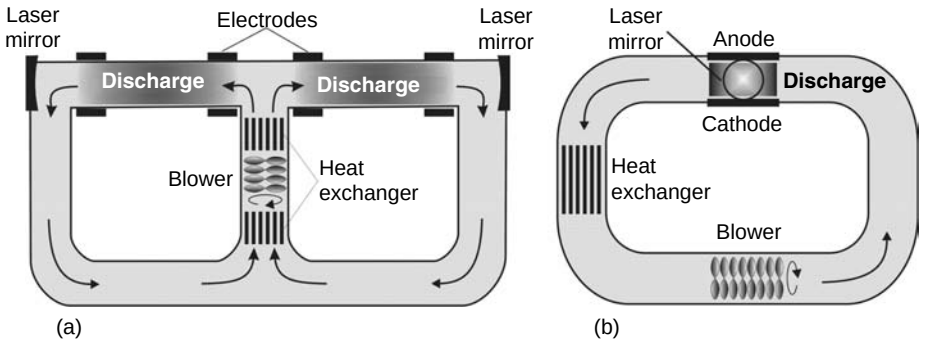

FIGURE 1.36 Schematic diagram of fast flow systems: (a) axial flow and (b) transverse flow with the flow perpendicular to the optical axis.

be extended by fan systems (low-power RF-excited CO_2 lasers). However, when the total delivered power exceeds about 300 W, it is necessary to apply liquid cooling systems. There are well-developed efficient cooling devices operating in close circulation with temperature control even below 0°C. Diffusion cooling systems are applicable when transverse dimensions of a laser discharge are relatively small (a few millimeters).

Temperature distribution in the cross section of a gas laser is governed by heat transfer differential equations (1.5) (see Section 1.2.3). Figure 1.35 demonstrates temperature distributions for a cylindrical DC CO_2 laser tube and RF-excited CO_2 slab waveguide laser.

1.9.2 Flowing Systems

Very high power laser systems require large volumes of gas media and as result of this, larger transverse dimensions. Multikilowatt power delivered into discharge cannot be removed by diffusion, particularly, when transverse dimensions exceed 1 cm. To improve heat removal from such a construction, the fast flow of gas medium should be applied. The excess heat absorbed by gas can be removed by the flowing gas, when the gas flow transit time is much shorter than the characteristic time for diffusion into the wall. The main reason of fast flowing is not only heat removal but also cooling discharge to keep population inversion. In practice flow velocity is about a few tens of meters per second.

There are two basic ideas of fast flowing systems: axial flow and transverse flow configurations (Figure 1.36). Axial flow is quite popular for molecular lasers with DC or RF excitation. Transverse flow systems are applied for higher DC-excited (multipin electrodes) molecular lasers or all kinds of transverse high repetition-pulsed molecular or excimer lasers.

REFERENCES

1. Siegman, A.E., *Lasers*, University Science Book, Mill Valey, California, 1986.
2. Verdeyen, J.T., *Laser Electronics*, Prentice Hall, Englewood Cliffs, New Jersey, 1995.
3. Svelto, O., *Principles of Lasers*, Plenum Press, New York, 1998.
4. Milonni, P.W., *Lasers*, John Wiley & Sons, New York, 1988.
5. Yariv, A., *Optical Electronics*, HRW International Edition, New York, 1989.
6. Yariv, A., *Quantum Electronics*, John Wiley & Sons, New York, 1989.
7. Eden, J.G., Ed., *Selected Papers in Gas Laser Technology*, SPIE Milestones Series, Vol. MS 159, SPIE Optical Engineering Press, Bellingham, 1999.
8. Charrington, B.E., *Gaseous Electronic and Gas Lasers*, Pergamon Press, Oxford, New York, 1979.
9. Brown, S.C., *Introduction to Electrical Discharges in Gases*, John Wiley & Sons, New York, 1966.

10. Hirsh, M.N. and Oskam, H.J., *Gaseous Electronics*, Academic Press, New York, 1978
11. Herzberg, G., *Spectra of Diatomic Molecules*, Vol. 1, Van Nostrand, Princeton, 1950.
12. Eisberg, R. and Resnick, R., *Quantum Physics of Atoms, Molecules, Solids, Nuclei and Particles*, Wiley, New York, 1974.
13. Liboff, R.L., *Introductory Quantum Mechanics*, Holden-Day, San Francisco, 1980.
14. Herzberg, G., *Electronics Spectra and Electronics Structure of Polyatomic Molecules*, Vol. 3, Van Nostrand, Princeton, 1967.
15. Fox, A.G. and Li, T., Resonant modes in laser interferometer, *Bell. Syst. Technol. J.*, 40, 453–488, 1961.
16. Schawlow, A.L. and Townes, Ch., Infrared and optical masers, *Phys. Rev.*, 112, 1940–1949, 1958.
17. Hodgson, N. and Weber, H., *Optical Resonators: Fundamentals, Advanced Concepts and Applications*, Springer, Berlin, New York, 1997.
18. Hall, D.R. and Jackson, P.E., Eds., *The Physics and Technology of Laser Resonators*, Adam Hilger, Bristol, 1989.
19. Yu, A. Anan'ev, *Laser Resonators and the Beam Divergence Problem*, Adam Hilger, Bristol, 1992.
20. Kossowsky, R., Jelinek, M., and Novak, J., Eds., *Optical Resonators—Science and Engineering*, NATO ASI Series, Kluwer Academic Publisher, Norwell, 1998.
21. Witteman, W.J., *The CO_2 Laser*, Springer, New York, 1987.

2 Fluid Dynamics

Anatoly S. Boreysho, Andrey V. Savin and Victor M. Malkov

CONTENTS

2.1 CW SUPERSONIC GAS LASERS

2.1.1 Introduction

Supersonic gas lasers (SGL) are lasers where gas is pumped through the resonator cavity at a supersonic velocity. They have always been of great interest in gas flow continuous wave (CW) lasers. In the 1970s, they were gas dynamic lasers (GDL) whereas nowadays, they are called chemical HF(DF)-lasers and oxygen–iodine lasers (COIL). The chemical systems are so appealing primarily owing to their ability to generate extremely powerful radiation. Because of the high rate of radiation energy of a laser medium mass unit (high efficiency), it is possible to pump quite a high flow rate of work gas through the resonator in chemical lasers. Apart from this, SGL can serve as a basis for stand-alone mobile laser complexes.

Similar projects—high-power stand-alone laser complexes—have already been realized. First, this is an airborne test-bed ALL-CO_2GDL installed on a K-135 aircraft. The technical features of the complex and the history of its development can be found in [1]. One of the examples of a DF-laser-based megawatt class stand-alone complex is the ''Nautilus'' project currently accomplished [2]. A large-scale ABL–COIL project of several megawatt output is on-board Boeing 747 [3].

All these lasers can be combined to form a group based on their structure, that is, from the point of view of the main structural component solution. They all incorporate gas generators, multinozzle banks(MNB), resonator cavities, exhaust systems, and so on. Second, from the point of view of gas flow arrangement in the laser's rectangular operating channel, that is, from the viewpoint of gas dynamics, these systems have a great deal in common. Further, we consider the characteristics of supersonic flows behind the MNB and the impact that the density nonuniformities generated by the banks have on the optical quality (OQ) of a flow in the resonator cavity. Exhaust systems are described in an individual section.

2.1.2 Supersonic Lasers' Main Structural Units (GDL, DF(HF), COIL)

Figure 2.1 shows a very general representation of block design diagrams: sequence of the main structural units of SGL lasers. When we mention powerful laser systems, we mean combustion systems. It is the gas generators that help create a high gas flow rate of a required chemical composition, pressure, and temperature.

Gas generator (GG). As its task is to generate the flow rate of a gas of a certain composition it requires special-purpose fuel and oxidizers; quite often these fuel components are toxic.

Multinozzle bank. The physical principle of a laser operation requires small dimension nozzles that have a small critical section. In order to form a high flow rate one needs to apply nozzle grids—MNB. Operation mixture expansion to the supersonic velocity in a nozzle allows reducing the flow static temperature though it decreases the laser's lower level population and forms favorable conditions for inverse population. High flow velocity also helps in

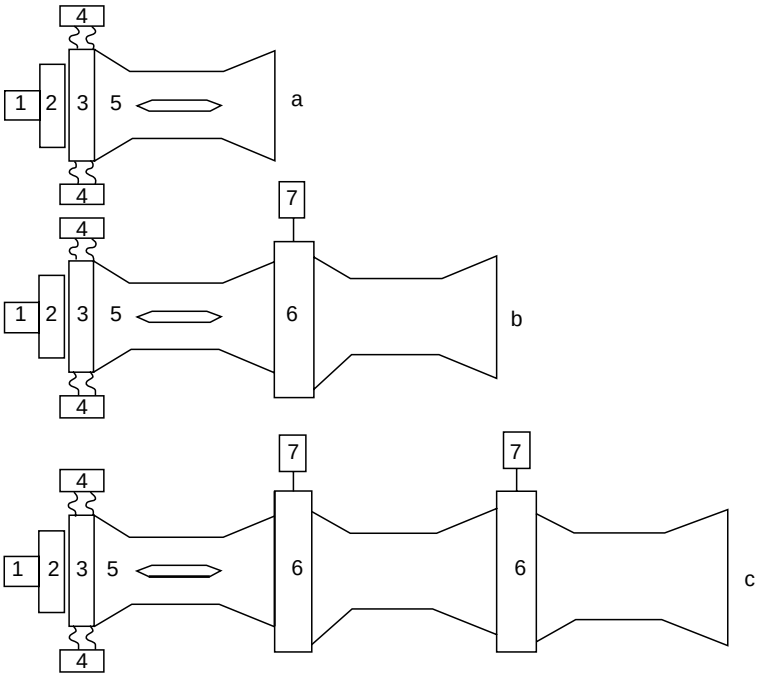

FIGURE 2.1 Block diagram of supersonic lasers: (a) CO_2-GDL; (b) DF-CCL with PRS; (c) COIL with PRS on the base of double-stage ejector; 1—generator, 2—multinozzle bank, 3—laser chamber with shutters, 4—vacuum capacities for mirrors' placing, 5—diffuser, 6—ejector, 7—gas-generator.

taking away the useless heat generated during the generation process from the resonator area. MNB forms a homogeneous flow in a laser cavity and it is required that density nonuniformities formed behind certain blades are perpendicular to the resonator's optical axis.

Laser chamber (cavity) comes right after the MNB and is an input point for the diffuser. Its task is to provide homogeneous supersonic flow. That is the reason why the laser chamber's walls are profiled according to the processes that take place in a gas. Therefore, in the case of chemical lasers the profile needs to be flared, first to prevent a flow from choking because of the heat emission; and second, it is desirable to arrange a flow free of impact waves to reduce the total pressure loss in a flow. Vacuum cavities for mirror arrangement are fixed to the chamber's side walls (usually with vibro-insulator).

Opening shutters are often installed on the vacuum cavities' input. There are two reasons for this. The cavities at the side walls—called caverns in aerodynamics—cause an increase in the diffuser start pressure. At that point, the degree of negative effect depends on cavern dimensions—combination of depth and length, and there is an area of these parameters where the diffuser start pressure increases abruptly. This is why caverns need to be closed at the start. Apart from this, at the start of the pressure recovery system's generators when the fuel mixture is rich, soot emerges. Therefore, shutters are also necessary to protect resonator mirrors.

Diffuser is necessary to reduce the supersonic flow. In order to reduce the diffuser's length, its inner channel is divided into parts by pylons, that is, a multisection diffuser is used.

Ejector. When the recovery pressure behind the diffuser is lower than the ambient pressure (which is correct for DF-lasers and COIL), supersonic ejectors are needed for exhaust arrangement. In the case of DF-lasers, they are called single-stage systems, and in the case

of COIL they are two-stage systems. (In this case, we mean ground-based versions of laser complexes). To form the required ejecting gas flow rate, special-purpose gas generators are applied.

The complex's exhaust part (diffuser and ejector) is usually called a pressure recovery system (PRS). In the case of DF-lasers, the PRS can incorporate a heat exchanger. Hot laser flow cooling allows reducing the ejecting gas flow rate demand thus reducing both the weight and the dimensions of the supply and storage system (SSS) for fuel and oxidizer components.

SSS. Figure 2.1 does not show it; however, obviously all the complexes incorporate such a system as it provides operation of both the laser generator and the PRS gas generators. It includes various vessels and high-pressure bottles, fittings (reducers, valves, vents, etc.), and connecting lines. It is necessary to mention that the SSS is fundamental from the viewpoint of weight and dimension as its share in a mobile complex is the most significant.

2.1.3 Special Features of Supersonic Lasers

Though similar in structure, these lasers are certainly different. Their operational parameters are different (pressure, temperature) because in GG a different fuel is applied, which means, the active media are of absolutely different chemical compositions, means and methods of inverse population formation and operational molecules are different. In other words, the lasers have different wavelengths.

CO_2-GDL [4–6]. Figure 2.2 shows a laser principle scheme, whereas Figure 2.3 shows a diagram of the lower vibration energy level of the main molecules taking part in the physical process: CO_2, N_2, and H_2O. Population inversion at molecule level occurs because excited vibration energy levels of the CO_2, N_2, and H_2O molecules possess different relaxation times. Level excitation is achieved due to the gas mixture's high temperature, which forms in the gas mixture on corresponding fuel combustion. On expansion of the hot gas mixture at a small-scale nozzle's output, the population of the lower vibration energy level of the N_2 molecules is defined by the temperature close to the one in a prechamber as the level relaxation time is considerable (a N_2 molecule is symmetrical). The characteristic time of molecule stay in the critical section area shall be less than that of the relaxation time. Hence, one obtains the condition to calculate a nozzle critical section dimension.

H_2O molecule level population is on the contrary defined by the temperature close to the nozzle output flow static temperature (i.e., low), as level relaxation time is less (a H_2O

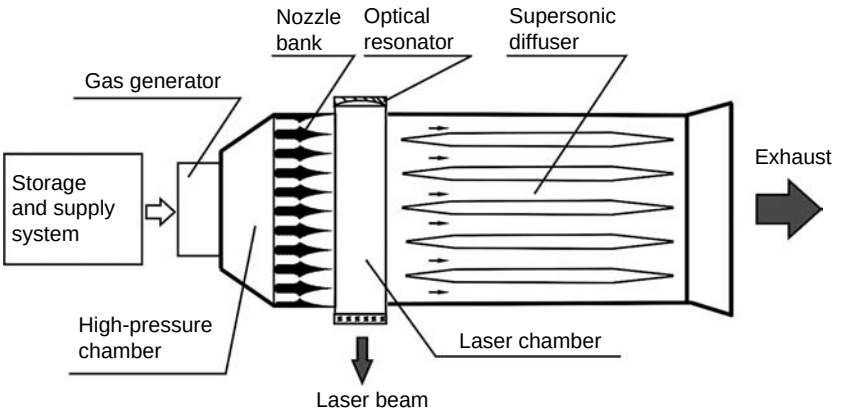

FIGURE 2.2 Scheme of CO_2-GDL.

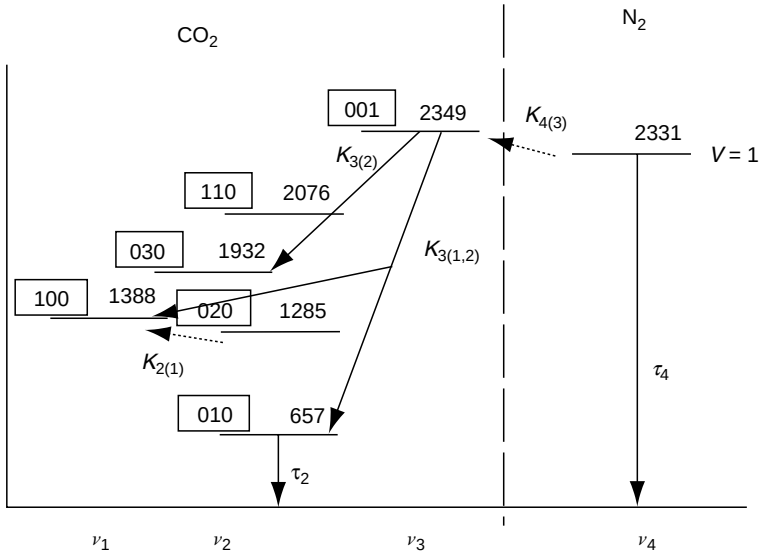

FIGURE 2.3 Relaxing channels in molecules' system CO_2 and N_2.

molecule is nonsymmetrical). In order to reduce the flow's static temperature, the mixture is accelerated in a supersonic nozzle to major values of Mach Number $M \approx 5$.

That is the reason why in the $CO_2 + N_2 + H_2O$ gas mixture, level population (001) of a CO_2 molecule is specified by the lower vibration energy level population of the N_2 molecules. The energy fault between these levels is minor and energy transmission probability is very high. The lower-level population is defined by the H_2O molecules' population. Thus, at the nozzle output, inverse population in CO_2 molecule's energy levels is realized in a gas flow. A brief description of the process is as following: energy is stored in N_2 molecules, the CO_2 molecule converts the energy into radiation, and H_2O molecules relieve the lasing transition's lower level thus creating an appropriate generation environment. The inverse population formation method described here is called heat pumping. The wavelength of radiation of CO_2-GDL is 10.6 mcm.

GDL gas generator's task is to form the required hot mixture ($CO_2 + N_2 + H_2O$) flow rate. Generally, application of hydrocarbon fuel can also fulfill this task. However, to achieve efficient laser operation it is necessary to make sure that the combustion products will include little water (mass fraction must be ~2%–3%). This is the reason why not every fuel type is ustable. Fuel composition shall rather include liquid components (SSS weight decreases), such as toluene and benzole. If nitrous oxide is used as an oxidizer rather than air, the combustion product compositions becomes not quite optimal but appropriate enough to obtain a high value of stored energy in a gas flow.

The system's gas dynamic parameters: temperature in the forechamber of the nozzle unit shall be in the range of 1800–1900 K, and the pressure in 40–60 atm. The flow velocity at the nozzle output will be $M \sim 5$–5.5, whereas static pressure in the resonator cavity will be in the range of 40–50 Torr. In the case of GDL, flow energy is enough to provide gas emission into the atmosphere with the help of a diffuser.

Specific energy stored in a gas flow in optimal conditions is ~20–25 kW/kg/sec, and the energy converted to radiation is about 10 kW/kg/sec. CO_2-GDL is an inefficient laser as only 1%–2% of the total heat energy is stored in the N_2 molecule vibration energy levels.

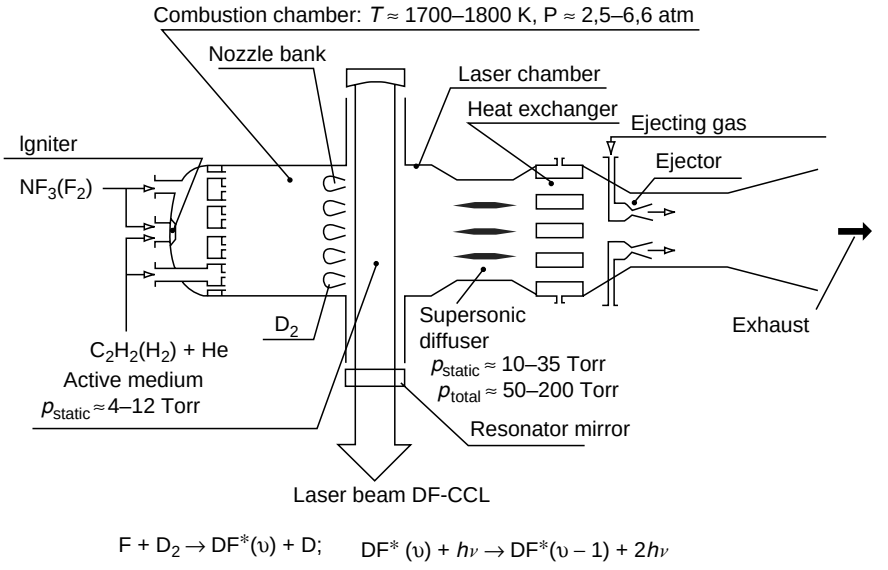

FIGURE 2.4 Principal scheme of DF-laser operation.

DF(HF)-laser [7,8]. Chemical lasers are more efficient than gas dynamic lasers. Figure 2.4 shows a basic DF/HF-laser operation scheme. A gas generator's task in this case is to generate a gas flow containing F atoms (in this case a GG is called a generator of atomic fluorine (GAF). In this type of a generator, fluorine-containing fuel is applied, such as NF_3 (nitrogen trifluoride); C_2H_4 can serve as oxidizer (generally, fuel compositions can be different). At temperatures 1700–2000 K in the GAF, molecular F_2 splits into atoms.

At the nozzle output, H_2 (or D_2) is injected into the flow. The $F+H_2 \rightarrow HF^* + H$ reaction product is vibrationally excited. The main task is to capture the energy as radiation as the HF* lifetime is rather short. This is the reason why pressure in the laser chamber's resonator cavity needs to be maintained low, ~7–15 Torr.

H_2 (or D_2) is injected either at the nozzle output or at the supersonic section of the nozzle. There are various nozzle unit arrangements; one of the versions is shown in Figure 2.5. There are two rows of injectors in the nozzles' supersonic section. The first row is fed with He, while H_2 (or D_2) is fed to the second one. The presence of He as a diluting agent allows slowing the process of mixing F and H_2 and thus prolongs the active area where generation takes place. If He is not added, the area turns out to be too short (2–3 cm), whereas the mirror load upon considerable radiation energy output is severe.

System's characteristic gas dynamic parameters. Pressure in the GAF ~ 1–7 atm, the Mach number at the nozzle edge $M \approx 4$–4.5. As the combustion process ($F + H_2$) takes place right after the nozzle unit, the heat is fed to the supersonic flow. It is known that in this case the flow starts slowing down. In order to avoid the chocking effect, meaning transfer of a supersonic flow mode into the subsonic, the laser chamber is extended and walls are profiled. Usually a degree of chamber expansion is selected so that at the diffuser's input the Mach number made $M \sim 2$. If the velocity is higher than the total pressure losses upon flow slowing down in the diffuser are large—a function that specifies total pressure loss falls abruptly as the M number grows. However, if the flow is decelerated harder, the possibility of supersonic flow failure increases.

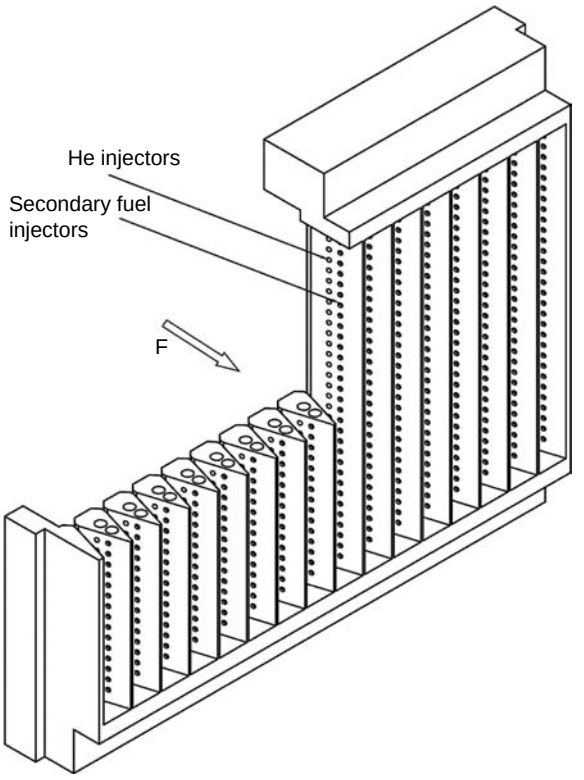

FIGURE 2.5 A nozzle bank variant.

In the general case because of gas dynamic losses or shock waves, losses as a result of heat generation and total pressure after the exhaust diffuser make 70–100 Torr. Such flow energy is not enough to provide exhaust into the atmosphere with just the diffuser. In order to arrange exhaust the ejector needs to be applied, that is, the PRS system.

As the compression ratio provided by the ejector is rather small (5–10—depending on the pressure after DF), the PRS of the DF/HF-laser can be built on the basis of a single-stage ejector. If an efficient heat exchanger is applied at the ejector's input, its ejection ratio can be increased, that is, the flow rate demand of ejecting gas can be reduced. In other words, the SSS weight can be reduced, and thus mass-dimension characteristics of the entire laser complex can be improved.

A task of efficient ejector construction involves jet mixing (subsonic flow and supersonic flow). However, the task of mixing them in the laser's nozzle is mostly an issue of penetration of fine-scale jets and of achieving a homogeneous flow, and the task of mixing them in the ejector is an issue of process arrangement at minimal loss of impulse in the system.

Chemical laser efficiency—specific energy obtained from a mass unit of active medium—is much higher than that of the gas dynamic systems. However, this value is considerably reduced (by 5–10 times) when one estimates the efficiency of the system in general considering ejecting gas flow rate in the PRS [9,10] (see part 6).

COIL [11]. This laser type differs significantly from the earlier ones. The laser's basic scheme is shown in Figure 2.6. There is no combustion in the laser's gas generator

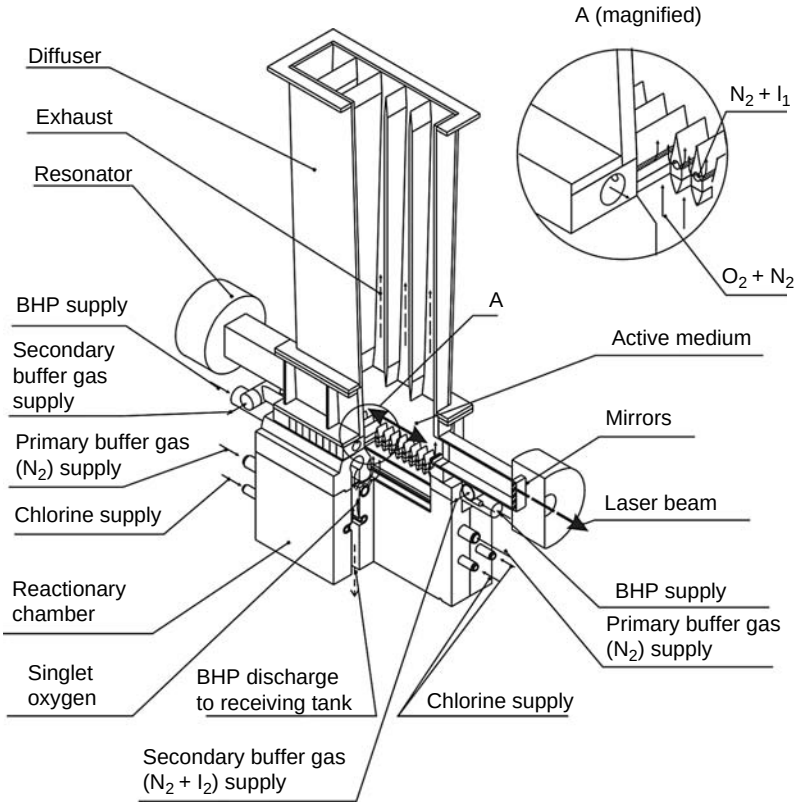

FIGURE 2.6 Principal scheme of COIL operation.

but a gas–liquid reaction. Alkali (e.g., KOH) dissolved in hydrogen peroxide (H_2O_2) is fed from the top through a special-purpose fine grid, that is, the solution shower is arranged. This method of feeding liquid chemical agents provides a much extended surface as the basis for gas reaction. Cl_2 is applied as a gas chemical agent fed from below. This is a very general operation scheme of the most efficient generator so far—called the singlet oxygen generator (SOG).

The $KOH + H_2O_2$ solution is fed from above the SOG from a thermally insulated container equipped with a cooling device. The solution temperature is kept in the range of $-15^{\circ}C$ to $-20^{\circ}C$. After subjecting to showering in the SOG, the liquid is poured into a receiving tank. It should be mentioned that one of the laser's advantages is that its active medium is cool and the laser chamber can be made of plexiglass.

Excited molecular oxygen—singlet oxygen $O_2(^1\Delta)$—emerges as a result of the reaction at the generator's output. The energy generated by the chemical reaction is stored at electron levels of a molecule (unlike the laser types described above where the point was in vibrational–rotational energy levels). From the SOG, oxygen is supplied to the mixing multinozzle bank. The supply is carried out in an environment of specially fed helium or nitrogen. A dilutant is required to reduce the speed of quenching $O_2(^1\Delta)$ and to reduce the time of singlet oxygen supply to the nozzle.

Based on its structure, the mixing nozzle bank is similar to a bank applied in DF-lasers. However, here gaseous I_2 is injected through rows of nozzle openings (to do this I_2 crystals are

first evaporated–heated). Iodine injection openings are placed in subsonic and supersonic sections of a nozzle, but they can also be placed in a transonic nozzle section.

Although gas dynamic systems of flow arrangement are similar in a DF-laser and a COIL, the inverse population process itself is much more complicated in COIL. First, the energy stored in $O_2(^1\Delta)$ is used to split the I_2 molecules, and only after that the iodine atoms are filled with energy stored in a singlet oxygen. It is considered that it takes 4–5 $O_2(^1\Delta)$ molecules to pump one iodine atom. Figure 2.7 shows an operational level's scheme. Generation is carried out at atomic iodine transfers.

After passing through the resonator cavity, the operation mixture is emitted either to a vacuum vessel or is pumped out with a pump (e.g., ejector). Parameters of the gas in the resonator cavity: the Mach number—1.5–2, static pressure 3–6 Torr, total temperature at a level 300 K.

If a PRS is designed for COIL exhaust it will cause a number of difficulties. First, widespread diffuser design methods applied in aerodynamics do not work in this case. The point to be noted here is that after the operation gas has passed through the resonator it still contains a considerable share of excited molecules of singlet oxygen (~30%). As it moves through the channel there takes place the process of quenching, that is, the electronically excited level's energy is converted into the molecules' translational degree of freedom, that is, gas temperature increases up the channel. It is known that heat supplied to a supersonic flow causes its slowing down and extra total pressure loss. That is the reason why usual recommendations on diffuser length selection (based on aerodynamic wind tunnel experiments, that is, in flows where heat is not supplied) do not work. Besides that, Re numbers are low—the boundary layers are thick, thus the total pressure after the diffuser turns out to be too low.

As a result, the required compression ratio the PRS is intended to provide for exhaust into the atmosphere makes 30–50. In order to get such compression ratios, it is necessary to apply a double-stage ejector. This means considerable ejector dimensions and high ejecting gas flow rate. Generally, cryoadsorption pumps [12] can be applied in the systems of moderate flow rate.

In spite of all the differences, the fact that the MNB-generated supersonic flow is present in the resonator cavity allows considering all the three laser types in one group. As main gas

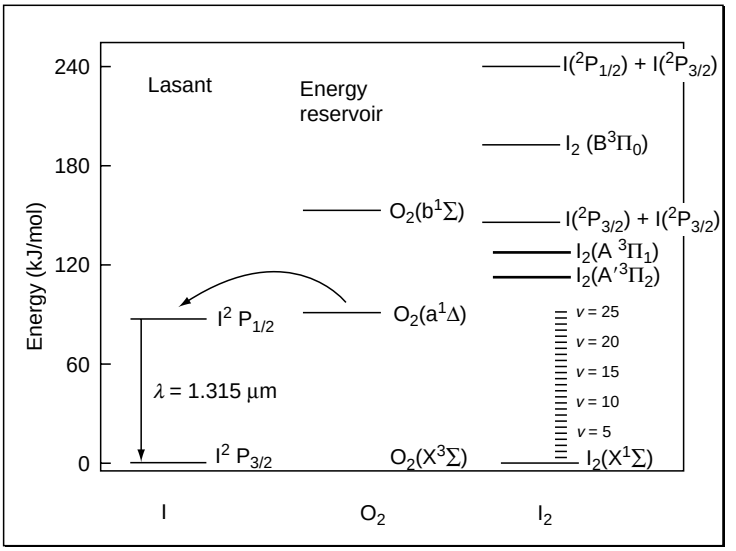

FIGURE 2.7 Working energy levels and transitions in COIL.

dynamic tasks and issues to be solved when designing such systems are general for all the type of lasers in question. This as well as forming a homogeneous flow by multinozzle bank and gas flow in rectangular channels, and tasks of supersonic flow deceleration and mixing, and so on. Therefore, the following sections consider the general consistent patterns of flow generation behind MNB of both homogeneous and mixing structures, both two-dimensional "flat nozzles" and three-dimensional "screen nozzles" type structures.

2.2 FLOW STRUCTURE IN THE LASER CAVITY AFTER MNB

2.2.1 Introduction

The chapter represents research results for supersonic flow features behind the MNB: two-dimensional—blade nozzle banks (BNB) and three-dimensional—screen nozzle banks (SNB). Optical flow visualization behind the MNB has been carried out according to the well-known Schlieren method. A typical optical device consisting of a parallel light beam radiation system and a receiving section has been used during the research. A sparker of $\Delta\tau \approx 10^{-6}$ sec pulse time was used as a pulse light source. The knife position in the receiving section of the optical device varied.

Flow parameters behind the nozzles were measured with the following pressure probes: total-pressure probes—Pitot tubes—and static pressure probes. The Mach number was estimated using the ratio of P_0' the Pitot tube pressure to P_{st} the static pressure.

2.2.2 Blade Nozzle Bank and Two-Dimensional Flow Pattern

2.2.2.1 Blade Bank Models

The models' outer appearance is shown in Figure 2.8. Each of these banks incorporated three central blades two sides of which were profiled and two side ones with one profiled side (semi blades). Thus, a model unit consisted of four blade nozzles, in which, walls of the uttermost nozzles were flush joined to the working channel walls. Bank blades were spaced with special polished plates thus allowing setting critical cross-section height in individual nozzles with higher accuracy—the entire structure was tightened with studs (the picture shows spacing plates between the blade arms. Along the perimeter of the nozzle box there is a rubber seal).

In all, the MNB blade supersonic section's profile was a minimal length outline calculated by the method of characteristics on Mach number $M = 5$ (adiabatic index $k = 1.4$) with correction for a boundary layer displacement thickness. Critical cross-section dimension was $h^* = 0.49$ mm, and the output cross-section height made $H = 13.45$ mm. Supersonic section length was $L_c = 37$ mm. Blade thickness t at the end where trail angle was $\alpha = 0$, varied: banks I–IV had $t = 0.75$, 0.5, 0.35, and 0.15 mm blades. Banks III(1) and IV(1) were assembled from the same blades as banks III and IV, but preliminary shortened by 7 and 11 mm respectively. Therefore, their α angle appeared to be 2.5° and 4°, and $t = 0.75$ and 1 mm. (Figure 2.8 shows one bank with integer blades and the other with shortened ones.) One more bank was assembled from blades with different t: one $t = 2.3$ mm central blade and two $t = 0.35$ mm blades. All the nozzles had the same subsonic contour: straight-line inlet of 60° to the axis conjugated by its radius $r \approx 1$ mm with a straight-line section in throat ($l \approx 0.5$ mm).

2.2.2.2 Flow Pattern

Schlieren photographs of the flow behind the banks I–IV (without shortened blade) are shown in Figure 2.9 and Figure 2.10. Photographs in Figure 2.9 and the first row in Figure 2.10 have been obtained from the spark light source, that is, at exposures $\Delta\tau \approx 10^{-6}$–$10^{7}$ sec.

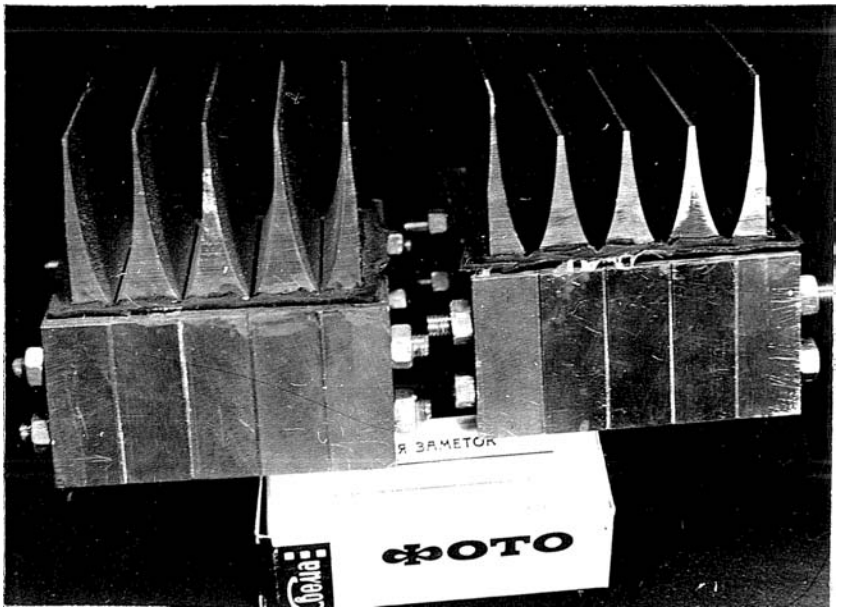

FIGURE 2.8 Blade nozzle bank—models for tests.

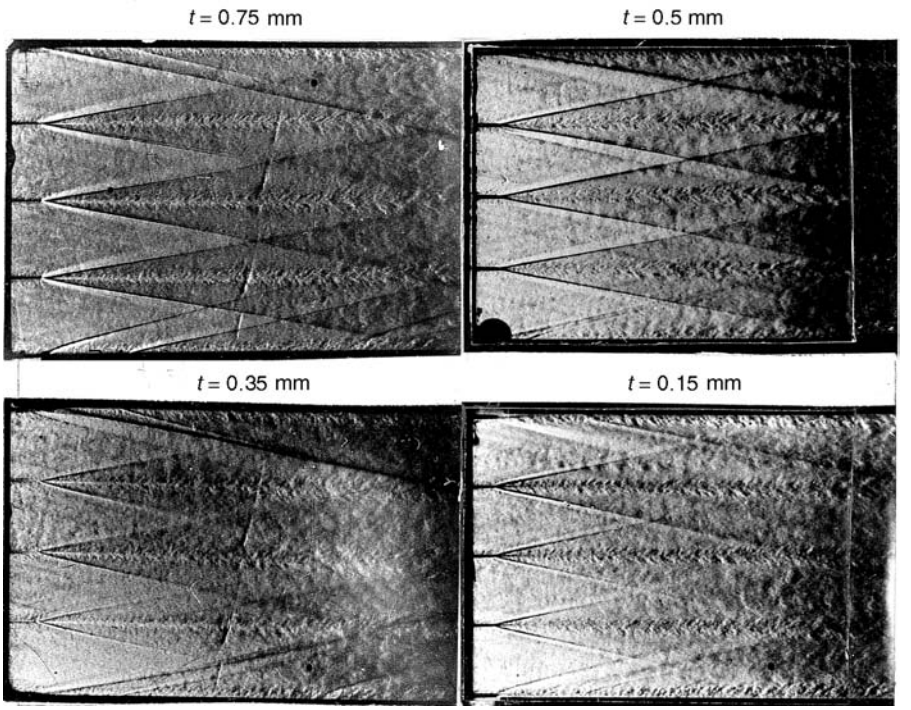

FIGURE 2.9 Flow fields after nozzle banks with different thickness (t) of blades (top view).

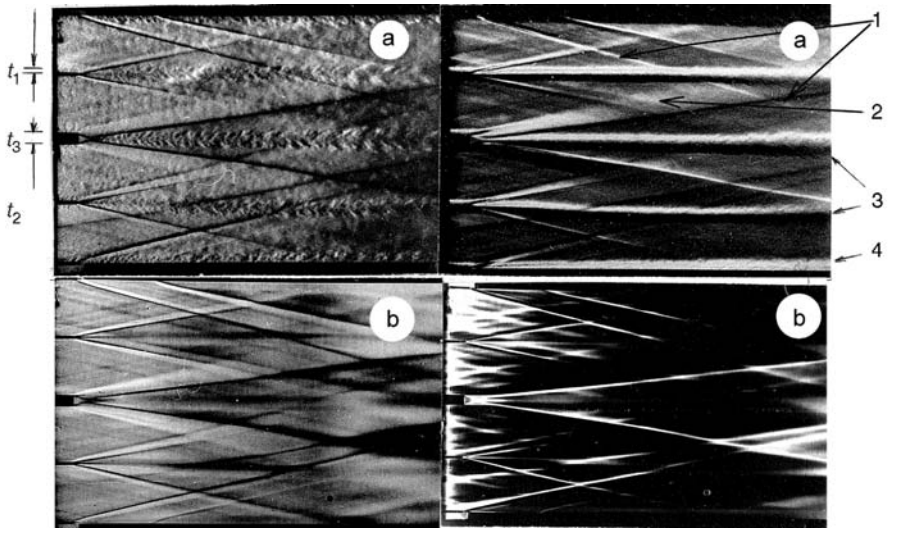

FIGURE 2.10 Schlieren photos of flow: (a)—spark light source ($\Delta\tau \approx 10^{-6}$ sec); (b)—CW source of light; top right photo—knife position is horizontal, others—knife position is vertical; $t_1 = t_2 = 0.35$ mm; $t_3 = 2.3$ mm. 1—Shock wave; 2—expansion wave; 3—wake; 4—boundary layer.

For comparison in the bottom row in Figure 2.10 there are photographs obtained at exposures set by a camera of $\Delta\tau \approx 10^3$ (i.e., minimal possible for a camera while continuous light source in this case was a mercury-vapor lamp).

All but one Schlieren photograph shown here were obtained in vertical knife position in the optical system. In the majority of the photographs, its position is such that the vacuum areas are represented as light lines whereas compression shocks are represented as dark lines. When a blade is led from the other side, compression shocks are represented, on the contrary, as light lines and the fan-shaped beam of expansion waves—as a dark area. Such a photograph is shown in Figure 2.10 (bottom right) representing a thick blade ($t = 2.3$ mm) bank. The same bank is represented in the photograph (top right) when the blade was positioned horizontally. Such a knife position allows marking off at once the nonuniformities stretching along the channel axis (wakes in this case). Thus, variation of knife position allows visualizing certain flow points in more detail. Spark shooting allows observing boundary-layer troughs on the walls, flow pattern there (turbulent in this case), flow pattern in the wakes and in the entire flow.

As one can see in the photographs, there are no compression shocks but trailing-edge ones in the flow core. This proves the high accuracy of the blade profile production: the profile was finished at a special-purpose PC grinder equipped with a laser tool scanner (only one nozzle was defective—the bottom one in the $t = 2.3$ mm blade bank. In this spot, a shock wave is generated in the flow core). Extra shocks generated at the channel walls: one emerged at the joint of the uttermost blade and the channel, and the other—further down the stream—at the spot where the sidewall window started. That is the reason why on pressure pattern measurement these spots were plastered.

Details of flowing around the edge are most clearly observed view at the $t = 2.3$ mm blade. The intensity of trailing shock and expansion wave depends on t and α (see Figure 2.13). Their intensity weakens as the value of t decreases and the trailing wave's inclination angle to the wakes axis increases and tends to the Mach angle of weak disturbance arcsin $(1/M)$. In the $t = 2.3$, 0.75, 0.5, 0.35, and 0.15 mm blades (at $\alpha = 0$) wave inclination angle was 8.5°, 10°,

10.7°, 11.2°, and 11.7° relatively (the Mach number at the nozzle outlet was $M = 5$ and the corresponding Mach angle was 12°).

Therefore, in the flow behind the blade MNB there emerges a typical diamond-shaped structure of shock waves and expansion waves. The last element was not specified in references [1–4]. However, the fan-shaped beam of expansion waves is formed on flow around the trailing edge and it closes by a shock wave. Impact synchronism of these two disturbing factors coming from adjoining edges and actually compensating for each other does not cause any visible change in the wake development pattern (the fact is confirmed by direct wake parameter measurements, but this is valid for moderate values $t < 1$ mm and $\alpha \leq 4°$, whereas at $t = 2.3$ mm deviations are observed). However, as one knows, a single shock wave impact breaks laws of free wake formation.

The wake forms a boundary layer flowing around the blades. One can see that in the set conditions the boundary layer at the blade edges is turbulent at the entire wake. Vortex periodic system is clearly seen in the wake, the vortexes' dimensions increase as the wake thickness grows. Effect of t and α values on the turbulent structure is not obvious here but an increase in the turbulent scale of density fluctuation behind the $t = 2.3$ mm blade when compared with ''thin'' blades is noticeable.

2.2.2.3 Average Parameter Distributions in a Flow

Overall picture. Figure 2.11 shows a total-pressure distribution pattern behind the normal shock (Pitot) and static pressure: $\overline{P}_0'(y)$ and $P(y) = P_{st}/P_{00}$ measured by corresponding probes at the exit of bank I at $x = 1$ mm ($x = 0$—from now on—blade end; P_{00} is the pressure in the nozzle bank forechamber)—$M(y)$ the Mach number distribution, $\sigma(y)$ the total pressure recovery coefficient (the ratio between flow total pressure and P_{00}), and $\bar{\rho}(y)$ the density were calculated on the basis of these data assuming that the stagnation temperature T_{00} is constant. The coordinate y is measured from the channel wall. Narrow holes along distributions—wake areas. Behind each nozzle in a flow core (the area between the adjoining wakes) distribution of numbers M and $\rho(y)$ is almost homogeneous, the M numbers coincide with the calculated values and the σ ratio is close to 1.

Similar data were obtained for each bank in several cross sections. The cross sections were selected depending on the visualization results. Apart from this exit measurements were carried out in the area of $x \leq 20$ mm (to obtain data on shock and expansion waves intensity the measurements were made behind two nozzles). Further on cross sections were selected in the area of $x = 35$–45 mm, where shocks crossed in the flow core. The cross section in the area of $x = 70$–90 mm was selected right after the spot where the wake was crossed by disturbances, to get an idea of the impact influence on the wake. The last cross section—at $x = 150$–160 mm—was remote enough from the bank exit. Here, to research the behavior of flow mean characteristics in the wake area more detailed measurements were carried out in the wake than those specified in the overall picture, at various P_{00} pressure values (for details of the research and results please see [5]).

Figure 2.12 shows an example of another common parameter distribution for bank I at $x = 22$ mm. It is here at $y = 18$ and 24.5 mm that disturbance from the blade ends (expansion shocks and waves) pass through the flow core. One can see clearly that density is reduced in the expansion wave to the same extent as it almost recovered in the shock wave and nearly returned to the undisturbed area value—in the core's center, that is, the shock actually compensates for the expansion wave's impact on the flow. The entire disturbance system's intensity (expansion wave and shock wave) can be specified by the value $\Delta\rho/\tilde{\rho}_{\tilde{n}\tilde{e}}$, where $\Delta\rho$ is the difference between the recorded minimum value ρ in the expansion wave and the value

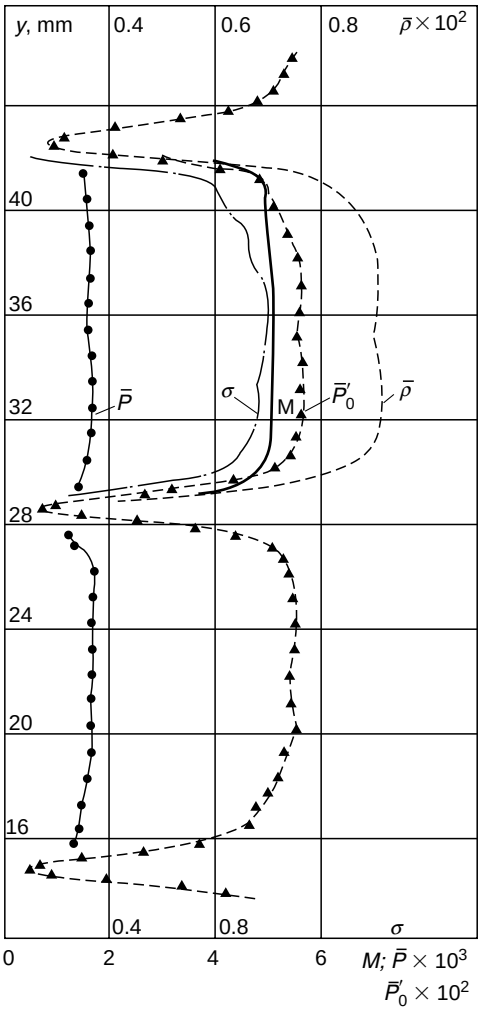

FIGURE 2.11 Parameter distributions at nozzle outlet—$x = 0$ (general picture).

after the shock, and $\tilde{\rho}$ is an average value in the flow core. Figure 2.13 shows these values: disturbance intensity rises as t grows and the α angle increases.

Boundary layer at the blade. In order to define the boundary layer's properties, profiles $P'_0(y)$ and $P(y)$ were gained at $x = -1$ mm. Based on these profiles the velocity distribution U/U_E is calculated (index E stands for the parameters at the wake boundary). Velocity distribution in the boundary layer is shown in Figure 2.14a (for two P_{00} values). The results can be approximated by the following exponential function (typical for turbulent flow mode):

$$U/U_E \sim (y/\delta^*)^n, \quad \text{at } n = 1/7.$$

The number Re_L according to the flow parameters in the nozzle's output section and its length equals $(1-4)\times 10^6$ at $P_0 = 7-30$ atm. Displacement thickness δ^* and momentum thickness θ_w is calculated by the usual method.

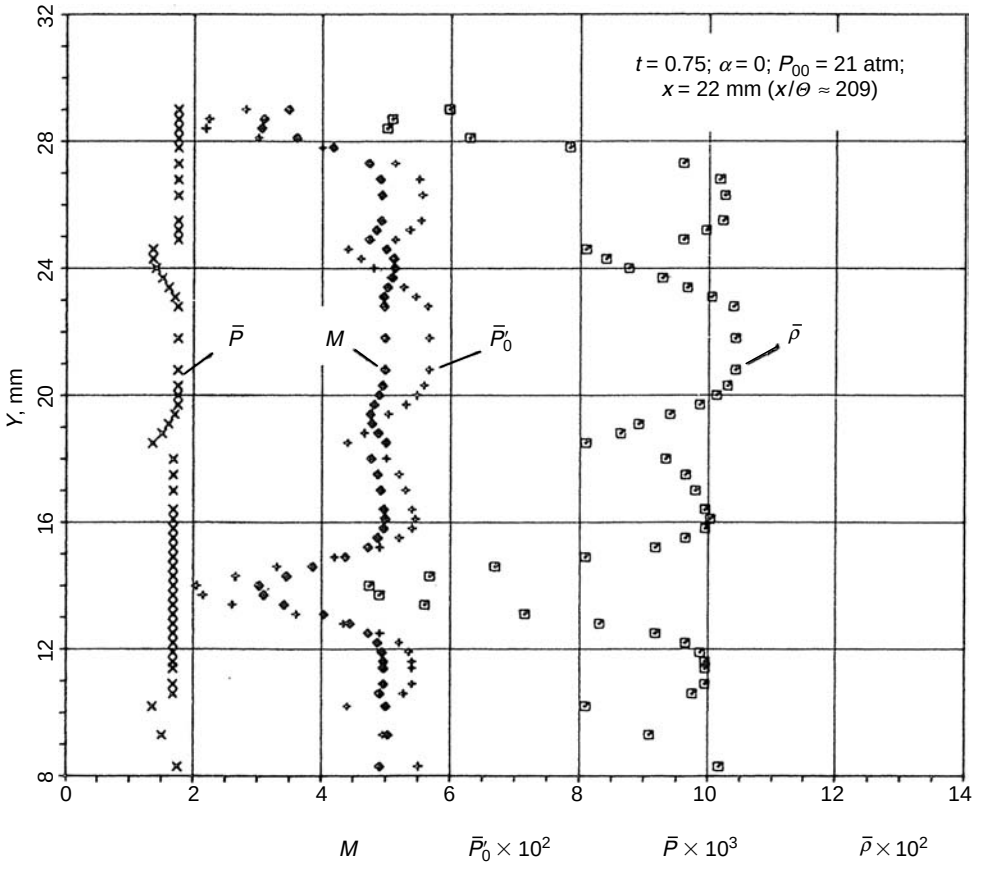

FIGURE 2.12 Flow parameters at $x = 22$ mm ($t = 0.75$ mm, $\alpha = 0$; $P_{00} = 21$ atm).

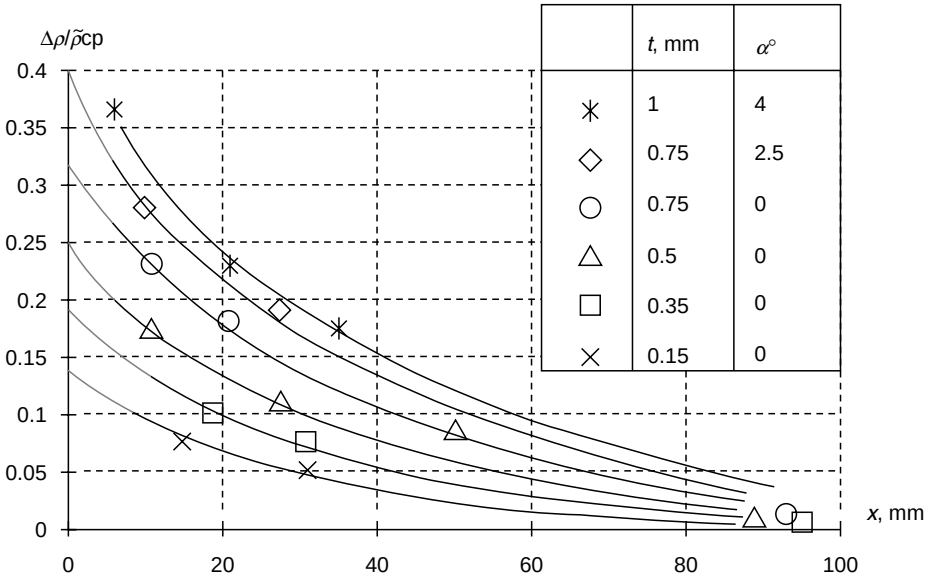

FIGURE 2.13 Intensity of expansion and shock waves system along the working channel.

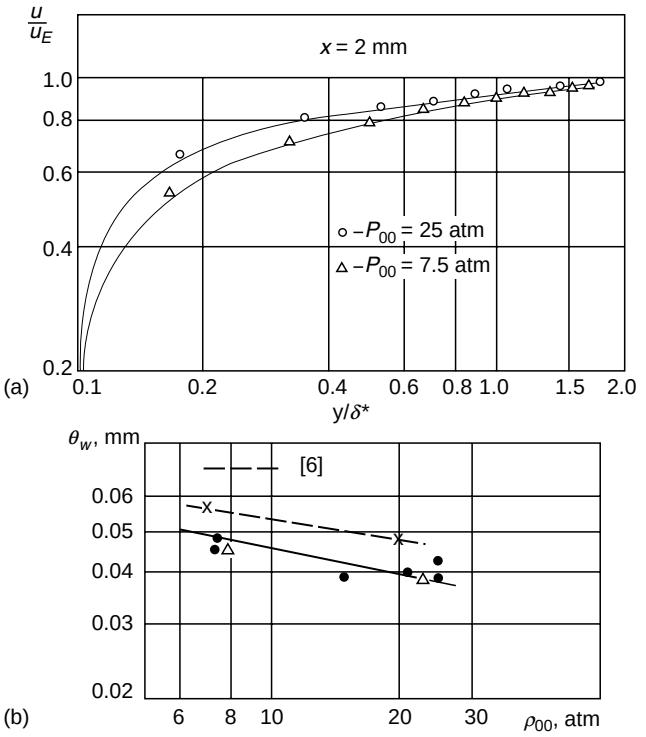

FIGURE 2.14 (a) Distribution of velocities in wall boundary layer at nozzle outlet: and (b) momentum thickness.

The obtained θ_w values at the nozzle exit are shown in Figure 2.14b. Here, $\delta^* = \int_0^\infty \left(1 - \frac{\rho U}{\rho_E U_E}\right) dy$ and $\theta_w = \int_0^\infty \frac{\rho U}{\rho_E U_E}\left(1 - \frac{U}{U_E}\right) dy$.

The results are represented in a dimensional view, though the nondimensional representation is more frequently used

$$\theta_w / L = f(Re_L).$$

The obtained data satisfy the approximate ratio $\delta^* \sim 1/P_\phi^{0.2}$ or the corresponding relation $\delta^*/x \sim 1/Re_x^{0.2}$, typical for a turbulent boundary layer.

As a reference, the picture shows the results of numerical calculation carried out in the narrow channel approximation. In [6], calculation was done by the integral method at a wall of minimum length nozzle (with an angular point at the contour) with application of a flat plate friction law. The data are represented as following:

$$\frac{4\theta_w Re_H^{1/7}}{H} = f(M),$$

where Re_H is calculated according to the parameters at the nozzle exit and the output section height. At $M = 5$ and $\kappa = 1.4$, the complex value is 0.110. As one can see numerical results coincide but they are a little higher than the experimental values. Since the calculation was carried out several times with application of various probes and they did not differ from each other, further on the test results for θ_w were assumed to be preferable.

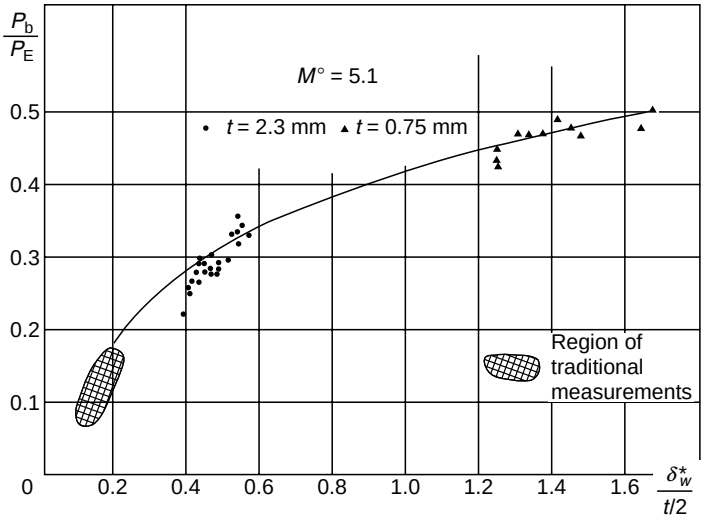

FIGURE 2.15 Base pressure at blade's edge.

Base pressure P_b. The value P_b has a telling effect on the nearest wake structure, for example, on step flowing [7]. On thick edge flowing intensive expansion waves completed by a shock wave emerge (Figure 2.10). The value P_b is influenced by relative thickness of the boundary layer δ/t. There are a lot of references on P_b dependence from δ/t, but they are generally obtained on numbers $M \leq 4$ and minor values of this parameter. Figure 2.15 specifies the approximate area of the existing results, that is, the obtained results widen the researched range by M and δ/t.

Flow core parameters. Figure 2.16 demonstrates the changes in the M number, pressure, and density along the flow in the core at the nozzle's axis: M_{E0}, $\overline{P}_{E0}$, and $\bar{\rho}_{E0}$ (pressure and

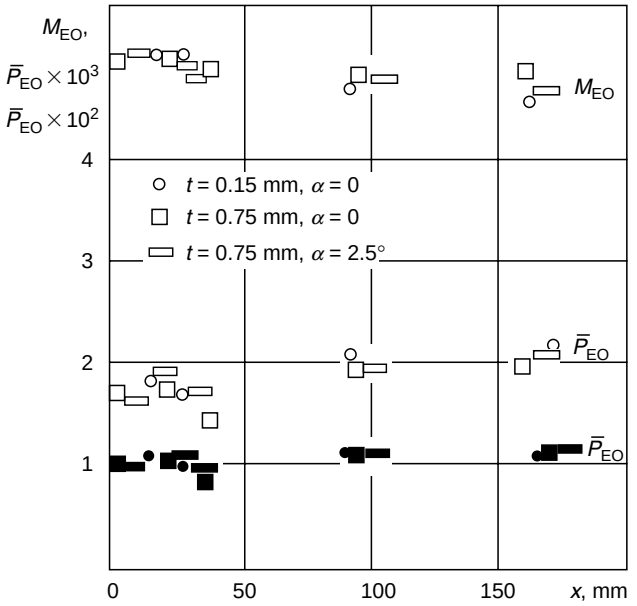

FIGURE 2.16 Flow parameters at nozzle axis along the resonator cavity.

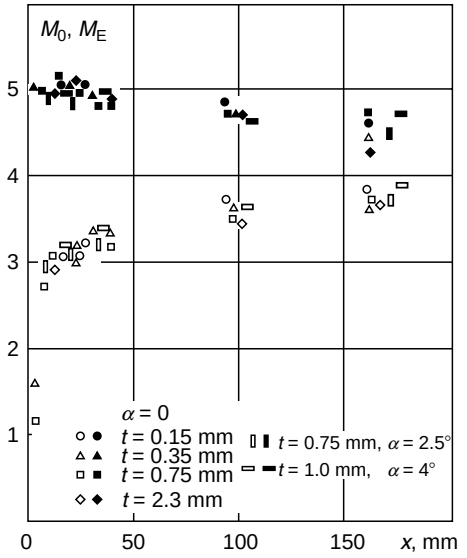

FIGURE 2.17 Mach numbers at axis and boundary of wake; light points—axis of wake; black points—boundary of wake.

density are related to their values in the forechamber). At the nozzle exit, the values as already mentioned are close to the rated values specified by the degree of nozzle expansion, while variations along a channel length are, as is obvious, minor. Moreover, to a great extent they are caused by the boundary layer growth at the model channel walls (the channel had constant cross-sectional area). At the spots where the expansion waves and shock waves coming from the blade edges pass the flow, parameters certainly experience disturbance—there emerge nonuniformities. Figure 2.13. gives a general idea of nonuniformities' extent for density. It is obvious that down the stream from the bank exit disturbance intensity decreases and behavior of M_{E0}, ρ_{E0} depends greatly on the live channel section. Estimation of boundary-layer displacement thickness proves that more than a half of the effect refers to this factor and the rest refers to flow non-isoentropy in the channel (weak disturbances from the walls, shocks, and friction).

Wake properties. Figure 2.17 through Figure 2.19 collate values along the axis and at the wake boundary—the Mach number—M_0 and M_E, density $\bar{\rho}_0$ and $\bar{\rho}_E$, pressure $\overline{P}_0$ and $\overline{P}_E$ (ρ and P refer to the forechamber values; picture symbols are common, they are shown in Figure 2.17).

In aerodynamics, wake research tests are generally carried out on a condition when the parameters are constant at the wake boundary, whereas here, it is not the case. The data also demonstrate parameter variation limits across the wake. Influence of t and α on the results has not been found for that matter ($t \leq 1$ mm and $\alpha \leq 4^\circ$).

It is a common practice that upon wake research, results are represented in the "far-field" wake variables. Far-field wake is an area with set universal mean motion properties (velocity and density) distribution, that is, the motion becomes self-similar. In this area, the wake's halfwidth b and maximum velocity fault $W_0 = U_\infty - U_0$ are described by asymptotic laws: $b \sim x^{1/2}$, $W_0 \sim x^{-1/2}$. A typical linear scale for a wake problem is the momentum thickness θ (as it is known [8,9] θ is a constant along the entire wake area). That is the reason why in nondimensional representation the coordinates are made nondimensional by θ, and the parameter distribution in section is given as fault variation—for example, for velocity as $(U_\infty - U)/(U_\infty - U_0)$.

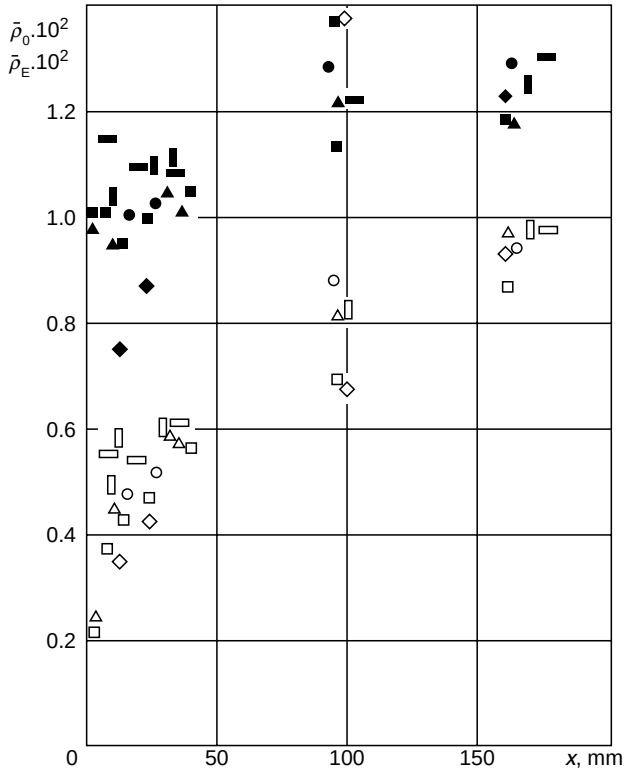

FIGURE 2.18 Density at axis and boundary of wake along the cavity.

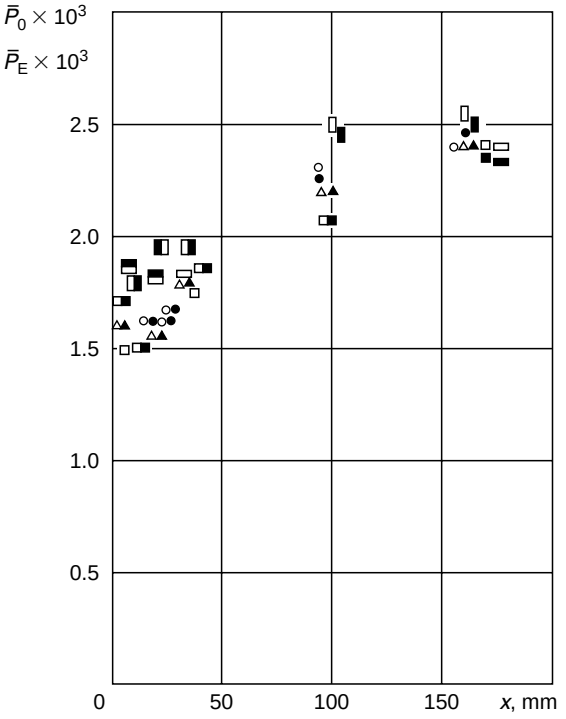

FIGURE 2.19 Pressure at axis and boundary of wake along the cavity.

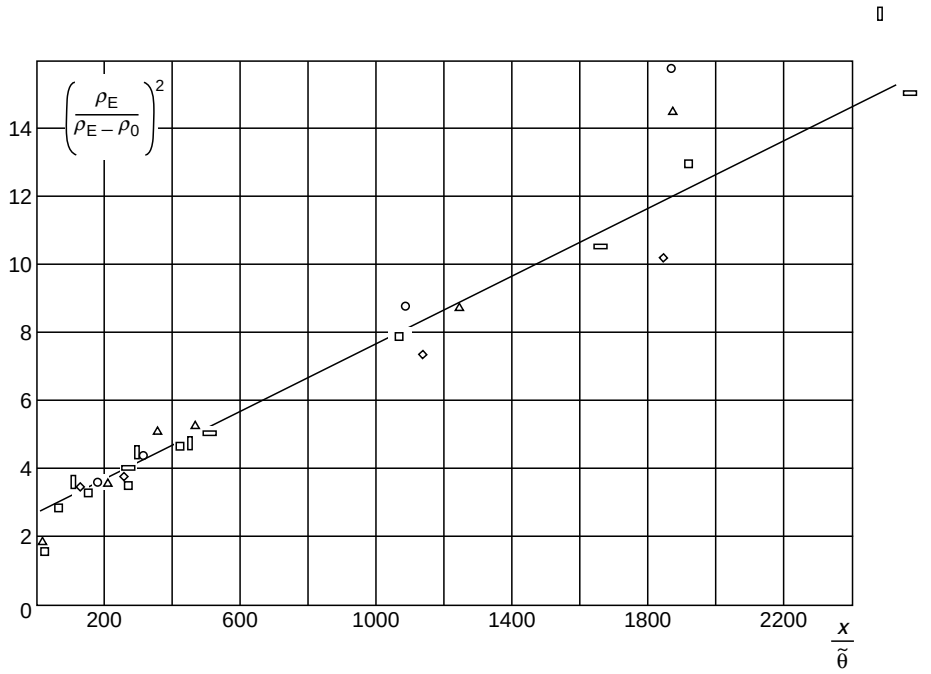

FIGURE 2.20 Density defect at wake's axis.

It is obvious that the border for separating a wake into near-field and far-field areas is not absolutely strict. In [10,11] one can see that a wake shall be specified by three areas. In the area of a near-field wake $x < 25\theta$—rate of growth b/θ and U_∞/W_0 are large when compared with their rate of growth in the asymptotic state. Geometry and rear edge thickness influence the stream here. In the "intermediate" area–$25\theta \leq x \leq 350\theta$, the wake is developing as a free turbulent stream and it is here that the asymptotic distribution for velocity is established, that is, local self-similarity [12]. In addition, when $x > 350\theta$, there is the far-field wake area. From a physical standpoint, as proved in [13], these three wake development areas are specified by a mixing degree of two boundary layers coming from the rear edge.

Variation of maximum faults of density and velocity behind the nozzle blades is shown in Figure 2.20 and Figure 2.21 (external flow conditions are applied here U_E and ρ_E rather than conditions at infinity U_∞ and ρ_∞). One can see that maximum faults are altered in proportion $(x/\tilde{\theta})^{1/2}$ that is, in our case we also obtain certain wake theory ratios. The point is that here $\tilde{\theta}$ is taken as a nondimensionalizing parameter—it is the average momentum thickness value for the entire measurement area and for all the blades. As mentioned before for the unlimited flow $\theta = constant$ in our conditions, there exists an axial pressure gradient and θ alters slightly. That is the reason why during processing $\tilde{\theta}$ is applied (for information on the value $\tilde{\theta}$ see below). The line in Figure 2.21 corresponds to the measurements obtained in an incompressible isobaric wake [8,11,14]. Results obtained in [9,10] at $M = 2$ and 3 relatively, that is, in a compressible case actually come in line with these data. Whereas in our tests at $M_E = 5$, velocity fault at the wake axis decreases more slowly.

Cross-section distribution of flow parameters in the wake in far-field wake variables is shown in Figure 2.22. There are results for a thick blade where $c\ t = 0.75$ mm and a thin one where $t = 0.15$ mm. Points are plotted from all the cross sections. The value b is the wake's half-width(it is related to $\tilde{\theta}$) and is defined with the coordinate where velocity equals half of

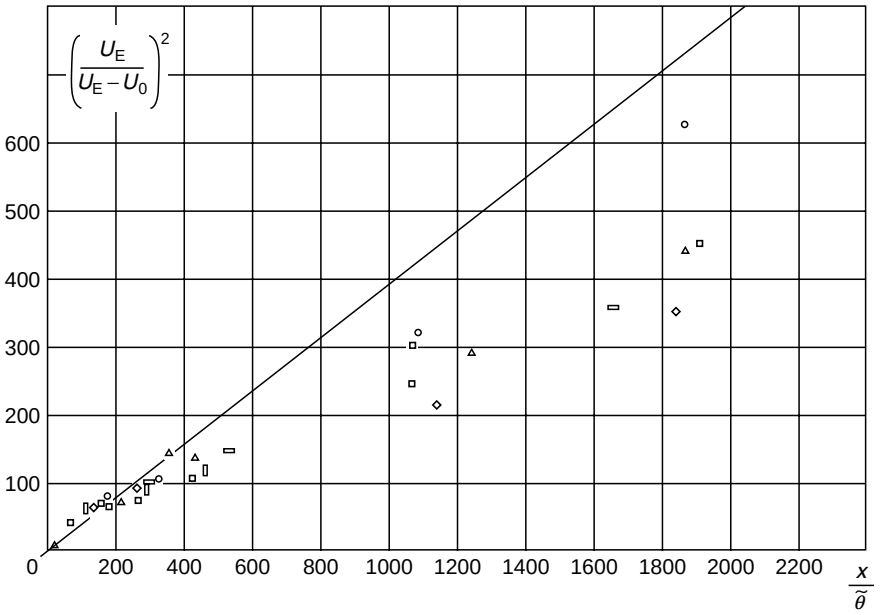

FIGURE 2.21 Velocity defect at wake's axis.

the sum of U values at the axis and at the boundary, that is, at $U=(U_E + U_0)/2$. Upon $y=0.5b$ velocity fault $(U_\infty - U)/(U_\infty - U_0)=0.5$. The results prove that in spite of the presence of disturbing factors all the points (taking into account experimental dispersion extent) fall on a universal curve. It all goes to show that the flow pattern in a wake and in our case is actually left self-similar and that t and α did not affect the flow pattern (data for all the other banks coincide with the ones shown in Figure 2.22). Thus, the idea of flow self-similarity in a wake expressed in [15] and supported in numerous tests both in incompressible and compressible flows, for example in [8–11,14], is also true both for the problem considered at $M=5$ and when a wake is under the impact of disturbances of special character (expansion wave and shock wave).

Just as in other researches velocity distribution is approximated (as well as in the case of the incompressible isobaric wake)

$$\frac{U_E - U}{U_E - U_0} = \exp\left[-0.69\left(\frac{y}{b/2}\right)^2\right].$$

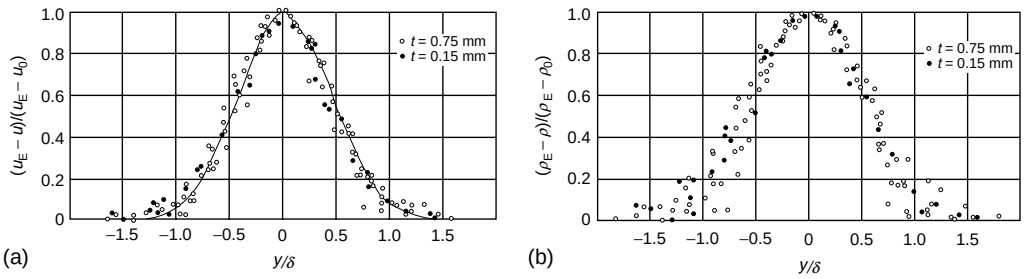

FIGURE 2.22 (a) Transverse velocity profile and (b) density profile in terms of far wake.

As emphasized above, the parameters in the wake were calculated on the basis of a condition of consistency of T_{00}, that is, as a matter of fact, the identity of temperature and dynamic profiles was established, even though the incompressible fluid experiments proved that the temperature profile is a little wider.

$$\frac{T_E - T}{T_E - T_0} = \exp\left[-0.45\left(\frac{y}{b/2}\right)^2\right]$$

As the velocity distribution in our tests coincided with the acknowledged results, it was also assumed that the temperature profiles would be the same as in [9,10] at $M = 2$, 3. The density profile has a similar view. It can also be defined on the basis of the temperature profile with the constitutive equation and the condition of pressure consistency across the wake.

Momentum thickness and wake thickness. Thus, the momentum thickness θ is a typical linear scale in the wake theory. This value as demonstrated in [8,9] equals the body resistance factor—wake generator—by virtual body thickness, that is, the value is constant. In our case, as the flow is not unlimited and there are variations of P_E along the wake, it is not observable. For a plate in an unlimited incompressible flow, the theory and the experiment provide a mere connection of θ and the momentum thickness in the boundary layer at a plate's end: $\theta = 2\theta_w$.

Figure 2.23 represents the data observed in our conditions. The same way as earlier, points for all the blades are plotted; they were obtained at $P_{00} \approx 20$ atm. It is obvious that the points are located a little higher than the line $\theta/2\theta_w = 1$. On flowing round the edges of some thickness the boundary layer coming from a blade first undergoes an intensive expansion wave impact and apparently a trailing shock wave does not compensate this impact completely. Thus, points for a very thick blade ($t = 2.3$ mm) on all the parameters' processing (e.g., wake thickness) are always located higher than others. However, noticeable difference of θ from an average value is only observed at the beginning of the wake ($x < 20$ mm). That is the reason why in the case of practical applications, average value of $\theta - \tilde{\theta}$ can be assumed constant

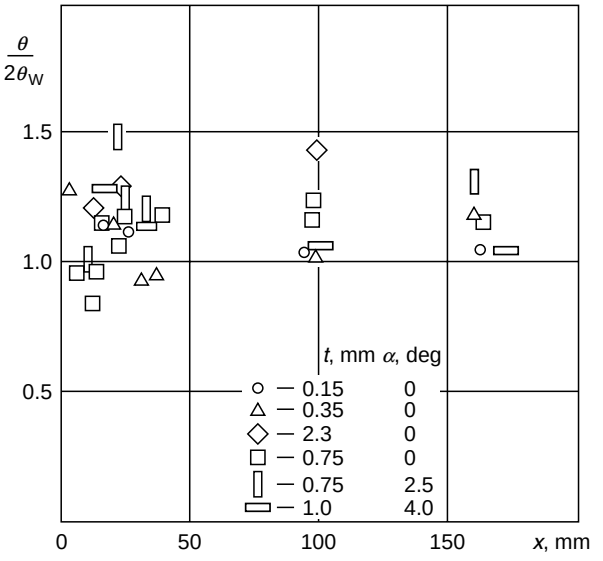

FIGURE 2.23 Momentum thickness in wake.

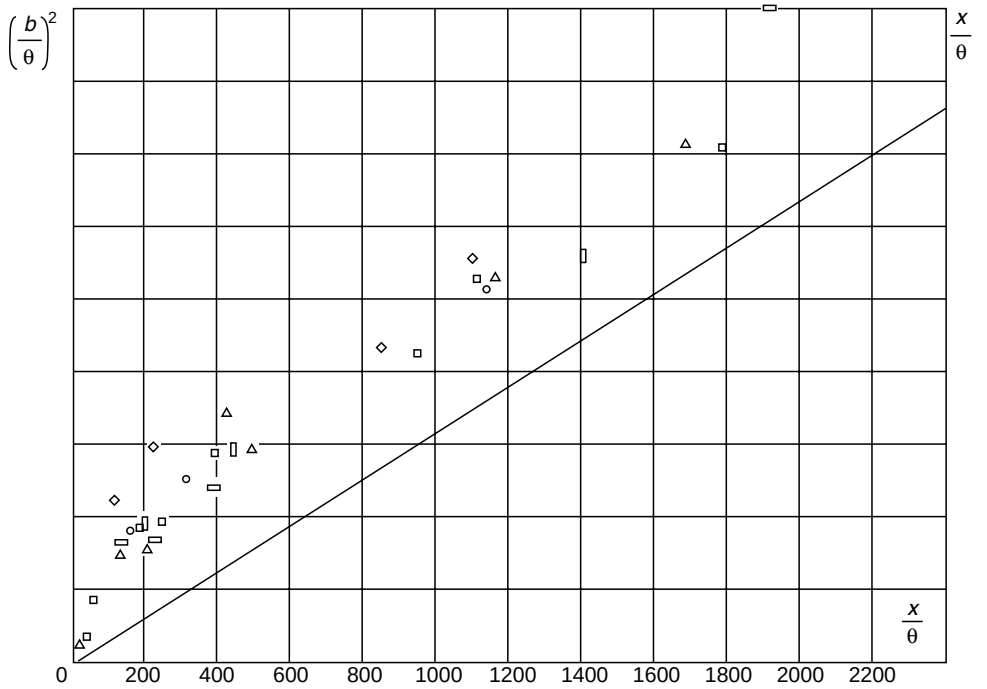

FIGURE 2.24 Wake thickness along the flow (θ—local momentum thickness value).

along the entire area and one can consider that $\tilde{\theta}$ is not affected by the t and α parameters (in the value range under consideration: $t \leq 1$ mm, $\alpha \leq 4^\circ$), and its value is $\tilde{\theta} = 2.2\,\theta_w$.

Figure 2.24 shows the dependence of the wake thickness b on distance and θ is a local momentum thickness value. It is obvious that the obtained results are colligated as usually by the connection $(b/\theta) \sim (x/\theta)^{1/2}$. The diagram line stands for connection $b(x)$ for an incompressible case [8,14], that is, points for this wake generator lay higher. Generally to combine the location of experimental points with the central point of coordinates, a virtual wake origin x_0 is introduced. The parameter x_0 is defined for each wake generator in an experiment, that is, it is empiric and depends on the generator's configuration and the R_e number. (Technically, it means transferring wake thickness increase mechanisms to the laws of wall boundary layer growth). In this case, it was obtained $x_0/\theta = 380$.

Figure 2.25 shows the results of correlation $b(x)$ for the GDL blades but rebuilt with respect to x_0, and instead of θ there is an average value $\tilde{\theta}$, which basically extended the spread of points but it makes practical application of the data obtained easier. Noticeable difference of the points from linear dependence for the incompressible case is only observed at the initial cross section $\tilde{x}/\tilde{\theta} \leq 500$. This dependence can actually be considered as an expression of the Townsend law of wake independence on Reynolds number.

On pulsation properties in a wake. Detailed studies of turbulence characteristics in a supersonic wake behind a thin plate were carried out [16,17]. The transition of flow stream from laminar conditions to turbulent ones [17], that is, all the three wake areas have been reflected: near-field, intermediate, and far-field ones. Figure 2.26 and Figure 2.27 represent the data, which are of the greatest importance to us.

Figure 2.26 shows variations in the pulse intensity ρ and U along the wake, and Figure 2.27 shows variations in integral scale of density turbulent pulses Λ_L. As one can see, pulse

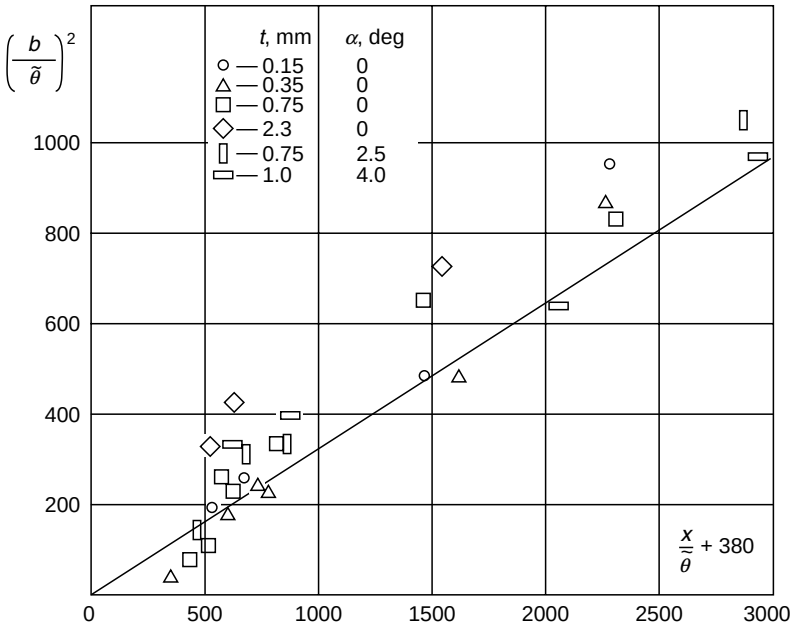

FIGURE 2.25 Wake thickness ($\tilde{\theta}$—averaged value θ; x_0—virtual wake beginning).

intensity ρ in the turbulent wake area almost stops altering and the scale $\Lambda_L \sim L$ (L is the transversal scale in a wake, e.g., its half-width).

Depicted results can be considered an empiric method of defining mean flow parameters behind the blade nozzle bank in the first approximation. The flow is reckoned to consist of a core, in which the parameters are constant in a transversal direction and vary along the stream and a wake area. Parameters at the exit of a certain nozzle are defined by its expansion degree with correction on boundary-layer displacement thickness δ^*. There are

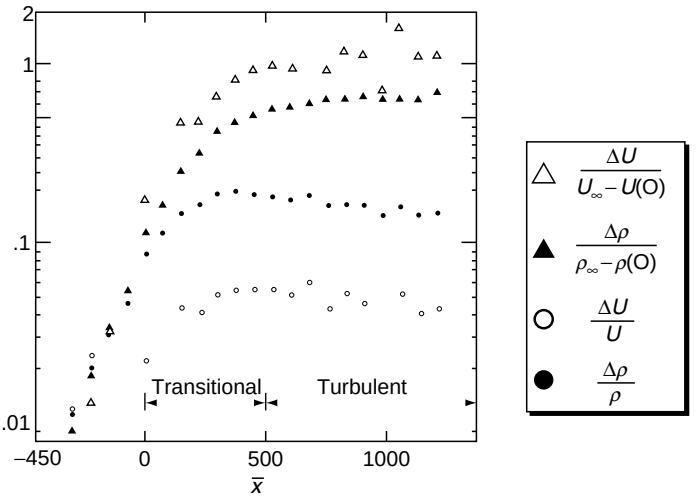

FIGURE 2.26 Intensity of pulsations in wake.

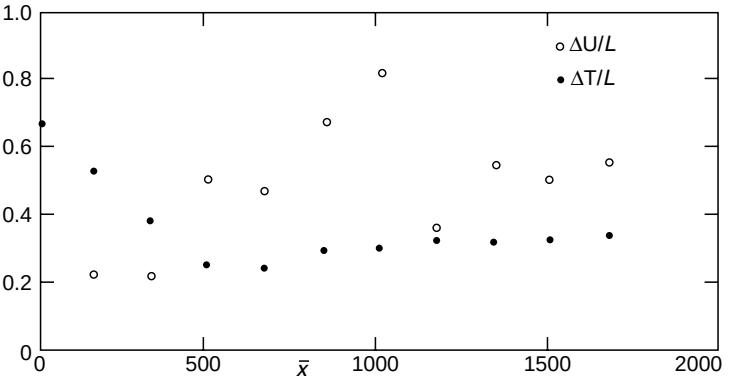

FIGURE 2.27 Integral scale of density pulsations Λ_T (L—wake's width).

a number of calculation methods and empiric correlations including the ones mentioned in this research to estimate δ^* and momentum thickness at nozzle exit θ_W. Core parameters correspond to the conditions at the wake's external boundary and they are estimated on the basis of Figure 2.17 through Figure 2.19. The point is that it is necessary to take into account that the model channel walls' boundary layer had considerable impact on the extent of parameter variations. In real conditions when a channel's height is substantially higher, the effect will lessen. At that the extent of parameter variation will approximately be less by half. Thus, the velocity variation at a 160 mm length is 2.5%, if there is no boundary layer impact the variation will be 1.2%. Parameter variation pattern can be approximated by lines (e.g., $\rho_E/\rho_{E0} = 1 + ax$). Wake axis parameters will be defined on the basis of their defect distribution in Figure 2.20 and Figure 2.21, at $\tilde{\theta} = 2.2\theta_W$. Parameter distribution in a wake's cross section is found with approximation expressions for U, ρ, and T.

The main conclusion is as following: within the range of the executed measurements ($x \leq$ 160 mm) the distribution of mean velocities and density in a wake behind a certain blade of a blade MNB is universal in spite of disturbances coming from the adjoining blades, and the wake width is described by the asymptotic law: $b \sim x^{1/2}$.

2.2.2.4 Impact of Real Blade Nozzle Bank Assembly Defects on Flow Gas Dynamics

In the previous paragraph, we considered flows behind the banks of an ideal assembly: there was no displacement of the blades forming one nozzle in relation to each other; all the nozzles were of the same critical cross section permanent along the entire blade length, and so on. In reality, some way or another, the situation is reversed: there are both displacements and dispersion in throat dimensions. Apart from this, uncooled blades of big size (more than 150 mm) bend right after the first starts when affected by thermal stresses. The fact causes an increase in throat dispersion and throat inequality in the blade height. Thin blade edges break off. Therefore, the impact such defects have on mean flow parameters is examined in this section briefly.

Deviation of a certain bank nozzle's throat dimension from the design value. Figure 2.28 juxtaposes an overall pattern of a flow behind an ideally assembled bank (Figure 2.28a) and the cases when a bank has a defective nozzle the throat of which differs from the designed one h_0^*. First of all, it is obvious that as soon as such a defect emerges the wakes start distorting. They bend toward the side of the smaller density flow: when $h_1^* < h_0^*$—the throat in the

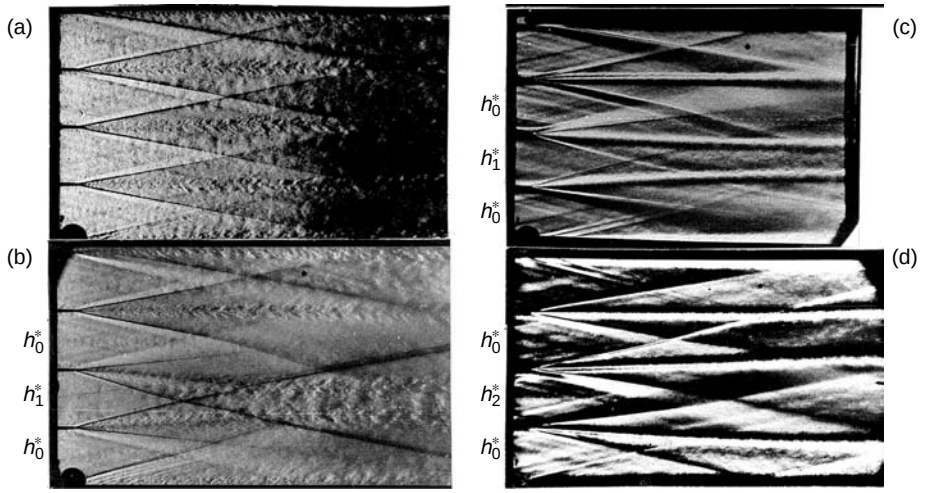

FIGURE 2.28 Photos of flow behind the nozzle bank with deformed nozzles: (a) all throat equal ($h_0^* =$ 0,49 min); (b),(c),(d) $h_0^* = 0.49$ mm, $h_1^* = 0.22$ mm, $h_2^* = 0.8$ mm.

adjoining nozzles, in this case the wakes converge, and, on the contrary, the wakes diverge when $h_2^* > h_0^*$. The case of "converging" wakes is represented by pictures obtained with a vertical and horizontal knife (Figure 2.28b and Figure 2.28c), the case of "diverging" wakes—with a horizontal one (Figure 2.28d). Wakes converge (or diverge) until the densities in adjoining flows divided by wakes get leveled off, and then they become parallel again.

Violation of the strict pattern of a flow's layered structure with parallel wakes, is only possible during ideal assembly (Figure 2.28a and Figure 2.9), emerging of areas with nonparallel boundaries and density varying visibly along the flow causes, first, difference in mean optical paths by resonator's aperture, that is, decrease in optical quality of the medium (and consequently decrease in laser radiation quality), and second, it also causes resonator deficiency because of its beam course deformation. In this case, the beams will diverge, that is, experience a refraction effect, as they do not pass completely perpendicular to the boundaries of various densities media the same way as on ideal assembly (the resonator is generally located right behind the blade bank exit). Direct measurements of W—output GDL radiation power—prove it. The more considerable is h^* dimensions dispersion in a bank, the greater is the W value reduction—with other conditions similar—than in the case of ideal MNB assembly, that is, the resonator's efficiency really decreases.

Apart from wake deformation, there may also emerge alteration of a flow mode in a narrowing flow core. Figure 2.28b shows that starting with $x = 30$ mm when wakes come close enough to each other they start interrelating and turbulize the entire flow area between the wakes. Since the flow area in the resonator cavity occupied by the turbulent flow grows, such an effect causes a decrease in the optical quality of the medium.

Further on, in reality the critical cross section does not change uniformly along the entire blade length as it happens in this model experiment. Bank blades can bend and consequently areas with different mean density by channel height emerge in the flow, that is, optical paths by resonator's aperture become different, and this factor as mentioned above means deterioration in the output radiation quality.

Blade slots. Because of thermal stress, a blade bends and its thin edges break off. In order to reduce the effect it was offered to make slots in a blade to relieve the edges from the stress. Such a bank ($t = 0.5$ mm, $\alpha = 0$) with slots exit in the middle of blades was tested. Notch width

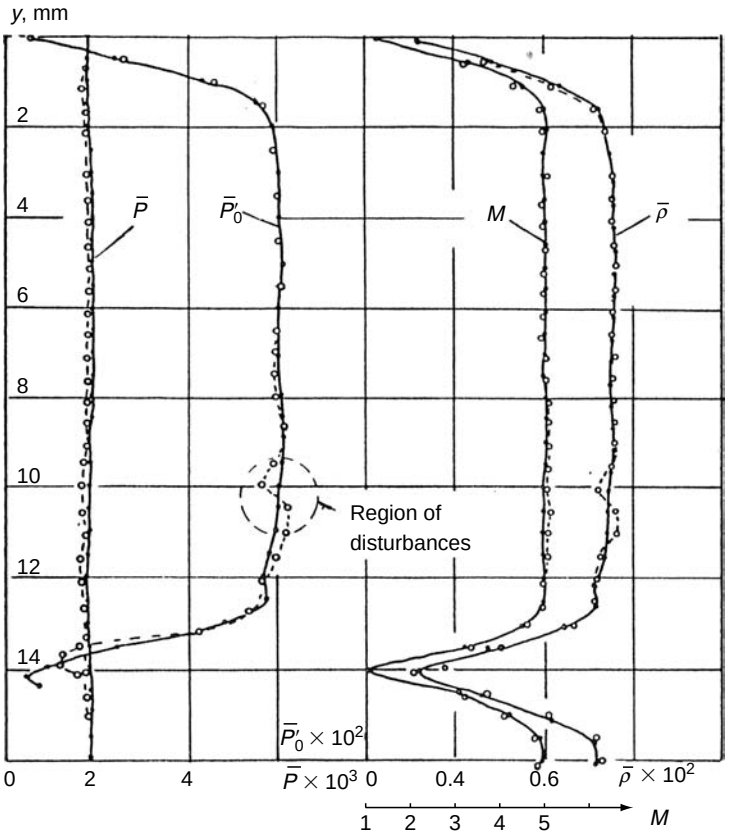

FIGURE 2.29 Influence of slots in blades on flow parameters at nozzle bank outlet; $x = 0$, $\Delta = 0$, slot; •—closed, ○—opened slot.

was $\Delta = 0.35$ mm, length = 15 mm. Figure 2.29 shows the nozzle exit parameter distribution ($x = 0$) for an ideal assembly bank. The measurements were made in the slot plane. Measurement of coordinate y is made from the middle of an end-butt of an adjoining blade. Light points mean that a slot is open, dark points mean that a slot is puttied and the slot's profile is restored completely. Parameter disturbance in the area $y = 9$–11 mm is the result of the slot exit in a blade. Maximum density variation is $\Delta\rho/\tilde{\rho} \approx 5\%$.

The pattern of slot flowing around is the same as in a blade edge: in the slot root, at the step corner the flow turns round—there emerges an expansion wave (in cross section $x = 0$ this area passes through $y = 9$–10 mm), and the shock wave where the flow turns back passes through $y = 10$ mm. Disturbances from the slot beginning spread under approximately the same angles as the disturbances from the blade edge and fade out at about $x = 30$ mm distance (in case of the ideal bank assembly).

Disturbances consist of compression and expansion areas, but density deviations from the average value are close, that is the reason why the optical path along the slot will be the same as above and below the slot, that is, wavefront aberration by aperture are minimal. However, the pattern changes when a bank is distorted.

Combined effect of blade slots and throat dimension fringe in a bank. There are results for a bank with a distorted nozzle of critical cross section $h^* = 0.22$ mm, and the others are of

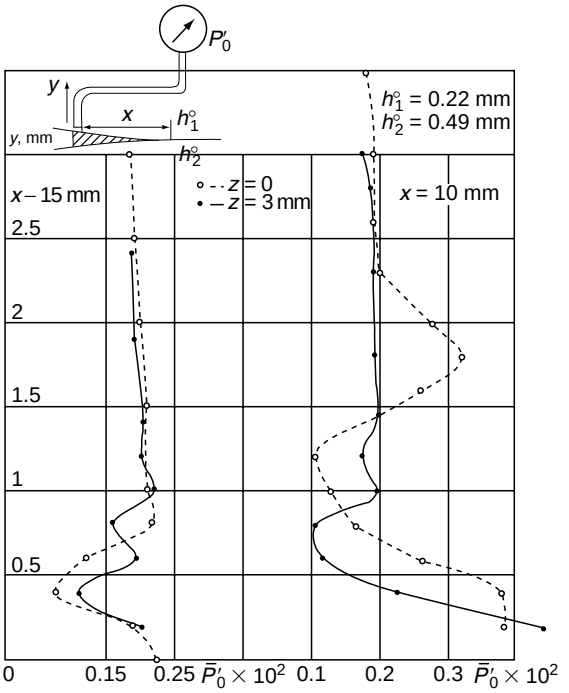

FIGURE 2.30 Results of measurements by vertical Pitot tube under slot ($z = 0$) and not under slot ($z = 3$ mm).

a design critical cross section $h_0^* = 0.49$ mm. First, P'_0 was measured inside the nozzle with a special-purpose vertical probe right above the slot ($z = 0$ mm) and a little away from the slot ($z = 3$ mm). Figure 2.30 shows the results and the test diagram. The $\overline{P}'_0$ values above the slot and beside it do not differ much ($\overline{P}'_0$ is much less than the value measured in this spot by the horizontal Pitot tube), that is, actually the gas is not blown through the slot in a nozzle with minor H/h^*.

Figure 2.31a represents the flow parameters at a bank exit from both parts of a blade (a slotted one), which divides distorted nozzles of $h^* = 0.22$ mm and an undistorted one. It is obvious that the wake in the slot plane does not coincide with the wake of the entire blade (unlike the ideal bank assembly case). The wake behind the slot step is distorted in the same way as the entire blade's wake but it begins earlier (at $x = -15$ mm) and to the blade exit ($x = 0$ mm) is had already diverged from the axis by 2 mm. As it is observed on the basis of measurements, in the cross-section 7, 20, and 50 mm (the cross-section 7 is shown in Figure 2.31b), the further slot wake development leads to the fact that a layer with properties differ greatly from the adjoining areas is formed in this plane. It is a layer of significantly expanded wake. Nonuniformity covers all the flow core area from one wake to the other.

It was even possible to visualize a narrow layer with different density in a flow behind the slot. Figure 2.32 shows the corresponding pictures (the blade is horizontal). The top picture represents an ideal assembly case where all the critical cross sections are equal, and the bottom one represents a bank with a distorted nozzle. The pictures are taken across the blades rather than along them as in Figure 2.28 (through the top and bottom windows), that is, along the

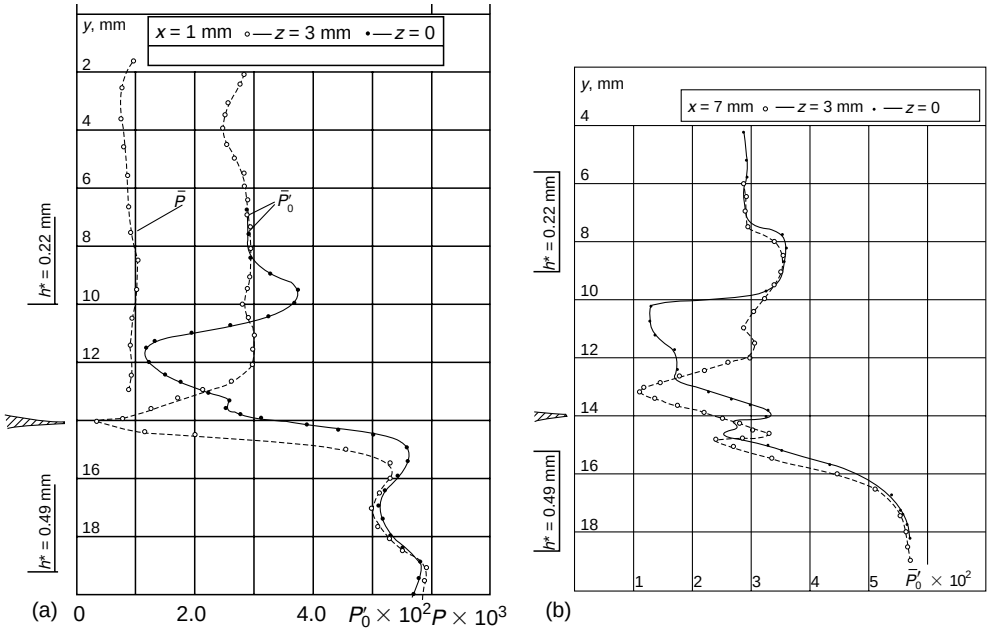

FIGURE 2.31 Joint influence of slot and difference of h^*: (a)—cross section $x = 1$ mm; (b)—cross section $x = 7$ mm.

axis of an assumed resonator (through the side windows). The shock waves coming from the nozzle neck and from the glass joints (at the top and bottom windows) with the operation area have been marked. It is obvious that the shock inclination angle from the neck depends on the nozzle's expansion degree. That is the reason why for an ideal assembly bank all the shocks coming from the throat area converge into one in the picture, whereas in the distorted bank case as much as two shocks have been recorded. The fact that the flow area occupied by the shock waves whose plane is parallel to the resonator's axis increases in the second case is also a disadvantage from the point of view of optical quality of the flow.

Thus nonuniformity forms along the resonator's axis in the slot plane in a distorted nozzle bank that will cause wavefront aberration at the resonator's output, that is, it causes radiation quality deterioration (apart from the results represented here some data for other h^* values that differ from h^*_0 to a smaller extent also have been obtained. From the qualitative standpoint all the effects observed in the flow are preserved). As it is impossible to avoid differences in h^* in a real bank and right after the first starts the h^* values variation generally increases, the structural solution of the blade edge "relief" as a slot cannot be considered satisfactory one.

Blade displacement relative to each other. Figure 2.33 demonstrates the result of a nozzle's halves displaced relative to each other. The data are obtained for different displacements Δ, and there were selected different h^* so that distributions $\overline{P}'_0$ and $\overline{P}$ could not converge on the graph. Displacement leads to a situation when at a nozzle's output from one side a shock wave is recorded and on the opposite side an expansion side is recorded. Disturbances are certainly formed in the neck. Upon displacement of $\Delta \approx h^*$ (such displacements are real taking into account the fact that in the present day GDLs $h^* = 0.1$–0.2 mm) disturbances become noticeable.

The measurements prove that in a general case disturbances caused by various factors (slots, displacements etc.) a summed up intensifying each other. In addition, from the

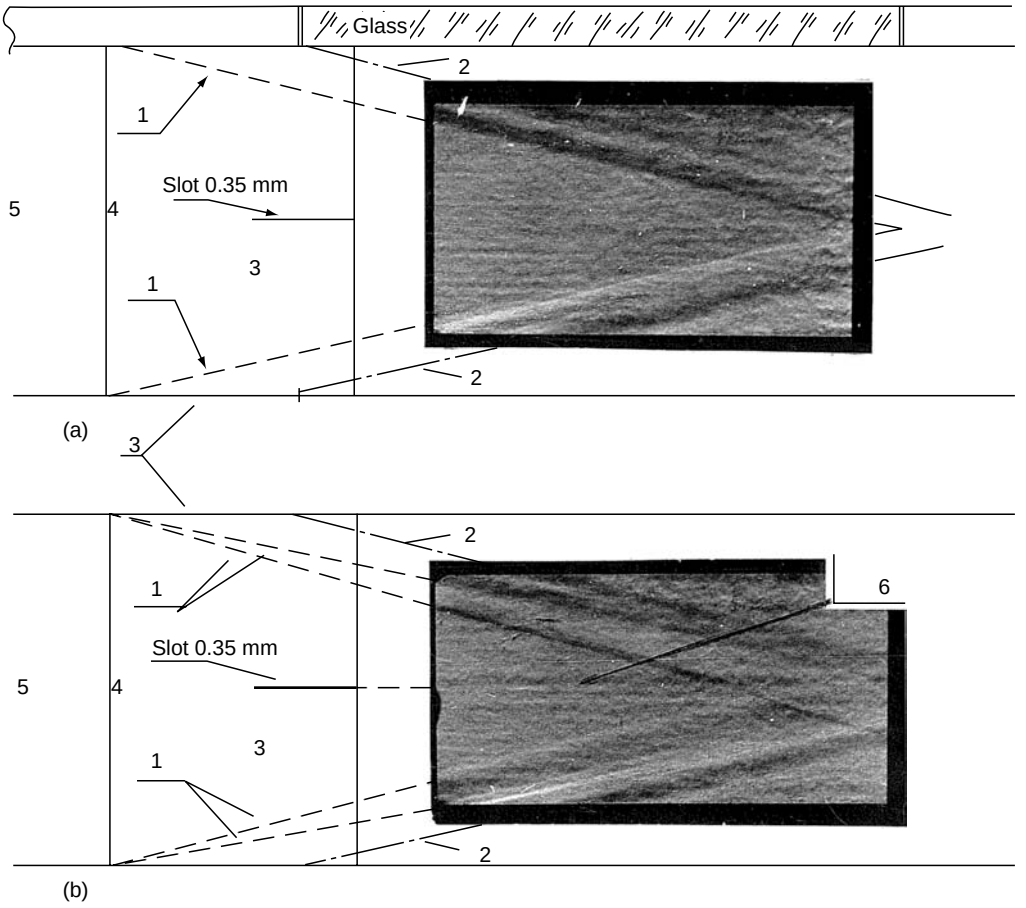

FIGURE 2.32 Flow field behind the blades with slot. 1—Shock waves from the throat; 2—shock waves from the joint of glass with wall; 3—supersonic part of blade; 4—throat of nozzle; 5—subsonic part of blade; 6—wake as a result of slot existence. (a) All throats are equal; (b) throats are different.

standpoint of their influence on optical flow uniformity they are similar. All the faults cause emerging of density nonuniformities and flow symmetry violation, whereas in a general case both these factors affect the optical quality of the medium. Thus, the tests prove that the flat structure of nozzle banks (especially when blades are of a big height) turns to be quite sensitive to the effects of real assembly factors and real operation conditions. A screen MNB structure appears to be more "stable" from the mentioned standpoint.

2.2.3 Three-Dimensional Structure of Flow after SNB

2.2.3.1 Models and Their Geometry

A screen nozzle bank—in its most simple version—is a plate with small-dimension axisymmetric nozzles drilled in it. The plate is fixed between flanges separating the forechamber from the operation channel. It is such a version that was applied in gas dynamic tests. Figure 2.34 shows a bank's layout drawing for an operation channel of the 21×80 mm cross section. Also channels of the 41×80 mm and 51×60 mm cross sections were used. The 41×80 mm

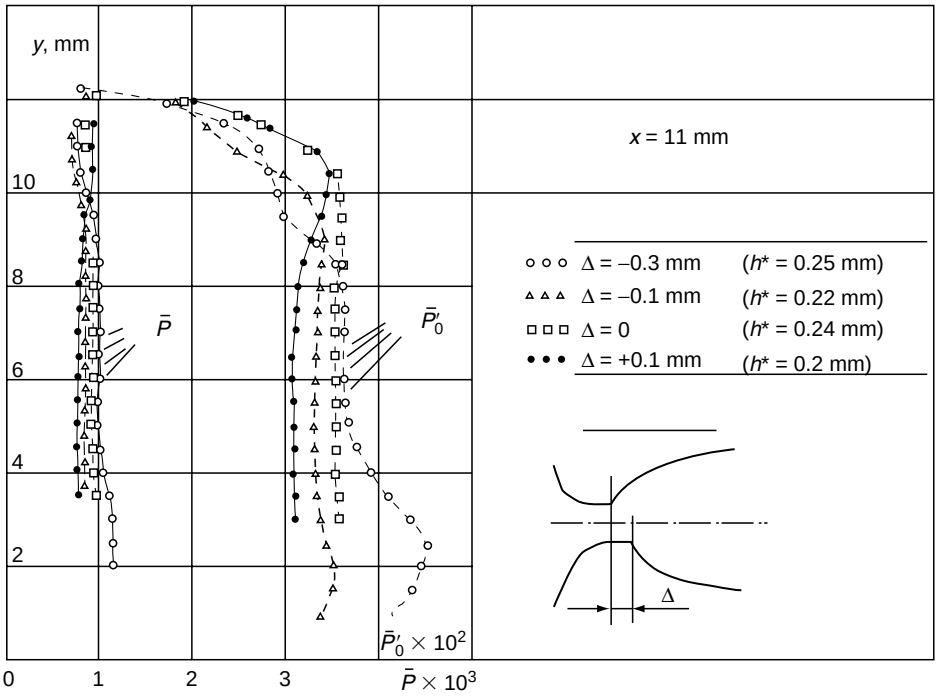

FIGURE 2.33 Blades' displacements relative to each other (distribution of parameters at $x = 11$ mm).

channel banks are similar plates with a big amount of nozzle rows (for the 51×60 mm channel—the bank view is shown in Figure 2.59, they were mostly used in aero-optical tests).

The subsonic section of SNB was of the same type: each micronozzle had a conic input of the 60° semiangle. Critical cross section of all the micronozzles is a cylinder area of ~0.5 mm, and the supersonic section is either conic or profiled. The bank's main geometrical parameters are specified in the table below.

Here d^*, d_e are the diameters of an output and a critical cross section of a micronozzle; l the length of the profile's supersonic section; A^*, A_e the areas of a throat and an output cross section of an individual micronozzle; ΣA^*, ΣA_e the total areas of the throats and the output

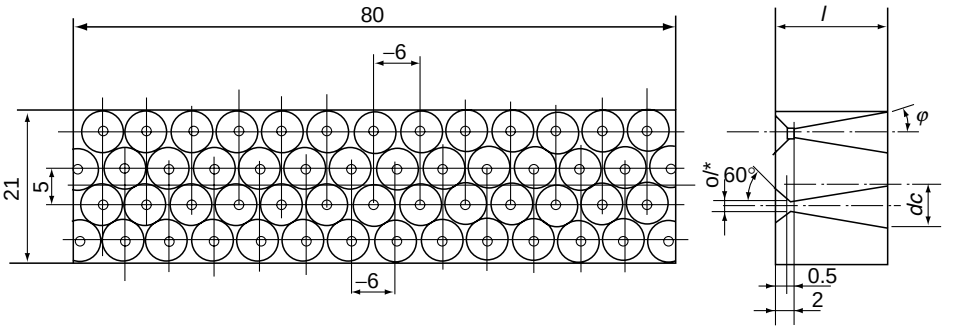

FIGURE 2.34 SNB geometry.

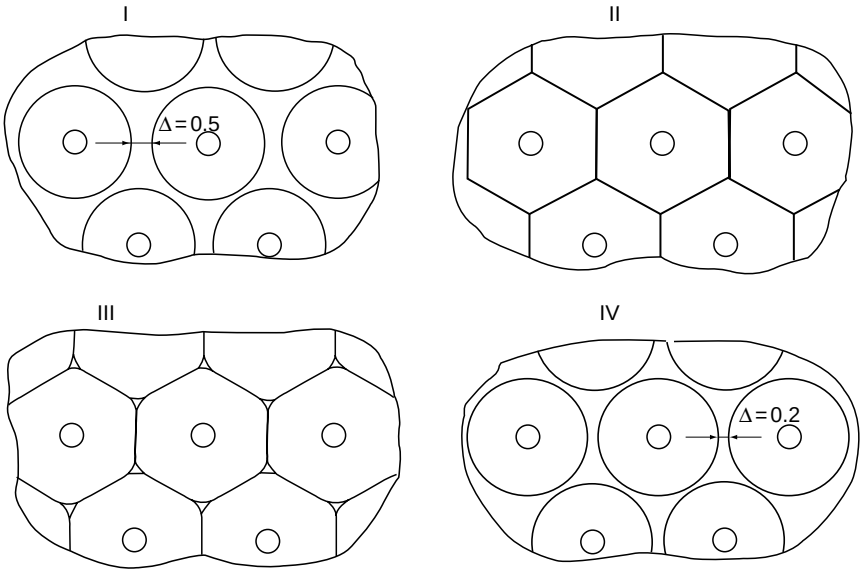

FIGURE 2.35 Base areas of different models.

cross sections in a bank; A_f the channel cross-section area; M_e^0 and M_f^0 the geometrical Mach numbers defined on the basis of correlation A_e/A^* and $A_f/\Sigma A^*$ relatively; φ is the semiangle of a micronozzle's conic expansion.

Versions of banks III, IV had profiled micronozzles (calculation methods for the profiled nozzles are specified, for example, in reference [18]). However, the nozzles had an exit profile rather than a full-size one: in bank III at the spot where the flow trailing angle is $\alpha = 1^\circ$, and in bank IV, $\alpha = 4^\circ$. Owing to this difference in bank widths, the l value of the base areas changed. Figure 2.35 shows details of the banks' output cross sections. In banks II and III, cross sections of adjoining micronozzles intercrossed and in the table, the value A_e corresponds to this hexagon. $\Sigma A_e/A_f$ specifies the base areas value and it is not equal to 1 even for bank II, as there are base areas at the bank edges ($\Sigma A_e/A_f$ is closer to 1 for bigger channels). Nozzle packing in bank V corresponds with version I. Measurement results for SNB were compared with the blade nozzle data the geometry of which is also specified in the table.

2.2.3.2 Pressure Field Measurement Results—Overall Pattern

Pictures of flow patterns behind the conic banks of $\varphi = 10^\circ$ are shown in the next part in Figure 2.59, Figure 2.62, and Figure 2.63 (on visualization in the 51×60 mm channel the $d_e = 5$ mm MNBs were used; the entire bank geometry is specified in a table of Section 2.4 of Chapter 3). Pictures made with a vertical knife (Figure 2.59) show a shock-wave structure—the shocks are formed right at the micronozzles' output. However, at a distance of $x = 60$–70 mm from the bank exit the shock intensity reduces and further on they are not recorded any more even with the Schlieren method. Pictures made with a horizontal knife (Figure 2.63) show that in the flow field a layered structure of nonuniformities is clearly seen starting at $x = 50$–60 mm. It is specified by the presence of wakes that are formed behind the banks' base areas—by intersections between the rows. Wakes are formed not only behind

the solid intersections (Figure 2.62, View B—wake period 4.5 mm), but they form a complete wake also behind the intersections that come in a row (Figure 2.63, View A of wake period 2.5 mm). As it is known, wakes in the supersonic conditions stretch for a long distance; they are recorded clearly in the area of $x = 200$–250 mm. The wakes specify the main structure of regular density nonuniformities in the resonator's cavity.

Pressure field measurements were carried out for all the banks in the cross-section range of $x \approx 2$, 10, 30, 130, 220, 285, 365 mm from the bank exit along the channel symmetry axes. Transverse coordinates y, z are read from the channel walls. Further on, only some examples of these measurements are examined.

Figure 2.36 shows profiles $P_0'(y)$ next to the screen output cross section ($x = 2$ mm). For the convenience of analysis, there is a nozzle section drawing shown in the same scale as the diagram. The drawing shows the probe trajectory (A) and dimensions of its cylindrical receiving section (B). The diagrams include combined data of versions I, IV, and II, III—the screens with similar nozzle length. Static pressure in cross section $x = 2$ mm was not measured as receiving openings of the probe were located at 10 mm distance away from its tip.

Flow parameters in the jets coming out of each micronozzle are more homogeneous in profiled nozzles—versions III, IV. The stream area occupied by boundary levels is considerable. The jet core where $\overline{P}_0'$ is almost a constant makes a value of ~4 mm (d_e ~ 6 mm). It is obvious that for a full-size profile whose length in our case exceeds 20 mm, the core would be of even a smaller dimension. Among the examined versions, the IV nozzle bank's jet core is the biggest.

For all SNB the value $\overline{P}_0'$ reduces abruptly behind the intersections ($y = 6$–9 mm and $y = 16$–21 mm), and in the area of a triangular base exit $\overline{P}_0'$ tends to the base pressure value that makes 0.25–0.5 of the static pressure value in a jet [7] (concordance of minimums $P_0'(y)$ with the nozzle crossing area proves that the probe was moving along the line (A)).

Apparent difference of $\overline{P}_0'$ in $y = 6$–9 mm for the first version if compared with the other refers to the fact that the intersection thickness of the other banks is smaller. In these cases

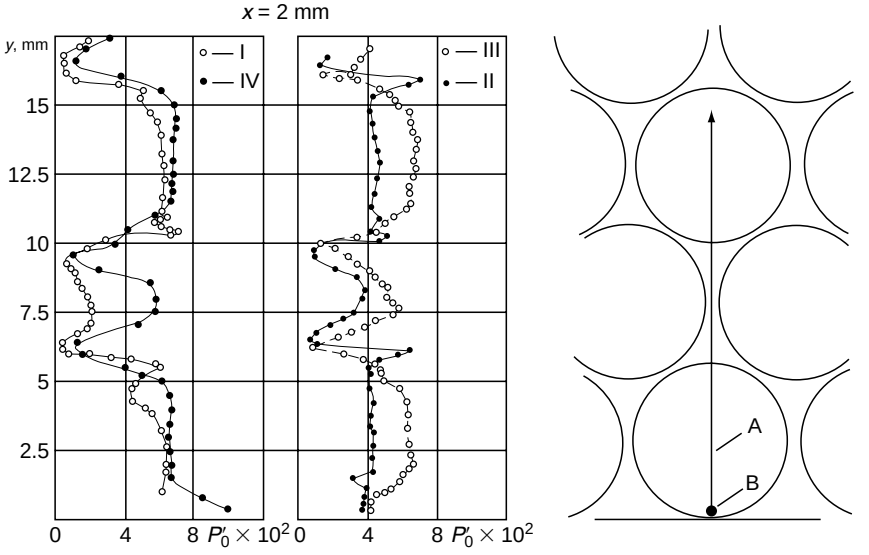

FIGURE 2.36 $\overline{P}_0'$ distribution near the nozzle bank outlet ($x = 2$mm).

TABLE 2.1
Geometrical Parameters of SNB

No	d^*, mm	d_e, mm	l, mm	A_e/A^*	$A_f/\Sigma A^*$	M_e^0	M_f^0	$\Sigma A_e/A_f$	φ°
I	1.1	5.7	15	26.8	35.3	5.1	5.44	0.76	10°
II	1.1	6.6	18	29*	35.3	5.19	5.44	0.9	10°
III	1.2	6.3	18.8	25*	29.7	5	5.22	0.85	Profile
IV	1.2	5.8	15	24.2	29.7	4.98	5.22	0.8	Profile
V	1.1	5.7	8.5	26.8	35.3	5.1	5.44	0.8	20°
	$h^* = 0.72$	$H = 21$	56	28.6	30	5.17	5.23	—	Blade nozzle

(versions II, III, IV), a probe is much wider than the intersection, and it already feels the impact from the adjoining jets. Lower values of $\overline{P}_0'$ in the jet core for the second bank refer to a greater degree of the nozzles' expansion (Table 2.1).

As it follows from the diagrams, it is typical for a conic nozzle to have shocks along the generatrix—peaks of $\overline{P}_0'$ at distances $y = 6$, 10.5, and 15.5 mm. Profiles of nozzles of $\overline{P}_0'$ are smooth at the output but the shocks as illustrated below are formed here almost in the output cross section.

Figure 2.37 shows all the flow parameters in the cross section $x = 11$ mm for version III of the screens. The flow pattern that can be represented according to these measurements is also shown here (probe trajectories are specified). This shock structure explains the failure of $\overline{P}_0'$ in

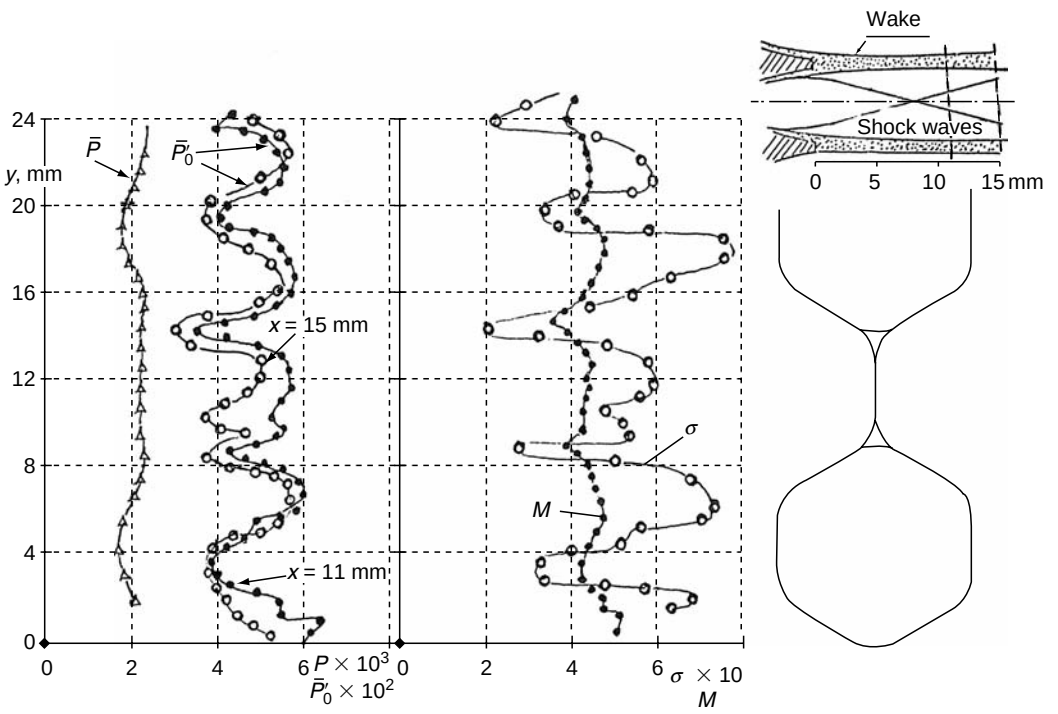

FIGURE 2.37 Flow parameters at $x = 11$ mm (model III).

the jet center ($y = 13.5$–15, 2–4 mm) and an increase in the failure's size, as seen in the diagram, upon the probe's shift further down the stream to the cross section $x = 15$ mm. Here it is possible to define the shock inclination angle approximately. Based on these measurements, it is certainly difficult to estimate that a bulk of the shocks is generated inside the nozzle because of the difference between a profile implemented in the metal and the designed one, and the other bulk is generated already at the output on jet interrelation and their relation with intersection wakes. To find this, additional detailed measurements for an independent nozzle of this kind with flow visualization are required. However, an indirect evidence of presence of shocks inside a micronozzle is the fact that the rated Mach number value is not reached at the output of axisymmetric profiled nozzles: maximum measured value was $M = 4.7$, while $M_e^0 = 5$.

The flow pattern behind the conic SNB is examined in detail in [2,4]. Shock waves emerge right behind the bank exit as a result of the divergent jets interrelation impact. But behind them unlike the profiled ones the rated Mach number is reached. Flow nonuniformities' (or disturbances') intensity was specified by the following values:

$$\overline{\Delta}P_0' = \left(P_{0\max}' - P_{0\min}'\right)/\widetilde{P}_{0\max}' \quad \text{and} \quad \overline{\Delta}M_0' = \left(M_{0\max}' - M_{0\min}'\right)/\widetilde{M}_0.$$

Maximum and minimum values in distribution were taken outside the limits of the boundary layer and depending on them an average value along the cross section was defined. Behavior of $\overline{\Delta}P_0'$ and $\overline{\Delta}\,\overline{M}$ along the channel is shown in Figure 2.38. It is obvious that, first of all, the base areas' value affects the results—data for bank I are located above the others (the results will be examined in more detail in section 2.2.4)

If the measurement results for the pressure fields in all the cross sections are described in a very general view, data correlation for "intercrossing" conic banks and "noncrossing" ones (versions I and II) proves that the total pressure loss levels do not differ much, the M number values are close though in bank I they are somehow lower. In general different base area value does not affect the jet mixing process.

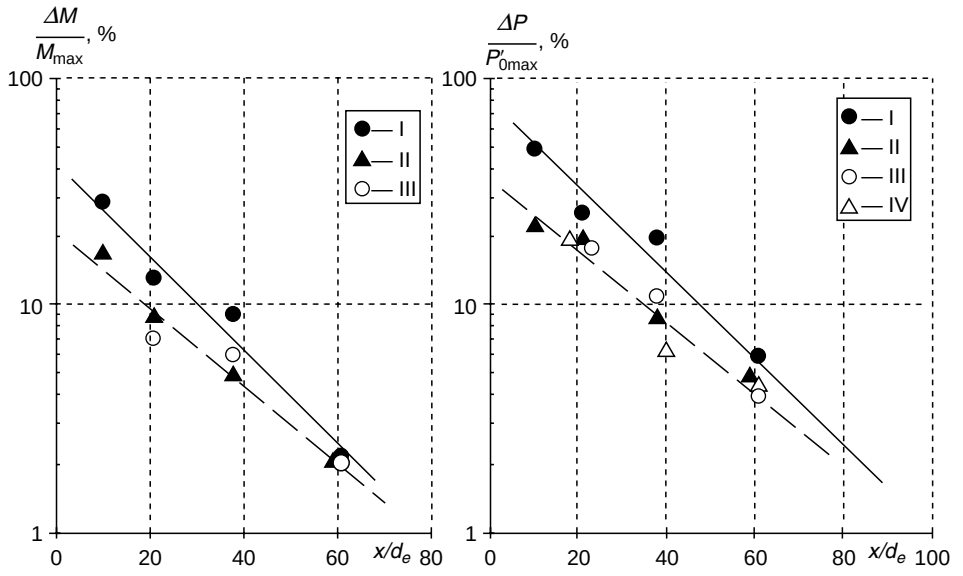

FIGURE 2.38 Nonuniformity intensity in distribution of averaged flow parameters in different cross sections.

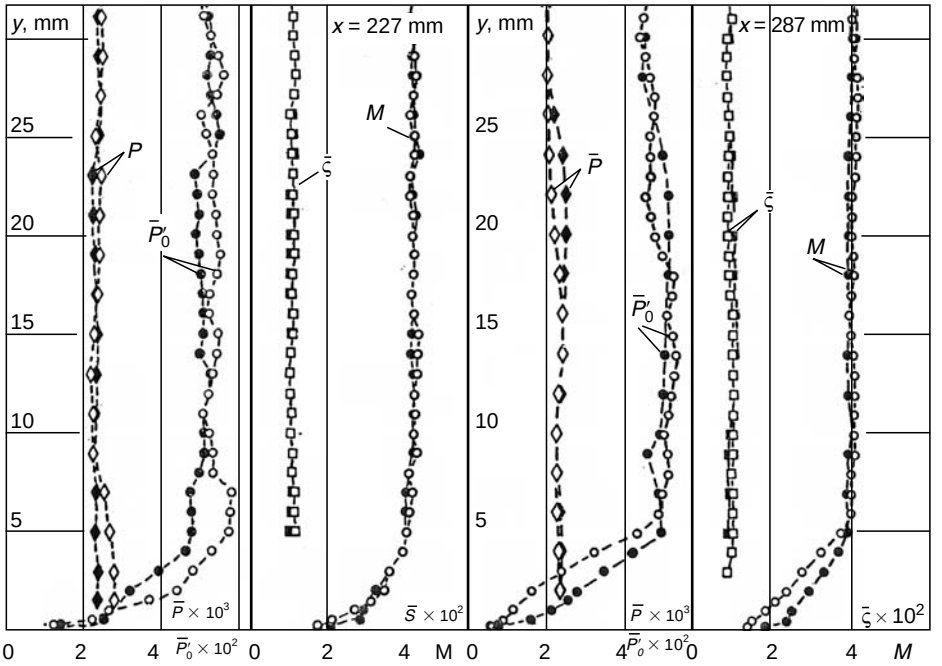

FIGURE 2.39 Flow parameters at $x = 227$ and 287 mm for screen MNB with $\varphi = 10$ and 20°; $\varphi = 10°$, ●◆■— $\varphi = 20°$.

Result comparison for the banks with different profile types indicates that the distribution pattern for these banks in all the cross sections is similar also from the qualitative standpoint, and parameters do not differ much quantitatively. It means that the nonuniformities structure is similar and their intensities are close. The micronozzle profile type influences the total pressure loss value—behind the conic banks as it is higher, while the Mach number is lower. This effect is tracked along the entire length of the resonator's cavity and is specified by pressure loss on flow turning in the conic jets.

At a distance of $\bar{x} = 40$–50 calibers profiles are noticeably leveling out. Figure 2.39 presents an example of result comparison for conic banks of $\varphi = 10$ and 20° angles. Variation of φ did not affect mean parameters distribution, that is, the regular patterns of flow formation remained the same. Variations took place in flow pulsation characteristics as pointed out below.

It is necessary to emphasize that because of wall proximity effect in narrow channels distinctness of the regular structure present behind the SNB is smeared. As an example Figure 2.40 shows the distributions by z in a 51×60 mm channel; one can clearly observe the flow layered structure—minimum in distribution of P'_0 passes through 2.5–3 mm, which corresponds to the wake structure, as is stated in Figure 2.63.

2.2.3.3 Base Pressure and Pressure Recovery in the Channel Located behind the Screen Banks

Dependence of the base pressure P_b of the Re_d number is represented in Figure 2.41. Pressure P_b was measured with the help of a drainage outlet in the center of a curvilinear triangle between the adjoining micronozzles (Figure 2.35, bank I). One micronozzle was drained to measure the pressure at the nozzle exit P_e. It is natural that the drainage outlet appeared not

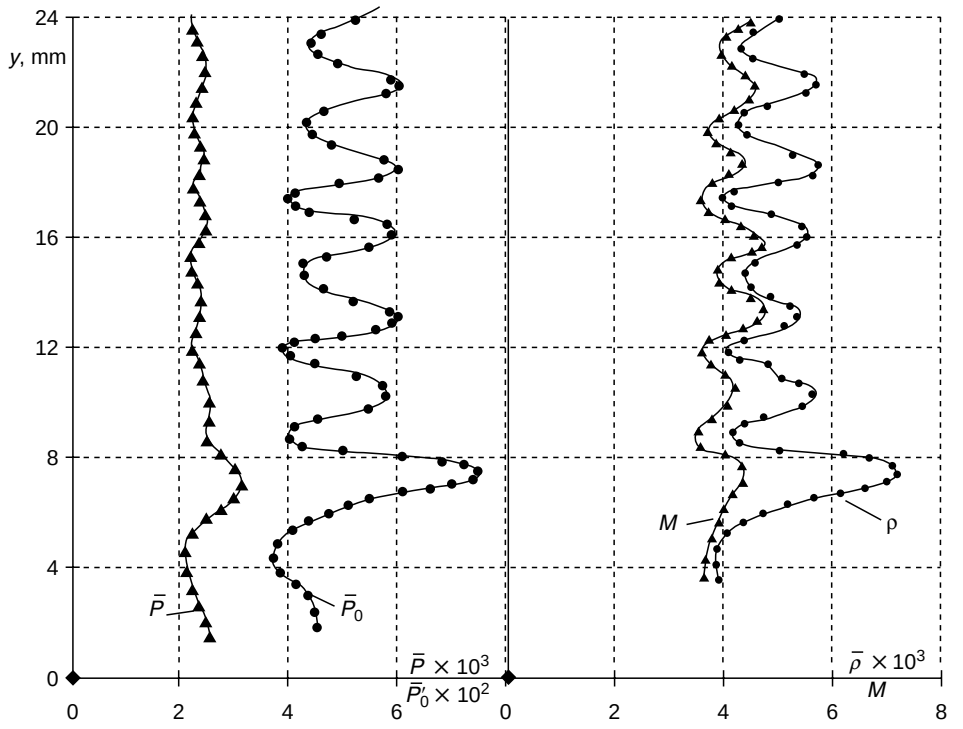

FIGURE 2.40 Flow parameters for SNB ($x = 28$ mm).

at the very exit but it was taken into account for result processing. The number Re_d calculated on the basis of the nozzle exit parameters and d_e, varied due to pressure variation in the forechamber P_{00}. Comparing the results with the data [6] for external flow around a body for similar M numbers indicates that P_b/P_e for an SNB is 2–3 times greater.

The problem of supersonic diffusion and pressure recovery in the channels will be examined in the PRS chapter in detail. Here we will briefly mention the result comparison in a channel of a constant cross section when screen MNB were applied as a nozzle device.

In the channel, a zone of transition of supersonic flow into a subsonic one is called a pseudoshock. The flow pattern here is rather complicated: three-dimension structure, shock, and the boundary layer interrelation at the walls, peeling-off, etc. However, in practical application flow details are not that important: it is required to be aware of the

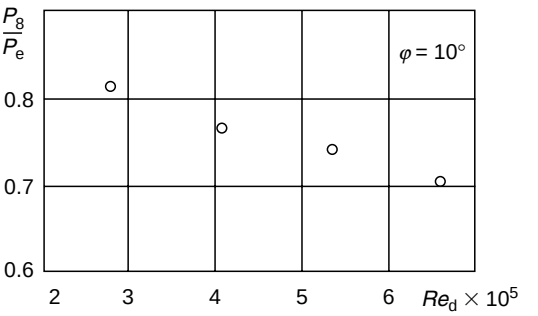

FIGURE 2.41 Base pressure.

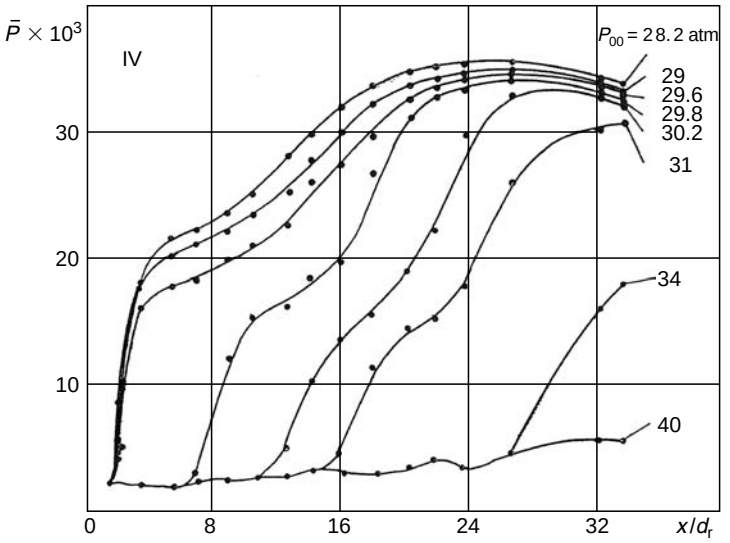

FIGURE 2.42 $\overline{P}$ distribution in channel in zone of pseudoshock at different P_{00}.

pseudoshock length and maximum pressure in the subsonic section. The first value defines the diffuser's length and the second one defines its efficiency (and starting pressure).

Figure 2.42 shows the pressure distribution along a channel wall in a flow behind bank IV for different P_{00}. Relative distance from the bank exit is $\bar{x} = x/d_h$, that is, hydraulic diameter $d_h = 4A_f/L_{ch}$ is selected to serve as a typical size, where L_{ch} is the channel perimeter. Pseudoshock length l_s is the distance from the cross section where an abrupt increase in pressure starts until the area where maximum pressures P_{max} are realized. As P_{00} starts reducing, a pseudoshock starting point shifts up the stream. The curve line of maximum pressure buildup corresponds with the pseudoshock starting point at the nozzle bank exit.

Figure 2.43 shows curves P_{max} for all the SNB as compared with the blade nozzle data. One can see that the pseudoshock's length is similar in all the cases though the blade nozzle's flow structure differs from the screen nozzle's structure. Further on it will be illustrated that l depends, first of all, on the shape of a channel.

Pseudoshock efficiency is generally defined as the ratio between maximum pressure at the end of a pseudoshock P_{max} and some reference value. There are various approaches used to select the latter value, which makes it difficult to compare the results. One of the frequently used parameters is $\eta_0 = P_{max}/P_0$, where P_0 is the pressure behind the normal shock at geometrical Mach number of $M = M_f^0$ which is specified only by the value $A_f/\Sigma A^*$. The value P^0 is the maximum recovery pressure corresponding to an ideal isoanthropic flow in a nozzle with a normal shock at the output cross section. It is worth noting that the parameter η^0 allows comparing data for various numbers M_f^0 and adiabatic line's values k.

On the basis of the values P_{max} estimated on the data in Figure 2.43, and P^0 projected according to the values $A_f/\Sigma A^*$ specified in Table 2.1, the values of η^0 for all the nozzle banks were defined: $\eta^0 = 0.76$, 0.75, 0.78, and 0.77 relatively for versions I–IV of SNB. In case of a blade nozzle $\eta^0 = 0.82$ (in other blade nozzle tests the value of η^0 varied within the range of 0.8–0.88 [19,26]). It is possible to state that the total losses in the case of screen nozzles does not depend much on a certain nozzle's profile shape and they are somehow higher than those in the blade nozzle tests. For comparison we can specify the value of η^0 in the known tests [20] in a round tube with a well-profiled nozzle where $\eta^0 \approx 0.9$ which does not exceed the values obtained in the present tests much.

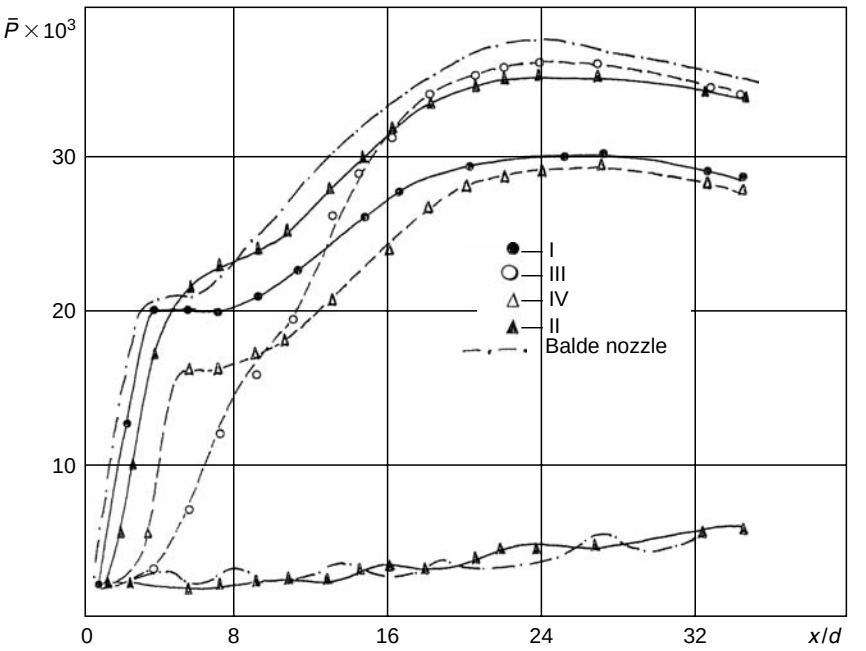

FIGURE 2.43 $\overline{P}$ distribution in channel behind the different screen MNB.

Figure 2.44 represents the measurement results for total pressure profiles behind a pseudoshock (in a subsonic flow). With the help of these data one can distinguish average values by the cross section $\tilde{P}_0$ and calculate the parameter $\eta_0^0 = \tilde{P}_0/P_0^0$ representing the ratio between the measured total pressure and maximum possible total pressure value P_0^0 behind the normal shock at an ideal isoanthropic flow in a nozzle. In the screen nozzle tests

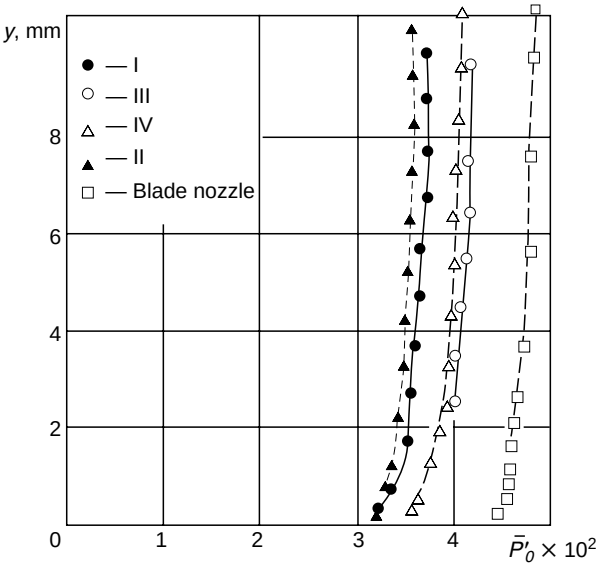

FIGURE 2.44 P'_0 distribution after pseudoshock zone.

$\eta_0^0 = 0.8$–0.85, for a blade nozzle $\eta_0^0 = 0.9$. The difference is not significant as well as upon η^0 value comparison.

Another way to define pseudoshock efficiency is to consider the losses only in the pseudoshock. According to [20], first, an average value of velocity ratio λ_1 is defined in the initial cross section of the pseudoshock with the measured wall pressure in this cross section P_1; next, pressure behind the normal shock wave P_2 is determined at $\lambda = \lambda_1$. Pressure recovery efficiency in a pseudoshock equals $\eta_1 = P_{\max}/P_2$. In the screen nozzle tests $\eta_1 = 0.8$ for versions I–IV, for a blade nozzle with the same expansion degree $\eta_1 = 0.86$ (in other blade nozzle tests maximum value of $\eta_1 = 0.94$ [19]). The fact that the value of η_1 differs from 1 refers to the wall friction impact that can be anticipated [19].

Thus, the difference in the flow structure does not influence the pressure recovery efficiency in the pseudoshock much. In addition, from this standpoint profile SNB banks do not differ much from a blade nozzle. $P_{\max}$ is somehow lower at the conic SNB but advantage of the profiled ones is not so great (though differences in the M numbers are not taken into account). With the η^0 and η_1 values obtained during the tests one can define the pressure in the end of a pseudoshock and the starting pressure.

2.2.3.4 Flow Pulsation Characteristics behind the Nozzle Banks

As measurements of pulsation characteristics were carried out on a special-purpose installation (highly clear air is required as dust particles can tear wires of an anemometer) of a 40×40 mm channel other models were applied for the tests. The main dimensions of new banks differed a little from the ones specified in Table 2.1. The title of Table 2.2 is the same.

The results were compared with the data obtained for a standard one upon a blade nozzle installation ($h^* = 3{,}6$ mm, $l = 155$ mm) rated for the number of $M_e = 4$. It is close to the value of M, which has been realized in a mixing zone in a flow behind the screen nozzles.

Pulsation characteristics measurement method included measurement of mean parameters distribution by the total pressure and the static pressure probes. Some results are represented in Figure 2.45. There is distribution of $\overline{P}$ and the numbers M. In Figure 2.45a and Figure 2.45b, there are profiles in a flow behind a screen nozzle, on Figure 2.45d, behind the blade (x is measured from the nozzle exit). Results of mass flow rate pulsation measurements are shown in Figure 2.46 (relative values $\langle \overline{m}' \rangle = \sqrt{\langle \overline{m}' \rangle^2}/\langle m \rangle$). As well as the mean characteristics the pulsation ones are strongly nonuniform along the cross section in the beginning of the channel (light spots depict a screen nozzle and dark spots depict a blade one). Peaks in the diagrams in cross sections $\bar{x} = 10$ and 21 correspond to the wakes formed behind the base areas. Profile $\langle \overline{m}' \rangle$ leveling occurs somehow sooner than the leveling of profiles of the numbers M and P_0' at a distance of 42 calipers in a flow core (outside the boundary layer) distributions are uniform enough but the average value $\langle \overline{m}' \rangle$ in the flow core is higher than that behind a blade nozzle by 2–3 times. As the distance increases, the difference reduces.

Micronozzle profiling impact on flow characteristics in the mixing zone. In general, the pattern of parameter variation along the channel length is specified by loss of the vertical

TABLE 2.2
Geometrical Parameters of SNB for Pulsation Measurements

Bank	φ°	d^*, mm	d_e, mm	A_e/A^*	$A_f/\Sigma A^*$	$A_f/\Sigma A_e$	M_e^0	M_f^0
1	10	1.35	5.0	13.72	16.45	1.2	4.28	4.49
2	20	1.00	5.0	25.00	30.00	1.2	5.00	5.23

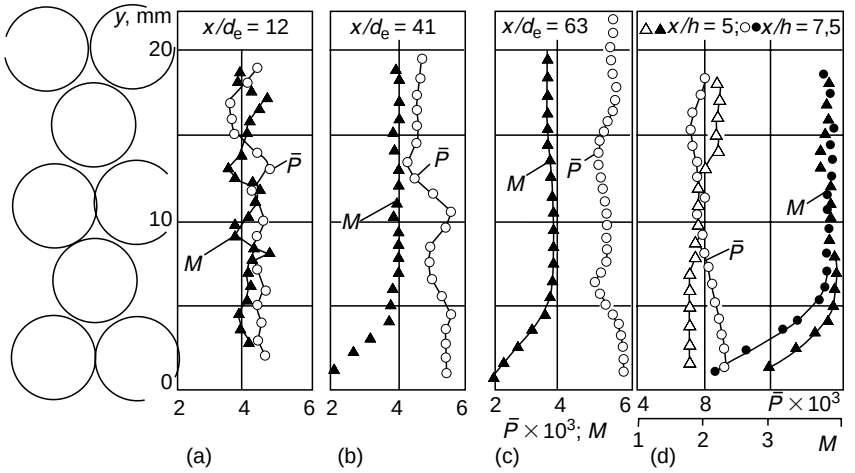

FIGURE 2.45 Averaged flow parameters for models, which were used at measuring of pulsations.

component of motion quantity. That is the reason why the total pressure loss in a flow behind conic banks is higher than profiled ones behind (the value σ is less in each cross section—an example is shown in Figure 2.39; the total pressure losses are also represented in Figure 2.44), whereas the Mach number values in the complete mixing zone—M_f is higher behind the profiled banks. For both the conic versions, the M number in the mixing zone is lower than that for the profiled banks. Such an effect—lower Mach numbers at large pressure losses—leads to the fact that when recovery pressures and $\overline{P}_{max}$ in one and the same channel behind the banks of different profiling do not differ much (Figure 2.43), η^0 are close (the fact that the recovery pressure in a diffuser of one and the same throat will not differ much upon using screen and blade nozzles was also mentioned in [2]). However, if the M_f numbers difference behind the banks is taken into account the differentiation increases.

It is also interesting to compare the losses during a pseudoshock when its beginning is located in the complete mixing zone, and the numbers M_f here are equal. Complete mixing cross section is $x/d_e \approx 10$. When a pseudoshock originates in B $\bar{x} = 10$ for bank I the value is

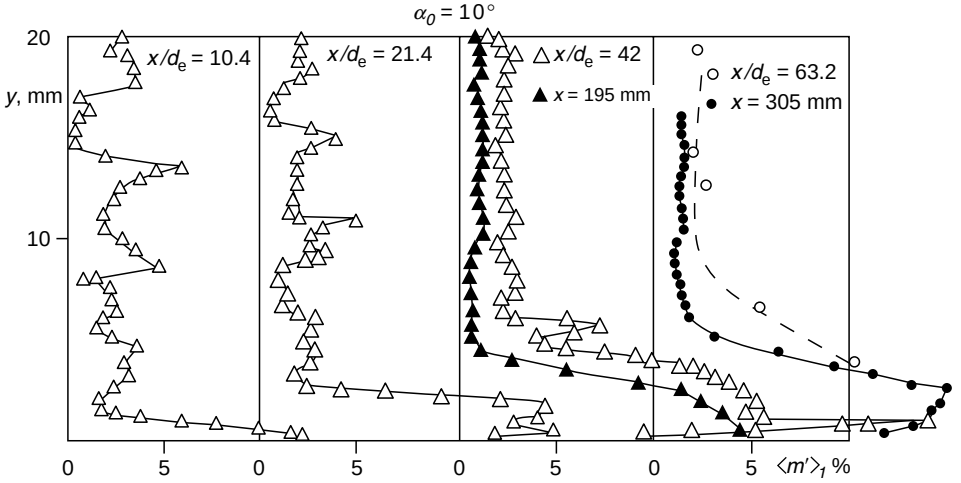

FIGURE 2.46 Profiles of distributions of mass flow rate pulsation.

$\overline{P}_{\max} \approx 29\times10^{-3}$, for version IV the value is $\overline{P}_{\max} \approx 32\times10^{-3}$, (Figure 2.42 and Figure 2.43). That for bank IV in the mixing zone $M_f = 4.2$ (at $A_f/\Sigma A^* = 29.7$), and for bank I, $M_f = 4.05$ (at $A_f/\Sigma A^* = 35.3$). If M_f is brought into compliance (e.g., to increase the micronozzle expansion degree in a conic bank, to calculate the pressure behind the normal shock and, on the basis of the obtained value of η^0, to estimate $\overline{P}_{\max}$), the difference of $\overline{P}_{max}$ for the conic and profiled versions of SNB will grow from 10% to 15%. Consequently, the profiled banks provide less losses at similar M_f. In full-scale conditions for large-size channels, this difference may even increase as the pseudoshock's start is located at a distance of $d_e = 1 - 2$ from the bank exit.

It is necessary to mention that the conclusion was obtained on the basis of the tests when micronozzles were of the same length both in the conic and profiled banks. It was achieved due to the fact that a calculated contour taken for a profiled micronozzle was not total, but truncated. There, the selected contour expansion degree was smaller than A_e/A^* at a conic micronozzle (it is known that the length of a calculated profile depends greatly on the value of A_e/A, see Table 2.1). At the same time using micronozzles of a complete profile in a bank (at A_e/A^* similar to the conic one) causes noticeable losses if compared with the conic banks especially at minor values of $P_0{\cdot}d^*$ (Figure 2.47). It relates to the fact that the boundary layers occupy a much bigger part of the outlet cross section of a profile's micronozzle due to its bigger length.

As on flow formation this ratio between a boundary layer's thickness in an outlet cross section and diameter d_e plays a significant role and influences flow parameter values in the complete mixing zone, the ratio δ^*/d_e difference shall be taken into account while comparing the measurements–"cool" ones ($T_0 = 300$ K) and measurements [2]—"hot" ones ($T_0 = 2000$ K). One needs to estimate the ratio of $P_0{\cdot}d^*$ in the cool tests to $P_0{\cdot}d^*$ in the hot conditions. If we assume that the boundary layer is laminar in micronozzles, the value δ^* can be estimated by a regular method: $\delta^*/l \sim Re^{-0.5}$. The $P_0{\cdot}d^*$ parameter ratio in the cool tests to the hot ones comes to about 15. (The estimation was carried out for particular environment of out tests, that banks still had different A_e/A. It is examined in more detail in [21]). Thus, our data

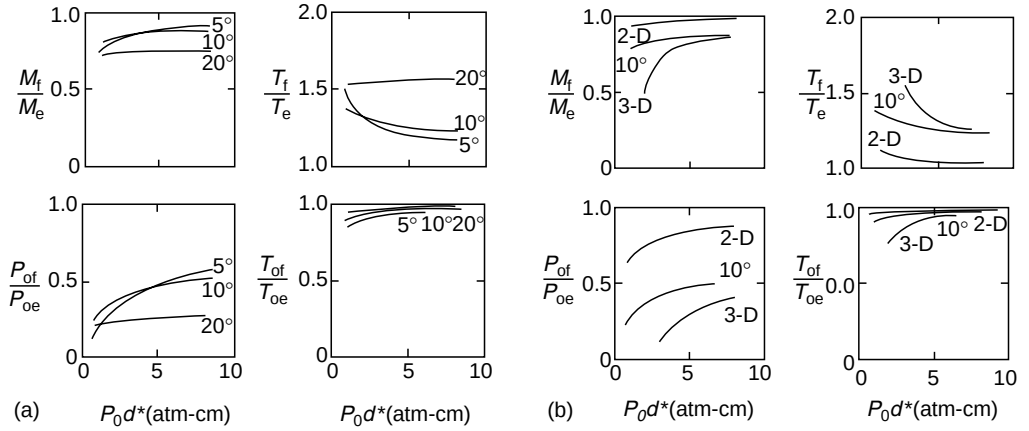

FIGURE 2.47 Results of flow parameters calculation in region of completed flow mixing: *a*—for screen MNB with different φ; *b*—results' comparison for screen conic nozzles with $\varphi = 10^\circ$; screen profiled (3-D) MNB and blade (2-D) nozzles. (From Russel D.A., Neice, S.E., Rose, P.H. Screen nozzles for gasdynamic lasers. *American Institute of Aeronautics and Astronautics Journal*, 1975, Vol. 13, No. 5, pp. 593–599.)

correspond to the bigger values of $P_0 \cdot d^*$ in calculations in [2], where relations are already clearly observed (Figure 2.47), when $P_0 \cdot d^* > 5$.

One more condition shall be considered. When tests are carried out in narrow channels, influence of the boundary layer built up on the channel walls upon the flow parameters in the core becomes noticeable. Displacement thickness δ^* in cross sections was estimated on the basis of measurement results (the M numbers profile was defined upon distributions $\overline{P}_0'(y)$ and $\overline{P}(y)$, and the data were a basis for estimating the velocity distribution $\overline{U}(y)$, and by integration the known ratios δ^* were defined). Figure 2.48 represents an example: velocity profile in $x = 365$ mm in a 21×80 mm channel. The profile's form is standard for a turbulent layer—U/U_0 is approximated by an exponential function with index $1/10$ (the number Re_x calculated on the parameters at the external edge of the boundary layer and distance from the bank is equal to 3.7×10^7). For bank I in cross section $x = 365$, the measured value of $M_f = 4.05$ and $\overline{\delta}^* = \overline{\delta}^*/(H/2) = 0.2$. Then, the Mach number in the channel for the condition of $\overline{\delta}^* \to 0$ (physically it corresponds to wide channels where the boundary layer influence is minor) makes $M_f^1 = 4.35$. The estimation is received with the flow rate equation assuming that in the both cases (when $\overline{\delta}^* = 0.2$ and $\overline{\delta}^* = 0$) T_0 is similar (for more details, see [21,22]). For bank III, the value M_f^1 is ~4.45. Then, the ratio of the numbers M_f^1 to M_f^0 defined only by area ratio makes for the conic banks is about 0.8, and for the profiled ones it is about 0.85. The value 0.8 for the conic banks with $\varphi = 10^\circ$ is very close to estimations of [2] on the values of $P_0 \cdot d^* > 5$.

Thus, the calculated results [2,4] and our tests and estimations are very close. Correlation [2] can be used for a prognosis of flow mean characteristics in the complete mixing zone in the hot conditions. However, parameter ratios obtained during the test behind the banks compared will remain. That is why from the standpoint of mean parameters (total pressure losses, values M_f and $\overline{P}_{max}$) the shortened profiled banks have an advantage over the conic ones. The shortened profiled banks are more preferable than the conic ones with $\varphi = 10^\circ$ also because in this case the contour start angle in a micronozzle is bigger. It means that vibration energy freezing conditions are better there.

Therefore, we need to note that while examining flows in a nozzle with nonequilibrium excitation of molecules' vibration freedom degrees, the value of $P_0 \cdot d^*$ is generally applied as a similarity parameter [25]. However, as specified [23,24] it is more accurate to define a flow with the parameter $P_0 \cdot d^*/\mathrm{tg}\varphi$ that allows generalization of the data by a unified dependency, for example, the gain factor, obtained in media behind different nozzles.

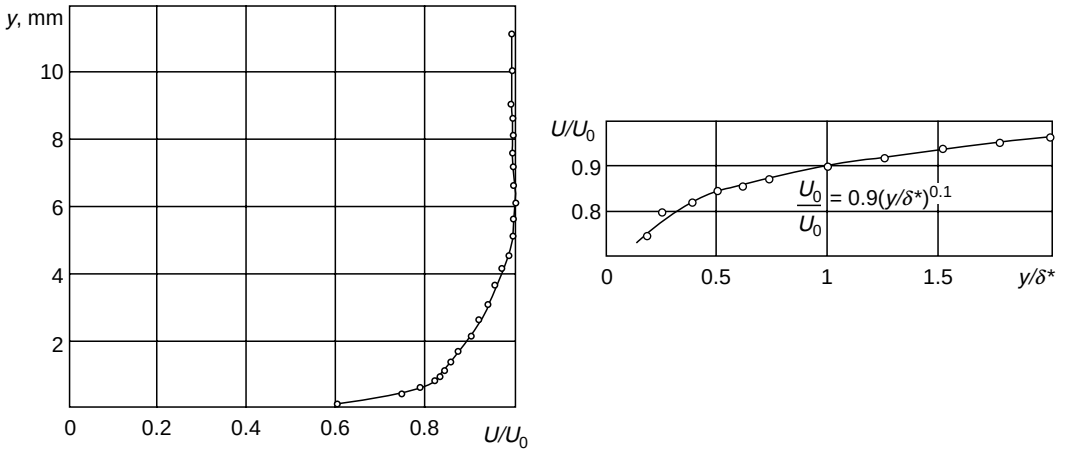

FIGURE 2.48 Velocity profile near the wall at channel's cross section $x = 365$ mm.

Nevertheless, this information—on gas dynamics of mean flows and energy characteristics—is not enough to make a final conclusion on which banks are preferable when applied to a laser. Though the summary made [2] is in favor of the conic banks with $\varphi = 10^\circ$ (in the banks with $\varphi = 20^\circ$ total pressure losses were anticipated to be too high; see Figure 2.47), the determinant information as it is proved in Chapter 3 is the data on supersonic flow optical quality.

Base areas and base pressure influence. Figure 2.38 represents the behavior of intensity of the number M and $\overline{P}'_0$ fields' nonuniformities along the channel. Values $\overline{\Delta}\,\overline{P}'_0$ and $\overline{\Delta}\,\overline{M}$ are laid on the axis of abscissas in a logarithmic scale (It is appropriate at this point to recall that $\overline{\Delta P}'_0 = \left(\tilde{P}'_{0\max} - \tilde{P}'_{0\min}\right)/\tilde{P}'_{0\max}$, and so on, where $\widetilde{P}'_0$, $\overline{M}$ – cross-section-averaged values were calculated, minimum and maximum values were taken outside boundary layer. It is obvious that nonuniformity intensities decline exponentially. The M number fields' leveling and, consequently, densities also, occur faster than the P'_0 fields' leveling. In the first case, a distance of about 60 calipers is required, and in the second case, it is 100. The value $\bar{x} = 100$ needed to level density nonuniformity was obtained in [2,4] also.

According to this result [2], it is recommended to place the resonator at $\bar{x} = 100$. However, to resolve this issue as well as the issue of bank micronozzles profiling it is required to obtain information on flow optical quality behavior along the resonator cavity. The data on behavior of mean density nonuniformities related to a regular flow structure is not enough.

As Figure 2.38 proves the profiling does not influence the behavior of the nonuniformities intensity—the data for banks II, III, IV agree. The results were influenced by base areas' dimensions. The direct line for bank I with the biggest intersections between the micronozzles' outlet cross sections (see Figure 2.35) is always higher than the others. It is explained by the fact that the main structure specifying the behavior pattern of the nonuniformities in the flow field is the wakes formed behind the base areas. The thicker the intersections are, the greater the expansion generated in the wake behind them, that is, $\overline{\Delta}\,\bar{\rho}$, $\overline{\Delta}\,\overline{P}'_0$ and $\overline{\Delta}\,\overline{M}$ increase. It can be easily tracked in the two-dimension case of flows behind the blade nozzles (Figure 2.13). Nonuniformities' intensity behind bank I is higher than the others and this difference remains till the complete mixing zone in $\bar{x} = 80$–100.

It is because the base areas of banks I and V are similar that the behavior of $\Delta\rho/\rho$ and $\Delta M/M$ in these two cases is almost the same (see Figure 2.49) (within the range of data spread). If the main regular structure specifying the flow nonuniformities behavior pattern had been a shock wave one as reckoned in [2,3] rather than wakes, then at such a juxtaposition when angle φ increases by two times, the results should have been different. However, the data spread is only observed in the initial section $x/d_e \leq 10$, where shock waves'

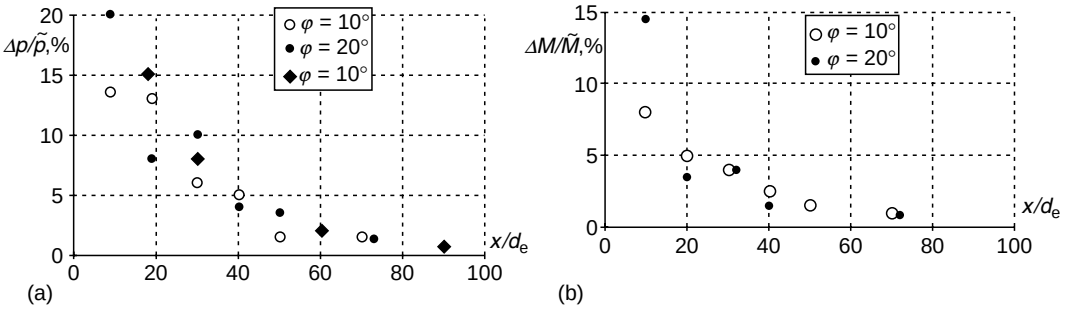

FIGURE 2.49 Nonuniformities' intensity, determined by regular flow structure, behind screen MNB with $\varphi = 10$ and 20°: (a)—density fields, (b)—Mach numbers fields, ◆ data. (From Russel, D.A., Neice, S.E., Rose, P.H. Screen nozzles for gasdynamic lasers. *American Institute of Aeronautics and Astronautics Journal*, 1975, Vol. 13, No. 5, pp. 593–599.)

impact is certainly significant. (Figure 2.49 also represents results of [2], obtained on the basis of interferometric measurements).

Experimental values of the base pressure P_b at the exit of bank I were presented in Figure 2.41 and as mentioned before the value P_b is much higher than the values obtained in aerodynamics for standard cases of streamline of shelf, missiles, and so on [7]. The impact of the pressure P_b on the flow parameters in the mixing zone is shown in Figure 2.50 at M_f. In a general case, reducing P_b causes a reduction in M_f and an increase in the total pressure. P_b reduces as the base areas increase (in the two-dimension case; see Figure 2.15). Thus, the presence of large base areas—thick intersections between micronozzles—is not desirable. It causes an increase in the regular nonuniformities' intensity, increase in the total pressure losses, and reduction in the numbers M_f.

In general, as Figure 2.50 shows, influence of P_b is not so crucial. Influence of displacement thickness δ^* at micronozzles' exit is more noticeable (values of δ^* were estimated on the basis of calculation results of laminar boundary layer characteristics at the plate [27]). Diagram of function $M_f/M_f^0 = f(\delta^*)$ reflects the influence of the main loss sources related to flow turning and friction at the nozzle walls. We need to note the following: in the executed tests relative thickness of $\overline{\delta}^* = \overline{\delta}^*/d_e$ is not big—$\overline{\delta}^* \leq 0.03$ and that is the reason why the values M_f/M_f^0 are quite high. Even for $\varphi = 20^\circ$, $M_f/M_f^0 = 0.76$, and for $\varphi = 10^\circ$ $M_f/M_f^0 = 0.9$ as the Mach number grows the loss factor increases and as a result M_f/M_f^0 reduces with other conditions similar (Figure 2.50b). Values of the M_f number in full-scale conditions of laser operation—during warm starts—can be estimated on the presented correlation $M_f = f(\delta^*)$, that is, values of M_f/M_0^0. will be lower than the ones obtained during cool tests. However, the recovery pressure behind the pseudoshock (in a diffuser of similar geometry) will not differ much in hot and model experiments.

Losses of friction in micronozzles of a screen bank and of flow turning cause an increase in flow total pressure (see Figure 2.43). At the same time, the same factors cause a reduction of the mixed flow's Mach number, which in its turn adds to pressure recovery efficiency P_0 in a normal shock. As a result the values of P_0 remain, as pointed out before, almost the same as in the case of an ideal nozzle with the same area ratio $A_f/\Sigma A^*$ (see Figure 2.44). Mixed flow parameters were basic for estimating the recovery pressure P_0 behind the normal shock at $M = M_f$, which were later equal compared with the P_0^0 corresponding isentropic expansion in a nozzle with area ratio $A_f/\Sigma A^*$ with following recovery in the normal shock at $M = M^0_f$. Thus, the ratio $\eta^0_0 = P_0/P_0^0$ specifies deviation in the screen nozzle installation start conditions

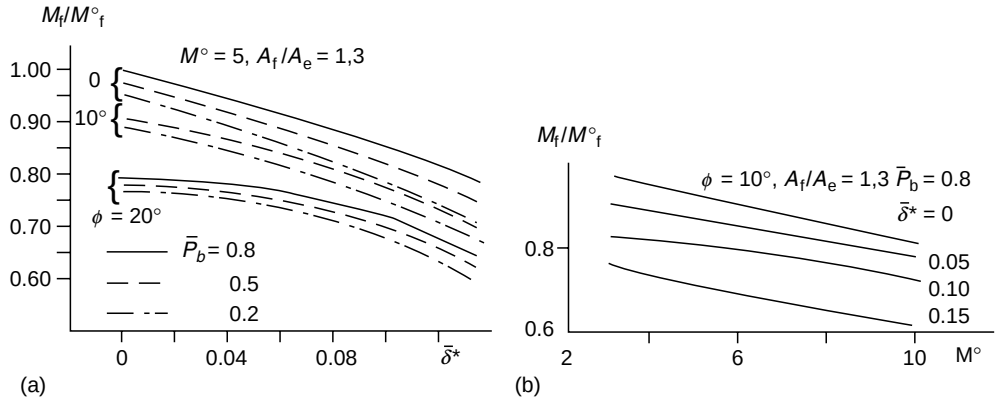

FIGURE 2.50 Influence of following factors on flow parameters: base pressure P_b, displacement thickness at outlet cross section of nozzle δ^*—(a) and Mach number M_0—(b) in region of completed mixing.

when compared with the ideal nozzle one with the same ratio between the channel area and the critical one. As a result even in the least favorable case ($\varphi = 20^\circ$, $\overline{\delta}^* = 0.15$) $\eta_0^0 \approx 0.88$.

On micronozzle expansion angle's influence in a conic bank. The issue has already been discussed in the previous paragraphs. First of all, angle φ influences the energy characteristics: as φ increases stored energy at nozzle exit multiplies. However, the total pressure losses increases also but due to the fact M_f in complete mixing zone reduces (Figure 2.50a) the recovered pressure do not vary much in the channel after the pseudo-shock (Figure 2.43).

Angle φ did not affect the value and pattern of regular nonuniformities' intensity behavior behind the bank much (Figure 2.49). However, the parameter's effect was observed at the flow's pulsation characteristics. Mass flow rate pulsation profiles $\langle m'(y) \rangle$ were presented in Figure 2.46 (light spots represent SNB; dark spots represent a blade one). The behavior of maximum $\langle m' \rangle$ values in the flow core along the channel length outside the boundary layer (but in this case it also reflects average values of $\langle m' \rangle$ by cross section) is presented in Figure 2.51. As the experiments were executed with the models whose dimensions were slightly different (these dimensions are specified in Table 2.2), the behavior of $\Delta M/M$ for these banks is also presented here. The obtained results—correlation between mass flow rate pulsation and φ and the behavior pattern of $\langle m' \rangle$ along the channel—turned out to be important for interpretation of the flow's optical quality measurements.

It is also necessary to note that turbulent properties of flows are important not only for laser systems. SNB were also suggested for aerodynamic tunnels in early 1950s [28,29]. But as

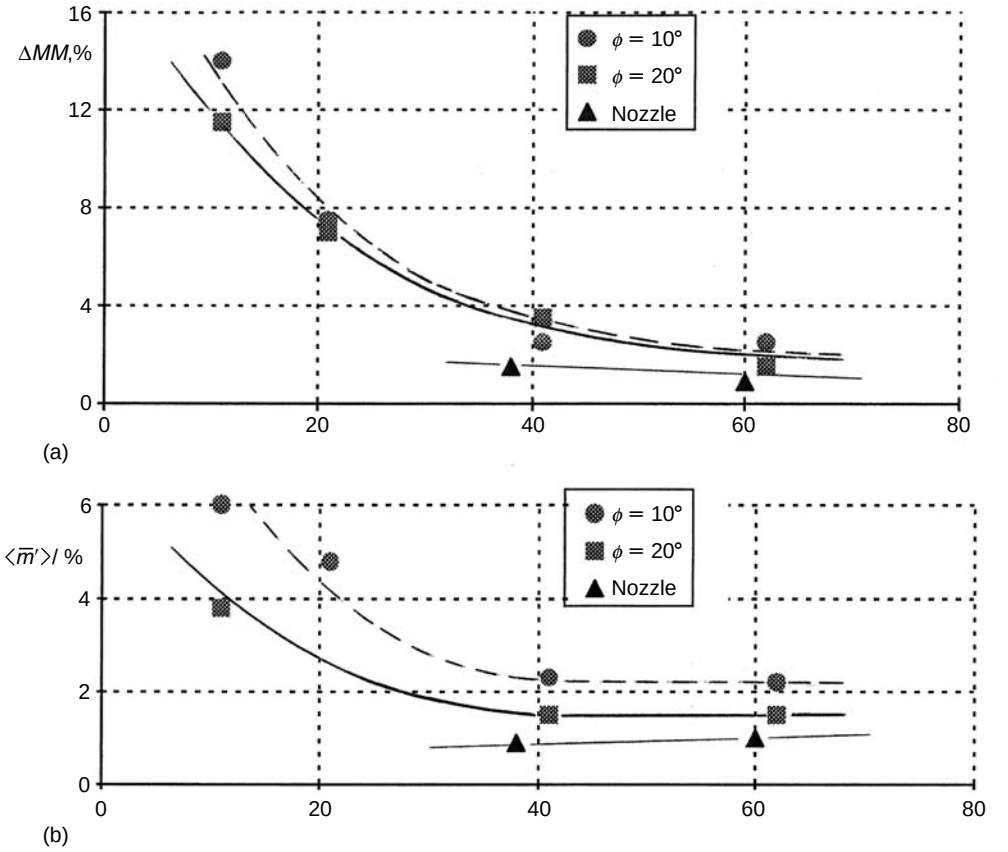

FIGURE 2.51 Nonuniformities in Mach number distributions in different cross sections of working channel (a) and pulsation's intensity of mass flow rate along the channel (b).

quite big axisymmetric nozzles were applied in the banks at those times, the obtained data were not encouraging. Application of micronozzles improves the case—uniform fields of high M numbers were obtained at small distances from the nozzle exit. Possibilities of application of such screen nozzles for aerodynamic tunnels were discussed in [30,31]. However, data on pulsation characteristics of the flows behind the screen banks restrict the opportunity. As is known, intensity of flow turbulent pulsation affects aerodynamic characteristics of streamlined bodies as it influences the process of the laminar boundary layer transition into the turbulent one. It is obvious that intensity of $\langle m' \rangle$ behind the screen nozzle is 2–3 times higher than in the flow core behind a regular aerodynamic nozzle.

The main disturbance type in a flow behind screen banks specifying the regular nonuniformities' pattern is wakes behind the base areas. The shock wave structure influence is only significant at the beginning of the flow. That is the reason why the micronozzle profile does not influence the behavior pattern and the intensity value of nonuniformities behind the bank; the intensity value of nonuniformities is affected by the dimensions of the base areas.

From the viewpoint of mean gas dynamic parameters of a flow the shortened profiled banks have advantages over the conic ones: the Mach numbers in the mixing zone behind such banks—and similar nozzle expansion degrees—are higher, total pressure losses are lower and that is why the recovery pressure in the channel behind the pseudoshock is higher. But these advantages are not determinative. It is impossible to make the final decision on preferability of a micronozzle profiling type in a bank only on the basis of analysis of mean gas dynamic parameters behavior—it also requires data on the optical quality of flows. Therefore the obtained data on the pulsation characteristics behavior behind the conic banks are important.

Mean flow parameters behind the screen MNB are worse than those behind the blade nozzles (the M numbers are lower; the total pressure losses are higher). But an important advantage of screen nozzles over the blade MNB is that they do not have any defects related to assembly of individual nozzles into a bank, and do not have any dispersion in the critical cross-section dimensions, that increases in the blade structures during operation in full-scale (hot) conditions. All the defects, including critical cross-section dispersion, cause a decrease in the flow optical quality. While comparing MNBs of different types (screen and blade ones), information on optical properties of the flows realized behind the banks is required for definition of their advantages from the standpoint of application in lasers, including anticipation of flow optical characteristics behind the banks during operation.

2.3 OPTICAL QUALITY OF FLOW IN THE LASER CAVITY AFTER MNB

2.3.1 Introduction

Radiation intensity in the far-field zone in the focal spot is defined not only by the power of a laser system but also by beam divergence, that is, radiation quality. Radiation quality is a vital parameter of every laser. In SGL it is determined by the OQ of a flow in a resonator, that is, the wavefront aberration pattern that is acquired during radiation generation in the resonator upon density nonuniformities found in the flow. In its turn, the pattern of the flow density nonuniformities that distort the radiation wavefront is specified by the structure of an MNB applied in a certain SGL.

That is the reason why to enhance the efficiency of a laser system it is required to resolve the problem of construction of an efficient MNB, among many other issues (including increase in specific power, resonator's efficiency factor, etc.). MNB's efficiency shall be estimated not only from the standpoint of obtaining high inverse population in a flow behind the nozzle

bank but also from the standpoint of the flow's OQ. To be able to improve the flow OQ one needs to be aware of the relation between an MNB's design features and features of the flow realized behind it, as well as to know how flow OQ depends on these features. Only these data can help improving flow OQ and, consequently, reducing laser radiation divergence.

2.3.2 Objectives of Aero-Optics for SGL Lasers

In the general case, wavefront distortion in a light beam upon passing through density nonuniformities of the air medium is called aero-optical effect. The effect is stipulated by refraction index variation linearly connected with the medium density. Phase aberrations occur on passing both regular structures (shock wave systems, contact surfaces) and turbulent ones.

Electromagnetic-wave propagation through the air medium used to be an object of thorough investigation of the atmosphere optics and currently there are a number of studies in this field, such as well-known treatises [1,2]. The following issues have been examined: radio wave propagation in the atmosphere, atmosphere's impact upon star image generation in telescope lens, and so on. The difference between aerooptics and atmosphere optics is that the former studies the cases when a typical scale of density disturbances, turbulent pulses, in particular, is much less than the beam aperture, that is, the situation opposite to the one typical for the atmosphere optics. Though the applied mathematical apparatus is similar in the both cases, the results are different [3].

The aero-optics objectives were singled out as an individual subject (for more details on the aero-optics see [4,5]) mainly due to the birth of lasers. The main problems of aero-optics for SGL lasers (including mixing systems both chemical and gas dynamic) are generated by needs of MNB usage to obtain larger active medium mass flow rate values. Such banks have an extensive base area and, thus, wakes, shock wave and expansion wave systems emerge upon flowing it around (see part 2). It means that radiation is generated in a medium including density nonuniformities and that is why the wavefront is not ideal, that is, plane at the resonator's output. Consequently, radiation divergence will be more than diffraction scattering, whereas the radiation intensity in the far-field zone in the spot center will be less when compared with an ideal case. That is the reason why the objective of the study is to try to achieve minimum laser radiation divergence by means of an adequate design of a nozzle bank. The degree of distortion of the plane radiation wavefront when passing through a medium is specified by the OQ of the medium. The issues of the flow's OQ behind the screen nozzle banks applied in a GDL were considered [6–8,53,54,68], and behind the banks applied in mixing-type lasers [9,10] behind the banks of the chemical SGLs.

The second type of aerooptical objectives referring to SGL is phase disturbances generated by aerodynamic windows that are required to emit high power radiation. Such windows are a plane gas jet separating the lower pressure resonator cavity from the outer medium. Specially selected jet geometry and the flow pattern behind it allow actuating the entire pressure differential right on the jet itself. However, turbulent mixing layers are formed at the jet boundary. Decrease in the quality of the radiation that passed through such a window was examined [11–14], where various window structures are suggested.

Scientists faced another scope of problems upon allocating lasers on airplane board. The objectives referring to eliminating radiation through a boundary layer formed on the hull surface in-flight. Decrease in radiation quality in this case refers to turret aerodynamics, and was considered in numerous studies, for example [15–17], while description and results of full-scale experiments, obtained in an airborne laboratory on board KS-135 are shown in [18]. Apart from that, application of optical guidance systems in modern supersonic missiles caused objectives related to correct interpretation of a signal received from a radiation sensor. Before it gets into the sensor's receiving window a beam passes through a shock wave and

turbulent mixing layer of cool gas cooling the window with an external flow. And it means that temporally a signal also depends on the conditions implemented upon the aircraft flowing around and the fact needs to be taken into account when elaborating control commands [19,20].

In the context of aerooptics objectives one can also mention the problem of implementation of optical gas phase-shifting devices [21]. Such a device is integrated into a radiating system to maintain laser beam coherence. The device can be used to eliminate static and dynamic phase distortions emerging in the laser itself. Similar systems are called coherent optical adaptive techniques [22]. The scope also includes gas light guides [23]. Thus, the scope of aero-optics objectives is quite wide but in one way or the other objectives refer directly to lasers: or passing of laser beam, or laser radiation generation.

Propagation of light—electromagnetic oscillations—in absorbing and scattering media is depicted, as it is known, by the Maxwell equations that are the basis of the scalar wave equation [24]:

$$c^2\nabla^2 u = \frac{\partial^2 u}{\partial t^2},$$

where $c = c_0/n$ is the velocity of light wave propagation in a medium.

Medium properties are included in the equation through the refraction index n, which is proportional to the medium density. Consequently, one needs to know the density fields of the medium studied. In general, precise numeric solution of the Navier–Stokes equations by means of the direct numeric simulation method allows defining the density fields and solving the aerooptical task [25]. However, even when the most powerful computers are applied it is only possible for idealized simple flows, when the Reynolds numbers are low.

Utilizing the large-scale vortex models when small-scale turbulence is considered statistically uniform and isotropic, that is, it can be described by statistic models and nonisotropy of a flow is only defined by large-scale vortexes—such an approach allows reducing required computational capability for calculation and advancing by the Reynolds numbers [26,27]. However, this is still far from practical applications.

That is the reason why currently the entire calculation procedure in aerooptical study program packages is divided into several steps. First, mean density fields are defined by solving averaged Navier–Stokes equations, and the flow's turbulent properties in corresponding areas are estimated with help of statistic turbulence models. And thus a complete aero-optical analyses consist of solving the Maxwell equations first for the mean density fields—low order aberrations are estimated, and then the light scattering problem is solved upon turbulent pulses on the basis of the flow properties estimated with the turbulence models (e.g., (k–ε) or (k–ω) models). Often, the phase distortions are calculated as the difference of optical paths and it is assumed that beams passing such nonuniformities do not distort that is, actually geometrical optics approximation is applied [25].

The objective of light scattering in an optically adequate laser medium when it incorporates random density nonuniformities was apparently considered for the first time in [3] (earlier the objective of scattering in a neutral medium was examined in [1,2], where the main principal results were obtained). In [3,4] the objective is studied with due consideration of the specific nature of aerooptics: density fluctuation scale is less than the beam aperture. The solution for the wave equation for a periodic wave $u \sim \exp(i\,\omega t)$ is known to be written as:

$$u(x,y,R) = \frac{i}{\lambda}\int \frac{u_0(x,y,0)}{r} \mathrm{e}^{ikr} dA_0,$$

where A_0 is the area of aperture, λ the wavelength, u_0 the initial field distribution along the aperture prior to entering the medium, $u(x,y,R)$—field in point $z = R$, and R the distance between planes $(x,y,0)$ and (x,y,R), $k = 2\pi/\lambda$.

Actually it is the Huygens–Fresnel integral. When $z = 0$, there is phase distortion (wavefront distortion) $\varphi(x,y)$ the integration element is multiplied by $\exp(-i\varphi)$. Usually field distribution in the far-field zone is described with a time-averaged transfer function as we are interested in big periods by t:

$$\langle \tau(x,y) \rangle \;=\; \langle u(x,y,z) u^*(x,y,z) \rangle \big|_{z=R}$$

Fourier transformation of $\tau(x,y)$ provides radiation intensity distribution in the far-field zone (in optics the Fraunhofer diffraction case more important from the practical standpoint is more frequently considered [24]):

$$I(\theta_x,\theta_y) \sim \int\int \tau(\xi,\eta) \mathrm{e}^{ik(\theta_x \xi + \theta_y \eta)}\, d\xi\, d\eta \tag{2.1}$$

(θ_x,θ_y are the angles in the focal plane, ξ and η are the Fourier coordinates).

In the general case, $\tau(x,y)$ is product of transfer functions calculated for the case when a beam is affected by an average and turbulent flows. The field of averaged nonuniformities causes a common beam withdrawal (a constant component specifying the wavefront inclination), whereas the turbulent one causes ray and the entire beam scattering and jittering (wavefront distortion). While, generally, the first effect is fixed by regular optical means the scattering causes inevitable decline in intensity of field I in the far-field zone on the target when compared with the case of diffraction-limited divergence of light beam I_0. That is the reason why the turbulent component of the transfer function $\tau_{\mathrm{m}}(x,y)$ is vital.

In [3,4] after wave equation integration and obtaining $u(x,y,z)$ the following is demonstrated:

$$\tau_m \sim \exp\left\{ 2k^2 \int_0^L \langle \Delta n^2 \rangle \left[\Lambda(x,y,z) - \int C(\xi,\eta,\zeta)\, d\zeta \right] dz \right\} \tag{2.2}$$

$\xi = x - x'$, $\eta = y - y'$ is the shift in coordinates, while ζ and z are the beam propagation direction; $\langle \Delta n^2 \rangle$ is the pulsation root-mean-square value n; $\Lambda(x,y,z)$ is the integral turbulent scale; L is the scattering layer thickness; $k = 2\pi/\lambda$; C is the turbulence correlation function.

Fourier transformation of the first member provides Airy distribution (diffraction angle of scattering $\theta_D \sim \lambda/D$). The second member specifies the diffraction pattern related to scattering at density pulsation ($\theta_m \sim 2/k\Lambda$). For the case of Gaussian correlation function, at $D \gg \Lambda$, α is the damping factor:

$$\alpha = 2k \langle \Delta n^2 \rangle \Lambda(x,y,z).$$

The integral of this expression is actually a root-mean-square phase error $\langle \Delta\varphi^2 \rangle$ accumulating along the optical path length

$$\langle \varphi^2 \rangle \;=\; 2k^2 \int_0^L \langle n^2 \rangle \Lambda\, dz. \tag{2.3}$$

Intensity correlation in the far-field zone I and I_0 in the presence of wavefront aberration in a beam and without it, is estimated with the Strehl ratio [24]:

$$Sr = I/I_0 \sim \exp[-\langle \Delta\varphi^2 \rangle]. \tag{2.4}$$

Thus, when light passes through a boundary layer, for example, radiation intensity in the spot center in the far-field zone on a target fall when compared with the case when this scattering layer is not found on the light's way. However, it is important to note that if a scattering medium is close to a homogeneous and isotropic medium in its properties, the diffraction pattern (at $D \gg \Lambda$ and $\alpha L \ll 1$), as it is shown [3,28], does not change. The same distances between maximum and minimum remain at the distribution, scattered energy drains to the distribution wings, a halo appears—the diffraction pattern contrast declines, effective beam divergence angle generally increases.

That is why we are not interested in intensity distribution upon plane in the far-field zone but merely in I reduction in the central spot in the curve line peak. This provides information on a common degree of wavefront distortion—$\langle \Delta\varphi^2 \rangle$—averaged by aperture and the fact gives an idea of the optical quality of the medium the probe radiation passed through. This is the idea in the focal spot method.

We need to mention it once again that calculations generally involved the case of homogeneous and isotropic turbulence and the geometric optics approximation, that is, the phase difference is calculated as optical paths difference (2.3). It is often feasible as refraction ratio variations in a turbulent air medium are minor $\Delta n \sim 10^{-6}$, while beam distortion is consequently small at relatively short optical paths (boundary layers, mixing layers), the Fresnel condition is fulfilled $\lambda L/\Lambda^2 \ll 1$ [25]. However, it is known that there are no universal statistic turbulence models have yet described the turbulent flow properties. In various parameter ranges for various flow types, different models are applied (new or modified well-known ones). Thus, program packages need to be evaluated and the anticipation itself for a certain case needs to be checked. And certainly a test is required to develop calculation methods in aero-optics further on, which is usually emphasized [29].

The main bulk of earlier issued studies refer to investigation of radiation advance either through a boundary layer [30], or through a mixing layer [31–33] (also including the studies on how turret flow around aero-dynamics affects the produced beam quality [15–18]). Examinations of aerodynamic windows [11–14] shall be related to the latter. There are a number of studies where aberration source is a circular jet, for example [34].

As a complete theoretical analysis of aero-optical effects is complicated enough, the tests usually consider a possibility, first, to apply approximating Schtrel ratio to estimate I/I_0 in the far-field zone. Second, to define phase difference behavior, more expedient approximate expressions are suggested based on physical estimations and containing pulsation members that can be measured (for example, with a thermal anemometer), or aerooptical effect is estimated on the mean parameter measurement of the flow (boundary layer thickness, density gradient through a mixing layer, etc.).

During airborne full-scale tests [35–38] (subsonic velocity $M < 0.9$), upon probing beam passing through the boundary layer the values of I/I_0 obtained as results of aerodynamic and optical measurements were compared. A thermal anemometer and a laser Doppler velocimeter were applied for aerodynamic measurements of ρ' and u'. After the integral turbulent scale had been defined, integration across the boundary layer according to Equation (3.3) gives $\langle \Delta\varphi^2 \rangle$ and on the basis of (2.4) $I/I_{0\text{aero}}$ are obtained. Optical measurements: with a special rapid-shift interferometer [39] the modulation transfer function τ is measured and this allows calculating intensity ratio—$I/I_{0\text{opt}}$ in the far-field zone. Thus, we can obtain correlation between the aerodynamic and optical measurements results.

Actually, a possibility of applying correlations obtained in [3] for real flows was verified. Disagreement of values I/I_0 obtained by these two methods especially when the turbulent boundary layer was thickened with porous screens was noted in [40,41] where aerodynamic tubes experiments were described. Optical measurements and calculations conformity was verified [63] on the formula [3] in case of shear layers at low pressure and minor subsonic velocity. A similar attempt for the shear layer case was made [55]. Here it was proposed to define optical properties of transmitted radiation on the basis of a mean density gradient through this layer. The results of such an approach application were numerically tested in [56,57].

In addition, apparently, at thorough measurements of the properties of a boundary layer's pulsation, which is possible at subsonic velocity, when it is easy to apply a laser Doppler velocimeter, $I/I_{0\text{aero}} = I/I_{0\text{opt}}$. In case of supersonic velocity, the issue is more complicated. It is more difficult to measure velocity pulsation u' and separate pulsations ρ' and U' (thermal anemometer measures mass flow rate pulsations). That is the reason why in [30] it was analyzed a bigger number of experiments executed by NASA, and it was demonstrated that pulsation properties in a boundary layer could be estimated on the basis of mean values. Figure 2.52a shows how turbulent scale depends on a boundary layer thickness, and Figure 2.52b presents an estimation of pulsation intensity in a flow and at a wall. Similar results allow a prompt estimation of aerooptic effect for a turbulent boundary layer.

The number of studies referring to OQ of SGL medium is much less as usually sufficient attention was paid to energy parameters directly: energy stored in a flow, amplification factors, or output power. There were no attempts to connect certain parameters and flow peculiarities behind the MNB applied in a laser with optical properties of the medium and, consequently, radiation quality of the laser. This is somewhat clear, as on the whole a flow in a resonator cavity is more complicated than an individual boundary layer or mixing layer.

In [6] flow OQ behind the GDL screen nozzles was examined. The distance at which complete mixing of jets from adjoining nozzles occurs was indicated, that is, the distance where density disturbance level related to a regular flow structure was reduced to the value of ~1% was defined. It was proposed to install a resonator at this very location. Concerning turbulent pulsations it was noted that they affect the OQ value to a much lesser degree than that of regular structures. A partially reasoned—as further investigations of [53,54,68] have shown—conclusion stating that a determining factor of a flow's OQ is only regular

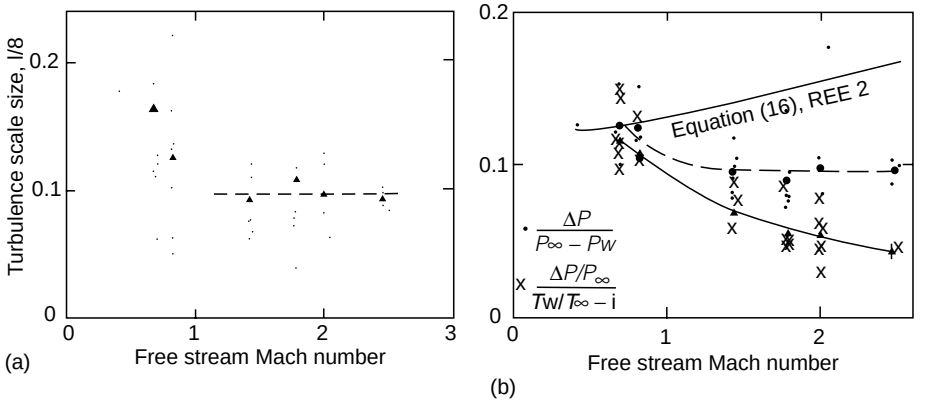

FIGURE 2.52 (a) The relation of scale of turbulent pulsations to boundary layer thickness. (b) The intensity of density pulsations in boundary layers. (From Sutton, G.W., Aero-optical foundations and applications. *American Institute of Aeronautics and Astronautics Journal*, 1985, Vol. 23, No. 10, pp. 1525–1537.)

nonuniformities, was also repeated in [9] while analyzing the flow behind mixing MNB for mixing laser systems. The basis for the conclusion was that a phase shift caused by regular nonuniformities was $\sim L$, and the one caused by random nonuniformities was $\sim\sqrt{L}$ [67]. But a shift for regular nonuniformities exists if there is $\Delta\rho$ along the aperture diameter, and if a sandwich of layers with $\Delta\rho$ is located perpendicular to the beam and along the entire aperture at once, the shift does not take place. While random nonuniformities do always cause it and that is implemented in the case of a flow behind the nozzle screens.

The conclusion on impact by regular nonuniformities only related perhaps to difficulty of interpretation of interferential patterns obtained upon flow probing at high M numbers and low density. As seen from the pictures presented in [6] the lines were wide and blurred, which refers to exposure period. At this rate in [34], where light passing through gas jets was examined, it was indicated that at exposure $\tau \sim 10^3$ sec interference fringes actually become wide as at such exposure turbulent pulsation effect gets averaged in time, and they can be resolved certainly with an instant shooting only ($\tau \sim 10^7$ s). The exposure period in [6] was most probably defined by shock tube operation period ($\tau \sim 10^3$ sec).

Therefore, an accurate estimation of the impact of the flow's random nonuniformities on OQ is possible at minor exposures. However, as we are still interested in phase behavior at quite long time periods, that is, mean phase behavior, in this case imposing result averaging requires bigger amount of shots (several tens if regular methods of interferogram processing are applied [34]).

Actually, it is clear that when considering the overall picture while estimating possible aberrations generated by all the systems of a powerful SGL (these certainly include beam emitting and aligning systems, mirror cooling systems, that is, effects of heating and deforming both structure elements and reflecting and radiation forming mirrors), wavefront disturbances specified by the turbulent pattern of active medium flow is, by all means, a part of the analyses [52,58]. But available works include very little data on the active medium's OQ.

Reference [10] estimates level of aberrations generated by an active medium of a chemical SGL equipped with various types of nozzle banks, including even screen ones, but the amount of numeric calculations obtained both with geometry optics approximation and diffraction effect consideration is limited. The study actually describes program package for aero-optic investigations. On the basis of Talbot interferometry [60] in [59] data on distribution of I/I_0 in the far-field zone for screen MNB mixing lasers are obtained. It demonstrates that the OQ of the flow deteriorates when the CO_2 admixing system is running, that is, when the system is running in the mixing mode, when compared with the homogeneous operation mode, that is, pure GDL. The task of correlating optical flow properties and its turbulent properties, which in their turn refer also to the bank structural features, and mixing process arrangement features—this task was not resolved during the work, which is reasonable considering its complicated nature. However, as two types of nozzle banks with different CO_2 admixing systems were tested, the influence of this factor—admixing method—on I/I_0 was disclosed in the study.

On account of the aero-optics objectives considered, it is necessary to mention adaptive optics capabilities [61,62]. For example, it is possible to adjust a wavefront pattern so that the distortion caused by atmosphere turbulence along the beam propagation path is compensated and thus optimal radiation propagation is provided from the point of view of achieving maximum energy intensity at a target. But it is difficult to count on such a possibility of correcting wavefront disturbances caused by random density pulsations in a laser's active medium. Pulsation frequencies are too high to be tracked with the help of deformable mirrors.

This is the reason why it is crucial to define the relationship between gas dynamic properties of a flow in a resonator cavity and MNB design parameters, as well as the connection between

these flow properties and the optical ones, that is, the flow's OQ. Such task was solved in [68, 69] for nozzle banks without mixing. This is a good basis to determine general approaches to the question of improving OQ of a laser's active medium due to adequate design of a nozzle bank.

2.3.3 On Experimental Methods of Optical Quality Research

On interferometry. The findings of flow OQ research with the focal spot method are presented below. The idea of the method is to measure the radiation intensity in far-field zone in the central spot. The optical diagram of method implementation is shown in Figure 2.53. Interferometry is frequently applied in aero-optics when, on the contrary, information on the wavefront distortion is obtained from the near field zone, and with the Schtrel correlation (2.4) intensity is calculated in the far-field zone in the central spot. The Schtrel correlation actually combines these two methods.

As mentioned earlier, however, while examining the impact of the pulsation properties of the flow on its OQ one needs to receive multiple instant interferograms and execute corresponding result averaging. Thus as where the measurement data of these two methods were compared [34], it was noted that ten photos are required for imposing result averaging. (it is clear that it is time-consuming to process such a number of interferograms to obtain one point). Otherwise point data are too scattered. In [51] it is stated that typical deviation of points obtained on the basis of single-piece interferograms comes to more than 20%. Apart from that one needs to keep in mind that an error in measuring the $\Delta\varphi$ phase root-mean-square deviation leads to major errors in the intensity value, as $\Delta\varphi$ is an exponent indicator in the Schtrel correlation. That is the reason why it appears that to identify the impact of the main physical mechanisms on light scattering in a flow it is more convenient to apply the focal spot method as a direct method.

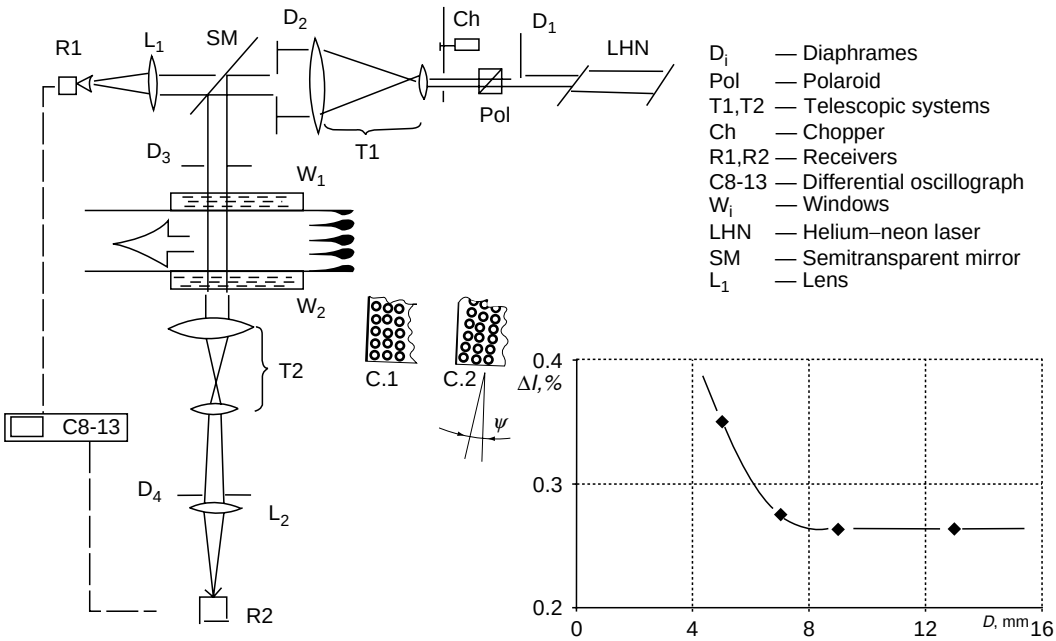

FIGURE 2.53 Scheme of measuring of flow OQ (a) and dependence of $\Delta\bar{I}$ value on probing beam diameter (b) screen MNB–SNB.

It is important to note that speaking about interferometry we mean conventional methods. In general, the methods of photometric measurements for interference fringes or fringe contrast measurements with shearing interferometers [42] allow obtaining information on stochastic processes on the basis of a single interferogram.

On a narrow aperture version of the focal spot method. The scheme presented in Figure 2.53a is not unique. Different versions of the focal spot method implementation can be found in [34,43]. Application of the narrow aperture measurement version as opposed to the commonly used wide aperture method, when they strive to probe the entire resonator cavity, allows resolving measurements in space. It is required when an objective of a research is to define how individual components of a flow's complicated structure affect the flow's OQ.

Selection of a certain dimension for a probing spot is imposed by the object under survey. First, we look forward to resolving a regular structure assigned, for example, by shock waves, and on the other hand a beam cannot be too thin, as its diameter shall house averaging by the turbulent structure for the results not to depend on the probing beam aperture dimension. This is the reason why, apart from general considerations, a certain dimension of a probing beam is imposed by a nozzle bank geometry, which assigns the typical dimensions of the structure of the flow. The results in Figure 2.53b are presented to illustrate the above stated. It indicates a relative value of a scattered portion of light $\Delta I/I_0$, obtained in a flow behind a nozzle bank when measuring diameter D_3 of a probing beam. One can observe that in the case of such a bank geometry the result ceases changing after 7 mm. The geometry of the tested banks will be described further, but as the output diameter of individual micronozzles in a screen MNB was maximum 5 mm and at a close-packed staggered structure the distance between rows made about 4 mm, application of a probing beam of 9–10 mm in diameter in tests is reasonable.

The selected beam diameter is admittedly bigger than vortexes in the wakes behind the flat blades in the case of two-dimensional banks application, and in the screen nozzle banks' case—as it follows from Figure 2.53—the same diameter already housed averaging also by the regular structure. What we mean is not only the shock wave and expansion wave systems but also sandwiched layers of different mean density. Density of one type of layers is defined by a parameter of the flow behind the intersection between adjoining rows of micronozzles (these intersections form the main area of the bank's base areas), that is, it is the wake density. While density of the other type of layers—in the center of the nozzle rows—is defined mainly by the density of the flow core behind an individual micronozzle. That is why the results for $\Delta I/I_0$ did not change if the probing beam of $D = 9$ mm shifted vertically. (Patterns of the flows behind the flat banks are presented in Figure 2.8 and Figure 2.9, and behind the screen MNB—in Figure 2.59, Figure 2.62, Figure 2.63.)

Now we need to point out the following. Application of a probing beam of a relatively small diameter leads to the fact that phase progression caused by a large-scale parameter variation, for example, with density growth along the entire resonator's length—the optical wedge, is eliminated from the consideration. Potential heavy density disturbances at the resonator cavity edges are not included in the examination either. That is why averaged phase variations obtained for a beam of a relatively small diameter can appear less than in the case of probing along the entire aperture. But, generally all these factors can be taken into account.

Thus, on interpretation of the results obtained with the narrow aperture version of the measurement method one should proceed from the following. The flat nozzle banks where shock wave structure was allowed (meaning the shocks from the top and bottom walls of the working channel, coming from the nozzle neck see Figure 2.32), are specified by the case when the transfer function $\tau(x,y)$ in expression (2.1) is only defined by the turbulent section. As when scattered at the turbulent wakes the probing beam passes through the shock wave

structure emerging behind the blade edges transversely, and the shock waves and expansion waves compensating each other do not change the average level of the mean density. In the screen nozzles the result is described by the transfer function, which already has both the turbulent portion and the portion related to the regular structure of averaged flow parameter variation. As in this case, as mentioned above, result averaging for several sandwiched layers of different density takes place along the probing beam aperture (and if near the bank exit averaging takes place also according to the shock wave structure).

Finally, if the opening or the diameter of the probing beam is of a finite size when compared with the turbulence scale, the transfer function (2.1) has also the portion defined by this diameter—an instrumental one [3]. In our case it is a constant member (D did not change during the tests and $D \gg \Lambda$) and it can be excluded from the analyses as relative values are considered—I/I_0.

On the role of diaphragm D_4. As the probing beam took shape with the help of a circular diaphragm D_2, as it is known, the Fraunhofer diffraction pattern is realized in the far field zone at a circular opening: interstratified dark and bright rings with a bright Airy disk in the center [24]. In addition, to estimate the value of the aperture root-mean-square wavefront distortion it needs—as the Schtrel formula requires—to measure intensity correlation in the central spot in the peak of the curve line describing intensity distribution across the beam (if there are disturbances at the beam's path—it is I, if there are no disturbances—I_0).

Intensity distribution is obtained, for example, with video windows—a sensing matrix—with an instant-return diaphragm, as for example in [43]. It takes one diaphragm aperture to make a complete picture of distribution of I in a plane. But one can proceed the other way. Diaphragm D_4 is set by the first dark ring right behind the disk and thus I distribution wings are detached at once. The radiation generated by the disk is collected by a lens on a receiver, that is, the integral value is measured—the integrated disk radiation, where the distributions curve is a strongly marked narrow peak. As the diffraction pattern does not change on scattered radiation at the turbulent layer [3,28], it is only that its intensity decreases, the correlation of the measured integral values corresponds to I/I_0 in the curve peak as the signal is averaged on one and the same diameter.

2.3.4 Asymptotic Estimation of the Radiation Scattered Portion Behavior on Flow Probing behind the BNB

As we pointed out before, in [3], the wave equation had been integrated for the case of the homogeneous and isotropic turbulence and the Gaussian correlation function. The expression (2.3) has been obtained for $\Delta\varphi$. In case of minor aberration relative intensity of the radiation $\Delta I/I_0$, that has passed the turbulent layer of thickness L (if we regard that n' and Λ do not change much across the layer, and $\Lambda \ll L$), can be written, on the basis of (3.3) and (3.4) as the following:

$$\frac{I - I_0}{I_0} = \frac{\Delta I}{I_0} \approx 2\left(\frac{2\pi}{\lambda}\right)^2 \langle n'^2 \rangle \Lambda L.$$

In [31] it was suggested that one should estimate $<n'>$ on the basis of the Gladstone–Dale correlation:

$$\langle n'^2 \rangle \approx 4\beta \frac{\langle \rho' 2 \rangle}{\langle \rho \rangle^2} \frac{\langle \rho \rangle^2}{\rho_{ref}^2},$$

where ρ_{ref}^2 is the density in normal conditions, when the Gladstone–Dale constant β is defined. It is correct when mixing of various gas flows takes place in the shear layer and at that it is assumed that fluctuations β' are equivalent to fluctuations ρ'. In the case when similar gases are mixed the same expression is derived but without coefficient 4. Then it can be written as following:

$$\Delta I = \frac{\Delta I}{I_0} \approx \frac{8\pi^2}{\lambda^2} \beta^2 \Lambda L \frac{\langle \rho'^2 \rangle}{\langle \rho \rangle^2} \frac{\langle \rho \rangle^2}{\rho_{ref}^2} \tag{2.5}$$

This expression is frequently applied to calculate ΔI, and further on it will be used to interpret experimental findings. Now let us estimate the asymptotic behavior nature of the value of $\Delta \bar{I}$ for the radiation that has passed a supersonic flow behind the blade nozzle bank. The main disturbance factors in the flow in this case, as mentioned before, are the shock waves and the expansion waves emerging behind the blade edges, and the wakes. In the case of the narrow aperture measurement version when we resolve the regular structure related to the shock waves coming from the flat channel walls from the nozzle neck (see Figure 2.32) (while the shock and expansion waves coming from the blade edges are crossed transversely by the probing beam), the main reason for scattering the probing radiation shall be the turbulent nature of a flow in the wakes.

There are numerous experimental findings on the structure and properties of turbulent wakes and mixing layers, so it helps to make the following estimation. Turbulent scale Λ is proportional to the thickness of layer L: according [44] for shear layers $\Lambda \approx 0.25L$; for boundary layers, as the analyses of results in [30] prove, approximation is acceptable $\Lambda \approx 0.1L$ (see Figure 2.52a). Measurements in a wake behind a flat body [45] resulted in $\Lambda \approx 0.3L$ (see Figure 2.27). Thus, it occurs that $\Lambda \sim L$.

The behavior of relative intensity of density pulsation ρ'/ρ in a wake was illustrated earlier in Figure 2.26. As one can see ρ'/ρ alters only in the beginning at the transition section, whereas in the section of developed turbulence ρ'/ρ becomes almost a constant value.

On the layer thickness $L(x)$. It was shock waves and expansion waves impact on a wake that made the difference between the problem on a wake behind flat blades considered in Chapter 2 and a regular aerodynamic problem on a free wake. The implemented measurements proved that the self-similarity of a flow in a wake behind a blade (within the limits of measurement accuracy) remains in our case also, that is, the parameter distributions across the wake represented in the corresponding coordinates intercoincide with any cross section. And, thus, a result well known in the wake theory was obtained: $L(x) \sim \sqrt{x}$. First of all, it refers to the fact that the expansion area in the flows under consideration always closes with a shock wave and these two factors sort of compensate each other. Impact of just one shock causes exactly flow self-similarity violation, its thickening.

So, if the main reason for probing beam scattering is turbulent density pulsation in flat wakes behind the blades, than inthe formula (3.5) the main members' behavior asymptotics is estimated the following way: wake thickness along the flow $L(x) \sim \sqrt{x}$, turbulent integral scale $\Lambda \sim L$, and density pulsation intensity $\rho'/\rho' \approx constant$. Then from (3.5) it easily follows that:

$$\Delta I / I_0 \sim x \cdot \rho^2 \tag{2.6}$$

2.3.5 Optical Quality of Supersonic Flows behind the BNB

The same nozzle banks (consisting of three central blades and two side ones) were applied in the optical tests as those applied in the gas dynamic measurements: each individual nozzle was

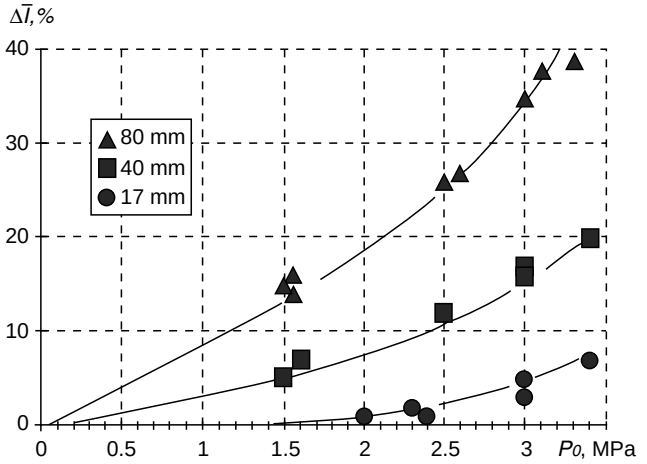

FIGURE 2.54 Dependence of $\Delta\bar{I}$ value on pressure (blade MNB – BNB).

of a critical cross section of $h^* = 0.49$ mm and expansion degree designed for number $M = 5$ (taking into account the boundary layer displacement thickness). During the experiments, blade edge thickness t changed along with the flow's exit angle α.

Figure 2.54 and Figure 2.55 present the data for ΔI at $x \leq 90$ mm (in the first window of the aerodynamic channel). As one can see the results are in agreement with estimation (3.6): dependency on pressure P_0 is nonlinear close to a quadric one, while on x—it is linear, ΔI increases as x grows (in all the cases the end of the supersonic section was counted as the reference starting point of x, including the shortened blade banks). The fact that the experiments confirmed estimation (3.6) proves that, first of all, scattering in our case really occurs mainly in the turbulent wakes. If the determining factor for wavefront distortion had been stationary density nonuniformities related to the intensity of the shock wave structure behind

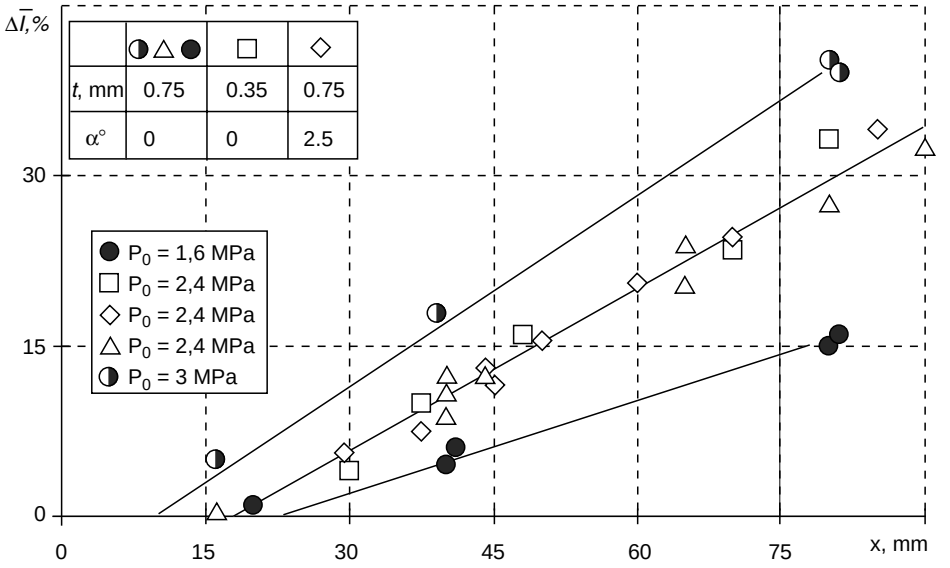

FIGURE 2.55 Behavior of $\Delta\bar{I}$ value along the resonator cavity ($X < 100$ mm) (BNB).

the blades, then the value of $\Delta I/I_0$ would have reduced as the intensity of the shocks decreased along the flow. Figure 2.13 illustrates the decrease (the intensity rate is counted as ratio $\Delta\rho_{ck}/\tilde{\rho}$ is the density difference before and after the shock to an average level of ρ in the flow core), and as one can observe, intensity of the disturbances related to the shock waves behind the blades depends on the values of t and α.

The found effect (growth of $\Delta\bar{I}$ with the increase of x) somehow resembles an optical wedge, whose presence was mentioned in the studies before, but it was related to the density increase in the channel. The presented results prove that increase in $\Delta\bar{I}$ cannot be explained in this case by density gradient only. According to gas dynamic measurements increase in ρ at a distance of 100 mm makes ~5% (see Figure 2.16), whereas the scattered radiation portion at a distance of 50 mm increases by two times and depends greatly on the pressure level. It shall be noted as the genuine optical wedge, related only to the constant density gradient along the flow, would have been eliminated by a corresponding resonator setting as such a gradient only causes a common wavefront inclination. The obtained data proves that phase alteration in a flow behind flat banks cannot be compensated by a resonator adjustment as it relates to a turbulent nature of a flow in wakes. There is an averaged root-mean-square phase difference, $\langle\Delta\varphi^2\rangle$, defined by density pulsation in a wake, and it increases along the flow due to the layer thickness L growth and, consequently, the turbulent scale Λ.

It appeared to be unexpected that results for all the flat banks were almost the same. To illustrate this Figure 2.55 shows points for three banks with different t and α at $P_0 = 2.4$ MPa. One can observe that all the points lay in one line (that is why Figure 2.54 and Figure 2.55 present data only for some banks). Aerodynamic measurements actually showed (see Figure 2.25) that in our case the wake thickness for all the blades is similar. Though it was expected that turbulent wake flow characteristics variation is possible, especially for the shortened blades, when the flow exit angle at a blade's end made a considerable value. At least comparison of the pictures of flows behind the banks (see Figure 2.9 and Figure 2.10) provided a qualitative indication on some increase in Λ. At the same time intensity of the shocks behind the blade edges, as it was mentioned before, was substantially different (Figure 2.13).

Similar $\Delta\bar{I}$ indicates that the influence of the shock wave structure and regular nonuniformities related to it is minor. Influence of the parameters α and t upon $\Delta\bar{I}$ (turbulent flow characteristics may change on variation in the parameters), was not found in this series of experiments. It is so because, first of all, the parameter variation range was not big. Moreover, second, the shortened blades were manufactured in such a way that when t grows α simultaneously increases. The effect of the factors is opposite: as the nozzle bank experiments proved increase in α causes decrease in pulsation intensity ρ'/ρ, while increase in t shall cause an increase in Λ.

The pattern of results obtained in the second window ($x > 150$ mm) differs vastly from the data for $x < 90$ mm that is specified by the change in flow structure in this section. Behavior of $\Delta I/I_0$ in the sections of $x > 100$ mm is of certain interest because the size of resonators of powerful SGL lasers can reach as much as 200 mm and more. However, at a bigger distance from the bank exit as the flow wake thickness grows their interaction is inevitable and it means that the wakes cannot be considered to be free.

To confirm this Figure 2.56 presents a pattern of the flow behind the flat nozzle, the pattern is obtained on the basis of two windows moving in succession (distance from the blade ends is indicated under the pictures) upon two positions of the knife. A bank with a thickness ($t = 2.3$ mm) blade in the center was selected on purpose as many particularities of the wake flow are observed more clearly. Simultaneous correlation with a flow behind a thin ($t = 0.35$ mm) blade qualitatively indicates how the t parameter influences a wake structure.

All the disturbing factors are clearly seen in the first window: a shock wave system (1) and an expansion wave system, (2) emerging due to the flow turning at the blade ends, wakes

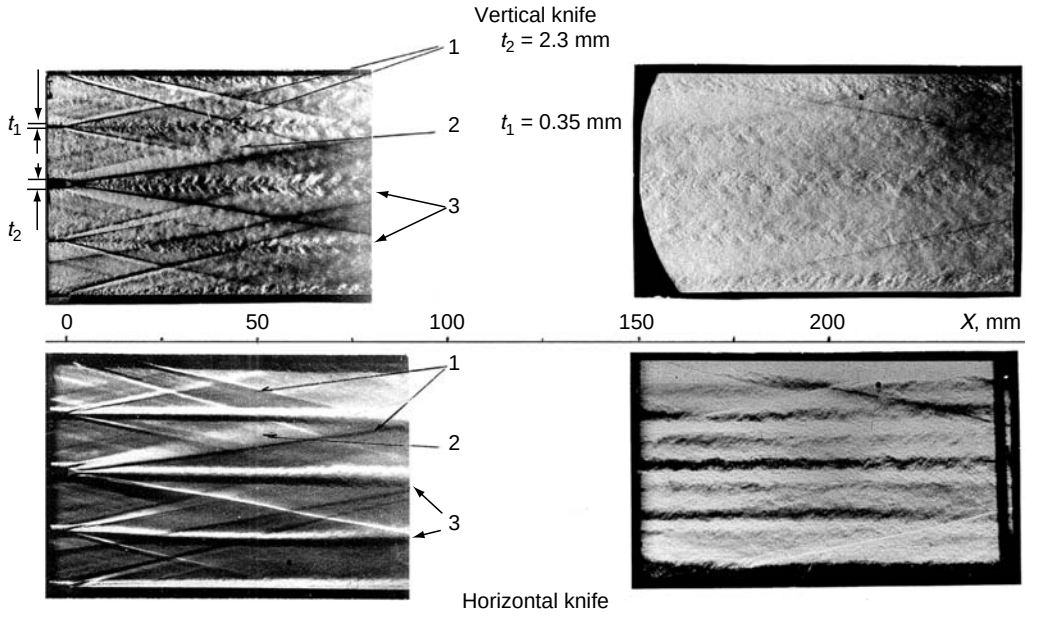

FIGURE 2.56 The wakes behind the blades of BNB.

(3) where vortex structure of the flows developed into a large-scale one. In the second window flow structure actually changes its type. In the area of $x \sim 150$ mm adjoining wakes start to overlap and to interact between themselves. During this time (as one can see on the pictures obtained with the vertical knife) large-scale vortexes develop in a wake, the entire flow gets turbulized, one cannot distinguish a flow core and a wake. Thus, the entire flow—from the optical standpoint—becomes almost homogeneous and with a distinctively smaller turbulence scale when compared with the one recorded in the wake at the first window's end.

Though pressure probe measured distributions of the flow averaged parameters along the channel cross sections still indicate typical breakdowns in distributions related to the presence of wakes. It is clearly seen also on the pictures obtained with a horizontal knife when lateral density nonuniformities stand out strongly. A regular flow structure defined by the wakes still exists and, thus, complete flow mixing—from the gas dynamic standpoint—has not occurred yet (the issue of poor wake mixing in supersonic flows has been known in aerodynamics long ago).

As one can see in Figure 2.57 (it presents data on two values of stagnation pressure P_0), behavior of $\Delta I(x)$ obtained along the entire working channel's length visibly represents the pattern of flow development described here. Values of $\Delta \bar{I}(x)$ after linear growth up to $x \approx 100$ mm in the area of $x \approx 150$–170 mm have reduced. The result is certainly explained by the flow structure variation, and, first of all, variation of the turbulent scales, which is clearly qualitatively recorded in the pictures. The quantitative estimation requires measurements of density pulsation intensity as the result $\bar{\rho}' \approx constant$ from [45] was obtained for a free wake, which in our case at $x > 150$ mm is not fulfilled (the wakes interact and become plane-parallel layers). And, most likely, ρ' will change. We need to note that formula (2.5) is correct for homogeneous and isotropic turbulence, while in a nonuniform nonisotropic case, as it was underlined in [46], large-scale vortexes influence is stronger as compared to small-scale ones.

The results presented in Figure 2.57 are common for all the flat banks with different t and α. Within the measurement accuracy limits, no differences were detected. (though as it is identified below the screen banks, results prove that α effect exists).

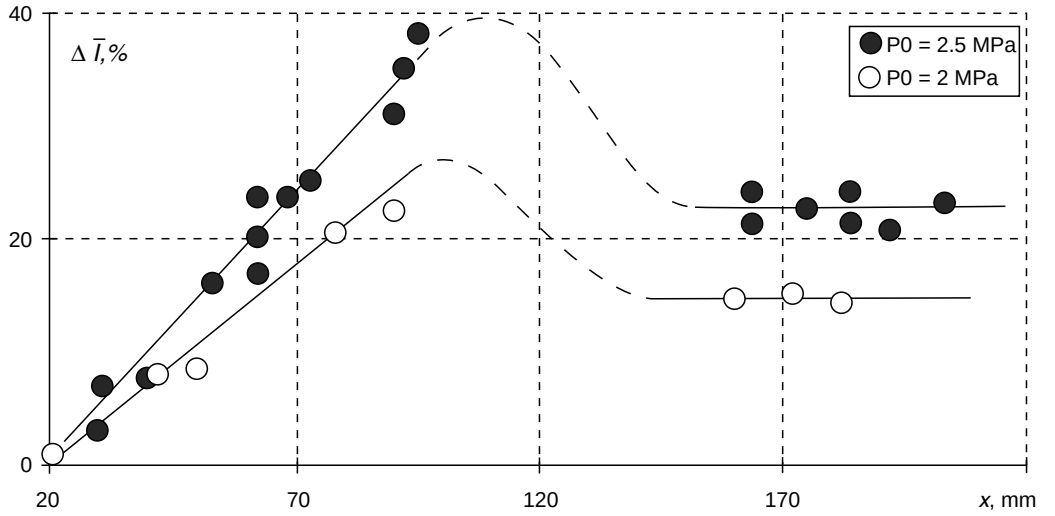

FIGURE 2.57 Behavior of $\Delta\bar{I}$ value along the resonator cavity ($x > 100$ mm) (BNB).

Unfortunately, experimental points have not been obtained for the area of $100 \leq x \leq 150$ mm—it is the place where the intersection between windows is located. That is the reason why shape of $\Delta\bar{I}(x)$ in this location is presumable. But it is natural to assume that $\Delta\bar{I}(x)$ can grow after $x = 90$ mm. The wakes in the first window do not join yet; their thickness will still be increasing along the flow and, consequently, Λ will grow. It is also clear that inflection of curve $\Delta\bar{I}(x)$ will take place earlier if the distance between the adjoining blades is reduced—a smaller critical cross section is taken for the nozzles while the same expansion degree is remained, that is, the average density in the flow remains the same. At that, presumably, the turbulence scale will also be smaller in the wake mixing zone—the mixing will start at smaller absolute dimensions of the wakes. It is such a mechanism of quite a rapid formation of a turbulent uniform—from the optical standpoint—flow at minor absolute dimensions of individual nozzles in a bank that explains screen banks results outlined in the following section.

In actual laser operating conditions, at high temperature and pressure (for a GDL case), deformations occur in a flat nozzle bank, and the blades bend. In particular, it causes the situation when critical cross sections of individual nozzles in a bank change. Figure 2.29 presents flow patterns when critical cross sections of one of the nozzles are smaller or bigger than those of the others. Note that it causes wake distortion and common flow turbulization between the wakes that came together and, consequently, an increase in area occupied by the turbulent flow.

To model the impact of critical cross-sections fringe in a bank upon flow's OQ, a MNB of nozzles was assembled where the critical cross-section dimensions h^* came in series: 0.3, 0.7, 0.3: and 0.7 mm. The total area of critical cross sections with respect to a regular nondeformed bank (where $h^* = 0.49$ mm) is preserved, that is, expansion degree of a flow in general behind the bank is unaltered so that the average density level of the flow for the two banks under comparison would remain the same. It is only under such a condition that it is possible to compare results for different banks, as the value of $\Delta I/I_0$ according to (2.5) depends strongly on a flow's average density.

Results of $\Delta\bar{I}$ for two banks—the deformed bank and the ideal assembly bank—are compared in Figure 2.58. As one can see that though it is not significant, an increase in $\Delta\bar{I}$ is detected both x when $x = 40$ mm and when $x = 80$ mm, covering the entire resonator area. In reality, impact of the blade distortion upon the flow OQ will still be considerable. First of all,

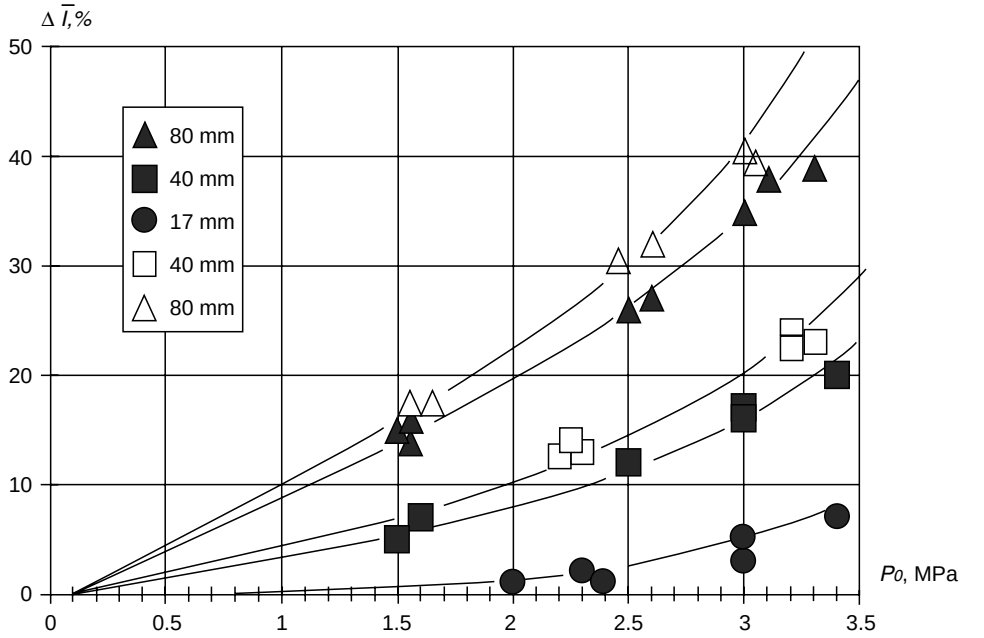

FIGURE 2.58 Comparison of results for ideal (dark symbols) and deformed (opened symbols) BNB.

there will not be such a symmetrical variation of h^* as it is in a model experiment, and the main thing is that right after the first start, the critical cross section becomes changeable along the blade's height (and in this case bigger blades' systems are in the worst conditions). It means that stationary density nonuniformities also occur along the aperture's diameter. And, consequently, the shift of phase specified by the turbulent pattern of a flow will be accompanied by effects of wavefront distortion upon these stationary nonuniformities—unequal averaged optical paths in various aperture points, which does not occur for an ideal assembly of a flat bank.

We need to remember that when there is a fringe in dimensions of critical cross sections, a direct reduction in output radiation power is observed. Apart from the decrease in $\Delta \bar{I}$ in the far-field zone (Figure 2.58) because of aberrations—wave front distortions emerging in a light beam when it passes through nonuniformities in a resonator cavity due to diffraction effects of beams' path in the resonator—changes also occur because of violation of strict uniformity and symmetry of the flow pattern due to distortion of wakes behind the nozzle blades (the latter refers to the geometrical optics). Thus, inevitable flat bank deviations from the ideal assembly case caused by defects emerging both from operation and from the actual assembly deteriorate the laser's power characteristics and the quality of its radiation.

In this regard, screen MNBs are a good alternative to the flat banks, thanks to their structure similar deformations—variations in areas of individual nozzle necks—cannot take place in MNBs (either the neck remains the same or the bank is destroyed). However, the question of the flow OQ behind them has always been there. This problem is examined in the next section.

2.3.6 Optical Quality of Supersonic Flows behind the SNB

The GDL screen nozzles as an alternative to the flat banks were suggested for the first time in [8]. Further development of the idea was application of their elaborated modifications in mixing lasers [9] and chemical lasers [10]. In the general case, a screen nozzle has a screen of densely arranged conic or similarly profiled micronozzles (in the case of a GDL) or

micronozzles of two types (for mixing or chemical systems). There are results for MNBs consisting of similar micronozzles. In the banks designed for optical measurements, they had the expansion degree of 25 and similar subsonic section—a conic one with the inlet angle of 120°. The main geometrical dimensions of the tested models are presented in the table below.

Bank	d^*, mm	d_e, mm	α	ψ	L_{sp}, mm
c-1	1	5	10	0	11
c-2	1	5	10	13	11
c-3	1	5	20	0	5.4
c-4	1	5	20	13	5.4
c-5	0.7	5.5	20	0	3.75
c-6	1	5	5	13	10.5

d^*—dimensions of a critical cross section, and d_e—dimensions of an outlet cross section of micronozzles in a bank.

Banks (c-1)–(c-5) consist of conic micronozzles that explain why their expansion half-angle φ and flow exit angle α coincide. Bank c-6 consists of profiled micronozzles—the profile is calculated according to the method of characteristics. It was a cut profile and not a complete profile, so the exit angle was 5° (the supersonic section of the profile was $L_{sp} = 10.5$ mm). As compared to the nozzle devices applied in gas dynamic measurements, these models had an extra parameter, ψ the inclination angle of rows of micronozzles about the optical axis. The overall view of the models and layout of the micronozzle cross section in the banks are presented in Figure 2.59 (it also includes pictures of the flows (View A) behind the banks of $\psi = 0°$ and 13°). The total area of the critical cross sections of all the micronozzles complied with the total area of cross sections in the flat nozzle banks. As the measurements were carried out in the same channel it provided a similar mean density level in a flow for all the MNBs compared. As it was pointed out in the previous section, it is this very factor that allows correctly comparing the measurement results for ΔI of blade-BNB and screen-SNB banks.

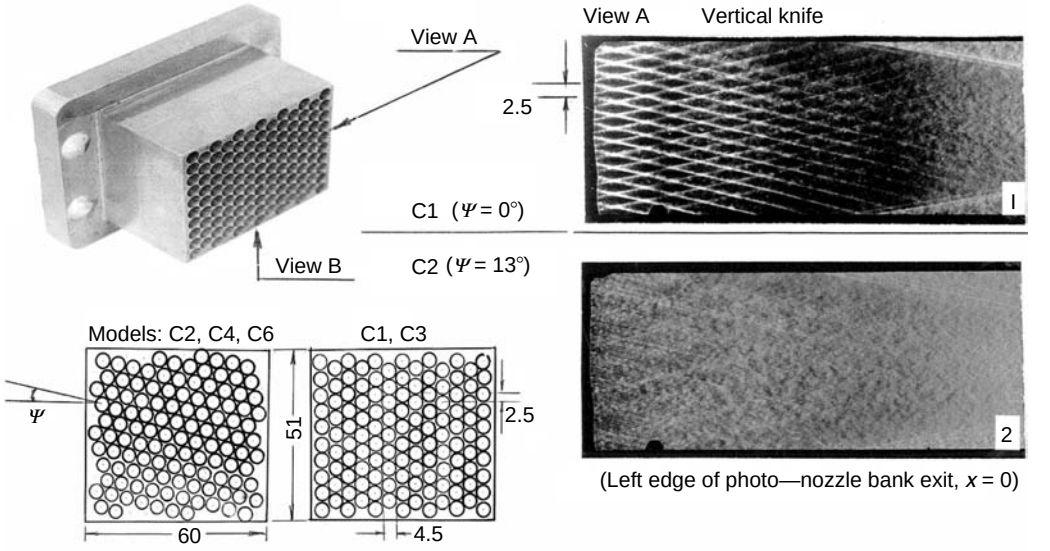

FIGURE 2.59 General view of SNB model, flow field in first window ($x < 100$ mm).

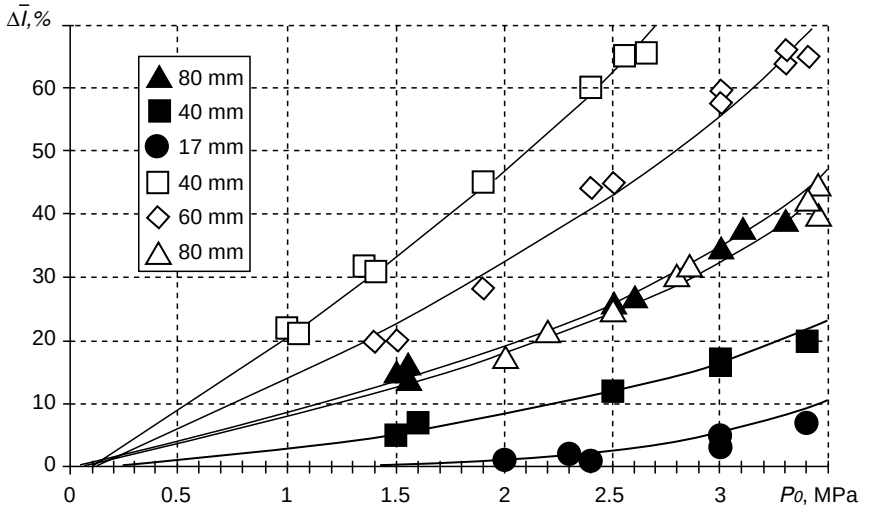

FIGURE 2.60 Comparison of dependences of $\Delta\bar{I}$ value on pressure for BNB (dark symbols) and SNB (opened symbols).

Figure 2.60 presents dependence of the relative portion of scattered light $\Delta\bar{I}$ from pressure at various distances from the screen bank exit as compared to the flat banks data (empty keys stand for the SNB results, black keys stand for the BNB results). The pattern of the dependence is similar for all the screen banks and, as it follows from the diagram, it is the same as for the flat banks. It is natural that $\Delta\bar{I}$ depends on the mean density of a flow but unlike the case of the blade MNBs the total value of ΔI reduces as the distance to the screen bank exit increases.

The overall dependence $\Delta\bar{I}(x)$ along the channel length for the banks with different exit angles α is presented in Figure 2.61. Thus, behavior of $\Delta\bar{I}(x)$ in flat banks and screen banks is polar; though, in both the cases the intensity of regular density nonuniformities of the shock wave structure reduces along the flow. Consequently, this is another point supporting the idea that not these stationary nonuniformities in our case define the behavior of $\Delta\bar{I}$ in the resonator cavity.

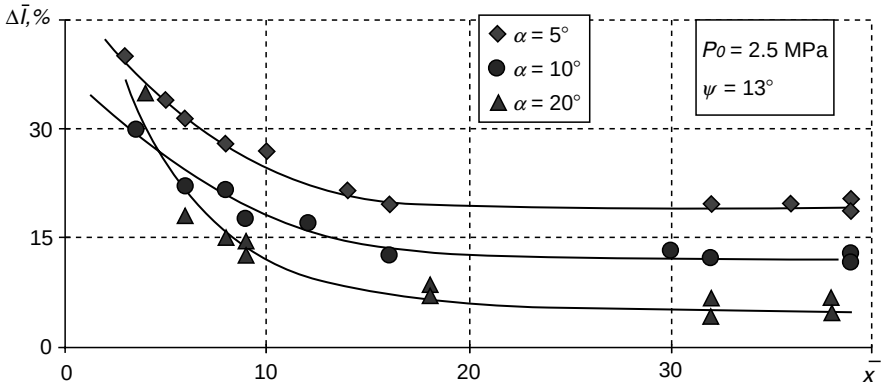

FIGURE 2.61 Influence of micronozzle exit angle α of SNB on flow OQ in resonator cavity (◆—profiled; ●, ▲—conic micronozzles).

Figure 2.61 indicates that as α increases the scattered radiation decreases. This factor and the qualitative run of the curves $\Delta\bar{I}(x)$ can be explained by the data on mass flow rate pulsation intensity $m'(x)$ (this crucial result dependence $\langle m'(x)\rangle$—is represented in Figure 2.51b). Comparison of results for $\Delta\bar{I}(x)$ and $m'(x)$ proves that while for the BNB the behavior of $\Delta\bar{I}(x)$ was mainly defined by the scale effects—increase in wake thickness and its integral scale, in the case of the screen banks—the pattern of dependence $\Delta\bar{I}(x)$ is to a great extent defined by density pulsation intensity $\bar{\rho}'$. Qualitative behavior of the curves $\Delta\bar{I}(x)$ and $m'(x)$ is the same. (The thermal anemometer's signal is proportional to m', but as the main portion is introduced to the signal by density pulsations, the behavior of ρ' and m' remain similar. Separation of ρ' and velocity is generally possible at special allowances.)

The second parameter that could influence the dependency pattern $\Delta I(x)$ is the integral scale Λ. As the pictures of the flow behind the screen banks (Figure 2.59 and Figure 2.62) show the flow gets almost homogeneous from the optical standpoint when a single scale Λ is somewhere at a distance of $\bar{x} \approx 15$–20. Here, as View A and View B illustrate, the shock waves almost completely attenuate (moreover, they are not recorded upon measurements carried out with the pressure probes). Examination of values of Λ behind the perforated screens performed [48] proved that Λ really changes slightly along the flow (experimental points are obtained up to $x \leq 40$) and depends on the screen dimensions. This is the reason that for the banks with similar d_e and nozzle arrangement, Λ in the flow will be similar along the channel $\Lambda \approx constant$ also. On account of both this fact and the behavior of $m'(x)$, the value of $\Delta I(x)$ stops changing after $\bar{x} \approx 20$ as shown in Figure 2.61—that is, from the optical standpoint, in the area of $\bar{x} > 20$, the flow becomes almost homogeneous.

But, complete mixing of the wakes and individual jets, from the gas dynamics perspective—as it was mentioned earlier, and for flat nozzles—takes place much farther. It is also indicated in Figure 2.62. The pictures in the area of $x \approx 200$ mm (in the second window) were made with a horizontal knife on purpose. It can be seen in bank c-1 the layered flow pattern is observed

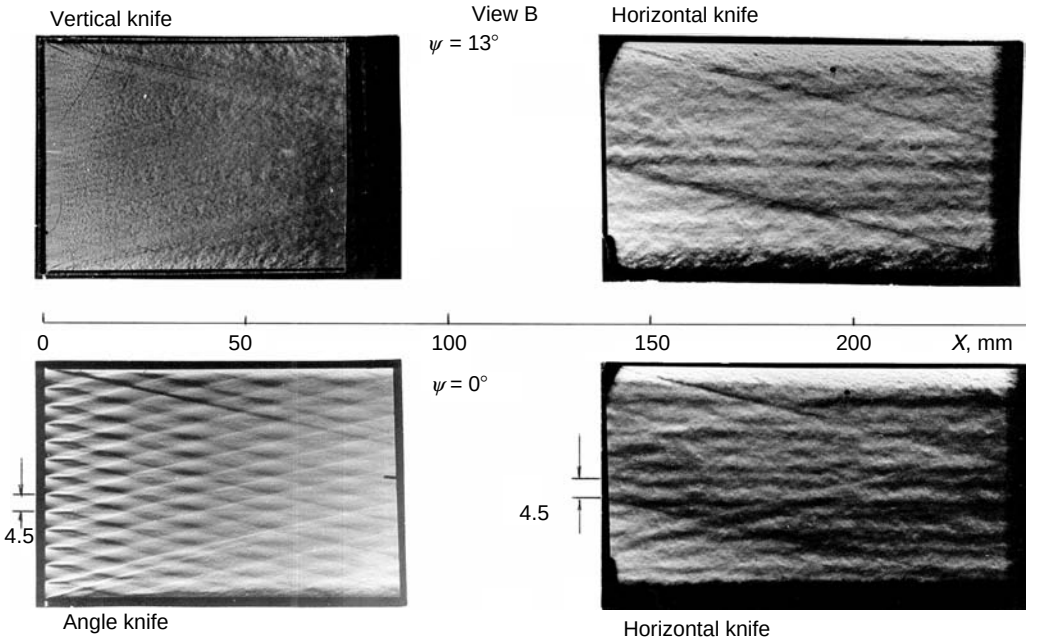

FIGURE 2.62 Flow field behind the SNB.

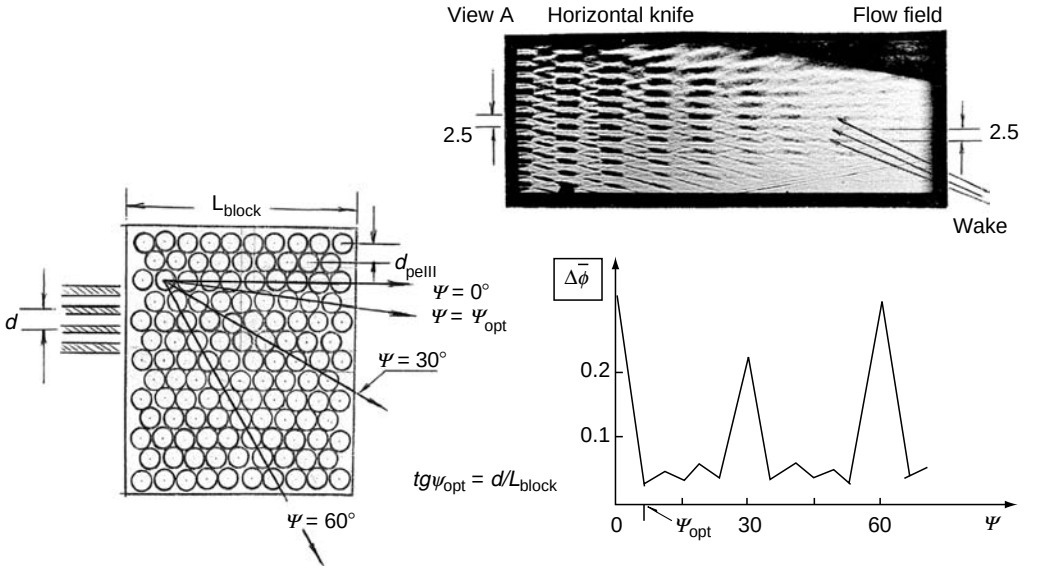

FIGURE 2.63 Choice of optimal angle ψ of micronozzles' rows skewing in SNB (regarding to resonator axis).

clearly, and the pattern refers to the difference in the flow density behind the base areas and the flow density along the nozzle axes. It is clear that the period of layers' alteration is defined by the bank outlet cross-section geometry (Figure 2.59), that is, in View B, the period makes 4.5 mm, whereas in View A it makes 2.5 mm (see Figure 2.63).

Comparison of the flow patterns for banks c-1 and c-2 in Figure 2.62 demonstrates how optical flow uniformity is improving upon misalignment of micronozzle arrangement axis, and how flow layering disappears in the second window if looked in a specific angle. In Figure 2.59, View A shows how the pattern of the shock wave structure changes. (Oblique shocks through the entire field were recorded and are shown in the second window in Figure 2.62; they are produced by various joints of the channel and, in particular, the joint between the nozzle bank itself and the channel.)

The registered flow peculiarity—occurrence of regular structure of averaged density nonuniformities (layering)—should have become apparent in results of measurement of $\Delta\bar{I}$ for the banks with different values of ψ. Figure 2.64 presents comparison of such data for the flows behind banks c-1 and c-2, c-3 and c-4, which only differ in the value of the angle ψ. As one can see, differences in $\Delta\bar{I}$ for the banks, where rows of micronozzles are arranged diversely, remain further along the flow, though after $\bar{x} = 20$ they become minor (density difference between the layers is already minor here and it can, for example, be visualized only with the help of the Schlieren method upon knife's horizontal position).

It is clear that differences for $\Delta\bar{I}$ will eliminate only in the place where the flow becomes completely homogeneous from the gas dynamics standpoint also. Figure 2.49 discloses variation of density nonuniformities intensity along the flow behind the conic SNB ($\Delta\tilde{\rho}$-mean value of the maximum deviations—outside the boundary layer—of the averaged density along the cross section from the averaged density value $\tilde{\rho}$ in this cross section, that is, $\Delta\tilde{\rho}$ is defined by the averaged flow's layered pattern itself than the pulsation properties of the mixing zones). As one can observe, $\Delta\tilde{\rho}/\tilde{\rho}$ falls down to the level of 1–1.5% somewhere in the area of $\bar{x} = 80$–100, that is, here the flow becomes homogeneous in terms of gas dynamics, and consequently, here $\Delta\bar{I}$ for the banks with different ψ will quit is different.

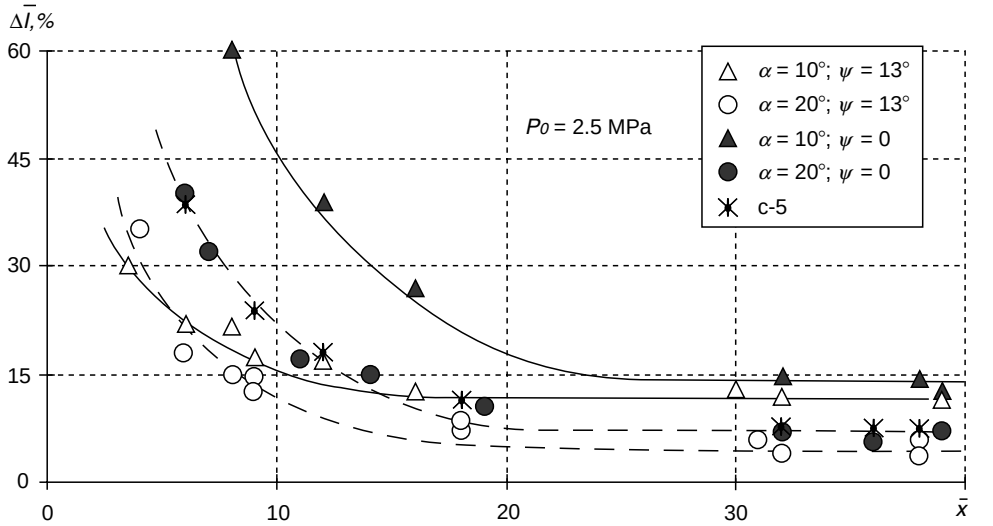

FIGURE 2.64 Influence of angle ψ on flow OQ in resonator cavity for SNB with $\alpha = 10$ and 20° (*—bank c-5).

The fact that improvement in the flow quality for the banks with the misaligned micronozzles' axis is remarkable. The flow's OQ improvement is detectible to the highest degree at the initial section where the regular structure's influence is still strong, and the structure refers directly to the jet nature of the flow from individual nozzles of the bank; the process of their jet mixing has just started here.

But, the represented result—dependence of $\Delta\bar{I}$ from the flow's regular structure—differs from the conclusions of study [6–8], where the shock wave structure emerging behind the screen bank exit was considered the determinative one, and the turbulent pulsation impact upon $\Delta\bar{I}$ was considered minimal—the wakes were not reviewed. It is the fact that $\Delta\bar{I}(x)$ achieves its least values at the distance of 20–30 caliber than $\bar{x} = 80$–100, that proves that the flow's OQ is affected, first, by the behavior of the flow's turbulent properties. It is also confirmed by the dependence of $\Delta\bar{I}$ from the angle α. If the shock wave structure had been the main factor specifying distortion of the wavefront of the probing beam than upon increase in the value of α, the value of $\Delta\bar{I}$ should have increased (the shock intensity is growing). But, what actually happens is that the flow's OQ improves with the value of α (at $\bar{x} > 10$, Figure 2.61).

The idea that the flow's OQ depends on the resonator's optical axis alignment was stated long ago [7,8]. Increase in intensity of the probing beam radiation in the far-field zone, as we have observed, was really recorded during the experiments with the banks of $\psi = 13°$ as compared to similar banks of $\psi = 0$. The effect refers to improvement in the flow uniformity considering its averaged structure. In terms of the qualitative approach the main point of the effect was illustrated by comparison of the flow patterns presented in the pictures obtained with a horizontal knife. Distortion of the radiation wavefront is specified by the difference of averaged optical paths at the probing beam's aperture. In the flow behind the SNB—with a strict order of micronozzles' rows arrangement—the beam coming behind the base areas of the wake along the intersections between the rows, and the beam coming along the nozzle axis, move through the media of different averaged density. It means that the transfer function (2.1) apart from the turbulent part will also have a member specified by the regular averaged flow structure. The optical axis direction under the angle ψ toward the nozzle rows line levels the optical paths. It is clear that there are optimal angles ψ.

Hence, in the flow behind the screen MNB the wavefront distortion generally occurs both at random nonuniformities and regular ones. However, first, influence of the regular nonuniformities after $\bar{x} \geq 20$, as it follows from Figure 2.64, is already minor. And, secondly, these nonuniformities do not refer to the shock wave structure but to the wakes that are formed behind the base areas of the banks and that specify the layered nature of the flow, which can be observed from the pictures (upon knife's horizontal position).

It is clear that layered nature is observed at registration of flow picture on flat. Actually, the wake present after each micronozzle is cylindrical; it joins with the next so that overall wake cross section repeats the form of SNB base area. The shock waves after $x = 70$ mm are practically not recorded any more (Figure 2.59), while the flow's layered nature remains for a long time (complete wakes mixing requires 100 caliber (500 mm); refer Figure 2.49). Consequently, phase incursion at the regular nonuniformities is specified by the difference in the flow's averaged densities in the wakes, and densities in pure flows along the axis of micronozzles.

Then it becomes clear that to define optimal misalignment angles ψ, it does not require calculation of the shock wave geometry [7], calculation of pressure drops in them, etc. Everything is defined by the geometry of the base areas in a block, which sets the period of arrangement of layers of different densities in the bank. The layered nature of the flow is clearly observed in the horizontal knife pictures. In Figure 2.63, the distance between the layers is 2.5 mm, which corresponds to the geometry of the intersections between the micronozzle rows in View A (see diagram in Figure 2.59). That is the reason why to level the optical paths it requires to rotate the resonator's axis so that the absolute value of the displacement on the bank's length L_{block} owing to turn—with regard to the initial position at $\psi = 0$—could make an entire period, that is, distance between the two layers (see diagram in Figure 2.63). This way, $\text{tg}\psi_{\text{opt}} = d/L_{\text{block}}$. At such a displacement angle, any beam will cross the wake and the area of the pure flow between the wakes once, and the optical paths—according the averaged flow structure—will level for all the beams.

As can be seen from the scheme, the dense nozzle arrangement is triangular; upon rotation by the angle of $\psi = 60^\circ$, the same situation at $\psi = 0^\circ$ is restored. At $\psi = 30^\circ$ an ordered arrangement of micronozzles also takes place but here the beam passes through the intersections in a time already, and consequently the phase shift will be less than that at $\psi = 0$. Therefore, the qualitative pattern of the flow's OQ dependence upon row rotation angle in a screen MNB unambiguously results from the bank's geometry (in the square arrangement the angles of flow's OQ deterioration are $\psi = 0$, 45° and 90°). Figure 2.63 presents a diagram of [7]. As pointed out before, the jet geometry was calculated here. That is why the result—from the standpoint of anticipating the angles where $\Delta\bar{I}$ increases sharply—will certainly be correct but only for angles ψ, and not for the phase shifts values (angle of turn $\psi = 13^\circ$ is not optimal for our models as it is far away from the value of $\psi = 30^\circ$; the value of ψ_{opt} is specified in the diagram).

Figure 2.64 also represents results for bank c-5. On comparison with bank c-3, no improvement has been observed. Such a minor decrease in d_e and increase in the arrangement density did not affect flow properties much. That is why we can declare that it is not possible to improve the flow's OQ in practice by reducing a bank's typical scale (according to [48], Λ also depends on the screen's typical dimensions), as greater decrease in dimension of individual micronozzle is hardly possible for real systems, firstly, because of manufacturing complexity.

Thus, improvement of the flow's OQ for screen MNBs is possible when rows of the micronozzles are displaced according to the resonator's axis. The fact was known before the research reported in [7,8]. However, a similar effect can be achieved by reducing the amount of the light scattered at the turbulent nonuniformities by altering micronozzle contour.

The effects, in this case, are the properties of turbulence: increase in the expansion angle φ of the conic micronozzles causes a reduction in density pulsation intensity and, hence, a decrease in $\Delta\bar{I}$ in the far-field zone. The most unfavorable nozzle banks, from the point of view of the flow's OQ, are the profiled micronozzle banks, when the flow ramp angle $\alpha = 0$.

In addition, the last thing is regarding the conic SNB. After a number of evaluations of the study [8] have been carried out, it was arrived that the most acceptable are the SNB banks of $\varphi = 10^\circ$. The conclusion was based on the fact that the total pressure losses for the flow's turning and jet mixing became significant at $\varphi > 10^\circ$. But, the experimental findings [49,50] (presented in part 2) on pressure recovery in a rectangular channel of a constant cross section (the most simple diffuser type) indicated that the value of P_f behind a $\varphi = 20^\circ$ bank is close to the case of $\varphi = 10^\circ$. Generally, increase in the total pressure loss upon the φ angle growing takes place, but this increase is small (the reasoning behind this is that the effective Mach number at the diffuser's inlet in a flow behind a $\varphi = 20^\circ$ SNB is somehow smaller, and therefore the function of the total pressure loss $\sigma(\lambda)$ is bigger than behind the $\varphi = 10^\circ$ banks).

To exemplify that, we refer to Figure 2.65. It compares distribution of static pressure $\overline{P}$ along the channel wall for two cases: (1) a big single standard nozzle is applied in a plant and (2) a screen nozzle (wherein the total of critical cross sections in a bank and the critical cross section of an individual nozzle are the same). Curves are present when a pseudoshock area that can be displaced by a reverse pressure value at the exhaust outlet by adjusting the ejector starts close to the nozzle exit, that is, when the maximum value of $\overline{P}$ is achieved. It can be observed that P_{max} differs by a value not exceeding 10% of $\overline{P}$. Consequently, the plant starting pressures for these two cases will also differ by a value of about 10% (upon the condition that the same diffuser is applied). To verify this statement, refer to Figure 2.44. The figure indicates fields of total pressures at the diffuser's output (present in the subsonic area) for the cases when different screen banks are applied. The data are presented in comparison with a flat nozzle—the differences are minor. Thus, when selecting an optimal geometry of SNB, recovery pressure behind the diffuser is not a critical parameter; so, conic banks of $\varphi > 10^\circ$ are acceptable.

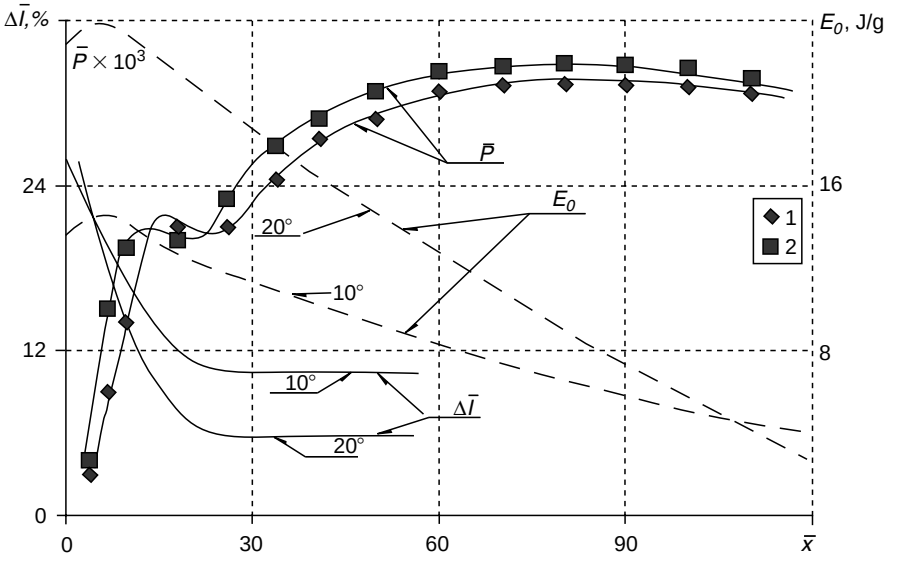

FIGURE 2.65 Flow characteristics in resonator cavity behind the SNB.

The main conclusions are made based on comparison of data igure 2.65 on the energy E_0 stored in the flow and the flows' OQ when conic SNBs of $\varphi = 10^\circ$ and 20° are applied in a CO_2-GDL as nozzle devices. The fact that the expansion angle is more favorable from the standpoint of E_0 application of the banks with a large nozzle, becomes obvious as freezing of the vibration energy and breakaway of the vibrational-band temperatures from the translation ones in the area of a nozzle neck in this case occurs with greater effect. In this example, E_0 gains almost a two-fold advantage. But, the advantage is realized only if the resonator is located not far from the bank's exit.

The presented OQ measurement results prove that in the screen banks with an offset nozzle axis ($\psi \neq 0$) the resonator shall be installed not at the distance of $\bar{x} = 80$–100 with the low level of averaged parameters disturbance, but at the distance of $\bar{x} = 20$–30, where a low level of turbulent pulsation intensity is achieved. As one can observe, here the portion of E_0 does not crucially differ from the maximum possible values, whereas in $\bar{x} = 80$–100 it makes just a small part of the maximum (it is true that application of helium instead of water to unload the lower laser level in the working mixture allows extending the area of maximum values of E_0, but application of helium is unreal for powerful systems with a considerable mixture mass flow rate). This very conclusion determines the importance of the obtained results. The behavior of flow pulsation properties in the resonator cavity imposes the resonator's location, and the structure of the averaged density nonuniformities in a flow assigns the displacement angle for micronozzle rows in a bank according the resonator's axis. Thus, information on the flow's OQ behind the screen nozzles unambiguously resolves the question of preference of one or the other profiling type of the micronozzles in favor of the conic one with a big expansion angle.

Numerous studies verified the results on intensity variation of the light that had passed through the density nonuniformities obtained with purely optical measurements and aerodynamic measurements, that is, estimated with the formula of [3] (on the basis of the measured gas dynamic properties of these nonuniformities). However, normally a single mixing, shear or boundary layer was used as an object. It was natural to verify compliance in our case of flows in resonator cavity also, when layers are numerous. The compliance results are shown in Figure 2.66a and Figure 2.66b. For a flat nozzle case, the layer thickness is summarized.

For the blade MNB (Figure 2.66a) the compliance is reasonably good. It is the very case when the transfer function in (2.1) is defined only by the turbulent part. In the screen banks the situation is different. Dependence on the angle ψ means that the transfer function contains a multiplier specified by the regular nonuniformities. That is why divergence in the area of $\bar{x} < 15$ is significant. But for the area of $\bar{x} > 20$, where the flow is already homogeneous, that is, when the averaged optical paths are close in aperture, application of formula (2.5) is reasonable (for an SNB, with ψ far from the angles and OQ deteriorating).

This way it is possible to estimate what the results obtained in the model banks correspond to in reality. The problem of adjustment of the model experiment results to natural conditions can be resolved on the basis of correlation (2.5), for transition to new wave lengths does not alter the situation qualitatively because of one of the main parameters outlining the solution of the aero-optical problem—correlation between the aperture and the turbulence scale [5] remain the same: $D/\Lambda \gg 1$.

To make it more apparent let us consider operational conditions of second generation CO_2-GDL [47]: $P_0 \sim 100$ atm, $T_0 \sim 2000$ K, and corresponding nozzle expansion levels. The thickness of the wakes behind the blades depends on the Re number very weakly ($b \sim Re^{-0.1}$), though it certainly will increase in hot experiments as compared to the cool ones in the model experiments (corresponding increase in Λ shall also be taken into account). Most likely, the relative wake pulsation intensity will not change much. In this case, the measured values of $\Delta I/I_0$ in the model experiments at a wavelength of $\lambda = 0.63$ μm and upon

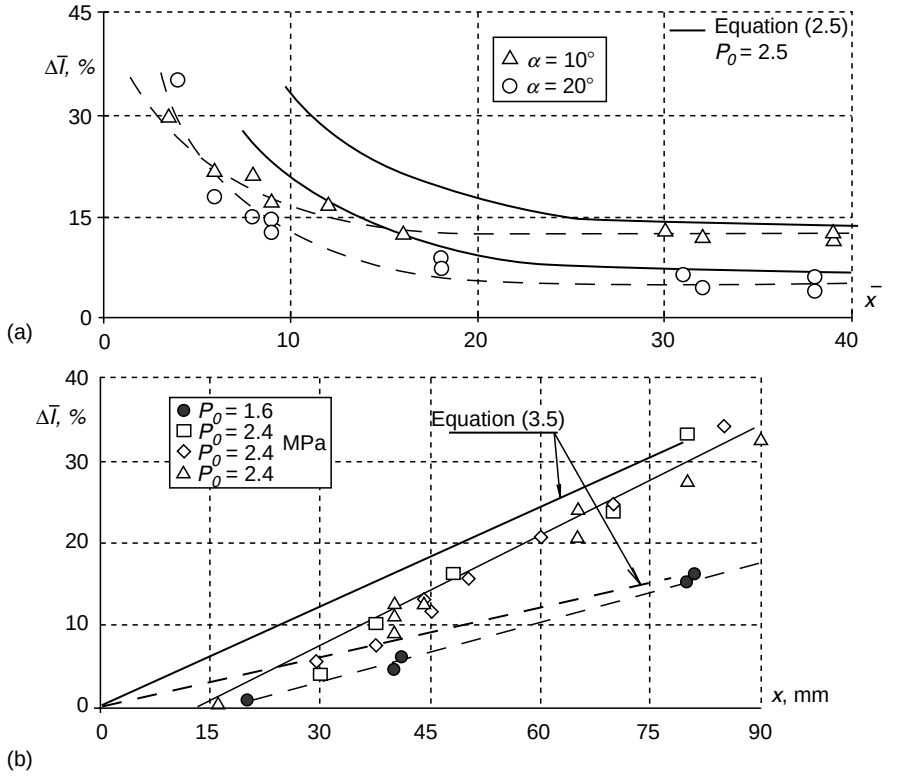

FIGURE 2.66 Comparison of experiment data with estimation under the formula (2.5): (a) SNB with $\psi = 13^{\circ}$; (b) BNB.

the resonator cavity's length of 50 mm will correspond with the results that are obtained for real operating conditions of a CO_2-GDL—$\lambda = 10.6$ mcm upon the optical path's length of several tens of meters (it depends on a certain level of nozzle expansion). It also needs to be taken into account that multiple-pass resonators are normally applied in a GDL. Thus, model conditions of the current experiments are close to the operating conditions typical for large-scale assemblies where the resonator's dimensions are ~3–4 m. Similar GDLs have been implemented in practice.

Now, let us consider the problem of how much one can increase the resonator's active zone lengths—and simultaneously the total mass flow rate of the installation, to obtain even greater radiation intensity in the far-field zone. It is obvious that the radiation power of an SGL laser—N_{rad} in the near-field zone grows as the mixture flow rate pumped through the resonator increases. For a GDL, N_{rad} is easily estimated [47]: $N_{\text{rad}} \sim G$, that is, directly proportional to the flow rate. The flow rate can be increased by a pressure rise in the forechamber P_0 and extending the size of the entire system, that is, the nozzle bank dimensions and consequently, the resonator's dimensions. But, significant values of L, the active zone length or the working channel width, cause increase in $\Delta I/I_0$ in the far-field zone. Let us evaluate the output radiation intensity I_0 at a mirror of dimensions ($H \times D$), where H—the height of the laser's working channel, and D—size of the mirror along the flow (the dimensions of the outlet cross section of the nozzle bank are, respectively, $L \times H$)

$$I_0 \sim \frac{N_{\text{rad}}}{HD} \sim \frac{G}{HD} \sim \frac{\rho LH}{HD} \sim \rho L,$$

where D is a definite value. Intensity in the far-field zone can be written as

$$I \sim I_0 \exp\lfloor -K(\lambda)\rho^2 L \rfloor \sim \rho L \exp\lfloor -K(\lambda)\rho^2 L \rfloor.$$

$K(\lambda)$—function λ (see (2.5)), the other values included in $K(\lambda)$ ($\rho'/\langle\rho\rangle$ and Λ), for the standard GDL conditions can be considered the values that vary a little within certain limits. That is the reason why maximum I can be estimated for a set pressure in the forechamber P_0 the same way as for the function $I = I(L)$ (derivative from $I(L)$ equate with zero). Then, the dependence of the resonator's optimal length that is a condition I maximum is realized in the far-field zone, on λ and ρ will be:

$$L_{\text{opt}} \sim \frac{1}{K(\lambda)\rho^2} \sim \frac{\lambda^2}{\langle\rho\rangle^2}$$

As one can see, estimation of L_{opt} strongly depends on the working length of the laser wave and active medium's density. Increase in the laser system's dimensions, when a resonator's length exceeds L_{opt}, no longer causes increase of I in the far-field zone at the target, though the output capacity of the radiation in the near-field zone increases. Estimation of L_{opt} for standard GDL conditions makes several tens of meters (but this value shall be divided by the number of radiation passes in the resonator). But, nevertheless, real systems have $L < L_{\text{opt}}$, and it means that in a properly designed GDL it is possible to achieve high radiation quality.

In chemical systems, for example HF/DF-lasers, it is more complicated to estimate the radiation quality. It certainly depends on a flow rate, but also on how a chemical agent mixing system is implemented, for example. Though it is possible to estimate the resonator's dimensions upon which flow density nonuniformities will start markedly affecting the radiation quality, that is, the value of $\Delta I/I_0$ in the far-field zone in the central spot. In chemical systems, low pressure in the resonator cavity is typical, and the fact is specified by the chemical reaction kinetics. That is why the main pattern of the flow nonuniformities will not be defined by the wake turbulence (they will more likely be nonturbulent), but by the vortex pattern of the flow in the chemical agent injection points—through a system of regular openings and a system of regular nonuniformities, specified by spatial arrangement of the chemical agents jets themselves, as their densities differ considerably (we mean blade MNBs).

Thus, the scale of nonuniformities—both regular and irregular—in an SGL chemical laser's resonator will be set, one way or another, by the geometry of the bank's injector system. In particular, by the distance between the openings of chemical agent injection, as it is impossible to mix components instantly and the energy pick-up is carried out next to the nozzle bank exit because inversion along the flow in a chemical laser declines very fast. Relative intensity of density pulsations in vortexes can be high due to significant difference in density of the chemical agents H_2 and F_2 (the same is applied for iodine–oxygen systems where I_2 and O_2 are mixed). However, if for estimation we take $\rho'/\langle\rho\rangle \sim 10$–$20\%$, upon the static pressure level of ~10 Torr in the resonator cavity, then $\Delta I/I_0$ can exceed 10% in the HF-systems already upon the resonator's length of ~1 m, that is, starting with these resonator dimensions the flow's OQ becomes an important parameter. Consequently, even relatively small HF-systems require considering the flow's OQ in general while designing a nozzle bank and mixing systems.

The mixing process in the chemical lasers' banks can certainly be examined by experiment. Effect of the trips injected from the nozzle walls on the flow was studied in [65,66] with the LIF method (Laser Induced Fluorescence). But the process is complicated and labor consuming. Modern computational means allow modeling 3D complicated flows accounting for

viscosity and the entire chemistry of the processes (getting an overall idea of a reacting jet mixing in a cross flow).

Numeric modeling of the processes in the mixing banks of supersonic chemical lasers is the topic of the next part.

2.4 PROBLEM OF MIXING IN THE NOZZLES OF SUPERSONIC CHEMICAL LASERS

2.4.1 Introduction

Mixing-type MNBs are applied in mixing GDLs and in chemical lasers (CL). These are either two-dimensional structures—an blade nozzle bank with an injection system, or three-dimensional ones—an SNB of two nozzle types of different chemical agents are fed through. Examination of the OQ after the similar banks' models (part 3) proved that if the physics of the active medium processes allows installing a resonator far enough downstream from the nozzle exit plane (NEP) of MNB (20–30 micronozzle diameters), then the SNB type banks can be applied. A similar approach was employed effectively on implementation of a mixing GDL [1]. However, typically, in the chemical systems a resonator is located just after the NEP. In this case, application of the SNB structure type is not feasible because there emerge regular density nonuniformities of high intensity after the NEP.

That is the reason why BNB are generally applied in chemical supersonic systems (in DF/HF-lasers, as well as in COIL). The feed of the second chemical agent and the dilutant are carried out through the system of injectors installed on the MNB forming blade walls. The feed can be performed in the subsonic, transonic, or in the supersonic section of a nozzle. It is obvious that injection of additional flow rate into the main flow causes sophistication of the flow's gas dynamic pattern in the resonator cavity. Extra disturbances related to jets' interrelation with the cross-flow overlap the basic features of a flow after the MNB (examined in part 2).

2.4.2 Mixing Process Features in the Chemical Laser Case

It is complicated to investigate jet system mixing phenomena in a small-scale nozzle experimentally. The results of visualization of a flow after one of the HF-laser's MNB structures obtained [2] can serve as an illustration. The nozzle bank geometry is shown in Figure 2.67. A unique flow visualization technique was implemented upon the LIF method [3]. The idea of the LIF method is as following: the I_2 molecules are added to the flow and fluoresce by the action of argon (or adjusted krypton) laser radiation. A laser knife was applied as highlighting tool in [2]. The information received in the knife's plane was recorded by a video recorder, and the beam plane was successively scanned through the flow under investigation perpendicularly to the output cross section of a nozzle bank (xy-plane) as shown in Figure 2.67.

On the basis of the obtained information, a computer builds up a flow's image in the yz-plane, parallel to the output cross section of an MNB, and a three-dimensional image (it is impossible to obtain an image in the selected yz-plane by direct optical method). The figure shows two-dimensional computer photographs in the yz-plane at a distance from the nozzle exit, which can explain the essence of the process. Here, flows come from the main (primary) nozzles, and from the secondary ones (for the visualization, I_2 was first fed to one nozzle section and then to another; I—when gas is not blown through so called trips—minor holes located at the surface of the main nozzles (see the bank scheme); II—when gas is blown through the trips). One can observe that in the second case the flows' contact surfaces from the primary and secondary nozzles increased due to the distortion of surfaces. Extension of

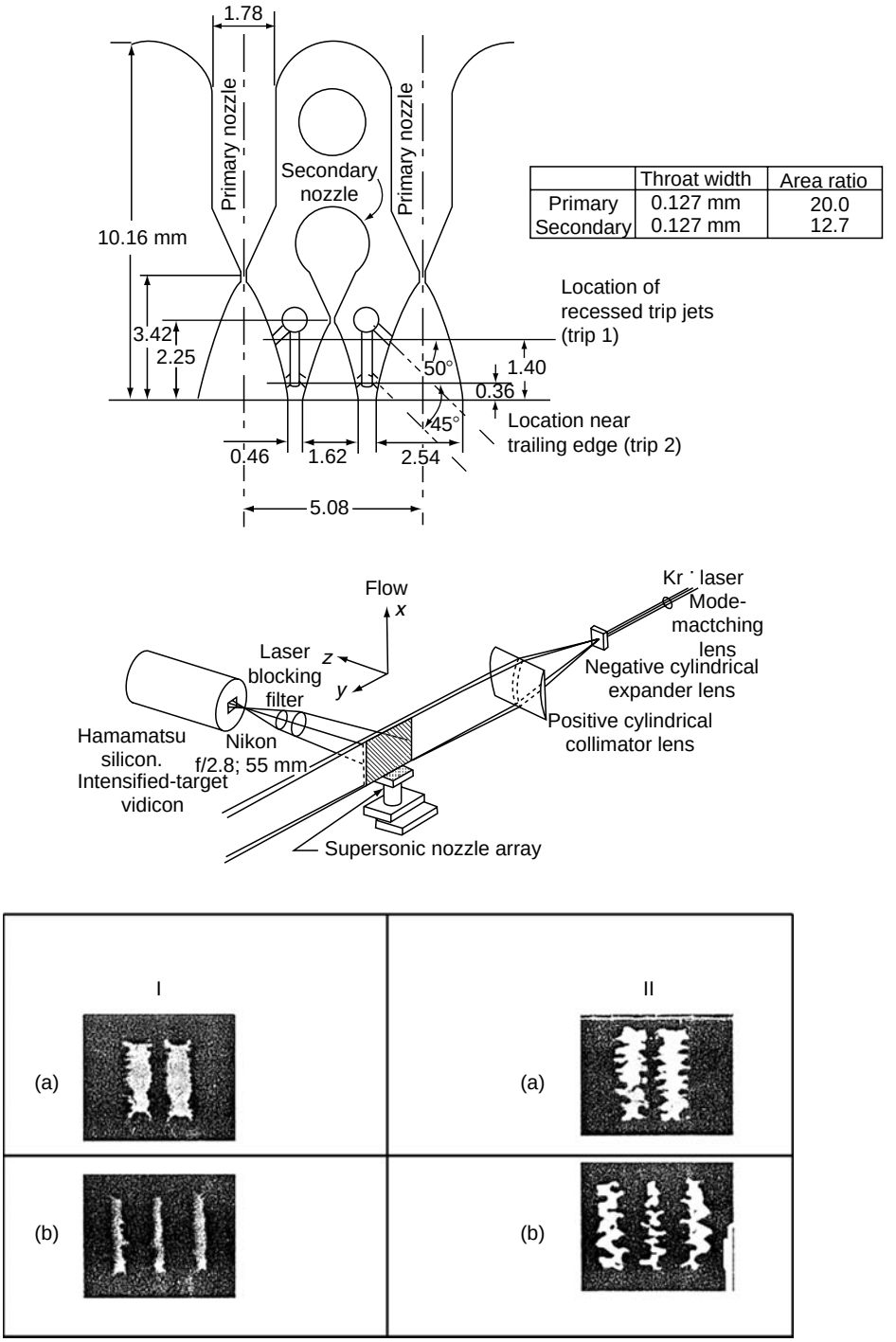

FIGURE 2.67 Flow visualization after MNB ($x = 4.8$ mm) of HF-laser. (From Rapagnani, N.L., Davis, S.J., Laser-induced fluorescence: a diagnostic for fluid mechanics, *Lasers & Applications*, Vol. 14, No. 5, 1985, pp. 127–131.)

the contact surface causes mixing process intensification and increasing of the reaction product output in general, that is, it was possible to increase the laser's output capacity with the help of the trips.

But, the information that can be obtained with such a technique (a laborious one and requiring special-purpose methods creation) can only be qualitative. It is impossible to resolve the issue of the OQ of such a flow upon the obtained data. It is obvious that when trips are running in a flow there emerge additional regular averaged structures (jet systems) and vortex structures—lateral vortexes occurring as the result of interrelation of injected jets and the cross flow. To estimate OQ of such a flow it requires accurate data on all the flow parameters or extra research (which in its turn will require creating a new special-purpose experimental installation).

At the same time, nowadays, high enough computational capabilities are available that allow performing detailed three-dimensional numerical simulation of a nonstationary flow of CL's active media that takes into account all the physical features—chemical, mechanical and kinetic. Upon numerical simulation, it is possible to visualize the entire process of flow mixing in nozzles in detail and obtain quantitative information on the flow parameters as well.

Further, it will be displayed by the example of investigation of a COIL nozzle mixing process (physical principles of COIL operation were briefly described in Part 1). The essence of the main gas dynamic process determining the laser operation is as follows. Iodine and nitrogen jets are injected into the excited oxygen flow in the transonic section of each MNB's nozzle (Figure 2.68). It is required not only to mix the components evenly but also execute it rapidly enough to minimize loss of the stored energy in singlet oxygen, and increase maximum laser radiation capacity.

Then, the general task is to carry out a parametric analysis of the nozzle bank operation and come to a constructive solution close to the optimal one. As soon as powerful commercial CFD simulation software and multiprocessing computing platforms appear, it will be

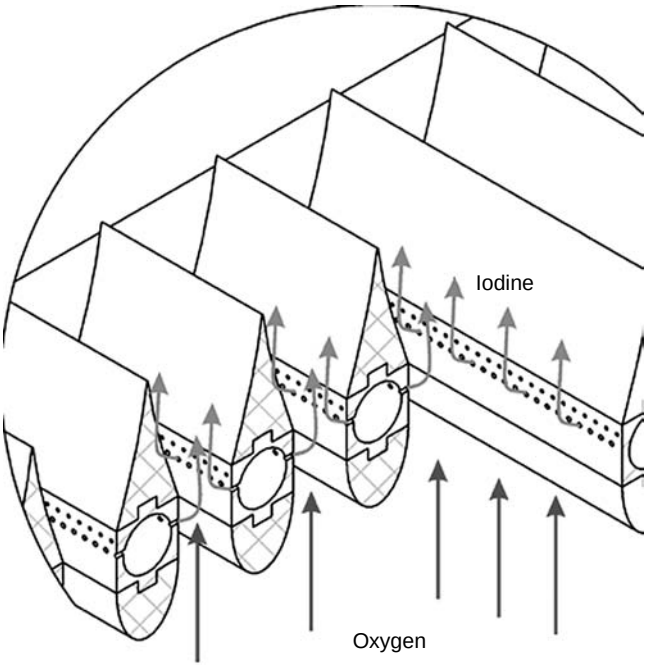

FIGURE 2.68 Injection of molecular iodine into the oxygen flow in COIL nozzle.

possible to resolve such a problem during the design stage. Nevertheless, practical implementation of this principle possibility requires the CFD-software adaptation to the peculiarities of the physical processes that take place upon preparing active media for chemical lasers.

Supersonic gas laser active media flow features. In a gas dynamic CO_2-laser, the energy efficiency measured as a degree of conversion of fuel chemical energy into radiation energy is relatively minor: 2–3%. The flow Mach number value is about ~5, which corresponds to velocity more than 1000 m/sec upon the stagnation temperature of 1500–1700 K. Pressure in the resonator cavity is several tens of Torr. Within such conditions gas dynamic processes do not suffer strong influence from the optical ones. The laser radiation optical quality is determined by nonuniformities of the active medium refraction index [4].

In HF/DF-lasers, the thermal energy released during the chemical reaction that takes place after the MNB's exit strongly affects the flow's gas dynamics in the resonator cavity by making the flow stagnated (that is why the cavity needs to be made divergent). In the low pressure HF-lasers, this process is mainly controlled by the kinetics of the secondary fuel combustion reaction $H_2 + F \rightarrow HF(v) + H$. In the DF-lasers similar to [5], with an active medium of high pressure, the heat production energy is specified by mixing the oxidizer and the secondary fuel flows. While designing a gas dynamic duct and the pressure recovery system, the processes causing heat production shall be taken into account [6,7].

In COIL's active medium, hidden energy stored in electronic levels of molecules' energy exceeds the total enthalpy of the flow specified by the progressive motion (both averaged and chaotic). That is why conversion of the hidden energy into heat during the relaxation process significantly affects the gas dynamics of the flow along the entire laser's channel. We can assume that this causes reverse coupling between the process of active medium supersonic flow's stagnation and the process of excited particles relaxation. There appear effects that are not observed in other CL types: the flow mode in the resonator cavity depends on how much energy is removed from the flow during the generation process, that is, the flow mode depends on the efficiency of the resonator operation [8,9].

Let us now consider the basic factors that determine the pattern of gas dynamic processes in a supersonic CL. These factors are: a typical velocity of exited particle relaxation and the temperature.

1. *By the relaxation velocity* all possible cases are divided into two classes.

a. For fast kinetic systems (for example, a continuous DF-laser with active medium of high pressure) the relaxation time scale τ_r is much less than the gas dynamic transport time $\tau_g = L/U$ (L is the length of the resonator cavity along the flow, U is the active medium velocity). It has a corresponding dimensionless criterion, the Damkeller number $D_a = \tau_r/\tau_g = \tau_r U/L \ll 1$. In this case, the active medium formation is controlled by component mixing and that is why the active medium cannot be optically homogeneous.

b. For slow kinetic systems ($D_a \geq 1$), the situation is opposite. In the COIL's active medium the main processes are the iodine dissociation $I_2 + O_2(^1\Delta) \rightarrow I_2^* + O_2(^3\Sigma)$; $I_2^* + O_2(^1\Delta) \rightarrow 2I + O_2(^3\Sigma)$ and pumping: $I + O_2(^1\Delta) \rightarrow I^* + O_2(^3\Sigma)$. Time scales of these processes are specified by component concentrations and reaction rates. In typical conditions, these time scales are of the same order as the gas dynamic time [10]. In this case, the optimal solution appears to be the one when components of the active medium are completely mixed before the medium is fed to the optical resonator's cavity. That is why the COIL's medium can be optically homogeneous, if mixing is properly arranged.

2. *The temperature factor* is estimated as the correlation between the laser transition energy and the medium's total heat content:

$$\theta = \frac{N_A h\nu}{C_p T_0 D} = \frac{\gamma - 1}{\gamma} \frac{hc}{k} \frac{1}{\lambda T_0 D}, \tag{2.7}$$

where h is the Planck constant, c the light velocity, k the Boltzmann constant, N_A the Avogadro number, $-C_p$ the molal heat capacity, λ the wavelength, T_0 the stagnation temperature, and D the flow dilution rate.

While examining supersonic gas lasers one can distinguish two extreme cases by the temperature factor.

a. In CO_2-GDL and DF-CL, the medium is of high stagnation temperature, whereas the laser transition energy is minor, causing $\theta \ll 1$. The laser generation efficiency does not affect gas dynamic processes significantly.
b. In COIL lasers, the situation is opposite: upon T_0 of about 300 K and high laser transition energy, $\theta \gg 1$. Upon generation, the portion of the energy stored at the electronic levels of O_2 is retrieved from the medium by the electromagnetic field. The rest of the energy is converted into heat and this causes considerable increase in T_0 of the flow. From the physical standpoint, it is the volume source of heat in the supersonic flow, and it means that the flow pattern in the resonator cavity and the diffuser shall change upon generation efficiency variation [8,9]. In turn, the radiation generation efficiency also depends on the active medium flow pattern. It is obvious that upon modeling such a flow, one needs to consider the heat sources whose intensity is determined by the kinetics of proceeding chemical reactions and the medium-radiation relationship of the energy equation.

2.4.3 Injection into the Cross-Flow in the Narrow Channel Conditions

Here are representative values of the properties of CL working media where mixing takes place.

		COIL(He)	COIL(N_2)	HF/DF
M	—	2	2	4.5
P	Torr	4	4	4
γ	—	1.5	1.4	1.5
μ	G/mole	9	29	9
μ^0	Pa*sec	1.96E-05	1.75E-05	1.96E-05
T	K	250	250	250
Re/L	1/m	160000	310000	360000

The specific Re number is estimated in the following way:

$$\frac{Re}{L} = \frac{MPT_0{}^{0.75}\sqrt{\gamma\mu}}{\mu_0\sqrt{R_0}}T^{-1.25}, \tag{2.8}$$

where T^0 is the normal temperature, μ^0 the viscosity in regular conditions, μ the molecular weight, R_0 the universal gas constant, γ the adiabatic index, M, P the Mach number and pressure, and T is the static temperature. In this estimation, the exponential function of viscosity to temperature μ is applied: $\mu = \mu_0(T/T_0)^{0.75}$.

Comparison of the specific Re number proves that the values for a COIL laser when nitrogen is used as a dilutant are close to the HF/DF-laser parameters because the difference in the Mach numbers is almost compensated by the difference in molecular weights. The Mach number itself influences the mixing mechanism but indirectly. At the same time, similar

values of specific R_e numbers mean similarity of mixing mechanisms in similar geometrical configurations. The fact can be the basis, for example, for applying the experience of HF-DF laser nozzle banks' production in COIL nozzle bank development. The difference in the mechanisms of physical and chemical processes is definitely taken into account when making certain technical solutions.

The main idea of the mixing MNB structure is lateral injection of jets into the cross-flow in the narrow channel conditions (acceleration of the nozzle flow). Normally, the basis for the bank design is the empirical relationships from the studies popular in gas dynamics, where regular injection patterns of an individual jet in the bottom of a semi-infinite cross-flow were examined [11].

The jet, axisymmetrical in the beginning, becomes horseshoe-shaped at a closer distance from the outlet opening. The jet deformation can be explained by the pattern of its interrelation with the cross-flow. The side surface of the jet suffers more intense influence from the cross-flow due to the mixing process. The jet particles located at the periphery are distorted by the cross-flow to a greater extent and move along a more arched trajectory which causes the horseshoe formation. Symmetric circulation areas are formed which come from the jet symmetry plane. Side lobes of the horseshow draw apart.

Generally, the experimental data are represented as dependence on the momentum ratio (here is the formula taken form [11]):

$$\frac{x}{d} = \frac{q_{01}}{q_{02}} \cdot \left(\frac{y}{d}\right)^{2.55} + \frac{y}{d}\left(1 + \frac{q_{01}}{q_{02}}\right) \cdot c\mathrm{tg}\alpha, \tag{2.9}$$

where x, y are the coordinates (Figure 2.69), d the nozzle diameter, α the angle between the nozzle axis direction and the cross-flow direction, $q_{01} = \rho_\infty {V_\infty}^2/2$, $q_{02} = \rho_0 {V_0}^2/2$ are the velocity heads of the cross-flow and the jets in the initial cross section.

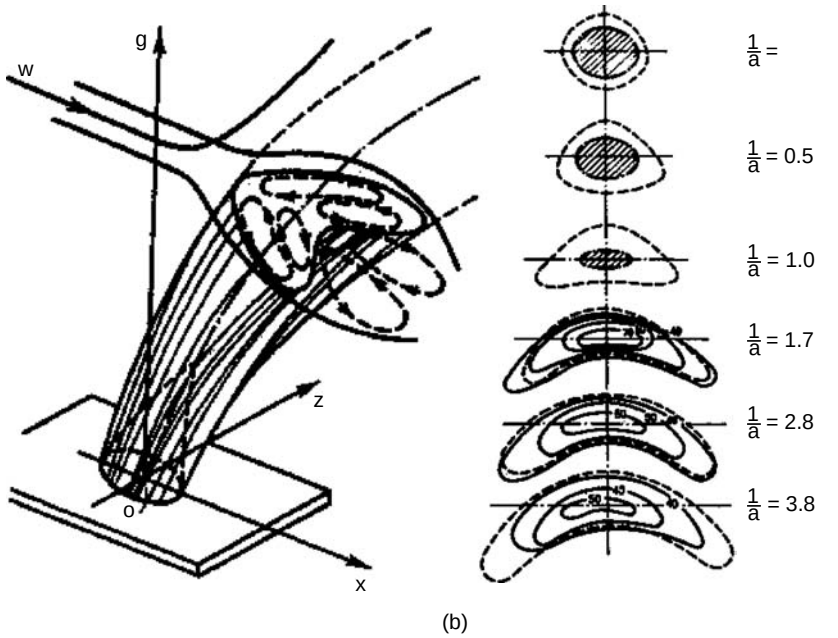

FIGURE 2.69 (a) Scheme of a jet flow in a cross-flow. (b) Shape of a lateral jet cross section in a side flow at various distances from the initial jet cross section. (From Zlobin V., Izvestiya Akademii Nauk Estonskoy SSR, 20, 66, 1971 (Russian-News Academy of Science of Estonia SSR).)

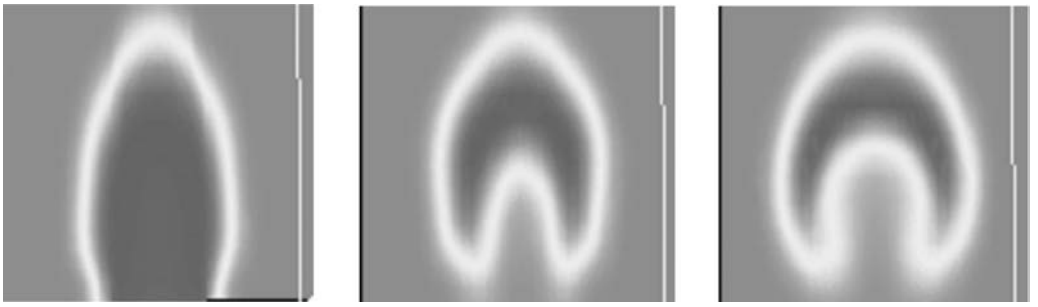

FIGURE 2.70 Jet lateral cross section of the injected jet at the distance of $1/d = 1, 1.5, 2$ (There is no water vapor around the jet. Maximum water concentration is in the core. Increasing of the intensity from white to black inside the jet corresponds to increasing of water concentration).

Figure 2.70 shows a pattern of injected jet development at the initial section of its trajectory according to the results of the numerical simulation. The three-dimensional nonstationary Navier–Stokes equations were resolved in the design volume as they are an element of the COIL nozzle assembly symmetry. The calculations were carried out with the help of program packages CFX5.7 and VICON-C. To describe the gas-phase chemical and kinetic processes a kinetic scheme containing 34 reactions and 12 gas mixture components was applied [10].

It can be observed from the qualitative standpoint that the process of jet development in a nozzle does not differ from development of an individual jet in the bottom of an unlimited cross-flow. Nevertheless, a detailed examination of a jet mixing system proves that in this case considerable differences do appear. To illustrate this, see Figure 2.71. It compares trajectories of an axis of jets coming from a single-row injector that are injected in a channel and in an

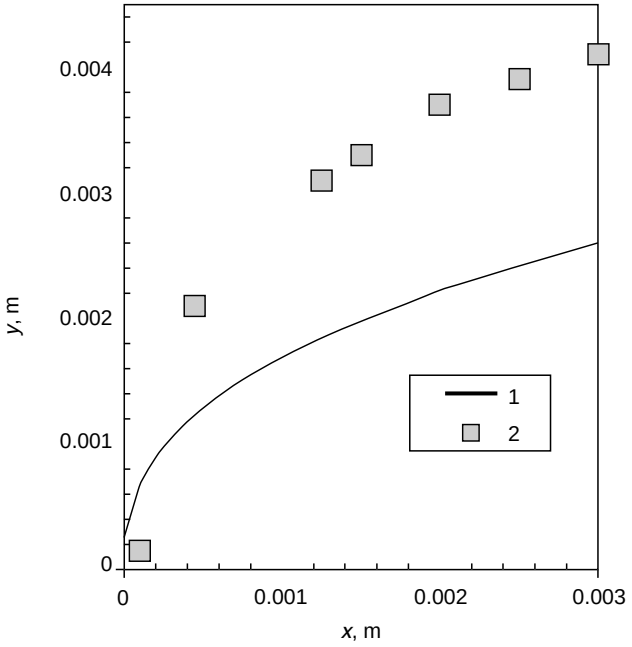

FIGURE 2.71 Trajectory of the system of jets injected in a plane-parallel channel according to the numerical modeling results (points)—solid line. (From Zlobin V., Izvestiya Akademii Nauk Estonskoy SSR, 20, 66, 1971 (Russian-News Academy of Science of Estonia SSR).)

axis of an individual jet [11,12]. Actually, a two-dimensional case trajectory (a plane jet) is compared here (the injector jets are located close to each other and at a certain distance they form a common structure) to a three-dimensional one (a circular single jet). It can be observed that the plane jet's trajectory is higher than the one for the circular single jet.

It is in the COIL's nozzle bank that we deal with a complicated jet system rather than with a single jet. That is why, first, the jet development takes place in the area limited by the nozzle symmetry plane, and the jets injected toward each other from the opposite walls of a nozzle interfere. Next, the jets of one row in a single-row injector influence each other; the first and the second rows' jets affect each other in a double-row injector.

It is clear that the presence of the above-mentioned factors, as well as the chemical kinetics impact upon the process cannot allow directly applying the quantitative empirical dependences obtained earlier in gas dynamics to analyze secondary flow penetration in a COIL nozzle.

To analyze the mixing mechanism's peculiarities upon transonic injection of chemical agents in a CL's nozzles let us consider the flows behind the banks of various configurations of injecting systems. Let us examine the schemes of secondary flow transonic injection through single-row and double-row injectors (with a successive opening arrangement and a staggered opening arrangement). The problem description is included the Reynolds-averaged Navier–Stokes (RANS) equations, turbulence model of the k-ω SST type (Menter), and a standard model of the COIL medium kinetics [10]. The nozzle assembly symmetry element (Figure 2.73) contained about 1 million cells; both regular bank and irregular tetrahedral screens were applied with concentration in the large gradient areas.

The calculation results on the secondary flow jet's penetration into the primary flow for various types of injectors are shown in Figure 2.72. It also depicts consolidating dependence

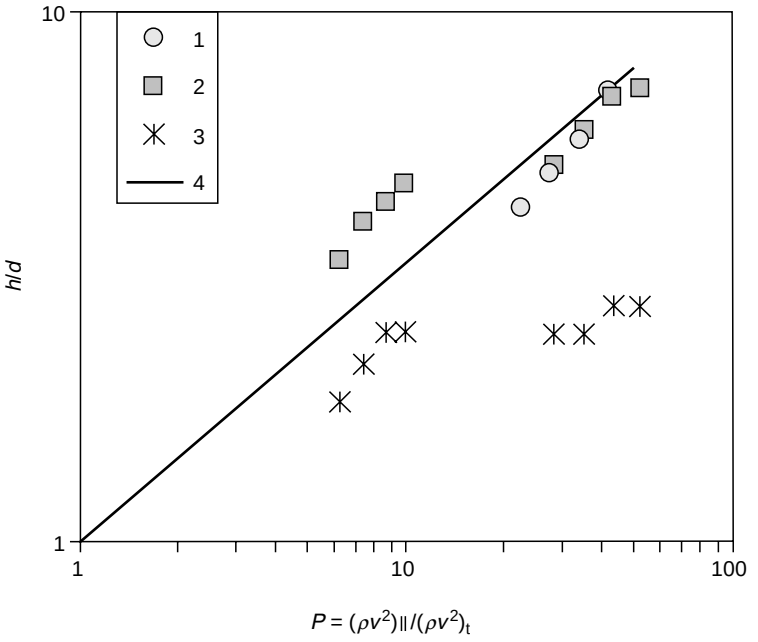

FIGURE 2.72 Dependence of the injected jet's penetration depth on the momentum ratio. 1—Single-row injector, 2—double-row injector with the staggered opening arrangement, first row, 3—the same, second row, 4—penetration for a single jet. (From Zlobin V., Izvestiya Akademii Nauk Estonskoy SSR, 20, 66, 1971 (Russian-News Academy of Science of Estonia SSR).)

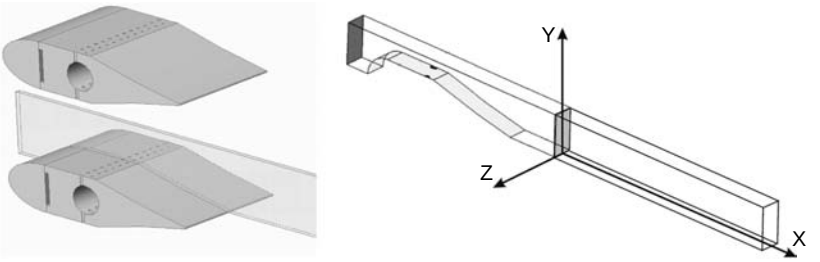

FIGURE 2.73 Computational domain and symmetry element.

for a single jet injected into an unlimited cross-flow [13]. In the case of a double-row injector, the penetration depth differs from the standard aerodynamic dependence because of mutual influence of the different injector rows' jets. This effect causes decrease in nozzle flow mixing efficiency, and a nonuniform distribution of components' concentration in the resonator cavity (Figure 2.74).

A double-row injector can serve as an example for brief consideration of mixing process details. Figure 2.74a and Figure 2.74b show distribution of water vapor concentration in lateral cross sections located in succession along and behind the nozzle (cross sections 1–4 are located in the nozzle's transonic section, 5–7 in the supersonic section, cross section 8 is located behind the nozzle exit; growth of the figure dimensions corresponds with increase in the nozzle cross-section dimension). The results are presented for two values of the total pressure—P_{02} of the injected flow.

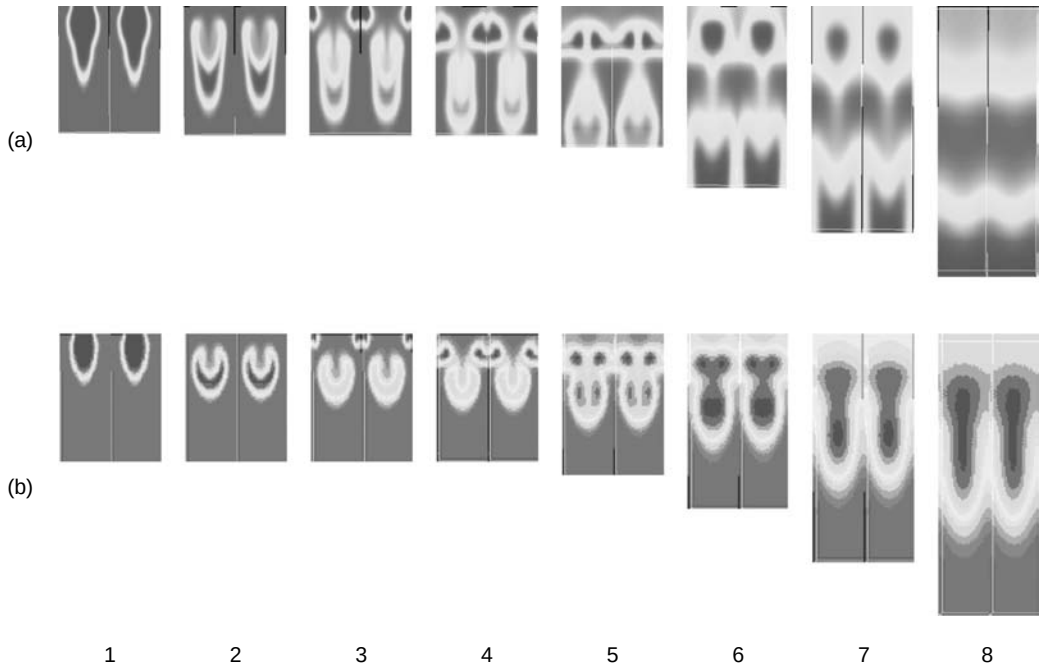

FIGURE 2.74 Water vapor concentration distribution in separate lateral cross sections: in 1 and 2 cross sections—the first row jets are recorded; in 3—the second row jets emerge; in 5–6—the common jets structure of both rows is observed; 8—cross-section area at the distance of 60 mm from the outlet nozzle cross section, (a) $P_{02} = 160$ Torr, (b) $P_{02} = 88$ Torr.

As shown, the experiments proved that a single jet quickly becomes horseshoe-shaped with two vortexes when injected into a cross-flow. A similar effect is observed upon transonic iodine injection also.

A first row jet forms a classic horseshoe-shaped structure (it is clearly seen in cross section (2), which is confirmed by a pair of lateral vortexes. However, at that cross-section flow field of the vortex pair causes a brake in the second row jet (cross sections 4, 5). Instead of forming a horseshoe-shaped structure, the second row jet shapes two disconnected vortex bands whose motion is completely dependent on the first jet's vortex field (cross section 6). As a result, a common structure is formed, which looks like a localized zone of high iodine concentration, when the vortex motions have damped (cross sections 7, 8).

When the secondary flow's flow rate is minor (low value of P_{02}) an incomplete jet penetration mode emerges and the iodine concentration remains nonuniform along the entire rated area (Figure 2.74b). The effect of the jets' mutual influence does not allow uniformity of concentration distribution even at high values of the parameter of P_{02}—in this case, at the nozzle outlet two areas of high iodine concentration are formed (Figure 2.74a, cross section 8).

The analyses of the mixing mechanism and the three-dimensional structure of the flows emerging upon transonic secondary flow injection allow formulating the following principles one needs to adhere to when designing efficient patterns of mixing arrangement in a COIL nozzle:

1. Injector openings' arrangement and the secondary flow injection parameters need to provide for formation of a vortex structure that could cover the entire lateral cross section of a flow. The mutual influence of injected jets shall not cause localized structures formation;
2. The time scale of molecular diffusion shall agree with the motion time of the vortex structures and also with the time of longitudinal convection of the active medium from the injection point to the resonator cavity;
3. The transversal scales of the mixing flows need to be minimized by reducing the nozzle dimensions.

Let us now examine a transonic single-row injector's operation based on these criteria.

Figure 2.75 and Figure 2.74 show a sequence of flow lateral cross sections in a nozzle starting with the iodine injection point They also show connection of two mirrored halves to demonstrate the flow in the nozzle's full cross section: injection coming from the top and bottom walls, where the injectors' openings are located in front of each other. The vortex structure is built in such a way that a succession of plane layers is formed toward the nozzle's outlet opening, the distance between the layers equals the injector opening's spacing. Further, the concentration leveling process is performed due to the molecular diffusion.

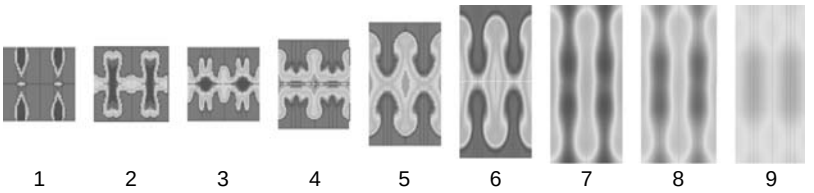

FIGURE 2.75 Water vapor concentration distribution in separate lateral cross sections: case of a single-row injector (P_{02} = 256 Torr). 1—Cross section in injection points; 2, 3—cross sections in transonic part of nozzle; 4–6—cross sections in supersonic part of nozzle; 8, 9—in laser cavity (9–60 mm from the outlet nozzle cross section).

We can assume that there are two stages of the mixing process. During the first stage, concentrations are leveled in the direction of injection at the scales of the lateral cross section of the oxygen nozzle. The process relates to the vortex structures formation and is mainly of a nonviscous nature. The time scale for this process can be estimated as $t_1 \approx d/(2u_2)$, where d is the nozzle's lateral dimension, u_2 the efficient lateral velocity of the injected jets. The second stage is mainly controlled by diffusion and its time scale of t_2 is proportional to $(a/2)^2/\nu$, where a—injector openings' spacing, ν—kinematic viscosity coefficient. Proportions and absolute dimensions of a nozzle assembly have been selected so that the time scales agreed mutually and to the convective time $t_c \approx L/u_c$, where L is the longitudinal flow's dimension, and u_c is the time scale of the longitudinal motion of the injected medium.

Thus, at this moment, it is possible to select an optimized structure of a nozzle bank at the stage of the numeric three-dimensional modeling design, to the first approximation. It is clear that the calculations that take into account a big amount of chemical and kinetic reactions (by applying a considerable amount of empirical and semi-empirical velocity constants for these reactions) need to be verified. And then, on the basis of the experimental data and the rectified calculations the nozzle bank structure can be refined. That is just where inextricable connection between a theory and an experiment is.

2.5 RESONATORS OF HIGH-POWER SGL LASERS

2.5.1 Classifications of the Powerful Laser Resonators

A resonator is the most important component in a power laser. The main task of a resonator is to generate powerful radiation from a minor angle divergence. A resonator specifies the laser output, angle divergence, and the aperture's shape.

Resonator can be classified from view point: (1) stability, unstable, plane-parallel; (2) number of passes in active medium (single, multi-path); (3) usage of field rotation (with rotation, without rotation); (4) aperture's shape (compact aperture or ring aperture, symmetrical or asymmetrical).

The main parameters of a resonator are:

(1) The Fresnel number that is specified for a stable resonator as $N_F = \frac{d^2}{4\lambda \cdot L}$, where d is the lateral dimension of an aperture, λ the radiation wave length, L the resonator's length.
(2) Transmittance ratio t.
(3) Stability parameters $g_1 = 1 - L/R_1$, $g_2 = 1 - L/R_2$, $R_{1,2}$—mirror curvature radiuses.
(4) Enlargement ratio M for an unstable resonator (UR).

From the point of view of the power lasers, URs—whose angle of divergence is minor and capacity is quite high—are of particular interest. Formation of radiation mode structure in a UR takes place in a narrow paraxial zone with a lateral dimension of about $2\sqrt{\lambda \cdot L}$, which provides decent spatial radiation characteristics. Next, light propagates from the paraxial zone to the peripheral zone; and enhances but preserves the lower-order mode's spatial structure formed at the paraxial zone. The equivalent Fresnel number of a UR determines a certain type of distribution of intensity and phase in the output aperture. For more widely spread positive leg confocal resonators this number:

$$N_E = \frac{d^2}{8\lambda \cdot L}(M - 1).$$

Figure 2.76 represents rated distributions of intensity and phase at an output mirror of UR upon various values of the equivalent Fresnel number.

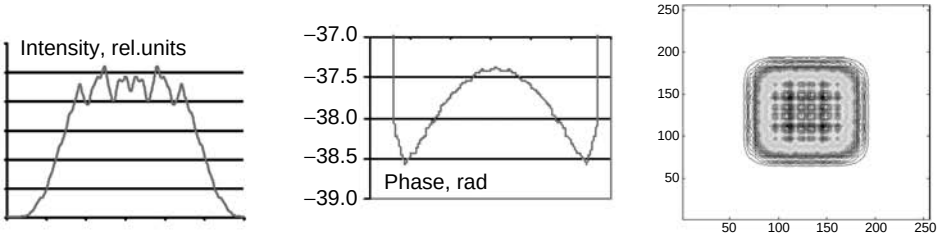

$M = 1.1$; $N_E = 0.6$, $L = 5$ m, $d = 0.05$ m, $\lambda = 10.6$ μm

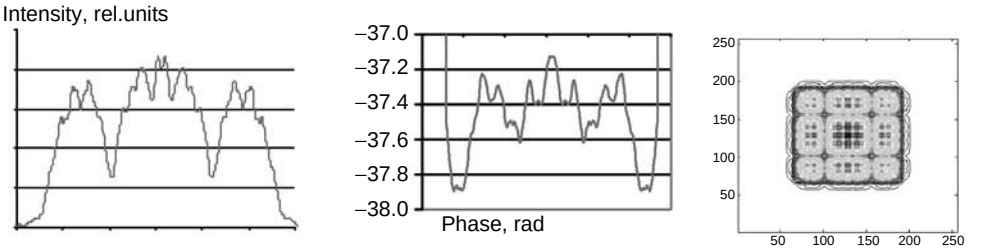

$M = 1.5$; $N_E = 2.954$, $L = 5$ m, $d = 0.05$ m, $\lambda = 10.6$ μm

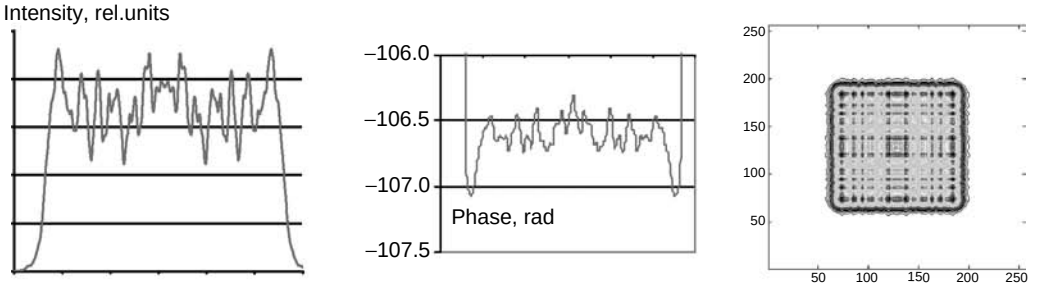

$M = 1.3$; $N_E = 7.5$, $L = 5$ m, $d = 0.1$ m, $\lambda = 10.6$ μm

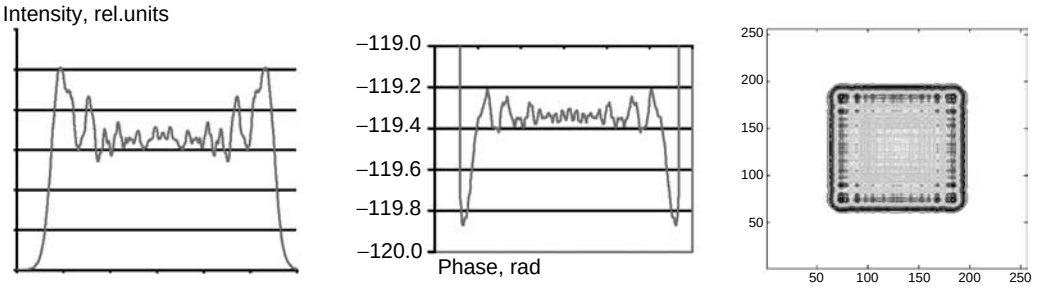

$M = 2$; $N_E = 23.5$, $L = 5$ m, $d = 0.05$ m, $\lambda = 10.6$ μm

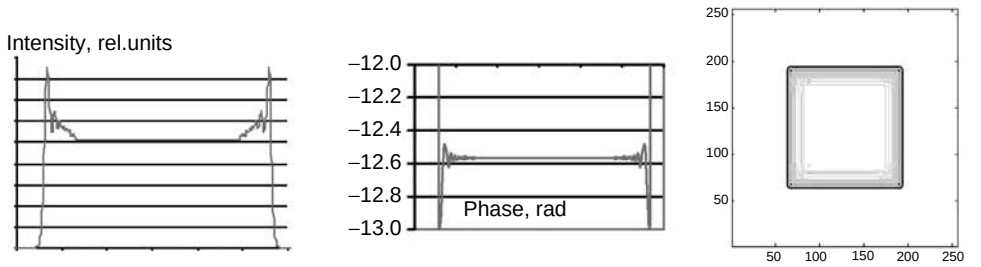

$L = 5$ m; $d = 0.1$ m, $\lambda = 10.6$ μm, $M = 1.5$, $N_E = 95$

FIGURE 2.76 Mode structure of unstable resonator.

As one can see from these diagrams, as the equivalent Fresnel number increases, the intensity distribution efficiency grows. This allows recommending it for powerful lasers.

2.5.2 Large-Scale Nonuniformities' Influence on Unstable Resonator Operation

Figure 2.77 presents a provisional classification of intracavity optical nonuniformities. As it is observed in the figure, the nonuniformities are divided into amplitude nonuniformities that are related to irregularity of the amplification ratio of the active medium or mirror reflection, and phase nonuniformities that are related to irregularity of the refraction factor of the active medium (AM) or resonator optics aberrations. By their position, the nonuniformities are divided into distributed nonuniformities, located along the entire resonator aperture, and paraxial nonuniformities, located next to the optical axis. Acknowledgment of the latter is especially important for the unstable resonators, as the paraxial area is responsible for the resonator mode formation. By spatial scales, the uniformities are classified as large-scale uniformities, whose lateral dimension is comparable to the aperture's dimension, and small-scale uniformities comparable to the Fresnel zone dimension. Apart from these, the non-uniformities can also be divided by the nature of impact upon radiation characteristics that influence capacity, divergence, or beam propagation direction.

To estimate the influence of the large-scale phase nonuniformities on radiation parameters of an unstable resonator one can use an aberrational ratio apparatus.

Let us assume that distribution of the refraction factor in an AM is an exponential series of the following view:

$$n(r) = n_0 + n_1 r + n_2 r^2 + n_3 r^3 + \cdots = \sum_{k=0}^{\infty} n_k r^k.$$

Then it is possible to demonstrate that the wavefront phase distribution at the output of an unstable resonator will be of the following view [1]:

$$\Delta\varphi(r) = \frac{2\pi}{\lambda} \cdot L \sum_{k=1}^{\infty} n_k \left[1 + \frac{1}{k+1} \frac{M^{k+1} - 1}{(M-1)M^k}\right] \times \left[r^k + \left(\frac{r}{M}\right)^k + \left(\frac{r}{M^2}\right)^k + \cdots\right].$$

if we take into account that $\left[r^k + \left(\frac{r}{M}\right)^k + \left(\frac{r}{M^2}\right)^k + \cdots\right] = \frac{1}{1 - 1/M^k} r^k$ and introduce identification:

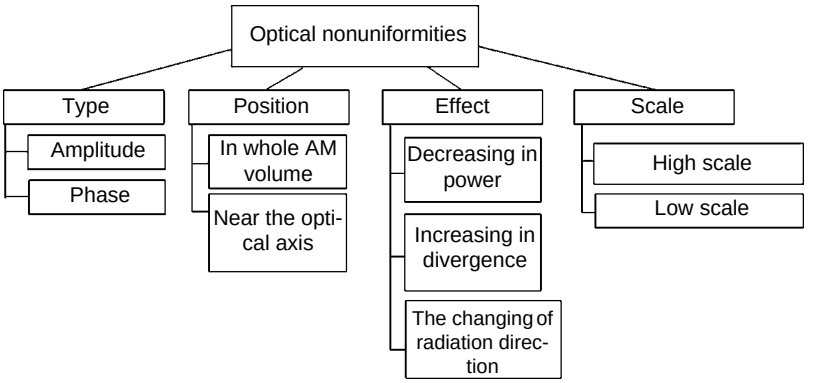

FIGURE 2.77 Classification of internal resonator nonuniformities.

$\alpha_k(M) = \left[1 + \frac{1}{k+1}\frac{M^{k+1}-1}{(M-1)M^k}\right]\frac{1}{1-1/M^k}$, then for a radiation wavefront behind an unstable resonator can be written as:

$$\Delta\varphi(r) = L\sum_{k=1}^{\infty}\alpha_k(M)n_k r^k.$$

The applied $\alpha_k(M)$ are called aberrational coefficients. They indicate to what extent a nonuniformity of order k develops stronger in UR as compared to single-pass amplifiers.

As the M-ratio increases, the resonator's sensitivity to aberrations decreases. The most frequently accounted types of large-scale aberrations in the powerful lasers are the aberrations of the first order (optical wedge) and the aberrations of the second order (spherical ones). The optical wedge refers to mirror misalignment in a resonator or to uneven downstream distribution of a refraction factor. The spherical aberration is mainly caused by thermal deformation of mirrors, inaccuracies of their fabrication or faults in installation.

Figure 2.78 shows an example of alteration in the resonator mode configuration when there is mirror misalignment by an angle of α for an unstable resonator of the following parameters $M = 1.5$, $d = 0.1$, $L = 5$ m, $\lambda = 10.6$ μm.

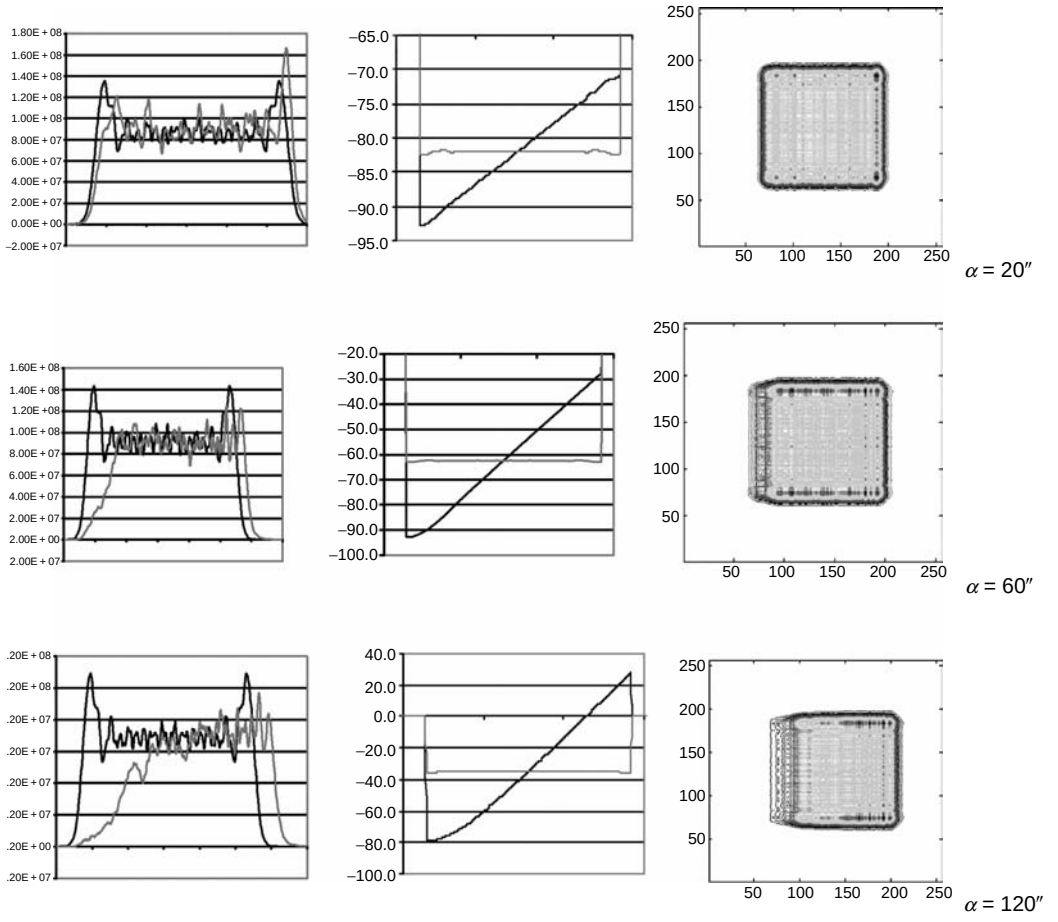

FIGURE 2.78 The influence of misalignment on mode of unstable resonator.

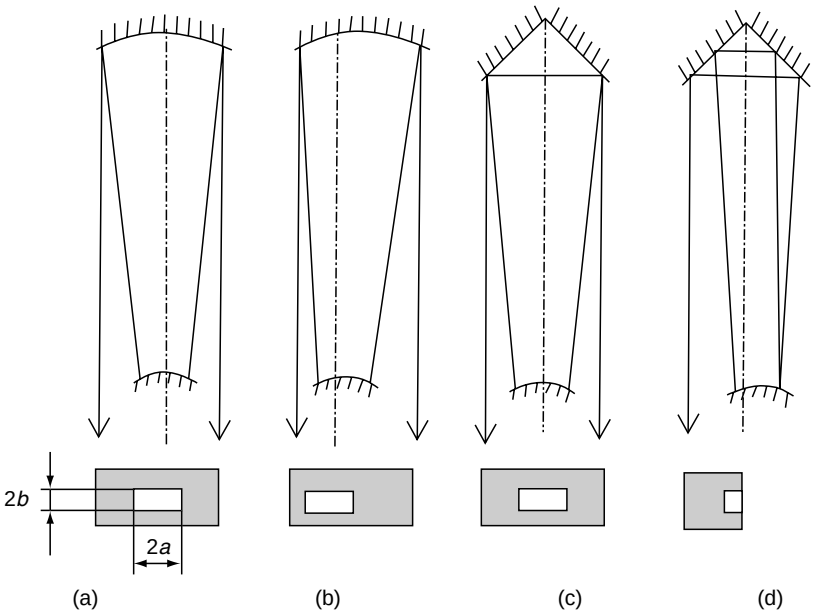

FIGURE 2.79 Schemes of GDL resonators: (a) classic UR with symmetrical aperture; (b) resonator with unsymmetrical aperture; (c) resonator with field rotation on roof mirror; (d) resonator with field rotation on roof mirror and unsymmetrical aperture.

As far as the large-scale amplitude nonuniformities are confirmed, as it was mentioned before, they mainly refer to uneven distribution of the amplification ratio of a weak signal of the active medium.

The spatial form of the gain distribution depends on a laser type. For example, in a supersonic GDL monotonous decline of the gain downstream is observed, while in a COIL right behind the nozzles, the gain increases to a certain maximum and then declines. Similar nonuniformities of the gain lead to a corresponding nonuniformity in radiation intensity distribution in the output aperture. To compensate them partially, angle reflectors can be applied in a resonator, which turn a beam so that a section of the beam coming to the angle reflector along the zone of high amplification after getting reflected from the angle reflector goes back along the zone of lower amplification. This way, intensity distribution in the beam cross section turns to be more uniform.

For example, in Figure 2.79 there are various schemes of an unstable resonator of GDL.

Figure 2.80 shows rated downstream intensity distributions by the output mirror aperture at various magnification ratios for resonators of a standard scheme (Figure 2.79a,b). While Figure 2.81 shows similar dependencies but for a UR with a field rotation (like Figure 2.78c and Figure 2.78d).

It is obvious that if the field rotation is applied, the intensity distribution in the output aperture becomes more uniform.

Figure 2.82 indicates intensity distributions in the aperture of the supersonic COIL—for a single-pass resonator, U-bend resonator, and a resonator with two field rotations at two angle reflectors. The latter scheme that provides uniform intensity distribution in a beam that completely corresponds to the gain distribution.

So, the large-scale nonuniformities can be compensated by uncomplicated passive methods. That is why the small-scale nonuniformities are of special importance as it is complicated to

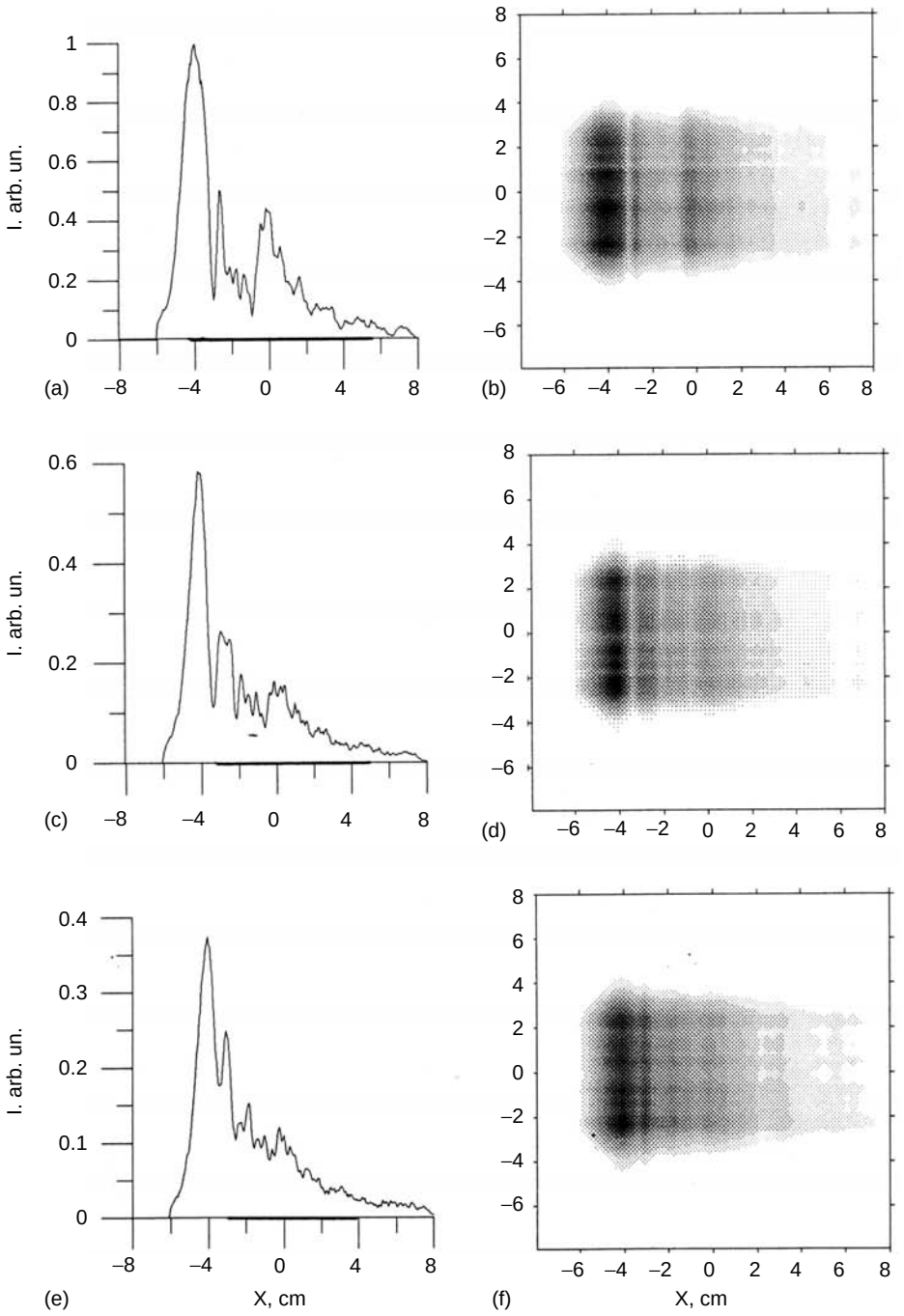

FIGURE 2.80 Calculated distributions of intensity by output mirror aperture along the flow at different magnification coefficients for resonators of classical scheme (a), (b)—$M = 1.4$; (c), (d)—$M = 1.8$; (e), (f)—$M = 2$.

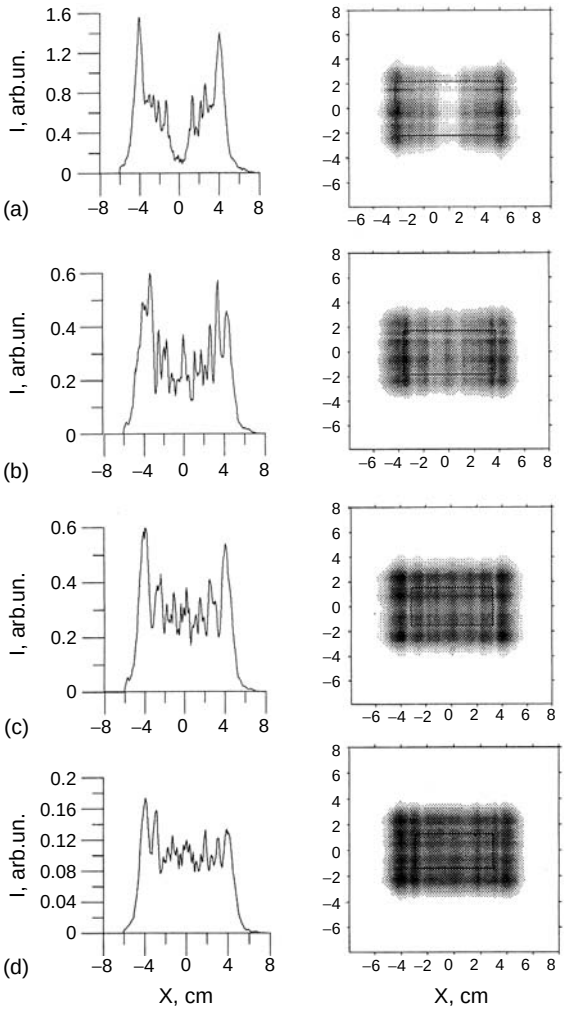

FIGURE 2.81 Calculated distributions of intensity on output mirror aperture along the flow at different magnification coefficients for resonators with field rotation; $M = 1.4$—(a), $M = 1.6$—(b), $M = 1.8$—(c), $M = 2$—(d).

compensate them, whereas the amount of their impact upon the radiation parameters may be significant.

2.5.3 Small-Scale Nonuniformities' Influence on Unstable Resonator Operation

Let us consider the influence of the periodic disturbance of AM's refraction factor upon an unstable resonator's efficiency. To do that, let us carry out numeric resonator modeling upon diffraction approximation.

To describe the refraction factor's periodic distribution in a certain AM cross–section orthogonal to the optical axis, one can apply the following approximation [2]:

$$n(x,y) = n_0 + a_{xy}\left[\frac{\sin^2(a_x \cdot x)}{a - \sin^2(a_x \cdot x)} + \frac{\sin^2(a_y \cdot y)}{a - \sin^2(a_y \cdot y)}\right],$$

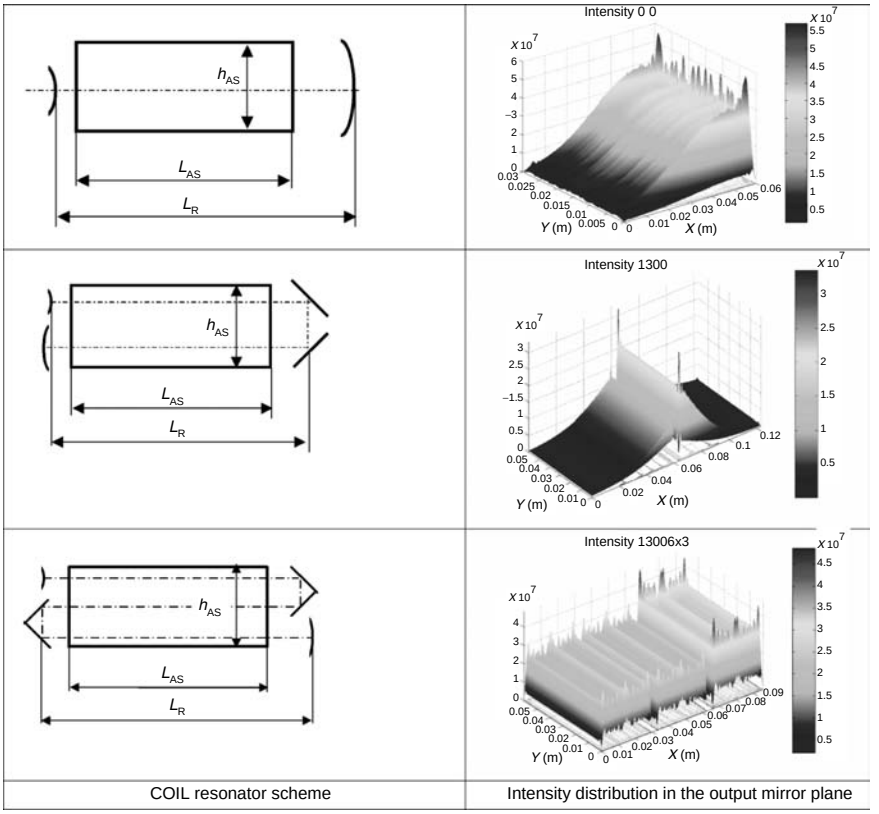

FIGURE 2.82 Intensity distributions in the output mirror plane for different resonator scheme.

where a_x, a_y, a_{xy}, a are the factors by varying which the following can be changed: number of nonuniformities' periods, the refraction factor's fringe relative to the average value of n_0, and configuration of the periodic nonuniformity in the cross section.

Figure 2.83 shows typical dependence of a radiation divergence angle by three levels of energy build-up of the directional diagram 20%, 50%, and 80% on the number of periods f

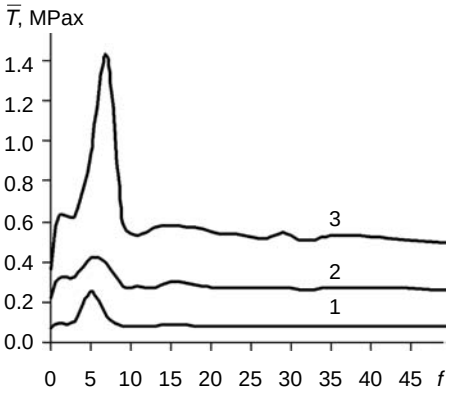

FIGURE 2.83 The dependence of beam divergence on period's number (spatial frequency) of phase nonuniformity on resonator aperture; 1—by level of energy filling of direction diagram 20%; 2—50%; 3—80%.

(spatial frequency) of nonuniformities in an aperture of a positive leg telescopic resonator for a radiation wave length of $\lambda = 10.6$ μm, equivalent distance between the mirrors $L = 4.1$ m and the resonator's enlargement ratio $M = 2$ at the output aperture in a shape of a square frame of the external dimension of 0.1 m. Radiation phase dispersion in an aperture during one pass through the nonuniform AM was assumed to be $D = 0.11$ rad^2 (which corresponds with the Schtrel number of ~0.9). Phase nonuniformity in the paraxial zone corresponded with the provisional collecting lens.

The diagrams make it obvious that the least favorable situation takes place when the number of wavefront (WF) aberration periods in the resonator's aperture $f \sim 5$–10, which confirms with the linear dimension of the nonuniformity period ~0.02–0.01 m. It is typical that minimal power of the radiation generation is also observed upon that.

Dimensions (diameter) of the first Fresnel zone of a resonator can be calculated with the following formula:

$$d_F = 2 \cdot \sqrt{\frac{2\lambda L}{M-1}}, \tag{2.10}$$

that is, for the resonator under consideration it will make ~0.01 m. It becomes obvious that the worst UR operating conditions occur when the phase nonuniformity period in the AM coincides to an extent with the first Fresnel zone dimensions. In addition, qualitatively, radiation divergence dependence on the number of UR aperture's periods retains its tendency for various levels of D.

When the nonuniformity period differs greatly from the Fresnel zone dimension d_F, more acceptable values of both generation capacity and radiation divergence (see Figure 2.82) take place if the nonuniformity period exceeds the first Fresnel zone dimension ($f < 5$) in the generation zone of a UR; that is, in the paraxial area limited by the first Fresnel zone dimension, phase fringe becomes less than the value of D at a complete period of spatial disturbance.

Upon $f > 8$, the generation zone houses several complete periods of spatial disturbance, exhibits decline in radiation divergence and preserves the level if f is increased. This feature can be explained by the fact that the spatial disturbance in the generation zone can be considered as a phase diffraction screen. The energy build-up of the zero diffraction order, which is responsible for meeting the requirement of stationary generation in a UR, does not actually depend on the screen period but depends only on the disturbance amplitude.

When the disturbance levels are not very high, the radiation portion scattered into the side diffraction gratings does not influence the formed resonator mode, that is, the radiation divergence. For example, upon $f \sim 16$ (in the resonator's configuration considered two disturbance periods fall within a Fresnel zone) the radiation propagation angle of the first diffraction grating already exceeds the angle dimension of the first Fresnel zone and because of that this portion of radiation leaves the resonator quite rapidly with no significant impact upon its formed mode.

As the resonator's geometrical parameters vary the maximum of the curves, Figure 2.83 shows the shift according to the resonator's Fresnel zone dimension variations relative to the spatial disturbance period. Approximate position of maximum unfavorable radiation divergence can be estimated on the basis of the equation of a nonuniformity period and the Fresnel zone dimensions though its actual position upon the frequency scale can differ a little as the Fresnel zone dimension for a resonator is conditional.

The detected tendency is also preserved if nonuniformity in the paraxial area of a resonator is of a divergent lens type, and that the maximum radiation divergence is achieved at the same

number of periods of aperture nonuniformities, and the angle divergence value is almost the same as in a collecting lens type nonuniformities.

If the following parameters are introduced, then one can write a condition when a local stable resonator is formed in a small-scale nonuniformities' resonator:

1. $\varepsilon = \dfrac{\Delta\varphi}{2\pi}$—relative phase dispersion after a single pass through the active medium
2. $\Delta = \dfrac{a_m}{a_u}$—relative nonuniformity dimension (a_u—lateral nonuniformity, a convex reflector diameter)

$$\frac{\pi^2\varepsilon}{N_{Eu}} < \frac{M-1}{M+1}, \qquad N_{Eu} = \frac{a_u^2}{4L\lambda}\left(M - \frac{1}{M}\right).$$

Figure 2.84 shows examples of intensity distributions and a radiation phase at the resonator's output upon two different values of Δ: at $\Delta = 1$ (a large-scale nonuniformity of a lens type) and at $\Delta = 15$ (small-scale aberration) for a resonator of $M = 1.5$, $L = 1$ m, $d = 0.1$ m, $\lambda = 10.6$ μm, $\varepsilon = 0.12$.

The presented analyses make it obvious that the least favorable situation (maximal divergence and minimal radiation output capacity) occurs when the period of a spatial nonuniformity in the AM is close to the equivalent Fresnel zone dimension of a selected resonator scheme. Apart from that, as the absolute nonuniformities level grows, that is, the difference between maximum and minimum value of the AM's refraction factor, the divergence of the generated radiation also increases. Accordingly, one can state that for a set nonuniformity

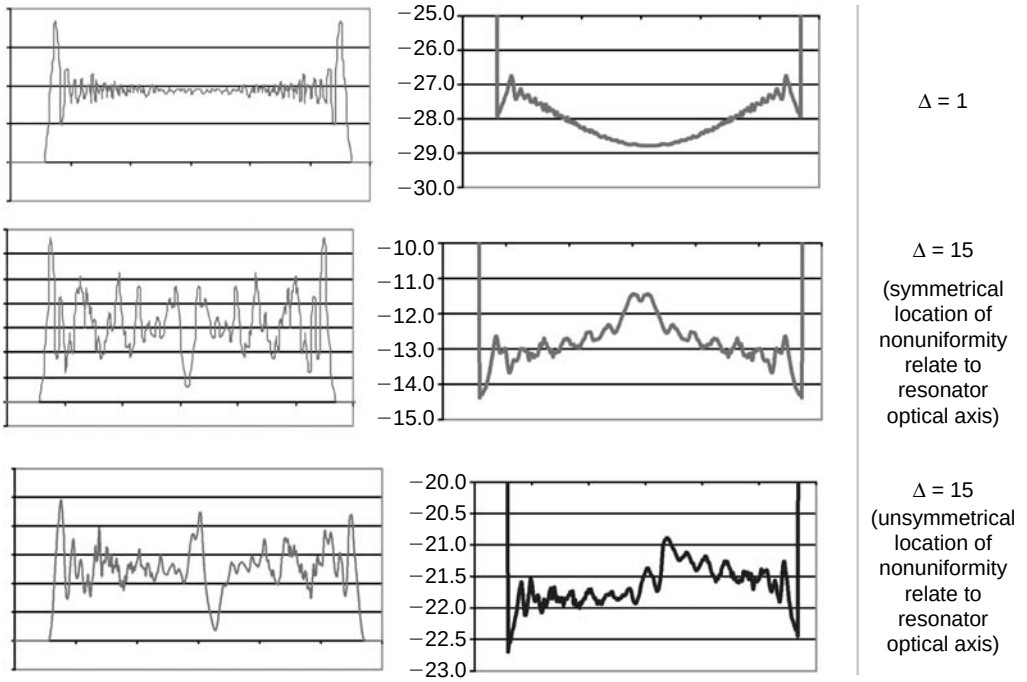

FIGURE 2.84 Distribution of intensities and phase in resonator aperture.

structure specified by the design particularities of the laser activation system the UR efficiency upgrading methods shall not only be intended to reduce integral phase dispersion of disturbances along the UR's optical axis, but also to provide advantageous correlation between the resonator's Fresnel zone dimension d_F and a nonuniformity period p

$$d_F \neq p(d_F > p \text{ or } d_F < p).$$

For the small-scale nonuniformities related, to the gas flow turbulence in particular, it is impossible to compensate them with the mentioned methods, as there is no regular structure in this case.

2.5.4 Resonator Design

The main components of a laser resonator are:

– active medium,
– bearing structure of a resonator,
– adjusting positioner,
– mirrors,
– mirror cooling system (if necessary), and
– control system for an automative resonator alignment.

Table 2.3 presents the basic requirements of a resonator design.

Figure 2.85 shows possible principle layout diagrams of a resonator and a gas flow section. From the standpoint of resonator's vibration isolation, the optimal scheme is presented in Figure 2.85c, though, it can cause radiation losses in the Brewster windows, and apart from that it is difficult to manufacture wide aperture windows for the far infrared band. The resonator shown in Figure 2.85b is the most affected by the external pressure load, though it is of smaller dimensions than the resonator shown in Figure 2.85a.

TABLE 2.3
Basic Requirements of a Resonator Design

Basic Requirements toward the Design	How to Fulfill
Mutual immobility of the resonator mirrors	Structural stiffness A special-purpose structure of adjusting positioner
Vibration proof resonator optics	An individual foundation for a resonator Vibration isolation between the gas flow section and the resonator A special-purpose structure of adjusting positioner
Leakage proof gas flow section	Tight connection between the resonator and the gas flow section or sealing the gas flow section of an independent resonator
Assurance of required alignment accuracy	A special-purpose structure of adjusting positioner Resonator's vibration control.
A required number of mirrors	High requirements toward production Mirror protection upon laser operation
A regular radiation dose exposed upon the mirrors	A proper resonator scheme Application of mirror cooling system if necessary

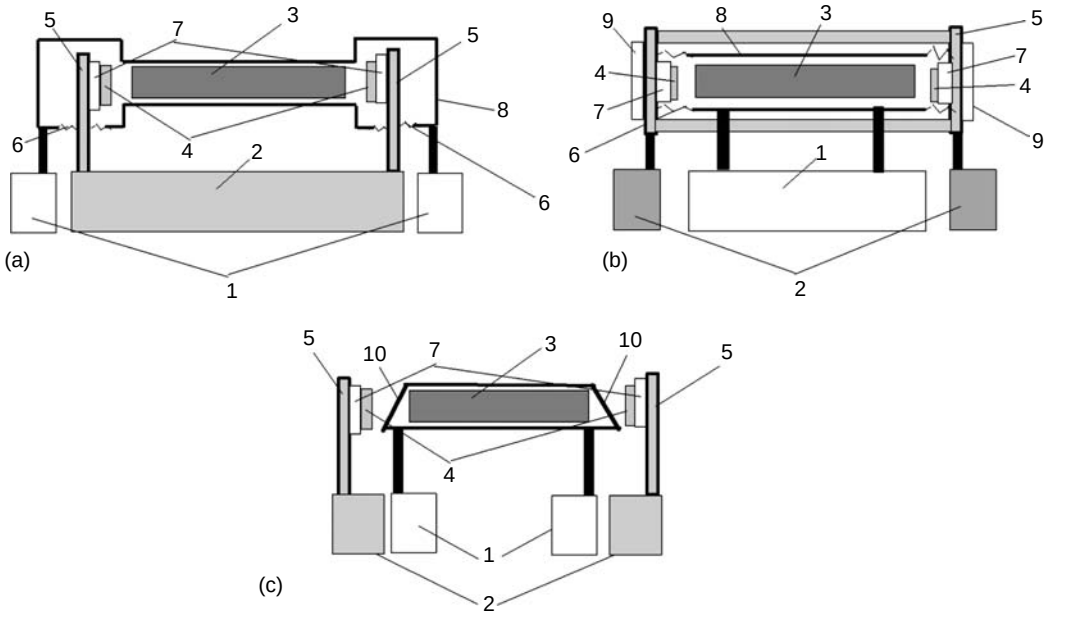

FIGURE 2.85 Schemes of resonator design: 1—base of gas-flow part; 2—base of resonator; 3—nozzle bank; 4—mirrors; 5 –frame structure of resonator; 6—hermetic sylphons; 7—adjusting brackets; 8—gas-flow part; 9—hermetic resonator's covers; 10—Brewster windows.

2.6 PRESSURE RECOVERY SYSTEMS FOR CHEMICAL SGL

2.6.1 General Information

As it was noted in the introduction, operating pressure in resonant cavity of SCL is low (10–20 Torr). So, the exhaust problem exists for such systems. For laboratory laser with low mass flow rate (and short operating time), the vacuum capacity can be used for exhaust. For systems with a big mass flow rate, especially for mobile, PRS design is required [1–4].

The demands to PRS of various types of lasers are shown with conditions in Figure 2.86. Only combustion driven CO_2-GDL can operate normally without consuming additional energy, using regular passive diffusers. However, even in this case the diffuser size is critical for the size of the whole laser system. Operation of chemical laser with a high power (HF/DF-laser, COIL) creates the need for active PRS; the latter is a large-scale chamber including a diffuser and high-energy ejection (or compression) station. For HF(DF)-lasers, one-stage ejector with compression level 10–12 is enough. But, for a COIL, we have to use a two-stage ejector with the total compression of about 50–60. Only if we put this COIL at a height of 10–12 km (the height of aircraft flight) will one-stage ejector be enough.

Figure 2.87 demonstrates the proportions between the size of HF(DF) supersonic laser and its pressure recovery system. Here, one can see a laboratory laser with a low mass flow rate (PRS on base of multitube ejector station for powerful laser is shown on Figure 2.101). Even without the system of component storage and feeding (gas cylinders, reservoirs, pipelines, etc.), the scales of the laser and PRS are incomparable. For a COIL system, this difference becomes even greater. The estimates for the flow rate of ejection gas reveal that it may be dozens of times higher than the total consumption of laser generation gases. That is why the PRS design is as important as laser itself for technical solutions and design of a high power SCL–HPSCL (on-land basing); it is crucial for power and gas consumption, as well as for

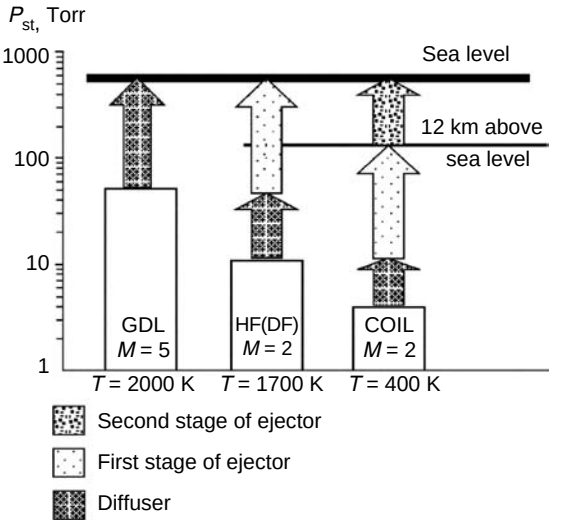

FIGURE 2.86 Pressure recovery in gas lasers with supersonic stream.

manufacturing, assembling, and operating costs. If we take into account operation of the PRS in analysis of HPSCL efficiency, the total estimates become quite different. Similar calculations for HF(DF)-lasers are published [5]. The estimates of specific power for other types of HPSCL are shown in Figure 2.88. These data are given for the laser power in the near-field zone, that is, the problems of radiation divergence, transmission, and dispersion in atmosphere have not been taken into account. We can state that estimates for specific energy outlet

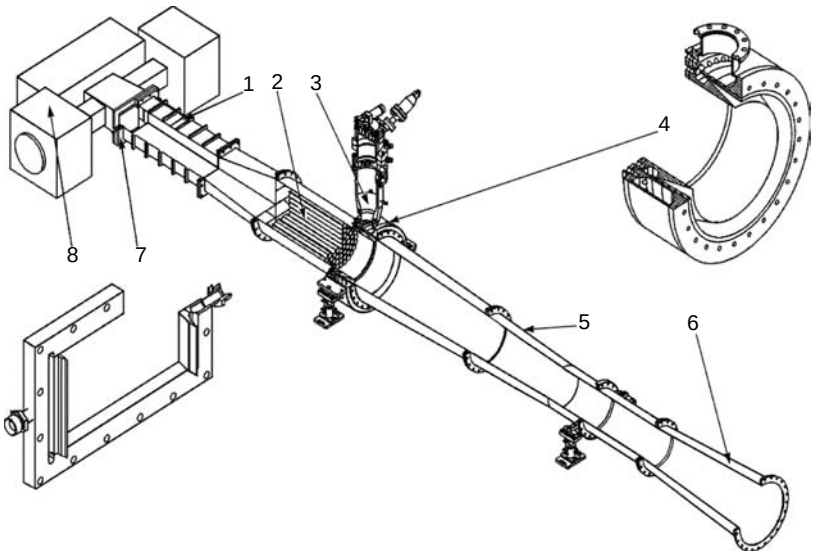

FIGURE 2.87 General view of PRS and HF(DF)-laser: lab small-scale installation. 1—Supersonic diffuser, 2—heat-exchanger, 3—vapor-gas generator, 4—ejector nozzle, 5—mixing chamber of ejector, 6—subsonic diffuser, 7—booster, 8—laser.

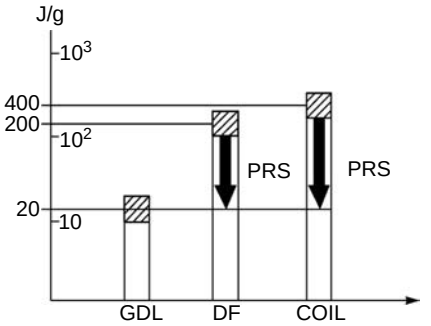

FIGURE 2.88 Specific power for different types of lasers taking in account PRS mass flow rate.

characteristics made for a chemical HF(DF)-laser and a COIL, with and without considering the mass flow rate of PRS components, are very different regardless of the calculation methods; this difference exceeds one order in magnitude.

So, success in creation of mobile laser complex mainly depends on luck in solving the problem of effective PRS creation.

2.6.2 Diffuser

In general, operating channel of PRS consists of diffuser (SD), ejector (EJ), and heat-exchanger.

It is known that the slow down process of supersonic flow in channel occurs in a series of oblique shocks (Figure 2.89) that arise on walls of channel as a result of boundary layers increasing on these walls [6]. It has been shown [7], that in round tubes (at enough big R_e numbers) pressure behind this system of shocks—pressure recovery—is neighbor to pressure behind normal shock (the system of oblique shocks is known as pseudoshock).

At the start of any kind supersonic gasdynamic installation it is necessary to create in forechamber sufficient pressure $\mathbf{P_0}$—before a supersonic nozzle—for pushing normal shock into an atmosphere through a test section, that is, pressure behind normal shock-P_0', for given Mach number M of flow (or $\boldsymbol{\lambda}$) in a test section should exceed atmospheric, that is,

$$P_0' = \kappa P_0 \times \sigma(\lambda) < 1. \tag{2.11}$$

Where $\sigma(\lambda)$ is the standard gasdynamic function determining losses of stagnation pressure behind normal shock and κ the empirical factor which is close to unit for round tubes (for correctly designed cylindrical diffuser it is determined actually by friction losses).

On the basis of normal shock ratio, one can also easily estimate both pressure of unstart and pressure recovery which already depend on the channel geometry of supersonic diffuser–SD

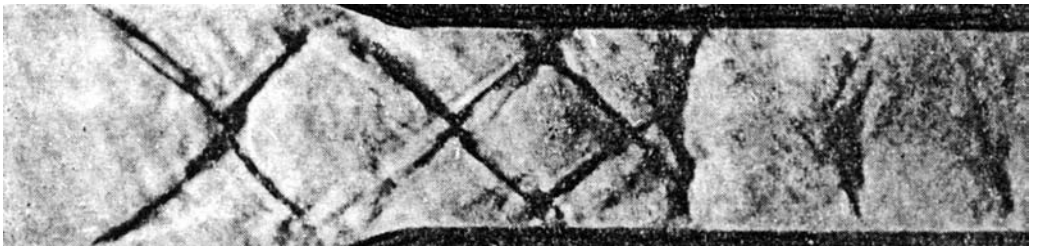

FIGURE 2.89 Pseudoshock (system of X-type oblique shocks) in converging channel.

(depends on a restriction degree). However, experimental SD characteristics and the estimations based on the one-dimensional integrated theory of normal shock are close only if the SD length-L_D, used in experiment, is equal to pseudoshock length—L_P. Otherwise, SD-characteristics become worse [8,9].

For a finding L_P that is necessary for the given flow Mach number, the generalized experimental dependencies $L_P/d_{eff} = f(M)$ are used. Thus, for round tubes the diameter of tubes was used as the generalizing parameter d_{eff}. In case of rectangular channels (with a different ratio of the sides $b/h > 1$) for generalization of results, it was necessary to enter the special effective diameter d_{eff} which does not coincide with hydraulic diameter [9]:

$$d_{eff} = h^{0.3} \times b^{0.7}$$

(where h is the height, and b is the width of the rectangular channel). Generalized dependence $L_P/d_{eff} = f(M)$ for rectangular and round channels is given in Figure 2.90. This half empirical method of an estimation of SD parameters is working well in case of GDL and aerodynamic wind tunnels.

However, such simple technique of estimation of SD parameters ceases to work in case of SCL. A principal cause of it is the heat generation in a supersonic flow of laser gas. In case of the DF-laser the heat generation is connected with the burning of secondary fuel and takes place instantly near the nozzle bank in the laser chamber, that is, before SD. In case of COIL, the heat generation is determined by the process of thermolysis of singlet oxygen molecules.

In [10] interesting data about behavior of temperatures of laser stream along the COIL channel are given (see Figure 2.91). Generally, the flow temperature grows along a stream, and grows almost linearly. It means, that process of a heat generation occurs gradually with almost constant intensity in the beginning of the channel. Therefore it is possible to influence by the form of channel slow down process of stream, on the general pseudoshock length.

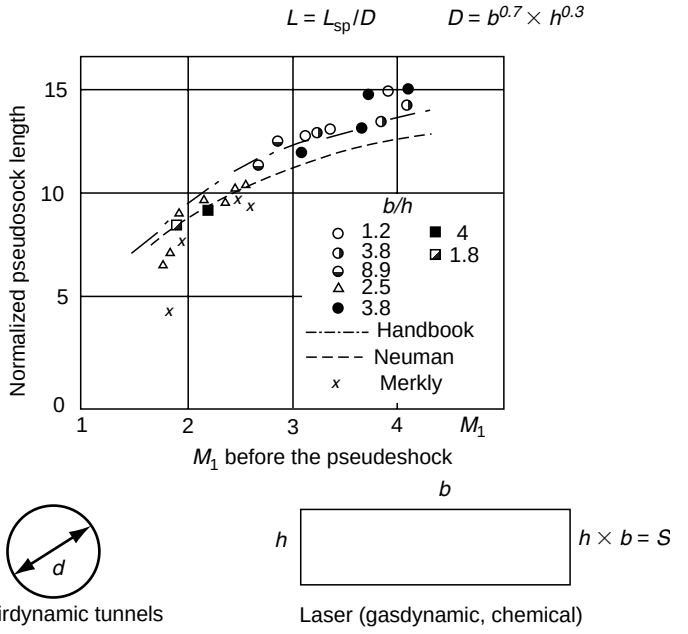

FIGURE 2.90 Dependence of normalized pseudoshock length on Mach number of incident flow (for round and rectangular cross-section channels).

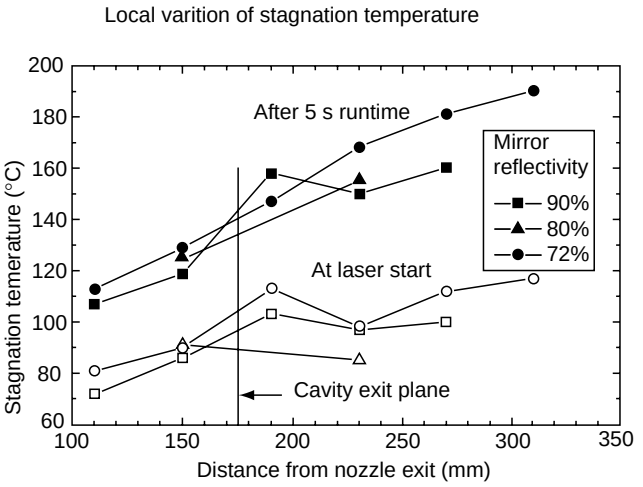

FIGURE 2.91 Variation of stagnation temperature along COIL's channel. (From Schall, W.O., Grunewald, K., Handke, J., COIL diffiser investigations, *COIL R&D Workshop*, May 2001, pp. 28–29, Prague.)

According to the known equation [11] describing change of flow speed **W** at external influence:

$$(M^2 - 1)\mathrm{d}W/W = \mathrm{d}F/F - \mathrm{d}Q \tag{2.12}$$

For the sake of simplicity only two members are indicated: the first characterizes the change of geometry of channel, and the second corresponds supply of heat, at a supply of heat-d$Q >$ 0 in a supersonic stream—$M > 1$, in the constant cross-section channel-$\mathbf{F} = F = const$ant, the change of speed is negative-d$W < 0$, that is, the stream is reduced.

Thus, in channels of supersonic chemical lasers to gasdynamic slow down mechanism in shocks (the separation zones, arising in the channel as a result of interaction of shocks with a boundary layer on walls take part in slow down of flow too), the slow down mechanism connected with heat generation is still added. It has resulted in reduction of pseudoshock length in comparison with L_{P} received in experiments without heat generation.

It is known that the supply of corresponding amount of heat to supersonic flow in the constant cross-section channel results in lock-out effect, that is, impossibility of existence of supersonic flow. Therefore, to avoid lock-out it is necessary to make the channel of the supersonic chemical laser, as follows from the equation (2.12), as an expanding one.

In Figure 2.92, distributions $P_{\mathrm{st}}(x)$ for the channel along with the divergence angle of laser chamber 1.7°, 2.5° and 4° are shown (for Mach number $M = 2$ at SD entrance). The data for angle 2.5° are taken from [10]. Apparently, expansion of the channel compensates heat generation in some sense: the more angle, the more zone of slow down. And on the contrary: the divergence angle is less, the flow slow down is faster, that is, the pseudoshock length is less, and it is possible to consider that the heat generation as more intensive.

SD with length more than the pseudoshock length operates ineffectively. However, the reduction in length corresponding with data at Figure 2.92 is impossible. Boundary layers in the COIL channel are very thick. Influence of outlet conditions is transferred to the nozzle easily.

Pressure distribution $P(X)$ in channel of SD with divergence angle 4° at different back pressures at SD exit is shown in Figure 2.93. The pseudoshock length at heat generation decreases in comparison with results in [8,9], which is obtained in SD without heat

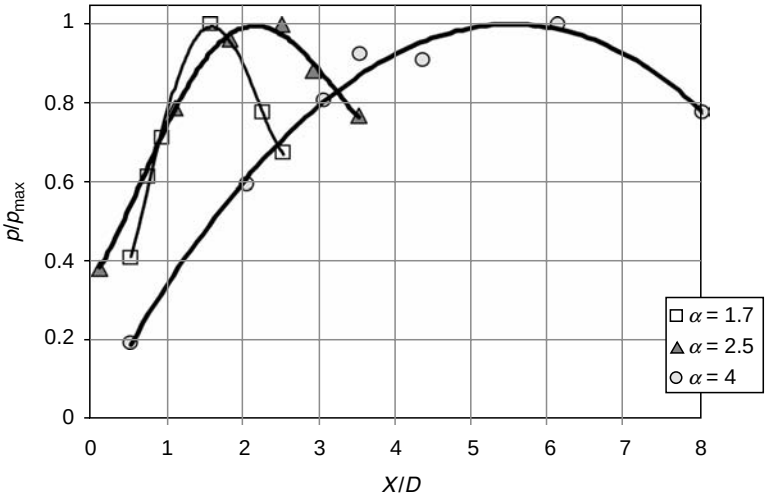

FIGURE 2.92 Static pressure distribution along COIL diffuser: α—initial divergent angle of laser chamber, x/D—normalized length of channel (D—see Figure 2.90).

generation. In channels without heat generation *(Q)*, pseudoshock displaces along channel depending on backpressure level. Here, it begins just after laser chamber: heat generation influences to slow down process and it begins exactly here. And, at reducing in length the conditions at exit is carried forward—pseudoshock moves to nozzle and supersonic flow in resonant cavity is unstarted quickly. Therefore, for reducing in SD length—in case of COIL—it is necessary to make particular actions: for example, to organize the exhaust of boundary layer [12] or blow it with help of high-pressure nozzles.

Hence, the slow down process of supersonic stream in conditions of chemical laser greatly depends on heat-generation process. It depends on the large number of concrete working parameters of the given laser, including constructive. It depends on composition of the active

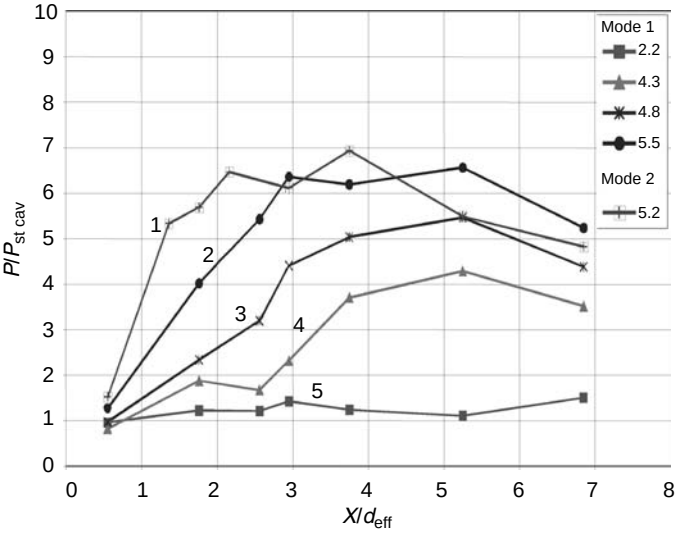

FIGURE 2.93 Static pressure distribution along COIL diffuser ($\alpha = 4°$): lines from 5 to 1 correspond to increasing of back pressure after diffuser.

laser medium (varies with the diluent used: helium or nitrogen), gasdynamic parameters of medium (pressure, speed), the particularities of work of singlet oxygen generator, the adulteration scheme of iodine into stream, etc. Therefore, the formulation of universal recommendations and delivery of simple dependencies as in [8,9] and simplifying SD design—in case of the chemical laser—are actually impossible.

Hence, the effective COIL SD cannot be projected independently from design of the nozzle bank and the laser chamber, and it is required to consider how physical process in the given laser is organized. If the knowledge of flow Mach number in test section is quite enough for SD creation of a wind tunnel, which means, SD can be projected separately, as the independent device, in case of chemical laser SD and the laser are uniform-integrated devices. It is the basic complexity in calculating and creating effective SD for chemical lasers.

When creating SD for chemical laser, it is possible to go in the empirical way: first, finding out the pseudoshock behavior in the channel of the given laser for operational conditions. It is possible to simulate numerically three-dimensional flow in the laser test section and to select SD channel for effective slow down of flow. But, the choice of model of chemical and kinetic processes that adequately reflects all COIL physics is not a simple matter.

In case of DF-lasers, the situation is easier: heat generation occurs only in the laser chamber in a zone of secondary fuel burning. Here a stream—if one examines it as the average flow—is reduced from Mach number $M = 4$–4.5 to $M \approx 2$ approximately. The initial expansion angle of the chamber of DF-laser usually makes 8°–10°. If flow parameters at SD entrance are known, SD characteristics can be estimated with the help of the traditional integrated technique. More details about SD of SCL can be found in [13,14].

2.6.3 Supersonic Ejector

Like for SD, calculation of the working parameters of EJ and its geometry starts from a standard one-dimensional inviscid model based on integral relationships of conservation equations [11]. Here, the length of mixing chamber is the key empirical parameter. It depends on the method of mixing. It is known that for the peripheral scheme (injection of induced gas along the wall of mixing chamber), the length of mixing is 4–5 caliber (chamber diameter) [15], and for the central injection it is 8–10 caliber [11]. The mixing chamber can be cylindrical or conic (converging). The converging degree is chosen from different terms: the pressure is kept along the chamber, or flow crisis occurs in its neck. The contraction ratio may be chosen from the search for optimal velocity ratio between λ_2—the subsonic flow behind SD (i. e., the ejector inlet) and λ_3—the flow at the mixing chamber outlet (i.e., at the inlet of mixing chamber neck). For this case, the mixing chamber will be shorter and the neck will be longer than that for ejector calculation with crisis in the throat.

Calculated ejection coefficients n are shown in Figure 2.94 depending on flow velocity λ_3 at the inlet to the mixing chamber at various ratios of flow compression for a single-stage ejector: each curve corresponds to a constant compression ratio marked there. It is obvious that optimal values of λ_3 exist. However, λ_3 is a calculated value of the model in the framework of the one-dimensional inviscid scheme. Therefore, for SD, ejector parameters and geometry chosen via the inviscid model are considered as the first approximation. Then the three-dimensional flow pattern is calculated for preliminary geometry using the complete Navier—Stokes equations. Start-up and breakdown characteristics, time of regime stabilization, etc. are then determined.

The flow pattern for ejector that has been operating in composition of DF-laser PRS is shown in Figure 2.95. The fields of Mach number are shown by color. The ejector nozzle was calculated for $M = 4.5$. Gas vapor at $T_0 = 1300$ K was used as the working medium. At ejection coefficient $n = 0.06$, the achieved degree of flow compression was ≈ 14. The calculated

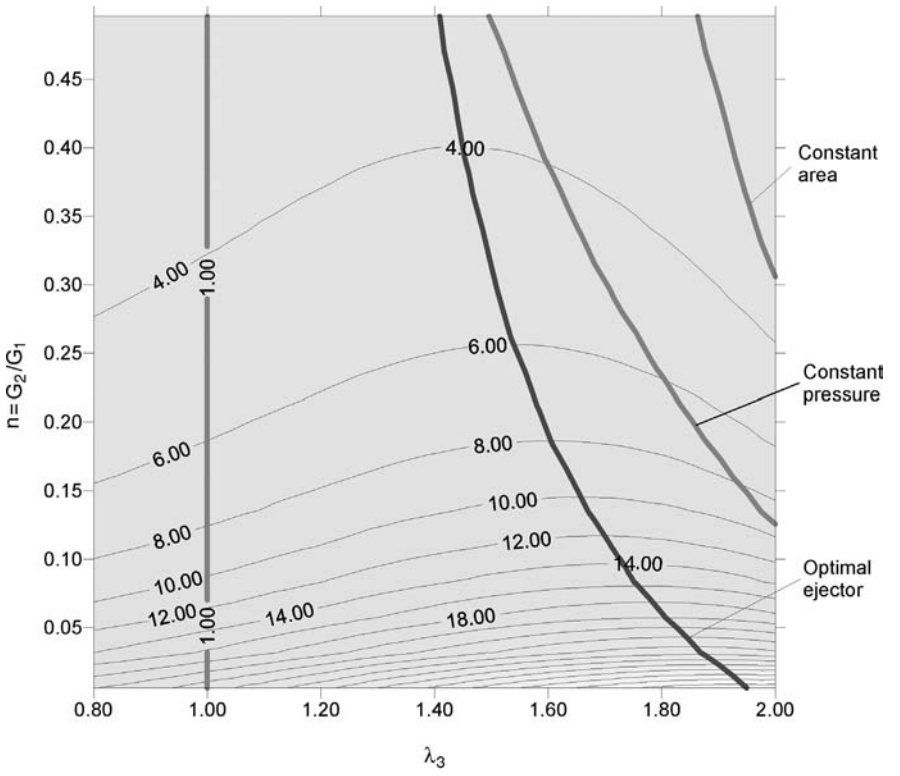

FIGURE 2.94 Dependence of ejection coefficient on velocity of flow at inlet of ejector throat: isolines correspond to constant ejector compression ratio.

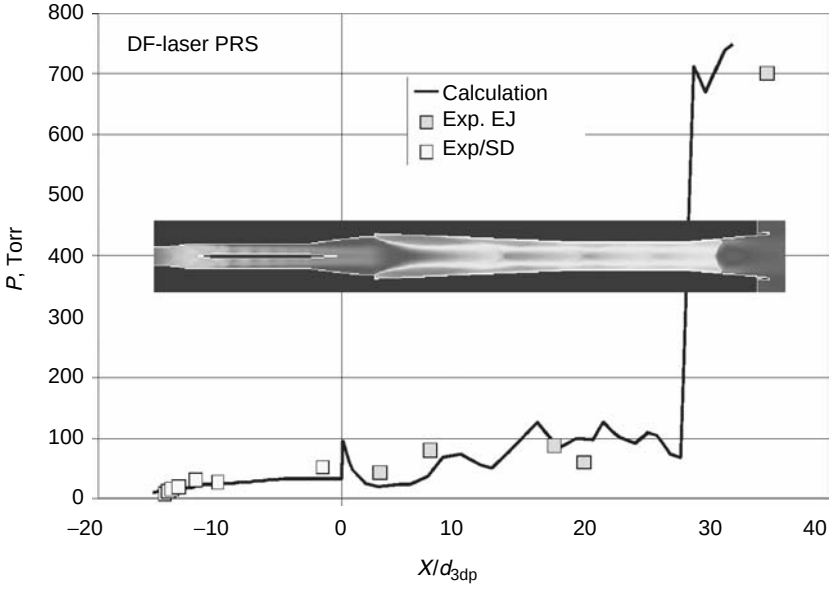

FIGURE 2.95 Static pressure distribution along PRS channel, comparison of experimental and numerical data.

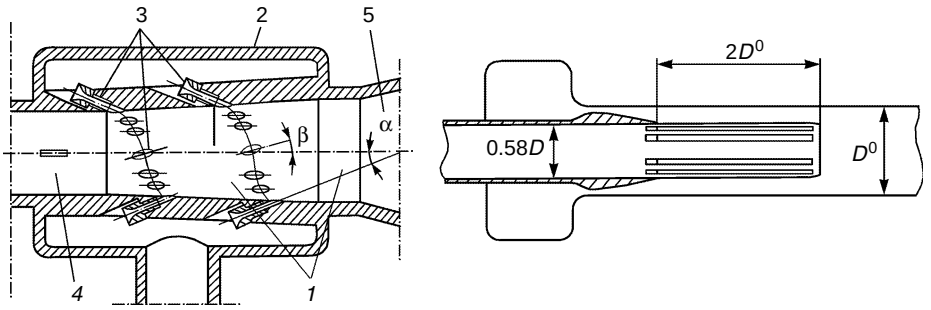

FIGURE 2.96 Principal schemes of ejectors with intensification of mixing.

curve of pressure distribution over the wall along the whole track of DF-laser PRS is plotted in Figure 2.95 against experimental data. Evidently, the simulation model gives an adequate representation of processes occurring in SD and EJ. There is not only qualitative, but also quantitative agreement. This model gives us an opportunity to predict PRS characteristics with good accuracy.

However, it is difficult to increase the compression ratio ε to more than 14 with the help of one-stage ejector. In the case of COIL PRS, compression ratio ε ranges from 30 to 40. In this case, it is possible to use the multistage ejectors. The same EJs are used for aerodynamic wind tunnels with big Mach numbers in test section. However, debugging of multistage ejectors—to make system operate on calculated parameters—is difficult. Besides, these multistage systems are very inept. Therefore, it is very difficult to use in mobile systems.

The schemes, which realize the principle of operations, are known as differential EJ [16]. Two types of such EJs are shown in Figure 2.96 from [17,18]. Mixing process is adjusted by geometrical sizes of slits and layout of nozzles, providing the effective mixing of low- and high-pressure streams. Differential EJ is used for aerodynamic wind tunnels with big Mach numbers. It is used because of such EJ help achieve the big compression ratio (~300 in the absence of passive gas). The three-dimensional picture of flow in mixing chamber of slit EJ is shown in Figure 2.97. The results of three-dimensional visualization explains the operation mechanism of slit EJ. Effluent jets from slits are accelerated to big Mach numbers by turning the stream. If the main nozzle is kept to Mach numbers less than 4, then Mach numbers in jets are increased upto 7. This provides the reach of big compression ratio ε.

However, differential EJ yields to multistage systems from the view of ejection coefficient. Today, the main task for differential EJ is achievement of the coefficient of ejection which is close to ejection coefficient of multistage systems. The differential schemes use the devices (head, nozzle system etc.) that intensify the process of mixing. Besides the schemes shown in Figure 2.96, it can be seen that more schemes that are effective are also possible. The main task in this case is not to make the big pressure losses in active gas stream at using such devices. Then it is possible to obtain the ejection coefficients, which are tolerant for PRS.

2.6.4 Vapor-Gas Generator

The efficiency of ejector use is determined by high specific power parameters of the ejecting gas: pressure and temperature at a low molecular mass. Modern gas generators working on combustion products of different kinds of fuel yield high-temperature gas with almost unlimited volume. The efficiency of vapor-gas generators (VGG) increases with pressure and

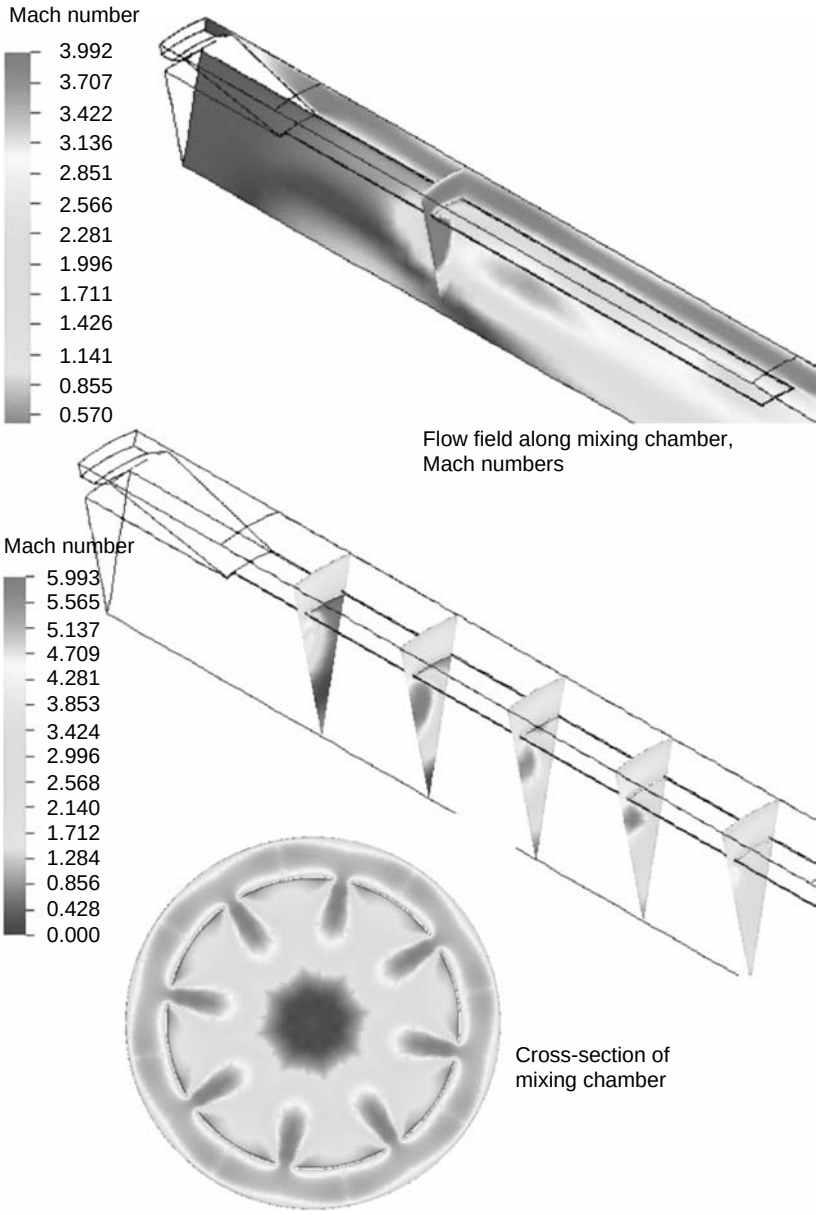

FIGURE 2.97 Numerical results of flow picture in mixing chamber of slot ejector.

temperature of combustion products. Usually these parameters reach the level of 100 atm and 2000–2500 K. The list of possible fuel components for vapor-gas generators is given.

Use of liquid components seems to be attractive for reduction of mass and sizes of the entire system, but they might be toxic and bring some additional engineering demands. Therefore, we have to consider not only on the energy characteristics of fuels, but also on the aspects of convenience, storage, availability, and safety.

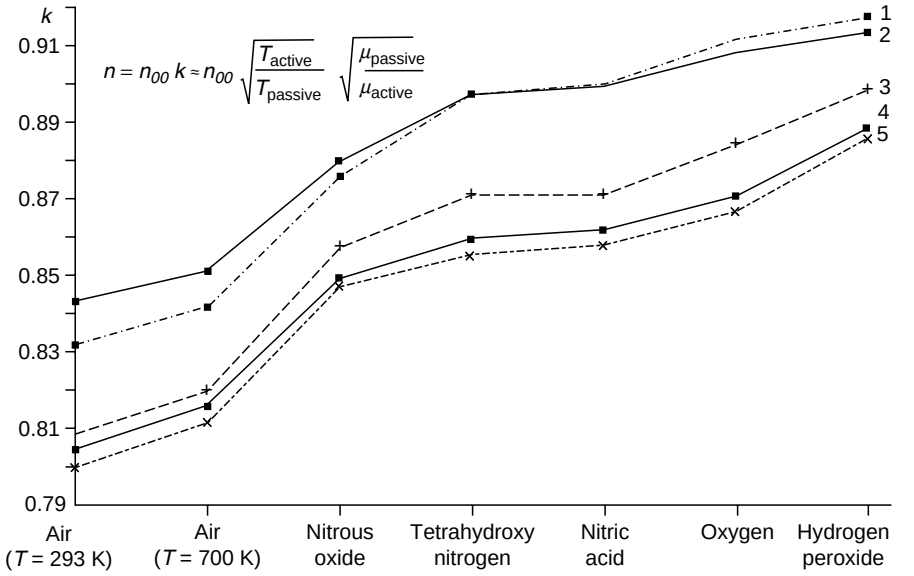

FIGURE 2.98 Effect of fuel choice on the ejection coefficient. 1—hydrazine, 2—ammonia, 3—methane, 4—ethyl alcohol, 5—kerosene. $T = 1100$ K.

Fuel Ethyl alcohol (C_2H_5OH), methyl alcohol (CH_3OH), kerosene, hydrazine (N_2H_4), methane (CH_4), ammonia (NH_3), benzene (C_6H_6)

Oxidizer Air, hot air ($T = 700$ K), oxygen (O_2), hydrogen peroxide (H_2O_2), nitrous oxide (N_2O), tetrahydroxy nitrogen (N_2O_4), nitric acid (HNO_3)

The estimates of the effect of fuel and oxidizer on the ejection coefficient are plotted in Figure 2.98. As for the thermodynamic efficiency, kerosene, ethyl alcohol, and methyl alcohol are very close. The type of oxidizer has more influence on the result. The highest effect is achieved with tetrahydroxy nitrogen and nitrous oxide, but they are toxic. That is why the most promising is the use of hydrogen peroxide H_2O_2. The operation of gas generators with this oxidizer faces certain difficulties, but today, the improved technologies and experience in operation with these gas generators are seen.

There are some limitations on the pressure and temperature of combustion products of VGG, that depend mainly on the materials used for making the gas-dynamic track. It is inexpedient to cool the wide surfaces of a large-scale construction. Therefore, the temperature of the ejecting gas must be limited to 900–1000 K. But, the use of modern materials may provide a reliable operation of PRS at gas temperature upto 1300–1400 K, making additional increase in the ejection coefficient by 20%. Moreover, this increases the limits of water vapor condensation in the ejector nozzle, so the pressure of the ejecting gas may also increase together with the Mach number. This gives us an opportunity to increase the ejector efficiency by 300%–50%. The required temperature of the ejecting gas is achieved by diluting the combustion products with water. This makes the molecular mass of the mixture lower and the ejection coefficient higher.

2.6.5 Heat Exchanger

The meaning of heat-exchanger application is as follows. Under conditions of varying ejecting and ejected media with different temperatures, the ejection coefficient can be presented as [19]:

$n = n_{00}\sqrt{\frac{T_{act}}{T_{pas}}}\frac{\mu_{pas}}{\mu_{act}}$, where n_{00} is the ejection coefficient under conditions of similar temperatures and compositions of active and passive gases, T is the temperature, and μ is the molar mass, n_{00} is a function, which depends on pressures and ejector's geometry, that is, perfection of gas-dynamic channel of ejector. Therefore, by decreasing the temperature of a passive gas, we can reduce demands for the ejector by consuming a required active gas (or increase the compression degree at a constant ejection coefficient). The effect of decreasing temperature is more than effect of decreasing stagnation pressure in gas because of friction. Therefore, the task of heat-exchanger is creation of a framework. The result of using a heat-exchanger is an increased ejection coefficient in the system. That is, effect of decreasing temperature is more than effect of decreasing n_{00} because of stagnation pressure losses in gas.

This is multiparameter optimization task. The result depends on a number of parameters: layout of cooling elements, its materials, material, size of edges, etc. This task is of engineering type that can be solved.

2.6.6 Problem of Operation of Laser with PRS

Starting conditions of laser with PRS is discussed [1,20] from the viewpoint of gas dynamics (general condition is coordination of SD and EJ characteristics). Let us recall that laser channels distinguish from traditional gas dynamic channels such as, aerodynamic wind tunnel channels. In Figure 2.99 the view of powerful laser with PRS is shown. Some details of starting conditions of such system are discussed.

2.6.6.1 Necessary Conditions for PRS Start

After SD and EJ work has been examined separately, it was possible to determine a condition of their coordination characteristics that would ensure starting of a whole PRS. It is clear that PRS will work if pressure after SD under a definite load is higher than pressure provided by ejector before the ejector's entrance in case of the same load.

The type of ejector and SD characteristics are shown in Figure 2.100. A dependence of pressure P_{02} before ejector on mass flow rate of passive flow G_2 is indicated here. P_{02} is value inversed to compression index of flow. G_2 is a value proportional to ejection coefficient. A hysteresis exists for EJ with a converging chamber, just as for SD with constriction: there is a starting characteristic, that is, a minimal pressure in prechamber of EJ nozzle (as well as in

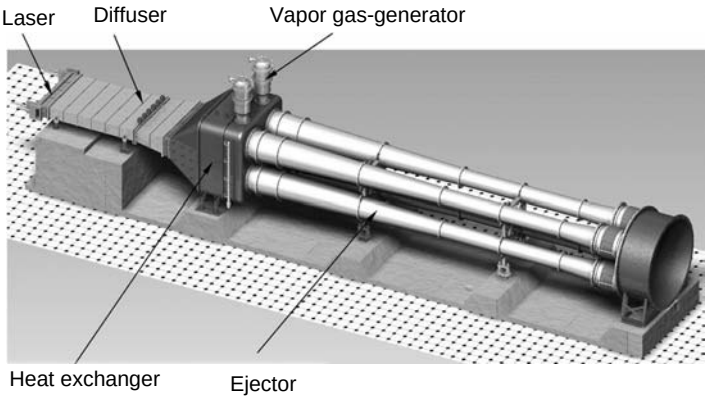

FIGURE 2.99 General view of PRS for powerful laser.

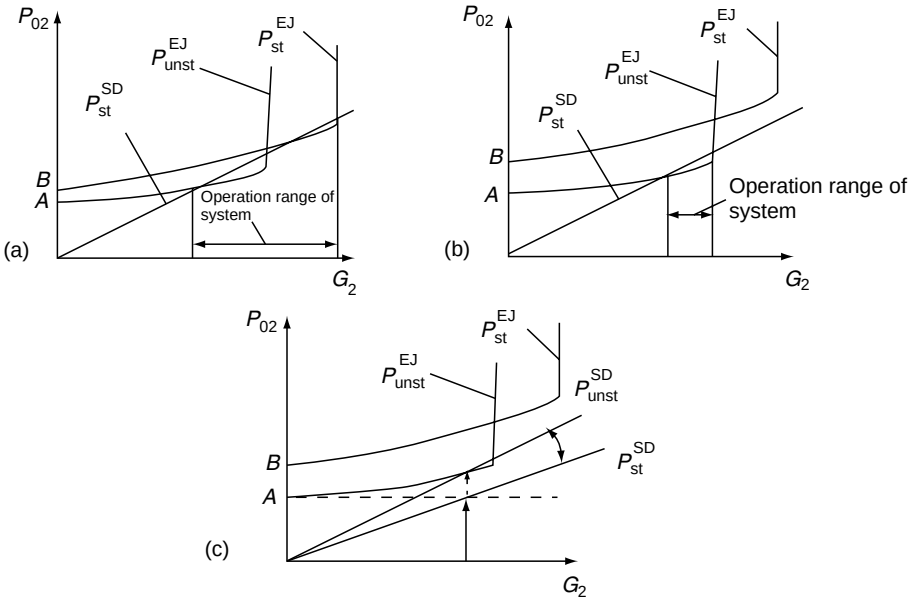

FIGURE 2.100 Conditions of PRS start: different variants of coordination of diffuser and ejector characteristics.

gas generator chamber) under which a nozzle and a whole channel of ejector are started. After the channel is started, pressure in prechamber can be reduced to a value P_{unstart}, where, $P_{\text{start}} > P_{\text{unstart}}$. Under the condition when $P_0 = P_{\text{unstart}}$, a general level of pressure of PRS channel is lower, but a working area of EJ at a load is reduced.

The starting characteristic of SD—a dependence of pressure after SD on a mass flow rate—is also shown here. This dependence is linear and a slope angle depends on Mach number of a flow at PRS inlet. PRS starts when EJ and SD characteristics curves are intersected. Yet, different variants are possible here. In the situation indicated in Figure 2.100a, laser can start to work at the starting characteristic and range of its work throughout mass' flow rates can be changed widely (with appropriate change of P_0). As for the situation in Figure 2.100b, range of laser's work is much narrower. Besides, a gas-generator work sequence should be dual-mode in this case. At first, short-term mode with $P_0 = P_{\text{start}}$ executes at which a whole EJ channel starts, and after this, a gas generator moves to fore-unstart (fore-breaking) mode with $P_0 = P_{\text{unstart}}$ at which laser starts with appropriate mass' flow rate. The more efficient mode is EJ work at fore-breaking characteristic.

The location of points A and B in the diagrams is determined by performance parameters of EJ and by Mach number of ejecting flows. Generally, the higher Mach numbers allow to reach the more high depression range and to get the more high ejection factor at a working mode of PRS. But then, it is necessary to have more high pressures in prechamber of EJ nozzle in the gas generator.

In the figures (a) and (b) variants of starting terms, when SD and EJ are connected practically in direct way (see Figure 2.87), have been examined. In such a connection, it is possible to examine a starting characteristic of SD only. Yet, a PRS channel for laser system with large mass' flow rate is made in another way. An ejector station that is connected to laser's diffuser through a large vacuum tank is used here (see on Figure 2.99). For such a channel, the situation indicated in figure (c) can be realized. At the first moment of laser start,

pressure in tank will not follow an ejector characteristic immediately (more the volume, more slow the pressure gets changed: this characteristic can be calculated); it will stay nearly at points' A or B level, that is, the pressure level on SD's outlet will be lower than in case of (a) and (b). And if SD starting characteristic crosses this level of pressure than at the first moment, PRS starts and later on a flow mode in SD will be changing accordingly to pressure changes on SD's outlet until it moves at unstarting characteristic. If SD unstarting characteristic crosses EJ characteristic, then working mode of PRS is saved. This scheme of work is most advantageous as demand to ejector on a flow compression degree and mass' flow rates of ejecting gas are decreasing.

A distinction value between SD's starting and unstarting characteristics depends on a rate of channel section constriction in SD. Therefore, it is very important to define the maximum possible value (S/S*) of SD constriction. This does not mean that work of channel with vacuum tank is more advantageous than in the case of line scheme at direct connection of SD to EJ. At line scheme, energy of passive flow is used though it is not very high (ejection factor $n < 0.1$). In the second case, energy of passive flow is not used and the flow is stopped completely. Moreover, additional losses by friction appear and channel starts to be more complicated. All these are qualitative arguments; quantitative characteristics are to be defined separately for every parameter of the flow. In the line scheme, PRS works at starting characteristic of SD and in the case of vacuum, it can work at unstarting characteristic of SD. This can be realized only at definite conditions. The important parameter for such a mode realization is speed of laser start.

2.6.6.2 Start of Complex Channel

Aerodynamics usually examines a case of start of mononozzle in smooth simple channel (nozzle contour is continued by channel's walls; the channel itself, as a rule, is axisymmetric; windows are flush-mounted with walls; constriction in diffuser is made due to curve of channel walls). Character of start of multinozzle bank differs from traditional aerodynamics noticeably. Distinctions are especially sizeable when it is a question of start of large bank in channels of complex shape, such as channel of supersonic chemical laser. Distinctions become noticeable for large nozzle banks in particular, whereas in small model sets, they can be insensibly (it happens due to influence of scale factor usually mentioned about during large systems design and development).

Many factors have influenced the type of start of multinozzle bank in laser channel. First, it is the character of flow establishing in rectangular channels that leads to forming of separation zones along narrow sides while starting. Then, it is the fact that in any laser a multinozzle bank is set in channel with some ledge. In Figure 2.101, laser channel (complex channel) is shown. In chemical laser except for such ledges, there are large base areas of nozzle bank itself. Laser chamber, that usually has a divergency (divergence), is beginning with resonator cavities. Resonator cavities have especially strong influence on type of stream as they define stream in the extreme channels of diffuser. In supersonic lasers, as a rule, multisectional diffusers—wide rectangular channel divided to parts by pylons—are used. This allows shortening of physical length of diffuser. Necessary degree of constriction of diffuser's throat is achieved by selection of pylons of definite thickness.

All these are necessary and unavoidable peculiarities of structure of gas-dynamic section of laser. And, evenly these peculiarities lead to the fact that strength in complicated channel during gas flow is more than in plain channel. Except increasing of frictional strength (due to more developed surface of walls), an additional shock-wave strength arises (in spite of aerodynamic shape of pylons due their opposite to supersonic flow standing during streamline, a shock-wave structure appears). That is why for gas flow in channels with constriction

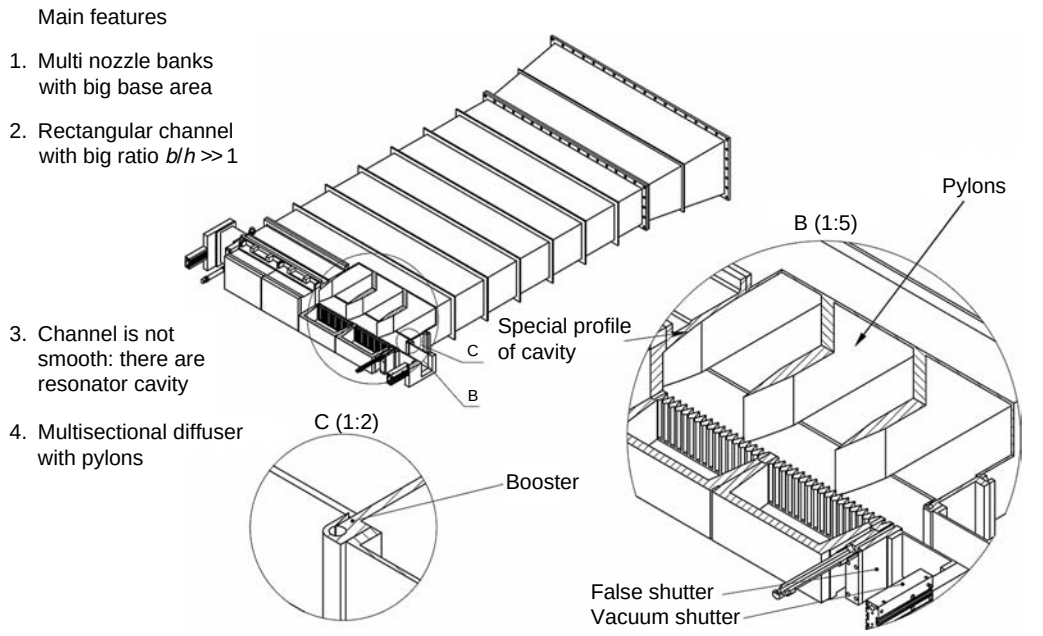

FIGURE 2.101 Scheme of laser channel of powerful chemical laser.

especially in complicated channels, effect of hysteresis appears, that is, pressure of channel starting is larger than pressure at which supersonic flow is breaking (unstarting). Here, a starting type of complicated channel becomes different from aerodynamic channel starting (Figure 2.102).

In smooth channel, a flow comes to its calculated value practically at once, when pressure in prechamber reaches the determined value. And, in aerodynamic experiments, a moment of start is usually recorded according to abrupt drop of static pressure in working section

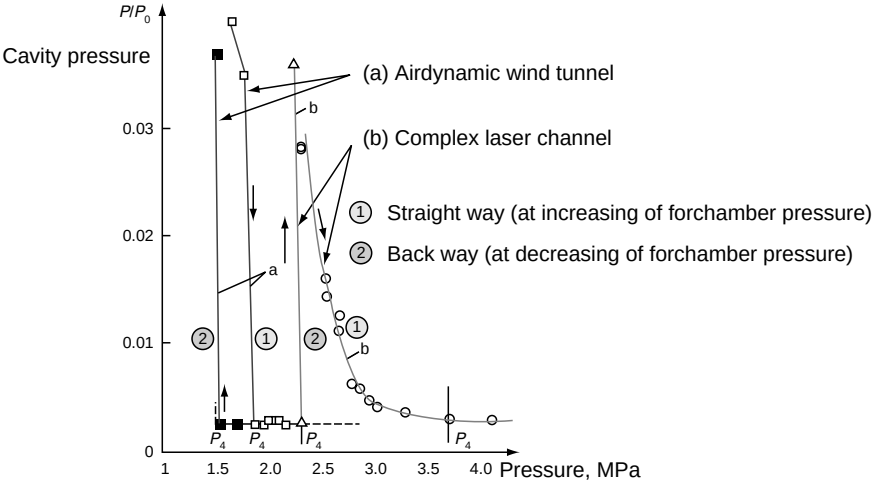

FIGURE 2.102 Comparison of character of start and unstart processes in case of laser channels and wind tunnel channels.

(curve 1a), but in case of complicated channel it happens in another way. Complicated channel needs several stages to start. Formally, at initial drop of pressure in working section it is possible to consider diffuser to be started (curve 1b primary points): pressure in resonator cavity (speaking about laser) dropped; there is process of pseudoshock in diffuser with supersonic flow before it. However, the initial drop of pressure does not mean the final start as the pressure in resonator cavity at this moment, as a rule, does not reach a calculated value, that is, calculated mode; in other words a channel is understarted (curve 1b primary points).

At that, difference of pressure in cavity from calculated value cannot be very sizeable and is quite allowable for aerodynamics' aims (Mach numbers will be different in very little value). But, as long as laser is a resonance system, such difference has very negative effect on working process in laser. It leads to decrease of radiating power as experiments prove.

Understarted state is stable and if necessary a further increase in either pressure in the prechamber of the nozzle bank (Figure 2.103) or increasing of the ejector productivity is demanded (if it is the start of laser channel with ejector pressure recovery system), or the operational sequence of the whole system should be modified. A process of coming to calculated mode of flow in resonator cavity of DF-laser that works with PRS is shown in Figure 2.103 as a practical example (pressure distribution comes to its minimal values in accordance with the gradual growth of mass flow—growth of mass flow rate means the appropriate growth of pressure in the prechamber).

Achievement of a calculated pressure in resonator cavity at a little understart is possible by making some impulse disturbance at diffuser entry by means of low-sized special blowing nozzles.

Single-valued flow type is established in smooth channel with mono nozzle at once and it is realized practically at the same drop of pressure over all the experiments. A process of stream establishment in complicated channel is dissimilar, it has different stages and the start itself is realized at different drops and, as experiments prove, depends even on way character of pressure running to operate mode value. This is caused due to hollows and ledges, where differing types of stable flow can be realized at different way characters (abrupt, slowed, step-like etc) of pressure runs to operating mode. Although the start pressure of a complicated

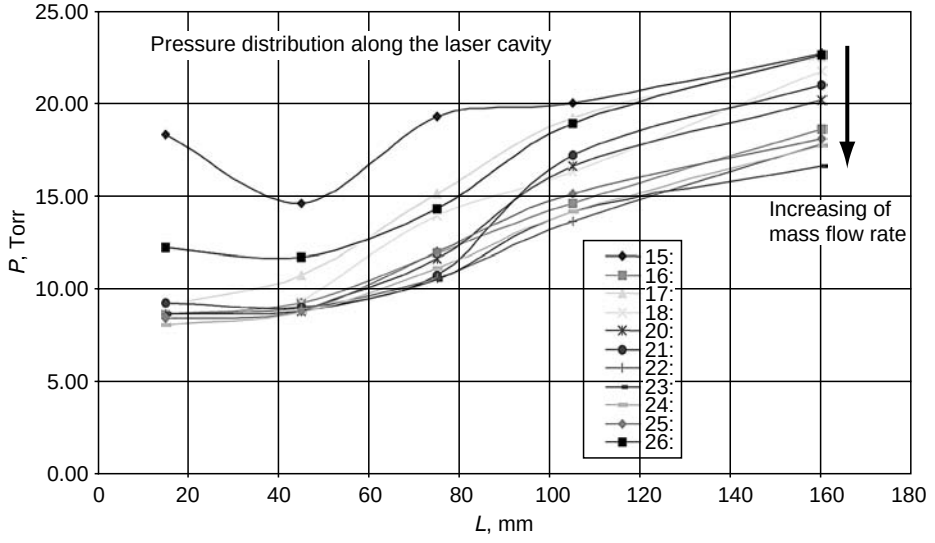

FIGURE 2.103 Changing of static pressure distribution in DF-laser channel at increasing of mass flow rate of laser.

channel (multinozzle device and irregular shaped channel) could not be differed too much (≈10%–15%) at various starts in different ways in the character of pressure running to the mode there is always ambiguity, as the experiments show. That is why the starting characteristics (for example, dependence of the diffuser start pressure on the channel constriction degree or on the diffuser length) is the field of points in the area of integrating curve but it is not a strict curve, that is, it is impossible to obtain the absolutely repeatability of results.

Interestingly, stall characteristics are more stable in this sense: points are plotted with much lesser scattering. It is clear from the standpoint of qualitative factor. If starting is determined by conditions of flow arising in the channel before diffuser, that is, in complicated channels with resonator cavities where different variants of flowing could be realized, then the stall is determined by conditions in the diffuser throat—in a more simple channel where conditions for the flowing stall are more specific. During starting, the structure of shocks is forced through the channel according to increasing prechamber pressure. During stall, the inverse process is realized: the shocks gradually creep back into the channel according to decreasing prechamber pressure till the moment of full stall of supersonic flow in the laser chamber.

The data for the large-scale GDL (exhaust is realized by a diffuser directly into atmosphere) are presented in Figure 2.104; the data illustrate effect of way character of pressure running to operating mode value on laser channel starting. The character by prechamber pressure decisively influences on the flow regime setting in resonator cavity. In the case of abruptly coming to the mode (blue curve) the pressure in resonator cavity is noticeably higher and it has not come to the expected level. In case of stepped start static pressure in cavity reach the expected level. Gain coefficient is changed correspondingly in these two modes: at abrupt starting, the gain coefficient slowly (like the resonator cavity pressure) reaches its maximum value because of understarting. The absolute values of gain coefficients are not considered (they are different because of various composition of working mixtures), that is, the behavior pattern of the gain coefficients. It is clear that the laser strongly loses power by slowly coming to the mode.

If character of coming to the working mode by the prechamber pressure influences flow setting in the channel then the character of changing backpressure after diffuser influences the starting process too (as it is realized in the ejector PRS). Starting as a whole is determined by the pressure drop at inlet and outlet of the channel; therefore these two factors (increasing of pressure in prechamber and decreasing of pressure at the diffuser outlet) are equivalent.

That is why the starting of nozzle bank and starting of diffuser should not be considered separately in our case (multinozzle bank + irregular shape channel) as it is realized in traditional gas dynamics where these processes are unambiguous enough. It is necessary to consider the flow setting along the channel as a whole, that is, with time (including nonstationary effects). So it is necessary to consider all elements of the channel including the vacuum tank before the ejector station. It is necessary to consider the ejector operation under loading, course of the changing vacuum tank pressure, that is, considering the evacuation rate of this tank by determining its volume. It determines the character of backpressure behavior after the diffuser and its starting consequently. Initial pressure in the tank and the changing tank pressure during simultaneous operation of laser and ejector determine the sequence of whole installation (more detailed information is presented in the next part).

At the same time it is necessary take into account that the starting of big diffuser (for installation with big mass flow rate) is more complicated than starting of small models. Difference of characteristics from the theoretical estimations is more, that is, there is the scale factor effect. All could not be simulated on the small installations: the channel division is different for the channel with big ratio of sides; all that was permissible for the small installation channel could not be realized on the large-scale one. Total pressure losses are huge. It is connected with the fact that the absolute dimension is used in the processes of viscous interaction at laminar flow transferring to turbulent one.

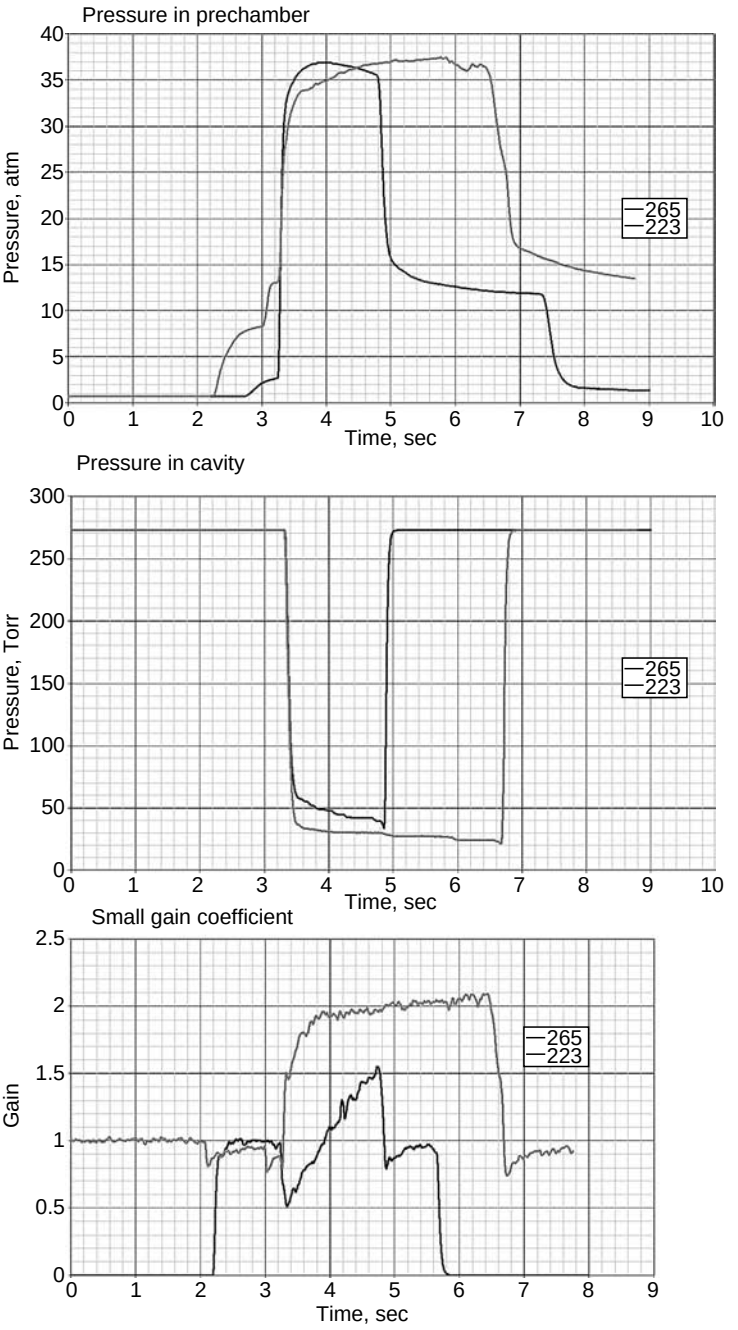

FIGURE 2.104 Behavior of main operation parameters of CO_2-GDL: case of two variants of start regimes.

It is clear from the above statement that solution of the starting problem of irregular shape channel demands consideration of all features: flow in rectangular section channel with big ratio of sides, pylons in the channel; the flow in deep cavities; the flow behind edges; the flow at the bottom of multinozzle devices. As a rule, these cases are considered separately (as the stationary variant) in aerodynamics; but it is necessary to consider all the effects simultaneously

with time, that is, the time-dependent variant in our case (analyzing of starting of the chemical laser channel). It is clear that it is not simple and the detailed consideration of all effects is possible only on the base of calculations using the transient equations of Navier—Stokes.

2.6.6.3 Some Technical Problems in Operation of Lasers with PRS

Besides the gas-dynamic problems (that had been examined in previous section), technical problems of operation of laser with PRS also exist. For example, the task about switch-off VGG and correspondingly the stalling of EJ from operation mode. If some actions are not made, at the switching off gas-generator the back suction of combustion products (CP) to laser cavity arises with big velocity, where CP contain water and soot. If this task is solved easily, then problem of vibrations influence, appearing at VGG operation, demands some efforts.

Turbulent flow in the vapor-gas generator causes strong vibrations of the entire installation frame: high-frequency oscillations (~10^3 Hz) and the low-frequency oscillations (10^1–10^2 Hz). The pressure oscillations inside the VGG combustion chamber lead to the disturbing forces acting on the PRS and the laser installation as a whole.

These forces induce the set of oscillating modes of the laser system as a whole and particularly the resonator mirrors. Such vibration leads to deflection of the optical axis of radiation. Therefore investigation of the magnitude and frequency spectrum of such oscillations has great impact in the integration design of laser with PRS. Some data on these vibrations gotten on laboratory for DF laser with PRS based on the one-stage ejector [20] are shown in Figure 2.105. Vibration sensors (piezo-accelerometers) have been installed on the VGG and on the optical resonator.

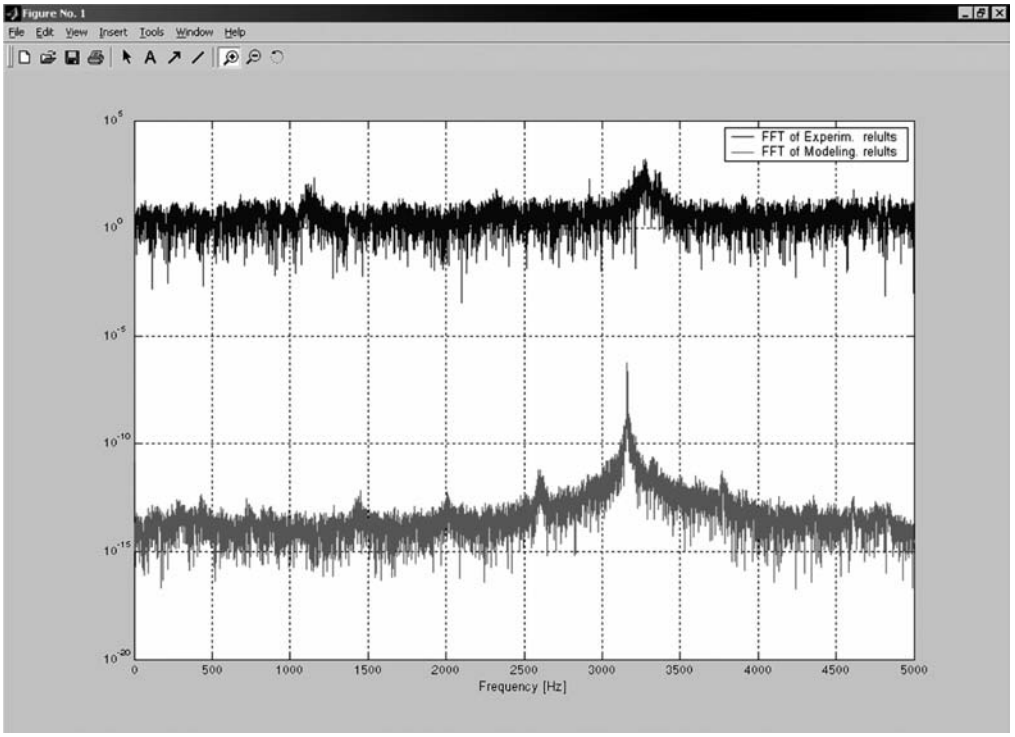

FIGURE 2.105 Spectra of the vibration acceleration; 1—VGG (upper curve), 2—laser resonator (lower curve).

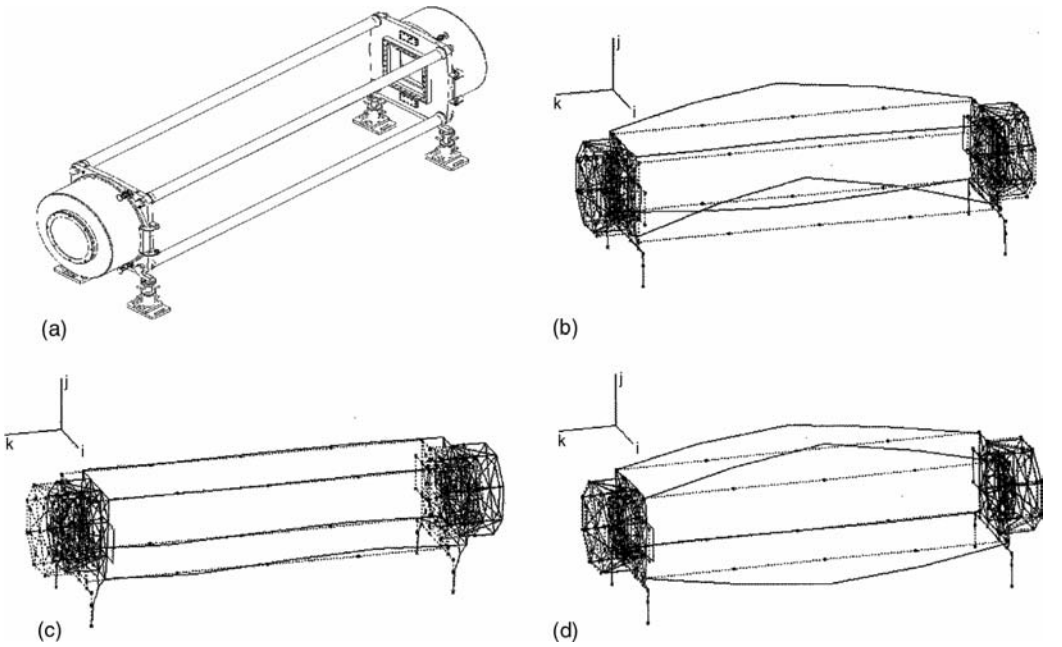

FIGURE 2.106 Laser resonator: (a)—layout; (b–d)—oscillation modes.

Discrete spectral components caused by high-frequency and low-frequency pressure oscillations in VGG combustion chamber are clearly visible against the wide-band background.

Analysis of the mode composition of the resonator vibrations is shown in Figure 2.106. The most powerful modes are related to oscillations of the two resonator assemblies as a whole relative to each other. Time dependencies of the oscillating angle of the resonator mirror at the typical shock action are given in Figure 2.107. Natural frequencies are about 300 Hz, magnitude is about a few angular seconds. It means the low-frequency pressure oscillations have greatest importance at the integration of the laser with PRS.

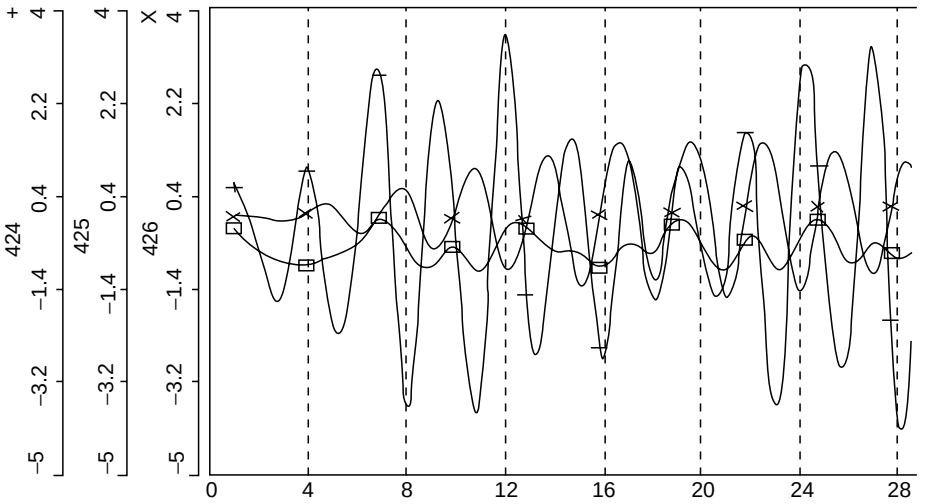

FIGURE 2.107 Oscillating angles of the resonator mirrors under the typical shock force.

Numerical simulation of the forced oscillations let us to find design solution to decrease the influence of these vibrations. One of the typical Matlab models is shown in Figure 2.108 intended for the analysis of the resonator vibrations under the action of the experimentally measured vibration disturbances. Models of such kind allow selecting natural frequencies and study the damping efficiency.

Besides vibrations related to the PRS operation the problem of carrier vibrations exists for mobile system. This problem becomes more serious in case of aviation carriers. Passive damping tools are effective for high frequencies—more than 10^3 Hz—particularly for distributed systems. Active tip-tilt mirrors with closed-loop frequencies from 300 to 500 Hz are necessary for low-frequency vibrations compensation.

Let us consider briefly the problem of carrier selection. Technical specifications define the intensity in the central spot in far field. The intensity depends on many parameters:

$$I = I(P_{\mathrm{W}},\lambda,D,L,T_{\mathrm{atm}},C_{\mathrm{n}^2},\beta,\ \mathrm{Location},\ \mathrm{H,h},\ldots),$$

where P_{w} is the laser power, λ, D the wavelength and output aperture diameter, defining the diffraction limit of the divergence, L the operating distance, T_{atm} the atmospheric attenuation (molecular and aerosol), and C_{n^2} is the structural constant of the atmospheric turbulence. Climatic condition (denoted by Location), elevation angle β, as well as height of the target (H) and the carrier (h) influence the final spot intensity strongly.

The main goal of such analysis is to calculate the required laser power. The power defines flow rate of laser medium as well as flow rate of PRS ejecting gas. Consequently, the size and weight of the whole laser installation can be calculated. Finally, parameters of the carrier became clear. Minimization of weight and size became the main problem during

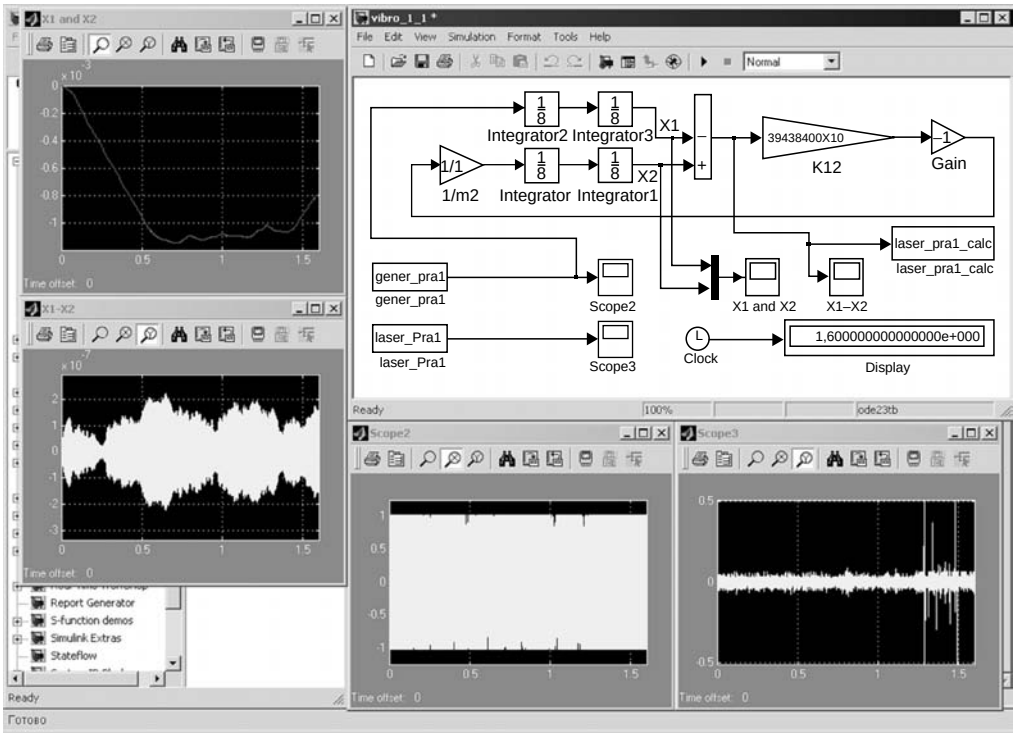

FIGURE 2.108 A Matlab model for simulation of the resonator oscillations.

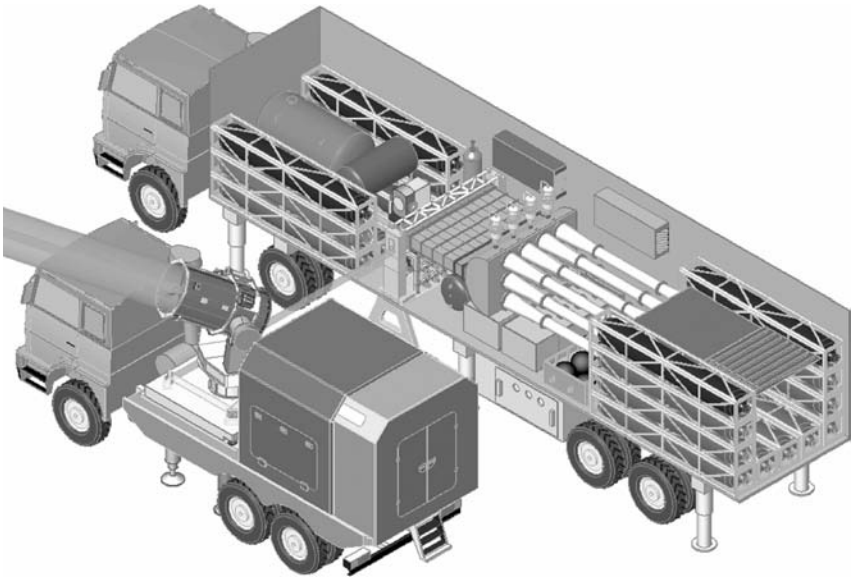

FIGURE 2.109 (**See color insert following page 336**.) Mobile DF-laser complex.

the integration of the HPSCL on mobile carrier. The typical integrated design of the mobile DF-laser complex is shown in Figure 2.109. The tracking/pointing system is located on the separate track and the whole complex consists of two tracks.

Another integrated one-track laser complex is shown in Figure 2.110. It is clear in that case, that vibro-insulation of tracking system from PRS is very severe in case of laser operating with PRS. Such kind of integrated design is suitable. In Figure 2.110 multifunctional laser sounding system (lidar) consisting of eight transmitting-receiving laser channels is shown. However, most of the problems of laser system's integration with mobile platform are general.

FIGURE 2.110 Mobile one-track laser system.

Such example is very interesting because the tracking system is based on the fixed focusing telescope and flat-mirror scanner. The layout of such type is most attractive for moderate apertures (<0.5 m) and operating distances less than 6 km (<5–6 km).

REFERENCES

2.1 CW Supersonic Gas Lasers

1. Daffner, R.F., Airborne Laser, *Bullets of Light*, Plenum Press, NY, 1997.
2. Shwartz, J., Wilson, G.T., Avidor, J., Tactical High Energy Laser. SPIE Proceeding, Vol. 4632, 2002.
3. Koop, G., et al., Airborne laser flight-weighted laser module (FLM) and COIL modeling support. American Institute of Aeronautics and Astronautics, paper No. 2000-2421, 2000.
4. Losev, S.A., *Gas Dynamic Lasers*. Moscow Publisher: Nauka, 1977 (Russia).
5. Anderson, G., *Gasdynamic Lasers: An Introduction*. Academic Press, NY, 1976.
6. Russel, D.A., Gasdynamic lasers. *Astronautics & Aeronautics*, 1975, Vol. 13, No. 6, pp. 50–55.
7. Warren, W.R., Chemical lasers. *Astronautics & Aeronautics*, April, 1975, Vol. 13, p. 36.
8. Bashkin, A.S., Igoshin, V.I., Nikitin., A.I., Oraevsky, A.N., Chemical lasers. *Science and Technology Results Radio Technology Series*, Vol. 8, Moscow Publisher: VINITI, 1975 (Russia).
9. Ratliff, A.W., McDanal, A.J., Kurzius, S.C., ZMartin, W.D., Power and pressure recovery analysis of chemical laser devices. American Institute of Aeronautics and Astronautics, paper, No. 75-721, 1975.
10. Boreisho, A.S., Malkov, V.M., Savin, A.V., et al., Pressure recovery system for high-power gas and chemical laser. *Journal of Thermophysics and Aerodynamics*, 2001, Vol. 8, No. 4, pp. 571–587 (Russian).
11. Yuryshev, N.N., Oxygen–Iodine laser with chemical pumping. *Quantum Electronics*, Vol. 23, No. 7, 1996 (Russian).
12. Vetrovec, J., Chemical oxygen–iodine laser with a cryosorption pump. Proceedings of SPIE, 2000, Vol. 3931, p. 60.

2.2 Flow Structure in the Laser Cavity After MNB

1. Russel, D.A., Fluid mechanics of power grid nozzle lasers. American Institute of Aeronautics and Astronautics, paper No. 74-223, NY, 1974.
2. Russel, D.A., Neice, S.E., Rose, P.H., Screen nozzles for gasdynamic lasers. *American Institute of Aeronautics and Astronautics Journal*, 1975, Vol. 13, No. 5, pp. 593–599.
3. Vaidyanathan, T.S. Russel, D.A., Wave-generated disturbance downstream of nozzle array. *American Institute of Aeronautics and Astronautics Journal*, 1985, Vol. 23, No. 5, pp. 749–751.
4. Russel, D.A., Neice, S.E., Rose, P.H., Screen nozzles for gasdynamic lasers. American Institute of Aeronautics and Astronautics, paper No. 74-549, NY, 1974.
5. Malkov, V.M., Ktalherman, M.G., Klimchik, G.V., Ruban, N.A., Flow characteristics behind the supersonic blade nozzle bank. Siberian Branch Academy of Science USSR, Institute of Theoretical and Applied Mechanics (ITAM), Report No. 2090, Novosibirsk, 1991 (Russian).
6. Demetriades, A., Linearized theory of gas-dynamic laser nozzle wakes and applications. Aeronautronic Publication. No U–6276: Ford Aerospace & Communication Corp., Calif., October 1976.
7. Chang, P.K., Separation of Flow. Pergamon Press, 1970.
8. Wignanski, I., Champagne, F., Marasly, B., On the large-scale structures in two-dimensional, small deficit, turbulent wakes. *Journal of Fluid Mechanics*, 1986, Vol. 168, pp. 31–71.
9. Demetriades, A., Turbulent mean flow measurements in two-dimensional supersonic wake. *Physics of Fluids*, 1969, Vol. 12, No. 1, pp. 24–32.
10. Bonnet, J.P., Jayaraman, V., de Roquefort, T.A., Structure of a high Reynolds–number turbulent wake in supersonic flow. *Journal of Fluid Mechanics*, 1984, Vol. 143, pp. 277–304.

11. Ramaprian, B.R., Patel, V.C., Sastry, M.S., The symmetric turbulent wake of flat plate. *American Institute of Aeronautics and Astronautics Journal*, 1982, Vol. 20, No. 9, pp. 1228.
12. Chevray, R., Kovasznay, L.S.G., Turbulence measurements in the wake of a thin flat plate. *American Institute of Aeronautics and Astronautics Journal*, 1969, Vol. 7, pp. 1641–1643.
13. Andreopoulos, J., Bradshaw, P., Measurements of interacting turbulent shear layers in the near wake of a flat plate. *Journal of Fluid Mechanics*, 1980, Vol. 100, pp. 639–668.
14. Bonnet, J.P., Delville, J., Garem, H., Space and space–time longitudinal velocity correlations in turbulent far wake of flat plate in incompressible flow. *Experiments in Fluids*, 1986, Vol. 4, No. 4, p. 189.
15. Townsend, A.A., *The Structure of a Transverse Shear Turbulent Flow*. Moscow. IL, 1959.
16. Demetriades, A., Turbulent measurements in an axisymmetric compressible wake. *Physics of Fluids*, 1968, Vol. 11, No. 9, p. 1841.
17. Demetriades, A., Observations on the transition process of two-dimensional supersonic wake. *American Institute of Aeronautics and Astronautics Journal*, 1971, Vol. 9, No. 11, pp. 2128–2134.
18. Pirumov, U.G. Roslyakov, G.S., *Gas Flow in Nozzles*. Moscow, Publishers—Moscow State University, 1978 (Russian).
19. Ktalherman, M.G., Malkov, V.M., Ruban, N.A., Slow down of supersonic flow in a rectangular channel of constant cross-section. *Journal of Applied Mechanics and Technical Physics*, 1984, Vol. 28, No. 6, pp. 48–57 (Russian).
20. Neumann, E.P., Lustwerk, F., Supersonic diffusers for wind tunnels. *Journal of Applied Mechanics,* 1949, Vol. 16, No. 2, pp. 195–202.
21. Anikin, M.A., Ktalherman, M.G., Malkov, V.M., Sinitzin, A.P., Flow parameters relation to an individual nozzle expansion angle. Gas dynamics of GDL's flowing channel. Proceedings of Siberian Branch Academy of Science USSR, Institute of Theoretical and Applied Mechanics (ITAM), Novosibirsk, 1987 (Russian).
22. Baev, V.K., Ktalherman, M.G., Malkov, V.M., Ruban, N.A., Flow characteristics and pressure recovery in a rectangular channel behind an axisymmetric nozzle screen. Gas dynamics of flow in nozzles and diffusers. Proceedings of Siberian Branch Academy of Science USSR, Institute of Theoretical and Applied Mechanics (ITAM). Novosibirsk, 1982, pp. 25–40 (Russian).
23. Malkov, V.M., Ktalkherman, M.G., Ruban, N.A., Influence of flow structure on optical gain in gasdynamic lasers. *Progress in Astronautics*, Vol. 88, Flames, Lasers, Reactive Systems. NY, AIAA, 1983.
24. Malkov, V.M., Ktalkherman, M.G., Shevyrin, A.V., Sheitelman, G.Y., Nozzle dimension and contour expansion parameters impact upon gain in a GDL upon combustion products of liquid hydrocarbon fuels. *Journal of Physics of Combustion and Explosion*, 1979, Vol. 15, No. 6, pp. 64–76 (Russian).
25. Losev, S.A., *Gas Dynamic Lasers*. Moscow Publisher: Nauka, 1977 (Russian).
26. Ktalkherman, M.G., Malkov, V.M., Ruban, N.A., Pseudo shock in a rectangular channel of constant cross-section. Gas dynamics of flow in nozzles and diffusers. Proceedings of Siberian Branch Academy of Science USSR, Institute of Theoretical and Applied Mechanics (ITAM) Novosibirsk, 1982, pp. 125–155 (Russian).
27. Abramovitch, G.N., Applied Gas Dynamics. Moscow Publisher: Nauka, 1969 (Russian).
28. Panherst, R., Holder, D., Experimental Procedure in Aerodynamic Tunnels. Moscow Publisher: Foreign Literature, 1955 (Russian).
29. Cronvich, L.L., Faro, I.D.V. Handbook of Supersonic Aerodynamics. Section 17. Ducts, Nozzles and Diffusers. NAVWEPS Report 1488, Vol. 6, January 1964, pp. 269–305.
30. Zinoviev, V.N., Ktalkherman, M.G., Lebiga, V.A., Malkov, V.M., Mean and pulsation characteristics of a supersonic flow in an aerodynamic tunnel with a screen nozzle. Izvestiya of Siberian Branch Academy of Science USSR (*Journal of News of SB AS USSR*) Series Technical Science. 1989, No. 5, pp. 37–43 (Russian).
31. Zinoviev, V.N., Ktalkherman, M.G., Lebiga, V.A., Malkov, V.M., Supersonic flow in an aerodynamic tunnel behind a screen nozzle. Problems of modeling in aerodynamic tunnels. International seminar papers, Novosibirsk, July 27–29, 1989.

2.3 Optical Quality of Flow in the Laser Cavity After MNB

1. Tatarsky, V.I., Wave Propagation in A Turbulent Environment. Moscow Publisher: Nauka, 1967 (Russian).
2. Chernov, L.A., Wave Propagation in A Medium With Random Non-Uniformities. Moscow Publisher: Academy of Science USSR, 1958 (Russian).
3. Sutton, G.E., Effect of turbulent fluctuations in an optically active fluid medium. *American Institute of Aeronautics and Astronautics Journal*, 1969, Vol. 7, No. 9, pp. 1737–1743.
4. Sutton, G.W., Aero-optical foundations and applications. *American Institute of Aeronautics and Astronautics Journal*, 1985, Vol. 23, No. 10, pp. 1525–1537.
5. Jamper, E.J., Fitzgerald, E.J., Recent advances in aero-optics. *Progress in Aerospace Sciences*, 2001, Vol. 37, pp. 299–339.
6. Russel, D.A., Neice, S.E., Rose, P.H., Screen nozzles for gasdynamic lasers. *American Institute of Aeronautics and Astronautics Journal*, 1975. Vol. 13, No. 5, pp. 593–599.
7. Vaidyanathan, T.S. Russel, D.A., Wave-generated disturbance downstream of nozzle array. *American Institute of Aeronautics and Astronautics Journal*, 1985, Vol. 23, No. 5, pp. 749–751.
8. Russel, D.A., Neice, S.E., Rose, P.H., Screen nozzles for gasdynamic lasers. American Institute of Aeronautics and Astronautics, paper No. 74-549, NY, AIAA, 1974.
9. Cassady, P.E., Newton, J., Rose, P., New mixing gasdynamic lasers. American Institute of Aeronautics and Astronautics, paper No. 76-343, NY, AIAA, 1976.
10. Zelazny, S.W., Chambers, W.A., Van Tassel, W.F., Brandkamp, W.F., Medium inducted phase aberrations in continuous wave hydrogen fluoride chemical lasers. *Wavefront Distortions in Power Optics*. Vol. 293, edited by Fuhs, A. and Fuhs, B., Wash., SPIE, 1981.
11. Parmentier, E.M., Greenberg, R.A., Supersonic flow aerodynamics windows for high-power lasers. *American Institute of Aeronautics and Astronautics Journal*, 1973, Vol. 11, No. 7, pp. 943–950.
12. Gilerson, A.A., Panchenko, V.I., et al., Study of optical properties of free-vortex aerodynamic windows. *Journal of Technical Physics*, 1990, Vol. 60, No. 12, pp. 29–34 (Russian).
13. Guile, R.N., Hilding, W.E., Investigation of a free-vortex aerodynamic window. American Institute of Aeronautics and Astronautics, paper No. 75-122, NY, AIAA, 1975.
14. Malkov, V.M., Trilis, A.V., Savin, A.V., Druzhinin, S.L., One-stage free-vortex aerodynamic window with pressure ratio 100 and atmospheric exhaust. Proceeding of SPIE Vol. 5770, part I, 2004.
15. Laderman, A.J., Motooka, W.D., Barber, D.D., Aero, Optics effects of airborne laser turrets. American Institute of Aeronautics and Astronautics-paper, No. 87-1397, NY, AIAA, 1987.
16. Clark, R.L., Farris, R.C., A numerical method to predict aero-optical performance in hypersonic flight. American Institute of Aeronautics and Astronautics, paper No. 87-1396, NY, AIAA, 1987.
17. Fuhs, A.E., Overview of aero-optical phenomena. *Wavefront Distortions in Power Optics*. Vol. 293, edited by Fuhs, A. and Fuhs, B., Wash., SPIE, 1981.
18. *Aero-Optical Phenomena*. *Progress in Astronautics and Aeronautics*. Vol. 80, edited by Gibert, K.G., Otten, L.J., NY, AIAA, 1982.
19. Kathman, A.D., Brooks, L.S., Kalin, D.A., A time-integrated image model for aero-optics analysis. American Institute of Aeronautics and Astronautics, paper No. 92-2793, NY, AIAA, 1992.
20. Haveren, G., Optical wavefront variance: a study on analytic use today. American Institute of Aeronautics and Astronautics, paper No. 92-0694, NY, AIAA, 1992.
21. Insuik, R.J., Bogdanoff, D.W., Christiansen, W.H., Demonstration of laser phase correction using supersonic gas jets. *American Institute of Aeronautics and Astronautics Journal*, 1982, Vol. 20, No. 10, pp. 1410–1413.
22. Pearson, J.E., Bridges, W.B., et al., Coherent optical adaptive techniques: design and performance of an 18–element visible multidither COAT System. *Applied Optics*, March 1976, Vol. 15, pp. 611–621.
23. Christiansen, W.H., Bruckner, A.P., Fluid mechanical light guide. *Applied Optics*, July 1975, Vol. 14, pp. 1556–1564.
24. Born, M., Wolf, E., *Principal of Optics*. Pergamon Press, 1968.
25. Truman, C.R., Effects of organized turbulence structures on the phase distortion in a coherent optical beam propagating through a turbulent shear flow. *Physics of Fluids*, *A*, 1990, Vol. 2, No. 5, pp. 851–857.

26. Hong and Payne, F.R., Development of large eddy interaction model for inhomogeneous turbulent flow. American Institute of Aeronautics and Astronautics, paper, No. 87-1248, NY, AIAA, 1987.
27. Tsai, Y.P. and Christiansen, W.H., Two dimensional numerical simulation of shear layer optics. *American Institute of Aeronautics and Astronautics Journal*, 1990, Vol. 28, No. 12, pp. 2092–2097.
28. Knight, C.J., Sutton, G.W., Berggren, R., Phase aberration and laser output beam quality. *Wavefront Distortions in Power Optics*, Vol. 293, edited by Fuhs, A. and Fuhs, B., Wash., SPIE, 1981.
29. Clarc, R., Banish, M., Hammer, J., Fundamentals of aero-optics phenomena. American Institute of Aeronautics and Astronautics, paper No. 94-2545, NY, AIAA, 1994.
30. Sutton, G.W., Optical imagine through aircraft turbulent boundary layers. *Progress in Astronautics and Aeronautics: Aero-Optical Phenomena*, Vol. 80, edited by Gilbert, K. and Otten, L., NY, AIAA, 1982, pp. 15–39.
31. Legner, H.H., Otis, J.H., Theophanis, G.A., Feinberg, R.M., Laser beam degradation through turbulent interfaces. American Institute of Aeronautics and Astronautics, paper No. 78-71, NY, AIAA, 1978.
32. Vu, B.T., Sutton, G.W., Theophanis, G.A., Laser beam degradation through optically turbulent mixing layers. American Institute of Aeronautics and Astronautics, paper No. 80-1414, NY, AIAA, 1980.
33. Craig, J.E., Rose, W.C., Wavelength effects on images formed through turbulence. American Institute of Aeronautics and Astronautics, paper No. 87-1398, NY, AIAA, 1987.
34. Bogdanoff, D.W., Optical quality of supersonic jets of various gases. *Applied optics*, 1982, Vol. 21, No. 5, pp. 893–903.
35. Gilbert, K.G., Lear jet boundary-layer/shear-layer laser propagation measurements. *Aero-Optical Phenomena. Progress in Astronautics and Aeronautics*, Vol. 80, edited by Gilbert, K.G. and Otten, L.J., NY, AIAA, 1982, pp. 249–260.
36. Kelsall, D., Optical measurements of degradation in aircraft boundary layers. *Aero-Optical Phenomena. Progress in Astronautics and Aeronautics*, Vol. 80, edited by Gilbert, K.G. and Otten, L.J., NY, AIAA, 1982, pp. 261–293.
37. Rose, W.C., Johnson D.A., Otten L.J., Summary of all cycle aerodynamic shear—and boundary—layer measurements. *Aero-Optical Phenomena. Progress in Astronautics and Aeronautics*, Vol. 80, edited by Gilbert, K.G. and Otten, L.J., NY, AIAA, 1982, pp. 294–305.
38. Gilbert, K.G., KC–135 aero-optical turbulent boundary-layer/shear-layer experiments. *Aero-Optical Phenomena. Progress in Astronautics and Aeronautics*, Vol. 80, edited by Gilbert, K.G. and Otten, L.J., NY, AIAA, 1982, pp. 306–324.
39. Kelsall, D., Rapid interferometric technique for MTF measurements in the visible or infrared region. *Applied Optics*, 1973, Vol. 12, No. 12, p. 1398.
40. Buell, D.A., Overview of 6×6 ft wind-tunnel Aero-Optics tests. *Aero-Optical Phenomena. Progress in Astronautics and Aeronautics*, Vol. 80, edited by Gilbert, K.G. and Otten, L.J., NY, AIAA, 1982, pp. 139–188.
41. Verhoff, A., Prediction of optical propagation losses through turbulent boundary/shear layers. *Aero-Optical Phenomena. Progress in Astronautics and Aeronautics*, Vol. 80, edited by Gilbert, K.G. and Otten, L.J., NY, AIAA, 1982, pp. 40–77.
42. Kromin, S.I., Lyubimov, V.V., Shehtman, V.N., Measuring a scattered component of a light wave. *Quantum Electronics*, 1986, Vol. 13, No. 5, pp. 962–966.
43. Baily, W.H., Line spread instrumentation for propagation measurements. *Aero-Optical Phenomena. Progress in Astronautics and Aeronautics*, Vol. 80, edited by Gilbert, K.G. and Otten, L.J., NY, AIAA, 1982, pp. 189–199.
44. Butt, R.G., Turbulent mixing of passive and chemically reacting species in a low–speed shear layer. *Journal of Fluid Mechanics*, 1977, Vol. 82, p. 53.
45. Demetriades, A., Observations on the transition process of two–dimensional supersonic wake. *American Institute of Aeronautics and Astronautics Journal*, 1971, Vol. 9, No. 11, pp. 2128–2134.
46. Truman, C.R.,The influence of turbulent structure on optical phase distortion through turbulent shear flows. American Institute of Aeronautics and Astronautics, paper No. 92-2817, NY, AIAA, 1992.

47. Losev, S.A., *Gasdynamic Lasers*. Moscow Publisher: Nauka, 1977 (Russian).
48. Kalizhnikov, V.S., One-dimension properties of turbulence behind screens of various types. Thermo-hydro-gasdynamics of turbulent flows. Proceeding of Siberian Branch Academy of Science USSR (SB AS USSR), Institute of Thermo-Physics (ITP), 1986, pp. 128–133 (Russian).
49. Anikin, M.A., Ktalkherman, M.G., Malkov, V.M., Sinitzin, A.P., Dependence of flow parameters behind a nozzle bank on an expansion angle of an individual micronozzle. Gas dynamics of a GDL's flowing channel: Proceeding of Siberian Branch Academy of Science USSR (SB AS USSR), Institute of Theoretical and Applied Mechanics (ITAM), Novosibirsk, 1987, pp. 65–78 (Russian).
50. Baev, V.K, Ktalkherman, M.G., Malkov, V.M., Ruban, N.A., Flow characteristics and pressure recovery in a rectangular channel behind an axisymmetric nozzle screen. Gas dynamics of flow in nozzles and diffusers: Proceeding of Siberian Branch Academy of Science USSR (SB AS USSR), Institute of Theoretical and Applied Mechanics (ITAM), Novosibirsk, 1982, pp. 25–40 (Russian).
51. Sutton, G.W., Hypersonic interceptor aero-optics performance predictions. *Spacecraft and Rockets*, 1994, Vol. 31, No. 4, pp. 592–599.
52. Hogge, C.B., Aberrations in power laser systems. *Wavefront Distortions in Power-Optics*, Vol. 293, edited by Fuhs, A. and Fuhs, B., Wash., SPIE, 1981.
53. Malkov, V.M., Ktalkherman, M.G., Aero-optics of gasdynamic laser nozzle banks. *Journal of Applied Mechanics and Technical Physics*, 1993, Vol. 34, No. 6, pp. 20–28 (Russian).
54. Malkov, V.M., Ktalkherman, M.G., Some aspects of aero-optics of GDL nozzle banks. American Institute of Aeronautics and Astronautics, paper No. 94-2447, NY, AIAA, 1994.
55. Bogdanoff, D.W., The optical quality of shear layers: prediction and improvement thereof. *American Institute of Aeronautics and Astronautics Journal*, 1984, Vol. 22, No. 1, pp. 58–64.
56. Baxter, M.R., Truman, C.R., Masson, B., Predicting the optical quality of supersonic shear layers. American Institute of Aeronautics and Astronautics, paper No. 88-2771, NY, AIAA, 1988.
57. Smith, R., Truman, C.R., Masson, B., Prediction of optical phase degradation using a turbulent transport equation for the variance of index-of-refraction fluctuations. American Institute of Aeronautics and Astronautics, paper No. 90-0250, NY, AIAA, 1990.
58. Zelazny, S.W., Rushmore, W.L., Limitations of power scaling for high energy short wavelength lasers. American Institute of Aeronautics and Astronautics, paper No. 87-1390, NY, AIAA, 1987.
59. Boreisho, A.S., Koryakovsky, A.S., et al., Study of the optical quality of gas flows formed by screen type nozzle banks. *Journal of Applied Mechanics and Technical Physics*, 1985, Vol. 55, No. 10, pp. 1943–1949 (Russian).
60. Koryakovsky, A.S., Marchenko, V.M., Interferometry of optical non-uniformities in laser active media on the basis of the Talbot effect, *Quantum Electronics*, 1980, Vol. 7, No. 5, pp. 1432–1438.
61. Hardly, J.W., Adaptive optics—problems and prospects. *Wavefront Distortions in Power Optics*, Vol. 293, edited by Fuhs, A. and Fuhs, B., Wash., SPIE, 1981.
62. Pearson, J. Adaptive optics: a state-of-the-art report. *Laser Focus*, September, 1981, p.53–61.
63. Chew, L., Coherent structure effects on shear layer optics. American Institute of Aeronautics and Astronautics, paper No. 90-0185, NY, AIAA, 1990.
64. Truman, C.R., Prediction and measurement of aero-optic effects through the dynamics of passive scalar in turbulent shear flow. American Institute of Aeronautics and Astronautics, paper No. 94-2549, NY, AIAA, 1994.
65. Rapagnani, N.L., Davis, S.J., Laser-induced fluorescence: a diagnostic for fluid mechanics. *Lasers and Applications*, May, 1985, p. 127–131.
66. Rapagnani, N.L., Davis S.J., Laser-induced I_2 fluorescence measurement in chemical laser flow field. *American Institute of Aeronautics and Astronautics Journal*, 1979, Vol. 17, No. 12, pp. 1402–1404.
67. Liepman, H.W., Roshko, A., *Elements of Gasdynamics*, NY, Wiley, 1957.
68. Malkov, V.M., Aero-optics of flow behind the nozzle banks of fast-flow lasers. *Journal of Applied Mechanics and Technical Physics*, 1996, Vol. 37, No. 6, pp. 794–800.
69. Malkov, V.M., Effect of turbulent supersonic flow structure born by multi-nozzle banks on optical quality of medium in resonator cavity. Proceedings of SPIE, 1998, Vol. 3574, pp. 179–186.

2.4 Problem of Mixing in the Nozzles of Supersonic Chemical Lasers

1. Cassady, P.E., Pindroh A.L., Newton, J.F., Performance potential of advanced GDL Concept. *American Institute of Aeronautics and Astronautics Journal*, 1979, Vol. 17, No. 8, p. 845–853.
2. Rapagnani, N.L. Davis, S.J., Laser-induced I_2 fluorescence measurement in chemical laser flow field. *American Institute of Aeronautics and Astronautics Journal*, 1979, Vol. 17, No. 12, pp. 1402–1404.
3. Rapagnani, N.L., Davis, S.J., Laser-induced fluorescence: a diagnostic for fluid mechanics. *Laser and Applications*, May 1985, Vol. 4, No. 4, pp. 127–131.
4. aMalkov, V.M., Effect of regular and turbulent supersonic flow structure born by multinozzle banks on optical quality of medium in resonator cavity. Proceedings of SPIE, Vol. 3574, pp. 179–186, 1998.
5. Shwartz, J., Wilson, G.T., and Avidor, J., Tactical High Energy Laser. Proceedings of SPIE, Vol. 4632, 2002.
6. Boreysho, A.S., Savin, A.V., Malkov, V.M., Problems and solutions in COIL gas dynamics. Proceedings of SPIE, Vol. 5777, 2004.
7. Malkov, V.M., Savin, A.V., Kiselev I.A., Diffusers of COIL and DF-lasers. Proceedings of SPIE, Vol. 5777, 2004.
8. Boreysho, A.S., Evdokimov, I.M., Vasiliev, D.N., Savin, A.V., Ten kilowatt chemical oxygen–iodine laser. Proceedings of SPIE, Vol. 5120, pp. 336–344, 2002.
9. Boreisho, A.S, Malkov, V.M., Savin, A.V., Vasil'ev, D.N., Evdokimov, I.M., Trilis, A.V., and Strakhov, S.Yu., A 12-kW continuous-wave chemical oxygen–iodine laser. *Quantum Electronics*, 2003, Vol. 33, No. 4, p. 307–311.
10. Boreysho, A.S., Barkan, A.B., Vasil'ev, D.N., Evdokimov, I.M., Savin, A.V., Highly efficient cw chemical oxygen–iodine laser with transonic iodine injection and a nitrogen buffer gas, *Quantum Electronics*, 2005, Vol. 35, No. 6, pp. 495–503.
11. Zlobin,V., Izvestiya Akademii Nauk Estonskoy SSR, 20, 66, 1971 (Russian—News Academy of Science of Estonia SSR).
12. Bayley, D.J., Hartfield, R.J., Jr., Experimental investigation of angled injection in a compressible flow. American Institute of Aeronautics and Astronautics, paper 95–2414.
13. Evdokimov, I.M., Vasiliev, D.N., Savin, A.V., Druzhinin, S.L., High efficiency mixing in high-power COIL: experiments and numerical simulation. Proceedings of SPIE, Vol. 5777, 2004.

2.5 Resonators of High-Power SGL Laser

1. Ananyev, J.A., Optical resonators and problem of laser beam divergence. Moscow Publisher: Nauka, 1979, p. 328 (Russia).
2. Lobachev, V.V., Strakhov, S.Yu., Efficiency of an unstable resonator with an active medium containing small-scale phase inhomogeneities. *Quantum Electron*, 2004, Vol. 34, No. 1, pp. 67–70.

2.6 Pressure Recovery Systems for Chemical SGL

1. Boreisho, A.S., Malkov, V.M., Savin, A.V., et al., Pressure recovery system for high-power gas and chemical lasers. *Thermophysics and Aerodynamics*, 2001, Vol. 8, No. 4, pp. 571–587.
2. Koop, G., Hartlov, J., et al., Airborne laser flight-weighted laser module (FLM) and COIL modeling support. American Institute of Aeronautics and Astronautics, paper No. 2000-2421.
3. Shwarts, J., Wilson, G.T., Avidor, J., Tactical High Energy Laser. SPIE Proceeding, Vol. 4632, 2002.
4. Aleksandrov, B.P., Bashkin, A.S., et al., Problems in the development of autonomous mobile laser systems based on a cw chemical DF laser. *Quantum Electronics*, 2003, Vol. 33, No. 1, pp. 25–30.
5. Ratliff, A.W., McDanal, A.J., Kurzius, S.C., Martin, W.D., Power and pressure recovery analysis of chemical laser devices. American Institute of Aeronautics and Astronautics, paper, No. 75-721, 1975.
6. Crocco, L., One-dimensional treatment of steady gas dynamic. *Fundamentals of Gas-dynamics*. Vol. 3, Princeton University Press, NY, 1958.
7. Neumann, E.P., Lustwerk, F., Supersonic Diffusers for Wind Tunnels. *Journal of Applied Mechanics and Technical Physics*, 1949, Vol. 16, No. 2, pp. 195–202.

8. Malkov, V.M., Ktalkherman, M.G., Ruban, N.A., Experimental investigation of GDL diffusers. American Institute of Aeronautics and Astronautics, paper, No. 90-1512, 1990.
9. Ktalkherman, M.G., Malkov, V.M., Ruban, N.A., Supersonic flow decelerated in a rectangular channel of a constant cross-section. *Journal of Applied Mechanics and Technical Physics*, 1984, Vol. 25, No. 6, pp. 48–57 (Russian)
10. Schall, W.O., Grunewaid, R., Handke, J., COIL Diffuser investigations. COIL R&D Workshop, Prague 2001, No. 28–29, May.
11. Abramovich, G.N., Applied Gas Dynamics. Moscow, Publisher: Nauka, 1976 (Russian).
12. Rodrigues, S.E. et.al., US Patent 5,735,469 April 7, 1998.
13. Malkov, V.M., Savin, A.V., Kiselev, I.A., Diffusers of COIL and DF lasers. SPIE Proceeding, GCL/HPL 2004, Prague, –30th August–3rd September, 2004.
14. Driscoll, R.J., Moon, L.F., Pressure recovery in chemical lasers. *American Institute of Aeronautics and Astronautics Journal*, 1977, Vol. 15, No. 5, pp. 665–673.
15. Taganov, G.I., Mezhirov, I.I., V.T. Kharitonov., Experimental study of a gas ejector at high pressure drop. Paper collection on research of supersonic gas ejectors. Publisher: TsAGI, Moscow, 1961, pp. 303–321 (Russian).
16. Uryukov, B.A., Theory of differential ejector. *Journal of Applied Mechanics and Technical Physics*, 1963, No. 5, pp. 41–47 (Russian).
17. Arkadov, Yu.K., Gas ejector with nozzle perforated by longitudinal slots. *Journal News of Academy of Science, Mechanics of fluid and gas*. 1968, No. 2, pp. 71–74 (Russian).
18. Arkadov, Yu.K., Compact gas ejector with a high compression and spiral-distributed nozzles. *Journal of Scientific Notes of TsAGI*, 1984, Vol. 15, No. 6, pp. 35–42.
19. Iskra, A.L., The ejectors with different ejected and ejecting gases. Paper collection on research of supersonic gas ejectors. Publisher: TsAGI, Moscow, 1961, pp. 303–321 (Russian).
20. Malkov, V.M., Boreisho, A.S., Savin, A.V., et al., On the choice of working parameters for the system of pressure recovery of supersonic chemical lasers. *Thermophysics and Aeromechanics*, 2001,Vol. 8, No. 4, pp. 589–600.

3 Optical Resonators

Anatoly P. Napartovich

CONTENTS

3.1 INTRODUCTION

Laser resonator is a crucial component of lasers. It provides a feedback necessary for the continuous wave (CW) operation of a laser and controls optical beam quality and laser spectrum. A number of excellent textbooks and monographs are known in which optical resonator theory is described in detail and rather extended lists of relevant literature sources are presented [1–4]. Therefore, no attempt is made here to describe the historical aspects in this field of science. It is assumed that the reader has basic knowledge about most popular resonator types and their destination in laser design. An application area—gas lasers—restricts the specific choice of topics considered in this chapter. To some extent, this choice reflects the personal interests of the author.

In section 3.2, basic equations are briefly discussed, and particular attention is paid to a description of modern computing methodologies allowing one to get detailed information about the modal properties of loaded resonators including compound systems. Laser resonator classification is given in Section 3.3 with an emphasis on specific resonators developed in connection with the appearance of new configurations of the gain media. Nonlinear effects associated with nonuniform gain saturation and refractive index variations induced by laser intensity are discussed in Section 3.4.

3.2 BASIC EQUATIONS AND METHODOLOGIES

3.2.1 Two-Mirror Resonators

3.2.1.1 Bare Resonators

The primary purpose of the laser resonator theory is to describe the so-called transverse (or spatial) optical modes in a bare resonator free of a gain medium. Many practical laser resonators consist essentially of two end mirrors with the gain medium in the middle. In gas lasers, the refractive index of the gain medium is close to unity and when unpumped it can be replaced by free space. The pioneering work of Fox and Li [5] exerted a profound influence on the development of laser resonator modeling. It has introduced most important concepts while using intuitive arguments. Mathematically rigorous theory for such resonators was formulated by Weinstein [1]. It is based on scalar and paraxial optics, approximations, which are usually valid for gas lasers. In these approximations, the propagation of a monochromatic wave field in the free space in the positive direction of the z-axis is described by the parabolic equation for complex amplitude of the wave field, A^+

$$2ik\frac{\partial A^+}{\partial z}+\frac{\partial^2 A^+}{\partial x^2}+\frac{\partial^2 A^+}{\partial y^2}=0. \tag{3.1}$$

Here, $k=2\pi/\lambda$ is the wave vector and λ is the wavelength; the real wave field was taken in the form: $E=A^+\ \exp(-i\omega t+ikz)+\text{c.c.}$, $\omega=ck$, where c is the light velocity in free space. Restricting further considerations by linear resonators, the wave field inside the empty resonator can be presented in a form of two counter-propagating waves with complex amplitudes A^+ (along the z-axis) and A^- (against the z-axis), the latter satisfying an equation as shown:

$$-2ik\frac{\partial A^-}{\partial z}+\frac{\partial^2 A^-}{\partial x^2}+\frac{\partial^2 A^-}{\partial y^2}=0. \tag{3.2}$$

End mirrors located at $z=0$ and $z=L$ transform an incident wave to the reflected one. In a simple case of mirrors with a smooth relief $h(x, y)$, the relationship between reflected and incident wave fields can be expressed in the form:

$$A_{\text{refl}}=A_{\text{inc}}\eta(x,y)\exp[2ikh(x,y)+i\psi], \tag{3.3}$$

where $\eta(x, y)$ is a stepwise-like function determining the shape of the reflecting mirror, $h(x, y)$ is the distance from the local position of the reflecting surface to a reference plane, and ψ is the phase advance introduced by reflection from the mirror surface (for a perfect metal mirror $\psi=\pi$). Equation 3.1, Equation 3.2, and boundary condition (3.3) posed at each of the two mirrors define the problem for laser resonator mathematically.

An injected into the bare resonator wave field will propagate between the mirrors and decay with a rate determined by radiation loss outward the resonator space. It means that the wave field frequency and wave vector have imaginary components [1]. For bare resonators, it is convenient to solve the problem reducing it to integral equations using the point-source (green) function for parabolic equation:

$$G(x-x',y-y',z)=\frac{k}{2\pi iz}\exp i\frac{k}{2z}[(x-x')^2+(y-y')^2]. \tag{3.4}$$

The convolution of the source function with wave field distribution in the plane $z = 0$ gives the wave field after propagation along the z-axis for z distance. The traditional procedure to derive resonator integral equations involves starting from the definition of the wave field amplitude on the surface of one of the mirrors, $u(x, y)$, then expressing the wave field on the surface of the second mirror with the help of the source function (3.4) and completing a round trip by retuning to the first mirror and using the source function again (3.4). By equating the wave field that arrives after the round trip to the starting point, the integral equation can be derived. In general, this equation is cumbersome. Therefore, we present here the integral equation for the simplest resonator, consisting of two plane metal mirrors aligned parallel with the distance between them equal to L (the so-called Fabry–Perot [FP] resonator):

$$u(x, y) = \frac{k \exp(2ikL)}{2\pi iL} \iint u(s, t) \exp \frac{ik}{2L}[(x - s)^2 + (y - t)^2] \, ds \, dt. \tag{3.5}$$

Here, integration is carried out over the surface of the first mirror, while the second mirror is taken unbounded (see Figure 3.1). This integral equation defines transverse optical modes, their resonant frequencies, and their losses. In gas lasers, the gain spectral bandwidth is many orders of magnitude less than the optical frequency. This allows us to replace the wave vector k by its reference value k_0 everywhere in Equation 3.5 except the exponential factor in front of the integral. It is known from textbooks on mathematical physics that Equation 3.5 has nontrivial solutions (they are called eigenfunctions) only at certain eigenvalues, which can be defined for Equation 3.5 as $\gamma = \exp(-2ikL)$. Because of the diffractive leakage of the wave field out of the FP resonator k is a complex number. Let us denote the eigenvalue for the transverse mode with number m as $\gamma_m = \exp(i\varphi_m - \delta_m)$. Then the modal frequency and loss per bounce can be expressed in the following forms:

$$\omega_{q,m} = c \, \mathrm{Re}(k_{q,m}) = \frac{c}{2L}(2\pi q - \varphi_m); \qquad \Delta_m = 1 - |\gamma|^2 = 1 - \exp(-2\delta_m), \delta_m = -2L \, \mathrm{Im} \, k.$$

The modal frequency depends on two indexes: q is an integer number counting the so-called longitudinal modes and φ_m corresponds to the frequency shift associated with the transverse m-th mode. Wainstein [1] found explicitly spatial patterns and losses for a number of transverse modes satisfying Equation 3.5 in the limit of large Fresnel numbers. For an arbitrary two-mirror resonator, an integral equation can be presented in a more general form:

$$\gamma u(x, y) = \hat{\boldsymbol{p}} u(x, y), \tag{3.6}$$

where $\hat{\boldsymbol{p}}$ is the round-trip operator and $\gamma = \exp(-2ikL)$ is an eigenvalue of this operator. The round-trip operator can be expressed in an integral form by applying the Green function (3.4) and boundary condition (3.3) for reflections from two mirrors.

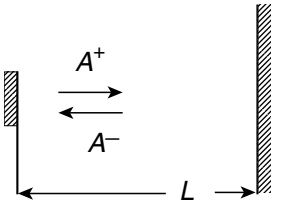

FIGURE 3.1 Schematic of the Fabry–Perot resonator.

Traditionally, the fundamental mode, which can be defined as one that has the lowest diffraction losses, is calculated by iterative techniques following the original work of Fox and Li [5]. This approach allows us to find only one mode with the lowest losses. In cases for which the discrimination of modes is low, many iterations are required to converge on the fundamental mode. Finally, at loss degeneracy points the iterative techniques do not give any result. More general techniques are based on matrix methods [6–9] allowing for extraction of the first few eigenvalues and modes. The Prony algorithm was first applied in References [6,7] to calculate a few modes with minimal loss in unstable resonators. More general approaches based on using Krylov subspace methods [8], compared with the Prony method, were discussed in Reference [9]. Among known methods for treatment of the eigenproblem in Krylov subspace, an Arnoldi algorithm [10] is noteworthy because of its simplicity and robustness. A sketch of the respective mathematical procedure is given next.

While performing numerical calculations, the round-trip operator $\hat{\boldsymbol{p}}$ acts in the discrete space of a high-dimension N, which is the total number of numerical mesh cells or Fourier harmonics in the wave field Fourier transform. From practical considerations, only the few modes with the highest possible values of $|\gamma|$ are of interest. One may expect that only a small part of the entire discrete space be involved in a search of optical modes with minimal losses.

To start with the Arnoldi iterations, an initial function $\nu(x, y)$ is to be determined. The appropriate way is to specify $\nu = \hat{\boldsymbol{p}}^{K}\psi$, where $\psi = \psi(x, y)$ is an arbitrary function, which can be thought of as a seeded wave field and K is the number of initial iterations (round trips made by this field). Solutions to the eigenproblem of interest to us are sought within the Krylov subspace spanned by Ω vectors calculated by subsequent iterations of the round-trip operator:

$$K_{\Omega}(\hat{\boldsymbol{p}},\nu) = \mathrm{span}\{\nu, \hat{\boldsymbol{p}}\nu, \hat{\boldsymbol{p}}^{2}\nu, \ldots, \hat{\boldsymbol{p}}^{\Omega-1}\nu\}. \tag{3.7}$$

Physically, this means that the preliminary K iterations select such a wave field distribution, which is composed of only modes with minimal losses. The number K of preliminary iterations and the Krylov subspace dimension Ω are chosen empirically. Furthermore, the Gramm-Schmidt orthogonalization technique is applied to create a basis in the Krylov subspace. Projection of the operator $\hat{\boldsymbol{p}}$ onto the Krylov subspace is realized by a Hessenberg matrix $\mathbf{H}_{\Omega}$ of $\Omega \times \Omega$ dimension. The eigenvalues $\gamma_1, \gamma_2, \ldots, \gamma_{\Omega}$ and eigenvectors $h_1, h_2, \ldots, h_{\Omega}$ of the matrix $\mathbf{H}_{\Omega}$ can be calculated using any relevant standard program. The numbers γ_1, $\gamma_2, \ldots, \gamma_{\Omega}$ approximate first Ω eigenvalues of the round-trip operator $\hat{\boldsymbol{p}}$. Approximate optical modes can then be expressed as linear combinations of vectors from the orthogonalized basis with eigenvector $\mathbf{H}_{\Omega}$ matrix weighting coefficients. This procedure gives a group of optical modes with relatively low losses and allows for evaluating the fundamental mode discrimination, which is a measure of single-mode stability.

Referring readers to the textbooks [1–3] for more details about properties of the integral equations for bare resonators, we briefly consider the modifications of mathematical procedures to include the nonlinear effects associated with gain saturation and phase self-modulation caused by the refractive index changes arising during laser operation.

3.2.1.2 Loaded Resonators

For typical conditions of a gas laser active medium, the refractive index is very close to unity. Therefore, we set a reference refractive index equal to 1 and the variation of index as $(n-1)$. Then the waves propagating in gaseous gain medium satisfy the following equation:

$$\pm 2ik\frac{\partial A^{\pm}}{\partial z} + \frac{\partial^2 A^{\pm}}{\partial x^2} + \frac{\partial^2 A^{\pm}}{\partial y^2} = ik[g + i2k(n-1)]A^{\pm}, \tag{3.8}$$

where g is the gain coefficient. Generally, the gain coefficient in an operated laser that can be found from a system of kinetic equations specific for a type of gas laser. Numerical simulations of optical equations constitute an essential part of self-consistent laser modeling and require the elaboration of effective and fast algorithms equally applicable to any laser. The appearance of spatially variable quantities g and n in the right-hand part of Equation 3.8 requires using new approaches, because the point-source function $G(x, y, z)$ for Equation 3.8 is not known in a general case.

The simplest way to simulate optical modes in a resonator loaded with an active medium is to replace spatially extended saturable gain by a set of thin sheets, between which the free-space propagation is assumed [4,11–13]. In more general terms, the split-operator technique was developed in Reference [14] for numerical simulations of laser light propagation in the atmosphere. This technique was applied for the first time to numerical simulations of a laser resonator in Reference [15]. In the split-operator technique, a step along the propagation axis, h_z is splitted to diffraction and gain/index steps. There exist methods to calculate the diffractive-propagation step of an arbitrary length with a high accuracy (Fresnel-Kirchgof integral and fast Fourier transformation [FFT] technique), and the length of the propagation step is restricted only by an accuracy of the gain or index step evaluation. For many gas lasers, the maximum step still providing a satisfactory accuracy of calculations is comparable with the resonator length. In this case, computing optical modes using even a single gain-phase sheet seems to be reasonable and is routinely done. However, such approximation is seen to be unacceptable when the detailed structure of the intracavity field is desired, particularly when considering peak power loading on intracavity elements.

When starting simulations of laser beam propagation, the gain coefficient and nonlinear part of the index are unknown. Combining a system of kinetic equations governing the behavior of gain or index in an active medium and paraxial optical equations results in a rather complicated mathematical problem. The natural way to settle the problem is to employ the method of iterations ideologically similar to the Fox–Li method. In contrast to passive optical cavity simulations, not only the wave field spatial pattern and phase, but also its intensity has to converge to some limit value after the series of round trips. In other words, if the round-trip operator in Equation 3.6 includes effects of laser beam interactions with the gain medium, then for CW single-mode lasing, $|\gamma| = 1$. This is exactly the condition under which the established laser intensity is found.

Generally, the question whether the iteration procedure will converge or not is a key problem in laser physics that has no general answer. Numerous experiments demonstrate that the single transverse and longitudinal mode operation was never realized spontaneously. As a rule, conscious efforts are required to achieve and support single-mode operation. A mechanism causing instability of a single-mode lasing is of quite a general nature. The gain coefficient at the given location is saturated by the intensity of the wave field at the same location. The resulting gain spatial profile has dips at the oscillating mode peaks and maximums in regions of the low-mode intensity (see illustration in Figure 3.2). Then, the modal gain defined as the gain coefficient weighted with mode intensity profile is equalized to the threshold value for the oscillating mode. However, for another mode with a different spatial profile and somewhat higher threshold, the modal gain overcomes its threshold at some level of pumping. Such a mechanism is called a ''gain spatial hole burning'' (GSHB) effect.

For the first time, this mechanism was considered when analyzing the competition of longitudinal modes in References [16–18]. The spatial profile of longitudinal mode intensity

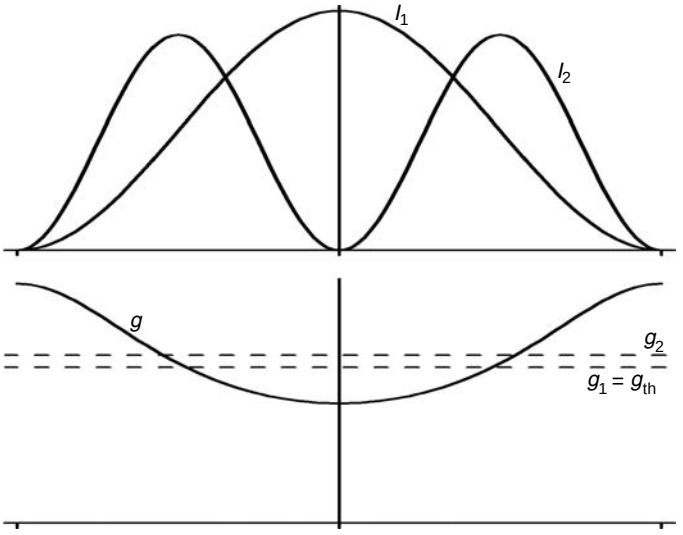

FIGURE 3.2 Illustration of gain spatial hole burning (GSHB) effect. I_1 and I_2 are the intensity profiles of the oscillating and competing modes, respectively; g_{th} is the threshold gain for the oscillating mode; g_1 and g_2 are corresponding modal gains defined as: $g_1 = \left(\frac{\int gI_1\,dx}{\int I_1\,dx}\right) = g_{th}$ and $g_2 = \left(\frac{\int gI_2\,dx}{\int I_2\,dx}\right) > g_1$. The effect of local gain saturation is expressed by the expression: $g = \left(\frac{g_0}{1+I_1/I_s}\right)$.

is formed by the interference of counter-propagating modes, and can be presented roughly as $I_0 \sin^2(\frac{\pi qz}{L})$. Taking into account that $L/q = \lambda/2$, the period of intensity modulation is $\lambda/2$. In gas lasers, diffusion processes exist that can smooth out small-scale nonuniformities of gain induced by interference fringes in the mode intensity. The diffusion rate is inversely proportional to gas pressure, so its influence is strong at low pressure and weaker at higher gas pressure. The typical spatial scale of mode intensity transverse nonuniformities is on the order of mirror sizes. Diffusion processes are, as a rule, not effective in smoothing out such large-scale nonuniformities. Therefore, the role of the GSHB in destabilizing a single-transverse-mode regime is rather important. Along with this versatile mechanism, there exist a number of more specific effects causing single-mode regime instability. Some of them are spatial nonuniformities of pumping rate and gas temperature, appearance of equal-loss modes, sources of in-cavity light scattering, and aberrations of optical elements.

In numerical simulations of loaded resonators, it would be very useful if theory were able to predict the limits of stable single-mode operations. An idea of how to tackle this problem was formulated and realized numerically in References [19,20]. The idea, in short, is as follows. Practically, when one desires to ensure a single-mode operation, additional losses for all modes except the selected mode should be introduced. Such a situation can be easily realized in numerical simulations. However, to distribute losses in such a manner that they attenuate the wave field of other modes and do not affect the selected mode, one needs to know wave field patterns for all modes. The numerical procedure consists of two alternating steps: classic iterations for a loaded resonator and matrix calculations of a mode spectrum at fixed gain and nonlinear index spatial distributions found at the iterative step. The key trick is then introducing artificial damping to all modes except the selected one. In such a method, characteristics of any prescribed mode can be found, even if modes with gain above the threshold exist. The procedure described allows one to find the exact parameters where single-mode operation fails. Implementation of this procedure in studies on a strip confocal unstable resonator with

saturable gain [20] demonstrated that there exist parameters of this resonator when no stable single-mode operation is possible. Besides, this approach accelerates the convergence of iterations in case of resonator parameters near the degeneracy point.

3.2.2 Compound Resonators

Along with the laser resonators relying on a two-mirror configuration with the gain medium in the middle, more complicated systems are in progress. In pursuit of achieving a high-power laser beam of good optical quality, many new resonator constructions were proposed and studied. Excellent reviews of the history of how most advanced resonator designs were developed can be found in References [2,3]. From the viewpoint of resonator theory, it is worth considering problems of numerical simulations of composite (compound) resonators incorporating additional mirrors, stop apertures, coupled resonators, and other optical elements.

It is known that the so-called unstable resonators [2–4] are, in many cases, the best way to produce single-mode high-power laser beams. In addition, minor modifications of laser schemes are possible, allowing for an effective control of laser spectrum. Figure 3.3a,b illustrates two such schemes: injection of a low-power signal from the master oscillator to a high-power slave laser (a); and an arrangement of a diffractive grating on the resonator axis behind the hole in the mirror (b).

Traditionally, the injection-controlled laser is analyzed in terms of empty cavity modes and coupling coefficients independent of exact wave field frequency and ignoring in-cavity diffraction, which actually controls the transverse patterns of the optical mode and of the injected signal. In this approximation, the coupling coefficient, responsible for a degree of oscillation control by the injected signal, cannot be calculated accurately. Besides, it is impossible to accurately evaluate the locking range because the modal selectivity in the unstable resonator with a central hole in the mirror is lower, and characteristics of a competing mode first approaching its threshold are not known in advance.

The diffraction numerical model of the injection-controlled laser shown in Figure 3.3a was developed in Reference [21] for a stripe telescope resonator, taking into account gain saturation effects. The minimal power needed for the slave laser locking was found for different aperture diameters and the frequencies of the external signal. It was shown that the locking range and the pattern of the mode excited by the injected signal are rather sensitive to gain kinetics. In general, by varying the signal frequency one can change a transverse mode in the slave laser.

In a three-mirror resonator of the type shown in Figure 3.3b, the phase of the beam injected into the hole in the concave mirror is controlled by the phase shift gained by the beam round trip: the hole → grating → the hole. This phase shift constitutes, as a rule, multiple wavelengths. In the cavity, this beam is combined with the radiation reflected from the concave

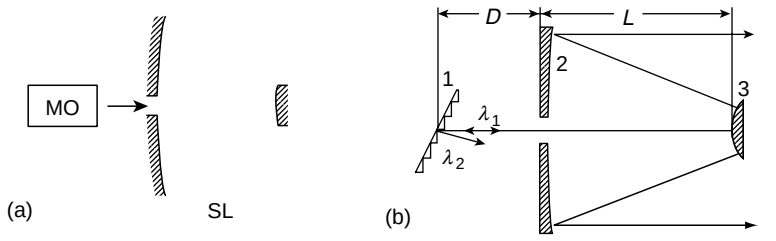

FIGURE 3.3 (a) Schematic of a laser with the unstable resonator controlled by the injected signal. MO is the master oscillator and SL is the slave laser. (b) Schematic of wavelength control in a laser with an unstable resonator and grating.

mirror. This is quite a new feature characteristic of compound systems. Interference patterns between beams reflected from the grating and the mirror change quasiperiodically with variations in the distance between the grating and the mirror or of the wavelength. This dictates the necessity to control relative locations of resonator components within fractions of the wavelength. To describe optical modes in such systems, it is not sufficient to construct one round-trip operator. An equation for the laser cavity shown in Figure 3.3b was derived in References [22,23]. Replacing diffraction grating with an effective perfect reflector with a spectral bandwidth much greater than an intermodal beating frequency, the resulting equation can be expressed in the form:

$$\left(\hat{\boldsymbol{p}}_1 + e^{i\psi}\hat{\boldsymbol{p}}_2\right)u(x,y) = \gamma u(x,y). \tag{3.9}$$

Here $\psi = 2kD$, where D is the distance between the grating and concave mirror (see Figure 3.3b); $\hat{\boldsymbol{p}}_1$ is the round-trip operator for the resonator formed by mirrors 2 and 3; $\hat{\boldsymbol{p}}_2$ is the round-trip operator for resonators formed by mirrors 1 and 3 and limiting diaphragm; and $\gamma = \exp(-2ikL)$. The important new feature is the appearance of the wave vector k in two different exponential functions. For the resonator with some fixed positions of the mirrors and grating, we can find the resonant frequency for the fundamental mode as a function of the phase ψ. Because the resonant frequencies of higher-order modes differ from the fundamental mode frequency, the phase ψ should also be changed. Hence, a procedure of calculations of a number of optical modes in this case is subject to modifications: a solution is to be sought in two-parameter space (ψ,γ). To find the critical conditions for a stable frequency control of the laser with the grating, a comparison should be made between modal gains reduced to the respective thresholds for two resonators: the entire compound one and the resonator formed by mirrors 2 and 3 (2–3). These calculations are to be done for the gain spatial distribution established under lasing of the fundamental mode of the compound resonator. When the gain of a mode of the resonator (2–3) reaches its threshold, it means instability of the wavelength-controlled operation. The described procedure was applied in Reference [23] to numerical simulations of CO_2 laser with the grating control of operative wavelength experimentally studied in Reference [24]. Conditions favorable for a reliable wavelength control were indicated. Results satisfactorily agree with the experiment [24].

In the 1980s–1990s, much attention was paid to the problem of a few gas lasers phase locking (extensive reviews of this activity can be found in References [25–27]). The methodology of diffractive simulations of a system of individual lasers with different methods of their optical coupling is similar to the one described previously. An essential property of modeling optically coupled lasers is the complication of basic equations. Instead of one equation (Equation 3.6), a system of equations, which incorporates terms responding to laser beam propagation in each resonator and in the space between them, is subject to computing.

We illustrate general ideas on a system of two axi-symmetric unstable resonators [23,28], coupling between which is provided by central holes in concave mirrors as shown in Figure 3.4. The equations solved to determine the modes of the system have the form:

$$\begin{pmatrix} \hat{\boldsymbol{p}}_1 & e^{i(\psi+\chi)}\mathbf{T}^{21} \\ e^{i\psi}\mathbf{T}^{12} & e^{i\chi}\hat{\boldsymbol{p}}_2 \end{pmatrix} \begin{pmatrix} \nu \\ f \end{pmatrix} = \gamma \begin{pmatrix} \nu \\ f \end{pmatrix}. \tag{3.10}$$

Here, $\nu = A^+(r, L+d), f = A^-(r, -L-d-\Delta), \psi = 2kd(\mathrm{mod}\ 2\pi), \chi = 2k\Delta(\mathrm{mod}\ 2\pi)$, and Δ is the resonator length detuning. The operators $\hat{\boldsymbol{p}}_{1,2}$ describe a round-trip propagation in each resonator, and $\mathbf{T}^{21}$ and $\mathbf{T}^{12}$ describe the propagation of the coupling beam from resonator 2 to resonator 1, and from resonator 1 to resonator 2, respectively. It is evident that the

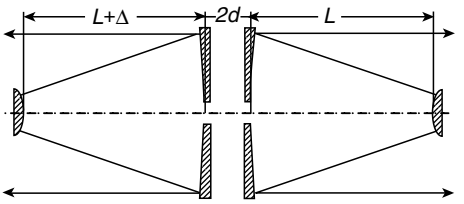

FIGURE 3.4 Schematic of lasers optically coupled through the holes in unstable resonators.

characteristics of the system of two resonators shown in Figure 3.4 are quasiperiodic functions of the resonator length detuning and the coupling path length with the period $\lambda/2$. Variations of ψ and χ within 2π correspond to changes in the respective lengths on $\lambda/2$. Numerical simulations made in Reference [23] for the system in Figure 3.4 demonstrated high sensitivity of collective mode properties to exact values of parameters ψ and χ. This means that the control of resonators detuning and the length of the coupling channel within fractions of the wavelength is a crucial condition for achieving laser array phase locking. It was shown in Reference [23] that, with a proper choice of these parameters and a strict control of them, effects of gain saturation result in breaking the phase-locked operation of lasers but at a reasonably high value above the threshold gain. A similar approach was realized in Reference [29] for adjoint-coupled stripe unstable resonators without regarding gain saturation effects. Later [30], a full model was developed for studying the phase locking of two CO_2 lasers with optically coupled hybrid resonators (see Figure 3.5) using beams diffracting over the edges of convex mirror in a waveguide—asymmetric unstable resonator. Three-dimensional diffraction code was applied taking into account refractive index gradients and gain saturation effects in combination with diffraction and waveguiding effects in the entire optical tract including the coupling channel. Key parameters for phase locking were defined: optical coupling channel length and position of the resonator optical axis relative to the nearest edge of the convex mirror. The numerical simulations evaluated tolerances for the length of the optical coupling channel. A range of the key parameters providing in-phase mode stable operation at high values above the threshold conditions was found for a particular laser construction.

3.3 TYPES OF RESONATORS

A large variety of different resonator constructions were proposed and studied in the past. Properties of a gain medium vary very strongly depending on the type of the gas laser. To provide high laser efficiency and good beam quality, the resonator configuration should

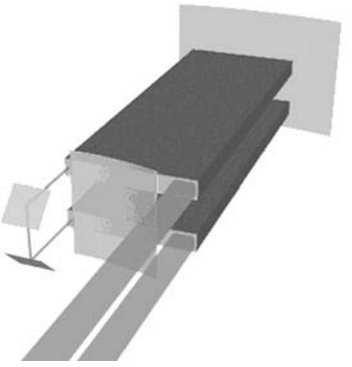

FIGURE 3.5 Schematic of two slab lasers with hybrid resonators coupled by a beam diffracted over the edge of the convex mirror.

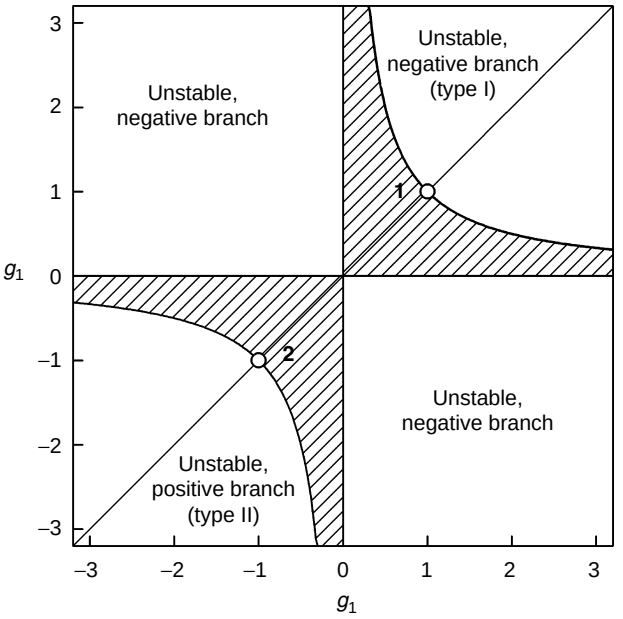

FIGURE 3.6 Stability diagram for resonators with spherical mirrors.

satisfy restrictions laid by geometry of gain volume and the typical value of a small signal gain. In general, all resonators can be divided into two large classes: stable and unstable. In terms of geometric optics, the stable resonators can confine optical rays infinitely for a long time. In the unstable resonators, all light rays leave the resonator after a few cycles (an exceptionally long-lived trajectory may exist but the diffraction effectively destroys such a trajectory). However, this classification can hardly be applied to resonators with mirrors that have an arbitrarily complex surface because of the mathematical complexity of ray trajectories' description. The simplest type of optical resonators is a resonator formed by two spherical mirrors. Figure 3.6 shows a diagram classifying resonators with spherical mirrors into stable and unstable ones. To be rigorous, this classification of resonators [2,3] is derived in paraxial approximation. It means that this classification is certainly valid for resonators with parabolic mirrors only. Otherwise, two parameters $g_{1,2} = 1 - L/R_{1,2}$ (L is distance between mirrors, $R_{1,2}$ radius of curvature of mirror 1 or 2) are insufficient to fully characterize resonators. Aberrations of mirrors can disturb the traditional stability diagram shown in Figure 3.6. Generally, such disturbances may become important for resonators with parameters falling in this diagram close to boundaries between regions of stability (marginally stable resonators). Properties of resonators with spherical mirrors are discussed in detail in many textbooks and handbooks to which the reader is referred—besides the already cited references [1–4], the textbooks on laser physics could be added [31–34] where principles of the resonator theory are reported.

3.3.1 Stable Resonators with Spherical Optics

The general approach for the description of modal properties of stable resonators with spherical mirrors is traditionally based on considerations of Hermite–Gaussian or Laguerre–Gaussian beams propagating between mirrors in the absence of restricting beam aperture effects like hard-edged stops or mirror edges. For such situations, a generalized ABCD matrix

[2] approach was formulated allowing for inclusion of resonators with variable reflectivity mirrors and multielement stable resonators into an analysis. The wave field of transverse optical modes found in this way should be located well within the minimum mirror aperture, that is, when diffraction losses are negligible. Provided the wave field reaches an edge of a mirror, this analysis fails, and the mode suffers from a transverse pattern distortion induced by diffraction from the mirror edge. Such effects can be described only numerically by a direct solving Equation 3.6. In the limit of negligible diffractive losses, the problem of multimode laser operation arises. The result of simultaneous oscillation of many modes is degradation of the output beam's optical quality. Typically, the radius of the optical beam for the fundamental mode that possesses the highest beam quality is limited by the order of magnitude by $(L\lambda)^{1/2}$. Taking into account a restriction on the laser intensity put by the destruction of optical elements, the total single-mode laser beam power turns out to be strictly limited at a value, which excludes many practical applications of lasers. Nowadays, it is well known that the best way to avoid such a limitation on the output beam power of a single-mode laser (diffraction-limited optical quality) is a choice of the so-called unstable resonator.

3.3.2 Unstable Resonators with Spherical Optics

Soon after the pioneering paper by Siegman [35], studies of unstable resonator properties have resulted in realizing the fact that these types of resonators can resolve the problem of a single-spatial-mode operation for high-power lasers and achieve high output beam quality. Applications of unstable resonators in laser technique have become very popular and led to a great success in solid-state and gas lasers. Respectively, optics of these resonators were studied in detail, and rather exhaustive texts with a description of the history of their development and properties of lasers implementing these resonators can be found in References [2–4,33,36].

A very useful concept of the laser with an unstable resonator was proposed by Anan'ev [36], who suggested considering it as an optical system comprising a driving generator and an amplifier with a matching telescope between them, particularly for the active cavity case. The central intensity core, which is defined by the central Fresnel zone of the cavity, plays the role of a generator and the remaining peripheral zone of the cavity plays that of the amplifier, with the edge-diffracted field at the feedback aperture edge providing the controlling feedback to the central intensity core. This mechanism of diffractive feedback into a converging wave field determines the diffractive properties of the cavity mode structure. Complicated interplay between this low-intensity converging field and the expanding spherical wave was a subject of numerous studies analyzed in depth in monographs [2,3].

Exploitation of unstable resonators demonstrated that the final goal to generate a high-power laser beam with high optical quality is easily achieved when an active medium possesses a high gain coefficient including short pulse lasers [37]. The underlying reason for this fact is the diffraction of the output beam on edges of the outcoupling mirror. The point is that such diffraction plays the more adverse role the smaller the magnification number, M, characterizing the increase in laser beam diameter after the completion of the resonator round trip. Approximately, resonator round-trip loss [2,3] is equal to $(1-1/M^2)$. This is why a low-gain medium needs a resonator with a low magnification ($M-1 \ll 1$).

For resonators with low magnification, an additional problem exists associated with the shape of the output laser beam. An intrinsic property of the unstable resonator is the fact that the output beam has a form of a ring with the width $(M-1)R_M$. Here, R_M is the radius of the output mirror, which can be a function of an azimuth for an arbitrary shape of the output mirror. The far-field pattern of a narrow ring-shaped beam has a multipeak form, which is inconvenient for most of the applications. A partial solution to this problem is the use of an

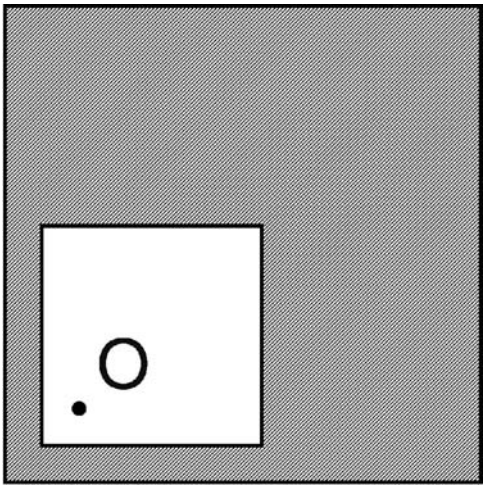

FIGURE 3.7 View from the output of the off-axis unstable resonator with the optical axis in the corner of the convex mirror.

off-axis unstable resonator [38], for which R_M measured from the optical axis strongly varies in azimuth. For example, a comparatively compact output beam can be produced by placing the optical axis at the corner of a rectangular output mirror (see illustration in Figure 3.7). One more method to get a compact-shaped output beam from an unstable resonator was proposed in Reference [3] and studied theoretically in Reference [39]. A key idea is to combine laser beam rotation within the cavity by a proper arrangement of mirrors and outward shift or magnification of this laser beam. Organized in such a manner, the evolution of the laser beam results in averaging gain or index spatial nonuniformities over multiple passes within the cavity and gives an opportunity to couple out of the resonator the laser beam of compact form. In experiments with CW fast-flow CO_2 lasers [40], the inner radius of the output ring-shaped beam was increased with the help of conical optics while the width of the ring was kept the same. This transformation made the output beam more compact improving the far-field pattern. Actually, known measures to enhance optical beam quality in unstable resonators with low magnification number did not provide a solution acceptable for technological laser developers.

3.3.3 Specific Classes of Resonators

The evolution of gas laser techniques is dictated by consumer requests, which include among others requirements on laser efficiency, convenience in operation and safety. With respect to CW high-power lasers, the use of a fast gas flow assisting in heat removal from the gain volume necessitates the development of a complex gas-dynamic facility, which lowers plug-in efficiency and has a high level of noise. In recent years an alternative approach prevails, which is based on a diffusion cooling of the gain medium. Intensification of the diffusion cooling can be done by the reduction of at least one transverse size of the gain generator. The lasers with such geometry are called slab lasers. Evidently, resonators allowing for effective extraction of a laser beam of good quality from slab lasers are to be the specific ones. A satisfactory solution to this problem is the so-called hybrid resonator [41], which combines properties of stable or waveguide propagation in the transverse direction with an asymmetric unstable configuration in the lateral direction.

Some types of lasers (e.g., HF/DF supersonic chemical lasers [42,33], radio-frequency (RF) pumped CO_2 lasers [43]) have an annular-shaped gain region. A lot of work was done on the development of resonators for chemical lasers with megawatt-class output power: the ALPHA laser at the TRW Capistrano Test Site and the MIRACL laser at the White Sands Missile Range. The ALPHA laser has high extraction efficiency, decentered, annular ring resonator (HEX-DARR) configuration. This is a highly specialized and complicated structure, which provides a high-power output beam (wavelength around 2.7 μm) with high optical quality.

For industrial-scale annular-shaped gain generators in CO_2 lasers, a number of resonator constructions were considered [43–45]. In the annular-shaped gain medium, the thickness of the annular waveguide is much smaller than the diameter of the device. Therefore, conditions for wave field propagation in waveguide and azimuth directions are quite different. It is comparatively easy to provide preferential gain and loss balance for the fundamental mode in the waveguide. However, it is a challenge to achieve a single-azimuth-mode operation. Authors [43] have proposed to wind an unstable strip resonator as shown schematically in Figure 3.8. A couple of methods to do this were considered in Reference [43]: making a contour height of the mirror to vary quadratically (the strip analog is an off-axis telescope), linearly (the strip analog is a tilted mirror), or cos-like (the tilted toric mirror) with the azimuthal angle. The diffraction theory of these resonators predicted their satisfactory performance, and the experiments confirmed the ability to produce a satisfactorily efficient output beam quality for CO_2 laser with azimuthally unstable resonators with the helical mirror and the tilted toric mirror. In the latter case, the laser output was in the form of two beams emitted at two different angles relative to the axis of the laser.

Lapucci et al. [44] suggested and realized, for the annular CO_2 laser, a so-called quarter-Talbot resonator comprising two plane mirrors with an intracavity aluminum spatial filter, based on a circular array of 28 holes and placed close to one of the plane mirrors. The spatial filter creates a system of small-aperture resonators exchanging by wave field because of diffraction in the gain medium. The Talbot effect [46,47] is a phenomenon of self-reproduction of a transversely periodic wave field distribution over a distance $Z_T = 2\Lambda^2/\lambda$, where λ is a radiation wavelength and Λ is the transverse period of the wave field pattern. For the first time, the Talbot effect was used in Reference [48] for phase locking of a large two-dimensional CO_2 laser array composed of diffusion-cooled tubes packed in a triangular lattice. At the half-Talbot distance, the in-phase beam array forms an identical image but is shifted during a half

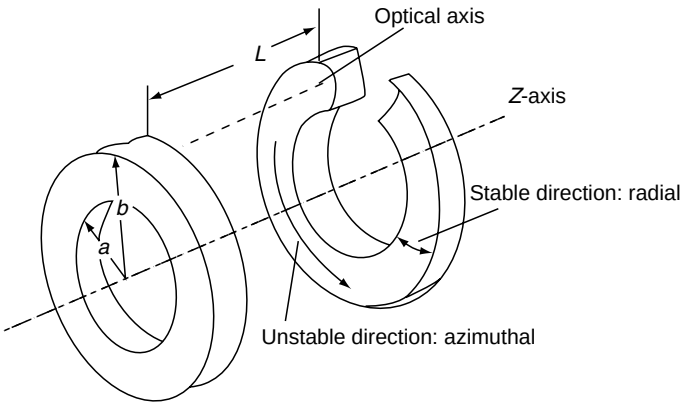

FIGURE 3.8 Schematic of the azimuthally unstable resonator. (Taken from Ehrlichmann, D. et al., *IEEE J. Quant. Electron.*, 30, 1441, 1994. With permission.)

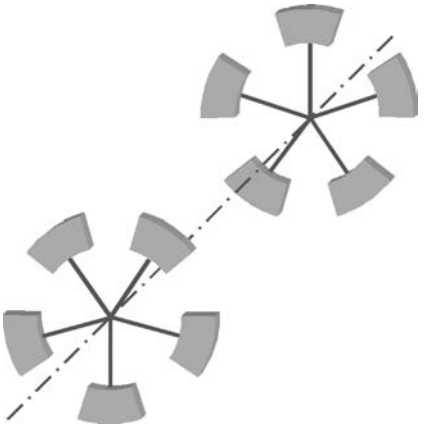

FIGURE 3.9 Schematic of Talbot resonator for annular gain medium.

of the period, while the out-of-phase (phase difference between the neighboring beams is π) beam array forms exactly the same distribution. At the Talbot distance, actually both in-phase and out-of-phase distributions are reproduced exactly. Therefore, authors [44] adjusted the period in the system of holes in the spatial filter and the distance between mirrors to form the quarter-Talbot resonator, which allows for the selection of a unique out-of-phase mode. Further, to improve the far-field pattern of the output beam they employed a phase plate that transforms the out-of-phase distribution to the in-phase one.

Napartovich et al. suggested to exploit the same quarter-Talbot resonator, but with reflectors in the form of segmented mirrors on each side turned to half of the period (see Figure 3.9). This resonator configuration allows one to select the in-phase mode, the diffraction losses for which are much lower than for other modes.

In a large-aperture active medium with a low-gain coefficient, implementation of the unstable resonator for selection of the fundamental mode suffers from the drawbacks (discussed earlier) associated with the necessity to apply a low-magnification resonator. A number of alternative ways to achieve a single-mode operation in lasers guaranteeing a good output beam quality with a gain area of a large size were considered in the literature. Most of them were not very successful to get a wide distribution. However, ideas underlying these methods might be still of interest. Referring the readers to the book [3] with information about numerous attempts to solve this problem made before 1979, let us discuss the recent progress.

Belanger and Pare, suggested an idea, which had a certain impact on further progress in designing laser resonators aimed to support a stable broad-area fundamental mode with a flat-top intensity distribution. Roughly, this idea was to fabricate one of the resonator mirrors with a surface profile that realizes the phase conjugate reflection for a desired light beam (following Belanger and Pare, let us call such mirrors "graded-phase mirrors" [GPM]). Practically, in designing such a resonator, one has to make a compromise between situations when the surface of the GPM is very complicated with fine features and when it is smooth, but higher-order modes have nearly the same threshold. It was found that this technique works for resonators with only low Fresnel numbers [51]. It was proposed in References [52–54] to add an intracavity phase plate introducing high spatial frequency phase disturbances, which, in turn, improve the selectivity of the designed GPM with respect to the reflection of the predescribed mode. Experimental realization of this proposal [53] for a solid-state laser confirmed that this trick allows achieving stable single-mode operation of the laser with the flat-top output beam at higher Fresnel numbers than the simple technique.

In the past, many efforts were made to study the effects of mirror reflection patterning on the modal properties of plane-parallel resonators [55–57]. In particular, periodical patterning of the reflection coefficient of one of the mirrors was carried out in a manner such that the distance between the mirrors turned out to be equal to the Talbot distance corresponding to this period, and the self-imaging waves experience minimal losses. Experiments [56] with such resonators confirmed the improvement of properties of the output beam, and further addition of a phase plate to correct the phases of the output beamlets [57] demonstrated, in agreement with expectations, that this method can lead to high output beam quality. Earlier studies on resonators with periodical patterning of mirror reflection [55–57] considered the limit of unbounded mirrors. Actually, diffraction losses and discrimination of modes essentially depend on the mirrors' sizes. Dependence of diffraction losses for a resonator comprising flat stripe mirrors, one of which has reflection coefficient values 0 or 1, on a variable fraction of perfectly reflecting surface, s, was studied in Reference [58]. Results of numerical simulations for losses per bounce for the out-of-phase mode can be approximated by an expression: $\delta = 0.78\ m/Ns$, where N is the number of reflecting segments of the patterned mirror and m is the resonator length reduced to $L_T/4$. For the quarter-Talbot resonator ($m = 1$) only the out-of-phase mode has minimal losses. In the half-Talbot resonator, the in-phase and out-of-phase modes have comparable losses till $s \leq 0.7$. For higher s values, the in-phase mode is preferable. In the limit $s \to 1$, the in-phase mode converts to the fundamental mode of the FP resonator with minimal losses, while the out-of-phase mode converts to the Nth order mode possessing higher losses. Therefore, the mirror with narrow regularly disposed absorbing streaks can be a good means to select the single in-phase mode.

In cases when the gain medium has irregular nonuniformities of refractive index, a useful method to partially cancel their adverse impact on the laser beam quality is the use of one of the resonator mirrors in a form of a retro-reflector array [59]. Experimental studies on such a resonator for photodissociation iodine laser demonstrated that individual resonators, each formed by a single triple prism and a flat counterreflector, have extensively exchanged the wave field. This results in the formation of a common wave field with simultaneous compensation of optical nonuniformities. The latter is caused by a property of the triple prism to return the reflected beam in exactly the opposite direction but shifted to a certain distance determined by the size of a single triple prism. The use of an intracavity Fourier filter formed by an aperture stop in the focal plane of two mirrors [59] allowed the authors to achieve a substantial improvement in the output beam in a pulsed photodissociation iodine laser.

3.4 GAIN SATURATION AND MODE–MEDIUM INTERACTION EFFECTS

As mentioned earlier, the gain saturation effect in combination with the nonuniformities of the optical mode spatial patterns is the major cause for the onset of multimode lasing. The same mechanism acts with respect to the broadening of a laser spectrum associated with the simultaneous operation of the laser on many longitudinal modes. For low-pressure gain media, the competition of longitudinal modes is suppressed by the diffusion leveling of the gain profile. In other words, the mechanism of the GSHB heavily relies on the response of the gain coefficient to local wave field intensity. In gas lasers with fast transverse flow of gain medium across the resonator aperture, the gain coefficient, as a rule, is not a function of the local intensity value. It is more appropriate to consider that the gain coefficient at a given location is determined by the history of the interaction of a gas portion flowing through the resonator region with laser intensity. Specifically, such nonlocality of gain saturation along the flow is a very important factor for gas-dynamic lasers [60,61] and electric-discharge CO_2 lasers with separated zones of the discharge and resonator [62]. In these lasers, the preexcited gas mixture enters into the resonator zone with a sufficiently high gain coefficient

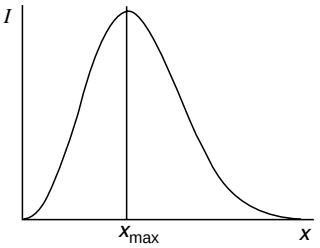

FIGURE 3.10 Intensity profile of the fundamental mode in the FP resonator with gain medium flowing in from the left.

and leaves it with a low excitation degree. Induced by stimulated emission, the gain gradient along the fast gas flow can strongly influence resonator modes. In the simplest approximation of a two-level system interacting with the laser field, the fundamental mode of the semi-infinite along the flow FP resonator was calculated in Reference [63]. It was found that the wave field of the fundamental mode is concentrated close to the mirror's upstream edge (see illustration in Figure 3.10). For the near-threshold operation of the laser, the position of the intensity peak within the cavity measured from the resonator zone entrance was explicitly found to be $x_{\max} \approx 3\sqrt{\left(\frac{2\lambda}{\pi(g_0 - g_{\text{th}})}\right)}$, where g_0 and g_{th} are the initial and threshold gain coefficients, respectively. The operating mode wave field extends over distance $(2 \div 3)\, x_{\max}$ along the gas flow.

In unstable resonators with the fast transverse flow, the gain saturation effect can induce auto-oscillations of the laser intensity [64]. Following Ananév's interpretation, the near-axis zone of the unstable resonator plays the role of the master oscillator, while the outer part of the resonator serves as a power amplifier. This interpretation is convenient for explaining the mechanism of oscillatory instability illustrated in Figure 3.11, where the unstable resonator is imitated by the combination of an oscillator and amplifier. Taking into account that light velocity is much higher than the gas flow velocity, the local value of the gain coefficient should be kept constant and equal to the threshold at the resonator axis. Evidently, a positive fluctuation of the laser intensity will result in additional diminishing of the gain in the

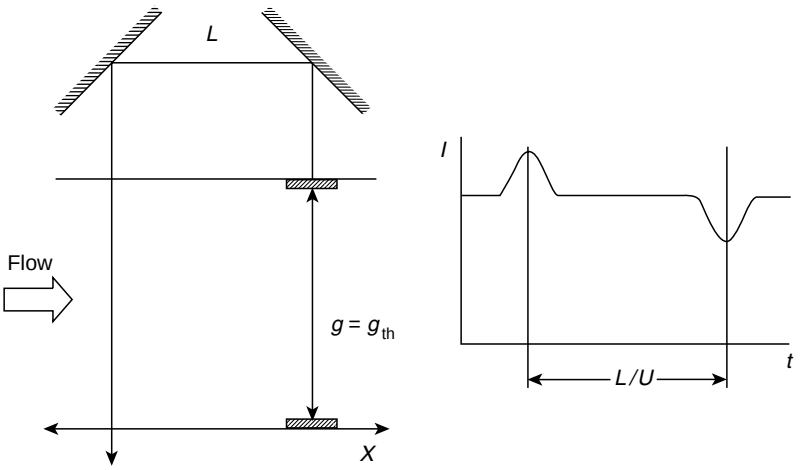

FIGURE 3.11 Schematic illustrating the mechanism of oscillating instability in a fast-flow laser with unstable resonator; L/U is the delay between the original intensity fluctuation and a response appearing after the arrival of the perturbed gain region to the resonator axis.

upstream zone of the resonator. When this negative disturbance of the gain coefficient arrived at the axis area, it induces a negative fluctuation of the laser intensity. It means that in this case a mode–medium interaction provides the negative feedback between fluctuations of gain and intensity. However, because of delay between the original fluctuation and the system response to it, L/U, an oscillating instability can evolve. The authors [64] using the simplest gain kinetic model have proved that the steady-state lasing of the fast transverse flow laser with an unstable resonator is unstable. Soon, oscillations of the CO_2 laser intensity in the fast-flow laser with the unstable resonator were revealed experimentally [65,66]. These observations initiated discussions of factors that could stabilize the predicted instability [67,68]. Authors [69,70] have studied the conditions for setting up the oscillatory regime in the fast-flow CO_2 lasers in much detail and formulated analytic criteria for its appearance. A number of stabilizing factors were analyzed and parameters of resonator and gain medium were found where no oscillatory operation was predicted in qualitative agreement with the experiments [65,66]. In particular, explicit criteria were derived for conditions when the oscillatory instability is stabilized by energy exchange processes between molecular vibrations of N_2 and CO_2 molecules; by gain medium excitation within the resonator zone and by nonuniformities of the gas flow velocity distribution along the optical axis. Destabilizing factors are wave field intensity gradient along the gas flow and finiteness of the light speed. In conditions typical for high-power electric discharge or gas-dynamic CO_2 lasers, the most important stabilizing factors are fluctuations of the gas flow velocity associated with gas-dynamic turbulence [70]. Even if the oscillatory instability is damped by gas flow nonuniformities, fluctuations of gain induced by the flow turbulence at the entrance into the resonator zone are resonantly enhanced at frequencies around the time of gas transit from the upstream mirror's edge to the optical axis [71]. This mechanism of resonant enhancement of any fluctuations of gain medium parameters at the entrance to the resonator is an underlying reason why fast-flow gas lasers with unstable resonators are so frequently subject to oscillatory instability.

In conclusion, gas lasers with fast transverse to the resonator axis flow manifest specific effects associated with gain saturation by stimulated emission: laser intensity concentration near the upstream resonator boundary and transition to the oscillatory mode of operation for unstable resonator configuration. In the absence of regular oscillations, a laser with the unstable resonator in turbulent gas flow is anomalously sensitive to gain fluctuations.

Comparatively high gas pressure and fast gas flow in high-power lasers introduce new features into interaction between laser field and medium. The refractive index of gases is proportional to the gas density (usually, the index changes associated with the resonant laser transition and difference in polarizabilities of molecules in different quantum states can be neglected). The gas density varies in space and time because of heating in relaxation processes and following gas expansion. Generally, the relaxation rate of excited species in gas depends on laser intensity. This dependence may have a complicated nature because of the complexity of real kinetics in the gain medium. It was found in CO_2 lasers and iodine photodissociation lasers that the gas-heating rate depends on laser intensity. The mechanism of this effect is intimately coupled with the difference in relaxation rates from the upper and lower levels of the laser transition. It is well known that for effective laser operation, the relaxation from the upper level should be slower than that from the lower level. As a result, a stepwise increase in the laser intensity is followed by an enhanced gas heating. An additional gas heating takes place on a time scale between relaxation times for lower and upper levels, respectively. In the steady-state laser operation, the stimulated emission extracts energy from the medium leading to relative cooling of gas. Hence, interaction of gain medium with the laser beam causes a rise in gas temperature at short times and cooling of gas at times longer than the relaxation time of the upper laser level. It means that spatial nonuniformities of the pulsed laser beam cause the formation of a respective nonuniform spatial distribution of gas temperature, which, in turn,

brings about acoustic disturbances. Refractive index gradients associated with gas density changes are a source of light scattering (aberration) reducing laser beam quality. Such a phenomenon was observed in Reference [72], where it was given the name "laser-induced medium perturbation" and manifests itself in a severe degradation of the laser beam quality of a pulsed electric discharge CO_2 laser with the unstable resonator. Then, similar phenomena were observed by a number of research groups studying pulsed CO_2 lasers pumped by an electron-beam-sustained discharges and UV-preionized discharges [73–77]. In all cases, a significant reduction of laser beam power approaching the far-field aperture took place at a time scale of microseconds. A number of models have been developed to describe this phenomenon [73,75–78] and to identify conditions for its occurrence. It was found that the development of medium perturbations was initiated by the stepwise spatial distribution of the laser intensity, typical for unstable resonators. The simplest trick to diminish the degradation degree of laser beam quality on a microsecond scale is the usage of helium-rich mixtures. Helium has about ten times smaller Gladstone—a Dale constant than other gases resulting in a decrease in the aberration amplitude. Besides, higher sound velocity helps to quickly remove the acoustic perturbations from the laser beam aperture.

This mechanism of the mode–medium interaction (self-action in the Russian literature) can cause an oscillatory instability and severe degradation of laser beam quality in CW fast transverse flow CO_2 lasers with high-pressure gain medium in a variety of ways [65,79–83]. Gas-dynamic perturbations induced by laser intensity fluctuations in the resonator can influence the threshold gain through the modulation of an optical wedge at the resonator axis and resonator magnification [80,81]. An explicit expression for the rate of the instability growth induced by these effects is given in Reference [81] for conditions typical for fast-flow CO_2 lasers.

Acoustic waves excited by laser field fluctuations propagating at a small angle, θ, to the optical axis $\theta \approx U/c_s$ (U is the flow velocity and c_s is the sound velocity), against gas flow, remains within the resonator zone for a long time [80,82]. An explicit criterion for the development of the opto-acoustical instability for typical conditions of the fast-flow CO_2 laser was derived by in Reference [82]. In an experimental construction of the fast-flow CO_2 laser, the necessity to form a uniform gas flow at the inlet of an active zone leads to the appearance, in the gas-dynamic duct, of units that reflect acoustic waves propagating along the flow. Then a resonator could be formed for the acoustic waves (it is expected that the length of such an acoustic resonator is much greater than the width of the optical resonator zone). Conditions when acoustic disturbances in such a resonator grow because of a positive feedback between light and sound fluctuations, produced by this mode–medium interaction, were analyzed in Reference [83].

The combination of the described mechanisms resulting in the onset of the spiky mode and the accompanying dramatic fall of the laser optical beam quality is the reason for stopping the program of development of high-power CO_2 lasers with excitation by the e-beam-sustained discharge [79,80].

Along with the development of optical nonuniformities with spatial sizes on the order of the resonator aperture, the formation of small-scale (0.2–0.4 mm) perturbations was observed in pulsed photodissociation iodine lasers within a few microseconds [84,85]. The mechanism of this instability was proposed in Reference [84]. It is essentially the same as the mechanism of the mode-medium interaction discussed here. The upper laser level in the photodissociation iodine laser is a metastable atomic level, while the lower level is the ground state of iodine atom. The most important relaxation processes in the photodissociation I laser are reactions of chemical recombination.

$$R + I \rightarrow RI \quad \text{and} \quad R + I^* \rightarrow RI.$$

Here, R is a radical formed by photodissociation of a source species, I, I* are the iodine atoms in ground and metastable states, respectively. Recombination reactions proceed with the release of a high-energy quantum into the translational motion. It turned out that the recombination of I atoms in the ground state is much faster than that in the metastable state. Because of this, wave field-induced transitions accelerate gas heating. Typical rates of gas heating stimulated by laser emission are rather high ($\sim 10^6$ s^{-1}). Therefore, in searching a response of the refractive index to fluctuations of the wave field, one has to consider both acoustic and temperature waves simultaneously. It corresponds to the parallel development of stimulated Rayleigh and Brillouin scattering (SRS and SBS). A linear theory of perturbations developed in Reference [86] for conditions of the photodissociation I laser has predicted that the rate of the SRS development is twice as high as that of the SBS. The linear theory predicted characteristic times and spatial scale in reasonably good agreement with the experiments [84,85].

Actually, deep similarities exist between the mode–medium interaction mechanisms in the photodissociation I laser and the electric-discharge CO_2 laser. The major difference is that the energy quantum released to gas heating in I laser is about an order of magnitude larger than in the CO_2 laser. Therefore, similar processes of the SRS and SBS are expected to occur in high-pressure CO_2 lasers, too. The theory of stimulated scattering in the inverted medium of CO_2 lasers was developed in Reference [87]. Specific features of development of these processes in CO_2 lasers, associated with the geometry of an unstable resonator were analyzed in Reference [88]. The role of converging waves appearing in the resonator because of scattering by gratings of gain and index induced by interfering waves was theoretically evaluated.

REFERENCES

1. Weinstein, L., *Open Resonators and Open Waveguides*, Golem, Boulder, 1969.
2. Siegman, A.E., *Lasers*, University Science Books, Mill Valey, California, 1986.
3. Anan'ev, Yu.A., *Laser Resonators and the Beam Divergence Problem*, Adam Hilger, Bristol, 1992.
4. Oughstun, K.E., Unstable resonator modes, in *Progress in Optics*, Vol. xxiv, Wolf, E., Ed., North-Holland Publishing Company, Amsterdam, 1987, p. 165.
5. Fox, A.G. and Li, T., Resonant modes in a maser interferometer, *Bell Syst. Technol. J.*, 40, 453, 1961.
6. Siegman, A.E. and Miller, H.Y., Unstable optical resonator loss calculations using the Prony method, *Appl. Opt.*, 9, 2729, 1970.
7. Murphy, W.D. and Bernabe, M.L., Numerical procedures for solving nonsymmetric eigenvalue problems associated with optical resonators, *Appl. Opt.*, 17, 2358, 1978.
8. Krylov, A.N., On the numerical solution of equations whose solution determines the frequency of small vibrations of material systems, *Izv. Akad. Nauk SSSR, Ser. Fiz.-Mat.*, 4, 491, 1931 (Russian).
9. Latham, W.P. and Dente, G.C., Matrix methods for bare resonator eigenvalue analysis, *Appl. Opt.*, 19, 1618, 1980.
10. Demmel, J.M., *Applied Numerical Linear Algebra*, SIAM, Philadelphia, 1997.
11. Rensch, D.B., Three-dimensional unstable resonator calculations with laser medium, *Appl. Opt.*, 13, 2546, 1974.
12. Siegman, A.E. and Sziklas, E.A., Mode calculations in unstable resonators with flowing saturable gain. 1: Hermite–Gaussian expansion, *Appl. Opt.*, 13, 2775, 1974.
13. Sziklas, E.A. and Siegman, A.E., Mode calculations in unstable resonators with flowing saturable gain. 2: Fast Fourier transform method, *Appl. Opt.*, 14, 1874, 1975.
14. Fleck, J.A., Morris, J.R., and Feit, M.D., Time-dependent propagation of high energy laser beams through the atmosphere, *Appl. Phys.*, 10, 129, 1976, App. A.
15. Lax, M. et al., Electromagnetic-field distribution in loaded unstable resonators, *J. Opt. Soc. Am. A*, 2, 731, 1985.
16. Kuznetsova, T.I. and Rautian, S.G., About instability of regime of monochromatic radiation generation in solid state optical quantum generators, *Sov. Solid State Phys.*, 5, 2105, 1963 (Russian).

17. Tang, C.L., Statz, H., and de Mars, G.A., Spiking behavior of solid-state lasers, *J. Appl. Phys*., 34, 2289, 1963.
18. Statz, H. and Tang, C.L., Multimode oscillation of solid state lasers, *J. Appl. Phys*., 35, 1377, 1964.
19. Korotkov, V.A. et al, Stability of phase-lokced lasing in a two coupled unstable resonator system, *SPIE Proc*., 1031, 229, 1990.
20. Elkin, N.N. et al., Influence of active medium on the mode structure of optical resonator near the loss degeneracy point, *SPIE Proc*., 1224, 172, 1990.
21. Elkin, N.N., Napartovich, A.P., and Troshchieva, V.N., Diffraction model of a laser locked by an external signal, *Sov. J. Quant. Electron*., 24, 40, 1994.
22. Elkin, N.N. et al., Diffraction calculations of the field in a composite 3-mirror unstable resonator, *Sov. J. Quant. Electron*., 18, 1026, 1988.
23. Apollonova, O.V. et al., Mathematical simulation of composite optical systems loaded with an active medium, *Laser Phys*., 2, 227, 1992.
24. Vitshas, L.N. et al., Control of the spectral structure of the radiation emitted from an atmospheric-pressure CO_2 laser with the pulse duration of 40 μs, *Sov. J. Quant. Electron*., 20, 50, 1990.
25. Latham, W.P., Rogers, M.E., and Palma, G.E., A review of laser device coupling techniques, *SPIE Proc*., 1224, 184, 1990.
26. Likhanskii, V.V. and Napartovich, A.P., Radiation of optically coupled lasers, *Sov. Phys. Usp*., 33, 228, 1990.
27. Glova, A.F., Phase locking of optically coupled lasers, *Quant. Electron*., 33, 283, 2003.
28. Elkin, N.N. et al., Collective modes of coupled unstable resonators, *Sov. J. Quant. Electron*., 19, 66, 1989.
29. Erkkila, J.Y., Shakir, S., and Hedin, V.E., Diffraction analysis of adjoint coupled unstable resonators, *SPIE Proc*., 1224, 210, 1990.
30. Elkin, N.N. et al., Simulation of phase locking of two lasers with hybrid resonators, *Quant. Electron*., 32, 692, 2002.
31. Yariv, A., *Quantum Electronics*, John-Wiley & Sons, New York, 1967.
32. Maitland, A. and Dunn, M.H., *Laser Physics*, North-Holland Publishing Company, Amsterdam, 1969.
33. Chodzko, R. and Chester, A., in *Handbook of Chemical Lasers*, chap. 3, Gross, R.W.F. and Bott, J.F., Eds., John-Wiley & Sons, New York, 1976.
34. Zvelto, O., *Principles of Lasers*, Plenum Press, New York, 1982.
35. Siegman, A.E., Unstable optical resonators for laser applications, *Proc. IEEE*, 53, 277, 1965.
36. Anan'ev, Yu.A., Angular divergence of radiation of solid-state lasers, *Sov. Phys. Usp*., 14, 197, 1971.
37. Anan'ev, Yu.A., Establishment of oscillations in unstable resonators, *Sov. J. Quant. Electron*., 5, 615, 1975.
38. Phillips, E.A., Reilly, J.P., and Northam, D.B., Off-axis unstable laser resonator: operation, *Appl. Opt*., 15, 2159, 1976.
39. Kuprenyuk, V.I. et al., On calculation of unstable resonators with field rotation in the wave approximation, *Sov. J. Quant. Electron*., 13, 1613, 1983.
40. Zavgorodneva, S.I. et al., On the conversion of the unstable-resonator laser radiation by means of the conical optics, *Sov. J. Quant. Electron*., 10, 79, 1980.
41. Jackson, P.E., Baker, H.J. and Hall, D.R., CO_2 large-area discharge laser using an unstable-waveguide hybrid resonator, *Appl. Phys. Lett*., 54, 1950, 1989.
42. Wildt, D., Space-based chemical lasers in strategic defense, *AIAA 92-2976*, AIAA 23rd Plasmadynamics & Lasers Conference, Nashville, TN, 1992.
43. Ehrlichmann, D. et al., Azimuthally unstable resonators for high power CO_2 lasers with annular gain media, *IEEE J. Quant. Electron*., 30, 1441, 1994.
44. Lapucci, A. et al., Beam quality enhancement for a radio-frequency excited annular CO_2 laser, *Appl. Phys. Lett*., 73, 2549, 1998.
45. Napartovich, A.P., Elkin, N.N., and Vysotsky, D.V., Simple way for in-phase mode selection in laser with annular gain region, *SPIE Proc*., 4184, 431, 2000.
46. Talbot, H.F., Facts relating to optical science. No. IV, *Edin. Soc. Philos. Mag*., 9, 401, 1836.
47. Rayleigh, Lord, On copying diffraction-gratings, and on some phenomena connected therewith, *Philos. Mag*., 11, 196, 1881.

48. Antyukhov, Y.V. et al., Effective phase locking of an array of lasers. *JETP Lett*., 44, 78, 1986.
49. Belanger, P.A. and Pare, C., Optical resonators using graded phase mirrors, *Opt. Lett*., 16, 1057, 1991.
50. Pare, C. and Belanger, P.A., Custom laser resonators using graded-phase mirrors, *IEEE J. Quant. Electron*., 28, 355, 1992.
51. Leger, J.R., Chen, D., and Wang, Z., Diffractive optical element for mode shaping of a Nd:YAG laser, *Opt. Lett*., 19, 108, 1994.
52. Leger, J.R., Chen, D., and Dai, K., High modal discrimination in a Nd: YAG laser resonator with internal phase grating, *Opt. Lett*., 19, 1976, 1994.
53. Leger, J.R., Chen, D., and Mowry, G., Design and performance of diffractive optics custom laser resonator, *Appl. Opt*., 34, 2498, 1995.
54. Napartovich, A.P. et al., Simplified intracavity phase plates for increasing laser-mode discrimination, *Appl. Opt*., 38, 3025, 1999.
55. Ablekov, V.K. and Belaev, V.S., A system approach to a problem of optical resonator, *Zhurnal Prikl. Spectroscop*., 23, 1110, 1975 (Russian).
56. Marchenko, V.G., A study into fields of wide-aperture flat resonators, *Sov. J. Quant. Electron*., 8, 1037, 1981.
57. Ablekov, V.K. and Marchenko, V.G., Intracavity transformation of wave fields in wide-aperture flat resonators, *Zhurnal Prikl. Spectroscop*., 44, 25, 1986.
58. Kozlov, S.N. and Napartovich, A.P., Numerical investigation of modes of a plane-parallel cavity with periodic mirrors, *Sov. Laser Res. J*., 13, 54, 1992.
59. Bagdasarov, Z.E. et al., A study into some features of shaping of laser radiation pattern in resonators with retroreflecting mirrors. *Sov. J. Quant. Electron*., 11, 1465, 1981.
60. Basov, N.G. and Oraeviskii, A.N., Attainment of negative temperatures by heating and cooling of a system, *Sov. J. Exp. Theor. Phys*., 44, 1742, 1973.
61. Gerry, E.T., Gasdynamic lasers, 9th Aerospace Sciences Meeting, *AIAA Paper No. 71-23*, New York, 1971. Also *IEEE Spect*., 7, 51–58, 1970.
62. Vedenov, A.A. et al., Calculation of energy characteristics of the electric discharge CO_2 laser, *Sov. J. Quant. Electron*., 5, 1404, 1975 (Russian).
63. Krasitskaya, L.S. and Napartovich, A.P., On calculation of Fabry-Perot resonator modes in fast-flow laser, *Teplofizika Vysokikh Temperatur*, 4, 1973 (Russian).
64. Drezin, Yu.A. and Dykhne, A.M., Self-oscillating instability of fast-flow lasers using unstable resonators, *JETP Lett*., 19, 371, 1974.
65. Yoder, M.J. and Ahouse, D.R., Output flux instabilities in a flowing-gas CW CO_2 electric discharge laser, *Appl. Phys. Lett*., 27, 673, 1975.
66. Artamonov, A.V. and Naumov, V.G., On stability of the stimulated emission from the fast-flow transverse-priming CO_2 laser, *Sov. J. Quant. Electron*., 7, 101, 1977.
67. Alme, L.M., Temporal oscillations in the output from a gas dynamic laser with an unstable resonator, *Appl. Phys. Lett*., 29, 35, 1976.
68. Mirels, H., Temporal stability of unstable resonator with cross flow, *Appl. Phys. Lett*., 28, 612, 1976.
69. Likhanskii, V.V. and Napartovich, A.P., On self-oscillation instability in fast-flow lasers with unstable resonators, *Sov. J. Quant. Electron*., 2 (Suppl. 10), 139, 1980.
70. Likhanskii, V.V. and Napartovich, A.P., Radiation dynamics of the fast-flowing CO_2 lasers with unstable resonators, *Izv. Akad. Nauk SSSR, Ser. Fiz*., 45, 399, 1981 (Russian).
71. Likhanskii, V.V. and Napartovich, A.P., Intensity response on the input fluctuations of the active medium parameters in the fast flow laser, *Opt. Commun*., 32, 309, 1980.
72. Roper, V.G. et al., Laser induced medium perturbation in a pulsed CO_2 laser, *Opt. Commun*., 25, 235, 1978.
73. Suhre, D.R. et al., Laser induced medium perturbation in a large CO_2 laser, *J. Appl. Phys*., 65, 954, 1989.
74. Dimakov, S.A. et al., Influence of thermal nonlinearity on the dynamics of radiation from an electron beam-controlled CO_2 laser with an unstable resonator, *Sov. J. Quant. Electron*., 17, 290, 1987.
75. Dente, G., Phase grating effects in pulsed CO_2 lasers, *SPIE Proc*., 293, 153, 1981.
76. Galushkin, M.G. et al., Self-interaction of radiation in a CO_2 laser resonator, *Sov. J. Quant. Electron*., 15, 570, 1985.

77. Dimakov, S.A. et al., Influence of self-interaction on the field structure of an electron beam-controlled CO_2 laser with an unstable resonator, *Sov. J. Quant. Electron.*, 15, 849, 1985.
78. Glessner, J.W. et al., Review of oscillator performance for electric lasers, *SPIE Proc.*, 1224, 44, 1990.
79. Perressini, E.R. and Parazzoli, C.G., Mode medium interaction in continuous wave (CW) flowing gas laser, *SPIE Proc.*, 138, 84, 1978.
80. Hill, R.A. and Peressini, E.R., Suppression of mode medium interaction in CW EDLs, in *Gas Flow and Chemical Lasers*, Wendt, J.F., Ed., Hemisphere Publishing Corporation, New York, 1979.
81. Deryugin, A.A., Likhanskii, V.V., and Napartovich, A.P., A novel mechanism of the output modulation in an unstable-resonator laser, *Sov. J. Quant. Electron.*, 15, 198, 1985.
82. Likhanskii, V.V. and Napartovich, A.P., On sound excitation in an unstable resonator laser, *Sov. J. Quant. Electron.*, 11, 96, 1981.
83. Deryugin, A.A., Likhanskii, V.V., and Napartovich, A.P., Sound vibrations in an unstable-resonator gas-flow CO_2-laser, *Sov. J. Quant. Electron.*, 16, 621, 1986.
84. Zuev, V.S., Netemin, V.N., and Nosach, O.Yu., Instability of iodine laser radiation wavefront and dynamics of development of optical inhomogeneities in the laser medium, *Sov. J. Quant. Electron.*, 9, 522, 1979.
85. Alyokhin, B.V. et al., Development of optical inhomogeneities in flashlamp photolysis lasers with short pump duration, *Sov. J. Quant. Electron.*, 10, 872, 1980.
86. Likhanskii, V.V. and Napartovich, A.P., On the development of fine-scale inhomogeneities in photo-dissociation lasers, *Sov. J. Quant. Electron.*, 11, 384, 1981.
87. Bel'dyugin, I.M. et al., Stimulated light scattering in an inverted carbon dioxide gas due to thermal nonlinearity, *Sov. J. Quant. Electron.*, 13, 523, 1983.
88. Deryugin, A.A., Likhanskii, V.V., and Napartovich, A.P., Stimulated light-scattering in an unstable resonator, *Sov. J. Quant. Electron.*, 16, 1123, 1986.

4 Electric Circuits

Vladimir V. Khukharev

CONTENTS

4.1 GENERAL ASPECT OF IONIZED GAS DISCHARGE

One of the most effective ways of pumping (excitation) a gas mixture in laser facilities is electric discharge. An electric field is applied within a gaseous medium; the field produces and accelerates the free electrons within that medium to velocities of 10^6 to 10^7 m/s [1]. These electrons then collide with the atoms or molecules in their ground state within the discharge and produce transitions at excited energy states. In electric-discharge gas lasers, the gas mixture turns into low-ionized nonequilibrium plasma. Vibrational energy levels of the working gas are excited by direct collision with the electrons and ions of a current or, more apparently and effectively indirectly, by collision with the atoms and molecules of other gases excited directly by the current. A glow discharge is a type of discharge that is most widely used in laser technologies. The glow discharge is a self-sustained discharge with a cold cathode, emitting electrons as a result of secondary emission, mainly under the action of positive ions. Its distinguishing feature is the presence of a layer with a strong field close to the cathode surface and a considerable potential fall (100 to 400 V and above) named the "cathode drop." The thickness of the cathode drop is inversely proportional to the pressure (density) of the gas mixture; for example, for an air with $p \times d = 39.5$ Pa $\times$ cm, where p is the air pressure and d is the cathode layer thickness. Near an anode, there is a layer of anode potential fall that is much less than a cathode fall. Between these two layers is located a positive discharge column, which is a less-ionized nonequilibrium plasma supported by an electrical field. Current density in the positive discharge column of the glow discharge is between 10^{-3} and 10^{-1} A/cm^2 and the voltage is between 100 V and 10 kV for pressures ordinarily used in laser technologies. The temperature of neutral atom and molecules and ions is about a few hundred kelvins. At the same time, electrons have a temperature that is of the order of thousands of degrees, or the electron energy is 1 to 2 eV. A glow discharge is an unstable type of discharge as it easily turns to an arc discharge mode.

Arc discharge is a self-sustaining discharge in which a cathode potential drop has a low value (~10 V). The cathode ejects electrons as a result of thermionic emission, field emission, or thermo-field emission. Arc current density is normally from 10^2 to 10^4 A/cm^2 but can reach even 10^7 A/cm^2. The voltage of arc discharge is between 10 and 100 V. Cathodes in

arc discharge mode are partially or entirely incandescent, and erode, that is, they crumble with the removal of the cathode material.

When a glow discharge slides down to the form of an arc, at first only the brighter light is seen by the spectator at a separate point, and the rest of the discharge zone remains occupied by a glow discharge. Current continues to increase in that local point; the glow discharge occupies less and less volume and then dies down. Only one bright line remains in the discharge volume. It is an arc. Sometimes during the operation of a gas-discharge laser devise, a process of glow discharge contraction into an arc line is seen.

There is an entire series of instabilities of a glow discharge in laser plasma. First of those are ionizing, overheating, and ionizing–overheating states [2]. For example, under conditions of constant gas pressure, electrical field voltage and current density, overheating instability develops according to the following diagram:

$$T_\alpha \uparrow \rightarrow n_\alpha \downarrow \rightarrow c_\mathrm{p} \downarrow \rightarrow T_\alpha \uparrow, \tag{4.1}$$

where T_α is the temperature in a local point, n_α the particle concentration at the same local point, and c_p is the heat capacity at the same local point.

It is seen that an increase in local fluctuating temperature leads to a decrease in density, and to a subsequent decrease in heat capacity, which, under conditions of constant heat input into the volume unit, results in further increase in temperature. Why is such temperature increase dangerous to gas discharge? Resistance of the discharge gap at a local spot decreases with temperature increase at the spot, and hence discharge currents also increase. It leads to further heating of increased volumes of gas and subsequent cathode heating, and the chain goes on. Finally, we have an increase in discharge current, decrease in discharge voltage, and a different mode of discharge, an arc mode. Glow discharge contraction destructively affects laser generation in the laser volume.

Another mechanism of losing stability is an ionization-overheating instability, acting as shown in the following diagram:

$$n_\mathrm{e} \uparrow \rightarrow jE \rightarrow T \uparrow \rightarrow N \downarrow \rightarrow E/N \uparrow \rightarrow n_\mathrm{e} \uparrow. \tag{4.2}$$

Here, n_e is the concentration of electrons, j the current density, E the electric field strength, T the gas temperature and N is the density of molecules number. Ratio E/N is a fundamental parameter, characterizing the efficiency of the optimal energy input for the excitation of necessary laser energy levels in case of electric discharge pumping. The value of E/N_critical is an important discharge parameter limiting energy input [2–4]. At the same time, parameter E/N characterizes ionization efficiency, which clearly depends on E/N [2].

In the case of accidental increase in electron concentration at some point of the discharge, conductivity and current density also increase; it also results in an increase in temperature at the same point and a decrease in the density of the molecule number. Hence, the ratio E/N also increases and the ionization process rate sharply increases. Electron concentration at this point increases even further and the chain of instability is closed.

What mechanisms promote discharge stability? All processes of heat and mass transmission equalizing temperature and concentration fields lead to dispersal of fluctuations and therefore to increase in discharge stability. Therefore, any means of increasing heat transmission coefficient lead to discharge stabilization. The following means are of this type: increasing of partition of gas with high heat conductivity, for example, helium; transition to turbulent flow and intensification and homogenization of turbulent pulsations, for example by installation of turbulence promoter on the inlet of the gas discharge chamber. An effective way of decreasing discharge instability is by pumping gas through the discharge chamber. It is a

method of effective cooling of a working gas mixture and at the same time it leads to the removal of the developed heat fluctuations from the glow discharge zone and results in an increase in discharge stability. However, increasing gas velocity demands additional energy consumption and is limited by some other reasons.

A discharge with short pulses is more stable than that with long pulses or DC discharge because during the shorter pulse there is not enough time for random fluctuation to develop into the contracting line. The stability of the discharge can be also enhanced by adding designing elements such as ballast resistors. They are located in an electric circuit serially with the discharge. At this discharge gap, voltage U is defined by the following relationship:

$$U = \varepsilon - I \times (R_{\mathrm{b}} + R_{\mathrm{ps}}), \tag{4.3}$$

where ε is an electromotive force (EMF), I a total discharge current, R_{ps} the resistance of the power supply, and R_{b} is the ballast resistance, which is much higher than R_{ps}. Analyzing this formula, one can see that when the current increases with a value of δI, the discharge gap voltage U falls with a value of $\delta I \times (R_{\mathrm{b}} + R_{\mathrm{ps}})$, which leads to a decrease in the total discharge current and gives a value of current back to the previous one. Another positive influence of the ballast resistor is that it limits the total discharge current to a value of

$$I_{\mathrm{sc}} = \frac{\varepsilon}{(R_{\mathrm{b}} + R_{\mathrm{ps}} + R_{\mathrm{dg}})}, \tag{4.4}$$

and hence preserves the power supply from damage.

Ballast resistors are physically united into a block. A diagram of a block of ballast resistors (BBR) joined into an electric circuit is shown in Figure 4.1.

Let us compare two variants of BBR: one with a sectioned electrode and a single common resistor for all electrode elements and the other with each plate element connected to its own resistor. In the first case, the voltage at the discharge gap is

$$U = \varepsilon - I \times R, \tag{4.5}$$

where I is the total current through all electrode elements and R is the resistance value. In the second case, by neglecting the inner resistance of the power supply the following value of the discharge gap voltage can be arrived at, which is common for all electrode elements:

$$U = \varepsilon - i \times r, \tag{4.6}$$

where ε is the EMF of the power supply, I the current through an element of the electrode's sectioned plate and r is the resistance value of the block resistor.

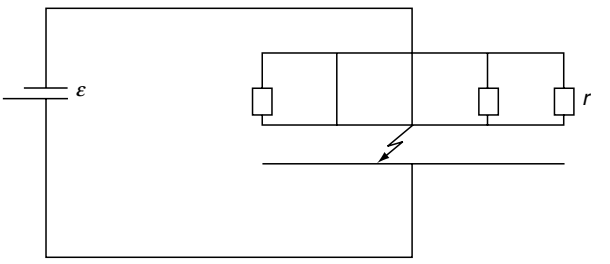

FIGURE 4.1 A diagram of the joined block of BBR.

Comparing the discharge with different BBR is necessary to consider the same energetic regime. Suppose the number of electrode elements is n, we receive

$$I = i \times n. \tag{4.7}$$

Equating discharge gap voltages in Equation 4.5 and Equation 4.6, we receive

$$R = r/n. \tag{4.8}$$

Parasitic heat generation in the BBR resistors is RI^2 for the first variant and $n(ri^2)$ for the second variant. Taking into account Equation 4.6 and Equation 4.7, we get

$$R \times I^2 = \frac{r}{n} \times (n \times i^2).$$

It means that no one variant has the advantage of comparing with another on the basis of energy loss.

If in a glow discharge in the discharge chamber a fluctuation of current δi through a single element appears, negative feedback response in the first BBR variant is $\delta U_1 = \delta i\, R$, as long as

$$U_1 - \delta U_1 = \varepsilon - (I + \delta i) \times R = \varepsilon - I \times R - \delta i \times R.$$

For the second BBR variant

$$U_2 - \delta U_2 = \varepsilon - (i + \delta i) \times r = \varepsilon - i \times r - \delta i \times r.$$

Taking into account Equation 4.8, we have

$$\delta U_2 = \delta i \times r = \delta i \times R \times n = \delta U_1 \times n.$$

Therefore, the stabilizing action of the BBR is n times more for the second BBR variant with the same energy loss. The second variant is more preferable because of successive ignition of glow discharge at all electrode elements.

For the stable operation of a discharge chamber, 20% to 40% of energy put into a discharge should be dissipated in a BBR. For example, let energy input in a discharge chamber be 40 kW, discharge current be 10 A and discharge voltage 4 kV. In that case, energy release in the BBR must be no less than 8 kW. Consider this figure as necessary to calculate parameters of resistors. As long as the maximum current through a single cathode element is 0.1 A, the necessary number of cathode elements, and hence the ballast resistors, is

$$n = \frac{I}{i} = \frac{10}{0.1} = 100.$$

Power dissipated in a separate resistor N_r is calculated as

$$N_\mathrm{r} = \frac{N_\mathrm{BBR}}{n} = \frac{8 \times 10^3}{10^2} = 80\ \mathrm{W}.$$

As soon as $N_\mathrm{r} = r \times i^2$, resistance value of one resistor is given as

$$r = \frac{N_\mathrm{r}}{i} = \frac{80}{0.1^2} = 8 \times 10^3\ \mathrm{Ohm}.$$

Therefore, under the assumption of equality of currents over all cathode elements and equality of their ballast resistor values, we have found that in the BBR there must be 100 resistors of 8 kΩ each with a current of 0.1 A through each and an energy dissipation of 80 W.

Good effect is obtained by sectioning one of the electrode plates, usually the cathode. This electrode is divided into separate elements, each of them connected to the power supply through its own ballast resistor. In this design, even transition of one or several elements (from the total number of hundreds or thousands) to the contracting regime does not distinctly influence the operation of other elements.

Other factors positively influencing the discharge stability are smoothing of flow velocity field, minimization of all possible heterogeneousness and injurious products of the working mixture decay, which provoke fluctuations of the gas mixture and discharge parameters.

A determinative feature of electrodischarge gas lasers is the directional shift of the charged particle groups in an electric field. When building advanced mathematical models of flow in a gas discharge chamber, many factors are taken into account, such as gas-dynamic, quantum-mechanical and electro-technical natures [3,4]. Nevertheless, in discharge and laser techniques people often digress from processes in the discharge gap using volt–ampere characteristics (VAC method) for gas-discharge description. VAC is a relation between discharge gap voltage and current through this gap. VAC does not give a unique value of current or voltage, but just connects them with each other by a relation of $U = U(I)$. There are many VACs of the discharge in the same gap of the gas depending on how one or the other value of the current was received, namely, rise or fall of current, what was the rate of the changing etc. In contrast to the dynamic VAC, differing from each other, there is only one static VAC, obtained at the stationary values of the current. To obtain VAC, a discharge gap is connected with an electric circuit in accordance with the diagram shown in Figure 4.2, where R_{gap} is the resistance of the discharge gap, R_{out} the resistance of the external circuit and ε is the EMF of the power supply.

Discharge gap voltage U may be expressed by the following relation:

$$U = \varepsilon - I \times R_{out}. \tag{4.9}$$

Considering Equation 4.9 together with the relation $U = U(I)$, which is discharge VAC, an equation is obtained to determine the working point:

$$\varepsilon - I \times R_{out} = U(I). \tag{4.10}$$

From Figure 4.2, it is obvious that the working point can be changed by varying ε or R_{out}. In Figure 4.3, the graphical means of determining a working point is shown [5].

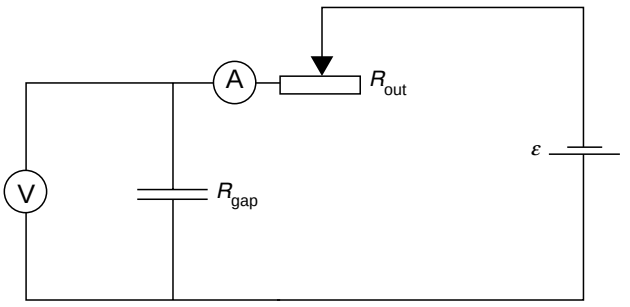

FIGURE 4.2 A diagram VAC recording.

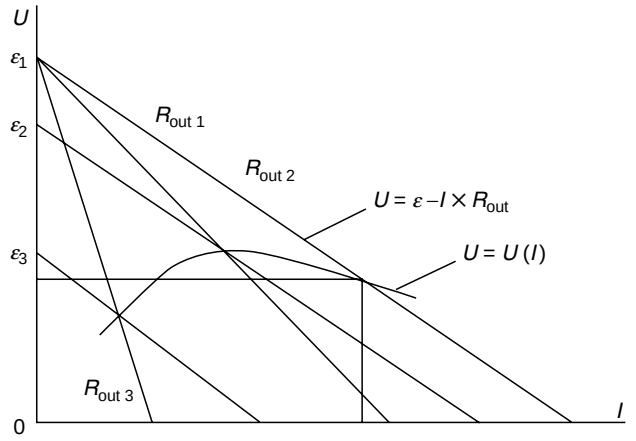

FIGURE 4.3 Finding a working point.

It is possible to receive a VAC curve by varying the values of ε and R_{out} separately or simultaneously and fixing U and I for every new value of ε or R_{out}. Typical gas-discharge VAC is presented in Figure 4.4 [5].

In the VAC shown in Figure 4.4, OABCD is a region of a non-self-sustained discharge, existing only under the condition of external ionization of gas in a discharge. Field energy is not enough to support the mechanism of delivery of new charged particles. Without connection to a source of external ionization, discharge does not exist in this region. DEFGHK is a region of self-sustained discharge. In this region, field energy is enough to support conductivity by gas ionization with electron impacts and by the secondary electron emission from a cathode because of bombing by positive ions. External sources of ionization are not needed. External ionizers that are sometimes used in facilities with a self-sustained discharge perform a secondary role of increasing the discharge stability and quality.

4.2 SELF-SUSTAINED VS. NON-SELF-SUSTAINED DISCHARGES

In the area OA of VAC (Figure 4.4), resistance of the gas gap is constant and dependence $U = U(I)$ is linear. In the area BC, the discharge current is constant, independent of discharge gap voltage and is referred to as saturation current. Area AB is a transitional zone between these areas. Electric field intensity growth over point C at the VAC curve leads to a situation

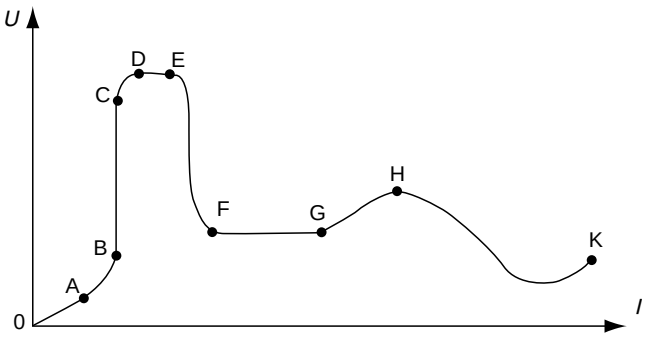

FIGURE 4.4 General view of gas-discharge VAC.

when electron energy becomes enough for the generation of considerable number of secondary electrons in the process of collision in a gas mixture. The number of electrons emitted by the cathode because of bombing by positive ions also becomes noticeable. Although the sum of the of generating and dying electrons is still negative, that is, a self-sustained discharge cannot exist, yet, in the area CD of VAC a growth of non-self-sustained discharge current is observed. Requirement for self-sustained discharge ignition is the equality of the number of electrons generated at the cathode surface plus the number of electrons generated in the discharge volume as the result of collisions with a number of dying electrons. Making up such a balance, a value of voltage for self-sustained discharge ignition (U_{ign}) is obtained as follows:

$$U_{ign} = \frac{p_0 \times H \times B}{\ln[p_0 \times H \times A/(1+\gamma^{-1})]},$$

where p_0 is the gas pressure, H the interelectrode gap height, γ the average number of electrons emitted by one positive ion reaching the cathode, and A, B are gas constants.

In Figure 4.5, Pashen's curves are presented describing the relationship $U_{ign} = U_{ign}(p_0 \times H)$ for different gases. The area DE of VAC is an area of self-sustained discharge existing at discharge ignition voltage. It is referred to as Townsend discharge or "dark discharge". The luminescence of the discharge cannot be seen and the current is rather small (10^{-10} to 10^{-5} A). Ordinary current-measuring devices cannot record such small values, but the presence of discharge and increasing current is justified by the fact that in spite of increase in ε, U does not increase (see Equation 4.3 and Equation 4.9).

With current growth over the point E, a field is formed near the cathode that is strong enough to comply with the self-sustaining discharge condition in the narrow area of the cathode potential drop. The field in the outside area just provides discharge gap conductivity. Total voltage at the discharge gap falls to a value less than U_{ign}. A glow discharge forms in the area that is on the right side of point F. From the beginning, it occupies only a part of the cathode area and the current density is referred to as "normal." With the increase

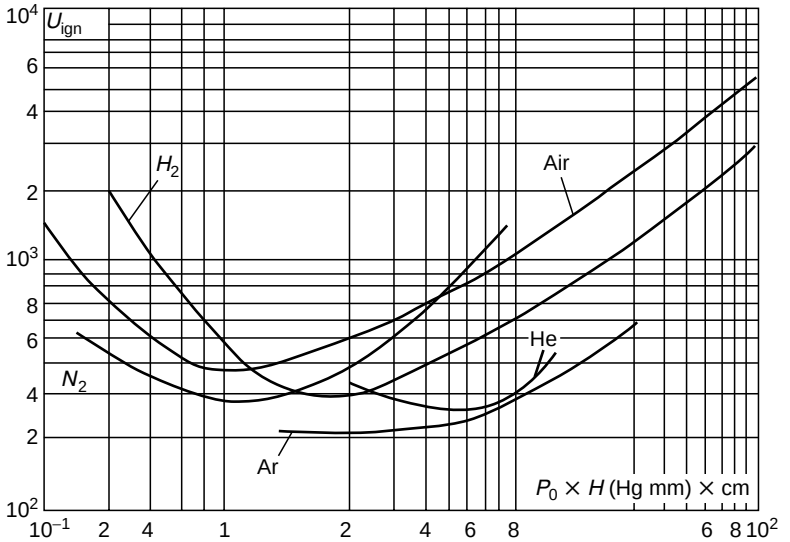

FIGURE 4.5 Pashen's curves for some gases.

in current, the cathode area occupied by the discharge increases and the current density remains "normal" (area FG). This takes place at almost constant discharge gap voltage. After all the cathode area is occupied by the discharge, current increases with simultaneous increase in current density and discharge gap voltage. This area, GH, is the area of "anomalous" glow discharge.

With further current increase, the cathode surface warms up and noticeable electron thermo-emission takes place. This results in even more warming up of the cathode surface. Positive feedback in this chain leads to the transfer of discharge to a new type—an arc discharge, which is the area to the right of point H.

The most effective method to get rid of discharge instability is the use of non-self-sustained discharge, in which functions of gas ionizing and electric power input for laser pumping are separated. This breaks the chain (Figure 4.2) in the last, most dangerous link: E/N increases do not have much influence on n_e.

In laser technology, there are three possible routine methods of non-self-sustained discharge creation in a given device: ionization by auxiliary pulse discharge, ionization by electron beam, and photoionization.

The following are the advantages of non-self-sustained discharge:

1. Possibility to work at optimal conditions of laser mixture excitation with discharge gap voltage from 0 to U_{ign}
2. Increased discharge stability, that is, the possibility to receive higher laser specifications
3. VAC increasing in all diapason that makes possible to work without ballast resistors and consequently without considerable energy loss

4.3 PULSING CIRCUITS

Factor limiting duration of a volume discharge in solid gases is the spontaneous development of spark channels with subsequent degradation of a glow discharge into an arc discharge. As a rule, to receive the utmost energy input, a forced (anomalous) mode of the glow discharge is used, characterized by higher current density and parameter E/N, which leads to consequent decrease in the maximum discharge duration.

Realized estimations show that, for example, molecular lasers of atmospheric pressure, excited by self-sustained glow discharge, can operate only in pulse or pulse-periodic modes with sufficiently large on–off time ratio.

For pumping pulse and pulse-periodic CO_2 lasers, different variants of systems with self-sustained discharge are developed and widely used [6]. Such systems are easier to operate; they do not demand protection against X-radiation appearing when an electron beam decelerates in a foil and in discharge electrodes, and the radiation energy that is generated by them is quite enough for different applications.

Consider various methods of forming pulse laser systems with a self-sustained discharge. A power supply pulse is formed either by the generator of pulse voltage (GPV) or the LC generator. A diagram of the GPV for feeding pulse lasers is presented in Figure 4.6 [7]. Here, R is the charging resistor; C the capacitance; C_1 and C_2 are the parasitic capacitances; D_1, D_2, and D_3 the discharges; D_{sh} a shorting discharger; R_l the load resistor; and U_{ch} is the charging voltage.

Designed output voltage defines the necessary number of GPV cascades. However, a large number of cascades make difficult the desirable decrease in generator inductance. Moreover, each discharger of the GPV must conduct total load current, which leads to axe their age.

LC generators (Figure 4.7) [7] do not have such disadvantages compared with an ordinary GPV.

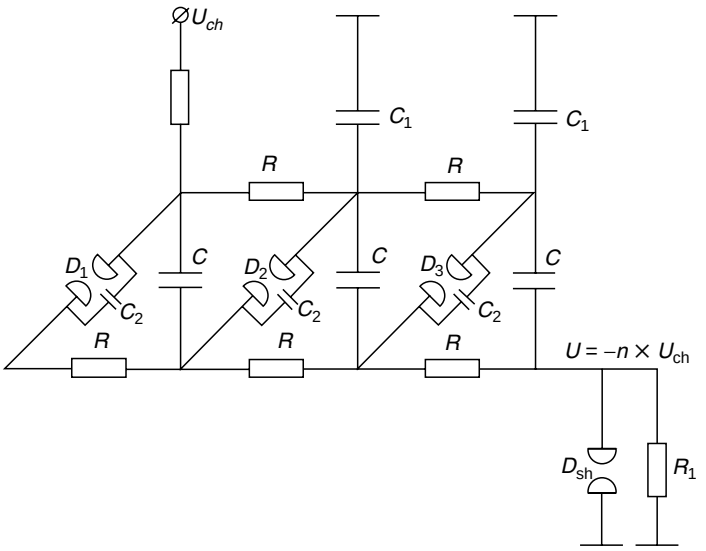

FIGURE 4.6 Generator of pulse voltage.

Inductance of the main circuit in an LC generator is less than in a GPV, as long as dischargers D_1, D_2, and D_3 are not included into the main circuit. From among known dischargers' designs, dischargers with field distortion have the best ignition stability [7] (Figure 4.8).

In these dischargers, trigger electrode 3 is a thin plate and is brought approximately in the line of the equipotential curve between the main electrodes 1 and 2. The potential on this electrode is maintained by the use of the ohmic divider (made up of resistors R_1 and R_2). The discharge gap is divided by the trigger electrode in the ratio of 2 to 1 (it is the best ratio, experimentally obtained) at which, this electrode is located closer to the main electrode that is earthed. Divider R_1R_2 shares the potential in the same ratio. For igniting the discharger, a pulse with front of 10 to 20 ns is put onto the trigger electrode. Such a pulse can be formed, for example, by using a thyratron scheme of ignition. A firing produces overvoltage of gaps 1–2 and 2–3 that leads to quick operation of dischargers. Such dischargers have a delay and the scattering of initiation in frames of 1 ns, at which the firing is of low power. This makes

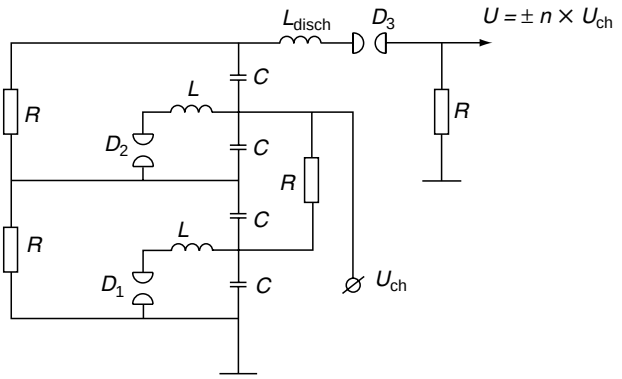

FIGURE 4.7 Circuit of an LC generator.

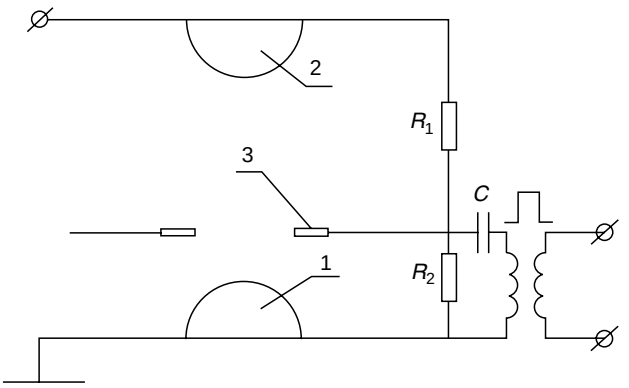

FIGURE 4.8 Discharger with field distortion.

possible the simultaneous initiation of several dischargers using a single firing. Such a design is especially convenient for GPVs.

Figure 4.9 shows the simplest scheme of pulse voltage provided by a GPV to the electrodes of the laser with self-sustained impulse discharge. High demanded values of E/N and difficulties of operation with high-voltage pulses make such schemes for laser medium excitation not much popular among users. Figure 4.10 shows the diagram of a Beaulieu laser [8] operating at atmospheric pressure of a working mixture and a rather low discharge voltage. In this design, sectioned cathodes of pins set, connected through resistors to the common bus, are used. Such cathode devices constrain (because of the negative feedback) prevalent rising of current through an individual cathode element and thus prevent conversion to an arc form. In this design, individual current channel fluorescence has a periodic arrangement.

Figure 4.11 shows another diagram of impulse power supply for a laser with sectioned cathode, where the cathode elements are small pipes; gas is blown through the pipes and then pumped out through the holes in the anode.

4.4 PREIONIZATION TECHNIQUES

As was mentioned earlier (in Section 4.2), there are three main methods of preionization of laser medium for creation of increased initial electron density in the discharge gap: ionization by auxiliary pulse discharge, ionization by electron beam, and photoionization.

In the first method (Figure 4.12), in addition to reduced waiting voltage there are high-voltage pulses produced, which generate sufficient number of charge carriers to initiate a self-sustained discharge.

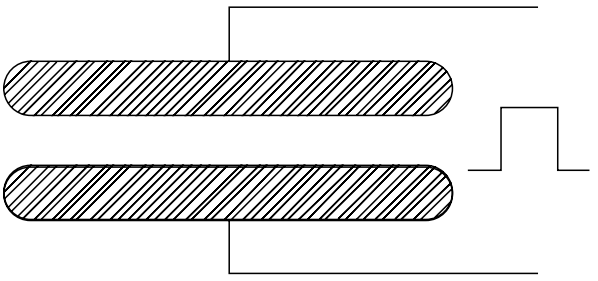

FIGURE 4.9 Scheme of pulse voltage feeding.

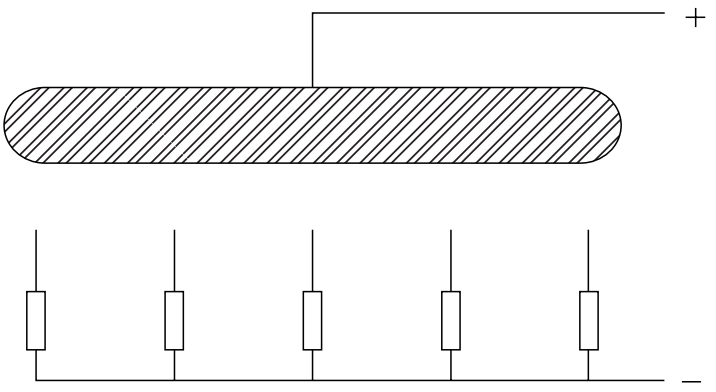

FIGURE 4.10 Beaulieu laser.

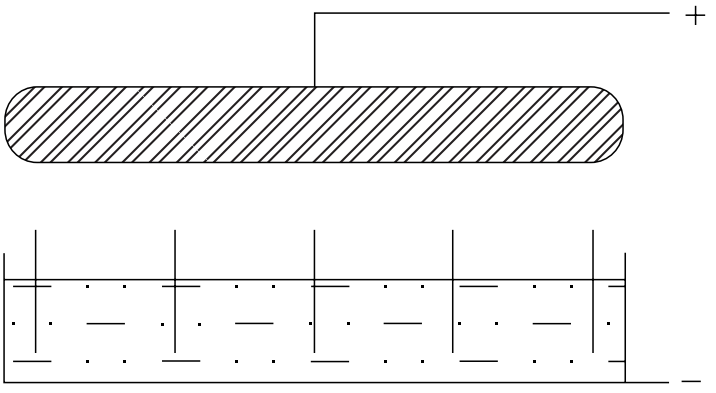

FIGURE 4.11 Pulse laser with self-sustained discharge.

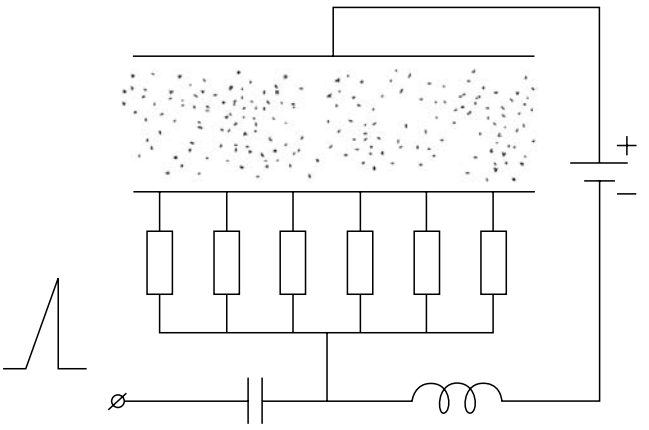

FIGURE 4.12 Preionizing by high-voltage pulse.

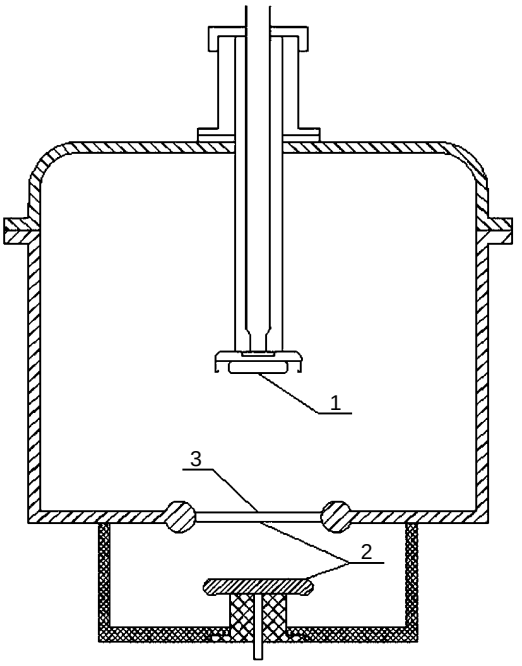

FIGURE 4.13 Laser with non-self-sustained discharge with electron beam preionization.

Ionization of gas in a discharge gap is produced by high-voltage independent subsidiary discharges periodically created using the same electrodes. The total voltage on the discharge gap in this case has a view of the periodic impulses against a background of the constant field. The value of the constant field is not high enough for supporting a self-sustained discharge but is just optimal to excite an active medium energy of secondary electrons. Generation of these electrons is produced at the stage of self-sustained discharge with increased values of current. In intervals between pulses in the discharge gap, there is non-self-sustained current in the decaying plasma [5].

In a scheme of non-self-sustained discharge with ionization by electron beam (Figure 4.13) [9], electrons ejected by the cold or hot cathode of the electron accelerator (called "gun") are accelerated on the accelerator electric field and are brought into the laser working volume through a foil on one of the electrodes. Acceleration is produced at a pressure of 10^{-7} to 10^{-10} Hg mm; so sealed foil must restrain pressure in the laser volume. Passing through a discharge gap, fast electrons produce homogeneous ionization of gas in the discharge gap and decelerate on the opposite electrode. Here, 1 is a cathode of electron accelerator; 2 the discharge gap electrodes; and 3 is a foil separating the accelerator chamber from the volume with the laser working medium.

Ionization by an electron beam is rather effective from an energy point of view. Nevertheless, this method has a disadvantage: the foil cost is too high and lifetime is too low, it needs frequent changing and this considerably raises the operating costs (though every year industry produces foils that are cheaper and have a longer lifetime).

In photoionization, a high-energy photon beam is created by special devices. For example, subsidiary discharge rich in utraviolet is ignited behind one of the electrodes. The light of this subsidiary discharge irradiates the main discharge gap through a hole in the electrode, producing gas ionization. In Figure 4.14, the most widespread schemes of positional

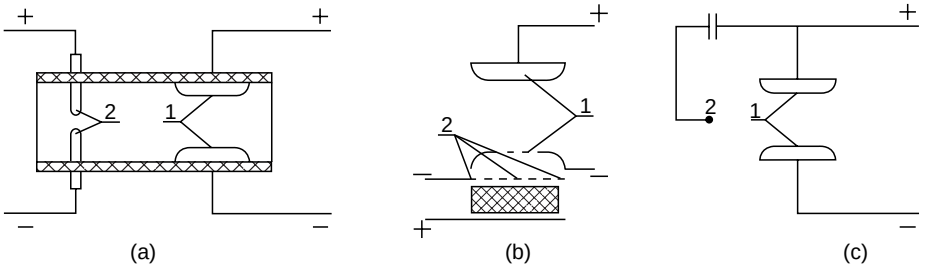

FIGURE 4.14 Schemes of positional relationship of the main and subsidiary discharges: (a) spark discharge, (b) creepage, and (c) corona discharge.

relationship of the main and subsidiary are shown (spark discharge [10,11], creepage [12,13] and corona discharges [14,15]). Here, 1 marks the main discharge electrodes and 2 the subsidiary discharge electrodes.

It is possible to create a preionization with a subsidiary discharge in a near-electrode area of the main discharge gap using a working surface of one of the electrodes of the main discharge [16] (Figure 4.15). Here, 1 marks a cathode; 2 an anode; 3 the subsidiary discharge electrodes; and 4 marks the insulators. The characteristic of this method is a combined participation of the photoionizing radiation of the subsidiary discharge plasma in the creation of an initial conductivity in the discharge gap volume. Such types of systems are usually referred to as lasers with double discharge. The most widely used are the following three schemes of the double discharge:

a. Discharge between a mesh cathode of the main discharge gap and a plane dielectric surface encompassing the main discharge electrode
b. Discharge between the nibbed zones of a profiled cathode and the surface of cylindrical insulators, embedded into grooves in a working cathode surface and containing thin wires, forming the electrode of the subsidiary discharge
c. Discharge between a mesh cathode of the main discharge and sectioned many-spiked electrode of the subsidiary discharge with resistor, capacitance, or inductive uncoupling between individual spikes

In the last variant, there are also continuous solid electrodes of cellular construction with surface discharge in every cell that is used. In Reference [17], a possibility of cascade connection of two volume discharges divided by the common mesh cathode is demonstrated.

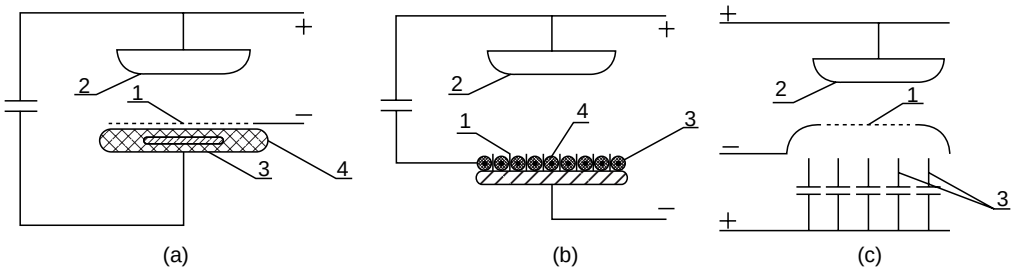

FIGURE 4.15 Schemes of preionization by a subsidiary discharge in the near-electrode zone of the main discharge gap.

4.5 RADIO-FREQUENCY EXCITATION CIRCUITS VS. DC GLOW DISCHARGE

Plasma in a discharge can be sustained by constant and alternating electric fields. A peculiar position among the alternating fields belongs to high-frequency fields with frequencies in RF diapason of 1 to 200 MHz.

There are many different methods to introduce high-frequency electric field into a discharge volume. They are logically separated into two main groups on the basis of whether electric field lines are closed in the discharge plasma or not; in other words, whether the field is rotational or potential [2].

The first group includes induction methods based on the usage of the effect of electromagnetic induction. The typical and the most widespread way to realize this method is the following (Figure 4.16). High-frequency current passes through a solenoid coil. The magnetic field of this current is also alternating and is directed along coil axis. Under the action of alternating magnetic flux, a vortex electric field is inducted inside the coil. Its lines of force are closed circles concentric with the coil. This electric field can support the discharge, at which the currents are also closed and run along circle lines of the electric field. The discharge can be stationary and impulse. Such a discharge is referred to as an induction discharge or a discharge of *H*-type. Induction discharges naturally are nonelectrode discharges.

In the methods of the second group, high frequency is applied on the electrodes. In the simplest and the most widely used geometry, two plane electrodes are located in parallel. Electrodes can be bared and kept in direct contact with the discharge plasma or can be insulated from the plasma with the dielectric (Figure 4.17). A system of two electrodes behaves relative to the alternating voltage like a capacitor; so discharges of this type, in contrast to the induced ones, are referred to as capacitive or discharges of *E*-type. Here, the letter *E* symbolizes the determinative role of the electric field. The term ''capacitive'' is mostly applied to the nonelectrode variant, in which electrodes are insulated from the cathode [18].

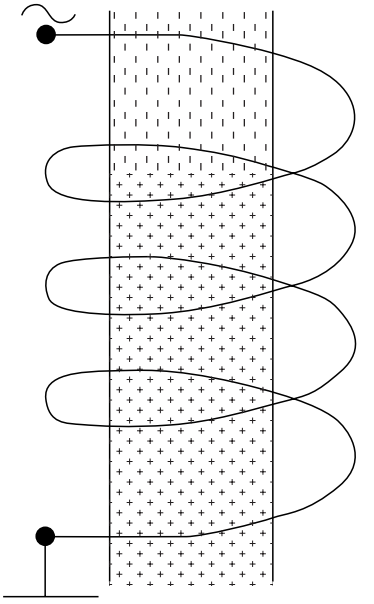

FIGURE 4.16 Diagram of inductive method of radio-frequency (RF)-discharge feeding.

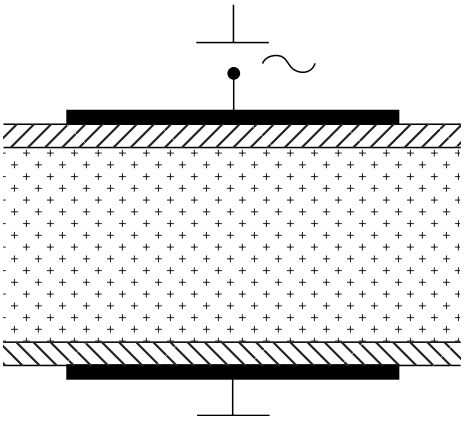

FIGURE 4.17 Diagram of capacitive nonelectrode method of RF-discharge realization.

In gas electrodischarge lasers for active medium pumping, a capacitive discharge is mainly used. The electrical schematic diagram of such a discharge is shown in Figure 4.18 [18].

In lasers at the base of the RF-discharge, heat rejection is produced from a working mixture through electrodes to which exciting RF-voltage is applied [19]. RF-plasma is as a rule low-ionized, nonequilibrium, and similar to the plasma of glow discharge.

The efficiency of an active medium excitation in many respects depends on the proportion between the frequency of the field variety and the frequency of the collisions of electrons with atoms [5]. At high frequencies of the electric field, the energy of the electrons varies slightly with time. Therefore, electrons produce ionization processes necessary for the discharge support as well as processes of particle excitation necessary for inversion creation with an almost constant rate during the period of the discharge. At a low frequency of the electric field, electron energy follows the electric field. In this case, a discharge in alternating electric fields looks like a non-self-sustained discharge with periodic ionization. Because of the exponential pattern of ionization rate dependence on electron energy, gas ionization is realized only in areas of maximum values of electric field strength, and during the interval between them non-self-sustained current runs in the decaying plasma [5]. The field amplitude necessary for the RF-discharge support is evaluated from the requirement of balance between

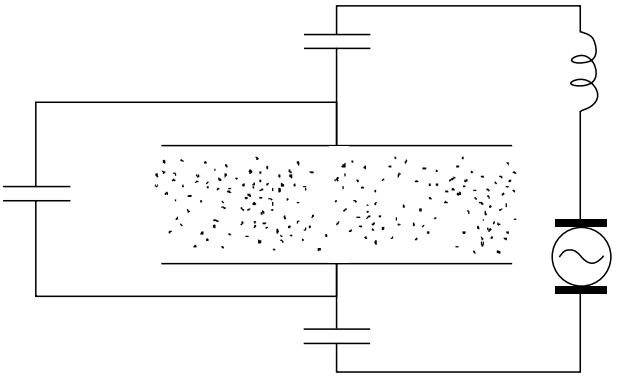

FIGURE 4.18 Schematic diagram for pumping working medium by capacitive RF-discharge.

the generation and death of electrons. For typical gas-laser conditions, it is closed to electric fields in the DC-discharge. Processes at RF-discharge electrodes play considerably less roles than in the case of the DC-discharges (in lasers with inductive discharge, there is no electrode).

In capacitive RF-discharges, near-electrode phenomena are important only for closing current in a discharge circuit. At low current density, conductivity of near-electrode layers is not high and current closure on electrodes is produced by displacement currents, running through the layer like through a capacitor. Such an RF-discharge mode is referred to as low current. With the increase in current, the voltage drop on the layer capacitance increases such that there occurs an electrical breakdown in the layer and the current in the layer consists of displacement and conduction currents. Such an RF-discharge mode is referred to as high current. It is necessary to note that the presence of insulating coating on current-conducting plates practically does not influence the running current.

The industry is interested in RF-discharge as applied to gas lasers because of its numerous advantages compared with DC-discharge. The main RF-discharge advantage is its higher stability in comparison with the DC-discharge owing to the periodic ionization mode in the case of RF-discharge. The point is that in RF-discharge, to provide a current running through a discharge gap there is no need to form a cathode layer, providing the current closure on an electrode. In RF-discharge, a cathode and an anode change their roles subject to RF-field phase and hence the current closure near electrodes; playing a cathode role in turn is provided by the displacement current.

The simplicity of the output power control and the possibility of operating at a lower voltage of power supply are among the advantages of lasers with RF-pumping. RF-discharge makes possible the excitation of large volumes of active medium without using external ionization sources. Furthermore, by using RF-discharge pumping it is possible to decrease parasitic energy losses in the discharge circuit using reactive elements, for example, capacitors as ballast loads. One more technical advantage is the possibility of use in laser with RF-pumping electrodes with dielectric coating. Finally, RF-pumping produces symmetric energy release in the discharge zone; therefore, medium density distribution across the resonator becomes much more symmetrical. This decreases the deviation of laser radiation from optical axes due to nonuniform refraction in the working gas.

REFERENCES

1. William T. Silgvast, *Laser Fundamentals*, Cambridge University Press, Cambridge, 1996.
2. Raizer, Y.P., *Gas-Discharge Physics*, New York, Springer-Verlag, 1991.
3. Smirnov, S.A. and Baranov, G.A., Gas dynamics and thermal-ionization instability of the cathode region of a glow discharge. Part I. *Tech. Phys.*, 46(7), 815–824, 2001.
4. Smirnov, S.A. and Baranov, G.A., Gas dynamics and thermal-ionization instability of the cathode region of a glow discharge. Part II. *Tech. Phys.*, 46(7), 825–830, 2001.
5. Golubev, V.S. and Lebedev, F.V., *Physics Fundamentals of Industrial Lasers*, Moscow, Vysshaya Shkola, 1988 (in Russian).
6. Golubev V.S. and Nath A.K., Design considerations and scaling laws for high power convective cooled CW CO_2 lasers. *Pramana J. Phys.*, 51(3&4), 436–479, 1998.
7. Velikhov, E.P., Baranov, V.Y., Letokhov, V.S., Ryabov, E.A., and Starostin, A.N., *Pulsed CO_2 Lasers and Their Application for Isotopes Separation*, Moscow, Nauka, 1983 (in Russian).
8. Beaulieu, J.J., Transversely excited atmospheric pressure CO_2 laser. *Appl. Phys. Lett.*, 16, 534, 1970.
9. Garnworthy, R.K., Mathias, L.E.S., and Carmichael, C.H.H., Atmospheric-pressure pulsed CO_2 laser utilizing preionization by high-energy electrons. *Appl. Phys. Lett.*, 19(12), 506–508, 1971.
10. Judd, O.P., An efficient electrical CO_2 laser using preionization by ultraviolet radiation. *Appl. Phys. Lett.*, 22(3), 95–96, 1973.

11. Cohn, D.B., Photoinitiated transversely sustained CO_2 laser. *Appl. Phys. Lett.*, 22(4), 138–140, 1973.
12. Richardson, M.S., Leopold, K. and Alcock, A.J., Large aperture CO_2-laser discharges. *IEEE J. Quant. Elec.*, 9(9), 934–939, 1973.
13. Browne, P.F. and Webber, P.M., A compact 50-J CO_2 TEA laser with VUV preionization and the discharge mechanism. *Appl. Phys. Lett.*, 28(11), 662–664, 1976.
14. Lamberton, H.M. and Pearson, P.R., Atmospheric pressure CO_2-lasers. *Electron. Lett.,* 7, 141–142, 1971.
15. Pearson, P.R. and Lamberton, H.M., Atmospheric pressure CO_2-lasers giving high output energy per unit volume. *IEEE J. Quant. Elec.*, 8(2), 145–149, 1972.
16. Kornyushin, V.N. and Soloukhin, R.I., *Macroscopic and Molecular Processes in Gas Lasers*, Moscow, Atomisdat, 1981 (in Russian).
17. Mazurenko, Yu.T., Rubinov, Yu.A., and Shakhverdov, P.A., New method for the excitation of a homogeneous discharge in a high-pressure CO_2 laser. *Quant. Elect.*, 5(10), 1273–1275, 1975.
18. Raizer, Y.P. Shneider, M.N., and Yatsenko, N.A., *Radio-Frequency Capacitive Discharges*, CRC Press, Boca Raton, London, Tokyo, 1995.
19. Colley, A.D., Villarreal, F., Cameron, A.A., Vitruk, P.P., Baker, H.J., and Hall, D.R., High power CW molecular gas laser using narrow gap slab waveguides, in *Gas Laser—Recent Developments and Future Prospects*, Witteman, W.J. and Ochkin, V.N., Eds., NATO ASI Series 3: High Technology, 1995, pp. 10, 89.

5 Electric Discharge CO Lasers

Andrey A. Ionin

CONTENTS

5.1 INTRODUCTION

Carbon monoxide laser is a very attractive object of research both from the standpoint of the development of high-power laser sources of coherent radiation in the mid-IR spectral region and from the standpoint of molecular kinetics. This is because an inversion population between the vibrational–rotational levels of a CO molecule is stipulated by vibrational–vibrational (V–V) exchange of CO molecules that are excellent examples for anharmonic oscillators. CO lasers have several specific properties that distinguish them from other high-power IR lasers. A CO laser can operate on more than a thousand vibrational–rotational lines belonging both to the fundamental band ($V+1\rightarrow V$), where V is the number of the vibrational level of the CO molecule, in the wavelength region of ~4.7–8.2 μm and to the first-overtone band ($V+2\rightarrow V$) in the spectral region of 2.5–4.2 μm. Therefore, a CO laser can run in the mid-IR spectral range within the extremely broad spectral band from 2.5 to 8.2 μm with a spectral hole of 0.4 μm width between the wavelengths of 4.2 and 4.7 μm (Figure 5.1). The CO laser has a few advantages when compared with CO_2 lasers. Fundamental band CO lasers have high output efficiency (~30%–50%) and high specific output energy that is 2–2.5 times that of CO_2 lasers. Experimentally obtained first-overtone CO laser efficiency is 11%; theoretical prognosis for the output efficiency is 25%, which places the first-overtone CO laser among the other high-power IR lasers such as CO_2-, fundamental band CO-, HF- and DF lasers. The spectral range of first-overtone CO laser covers that of well-known chemical HF-and DF-lasers, with the vibrational–rotational lines spacing several times less than that of those lasers. Many CO laser spectral lines coincide with a number of absorption lines of numerous organic and nonorganic substances such as H_2O, CO_2, CH_4, NO_2, NO, acetone, benzene, methanol, and so on (Figure 5.1). The diffraction limit of an angular divergence of fundamental band and first-overtone CO lasers is twice and thrice less than that of CO_2 lasers. Shorter CO laser wavelengths result in a lower plasma shielding effect. Several nonhygroscopic

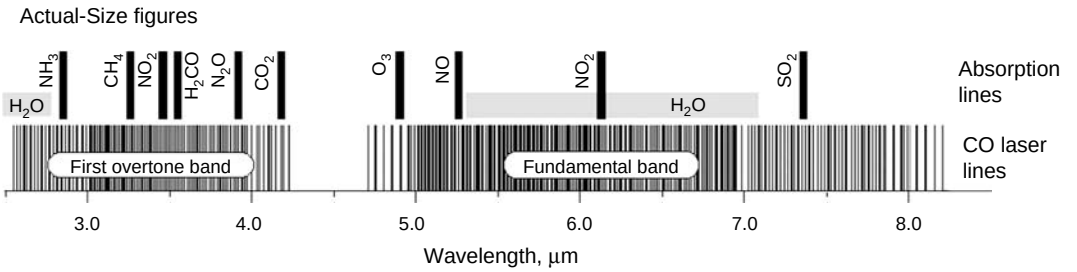

FIGURE 5.1 Position of fundamental band and first-overtone CO laser spectral lines and spectral lines corresponding to absorption of some molecules.

optical materials, which are transparent at the output wavelengths of a CO laser, have a greater resistance to laser damage and a greater mechanical strength. There exist optical materials that are transparent in the 5 μm spectral region and from which optical fibers with low optical losses can be fabricated. For many output wavelengths of fundamental band and first-overtone CO lasers, there are transparency windows in the atmosphere, in which the absorption is lower by a large factor than that for CO_2 laser radiation. Pulsed CO lasers have an order of magnitude laser pulses longer than those of CO_2 lasers. Finally, it has been demonstrated that 5 μm radiation interacts more effectively with some structural materials and human tissue.

5.2 HISTORICAL REMARKS

The supposition about the possibility of getting lasing on vibrational–rotational transitions of the ground electronic state of CO molecules was made [1] in 1964. In the same year, Patel and Kerl [2] for the first time observed lasing on the P-branch of vibrational transitions of a CO molecule when exciting carbon monoxide in a pulsed low-pressure electric discharge. One year later RF discharge CW CO laser was launched [3]. The CO laser was launched for the first time in the same year as the CO_2 laser. However, to the contrary of the latter, which became an object of very extensive research resulting in the development of high-power CO_2 lasers, at first, CO lasers were not given great attention. It was related to the poor output parameters of a CO laser obtained in first experiments (the output power was not higher than tenths of mW): lack of clear understanding of physical processes that result in inversion population, and technological problems.

The interest in CO lasers increased considerably in the early 1970s owing to experimental studies [5–9] in which Patel's suggestion [4] about CO laser active medium cooling was used and an output power of 95 W and output efficiency of 16% were obtained for CW electric discharge low-pressure CO laser. These experimental studies and theoretical research of Treanor et al. [10], who developed the theory of inversion population formation in the active medium of a CO laser by using a model of anharmonic oscillator ensemble, strongly stimulated the subsequent research and development of carbon monoxide lasers. In 1972, an output efficiency of 47% was obtained in cryogenically cooled CW low-pressure CO laser, and output efficiency of 12% was obtained at room temperature [11]. In the same year low-pressure fast-flow CW CO laser with an output power 400 W and 20% efficiency was launched [12].

At present, output power of cryogenic and room-temperature low-pressure fast-axial-flow CO lasers excited by self-sustained DC or RF discharge comes to approximately 1 kW at output efficiency ~20%–50%. Several cryogenic industrial 5 kW CO lasers and a transverse pumped 20 kW CO laser were developed in the 1990s. Application of non-self-sustained electron beam sustained discharge (EBSD) for excitation of CO lasers resulted in the development of pulsed EBSD lasers with an output energy ~0.5–1.5 kJ and output efficiency ~30%–40%, in the development of

industrial CW and repetitively pulsed CO lasers with output power ~12 and ~14 kW, respectively, and in the development of subsonic and supersonic flow EBSD lasers with output power ~80–200 kW running for a short period of time ~10^{-3}–5 s. Alongside with experimental research and development of CO lasers, theoretical studies of CO lasers have been carried out, the results of which have explained the mechanism of formation of inversion population in CO lasers and have helped in understanding the physical principles of CO laser operation.

5.3 MECHANISM OF FORMATION OF INVERSION POPULATION IN ELECTRIC DISCHARGE CO LASER

CO laser physics is quite different from that of a CO_2 laser. Unlike the well-known CO_2 laser that is a four-level quantum system, the CO laser active medium is a multilevel system. Carbon monoxide molecule in the ground electronic state $X^1\Sigma^+$ (Figure 5.2) is an excellent example of an anharmonic oscillator characterized by a set of vibrational levels O–V (Figure 5.3), the energy of which in standard spectroscopic symbols is as follows:

$$E_V = \omega_e\left(V + \frac{1}{2}\right) - \omega_e x_e\left(V + \frac{1}{2}\right)^2 \tag{5.1}$$

$$(E_V\ [\text{erg}] = hcE_V\ [\text{cm}^{-1}]),$$

where $\omega_e = 2169.8\ \text{cm}^{-1}$; $\omega_e x_e = 13.3\ \text{cm}^{-1}$ for the molecule $^{12}C^{16}O$. The quantity $2\omega_e x_e$ that is an energy difference between adjacent vibrational transitions is called a defect of vibrational

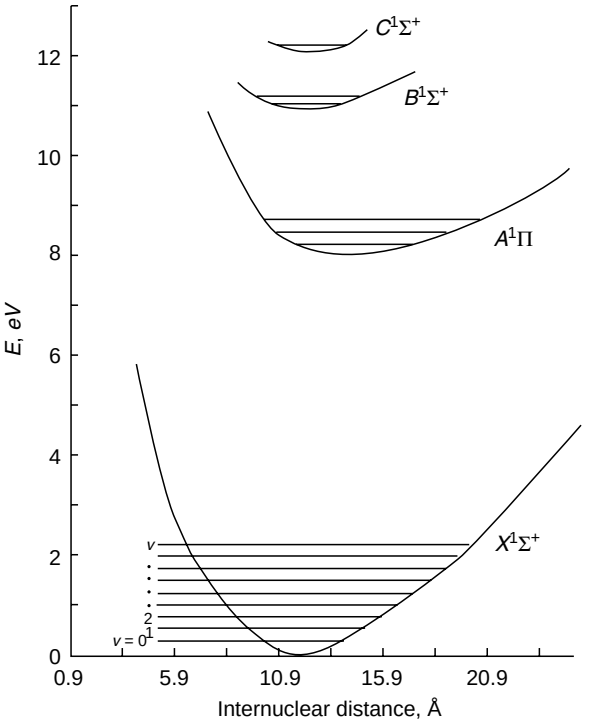

FIGURE 5.2 Diagram of electron-vibrational states of CO molecule.

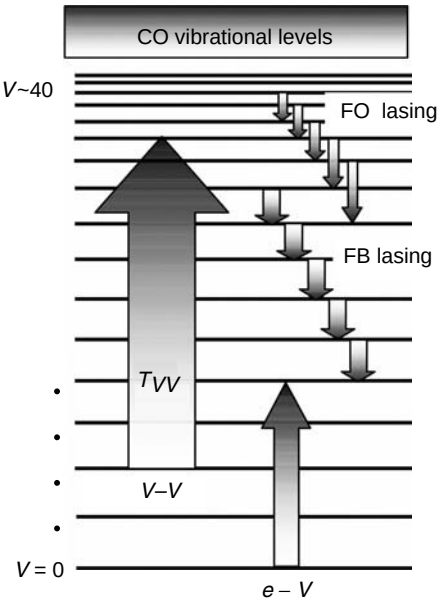

FIGURE 5.3 Schematic of vibrational levels of the ground state of CO molecule with pumping and lasing transitions.

quantum for these transitions and comes to ~1% of energy of the quantum. In an electric discharge, the excitation of lower vibrational levels of CO molecule by indirect (i.e., with the formation of intermediary ion CO^-: $e + CO \rightarrow CO^-$; $CO^- \rightarrow CO(V) + e$) electron collision takes place (e–V pumping) (Figure 5.3). Experimentally measured excitation cross-sections for the lower vibrational levels of CO molecule [13] are presented in Figure 5.4. The total excitation cross-section for the first eight levels is relatively high ($\sim 8 \times 10^{-16}$ cm^2) at the electron energy of ~2 eV that is of an order of magnitude higher for vibrational level $V = 1$ than for $V \cong 8$. The excitation efficiency for vibrational levels of CO molecule depends on the parameter E/N (where E is the electric field strength, and N is the gas density) and comes to 80%–90%. It means that about 80%–90% of energy loaded into an electric discharge can be transformed into the vibrational energy of the ground electronic state of CO molecule. In a CO laser using nitrogen content gas mixture CO:N_2, the energy transfer from vibrationally excited nitrogen to carbon monoxide molecules takes place as in a CO_2 laser. However, on the contrary to the CO_2 laser, the excitation just through electron collisions does not result in the formation of inversion population on vibrationally excited levels of CO molecule. The inversion population arises just because of anharmonicity of CO molecules, the existence of which causes the flow of vibrational energy to come up the ladder of energy levels in the course of the process of molecular collisions via V–V exchange (Figure 5.3).

Qualitatively, the mechanism of formation of inversion population in the ensemble of anharmonic oscillators can be understood following the simple four-level quantum model. Let two colliding molecules A and B be at the states 1, 2, 3, and 4 correspondingly (Figure 5.5). ΔE is a defect in vibrational quantum, that is, the energy that is the difference $\Delta E = (E_2 - E_1) - (E_4 - E_3)$ between energies of the two quanta. Molecule A is a model of lower vibrational state, and molecule B is a model of higher vibrational state of anharmonic CO molecule. Let us suppose that molecule A is initially in state 2, and molecule B is in state 3. Under the collision of molecules A and B, the exchange of their energies takes place (called vibrational–vibrational (V–V) exchange or relaxation). Molecule A performs transition 2→1, and

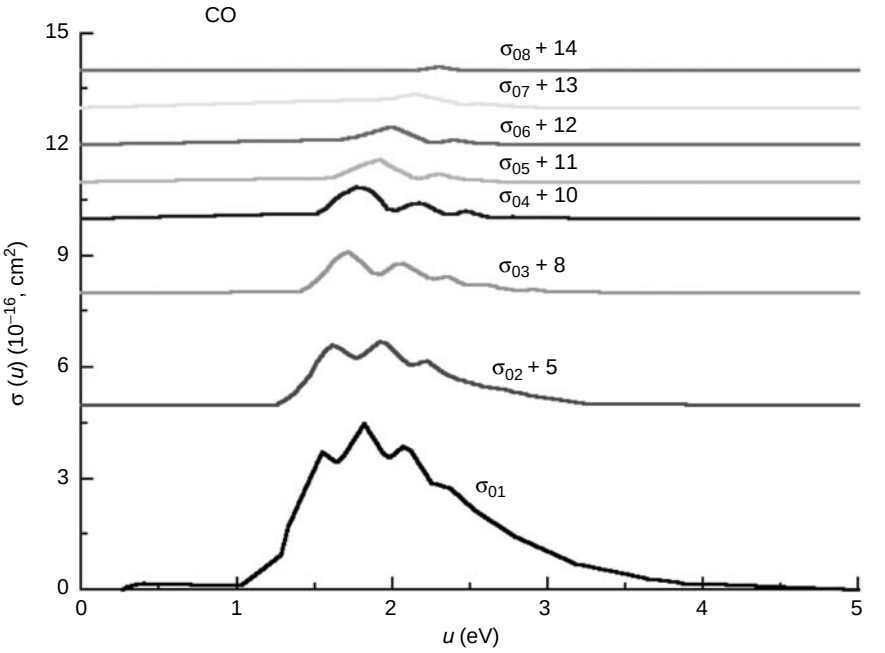

FIGURE 5.4 Experimental cross-sections σ_{0V} of the Vth vibrational level excitation by electron collisions vs. electron energy for CO molecule. (From Schulz, G.Y., *Phys. Rev.*, 135, 988, 1964. With permission.)

molecule B 3→4 (solid arrows in Figure 5.5a), with the energy ΔE transferred into rotational and translational degrees of freedom (eventually goes into gas heating). This direct process is characterized by the probability $P_{2\to1}^{3\to4}$. The reverse process going with the probability $P_{1\to2}^{4\to3}$ is depicted by the dashed arrows in Figure 5.5a. Following the principle of the detailed balancing, probabilities of the direct and reverse processes are connected by the relationship

$$P_{2\to1}^{3\to4} = \exp\left(\frac{\Delta E}{kT}\right) P_{1\to2}^{4\to3}, \tag{5.2}$$

where T is translational gas temperature. It follows from Equation 5.2 that $P_{2\to1}^{3\to4} > P_{1\to2}^{4\to3}$ at $\Delta E > kT$, and molecule B with low energy quantum is excited at the expense of molecule A

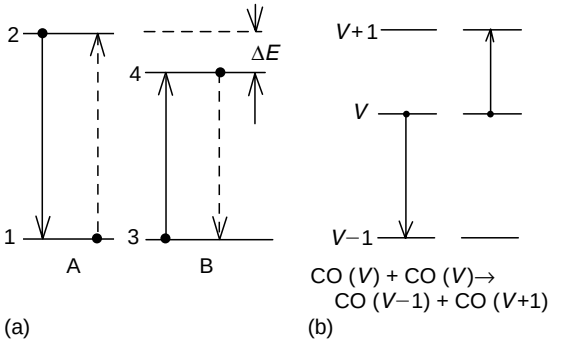

FIGURE 5.5 Diagram of energy exchange between two molecules A and B with different quanta (ΔE is quantum defect) (a); the same for two colliding CO molecules on vibrational level V (b).

with higher energy quantum. This process of $V-V$ pumping leads to the population growth of higher level of molecule B. Molecules A and B correspond, for example, to CO molecules in the state V and going under collision into the states $V-1$ and $V+1$ (Figure 5.5b). It can be seen from Equation 5.2 that the pump process is more effective at low gas temperature. That is why electric discharge CO lasers have maximum efficiency at low gas temperature close to the temperature of liquid nitrogen.

Treanor et al. [10] obtained for the first time the analytical expression for the vibrational distribution function (VDF) (i.e., the function of distribution of population over vibrational levels of anharmonic oscillators N_V), known as the Treanor distribution under the supposition of absence of the vibrational–translational (V–T) relaxation (i.e., of the process of transferring vibrational energy into the translational degree of freedom, in other words, into gas heating under molecule collisions):

$$N_V = N_0 \exp\left(-\frac{E_V}{k\theta_V^*}\right); \tag{5.3a}$$

$$\text{or} \quad N_V = N_0 \exp(-V\gamma)\exp\left(-\frac{E_V}{kT}\right), \quad \gamma = \frac{E_1}{k}\left(\frac{1}{\theta_1^*}-\frac{1}{T}\right); \tag{5.3b}$$

$$\text{or} \quad N_V = N_0 \exp\left(-\frac{VE_1}{k\theta_1^*}+\frac{VE_1-E_V}{kT}\right), \tag{5.3c}$$

where V is the number of vibrational level; E_V the energy of vibrational level V; T the translational gas temperature; and θ_V^* is the effective vibrational temperature for the vibrational level V (see Equation 5.3a), which is different for different vibrational levels.

There is following dependence between θ_V^* and θ_1^*;

$$\frac{\theta_V^*}{\theta_1^*} = \left\{\frac{VE_1}{E_V} - \frac{\theta_1^*}{T}\left[\frac{VE_1-E_V}{E_V}\right]\right\}^{-1}. \tag{5.4}$$

As follows from above expressions, in the case of harmonic oscillators ($E_V = VE_1$) distribution (5.3) is reduced to the Boltzmann distribution with temperature θ_1^*. It is also valid for low vibrational levels of CO molecule for which $E_V \approx VE_1$. When $\theta_1^* = T$, the distribution (5.3) is the Boltzmann one characterized by the temperature T. When $\theta_1^* \neq T$, the Treanor distribution differs from Boltzmann one with the temperature T. If $\theta_1^* > T$, the vibrational temperature θ_1^* rises with the number of vibrational level ($\theta_V^* > \theta_1^*$). At $\theta_1^* < T$ the vibrational temperature drops down with the number of vibrational level ($\theta_V^* < \theta_1^*$). It follows from formulae (5.3) that at $\theta_1^* > T$ the absolute inversion population $N_{V+1} > N_V$ is possible beginning from $V \geq V_{\min}$, where $V_{\min}$ is the number of vibrational level corresponding to the minimum of the Treanor distribution. Because the dependence $\ln(N_V/N_0)$ on the vibrational number is a parabolic one, the value of $V_{\min}$ can be easily found from the condition

$$\frac{\mathrm{d}}{\mathrm{d}V}\left(\ln\frac{N_V}{N_0}\right) = 0; \quad V_{\min} \approx \ln\left(\frac{N_0}{N_1}\right)\frac{kT}{2\omega_e x_e}.$$

A schematic depiction of the Treanor distribution N_V^{Treanor} is presented in Figure 5.6, from where one can see that the inversion population $N_{V+1} > N_V$ is positive for high vibrational levels $V > V_{\min}$, whereas at lower levels ($V \ll V_{\min}$) Boltzmann distribution takes place.

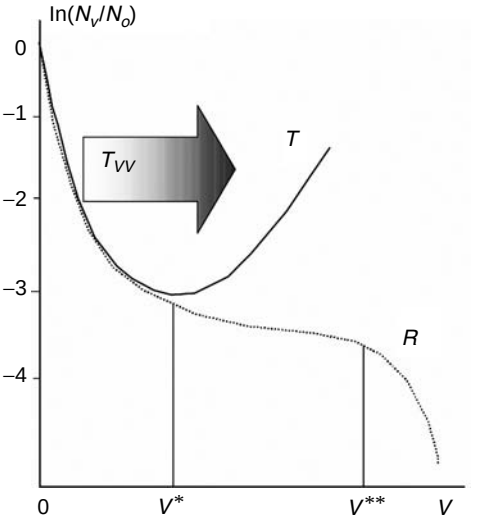

FIGURE 5.6 Schematic depiction of Treanor (T) and real (R) vibrational distribution function N_V normalized on population of the 0th vibrational level. "Plateau" region is between $V^* \sim V_{\min}$ and V^{**}.

The theoretical analysis of processes taking place in the active medium of a real CO laser, when compared with the Treanor calculations, takes into account not only V–V exchange but also the whole set of different factors: vibrational–translational (V–T) relaxation, radiative decay of vibrational levels, the excitation of these levels through electron collisions, the influence of buffer gases N_2, He, Ar, Xe, and others. The influence of V–T relaxation and radiative processes is very strong for highly excited vibrational levels ($V \geq 10$). It should be noted that the existence of the energy flow up the ladder of vibrational levels of CO molecule is possible because of the fact that the characteristic time τ_{VV} of V–V exchange and the time T_{VV} of VDF formation are a few orders of magnitude less than characteristic time of V–T relaxation τ_{VT} up to some vibrational level V for which $\tau_{VV} \sim \tau_{VT}$. The time τ_{VT} depends on gas pressure and laser mixture content. The real VDF N_V^{real}, which is found from numerical solution of equation system consisting of a few dozens of differential kinetic equations, differs considerably from the Treanor VDF at high values of V (Figure 5.6). The behavior of this function strongly depends on concrete experimental conditions. Conditionally, the region of its definition can be divided by three intervals: $0 < V < V^*$; $V^* < V < V^{**}$; $V^{**} < V$. Within the first interval $N_V^{\text{real}} \sim N_V^{\text{Treanor}}$ up to the vibrational number $V^* \approx V_{\min}$. In the second region N_V^{real} is characterized by a plateau, with N_V^{real} proportional to $1/V$. In the third interval at $V \geq V^{**}$ the function N_V^{real} steeply decreases. Such a behavior of the real VDF is related to the fact that $\tau_{VT} \gg \tau_{VV}$ for the interval $O < V < V^*$ and the VDF behavior is determined by the V–V exchange, that is, the real VDF is close to the Treanor one. At $V > V^{**}$ the reverse inequality $\tau_{VT} \ll \tau_{VV}$ takes place, that is, the rate of transferring vibrational excitation into heat prevails over the V–V exchange rate. Whereas the absolute inversion population $N_{V+1} > N_V$ is possible for the Treanor VDF, for the real VDF this fact practically never takes place in electric discharge CO lasers (the absolute inversion population was observed in optically pumped CO lasers).

Despite this fact, it is possible for inversion population to exist in the active medium of a CO laser in the plateau region of the real VDF owing to the existence of the manifold of rotational sublevels for each vibrational level. Because of the very short time T_{RT} of the process of rotational–translational relaxation ($T_{\text{RT}} \sim 1$ n sec at gas pressure ~1 atm), the

cross-section of which is of the order of magnitude close to the gas kinetic one, it is considered that the distribution of population over rotational sublevels $N_{V,J}$ for each vibrational level has Boltzmann behavior for the time scale $T \gg T_{RT}$:

$$N_{V,J} = N_V \left(\frac{B_V}{kT}\right)(2J+1)\exp\left(-\frac{B_V}{kT}J(J+1)\right), \tag{5.5}$$

where J is the number of rotational sublevel; $B_V = B_0 - \alpha_e(V+1/2)$ is the rotational constant for the vibrational level V; $B_0 \approx 1.931271\ \text{cm}^{-1}$; $\alpha_e = 1.7513\times10^{-2}\ \text{cm}^{-1}$; $k = 0.69\ \text{cm}^{-1}/\text{grad}$ is the Boltzmann constant.

The dependence of the energy of rotational sublevel on the number J is as follows:

$$E_J = B_V J(J+1) - D_V J^2(J+1)^2, \tag{5.6}$$

where $D_V = D_e + \beta_e(V+1/2)$, $D_e = 6.1198\times10^{-6}\ \text{cm}^{-1}$, $\beta_e = 0.9876\times10^{-9}\ \text{cm}^{-1}$.

Schematically, the distribution $N_{V,J}$ is presented in Figure 5.7a. The energy difference between two rotational sublevels J_1 and J_2 belonging to the vibrational levels with the numbers V_1 and V_2 can be found from the following equation:

$$\Delta E\begin{pmatrix} V_2 \to V_1 \\ J_2 \to J_1 \end{pmatrix} = \left[\omega_e\left(V_2+\frac{1}{2}\right) - \omega_e x_e\left(V_2+\frac{1}{2}\right)^2\right] - \left[\omega_e\left(V_1+\frac{1}{2}\right) - \omega_e x_e\left(V_1+\frac{1}{2}\right)^2\right] + B_{V_2}J_2(J_2+1) - B_{V_1}J_1(J_1+1) - D_{V_2}J_2^2(J_2+1)^2 + D_{V_1}J_1^2(J_1+1)^2. \tag{5.7}$$

It is possible for the inversion population to exist between vibrational–rotational sublevels (V_2J_2) and (V_1J_1) with population N_{V_2,J_2} and N_{V_1,J_1}: $N_{V_2,J_2} > N_{V_1,J_1}$ (the partial inversion population) despite the inequality $N_{V_2} < N_{V_1}$, and lasing can be on the transition $(V_2J_2)\to(V_1J_1)$ (Figure 5.7a). According to the quantum mechanical rule of selection for the ground electronic state, the radiative transition takes place at $\Delta J = +1$ (P-branch,

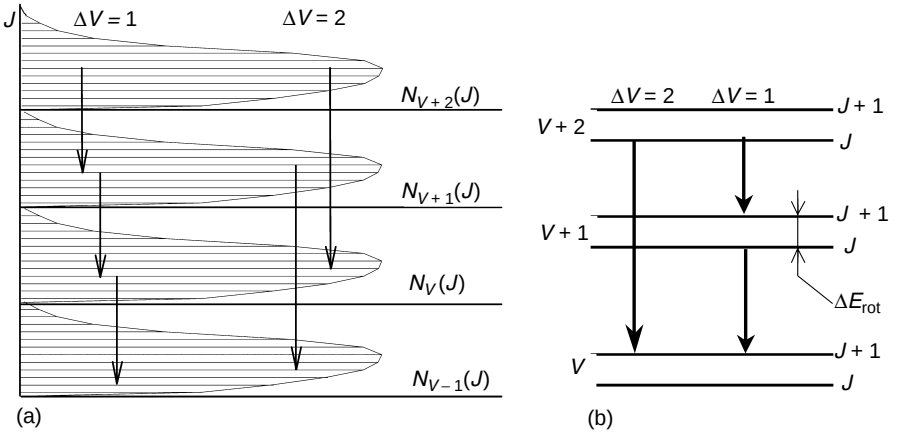

FIGURE 5.7 Diagram of rotational distribution within vibrational levels of CO molecule (a) and laser transitions (a, b).

transitions are denoted as P(J), that is, $J_2 = J \rightarrow J_1 = J+1$) (Figure 5.7b) and $\Delta J = -1$ (R-branch, transitions are denoted as R(J), that is, $J_2 = J \rightarrow J_1 = J-1$).

5.4 SMALL-SIGNAL GAIN AND CO LASER SPECTRUM

Lasing (amplification) in CO laser (laser amplifier) takes place only for those vibrational–rotational transitions for which small-signal gain

$$\alpha_{V_2, J \rightarrow V_1, J \pm 1} > \alpha_{\text{threshold}} = \frac{1}{2L} \ln\left(\frac{1}{R_1 R_2}\right),$$

where R_1, R_2 is the reflectivity of mirrors of laser resonator ($\alpha_{V2,\ J \rightarrow V_1,\ J \pm 1} > 0$ for a laser amplifier).

The small-signal gain for the radiation affecting a vibrational–rotational transition $(V_2,J) \rightarrow (V_1, J \pm 1)$, where $V_2 - V_1 \geq 1$ is represented by the following equation:

$$\alpha_{V_2,\ J \rightarrow V_1,\ J \pm 1} = \left(\frac{\lambda^2}{8\pi kT}\right) A_{V_2, V_1} S_J \times \left[N_{V_2} B_{V_2} \exp\left(-\frac{B_{V_2} F(J)}{kT}\right) - N_{V_1} B_{V_1} \exp\left(-\frac{B_{V_1} F(J \pm 1)}{kT}\right)\right] G(\lambda), \quad (5.8)$$

where $F(J) = J(J+1)$, sign "plus" corresponds to the P-branch, sign "minus" corresponds to the R-branch; $S_J = J+1$ for the P-branch transition, $S_J = J$ for the R-branch; A_{V_2, V_1} is the probability of spontaneous radiative transition $V_2 \rightarrow V_1$ (Einstein coefficient), λ is the wavelength of radiation, and $G(\lambda)$ is the normalized profile of the spectral line. The dependences of small-signal gain on the rotational number J for different parameters N_{V_2}/N_{V_1} and gas temperatures $T = 100$ K and 300 K are presented in Figure 5.8a and Figure 5.8b. In case of partial inversion $N_{V_2}/N_{V_1} < 1$, the small-signal gain is positive (amplification) only for the P-branch (solid curves A and B in Figure 5.8) and negative (absorption) for the R-branch (dotted curves A and B in Figure 5.8). Analytical expression for the spectral profile $G(\lambda)$, for

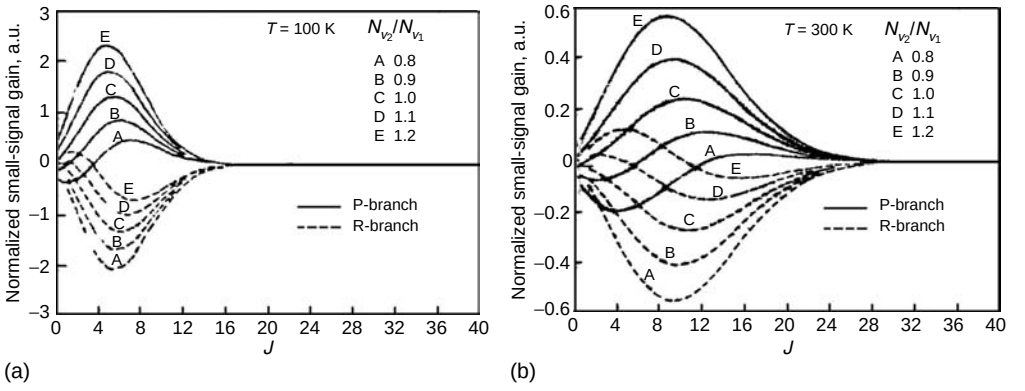

FIGURE 5.8 The dependence of small-signal gain for P- and R-branches of vibrational transition $V = 7 \rightarrow V = 6$ on the rotational number J. $T = 100$ K (a); $T = 300$ K (b). The gain is normalized to N_{V_1} and factors out of square brackets except S_J and function of T. Doppler broadening. See Equation 5.8 and Equation 5.9. Arbitrary unit is the same for both figures. (From Patel, C.K.N., *Phys. Rev.*, 141, 71, 1966. With permission.)

which collisional and Doppler broadening of a spectral line of amplification is taking into consideration, is as follows:

$$G(\lambda) = \left(4\ln\frac{2}{\pi}\right)^{1/2}\frac{H(b)}{\Delta\nu_D},$$

$$H(b) = \frac{b}{\pi}\int_{-\infty}^{\infty}\frac{\exp(-z^2)}{z^2+b^2}\mathrm{d}z = [1-\Phi(b)]\exp b^2,$$

$$\Phi(b) = \frac{2}{\pi}\int_{0}^{b}\exp(-x^2)\mathrm{d}x,\ b = \frac{\Delta\nu_L}{\Delta\nu_D}\sqrt{\ln 2}\ , \tag{5.9}$$

where $\Delta\nu_{\mathrm{L}}$, $\Delta\nu_{\mathrm{D}}$ are the spectral line widths for collisional and Doppler broadening. The expression for the Doppler broadening is: $\Delta\nu_{\mathrm{D}} = (\nu/c)\sqrt{(8kT/M)\ln 2}$ ($\nu = 1/\lambda$, if $\Delta\nu_{\mathrm{D}}$ is measured in cm^{-1}). At low pressures of active medium ($\leq$ ~10–20 torr) the spectral width is determined by Doppler broadening and does not depend on gas pressure. At gas pressure higher than ~70–100 torr collisional broadening is considerably higher than Doppler one. The collisional broadening depends on gas temperature and partial pressure of laser mixture components and is calculated according to the formula $\Delta\nu_L = Y/\sqrt{T}\sum_i \gamma_i p_i$, where T is the gas temperature, p_i the partial gas pressure for the ith component of laser mixture, and γ_i is the spectral line width stipulated by collisions of CO molecule with molecules of the ith component. The values of coefficients Y and γ_i can be found in Reference [14].

It follows from Equation 5.8 at $V_1 = V-1$ that, as partial inversion population takes place, the amplification ($\alpha_{V_2,\ J\to V_1,\ J\pm 1} > 0$) exists only for the spectral lines for which the following relation is valid:

$$J > J^* = -\frac{kT}{2B}\ln\left(\frac{N_V}{N_{V-1}}\right) \quad (B_V \approx B_{V-1} = B). \tag{5.10}$$

Small-signal gain in a CO laser strongly depends on gas temperature. At the same value of ratio N_{V_2}/N_{V_1} the small-signal gain is of the order of magnitude higher for a CO laser running at gas temperature 100 K than at room temperature (compare Figure 5.8a and Figure 5.8b). Therefore, when cooling the active medium of a CO laser, small-signal gain increases considerably, the probability of populating high vibrational levels increases, and V–T relaxation rate decreases, which results in an enhancement of output power and laser efficiency. As a rule, partial inversion population does exist in electric discharge CO lasers, that is, $N_{V_2}/N_{V_1} < 1$. Therefore, amplification and lasing takes place only for P-branch of vibrational–rotational transitions. Within each vibrational band $V+\Delta V\to V$ CO lasing can take place on a set of rotational lines designated as $P(J)$ and corresponding to the vibrational–rotational transition $V+\Delta V\to V$; $J\to J+1$. Most CO lasers operate on fundamental vibrational transitions $V+1\to V$, that is, $\Delta V = 1$. The maximum value of a small-signal gain in active medium of an electric discharge fundamental band CO laser depends on many factors such as gas temperature, pump power or energy, laser mixture content, etc., and comes to ~10^{-2}–10^{-1} cm^{-1}. The radiative probability of transition on first vibrational overtone $V+2\to V$ ($\Delta V = 2$) is low. However, this probability, that is, the Einstein coefficient $A_{V+2,\ V}$, increases with the number of vibrational level V to V~40; the ratio of Einstein coefficients for the first overtone and fundamental transitions $A_{V+2,V}/A_{V+1,V}$ grows with the number V and even higher than one for highly excited vibrational transitions [15] (Figure 5.9). Small-signal gain for overtone transitions can be close to that of fundamental ones as it is ~10^{-3}–5×10^{-3} cm^{-1}.

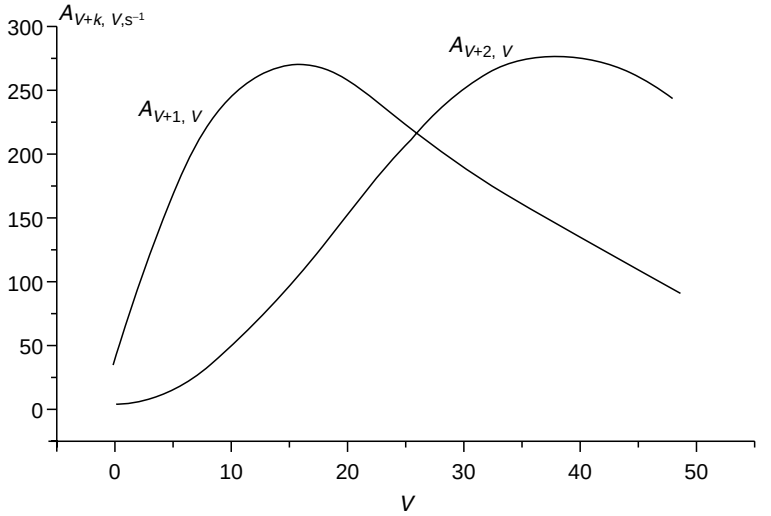

FIGURE 5.9 Einstein coefficients $A_{V+k,V}$ for fundamental ($k = 1$) and first-overtone transitions ($k = 2$) vs. vibrational number V. The dependencies are plotted by using data from (Langhoff, S.R. and Bauschlicher, C.W., Jr., *J. Chem. Phys*., 102, 5220, 1995).

It should be noted that second-overtone lasing with $\Delta V = 3$ was not experimentally observed in a CO laser. Therefore, CO laser can run on vibrational–rotational transitions of fundamental band $P_{V+1\to V}(J)$ with laser frequency $\omega_{V+1\to V}^{J\to J+1}$ in the wavelength range ~4.7–8.2 μm [16,17] and on first-overtone transitions $P_{V+2\to V}(J)$ in the wavelength range 2.5–4.2 μm [18–21] with laser frequency that can be found from the simple equation (Figure 5.7b):

$$\hbar\omega_{V+2\to V}^{J\to J+1} = \hbar\omega_{V+2\to V+1}^{J\to J+1} + \hbar\omega_{V+1\to V}^{J\to J+1} + \Delta E_{\text{rot}}. \tag{5.11}$$

The partial inversion population in CO laser arises between adjacent vibrational states lying in the plateau region of VDF. The lasing in adjacent vibrational bands results in cascade lasing (Figure 5.3 and Figure 5.7) within the manifold of vibrational levels belonging to the plateau region. Actually, the lasing corresponding to the fundamental band $V\to V-1$ leads to the population growth on the vibrational level $V-1$ and decreases the population of the level V, which, in turn, improves the condition for the enhancement (or formation) of inversion population on the vibrational transitions $V+1\to V$ and $V-1\to V-2$. A CO molecule that has emitted on the transition $V+1\to V$ partakes in the lasing on the vibrational transitions $V\to V-1$, $V-1\to V-2$ and so on, within the plateau region of the VDF N_V^{real}. Time behavior of laser pulses demonstrating the cascade mechanism of lasing is presented in Figure 5.10. Since the lifetime of CO molecules in excited vibrational states, which is determined by V–T relaxation, is long, CO molecule getting into the lowest laser level because of lasing can be transferred into higher vibrational levels due to V–V exchange (V–V pumping) without getting into the ground ($V = 0$) vibrational state. Such a circulation of CO molecules over the manifold of vibrational levels proceeds permanently in the course of CO laser free-running and stipulated its extremely high physical efficiency (~40%–50% for fundamental band CO laser), that is, the ratio of output laser power (energy) to the electric power (energy) loaded into electric discharge. The same process also takes place in an overtone CO laser. As a result, the experimentally observed output efficiency of a first-overtone CO laser comes up to

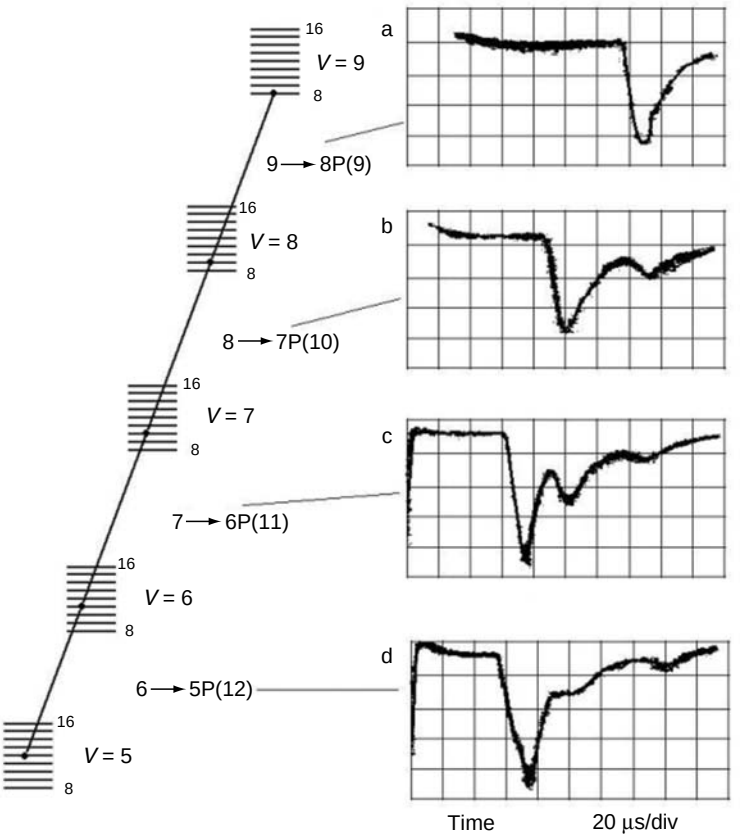

FIGURE 5.10 Time behavior of CO laser pulses demonstrating the cascade mechanism of CO lasing. (From Patel, C.K.N., *Phys. Rev.*, 141, 71, 1966. With permission.)

11%, the theoretically predicted one coming up to ~20%–25%. Moreover, at definite conditions, there is a possibility for two independent lasing cascades to arise for vibrational transitions with even and odd vibrational numbers, which results in intensity alternation of vibrational bands in overtone CO laser spectrum [22] (Figure 5.11).

The radiation spectrum of free-running CO laser consists of a set of vibrational bands that are apart from each other by the spectral interval of ~20–30 cm^{-1}, corresponding to the quantum defect. The minimum number of vibrational levels, beginning from which arises the deviation of the VDF from the Boltzmann distribution and, as a result, CO laser running is possible, can be estimated following the next consideration. The inequality $P_{2-1}^{3-4} > P_{1-2}^{4-3}$ is valid at $\Delta E > kT$. CO molecule transition into the vibrational state with the number V proceeds with maximum probability according to the following reaction $CO(V-1)+CO(V'=1) \rightarrow CO(V)+CO(V'=0)$ The quantum defect ΔE is maximum in this case:

$$\Delta E = [E(1) - E(0)] - [E(V) - E(V-1)] = 2\omega_e x_e (V-1). \tag{5.12}$$

Minimal value $V_{\min}$, at which lasing can arise can be roughly estimated from the expression

$$2\omega_e x_e (V_{\min} - 1) \approx kT. \tag{5.13}$$

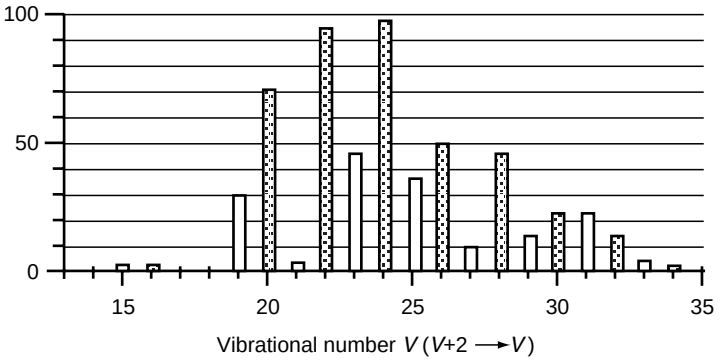

FIGURE 5.11 Distribution of output energy of pulsed first-overtone CO laser over vibrational bands demonstrating two lasing cascades with even and odd numbers. (From Ionin, A. et al. *Opt. Commun.*, 178, 377, 2000. With permission.)

One can see from this estimation that the number of the lowest vibrational levels, beginning from which the lasing can take place, increases with the gas temperature. At room temperature $T = 300$ K the lasing can arise beginning from $V_{\min} \sim 8$, whereas at the temperature of liquid nitrogen 77 K $V_{\min} \sim 2$. There are one or several rotational lines in each vibrational band separated from each other by the spectral interval:

$$\delta\nu \approx [B_{V_1}(J+1)(J+2) - B_{V_1}J(J+1)] - [B_{V_1}(J+2)(J+3) - B_{V_1}(J+1)(J+2)] = 2B \approx 4\ \text{cm}^{-1}. \tag{5.14}$$

At constant ratio N_V/N_{V-1}, CO laser spectrum shifts to the higher values of J as gas temperature increases. As a rule, the values of J in experiments lie within ~15–25 for the room temperature and ~5–10 for the temperature of liquid nitrogen. The approximate expression for the rotational number J_{opt}, corresponding to the maximum small-signal gain is as follows [23]:

$$J_{\text{opt}} \approx \left[\left(\frac{J^*}{2}\right) - \left(\frac{1}{4}\right)\right] + \left\{\left[\left(\frac{J^*}{2}\right) - \left(\frac{1}{4}\right)\right]^2 + \left(\frac{3kT}{2B}\right)\right\}^{1/2} \tag{5.15}$$

as for J^*, see Equation 5.10.

Therefore, the data about rotational structure of CO laser spectrum gives information about the temperature of active medium and the degree of vibrational pumping characterized by the N_V/N_{V-1} ratio.

In experiments the spectrum of free-running fundamental band CO laser lies, as a rule, within the spectral interval of ~4.9–5.5 μm. (By using special procedures this spectrum can be stretched to the spectral interval of ~4.7–8.2 μm. The spectrum of a first-overtone CO laser is within ~2.5–4.2 μm.) The distribution of output power (energy) over a CO laser spectrum depends on many factors. The spectral width of a single vibrational–rotational line corresponding to a spectral profile of small-signal gain ($\Delta\nu_{\text{ampl}} \sim 0.1\text{cm}^{-1}$ at gas pressure of ~1 atm for high-pressure CO lasers) is far less than the spectral interval between adjacent vibrational–rotational lines (~4 cm^{-1}).

Incorporation of selective elements into a CO laser resonator (diffraction grating, for instance) enables one to select a single vibrational–rotational line. However, the output efficiency of such a CO laser does not exceed a few percent because of disrupting cascade

mechanism of CO lasing. Application of multicavity selective schemes selecting one vibrational–rotational line in each vibrational band partaking in free-running lasing gives the opportunity of keeping cascade mechanism of lasing and output efficiency of CO laser, and to increase its spectral brightness.

5.5 PULSED MODE OF CO LASER OPERATION

Under pulsed excitation in electric discharge, it needs time T_{VV} for population to go up the ladder of vibrational levels of CO molecule and form the plateau in VDF (Figure 5.3 and Figure 5.6). This time depends on the rate of V–V exchange, and, hence, on gas pressure of laser active medium and the number V of vibrational level. The higher the vibrational level, the longer the time needed for population to reach this level, and hence the longer the time for formation of inversion population. The lifetime of the inversion population is determined by the rate of the V–V exchange and V–T relaxation time. Usually, electric discharge pump time for pulsed CO lasers is ~1–100 μs. The pulse duration of a free-running pulsed CO laser is usually longer ~0.1–1.0 ms^{-1}. To make the CO laser run with a shorter pulse one needs to use a Q-switching of the laser resonator. Q-switching by a rotating mirror [24] enables one to get a CO laser pulse of microsecond or submicrosecond duration. However, the efficiency of getting a microsecond pulse is 5–10 times less than that of a free-running CO laser. The cause of this efficiency reduction is the fact that most of the vibrational energy is concentrated in lower vibrational levels. A time T_{VV} is required for this energy to transfer to the plateau as a result of the V–V exchange (Figure 5.3 and Figure 5.6). To extract the energy close to that of free-running pulsed laser output, one needs to launch a series of short microsecond pulses with interval $T \geq T_{VV}$. The above Q-switched CO laser operates in multiline mode. Rotational–vibrational line selection also results in laser efficiency decline, because the single-line lasing of short microsecond pulse affects only one vibrational transition. As a result, the efficiency of the laser emitting a single short microsecond pulse on a single rotational–vibrational line is a few tenths of a percent coming up to ~1%, 5–10 times less than that of a multiline Q-switched CO laser.

Nanosecond pulse CO lasing makes the situation more complicated because it is limited by two factors. One of them is the distribution of the vibrational level population over the rotational structure. Another one is the limitation of pulse length by the width of the spectral line. Both factors are determined by gas pressure p of gas mixture used in an electric discharge CO laser or CO laser amplifier. A single-line nanosecond pulse extracts energy from one selected rotational–vibration transition (Figure 5.12) because its pulse length t_{out} is about or less than the (RR) relaxation time $T_{\text{RR}} \geq 10^{-9}$ s at $p \leq 1$ atm. Thus, the output efficiency of a single-line nanosecond pulse CO laser is 0.1%, an order of magnitude less than for microsecond pulse lasing and close to the value estimated in [25]. To increase ultrashort pulse CO laser efficiency one has to use a train of such pulses following with interval $T > T_{\text{RR}}$.

The second factor is that a nanosecond pulse duration t_{out} is limited by the spectral line width $\Delta\nu$: $t_{\text{out}} \sim (\Delta\nu)^{-1}$. The rough estimation for a CO laser mixture gives ~300 torr for getting an ~1 ns pulse. Both factors were experimentally analyzed not for CO lasers, but for 10.6 μm CO_2 lasers and amplifiers in hundreds of publications as the idea of using nanosecond high-energy CO_2 laser pulses for inertial fusion was developed in the 1970s and 1980s. However, for a CO laser there is only one publication [26] in which a train of ~2 ns pulses with energy of ~1 μJ/pulse (gas pressure ~350 torr) was experimentally obtained.

It should also be noted that an active medium of CO laser has a unique distinction related to the very wide vibrational–rotational spectrum of CO molecule (Figure 5.1). The full width $\Delta\nu$ of a CO laser spectrum corresponding to the wavelength region 2.5–8.2 μm is $\Delta\nu \sim 3000$ cm^{-1}. At gas density ~15–20 atm all these spectral lines could overlap and as a

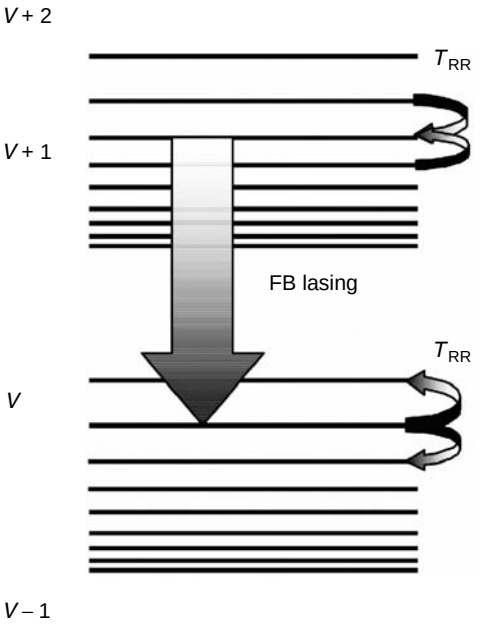

FIGURE 5.12 Schematic of singe-line ultrashort fundamental band CO lasing.

result one can obtain a very broadband laser medium suitable for producing ultrashort ($\Delta t \sim 1/(c \cdot \Delta\nu) \approx 10$ femtosecond) laser pulses in the mid-IR spectral region.

5.6 THEORETICAL MODEL OF ELECTRIC DISCHARGE CO LASER

Theoretical description of electric discharge CO lasers is based on the mathematical model consisting of the system of kinetic equations describing vibrational population N_V, density of photons I_V in a laser resonator on frequencies of quantum transitions under consideration, the change of translational–rotational temperature T of laser mixture. This system of equations characterizing under one-quantum approximation the lasing process in a CO laser is as follows [30]:

$$\begin{aligned}\frac{dN_V}{dt} = {} & \frac{R_V W}{E_V} - c(\alpha^V_{\text{ampl}} I_V - \alpha^V_{\text{ampl}} I_{V+1}) - N_V \sum_{V'} (P^{V',V'+1}_{V,V-1} N_{V'} + P^{V'+1,V'}_{V,V+1} N_{V'+1}) \\ & + \sum_{V'} P^{V'+1,V'}_{V-1,V} N_{V'+1} N_{V-1} + \sum_{V'} P^{V',V'+1}_{V+1,V} N_{V'} N_{V+1} \\ & - \left\{ \begin{array}{l} P_V \left(N_V - N_{V-1} \exp\left[-\frac{(E_V - E_{V-1})}{kT} \right] \right) \\ + P_V \left(N_{V+1} - N_V \exp\left[-\frac{(E_{V+1} - E_V)}{kT} \right] \right) \end{array} \right\} N - N_V (A_V + A_{1V}) \\ & + N_{V+1} A_{V+1} + N_{V+2} A_{V+2}; \end{aligned} \tag{5.16}$$

$$\frac{dT}{dt} = \frac{1}{C_r} \left\{ \begin{array}{l} W(1 - \sum_V R_V) + \sum_V P_V \left(N_V - N_{V-1} \exp\left[-\frac{(E_V - E_{V-1})}{kT} \right] \right) N (E_V - E_{V-1}) \\ + \sum_V \sum_{V'} (P^{V',V'+1}_{V,V-1} N_V N_{V'} - P^{V'+1,V'}_{V-1,V} N_{V-1} N_{V'+1})(E_V - E_{V-1} + E_{V'} - E_{V'+1}) \end{array} \right\}; \tag{5.17}$$

$$\frac{dI_V}{dt} = c\alpha^V_{\text{ampl}}(I_V + 1) - \tau^{-1}_{ph} I_V, \tag{5.18}$$

where N is the gas density; N_V the density of molecules on the vibrational level V; I_V the photon density in the laser cavity; W the specific input power, that is, the power loaded into electric discharge; R_V the fraction of energy going into the excitation of vibrational level V of CO molecule; α^V_{ampl} the small-signal gain on vibrational transition $V \rightarrow V-1$; τ_{ph} the photon lifetime in a laser cavity; c the speed of light; C_r the specific heat capacitance; A_V, A_{1V} the probability of spontaneous emission from vibrational level V for transitions $V \rightarrow V-1$ and $V \rightarrow V-2$; E_V the energy of the vibrational level V; and $P^{V',V'+1}_{V,V-1}$ is the rate of V–V relaxation for the process $CO(V)+CO(V') \rightleftarrows CO(V-1)+CO(V'+1)$. P_V is the rate of V–T relaxation for the process $CO(V)+M \rightleftarrows CO(V-1)+M+\Delta E$, where M is any other molecule or atom.

For laser mixtures with molecular buffer gas (nitrogen, for instance) or inert gases (helium, argon, etc.) one should introduce additional terms into the system of equations describing collisions of CO molecule with molecules and atoms of other gases taking into account appropriate rates of relaxation and vibrational energy exchange with molecular gases. Moreover, equations describing excitation of vibrational levels of the molecular gases in electric discharge should be incorporated in the system of equations 5.16.

When solving the system of equations, one needs to know information about kinetic constants characterizing the processes of V–V exchange, V–T relaxation, and radiative decay. An order of magnitude for the rates of the V–V exchange between CO molecules and also between CO and N_2 molecules can be estimated when considering following processes [27,28]:

$$CO(V=1) + N_2(V=0) \underset{k_{21}}{\overset{k_{12}}{\rightleftarrows}} CO(V=0) + N_2(V=1) - 188\ \text{cm}^{-1}, \tag{5.19}$$

$$CO(V=1) + CO(V=1) \underset{k'_{21}}{\overset{k'_{12}}{\rightleftarrows}} CO(V=0) + CO(V=2) + 27\ \text{cm}^{-1}. \tag{5.20}$$

At $T = 300$ K $K_{12} = 177 + 16$ torr^{-1} s^{-1}; $K_{21} = 440 + 40$ torr^{-1} s^{-1}, $K'_{12} = (1.26 + 0.18)\times 10^5$ torr^{-1} s^{-1}; $K'_{21} = (1.10 + 0.16)\times 10^5$ torr^{-1} s^{-1}. As gas temperature drops down to 175 K, the constants decrease the order of magnitude.

The V–T relaxation time is several orders of magnitude longer than the V–V exchange time and comes up (for instance at $T = 300$ K and gas pressure 1 atm) to ~1 s and ~10^{-3} s for CO–CO and CO–He interaction, respectively [29]. Einstein coefficients for fundamental and overtone transitions can be found in [15]. Their dependencies on the vibrational number V obtained from the data of [15] are in Figure 5.9.

The probability of spontaneous emission reaches a high value at $V > 10$ (for fundamental band transitions) and renders high influence on CO laser kinetics, especially, at low gas pressure. The fraction of energy of excitation of the vibrational level V of CO molecule R_V and the fraction of pump energy going into the gas heating can be theoretically calculated by considering the balance of electron energy in an electric discharge and solving the kinetic Boltzmann equation for the electron energy distribution function.

The mathematical model of electric discharge CO laser represented by Equation 5.16 through Equation 5.18 is complicated, because it consists of the system of a few dozens of differential equations. Its solution obtained, as a rule, by numerical calculations strongly depends on values of kinetic rates and cross-sections of physical processes, which in many

cases are also calculated by theoretical methods. Moreover, the theoretical description of electric discharge CO laser is strongly determined by the degree of completeness of physical processes taken into consideration. The theoretical studies of a CO laser have been extensively developed since its launch (see, for instance, [30–43]); also discussed in several reviews [23,29,44–47]. Nowadays, the theoretical study of CO laser are developing in the following directions: modification of the theoretical model itself taking into account multiquantum VV exchange going according to the reaction $CO(V)+CO(V') \rightleftarrows CO(V-n)+CO(V'-n)$ $(n \geq 2)$, where n is the number of vibrational quanta exchanged, and more precise definition of physical constants used in the model [47].

The first experimental indication of the importance of collisional exchange of CO molecules by more than one vibrational quantum was claimed for $V > 15$ [48]. Later, it was demonstrated [49,50] that for the correct description of a first-overtone CO laser it is necessary to employ multiquantum exchange (MQE) theory. The transition to a more complicated description using MQE depends critically on the existence of reliable data about V–V exchange processes for different gas temperatures and all vibrational states. It is practically impossible to measure all the necessary rate constants. Therefore, the leading role in the progress should be played by the theory of molecular collisions. The first simplified theories, mostly first-order ones, were introduced in the 1950s and 1960s. Concerning V–V energy transfer, the Rapp–Englander-Golden model [51] for transitions induced by short range forces, and the Sharma–Brau model [52] for transitions induced by long range multipole interactions accounting for exactly resonant transfer became very popular. These simplified theories, especially the Sharma–Brau approach, generally show a good qualitative agreement with the experimental behavior of rate constants as a function of temperature. However, because the whole range of interaction forces (short range, long range, and dispersion contributions) and their interference effects are neglected, the quantitative results are in most cases not accurate enough. Moreover, these models also fail to qualitatively reproduce the correct rate constant behavior at temperatures lower than 200 K. This is a consequence of the fact that rotational motion and the centrifugal stretch coupling are not included, although they give a substantial contribution at low energies. A method to simplify the computational load of accurate determinations of V–V rate coefficients, without resorting to drastic approximations, is based on semiclassical considerations and has been introduced and developed by Billing [53–56]. This approach consists of treating the rotational and translational motions of the molecules classically, whereas the vibrations and vibrational–rotational coupling are treated quantum mechanically. The coupling between the two systems is achieved by using an averaged potential for the solution of the classical equations of motion. Evidently, such a theory requires a good knowledge of interaction potentials at short and long distances, and their choice can seriously affect the accuracy of the results. The rate constants for the CO–CO vibrational exchange process reported in Reference [57], together with those presented earlier in Reference [58], constitute a very large set of semiclassical rate coefficients in a wide temperature interval either for single or multiquantum processes, including those where an asymmetric number of vibrational quanta are exchanged. Thus, the number of computed rate constants is sufficient to construct the full matrix of V–V rate constants without resorting to heuristic suggestions based on extrapolation or interpolation. Inclusion of the asymmetric one-to-two quanta exchange processes allows one to explain naturally the abrupt reduction of vibrational populations at these levels observed experimentally in [59], where it was explained by the introduction of a V–E (vibrational–electronic) nonadiabatic collisional process. The sensitivity of CO overtone lasing characteristics to the choice of the rate constant set is strong, and thus only an accurate and complete set published in [57,58] should be recommended. Furthermore, the main and undeniable advantage of the new semiclassical set is its capability to more adequately describe nonstationary processes, which takes place after

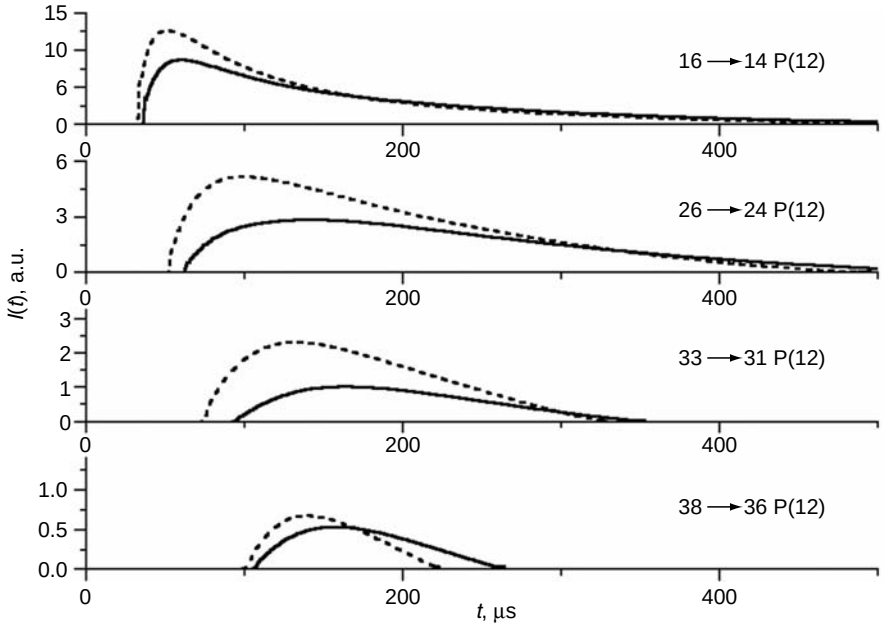

FIGURE 5.13 Laser pulses for frequency selective first-overtone EBSD CO laser calculated for high overtone transitions with different models: SQE model (*dashed curve*) and MQE model (*solid curve*). (From Napartovich, A.P. et al., *Proc. SPIE*, 5777, 408, 2005.)

sudden perturbations of the VDF. To illustrate effects produced by transition from the model in single quantum exchange (SQE) approximation [60] to a full MQE theory [57], single-frequency overtone lasing for a number of vibrational levels was calculated for conditions close to those realized experimentally in [61] for the first-overtone CO laser. Laser mixture CO:He = 1:4 at temperature 100 K and gas density 0.2 amagat (Amagat is a reduced gas density unit corresponding to the number of moles in the mole volume 22.4l) was assumed to be excited by the EBSD with duration 30 μs and energy input density ~200 Jl^{-1} amagat. Time behavior of laser pulses is shown in Figure 5.13. It is seen that the simplified SQE theory overestimates the intensity magnitude and rate of inversion formation. Full MQE model predictions are remarkably closer to the experiment. It is worth noting that corrections to SQE approximation are larger for medium vibrational levels.

Ab initio rate coefficients calculations for asymmetric V–V' energy exchange processes in CO–N_2 collisions were performed in [62] using a semiclassical coupled-state method and a slightly modified interaction potential discussed in the previous paper [63]. Rate coefficients for asymmetric exchange between CO molecules on high vibrational levels and ground state CO and N_2 molecules are shown in Figure 5.14 for two gas temperatures 100 and 300 K. The maximum of rate coefficient for N_2, as it is a molecular collision partner although much lower than that for CO partner, is shifted down five levels. As a result, when N_2 concentration is above a few percent, energy exchange with N_2 controls populations of CO molecules on levels $V > 38$. This effect was experimentally observed [61], where a first-overtone CO laser spectrum was detected for laser mixtures with and without nitrogen. The new set of rate coefficients for asymmetric one-to-two quanta in V–V' energy exchanges was calculated and used in the kinetic modeling for the CO:He(Ar):N_2 lasing mixtures at different N_2 concentrations [62].

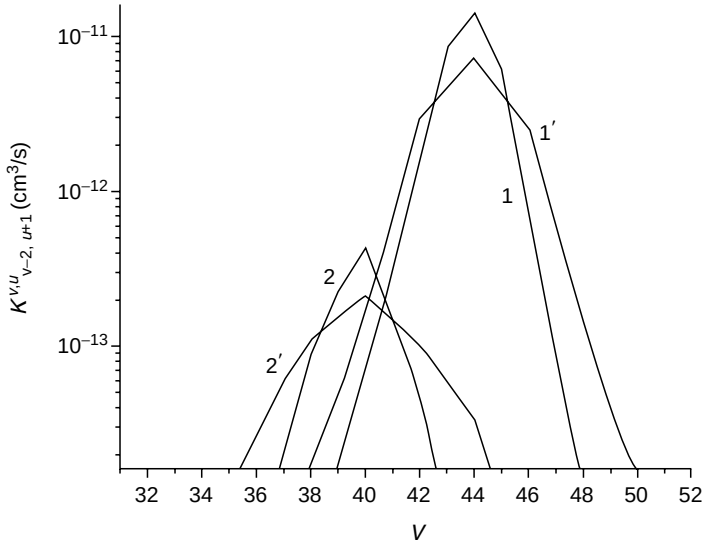

FIGURE 5.14 Rate coefficients of the asymmetric processes $CO(V) + CO(0) \rightarrow CO(V-2) + CO(1)$ (1, 1′) and $CO(V) + N_2(0) \rightarrow CO(V-2) + N_2(1)$ (2, 2′) vs. the number V of vibrational levels at $T = 100$ K (1, 2) and $T = 300$ K (1′, 2′). (From Napartovich, A.P. et al., *Proc. SPIE*, 5777, 408, 2005. With permission.)

A complete numerical model of CO laser is based on the theory of multiquantum V–V exchange. Actually, a full kinetic model of the laser incorporates plasma kinetics module also, which, in turn, is based on solving electron Boltzmann equation for an electron energy distribution function. Electron–molecule interactions govern efficiency of excitation of molecular vibrations in a discharge. For correct description of these processes, reliable information is needed about cross-sections for vast variety of processes including elastic and inelastic processes, electron attachment, ionization, dissociation, etc. Since energy release in the electric discharge is followed as a rule, by gas dynamic expansion, this process should be taken into account in the model. Because of a great complexity in the processes involved, and still existing restrictions on computing rate, zero-dimensional model is usually employed. In such a situation, experimental data should be measured in well-controlled conditions with proper care about the role played in reality by spatial nonuniformities. Comparison between such data and results of numerical simulations verifies an applicability of the theory to the description of experiments.

Small-signal gain in dependence on vibrational number is a direct measure of vibrational distribution function provided the gas temperature is known. However, a technique required for its measurements is complicated. Extensive experimental studies on small-signal gain spectrum dynamics in EBSD CO laser were performed, first using the selective intracavity losses [64] to measure the small-signal gain on first-overtone transitions. Later, a master oscillator-laser amplifier system was developed and implemented to measure small-signal gain spectrum in the fundamental band [65]. It was shown that a satisfactory agreement of the theory with experiment takes place in the case when the specific input energy loaded into an electric discharge taken in calculations was reduced by ~30%–40% relative to space-averaged experimental specific input energy value. Such a correction in the local value of the specific input energy when compared with the experiment value leads to a good agreement between the theory and measurements for a wide range of vibration transitions and for various gas mixtures and densities. Figure 5.15 illustrates the correspondence of the theory to the

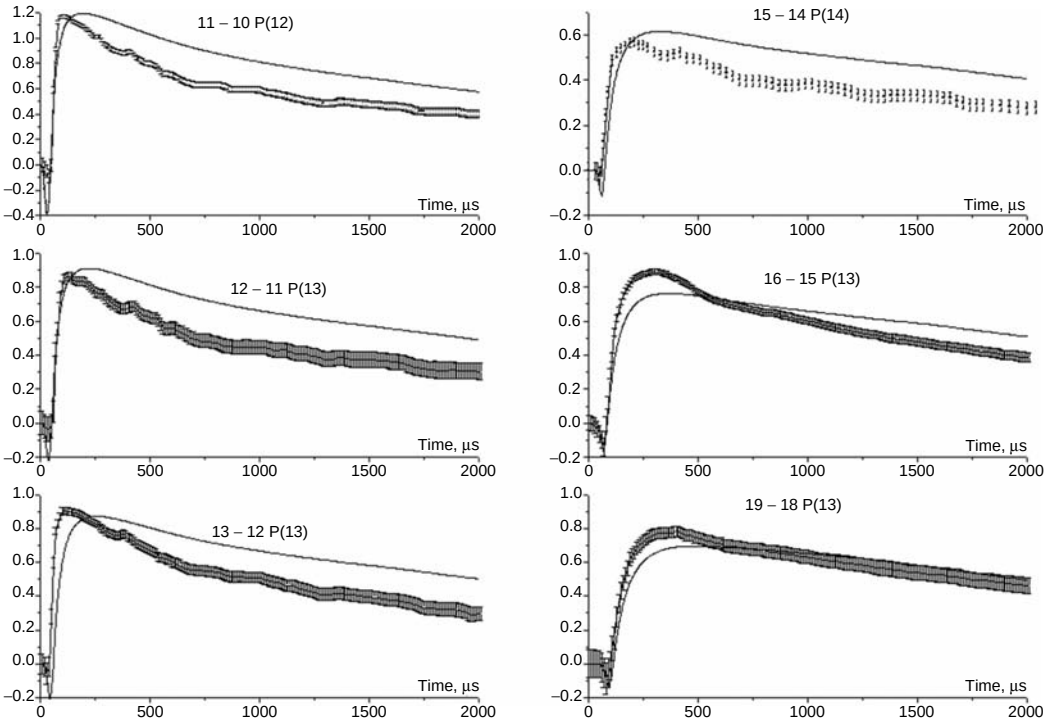

FIGURE 5.15 Small-signal gain time behavior for different vibrational transitions. CO:He = 1:4, gas density 0.12 amagat, initial temperature 120 K. Solid lines show theoretical results for specific input energy ~100 JL^{-1} amagat. The experimental data for average specific input energy ~150 JL^{-1} amagat are plotted by bars showing the experimental error. (From Napartovich, A.P. et al., *Proc. SPIE*, 5777, 408, 2005. With permission.)

experiments for the mixture CO:He = 1:4 where measured small-signal gain time behavior for six vibrational–rotational fundamental band transitions is compared with the results of calculations [66]. The progress in theory of multiquantum V–V exchange results in much better ability of the full kinetic model to describe available experimental data. Small-signal gain time behavior in the fundamental and overtone bands was experimentally studied allowing kinetic model successful verification. A great role of asymmetric V–V' exchange in the formation of CO vibrational distribution function on high levels at low additions of N_2 was shown.

5.7 EXPERIMENTAL RESEARCH AND DEVELOPMENT OF FUNDAMENTAL BAND CO LASERS

The methods of excitation of carbon monoxide lasers are close to those of widespread CO_2 lasers. First CO lasers [2–9] operated when their gas mixtures CO:He or CO:N_2:He were excited by self-sustained RF of DC discharge ignited in an electric discharge tube. Since the beginning of the 1970s scientists and engineers have been paying great attention to the experimental research of lasing mechanism taking place in a CO laser, to the analyses of VDF, to the research of elementary processes going in low-temperature plasma of a CO laser, spectral properties of a CO laser operating in spectrally selective and nonselective mode of

operations, small-signal gain measurements, the development of different sorts of CO lasers including CW, pulsed, repetitively pulsed ones, sealed-off and gas flow CO lasers, excited by self-sustained and non-self-sustained discharge (see for instance [67–89]). Many such studies were discussed in the reviews [44,90–96].

CO lasers can run in so-called sealed-off mode of operation [72,73,97–100] (i.e., without changing the gas mixture), when heat released in the course of electric discharge is removed by diffusion of gas to the wall of a tube and in gas flow regime. Specific output power ~30 W/m at efficiency of ~15% was obtained in the sealed-off CO laser [98]. A sealed-off water-cooled CO laser with a laser tube of ~1 m length operating in nonselective multiline mode of operation normally has an output power of ~10 W. The output power of sealed-off CO laser consisting of many electric discharge tubes comes to ~100 W [100]. A replacement of in an active medium in the zone of excitation and its cooling down to −10°C resulted in the development of DC discharge axial-flow CO laser consisting of 20 successive sections each of 30 cm long with a total output power of 4 kW. Laser mixture CO:He:N_2 = 1:20:1 at an operating pressure of 120 mbar –130 mbar with a small amount of oxygen and xenon was used. The optimal flow rate was 0.1 l min^{-1}. Under sealed-off geometry, the same laser had an output power up to 3 kW and an output efficiency up to 8%. Wall-plug efficiency of the CO laser was 3% [101]. Cooling laser mixture down to cryogenic temperature ~100 K and using fast axial gas flow resulted in the development of DC discharge CO laser with 49% efficiency and output power ~1 kW [102].

RF discharge is becoming more and more popular for the excitation of both CO_2 and CO lasers and is widely applied to waveguide, slab, transversely excited, and axial-flow CO lasers. An output power ~1 kW, efficiency 28%, and specific output energy 2.4 kW/m (9.5 W/cm^{-3}) were obtained in the cryogenically cooled fast-axial-flow CO laser consisting of two sections each of 24 cm length and excited by RF discharge (excitation frequency f = 27 MHz). The running time was limited by the liquid nitrogen storage capacity to 50 min at 950 W and 2 h at 750 W. The inlet gas temperature was −135°C [103]. Laser efficiency of 17% was detected for the fast-axial-flow ~1 kW RF discharge CO laser (f = 13.56 MHz) running at gas temperature close to that of the room [104].

In [106], RF discharge transverse-flow CW CO laser previously cooled by liquid argon and operated at 200 K with output power 1.32 kW and output efficiency 28.1% [105] was researched at gas temperature 286 K. An output power of ~1 kW and output efficiency of 15% were achieved using laser mixture of He, N_2, CO, and O_2 without the addition of xenon. Room temperature operation was claimed to be superior because of more uniform excitation and higher optical quality of CO laser radiation. Repetitively pulsed modification of the above CO laser operating also at room temperature was reported in [107], where a peak power of 920 W, which is 1.6 times the CW output power, was observed.

RF discharge was successfully applied for pumping CO lasers with slab geometry of excitation (Figure 5.16) (slab CO lasers). In such lasers heat generated in the excitation zone, with interelectrode gap of a few millimeters and width of several centimeters, is withdrawn through the thermal diffusion to the cooled electrodes. That is why these lasers operate without gas flowing. An output power of 120 W, efficiency 17%, and specific output power 15.5 kWm^{-2} were obtained in compact slab CO laser at gas temperature −30°C. The same CO laser had an output power of 50 W when running at room temperature. For a laser with an unstable resonator, the output power came to 80 W, with the output efficiency 12% at gas temperature −30°C [108]. The specific output power was enhanced to 26 kWm^{-2} in [109]. It should be noted that laser radiation within the laser slab propagates as in one-dimensional waveguide. At cryogenic cooling RF discharge slab CO laser with active volume 500×178×2 mm^3 emitted IR radiation with power ~1 kW with efficiency 25% [110]. When decreasing the electrode width down to the size comparable with the interelectrode gap of ~1–2 mm, the

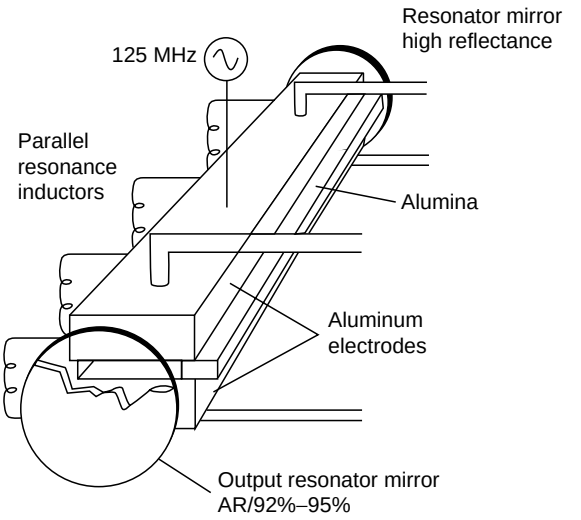

FIGURE 5.16 CW slab CO laser excited by RF discharge. (From Villarrea, F. et al. *CLEO'95, Technical Digest*, 44, 1995. With permission.)

mode of slab laser operation transforms into a totally waveguide regime. Waveguide RF discharge CO lasers are characterized by small dimensions of active region (~$2\times2\times200$ mm^3) and output power ~1–10 W (see review [93]). For instance, an output power of 0.5 W was obtained in CO laser with an active volume of $1.5\times1.5\times180$ mm^3 [111].

Apart from RF discharge, MW discharge is also applicable to CO laser excitation. Output power 440 W with efficiency 8% and specific output power 1.4 kWm^{-1} was observed in fast-flow MW discharge CO laser ($f = 2.456$ GHz) running at room temperature [112], which was later increased to 700 W ($\eta = 6.8\%$) [113]. Two magnetrons with power 6 kW each at frequency 2.46 GHz were used for excitation of the gas mixture He:N_2:CO:Xe = 79.5:7.5:8.5:4.5 circulated in a closed loop. CO concentration was controlled. Addition of an optimized amount of O_2 with adsorption of CO_2 in the zeolithe traps stabilized gas composition.

Following the main principles of V–V exchange (see earlier), one needs to cool the CO laser active medium to liquid nitrogen temperature to reach its highest efficiency. The application of liquid nitrogen is not very convenient, in particular, for autonomous and mobile laser systems. Adiabatic gas expansion through a supersonic nozzle enables one to cool down the laser mixture and form a supersonic gas flow with the Mach number

$$\mathrm{M} = \sqrt{\left(\frac{T^*}{T} - 1\right)\frac{2}{(C_p/C_v - 1)}}.$$

Electric discharge excitation of such a supersonic CO laser is possible both in supersonic flow and subsonic flow in a plenum chamber. Different types of the electric discharges, self-sustained and non-self-sustained, can be used for supersonic CO lasers pumping [114–128]. Application of transverse-flow RF discharge for excitation of supersonic CO laser in a plenum subsonic zone resulted in the development of closed-loop 1 kW CO laser (Figure 5.17) [124,125] and 7 kW CO laser running in the course of ~10 s [126,127]. An output power ~2 kW and efficiency of ~20% were obtained in RF discharge supersonic CO laser [128] by using the strongly modified laser facility used in [124,125]. It is shown in Figure 5.18.

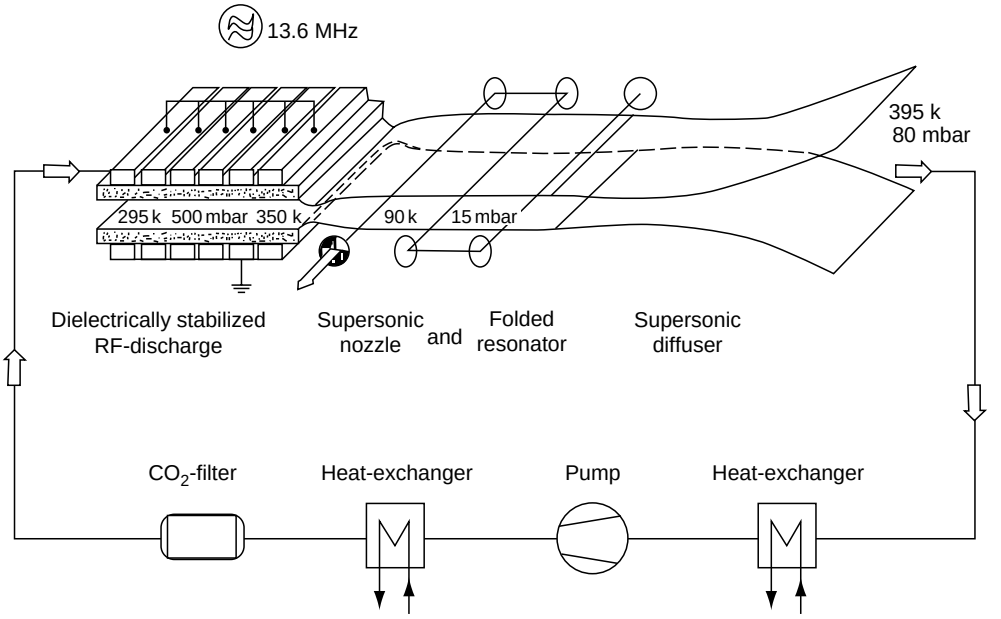

FIGURE 5.17 CW closed-loop supersonic CO laser with RF excitation. (From von Bülow, H. and Zeifang, E., *Rev. Sci. Instr.*, 64, 1764, 1993. With permission.)

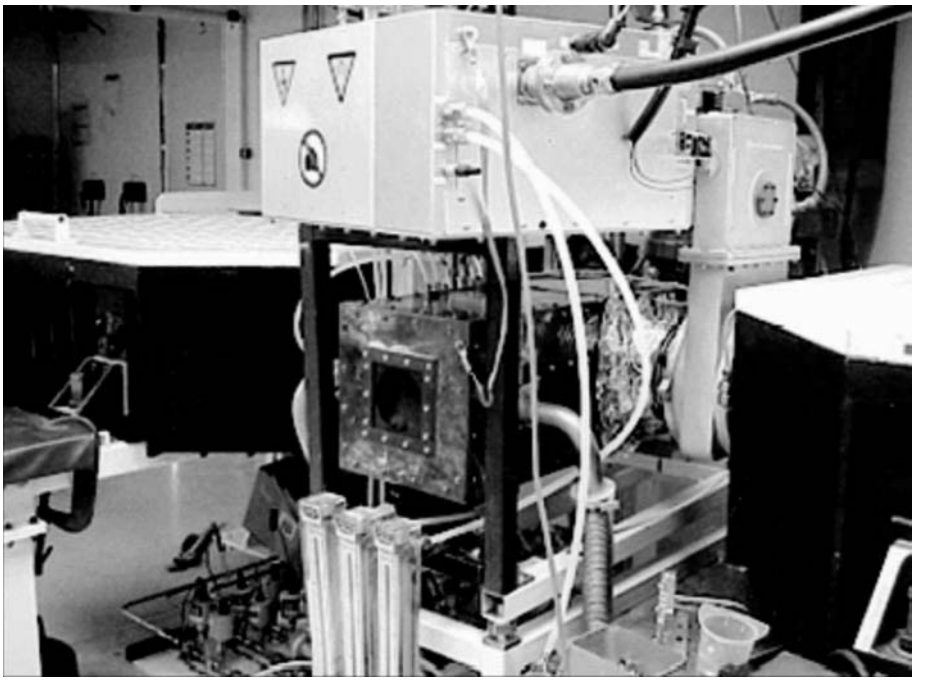

FIGURE 5.18 CW supersonic fundamental and first-overtone band CO laser [http://www.afrl.af.mil/successstories/2001/emerg_tech/01-de-17.pdf].

As for the output power, different types of electric discharge CO lasers can conditionally be classified as follows. Output power ~1–10 W: waveguide lasers, room-temperature sealed-off lasers; output power ~10–10^3 W: lasers pumped by DC, RF, and MW discharge, lasers with axial gas flow, with diffusion cooling; slab lasers; output power ~10^3–10^5 W: lasers with transverse gas flow and transverse electric excitation including electron-beam sustained discharge (EBSD) lasers. One can see that transverse electric excitation (electric field is perpendicular to the optical resonator axis) and transverse gas flow perpendicular to both electric field and the axis of optical resonator are used for the development of high-power CO lasers with an output power of tens and hundreds of kW. A set of high-power CW transverse-flow CO lasers excited by DC self-sustained discharge was developed in [129]. The first one is cryogenic CW TE 5 kW CO laser excited by DC discharge, with a commercial CO laser also constructed. Its discharge zone dimension is 6.2 cm (gap) × 140 cm (length). A folded three-pass stable resonator with cavity length 6.6 m and optical aperture 55 mm in diameter was used. Gas mixture $CO:N_2:He:O_2 = 6:16:78:0.4$ at gas temperature 150 K, gas pressure 50 torr and gas flow velocity 22 ms^{-1} was used. Operating time was several hours. More powerful cryogenically cooled CO laser with an output power of 20 kW and output efficiency of 15% was also developed [129] (Figure 5.19). The laser had transverse excitation configuration and was excited by DC discharge with a dimension of 6.2 cm (gap)×400 cm (length). Stable resonator with cavity length 8.4 m and optical aperture 57.5 mm in diameter was used. Operating conditions: gas temperature 150 K, gas pressure 40 torr, and gas flow velocity 20 ms^{-1}.

One type of transverse electric discharge and transverse gas flow lasers is the EBSD laser. EBSD is a non-self-sustained discharge in which conductivity is created under ionization of

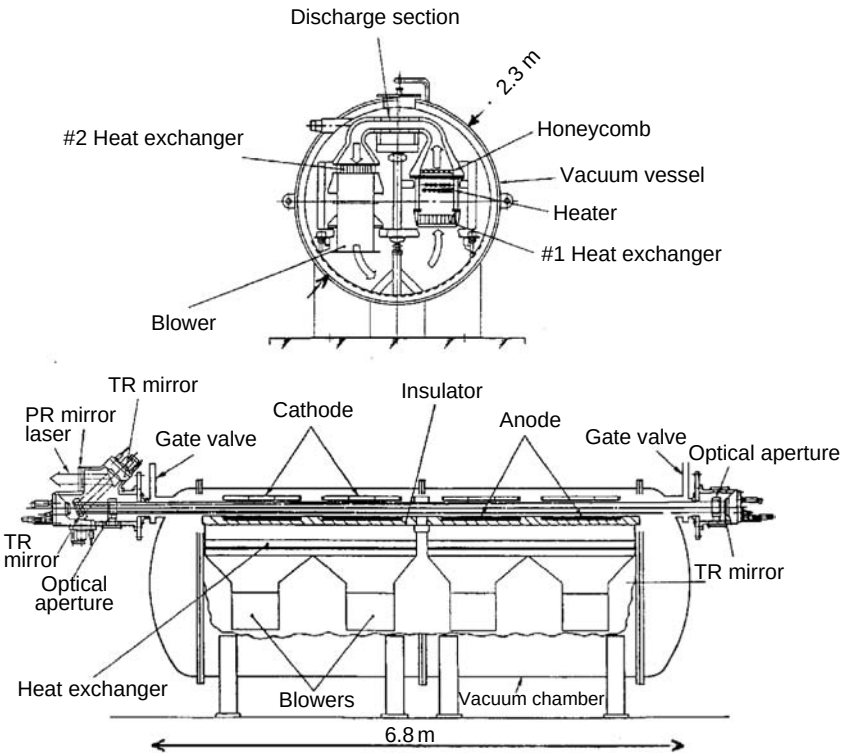

FIGURE 5.19 High-power 20 kW CO laser with transverse gas flow. (From Kuribayashi, S. et al. *Proc. LAMP'92,* Nagaoka, Japan, 51, 1992. With permission.)

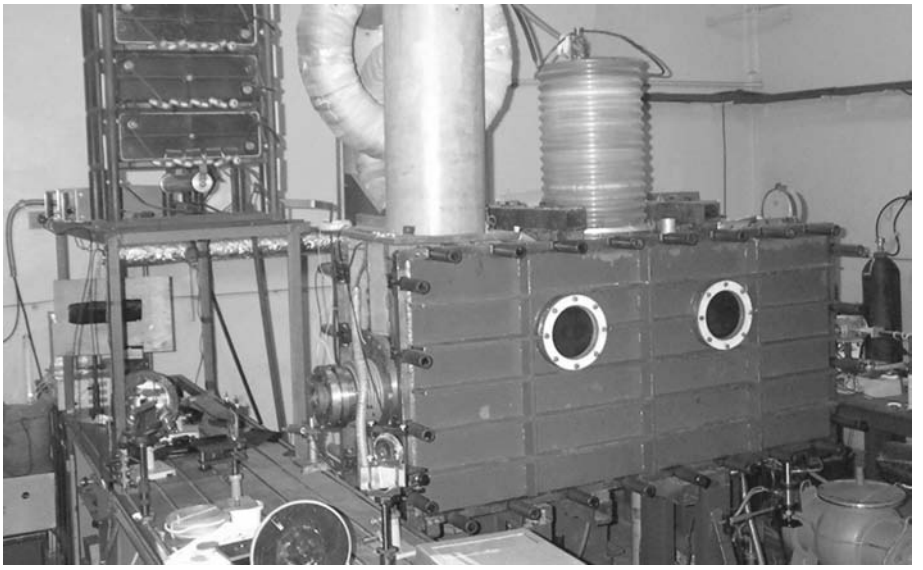

FIGURE 5.20 Pulsed EBSD CO laser with output energy 800 J (fundamental band) and 50 J (first-overtone). (From Ionin, A. et al. *Proc. First Symp. Beamed Energy Propulsion*, Pakhomov, A., Ed., Huntsville, AL, November 2002, American Institute of Physics, 697, 2003. With permission.)

active medium by external electronic beam. Electric energy is loaded from a high-voltage power source into the active medium that has conductivity with electron concentration of 10^{10}–10^{13} cm^{-3}. The advantage of EBSD lasers is the possibility of increasing gas pressure and controlling E/N (E/p) parameter on which the efficiency of electric discharge pumping depends strongly. The proposition about excitation of high-pressure CO laser by EBSD was made in [130]. First, room-temperature pulsed EBSD CO lasers were developed in [35,131,132] on the basis of CO_2 laser facilities. However, output characteristics of such lasers were inferior to those of CO_2 lasers. Further efforts were aimed at cryogenically cooled pulsed EBSD CO lasers [133,134]. The data obtained for these lasers under the same experimental conditions were to some extent contradictory: ~60% efficiency in [134] and ~15% in [133]. The EBSD method of CO laser pumping enabled one to increase the gas density of laser mixture up to 10 Amagat [135]. Cryogenic single pulsed EBSD lasers (Figure 5.20) were also developed in [87,136–139], their energy coming to ~0.5–1.5 kJ with laser efficiency ~30%–40%. Repetitively pulsed EBSD CO laser operating with a repetition rate of 100 Hz and emitting 10 kW average output power with efficiency 15% was developed in [140]. The CO laser ran for 10 s. Industrial EBSD CO laser with CW ~10–12.4 kW and repetitively pulsed 14.2 kW output power (Figure 5.21) was developed and applied for laser welding of 10 mm width stainless steel [141–143]. Repetitively pulsed mode of the EBSD pumped cryogenic CO laser was also realized in [144], and comparative studies were performed on efficiency of perforating of different metals for CO_2 and CO lasers for similar energetic characteristics of both (pulse energy 5–30 J). The material removal rate per pulse for CO laser was higher than for CO_2 laser: 1.4 times for copper, 1.86 times for steel, and 4.5 times for aluminum. Authors indicate the existence of an optimum repetition rate of about 110 Hz at pump pulse duration 100 μs. Increasing repetition frequency resulted in laser beam optical quality becoming worse. The room temperature repetitively pulsed EBSD CO laser was studied in [145,146]. A train of 1000 pulses with a repetition rate of 100 Hz and output energy 80 Jl^{-1} bar at output efficiency 20% was obtained [146]. Cryogenic CW CO laser excited by the EBSD was developed in [147]. The laser operated with laser mixture $CO:N_2 = 1:9$ and subsonic gas flow rate of 1 kgs^{-1} of

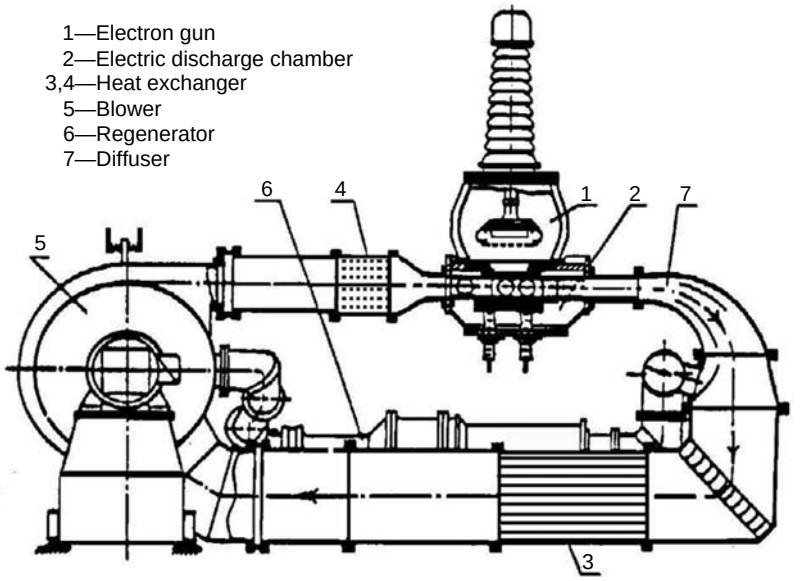

FIGURE 5.21 High-power industrial CW and repetitively pulsed CO laser. (Averin, A., et al., *Proc. SPIE*, 2206, 1994. With permission.)

precooled gas (temperature 90 K). Total power 85 kW was demonstrated at electro-optic efficiency ~25–30%. Output laser beam had sizes 10×5 cm^2, operating time up to 5 s.

First experiments on the development of supersonic EBSD CO laser were started in the 1970s [91,92,148], with output power of 110 kW and 18% efficiency obtained for 2 ms^{-1}. The output power reached 250 kW for shorter running time [91]. Supersonic CO lasers with output power ~80–200 kW with running time ~10^{-3}–1.0 s were developed in [149–152]. Authors [152] launched CO laser with EBSD excitation in supersonic flow of gas mixture CO:Ar of density 0.2 amagat at flow Mach number 2.9 and gas temperature 80 K. At gas flow rate 6.3 kgs^{-1}, the laser power of 200 kW was achieved with an efficiency of 40% at 100–300 ms. Specific laser power amounted up to 90 Jg^{-1}. This CO laser was supposed to be situated on a truck. It should be noted that NASA considered high-power EBSD CO laser as a very promising candidate for space based laser system intended for laser transmission of energy transformed from solar radiation from space to the Earth [153]. A comparison of EBSD CO laser with electric discharge and gas dynamic CO_2 lasers, iodine and chemical lasers, and so on, demonstrated that only supersonic CO laser has the best efficiency and the least mass and dimensions. The project of CW supersonic CO laser with output power of ~1 GW was discussed in [154].

Apart from the above efforts aimed at the development of different sorts of CO lasers, a study of various physical processes in the active medium of CO lasers has been taking place. Optical pumping of CO molecule is very promising for studying CO laser kinetics, because there is no influence of plasma electrons on vibrational and rotational kinetics in this case. Since the first research work in the field [155], several other papers have been published [156–166]. Ionization in optically pumped CO was investigated in [159], where carbon monoxide was excited by resonance absorption of CO laser radiation. As a result, a non-self-sustained electric discharge, supported by the laser, was ignited between the two electrodes. It was shown that the CO vibrational levels were strongly overpopulated up to the vibrational level

$V = 40$ and a correlation took place between the discharge current and the high vibrational level population. The transfer of vibrational energy to electronically excited states in optically excited V–V pumped CO was studied in [160] both theoretically and experimentally. Quenching of high vibrational levels of the CO ground electronic states was shown to decrease the emission from the electronic excited states of CO (and C_2) considerably, indicating that their formation strongly depends on the vibrational excitation in the ground state. Lasing in optically pumped CO laser was observed in [162]. Multiline CW CO laser operating on vibrational transitions from 1→0 to 7→6 was used as a pump source. Optically pumped lasing was observed on vibrational transitions from 11→10 to 15→14. The observed conversion efficiency was ~10%. Repetitively pulsed optical parametric oscillator was used in [163, 164] for carbon monoxide overtone transition 0→2 pumping. Multiline [163] and single-line [164] CO lasing on 2→1 vibrational transition was observed, with the absolute inversion population realized. The shortest CO laser wavelength seems to be obtained in such optically pumped laser for 2→1 R(11) vibrational–rotational spectral line with wavelength ~4.6 μm [164]. The short pumping pulse length (~8 ns) enables one to study the rotational kinetics of population over the vibrational level [165,166].

Explosive absorption that was theoretically predicted [167] and calculated for CO laser [168] was experimentally observed in [157], where CO laser mixture at room temperature slightly excited by EBCD was optically pumped by spectrally selective CO laser. An increase in absorption coefficient with an intensity of input radiation was detected. Such a behavior of the absorption coefficient is quite different from that of the two-level quantum system and is explained by vibrational–vibrational exchange, which populates the lower level of absorbing transition.

Amplification of CO laser radiation and its peculiarity due to its multiline spectrum was observed in [169,170]. The saturation parameters for multilevel active medium of CO laser amplifier were estimated for both long-pulse (100–1000 μs) and short-pulse (~1 μs) laser input. The effect of transformation of multiline spectrum for CO laser radiation passing through the CO laser amplifier was experimentally observed, which was associated with the multilevel structure of the amplifying medium. The data obtained are important for the development of high-power master-oscillator power amplifier systems using carbon monoxide as an active medium.

Phase conjugation effect, which could be useful for optical quality improvement, was observed in [171,172]. An optical scheme, in which the probe signal was directed into the CO laser active medium under the small angle to the intracavity waves resulting in diffraction gratings of saturated gain and refraction index, was used. Phase-conjugated signal diffracted back to the probe and an efficiency 0.2% and ~2% was observed for single-line and multiline probe signals, respectively. The amplitude (i.e., saturated gain) mechanism was shown both experimentally and theoretically to be the predominant mechanism of phase conjugation, when using an active medium of CO laser as phase-conjugation mirror.

Frequency selective Q-switching and mode-locking were studied in the 1970s [26], with the output energy not higher than 1 μJ. For a nonselected Q-switched mode of operation laser, the output came to a few joules with an output efficiency of 5% [173]. A frequency selective tunable Q-switched CO laser was studied in [174]. The laser emitted short (~1–10 μs) pulses with energy 0.1–0.5 J at a wavelength in the range 4.9–6.5 μm. A special optical system was developed for studying the influence of suppression and locking inside the cavity of various parts of the laser spectrum on the output energy and efficiency. In the single-pulse mode of operation ($t_{0.1} = 5$ μs), the efficiency was 0.6% at $\lambda \sim 5.2$ μm (near the maximum of the spectrum obtained in the free-running mode) and 0.1% at $\lambda = 6.0$ μm. Frequency selective lasing of a series of short pulses resulted in output efficiency 0.6% at the long-wavelength edge of the spectrum, with 0.5 J as the total output energy. The fine temporal structure of the

laser pulses was studied with nanosecond resolution. The laser was used in polymer materials surface heat treatment [175] and to study vibrational exchange kinetics on highly excited vibrational levels of CO molecule [50].

5.8 RESEARCH AND DEVELOPMENT OF OVERTONE CO LASERS

For electric discharge CO laser CW first-overtone (FO) CO lasing was observed for the first time in the experiment by Bergman and Rich [18], where supersonic expansion and cooling of preexcited CO:He:O_2 mixture was used. Gas mixture CO:He:O_2 = 78:92:1 at intracavity gas pressure 2.75 torr and gas temperature ~40 K (Mach number 4.2) was used. The active gain path was 20 cm at the optical axis. The output mirror provided ~1% transmission and 99% reflectivity over a 2.6–3.1 μm band pass, with a reflectivity of 30% in the 4.8–6.0 μm range of fundamental band (FB) CO lasing. The rear cavity mirror was a 4 m radius-of-curvature total reflector with 99% reflectivity. FO CO lasing took place on 25 vibrational–rotational lines, ranging from P(5) line of $V+2 \rightarrow V = 12 \rightarrow 10$ vibrational band at $\lambda = 2.688$ μm to the P(6) line of 21→19 at 3.066 μm. FO CO laser power and output efficiency were 20 W and 0.6%, respectively, with the total output power (FO+FB) of 88 W.

Six months later FO CO lasing was observed in a pulsed EBCD CO laser [19] with active volume of ~5 l. A laser resonator was used with output mirror with a reflectivity of ~84% for 2.8–3.2 μm spectral range and ~14% for 5.0–5.6 μm range. Laser mixture CO:N_2:He = 1:9:10 at gas density 0.5 amagat. Pump pulse length was 50 μs. The output energy was 9 J at specific output energy (SOE) 3.5 Jl^{-1} amagat and output efficiency 3.1%. The total (FO+FB) efficiency was 30%. FO CO lasing was observed within 2.7–3.0 μm spectral range corresponding to the vibrational bands $V+2 \rightarrow V$ from 13→11 to 16→14.

An optimization of pump conditions and output mirrors enabled the authors of [176,177] to extend FO CO lasing range from 2.7 to 3.3 μm and to enhance SOE and output efficiency up to 10 Jl^{-1} amagat and 5%, respectively. FB CO lasing was not suppressed yet. Although the authors of [176,177] carried out detailed parametric study of the FO CO laser, they failed in further increase in output efficiency and extension of lasing spectrum, which seemed to be affected by the poor characteristics of cavity mirrors. The maximum output energy of ~50 J at output efficiency of 5% and SOE 10 Jl^{-1} amagat was obtained in [178] for the FO CO laser with active volume of 10 l (Figure 5.20).

Attention was paid to low-power FO CO laser that could be used for spectroscopy [179]. Single-line low-pressure CW FO CO laser was developed in [20,179–181], which operated on 330 rotational–vibrational lines (150 lines in [20]) and was frequency tuned within a spectral range of 2.62–4.07 μm corresponding to overtone transitions from 10→8 to 37→35. The same laser was also used for obtaining CW lasing on the FB 1→0 transition [182]. The laser tube of 90 cm length and 13 mm diameter was cooled by liquid nitrogen (Figure 5.22). The laser mixture CO:N_2:He:Ar at gas pressure 17 mbar was pumped by a DC discharge. The laser cavity consisted of a gold-coated concave ($R = 10$ m) mirror and a reflection grating in Littrow configuration (450 grooves/mm). This laser with low output power of ~0.55 W (no data about output efficiency) was used for spectroscopic applications [181], which do not need high output power and output efficiency. Theoretically, the opportunity of achieving FO CO lasing in an electric discharge laser was predicted in [183]. Numerical studies on characteristics of FO CO laser were also performed in [184]. Analytical theory of the steady-state operation of FO CO laser was developed in [185]. Numerical calculations were performed in [186] on simultaneous FB and FO lasing. Because of the lack of experimental data on vibrational–vibrational exchange rates for highly excited levels of CO molecule, normally extrapolation of low-level kinetic constants is used for modeling lasing on high vibrational transitions [183–189]. For instance, based on an agreement between the theory and experiment for FB CO laser operating

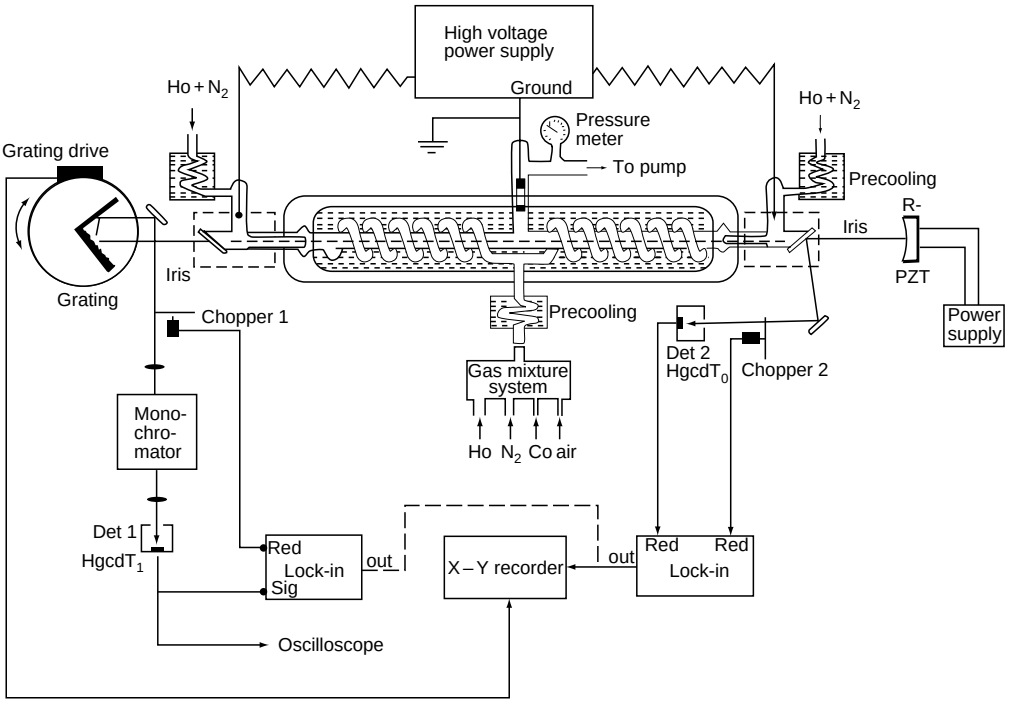

FIGURE 5.22 Frequency selective DC discharge CW first-overtone CO laser cooled by liquid nitrogen. (From Urban, W., *Laser und Optoelectronik*, 23, 56, 1991 and George, T. et al. *Appl. Phys.*, B53, 330, 1991. With permission.)

on vibrational transitions from 5→4 to 16→15, the authors of [189] used the same set of kinetic constants for an estimation of potential characteristics of supersonic FO CO laser operating on vibrational transitions up to 44→42 with output power up to ~20 MW and output efficiency up to 34%. However, for such high vibrational levels the very applicability of the extrapolation method is questionable and has to be verified by a comparison of experimental and theoretical data. Such a comparison was done in [188], where multiline FO CO laser pumped by a short (~1.5 μs) electric discharge pump pulse was researched both experimentally and theoretically. The authors of [188] observed good agreement between the theory and experiment, but FO CO laser spectrum range was narrow (11 lines on low vibrational transitions from 14→12 to 19→17) and the output efficiency was low: 1.2% at SOE 12 Jl^{-1} amagat. Modern theory of an FO CO laser based on the multiquantum *V–V* exchange is discussed at the end of Part 5.6.

Since 1997, FO CO laser physics has been studied both theoretically and experimentally by the joint research team of the Lebedev Physics Institute (Russia), the Troitsk Institute for Innovation and Fusion Research (Russia), and the Air Force Research Lab (USA). Even the first experiments using intracavity spectral filters suppressing FB CO lasing demonstrated [60] that pulsed FO CO laser spectrum could be extended to 2.7–3.6 μm, with an output efficiency of 5%. Theoretical calculations taking into consideration all the real intracavity optical losses predicted an output efficiency of 20%. When using broad band dielectric mirrors with a high reflectivity for FO band and low reflectivity for FB, pulsed FO CO laser spectral band was extended up to 2.5–4.1 μm, with an output efficiency of 11% [21,190,191]. Frequency tuned single-line lasing on 413 vibrational–rotational lines within 2.7–4.2 μm spectral range with maximum efficiency up to 0.6% was obtained [21,61,192]. The total number of spectral lines for both multiline and single-line FO CO lasing was 430.

The latest achievements in CO overtone laser technique are associated with the realization of pulsed and repetitively pulsed lasing at temperature close to that of room [146,193] and with operation of CW supersonic RF discharge FO CO laser [128]. Lasing at room temperature was achieved by means of pumping by short and intense EBSD pulses gas mixture $CO:N_2:He = 1:3:4$ at pressure 325–400 mbar and initial temperature 5°C. The specific pulse energy in optimized conditions amounts to 16 Jl^{-1} bar. In burst mode of repetitively pulsed operation, up to 100 pulses at a repetition frequency of 30 Hz have been achieved resulting in an average laser power of 60 W [193]. Pulsed energy of 25 J with output efficiency 1.5% was obtained for the active volume of 71 [146]. The authors of [146] claimed that an average output power of 4 kW can be expected for their laser facility. Finally, CW operation of CO laser in the overtone band with an output power of 50 W was realized [128,194] by international cooperation of groups from the Air Force Research Lab (USA), the Lebedev Physical Institute (Russia), and the DLR (Germany) (Figure 5.18).

REFERENCES

1. Legay, F. and Legay-Sommair, N., The possibility of obtaining an optical maser using vibrational energy of gases excited by active nitrogen, *Acad. Sci.(Paris) Comp. Rend.*, 259B, 99, 1964.
2. Patel, C.K.N. and Kerl, R.J., Laser oscillation on $X^1\Sigma^+$ vibrational–rotational transitions of CO, *Appl. Phys. Lett.*, 5, 81, 1964.
3. Legay-Sommair, N., Henry, L., and Legay, F., A laser using the vibrational energy of gases excited by activated nitrogen (CO, CO_2 and N_2O), *Acad. Sci.(Paris) Comp. Rend.*, 260B, 3339, 1965.
4. Patel, C.K.N., Vibrational–rotational laser action in carbon monoxide, *Phys. Rev.*, 141, 71, 1966.
5. Osgood, R.M., Jr. and Eppers, W.C., Jr., High-power CO–N_2–He laser, *Appl. Phys. Lett.*, 13, 409, 1968.
6. Osgood, R.M., Jr. and Nichols, E.R., A powerful CO laser, *Laser Focus*, 5, 37, 1969.
7. Eppers, W.C., Jr., Osgood, R.M., Jr., and Greason, P.R., 75 Watt CW carbon monoxide laser, *IEEE J. Quant. Electron.*, 6, 4, 1970.
8. Osgood, R.M., Jr., Eppers, W.C., Jr., and Nichols, E.R., An investigation of the high-power CO laser, *IEEE J. Quant. Electron.*, 6, 145, 1970.
9. Osgood, R.M., Jr., Nichols, E.R., and Eppers, W.C., Jr., Further studies of the high-power CO laser at 5 μm, *IEEE J. Quant. Electron.*, 6, 173, 1970.
10. Treanor, C.A., Rich, J.W., and Rehm, R.G., Vibrational relaxation of anharmonic oscillators with exchange-dominated collisions, *J. Chem. Phys.*, 48, 1798, 1968.
11. Bhaumik, M.L., Lacina, W.B., and Mann, M.M., Characteristics of CO laser, *IEEE J. Quant. Electron.*, 8, 150, 1972.
12. Kan, T. and Whitney, W., Forced-convective flow carbon monoxide laser, *Appl. Phys. Lett.*, 21, 213, 1972.
13. Schulz, G.Y., Vibrational excitation of N_2, CO and H_2 by electron impact, *Phys. Rev.*, 135, 988, 1964.
14. Patel, B.S., Collisional broadening of high pressure CO and CO_2 transition, *Phys. Lett.*, 45A, 137, 1973.
15. Langhoff, S.R. and Bauschlicher, C.W., Jr., Global dipole moment function for the $X^1\Sigma^+$ ground state of CO, *J. Chem. Phys.*, 102, 5220, 1995.
16. Yardley, J.T., Laser action in highly-excited vibrational levels of CO, *J. Molec. Spectr.*, 35, 314, 1970.
17. Djeu, N., CW single line CO laser on the $V = 1 \rightarrow V = 0$ band, *Appl. Phys. Lett.*, 23, 309, 1973.
18. Bergman, R.C. and Rich, J.W., Overtone bands lasing at 2.7–3.1 μm in electrically excited CO, *Appl. Phys. Lett.*, 31, 597, 1977.
19. Basov, N.G. et al., Cooled electron-beam-controlled laser based on two-quantum transitions in CO molecules, *Sov. J. Quant. Electron.*, 8, 1058, 1978.
20. Gromoll-Bohle, M., Bohle, W., and Urban, W., Broadband CO laser emission on overtone transitions $\Delta V = 2$, *Opt. Commun.*, 69, 409, 1989.

21. Basov, N.G. et al., Efficient pulsed first-overtone CO laser operating within the spectral range of 2.5–4.2 μm, *IEEE J. Quant. Electron*., 36, 810, 2000.
22. Ionin, A. et al., Alternation of vibrational band intensities in multiline pulsed first-overtone CO laser spectrum, *Opt. Commun*., 178, 377, 2000.
23. Bubyakin, G.B., Eletsky, A.V., and Populovsky, V.F., Carbon monoxide laser, *Uspekhy Fizicheskih Nauk*., 106, 723, 1972 (in Russian).
24. Osgood, R.M., Jr., Nichols, E.R., and Eppers, W.C., Jr., Q-switching of the carbon monoxide laser, *Appl. Phys. Lett*., 13, 409, 1968.
25. Hopf, F.A., Short pulse energy extraction in CO amplifiers, *Opt. Commun*., 9, 38, 1973.
26. Nurmikko, A.V., Mode-locking of a TEA CO laser, *Appl. Phys. Lett*., 26, 465, 1974.
27. Stephenson, J.S., Vibrational excitation and relaxation of CO ($V=1$) and CO ($V=2$) states, *Appl. Phys. Lett*., 22, 576, 1973.
28. Allen, D.C. and Simpson, C.J., Vibrational energy exchange between CO and isotopes of N_2 between 300 K and 80 K, *Chem. Phys*., 45, 203, 1980.
29. Sobolev, N.N. and Sokovikov, V.V., Carbon monoxide laser. Mechanism of inversion population formation, *Uspekhy Fizicheskih Nauk*., 110, 191, 1972 (in Russian).
30. Basov, N.G. et al., Theoretical study of characteristics of EBSD CO laser, *Preprint #1 of the Lebedev Physical Institute*, Moscow, 1976.
31. Rich, J.W., Kinetic modeling of the high-power carbon monoxide laser, *J. Appl. Phys*., 42, 2719, 1971.
32. Center, R.E. and Caledonia, G.E., Theoretical description of the electrical CO laser, *Appl. Phys. Lett*., 19, 211, 1971.
33. Yardley, J.T., Population inversion and energy transfer in CO lasers, *Appl. Opt*., 10, 1760, 1971.
34. Caledonia, G.E. and Center, R.E., Vibrational distribution functions in anharmonic oscillators, *J. Chem. Phys*., 55, 552, 1971.
35. Lacina, W.B. and Mann, M.M., Transient oscillator analysis of high-pressure electrically excited CO laser, *Appl. Phys. Lett*., 21, 224, 1972.
36. Nighan, W.L., Electron kinetic processes in CO lasers, *Appl. Phys. Lett*., 20, 96, 1972.
37. Hall, R.J. and Eckbreth, A.C., Kinetic modeling of CW CO laser, *IEEE J. Quant. Electron*., 10, 580, 1974.
38. Smith, N.S., Hassan, H.A., and McJuville, R.M., Small-signal gain calculations for high-flow CW CO discharge lasers, *AIAA J*., 12, 1619, 1974.
39. Center, R.E. and Caledonia, G.E., Parametric performance predictions for high-power pulsed electric CO lasers, *J. Appl. Phys*., 46, 2215, 1975.
40. Lacina, W.B. and McAllister, G.L., Scaling generalizations for a CO electric laser, *IEEE J. Quant. Electron*., 11, 235, 1975.
41. Stanton, A.C., Hanson, R.K., and Mitchner, M., Vibrational kinetics in CO electric discharge lasers, *J. Appl. Phys*., 51, 1360, 1980.
42. Iyoda, M., Murota, T., Akiyama, M., et al., Two-dimensional computer modeling of discharge-excited CO gas flow, *Proc. SPIE*, 1397, 457, 1991.
43. Iyoda, M., Taniwaki, M., and Sato, S., Network based simulation of CO laser, *Proc. SPIE*, 3092, 293, 1997.
44. Center, R.E., High power efficient electrically excited CO lasers, in *Laser Handbook*, Smith, M.L., Ed., North-Holland Publishing Company, The Netherlands, 1979, 89.
45. Rich, W.J., Relaxation of molecules under the exchange of the vibrational energy, in *Applied Atomic Collision Physics, 3. Gas Lasers*, McDaniel, E.W. and Nighan, W.L., Eds., Academic Press, New York, 1982, 125.
46. Napartovich, A.P., Physics of high-power CO lasers, in *Gas Lasers—Recent Developments and Future Prospects, NATO, ASI Series, Ser.3: High Technology*, Vol.10, Witteman,W.J. and Ochkin, V.N., Eds., Kluwer Academic Publishers, Dortrecht–Boston–London, 1996, 20.
47. Napartovich, A.P. et al., CO laser: advances in theory and experiment, *Proc. SPIE*, 5777, 408, 2005.
48. Brechignac, Ph., Near-resonant VV-transfer rates for high-lying vibrational states of CO, *Chem. Phys*., 34, 119, 1978.

49. Konev, Yu.B. et al., A kinetic model of multi-quantum vibrational exchange in CO, *J. Phys. D: Appl. Phys.*, 27, 2054, 1994.
50. Ionin, A.A. et al., Theoretical modeling and experimental studies of the multi-quantum vibration exchange in vibrationally excited CO molecules, *J. Phys. D: Appl. Phys.*, 34, 2230, 2001.
51. Rapp, D. and Englander-Golden, P., Resonant and near-resonant vibrational–vibrational energy transfer between molecules in collisions, *J. Chem. Phys.*, 40, 573, 1964.
52. Sharma, R.D. and Brau, C.A., Energy transfer in near-resonant molecular collisions due to long-range forces with application to transfer of vibrational energy from ν_3 mode of CO_2 to N_2, *J. Chem. Phys.*, 50, 924, 1969.
53. Billing, G.D., Semiclassical three-dimensional model for vibrational energy transfer in diatomic molecules, *Chem. Phys.*, 5, 244, 1974.
54. Billing, G.D., Cross sections and rate constants for rotational and vibrational excitation of H_2 and D_2 colliding with ^{4}He, *Chem. Phys.*, 30, 387, 1978.
55. Billing, G.D., The semiclassical treatment of molecular ro/vibrational energy transfers, *Comput. Phys. Rep.*, 1, 237, 1984.
56. Billing, G.D., Rate-constants for vibrational transitions in diatom-diatom collisions, *Comput. Phys. Commun.*, 44, 121, 1987.
57. Billing, G.D. et al., Sensitivity of molecular vibrational dynamics to energy exchange rate constants, *J. Phys. B: At. Mol. Opt. Phys.*, 36, 1175, 2003.
58. Coletti, C. and Billing, G.D., Rate constants for vibrational energy transfer in carbon monoxide, *J. Chem. Phys.*, 113, 4869, 2000.
59. Deleon, R.L. and Rich, J.W., Vibrational energy exchange rates in carbon monoxide, *Chem. Phys.*, 107, 283, 1986.
60. Ionin, A. et al., Parametric study of first overtone CO laser with suppressed fundamental band lasing: experiment and theory, *Opt. Commun.*, 155, 197, 1998.
61. Basov, N.G. et al., Pulsed first-overtone CO laser operating in 2.5–4.2 μm spectral range. II. Frequency selective regime, *Quant. Electron.*, 30, 859, 2000.
62. Cacciatore, M. et al., Vibrational energy exchanges between N_2 and strongly excited CO molecules: their role in vibrational kinetics, *J. Phys. B: At. Mol. Opt. Phys.*, 37, 3379, 2004.
63. Kurnosov, A.K., Cacciatore, M., and Billing, G.D., State-to-state rate constant calculations for V–V energy transfer in CO–N_2 collisions, *J. Phys. Chem. A.*, 107, 2403, 2003.
64. Basov, N.G. et al., Pulsed laser operating on the first vibrational overtone of the CO molecule in the 2.5–4.2 μm range: 3. The gain and kinetic processes on high vibrational levels, *Quant. Electronics*, 32, 404, 2002.
65. Ionin, A. et al., Small signal gain time behavior on high vibrational transitions ($V > 15$) of pulsed CO laser amplifier, *Proc. SPIE*, 5479, 156, 2004.
66. Klimachev, Yu. et al., Time behavior of small-signal gain on high vibrational transitions for pulsed CO laser amplifier with gas mixtures CO:He, CO:N_2, and CO:O_2, *Proc. SPIE*, 5777, 418, 2005.
67. Mantz, A.W. et al., CO laser spectrum studied with a 10-meter vacuum IR grating spectrometer, *J. Molec. Spectr.*, 35, 325, 1970.
68. Legay, F., Legay-Sommair, N., and Taieb, G., Mechanism of CO–N_2 laser. I. Study of vibrational population, *Can. J. Phys.*, 48, 1956, 1970.
69. Anokhin, A.V., Markova, S.V., and Petrash, G.G., Pulsed lasing on vibrational transitions of CO at gas cooling, *Soviet Physics—Lebedev Institute Reports (Kratkie soobscheniya po fisike)*, #8, 13, Allerton Press Inc, 1970.
70. Mantz, A.W. et al., CO laser spectrum studied with a 10-meter vacuum IR grating spectrometer, *J. Molec. Spectr.*, 35, 325, 1970.
71. Anokhin, A.V., Markova, S.V., and Petrash, G.G., Life-time of inversion on vibrational transitions of CO molecule, *Soviet Physics—Lebedev Institute Reports (Kratkie soobscheniya po fisike)*, #2, 30, Allerton Press Inc, 1970.
72. Freed, C., Sealed-off operation of stable CO lasers, *Appl. Phys. Lett.*, 18, 458, 1971.
73. Seguin, H.J., Tulip, J., and White, B., Sealed CO laser at room-temperature, *Can. J. Phys.*, 49, 273, 1971.

74. Mikoberidze, A.A., Ochkin, V.N., and Sobolev, N.N., Measurement of vibrational temperatures in CO laser, *Zhurnal Tekhnicheskoi Fiziki*., 42, 1464, 1972 (in Russian).
75. Lotkova, E.N., Mercer, G.N., and Sobolev, N.N., Population, gain and excitation mechanism of the CO laser, *Appl. Phys. Lett*., 20, 309, 1972.
76. Cohn, D.B., CO TEA laser at 77 K, *Appl. Phys. Lett*., 21, 343, 1972.
77. Champagne, L., Cryogenically cooled CO–He TEA laser, *Appl. Phys. Lett*., 23, 158, 1973.
78. Kacheva, T.F., Ochkin, V.N., and Sobolev, N.N., Carbon monoxide operating laser at room temperature, *Sov. J. Quant. Electron*., 3, 484, 1973.
79. Brechignac, P., Martin, J.P., and Taieb, G., Small-signal gain and vibrational distribution in CO, *IEEE J. Quant. Electron*., 10, 797, 1974.
80. Cohn, D.B., Griffin, W.S., and Mendoza, P.J., Improved convective flow longitudinal discharge CO laser, *J. Appl. Phys*., 46, 2790, 1975.
81. McAllister, G.L., Draggo, V.G., and Eguchi., Acoustical wave effects on the beam quality of a high energy CO electric discharge laser, *Appl. Opt*., 14, 1290, 1975.
82. Keren, H., Avivi, P., and Dothan, F., The influence of oxygen on CO laser performance, *IEEE J. Quant. Electron*., 11, 590, 1975.
83. Smith, A.L.S., Effect of xenon on the temperature in carbon monoxide lasers, *IEEE J. Quant. Electron*., 13, 59, 1977.
84. Lim, D.G., Mendoza, P.J., and Cohn, D., Characteristics of a 600 W convective flow CO laser, *Rev. Sci. Instr*., 48, 1430, 1977.
85. Monson, D.J. and Srinavasan, G., A pulser-sustainer carbon monoxide electric discharge supersonic laser, *Appl. Phys. Lett*., 31, 828, 1977.
86. Avtonomov, V.P. et al., Lasing line selection in an electric-discharge CO laser, *Sov. J. Quant. Electron*., 8, 1074, 1978.
87. Basov, N.G. et al., Experimental investigation of pulsed electron-beam controlled carbon monoxide lasers, *J. Sov. Laser Res*., 1, 311, 1980.
88. Baranov, V.Y. et al., Experimental and theoretical study of non-cooled CO laser with short pulse pumping, *IEEE J. Quant. Electron*., 19, 1463, 1983.
89. Sato, S., Fujioka, H., and Saito, H., High-power-closed cycle subsonic CW CO laser excited by a transverse self-sustained discharge, *Appl. Phys. Lett*., 46, 537, 1985.
90. Sobolev, N.N. and Sokovikov, V.V., The carbon monoxide laser. Review of experimental results, *Sov. J. Quant. Electron*., 2, 305, 1972.
91. Bhaumic, M.L., High-efficiency electric discharge CO lasers, in *Lect. Summer School on Physics and Technology*, Capri, October, 1975, Inst. Phys. Conf., Ser 29, 1976, 243.
92. Mann, M.M., CO electric discharge lasers, *AIAA J*., 14, 549, 1976.
93. Ionin, A.A. et al., Electric discharge high-pressure IR lasers and their applications, *Itogi nauki i tekhniki*, *ser. Radiotekhnika*., 32, VINITI, Moscow, 1984 (in Russian).
94. Ionin, A.A., High-power CO lasers in Russia, *Quant. Electron*., 23, 93, 1993.
95. Ionin, A. and Spalding, I., CO lasers—state of the art and potential of applications, in *Gas Lasers—Recent Developments and Future Prospects, NATO, ASI Series, Ser.3: High Technology*, Vol. 10, Witteman, W.J. and Ochkin, V.N., Eds., Kluwer Academic Publishers, Dortrecht–Boston–London, 1996, 279.
96. Ionin, A., Carbon monoxide lasers: problems of physics and engineering, *Proc. SPIE*, 889, 24, 2000.
97. Asawa, C.K., Compact 1.1 W sealed-off waveguide CO laser, *Appl. Phys. Lett*., 24, 121, 1974.
98. Peters, P.J.M., Witteman, W.J., and Zuidema, R.J., Efficient simple sealed-off CO laser at room temperature, *Appl. Phys. Lett*., 37, 119, 1980.
99. Dubovsky, P.E. et al., Sealed waveguide CO laser, *Sov. J. Quant. Electron*., 12, 800, 1982.
100. Aleinikov, V.S. and Masychev, V.I., Carbon Monoxide Lasers, *Radio i Svyaz'*., Moscow, 1990 (in Russian).
101. McNaught, W.G. and Wlodarczyk, G., A 3 kW industrial CO laser operating at room temperature, *Proc. SPIE,* 3092, 440, 1997.
102. Abrosimov, G.V. et al., Experimental research of fast-flow CO laser operating in CW regime, *Zhurnal Tekhnicheskoi Fiziki*., 47, 235, 1977 (in Russian).

103. Hall, D.R. et al., New technology for industrial carbon monoxide lasers, *Proc. Int. Conf. Laser Advanced Material Processing LAMP'92*, Nagaoka, Japan, 55, 1992.
104. Shimizu, K. et al., High-power room temperature operated CO laser, *Proc. SPIE*, 3889, 433, 2000.
105. Kanazawa, H. et al., Characteristics of a transverse-flow CO laser excited by RF discharge, *IEEE J. Quant. Electron.*, 30, 1448, 1994.
106. Uehara, M., Kanazawa, H., and Kasuya, K., Recent studies of high-power CO laser under room-temperature operation, *Proc. SPIE*, 2502, 38, 1995.
107. Uehara, M. and Kanazawa, H., A room temperature operating pulse RF discharge excited CO laser, *Proc. SPIE*, 3092, 436, 1997.
108. Zhao, H., Baker, H.J., and Hall, D.R., Area scaling in slab RF excited carbon monoxide lasers, *Appl. Phys. Lett.*, 59, 1281, 1991.
109. Villarrea, F. et al., High-pressure CW molecular gas lasers using narrow-gap slab waveguides, *CLEO'95, Technical Digest*, p. 44, 1995.
110. Xin, J., Zhang, W., and Jiao, W., Radio frequency discharge excited diffusively cooled kilowatt carbon monoxide slab waveguide laser with a three mirror resonator, *Appl. Phys. Lett.*, 75, 1369, 1999.
111. Gerasimchuk, A. et al., Frequency tuned carbon monoxide waveguide laser with RF pumping, *Appl. Phys.*, B48, 513, 1989.
112. Luo, X., Schäfer, J.H., and Uhlenbusch, J., High power room temperature operating CW CO laser excited by microwave discharge, *Proc. SPIE*, 2502, 69, 1995.
113. Schäfer, J.H., Uhlenbusch, J., and Wierich, M., Microwave excited CW CO laser at room temperature, *Proc. SPIE*, 4184, 242, 2001.
114. Rich, J.W. et al., An electrically excited gas dynamic carbon monoxide laser, *Appl. Phys. Lett.*, 19, 230, 1971.
115. Brunet, H. and Mabru, M., Electrical CO-mixing gas dynamics laser, *Appl. Phys. Lett.*, 21, 432, 1971.
116. Kan, T., Streagack, J.A., and Watt, W.S., Electric-discharge gas-dynamic laser, *Appl. Phys. Lett.*, 20, 137, 1972.
117. Shirley, J.A., Hall, R.J., and Bronfin, B.R., Stimulated emission from carbon monoxide transitions below 5 μm excited in supersonic electric discharge, *J. Appl. Phys.*, 45, 3934, 1974.
118. Rich, J.W., Bergman, R.C., and Lordi, J.A., Experimental and theoretical investigation of the electrically excited, supersonic flow carbon monoxide laser, *AIAA J.*, 13, 95, 1975.
119. Daiber, J. and Thompson, H., Performance of a large CW preexcited CO supersonic laser, *IEEE J. Quant. Electron.*, 13, 10, 1977.
120. Krause, S. and Maisenhalder, F., Gasdynamic CO laser with closed-cycle gas flow, *Appl. Phys.*, 22, 421, 1980.
121. Stanton, A.C., Hanson, R.K., and Mitchner, M., Performance of a CW double electric discharge for supersonic CO lasers, *J. Appl. Phys.*, 51, 1370, 1980.
122. Schock, W. et al., CW carbon monoxide laser with RF excitation in the supersonic flow, *Appl. Phys. Lett.*, 37, 119, 1980.
123. Hoffman, P. et al., CW carbon monoxide laser with microwave excitation in the supersonic flow, *Appl. Phys. Lett.*, 37, 673, 1980.
124. von Bülow, H. and Zeifang, E., Gas dynamically cooled CO laser with RF excitation, *Proc. SPIE*, 1397, 499, 1990.
125. von Bülow, H. and Zeifang, E., Supersonic CO laser with RF excitation, *Rev. Sci. Instr.*, 64, 1764, 1993.
126. von Bülow, H. and Schellhorn, M., High-power gas dynamically cooled carbon monoxide laser, *Appl. Phys. Lett.*, 63, 287, 1993.
127. von Bülow, H. and Schellhorn, M., High-power gas dynamically cooled CO laser with unstable resonator, *Proc. SPIE*, 2502, 63, 1994.
128. McCord, J.E. et al., Supersonic RF discharge CO laser operating in fundamental ($\Delta = 1$) and overtone ($\Delta = 2$) spectral bands, *Proc. SPIE*, 5448, 379, 2004.
129. Kuribayashi, S. et al., Current status of the high-power CO laser program, *Proc. LAMP'92*, Nagaoka, Japan, 51, 1992.

130. Basov, N.G. et al., About the possibility of development of tunable IR gas lasers, *Pis'ma v Zhurnal Experimental'noi i Teoreticheskoi Fiziki*., 14, 545, 1971 (in Russian).
131. Basov, N.G. et al., Electron-beam sustained discharge pulsed CO laser, *Soviet Physics—Lebedev Institute Reports (Kratkie soobscheniya po fisike)*, #6, 1, Allerton Press Inc., 1974.
132. Basov, N.G. et al., Electron-beam sustained discharge CO laser with output energy 100 J, *Sov. J. Quant. Electron*., 4, 1412, 1974.
133. Center, R.E., High-pressure electrical CO laser, *IEEE J. Quant. Electron*., 10, 208, 1974.
134. Mann, M.M., Rice, D.K., and Eguchi, R.G., An experimental investigation of high energy CO lasers, *IEEE J. Quant. Electron*.,10, 682, 1974.
135. Basov, N.G. et al., Lasing in e-beam sustained discharge high-pressure CO laser, *Pis'ma v Zhurnal Tekhnicheskoi Fiziki*., 2, 817, 1976 (in Russian).
136. Boness, M.J.W. and Center, R.E., High-pressure electrical CO laser, *J. Appl. Phys*., 48, 2705, 1977.
137. Basov, N.G. et al., Cooled e-beam sustained discharge carbon monoxide laser with active volume 5 liters, *Pis'ma v Zhurnal Tekhnicheskoi Fiziki*., 3, 385, 1977 (in Russian).
138. Basov, N.G. et al., Pulsed EBSD lasers with cryogenic cooling of active medium, *Zhurnal Tekhnicheskoi Fiziki*., 55, 326, 1985 (in Russian).
139. Ionin, A. et al., Pulsed laser facilities operating from UV to IR at the Gas Laser Lab of the Lebedev Institute, in *Proc. First Symp. Beamed Energy Propulsion*, Pakhomov, A., Ed., Huntsville, AL, November 2002, American Institute of Physics, 2003, 697.
140. Averin, A.P. et al., Repetitively pulsed EBSD carbon monoxide laser, *Sov. J. Quant. Electron*., 20, 427, 1990.
141. Basov, N.G. et al., High-power electroionization CO_2 and CO lasers for industrial applications, *IEEE J. Quant. Electron*., 21, 342, 1985.
142. Spalding, I. et al., *Final Report of Eureka EU113 CO Eurolaser Project, Doc. No. TLC/EU 113/PM/40, Sub-project group 4, Generic Applications and Process Research*, 62, 1996.
143. Averin, A. et al., High power CO lasers for material processing, *Proc. SPIE*, 2206, 1994.
144. Rodin, A.V. et al., Pulsed powerful e-beam sustained CO laser with a subsonic flow of the active gas mixture, *Proc. SPIE*, 4065, 836, 2000.
145. Ionin, A. et al., Room temperature repetitively pulsed e-beam sustained carbon monoxide laser, *Proc. SPIE*, 2502, 44, 1994.
146. Bohn, W.L. et al., High power CO overtone laser, *Proc. SPIE*, 4760, 486, 2002.
147. Golovin, A.S. et al., Continuous wave electron-beam stabilized CO laser with subsonic flow of the active medium, *Quant. Electron*., 26, 395, 1996.
148. Jones, T.G. et al., Electron-beam stabilized CW electric discharge laser in supersonically cooled $CO/N_2/Ar$ mixtures, *AIAA Paper 74–562*, 1974.
149. Klosterman, E.L. and Byron, S.R., Electrical and laser diagnostics of an 80 kW supersonic CW CO electric laser, *J. Appl. Phys*., 50, 5168, 1979.
150. Maisenhälder, F., High power CO lasers and their application potential, *Proc. SPIE*, 1031, 98, 1988.
151. Ionin, A. et al., Supersonic electron beam controlled discharge CO laser, *Proc. SPIE*, 1397, 453, 1990.
152. Dymshits, B.M. et al., CW 200 kW supersonic CO laser, *Proc. SPIE*., 2206, 109, 1994.
153. Monson, D.J., Systems efficiency and specific mass estimates for direct and indirect solar-pumped closed-cycle high-energy lasers in space, in *Radiat. Energy Convers. Space Techn. Pap. 3rd NASA Conf*., Moffet Field., CA, NY, 333, 1978.
154. Coneybear, J.F., The use of lasers for the transmission of power, in *Radiat. Energy Convers. Space Techn. Pap. 3rd NASA Conf*., Moffet Field., CA, NY, 279, 1978.
155. Rich, J.W., Bergman, R.C., and Raymonda, Y., Vibrational–vibrational pumping of carbon monoxide initiated by an optical source, *Appl. Phys. Lett*., 27, 656, 1975.
156. Cohn, D.B. et al., Optical pumping of CO by a convective flow CO laser, *IEEE J. Quant. Electron*., 22, 723, 1986.
157. Anan'ev, V.Yu. et al., Nonlinear absorption and spectral conversion of laser radiation by carbon monoxide molecules excited in an electron-beam-controlled discharge, *Sov. J. Quant. Electron*., 17, 1287, 1987.
158. Urban, W. et al., Treanor pumping of CO initiated by CO laser excitation, *Chem. Phys*., 130, 389, 1989.

159. Adamovich, I. et al., Vibrationally stimulated ionization of carbon monoxide in optical pumping experiments, *Chem. Phys*., 173, 491, 1993.
160. Wallaart, H.L. et al., Transfer of vibrational energy to electronic excited states and vibration enhanced carbon production in optically excited V–V pumped CO, *Chem. Phys*., 196, 149, 1995.
161. Kochetov, I.V. et al., Optical pumping of mixture containing CO by multifrequency CO laser radiation, *Quant. Electron*., 25, 655, 1995.
162. Schulz, O. et al., Optical pumping of CO and laser emission, *Contributed papers, III Int. School-seminar ''Nonequilibrium processes and their applications''*, Minsk, Belarus, September, 8–13, 1996, 40.
163. McCord, J.E. et al., Experimental investigation of an optically pumped mid-infrared carbon monoxide laser, *IEEE J. Quant. Electron*., 35, 1602, 1999.
164. McCord, J.E. et al., Frequency tunable optically pumped carbon monoxide laser, *IEEE J. Quant. Electron*., 36, 1041, 2000.
165. Phipps, S.P. et al., Investigation of the state-to-state rotational relaxation rate constants for carbon monoxide (CO) using infrared double resonance, *J. Chem. Phys*., 116, 9281, 2002.
166. Hostutler, D.A. et al., State to state rotational relaxation rate constants for the CO+X series (X = CO, He, and Ne) using IR–IR double resonance experiments. Comparing theory to experiment, *Proc. SPIE*, 5448, 906, 2004.
167. Oraevsky, A.N. and Protsenko, I.E., Explosive absorption of radiation, *Sov. J. Quant. Electron*., 15, 1509, 1985.
168. Shmelev, V.M. and Margolin, A.D., Optical instability of molecular gas under non-isothermal conditions, *Khimicheskaya Fizika*., 4, 873, 1985 (in Russian).
169. Anan'ev, V.Yu. et al., Pulsed EBSD carbon monoxide laser amplifiers. I. Amplification of radiation of free-running EBSD CO laser, *Sov. J. Quant. Electron*., 19, 4, 1989.
170. Anan'ev, V.Yu. et al., Pulsed EBSD carbon monoxide laser amplifiers. II. Amplification of pulsed radiation of EBSD CO laser with controlled spectral and time parameters, *Sov. J. Quant. Electron*., 19, 10, 1989.
171. Afanas'ev, L.A. et al., Active medium of molecular CO_2 and CO lasers as a nonlinear component of phase-conjugating mirror, *Quant. Electron*., 24, 513, 1994.
172. Ionin, A.A. et al., Intracavity phase-conjugation of the radiation from a pulsed frequency selective CO laser, *Quant. Electron*., 30, 342, 2000.
173. Anan'ev, V.Yu. et al., Enhancement of the efficiency of Q-switched electron-beam-controlled CO laser by generating a series of laser pulses, *Sov. J. Quant. Electron*., 15, 1096, 1985.
174. Ionin, A. et al., Pulsed frequency selective tunable Q-switched EBSD CO laser, *Quant. Electron*., 27, 189, 1997.
175. Ionin, A. et al., Application of CO laser for frequency selective surface heat treatment of polymer materials, *Proc. SPIE*, 3343, 1032, 1998.
176. Basov, N.G., Kazakevich, V.S., and Kovsh, I.B., Electron-beam-controlled laser utilizing the first overtones of the vibrational–rotational transitions of the CO molecule. I. Time-resolved spectral characteristics, *Sov. J. Quant. Electron*., 10, 1131, 1980.
177. Basov, N.G., Kazakevich, V.S., and Kovsh, I.B., Electron-beam-controlled laser utilizing the first overtones of the vibrational–rotational transitions of the CO molecule. II. Energy characteristics, *Sov. J. Quant. Electron*., 10, 1136, 1980.
178. Basov, N.G., Ionin, A.A., and Kovsh, I.B., The electroionization CO laser: a multiwavelength IR oscillator ($\lambda = 2.7$–3.3 μm; 4.9–6.0 μm), *Infrared Phys*., 25, 47, 1985.
179. Urban, W., The carbon monoxide laser as spectroscopic source, *Laser und Optoelectronik*, 23, 56, 1991.
180. Bachem, E. et al., Recent progress with the CO overtone $\Delta V = 2$ laser, *Appl. Phys*., B57, 185, 1993.
181. Murtz, M. et al., Tunable carbon monoxide overtone laser sideband system for precision spectroscopy from 2.6 to 4.1 μm, *Opt. Lett*., 23, 58, 1998.
182. George, T. et al., Saturation stabilization of the CO fundamental-band laser, *Appl. Phys*., B53, 330, 1991.
183. Konev, Yu.B. et al., Investigation of a possibility of getting lasing on overtones of CO molecule at electric discharge pumping, *Pis'ma v Zhurnal Tekhnicheskoi Fiziki*., 3, 1267, 1977 (in Russian).

184. Suchkov, A.F. and Shebeko, Yu. N., Theoretical investigation of the energy and spectral characteristics of a laser utilizing the first overtones of the vibrational–rotational transitions of CO molecule, *Sov. J. Quant. Electron*., 9, 565, 1979.
185. Zhdanok, S.A. et al., Analytical theory of steady-state lasing on overtone of CO molecule, *Inzhenerno Fizicheskii Zhurnal*., 38, 273, 1980 (in Russian).
186. Konev, Yu.B. et al., Investigation of characteristics of gas discharge CO laser at overtone lasing. II. Simultaneous lasing on fundamental band and overtone in pulsed regime, *Inzhenerno Fizicheskii Zhurnal*., 41, 514, 1981 (in Russian).
187. Konev, Yu.B. et al., Investigation of characteristics of gas discharge CO laser at overtone lasing. I. Steady-state regime, *Inzhenerno Fizicheskii Zhurnal*., 41, 289, 1981 (in Russian)
188. Belykh, A.D. et al., Pulsed CO laser based on the first vibrational overtone, *Quant. Electron., 25*, 315, 1995.
189. Aleksandrov, B.S. et al., Energy and spectral characteristics of a supersonic electron-beam-sustained CO laser based on the first vibrational overtone and also operating in a selection regime, *Quant. Electron*., 27, 584, 1997.
190. Ionin, A. et al., Pulsed first-overtone CO laser: effective source of IR radiation in spectral range 2.5–4.0 μm, *Opt. Commun*., 160, 255, 1999.
191. Basov, N.G. et al., Pulsed first-overtone CO laser with output efficiency higher than 10%, *Opt. Commun*., 171, 107, 1999.
192. Basov, N.G. et al., Frequency tunable single-line first-overtone carbon monoxide laser, *Opt. Commun*., 180, 285, 2000.
193. Zeifang, E., Mayerhofer, W., and Walther, S., Room-temperature repetitively pulsed CO overtone laser, *Proc. SPIE*, 4184, 230, 2001.
194. Bohn, W., et al., High power supersonic CO laser on fundamental and overtone transitions, *Quant. Electron*, 35, 1126, 2005.

6A DC-Excited Continuous-Wave Conventional and RF-Excited Waveguide CO_2 Lasers

Edward F. Plinski and Krzysztof M. Abramski

CONTENTS

6A.1 INTRODUCTION

Stephen J. Matthews, a contributing editor in *Laser Focus World*, probably gave the best description of the role a carbon dioxide (CO_2) laser played in laser engineering development. Matthews compared the laser to an Olympic weightlifter who attained his peak at 40 years of age, when his muscles are the strongest [1].

Chandra Kumar Naranbhai Patel announced the development of the first CO_2 laser at Bell Laboratories in 1963, and published it in 1964 [2]. In addition, his laser device was not "waiting for a job" too long. The CO_2 laser satisfied expectations of scientists and engineers concerning high-power lasers and, consequently, applications of a laser as such in many branches of science and technology. Today, CO_2 lasers are applied in industries for cutting, welding, drilling; in medicine for surgery (some noncontact and noninvasive procedures), using photons, rather than scalpels; in the environment to detect pollution and to analyze some compositions of the atmosphere; in communications; and in military applications (see "Star Wars").

6A.1.1 Carbon Dioxide Molecule

Figure 6A.1 shows some visual representations of vibrational modes of the CO_2 molecule. It is a linear form of molecular structure, and it can vibrate in three ways giving an asymmetric stretch mode, bending mode, and a symmetric stretch mode. The bending mode, as seen in Figure 6A.1c, can be created in two ways, not recognized by the observation. Hence, it is called a double-degenerated mode.

The molecule can vibrate and rotate simultaneously. Rotational modes are also quantized. In that way, the molecule in some vibrational mode actually exists at one of the rotational modes. The rotational states accompany each vibrational state.

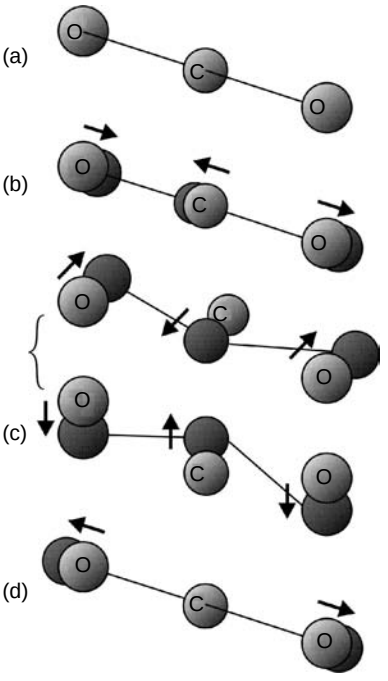

FIGURE 6A.1 Vibrational modes of the CO_2 molecule: (a) the linear shape of the CO_2 molecule, (b) the asymmetric stretch mode, (c) double-degenerated bending mode, (d) the symmetric stretch mode.

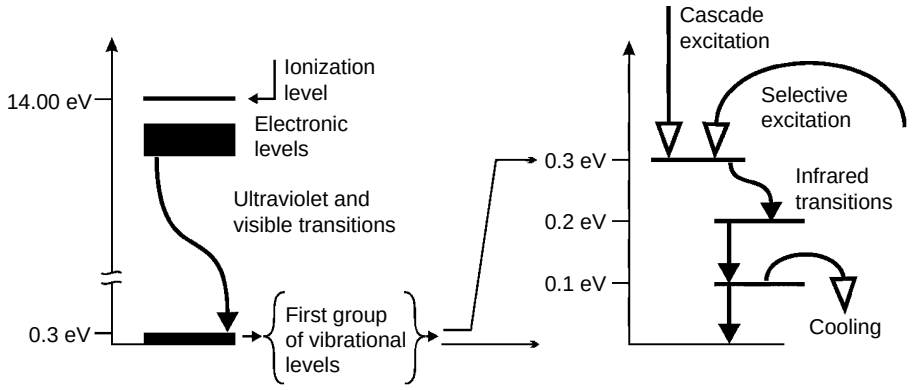

FIGURE 6A.2 Energy level structure of a CO_2 molecule. Left—structure with electronic levels and first group of vibrational levels; right—zoom of the vibrational levels. Two mechanisms of excitation are visible: via electrical DC or RF current (cascade from higher electronic levels), and some selective mechanism increasing the population inversion. A mechanism of cooling is also indicated.

Although the process of excitation of atoms requires much energy, excitation of a molecule to the vibrational state is much easier. As seen in Figure 6A.2, excitation of a CO_2 molecule to first vibrational levels needs only about 0.3 eV of input energy compared with the excitation of the molecule to the first electronic level which needs ~10 eV of energy. This fact is very promising. An efficient molecular laser should be build very easy. Kumar Patel believed that because of the nearness of the possible lasing levels to the ground state such a laser should give a high output power with high efficiency.

Unfortunately, a mechanism of CO_2 vibrational level excitation by electric discharge gives relatively low inverted population of upper and lower laser levels. Kumar Patel solved the problem. He had realized that to increase the power of the laser he needed some selective excitation mechanism. The paper by Morgan and Schiff on quenching of a vibrationally excited nitrogen molecule by a CO_2 molecule was very helpful [3]. (In a low-pressure nitrogen discharge, approximately 30% of the N_2 molecules is excited to the $\nu = 1$ state, where energy difference between the N_2 and CO_2 states (see Figure 6A.3) is only 18 cm^{-1} (0.0022 eV.) Thus, easy transfer of energy to the CO_2 molecule.) Patel had immediately understood that nitrogen was the searched donor molecule [4,5]. Adding helium as a cooling gas was only a question of short time (a typical composition of the laser gas CO_2:N_2:He mixture is from 1:1:3 to 1:1:8). In that way, a high-power laser molecular system became a fact. From 1 mW to 100 W in one year [6]. Certainly, it is one of the most spectacular records in the laser physics development.

Figure 6A.4 shows more details about the energy structure of the CO_2 molecule. Two vibrational states ν_1 and ν_2 are shown in the figure. Each vibrational state ν is split into a number of rotational levels J (see Chapter 1.3). They create P and R branches of the CO_2 spectrum bands. The rule is as follows: the P-branch corresponds to $\Delta J = +1$, the Q-branch corresponds to $\Delta J = 0$, the R-branch corresponds to $\Delta J = -1$. The transitions between (001) and (100) centered at 10.6 μm (P-branch) give the strongest lasing lines (see Figure 1.6 in Chapter 1). Whereas the transitions between (0 0 1) and (0 2 0) centered at 9.6 μm give the relatively lower lasing.

A CO_2 molecule remains in the upper laser level for about 2 msec. At that time due to intermolecular collisions, the molecule changes the rotational levels approximately 20,000 times (so-called the thermalization effect). It is why lasing occurs on one chosen transition from the set of possible rotational levels of the same vibrational state. This effect directly leads to the phenomenon called a laser "signature."

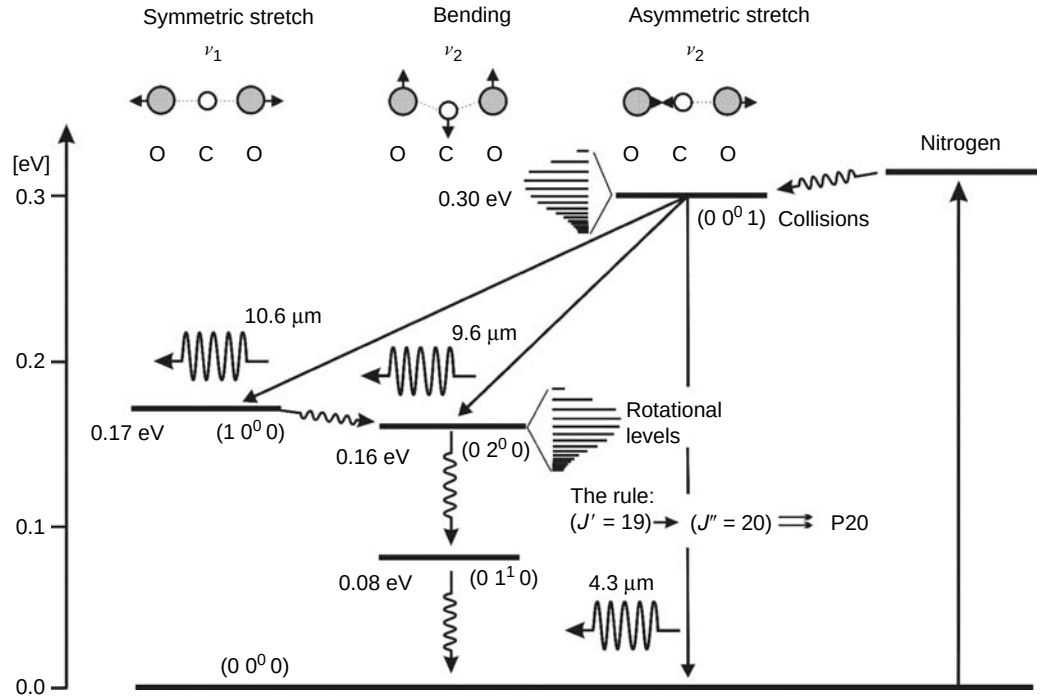

FIGURE 6A.3 Vibrational–rotational CO_2–N_2 laser energy level diagram. The vibrational energy state of a CO_2 molecule is described by three quantum numbers: ν_1—symmetric stretch quantum number, ν_2—bending quantum number, ν_3—asymmetric stretch quantum number. For example CO_2 ($\nu_1\,\nu_2\,\nu_3$) = (0 0 0) indicates a molecule in the vibrational ground state. Vibrational state $\nu = 1$ of nitrogen is also indicated.

6A.1.2 Regular, Sequence, and Hot Transitions

The rich vibrational spectrum of the CO_2 molecule gives possibility to lase on many emission lines. One of the possibilities is the so-called sequence-band lines. They involve upper state

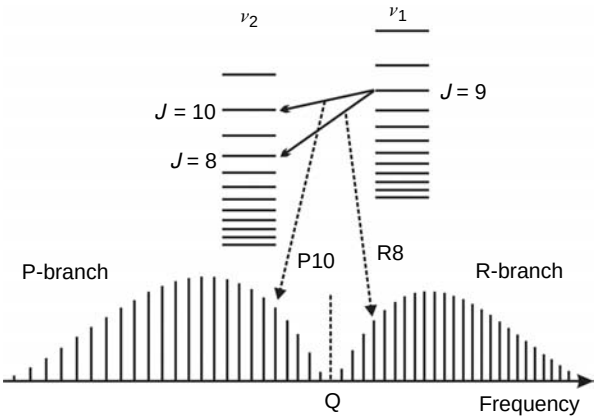

FIGURE 6A.4 Triatomic linear molecule spectral band. Two vibrational states ν_1 and ν_2 are indicated. They are split into a number of rotational levels J. Examples of transitions are shown to demonstrate how P- and R-branches are created.

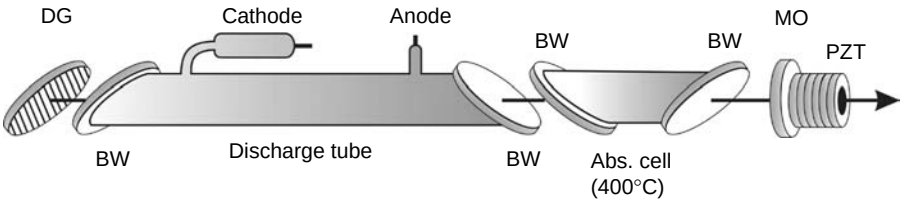

FIGURE 6A.5 Setup for investigation sequence bands of the CO_2 molecule. The laser tube and hot absorption cell (heated with electrical heater) are inserted into the common optical resonator. DG—diffraction grating, BW—Brewster window, MO—output mirror, PZT—piezoceramic transducer.

levels of CO_2 ($\nu_1\,\nu_2\,\nu_3$) for ν_3 higher than 1. To observe the sequence-band lines, some additional instrumentality is necessary. They are too weak to observe them in a simple experiment. First, they have a small gain and second, they are very close to regular ones. Hence, an absorption intracavity cell filled with hot CO_2 is used in the experiment to suppress the laser radiation on regular transitions [7,8]; see Figure 6A.5.

When other special instrumentality is used, it is possible to observe hot-band lines from 9.3 to 11.1 μm [9,10]; see Figure 6A.6. About 4.3 μm fluorescence is indicated in the figure (very convenient for laser line center stabilization to a saturation Lamb dip [11,12]). It is also possible to observe sequence-band lines without the hot CO_2 absorption intracavity cell—as known, difficult to separate. A non-Littrow mounting of the diffraction grating was applied in the laser arrangement [13].

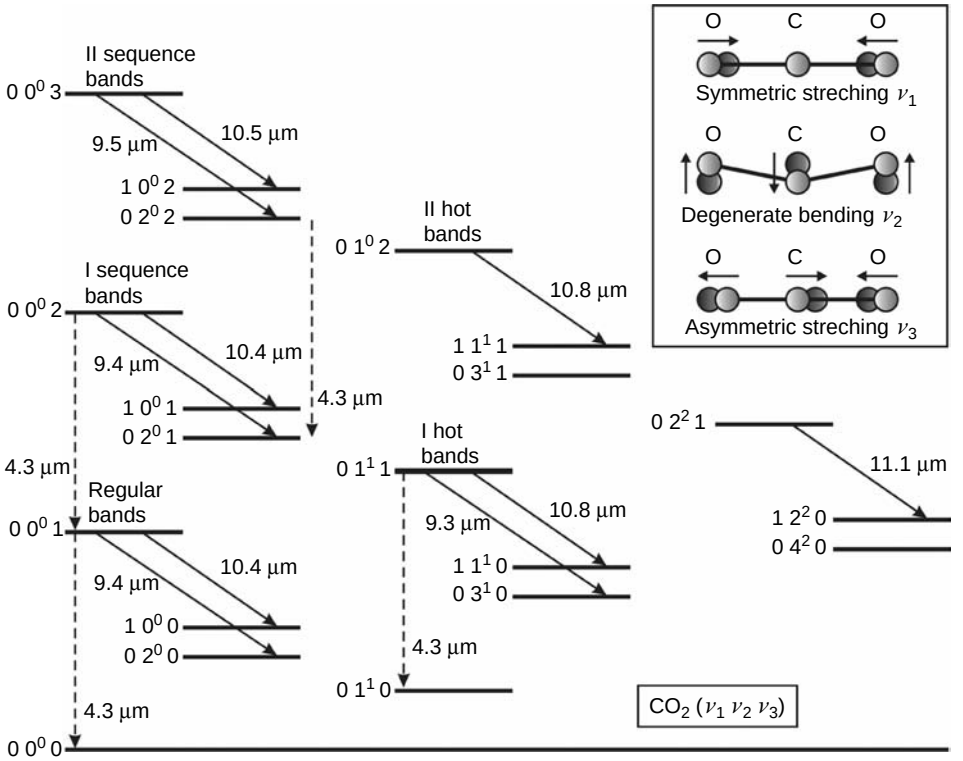

FIGURE 6A.6 Regular, hot, and sequence transitions in CO_2 laser medium. Possible vibrations of the CO_2 molecule are shown (described by quantum numbers ν_1, ν_2, and ν_3).

6A.1.3 Isotope Spectral Displacement

Spectral properties of a molecule depend on the mass of all atoms contributing to the molecule structure. The mass of a molecule can be changed without the distortion of the molecular structure changing atoms into their isotopes. In the case of a CO_2 molecule, we can change atoms of carbon and oxygen. Instead of the basic atoms ^{12}C and ^{16}O, we can use ^{13}C and ^{14}C or ^{17}O and ^{18}O isotopes. In that way, it is possible to get combinations like: $^{12}C^{16}O_2$ (basic), $^{13}C^{16}O_2$, $^{14}C^{16}O_2$, $^{16}O^{16}O^{18}O$, $^{12}C^{17}O_2$, $^{13}C^{18}O_2$, and $^{14}C^{18}O_2$.

$$\frac{\omega_1^i}{\omega_1} = \sqrt{\frac{m(\mathrm{O})}{m(\mathrm{O})^i}}, \qquad \frac{\omega_2^i}{\omega_2} = \frac{\omega_3^i}{\omega_3} = \sqrt{\frac{m(\mathrm{O})\left(1+\dfrac{2m(\mathrm{O})^i}{m(\mathrm{C})^i}\right)}{m(\mathrm{O})^i\left(1+\dfrac{2m(\mathrm{O})}{m(\mathrm{C})}\right)}} \tag{6A.1}$$

Mode frequencies, such as symmetric ω_1, bending ω_2, and asymmetric ω_3, are modified according to Equation 6A.1. Where m(O) and m(C) are the atom masses of the oxygen and carbon, respectively, the subscripts 1, 2, and 3 indicate mode frequencies, superscript i indicates an isotope [14].

Figure 6A.7 shows up to what extent a CO_2 regular band can be shifted when different isotopes are used in the molecule composition. The shift can be as much as even 10%; see Figure 6A.8.

As seen, carbon isotopes significantly influence the frequency shift. In consideration of earlier results, it is clear why the CO_2 laser signatures can be so different for the same length of the laser resonator when isotopes of carbon or oxygen are used.

The CO_2 CW laser plays an important role as a precise coherent pumping source for many FIR lasers (see Chapter 11.4.2). Hence, for many cases of pumping, it is necessary to use isotopes to shift frequency radiation of a CO_2 laser to cover it with an upper level of FIR radiation (see Figure 11.21, Chapter 11). The isotope shift method is very convenient to obtain a CO_2 laser spectral operation in the 12 μm region [14].

6A.1.4 Basic Spectral and Gain Parameters of CO_2 Laser Media

According to the explanations given in Chapter 1.4, a short overview of line shapes of CO_2 molecule is given later. The line width of CO_2 laser is homogenously broadened almost for all

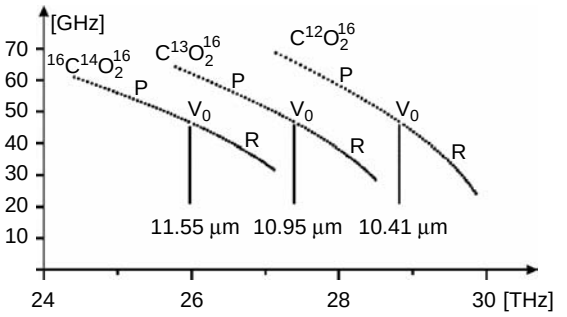

FIGURE 6A.7 Frequency displacement of a CO_2 regular band for different isotopic configurations of a CO_2 molecule. Points represent position of CO_2 emission lines in frequency. A vertical axis represents the differences in frequency of neighbor lines (as seen, the difference between neighbor lines changes from ~30 to ~60 GHz along the band).

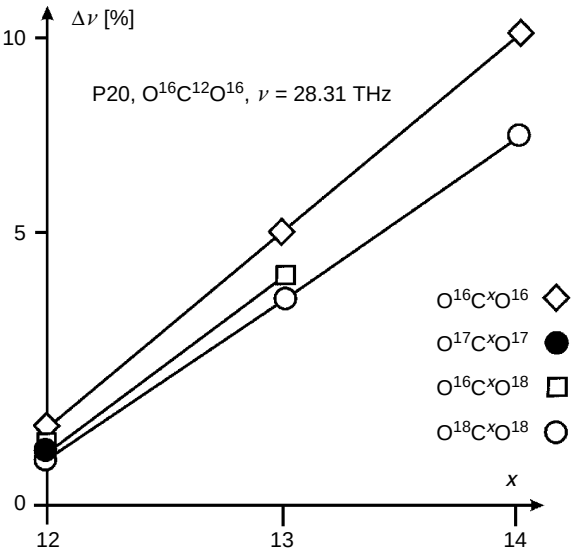

FIGURE 6A.8 Relative frequency shift of different isotopomers of a CO_2 molecule with respect to a basic $^{12}C^{16}O_2$ P20 line (28.31 THz). *x*—carbon isotopes.

practical cases, because its Doppler broadening is about $\Delta\nu_p \approx 60$ MHz. The pressure broadening of CO_2 laser lines is given by a formula [15,16]

$$\Delta\nu_p = 7.58\left(\psi_{CO_2} + 0.73\psi_{N_2} + 0.64\psi_{He}\right)p\left(\frac{300}{T}\right)^{1/2} \text{MHz}, \tag{6A.2}$$

where ψ is the fraction of the gas in the laser mixture and p is the pressure of the laser medium in torrs.

This formula can be replaced by a practical rule that says, increasing pressure by 1 Torr broadens the spectral line about 4.8 MHz (for assumed temperature of the gas mixture $T = 400$ K, for the typical CO_2:N_2:He = 1:1:3 mixture used in CO_2 RF-excited waveguide lasers, and composition $\psi_{CO_2} = 0.2$, $\psi_{N_2} = 0.2$, $\psi_{He} = 0.6$).

It can be noted that for about 12 Torr pressure, both Doppler (inhomogenous) and pressure (homogenous) broadenings are compared. The CO_2 laser usually operates at pressures higher than 12 Torr (DC-excited low-pressure lasers operate at about 20 Torr, RF-excited lasers at 100 Torr, and TEA lasers at 1 bar). Therefore, we can assume that for the most of CO_2 lasers their emission lines are homogenously broadened.

The other important parameters that determine the operation condition of CO_2 lasers are the small-signal gain g_0 and the saturation intensity of medium I_s. The small-signal gain and saturation intensity depend strongly on pressure. Hence, for low-pressure mixtures (20 Torr DC-excited laser)—see Chapter 1, Table 1.4—values are $g_0 \approx 0.3$ m^{-1}, $I_s \approx 20$ W/cm^2 and for high-pressure mixtures (RF-excited lasers) the values are $g_0 \approx 0.6$ m^{-1}, $I_s \approx 10$ kW/cm^2, respectively. It is clear from the earlier discussion that pressure influences the parameters of CO_2 laser operation strongly.

6A.1.5 Sealed-Off Conditions of a CO_2 Laser

The CO_2 DC discharge operation in some chosen geometry of the laser structure depends on the total pressure and current density. Components of the CO_2 laser gas mixture in conditions

of the weakly ionized plasma, about 10^{-7} of ions to particles ratio, are dissipated into many products. A main problem with CO_2 lasers operating in sealed-off conditions is the dissociation of a CO_2 molecule in reactions by electron impact: $CO_2 + e \Rightarrow CO + O + e$ or $CO_2 + e \Rightarrow CO + O^-$ [17].

- **Laser chemistry**
  If we take into account the dissociation of nitrogen (usually present in a CO_2 laser mixture) $N_2 + e \Rightarrow 2N + e$, thenwe have many different products in the laser gas medium—it is called laser chemistry—such as CO_2 (basic), O, O_2, O_3, NO, and N_2O [18,19]. The process of dissociation in sealed-off CO_2 lasers yields about 70% of dissociated CO_2 molecules. It decreases the population inversion and even influences the stability of the discharge. (The only solution in open systems is the application of flowing gas through the laser structure). To decrease the degeneracy of the gas mixture, usually water or hydrogen is added to the laser chamber [19,20].
  Another problem is the released oxygen, which is immediately captured by metal electrodes. One of the methods to minimize the effect is to use suitable metals as a material for electrodes. Gold or platinum seems to be the best solution [21]. Both metals significantly support a sufficient amount of CO_2 in the laser mixture.

- **Catalysis**
  Gold can also be used as an internal catalyst. It is usually sputtered on the inside of the glass laser tube [22]. The gold catalyst is activated in the presence of the discharge by adding 1% of hydrogen or 8% of carbon monoxide to the gas mixture. The gold catalyst can also be applied in RF-excited CO_2 waveguide laser structures [23].
  A more sophisticated method to avoid the decomposition of the CO_2 laser mixture is using catalytic electrodes covered by perovskite-type oxide, such as $Ln_{1-x}M_xCoO_3$, where Ln is a lanthanide (e.g., La, Nd) and M is an alkaline earth metal (e.g., Sr) [24,25].

- **Ionization potential**
  It is necessary to mention the role of xenon as an addition in sealed-off CO_2 laser systems. Xenon significantly improves the performance of DC, AC, and RF discharge, as well, in CO_2 electrically excited laser systems. The addition of a small amount of Xe to a CO_2 laser electrical system introduces a lower ionization potential, that is, about 2 eV less than in the case of a CO_2 molecule (see Figure 6A.2). The excitation and pumping of a laser gas medium are easier, and the output power of an RF-excited CO_2 waveguide laser can be increased by more than 20% [26]. It decreases the average energy of electrons and improves the efficiency of the excitation mechanism.

6A.1.6 The CO_2 Laser Structure—Mechanical, Electrical, and Optical

The active medium in a conventional diffusion-cooled CO_2 laser at the DC excitation is usually enclosed in a glass tube. It has to be cooled externally because of the relatively high power delivered to the laser plasma—currents up to a few tens of milliamperes at 5–10 kV of voltage. A water jacket is usually used to enclose the laser plasma tube (see Figure 6A.9). Because the temperature of tap water (usually used) can change with the season, some changes in output power can be observed. The practical rule says that 1 K change of water-cooled temperature causes 0.5% of the CO_2 laser output power. People dealing with CO_2 lasers observe that the same laser operates with a few percent higher power during winter time. Additional, and very important, the method of cooling is adding helium. It cools lower

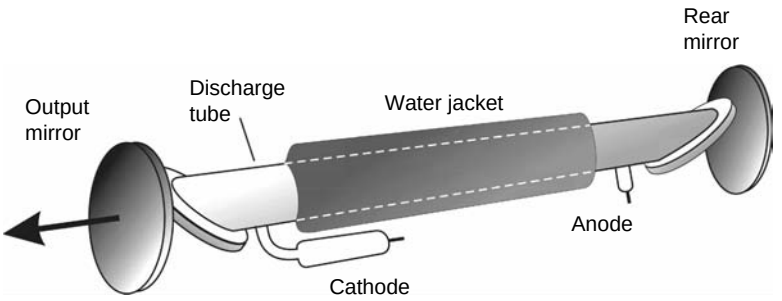

FIGURE 6A.9 A typical glass structure of the CO_2 laser tube. The tube can be terminated with Brewster windows or mirrors directly fixed to both ends of the tube, usually made of ZnSe (zinc selenide) polycrystals.

CO_2 molecule levels (see Figure 6A.2). Typically, helium is added to the laser gas mixture in the proportion of CO_2:N_2:He = 1:1:3 to 1:1:8.

The pressure of the laser gas mixture applied in conventional DC-excited CO_2 lasers does not exceed a few tens of Torrs. Under these conditions (pressure and above mentioned currents and voltages applied), CO_2 outputs are approximately a few tens of watts from a 1 m long laser tube, at an efficiency about 10%. For the 1 m long tube, one can expect even 50 W output power [20].

A glowing plasma exhibits the so-called negative dynamic resistance. Hence, an additional element—a ballast resistor—should be connected in series to a power supply and the laser tube to get stable conditions for the plasma (see Chapter 1.8.1). Figure 6A.10 gives an explanation of the electrical setup. The characteristic visible at the left is inverted to the one shown in Figure 1.22 (Chapter 1.8.1) to give a better explanation of the phenomena. When voltage on a discharge tube exceeds some critical point U_{ignition} (when a glowing discharge is created), the operating point at the characteristic $I_{\text{laser}} = f(U_{\text{laser}})$ goes to some point determined by crossing an auxiliary characteristic (dashed line) called a load line and dynamic characteristics of the plasma resistance. The load line is created by two points: power supply voltage U_0 and

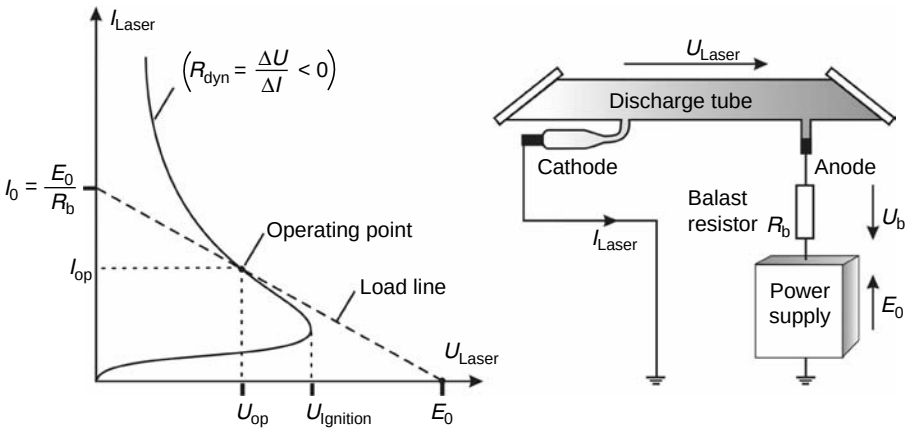

FIGURE 6A.10 Left—dynamic charactersitics of the laser plasma resistance R_{dyn}. Operating point for laser tube current I_{op} and voltage U_{op} is indicated. E_0 is the power supply voltage. Right—electrical setup of the laser. U_{laser} is the voltage on the laser tube and U_b is the voltage on the ballast resistor R_b. As seen, an operating point can be controlled by changing the value of the ballast resistor R_b.

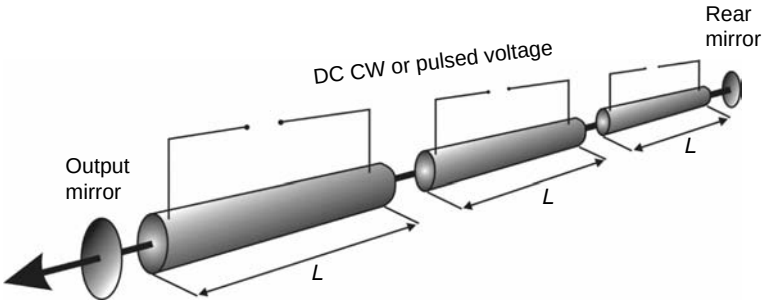

FIGURE 6A.11 Linear scaling of the DC-excited CO_2 laser. The long laser tube is often divided into a few electrically separated sections.

laser tube current $I_0 = U_0/R_b$, where R_b is a ballast resistor. As seen, the position of the operation can be easily controlled by choosing a suitable value of the ballast resistor.

It is obvious that a longer laser medium corresponds to higher output power. In the case of DC excitation, it creates some problems with plasma ignition. DC-excited conventional CO_2 lasers are often designed as a system of tubes in series to increase the length L of the common laser resonator (see Figure 6A.11). In this case, it is called linear scaling (longer tube, higher output).

Sealed-off and slow gas flow conventional CW DC-excited laser systems can be arranged in different ways. We can classify them as shown in Figure 6A.12, where the heat is removed by diffusion through the wall of the glass tube. In all presented systems, the laser beam, gas flow, and excitation are arranged along a common axis.

Figure 6A.13 shows possible optical configurations of the DC-excited CO_2 lasers. The first one (a) is equipped with Brewster windows, which determine a linear polarization of the output radiation. The total reflecting rear mirror can be moved with a piezoceramic transducer to tune the laser. In the second structure (b), the rear mirror is substituted with a diffraction grating. It makes it possible to tune the laser to a chosen emission line—a typical configuration for frequency stabilization of the laser (see Section 6A.1.7.1). A simple structure shown in (c) is convenient in applications, where a polarization and emission line are not important (laser technological systems hardening).

For some applications, the operation in a basic mode TEM_{00} plays a significant role. A CO_2 laser with an internal, relatively wide tube (about 6 mm in diameter) exhibits inclination to oscillate at higher-order modes. Different methods are used to suppress them. The simplest one is shown in Figure 6A.14. The diaphragm placed centrally in the path of the laser beam successfully suppresses higher-order modes by introducing suitable losses to the laser cavity.

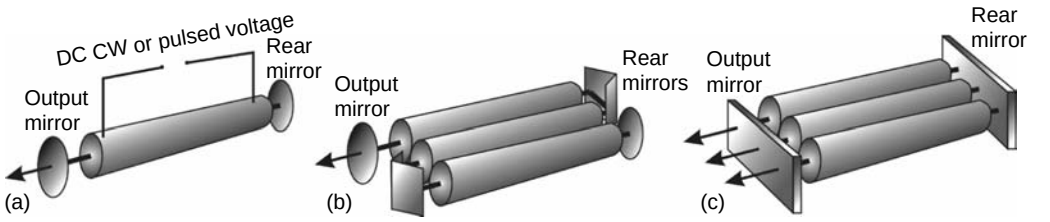

FIGURE 6A.12 CW conventional DC-excited CO_2 lasers (water-cooled discharge tubes): (a) excitation with DC current along the axis of the laser tube, (b) laser tubes arranged in series (multifold structure), (c) laser tubes arranged parallel.

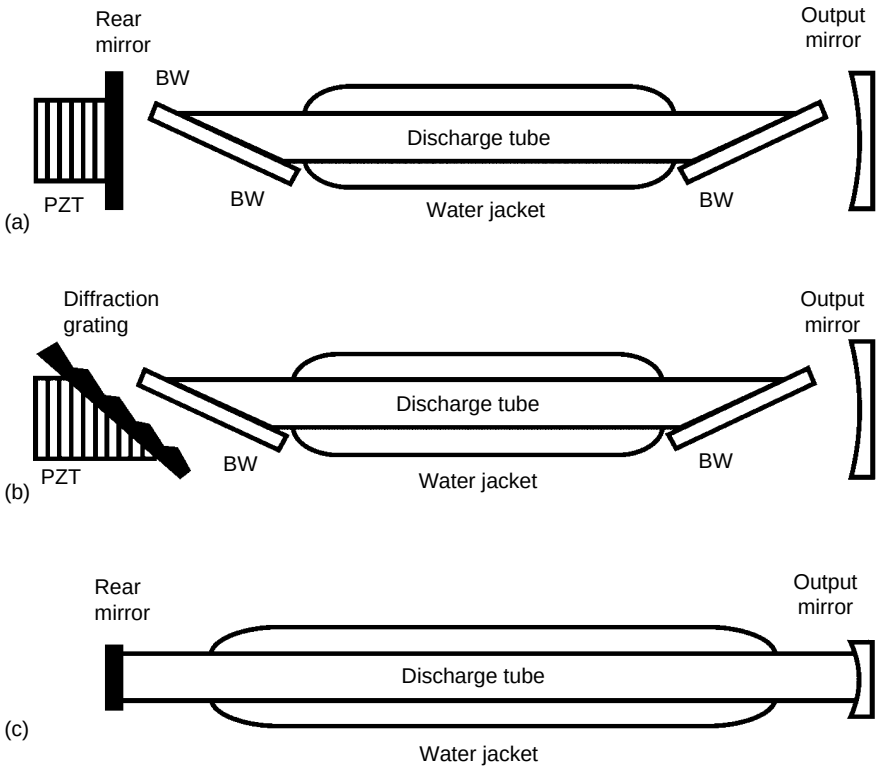

FIGURE 6A.13 Possible configurations of DC-excited conventional CO_2 lasers: (a) the discharge tube closed with Brewster windows BW, the laser can be tuned with a piezoceramic transducer PZT, (b) a diffraction grating instead of the rear mirror is used to tune the laser to a chosen emission line, (c) a simple structure with mirrors directly fixed to the ends of the tube.

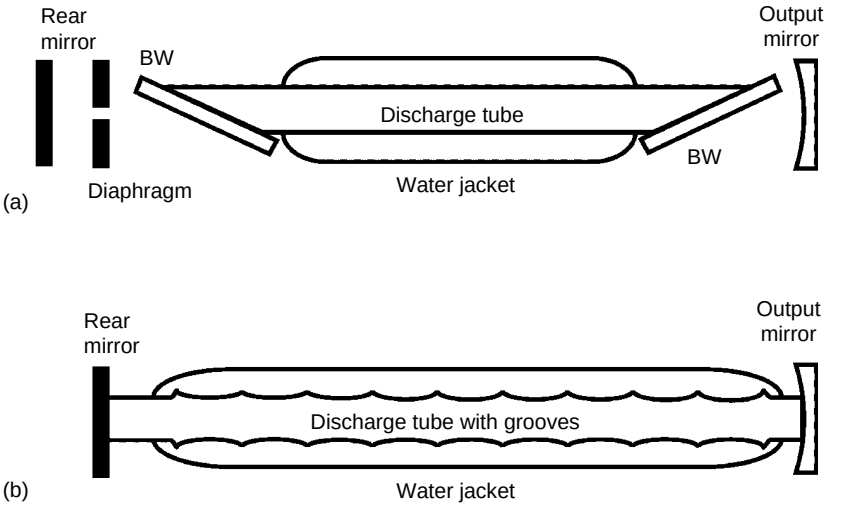

FIGURE 6A.14 Methods of suppressing laser higher order modes: (a) using a diaphragm inside the laser cavity, (b) using an internally profiled laser tube (BW—Brewster windows).

The second method (b) is much more sophisticated. The laser tube is internally profiled to suppress the operation of higher-order laser transverse modes.

6A.1.7 Tuning and Single-Frequency Operation

Laser action occurs when the resonator mode frequency overlaps the profile of the laser gain curve. In the case of CO_2 laser, there are many emission lines (Figure 6A.4), where the CO_2 laser oscillates on the strongest line coinciding with the laser cavity resonance. When the laser is tuned, the profile of the emission line is monitored by the laser longitudinal mode and it is observed in the output power as a specific shape of the gain curve. This shape is reproduced with each half-wavelength of tuning (from node to node of the standing wave in the resonator cavity); see Figure 6A.15.

When a spectrum of the laser medium has many emission lines (like in CO_2), then tuning the laser resonator gives a very specific picture of the laser output. Different resonant frequencies of the optical resonator can be in coincidence with frequencies of the emission lines of a CO_2 laser medium. As a result, the laser operation does not occur on one emission line, but "jumps" from line to line. Theoretically, the laser can operate on many emission lines simultaneously. However, the CO_2 laser operating only on the basic transverse mode TEM_{00} oscillates only on one longitudinal mode, which has the highest gain. It is a result of strong competition between rotational levels in the medium. Due to thermal effect (high-frequency collisions: ~10^7 collisions per second), there is an internal equalization process of population inversion along rotational levels. This strong competition between rotational levels in the CO_2 medium results in a "line-hopping" effect: the laser usually operates only on one chosen line [27], as long as an optical length of the resonator is not changed (mechanically or because of temperature drift or other perturbations). The observed picture of the output laser power is called the laser signature [28].

Figure 6A.16 shows a typical laser signature obtained from CO_2 laser [29]. The signature is reproducible with each half-wavelength $\lambda/2$ of tuning ΔL. The laser signature is stable and can be calculated for the chosen length L of the optical resonator [30]. According to Schiffner [31], the profile of the laser output gain curve can be described by a formula

$$\frac{I(d)}{I_s} = \frac{\alpha_0}{a} - 1 - 4\frac{(d-d_0)^2}{\Delta d^2}, \tag{6A.3}$$

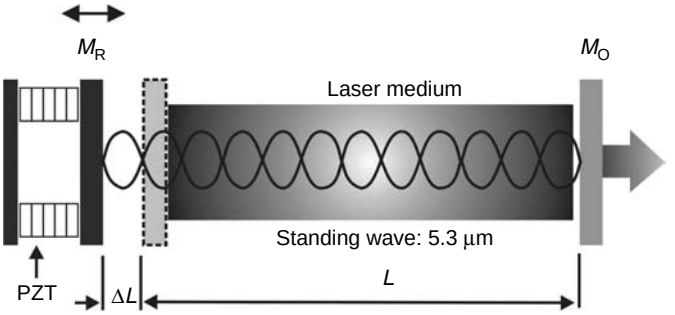

FIGURE 6A.15 Explanation of the laser tuning. The optical resonator is tuned with a piezoceramic transducer PZT of a few values of the half-wave ΔL, where the half-wavelength is assumed as 5.3 μm for a CO_2 laser. M_R—rear, total reflective mirror, M_O—output mirror, L—resonator length.

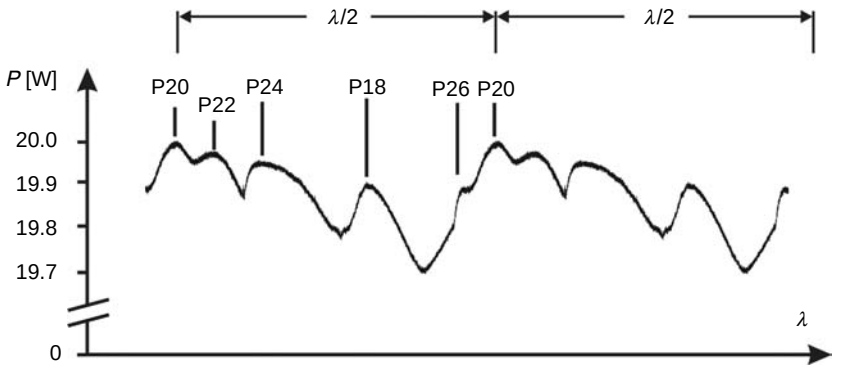

FIGURE 6A.16 Experimental results of a CO_2 laser tuning of two half-wavelengths $\lambda/2 \approx 5.3$ μm. Different P branch lines are responsible for laser output power maxima visible in the picture.

where $I(d)$ is the radiation intensity inside the resonator, I_s the saturation intensity, α_0 the small gain coefficient, a the absorption coefficient, d and d_0 denote the tuning and normalized tuning of the laser, respectively, and Δd is the "geometrical" width of the laser line.

As easily shown, the formula approximates output laser gain curves with inverted parabolas. The formula was derived by assuming the existence of only longitudinal modes in the laser cavity (no transverse modes). It assumes that the radii of the laser mirrors are much greater than the changes in their positions d. It also assumes homogeneous broadened lines because of pressure applied in CO_2 lasers. Another assumption is that a refractive index of the laser medium is not sensitive to changes in the laser operation frequency. Losses a are assumed to be homogeneously distributed along the laser cavity. Despite many assumptions and simplicities, the formula gives signatures easily confirmed by experiments. Figure 6A.17 shows schematically the idea described here. A line-hopping effect occurs in those places where curves cross each other.

Schiffner's procedure can be simplified much more drastically. A simplified algorithm is limited only to investigations of the frequency distance between longitudinal modes and centers of the emission lines. It does not take into account both gain and width of the chosen

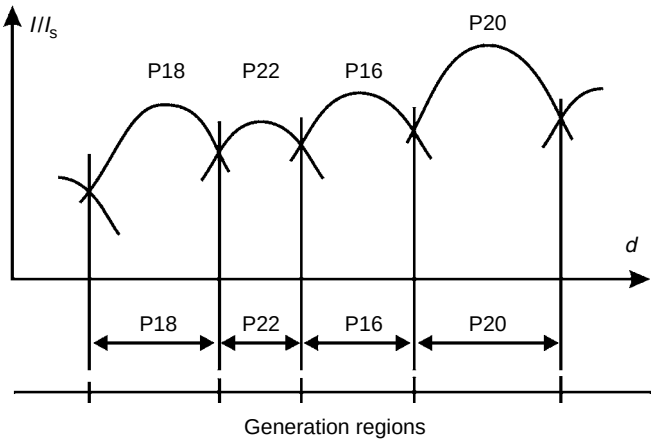

FIGURE 6A.17 Explanation of Schiffner's procedure. Line-hopping effect occurs when laser gain curves cross each other.

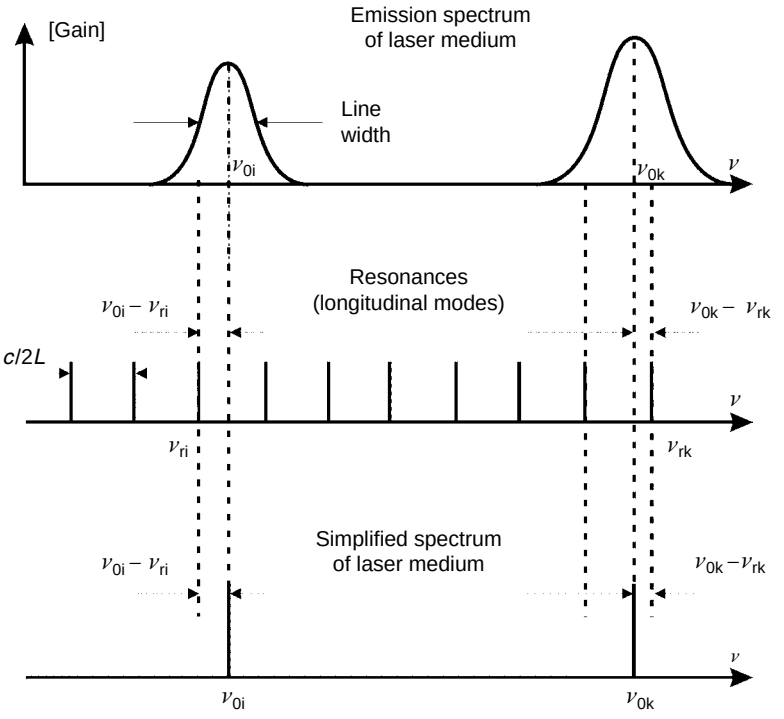

FIGURE 6A.18 Explanation of Schiffner's procedure (top) and simplified procedure (bottom). The first one takes for calculations a shape of the laser gain, another one is sensitive only for a frequency distance ν_{0i}, $-\nu_{ri}$, ν_{0k}, $-\nu_{rk}$ between laser modes ν_{ri}, ν_{rk}, and centers ν_{0i}, ν_{0k}, emission lines (bottom). The frequency distance between longitudinal modes is $c/2L$ (middle).

emission line; see Figure 6A.18. After all, it successfully reconstructs signatures that are obtained experimentally [30]. Figure 6A.19 shows some sophisticated examples of laser signatures calculated for different isotopes of carbon and oxygen as elements of a CO_2 molecule structure (for $L = \sim 408.8$ mm long optical resonator). As seen, it is possible to get a desired signature, and obtain even a "poor" signature where only one chosen emission line is generated by a laser. Figure 6A.19 (top) shows an example, in which the laser can operate on line P20 even when it is a few micrometers tuned. Choosing such a signature gives better conditions for passive stabilization of the optical resonator length. The signature on top of the figure also exhibits some convenient effect: the laser operation "jumps" from line to line according to the order of the CO_2 molecule spectrum (well-ordered laser signature [30]). As seen, it is possible to create a CO_2 laser operated on a single line during a half-length wave tuning [32,33]. A single line operation is possible even in a pulse regime of the CO_2 laser for a carefully chosen signature [32,34]. This earlier analysis deals with relatively short resonators. For long resonators (L more than 5 m), where a free spectral range $\Delta\nu_{FSR} = c/2L$ is much smaller than the emission line width, a CO_2 laser operates permanently on the strongest P20 line.

6A.1.7.1 Frequency Stabilization of a CO_2 Laser

CO_2 lasers can be used as precise frequency references for laser spectroscopy. The band of such a spectroscope is determined by the width of the laser emission line. In the case of the CO_2 molecule used as a laser medium, the laser gain curve width does not exceed a few tens of

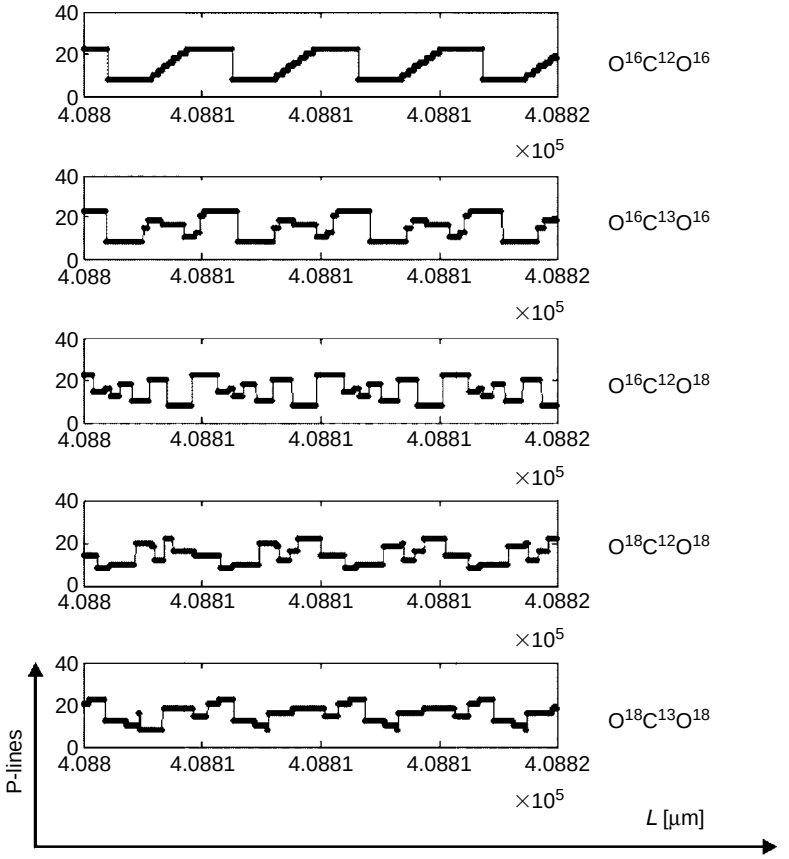

FIGURE 6A.19 Examples of laser signatures calculated theoretically for chosen isotopes of carbon and oxygen as components of CO_2 laser. Vertical axis is the names of lines from P branch of CO_2 spectrum, horizontal axis is the laser tuning from $L = 408.80$ to $L = 408.82$ mm. (Top: an example of the signature, when the laser does not suffer a "line hoppings" effect even for a few micrometer tuning).

megahertz in the case of a conventional low-pressure CO_2 laser (it can be assumed that the emission lines of the CO_2 lasers are homogeneously broadened for pressures higher than 10 Torr; see Chapter 1.4.2). It can reach hundreds of megahertz in the case of RF-excited waveguide lasers to a few tens of gigahertz for atmospheric and high-pressure lasers. (The pressure broadening is ~5 MHz per Torr for CO_2 lasers.)

A method of laser saturation spectroscopy is based on coincidence of the laser gain curve with a dense molecular spectrum of the absorber. Figure 6A.20 shows a simplified setup of the saturation spectroscopy experiment. A laser beam penetrates an investigated absorption medium in the absorption cell and saturates the absorber. Next, the saturating beam leaves the absorber and is attenuated and reflected back to the absorption cell as a weak, detecting (probe) beam. As known, particles traveling in perpendicular direction to the observer (here, to saturating or detecting beam direction) are responsible for the center of the absorption line. It is a consequence of a Doppler effect (see Chapter 1.4.3). If the laser output frequency is tuned to the center of the absorption line, then the absorber saturated by a saturating beam is transparent for the weak, detecting beam. In that way, for just that frequency a peak of the detecting beam intensity is registered. Absorption for the frequency of the center of the absorption line is lower, and this effect is known as an inverted Lamb dip. When an

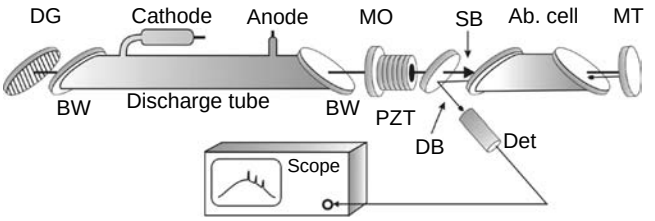

FIGURE 6A.20 Arrangement for the laser saturation spectroscopy using a CO_2 laser. An output laser beam, as a strong saturating beam, saturates investigated absorber in an absorption cell (usually under pressure of a few, or a few tense of millitorrs), DG—diffraction grating to choose a desired CO_2 emission line, MO—output mirror, BW—Brewster windows, PZT—piezoceramic transducer to tune the laser in the range of an emission line width, MT—mirror with some attenuator (it can be partly transmitting to attenuate the return, weak detecting beam), SB—strong laser beam output, DB—weak, detecting beam, Det—optical detector.

investigated absorber exhibits many absorption lines, they will be visible as absorption peaks at the detecting signal profile when the laser is tuned. The number of monitored absorption peaks depends on the absorber and the width of the laser emission line.

Figure 6A.21 gives a clearer explanation of the method. Three absorption lines are hidden: their relative positions cannot be determined accurately (using the methods of the traditional spectroscopy) because of the Rayleigh criterion. When the absorber is monitored with a saturation spectroscopy method, all three absorption lines can be recognized as absorption peaks at the profile of the laser detecting beam signal.

The effect of the absorption peak can be used for frequency stabilization of the laser. Sulfur hexafluoride SF_6 is a suitable absorber in the case of a CO_2 laser. An SF_6 absorption band covers many CO_2 laser emission lines. Let us consider a simpler case, without the absorber. Figure 6A.22 shows a setup for laser frequency stabilization using the first derivative method.

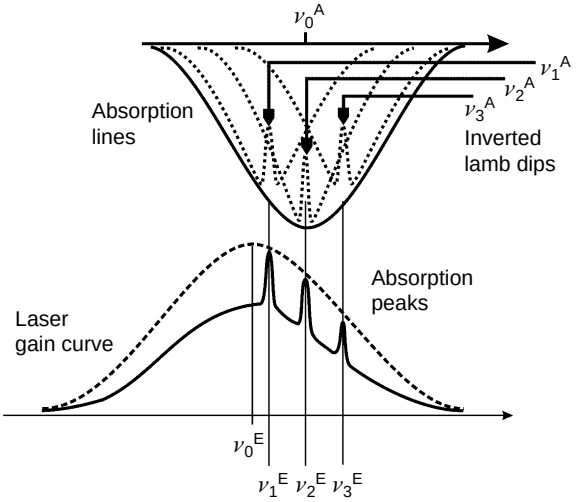

FIGURE 6A.21 Laser saturation spectroscopy principle. The absorption line consists of three lines hidden because of the Rayleigh criterion. Using a method of the laser saturation spectroscopy it is possible to recognize all three lines, visible at the profile of the laser gain curve as absorption peaks. (It is an interesting example where a physical principle was "broken.")

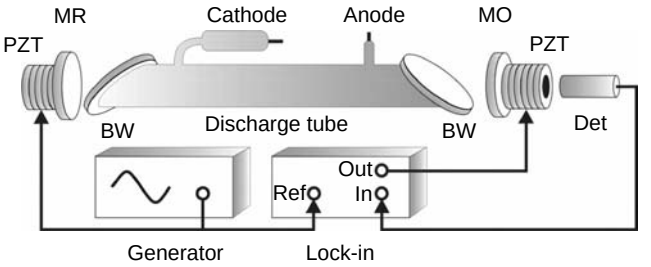

FIGURE 6A.22 Setup for the laser frequency stabilization to the center of the laser gain curve (to the center frequency of the emission line). MR—rear mirror, MO—output mirror, PZT—piezoceramic transducers, BW—Brewster windows, det—optical detector, lock-in amplifier is put as a phase sensitive detector (with PZT and generator creates the electronic loop of the servomechanism), Ref—input of the reference signal (from acoustical generator), In—input signal from the detector, Out—output signal to control PZT and stabilize the laser.

Laser frequency is modulated (a few kilohertz "dither") by a mirror fixed to a piezoceramic transducer PZT. The output laser signal (Figure 6A.23a) is detected by a phase-sensitive detector (synchronous detection). An error signal (or discriminant signal) at the output of the phase-sensitive detector looks like the one shown in Figure 6A.23b [35]. In fact, this signal is a first derivative of the laser gain curve. Thus, the name of the method of stabilization. In practice, it is frequency stabilization to the center of the laser gain curve. The servomechanism (PZT and electronic loop) is sensitive to detuning the laser off from the center of the gain curve. Then, the error signal appears at the output of the phase-sensitive detector; it is amplified and directed to the PZT. Finally, the servomechanism corrects the frequency of the laser radiation, tuning the laser frequency to the center of the emission line. A diffraction grating is used as one of the laser mirrors in the case of a CO_2 laser to choose a desired emission line.

A setup for the stabilization to the center of the absorption peak is the same. The slope of the first derivative signal of the peak is higher than the signal created from the laser gain curve. Hence, the level of the frequency stabilization is higher.

Sometimes the method of the third derivative is used. It gives a very convenient advantage: the background of the laser gain curve is sufficiently reduced. It is especially important in cases when the absorption peak does not appear at the center of the laser gain curve. The picture in Figure 6A.24 shows the laser gain curve with an absorption peak and the first, second, and third derivatives of the gain curve. A signal of the second derivative is useless because it is symmetrical, and it gives the same sign of the error signal independently of laser frequency detuning. Next, a third derivative signal is useful, and, as seen, it has a much higher slope than the first derivative signal. The third derivative method is very successful in

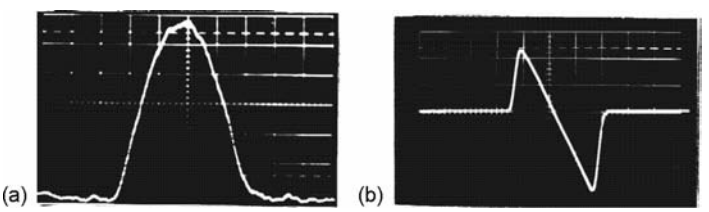

FIGURE 6A.23 (a) CO_2 laser output gain curve. (b) First derivative of the curve (discrimination signal) electronically obtained.

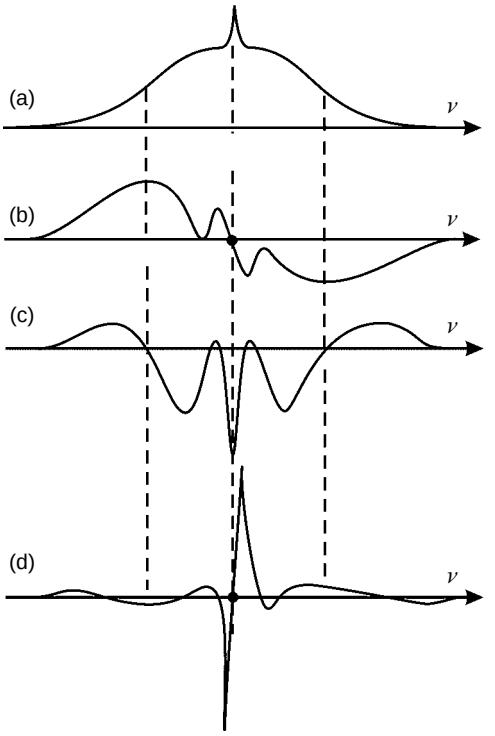

FIGURE 6A.24 Principle of the laser frequency stabilization using a method of the saturation absorption: (a) gain curve with an absorption peak, (b) first derivative of the gain curve, (c) second derivative (useless because of the symmetry of the signal), (d) third derivative of the laser gain curve (the background is almost removed).

laser saturation spectroscopy to recognize relatively weak absorption peaks. For example, in the case of OsO_4 molecule absorption spectrum [36,37]. This method gives much higher resolution of such a spectrometer.

Another method is the stabilization to the center of the inverted Lamb dip at the absorption profile of a CO_2 molecule. The absorption cell is placed inside the CO_2 laser resonator cavity (see Figure 6A.25). In this case, the so-called side-light radiation is detected at the wavelength of 4.3 μm.

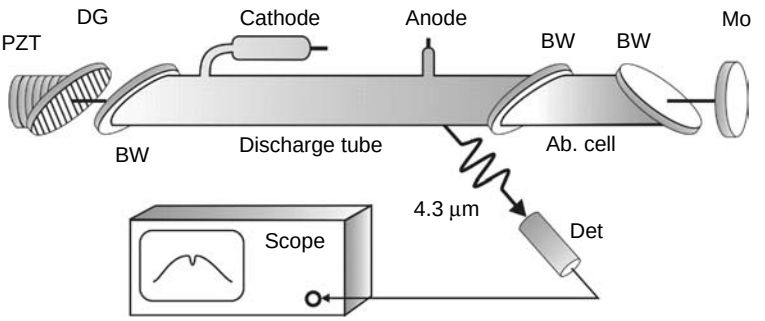

FIGURE 6A.25 Setup for the frequency stabilization of a CO_2 laser using a signal of the side-wall radiation at 4.3 μm. DG—diffraction grating to choose a desired emission line (it serves as a total reflecting mirror), MO—output mirror, BW—Brewster windows, Det—optical detector.

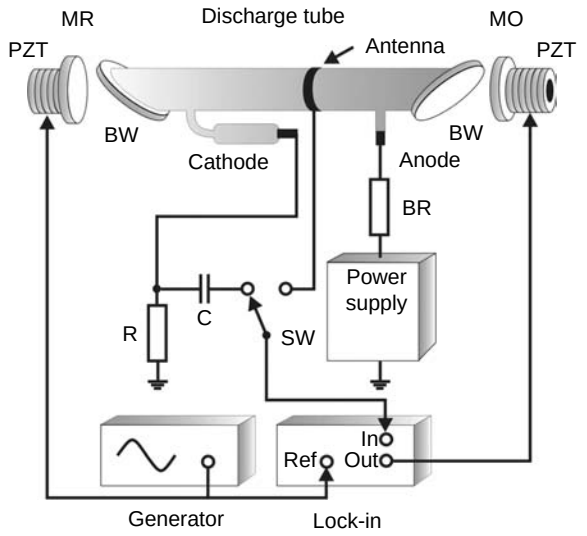

FIGURE 6A.26 Setup for optogalvanic stabilization of the CO_2 laser frequency. PZT—piezoceramic transducer, MR—rear, total reflective mirror, MO—output mirror, BW—Brewster windows, BR—ballast resistor for compensation of the negative impedance of the DC plasma, R—resistor (ex. 1 Ω), C—capacitor, SW—switch to choose the optogalvanic signal, lock-in amplifier is put as a phase sensitive detector (with PZT and generator creates the electronic loop of the servomechanism).

The CO_2 laser power changes are represented in changes of the laser plasma impedance, which is called the optogalvanic effect [38,39]. (A very specific phenomenon in gas lasers.) It can be easily used for frequency stabilization to the center of the laser gain curve. When the laser is tuned, the laser gain curve is observed at the output, which will also be represented in the optogalvanic signal. A servomechanism uses the signal taken from the circuit of the laser electrical supply instead of the optical detector signal. (It is a good way to avoid an expensive infrared detector.) Figure 6A.26 explains this method.

The experiment can be performed in two ways: with discharge current stabilization or voltage stabilization on the electrodes. When current is stabilized (easier case), the signal (in this case—optovoltaic signal) can be detected at the resistor R connected in series, as shown in Figure 6A.26. The servomechanism works in the same way as explained here. The optogalvanic signal can also be detected using a small antenna placed close to the laser discharge [40,41]. The signal is detected by the electromagnetic field changes around the laser discharge tube (see Figure 6A.26).

A stabilization about 10^{-8} ($\Delta\omega/\omega_0 = 10^{-8}$, where ω_0 is the center of the laser line and $\Delta\omega$ is the frequency stabilization) is obtained with the stabilization method to the center of the laser line, when a free-running laser gives the value of 10^{-6}. For the saturation absorption method, the frequency stabilization reaches the value of 10^{-13} (it means 1 Hz or even less) in the case of CO_2 lasers.

6A.1.8 RF-Excited Waveguide CO_2 Laser

When the basic part of the optical laser resonator is formed by optical waveguide, and its walls play a crucial role in propagating properties and the shape of a laser beam formed inside the resonator, they are called waveguide resonators (Figure 6A.27). Practically the waveguide resonator is defined by a simple criterion—the Fresnel number N_F should be lower than unity:

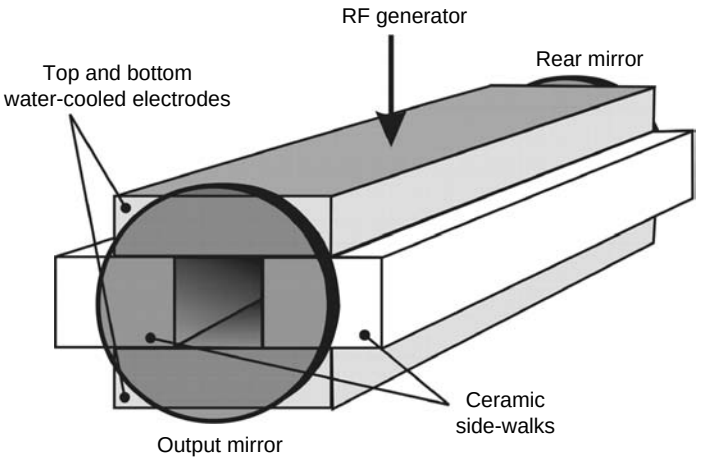

FIGURE 6A.27 Sandwich-type structure of an RF-excited CO_2 waveguide laser. Metal electrodes, ceramic side walls, and both rear and output plane mirrors create the laser waveguide cavity.

$$N_F = \frac{a^2}{\lambda L} < 1, \tag{6A.4}$$

where a is half of the resonator aperture, λ the wavelength, and L is the resonator length.

For example, for a typical CO_2 waveguide with the square transverse dimensions $2a \times 2a = 2 \times 2$ mm^2, $L = 400$ mm, and $\lambda = 10.6$ μm, the Fresnel number is ~0.2. When the Fresnel number exceeds unity, the resonator can be treated as an open resonator. In practice, for a CO_2 laser with the same length L and transverse dimension $2a \geq 5$ mm, the resonator becomes an open one ($N_F \approx 1.5$). In that case, a Gaussian resonator should be applied.

The advantage of using waveguide resonators for molecular CO_2 lasers lies in the fact that it allows to decrease transverse dimensions of the beam inside the waveguide. Small transverse dimensions allow to increase diffusive cooling efficiency (see Figure 6A.2, where 010 level is depopulated by collisions with helium atoms, which transport waste heat to the walls). There is another advantage: due to better cooling condition, the pressure of the mixture can be increased considerably, according to the practical formula

$$pd \approx 25 \text{ (Torr cm) for waveguide structures,} \tag{6A.5}$$

$$pd \approx 19 \text{ (Torr cm) for planar structures,} \tag{6A.6}$$

where p is the pressure and d is the transverse dimension of the waveguide or slab (for planar structure).

For $d = 2$ mm, the total pressure of mixture more than 100 Torr can be applied. Higher pressure means higher density of gain medium and higher output power. Hence, waveguide lasers require much shorter length to obtain the same output power than the low-pressure DC-excited CO_2 lasers.

6A.1.8.1 Waveguide Modes in Rectangular Symmetry

The waveguide channel can be formed by glass or ceramic capillary (with typical internal diameter of 1–2.5 mm) or more often in rectangular configuration as shown in Figure 6A.28. The sidewalls can be all dielectric or they can be formed in the "sandwich"

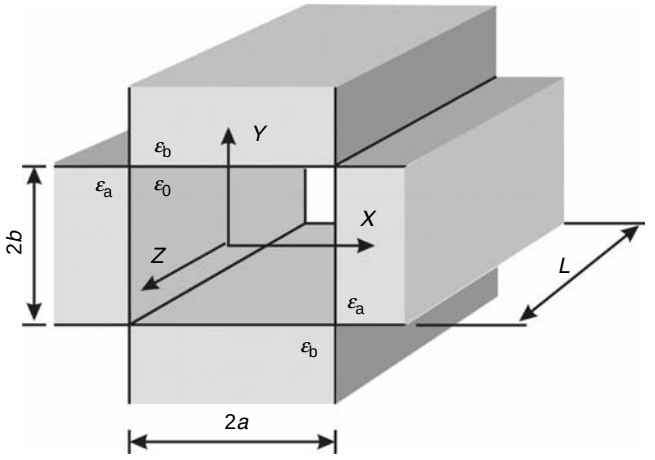

FIGURE 6A.28 Schematic picture for calculations of the electromagnetic field components propagating along the waveguide channel.

structure, where opposite walls are dielectric or metal (usually aluminum) and they operate as the RF electrodes. For the frequencies of CO_2 laser radiation (28 THz), neither dielectric nor metal behaves like pure dielectric or pure metal. They are lossy materials; however, their losses can be much smaller than the total gain in such structures. The waveguide structure can propagate typical hybrid waveguide EH_{mn} modes, which express x- or y-polarized component of the electrical field:

$$E_y = E_0 \begin{bmatrix} \cos\left(\frac{m\pi x}{2a}\right)\cos\left(\frac{n\pi y}{2b}\right) & m, n & -\text{ odd} \\ \cos\left(\frac{m\pi x}{2a}\right)\sin\left(\frac{n\pi y}{2b}\right) & m & -\text{ odd}, \quad n \quad -\text{ even} \\ \sin\left(\frac{m\pi x}{2a}\right)\cos\left(\frac{n\pi y}{2b}\right) & m & -\text{ even}, \quad n \quad -\text{ odd} \\ \sin\left(\frac{m\pi x}{2a}\right)\sin\left(\frac{n\pi y}{2b}\right) & m, n & -\text{ even} \end{bmatrix} \tag{6A.7}$$

Figure 6A.29 graphically explains formula 6A.7, where different EH_{mn} modes propagate along the optical z-axis of the waveguide.

Figure 6A.30 shows patterns of real EH_{mn} modes obtained for RF-excited waveguide CO_2 laser with 2.2×2.2 mm^2 cross section and 380 mm length [35]. The most required EH_{11} mode in the rectangular waveguide is similar to TEM_{00} mode for a free space Gaussian resonator.

6A.1.8.2 RF-Excited Discharge

The method of laser active medium excitation plays a significant role to ensure the maximum population inversion of levels taking part in laser action. It has an important influence on the level of output power, laser efficiency, and quality of the laser beam. The possibility to decrease the transverse dimensions of the guiding channel (like in Figure 6A.27) of the CO_2 laser implies RF excitation of such a structure. The RF technique of excitation appeared to be optimal for waveguide molecular lasers.

Transversal excitation with a radio frequency (RF) current of CO_2 laser plasma exhibits many advantages compared with DC excitation along the laser tube. The main advantages are low excitation voltage (a few hundred volts), better discharge stability, and better efficiency of the excitation.

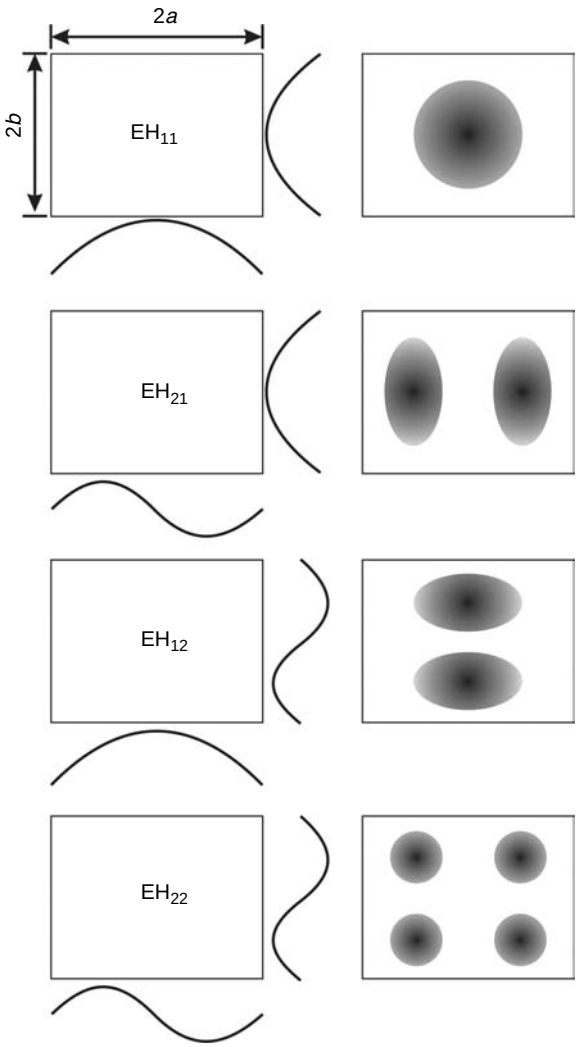

FIGURE 6A.29 Left—modes formed across *xy*-axis of the waveguide according to formula 6A.7, and right—intensity distribution of the respective modes.

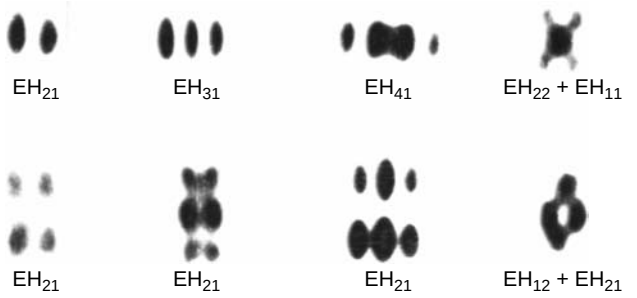

FIGURE 6A.30 Some waveguide laser modes (experimental results) formed in the channel of $2.2 \times 2.2\,\text{mm}^2$ cross section and 380 mm long.

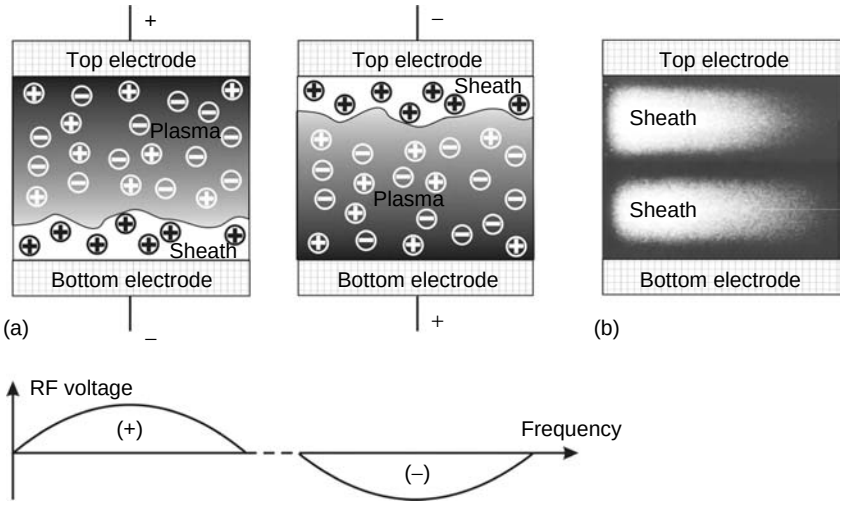

FIGURE 6A.31 (a) A schematically shown model of RF-excited plasma and explanation of sheath creation, (b) experimental result—glowing plasma in the laser 2×2 mm^2 waveguide channel (asymmetry is caused by a tilted camera).

A specific feature of RF discharge is nonuniformity of the plasma near electrodes. It is of fundamental importance to form alpha- or gamma-discharge [42]. In the case of alpha-discharge, positive ion sheaths create the above-mentioned plasma nonuniformity along the electrode surface. A neutral discharge occupies the area between electrodes, where population inversion process occurs and laser action as a consequence. The mechanism of sheath creation can be explained as follows: for RF excitation the cloud of neutral plasma oscillates, and in that way it uncovers slow, heavy ions in the neighborhood of electrode surfaces (see Figure 6A.31).

The investigations show that sheaths play an important role in stabilization of the alpha-type discharge. For the typical conditions of the CO_2 waveguide or slab-waveguide laser operation excited with RF discharge, the alpha-type discharge is very stable. For such parameters as pressure in the range of 13–800 hPa (10–200 Torr), 1.5–2.5 mm gap between water-cooled aluminium electrodes and 40–300 MHz excitation frequency, the probability of alpha- to gamma-type discharge transfer is very low.

Analysis of the available data gives a description of the RF alpha-type discharge [43]:

- High density of the discharge current and relatively low plasma voltage compared with a voltage drop on sheaths, which indicate that the alpha-discharge behaves like a pure capacity load, particularly at relatively high input power and pressure.
- For optimum RF-excited slab-waveguide laser operation conditions,pressure of 93 hPa (70 Torr) and delivered input power per unit area of about 20 W/cm^2, plasma resistance is ~200 Ω/cm^2 (it gives 0.4 Ω for 10 kW of delivered power).
- The positive slope of current–voltage characteristic of alpha-discharge is a result of sheath properties but not plasma as such.
- The total thickness of sheaths is a result of the slowly rising function of current density and it is independent of gas pressure. It is equal to ~0.35 ± 0.03 mm, for current density of 30–1000 mA/cm^2 and relatively small compared with an interelectrode gap of ~2.5 mm. It means that for typical waveguide RF-excited laser operation conditions most of the waveguide laser channel is occupied by plasma [44].
- Figure 6A.32a shows an equivalent circuit of the RF-excited plasma. It is a combination of plasma resistance R_P, plasma capacity C_P, and plasma sheath capacity C_S. As was

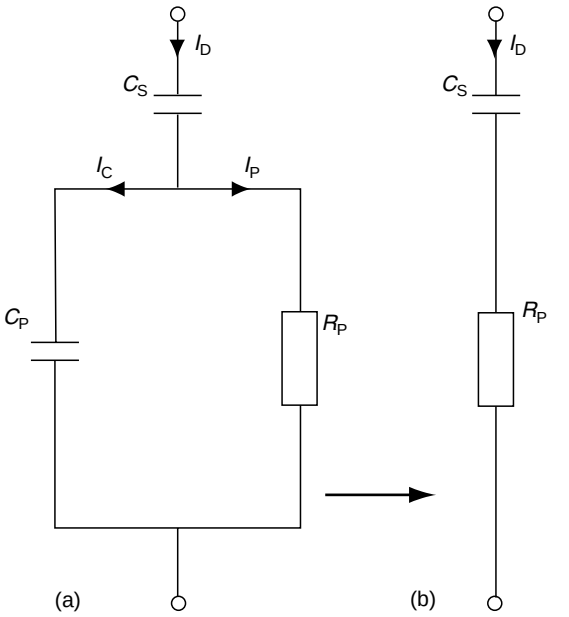

FIGURE 6A.32 (a) Equivalent circuit of RF plasma in the alpha phase. R_P, C_P, C_S plasma resistance, capacity, and sheath capacity, respectively; I_D—sheath current, I_P—plasma current, I_C—capacity current of the plasma. (b) Circuit without plasma capacity current I_C.

experimentally proved, plasma capacity current I_C covers only a few percent of total discharge current I_D. Hence, an equivalent circuit of RF plasma can be expressed as shown in Figure 6A.32b (only plasma resistance R_P and plasma sheath capacity C_S).

Considerations presented earlier show that alpha-type discharge is very stable because of its own internal structure. The existence of sheaths (exactly equivalent capacity of the sheaths) fulfills a protective role for some undesired temperature instabilities. A general conclusion is that in typical operation conditions of RF-excited CO_2 waveguide lasers the probability of alpha-type discharge transfer to gamma type is low.

It was experimentally confirmed that alpha–gamma transfer is strictly related to changes in sheaths, but not in the main plasma column. To explain the phenomenon, the physical model is assumed where the electrical field in sheaths rises with an excitation frequency. In that way, the time necessary for electrons presented in sheaths (gamma electrons) to be transferred to the plasma column is longer than one cycle of the excitation frequency. It means that for short excitation time, gamma electrons are captured in the sheaths.

On the other hand, it is known that the necessary voltage to maintain the discharge can be increased without increasing the excitation frequency by covering the electrode surfaces with materials of weak emissive properties. Then, the used alpha-discharge current (in the plasma column) can be higher and still low enough not to be transferred to gamma discharge, useless for the laser medium pumping (still in waveguide configuration). It should be emphasized here that increasing excitation frequency creates problems with the uniformity of the voltage distribution along the laser electrodes. It will be considered in later sections.

Optimum conditions of the gas laser discharge medium necessary for maximum extraction of the power from the medium need correlation of many factors that are responsible for properties of the laser discharge. Mutual dependence of parameters such as voltage on the plasma column, discharge current, gas pressure, electrode dimensions, and distance between

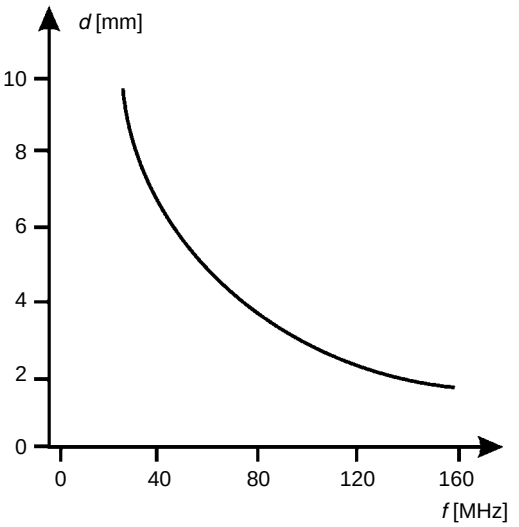

FIGURE 6A.33 Approximation (electrode distance vs. optimum frequency) of the experimental results collected from available data in literature.

them is very complicated. Usually, it is difficult to present them in analytical forms, but as experimental characteristics. Description of all possible physical states of the plasma would have to take into account many possible combinations of different parameters. Usually parameters are grouped to make the plasma description easier. Hence, investigations of scaling laws are carried out. One of the most known laws is the Pashen curve $V = F(pd)$, which joins plasma votage V, gas pressure p, and inter-electrode distance d. For example, scaling laws for conventional lasers excited with CD current along the laser discharge tube show that for some optimum conditions of laser operations and for a given diameter of a laser tube the optimum pressure rises with a decrease in the tube diameter and the specific output power (power per laser tube length) remaining constant.

Calculation of optimum conditions of RF-excited waveguide CO_2 lasers is more difficult. However, some manipulation is possible through changes in the excited frequency. Moreover, interelectrode distance is an additional factor. Data collected from the literature [45–47] can be presented in the form of the characteristic $d = F(f)$, interelectrode distance d vs. excited frequency f (see Figure 6A.33). The curve in the figure can be expressed as dependence $d(f) = F_1/f$, where F_1 is a constant, and it is one of the scaling laws of such a laser system: $F_1 = fd$ (in the case of RF-excited CO_2 waveguide lasers: $F_1 = 28$ cm MHz). From the above approximations, a practical formula describing df product for optimal conditions can be written as

$$df \approx 28 \text{ cm MHz}. \tag{6A.8}$$

6A.1.8.3 Equivalent Circuitry

The sandwich structure, as shown in Figure 6A.27, centrally fed with RF voltage behaves like a symmetrically supplied opened transmission line [48]. When the wavelength of the RF excitation is compared with the length of the transmission line (in our case the length of the waveguide), the distribution of RF voltage along the waveguide is not uniform, as shown in Figure 6A.34a. For the typical sandwich metal-ceramic structure of the waveguide made of aluminum and Al_2O_3 ceramic (where a relative permittivity is 9), the quarter wavelength

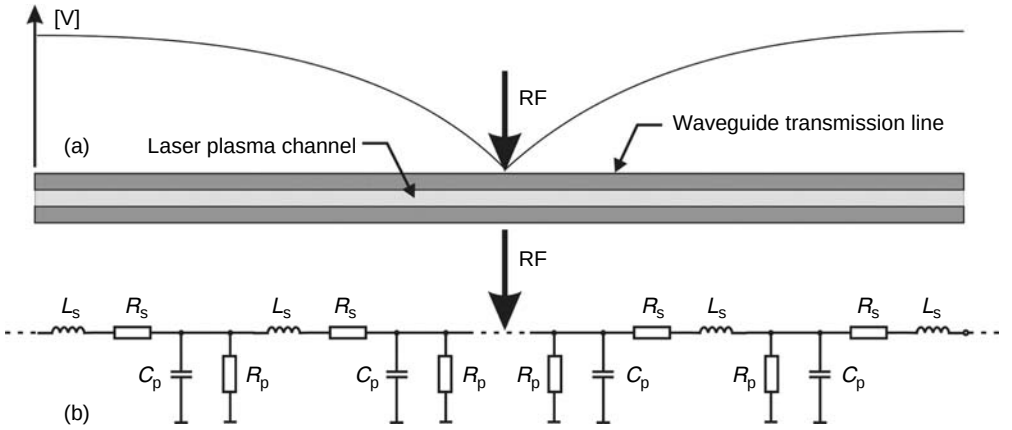

FIGURE 6A.34 Equivalent circuit of the laser waveguide cavity (a). L_s, R_s—series inductivity and resistance, C_p, R_p—capacity of the laser structure and resistance of the laser plasma, respectively, L_p—shunt inductor. High nonuniformity of the voltage distribution along the laser channel is shown (b). In real structures, ~40 cm long, nonuniformity can exceed 40% at both ends of the channel.

of the excitation wave is equal to ~20 cm for the frequency of 125 MHz. Voltage nonuniformity (caused by an RF standing wave effect) for a typical 40 cm long waveguide structure can be as high as 40%. It causes nonuniform distribution of the laser plasma excitation in the laser waveguide cavity and finally reduces the output power significantly.

The single-channel waveguide with aluminum electrodes separated by ceramic bars is considered here as a low-loss transmission line. A voltage $V(x)$ distribution along the waveguide consists of two opposite V_1 and V_2 propagating waves and can be described as [48,49]

$$V(x) = V_1 e^{\sqrt{zy}x} + V_2 e^{-\sqrt{zy}x}, \tag{6A.9}$$

where z and y are impedance and admittance of the equivalent transmission line, respectively, and $z = R_s + j\omega L_s$, $y = G_p + j\omega C_p$, $G_p = 1/R_p$.

Introducing characteristic impedance of the line $Z_0 = \sqrt{z/y}$ and propagation constant $\gamma = \sqrt{zy}$, the expression (6.9) can be rewritten as

$$V(x) = V_1 e^{\alpha x} e^{j\beta x} + V_2 e^{-\alpha x} e^{-j\beta x}. \tag{6A.10}$$

Assuming lossless and open transmission line ($\alpha = 0$), only one part of the expression (6.10) can be considered:

$$V(x) = V_1 \cos Bx, \tag{6A.11}$$

where $B = -j\gamma$, and V_1 is the voltage at the end of the line. The expression shows nonuniformity of voltage distribution along the waveguide channel excited with radio frequency. There are a few practical techniques to improve the uniformity of voltage distribution along the waveguide. We demonstrate two of them.

The effect of the RF standing wave along the waveguide can be corrected by smoothing the voltage distribution using inductive-terminated technique, where inductive coils L_p (see Figure 6A.35) are fixed at both ends of the laser electrodes.

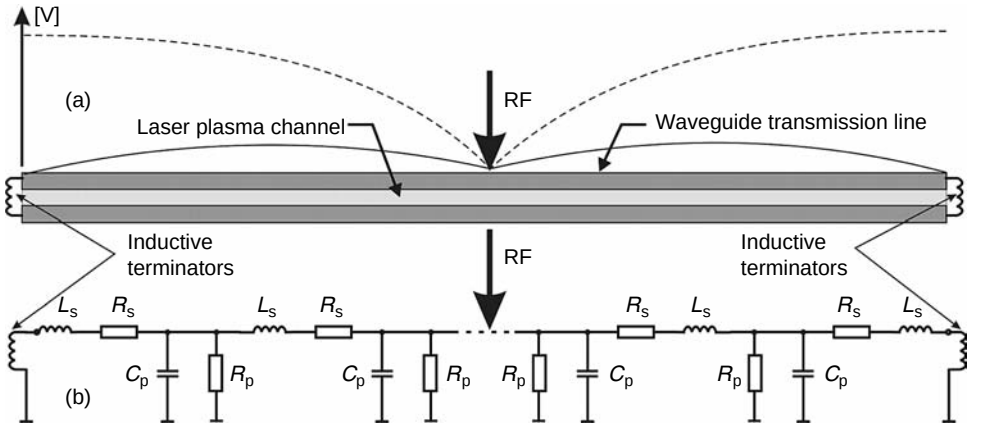

FIGURE 6A.35 Waveguide laser channel inductive terminated with coils. In a real case, for ~40 cm long waveguide, nonuniformity of the voltage along the channel can be suppressed from 40% (dashed line) to 5% (solid line).

For the lossless transmission line ($\alpha = 0$) loaded with the pure inductance L_p ($Z_p = j\omega L_p$), the voltage distribution can be expressed by the formula [48,49]

$$V(x) = V_0(\cos Bx + jD \sin Bx), \tag{6A.12}$$

where $D = Z_0/\omega L_p$.

Analysis of Equation 6A.12 shows that the best results are for $D \approx 0.3$.

The earlier presented method can be modified to the method of parallel resonance given by Chenausky [50]. The shunt inductors are chosen in such a way that each of them forms a parallel circuit with a distributed capacity of the waveguide structure. It means that a distributed reactance C_p of the waveguide is compensated by reactance L_p of the shunt inductors connected in parallel. It can be expressed as a condition of the resonance:

$$\omega L_p - 1/\omega C_p = 0 \quad \text{or} \quad \omega^2 C_p L_p = 1. \tag{6A.13}$$

See Figure 6A.36.

A similar approach based on transmission line theory applied for slab-waveguide (large area) laser structures is given by Strohschein [51]. The technique of parallel resonance is commonly applied as most practical and efficient.

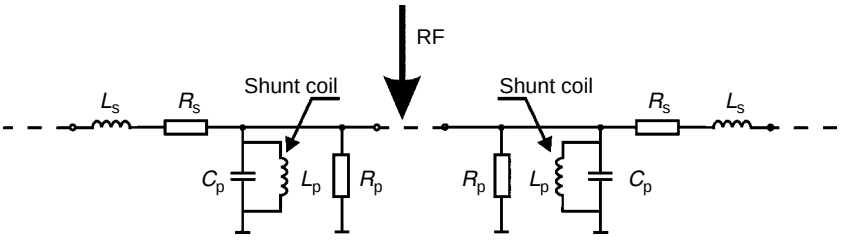

FIGURE 6A.36 Equivalent circuit of the laser waveguide cavity with shunt inductors L_p. L_s, R_s—series inductivity and resistance, C_p, R_p—capacity of the laser structure and resistance of the laser plasma, respectively.

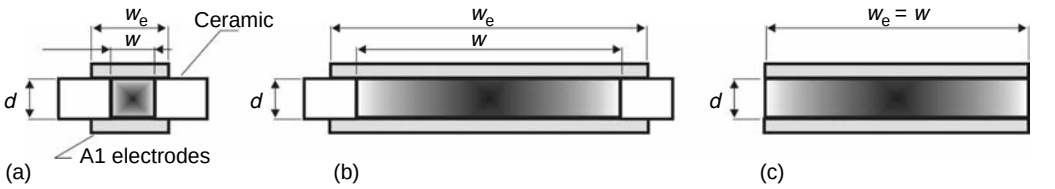

FIGURE 6A.37 (a) Sandwich structure of the laser waveguide: d is the interelectrode gap, w_e is the electrode width, w is the waveguide channel width; (b) large-area laser with ceramic side walls; (c) large-area laser without side walls.

A natural consequence of the RF-excited CO_2 waveguide laser development was the process of the widening lateral dimension of the guiding channel (see Figure 6A.37). The RF technique also ensures homogeneity of plasma between the large-area electrodes (see Section 6A.1.10). However, large-discharges cause new problems compared with a single waveguide laser, where the plasma electrical parameters like conductivity allows using the approximation of the low-loss transmission line. In the case of slab-waveguide lasers, the plasma plays a dominating role in the description of the RF wave propagation in the laser channel. There are two main effects complicating the electrical equivalent circuit of the slab structure.

The first one is plasma resistance, which dramatically decreases with the area of electrodes. The value of the plasma resistance R_p can be as low as a fraction of ohms. It creates problems with electrical matching of the laser head to the RF supply. It means that the large-area laser channel with plasma is the transmission line with high losses. Consequently, it worsens uniformity of RF voltage distribution along and across the large-area laser channel.

The second effect substantially influencing transmission parameters of the laser channel is the plasma sheath effect. Plasma sheaths appear near the surface of the electrodes as a Section 6A.1.8.2 consequence of RF excitation (Section 6A.1.8.2). The sheaths introduce additional capacitance C_s in series with resistance R_p of plasma. A simplified interpretation of that phenomenon is illustrated schematically in Figure 6A.38. The capacitance C_s of the sheaths dominates in the equivalent circuit of the laser head.

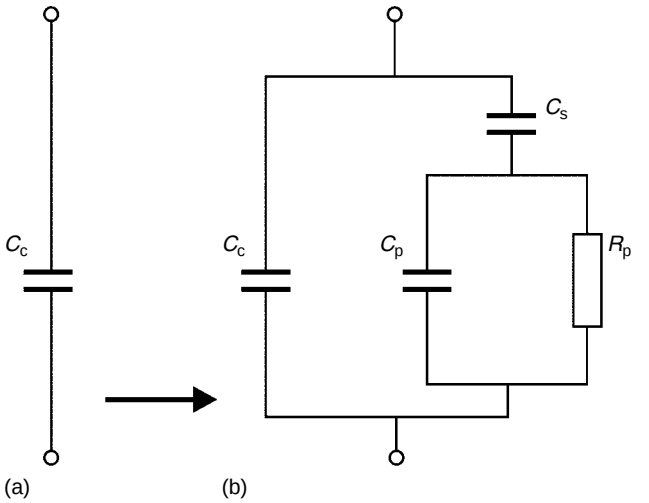

FIGURE 6A.38 Equivalent circuits of the laser slab-waveguide without side walls: (a) without plasma, (b) with plasma. C_c is the interelectrode capacitance, R_p, C_p resistance and capacitance of plasma, respectively, C_s is the capacitance of sheaths.

For some chosen slab-waveguide structures without sidewalls (Figure 6A.37c), the influence of the sheath capacity is particularly high. The sheath capacity can reach the value four times higher than the capacity of the laser head without plasma [52]. It means that using the parallel resonance technique, the resonant frequency of the "cold" laser head should be as much as two times higher than the frequency of the supply generator. It is necessary to mention that, in this case, the matching of the RF supply and laser head is far from the optimum, and problems with ignition of the plasma can be quite serious. Thus, it is necessary to find some compromise or use some methods to make the ignition easier.

Researchers usually solve the problem with inhomogeneity distribution of RF voltage and matching large-area discharge to the RF supply in many individual ways. The most promising technique seems to be supplying with a high-power transistor amplifier array distributed along the electrodes.

6A.1.8.4 Basic Data of Waveguide CO_2 Lasers

Many investigations showed that the optimum (but not critical) mixture in a waveguide CO_2 laser is CO_2:N_2:He = 1:1:3 with extra 5% of xenon. The role of xenon was described in Section 6A.1.5. The optimum pressure, at which one can expect a maximal output power, depends on waveguide transverse dimensions according to a practical rule (Equation 6A.5)—smaller transverse dimensions accept a higher pressure ($pd \approx 25$ Torr cm). A similar parameter joining the transverse dimensions d and the optimum frequency excitation f can be expressed in the practical engineering formula 6A.8 ($df \approx 28$ cm MHz).

Hence, a typical CO_2 waveguide laser has a square cross section of 2.25×2.25 mm^2 with a total length of about 400 mm, at 125 MHz frequency excitation, with output power higher than 30 W [53,54]. The typical output power characteristics as a function of the delivered RF power and different pressures are shown in Figure 6A.39 [55]. The laser was equipped with ZnSe dielectric-coated flat mirrors (99.8% rear and 92.0% output mirrors).

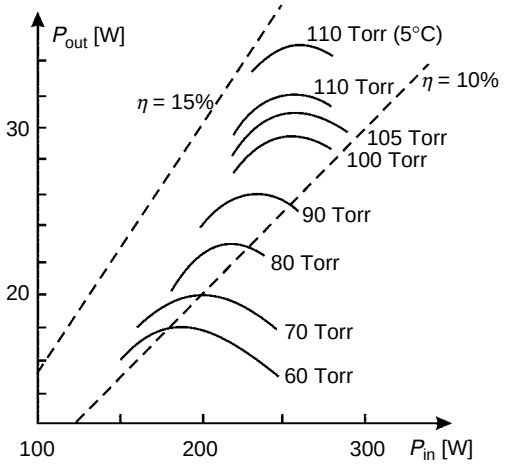

FIGURE 6A.39 Output power vs. RF delivered power for a waveguide CO_2 laser with dimensions $2.25 \times 2.25 \times 376$ mm^3 for the mixture CO_2:N_2:He = 1:1:3 + 5% of xenon. Cooling temperature was 14°C, the top characteristic shows the maximum power obtained for 5°C. It demonstrates the power increasing effect due to cooling process (efficiency η is shown).

The simple model based on the Rigrod procedure [56,57] gives a simplified formula of laser output power for homogeneously broadened medium:

$$P_{\text{out}} = \frac{I_s \cdot T_2 \cdot S}{\left(\sqrt{R_1} + \sqrt{R_2}\right)\left(1 - \sqrt{R_1 R_2}\right)} \left(g_0 L - \frac{1}{\sqrt{R_1 R_2}}\right), \tag{6A.14}$$

where g_0 is the small-signal gain, I_s the saturation intensity, L the resonator length, S the effective cross section of the laser beam, $R_1 = 1 - T_1 - A_1$, $R_2 = 1 - T_2 - A_2$ are the reflection coefficients of rear and output mirrors decreased by internal losses of the resonator, T_1, T_2 are the transmission coefficients of rear and output mirrors, respectively, and A_1, A_2 are the internal distributed losses in both directions of the resonator.

Modeling has to be limited to some estimations. The small-signal gain g_0 is difficult to measure accurately but some basic measurements allow estimating it at the level $g_0 = 0.65\ \text{m}^{-1}$ (for 110 Torr). For experimental data $P_{\text{out}} = 32$ W, $R_1 = 0.98$, $R_2 = 0.90$, $T_2 = 0.08$, $L = 386$ mm, $g_0 = 0.65\ \text{m}^{-1}$, $S = \pi w_0^2 = 1.95\,\text{mm}^2$ (where $w_0 = 0.35d$ is the effective radius of the laser beam cross section inside the waveguide, and d is the internal dimension of the waveguide), the saturation intensity fitting Equation 6A.14 can be estimated as $I_s = 12\ \text{kV/cm}^2$. A waveguide laser is characterized by high value of saturation intensity I_s on the kW/cm^2 scale compared with low-pressure DC lasers with I_s on the level of tens of W/cm^2 [1.21].

Owing to high pressure (more than 100 Torr), the line width of the lasing lines has the value at the level of 500 MHz, and it is homogeneously broadened. A free-running waveguide laser without any frequency stabilization causes line hoppings among a few strong lines with a dominating P20 line. The waveguide forms a well-guided channel. However, there is a problem with efficient coupling of the laser beam (propagating inside the waveguide) with the external mirror. The beam leaves the waveguide channel into free space (the gap between the channel end and mirror surface), and after reflection on the mirror it has to be optically matched to the waveguide. Practical efficient coupling (the coupling losses are negligible) is ensured when a flat mirror is placed as near the waveguide edge as possible (about 2 mm). The estimated plasma resistance is about 150–250 Ω [55]. This resistance can be easily electrically matched to the 50 Ω cable of an RF supply through a simple LC matching circuit. Some RF-excited structures are built in such a way that the plasma in the waveguide is a component of the resonant circuit of a high-power oscillator (see Section 6A.1.8.3). Other structures use low-power master oscillators driving distributed RF amplifiers (RF high-power transistors) along the waveguide plasma channel.

6A.1.9 RF-Excited Waveguide CO_2 Laser Arrays

The monolithic construction of multiple parallel lasers in one- or two-dimensional arrays is a very attractive idea of scaling laser power, when there is a limit of a single laser device. Diffusion-cooled CO_2 waveguide lasers particularly benefit from this approach [58]. Figure 6A.40 demonstrates the ideas of one-dimensional and two-dimensional arrays of waveguide structures.

In Reference [58], two constructions, 1×13 and 3×13 waveguide array matrixes, were investigated. For the 1×13 array the maximum output power of 350 W was obtained, whereas for the 3×13 array the maximum was 750 W. In both cases, the arrays were equipped with the plane common mirrors. To get homogeneous distribution of output power across the array, it is necessary to ensure an equal distribution of cooling efficiency in the array.

For free-running regime, each laser channel is operated in an EH_{11} mode but at different emission lines (different frequencies) independently. In the far field, the beam of such a

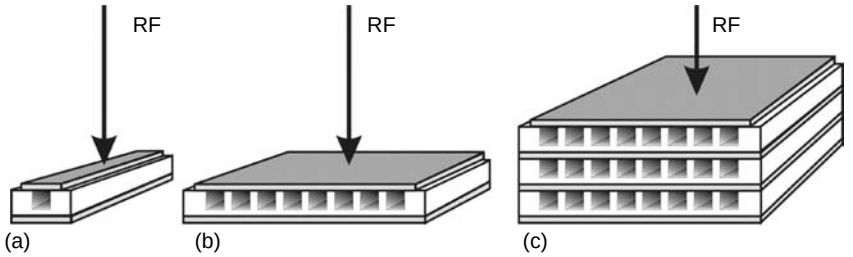

FIGURE 6A.40 Sealed-off diffusion-cooled RF transversally excited waveguide lasers: (a) single waveguide channel, (b) one-dimensional structure, (c) two-dimensional structure.

multichannel laser is formed as incoherent summation of all individual beams. The intensity I of N equal beams incoherently summed in the far field can be expressed as

$$I = N \cdot I_0, \tag{6A.15}$$

where I_0 is the intensity of an individual beam.

The array concept can be quite attractive when all beams are operated in the array in a synchronization regime. Physically, it means that all beams operate on the same emission line and the same frequency with controlled phases. When all N individual beams operate in phase (so-called phase-locking regime) the constructive interference appears to result in a strong increase in the total intensity in the far field according to

$$I = N^2 \cdot I_0. \tag{6A.16}$$

It is the example of a coherent summation. Phase locking of N beams increases N^2 times the intensity of the laser array, compared with only N increasing factor in the case of incoherent summation according to Equation 6A.15. The phase locking array concept was the inspiration of many solutions in the past. To phase lock the beams of the laser array, it is necessary to ensure some mutual coupling of energy between neighboring channels in the array. Some concepts of coupling are presented in Figure 6A.41 [59–61]. It has to be explained that these concepts found only scientific meaning. Phase locking can be observed and investigated in laboratory conditions, but it is difficult to keep it in an industrial environment.

6A.1.10 RF-Excited Slab-Waveguide CO_2 Lasers

RF-excited slab-waveguide lasers appeared as a natural consequence of waveguide laser development by enlarging a lateral dimension of the waveguide channel with only transverse

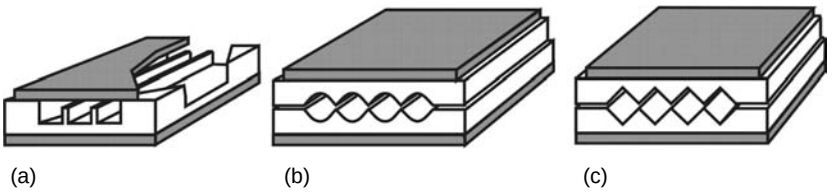

FIGURE 6A.41 Some examples of phase-locked array concept: (a) ridge hollow waveguide laser array, (From Newman, L.A., Hart, R.A., Kennedy, J.T., Canter, A.J., DeMaria, A.J., Bridges, W.B., *Appl. Phys. Lett*., 48(25), 1701–1703 (1986).) (b) self-focusing laser array, (From Bourdet, G.L., Mullot, G.M., Vinet, J.Y., *IEEE J. Quantum Electron*., 26(4), 701–710 (1990).) (c) diagonally coupled laser array (From Abramski, K.M., Colley, A.D., Baker, H.J., Hall, D.R., *Appl. Phys. Lett*., 60(5), 530–532 (1992).)

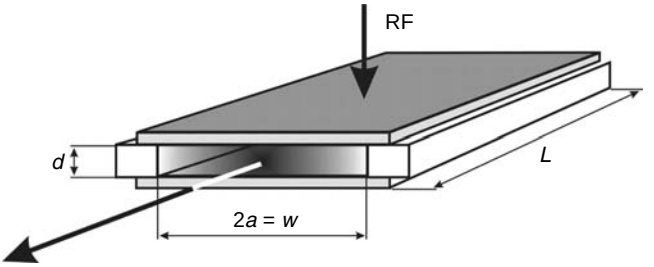

FIGURE 6A.42 Slab-waveguide laser structure with side walls.

waveguiding dimension remaining. The concept of RF-excited slab configuration is shown in Figure 6A.42.

These lasers are often called large-area discharge or planar lasers. Considering a uniform discharge obtained between cooled electrodes of width w, length L, and spacing d, the total power extraction P_{out} from the volume can be written as [62]

$$P_{\text{out}} = kP_{\text{L}}\left(\frac{w}{d}\right)L = kP_{\text{L}}\left(\frac{A}{d}\right), \tag{6A.17}$$

where P_{L} is the specific power for a sequence cross-section gain medium, with the value of about 80 W/m (32 W output power from 38 cm long CO_2 laser—see Figure 6A.39), k is the factor responsible for different cooling conditions for large-area discharge compared with the single waveguide structure and A is the discharge area ($A = w \times L$).

However, it is much more convenient to express the extraction power from a large-area discharge slab laser by the parameter that scales power per unit area of the gain medium P_{out}/A [W/m^2]. Elementary experiments showed that laser power per unit electrode area can reach values of 20–30 kW/m^2 [63]. The mode structure of a slab-waveguide laser with ceramic sidewalls is determined by dimensions of the slab. The output is usually the mixture of a few modes EH_{m1}, where m is the large integer number responsible for the lateral dimension. The mechanism of forming such modes is discussed in the later sections.

6A.1.10.1 Slabs with Sidewalls

The mode EH_{m1} in a slab-waveguide laser is created as an interference of two plane waves bouncing between sidewalls and laser mirrors. Figure 6A.43 illustrates the case well.

Two plane waves propagating in one direction and two identical plane waves propagating in an opposite direction form the mode structure in the slab-waveguide cavity. The electrical field of EH_{m1} is described by a formula

$$E_y = E_{0y}\left[e^{i\left(\frac{m\pi}{w}x+\beta_m z\right)} + e^{-i\left(\frac{m\pi}{w}x+\beta_m z\right)}\right]e^{\omega t}. \tag{6A.18}$$

The formula describes a sum (interference) of two plane waves propagating in a direction z at some small angle $\pm\theta_{\text{m}}$ (for a small angle θ_{m}, $\sin(\theta_{\text{m}}) \approx \theta_{\text{m}}$ and $\beta_{\text{m}} \approx 2\pi/\lambda$). Thus, the angle θ_{m} can be written as

$$\theta_m = \arctan\frac{m\pi}{w\beta_m} \approx \frac{1}{w}m\frac{\lambda}{2}. \tag{6A.19}$$

This situation is illustrated in Figure 6A.44.

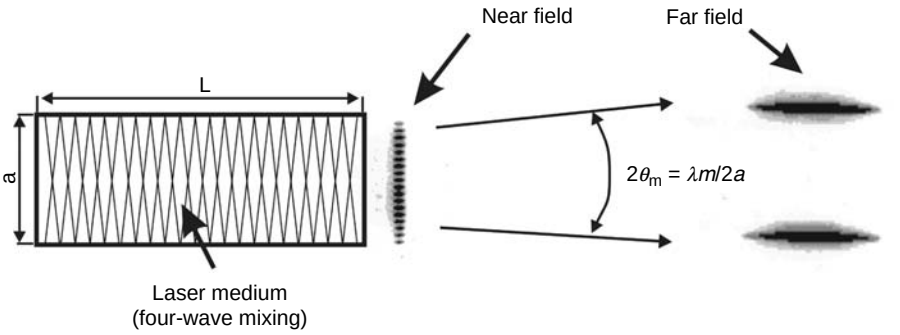

FIGURE 6A.43 Explanation of the four-wave mixing effect in a slab. Experimental results obtained in the near and far fields are also shown.

In typical CO_2 slab-waveguide lasers, the angle θ_m is in the range of 1–3 mrad (see Figure 6A.44). In the far field, two waves are separated in space and can be observed as lobs. In practice, the far field pattern of the laser beam is observed in the focal plane of a lens.

In real slab-waveguide lasers with side walls, the output power consists of a mixture of a few EH_{m1} modes (Figure 6A.45), where the number of modes and the order mode m depend on the state of alignment [64,66]. Some of them can operate on different emission lines.

There is possibility to control the mode structure in a slab-waveguide laser with sidewalls applying the Talbot effect [65,66]. It is enough to put some periodical filter at the end of the slab, or even better at both ends, (e.g., gold wires placed in the front of the mirrors) with a period D, which fulfills a Talbot condition

$$D = \sqrt{\frac{2\lambda L_T}{k}}, \tag{6A.20}$$

where λ is the wavelength, k is the integer number, L_T is the "Talbot" length of the optical resonator when we have reconstruction of the mode picture with a period D.

For example, for the length of the optical resonator $L_T = 400$ mm, $\lambda = 10.63$ μm, to obtain an EH_{101} mode (putting $k = 2$), the calculated period D of the Talbot selector is equal to 2.06 mm. Figure 6A.46 shows experimental results of EH_{101} and EH_{201} modes obtained using a Talbot selector.

Structures with sidewalls do not appear to be practical. The quality of the laser beams from slab lasers with sidewalls as the sum of a few modes is very bad (M^2 is much larger

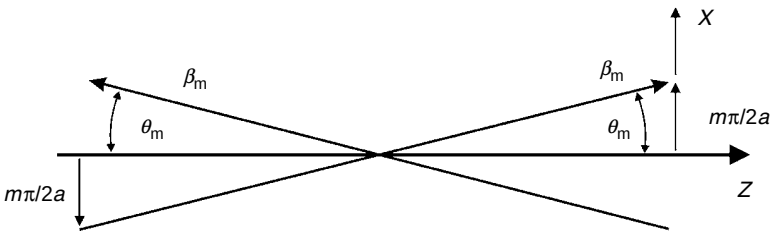

FIGURE 6A.44 Auxiliary drawing for the expression 6.19.

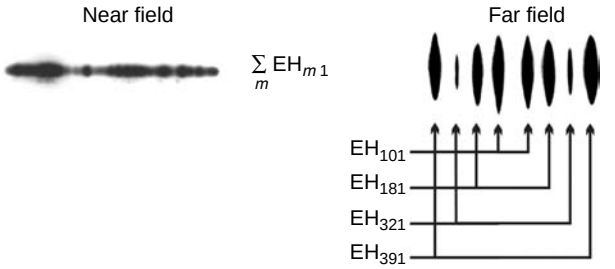

FIGURE 6A.45 Picture of the output radiation in the near field (left) for some mixture of waveguide modes (observed at the UV screen). The same modes in the far field (right) are shown (lobs). The patterns were taken from the RF-excited slab-waveguide laser with dimensions of $w = 20$ mm, $d = 2$ mm, $L = 400$ mm.

than 1; about quality parameters see [67]). Their focusability is poor and difficult to use in technology applications.

6A.1.10.2 Slabs without Sidewalls—Large-Area Lasers

Real applications found large-area slab-waveguide RF-excited lasers without sidewalls. Waveguiding conditions are still preserved between electrodes of the slab, but a free space propagation is reached in a lateral direction (see Figure 6A.37c). The fact that the medium is very wide in a lateral direction and fulfills free space conditions allows using unstable configurations of the optical resonator [68]. The unstable resonator ensures efficient filling of the basic laser mode in all open large-area cavities occupied by a laser active medium.

There are two practical types of unstable resonators termed confocal resonators. They are distinguished from the family of unstable resonators by the common feature: $R_1 + R_2 + L$,

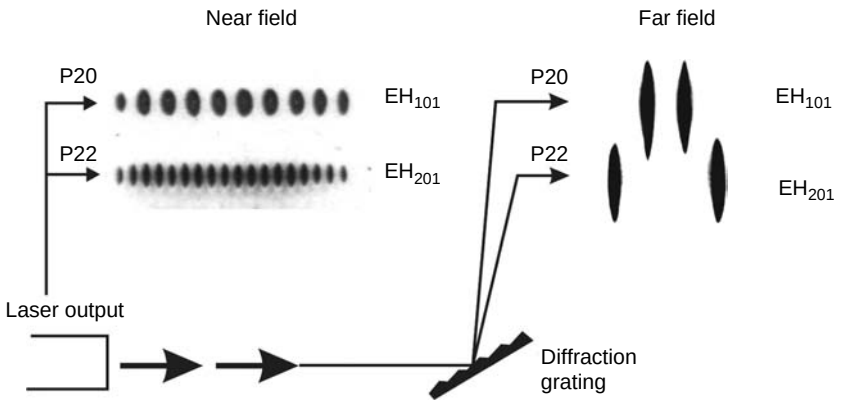

FIGURE 6A.46 Pictures of the output radiation in the near field (left) for selected waveguide modes, EH_{101} and EH_{201} modes obtained using a Talbot selector (observed at the UV screen). The same modes in the far field (right) are also shown. As seen, in many cases each mode can be generated on a different emission line. It can be observed deflecting the output laser beam at the diffraction grating (patterns of the near field are observed directly at the laser output).

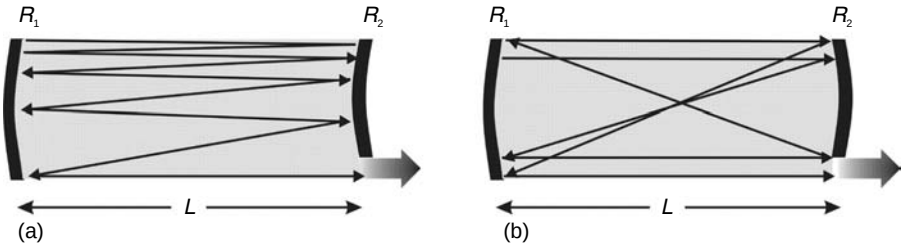

FIGURE 6A.47 Two possible optical resonators usually used in large-area open slab-waveguide structures: confocal from a positive branch of the universal diagram of stability (a), and confocal from a negative branch (b). R_1, R_2 mirror curvatures, L is the resonator length.

where R_1 and R_2 are the curvatures of the mirrors and L is the resonator length. Two cases fulfill the earlier confocality condition and they are shown in Figure 6A.47.

- "positive branch" resonator (R_1—concave, R_2—convex),
- "negative branch" resonator (both mirror concave).

Most popular is a "negative branch" version as more stable and more resistive to the mirror tilting [69]. Out-coupling transmission T of the unstable resonators can be expressed by a simple formula

$$T = 1 - \left|\frac{R_2}{R_1}\right|. \tag{6A.21}$$

The beam quality of the hybrid mode (waveguiding property, EH_{11}, in a transverse direction and Gaussian, TEM_{00}, in lateral direction disturbed by a diffraction effect at the edge of the output mirror) is quite high—M^2 parameter between 1 and 1.5. This property established the high position of slab-waveguide lasers in technological applications and they reached an advance technological level. They are available in the market with the laser output power from 10 W to kilowatts scale. For example, 1 m long and 10 cm wide RF-excited CO_2 large-area laser can reach an output of more than 2 kW. These lasers operate with 10%–15% of efficiency. A 1 kW output power laser requires 10 kW RF power supply.

6A.1.11 Sealed-off Diffusion-Cooled RF Transversally Excited All-Metal CO_2 Lasers

RF transverse excitation is successfully applied in all-metal structures of the CO_2 lasers [70,71]. A cross section of the structures is usually around 5×5 mm^2; it means it does not preserve waveguiding conditions between electrodes (see Figure 6A.48). The lasers are characterized by low-cost fabrication and gas conduction cooling, which is used for the comfort of the user.

6A.1.12 Temperature Distributions

CO_2 diffusion-cooled lasers have to be under special "temperature control." There are two reasons: the first one is that the heat obtained from delivered excitation power to

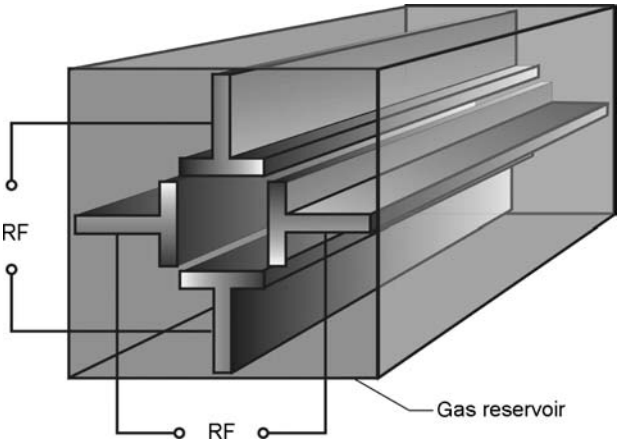

FIGURE 6A.48 The idea of an RF transversely excited all-metal laser.

the discharge has to be efficiently removed; the second reason is that the high temperature destroys the population inversion of the laser medium. Practical knowledge says that maximal accepted temperatures in the CO_2 laser plasma should not exceed a value of about 700 K.

Temperature distributions in diffusion-cooled systems was mentioned earlier in Chapter 1.9.1. Here, some generalized discussion about temperature distribution across the gas discharge column with arbitrary cross section is given. We consider here only the CO_2 laser mixture, which contains CO_2, N_2, He, and Xe.

The temperature distribution in a gas medium is governed by a differential diffusion equation:

$$\mathrm{div}(\lambda_{\mathrm{mix}}(T)\mathrm{grad}(T)) = -Q_{\mathrm{in}}, \tag{6A.22}$$

where λ_{mix} is the thermal conductivity of the analyzed mixture [W/mK], T is the temperature [K], Q_{in} is the density of the delivered power to the medium [W/m^3], and $\lambda_{\mathrm{mix}}(T)$ is the thermal conductivity of the analyzed gas mixture [W/mK].

Thermal conductivity of the gas mixtures can be expressed by a formula [72]

$$\lambda_{\mathrm{mix}} = \sum_{i=1}^{n} \lambda_i \left[1 + \sum_{\substack{k=1 \\ k \neq i}} G_{ik} \frac{x_k}{x_i} \right]^{-1}, \tag{6A.23}$$

where

$$G_{ik} = \frac{1.065}{2\sqrt{2}} \left(1 + \frac{M_i}{M_k} \right)^{-\frac{1}{2}} \left[1 + \left(\frac{\eta_i M_k}{\eta_k M_i} \right)^{\frac{1}{2}} \left(\frac{M_i}{M_k} \right)^{\frac{1}{4}} \right]^2, \tag{6A.24}$$

where η_i, η_k are the viscosities, M_i, M_k are the molar masses, x_i, x_k, are the fractions of i or k component, and λ_i is the thermal conductivity of i component.

Coefficients of thermal conductivity λ and viscosity η are dissipated in scientific literature and many handbooks, and it is convenient to use some approximation functions [73]:

$$\lambda_i(T) = A_i \times 10^{-4} T^{B_i} + a_i \times 10^{-2} + b_i T \times 10^{-5} + c_i T^2 \times 10^{-8} \quad \text{W/mK}, \tag{6A.25}$$

and

$$\eta_i(T) = K_i \times 10^{-6} T^{L_i} + k_i \times 10^{-5} + l_i T \times 10^{-8} + m_i T^2 \times 10^{-11} \quad \text{Ns/m}^2, \tag{6A.26}$$

where for CO_2: $A = 0.4255$, $B = 1.0631$, $a = -0.8537$, $b = 2.6980$, $c = -1.5910$,
$K = 0.2052$, $L = 0.7589$, $k = -0.2928$, $l = 0.9581$, $m = -0.5762$,
for N_2: $A = 2.9625$, $B = 1.0631$, $a = 0.2459$, $b = -0.8075$, $c = -1.5910$,
$K = 0.4706$, $L = 0.6417$, $k = -0.1670$, $l = 0.5520$, $m = -0.3348$,
for He: $A = 24.8795$, $B = 0.7187$, $a = 0.1279$, $b = -0.4273$, $c = 0.2576$,
$K = 0.4139$, $L = 0.6777$, $k = 0.0204$, $l = -0.0652$, $m = 0.0403$
for Xe: $A = 0.5039$, $B = 0.8349$, $a = -0.0438$, $b = 0.1430$, $c = -0.0853$,
$K = 0.2518$, $L = 0.8010$, $k = -0.3915$, $l = 1.2738$, $m = -0.7638$.

As an example, Figure 6A.49 shows the calculated temperature distribution in a typical RF-excited CO_2 slab-waveguide laser for dimensions of electrodes: $d = 2$ mm, $w = 40$ mm (cross-section of the slab) where the boundary integration areas are indicated as $r_w = r_d = 5$ mm.

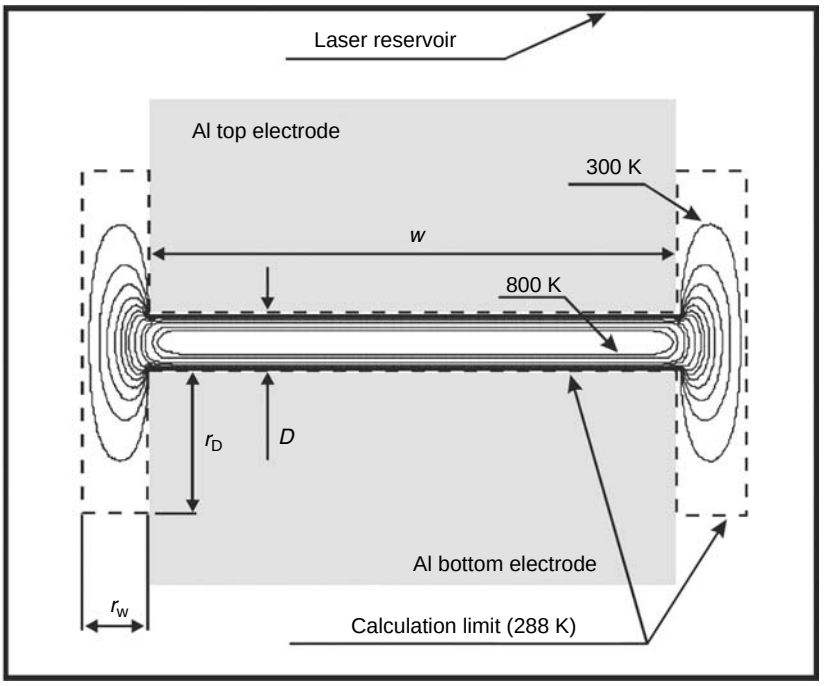

FIGURE 6A.49 Predicted temperature distribution of CO_2 laser plasma in the slab-waveguide laser 2×40 mm^2 cross-section structure. Temperature of a water-cooled aluminum electrode is assumed as 288 K. Calculations are performed for typical RF-excited slab-waveguide CO_2 laser parameters, like pressure, input power, and gas mixture.

A very convenient property of the slab-waveguide structure is the possibility to apply the same mechanical design of the laser cavity for different kinds of gas lasers, as CO_2, carbon monoxide, and xenon, as well [74,75].

6A.1.13 Dynamics of the CO_2 Laser

For many technological applications, like laser material processing, the pulse operation of CO_2 lasers was identified as much more attractive than the CW case. The pulse operation shows important advantages: it allows supplying the laser with optimum power delivered; the change of the average power is conveniently controlled by changing the duty cycle of the pulse train. In practice, frequencies up to 10^4 pps (pulse per second) are used.

DC-excited CO_2 lasers usually operate continuously. It is rather inconvenient to pulse high voltage supplies. The pulse technique found particular application in RF-excited lasers. RF supplies can be easily pulse modulated. In the following, some elementary description of the pulse forming as an effect of pulse excitation of a CO_2 laser medium is given.

Let us have a look at the CO_2 laser energy system shown in Figure 6A.50. The system is simplified—compared with Figure 6A.3—and reduced to the three-level one. The energy transfer from nitrogen is still considered.

The description of the dynamics of the laser operation is usually easier using rate equations for the laser levels and output intensity. The set of differential equations describing the considered system can be expressed as [76–79]

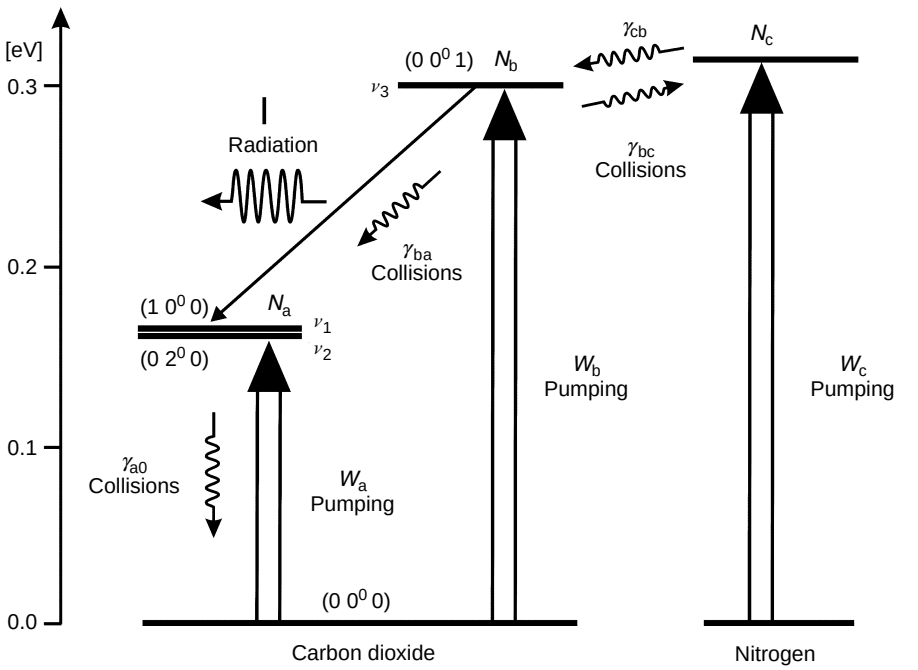

FIGURE 6A.50 Simplified diagram of CO_2 laser energy levels. I is the intensity of the output laser radiation, N_b is the higher CO_2 laser level, N_a is the lower laser level (total population of CO_2 molecules in the coupled ν_1 and ν_2 modes—see Figure 6A.3), N_c is the higher nitrogen level, W_b, W_a, and W_c denote pumping to higher CO_2 laser level, to lower level, and to nitrogen higher level, respectively. γ_{a0}, γ_{ba}, γ_{cb}, and γ_{bc} are the collisional deactivations from suitable levels like in the figure.

$$\frac{dI}{dt} = -\frac{I}{T_0} + \sigma c(N_b - fN_a)I + \frac{\sigma c N_b}{V} \tag{6A.27}$$

$$\frac{dN_a}{dt} = \sigma c(N_b - fN_a)\, I - \gamma_{a0}N_a + \gamma_{ba}N_b + W_a \tag{6A.28}$$

$$\frac{dN_b}{dt} = -\sigma c(N_b - fN_a)\, I - \gamma_{ba}N_b - \gamma_{bc}N_b + \gamma_{cb}N_c + W_b \tag{6A.29}$$

$$\frac{dNc}{dt} = \gamma_{bc}N_b - \gamma_{cb}N_c + W_c, \tag{6A.30}$$

where V is a cavity volume, and f is a fraction of the N_a that establishes the lower laser level density value.

A radiative cross section for the laser transition is given by [16]

$$\sigma = \frac{5 \times 10^{-17}}{x + 0.73y + 0.64z}\ (\text{cm}^2), \tag{6A.31}$$

where x, y, z are the partial pressures of CO_2, N_2, and He in torr, respectively.

The room-temperature collisional rates used in the model are [77]

$$\begin{aligned}
\gamma_{a0} &= (10x + 4.6y + 0.56z)\ [\mu s^{-1}] \\
\gamma_{ba} &= (0.27x + 0.08y + 0.06z)\ [\mu s^{-1}] \\
\gamma_{bc} &= 14.5y\ [\mu s^{-1}] \\
\gamma_{cb} &= 13.2x\ [\mu s^{-1}].
\end{aligned} \tag{6A.32}$$

The photon lifetime T_0 in the laser cavity can be written as [77]

$$T_0 = \frac{\dfrac{2L}{c}}{\log\dfrac{1}{RT}}, \tag{6A.33}$$

where R and T are the reflectivity and transmission of the output laser mirror, respectively, L is the resonator length, and c is the light speed. The equations can be solved numerically, and for $V = 40\ \text{cm}^3$ and $T_0 = 28 \times 10^{-9}$ s, results are given as shown in Figure 6A.51.

The pumping time t_p is 1 μs. Once the gain exceeds some threshold, the laser still needs some time to build up the laser intensity to saturating values. Then, when the laser overcomes the threshold value, one observes the first strong spike called gain switching. In addition, after that the laser still spikes. It saturates the gain below threshold, but the gain again recovers, and still spikes are observed until the steady-state conditions are reached, and the laser operates on some level of the intensity.

In the figure, the pumping is of the form of a square (relatively short) input pulse, and consequently the laser intensity expires after about 15 μs. In that way, it is possible to observe a nitrogen tail. It is owing to the longer lifetime of the higher level of nitrogen compared with CO_2 (compared with the right side of the characteristics in the figure where influence of nitrogen is not considered in the set of differential equations as given earlier). In that case, the laser output pulse after a few weak spikes is quenched.

Look again at the center and bottom characteristics in the figure. As seen, the difference in population inversions of higher and lower levels becomes constant during the laser operation. We observe the balance between lasing levels.

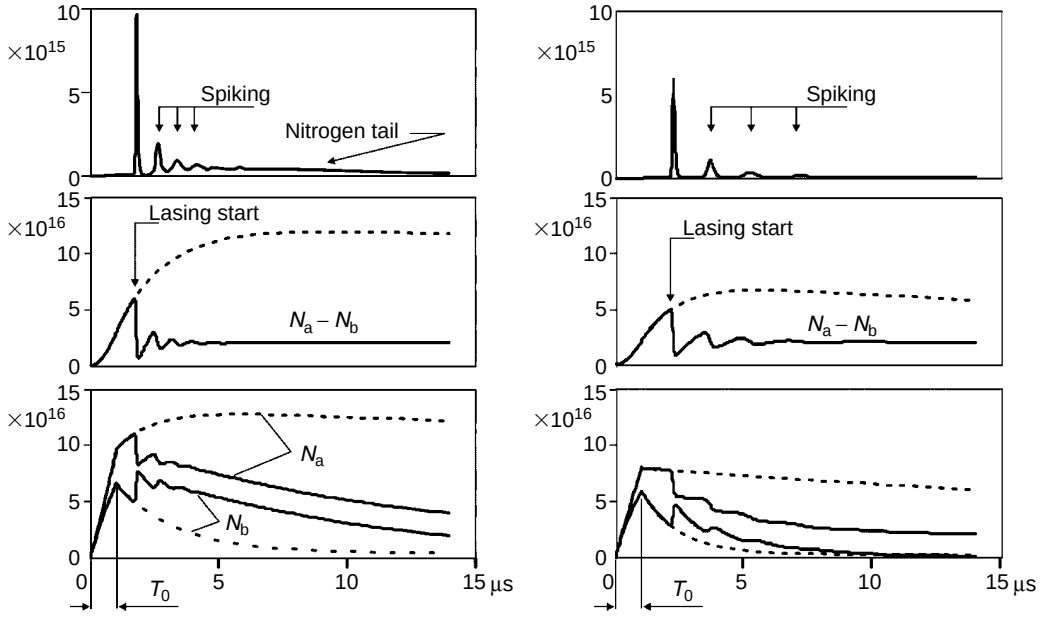

FIGURE 6A.51 Set of the characteristics obtained because of the differential equations solution. Left—with nitrogen, right—without nitrogen. Solid lines—with lasing, dashed lines without lasing. Top—intensity of the output radiation, center—difference in population of higher N_b and lower N_a laser levels, bottom—population of higher N_b and lower N_a laser levels.

The pulse operation of a laser as such is very convenient in many applications. In laser materials processing, a pulsed radiation, much more invasive and much easier, destructs the material in such processes like cutting or drilling. The same advantages are convenient in surgery. In high-power CO_2 laser systems, like TEA lasers, just the first spike (a gain switching pulse) is used.

6A.1.13.1 Pulsed RF Excitation of Waveguide and Slab-Waveguide Lasers

As mentioned earlier, pulse operation of the laser is very convenient in many kinds of proceeded materials. An RF-excited CO_2 laser is relatively easy to be pulsed. A switching pulse controlling the laser operation is usually not longer than 100 μs, usually 5–10 μs. As seen, the output laser pulse is consequently much longer than in the case of TEA lasers (nanoseconds). It is, of course, the effect of the physics of RF laser plasma excitation. Figure 6A.52 shows a typical characteristic of a pulsed RF-excited CO_2 laser (compare with Figure 6A.51).

Figure 6A.53 shows pulsing process typical for radio-frequency excited CO_2 waveguide laser [64]. The supply generator is controlled with square switching pulses of T period (where τ is an effective pulse). The RF pulses are a bit delayed of $\Delta\tau$ time. The output laser pulse is delayed of $\Delta\tau$ time. As seen, the laser pulse starts with a gain switching.

6A.1.14 DC or RF Excitation?

It seems that after some euphoria and promotion of RF excitation, DC excitation came off well from the competition. Sputtering electrodes usually was the argument used against DC excitation. Sputtering can destroy electrodes and contaminate the laser mirrors. However, a

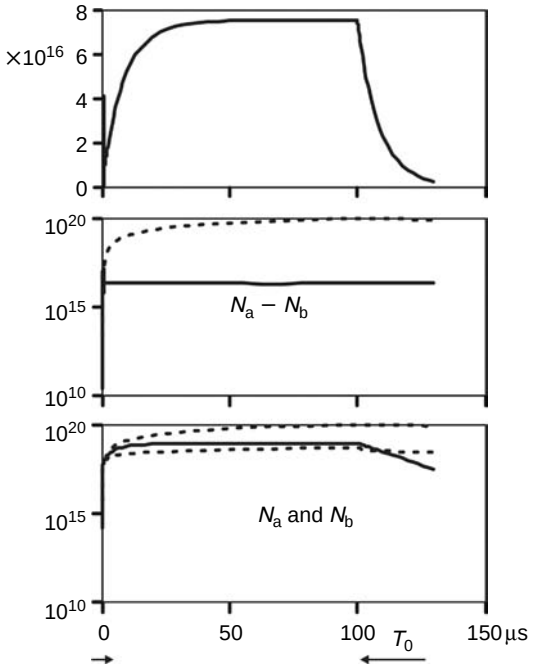

FIGURE 6A.52 Typical characteristics for a pulsed RF-excited CO_2 laser. A pumping pulse is relatively long: here 100 μs. Solid lines—with lasing, dashed lines without lasing. Top—intensity of the output radiation, center—difference in population of higher N_b and lower N_a laser levels, bottom—population of higher N_b and lower N_a laser levels.

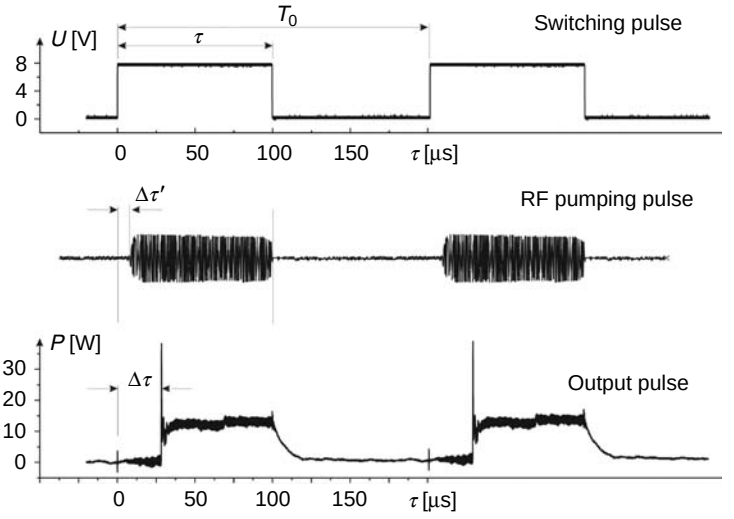

FIGURE 6A.53 Laser pulses experimentally obtained. Top—switching pulses controlling supply generator, center—pulses from supply generator, bottom—laser output pulses.

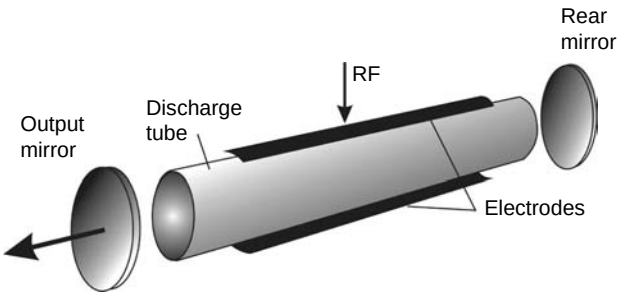

FIGURE 6A.54 A conventional laser tube transversally excited with RF voltage.

good design of electrodes can solve the problem. Another argument is the cathode fall. However, it is nothing for a supplying voltage of many kilovolts in big laser systems. On the other hand, one should remember about the sheath regions distributed along the laser electrodes, which decrease the total electrical efficiency of the RF power supplies. The efficiency of RF-excited lasers is a bit lower because of another problem: difficulties with keeping the homogeneous discharge between electrodes. Usually used slab-waveguide structures need unstable optical resonators applied, and give a slightly low beam quality than DC systems. From the other side, compactness of the RF systems is higher. Decision of the customer depends on how the laser is to be used and what is most important for the user: output power, beam quality, or dimensions and compactness? In addition, it is necessary to mention that RF excitation is sometimes applied to glass laser tubes as shown in Figure 6A.54. As seen, in this linear structure, excitation is transversal to the axis of the laser as in the RF-excited waveguides.

6A.1.15 Microwave Excitation of CO_2 Lasers

Microwave discharge excitation is a promising alternative to both RF and CW excitations. It gives high input power density and less gas contamination and degradation of laser optics—like in RF-excited lasers. Microwave supply voltage is lower as well. Cost of a magnetron is much lower (even with an accompanying electronic setup) than an RF exciter. Microwave excitation seems to be ideal to be applied for gas lasers. The main disadvantage is a problem with homogeneity of the discharge along and across the laser cavity. Thus, a few basic concepts have been developed.

One of the solutions is excitation of the discharge, where the microwave in TE_{01} mode is perpendicular to the axis of the laser tube (classical, waveguide, or multiwaveguide) [80]. To improve the efficiency of such a system, two orthogonal sets of magnetrons can be applied. It is used to randomize the electrical field in the excitation area; otherwise, high temperature and even an arc can be expected. The frequency of both magnetrons differs slightly giving a rotating electrical vector of the field in the discharge area. In that way, radial homogeneity of the discharge is obtained [81].

Longitudinal excitation with microwaves should give better efficiency of the laser system compared with DC excitation. It gives a small cross section of the discharge, and in waveguides (longitudinally excited) a high input should be observed compared with classical DC longitudinally excited systems. In practice, it is difficult to ensure longitudinal homogeneity of the discharge, which leads to limitation of the input power. Additionally, propagation of the microwave attenuates rapidly with a propagation distance. The solution is application of

the microwave in TM_{010} mode with a suitable tuning technique [82,83]. Helical coupling antennas are also used for longitudinal excitation [84].

To overcome problems with propagation of TE and TM microwave modes in the laser cavity, it is possible to convert, e.g., TE_{01} mode into TEM mode using a strip line, where a TEM mode is formed [85]. Another solution is used for a slab-waveguide laser structure. According to the scaling formula (Equation 6A.8), joining excitation frequency f and transverse dimension d of a RF-excited slab-waveguide laser, $df = 28$ cm MHz, one can conclude that increasing the frequency f toward a microwave region, the optimum d dimension can be decreased. Using the second scaling law (Equation 6A.6) for a slab CO_2 laser should allow application of higher pressure (according to $pd = 19$ Torr cm) at the level of hundreds of torrs. Higher pressure should give higher power extraction per unit area of slab than RF-excited structures. This idea motivated most researchers dealing with microwave-excited CO_2 slab lasers [86,87].

In the slab-waveguide laser structure, the microwave field is created in the prime microwave cavity in parallel to the laser sandwich kind metal-ceramic waveguide. A microwave electrical field goes into the laser cavity and is formed along the ceramic plate in parallel to the surface of the plate [88].

Despite many problems with homogeneity and propagation of the microwave in laser structures, it seems that microwave excitation shows many advantages over DC or RF discharge to create compact and high-efficiency gas laser systems. However, the preceding concepts have not found practical applications. Microwave excitation is still awaiting elegant, efficient, and clever solutions.

6A.1.16 Some Practical Formulas—Optical Properties of CO_2:N_2:He Mixtures

The investigator sometimes needs information about relations between thermodynamic and optical quantities. It can be described by the Gladstone–Dale formula defining the gas refractive index n as a function of the gas density N (m^{-3}). It can be written as

$$\frac{n-1}{N} = \gamma, \tag{6A.34}$$

where γ (m^3) is the Gladstone–Dale constant.

The changes of the laser gas density N are the result of changes of both pressure p and temperature T. It can be described according to the equation of state of an ideal gas as given later:

$$N = \frac{p}{kT}, \tag{6A.35}$$

where k is a Boltzmann constant.

In that way we have

$$n - 1 = \gamma \cdot \frac{p}{kT}. \tag{6A.36}$$

On the other hand, the refractive indices of three gas components applied in CO_2 lasers—CO_2, N_2, He—are given as follows [89]:

$$(n-1)^{CO_2} = 450 \times 10^{-6},$$
$$(n-1)^{N_2} = 300 \times 10^{-6},$$
$$(n-1)^{He} = 36 \times 10^{-6}. \tag{6A.37}$$

If we know the fractions $f_{CO_2}, f_{N_2}, f_{He}$ of the gas mixture applied, a refractive index can be easily calculated from a formula [90]

$$n - 1 = 10^{-6} \cdot (450 f_{CO_2} + 300 f_{N_2} + 36 f_{He}), \tag{6A.38}$$

A temperature- and pressure-dependent formula can be recalculated from Equation 6A.36 by taking into account Equation 6A.34 and Equation 6A.35:

$$n - 1 = 10^{-6} \cdot (450 f_{CO_2} + 300 f_{N_2} + 36 f_{He}) \cdot \frac{p}{p_0} \cdot \frac{T_0}{T}. \tag{6A.39}$$

For $T_0 = 273.16$ K and $p_0 = 760$ Torr, we have a convenient formula

$$n - 1 = 3.59 \times 10^{-7} \cdot (450 f_{CO_2} + 300 f_{N_2} + 36 f_{He}) \cdot \frac{p}{T}. \tag{6A.40}$$

For example, for CO_2 laser gas mixtures usually applied, CO_2:N_2:He = 1:1:3, we have

$$450 f_{CO_2} + 300 f_{N_2} + 36 f_{He} = 450 \cdot 0.2 + 300 \cdot 0.2 + 36 \cdot 0.6 = 176.1. \tag{6A.41}$$

The refractive index of the applied laser medium can be evaluated from interferograms (interferometric fringes) observed in a Mach–Zehnder interferometer, for example. Figure 6A.55 shows a suitable experimental arrangement schematically. A He–Ne laser is usually used as a source. The relation between changes in the refractive index Δn and a number of observed fringes at the detector is as follows:

$$\Delta n = \frac{\lambda}{L}, \tag{6A.42}$$

where L is the length of the optical resonator, and λ is the wavelength (0.63 μm for the He–Ne laser). These formulas can also be applied when a pulse regime of CO_2 lasers is considered.

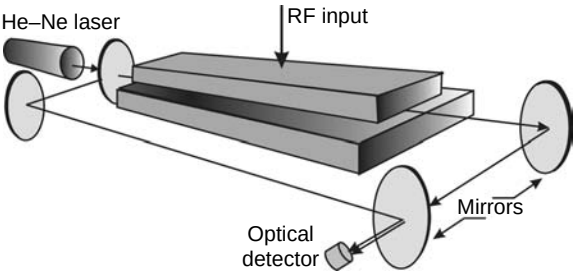

FIGURE 6A.55 A slab-waveguide CO_2 laser cavity in a Mach–Zehnder interferometer arrangement. The laser mirrors are removed.

Another formula provides the possibility of calculating a CO_2 laser linewidth for arbitrary values of laser gas mixture pressure p, and temperature T, and proportions of components of CO_2:N_2:He $= \psi_{CO_2}$:ψ_{N_2}:ψ_{He} [15,16]:

$$\Delta\nu_p = 7.58\left(\psi_{CO_2} + 0.73\psi_{N_2} + 0.64\psi_{He}\right)p\sqrt{\frac{300}{T}} \quad \text{(MHz)}. \tag{6A.43}$$

REFERENCES

1. Matthews, S.J., Heavy lifting, *Laser Focus World*, 37(10), 89–94 (2001).
2. Patel, C.K.N., Interpretation of CO_2 optical maser experiments, *Phys. Rev. Lett.*, 12, 588–590 (1964).
3. Morgan, J.E., Schiff, H.I., The study of vibrationally excited N_2 molecules with the aid of an isothermal calorimeter, *Can. J. Chem.*, 41, 903–910 (1963).
4. Patel, C.K.N., in This Week's Citation Classic, ISI Current Contents, 42, p. 20, Oct. 21, 1985 dedicated to C.K.N. Patel, continuous-wave laser action on vibrational rotational transitions of CO_2, *Phys. Rev.* A, 136, November, 1187–1193 (1964).
5. Patel, C.K.N., CW high power $N_2 + CO_2$ laser, *Appl. Phys. Lett.*, 7, July, 15–17 (1965).
6. Patel, C.K.N., Tien, P.K., McFee, I.H., CW high power CO_2—N_2—He laser, *Appl. Phys. Lett.*, 7, 290–292 (1965).
7. Reid, J., Siemsen, K., New CO_2 laser bands in the 9–11 μm wavelength region, *Appl. Phys. Lett.*, 29, 250–251 (1976).
8. Reid, J., Siemsen, K., Laser power and gain measurements on the sequence bands of CO_2, J. *Appl. Phys.*, 48, 2712–2717 (1977).
9. Evenson, K.M., Chou, C.-C., Bach, B.W., Bach, K.G., New cw CO_2 laser lines: the 9 μm hot band, *IEEE J. Quantum Electron.*, 30(5), 1187–1188 (1994).
10. Chou, C.-C., Evenson, K.M., Zink, K.R., Maki, A.G., Shy, J.-T., New CO_2 laser lines in the 11 μm wavelength region: new hot bands, *IEEE J. Quantum Electron.*, 31(2), 343–345 (1995).
11. Freed, C., Javan, A., Standing-wave saturation resonances in the CO_2 10.6-μm transitions observed in a low-pressure room-temperature absorber gas, *Appl. Phys. Lett.*, 17, 53–56 (1970).
12. Ya., S., Tochitsky, Chou, C.-C., Shy, J.-T., Frequency stabilization of the sequence-band CO_2 laser using the 4.3 μm fluorescence method, *IEEE J. Quantum Electron.*, 31(7), 1223–1230 (1995).
13. Solodukhin, A.S., Hot-cell-free sequence-band CO_2 laser, *J. Mod. Opt.*, 34, 577–589 (1987).
14. Wendland, J.J., Baker, H.J., Hall, D.R., Operation of a cw $^{14}C^{1.6}O_2$ laser in the 12 μm spectral region, *Opt. Commun.*, 154, 329–333 (1998).
15. Wood, O.R., High-pressure pulsed molecular lasers, *Proc. IEEE*, 62(3), 355–400 (1974).
16. Abrams, R.L., Broadening coefficients for the P(20) CO_2 laser transition, *Appl. Phys. Lett.*, 25(10), 609–611 (1974).
17. Wiegand, W.J., Fowles, M.C., Benda, J.A., Carbon monoxide formation in CO_2 lasers, *Appl. Phys. Lett.*, 16, 237–239 (1970).
18. Wiegand W.J. and Nighan, W.L., Plasma chemistry of CO_2–N_2–He discharges, *Appl. Phys. Lett.*, 22(11), 583–586 (1973).
19. Witteman, W.J., Rate determining processes for the production of radiation in high power molecular lasers, *IEEE J. Quantum Electron.*, 2, 375–378 (1966).
20. Witteman, W.J., High output powers and lifetimes of sealed-off CO_2 laser systems, *Appl. Phys. Lett.*, 11, 337–338 (1967).
21. Lotkova, E.N., Ochkin, V.N., Sobolev, N.N., Dissociation of carbon dioxide and inversion in CO_2 laser, *IEEE J. Quantum Electron.*, 7(8), 396–402 (1971).
22. Macken, J.A., Yagnik, S.K., Samis, M.A., CO_2 laser performance with a distributed gold catalyst, *IEEE J. Quantum Electron.*, 25(7), 1695–1703 (1989).
23. Heeman-Ilieva, M.B., Yu. B., Udalov. K. Hoen, Witteman, W.J., Enhanced gain and Output power of a sealed-off rf-excited CO_2 waveguide laser with gold-plated electrodes, *Appl. Phys. Lett.*, 64(6), 673–675 (1994).

24. Iehisa, N., Fukaya, K., Matsuo, K., Horiuchi, N., Karube, N., Perfomance characteristics of sealed-off CO_2 laser with $La_1.Sr_xCoO_3$ oxide cathode, *J. Appl. Phys.*, 59, 317–323 (1986).
25. Oh, H., Kim, S., Cho, U., An investigation of the catalytic effect with $Nd_1.Sr_xCoO_3$ perovskite in sealed-off CO_2 laser, *Bull. Korean. Chem. Soc.*, 13, 593–595 (1992).
26. He, D. and Hall, D.R., Influence of xenon on sealed-off operation of rf-excited CO_2 waveguide lasers, *J. Appl. Phys.*, 56(3), 856–857 (1984).
27. Mocker, H.W., Rotational level competition in CO_2 lasers, *IEEE J. Quantum Electron.*, 4, 769–776 (1968).
28. Waksberg, A.L., Boag, J.C., Sizgoric, S., Signature variations with mirror separation for small sealed CO_2 lasers, *IEEE J. Quantum Electron.*, 7, 29–35 (1971).
29. Plinski, E.F., Izworski, A., Witkowski, J.S., Calibration of an automatic system using a laser signature, *J. Systemics, Cybernetics Informatics*, 1(2), 76–80 (2003).
30. Plinski, E.F., Witkowski, J.S., Well-ordered laser signature, *Opt. Commun.*, 176(1–3), 207–211 (2000).
31. Shiffner, G., Prediction of CO_2 laser signatures, *IEEE J. Quantum Electron.*, 8, 877–881 (1972).
32. Plinski, E.F., Witkowski, J.S., Majewski, B.W., Abramski, K.M., Spectral aspects of a CO_2 slab waveguide design, *SPIE Proc.*, 5120, 202–205 (2002).
33. Baker, H.J., Field, P.A., Villarreal, F., Stratton, S.D., Ramirez, R.J., Hall, D.R., Line stabilisation of slab waveguide CO_2 lasers and the ''Laser Signature'' revisited, *SPIE Proc.*, 5120, 55–59 (2002).
34. Wojaczek, D.A., Plinski, E.F., Witkowski, J.S., Fortuna, P., Karlikowski, D., Abramski, K.M., Monitoring thermodynamic and optical parameters of the RF excited CO_2 pulsed laser plasma, *SPIE Proc.*, 5958, 1F1–1F6 (2005).
35. Plinski, E.F., Private Archive, Wroclaw University of Technology, Wroclaw, 1983.
36. Yu. A. Gorokhov, Kompanets, O.N., Letokhov, V.S., Gerasimov, G.A., Yu. I. Posudin, Narrow saturation resonances in the spectrum of OsO_4 induced by CO_2 laser radiation, *Opt. Commun.*, 7(4), 320–322 (1973).
37. Bazarov, E.N., Gerasimov, G.A., Yu. I. Posudin, Narrow resonances in the absorption saturation of OsO_4, *Opt. Spectrosc.*, 38(3), March 1975, 354–355.
38. Pliński, E.F., Abramski, K.M., Opto-voltaic representation of a gain profile in a cw CO_2 laser, *Opt. Commun.*, 50(3), 162–164 (1984).
39. Smith, A.L.S., Moffat, S., Opto-galvanic stabilized CO_2 laser, *Opt.Commun.*, 30(2), 213–218 (1979).
40. Nowicki, R., Pliński, E.F., Rzepka, J., The use of discharge electric field variations to CO_2 laser stabilization, *Opt. Commun.*, 53(2), 113–116 (1985).
41. Shin, D.J., Chung, Y.B., Lee, I.W., Stabilization of the CO_2 laser power by feedback controlling through an auxiliary electrode, *IEEE Trans. Instrum. Meas.*, 18(2), 535–536 (1989).
42. Levitsky, S.M., An investigations of the breakdown potential of a high-frequency and pressure transition regions, *Sov. Phys.-Tech. Phys.*, 2, 887–889 (1957).
43. Vitruk, P.P., Baker, H.J., Hall, D.R., Similarity and scaling in diffusion-cooled RF-excited carbon dioxide lasers, *IEEE J. Quantum Electron.*, 30(7), 1623–1634 (1994).
44. Vidaud, P., He, D., Hall, D.R., High efficiency RF excited CO_2 laser, *Opt. Commun.*, 56(3), 185–190 (1985).
45. Akimov, A.G., Koba, A.V., Lipatov, N.I., Mineev, A.P., Pashinin, P.P., Prokhorov, A.M., An effect of the exciting field frequency on performance of an RF pumped waveguide CO_2 laser, *Sov. J. Quantum Electron.*, 16, 938–944 (1973).
46. Duranti, S.M.A., Vidaud, P., Baker, H.J., Hall, D.R., Optimization of gain zone reduced fields in RF excited carbon dioxide lasers, CLEO'1988, Anaheim, CA, paper No. ThT4.
47. Hall, D.R., Hill, C.A., RF discharge excited carbon dioxide lasers, *Handbook of Molecular Lasers*, Cheo, P.K., Ed, New York, Marcell Dekker, 1987, Chapter 3, p. 328.
48. Johnston, W.C., *Transmission Lines and Networks*, New York: McGraw-Hill, 1950, p. 105.
49. He, D., Hall, D.R., Longitudinal voltage distribution in transverse rf discharge waveguide lasers, *J. Appl. Phys.*, 54(8), 4367–4373 (1983).
50. Chenausky, P.P., Hart, R.A., Newman, L.A., Hoffman, N.H., High-capacitance parallel-resonant rf-excited waveguide CO_2 lasers, CLEO'82 Conference, Phoenix, Technical Digest, paper No. THN2, pp. 88–90.

51. Strohschein, J.D., Bilida, W.D., Seguin, H.J.J., Capjack, C.E., Computational model of longitudinal discharge uniformity in RF-excited CO_2 slab lasers, *IEEE J. Quantum Electron.*, 32(8), 1289–1298 (1996).
52. Plinski, E.F., Witkowski, J.S., Abramski, K.M., Algorithm of RF-excited slab-waveguide laser design, *J. Phys. D: Appl. Phys.*, 33, 1823–1826 (2000).
53. He, D., Hall, D.R., A 30-W radio frequency excited CO_2 laser, *Appl. Phys. Lett.*, 43(8), 726–728 (1983).
54. Heeman-Ilieva, M.B., Yu. B. Udalov, Witteman, W.J., Peters, P.J., Hoen, K., Ochkin, V.N., RF excited 1.1 W/cm waveguide CO_2 laser, *J. Appl. Phys.*, 74(7), 4786–4788 (1993).
55. Abramski, K.M., Methods of analysis, control and locking of gas laser frequencies, Monographs No. 36, Wroclaw University of Technology Press, 1993.
56. Rigrod, W.W., Saturation effects in high gain lasers, *J. Appl. Phys.*, 36(8), 2487–2490 (1965).
57. Rigrod, W.W., Homogeneously broadened cw lasers with uniform distributed loss, *IEEE J. Quantum Electron.*, 14, 377–381 (1978).
58. Abramski, K.M., Colley, A.D., Baker, H.J., Hall, D.R., High-power two-dimensional waveguide CO_2 laser arrays, *IEEE J. Quantum Electron.*, 32(2), 340–349 (1996).
59. Newman, L.A., Hart, R.A., Kennedy, J.T., Cantor, A.J., DeMaria, A.J., Bridges, W.B., High power coupled CO_2 waveguide laser array, *Appl. Phys. Lett.*, 48(25), 1701–1703 (1986).
60. Bourdet, G.L., Mullot, G.M., Vinet, J.Y., Linear array of self-focusing CO_2 lasers, *IEEE J. Quantum Electron.*, 26(4), 701–710 (1990).
61. Abramski, K.M., Colley, A.D., Baker, H.J., Hall, D.R., Phase-locked CO_2 laser array using diagonal coupling of waveguide channels, *Appl. Phys. Lett.*, 60(5), 530–532 (1992).
62. Abramski, K.M., Colley, A.D., Baker, H.J., Hall, D.R., Power scaling of large-area transverse radio frequency discharge CO_2 lasers, *Appl. Phys. Lett.*, 54(19), 1833–1835 (1989).
63. Schackleton, C.J., Abramski, K.M., Baker, H.J., Hall, D.R., Lateral and transverse mode properties of CO_2 slab waveguide lasers, *Opt. Commun.*, 89(5,6), 423–428 (1992).
64. Plinski, E.F., Radiation properties of RF excited waveguide CO_2 lasers, Wroclaw University of Technology Press, Wroclaw, 2002.
65. Abramski, K.M., Baker, H.J., Colley, A.D., Hall, D.R., Single-mode selection using coherent imaging within a slab waveguide CO_2 laser, *Appl. Phys. Lett.*, 60(20), 2469–2471 (1992).
66. Plinski, E.F., Abramski, K.M., Witkowski, J.S., Optical resonators for slab-waveguide lasers, Optical Resonators—Science and Technology, Kossowsky, R., Jelinek, M., Novak, J., Ed., Kluwer Academic Publishers, NATO ASI Series, Vol. 45, pp. 267–279, (1998).
67. Siegman, A.E., How to (Maybe) measure laser beam quality, in *DPSS Lasers*: *Applications and Issues* (*OSA TOPS Volume 17*), Dowley, M.W., Ed., Optical Society of America, Washington D.S., 1998, pp. 184–199.
68. Jackson, P.E., Baker, H.J., Hall, D.R., A CO_2 large area laser using a hybrid waveguide-unstable resonator, *Appl. Phys. Lett.*, 54, 1950–1952 (1989).
69. Krupke, W.F., Sooy, W.R., Properties of unstable confocal resonator CO_2 laser system, *IEEE J. Quantum Electron.*, 5(12), 575–586 (1969).
70. Laakmann, P., Sealed-off RF-excited gas lasers and method for their manufacture, Patent USA, No. US 506 54 05 (1991).
71. Vitruk, P., All metal electrode sealed gas laser, Patent USA, No. US 595 33 60, 1999.
72. Mason, E.A., Saxena, S.C., Approximate formula for the thermal conductivity of gas mixtures, *Phys. Fluids*, 1(5), 361–369 (1958).
73. Plinski, E.F., Witkowski, J.S., Prediction of the thermal properties of CO_2, CO and Xe laser media, *Opt. Laser Technol.*, 33, 61–66 (2001).
74. Colley, A.D., Villarreal, F., Baker, H.J., Hall, D.R., High brightness slab waveguide carbon monoxide laser, *Appl. Phys. Lett.*, 64(22), 2916–2918 (1994).
75. Vitruk, P.P., Morley, R.J., Baker, H.J., Hall, D.R., High power continues wave atomic Xe laser with radio frequency excitation, *Appl. Phys. Lett.*, 67(10), 1366–1368 (1995).
76. Lachambre, J.-L, Lavigne, P., Verreault, M., Otis, G., Frequency and amplitude characteristics of a high repetition rate hybrid TEA-CO_2 laser, *IEEE J. Quantum Electron.*, 14(3), 170–177 (1978).
77. Lachambre, J.-L, Lavigne, P., Otis, G., Noel, M., Injection locking and mode selection in TEA-CO_2 laser oscillators, *IEEE J. Quantum Electron.*, 12(12), 756–764 (1976).

78. Moor, C.B., Wood, R.E., Hu, B-L., Yardley, J.T., Vibrational energy transfer in CO_2 lasers, *J. Chem. Phys.*, 46, 4222–4231 (1967).
79. Gilbert, J., Lachambre, J.-L., Rheault, F., Fortin, R., Dynamics of the CO_2 atmospheric pressure laser with transverse pulse excitation, *Can. J. Phys.*, 50, 2523–2535 (1972).
80. Choo, D., Takaneka, Y., Yamane, S., High Power microwave excited CO_2 laser oscillator, *Proc. SPIE*, 3092, 210–214 (1997).
81. Kato, M., Saito, K., Yajima, H., Sato, K., Kimura, M., Furuya, N., Łamane, S., Microwave-discharge-excited CO_2 laser using orthogonally crossing electric fields, *CLEO Conference*, paper CThM4, p. 445 (1996).
82. Freisinger, B., Pauls, M., Schaefer, J.H., Uhlenbusch, J., High-power CO_2 laser excited by 2.45 GHz microwave discharges, *Proc. SPIE*, 1397, 311–318 (1991)
83. Ikeda, T., Danno, M., Shimazutsu, H., Abe, T., Tanaka, J., TM_{010}-mode microwave excited high power CO_2 laser using a cylindrical resonant cavity, *IEEE J. Quantum Electron.*, 30(11), 2657–2662 (1994).
84. Ikeda, T., Danno, M., Monaka, T., Noda, M., Tanaka, J., A New helical coupling microwave antenna excited high-power CO_2 laser using a cylindrical resonant cavity, *IEEE J. Quantum Electron.*, 35(5), 721–729 (1999).
85. Shahadi, A., Sintov, Y., Jerby, E., Longitudinal coupled-cavity scheme for microwave-excited CO_2 slab lasers, *Microwave Opt. Technol. Lett.*, 36, 115–120 (2003).
86. Marz, M., Oestreicher, W., Microwave excitation of a diffusion-cooled CO_2 laser, *J. Phys. D*: *Appl. Phys.*, 27, 470–474 (1994).
87. Kruger, W., Grosse-Wilde, H., Gas lasers, in particular CO_2 lasers, Patent USA, No. US 5 224 117, 1993.
88. Tokoro, T., Matsuoka, N., Yasuda, M., Uchiyama, T., CO_2 laser excited by microwave discharge using stripline, *Proc. SPIE*, 3092, 235–238 (1997).
89. Gray, D.E., Ed., *American Institute of Physics Handbook*, McGraw-Hill, New York, 1972, pp. 6–110.
90. Kurosawa, T., Anomalous refractive indices of the amplifying medium in a waveguide CO_2 laser, *Appl. Opt.*, 25(21), 3816–3824 (1986).

6B High-Power Electric CO_2 Lasers

Alan E. Hill

CONTENTS

6B.2 INTRODUCTION

"In some way they (the Martians) are able to generate an intense heat in a chamber of practically absolute non-conductivity . . . This intense heat they project in a parallel beam against any object they choose, by means of a polished parabolic mirror of unknown composition . . . However it is done, it is certain that a beam of heat is the essence of the matter. What is combustible flashes into flame at its touch, lead runs like water, it softens iron, cracks and melts glass, and when it falls upon water, that explodes into steam".

H.G. Wells, *The War of the Worlds*, 1897

6B.2.1 Introduction and Historical Background

In this chapter, we explore the art and science of scaling CO_2 lasers to reach ever-increasing power or energy levels. Historically, the CO_2 laser became the first of a new breed of lasers—the molecular gas laser—and it possessed unique attributes that opened up for the first time the possibility of producing extremely high average laser power. Before the discovery of the CO_2 laser, scientists had visions of making laser weapons, as depicted in the famous James Bond movie, *Goldfinger*. In that movie, a giant flash lamp-pumped ruby-like laser was depicted because that represented the only known laser capable of producing high enough peak power pulses to interact with metal—that is, it could punch holes in razor blades. Of course, this category of lasers—including all the optically pumped solid state devices of today—lack the inherent properties needed to develop sustained high average power, near diffraction-limited beams. Mostly, these lasers are relatively inefficient, and their waste heat cannot be readily conducted away from the solid crystalline optical gain media. Hence, thermal stresses occur, which in turn produce irregularities in their index of refraction throughout their volume. Therefore, beam quality is severely degraded.

Let us now compare the relative merits of a molecular gas laser, and most specifically a CO_2 laser. This laser has a quantum efficiency of 41% and can easily produce 25% cavity efficiency in practice. However, we must still deal with the remaining energy: 75% of the applied electrical power, which gets transformed into heat within the gain media.

Fortunately, the CO_2 laser's gain media is a gas, and gas is very resilient. Heat is easily dispersed by convection and diffusion. Furthermore, the density of gas is extremely low as compared with that of a solid, so correspondingly, the magnitude of index of refraction gradients is minimal. Owing to these properties, an extremely simple and very early CO_2 laser achieved 80 W m^{-1} length of discharge tube containing a flow mixture of CO_2, N_2, and He. Power could be linearly scaled by increasing the discharge tube length—first to the 900 W level and then to the 8800 W level, where the cavity efficiency approached 20%. (Actually, 10 kW had been exceeded, but it was not reported because the government classified power level remained at 10 kW in the late 1960s). The laser was 750 ft long.

This giant leap practically fell out automatically, with very little engineering effort—purely as a result of the CO_2 laser media's remarkable physical attributes. However, a plateau in progress was rapidly reached. Each new level of power scaling would require a significantly growing effort, and the work became increasingly more costly. However, the United States and the Soviet Union both quickly realized[1] that the CO_2 laser had weapons potential, and this launched an arms race beginning in the early 1970s. Both countries then funded CO_2 lasers—and later chemical laser research—at a staggering level of support as the arms race escalated.

Consequently, CO_2 laser technology came to incorporate a combination of disciplines including gas dynamics, rocket combustion technology, molecular kinetics, chemistry, thermodynamics, pulsed power engineering, plasma physics, advanced resonator design, nonlinear optics, and many more diverse technological disciplines.

The high-power CO_2 laser of today has evolved to include an unprecedented combination of attributes: nearly unlimited levels of average power scalability, high electrical to optical conversion efficiency, near-diffraction limited beam quality, either CW or high-energy pulse repetition rate modes of operation, compact size, and relatively low cost.

6B.2.2 Technical Discussion: Early Developments

Let us trace the emergence of specific problems that blocked progress along the road to produce an ever-increasing level of laser power, and in turn, the solution(s) to these problems.

Oftentimes, different areas of engineering or principles of physics will be integrated into the core technology, wherein the scope of the discussion will be broadened.

At this point, it is suggested that the reader be familiar with CO_2 laser basics as presented in Plinski (this volume), in which, Kumar Patel's land-breaking discovery of the CO_2 laser in 1963 is referenced. Kumar Patel had realized that when N_2 is excited by a DC glow (or RF) discharge, some 85% of the energy input gets stored into its metastable $V = 1, 2, 3, \ldots$ vibrational states. Then, this entire energy reservoir trickles down the N_2 ($V = n$) vibrational manifold and gets transferred by making Fermi-resonant collisions from the $V = 1$ state to the upper laser state $V = (010)$ of the CO_2 molecule.

Patel's first laser produced only 1 mW of power because N_2 was RF excited separately, and then mixed it into a dilute CO_2 flow stream. In this configuration, CO_2 molecules are reused rapidly many times, thus draining the N_2 energy storage reservoir within a very short distance of travel along the optical path. Therefore, gain was limited to a small region where mixing occurred, so the gain-path length was too short to permit efficient laser power extraction. Interestingly, later mixing lasers of a similar sort achieved ~10 kW simply by means of incorporating much faster flow streams and transverse gain-path geometry, thereby stretching out the gain path length.[2]

Within a few months, Harrigan[3] readily achieved ~80 W m^{-1} of discharge simply by flowing premixed $N_2 + CO_2 + He$ down a water-cooled tube, bounded on its ends by cavity optics, and by maintaining a glow discharge that excited the entire length of the tube. A stable, arc-free, glow discharge was produced either by means of applying direct current across the tube and inserting a ballast resistor in series, or by means of supplying high-voltage AC from a saturable core ballasted transformer of the type used to power neon signs. The reader is referred to Khukharev (this volume), which covers the maintenance of normal glow discharges by means of inserting a negative impedance element to prevent arc formation.

This brings us to the plateau in progress mentioned in the Introduction. The power obtainable from CW longitudinal discharge lasers of the Harrigan–Whitehouse variety proved totally independent of their diameter or pressure—only their length mattered. Intuition might indicate that all three parameters should contribute extended power, as the total number of excited CO_2 molecules in the cavity increases whenever length, pressure, or diameter is increased, so clearly some controlling parameter must be negating the power scaling effect of increasing either diameter or pressure.

The laser simply shuts off at the point where the gas exceeds a particular temperature, T_{tb}. In addition, as the only means of escape for the heat was to diffuse to the water-cooled wall, it became clear why neither increasing the diameter nor the pressure affected power. The rate of wall heat transfer $\dot{Q}_{wall}$ is proportional to $1/d^2P$, where d is the tube diameter and P is the pressure. When P is increased, the total number of excited CO_2 molecules increases correspondingly. However, to avoid a temperature rise the power load to the discharge cannot be increased with P. The power deposition per molecule must be decreased in direct proportion to the number of molecules in the cavity. Therefore, the net available power generated remains unchanged.

Similarly, when the discharge diameter is increased, the available number of molecules is increased in proportion to d^2. However, as the rate of heat removal $\dot{Q}_{wall}$ is proportional to d^2, the power input per molecule must be decreased proportional to d^2. Moreover, the two effects cancel, and again the total power input remains unchanged.

Therefore, why does the laser turn off upon reaching some critical gas temperature, and what is that gas temperature? To find the answer, let us explore the collision processes depicted in the energy level diagram of Plinski and Abramski (this volume), and also Figure 6B.1, which applies more specifically to the discussion that follows.

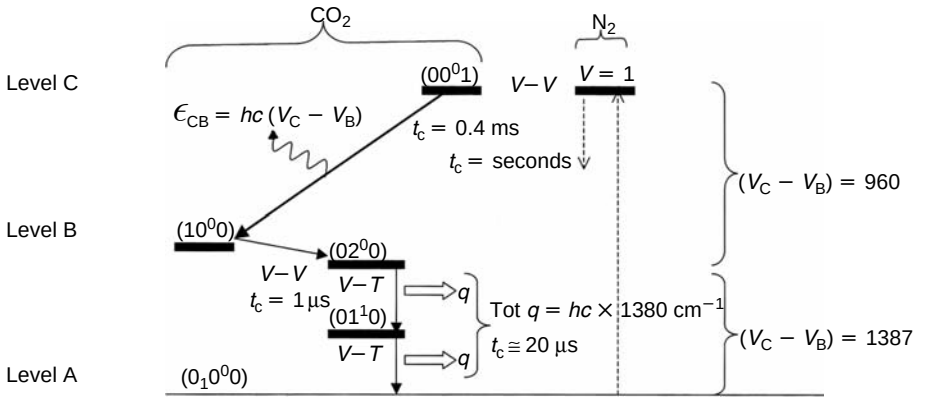

FIGURE 6B.1 Energy levels for N_2–CO_2 lasers.

The CO_2 [001] upper laser level and the vibrational manifold of N_2 ($V = 1, 2, 3, \ldots$) are efficiently excited by electron impact from the electric discharge. N_2 ($V = 1$) is metastable, lasting for seconds in the absence of CO_2. In the laser mixture N_2 [$V = 1$], the vibrational energy is transfered by collision to CO_2 [001] in less than 65 μsec (at 15 torr). Subsequently, nearly all the N_2 vibrational energy feeds into CO_2 [001]. Electron–molecule collisions create much greater molecular vibrational excitation than thermal excitation. Hence, about 85% to 90% of the electrical pump power can be ultimately stored into the upper laser level C.

The CO_2 molecule has three vibrational wave numbers ($\nu_1 = 667\ \text{cm}^{-1}$, $\nu_2 = 1387\ \text{cm}^{-1}$, and $\nu_3 = 2347\ \text{cm}^{-1}$). At 15 torr (nominal pressure for early CW-flowing lasers), level A (CO_2, [001]) is relatively long lived, and the collisional relaxation time is in the order of 20 μsec. In level B, CO_2 [$10^{0}0$] equilibrates with CO_2 [$02^{2}0$] within 500 nsec. Finally, level B relaxes to the ground state level A by two steps: CO_2 [$02^{2}0$] → CO_2 [$01^{1}0$], which relaxes in ~2 μsec, followed by CO_2 [$01^{1}0$] → CO_2 [$00^{0}0$], which relaxes in 18 μsec.

The energy per each molecular transition from level C to level B is $\in_{CB} = hc\ (\nu_C - \nu_B)$, where h is Plank's constant, c is the velocity of light, and ν_C and ν_B are the wave numbers for level C and level B, respectively. So, the quantum efficiency n_q is simply the ratio $\nu_C - \nu_B/\nu_C = 0.41$. The remaining energy is converted to heat because the level B to level A transitions undergo vibrational–translational (VT) collisions. The fraction of heat released is $\nu_B - \nu_A/\nu_C = 59\%$. Depending on the amount of power applied, some fraction ΔQ of the heat released remains in the gas; i.e., it never reaches the walls. Then ΔQ_g heats the gas, raising its temperature by ΔT, according to

$$\Delta T = \frac{\Delta Q_g}{\dot{m} C_p}, \tag{6B.1}$$

where ΔT is the rise in temperature, ΔQ is the thermal energy input, $\dot{m}$ is the mass of the gas mixture, and C_p is the specific heat of constant pressure of the gas mixture.

As the gas temperature ($T_g = T_{initial} + \Delta T$) rises, the laser media becomes a thermal reservoir that is capable of populating the lower laser level directly from heat. We know from statistical mechanics that the ratio of molecule densities in level B or level A at thermal equilibrium is simply the Boltzmann factor:

$$\frac{N_A}{N_B} = \exp\left[\frac{(\in_B - \in_A)}{kT}\right], \tag{6B.2}$$

where k is Boltzmann's constant 1.38×10^{-23} J K^{-1} and the energy difference $(\in_B - \in_A)$ corresponds to the optical energy equivalent $\in_{BA} = hc\ (\nu_B - \nu_A)$. We may ask at what gas temperature do half of the gas molecules have kinetic energies distributed above the CO_2 [101] kinetic energy? Or, what is T such that

$$\sqrt{2\pi} \int_{E(010)}^{\infty} \sqrt{E} e^{-\left(\frac{E}{kT}\right)} \mathrm{d}E \approx 0.5. \tag{6B.3}$$

The answer is $T_{BN} = 280°C$. Therefore, above this temperature, the depopulation of B to A is blocked, hence the population density $N_C - N_B$ becomes negative, as does the laser gain:

$$\alpha = \sigma(N_C - N_B), \tag{6B.4}$$

where σ is the stimulated emission cross section. For the most efficient operation, heat must be removed sufficiently fast so that the gas temperature remains less than ~150°C, such that $N_A/N_B \geq 0.37$.

This phenomenon is known as "thermal bottlenecking." Its experimental realization and subsequent solutions were found in 1970 by Hill,[4] and as a consequence, two significant events took place.

The first event was the generation of giant pulses from a small gas volume laser, where in a three orders of magnitude, energy amounting to 10 J $pulse^{-1}$ was achieved.[5] With this demonstration it was realized that power could in fact be scaled with pressure and volume—not merely with length. This was accomplished using large bore axial tubes, reaching up to 15 cm in diameter, and operating at extended (40 to 100 torr) pressures (by 1970 standards). Discharge stability was realized by means of preionization and the application of megavolt, fast-rise-time pulses.

The second event was the demonstration that average power could be scaled by means of exchanging the gas volume at high velocity; that is, scaling mass flow rate $\dot{m}$ instead of increasing the laser's length or volume.[4] These events flagged the eventuality that CO_2 lasers could be scaled to reach giant power levels operating in either continuous or rapid pulse mode. In rapid pulse mode operation, the role of thermal diffusion became experimentally easy to verify and quantify. In this case, an electrical pulse uniformly heats the gas, then following lasing, the heat diffuses radially outward to the wall according to the heat equation

$$\bar{K}_T \frac{1}{r} \frac{\partial}{\partial r} \left(r \frac{\partial' T(r,\tau)}{\partial r} \right) = \rho C_v \frac{\partial T(r,\tau)}{\partial T}, \tag{6B.5}$$

which has the solution

$$T_{(r,\tau)} = T_{wall} + \left(T_{gas} - T_{wall}\right) J_o \left(\frac{2.405}{R}\right) \times \exp\left[-\frac{K_o T^{\infty}}{P C_v} \left(\frac{2.405}{R}\right)^2 (t - t_o) \right], \tag{6B.6}$$

where R is the radius of the tube, r is the radius of the plasma element volume, $(t - t_o)$ is the time elapsed after thermal step increase, $K_o T^{\infty}$ is the thermal conductivity, $T_{(r,\tau)}$ is the temperature, and J_o is the Bessel function of zero order.

Following the temperature increase step, the temperature falls exponentially with a time constant that is proportional to $R^2/\bar{\lambda}\,\bar{c}$, where $\bar{\lambda}$ and $\bar{c}$ are the average molecular mean free

path and average thermal velocity, respectively. For example, Equation 6B.1 predicts that inputing 50 J to the laser cavity (a tube 7.6 cm in diameter $\times$ 2.44 m in length) with a $CO_2/N_2/He$ mixture of 7/7/28 torr, respectively, heats the gas by a temperature step $\Delta T = 90°C$, where the temperature relaxes with an exponential time constant of $\tau_r = 33$ msec.

Data showed that when the tube diameter was decreased by two-thirds, then by one-third, the thermal relaxation time correspondingly decreased by the factors $1/(2/3)^2$ and $1/(1/3)^2$, confirming that the exponential relaxation time constant scales as $1/R^2$. Furthermore, the laser output power scaled directly with R^2 and also with P. Therefore, provided the specific power loading (SPL) is held below the thermal bottlenecking criteria, $T_{gas} < T_{TB} \approx 280$ K, the energy output for this device scales directly with the molecular number density in the N_2 vibrational manifold times the cavity volume.

In the foregoing experiments, the SPL was limited by discharge stability—still a serious limitation for high pressure, large volume plasmas at the time. Upcoming developments provided the means to acquire the full quota of SPL, which drove the gas temperature up to its thermal bottlenecking limit of 280°C.

In the meantime, the role of thermal bottlenecking was experimentally verified and characterized by means of pulsing the discharge rapidly and in the absence of helium. Thus, thermal diffusion was practically eliminated, whereas the gas temperature was incremented by 90°C steps. Using a 10 torr $N_2 + 10$ torr CO_2 mix, where initially $T_{gas} = 0°C$, the first, second, and third laser pulses reached calculated temperature changes of 0°C to 150°C, 125°C to 300°C, then 225°C to 400°C, respectively. The initial pressure pulse sustained an arc (because no preionization had been generated in a previous pulse), thereby producing minimal laser power. The second pulse met favorable thermal conditions, and temperature peaked just beyond T_{BN}. This produced 5J output—a power level that matched the optimum level achieved in the presence of helium. The third pulse produced on the order of 2.5J, since extraction terminated as the gas temperature passed through T_{TB} (280°C). The fourth pulse produced no laser output, since the gas temperature at its onset was 300°C, which already exceeded the thermal bottlenecking temperature limitation.

The data verified T_{BN} to be ~280°C, as calculated, and it also verified that the role of helium served primarily to thermally deactivate CO_2 states $[02^20]$ and $[01^10]$ to ground level. Helium also plays other important roles, such as modifying the electron energy distribution—in effect, lowering the electron temperature, which then increases the electron excitation efficiency of N_2. However, this role was not nearly as important as thermal relaxation, contrary to some earlier thinking.

Let us now consider the manner in which power scaling with increasing mass flow rate was discovered. The average power output from the axial pulsed laser was found to linearly increase with repetition rate until it peaked sharply, and then fell sharply. The clue was that repetition frequency at peak average power corresponded to an interpulse dwell time that closely matched the thermal diffusion time; i.e., that point where gas could no longer be cooled back to a level, which nearly matched the chilled wall temperature. Moreover, if the wall diameter d were doubled, the maximum repetition rate would be quadrupled according to the diffusion time constant's dependence on d^2. Therefore, although peak power scaled with d^2 and pressure P, average power remained nonscalable except by increasing length, as in the CW mode-of-operation case.

But now it had become clear that if one were to exchange the heated gas following a pulse for cold gas, the average power should depend on how rapidly the exchange could be made, rather than how long it took for heat to diffuse to the wall. This concept was verified experimentally using an axial rapid pulsed laser as previously described, but many flow conduits were added along opposite sides of the tube across which the gas volume could be

rapidly exchanged. In this configuration, the peak temperature rise during high repetition rate operation, that has reached steady state, becomes

$$\Delta T = \left[4.182 C_p n w \pi R^2\right]^{-1} P(1-\eta)\left\{\frac{l}{v}\left(\frac{3}{16}\frac{R^2}{\bar{\lambda}\bar{c}}\right)^{-1}\left(\frac{l}{v}\right)^2\right\}, \tag{6B.7}$$

where l is the length, R is the radius, v is the flow velocity, P is the input power, and η is the laser efficiency. Equation 6B.7 can also be applied to continuously excited axial flow streams where the gas exits at steady temperature $T_{\max} = T_i + \Delta T$, where T_i is the gas temperature flowing into the tube.

If the velocity and geometry are such that thermal diffusion can be neglected, Equation 6B.7 reduces to

$$\Delta T = \left(4.182 C_p n w \pi R^2 v\right)^{-1} P(1-\eta) = \frac{P(1-\eta)}{4.182 C_p \dot{m}} \tag{6B.8}$$

and the power can be raised without increase in gas temperature by means of scaling $\dot{m}$ in direct proportion to the power. As cavity storage densities exceeding 100 kW L^{-1} have been produced in pulsed plasmas where $\Delta T \approx 150^\circ C$, it became clear that, while operating at a comparable temperature and pressure, laser power should scale linearly with mass flow rate and correspondingly increased input power, whether CW or rapid pulsed.

6B.2.3 Basic Theory of Power Extraction

Let us now quantify the physics of power scaling in terms of gas kinetics. Beginning with the more familiar case of a longitudinal CO_2 laser with insufficient flow to overwhelm convection, the rate equations for the upper and lower lasing levels are

$$\frac{\partial N_u}{\partial t} = r_u - \frac{N_u}{\tau_u} - (N_u - N_l)\frac{\sigma I}{h\nu'}, \tag{6B.9}$$

$$\frac{\partial N_l}{\partial t} = r_l - \frac{N_l}{\tau_l} - (N_u - N_l)\frac{\sigma I}{h\nu'}, \tag{6B.10}$$

where N_u, N_l are the densities of the upper and lower states, respectively, r_u, r_l are the pump rates of the upper and lower states, respectively, τ_u, τ_l are the kinetic relaxation times of the upper and lower states, respectively, $h\nu$ is the laser photon energy, σ is the stimulated emission cross section, and I is the laser beam intensity. For typical $CO_2/N_2/He$ mixtures, $\tau_u = 1.6 \times 10^{-5}$ sec, $\tau_l = 4 \times 10^{-7}$ sec normalized to 1 atm total pressure, and each rate scales inversely with pressure.

For either CW or pulse lasers for which the pulse time is much longer than τ_l (which applies to all rapid pulsed lasers that are discussed herein), we may assume quasisteady-state conditions, where

$$\frac{\partial N_u}{\partial T} = \frac{\partial N_l}{\partial T} = 0 \tag{6B.11}$$

Hence, the gain α becomes

$$\alpha = (N_u - N_l) = \frac{\sigma(r_u \tau_u - r_l \tau_l)}{1 + \frac{\sigma I}{h\nu'}(\tau_u + \tau_l)}. \tag{6B.12}$$

Then, setting $I = 0$ yields the small signal gain α_o

$$\alpha_o = \sigma(\tau_u r_u - \tau_l r_l) \tag{6B.13}$$

Then by defining the saturation flux I_{sat} as the flux intensity required to reduce α by one-half (i.e., to extract one-half of the available laser power), then

$$I_{sat} = \frac{h\nu'}{\sigma}\left(\frac{1}{\tau_u - \tau_l}\right) \tag{6B.14}$$

and

$$\frac{\alpha}{\alpha_o} = \frac{1}{1 + \frac{I}{I_{sat}}}. \tag{6B.15}$$

Let us pause here to examine the effect of increasing pressure on power scaling. It can be shown that the maximum available power from a laser gain region of volume V is:

$$P_{max} = \iiint \alpha_o I_s \mathrm{d}V. \tag{6B.16}$$

In addition, α_o decreases linearly with pressure, as can be seen from Equation 6B.13, as τ_u depends on the gas collision rate, and hence it decreases as $1/P$. On the other hand, I_{sat} increases quadratically in proportion to P, as seen from Equation 6B.12. From the definition

$$\sigma = \frac{\lambda^2 A_{21}}{\Delta\nu}\left(\frac{1}{4\pi\sqrt{\ln(2/\pi)}}\right), \tag{6B.17}$$

where λ is the wavelength, A_{21} is Einstein's A coefficient, and $\Delta\nu$ is the pressure broadened line width, we note that the Doppler broadened line width $\Delta\nu$ increases with the collision frequency, and hence pressure, as likewise does τ_u and τ_l. Therefore, the product $\alpha_o I_{sat} \propto (1/P)(P)^2$ increases linearly with pressure. However, the saturated flux (i.e., the stored power density) scales quadratically with pressure. Consequently (now that the waste heat has been removed), we may scale laser power and at the same time reduce the laser's volume in direct proportion to raised gas pressure.

Another consequence of pressure scaling is that the laser intensity scales as the square of pressure, a situation that will at some point lead to mirror damage in the case of continuous lasers, and gas plasma breakdown in the case of pulsed or rep-pulsed lasers.

Let us now modify Equation 6B.9 and Equation 6B.10 to account for convective gas flow by adding mass transport terms for upper and lower laser levels:

$$\frac{\partial N_u}{\partial T} = r_u - \frac{N_u}{\tau_u} - (N_u - N_l)\frac{\sigma I}{h\nu'} + \frac{N'_u}{\tau_f} - \frac{N_u}{\tau_f} \tag{6B.18}$$

$$\frac{\partial N_l}{\partial T} = r_l - \frac{N_l}{\tau_l} - (N_u - N_l)\frac{\sigma I}{h\nu'} + \frac{N'_l}{\tau_f} - \frac{N_l}{\tau_f}, \tag{6B.19}$$

where τ_f is the flow cavity traverse time (in either axial or transverse configuration), and N'_u and N'_l are the population densities of the upper and lower states in the absence of stimulated emission, respectively.[6]

Solving Equation 6B.18 and Equation 6B.19 in the same manner as Equation 6B.9 and Equation 6B.10, we derive gain and saturation intensity expressions for fast-flow stream, convective-transport lasers:

$$\alpha_o = \sigma(r_u\tau_u - r_l\tau_l), \tag{6B.20}$$

$$I_{sat} = \frac{h\nu'}{\sigma}\left[\frac{\tau_u\tau_f}{\tau_u + \tau_f} + \frac{\tau_l\tau_f}{\tau_l + \tau_f}\right]^{-1}. \tag{6B.21}$$

Let us pause to explore the effect of adding a fast convective gas flow stream to power scaling according to Equation 6B.20 and Equation 6B.21. First, we see that Equation 6B.20 is unchanged from Equation 6B.13; that is, the small signal gain is not directly affected by rapidly exchanging the gas volume. Moreover, as should be expected, I_{sat} is not changed significantly either until the flow exchange time τ_f becomes small compared with either τ_u or τ_l. As τ_u/τ_f and τ_l/τ_f become much larger, then I_{sat} scales directly with the mass transport ratio. That is, mass-flow scaling reaches threshold when the convective heat removal rate is capable of maintaining a constant maximum temperature as the number of molecules sweep through the cavity per second can be increased, commensurate with an increase in applied power. The parameter I_{sat} is a measure of the total power extractable, which may be generated either by recycling a number of near-stationary CO_2 molecules through the kinetic manifold many times per second (which also necessitates heat transfer to the wall), or by means of flowing a larger number of excited (or excitable) molecules through the cavity per second.

Then, according to Equation 6B.16, the available power scales in direct proportion to mass flow rate and pressure as long as the electric power input is scaled in direct proportion. In addition, the available power increases as α_o is increased by means of increasing the electrical input power, and therefore the pump rate r_p, up to the point efficiency, starts to decrease as the gas temperature approaches the thermal bottleneck temperature limitation. In some cases the power output maximizes, but with reduced efficiency at SPL power load such that T_{gas} may somewhat exceed 280°C at the exit. This is because, although lasing has stopped short of the cavity exit, the pump rate r_B and $\alpha_{o(l)}$ may be considerably raised over an upstream portion of the gain media. How the designer may choose to optimize either maximum power or maximum efficiency, or choose to trade off power vs. efficiency will be shown later.

6B.2.4 Maximizing Power or Efficiency

Now we consider the fast axial flow-collinear optical cavity continuous laser. For the case of lower power extraction below ~10 kW, both transverse and axial cavity alignments with respect to flow can be analyzed in a similar manner. However, at higher power levels the transverse configuration encounters serious beam quality disturbance and must be handled in a special way.

First, gas dynamic effects are reviewed as they profoundly affect density, pressure, velocity, and temperature variations along the flow axis. In addition, Rayleigh heating—an effect of incompressible gas dynamics—can lower the gas temperature at an SPL level that would otherwise cause thermal bottlenecking, thus allowing SPL to be raised beyond its otherwise limiting value. Hence, higher α_o and correspondingly higher output power can be achieved.

Second, we explore how the resonator design may be optimized to achieve maximum output power, or maximum efficiency applying Rigrod theory.

6B.2.5 Optimal Use of Compressible Gas Dynamic Effects

Upon application of excitation power to the laser, P_{in}, some fraction of this power is extracted by the beam, and that energy which is left resides in the gas—either as internal vibrational/rotational states or as thermal power $P_g = (1-\eta_L)P_{in}$. If the flow is stationary, P_g is converted to a rise in gas temperature, as given by Equation 6B.1. However, if the gas is flowing at Mach $M \approx 0.3$—a point where the flow stream starts to become compressible—then the thermal power is partly converted to forward kinetic energy; that is, it is directed into a steadily increasing flow velocity. Correspondingly, the gas density decreases as flow velocity increases. Moreover, as thermal energy continues to be added by the discharge along the direction of flow, the gas temperature rise diminishes whereas the flow velocity increases. After sufficient power input, the Mach number reaches the value $M = 1/\sqrt{\gamma}$, where $\gamma = C_p/C_v$, (roughly $M = 0.8$ for a typical CO_2 mixture), at which point a remarkable thing happens. The flow stream entropy reverses so that, upon further addition of power, the gas stream temperature actually decreases. Instead of heating the gas, all additional energy goes into increasing velocity, while an additional increase in velocity occurs as an equivalent amount of heat gets extracted from the gas. Beyond this point the further addition of energy drives the Mach number to $M = 1$ and some gas cooling occurs. This phenomena is called "Rayleigh heating" and may be derived from the following irreversible relationships that relate pressure ($P_{1,2}$), temperature ($T_{1,2}$), density ($\rho_{1,2}$), and Mach number ($M_{1,2}$) at two distinct locations: an upstream location at position 1 and downstream location at position 2.

$$\frac{P_2}{P_1} = \frac{1 + \gamma {M_1}^2}{1 + \gamma {M_2}^2} \tag{6B.22}$$

$$\frac{T_2}{T} = \left(\frac{P_2}{P_1}\right)^2 \left(\frac{M_2}{M_1}\right) \tag{6B.23}$$

$$\frac{\rho_2}{\rho_1} = \frac{V_1}{V_2} = \frac{P_2}{P_1}\frac{T_1}{T_2}. \tag{6B.24}$$

In an incompressible flow stream, the input power to the gas is related to the stagnation temperature change T_0 according to

$$P_g = mC_p(T_{02} - T_{01}) = (1 - \xi)P_{input} \tag{6B.25}$$

$$T_{01} = T_1\left(1 + \frac{\gamma - 1}{2}M_1^2\right) \tag{6B.26}$$

$$T_{02} = T_2\left(1 + \frac{\gamma - 1}{2}M_2^2\right). \tag{6B.27}$$

Let T_0* be the stagnation pressure at Mach 1. Then the stagnation temperatures at the start point T_{01} and end point T_{02} can be related to the Mach number at the start point M_1 and end point M_2 by

$$T_{01} = \frac{2(1 + \gamma)M_1^2}{(1 + \gamma_1 {m_1}^2)^2}\left(1 + \frac{\gamma - 1}{2}{M_1}^2\right) \tag{6B.28}$$

$$\frac{T_{02}}{T_0^*} = \frac{P_g}{\dot{m}C_p T_{01}} + \left(\frac{T_{01}}{T_0^*}\right) \tag{6B.29}$$

and the exit Mach number is

$$M_2 = \sqrt{\frac{1 - \left(1 - \frac{T_{02}}{T_0^*}\right)^{1/2}}{1 + \gamma\left(1 - \frac{T_{02}}{T_0}\right)^{1/2}}}. \tag{6B.30}$$

Equation 6B.22 through Equation 6B.24 are solved sequentially for M_2, where the fraction of SPL that heats the gas $(1 - \xi) = \text{SPL} = P_g/\dot{m}$ is specified and M_1 is chosen to be variable. Then Equation 6B.29 and Equation 6B.30 are used to determine T_2, the flow stream temperature at the tube exit, and which drives thermal bottlenecking. Figure 6B.2 shows a family of curves of

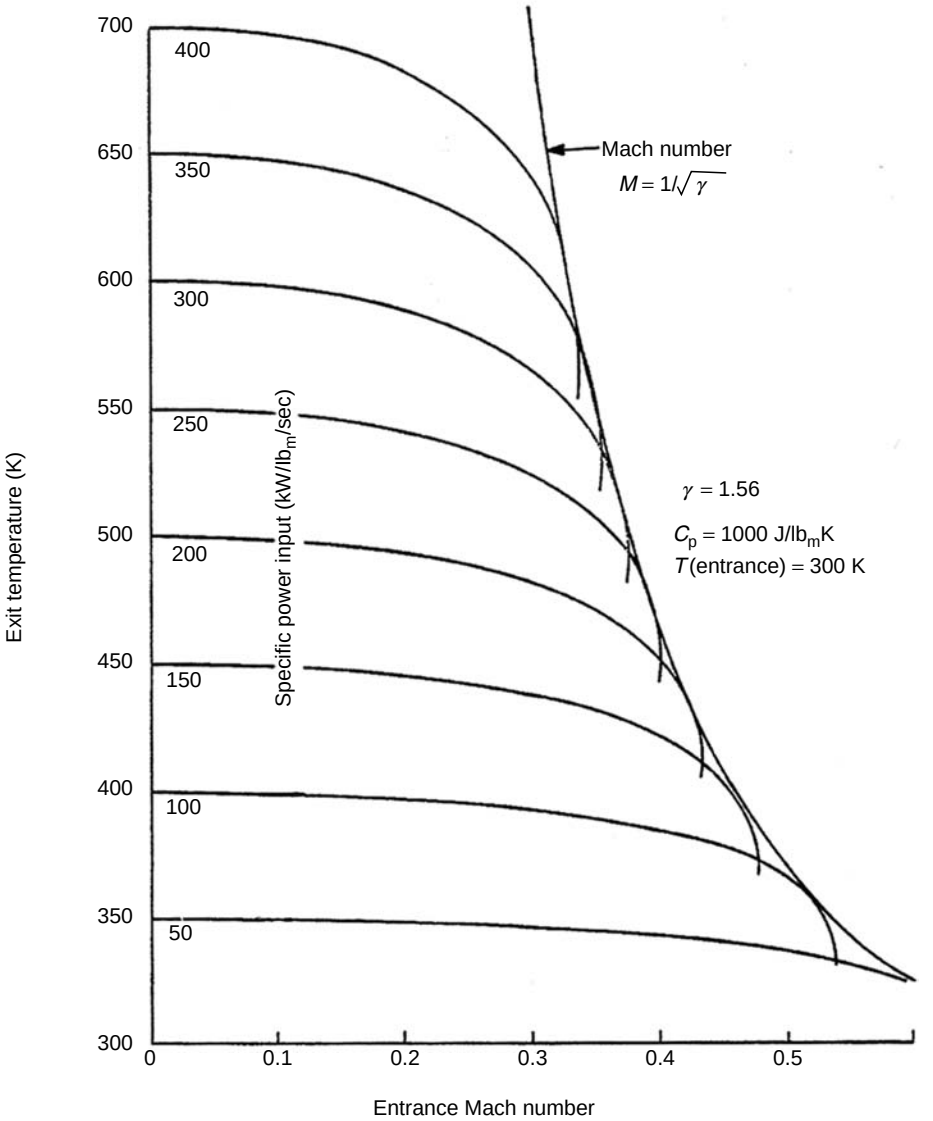

FIGURE 6B.2 Rayleigh heating curves.

exit temperatures vs. specific input power $P_g/\dot{m}$, where the starting temperature is 300 K. Note that for a given specific input power, the exit temperature continues to fall as M_2 approaches $1/\sqrt{\gamma}$.

At this point the maximum gas stream temperature is reached. In Figure 6B.2 the Mach number $M = 1/\sqrt{\gamma}$ is overlain, so that for a selected entrance Mach number, a corresponding curve may be traced back to the left vertical axis to determine the exit temperature. These curves are used to determine exit and entrance Mach numbers such that the maximum SPL can be achieved without heating the gas beyond tolerable limits. The "tolerable limit" depends on one's choice of whether to maximize power or efficiency, and upon cavity design parameters.

Let us visualize what goes on inside the laser gain region as it undergoes Rayleigh heating according to Equation 6B.29 and Equation 6B.30. Figure 6B.2 presents a family of curves covering a range of SPL power inputs (that part of the input channeled into gas heating). One selects a desired SPL (shown to the right on the vertical axis), which corresponds to an exit temperature (shown to the left). Next, one chooses an entrance Mach number along the horizontal axis, then draws a vertical line from the chosen Mach number to intersect with the curve that represents the selected SPL. Finally, one draws a horizontal line from the intersection point to the vertical axis. The horizontal line's intersection with the vertical axis then depicts the flow stream temperature at the exit. This is the temperature that bottlenecks the laser. As the vertical line's point of intersection moves to the left, the exit Mach number approaches the limiting value $M = 1/\sqrt{\gamma}$, which defines the highest stream temperature reached. One should apply that fraction of SPL input that heats the flow, exclusive of power removed by the laser beam; i.e., SPL (applied) $\times \xi$ should be used, where ξ is to be defined in Equation 6B.33. Figure 6B.2 is quite useful for designing lasers, but it does not provide a good picture in terms of Mach number variation along the gain path region. So let us display similar information differently so that the Rayleigh heating effects can be best visualized.

Figure 6B.3 illustrates directly how the Mach number increases along the flow stream as the SPL input is steadily added along the direction of flow. The family of curves represents different choices of starting Mach number, and shows that a given level of SPL input increases the Mach number only slightly for an initial $M_1 = 0.22$, but quite significantly for $M_1 = 0.34$. Also, note that the temperature contours bend over in the direction of increasing Mach number, indicating that more power can be added without further increasing the stream exit temperature for cases of higher starting M_1 and therefore largely extended M_2. The degree to which SPL can be increased without penalty with increasing Mach number is illustrated by the horizontal arrows in Figure 6B.3. For example, if one chooses $M_1 = 0.22$, the SPL = 250 kW lb^{-1} sec^{-1} may in fact be raised up to APL = 312 kW lb^{-1} sec^{-1} without exceeding 550 K. However, if one chooses $M_1 = 0.31$, then SPL = 350 kW lb^{-1} sec^{-1} can be further increased to 427 kW lb^{-1} sec^{-1} (this represents an excellent design choice).

Finally, let us plot the parameter ratios that are critical to laser performance along the direction of flow (Figure 6B.4). Specifically, we look at the exit end to input end ratios of pressure density and temperature. Here the cavity length has been normalized such that the Mach number reaches $1/\sqrt{\gamma}$ at the exit point. Most interestingly, we note that the gas density falls by a factor of 3 across the cavity, whereas the pressure has fallen nearly by a factor of 2.

Several concerns now come to mind: (1) How will this affect the uniformity of power loading along the cavity? and (2) What effect does the substantial density gradient and velocity gradient have on the laser beam?

Fortunately, despite the substantial axial density gradient, the SPL spatial deposition remains nearly constant over the full distance of flow for continuous, internally sustained, or "glow" discharges. This also holds true for transverse-cavity lasers, as long as the discharge current and direction of flow are aligned. This is because the $\vec{E}$-field gradient automatically

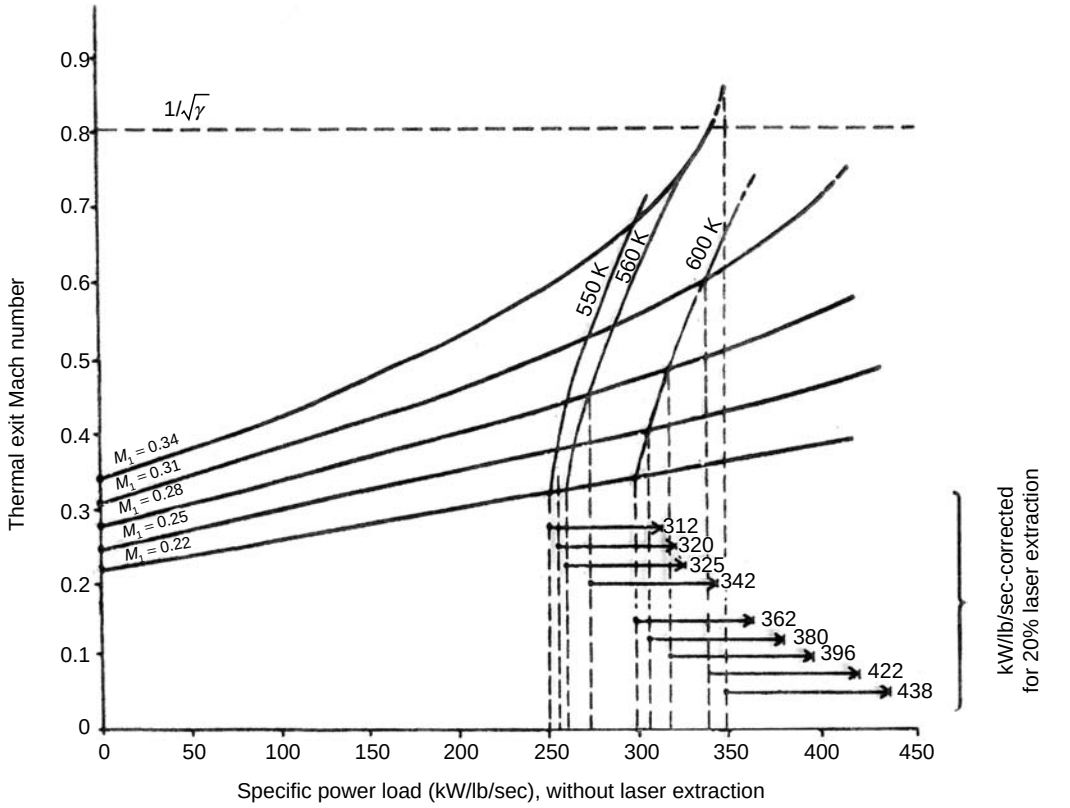

FIGURE 6B.3 Temperature vs. Mach number.

adjusts with pressure changes to sustain a balance between ionization production and ionization loss mechanisms. However, most of the very high-power lasers use externally sustained plasma generation and control. In this case, continuous will not maintain spatially uniform plasma control.

How the density gradient affects the beam depends on whether it is extracted along the direction of flow or transverse to the direction of flow. If all the three axes are collinear, then the density gradient is primarily along the optical axis, so that there is no pronounced index of refraction gradient $\vec{\nabla} n_R$ along the axis. However, in the case of slow-flowing or small tube diameter lasers, there may be an azimuthally symmetrical radial gradient of $\vec{\nabla} n_R$, where the resulting aberrations may be corrected by means of inserting a ZnSe lens into the cavity or by correcting a cavity mirror. Given a properly controlled plasma, there should not be an optical aberration problem that cannot be corrected for the case of a coaxial fast-flowing laser.

However, when the optical cavity is transverse to the flow, a substantial Doppler shift spread in frequency occurs, which is caused by the oscillator beam traveling both forward and backward along the direction of gas flow. This is not important for most applications that require very high-power CO_2 lasers. In these lasers, beam quality and far-field brightness generally are most important. When the resonator is transverse with respect to flow, the Doppler shift problem disappears, but beam quality may be severely affected for the case of transverse-flowing continuous lasers. Now the density gradients, and correspondingly the index gradient $\vec{\nabla} n_R$, lie across the beam, which causes it to bend. In addition, there are further SPL power deposition uniformity issues.

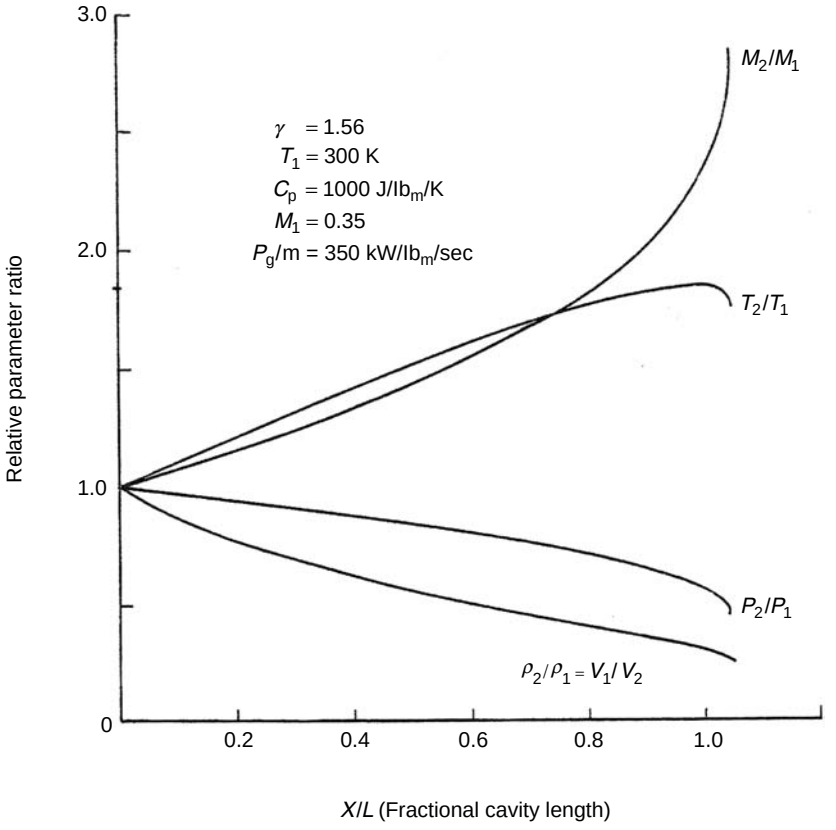

FIGURE 6B.4 Density, velocity, and temperature increase caused by Rayleigh heat addition.

6B.2.6 Optimal Cavity Design

Let us break out the laser efficiency η_L into five factors:

$$\eta_L = \eta_e \eta_q \eta_p \eta_{sat} \eta_{opt}, \tag{6B.31}$$

where η_e is the electrical transfer efficiency; η_q is the quantum efficiency = 0.41; η_p is the optical packing fraction, which for fast-flowing continuous lasers is essentially unity due to convection; η_{sat} is the saturation efficiency, or fraction of the kinetic stored energy transferred to the beam; and η_{opt} is the resonator or extraction efficiency. The quantity η_e depends on the gas mixture and on the reduced electric field, E/N, or its equivalent, E/P = volts/cm-amagat (1 amagat = 1 atm, STP pressure). (Later it will be shown that for the case of a glow- or self-sustained discharge, the E/N is clamped to a fixed number that depends only on the gas mixture.) For typical helium-rich mixtures used in fast-flow CW lasers, $E/P \approx 4600$ V/cm-A, and $n_e = 0.80$ to 0.87. The factor η_e can be increased for the case where E/P can be made lower using non-self-sustained discharges.

The extraction efficiency can be calculated from the cavity optics

$$\eta_{opt} = 1 - \frac{a_1 + a_2 + d_1 + d_2}{1 - r_1}, \tag{6B.32}$$

where a_1, a_2, d_1, and d_2 are the reflection, diffraction, and absorption losses for the cavity optics 1 and 2, respectively, r_1 is the reflection of the output coupler, and L is the cavity length.

During laser extraction, the fraction of power input imparted to gas heating is ξ

$$\xi = 1 - \eta_L\left(1 + \frac{a_1 + a_2 + d_1 + d_2}{1 - r_1 + a_1 + a_2 + d_1 + d_2}\right). \tag{6B.33}$$

When laser extraction is included, the gas temperature T_g reaches its maximum at the point $M = 1/\sqrt{\gamma}$. Then

$$T_{g\max} = T_i + \frac{P_{in}}{\dot{m}C_p}\xi = T_i + \frac{SPL}{C_p}\xi, \tag{6B.34}$$

where SPL is the total power input per kilogram into the gas and T_i is the initial incoming gas temperature.

If laser extraction can be made very efficient, and if gas expansion effects are fully used, then SPL can be markedly increased without further raising T_g since the laser beam removes a significant fraction of the electrical input power. Then α_o and hence power and efficiency are raised correspondingly.

Depending on how hard SPL is pushed toward its limit set to thermal bottlenecking, the gain distribution changes markedly along the flow direction. Available power is proportional to $\int \alpha_{o(l)}\mathrm{d}l$, and peaks when $\langle\alpha_o l\rangle$ is maximum, even though α_o may drop below the axis near the exit end.

Let us express the gain in terms of physical parameters that the designer can adjust. For steady-state operation the gain α_o at a point l along the tube of total length L is

$$\alpha_{o(l)} = \sigma N_o\left[[1 - \exp(-r_d t)]\frac{r_p}{r_d} - \exp\left(-\frac{E_{(01^10)}}{K\left(T_i + \frac{SPL\xi}{C_p}\frac{l}{L}\right)}\right)\right], \tag{6B.35}$$

where r_p and r_d are the CO_2 (001) pump and deactivation rates, respectively, and $E_{(010)}$ is the CO_2 (010) vibrational energy. Next, let us drop the initial transient term $[1 - \exp(-r_d t)] \to 1$, and we recognize that r_p is proportional to SPL; i.e., $r_p = \gamma \times \mathrm{SPL}$. Finally, to the first approximation we neglect the temperature dependence of r_d. Then,

$$\alpha_{o(l)} \cong \frac{A \times SPL}{L} - B\exp\left(-\frac{E_{(01^10)}}{K\left(T_i + \frac{SPL\xi}{C_p}\frac{l}{L}\right)}\right), \tag{6B.36}$$

where the nearly constant terms have been lumped together according to

$$A = \frac{\sigma N_o \gamma L}{r_d};\ B = \sigma N_o \tag{6B.37}$$

and, we seek $\langle\alpha_o L\rangle$ which is needed to determine the cavity optic parameters, I_s and finally η_i

$$\langle\alpha_o L\rangle \cong A \times SPL - B\int_o^L \exp\left[-\frac{E_{(01^10)}}{K\left(T_1 - \frac{SPL\xi}{C_p}\frac{l}{L}\right)}\right]\mathrm{d}l. \tag{6B.38}$$

The constants $\mathcal{A}$ and $\mathcal{B}$ (and also I_{sat}) may be calculated from the kinetic theory. Or, if the laser exists, $\mathcal{A}$ and $\mathcal{B}$ can be experimentally determined by measuring the SPL required to attain laser threshold using two output couplers of two different reflectivities. $\mathcal{A}$ is determined from a threshold power measurement using a high reflectance coupler such that the SPL pump power is low and the Boltzmann term becomes $\exp\left(-E_{(01^10)}/KT\right)$. Hence at threshold, and according to Rigrod analysis if,

$$\langle \alpha_o L \rangle = \int_o^L \alpha_{o(l)} dl = LA \times SPL - B \exp\left(-\frac{E_{(01^10)}}{KT_i}\right), \tag{6B.39}$$

then,

$$\langle \alpha_o L \rangle = \frac{1}{2} \log\left[\frac{1}{r_1 - \sum_i (a_i + d_i)}\right]. \tag{6B.40}$$

Next, a low-reflectance coupler is used so that the laser is substantially thermally bottlenecked; i.e., SPL is large and the laser is substantially bottlenecked at the threshold lasing condition. Now B can be determined from

$$L \times A \times SPL_2 - B \exp\left(-\frac{E_{(010)}}{K\left(T_i + \frac{SPL\xi}{C_p}\frac{l}{L}\right)}\right) = \frac{1}{2} \log\left[\frac{1}{r_2 - \sum_i (a_i + d_i)}\right], \tag{6B.41}$$

where the value of $\mathcal{A}$ obtained from Equation 6B.37 is inserted into Equation 6B.41 and $\xi = 1$ since threshold conditions prevail.

Alternative to solving for $\mathcal{A}$ and $\mathcal{B}$ as described, we could have solved for $\langle \alpha_o L \rangle$ directly by means of determining SPL input needed to achieve threshold oscillation using two output couplers of markedly different reflectivities. Then Equation 6B.42 is written for each case and then the two equations are solved for $\langle \alpha_o L \rangle$. This is the easiest method to use when dealing with lasers at this current level of sophistication. However, as we progress to higher powers, other phenomenon (e.g., mode media interaction) will set in. At that point, a detailed knowledge of spatially dependent saturation effects proves critical.

With the discussions established earlier, we determine I_{cav}/I_{sat} using Rigrod's equation:

$$\frac{I_{cav}}{I_{sat}} = \frac{t_c\sqrt{1 - (a_1 + a_{2)})} \times \langle \alpha_o L \rangle + \ln\left(\sqrt{1 - (a_1 + a_2)} \times \sqrt{1 - ((a_1 + a_2) - t_c}\right)}{\sqrt{1 - (a_1 + a_2)} \times (a_1 + a_2 + t_c) + (a_1 + a_2)\left(\sqrt{1 - (a_1 + a_2)} - t_c\right)}, \tag{6B.42}$$

where a_1 and a_2 are the cavity mirror and output coupler absorption, and t_c is the output coupler transmission.

And finally $I_{cav(l)}/I_{sat}$ may be inserted into

$$\eta_{ext} = \frac{\int dl \iint dA \left[\frac{\alpha_a I_{sat}}{1 + \frac{2I_{cav(l)}}{I_{sat}}}\right]}{\iiint \alpha_o I_{sat} dV} \tag{6B.43}$$

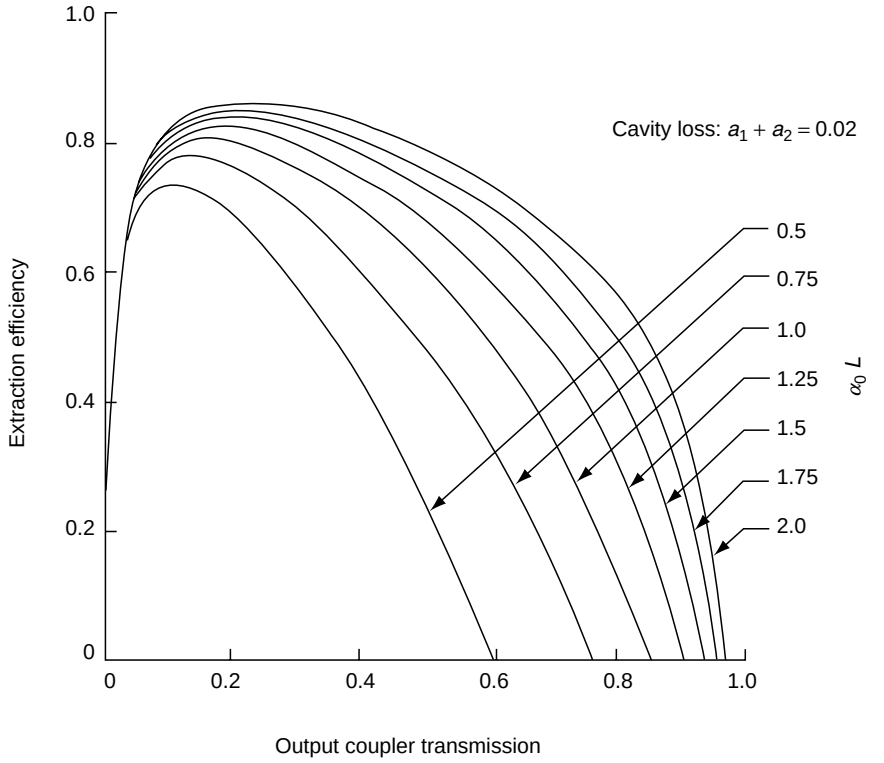

FIGURE 6B.5 Resonator design curves.

or

$$\eta_{\text{ext}} = \frac{1}{V} \int \mathrm{d}l \iint \mathrm{d}A \left[\frac{1}{1 + \frac{2I_{(l)}}{I_{\text{sat}}}} \right] \tag{6B.44}$$

for the case of uniform media. From Equation 6B.44, we note that η_{ext} does not contain α_o, and in fact both I_{sat} and η_{ext} depend only on the gas composition and pressure.

A family of solutions to Equation 6B.42 and Equation 6B.44 is presented in Figure 6B.5, which plots extraction efficiency (η_{ext}) vs. output coupler transmission (t_c) for a range of $\langle \alpha_o L \rangle$ values. These curves form the basis for designing an optimum resonator.

6B.2.7 Cavity Design Examples Pertaining to Continuous Transsonic Flow Axial Lasers

Two examples are given. The first illustrates a closed-cycle design that relies on driving the gain media at extremely high SPL levels to achieve compact operation, whereas achieving high power at high efficiency. The gain region occupies a 10 cm diameter by 75 cm long tube and operates at 40 torr. Given an SPL input of 770 kW kg^{-1} sec^{-1}, it produces 6 kW at 23.5% laser efficiency. And, given an input of 990 kW kg^{-1} sec^{-1}, it produces 7.5 kW at 22% efficiency, as shown in Figure 6B.6.

How is it possible to achieve such performance levels commensurate with an SPL input that seemingly should have bottlenecked the laser? The gain $\alpha_{o(l)}$ and the gain length product

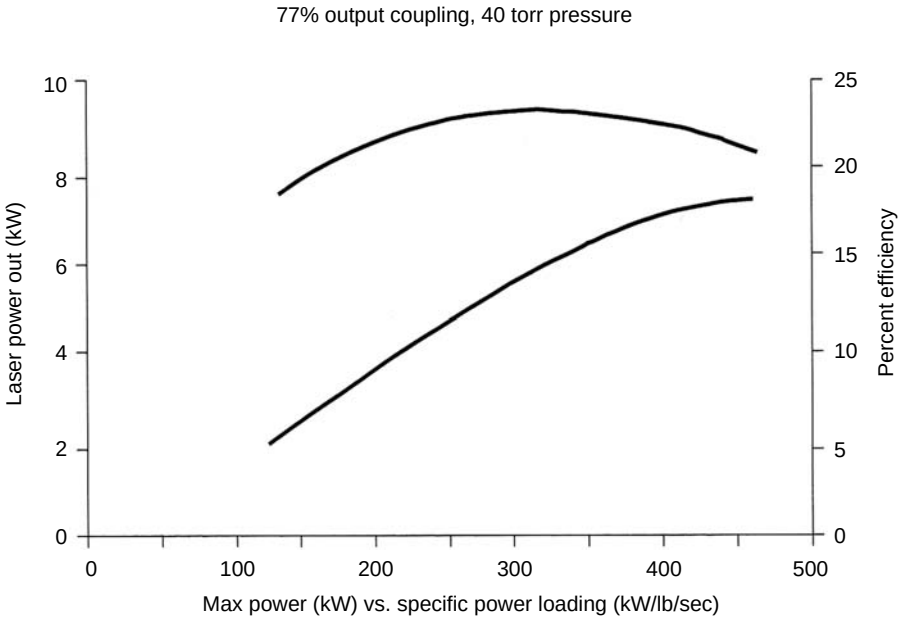

FIGURE 6B.6 Power and efficiency vs. SPL for controlled turbulence stabilized, 10 cm diameter × 75 cm axial flow laser.

$\int_o^L \alpha_{o(l)} dl$ are plotted vs. l using Equation 6B.36 through Equation 6B.38. From Equation 6B.38 we note that because SPL is much higher than normal (974 kW kg^{-1} sec^{-1}), α_o at the entrance is also much higher than normal ($\alpha_o = 0.033$). Thermal bottlenecking does indeed drive the gain negative before reaching the end of the tube; however, the integrated gain length produced continues to grow until it peaks at the distance of 70 cm. So $\langle \alpha_o L \rangle = \int_0^{70cm} \alpha_{o(l)} dl = 1.41$, and the output coupler's reflectance is 0.77. Applying these values to the extraction efficiency curves of Figure 6B.5, we determine $\eta_{ext} \approx 0.8$. Next, using resonator losses $a_1 + a_2 = 0.02$, $d_1 + d_2 = 0.02$, and $r = 0.77$ from Equation 6B.32, we determine $\eta_{opt} \approx 0.88$. Finally, from Equation 6B.31 we calculate the laser efficiency as

$$\eta_L = \eta_e \eta_q \eta_p \eta_{sat} \eta_{opt} \cong (0.8)(0.41)(1.0)(0.8)(0.88) = 0.23,$$

which almost perfectly agrees with the experimentally measured value. Because η_L is so large, it would appear that the larger than normal SPL input contributed little impact due to thermal bottlenecking.

So let us confirm what level of gas heating has occurred. From Equation 6B.33, we determine $\xi = 0.73$; though 25.5 kW is applied, only 18.6 kW goes into heating the 0.0273 kg sec^{-1} flow stream, which raises the gas temperature T_{02} from 283 K up to 593 K at the exit of the gain region. For this design, the flow enters at Mach $M_1 = 0.25$ and exits at $M_2 = 0.6$. (Lower Mach numbers are used for closed-cycle configuration to reduce the pressure drop ΔP and to cut the cost of recirculating pump power.) Then from Equation 6B.27, we determine that the 593 K exit stagnation temperature gets reduced by gas dynamic expansion to the flow stream temperature $T_2 \approx 500$ K, or 270°C. So the gas temperature does rise just beyond the brink of bottlenecking, at the point (70 cm) where Figure 6B.7 shows that α_o dips negative.

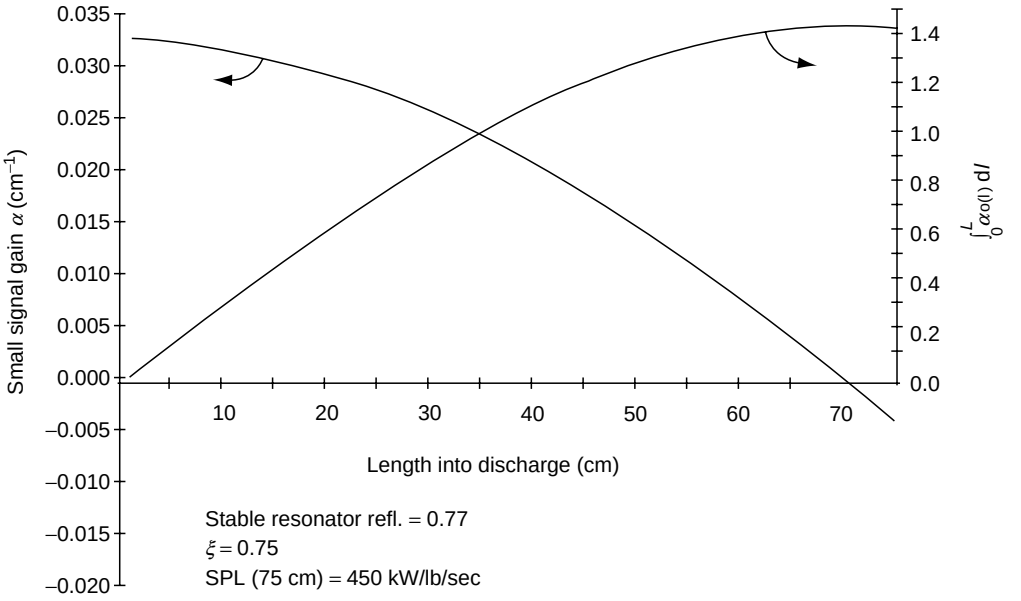

FIGURE 6B.7 Variation of α_o and $\int_o^L \alpha_{o(l)} dl$ vs. position along flow stream, operating at near optimal conditions.

This is consistent with our optimized performance expectations. The laser of this example was developed at Plasmatronics by the author in 1986, in response to an industry-driven set of requirements. Small size, low cost, and closed-cycle gas recirculation with relative ease were the primary considerations.

In our next example, the laser was developed by the author and his colleagues to serve in a military testing laboratory environment at Kirtland Air Force Base. In this case, high-power output was most important, and the laser needed to remain on for only 15 sec bursts. Cost was not a major issue and open-cycle operation was acceptable. The emergent gas was dumped into an evacuated 32 ft in diameter tank. The laser consists of two back-to-back, 10 cm in diameter axial flow tubes that have a total active gain path length of 1.54 m. The flow streams meet at the center as each stream exits at $M_2 = 1$, then turn outward and exit radially. The laser nominally generates 15.4 kW, CW at 26.5% efficiency, but a variation on its design could operate at $\eta_L = 31\%$. This laser was put into service in 1971. Within a few years of its completion, an up-scaled laser of this same design (called LHMEL) went into service at Wright Patterson Air Force Base. LHMEL consists of four sections instead of one section as described here, and its tube diameters are 15 cm instead of 10 cm. It sustains ~165 kW continuous for 30 sec bursts. It remains operational to this day.

Let us examine salient design features of the LHMEL laser. To begin, any time an open cycle configuration can be used, it is optimal to exit a longitudinal flow tube at $M_2 = 1$. Then the most important driving factor will depend on the capability of the chosen discharge method to uniformly excite larger volume flow streams at relatively high pressures to the requisite SPL levels. The longer gain path length (compared with the previous laser) allows a reduction in α_o ($\alpha_o = 0.01$) and therefore a reduction in SPL (now 880 kJ kg^{-1}, down by 10%). Moreover, the choice of a Mach 1 exit point further lowers $T_{g(max)}$. Finally, the attainment of a larger η_L lowers that fraction of SPL, which contributes to heat. The net effect is that α_o remains net positive over the entire length of the tube, and therefore η_L is increased.

Given the choice that 300 to 350 kW lb^{-1} sec^{-1} SPL has been selected, and referring to Figure 6B.2 we note that the resulting entrance Mach number is $M = 0.35$. This is fortuitous because flow expansion, and therefore gas cooling, sets in at $M = 0.35$.

6B.2.8 Some Pressure Scaling Considerations

The designer must initially chose a pressure range, and this choice determines power density. In turn, the optics and their dielectric coatings are damaged above some threshold power density, and therefore the cavity flux must remain safely below this level. For the case of typical CW laser gas mixes, such as $CO_2/N_2/He = 1/4/12$

$$I_{sat} \cong 500{,}000\left(\frac{P_{(torr)}}{760}\right)^2, \tag{6B.45}$$

that is, $I_{sat} \approx 500$ kW cm^{-2} at 1 atm. Furthermore, in order to nearly saturate the gain media; e.g., make η_{ext} near unity, the circulating flux must be made much higher than I_{sat}. Whether short pulse or long pulse, high rep rate lasers generally operate at or near 1 atm pressure but can tolerate these enormous pulsed flux levels. By comparison, mirror flux level for CW lasers must be much lower.

Yet, we continue to strive to scale continuous lasers to reach the highest power levels possible and to make them compact. Water-cooled optics can, at great cost, be capable of sustaining flux levels approximately 50,000 W cm^{-2}. Then, I_{sat} should perhaps be about 5000 to 10,000 W cm^{-2}, and correspondingly, cavity pressures about 100 to 125 torr should be considered for continuous CO_2 gain media. Then great care must be taken to maximize the product $\eta_{ext} \times \eta_{opt}$ such that the media is as saturated as possible without destroying the optics.

6B.2.9 Production and Control of Very Uniform, Large-Volume, High-Pressure Plasmas with Large Specific Power Input

In the foregoing section, we discussed the physics and optimization of fast axial lasers, then gave examples of several somewhat scaled-up devices in terms of their plasma volumes operating pressures, and rather formidable SPLs. In addition, it was acknowledged that none of this would work without invoking some mastery of the "care and feeding" of plasmas.

Therefore, we now pick up the story of the next major development: the generation and control of the plasma media that is well suited for laser applications. We begin this discussion by again considering slow-flow, wall-diffusion, cooled lasers of the Harrigan–Whitehouse variety.

Recall that these lasers did not scale by increasing either the pressure or the plasma tube diameter. However, this was not the only problem. Even if there had been no thermal bottlenecking limit, their plasmas could not have sustained an increase in diameter without decreasing their pressure. If this were attempted, the glow discharge would have collapsed into an arc. Recall that a glow discharge sustains a precarious balance between electron–ion pairs created by means of volume avalanche ionization and electron ion pairs lost to volume recombination, attachment, and wall diffusion. For this case, the ionization rate equation takes its simplest form

$$\frac{dn_s}{dt} = \left(\frac{\alpha_i}{N}\right)\vec{v}_d n_e - \left[\left(\frac{\alpha_a}{N}\right)\vec{v}_d n_e + D_a \nabla^2 n_e\right], \tag{6B.46}$$

where n_e is the electron density, v_d is the electron drift velocity, α_i is the ionization rate, α_a is the electron attachment coefficient, N is the number density, and D_a is the ambipolar diffusion constant. In steady state, $dn_e/dt = 0$, so that the rate of ionization is exactly matched by the loss of ionization to attachment and diffusion to the wall

$$\frac{\alpha_i}{N} = \frac{\alpha_i}{N} + \frac{1}{n_e v_d} D_a \nabla^2 n_e \tag{6B.47}$$

For a tube of radius R and length L, we approximate

$$D_a \nabla^2 n_e \cong \frac{D_a n}{\lambda^2}, \quad \text{where} \quad \frac{1}{\lambda^2} = \left(\frac{\pi}{L}\right)^2 + \left(\frac{2.405}{R}\right)^2 \tag{6B.48}$$

which arises from the Bessel function solution for $\nabla^2 n_e$ in cylindrical geometry. Consequently, the spatial distribution for the plasma has a significant Bessel function like spatial distribution, which peaks in the center and falls off to zero at the walls. This same spatial profile is reinforced by heat flow, as evidenced by the spatial component of Equation 6B.6, a Bessel function solution to the heat flow Equation 6B.5.

Let us now explore the role that diffusion plays regarding plasma stability. Wherever a concentration of ions exist, there will be a flow of ions from regions of higher concentration to regions of lower concentration. In addition, as negative ions flow more rapidly than positive ions, there will initially exist a net positive charge in the center of the tube. The space charge slows down negative ion diffusion and speeds up positive ion diffusion owing to the resultant electric field established. In equilibrium, equal quantities of positive and negative charges will be lost to the walls. Thus, wall diffusion plays a critical role in maintaining balance in Equation 6B.46, and in helping to spread the plasma column. Moreover, in a manner analogous to heat flow, the diffusion loss mechanism is reduced by the square of the tube diameter and linearly by an increase in pressure. So this time the plasma stability issues forbid an increase in tube diameter without making a corresponding reduction in pressure; i.e., again the d^2P product cannot exceed a fixed level. In practice, given typical CW laser mixtures (which consist mostly of helium), a combination of 5 cm diameter tube and 15 torr total pressure approximately characterizes this limitation. However, the thermal power deposition problem has been conquered by means of fast flow streams. Next, we must conquer the volume, pressure, or SPL power deposition problem. Interestingly, one solution to the problem is derived by means of mechanically manipulating the flow stream. Thus follows the next facet of our story.

We begin by introducing a plasma column into a large (15 cm diameter) bore tube through which a typical laser gas mixture is flowing at elevated pressure and at relatively high velocity—perhaps 100 $msec^{-1}$ or $M \approx 0.2$. Figure 6B.8 depicts this actual experiment. The flow transit time is orders of magnitude shorter than the wall diffusion time constant for the case of slow flow, so there is no charge neutralization at the wall, yet there is a stable plasma column as long as the SPL pump is kept below a critical level. Stability is primarily possible without walls and at extended pressure ($P \approx 40$ torr) because gas is swept through the tube before its internal temperature becomes excessive, which would in turn lower its density and raise the E/P to the point where the glow to arc transition occurs. Although the walls no longer play a role in stabilizing the plasma, thermal diffusion does, so the plasma's spatial distribution remains much the same—hot in the center, growing cold toward its outer diameter. Its shape and extent are now controlled by two opposing physical mechanisms. Because the temperature is highest in the center, the E/P value there is highest, so the ionization rate is highest, and plasma heating is increased. At this point total collapse of

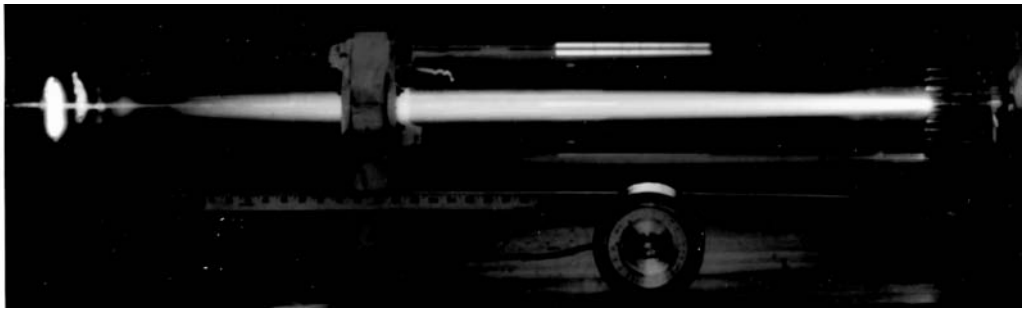

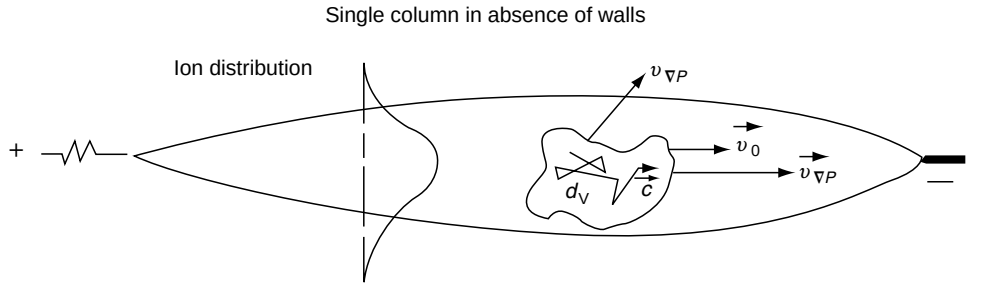

FIGURE 6B.8 Radial spread of a single plasma column in a high-speed axial flow stream.

the glow state into an arc would occur, except that diffusion compensates, driving the plasma radially outward with a force that grows stronger in opposition to an increased thermal collapse. The plasma diameter is established at the point where these two opposing forces come into equilibrium. Given a particular temperature, the diameter scales proportional to $1/P^2$, but again also depends on the gas composition. We note in Figure 6B.8 that the plasma's diameter increases along the direction of flow. This happens because its temperature continues to rise and its pressure lowers as energy is continuously added to the flow stream.

Figure 6B.9 illustrates how two adjacent plasma channels interact within a fast flow stream. The diffusion time constant is on the order of $d^2/\bar{\lambda}\bar{c}$, where $\bar{\lambda}$ is the mean free path which is inversely proportional to the pressure P. So, if we space the plasmas a distance L apart in a flow stream, which exits at velocity v such that $l/\vec{v} < d^2/\bar{\lambda}t$, then the two columns will not be driven together by forces resulting from the thermal gradient.

This suggested a reasonable first approach toward filling large volumes with plasma in the presence of high-pressure, high-velocity flow streams. Figure 6B.9 shows an experimental verification of this kind of volume filling. The device depicted occupies a plasma volume 2.5 cm deep $\times$ 7.5 cm across $\times$ 7.5 cm along the direction of flow. It was lased transverse to the direction of flow, and it produced ~150 W, whereas a somewhat larger version measuring $2.5 \times 15 \times 15$ cm produced 600 W. Historically, these may have been the first fast-flow transverse laser. At about the same time, William Tiffany and colleagues built a 1 m wide, closed cycle laser that produced ~1200 W.[7]

The problem with these early efforts was twofold. First, they could not achieve nearly the SPL needed to deliver high power and high efficiency. Second, their discharges were

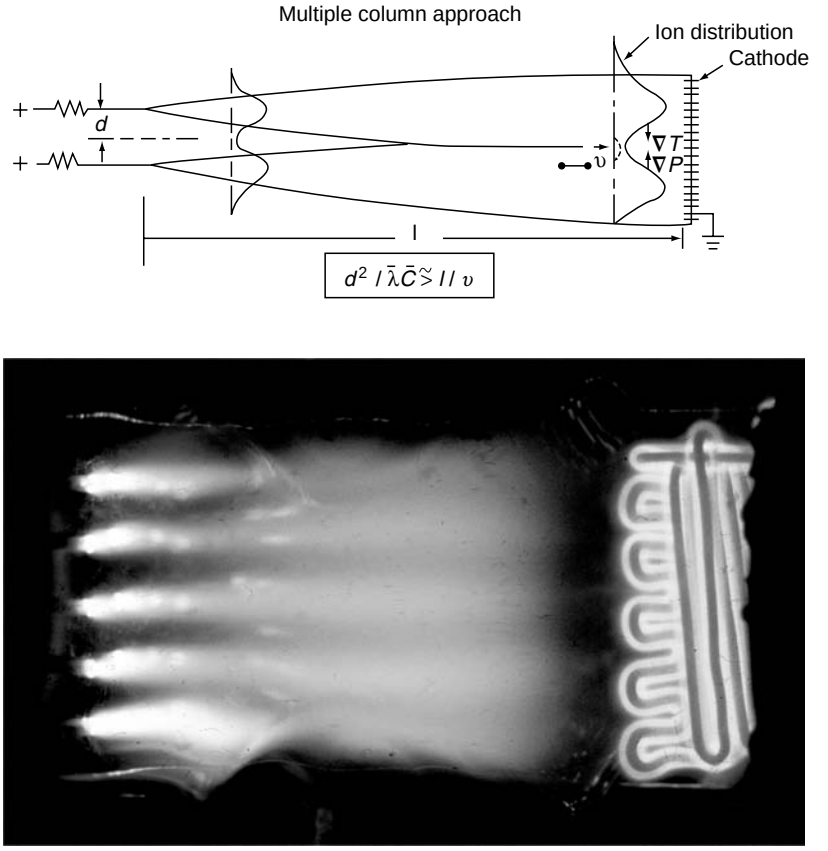

FIGURE 6B.9 Merger of multiple plasma columns in a high-speed axial flow stream.

segmented rather than homogeneous. The temperature gradients produce density gradients, which in turn produce index of refraction gradients. Therefore, for the case of segmented or otherwise filamented plasma gain media, high-quality beam extraction was no longer viable above perhaps 5 kW, CW. Both SPL and plasma gain media homogeneity difficulties resulted in a process referred to as the "Controlled Turbulence Stabilization," invented by the author in 1971.[8,9]

Let us now examine how this process stabilizes the plasma. In essence, an initially uniform continuous plasma density is to be created, then "frozen" in a nonsteady state, stable mode by means of applying aerodynamics in a fast flow stream, as suggested by Newton's second law, and resulting Ohm's law for the flow stream. Specifically, for electrons and ions in a flow stream with velocity ν, in the direction of ion conduction:

$$\rho_{e,i}\frac{dv_{e,i}}{dT} = -\vec{\nabla}P_{e,i} \pm ne\left(\vec{E} + \frac{1}{C}\vec{v}_{e,i} \times \vec{B}\right) - \frac{nm_{e,i}\vec{v}_{e,i}}{t} + \rho_{e,i}g \tag{6B.49}$$

leads to

$$\vec{J}_- = \sigma_e\left(\vec{E} - \frac{1}{n_e e}\vec{\nabla}P\right) = \sigma_e\left(\vec{E} - \vec{E}_{Pe}\right) \quad \text{for electrons} \tag{6B.50}$$

and

$$\vec{J}_+ = \sigma_e\left[\vec{E} + \frac{1}{n_e e}\left(\vec{\nabla}P_g - \rho_i \frac{dv_i}{dt}\right)\right] = \sigma_i\left(\vec{E} - \vec{E}_{Pg}\right) \quad \text{for ions.} \tag{6B.51}$$

Here J_- and J_+ are the electron and ion current densities, respectively; $\sigma_{e,i}$ is the electron or ion conductivity, respectively, where

$$\sigma_{e,i} = \frac{n_e e^2 t_{e,i}}{M_{e,i}},$$

where η is the electron number density, $\rho_{e,i}$ is the electron or ion mass density, respectively; e is the electron charge; $\vec{\nabla}P_{e,i}$ is the electron or gas pressure gradient, respectively; and $t_{e,i}$ is the electron or ion mean collision time with neutrals; and g is the gravitational constant. It is apparent that the pressure gradient terms in each Ohm's law are equivalent to additional electric fields $\vec{E}_{Pe}$ and $\vec{E}_{Pg}$. The electrons travel upstream with a drift velocity of 500 m sec^{-1}, and $\frac{1}{n_e e}\vec{\nabla}P_e \ll \vec{E}$. However, the electron and ion spatial distributions maintain charge neutrality, whereas for ions $(1/n_e e)\vec{\nabla}P_g = 250\,\text{kV/m}$ when $n_e = 5 \times 10^{10}$ electrons cm^{-3} and $\vec{\nabla}P_g = 15\,\text{torr/m}$. Of course, electrons quickly arrange their spatial distribution to nullify the ionic $\vec{E}$-field. This implies that ion spatial distribution and therefore electron spatial distribution are largely affected and can be controlled by aerodynamic forces.

The first implementation controlled aerodynamic stabilization is shown in Figure 6B.10. Rods are placed upstream of the anodes, where vortices are shed around each anode to rapidly diffuse the plasma, thus minimizing thermal gradients. A nozzle array placed down stream of the anodes drives the turbulated plasma stream supersonic, and then shocks it back to subsonic. The nozzles are nonconducting so that individual plasmas are isolated during mixing. The shock front breaks large amplitude, low-frequency turbules into small amplitude, high-frequency turbules, so that on subsequent merger of the individual plasmas, a single, homogeneous, large-volume plasma is produced. If still further plasma homogeneity is required, a fine mesh screen may be placed across the exits of the nozzle array. The screen can be made of conducting mesh as long as it is aligned directly along an $\vec{E}$-field contour line, such that the differences in potential gradient are made less than the gradient needed to extract electrons from the mesh.

With refined spatial homogeneity, the internal $\vec{\nabla}P$, $\vec{\nabla}\rho$, $\vec{\nabla}T$, and $\vec{\nabla}n_e$ have been reduced to microscopic proportions as the plasma enters the gain region. Those tiny perturbations that do remain can, and eventually will, grow into thermal instabilities, given sufficient time and SPL input power. Depending on pressure, mix, SPL, and the particular design of the controlled turbulence generator, growth instability time will vary, and the designer must insure that the plasma passes through or across its discharge volume in a sufficiently short time. At transsonic velocities, the plasma typically crosses a 1 m channel in less than 3 msec—a condition that generally proves adequate.

The occurrence of the shock proved to be essential for operation at extended pressure, or $\dot{m}$, as shown by the following experiment. Here a rectangular channel of dimensions 5×9 cm^2 cross section by 100 cm in the flow direction was used to evaluate the role of the turbulator

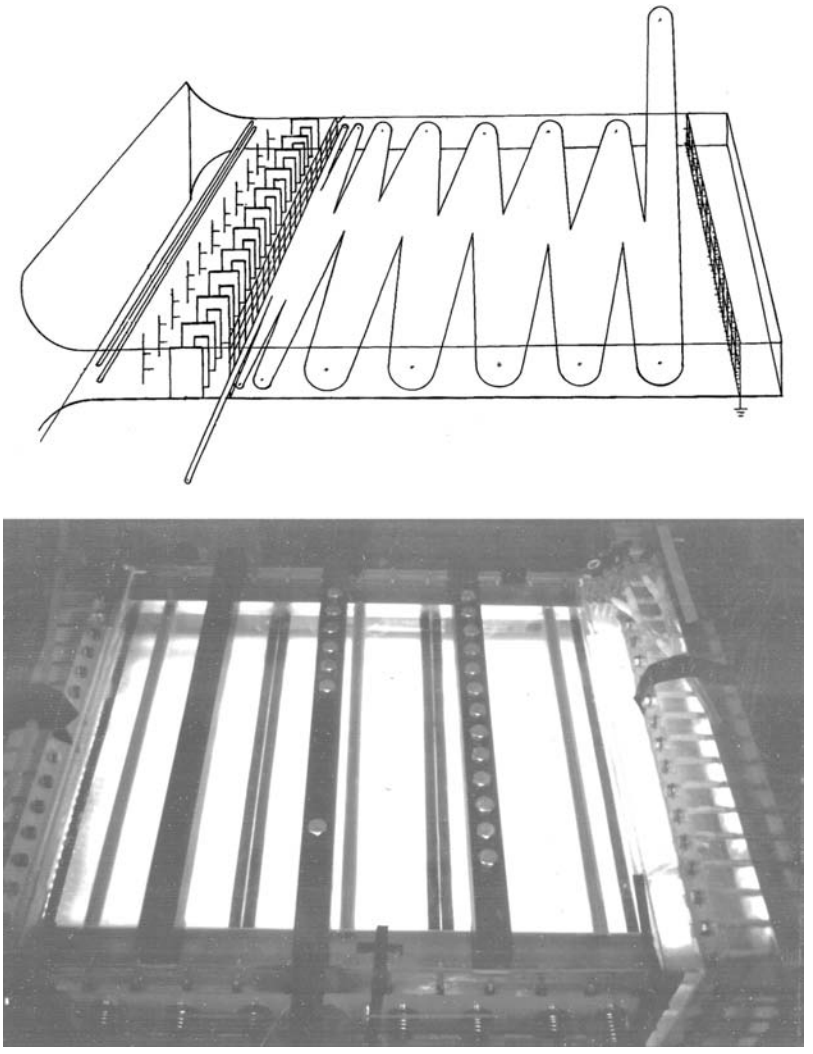

FIGURE 6B.10 (**See color insert following page 336**.) Electro-aerodynamic laser (EAL) geometry and plasma filling, which produces 20 kW of laser power.

device. It could be pumped at 2700 cfm for which case a shock always occurs, or at 2049 cfm, for which case a shock never occurs. Figure 6B.11 displays two maximum stable, SPL loading curves vs. pressure for the cases of shocked vs. nonshocked operation. Both curves indicate an acceptable SPL input at 40 torr operation. For the case of shocked flow, a constant SPL input (270 kW $lb^{-1}sec^{-1}$) can be maintained with stability with increasing pressure, from 40 to 150 torr. However, for the case where no shock occurs, there is no increase of power with increase in pressure.

6B.2.10 First 20 KW Class Compact Laser

A $5 \times 75 \times 100$ cm amplifier incorporating the turbulence stabilization structure shown in Figure 6B.10 produced 20 kW, single mode continuous power in closed cycle, master oscillator power amplifier (MOPA) configuration.[9,10] Its striking plasma uniformity is

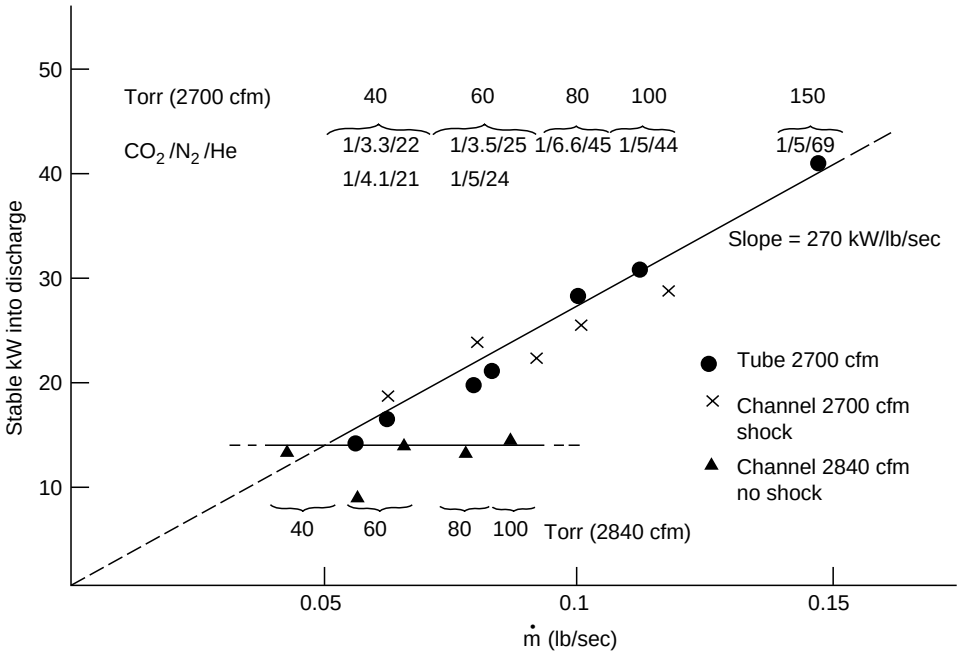

FIGURE 6B.11 Controlled turbulence stabilized plasma pressure scalability, with shock wave and without shock wave.

visually apparent in Figure 6B.10. The device, called the EAL (electro-aerodynamic laser), was developed by the author at Kirtland Air Force Base and installed at Wright Patterson Air Force Base 1971. This laser was a forerunner to the LHMEL laser previously described. This amplifier was driven by a 500 W, single-mode oscillator. The beam expanded from 0.5 cm to 5 cm diameter whereas making five, 80 cm transverse passes across the amplifier, then making 12 more columnated traverse passes as it "walked" across the 1 m long amplifier channel. Its SPL was held at 250 kW lb^{-1} mass to maintain its peak gain value over the entire channel length. Later in 1973, Tony DeMaria and Jack Davis at United Aircraft constructed a similar, but somewhat scaled-up, version of the EAL, which produced 27.2 kW.[11]

Immediately following its debut as a transverse laser stabilizer, the stabilizer apparatus was reconfigured to wrap coaxially around the front end of axial flow lasers, to inject turbulated plasma radially inward. The plasma was driven slightly supersonic, then shocked back to subsonic flow as it entered the tube at an oblique angle through a surrounding radial orifice. This stabilization method was implemented on all the axial flow lasers described previously, including the 150 kW LHMEL.

Despite its success as a provider of large volume plasmas, it also created a problem, namely, the pressure drop across the plasma increased. This is not a problem for open-cycle lasers, but it raises the cost of recirculating the gas back through the laser. Closed-cycle operation is preferred for continuously operating lasers because the cost of replenishing the gas (primarily helium) is nearly eliminated. Typically only 1% or less of the gas then needs to be replaced per pass instead of 100%. This 1% loss is caused by plasma-chemistry effects, the most prominent

problem is the loss of CO_2 to CO (see Plasma Chemistry discussion by Plinski and Abramski, this volume.) In addition, of course the primary reason for recirculating the gas is to remove the heat, which is accomplished by means of inserting a heat exchanger into the flow return path. Then the gas must be re-compressed sufficiently to overcome pressure losses, forcing the gas back through the laser. Typically, the additional heat introduced by the compressor must also be removed by passing the gas stream once more through a second heat exchanger.

There is an important class of low-power industrial lasers (<5 kW range) that pose very few design problems. These can operate in a transverse geometry where plasma uniformity is not critical, and flow velocities are <100 m sec^{-1}. Gas recirculation can be accomplished using low-pressure drop electric fans and so on.

However, in this section we deal with an extensive set of issues that occur primarily at higher power levels and particularly where beam quality or highly efficient operation is important. Therefore, with regard to these goals, the matter of pressure drop for closed-cycle operation remains paramount. Generally, these require Roots blowers or other clean pumps which can move large gas volumes at high pressures, and which can also develop relatively large compression ratios.

These factors suggested that a variation of the controlled turbulence technique was needed, wherein a positive pressure gain is produced across the generator instead of a pressure loss.[12] The revised turbulator incorporates ejector pumps. Both the recirculated gas stream and an additional plasma stream passes through an array of ejector pumps, which in addition to stabilizing the plasma, also serve as the primary recirculation pump. When used in an axial configuration, the closed-cycle recirculating gas is passed through a radially symmetric heat exchanger and gets returned coaxially over the plasma tube. This allows for extremely tight packaging. For example, Figure 6B.12 shows a compact ~20 kW class, axial laser that uses a single 15 cm diameter by 75 cm long plasma tube. This entire laser head, including the gas return loop and the heat exchanger, measures only ~50 cm diameter × 100 cm long.

A small fraction of the circulating gas (~20%) is removed from the central loop, compressed from 40 to ~200 torr, is then passed through a catalytic converter, and finally gets injected into the array or ejector pumps as shown in Figure 6B.12. Before injection, a helium plasma stream is premixed into the neutral gas, and then the neutral gas containing plasma is injected into the ejector pump at $M = 2$. As the injected plasma stream expands, it entrains the surrounding recirculated gas into an elongated, conically shaped, supersonic or subsonic boundary layer (see Figure 6B.12). Although crossing through this boundary layer, the plasma stream becomes highly turbulated, and is thus made homogeneous. The injected plasma flow stream spreads to completely fill the ejector pumps by the time the flow traverses their length. The fully mixed flow channels then radially coalesce into the axial discharge tube at $M \approx 0.35$. This method of turbulent stabilization is so effective that, even for pressures in excess of 50 torr, SPL can be raised well beyond the limits imposed by thermal bottlenecking. In fact, during testing, SPL was pushed to the point where the electrodes were melted, and even so, the discharge remained fully diffuse and streamer-free.

A regeneratively cooled 2000 cfm Roots pump was used to drive the ejectors, where the pump mass flow rate amounted to approximately one-fifth of the cavity mass flow rate. Furthermore, the 2000 cfm blower flow rate was leveraged by the ejector pumps to attain a cavity flow rate on the order of 10,000 cfm. The loop pressure drop made up by the ejector pump was $(P + \Delta P)/P \approx 1.18$. The remarkable plasma homogeneity of the 50 torr plasma can be seen in Figure 6B.12, where SPL = 1 MJ kg^{-1}. This device was developed at Plasmatronics

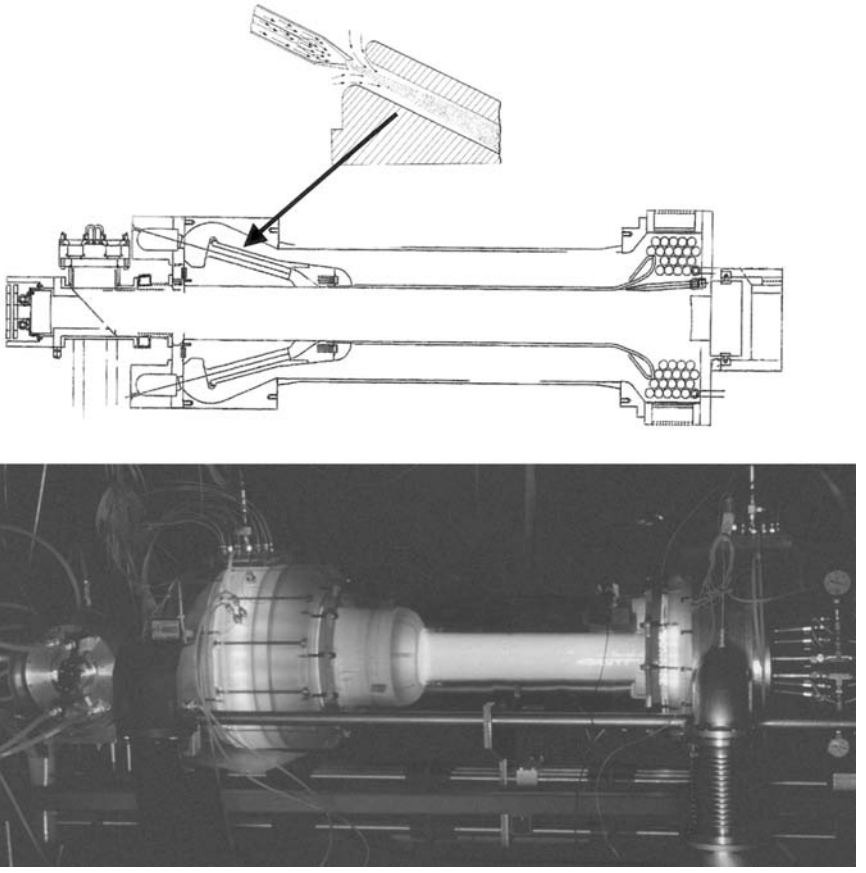

FIGURE 6B.12 (**See color insert following page 336**.) Upper diagram: ejector pumped, controlled avalanche stabilized laser. Lower diagram: closed-cycle, ejector pumped, stabilized laser with plasma characteristic of 20 kW laser extraction. The cavity, however, is blocked.

in Albuquerque, New Mexico in 1980.[12] A discussion of its laser characteristics resumes under the topic of mode-media interaction instabilities.

6B.2.11 Alternative Means of Large-Volume, High-Pressure Plasma Stabilization

Up to this point, we have been primarily discussing the self-sustained, or "ballasted glow" discharges and their application to medium high-power continuous lasers, which are quite inexpensive to implement. We now leave the self-sustained discharge category of lasers and instead pursue high-pressure, giant, pulsed-power lasers, or high repetition pulsed lasers capable of delivering high average power. These kinds of lasers again rely on uniform excitation of large volume plasma, but this time both pressure and plasma density can exceed that of earlier examples by orders of magnitude.

One of two opposite modes of *non*-self-sustained discharge may be used, depending on the power density and pulse length:

Case I: When very high output powers are required, lasting only a fraction of a microsecond or up to several microseconds, then a substantially overvolted (above-glow E/P), excitation-potential, short pulse is supplied. The plasma is very unstable but the discharge collapses before thermal instability drives the discharge into an arc condition. Such devices are generically referred to as "TEA lasers."
Case II. When a relatively long pulse (or repetition pulsed) lasting on the order of 20 microseconds/pulse, or when super high CW power (hundreds of kilowatts to megawatts) is desired, an undervolted (below-glow E/P) excitation potential is needed. The plasma usually remains stable continuously since there is no volume avalanche and since all the ionization is externally provided.

In turn, there are two important methods of externally sustaining plasma ionization for Case II:
Case IIA. A broad area, relatively low density, uniform electron beam (~100 to 200 kV) is directed into the laser cavity, which passes through a thin foil pressure barrier. This beam of "primary" electrons makes many collisions with neutral molecules, thereby creating a large number of low energy or "secondary" electrons. A DC, subbreakdown field (where E/N is below ionization level) is applied to the bath of secondary electrons creating current flow, which in turn vibrationally excites the N_2 ($V = 1, \ldots, n$) states, and also the CO_2 (001) state.
Case IIB. A string of very short duration (t = tens of nanoseconds), but extremely overvolted pulses (E/P is ~$20 \times$ glow E/P, initially) is applied to the gas at a rate of 10 to 50 kHz. Although the ionizing pulse duty cycle is only ~0.001, the residual electron density builds with each microavalanche up to a constant average residual value, although the current density fluctuates. Then as in the case of an electron gun ionizing source, a constant DC undervolted (the E/P_{pump} is below the ionization potential) is applied to the residual electrons that have been generated by the avalanche pulses, creating a current flow which energizes the molecular states, as for Case IIA. This method of sustaining subbreakdown excitation is referred to as the "Controlled Avalanche Discharge."

Several other variations on the controlled avalanche theme have spawned other unique and important lasers; in one case, a continuous string of 1 to 3 μsec flat top pulses at 200 PPS with pulsed and average power levels of 50 MW pulsed, 10 kW average, respectively. In a second case, a continuous steady 250 torr plasma, energized with 4 MW applied power, was used in an attempt to produce 1 MW continuous laser power. It failed to do so because of mode–mode media instabilities, which are to be discussed.

These approaches may be understood and compared by discussing variations on the relevant driving terms of the electron–ion production and loss rate equation

$$\frac{\mathrm{d}n_{\mathrm{e}}}{\mathrm{d}t} = S + \left(\frac{\alpha_i}{N}\right) N \nu_{\mathrm{d}} n_{\mathrm{e}} - \left(\frac{\alpha_{\mathrm{a}}}{N}\right) N \nu_{\mathrm{d}} n_{\mathrm{e}} - \alpha_{\mathrm{r}} N n_{\mathrm{e}}^2 - D_{\mathrm{a}} \nabla^2 n \tag{6B.52}$$

This equation has been expanded from Equation 6B.46 and contains several new terms. Here, S is an external ionization source term, and is defined according to its appropriate function. It may describe an input of primary electrons, X-rays, ultraviolet photons, metastable helium atoms, or external plasma injection; i.e., whatever kind of flux is used to create all of the ionization, or perhaps only pre-ionization. Then α_{r}/N is the reduced (normalized) three-body recombination coefficient. This term was omitted from Equation 6B.46 because the electron density, n_{e}, for the glow discharges discussed, is typically 2 to 5×10^{10} electrons

cm^{-3}. Therefore, in Equation 6B.46, α_a/N dominates α_r/N by several orders of magnitude. (However, for the cases we now discuss, α_r/N either dominates or at least plays a significant role.) At $n_e \approx 3 \times 10^{12}$, recombination becomes dominant over attachment for $P = 1$ amagat. Finally, diffusion, which was previously dominant, is dropped for most of the remaining cases that are presented here.

Equation 6B.52 can be approximately solved by assigning judicious constant values to α_i, α_a, α_r, and E/N, which is the ratio of the plasma to neutral density and which controls most plasma coefficients including α_i, α_a, α_r, and ν_d. Its underlying physical significance is that E/N is proportional to the energy an electron gains (on average) between making collisions. So in reality

$$\left(\frac{\alpha_i}{N}\right) \rightarrow \left(\frac{\alpha_{i(E/N)}}{N}\right), \left(\frac{\alpha_a}{N}\right) \rightarrow \left(\frac{\alpha_{a(E/N)}}{N}\right) \text{ and } \nu_d \rightarrow \nu_d(E/N).$$

In addition, most of these dependencies have been experimentally measured and plotted as a function of E/N.[13]

For continuous lasers $dn_e/dt = 0$, the parameters α_i, α_a, α_r, ν_d are constant. However, for pulsed lasers, E/N changes rapidly and so does $\alpha_{i(E/N)}$ and $\alpha_{a(E/N)}$ vs. E/N. Sometimes a curve actually reverses its slope as the E/N value continues to rise, leading to a reversal in balance between ionization production and loss. This causes an "attachment instability." Gases that exhibit changes in their $\alpha_{i(E/N)}$ vs. E/N slope are called "electronegative gases," of which H_2O vapor is a most notorious offender. Attachment instability can lead to many microstreamers and potentially to an outright arc, or they can trigger a thermal instability that certainly leads to an arc, but which might hold off until after the laser pulse has been produced.

Finally, there are many plasma-chemical reactions, ion formation, disassociations, and excited states that can be produced during the application of an overvolted pulse. The rate constants for such reactions depend seriously upon E/N, but they also depend on the electron energy distribution, which changes dramatically as E/N transitions between overvolted and undervolted states. To study these effects, the Boltzmann equation must be solved to determine the electron energy distribution over a range in E/N values. Finally, a gas kinetics code containing the relevant chemical species must be coupled to the Boltzmann equation solver, which provides electron energy distribution function dependent cross sections.

The technologies on which we now focus were developed mostly in parallel with the glow discharge scheme presented previously. Therefore, in keeping with our mostly historical line of developments, let us reset the time line back to around 1970.

6B.2.12 TEA Laser Development

The first realization of multijoule, megawatt power pulse occurred in 1970. As described earlier,[5] the achievement of three orders of magnitude increase in pulse power can be attributed to the nature of plasma excitation, in which highly overvolted, nonequilibrium electrical pulses were applied to a large volume, medium high pressure, CO_2 laser gas mixture. This first means of implementation, however, proved somewhat inconvenient. Megavolt pulses, generated by large Tesla-coil like pulse transformers, were applied across an axial-flowing, 2 m long tube. Sometimes electrical discharges would leap from the laser to the floor.

At this point a Canadian scientist Beaulieu[14,15] found a much more practical means to implement the overvolted pulse concept; hence, the TEA laser was born. TEA stands for Transverse Electric Atmospheric laser, an acronym that aptly describes this approach. The electric discharge was applied transverse to the direction of the beam, along a gain path length of perhaps 1 m, where the gas pressure was in fact 1 atm. Since the electrical path length had

been reduced to 2 cm (as opposed to 2 m), the overvolted pulse potential got reduced from the megavolt range down to the 30 to 50 kV range.

For the first TEA lasers there existed no effective means of filling the gas volume with uniform plasma, so an array of pin electrodes were aligned along adjacent sides of the discharge tube, across which quasidiffuse individual plasma streamers crossed the gain region. Each pin was resistively ballasted, and the two pin arrays rotated in a spiral fashion along the axis, which appeared like the structure of a DNA molecule. This improved azimuthal symmetry of the discharge, with respect to the cross-sectional area of the laser beam.

The choice to operate the TEA laser at or near 1 atm proved fortuitous. The overvolted electrical pulse has to be kept short to avoid discharge collapse into an arc, typically below one microsecond. The pulse E/N grows substantially above the arc potential, which is approximately twice the glow potential, then falls below the glow potential before an arc could form. The ensuing avalanche is arrested at the point where E/N falls below the glow maintenance level, after which the field continues to heat the electronics. These electrons collisionly excited N_2 ($V=1,\ldots$) and CO_2 (001) over a time period lasting several microseconds as the potential continues to decrease. The fortuitous part is, at $P=1$ atm, the $N_2 \rightarrow CO_2$ transfer rate is 0.5 μsec, which approximately matches the peak of the pump current duration. Also, the VT collisional relaxation time that drains the terminal laser state is on the order of 0.3 μsec from CO_2 (02^20) to CO_2 (01^10), then 0.5 μsec from CO_2 (01^10 to ground CO_2(000). In addition, all other competing transitions have relaxation transfer times on the order of 20 μsec. Therefore, we have a made-to-order setup for moving energy through the laser transition.

There are also other aspects of this early development that showed enormous potential. Among them, the saturation and optical extraction efficiencies were unusually high; $\eta_{sat} \approx 0.95$. These efficiencies happen because at $P=1$ atm, $I_{sat} \approx 500{,}000$ W cm^{-2}; yet, owing to the short pulse time (50% of the energy is extracted in ~0.2 μsec), cavity peak power density can readily exceed 10 to 15 times I_{sat}.

Some rather formidable problems were also encountered in early attempts. The most serious of these were (1) lack of plasma homogeneity, (2) much lower than optimal SPL than could be achieved, and (3) E/N ramped over a wide range during the period of electron collisional excitation of N_2 ($V=1,\ldots$) and CO_2 (001) states. The electric pumping efficiency η_e is highly dependent on E/N and in fact, peaks at one particular value. So initially, η_e and η_p were substandard. The most pressing need was to eliminate the individual pin electrodes, and instead form a stable plasma bounded by opposing planar electrodes that uniformly filled the intervening volume, and then, find a means of importing a significantly larger SPL to the gas.

Many early investigators realized that a pivotal requirement was to establish a uniform bed of weak plasma, or preionization, before delivering the overvolted discharge pulse. This preionization could either take the form of an ionized sheet distributed along the cathode, or as weak uniform ionization seeded throughout the gas volume. On the other hand, even better, establish both of these conditions before applying the discharge pulse. In either case, the charges provided a large, evenly distributed, number of nucleation centers, which when suddenly pulsed at high E/N, develop a huge number of avalanches that coalesce into a single uniform plasma. To achieve this desired effect, the pulse rate of E/N rise must be fast compared with all instability growth mechanisms, and E must be spatially uniform and free of regions where the field gets ''pinched'' and creates local charge concentration.

There are essentially three components needed to bring all the required physical conditions to bear:

1. The generation of a properly proportioned electrical pulse
2. The establishment of a well-controlled $\vec{E}$-field distribution
3. The generation of a correctly distributed preionization

Commonly used electrical pulse circuits that fulfill requirement (1) are described in the Circuits Chapter of this book. In short, these circuits typically incorporate fast, low inductance, energy transfer from a charged capacitor onto a very fast, low inductance peaking capacitor, which steepens the current rise time. In addition, in many cases, some of the stored energy is diverted into the production of sparks used to preionize the gas. The best electrodes are planar and uniform over the plasma conduction region, but tailored according to a mathematically derived contour along its edges, such that the $\vec{E}$ -field monotonically increases at its edges. The "Regowski" profile is often used to satisfy condition (2), as described by Cabine.[16]

If all other requirements are adequately satisfied, it takes a uniform volume distribution of only ~10^6 to 10^7 electron–ion pairs to properly launch a uniform plasma. It is interesting to note that nature nearly accomplishes this task for us. Cosmic radiation typically sustains a bed of secondary ionization amounting to $\eta_e \approx 10^3$ to 10^4. But not quite enough. The finesse with which the preionization task is accomplished determines to a large extent how well the laser works; most specifically, it determines plasma uniformity and maximum achievable SPL input. Many workers have tried a number of methods to accomplish this task. Two particular approaches are, in the author's opinion, far superior than the others in terms of results.

One of these preionization methods has been developed extensively by the Kurchartov Institute,[17] and also by other Russian laboratories. In this method, a very fast-rising, overvolted electrical pulse is applied across the surface of a dielectric barrier. The current return path is provided by a back-strap metal plate on the underside of the dielectric barrier, which is of extremely low inductance, and provides an intense electric field at the surface of the dielectric. This enhances plasma development, causing a high-density, uniform plasma sheet to be launched across the surface. The plasma sheet produces a uniform, intense, broad-area ultraviolet source that creates volume ionization, filling the cavity. The radiation may either shine through a bed of slots milled into a solid cathode, or the plasma sheet itself may serve as the cathode. In the latter case, the plasma sheet provides the initial electrons, and in addition, the UV photons produced ionizes the media volume. This concept does a superior job, but for high repetition lasers, it could also cause a buildup of contamination due to sputtering and also undesirable chemical reaction by-products.

The second and most superior method is to inject a broad area X-ray beam into the discharge region. This technique has been used quite widely, and is thought to have originated at Los Alamos Labs.[18] In this method, an electron gun, similar to that which might have been used to create an E-beam ionized plasma, is instead used to generate X-rays. The E-beam strikes a gold target, converting some of its energy into ~80 to 200 keV X-rays (depending on requirements set by the operating pressure and physical dimensions of the laser). Both X-ray preionization and X-ray full-ionization techniques are very expensive, but warranted for large systems. The main difference is that the X-rays penetrate thick structures and do not require fragile foils. Therefore, the technique is very reliable. Moreover, it neither creates a contamination nor a chemistry problem. Since the cross-section for electron–ion production is low, the ionization is very uniform. In addition, a relatively weak X-ray flux level of short time duration suffices to generate an adequate level of preionization.

The most common and much less-expensive approach is to create a large number of spark discharges directly behind a semitransparent wire mesh that serves as the cathode. A most impressive TEA laser of this type was developed by Martin Richardson and John Alcock at the Canadian Ministry of Defense.[19] This laser produced 300 J, several gigawatt pulses. It consisted of four discharge modules, each of 50 cm^2 cross-section $\times$ 50 cm long. Its performance in most respects was outstanding: it produced $\alpha_o = 0.05$, SPL = 300 JL-A^{-1}, using a mixture $CO_2/N_2/He = 0.3$, 0.2, 0.5, at 1 atm, which enabled most of the energy to be

extracted in the transient peak of ~250 nsec. Power output was limited by optical breakdown, both inside the laser media and on optical elements.

More typical TEA laser mixtures such as $CO_2/N_2/He = 1/4/5$ create a transient spike some 200 nsec wide, containing roughly half of the extracted energy. The other half of the energy dribbles out at a much lower power over an extended time period of 5 to 20 μsec, depending on the relative concentration of N_2.

A set of five coupled rate equations, which correctly predict pulse shape, is found in Duley's book on CO_2 lasers,[20] which is strongly recommended as a supplement to this section. In the same context, Wood's review paper[21] is also highly recommended.

A particularly interesting high repetition rate TEA laser has been developed by Vladimir Mezhevov and his colleagues for the application of separating Carbon-13 isotopes from Carbon-12 isotopes.[22,23] This device (including several variations) is a very compact, closed, recirculating loop TEA laser, which incorporates catalytic converters that clean up a small fraction of the recirculating gas. These lasers are photo-preionized using spark discharges, and are energized using a very fast, initially overvolted pulse that quickly decays. To this point, its design typifies a general format of "TEA" laser methodology, yet its performance is spectacular in that it achieves all the following parameters:

- Repetition rate: up to 600 PPS
- Pulse length: ~200 nsec
- Average power: 1800 W
- Energy out: 3 J pulse^{-1}
- Beam quality: single mode
- Tunability: from 9.4 to 10.8 μm, single rotational line tunable
- Total efficiency: ~7.5%
- Nonstop run time: ~6 months

In this regard, recall that typically single mode vs. multimode operation reduces power by perhaps 50%, whereas single line selection typically reduces power by an additional 50% over multimode, P20 line operation.

Let us examine several factors that set this laser apart from others. Its SPL is quite low (~60 kJ kg^{-1}), in comparison for example with the LADS (Laser Automated De-coating System), which operates at ~450 kJ kg^{-1} (to be described later). This reduction in SPL significantly lowers the gain and therefore requires a multipath folded cavity. Although the extraction efficiency is also reduced, this effect is somewhat recovered due to the short pulse length and therefore increased peak power density, which increases the saturation efficiency. Owing to a significantly extended optical path length plus superb resonator design, the output power and efficiency remain quite tolerable—particularly in consideration of its overall capability.

The benefits of operating at reduced SPL are:

1. Gas heating is reduced to $\Delta T = \sim 12$ K per pulse, or ~53 K per cavity exchange, during which ~4 pulses are fired. In turn, acoustic waves are minimized, which otherwise would become a significant problem when operating at 600 PPS.
2. Plasma cavity arcs become less frequent, even though simple and inexpensive pulse circuits are used.
3. Gain media thermal gradients are minimal at its operating pressure (0.5 atm); thus, a multipath resonator can operate without significant beam quality degradation.
4. Plasma chemistry effects are reduced, so that continuous periods of operation are extended.

5. The volume flow rate requirements are reduced from approximately three cavity gas exchanges per pulse as is normally required for heavily SPL lasers, to perhaps one-fourth of a cavity gas exchange per pulse. In addition, very small pressure drop gas recirculation pumps are needed owing to the reduced magnitude of acoustic waves. Stringent acoustic abatement methods require large pressure-drop pumps.

This example is included to show an optimized TEA laser design that achieves unique attributes. It operates in an SPL regime that is quite opposite to the device intended to reach ever-more average power with high beam quality, and upon which this section concentrates.

In concluding this TEA laser section, let us summarize this operation according to the ionization rate Equation 6B.52. Extracting the operative terms for this process, we have

$$\frac{\mathrm{d}n_\mathrm{e}}{\mathrm{d}t} = S_\mathrm{ip} + \left(\frac{\alpha_\mathrm{i}}{N}\right) N \nu_\mathrm{d} n_\mathrm{e} - \left(\frac{\alpha_\mathrm{a}}{N}\right) N \nu_\mathrm{d} n_\mathrm{e} - \left(\frac{\alpha_\mathrm{r}}{N}\right) N n_\mathrm{e}^2, \tag{6B.53}$$

where S_ip is the photo ionization rate at distance z from the spark(s) source, and t is the time and is derived as follows: the photon flux with frequency ν reaching the plasma at a distance z from the source at time t is

$$\Phi_{(\upsilon,\,\mathrm{z},\,\mathrm{t})} = \frac{P_{(\upsilon,\mathrm{t})}}{4\pi\ hz} \times \frac{\mathrm{e}^{-\mu_{(z)}z}}{z^2}, \tag{6B.54}$$

where $u_{(\mathrm{z})}$ is the photon attraction per unit length in the gas. The number of electrons $S_{\mathrm{i\ (v,\ z,\ t)}}$ produced per second by direct single-step photo ionization is

$$S_\mathrm{ip} = \sigma_{\mathrm{i(z)}} N \Phi_{(\mathrm{v},\,\mathrm{z},\,\mathrm{t})}, \tag{6B.55}$$

where $\sigma_{\mathrm{i(z)}}$ is the photoionization cross section and N is the gas density. Let us define the photon mean free path $l_{\mathrm{p(z)}}$

$$\frac{1}{l_{\mathrm{p(z)}}} = \sigma_{\mathrm{i(z)}} N = \mu_{(\mathrm{z})} \tag{6B.56}$$

so the total electron generation rate summed over the spread in photo energies becomes the photoionization source term

$$S_\mathrm{ip} = \int_0^\infty S_{\mathrm{i(v,\,z,\,t)}} \mathrm{d}\nu \tag{6B.57}$$

A concern is that, particularly for high repetition rate lasers, sparks in the open gas stream can lead to contamination buildup.

6B.2.13 Electron Beam Ionized CO_2 Lasers

Electron beam ionized lasers were invented independently at three different institutions: at Los Alamos by Keith Boyer and Charles Fenstermacker,[24] at Avco Everett Labs by Jack Daugherty[25] and James Reilly, and at the Lebedev Institute in Moscow by Nicholas Basov[26] and colleagues. This development marks the next major turning point in the evolution of giant pulsed lasers.

In the case of electron beam ionized CO_2 lasers, a broad-area, diffuse, electron beam is formed in a vacuum, and then extracted through a thin foil window into a high-pressure region in which the gas is contained. The ionization is formed and sustained throughout a large volume region entirely by secondary ionization. Typically, 50 secondary ion–electron pairs per primary electron from the beam are created per centimeter of travel at 1 atm pressure, and hence a primary that has 200 keV creates ~6000 secondary ion–electron pairs, expending about 32 eV per ionizing collision. Except for space-charge effects, there is no macroscopic electric field involved—in either creating or sustaining the plasma. In addition, an external electric field is applied between two electrodes bounding the plasma, and a current flows in response (no matter how small the electric field) as long as the net potential exceeds the cathode-glow potential. Since this pump field potential is held below the glow potential, it will not on its own accord substantially contribute to ionization, but will only impart energy to the plasma. Pumping is entirely disconnected from ionization. Furthermore, since avalanche ionization is no longer involved, the gas is raised to very high pressures and can also occupy very large volumes. Any choice of the E/N parameter falling between zero and that value which characterizes the glow condition is allowed. This freedom to administer the optimal choice of E/N often leads to increased efficiency in coupling energy into the desired process. For the first time, CO_2 lasers were excited at the $(E/N)_{\text{pump}}$ value, which maximizes η_L when $E/P = \sim 6700$ V/cm-A. Previously, the glow process had fixed $(E/N)_{\text{pump}}$ at ~10,000 V/cm-A, for which case η_e is reduced. In addition, either the continuous power deposition rate (CW) or the peak energy deposition (pulsed) could now be selected at will, and independently with respect to E/N, simply by controlling the electron beam.

It is not surprising that the range of plasma parameters and size of devices these plasmas support become greatly magnified for the case of electron beam ionized plasmas over their internally sustained normal-glow counterparts, as shown in Table 6B.1. In the usual configuration,

$$\frac{dn_e}{dt} = S_i \times j_{b(t)} - \frac{\alpha_a}{N} N\nu_d - \alpha_r N n_e{}^2, \tag{6B.58}$$

TABLE 6B.1
Electric Discharge Methods Compared

Parameter	E-Beam Ionized	Controlled Avalanche	Self-Sustained
Pressure range	~1 to >30 atm	100 torr to >10 atm	1 torr to >4 atm
Volume scalable	No fundamental limit	No fundamental limit	~24L-A achieved
Volume homogeneity	2nd best	1st best	Limited
Stability with electron attachers	2nd best	1st best	Prone to thermal & attachment instability
Specific power load (CO_2)	~500 J L-A^{-1}	~500 J L-A^{-1}	120 to 180 J L-A^{-1}
E/N range (sustained)	Near 0 to glow limit (typical 40 Td)	Near 0 to glow limit (typical 40 Td)	Only at glow limit (typical 40 Td)
E/N range (transient)	NA (except space charge)	80 Td to >>200 Td	NA
Pulse length	Continuous, down to ~10 nsec	Continuous, down to ~10 nsec	Ballasted CW, down to ~100 μsec, or transient 100–200 μsec
Current density	~50 mA cm^{-2} to >1000 A cm^{-2} (10 μsec)	50 mA cm^{-2} to >10,000 A cm^{-2} (~20 A cm^{-2} at 1 μsec)	10 mA cm^{-2} to ~100 A cm^{-2} (TEA)

where S_i is the number of secondary electrons per primary electron per centimeter distance, and $J_{b(t)}$ is the pulsed electron beam current density. Note that there is no avalanche ionization. For CW operation

$$n_e = \frac{S_i j_b}{\alpha_a \nu_d} \tag{6B.59}$$

since at $n_e \ll 10$,[12] the recombination term disappears.

Sometimes only the electron beam is used and there is no separate pump field. In this case, the E-beam must excite the upper laser directly. This is generally the case at extremely high gas pressures. High pressure is required to generate ultrashort, high peak-power pulses since pressure broadening will overlap the rotational lines to create the wide bandwidth that is necessary. Basov[27] directly pumped CO_2 lasers with an E-beam at pressures exceeding 30 atm.

A number of very large open cycle pulsed or rapid pulsed E-beam lasers were developed during the early 1970s in support of the laser weapons development in the United States and Soviet Union. Multikilojoule pulsed or hundreds of kilowatts average power rapid pulsed lasers were typically used in classified defense programs at the time. Repetition rates and pulse times were typically several hundred pulses per second and 20 to 50 μsec, respectively. Most were intended to operate at single mode. Huge gas "farms" and sometimes giant dump tanks were needed to support this type of open cycle, "flush and gush" mode of operation. At least the shock and acoustic waves could be readily managed for the case of operating closed cycle.

Several 10 to 20 kW class, E-beam, ionized, CO_2 lasers have been packaged into (nearly) closed-cycle, compact systems suitable for commercial application. The earliest of these was a continuous laser developed at Avco Everett Laboratories in Boston by Jack Daugherty and Evan Pugh in 1972.[28] The laser cavity measured on the order of $10 \times 10 \times 100$ cm, operated at perhaps 50 torr, and incorporated an unstable resonator and an aerodynamic output window. This laser produced ~20 kW CW, and was used in a heavy steel welding application.

An early example of a high rep-rate, E-beam, ionized, closed-cycle laser, producing 15 kW average power, was developed in Germany.[29,30] This laser produced 150 J pulses at 100 PPS and was intended for use in an aircraft paint-stripping application.

Both these developments are noteworthy, since they were the first to tackle and solve the beam quality problems associated with waste energy trapped within a tightly constrained closed flow loop. However, the methodologies required are quite different for the case of continuous vs. rapid pulsed systems. For CW operation, thermal gradients stir up convective cells with large density gradients. Therefore, smooth, uniform flow must be preserved by some means.

For the case of rapid-pulsed, closed-cycle operation, the cavity media remains uniform during laser extraction, but later expands explosively because its temperature has doubled due to electrical energy addition. These shock waves degenerate into intense acoustic waves, but they cannot dissipate before the occurrence of the next pulse. Generally, heroic efforts are required to absorb the acoustic waves and restore equilibrium pressure conditions during the time lapse between pulses.

Yet another class of very large E-beam ionized CO_2 lasers has centered on thermonuclear fusion research around the world. Such systems were designed to amplify a single 1 to 30 nsec pulse into tens of kilojoules, and split the beam into dozens of channels, all to be focused in a coherent manner onto a single pellet of deuterium within a large vacuum sphere. The first of these systems, called Antaries, was developed at Los Alamos National Labortory under the leadership of Keith Boyer and Charles Fenstermacher. Later, it was recognized that the wavelength of CO_2 laser was wrong for the fusion application, and efforts were channeled toward development of very short wavelength lasers.

Since the advent of electron beam controlled plasmas, other categories of externally sustained discharges have evolved. An important example is the two-step photoionized discharge.[31] Here, a chemical (usually tri-*n*-propylene) added to the gas is ionized by means of absorbing two UV photons of modest energy. Flash lamps may create substantial ionization even though the shortest wavelength photons that can penetrate their quartz tube housing are not energetic enough to create single-step ionization. (Sparks are often used without quartz cladding to generate hard UV and hence one-step ionization, but this is useful only to create rather low preionization levels of charge density.) This two-step process is capable of providing all the ionization required to import the full quota of energy allowable (in consideration of thermal bottlenecking processes) to excite very large CO_2 lasers for moderately long pulse-length applications. Once more, a subbreakdown field is applied to pump the lasing N_2 ($V = 1, \ldots$) manifold. This excitation process can produce many tens of kilojoules, CO_2 laser pulses by means of exciting cubic meters of gas at atmospheric pressure.[32] Unfortunately, the disassociation by-product contaminates the laser cavity, which is not conducive to enabling high-repetition rate operation.

Among the discharge categories discussed to this point, the electron beam ionized plasma clearly dominates the field of applications. However, for high average power applications the E-beam ionized plasma technology suffers from a serious reliability problem. The thin window through which the E-beam must pass from the near-vacuum region of the accelerator to the pressurized region of the laser cavity is subject to catastrophic failure. This window is blasted by shock waves as the heated laser plasma expands, and is also subject to puncture by accidental cavity arcs. Therefore, lasers those operate above a few kilowatts average power must often defer to less capable discharge techniques, or be relegated to laboratory study purposes where frequent breakdowns can be tolerated. For this reason, more durable means of creating plasmas have been sought that closely emulate the electron beam ionized plasma and retain its most salient properties.

6B.2.14 Controlled Avalanche Ionization Lasers

The author has adopted his "controlled avalanche discharge" approach[33] in lieu of using E-beam technology ever since 1973 for many diverse laser applications with pleasing results. Jim Reilly explored a similar technique, which is called the "pulser-sustainer" approach.[34] Further advances presented here center mostly on variations of the controlled avalanche theme. The controlled avalanche discharge, in a similar manner to the electron beam ionized discharge, permits independence of ionization and pump mechanisms, and offers freedom to choose the E/N parameter. Again, since the ionization phenomenon is not associated with the applied pump field, the pump field may be tuned at will to optimize the excitation of any particular molecular transition. And, like the electron beam ionization scheme, this condition provides uniform, stable excitation of very large volumes of very high pressures without arcing, and extremely high specific energy loads may be imported to the plasma, either continuously or in a giant pulsed mode of excitation.

6B.2.15 Compact Giant Single-Pulsed CO_2 Lasers

Single giant pulsed lasers operating at 1 to 10 atm are energized by means of applying a single, substantially overvolted, controlled avalanche pulse preceded by preionization (preferably X-ray) and followed by a subbreakdown potential pump pulse. Since the full amount of ionization (typically $n_e = 10^{13}$ to 10^{15} pairs cm^{-3}) must be developed from the initial preionized state (typically $n_e \geq 10^7$ pairs cm^{-3}) within a single avalanche, the controlled avalanche pulse must exceed the breakdown potential by a factor of perhaps 10 rather than

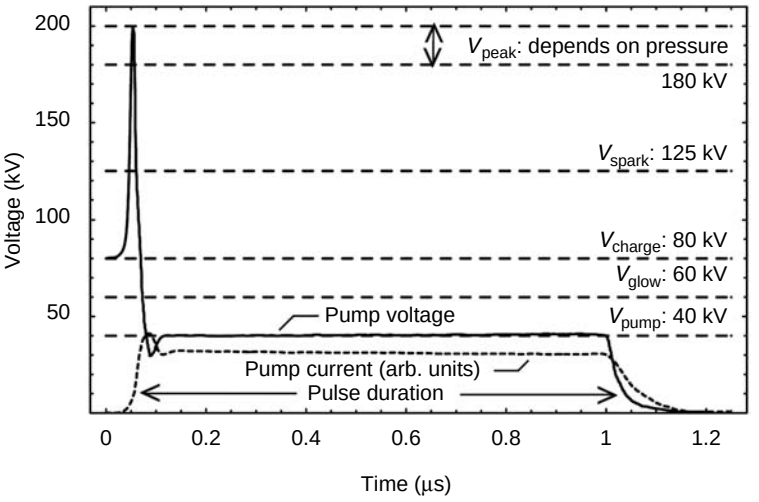

FIGURE 6B.13 Voltage temporal characteristics of a single-pulsed, controlled-avalanche discharge. Laser pulse is 1 μsec flat top for this excitation condition.

a factor of 2 or 3 corresponding to the case where substantial ionization is present at the onset of each avalanche. Also, the higher the pressure, the shorter the avalanche pulse must be to avoid the discharge collapsing into an arc, and to keep pace with three-body electron attachment-recombination rates, both of which increase linearly with pressure.

Figure 6B.13 illustrates the generic temporal structure of the controlled-avalanche and pump excitation voltage pulse. The main pump segment of the discharge falling below V_g may be extended as required by means of matching the pulse-forming network (PFN) impedance to the intended plasma impedance and matching the PFN discharge period to the desired pump-pulse period.

At medium pressure operation, which requires avalanche pulses not shorter than 30 nsec, discrete component circuits are used. For example, the present author obtained 100 J, 200 nsec pulses from a 1 atm-pressure, CO_2 laser cavity measuring $100 \times 10 \times 5$ cm, which used a saturable magnetic core isolation circuit. Others have obtained excellent results with large-volume, multijoule, excimer lasers operating at around 3 atm pressure using a similar circuit and controlled avalanche approach. To operate at extended pressures (e.g., ~10 atm), avalanche pulses need to be <5 nsec, yet rise to ≥ 600 kV. Such pulses have been generated using lumped circuit approaches, which may incorporate Blumlein lines.

6B.2.16 Compact, High-Repetition Rate CO_2 Lasers

Substantial progress has been made in the area of high-powered, high-repetition rate CO_2 lasers,[35] as exemplified by the LADS. The LADS is a 10 kW average power, 20% cavity efficient, 50 J pulse^{-1}, 200 PPS, 1.4 μsec pulse-duration laser developed at Plasmatronics and delivered to Hill Air Force Base in Ogden, Utah in 1995. This is a transverse discharge, subsonic-flowing laser with an active cavity volume measuring $5 \times 5 \times 75$ cm that operates at 0.5 atm. This laser is X-ray preionized, which uses acoustic and shock wave abatement techniques, and incorporates a four-step plasma formation process resulting in a factor of 2 enhancement SPL over previous variations of the controlled avalanche process. The steps are

- **Step 1:** An electron beam generated, broad-area, X-ray pulse is applied to the plasma, which generates a uniform bed of seed preionization ($n_{epreion} \geq 10^7$ electrons cm^{-3}) throughout the discharge volume.
- **Step 2:** Following a short delay, the seed ionization is caused to avalanche to the full working level electron number density (typically $n_{epump} = 10^{13}$ to 10^{14} electrons cm^{-3}, depending on pulse duration) by means of applying a single enormously high voltage pulse of ultrashort duration. The exact height and width of this pulse are application specific, but will most likely fall into the range of 100 kV to 2 MV, lasting 5 to 75 nsec. More specifically, it delivers an initial open circuit reduced field strength of typically 150 Td, which amounts to a factor of ~3 to 8 times the glow potential (depending on the gas mix and level of presiding preionization). The avalanche is completed as the pulse falls from its maximum field strength (~150 Td) to the loaded value (~75 Td). This field falls just below the sparking potential V_s, but well above the "normal glow" potential V_g.
- **Step 3:** In the final phase of creating ionization, the applied potential falls naturally from its intermediate value—which is the PFN charge voltage—to one-half of that value as the plasma impedance falls to match the PFN impedance.
- **Step 4:** The laser is continuously pumped under optimum conditions until terminated by the PFN. The system is designed so that as the plasma impedance comes into match with the PFN impedance, the voltage drops to one-half the PFN charge voltage, which has been selected to provide the optimal E/N conditions for pumping the laser. Since this E/N value falls below the glow condition (i.e., it produces little or no avalanche ionization) it may be maintained without forming an arc for a limited period of time. Typically, the PFN parameters will be selected to apply the maximum SPL afforded by thermal bottlenecking, subject to the desired pulse width. Figure 6B.14 illustrates a "hybrid" circuit in generic form, capable of delivering the required electrical pulse as described. Here, a useful trick is to incorporate an initial doubling of the avalanche pulse voltage as it first reflects from the initially open-circuit cavity back into the delivery line, but quickly falls as the discharge impedance decreases with ionization build-up. Hence, the plasma becomes a participating element, interacting with the network so that the process becomes self-regulated and stability is achieved.

The LADS laser and its discharge looking end-on are shown in Figure 6B.15.

6B.2.17 Compact, Continuous, Controlled Avalanche Ionized CO_2 Lasers

In 1973, this concept was introduced by the author[33] and then shown to be capable of operating into the megawatt continuous regime in 1977, but unpublished until a few details were released in 1989.[36] In this application, a medium-pressure flow stream (50 to 250 torr), CO_2 laser mixture is quasi-continuously ionized by means of applying a steady stream of 50 to 75 nsec pulses at about three times the breakdown potential at a rate of 20,000 to 50,000 PPS. The average electron density produced was ~10^{11} electrons cm^{-3}, where the loss in conductivity between ionizing pulses amounts to only 5% to 10% of its mean value. The kinetic processes integrate the corresponding modulation of pump power so that the laser beam is essentially continuous. Pumping is accomplished by applying a pure DC potential (without ballast) across the same transversely positioned electrodes that supply the controlled avalanche pulses. The pulses may simply ride on top of the DC power supply, or the corresponding DC and pulsed power components may be supplied by parallel circuits that are blocked from each other by the use of inductors and capacitors. Preionization

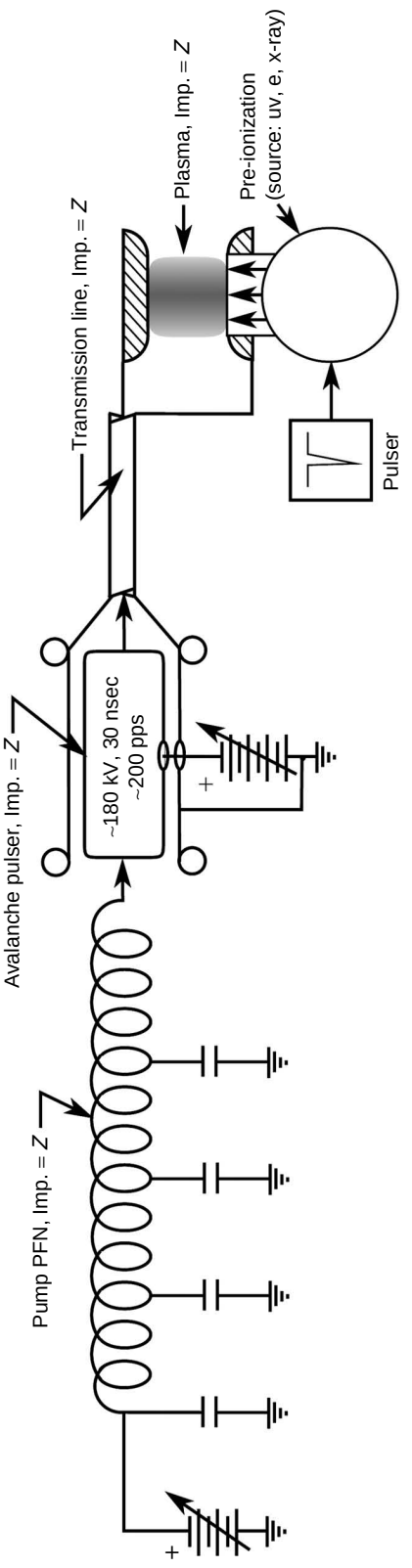

FIGURE 6B.14 Generic, single-pulse, controlled-avalanche, hybrid-pulse circuit.

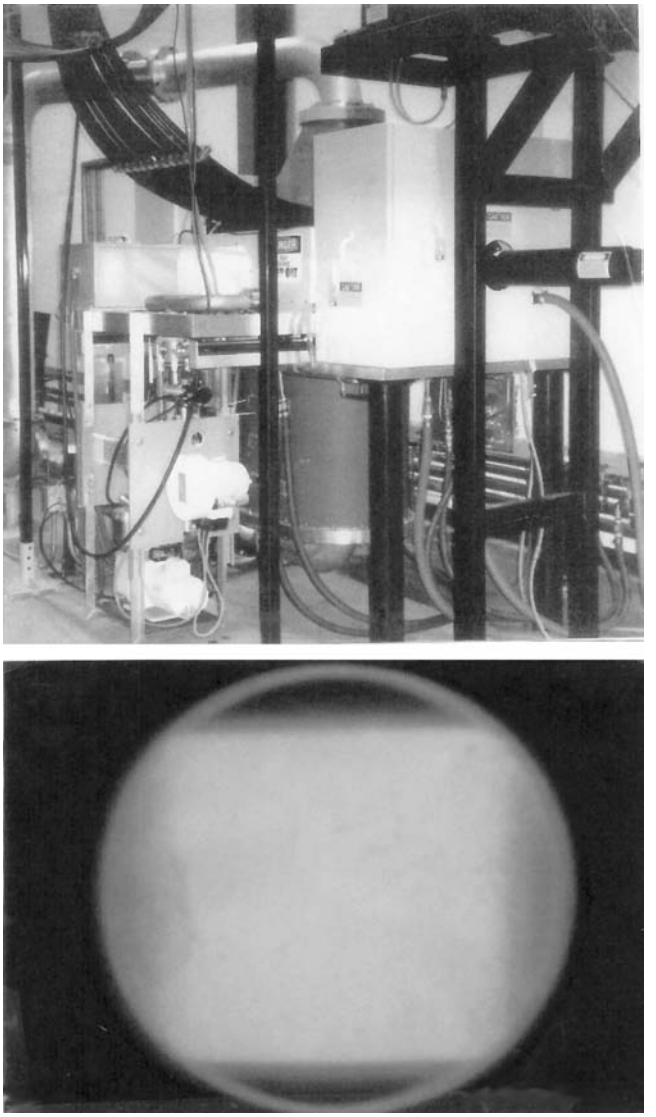

FIGURE 6B.15 Upper photo: LADS 200 PPS rep-rate, 50 J pulse^{-1}, controlled-avalanche laser. Lower photo: end view of discharge of LADS (looking into blocked laser beam). Cavity is $5 \times 5 \times 75$ cm.

must be provided to begin the process, but may be discontinued once steady-state operation is reached.

The current fluctuation may be modeled by solving the ionization rate equations, which correspond to the overvolted and undervolted states in an iterative manner and synchronized in time. Each segment of the solution then provides the initial conditions for the next segment. Figure 6B.16 shows the modeled solution for the case $N_2/He = 30/70$ torr, respectively, with $t_p = 75$ ns and the repetition rate = 20,000 PPS. Figure 6B.16 compares the measured current response in an experiment set up to reproduce the conditions of Figure 6B.16. The first pulse is overvolted more than the rest in order to "jump start" the ionization process.

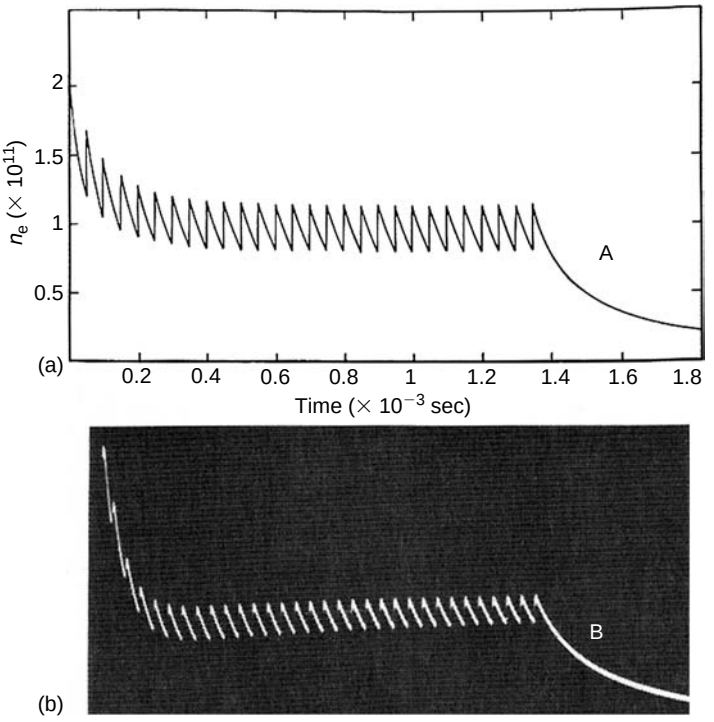

FIGURE 6B.16 Quasicontinuous, controlled-avalanche laser; controlled discharge 20,000 PPS, 75 nsec ionizing pulses. Upper: calculated pump current. Lower: corresponding measured pump current.

6B.2.18 Special Problems Associated with Very High Continuous Power

The CW controlled avalanche-based laser, built in 1978 at Kirtland AFB, was intended to operate at around 1 MW of power out, and at pressures up to 250 torr. The device did in fact power load a subsonic-flowing 1 m wide $\times$ 4 cm $\times$ 15 cm channel at 4 MW input sustained continuously, and beam control issues were pushed into unfamiliar territory. Many problems related to high-power operation were anticipated and dealt with by design. Other phenomena, including various kinds of mode–media interaction instabilities were discovered for the first time, which remained unsolved during the tenure of this laser. In fact, these instabilities surfaced at three locations almost simultaneously. The other two lasers were also large CW transverse flowing devices, but were E-beam ionized rather than controlled-avalanche ionized. These were built by Jack Daugherty at Avco Everett Labs and Gene Parasini at Hughes Aircraft.[37]

Let us first consider those problems for which we may most readily implement solutions by design. This requires a somewhat detailed description of the laser.

The Kirtland laser, illustrated in Figure 6B.17, was configured such that its optical path, gas flow path, and electric current flow path were mutually orthogonal. The device was capable of loading 4 MW of power into a diffuse plasma of controllable distribution at 250 torr pressure. The gas entered the channel at $M = 0.35$, providing $\dot{m} = 2.8$ lbs sec^{-1}. To lase at this power level, high pressure, fast-flow velocities and high-SPLs were required. All these conditions tend to degrade beam quality. The flow stream entered the channel at Mach $M = 0.35$ so that compressible gas dynamic effects could be used to transfer part of the waste heat into acceleration, thereby permitting higher SPL without killing the gain due to

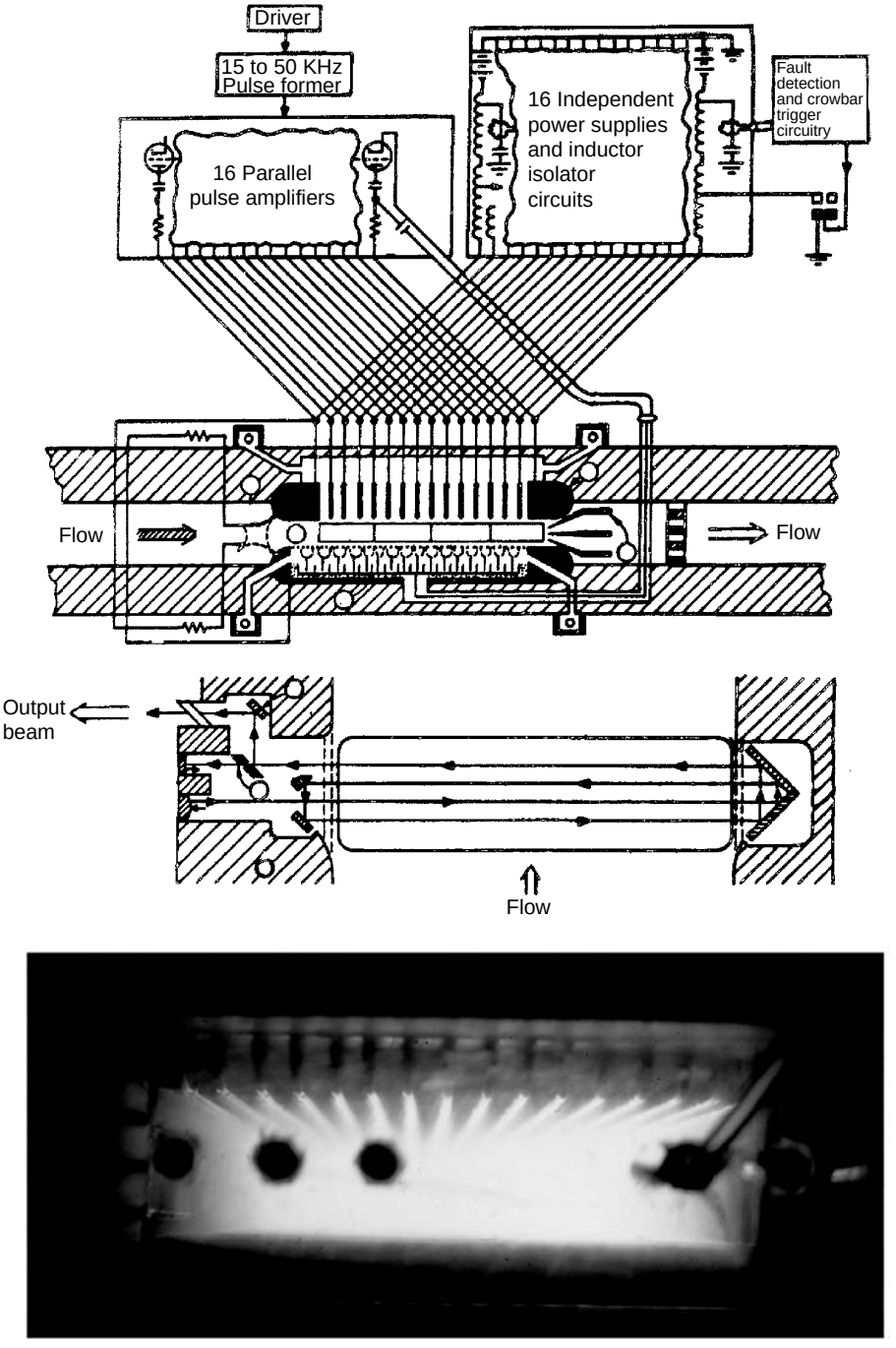

FIGURE 6B.17 High-power, continuous, controlled-avalanche laser developed at Kirtland AFB. Upper: design drawings. Lower: 4 MW plasma looking end on with mirrors removed. 16 electrodes carry ~16 A each; pump $\vec{E}$ is 16 kV vertical; heading right, flow is 4.5 kg sec^{-1}, 250 torr, and is mutually orthogonal to $\vec{E}_{pump}$ and beam.

thermal bottlenecking, and furthermore to increase the mass flow rate. The exit Mach number was limited by onset of flow instabilities beyond $M = 1/\sqrt{\gamma}$.

The consequences of adding the required SPL into a transsonic flow stream are illustrated in Figure 6B.4. The density changes by a factor of two to three along the direction of flow, which crosses the direction of beam propagation for the transverse geometry. Furthermore, $\rho_{(z)}$ is not linear, but has higher order terms ($\rho = \rho_o(1 + K_{1z} + K_{2z} + \cdots)$), owing to the gas dynamics of Rayleigh heating in the transsonic range.

Lensing effects were corrected by linearizing the density gradient by tailoring the electrical current distribution, and by tilting a resonator mirror to compensate for the remaining linear component of beam bending. The controlled avalanche scheme allows discharge pumping at E/N ratios that are spatially variable and are in no way clamped to the glow potential. The plasma is homogeneous, even when excited at high pressure to SPLs that are in excess of prudent levels set by bottlenecking considerations. Density linearization was accomplished by segmenting the cathode into 16 parallel, independently powered, 1 m long strips, each capable of delivering 16 A at 15 kV. The separate supplies were controlled from a central computer, which caused the calculated voltage distribution to appear along the channel, graded in the flow direction.

By solving the continuity equation, the energy conservation equation, the momentum conservation equation, and the ideal gas law, subject to the requirement that $\rho_{(z)} = \rho_i + kz$ (i.e., linear in the flow direction z), we determine the required $(E_y/N)_z$, and correspondingly the required SPL distribution $(j \cdot E)_{(z)} \times \xi$, which is

$$j \bullet E - Q_L = \frac{A}{(\rho_i - kz)^2} - \frac{B}{(\rho_i - kz)^3} \tag{6B.60}$$

$$E/P = \frac{W}{22.4} \times \frac{\sqrt{\frac{1}{\sigma_c}\left(\frac{A}{(\rho_i - kz)^2} - \frac{B}{(\rho_i - kz)^3}\right)}}{(\rho_i - kz)}, \tag{6B.61}$$

where σ_c is the plasma electrical conductivity, and

$$A = \frac{\rho^2 V_1 KT}{10^6}\left[4180\ C_p\left(P_i + \rho_1 V_1^2\right)\right] \tag{6B.62}$$

$$B = \frac{2\rho^3 V_1^3 K}{10^6}\left(\frac{\rho_1 T_1}{P_1} C_p \times 4180 - \frac{1}{2}\right) \tag{6B.63}$$

$$K = \frac{\rho_1 - \rho_f}{x_f - x_1} = \nabla\rho \tag{6B.64}$$

The cavity extraction efficiency drives the value of ξ, which is that part of SPL that goes into laser heating. Then ξ must be monitored and used to control mirror tile. In normal glow lasers that do not afford the flexibility of spatially controlling power deposition, the cross-sectional area may be tailored to linearize $\rho_{(z)}$. Here a computer controls the applied field distribution $E_{y(z)}$, which causes corresponding changes in temperature distribution, Mach number distribution, and $(E/N)_{(z)}$ distribution such that $\rho_{(z)}$ is linearized, as shown in Figure 6B.18.

The required mirror tilt may be derived from Fermat's Principle for a dispersive media,

$$\frac{\partial}{\partial_{0_{(z)}}} \sum \int n_{(l)} \mathrm{d}l = 0 \tag{6B.65}$$

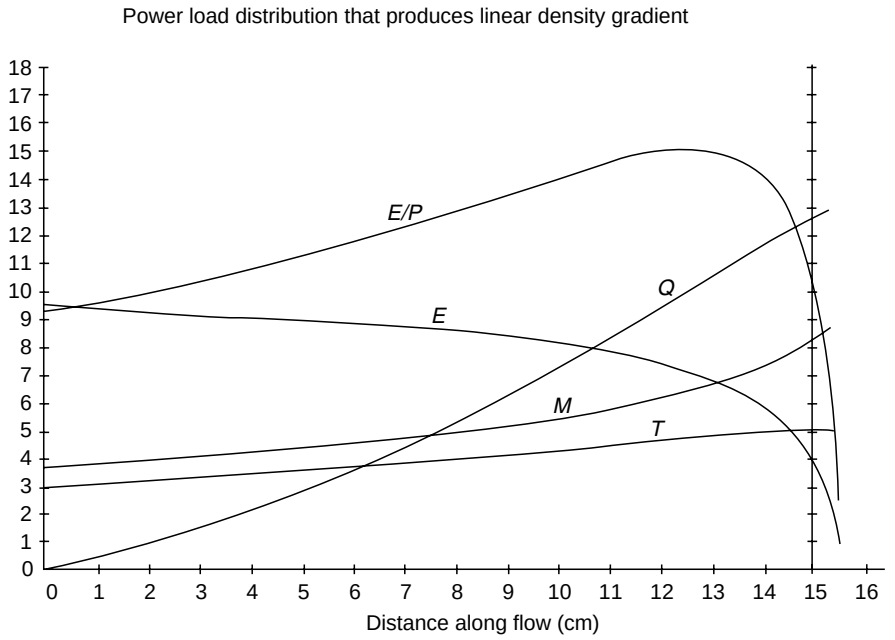

FIGURE 6B.18 Power load distributed to produce linear density gradient in direction of flow.

where $\theta_{(z)}$ is the beam angular derivation from normal propagation direction at position z along the direction of flow and l is the length along optical path, at nearly a right angle to z. In general, for known $\Delta\rho_{(y)}/\rho_1$,

$$\left\{\theta_t = \int_0^{y\,\max} \left\{\frac{1}{y}\right\} \times \left[\left\{\frac{n_{atm}-1}{1+(n_{atm}-1)\left(1+\Delta\rho_y/\rho\right)^2}\right\}\right] - \left[\left\{\frac{1}{y^2}\right\} \times \left\{\frac{n_{atm}}{1+(n_{atm}-1)\left(1+\Delta\rho_{y/\rho}\right)}\right\}\right]\right\} dy \tag{6B.66}$$

which has linearized $\rho = \rho_o + kz$, simplifies to

$$\left\{\theta_t = \left\{\frac{w}{y}\right\}\left[\left\{\frac{n_{atm}}{1+(n_{atm}-1)(1+\Delta\rho/\rho)} - 1\right\}\right]\right\}, \tag{6B.67}$$

where n_{atm} is the index of refraction of the laser mix at atmospheric pressure. Typically, $\theta \approx 0.5 \times 10^{-3}$ radians. The computer drove a servomotor which controlled the mirror tilt to match a given flow-SPL condition.

There are more deleterious effects that may be corrected by resonator design, as illustrated in Figure 6B.19. The left-hand drawing indicates the role that transverse separated Gaussian beams play in interacting with the saturated gain along the flow direction. Upstream the small signal gain increases with z as it is pumped in the absence of extracting radiation. As the flow

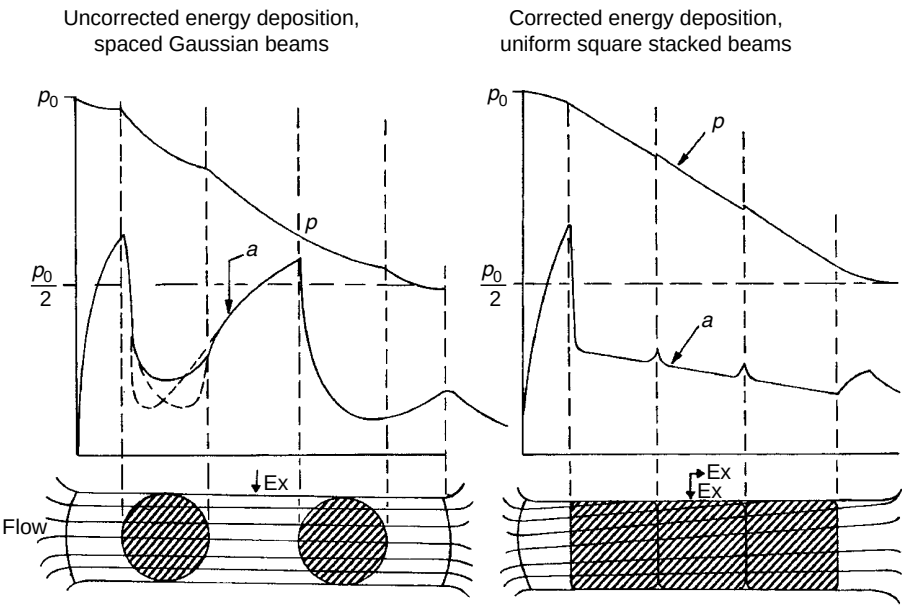

FIGURE 6B.19 Corrective resonator design scheme.

stream passes through the beam, the gain falls from its small signal value to its saturated value according to

$$\left\{ \alpha_{(z)} = \left\{ \frac{\alpha_{o(z)}}{1 + \left\{ \frac{2I_{(z)}}{I_{sat}} \right\}} \right\} \right\}. \tag{6B.68}$$

The extracted laser energy triggers a corresponding localized gas temperature increase as the lower laser level is populated by this extraction, which in turn, decays to the ground state through helium collisional deactivation, thus releasing heat. The increased gas temperature, in turn, causes the density to locally decrease. If the beam is Gaussian instead of flat, this process is further modulated by its spatial dependence; hence, the beam loses its radial symmetry in phase and amplitude. To offset these difficulties, a folded unstable resonator with square beam profiles was used as shown in Figure 6B.19. Its four-pass folded configuration eliminated the dead spaces and illuminated the cavity with uniform intensity. A further benefit arose by nature of the beam-folding scheme: its symmetry reversed with respect to upstream and downstream edges on successive passes. This helps to average out remaining phase front distortions. The accumulated effect of combining the folded unstable resonator with the density linearization and mirror positioning schemes is illustrated on the right side of Figure 6B.19. Both gain and density profiles are, in principle, linear with respect to the flow direction, and the effect of the linear gradient has been removed by means of mirror alignment correction. In practice, these spatial corrections successfully allowed the laser to perform with high beam quality and temporal stability at pressures of 50 torr or lesser. However, as the pressure is increased from 50 to 130 torr, the temporal oscillation amplitude increased from threshold to 100% modulated. Figure 6B.20 shows this laser's beam power temporal dependence for various pressures. The signal is chopped to identify the null power point on each scope trace. The oscillation frequency spectrum centers about 20 kHz

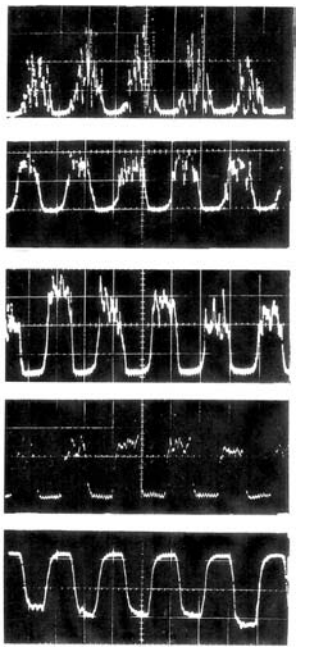

FIGURE 6B.20 Mode–media interaction instability growth with increase in pressure. Note that beam is chopped for clarity; note trace E.

and a net reduction in laser efficiency accompanies the increase in oscillation modulation level as the pressure is increased. As the pressure is increased, the oscillation modulation grows whereas efficiency and discharge stability degrade.

6B.2.19 Mode–Media Instabilities

To first order the inefficiencies of this lasing process provides heat that raises the plasma temperature and accelerates the flow velocity (Figure 6B.21). In turn, the neutral density is reduced in a nonlinear manner along the direction of flow owing to the complications of incompressible flow dynamics (Rayleigh heating). Next, the neutral density variations distort and bend the optical beam. These density variations also modulate the electric field/neutral density ratio (E/N), which spatially (and perhaps temporally) modulates the ionization process, and hence, the electrical current distribution. Next, this electrical perturbation spatially modulates the small signal gain distribution. The "real" gain, and correspondingly, the laser power output contribution from a particular volume element of gas media depend both on the small signal gain and the saturation of the stimulating beam at this point. The laser photon extraction is accompanied by a corresponding heat release $\Delta Q = h\nu\,(1-\eta_q)/\eta_q$. Thus, the feedback process is completed as the gas is further heated and accelerated, so the instability grows.

The reason that mode–media oscillations grow with increasing pressure becomes evident from the relationship of α_o and I_{sat} to gas kinetic parameters according to Equation 6B.20 and Equation 6B.21, which are restated here for the reader's convenience:

$$\alpha_o = \sigma(r_u\tau_u - r_l\tau_l) \tag{6B.69}$$

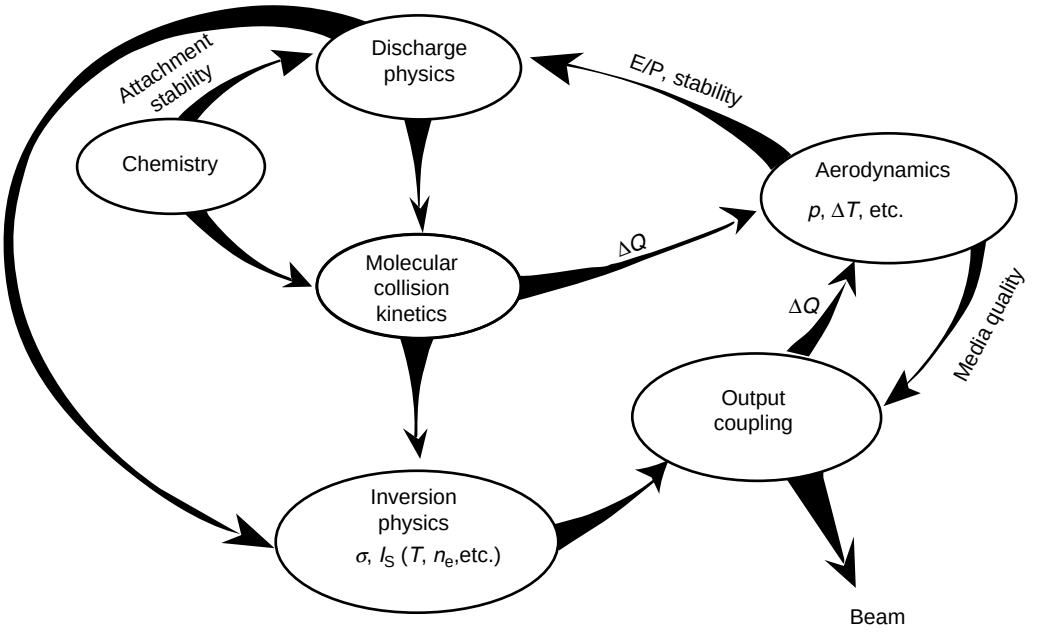

FIGURE 6B.21 Flow chart showing the development of a prominent mode media instability.

$$I_{\text{sat}} = \frac{h\nu'}{\sigma} \times \left[\frac{\tau_{\text{u}}\tau_{\text{f}}}{\tau_{\text{u}} + \tau_{\text{f}}} + \frac{\tau_{\text{l}}\tau_{\text{f}}}{\tau_{\text{l}} + \tau_{\text{f}}} \right]^{-1}, \tag{6B.70}$$

where r_{u}, r_{l} are the upper and lower level volume pumping rates, respectively; τ_{u}, τ_{l} are the upper and lower level volume collisional relaxation times, respectively; and τ_{f} is the cavity gas exchange time in the z direction. The parameters α_{o}, I_{sat} completely characterize the energy extraction properties of the gain media and determine the extraction efficiency (Equation 6B.42). Equation 6B.70 shows that I_{sat} depends only on gas kinetics that scale in proportion to P_2, and proportionate with the flow velocity when r_{f} becomes comparably small compared with τ_{l} or τ_2. However, α_{o} gets reduced proportional to an increase in pressure. Therefore, the net available energy $\iiint \alpha_{\text{o}} I_{\text{sat}} = \text{d}V$ increases linearly with P, but it becomes much harder to extract due to the reduction in gain. Hence, I/I_{sat} drops markedly and the extraction efficiency also drops. Three consequences of pressure scaling immediately aggravate mode–media interaction:

1. More energy is stored in the kinetic manifold (as opposed to being extracted as laser power). This fuels the instability.
2. The lasing efficiency is further lowered due to an increase in ξ, where $\langle \alpha_{\text{o}} L \rangle$ is reduced by an increase in thermal bottlenecking.
3. The increased pressure produces a greater optical wedge, thus bending transverse oscillator beams further out of resonance.

To recover lost extraction efficiency, the beam's cross-sectional area may be reduced or the cavity Q may be increased. In addition, the folded oscillator path may be increased in length to recover $\langle \alpha_{\text{o}} L \rangle$, that has reduced α by increasing P. But again, these actions have their deleterious consequences. By lengthening L, we extend the optical level arm while also

introducing more molecules in the optical path, which further increases beam bending. Corrective folding schemes then become mandatory.

Unstable resonators are often used at high-power levels since they support large mode volumes and alleviate the need to sustain damage producing intensity levels on mirror surfaces. However, unstable resonators used in cross flow configuration at high pressures create special problems. Unlike stable resonators, the unstable resonator must be operated at low magnification to avoid serious far-field diffraction power losses. Hence, its cavity Q is low, and the path length must be made long to preserve the necessary $\langle \alpha_o L \rangle$ product.

To make matters worse, the unstable resonator multiplies the density gradient induced wedge angle by the factor $2M/(M-1)$, where M is the magnification of a positive branch resonator.[38] As a further assault, the resonator's sensitivity to misalignment scales according to $\theta_{lt} = (D/L)\,((M-1)/2M)^2$, where θ_{lt} is the misalignment angle needed to totally extinguish oscillation, and D is the beam diameter. With L made quite long, the resonator's threshold to sustain relaxation oscillation becomes more sensitive to low-level, density gradient-induced, optical wedges.

Two significant steps seem prudent: (1) investigate large bore diameter axial systems wherein the gas flow, current flow, and optical axis (or axes) are mutually co-linear, since this (to the first order) decouples transverse bending, and (2) develop a means of homogeneously pumping at much higher than usual SPL levels while taking measures to minimize gas heating through efficient extraction designs. The higher pump rate maximizes

$$\langle \alpha_o L \rangle = \int_0^L a_{o(z)} \mathrm{d}z \tag{6B.71}$$

without increasing L.

These investigations have been carried out,[36] and a brief discussion of the significant findings will follow. The work was stimulated by the promise of a newly developed discharge technique,[12] which permits very homogeneous plasma excitation over large high-pressure gas volumes at SPL levels that exceed those normally achievable in quasiclosed cycle CO_2 lasers by a factor of 3. At this point, we return attention to the axial-flow controlled turbulence lasers discussed earlier. In these lasers $\langle \alpha_o L \rangle$ may be maximized, even for limited length (i.e., $L = 75$ cm or less). Therefore, very high extraction efficiencies result: for example $\eta_{ext} = 0.85$ when $\alpha_{opk} = 0.032$ and $\int_0^{75\text{ cm}} \alpha_{o(z)} \mathrm{d}z = 1.5$ at 40 torr. Using a 77% reflector stable multimode resonator, $\langle \alpha_o L \rangle$ peaked at SPL = 350 kW lb^{-1} mass, yielding 23.5% overall laser efficiency. The output power continued to rise to 7.2 kW at 19% efficiency and SPL = 500 kW lb^{-1} mass sec (Figure 6B.6). It seems remarkable on first glance that thermal bottlenecking does not prevent effective use of our recently acquired SPL capability. However, detailed calculations reveal a bootstrapping effect. As the input power is increased, then $\langle \alpha_o L \rangle$ increases so η_{ext} also increases, which decreases ξ. Hence, a lower percent of the applied power goes into gas heating. A small reduction in ξ helps a great deal since the gain is choked exponentially with increasing temperature owing to the Boltzmann factor in Equation 6B.38, whereas additionally the rate of laser power extraction scales with $\langle \alpha_o L \rangle$. This effect requires that the resonator be optimally coupled as provided by Equation 6B.42 and Equation 6B.44, which effect is plotted in Figure 6B.5. These results suggested that an unstable resonator, subject to favorable gain-length produce in axial configuration, should operate efficiently and avoid mode–media interaction. This did not happen, and the reasons are quite revealing.

Difficulties began when, to optimize far-field brightness at the expense of a "small" power and efficiency sacrifice, the resonator's magnification was reduced. This change should have cut the laser efficiency η_t from 0.235 to about 0.17. Instead, η_t dropped down to 0.05–0.08

depending on SPL, and severe mode–media oscillations at acoustic frequencies set in, accompanied by mode beating at 100 kHz frequencies.

Apparently, this compromise in cavity Q led to a runaway degradation of power and efficiency due to feedback through the thermal bottlenecking process—the exact opposite of the stable resonator bootstrapping process. Thus, the reduced resonator efficiency increased gas heating, which in turn lowered $\alpha_{o(z)}$ and therefore $\langle \alpha_o L \rangle$. As the extraction efficiency is lowered, it further increases ξ so that more heat is dumped into the gas flow stream, closing a feedback loop, and then runaway degradation occurs. It is well known that resonator efficiency is controlled by the gain, but now we have the additional mechanism whereby gas is, in turn, controlled (lowered) by the resonator efficiency, and the two effects feed on each other. This phenomenon is peculiar to the situation where the gain media is pumped at SPL levels that approach the thermal bottleneck limit, and the resonator's Q is somewhat lower than optimal. The 20 kW class laser was used in these experiments. A calculated gain distribution plot that illustrates the runaway resonator degradation is shown in Figure 6B.22.

Since $\langle \alpha_o L \rangle$ is no longer favorably large, the resonator (and particularly an unstable resonator) becomes more sensitive to mechanisms that can impart a time-varying radial component to the beam's intensity profile. Three mechanisms can readily pluck a transverse oscillation in an undersaturated, overpumped, axially symmetric laser. They are (1) velocity asymmetries, (2) beam profile gradients or dead areas, and (3) slight mechanical vibrations imparted to the resonator or stronger gas pressure fluctuations introduced by the pump.

Velocity asymmetries lead to thermal instabilities because slower moving gas streams get heated more than adjacent faster moving gas streams. A density disturbance results, wherein E/N rises, thus initiating runaway mode media oscillations. Transverse coupling occurs due to radial flow components that are created by the ensuing radial thermal gradient established between adjacent flow streams. Radially dependent heat release triggered by nonuniform beam saturation extraction can create radially dependent density and temperature changes,

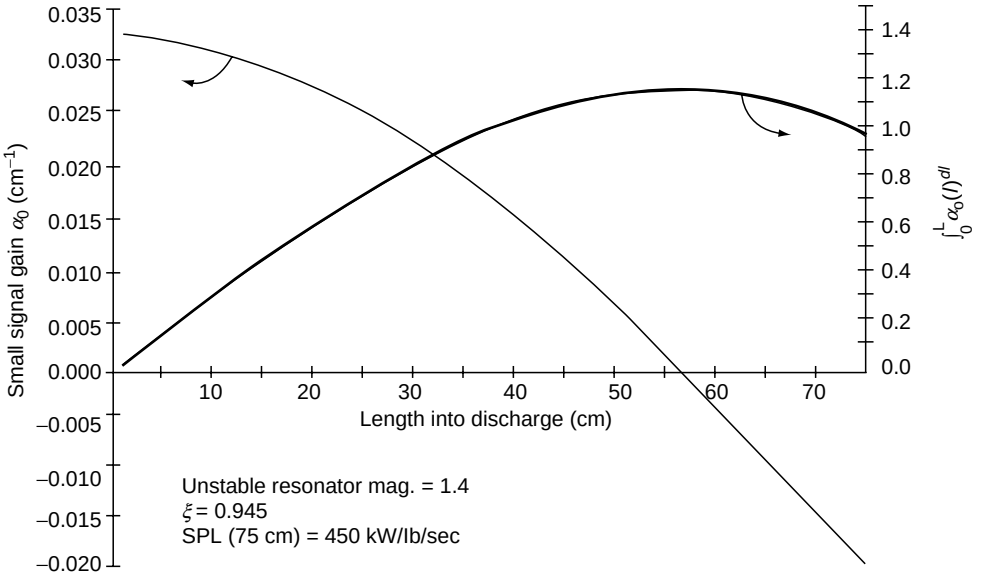

FIGURE 6B.22 A variation of α_o and $\int_o^L \alpha_{o(l)}{}^{dl}$ vs. position along a flow stream under highly nonoptimal conditions, wherein several mode–media interaction instabilities dominate.

thus leading to the same results produced by velocity shear. The beam gradient effects can be reduced by ensuring that the kinetic CO_2 (001) deactivation time is long compared with diffusion times, which are driven by thermally induced radial pressure gradients. Kinetics, beam profile, packing schemes, level of saturation, and turbulent scale size all play a role in dealing with this process. Resonator vibration directly introduces transverse beam oscillations, which get further magnified by the unstable resonator.

Thermal streamers or attachment instabilities that normally result under high-SPL conditions at high pressure are a significant source of radial density gradients, which also introduce transverse beam oscillation. The plasma is particularly well behaved under these conditions; however, the disturbances mentioned above can be reinforced (amplified) by the thermal instabilities they create.[36] Thermal instabilities can launch attachment instabilities, and vice versa. It is therefore helpful to remove electronegative plasma by-products using catalytic converters for closed (or quasiclosed) cycle operation, as has been experimentally verified.

By means of removing mechanical vibration coupled to the resonator, and by correcting slight flow asymmetries, we were able to suppress the transverse mode coupling mechanisms and thus eliminate the mode–media oscillation from the axial unstable resonator laser. However, the laser's efficiency and power were only slightly enhanced.

6B.2.20 Suggested Methodologies to Eliminate Mode–Media Interaction Instabilities

Whenever logistics allow, it is always preferable to use a MOPA configuration. Small oscillators with stable single-mode cavities may be precisely controlled. The oscillator beam can be slowly expanded, thereby maintaining saturation within a regenerative amplifier. For this case, limited cavity feedback is used to hasten amplification whereas an oscillator beam dominates control by starving the parasitic modes. Then power amplifier stages to follow should be void of any feedback return paths, and should be driven to a high level of saturation over its entire mode volume. If the regenerative amplifier does develop spatial perturbations, they can be corrected using phase conjugate optics if necessary.

In most respects, high repetition pulsed lasers are the easiest to control. Their gain media is fully saturated, and uniformly so over their entire volumes. Waste heat always causes problems—either thermal effects in real time for the case of continuous operation, or shock waves and other acoustical disturbances in the case of pulsed operation. In either case, we must proactively take action. In pulsed operation the pulse may (in principle) be delivered without difficulty, as long as the shock waves and acoustic waves are absorbed or deflected; that is, generally dissipated by ~60 dB during the intervening time period between pulses. Furthermore, the heated gas volume and preferably three-cavity volume exchanges should be completed as well within the intervening time between pulses. Finally, the pulse duration need to be made sufficiently short so as not to allow the pulsed cathode shock wave to travel into the gain extraction region. Therefore, now a different set of conditions must be met. In addition, there will always be constraints on design parameters. Nonetheless, here we are dealing with problems for which solutions do exist.

Finally, it is suggested that supersonic plasmas be explored for their potential as gain media, which would seem to provide enormous power, compact geometry, and would tend to correct most of the causes of power scaling dependent beam degradation. The approach entails longitudinal excitation of supersonic flow streams, which have been produced using a controlled turbulence stabilization method that operates supersonically.

When heat is added to a supersonic flow stream, the density increases whereas the flow velocity decreases; i.e., both parameters act in opposite directions compared with heat addition to a subsonic flow stream. The net effect is that $(\Delta\rho/\rho)_q$ changes sign, and the

overall feedback changes from positive to negative. Hence, we expect stability rather than oscillation. Furthermore, the magnitude of density change with heat addition becomes an order of magnitude smaller when adding a given SPL to a $M = 3$ flow stream compared with adding it to a $M = 0.35$ flow stream.

For supersonic flow, the density-length product is substantially reduced since power scaling is facilitated by molecular transport. That is, both α_o and I_{sat} increase with velocity. Therefore, the resonator optical path length may be reduced in addition to minimizing the number of interacting molecules within the mode volume.

Finally, the initial gas temperature is reduced to the freezing point of CO_2, and in fact, heat must be added to stay above this temperature. As a result, thermal bottlenecking is held off so that the SPL can be approximately doubled.

The controlled turbulence techniques have been modified to excite Mach $M = 2.8$ plasmas at 15 torr in a 15 cm longitudinal channel of 4 cm^2 cross-section area. Here, a power input of 12.5 kW produced a uniform, diffuse glow that decelerated the $M = 2.8$ flow stream to $M = 1.5$ as its exit. This experimental validation bodes well for the viability of the technique.

6B.2.21 Promising Areas of Development for the Future

There are exciting future applications of universal importance to be considered for high-powered, efficient lasers that have good beam quality. Among these potential applications are: space debris removal, energy transmission through space, ground-based launch of small satellites into near-earth orbit, and possibly the deflection of meteorites heading for earth. As far out as these ideas might seem, lasers of the several megawatt to 10 MW class could accomplish a few of these goals quite nicely. At this point, several lasers appear scalable to the necessary degree and possess excellent beam quality; i.e., the oxygen iodine laser and the CO_2 laser. Whatever the laser, it must be very efficient. Moreover, herein lies the opportunity.

Marlan Scully at Texas A&M University[39] has shown that it is possible to improve the efficiency of a classical Otto cycle (or variant cycle) heat engine by adding a laser system that can exhibit coherent laser energy from the thermally excited exhaust atoms or molecules. In addition, the author and his colleagues at Texas A&M University[40–42] have specifically shown how to do the reverse; that is, improve the efficiency of a CO_2 laser by using its waste thermal energy to power a heat engine. This is accomplished using a closed loop flow stream, which couples the laser and heat engine together. This can be done for either a pulsed laser coupled to a piston-type engine or a CW laser coupled to a Brayton cycle turbine engine. Then the extracted mechanical power generates electricity that partially powers the laser.

Either of these two basic approaches can be shown to have a new combined Carnot efficiency, which characterizes the coupled system as one, and that can reach on the order of 70% to 80% efficiency. However, one must find a practical way to implement the process, and this *has* been done, but only for the case of the CO_2 laser, which thermally drives the heat engine.

In 1959, Scovil[43] described the CO_2 laser itself as a heat engine. Specifically he demonstrated that the quantum efficiency for the CO_2 laser ($\eta_q = 0.41$) could not exceed a thermal limit, established by the vibrational temperature of the upper and lower states T_2 and T_1. That is,

$$\eta_q \leq \frac{T_2 - T_1}{T_2} = \eta_L \tag{6B.72}$$

Therefore, the laser itself can be viewed as a heat engine subject to the usual Second Law of Thermodynamics.

The work of Scully and colleagues shows that if a mechanical engine has a Carnot efficiency $= \eta_E$, then theoretically for either a laser-heat engine or heat engine-laser scenario, the combined system Carnot efficiency is very nearly

$$\eta_{tot} = \eta_e + \eta_E - \eta_l \eta_E. \tag{6B.73}$$

In carefully designed and analyzed systems, Hill and colleagues derived for the case of a pulsed CO_2 laser/reciprocating engine, $\eta_q = 41\%$, $\eta_E = 81\%$, hence $\eta_{tot} = 89\%$. However, this is not realistic since both laser and engine suffered engineering related losses. However, accounting for known system losses, a realistic efficiency may be $\eta_{tot} = 56\%$. For this case, the actual laser efficiency 0.23, so the net required electric input power is reduced by a factor of 2.4.

The case for a CW laser coupled to a Brayton engine showed significantly better results.[41] For this case, $\eta_L = 0.26$, $\eta_E = 83\%$, so η_{tot} (theoretical max) $= 87\%$. This time, after accounting for known system loss, a realistic estimate becomes $\eta_{tot} \approx 78\%$, thereby lowering the net power applied to the laser by a factor of three. Of course, there are external system losses not included, so the total performance projection must be somewhat further reduced. In another variation of this scheme, the waste heat generated in a rapid pulsed laser is harnessed to pump the laser gas around the closed cycle loop.[42]

It is hoped that this development will serve as an example of how CO_2 lasers continue to progress even after 40 years time, and that the community will continue to mature along lines that will launch a few of the exciting applications of the future.

REFERENCES

1. Eletskii, A.V. and Smirov, B.B., A pulsed carbon dioxide laser, *Doklady*, 15, 109, 1970.
2. Tony DeMaria, personal communication.
3. Harrington, R.E., Application of the theory of heat conduction to the absorption of blackbody radiation, *J. Appl. Phys.*, 38, 3266, 1961.
4. Hill, A.E., Role of thermal effects and fast flow power scaling techniques in CO_2–N_2–He lasers, *Appl. Phys. Lett.*, 16, 423, 1970.
5. Hill, A.E., Multijoule pulses from CO_2 lasers, *Appl. Phys. Lett.*, 12, 324, 1968.
6. DeMaria, A.J., Review of CW-high power CO_2 lasers, *Proc. IEEE*, 61, 731, 1973.
7. Tiffany, W.B., Tang, R., and Foster, J.D., CW operation of high pressure flowing CO_2 lasers, *Appl. Phys. Lett.*, 15, 91, 1969.
8. Hill, A.E., Uniform excitation of large-volume, high pressure, near-sonic CO_2–N_2–He flow stream, *Appl. Phys. Lett.*, 18, 194, 1971.
9. Hill, A.E., Uniform electrical excitation of large volume, high pressure gases with application to laser technology, *AIAA Mtg.*, Paper No. 71–65, New York, 1, Jan. 25–27, 1971.
10. Hill, A.E., Aerodynamic large volume gaseous electric discharge system, *U.S. Patent* No. 3,795,838, March 5, 1974.
11. Brown, C.O. and Davis, J.W., Closed-cycle performance of a high-power electric discharge laser, *Appl. Phys. Lett.*, 21, 480, 1972.
12. Hill, A.E., Large volume gaseous electric discharge system, *U.S. Patent* No. 4, 849, 984, July 18, 1989.
13. Brown, S.C., *Basic Data of Plasma Physics*, MIT Press, 1967.
14. Beaulieu, A.J., Transversely excited atmospheric pressure CO_2 lasers, *Appl. Phys. Lett.*, 16, 504, 1970.
15. Beaulieu, A.J., High peak power gas lasers, *Proc. IEEE*, 59, 667, 1971.
16. Cobine, J.C., *Gaseous Conductors*, Dover, 1958.
17. Vladimir Baronov, personal communication.
18. Dean Judd, personal communication.
19. Richardson, M.C., Alcock, A.J., Leopold, K., and Burtyn, P.A., 300-J multigigawatt CO_2 laser, *IEEE J. Quantum Electron.*, QE-9, 236, 1973.

20. Duley, W.W., *CO_2 Lasers*, Academic Press, 1976.
21. Wood, O.R., High-pressure pulsed molecular lasers, *Proc. IEEE*, 62, 355, 1974.
22. Mezhevov, S.V. personal communication.
23. Baranov, V.Y., Dyad'kin, A.P., Malyuta, D.D., Kuzmenko, V.A., Pigulsky, S.V., Mezhevov, V.S., Letokhov, V.S., Laptev, V.B., Ryabov, E.A., Yarovoi, I.V., Zarin, V.B., and Podoryashy, A.S., Production of carbon isotopes by laser separation, in Panchenko, V.Y., and Golubev, V.S. (eds.), Progress in Research and Development of High-Power Industrial CO_2 Lasers, *SPIE Proc.*, 4165, 2000.
24. Fenstermacher, C.A., Nutter, M.J., Leland, W.T., and Boyer, K., Electron-beam-controlled electrical discharge as a method of pumping large volumes of CO_2 laser media at high pressure, *Bull. Am. Phys. Soc.*, 16, 42, 1971.
25. Daugherty, J.D., Electron beam sustainer laser, *High Power Molecular Lasers Symp.*, Quebec, May 15–17, 1972.
26. Basov, N.G., Electroionization lasers, *VII Int. Quantum Electron. Conf.*, Montreal, May 8–11, 1972.
27. Nicholi Basov, personal communication.
28. Daugherty, J.D., Pugh, E.R., and Douglas-Hamilton, D., *Bull. Am. Phys. Soc.*, 17, 399, 1972.
29. Willie Bohn, personal communication.
30. Renz, G., Jung, M., Mayerhofer, W., and Zeyfang, E., Pulsed CO_2 laser with 15 kW average power at 100 Hz repetition rate, *SPIE Proc.*, 3072, 114–117, 1997.
31. Javan, A. and Levine, J.S., The feasibility of producing laser plasmas via photo-ionization, *IEEE J. Quantum Electron.*, QE8, 827, 1972.
32. Victor Apollonov, personal communication.
33. Hill, A.E., Continuous uniform excitation of medium-pressure CO_2 laser plasmas by means of controlled avalanche ionization, *Appl. Phys. Lett.*, 22, 670, 1973.
34. Reilly, J.P., Pulser sustainer electric discharge laser, *J. Appl. Phys.*, 43, 3411, 1972.
35. Hill, A.E., Compact, flexible, rapid-pulsed, molecular gas laser, *U.S. Patent* No. 6, 771, 684, 2004.
36. Hill, A.E., Coupled beam-gas dynamic ionization interactions in continuous laser plasmas: *14*th *Int. Conf. on Phenomena in Ionized Gases*, Belgrade, July 10–14, 1989.
37. Jack Daugherty and Gene Parasini, personal communication.
38. Siegman, A.E., *Lasers*, University Science Books, 1986.
39. Scully, M.O., The quantum Otto mobile, *Phys. Rev. Lett.*, 88, 050602, 2002.
40. Hill, A.E., Rostovtsev, Y.V., and Scully, M.O., The quantum Otto mobile and its application to directed energy, *SPIE Conf. Proc.*, 5448, Taos, 84, April 25–30, 2004.
41. Hill, A.E., Performance projection for a functional CO_2 laser coupled quantum heat engine, *J. Modern Optics*, 51, 2713, 2004.
42. Hill, A.E., Rostovtsev, Y.V., and Scully, M.O., Practical implementation of a CO_2 laser coupled quantum heat engine, *Phys. Rev.* A, 72, 043802, 2006.
43. Scovil, H.E.D. and Shultz-DuBois, E.O., Three-level masers as heat engines, *Phys. Rev. Lett.*, 2, 262, 1959.

7 Hydrogen and Deuterium Fluoride Chemical Lasers

Wilhelm H. Behrens and Peter D. Lohn

CONTENTS

7.1 OVERVIEW

This chapter covers the following topics:

A basic overview of hydrogen fluoride (HF*) and deuterium fluoride (DF*) continuous-wave combustion driven chemical lasers, the physics and chemistry of these lasers, fluid mechanics, and modeling of chemical lasers.

For arc driven CW chemical lasers, we refer the reader to the *Handbook of Chemical Lasers* [1]. For pulsed chemical lasers, the reader is referred to references [1] through [3]. An overall view of chemical lasers is given in [4] and more details are provided in [1]. An example of a high energy laser development program is presented in [5].

The lasing wavelengths for the HF* laser are between 2.6 μm and 3.0 μm with the main power around 2.7 μm. For the DF* laser the spectral lines are between 3.6 μm and 4.0 μm with the main power at about 3.8 μm.

Continuous wave combustion driven CW HF*/DF* lasers work on the principle of heat generative reaction of fluorine (F_2) or nitrogen trifluoride (NF_3) and deuterium (D_2) to produce fluorine (F) atoms. Fluorine with diluent, typically helium, is then reacted at supersonic speeds with hydrogen (H_2) in the lasing cavity to form vibrationally excited HF*. The reactions are similar in a DF* laser (see Figure 7.1).

HF Laser

Combustor reactions: $2NF_3 + 3D_2 \rightarrow 6DF + N_2 + \text{Sensible heat Q}$

$2NF_3 + Q \rightarrow N_2 + 6F$

Laser cavity reactions: $H_2 + F \rightarrow HF^4 + H$

DF Laser

Combustor reactions: $4NF_3 + C_3H_4 \rightarrow 2CF_4 + 4HF + 2N_2 + \text{Sensible heat Q}$

$2NF_3 + Q \rightarrow N_1 + 6F$

Laser cavity reactions: $D_2 + F \rightarrow DF^* + D$

Combustor and cavity chemistry

FIGURE 7.1 Combustor and cavity chemistry.

Propagation of HF* laser beams through the atmosphere is very poor because of the water content in atmospheric air. DF* laser beam propagation is much better. The laser beam atmospheric attenuation for HF lasing is more than 90%/km and for DF lasing it is less than 5%/km.

The main components of the chemical laser are depicted in Figure 7.2. The processes in HF* and DF* lasers are the same. Combustor reactants are fed into the combustor in a fine gas stream to facilitate thorough mixing of the reactants and complete combustion. The flow is subsonic and the combustor pressure is of the order of 25 to 250 psi (170–1700 kPa) and the adiabatic flame temperature is 1800 to 2000 K. Because of combustor heat loss, the gas temperature at the sonic throat of the supersonic nozzle cavity injector is of the order of 1500 K.

The cavity oxidizer (atomic fluorine) is injected together with diluent (helium and the other combustor products) into the lasing cavity where it is mixed at a very fine scale with the cavity fuel H_2 with some more helium diluent. The supersonic combustion product, vibrationally excited HF*, serves as the photon donor when a proper optical laser cavity mirror system extracts the laser beam. The pressure in the lasing cavity ranges from about 3 to 35 torr. Further discussion of the laser resonator and laser beam diagnostics is undertaken in other chapters.

The laser system requires additional components that are depicted in Figure 7.3 for a ground based DF* system. The fluid supply and the pressure recovery subsystems are two additional key elements of a chemical laser. The fluid supply system consists of high pressure gas tanks where the reactants and helium diluent are premixed. The water supply for the heat exchanger and ejector system gases are also shown. If required, a gas scrubber upstream or downstream the ejector pump is also added.

For a deuterium fluoride laser where the lasing cavity supersonic flow is at a pressure of 25 to 35 torr, the passive diffuser will recover the flow from 150 to 250 torr (with appropriate back pressure). The ejector pump then increases the pressure to the atmospheric level. To get a basic idea of the available laser power that can be extracted from the excited hydrogen fluoride, see Figure 7.4 (and Figure 7.5 for DF), which shows the various loss mechanisms. The reaction

$$F + H_2 \longleftrightarrow HF^* + H + 132.2 \text{ kJ/mole F}, \tag{7.1}$$

which is equivalent to 6964 J/g_F (as atoms). Subtracting all the losses including collisional deactivation, the HF/DF laser efficiency is roughly 800 to 1600 J/g_F, depending on

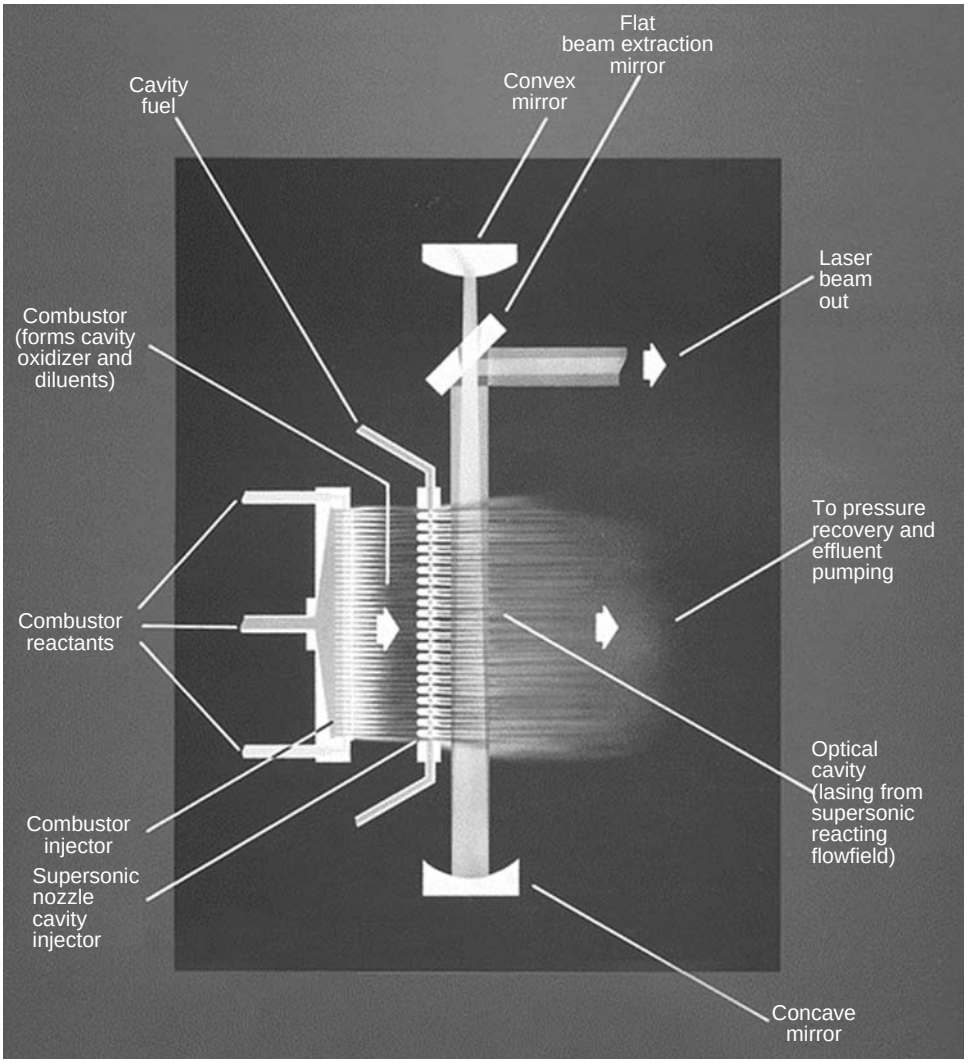

FIGURE 7.2 Main components of combustion driven HF/DF chemical lasers.

the laser cavity pressure. To first order, the lower the laser cavity pressure the higher is the chemical efficiency.

Laser performance, besides its chemical efficiency, depends strongly on the laser beam quality, which in turn depends on the lasing medium quality, the quality of the mirrors, the windows and jitter of the optical system. Jitter depends on vibration of the overall laser system. Laser brightness and intensity on target are key parameters as illustrated in Figure 7.6. Brightness is proportional to laser power and telescope diameter square and one over the square of the laser wavelength. Intensity is brightness over the square of the target distance. Considering that laser medium inhomogeneity and tolerance of mirror figure (wavefront error) are measured in terms of laser wavelength and the wavefront distortions scale with wavelength, it is important to note that the shorter the laser wavelength, the harder it is to achieve beam quality close to its diffraction limit.

For the convenience of the reader, important laser performance parameters are defined in Figure 7.7.

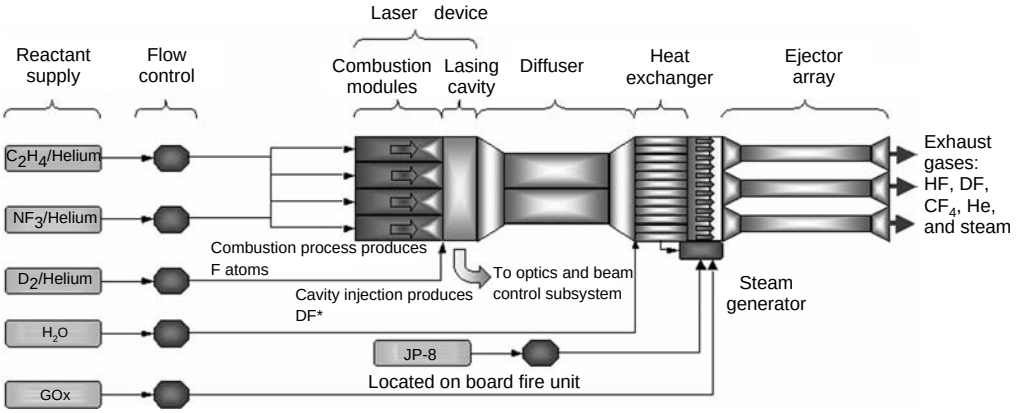

FIGURE 7.3 Laser system components.

Available laser power for HF laser

$$F + H_2 > HF^* + H + 31.8 \frac{kcal}{mole\ F}$$

$$\text{Chemical energy release } 6964 \frac{Joules}{g_{Flourine}}$$

$$\text{Thermal energy } 0.3 \times 6964 = 2089 \frac{Joules}{g_F}$$

$$\text{Vibrational energy } = 4875 \frac{Joules}{g_F}$$

$$\left.\begin{array}{l} HF^*(3) = 1365 \\ HF^*(2) = 2681 \\ HF^*(1) = 828 \end{array}\right\} 4875$$

Extractable power without collisional deactivation approximately ~3300 $\frac{Joules}{g_F}$

Present laser efficiencies ~600–1600 $\frac{Joules}{g_F}$

FIGURE 7.4 HF available laser power.

Available laser power for DF laser

$$F + D_2 > DF^* + D + 30.6 \frac{kcal}{mole\ F}$$

$$\text{Chemical energy release } 6742 \frac{Joules}{g_{Flourine}}$$

$$\text{Thermal energy } 0.28 \times 8742 = 1888 \frac{Joules}{g_{Flourine}}$$

$$\text{Vibrational energy } = 4854 \frac{Joules}{g_{Flourine}}$$

$$\left.\begin{array}{l} DF^*(4) = 1311 \\ DF^*(3) = 2136 \\ DF^*(2) = 1068 \\ DF^*(1) = 338 \end{array}\right\} 4854$$

Extractable power without collisional deactivation approximately ~3300 $\frac{Joules}{g_F}$

Present laser efficiencies ~600–1600 $\frac{Joules}{g_F}$

FIGURE 7.5 DF available laser power.

$$B \sim \frac{(P)(D^2)}{\lambda^2} \quad f(\text{Jitter, WFE}); \quad I_{\text{target}} \sim \frac{B}{R^2}$$

where

B = Brightness
P = Power of laser
D = Diameter of transmitting telescope
λ = Laser wavelength
Jitter = Measure of pointing stability of laser beam
WFE = Measure of quality of laser beam
(*Note*: WFE is a characteristic that differentiates laser from flashlight and a key measure of ability to focus beam at long ranges.)
I_{target} = Laser intensity at target
R = Range (distance) from laser to target

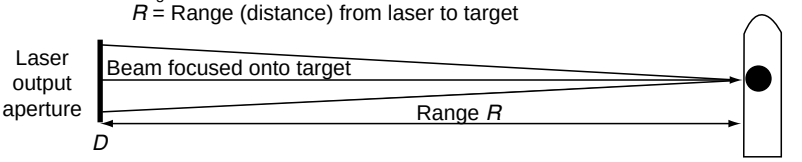

FIGURE 7.6 Laser performance factors: brightness defined, intensity on target calculated.

7.2 PHYSICS AND CHEMISTRY OF COMBUSTION DRIVEN CONTINUOUS WAVE CHEMICAL LASERS

In the combustor, free fluorine atoms are produced. The mixture ratio of the combustor reactions is crucial because it needs to be such that close to 100% dissociated fluorine is achieved in the combustor. An example of the fluorine dissociation as a function of combustor pressure and temperature for a representative combustor diluent ratio of 12 is shown in Figure 7.8. This graph holds for both HF and DF lasers. The combustor diluent ratio is defined in Figure 7.7.

Combustor dissociation fraction $\alpha = \dfrac{[F]}{[F_2] + [F]}$

Combustor diluent ratio $\psi_c = \dfrac{[He] + [other]}{[F_2] + \frac{1}{2}[F]}$

Cavity diluent ratio $\psi_L = \dfrac{[He] + [other]}{[F_2] + \frac{1}{2}[F]}$

Mixture ratio into laser cavity $R_L = \dfrac{[H_2]}{[F_2] + \frac{1}{2}[F]}$

Total laser molar diluent ratio $\Omega = \psi_L + \psi_C$

Specific power $\sigma = \dfrac{\text{Power}}{\text{Mass flow}} \dfrac{\text{kJ}}{\text{kg}}$

Nozzle power flux $\delta = \dfrac{\text{Power}}{\text{Nozzle frontal area}} \dfrac{\text{kW}}{\text{m}^2}$

Fluorine efficiency $\eta = \dfrac{\text{Laser energy}}{g_{\text{Flourine}}} \dfrac{\text{J}}{g_F}$

[] denotes a molar value

FIGURE 7.7 Laser parameters.

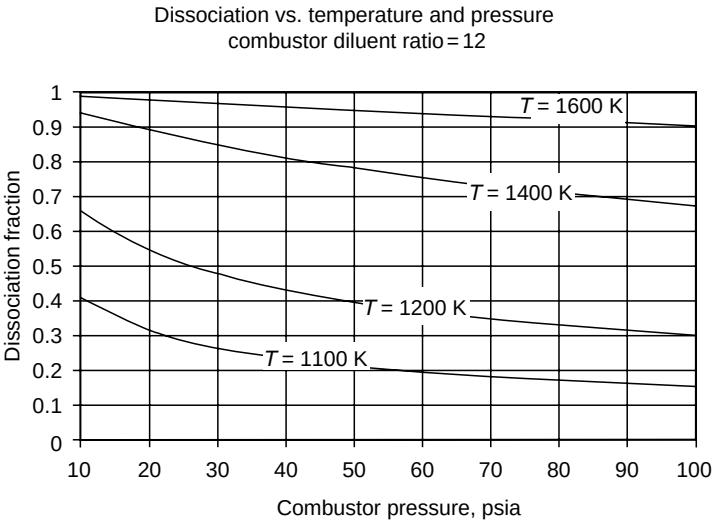

FIGURE 7.8 (**See color insert following page 334**.) Dissociation vs. temperature and pressure.

The combustor flow containing the fluorine atoms is then mixed with hydrogen or deuterium in the supersonic mixing region downstream the supersonic nozzles. The reaction between hydrogen and fluorine is hypergolic. As the fluorine atoms and hydrogen molecules collide, they spontaneously react and produce excited state HF (HF*). The energy levels for the reactions $F + H_2$ and $F + D_2$ are shown in Figure 7.9. The reactions producing HF* typically result in three vibrational states and those producing DF* result in four vibrational states beyond the ground state.

The HF laser energy levels along with the lasing wavelengths are shown in Figure 7.10. In this figure, the rotational states are the J-states and the vibrational states are the V-states. For the fundamental HF* transition $\Delta V = -1$ and $\Delta J = +1$. These are P-branch transitions. For the R-branch transitions, the R-branch $\Delta J = -1$. R-branch power is very difficult to obtain. Lasing in the fundamental mode is described in references [6] through [8].

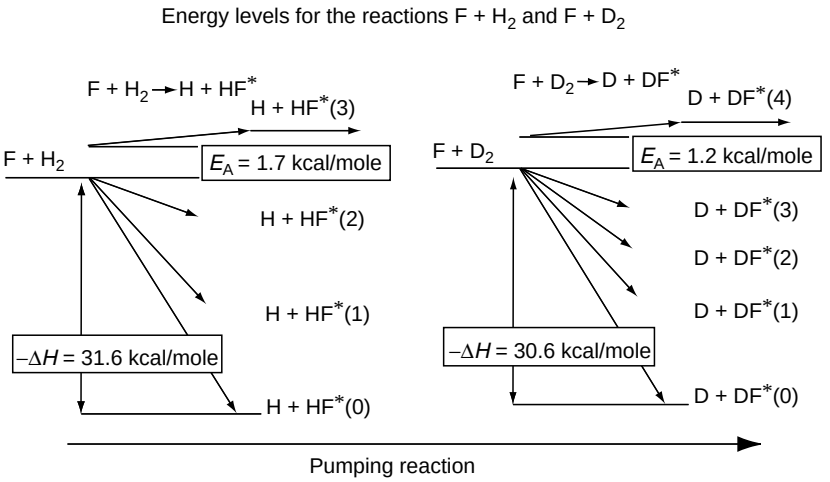

FIGURE 7.9 Energy levels for the reactions $F + H_2$ and $F + D_2$.

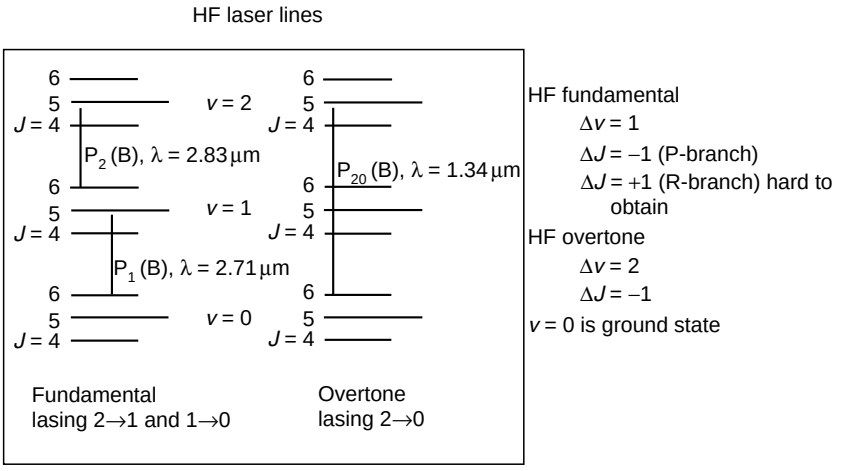

FIGURE 7.10 HF laser lines.

There are also the HF overtone transitions which result in approximately half the wavelength of the fundamental, that is, $\lambda \simeq 1.34$ μm. (Overtone lasing is harder to accomplish because the very large gain in the fundamental has to be virtually completely suppressed to achieve lasing at the overtone wavelength [9,10].

The basic chemistry and probabilities of achieving the vibrational states 1 to 3 of the *cold reactions* are shown in Figure 7.11 and Figure 7.12. The *hot reactions* are also shown but are much less likely to be achieved [1]. These reactions are called cold and hot reactions because of the different exothermissivities associated with these reactions (−31.6 kcal/mole for the cold reaction and −97.9 kcal/mole for the hot reaction). Rate coefficients for HF and DF kinetics are discussed in [11] and [12].

The light emissions, spontaneous, and lasing emissions are reviewed in [1]. In the case of lasing emissions, the incident lasing field stimulates emission of an additional coherent photon from the excited molecule. The initially excited molecule drops by one transition as it adds energy to and increases the gain of the lasing field.

Modeling of these processes is deferred to Section 7.4 of this chapter. Representative closed cavity lasing spectra are shown in Figure 7.13 and Figure 7.14.

- Pumping reactions (HF)
  - $F + H_2 \rightarrow HF(v,J) + H, v = 1–3$, Cold reaction

V	1	2	3
Probability	0.174	0.562	0.264

  - $H + F_2 \rightarrow HF(v,J) + F, v = 1–7$, Hot reaction
- Deactivation reactions
  - $HF(v') + HF(v'') \rightarrow HF(v' + 1) + HF(v''–1)$, v–v Transfer
  - $HF(v) + M \rightarrow HF(v–1) + M$, v—T Transfer—Energy shows up as sensible heat
- Spontaneous emission
  - $HF(v,J) \rightarrow HF(v–1) + hv$
- Lasing
  - $HF(v,J) + hv \rightarrow (v–1, J + 1) + 2hv$

FIGURE 7.11 Basic chemistry of HF chemical lasers.

- Pumping reactions (DF)
  - $F + D_2 \rightarrow DF(v,J) + D, v = 1–3$, Cold reaction

V	1	2	3	4
Probability	0.106	0.246	0.379	0.269

  - $D + F_2 \rightarrow DF(v,J) + F, v = 1–7$, Hot reaction
- Deactivation reactions
  - $DF(v') + DF(v'') \rightarrow DF(v'+1) + DF(v''–1)$, $v–v$ Transfer
  - $DF(v') + M \rightarrow DF(v–1) + M$, $v–T$ transfer –Energy shows up as heat
- Spontaneous emission
  - $DF(v,J) \rightarrow DF(v–1) + hv$
- Lasing
  - $DF(v,J) + hv \rightarrow DF(v–1, J = 1) + 2\,hv$

FIGURE 7.12 Basic chemistry of DF chemical lasers.

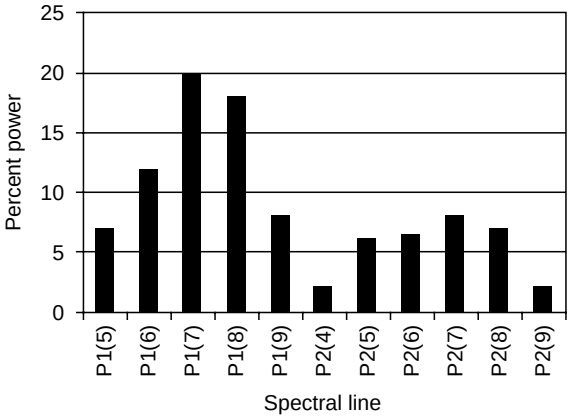

FIGURE 7.13 Representative HF power spectrum.

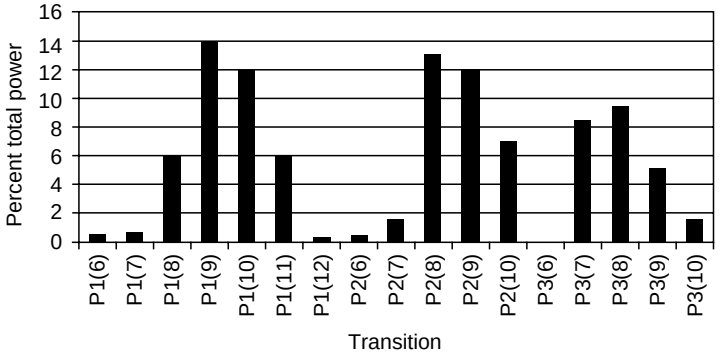

FIGURE 7.14 Representative DF power spectrum.

- Pumping reactions: $F + H_2 > HF\ (v) + H$; $v = 1, 2, 3$
- v–v Transfer: $HF^*(v1) + HF^*\ (v2) > HF(v3) + HF(v4)$; $v1 + v2 = v3 + v4$
  $HF^*(v1) + H_2^*\ (v2) > HF^*(v3) + H_2^*(v4)$; $v1 + v2 = v3 + v4$
- v–T Deactivation: $HF^*(v + 1) + M > HF^*(v) + M$; M can either represent another species or a weighted sum of all species: HF(0), HF*(1), HF*(2), HF*(3), HF*(4), DF, H, $H_2(0)$, $H_2(1)$, F, F_2, He, N_2
- Reaction rates of the form $k_t = Ae^{B/RT}/T^n$ where R is the universal gas constant. Approximately 70 reactions.
- Typical values are (units are cm, g mol, s, cal for binary reactions [A] = cm^3/mol–s; [B] = cal/mol)
  - Pumping: $A = 1 \times 10^{10}$; $B = -330$; $n = -1, 2$
  - v–v Transfer: $A = 2 \times 10^{16}$; $n = 1$; $B = 0$
  - v–T Transfer: two additive terms
    - ($A = 1 \times 10^6$; $n = -2, 3$; $B = 0$) and ($A = 5 \times 10^{12}$; $n = 1$; $B = 0$)

FIGURE 7.15 HF kinetics.

For HF lasing, only the cold reaction fundamental vibrational lines of the vibrational states 1 and 2 are measured and for DF lasing three vibrational levels of the cold reaction fundamental lines are observed. Kinetics rates for HF and DF lasers are outlined in Figure 7.15 and Figure 7.16.

The chemically available laser power was illustrated for HF lasing and DF lasing in Figure 7.4 and Figure 7.5 respectively.

7.3 FLUID MECHANICS OF CHEMICAL LASERS

In this section the laser internal flows from combustor and laser cavity to pressure recovery system will be discussed. The fluid supply system in an operational device is also important but established sound engineering practices will be able to deal with these systems. The laser elements are shown in a schematic shown in Figure 7.17.

- Pumping reactions: $F + D_2 > DF(v) + D$; $v = 1, 2, 3$
- v–v Transfer: $DF^*(v1) + DF^*(v2) > DF(v3) + DF(v4)$; $v1 + v2 = v3 + v4$
- $DF^*(v1) + D_2^*(v2) > DF^*(v3) + D_2(v4)$; $v1 + v2 = v3 + v4$
- v–T Deactivation : $DF^*(v + 1) + M > DF^*(v) + M$; M can either represent another species or a weighted sum of all species: DF(0), DF*(1), DF*(2), DF*(3), DF*(4), DF*(5), HF, D, $D_2(0)$, $D_2(1)$, $D_2(2)$, F, F_2, He, N_2, CF_4
- Reaction rates of the form $k_t = Ae^{B/RT}/T^n$ where R is the universal gas constant. Approximately 80 reactions.
- Typical values are (units are cm, g mol, s, cal for binary reactions [A] = cm^3/mol – s; [B] = cal/mol)
  - Pumping: $A = 5 \times 10^9$; $B = -460$; $n = -1, 2$
  - v–v Transfer: $A = 8 \times 10^{15}$; $n = 1$; B = 0
  - v–T Transfer: two additive terms
    - ($A = 2 \times 10^4$; $n = -2.4$; $B = 0$) and ($A = 4 \times 10^{15}$; $n = 1.3$; $B = 0$)

FIGURE 7.16 DF kinetics.

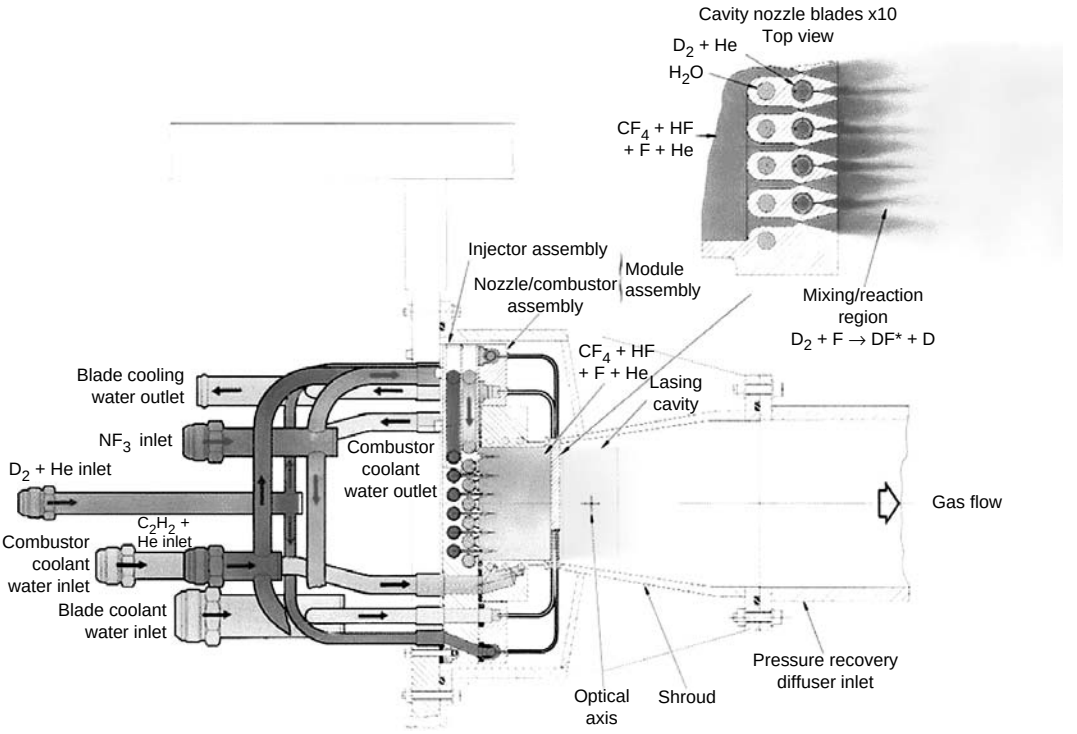

FIGURE 7.17 (**See color insert following page 336.**) Chemical laser features.

There is a plethora of fluid mechanical phenomena in laser cavity flows. Because of the low Reynolds numbers the flow is very viscous; mixing occurs on a small scale with large heat release at supersonic speeds; base flow regions are imbedded in high nonuniform supersonic flow; shock wave-boundary layer interactions with possible shroud boundary layer separation occur, as well as interaction and mixing of supersonic laser flow with optical duct purge flow.

7.3.1 Combustor Flow

The purpose of the combustor is to produce close to 100% atomic fluorine in as much a short combustor as possible. One typical configuration is a triplet injector array that has been used in propulsion systems since the 1950s.

A sketch of this triplet injector is shown in Figure 7.18. The design criteria for the design of this type of ejector, assuring rapid mixing was developed by Elverum and Morey [13].

To first order, as is stated in Figure 7.18, the momentum flux of the fuel (outer stream) and oxidizer streams are matched, that is, the momentum flux $\rho_1 U_1^2$ is nearly equal to $\rho_2 U_2^2$.

The size of the triplet dimensions determines how fast the combustor flows mix. The shorter the combustor, the lesser the wall heat transfer. With this type of small scale triplet design of the combustor, the turbulence scale is small and, hence, pressure roughness is low.

7.3.2 Nozzle Flow (Laser Cavity Injectors) and Lasing Cavity Flow

Because of the requirement of mixing very quickly in the lasing cavity, the laser cavity injector nozzles are very small. One has to differentiate between the requirements to maximize laser performance in terms of laser mass flow efficiency; by maximizing σ(kJ/kg) and minimizing

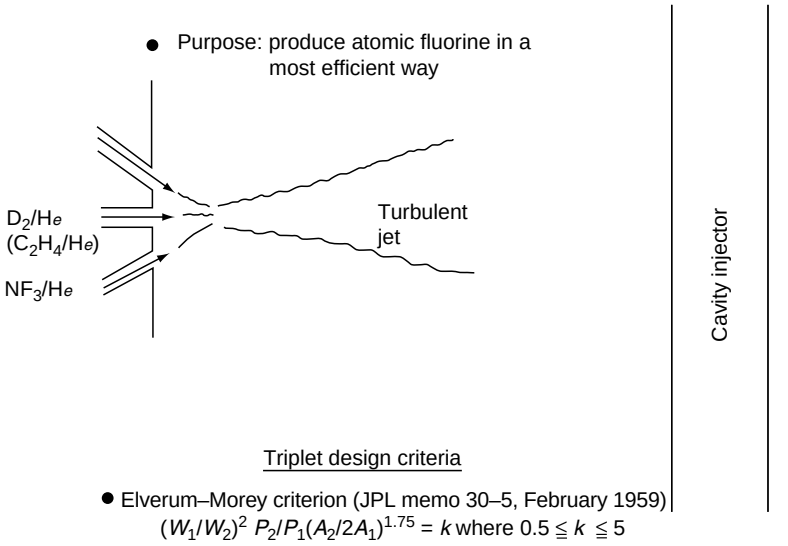

FIGURE 7.18 Combustor triplet injector.

laser size, δ (kW/m^2). In the first case, the size of the laser is secondary to the weight of the laser flow rates. If, however, smaller size is required, laser output power over laser frontal area δ (kW/m^2) is important, and a different set of criteria applies to the nozzle design.

If high laser mass efficiency is needed, the combustor pressure and hence, the laser cavity pressure will be very low: <5 torr. In this case the Reynolds number of the gas flow becomes relatively low and laminar mixing in two dimensions yields fast mixing of laser fluorine and cavity fuel (H_2 or D_2) so that close to all of the fluorine is reacted with the cavity fuel within the lasing zone.

The issue at these low pressures is then that viscous effects dominate the flow through the cavity injector nozzle. An example is shown in Figure 7.19 where virtually the whole inside of the nozzle flow is viscous. The maximum mean Mach number achievable at the exit in a nozzle with a sonic flow gap throat size of 0.125 mm and a combustor pressure less than 300 kPa is not higher than about 3. This limits the lasing efficiency because of a relatively high

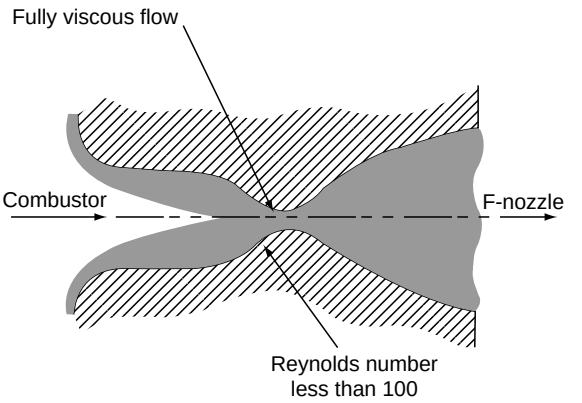

FIGURE 7.19 Low pressure cavity injector nozzle.

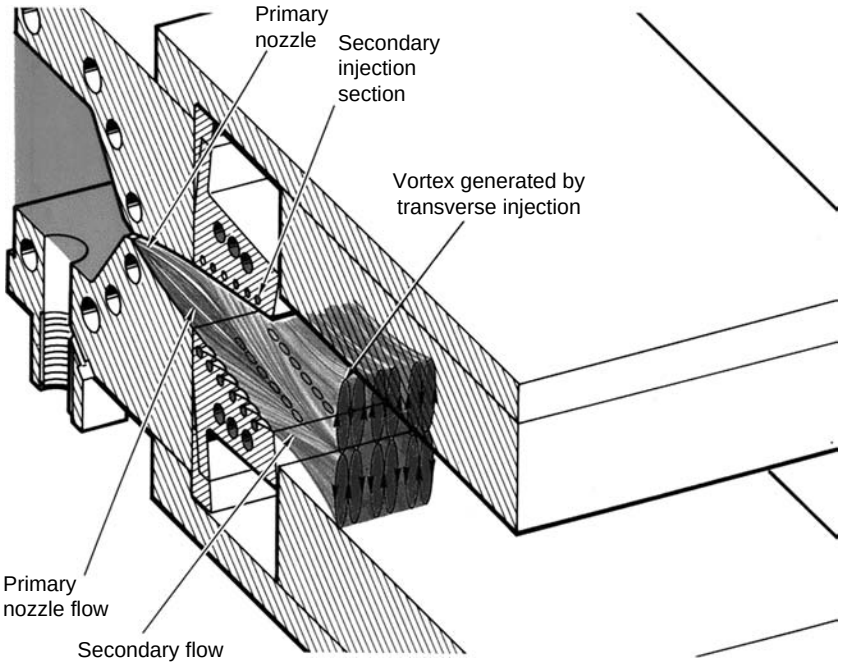

FIGURE 7.20 Low pressure hypersonic low temperature nozzle flow.

static temperature and density of the laser cavity flow. A nozzle configuration to ameliorate the viscous effect is shown in Figure 7.20.

This laser nozzle configuration is named the hypersonic low temperature (HYLTE) nozzle as described in [14]. It is designed to reduce viscous flow effects that result in higher flow speeds and lower static temperatures. In this configuration, the fluorine stream is injected from the combustor into a relatively large nozzle and the cavity fuel (H_2/He) is injected supersonically and obliquely to the fluorine stream. The mixing is enhanced by the formation of a small scale vortex structure in the lasing cavity (see Figure 7.20).

For reference, another configuration whose purpose is the same, that is, to create higher Mach numbers and lower static temperatures, is the hypersonic wedge nozzle (HYWN) configuration [15].

If compactness of the laser, that is, high nozzle efficiency (δ kW/m^2) is required, then the combustor pressure needs to be very high (>1000 kPa). In that case highly three-dimensional mixing is required to achieve this goal because the laminar kinematic viscosity is much smaller than at low pressures. See references [16] and [17].

This type of nozzle flow creates inherently three-dimensional flow at a very small scale and mixing occurs fast enough to produce good lasing efficiency. The complex flow at the entrance of the large cavity is also shown schematically in Figure 7.21. In reality, it is further complicated by the three-dimensional effects of the trip jets.

The resulting approximate average Mach numbers, temperatures, and pressures are also shown for the flow in the lasing cavity with and without chemical reactions (see Figure 7.22 through Figure 7.24).

Typical laser performance at these flow conditions is shown in terms of laser power density δ (kW/m^2) and laser mass efficiency σ (kJ/kg) in Figure 7.25. These results are shown and discussed in more detail in [16].

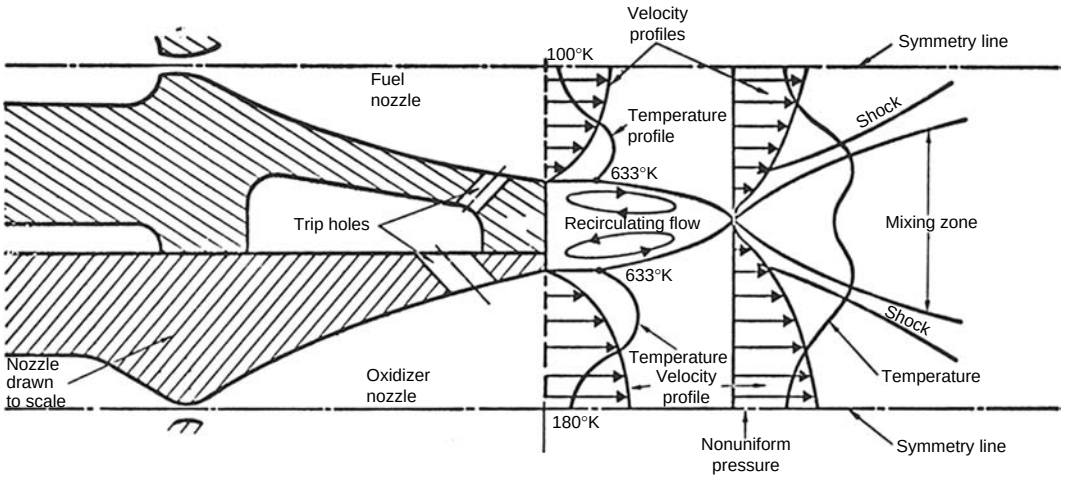

FIGURE 7.21 High pressure trip flow type cavity injector and schematic of flow at laser cavity entrance.

The fact that the lasing cavity pressure rises rapidly in the flow direction (Figure 7.24) makes the design of the laser cavity enclosure important. There are two reasons: (1) the prevention of boundary layer separation that creates shock waves in the lasing region, and (2) the interaction of lasing flow with the resonator optical duct flow and the pressure recovery system.

These flow structures are the flow nonuniformities that will have a strong influence on the resulting optical quality of the laser beam and the pressure recovery performance. The lasing-medium density variation normal to the laser beam affects the beam quality.

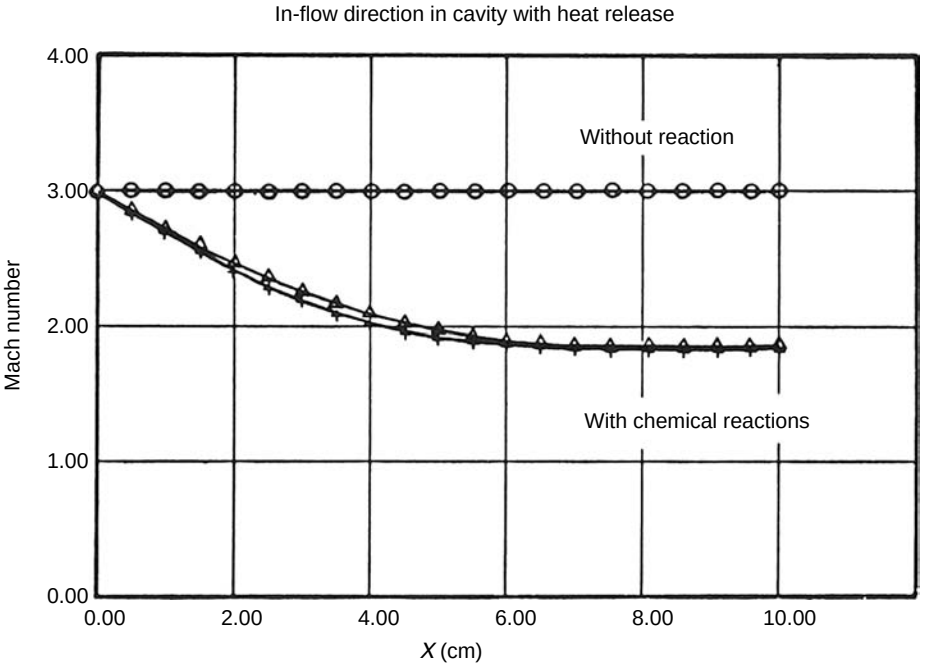

FIGURE 7.22 Laser cavity medium: mean Mach number distribution.

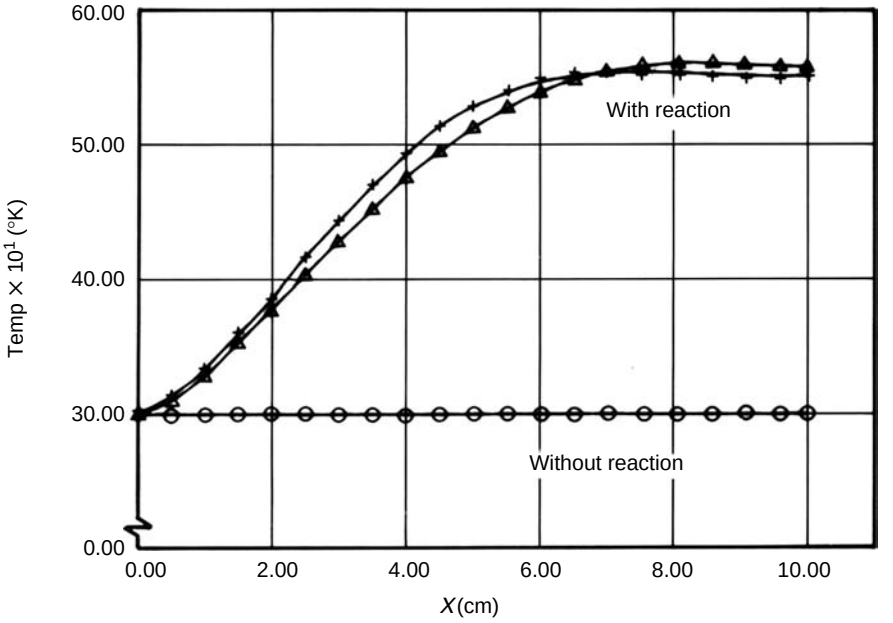

FIGURE 7.23 Temperature distribution in flow direction with heat release.

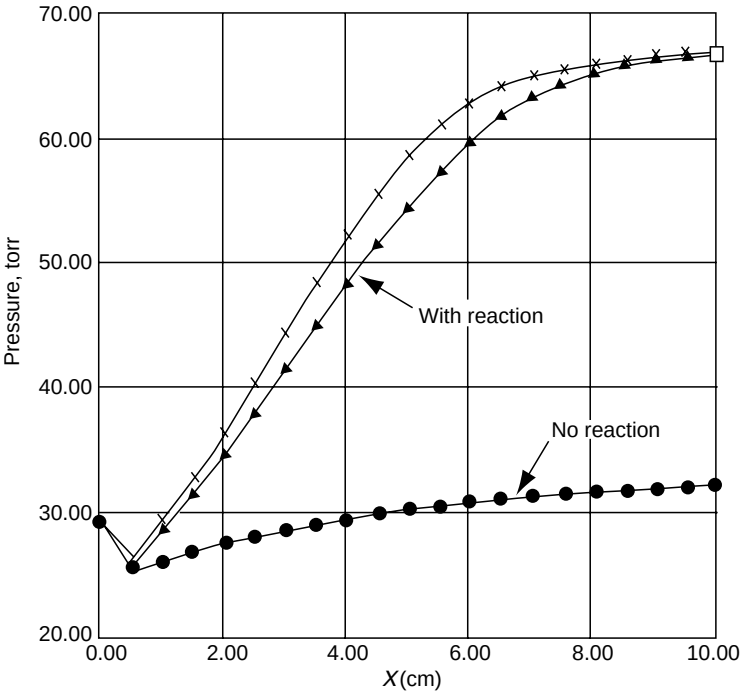

FIGURE 7.24 Mean pressure distribution in flow direction.

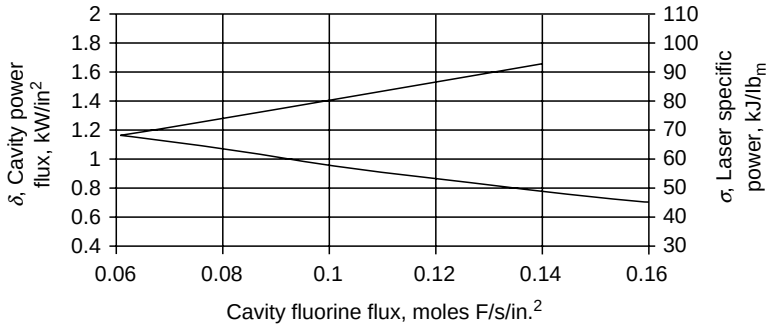

FIGURE 7.25 DF chemical laser performance.

The wavefront distortion is

$$\langle \Delta\phi \rangle = \frac{2\pi}{\lambda} \int \frac{\Delta n}{n} \mathrm{d}s, \tag{7.2}$$

where n is the index of refraction at mean density ρ in the lasing cavity, s the beam path coordinate, Δn the medium index distortion normal to the beam, λ the laser beam length.

For a gas

$$n - 1 = \beta \frac{\rho}{\rho_{\mathrm{ref}}}, \tag{7.3}$$

where β is the Gladstone Dale constant, ρ the density of gas in lasing cavity, ρs the reference density.

The resulting

$$\frac{I}{I_0} \approx 1 - (\Delta\Phi)^2 \sim 1 - \left(\frac{2\pi\Delta L}{\lambda}\right)^2, \tag{7.4}$$

where I is the laser beam intensity, I_0 the diffraction-limited intensity, and $\Delta L = \Delta n L$, L the path length along the beam path.

Note that a two dimensional weak shock wave normal to the beam, say $\Delta\rho/\rho = 0.1$, will result in $I/I_0 \simeq 0.5$, if $\lambda = 3.8 \times 10^{-6}$, and if the lasing mean cavity density is 30 torr and the Gladstone Dale constant $\beta = 10^{-4}$. Hence, the lasing medium (across the beam) has to be very uniform to generate a high quality laser beam.

A lasing cavity view in which the beam direction is normal to the plane of the paper is shown in Figure 7.26. It shows expanding sidewalls to avoid boundary layer separation and creation of shock waves. This expansion has to be kept to a minimum. Otherwise the excessive nonuniformity of the cavity flow density leads to significant degradation as discussed. In addition, the pressure recovery in the laser diffuser decreases as the flow cross-sectional area increases (see Section 7.3.3).

The laser cavity cross-section along the beam path (Figure 7.27) shows the regions where interaction of the optical duct purge flows with the supersonic laser cavity flow. Significant density nonuniformities can occur in these regions as well, leading to beam quality degradation and lower laser power or contamination of the laser mirrors. Three-dimensional numerical flow calculations are very helpful to quantify these effects.

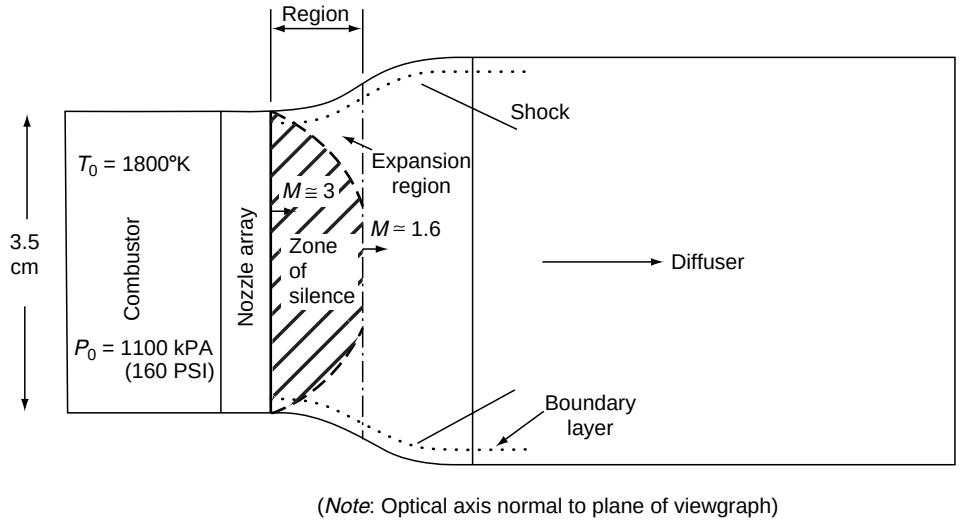

FIGURE 7.26 Laser side view.

7.3.3 Pressure Recovery

Since the lasing cavity flow is at a low pressure, typically a pressure recovery system is used to bring the laser pressure to atmospheric conditions. The laser gas could also be absorbed or adsorbed at low pressure by the right kind of substance (zeolite). This technology is another complex topic and is not addressed.

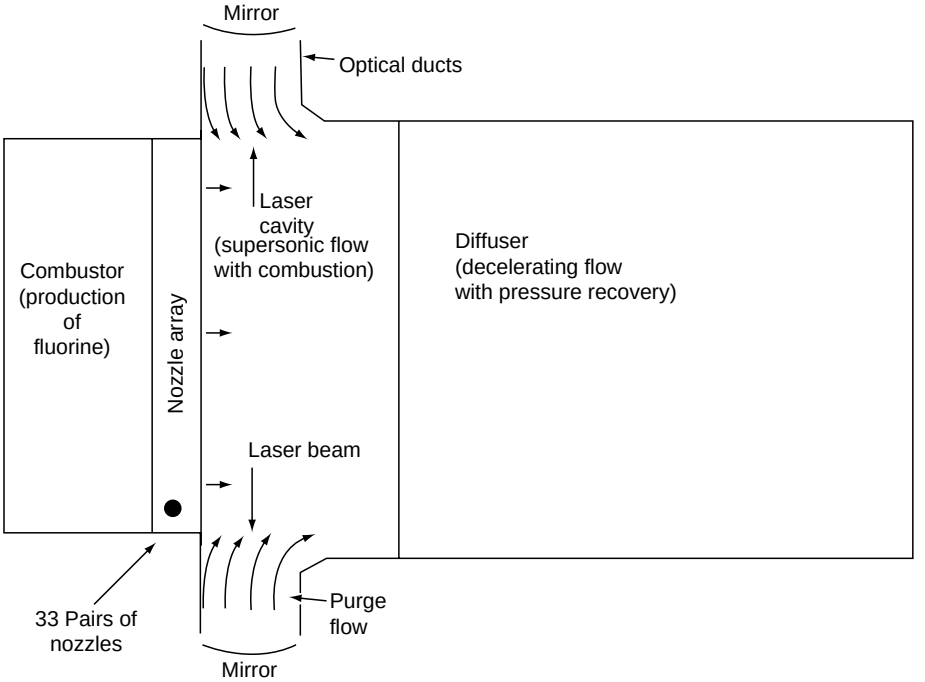

FIGURE 7.27 Laser top view.

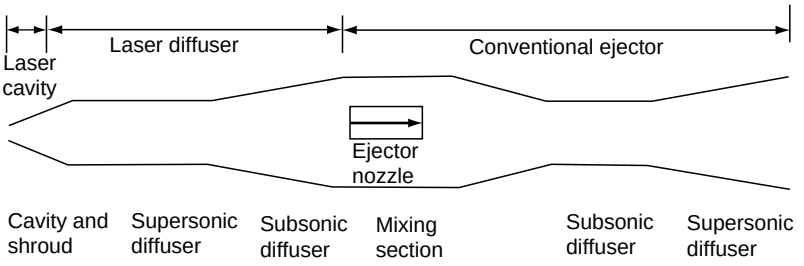

FIGURE 7.28 Diffuser/ejector configurations.

The pressure recovery system typically consists of a laser diffuser followed by an ejector system. Under some circumstances a gas scrubber system is also included. That technology, however, will not be discussed.

A schematic of the diffuser ejector system is illustrated in Figure 7.28. It consists of a constant area duct section where the flow is converted from supersonic to subsonic speeds and an increased pressure. The length of the constant area duct section is determined empirically from a great number of tests as shown in Figure 7.29; see reference [18]. A classic paper on supersonic diffusers is [19]. Two recent papers [20] and [21] are of interest and also lead to a number of interesting references.

In the subsequent subsonic expanding diffuser section, the flow is further reduced in speed and the pressure is increased further.

The diffuser is strictly a passive flow device that reacts to increased pressure downstream the diffuser. If the downstream pressure becomes too high, the high pressure will propagate upstream in the diffuser and if increased beyond the maximum recovery pressure, it will adversely affect the flow in the lasing cavity.

For a properly operating diffuser, a straight forward approximation has been derived [22] for an estimate of the achievable pressure recovery. The test results are remarkably close to this approximate analytical expression (see Figure 7.30). A number of suggestions for further improvements to diffuser performance have been made over the years, but have not been proven by test [23,24].

The ejector that is located downstream of the diffuser serves to increase the pressure, usually to the atmospheric pressure. There are two elements of an ejector. The first element is a gas generator with supersonic nozzles that produce gas at high supersonic Mach numbers, say $M = 4$, which is then mixed with the subsonic laser flow. In the second element, an ejector diffuser, the mixed supersonic flow (gas generator and laser flow) is then reduced in speed and increased in pressure, typically to atmospheric pressure.

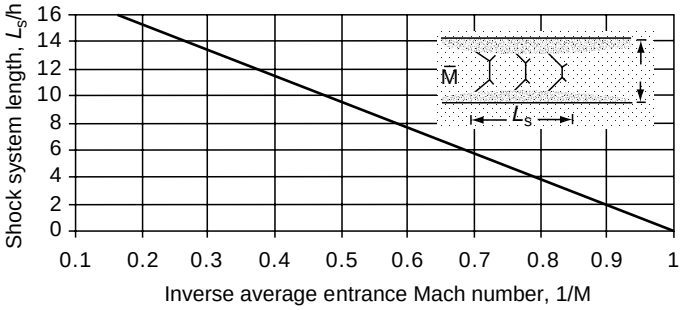

FIGURE 7.29 Shock length as a function of Mach number in a constant area duct.

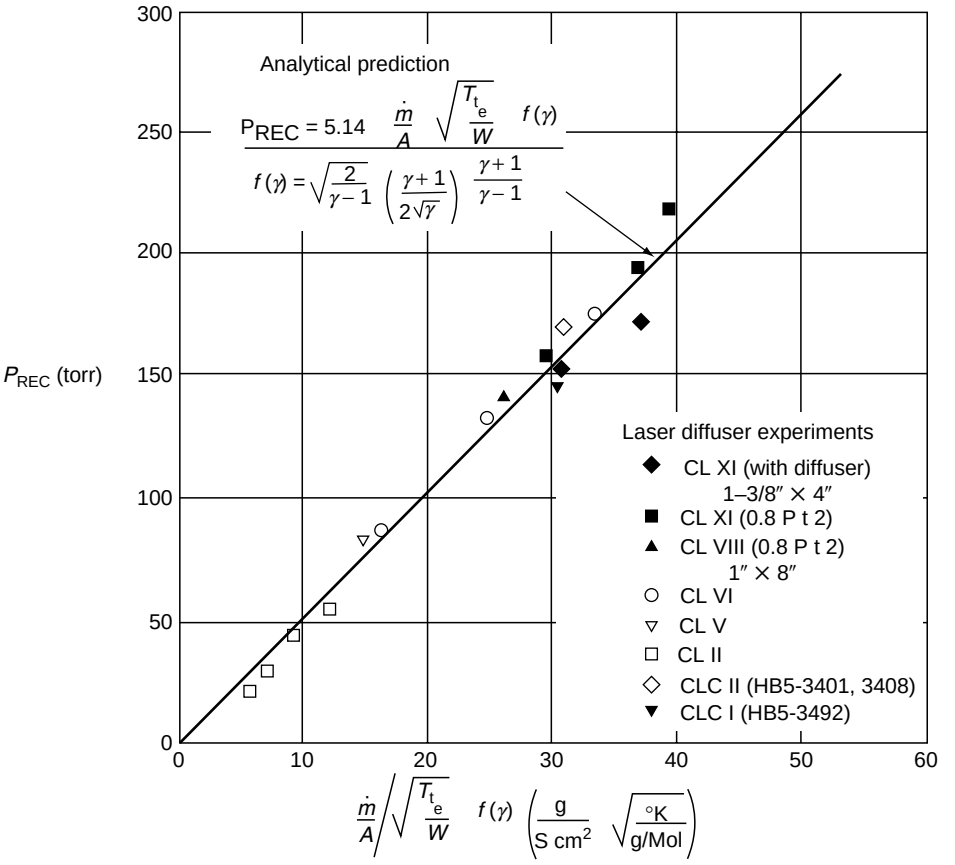

FIGURE 7.30 Pressure recovery test data comparison with analytical predictions.

The performance of an ejector in an all-gas system is approximated by a simple relation as shown in Figure 7.31, which demonstrates that

$$\frac{P_r}{P_{os}} = A\frac{m_p}{m_s}\sqrt{\frac{To_p}{To_s}}\frac{(M_w)_s}{(M_w)_p}, \tag{7.5}$$

where P_r is the pressure recovery, $(\ )_p$, refers to the primary flow (gas generator), $(\ )_s$ the secondary (laser) flow, and $(\ )_o$ the stagnation condition, m is the mass flow rate, M_W the molecular weight. For a steam ejector system the performance is somewhat better because of the two-phase nature of the stream. The performance calculations are somewhat more involved. They are described in [25].

Other papers dealing with supersonic ejector systems are cited in [26].

7.4 MODELING OF CHEMICAL LASERS

7.4.1 Introduction

Chemical laser flow modeling addresses the reacting, lasing flow in the laser cavity, performance of the laser combustor including chemical reactions, turbulent mixing, and heat loss to walls, and the general flow in the feed system, the surrounding cavity enclosure, and the

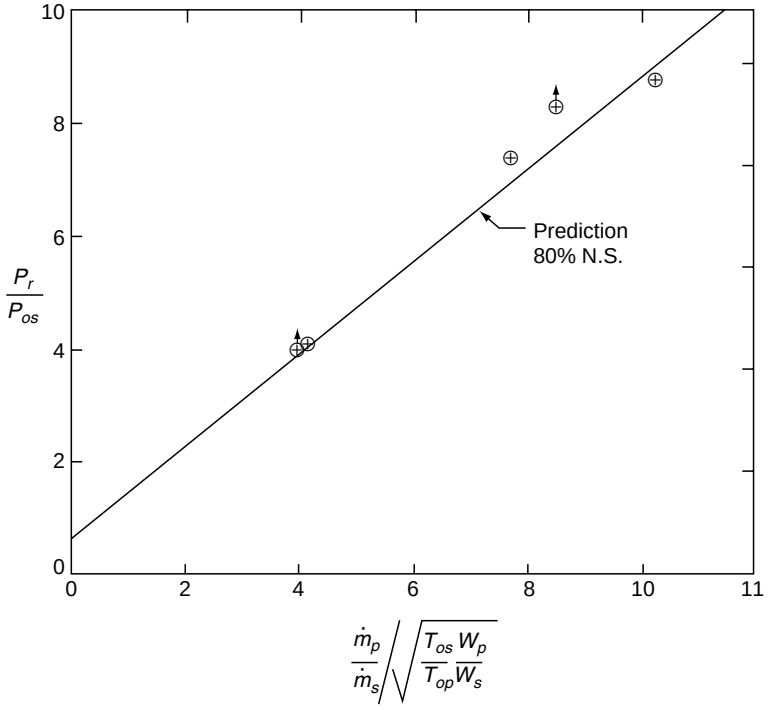

FIGURE 7.31 Ejector performance compared to 80% of normal shock.

pressure recovery system. This discussion is limited to continuous wave lasers operating in the P-branch, fundamental mode.

A chemical laser cavity performance model provides valuable insights into the design of both the cavity injector as well as the optical resonator. A detailed model of the cavity flowfield also provides useful inputs for cavity enclosure design as well as diffuser design. Such performance modeling requires the combination of fluid dynamics and nonequilibrium chemistry as well as accounting for extraction of energy from an optical resonator. It is a modeling challenge and several levels of modeling detail are used to support the design efforts.

The cavity flowfield is a supersonic flow of cavity fuel (D_2 or H_2) mixed with helium (secondary flow) and primary flow from the combustor and containing atomic fluorine. Mixing and reaction produce the excited state of the lasing molecule (DF* or HF*) whereas the resonator propagates a beam through the lasing medium extracting energy from the excited states. In general, the cavity is operated at low pressure to minimize collisional deactivation: a few torr for a space-based laser and about 30 to 40 torr for ground based operation. The resulting cavity flow is essentially laminar with little or no contribution from turbulent mixing. It should be noted that F_2 can combine with H or D atoms and also produce excited state HF/DF. In fact, the cold reaction produces H/D atoms that can react with F_2 to produce excited state HF/DF with the so-called hot reaction. The combination of hot and cold mechanisms can, in principle, form a chain of reactions that would lead to high laser efficiency. In practice the chain is difficult if not impossible to produce.

The combustor flowfield consists of highly exothermic dissociation reactions that produce F atoms which, when reacted with D_2 or H_2, produce the excited state lasing molecule in the cavity. The combustor pressure is in the range from 25 to 200 psia.

The dissociation reactions are fast and near to equilibrium. Recombination of F to F_2 after dissociation is slower and nonequilibrium chemistry is required. The entire mixing process in the combustor is turbulent. Additionally, heat loss to the combustor walls must be considered very carefully—in particular, the effects of free stream turbulence are key to calculating heat loss to walls. The combustor design must allow efficient production of F atoms and minimize wall heat loss to prevent recombination of F to F_2.

Modeling of flows in the feed system, the surrounding cavity enclosure, and the pressure recovery system involves a large number of phenomena. Feed system design must include issues associated with flow control and transient startup and shutdown. Compactness may require storing gas at high pressure where real gas effects are important. The cavity enclosure flows must be designed to maintain required low pressure in the cavity and to isolate laser gas from optical surfaces. Diffuser performance in the pressure recovery system must consider the effects of shock-boundary layer interactions as well as the effects of sensible heat addition caused by recombination of H/D atoms.

7.4.2 Equations for Reacting, Lasing Flow

The basic equations of fluid mechanics of a gas mixture are applicable. Modeling of laser cavity performance must account for laser power extraction. In particular, the continuity and energy equations are modified for lasing.

The continuum flow equations are presented in the following and are outlined in [27] and [28]. The time-dependent equations are also given. Most often, only the solution of the steady state is required. However, steady state solutions are often obtained by including the time derivatives and time stepping to a steady solution. These approaches are usually not time-accurate because only the final steady state is of interest. However, unsteady, transient solutions require time accurate solutions of the equations.

Continuity equations:

Overall continuity:

$$\frac{\mathrm{d}\rho}{\mathrm{d}t} + \rho \frac{\partial u_l}{\partial x_l} = 0, \tag{7.6}$$

where u_i is the velocity, ρ the mixture density, t time, x_i position (x, y, z), and $\partial u_l/\partial x_l$ the divergence of velocity (repeated indices imply summation). The material or total time derivative of a flow quantity is denoted by

$$\frac{\mathrm{d}()}{\mathrm{d}t} = \frac{\partial()}{\partial t} + u_l \frac{\partial()}{\partial x_l} = 0. \tag{7.7}$$

The partial derivative with respect to time is zero for steady state solutions. In particular, the divergence of the product of density and velocity is zero for steady state

$$\frac{\partial(\rho u_l)}{\partial x_l} = 0. \tag{7.8}$$

Species continuity for species k

$$\frac{\mathrm{d}\rho_k}{\mathrm{d}t} + \frac{\partial}{\partial x_l}(\rho_k u_l + j_{l,k}) = r_k + r_{Lk}. \tag{7.9}$$

The quantity $j_{l,k}$ is the vector mass flux of the species k relative to the mixture velocity or the diffusional mass flux. The r_k term accounts for chemical reactions. A second term, r_{Lk} accounts for the change in species concentrations caused by lasing. In general the second term is in proportion to the laser gain times the intensity divided by the photon energy for a particular line.

Momentum equation

$$\rho\left(\frac{\partial u_i}{\partial t}+u_l\frac{\partial u_i}{\partial x_l}\right)=-\frac{\partial p}{\partial x_i}+\left(\beta+\frac{1}{3}\mu\right)\frac{\partial}{\partial x_i}\frac{\partial u_l}{\partial x_l}+\mu\frac{\partial}{\partial x_l\partial x_l}u_i, \tag{7.10}$$

where the last term represents the Laplacian of the velocity vector, μ the viscosity, and β the dilatational or bulk viscosity. Body forces can be ignored for most gas laser flows and are not included here.

Energy equation

$$\frac{\mathrm{d}h}{\mathrm{d}t}=-\frac{\partial q_{\mathrm{l}}}{\partial x_{\mathrm{l}}}+\frac{dp}{dt}+\Phi_{\mathrm{v}}+\delta h_L, \tag{7.11}$$

where h is the mixture enthalpy per unit mass, q_i the heat flux, Φ_v the viscous dissipation, and δh_L the enthalpy required for lasing. In particular,

$$h=X_k h_k, \tag{7.12}$$

where X_k is moles of species k per mixture mass. The species enthalpy h_k includes the heat of formation for the individual species. Thus the sensible energy release by chemical reactions is accounted for in the energy equation.

The increase in enthalpy from the viscous dissipation function is

$$\Phi_v=\left(\beta-\frac{2}{3}\mu\right)\left(\frac{\partial u_l}{\partial x_l}\right)^2+2\mu D_{ij}D_{ij}, \tag{7.13}$$

where the rate of deformation tensor is

$$D_{ij}=\frac{1}{2}\left(\frac{\partial u_j}{\partial u_i}+\frac{\partial u_i}{\partial x_j}\right).$$

The lasing enthalpy extraction, δh_L, is proportionate to the sum over all transition lines of the laser gain times the laser intensity.

The tractability of modeling laser flows is greatly improved by treating the vibrational states as separate species as opposed to carrying along each vibrational–rotational state as a separate chemical species. As a practical matter this approach is required as the transfer rates between rotational–vibrational states are not available. The approach taken is to model the rotational state for each vibrational level as a rotational nonequilibrium distribution using published estimates of the nascent distribution. Rotational relaxation is approximated separately using approaches that take into account measured relaxation rates. As lasing removes power on a favorable transition, the rotational population of that state is reduced and can only be repopulated by rotational relaxation and toward a Boltzmann equilibrium distribution. If this relaxation were infinitely fast the population would always be in a Boltzmann distribution and the most efficient transitions would be instantly repopulated. The effect of

rotational nonequilibrium can reduce the predicted power from what might be calculated assuming rotational equilibrium. The effect on power may be a 20% reduction for HF and 10% for DF.

7.4.3 Chemical Reactions

Consider only the cold reaction and restrict to P-branch, fundamental lasing. The excited state is produced only by the reaction of atomic fluorine with cavity fuel; and the P-transition, fundamental lasing transitions are from $(v+1, J-1)$ to (v, J).

The chemical reactions for chemical lasers can be divided into three groups: pumping, deactivation, and v–v transfer.

Pumping reactions characterize F atoms reacting with cavity fuel (D_2 or H_2):

$$F + D_2 \rightarrow D + DF^*(v), \quad v = 1,2,3,4, \tag{7.14}$$

where DF* is pumped into four vibrational levels (HF* into three), and V–V transfer between vibrational levels.

$$DF^*(v1) + DF^*(v2) \rightarrow DF^*(v3) + DF^*(v4), \quad v1 + v2 = v3 + v4. \tag{7.15}$$

$$DF^*(v1) + D2^*(v2) \rightarrow DF^*(v3) + D2^*(v4), \quad v1 + v2 = v3 + v4. \tag{7.16}$$

Collisional deactivation or V–T transfer:

$$DF^*(v+1) + M_{cat} \rightarrow DF^*(v) + M_{cat} \tag{7.17}$$

with M_{cat} consisting of weighted values of DF*, HF, D, $D_2(0)$, $D_2(1)$, $D_2(2)$, F, F_2, CF_4, N_2 for a DF laser. M_{cat} is thus a catalytic species and enables calculation of the deactivation caused by several species with a single reaction.

The rate of change of fluorine, DF*(0), caused by a V–V transfer reaction is as follows:

$$\frac{dn_{DF^*(0)}}{dt} = k_f n_{DF^*(1)} n_{DF^*(2)} - k_b n_{DF^*(0)} n_{DF^*(3)}. \tag{7.18}$$

The quantity n is the molar species concentration and k_F and k_b are forward and backward reaction rates. The sum of all the rates of change equations each reaction involving DF*(0) is included in the r_k term in the species continuity equation.

The associated reaction rates are compiled in several sources in Arrhenius form. The determination of the rates from measurements and modeling is summarized in [29] and [12]. (Additionally, Reference [1] provides a wealth of information on chemical rates and modeling as well as most other aspects of chemical lasers.) Accurate laser power performance modeling can be achieved by anchoring the uncertainty in the rates to accurate small-signal gain measurements. About 80 reactions are used for DF laser modeling and about 70 reactions for HF (The number of reactions would be increased significantly if the catalytic species—the M_{cat}'s—were not used.)

7.4.4 Lasing Equations

The laser power performance can in principle be calculated by coupling the reacting flow equations with a resonator model that would, given a gain calculation from the flow model, calculate the lasing intensity distribution. An iteration scheme could be set up that would

converge to a consistent intensity and gain fields that satisfy the reacting flow equations, the laser radiation equations, and the resonator conditions. As a practical matter, this approach would be extremely slow given present computing speeds. We outline the laser equations to discuss approximate solutions that are achievable with realistic computing times.

Gain calculation

The P-transition, fundamental wave number is given as follows:

$$\Delta\omega_{v,J} = \omega_e - 2\omega_e x_e(v+1) - J[2B_e + \alpha(J - 2(v+1))], \tag{7.19}$$

where ω_e, α_e, $\omega_e x_e$, B_e, are spectroscopic constants.

The Einstein coefficients for stimulated emission and absorption are:

$$B_{v+1,v} = \frac{8\pi^3}{3h^3 c}\left(\frac{J}{g_{V+1}}\right)|M_V^{V+1}|^2, \tag{7.20}$$

where h is Planck's constant, c the speed of light, $g_{V+1} = 1$

and

$$B_{v,v+1} = \frac{2J-1}{2J+1} B_{V+1,V}, \tag{7.21}$$

and matrix elements,

$$|M_V^{V+1}|^2 = (a + bJ + cJ^2)(a_v + b_v[v+1]), \tag{7.22}$$

where the constants are curve fits of tabulated values in the Willow Run Laboratories report [30].

The gain can then be constructed for the P-branch, fundamental transition gain less loss difference using stimulated emission and absorption Einstein coefficients [31] and line shape outlined in [32]

$$\alpha_{V,J} = \frac{8\pi^3 \upsilon}{3hc} J|\mathrm{M}_V^{V+1}|^2\left(\frac{n_{V+1,J-1}}{2J-1} - \frac{n_{V,J}}{2J+1}\right)\phi, \tag{7.23}$$

where v is the transition frequency, $n_{V,J}$ the number density of the excited state. The multiplier ϕ is a broadening coefficient that has both Doppler and collisional, Lorentz components. It should be noted that source flow nozzles have flow components in the beam direction. Doppler broadening must be adjusted to account for these components. An interesting ramification is that small-signal gain measurements will be different depending on the orientation of the probe laser.

The number densities, $n_{V,J}$, are

$$N_V \mathrm{f}(V,J), \tag{7.24}$$

where N_V represents the population of vibrational level, V the totaled overall rotational levels, and f(V,J) represents the rotational distribution. If the excited species are in rotational equilibrium then a Boltzmann distribution describes the rotational distribution

$$\mathrm{f}(V,J) = \frac{2J+1}{\left(\frac{kT}{hcB_V}\right)} e - \left(\frac{hc}{kT} E_{V,J}\right) \tag{7.25}$$

with $B_V = B_e - \alpha(V + 1/2)$, and $E_{V,J} = J(J+1)B_V$, and k the Boltzmann constant.

Assumption of rotational equilibrium is sufficient to calculate small-signal gain. Rotational nonequilibrium can be important for accurate power modeling. It is useful to outline the approach for treating rotational nonequilibrium:

1. Only vibrational states are tracked directly in the reacting flow calculations
2. An initial rotational distribution is prescribed
3. Rotational relaxation is approximated based on experimental measurements [33]
4. As lasing occurs, the effect of reducing the rotational population for the lasing transition reduces the gain and therefore power. The effect of rotational nonequilibrium is to reduce power from the level that would be predicted if rotational equilibrium were assumed. (Reference [34] gives a good discussion of inclusion of rotational nonequilibrium effects in laser performance modeling; recent measurements outlined in [35] suggest that the effect of rotational nonequilibrium on power may be smaller than previously thought).

7.4.5 Resonator Modeling

Several approaches can be used to model the power performance of a chemical laser. The development of practical, and verifiable approaches to modeling has depended greatly on computing power, software developments, and the availability of measured data. The rapid development of better performing gain generators with good mixing forced the use of more approximate methods for both the fluid dynamics and the resonator modeling. In the immediate future the availability of high speed computing and sophisticated software tools can be expected to produce much higher quality resonator modeling.

Three paths can be taken when connecting the gain-producing fluid dynamics model with the power extraction of the resonator.

7.4.5.1 Simplified Fluid Dynamics and Detailed Resonator Models

The approach developed in the 1970s was to implement a simplified mixing model into detailed resonator calculation. The mixing model can be provided by detailed fluid dynamics models. One approach is to use calculated small-signal gains to anchor the simplified mixing model embedded in the detailed resonator model. The anchored model is then used to drive the power calculation with the full wave optics propagation of resonator model [36]. In general, a number of gain sheets are included and the simplified model, in effect, calculates separate fluid dynamics mixing for each gain sheet. A good example of this approach is found in [37]. Good agreement was found between calculations and experiment for small-signal gains, laser power, and cavity pressure.

7.4.5.2 Simplified Optics and Detailed Flow Models

Coupling of the reacting flow model and the laser intensity requires modeling the propagation of the laser through the gain medium. The line transition intensity is quantified by the gain:

$$\frac{dI_{V,J}}{ds} = \alpha_{V,J} I_{V,J}. \tag{7.26}$$

The length element ds, is along a ray in the gain medium. Integration of the intensity assisted by a ray tracing scheme is conducted separately from the flow model. It is consistent with the boundary conditions of the resonator and the scheme will drive the round trip gain to the

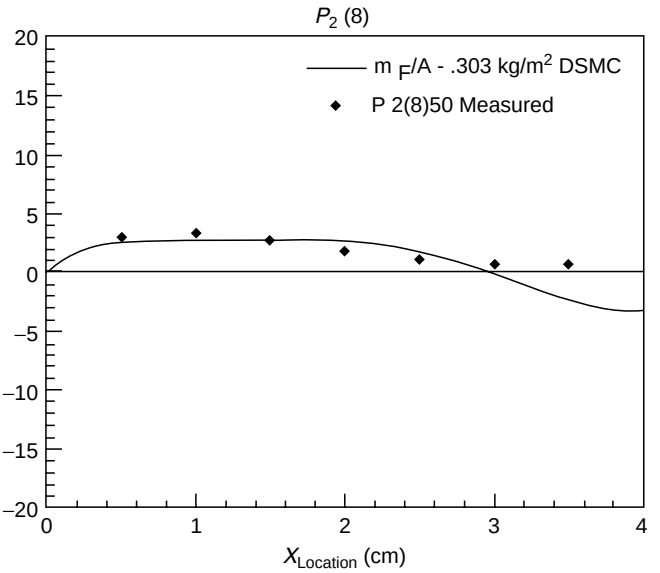

FIGURE 7.32 Small-signal gain: measured and calculated.

appropriate value. The simplest approach is a Fabry–Perot resonator. Whereas a reasonable estimate of power can be made, the lack of upstream–downstream coupling limits calculation of mode length with the Fabry–Perot approach. A second approach is to account for upstream–downstream communication with a roof top resonator or with a more detailed ray trace model. These approaches have until now involved compromise by not including the full resonator flow field but restricting to unit cell flow calculations which see an averaged intensity. These methods are primarily useful when calculating small-signal gain, screening potential designs, and evaluating experimental measurements. An example of small-signal gain from a detailed flowfield model is found in [38]. This method uses a direct molecular simulation approach to calculate the cavity flow field (an approach that produces a solution to the continuum, Navier–Stokes equations as discussed in [39]). An example of calculated and measured small-signal gain is shown Figure 7.32. This approach has been developed to give small-signal gain calculations that compare well with measured values.

7.4.5.3 Coupled Detailed Models

Detailed fluid dynamics models can be coupled with a detailed resonator model by iteration. The gain calculated with the fluid dynamics model is handed off to the resonator model and the intensity distribution is calculated. The intensity is fed back to the fluid dynamics model and the process is repeated till convergence is achieved. (The convergence scheme is designed to be stable and rapid.) The power of this approach is that the best numerical methods can be used. The drawback is that a tremendous amount of computer power is required. One can, however, envision fully parallelized fluid dynamics and resonator models calculating the power performance of complex chemical laser resonators on the next generation of processors (Figure 7.33).

Experience indicates that the gain (flow) calculations take more time than the resonator calculation. The process described here will be most efficient when the gain calculation is divided among the optimal number of processors. This selection will be based on the speed of

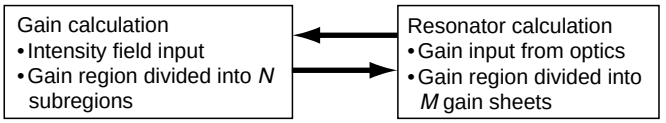

FIGURE 7.33 Iteration for detailed resonator analysis.

the processors, the message passing time, and the size of the gain field. The iteration scheme could either pass converged gain and intensity fields or partially converged fields to speed up convergence. Selection of the most efficient scheme will require a good deal of trial and error.

REFERENCES

1. Gross, R.W.F. and Bott, J.F., *Handbook of Chemical Lasers*, John Wiley & Sons, New York, 1976.
2. Gross, R.W.F., Cohen, N., and Jacobs, T.A., HF chemical laser produced by flash photolysis of F2 O–H mixtures, *Journal of Chemical Physics*, April 15, Vol. 48, no. 8, pp. 3821–3822, 1968.
3. Suchard, S.N., Kerber, R.L., Emanuel, G., et al., Effect of H_2 pressure on pulsed $H_2 + F_2$ laser experiment, *Journal of Chemical Physics*, Vol. 57, p. 5065, 1972.
4. Miller, J., Chemical lasers, *Quest*, TRW (NGST), Vol. 4, no. 3, pp. 3–21, 1980.
5. Wacks, M., Ryan, L., and Johannsen, D., The alpha program, *Journal of Directed Energy,* 1, pp. 317–331, Winter, 2006.
6. Emanuel, G., Analytical model for a continuous chemical laser, *Journal of Quantitative Spectroscopy and Radiative Transfer*, Vol. 11, pp. 1481–1520, 1971.
7. Mirels, H., Hofland, R., and Dunn, M.G., Simplified model of CW diffusion-type chemical, *American Institute of Aeronautics Astronautics Journal,* Vol.11, no. 2, pp. 156–164, 1973.
8. Broadwell, J.E., Effect of mixing rate on HF chemical laser performance, *Applied Optics*, Vol. 13, no. 4, pp. 862–967, April, 1974.
9. Chodzko, R., Multiple-Selected-Line unstable resonator, *Applied Optics*, Vol. 13, no. 10, pp. 2321–2325, 1974.
10. Sentman, L.H., Otto, J.W., Gordon, S.J., et al., Effects of gain length on HF overtone performance and line selection HF fundamental performance, American Institute of Aeronautics Astronautics Paper 1993–3185, 1993.
11. Cohen, N. and Bott, J.F., Review of rate data for reactions of interest in HF and DF lasers, *J.F. Chemical Kinetics*, SDTR-82–86, 1982.
12. Manke, G.C. and Hager, G.D., A review of recent experiments and calculations relevant to the kinetics of the HF laser, *Journal of Physical and Chemical Reference Data*, Vol. 30, pp. 713–733, 2001.
13. Elverum, G.W. and Morey, T.F., Criteria for optimum mixture-ratio distribution using several types of impinging-stream injector elements, Jet Propulsion Laboratory Report 30–5, February 25, 1959.
14. Hook, D.L. and Broadwell, J.E., Premixed cold reaction CW laser nozzle, United States Patent 4,785,461, November 15, 1988.
15. Hook, D.L. and Waypa, J., Jr., Transverse mixing hypersonic wedge nozzle chemical laser, United States Patent 4,237,429, December 2, 1980.
16. Wilson, L.E. and Hook, D.L., Deuterium fluoride CW chemical lasers, AIAA paper 1976–344, 1976.
17. Witte, A.B., Broadwell, J.E., and Hook, D.L., Chemical laser with mixing enhancement device for power improvement, United States Patent 4, 048, 586, 1977.
18. Merkli, P.E., Pressure recovery in rectangular constant area supersonic diffusers, *AIAA Journal,* Vol. 14, no. 2, pp. 168–172, 1976.
19. Neumann, E.P. and Lustwerk, F., High-efficiency supersonic diffusers, *Journal of the Aeronautical Sciences*, Vol. 18, pp. 369–374, June, 1951.
20. Malkov, V.M., Savin, A.V., and Kiselev, I.A., Diffusers of COIL and DF lasers, Proceedings of the SPIE, vol. 5777, pp. 164–169, Eighth International Symposium on Laser Metrology, 2005.
21. Lohn, P.D., Chan, W.R., Haflinger, D.E., et al., COIL laser diffuser design, *AIAA*-2001–3010, 32nd AIAA Plasmadynamics and Lasers Conference, June, 11–14, 2001.

22. Behrens, H.W. and Sugimura, T., Pressure recovery analysis, Tri-Service Chemical Laser Symposium, Kirtland AFB, NM, February 19–21, 1975.
23. Behrens, H.W., Supersonic gas flow device incorporating a compact supersonic diffuser, United States Patent 6, 302, 142, 1982.
24. Davis, J.A., Morr, G.F., and Moon, L.F., Investigation of a porous-wall compact diffuser for chemical lasers, *AIAA*-1982–1004, AIAA and American Society of Mechanical Engineers, 1982.
25. Hook, D.L., Magiawala, K., Haflinger, D.E., et al., An ejector system for space simulation of the alpha laser, *AIAA*-92-2981, AIAA 23nd Plasmadynamics & Lasers Conference, July 6–8, 1992.
26. Emanuel, G., Optimum performance for a single-stage gaseous ejector, AIAA, Fluid and Plasma-Dynamics Conference, July 14–16, 1976, p. 7.
27. Schlichting, H.S., *Boundary Layer Theory*, McGraw-Hill, New York, 1960.
28. Bird, R.B., Stewart, W.E., and Lightfoot, E.N., *Transport Phenomena*, John Wiley & Sons, New York, 1960.
29. Cohen, N. and Bott, J.F., Review of rate data for reactions of interest in HF and DF lasers, AFWL Report No. SD-TR-82–86, 1982.
30. Meridith, R.E. and Smith, F.G., Investigation of fundamental laser processes, Willow Run Laboratories. Vol. 2, Report 84130-39-T (II), U. Michigan, 1971.
31. Herzberg, G., Molecular spectra and molecular structure—I. *Spectra of Diatomic Molecules*, D. Van Nostrand, New York, 1961.
32. Mitchell, A.C.G. and Zemansky, M.W., *Resonance Radiation and Excited Atoms*, Cambridge Press, England, 1961.
33. Hinchen, J.J. and Hobbs, R.H., Rotational relaxation studies of HF using IR double resonance, *Journal of Chemical Physics*, Vol. 65, no. 8, 1976.
34. Thoenes, J., Hendricks, W.L., Kurzius, S.C., and Wang, F.C., Advanced laser flow analysis theory, AFWL-TR-78, 1979.
35. Manke, G.C. et al., On the presence of rotational non-equilibrium in a supersonic HF laser, AIAA Paper 2003–3753, 2003.
36. Anan'ev, Y.A., Laser Resonators and the Beam Divergence Problem, Institute of Physics, Adam Hilger, Bristol, 1992.
37. O'Keefe, D.O., Sugimura, T., Behrens, H.W., Bullock, D., and Dee, D., Comparison of LAMP and BLAZER code calculations with TRW CL XV measurements, *Optical Engineering*, Vol. 18, no. 4, pp. 363–369, 1979.
38. Lohn, P.D. et al., Fluid dynamics for space-based laser design, AIAA Paper 1999–3547, 30th Plasmadynamics and Lasers Conference, Norfolk, VA, 1999.
39. Lohn, P.D., Haflinger, D.E., McGregor, R.D., and Behrens, H.W., Modeling of near-continuum flows using the direct simulation Monte Carlo method, AIAA Paper 1990–1663, 21st Fluid Dynamics, Plasma Dynamics and Lasers Conference, Seattle, WA, 1990.

8 Excimer and Exciplex Lasers

Sergey I. Yakovlenko

CONTENTS

8.1 INTRODUCTION

In photochemistry, an exciplex (excited complex) is a chemical compound (or a complex), which is strongly bound in an excited electronic state, but which readily decays (dissociates) in the ground state [1]. An excimer is an exciplex consisting of identical atoms or fragments (a dimer, a trimer, polymer, and so on).

Exciplex molecules usually contain rare-gas atoms. The rare gases do not normally form chemical compounds in their ground state as their electron shells are filled (the exception is XeF_2). However, excited rare-gas atoms R* have chemical properties close to those of alkali metals: they have one weakly bound electron, the behavior of which is little affected by the interaction with the ''inner'' electrons. Lasing of excimers and exciplexes is the result of a photodissociative transition from a bound excited state to a repulsive ground state. The spectral width of a photodissociative transition is large [2] and this presents the main difficulty in lasing.

Houtermans discussed the idea of using photodissociative transitions directly to amplify stimulated radiation in the 1930s but he published it only in 1960 (see Reference [3]). The first experimental attempts [4–8] to achieve lasing were unsuccessful. This lack of success was not accidental.

First, following Houtermans [3], many experimentalists and theoreticians regarded a photodissociative transition as ''automatically'' inverting because of the short decay time of the ground state. However, in reality, inversion at a photodissociative transition requires in particular a sufficiently low gas temperature. Attempts to get lasing at high gas temperatures ended in failure.

Second, at that time, the majority of investigators of laser-active media began from pumping schemes not based on recombination but on ionizations of a gas by electrons heated in an external electric field, as it occurs in a conventional discharge. However, to achieve lasing as a result of a photodissociative transition, strong pumping of a dense gas is required because of the large spectral width of this transition. A conventional discharge in a dense gas not only heats electrons, but also heats heavy particles effectively.

Powerful electron-beam pumping, used by Basov et al. [9–11], made it possible to create a supercooled (in respect of the degree of ionization) recombining plasma with a low gas temperature and thus avoid the blind alley of the previous attempts. Basov et al. first achieved lasing directly on a photodissociative transition.

The work on pumping liquid xenon with an electron beam [9–11] stimulated experiments on electron-beam pumping of high-pressure rare gases. Lasing on the dimer Xe_2 ($\lambda = 172$ nm), and also on the dimers Kr_2 ($\lambda = 146$ nm) and Ar_2 ($\lambda = 126$ nm), as a result of pumping of dense gases was achieved in 1972–1974 almost simultaneously by several research groups [12–29].

Investigations of exciplex lasers using halides of rare gases were based on the detection of emission spectra of these molecules [2,30–36]. Lasing has been observed for XeBr (282 nm) [37], KrF (248 nm) [38–41], XeCl (308 nm) [38,42], XeF (351 and 353 nm) [43,44], ArF (193 nm) [41], and KrCl (222 nm) [45] molecules pumped with an electron beam and in a discharge for KrF [46–52], XeF [49–52,53–55], and ArF [51,52] molecules. The information about the potential curves of exciplex molecules is summarized in References [56–58]. One can find the review information in References [59–70].

Lasers utilizing exciplex molecules are quite frequently called excimers but not exciplex lasers, following the nomenclature of rare-gas dimer lasers. We shall adopt the more correct terminology.

8.2 RARE-GAS DIMER LASERS

8.2.1 Theoretical Aspects

8.2.1.1 Inversion Condition

The main features of exciplex lasers are related to the large width of the photodissociative-transition band and the important role played by chemical reactions in plasma formed by strong pumping of dense gases. These features are seen in excimer lasers based on the photodissociative transitions of rare-gas dimers R_2^* (R = Xe, Kr, Ar):

$$R_2^* \rightarrow R + R + \hbar\omega. \tag{8.1}$$

The example of rare-gas plasma provides the basis for the simplest analysis of the inversion of photodissociative transitions. Therefore, we shall consider rare-gas dimers in discussing the main aspects of the physics of the active media of exciplex lasers.

The R_2 molecule in the ground (i.e., repulsive) state (Figure 8.1) decays into atoms ($R_2 \rightarrow R + R$) in a time $\tau_d < 1$–10 ps during which the atoms of energy $\varepsilon_d \sim 1$ eV seem to "roll down" from a potential hill. The lifetime τ^* of an electronically excited excimer R_2^* is higher than 1 ns. Consequently, deactivation of the lower active state by the flying apart of atoms is very effective.

However, it does not follow that the inversion condition is satisfied "automatically," as assumed by Houtermans [3] and others. For example, light is not amplified but absorbed in a medium, which is in thermodynamic equilibrium. Conditions for amplification of radiation as a result of photodissociative transition were considered [71] before the first excimer lasers were realized. The inversion conditions demand that photodissociative transitions described by expression (8.1) should predominate over reverse photoassociative transitions:

$$R + R + \hbar\omega \rightarrow R_2^*. \tag{8.2}$$

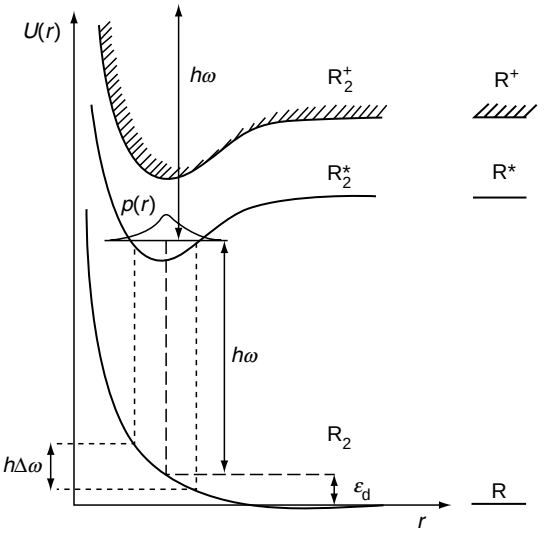

FIGURE 8.1 Basic term scheme of an R_2 dimer and the characteristics of a photodissociative transition: $\hbar\omega$ is the energy of the amplified radiation; $\Delta\omega$ is the effective line width; ε_d is the kinetic energy of atoms flying apart; $p(r)$ is the probability of finding nuclei at a distance r in a bound state.

In other words, it is necessary to ensure that there are fewer molecules on the "hill" of the ground electronic term than in the "well" of an electronically excited state. If the distribution of the heavy particles is Maxwellian, the population of this hill is proportional to $\exp(-\varepsilon_d/T)$, where T is the gas temperature. Consequently, the inversion condition reduces to the requirement of a sufficiently low gas temperature: $T < T_{cr}$.

A correct analysis [71] (see also References [59,61,72–75]) yields for the gain $\kappa = \kappa_{phd} - \kappa_{pha}$ the following formulas:

$$\kappa_{phd} = \sum_{vj} \sigma_{phd}(\varepsilon j, vj)[R_2^*]_{vj},\ \kappa_{pha} = \sum_{vj} \sigma_{phd}(\varepsilon j, vj)(2j+1)\left(\frac{2\pi^2}{\mu T}\right)^{3/2} N^2 \exp(-(E_{vj} - \hbar\omega)/T).$$

Here $\sigma_{phd}(\varepsilon j, vj)$ is the photodissociation cross section for the transition $vj \to \varepsilon j$, where v is the vibration number, j is the rotation number of R_2; ε is the kinetic energy of relative movement of atoms R; $[R_2^*]_{vj}$ is the population of the R_{2vj}^* sublevel; μ is the reduced mass of R_2 molecule; E_{vj} is the energy of excitation energy of R_{2vj} sublevel; and N is the gas density.

The simplified expression for photodissociation cross section looks like

$$\sigma_{phd} \approx (\lambda^2/4)(A/\Delta\omega).$$

Here $\lambda = 2\pi c/\omega$ is the wavelength of the transition; A is the rate of spontaneous radiative decay of the R_2^* molecule; $\Delta\omega = 1/Q(\omega)$ is the effective width of the transition band; and Q is the Frank-Condon factor.

Using these expressions after summation on v and integration on dj one has:

$$\kappa_{phd} = \sigma_{phd}[R_2^*], \quad \kappa_{pha} = \sigma_{phd}\left(\frac{2\pi\hbar^2}{\mu T}\right)^{3/2} \frac{\mu T r_e^2}{\hbar^2} \frac{e^{-\varepsilon_d/T}}{1 - e^{-\hbar^2\omega_{e/T}} N^2.}$$

Here $[R_2^*] = \Sigma_{vj}[R_2^*]_{vj}$ is the full population of the R_2^* state; r_e is the equilibrium nuclear separation in R_2^* molecule; $\hbar\omega_e$ is the energy of the first vibration transition in R_2^* molecule.

A rough estimation of the critical temperature can be obtained from these expressions for gain κ (for details, see References [59,61,71–75]):

$$T_{cr} \approx \varepsilon_d/10 \approx 0.1 \text{ eV}. \tag{8.3}$$

This estimate is quite close to the exact value because of the logarithmic nature of the dependence of T_{cr} on the plasma parameters.

In view of the low value of T_{cr}, arc plasma in which the gas temperature is very high ($T \approx 1$ eV) is obviously unsuitable for photodissociative-transition amplification.

8.2.1.2 First, Second, and Third Continua in Rare Gases

It is accepted to distinguish three continua in rare-gas spectra. The continuum beginning at a resonant line refers to the first continuum. It is followed by the second and third continua in the ascending of wavelengths (Table 8.1). The first continuum corresponds to radiation from high-excited vibration levels of the states $^{1,3}\sum_u^+$ of dimers R_2^* to the ground repulsive state $^1\sum_g^+$. The second continuum corresponds to the same electronic transition, but from the bottom vibration levels (Figure 8.1 and Figure 8.2). The basic hypotheses offered for an explanation of the nature of the third continua are considered in reviews [76,77]. The

TABLE 8.1
Wavelengths of the Resonant Transition, the Second and Third Continua in Various Inert Gases

Element	Resonant Transition, nm	Second Continua (Band Center), nm	Third Continua, nm
Helium	60	70–80	105–650
Neon	74.4	82	90–105
Argon	106.7	126	150–280
Krypton	123.6	146	180–360
Xenon	147.0	172	200–400

Note: Position of band maxima of the third continua and their form can strongly depend on experimental conditions. The first continua are displaced on some nanometers aside the large wavelengths from resonant transition.
Source: From Boichenko, A.M., Tarasenko, V.F., and Yakovlenko, S.I., *Laser Phys.*, 9(5), 1004–1020, 1999.

most reliable one for high pressure is that it is the transition in singly charged molecular ion Rg_2^{+*} (1) $\rightarrow Rg^+ + Rg + \hbar\omega$ (Figure 8.2).

It is clear that lasing on the transitions corresponding to the first continuum is practically impossible. There were publications about detection of radiation amplification on the third continua. However, these publications have not proved to be true. Theoretical consideration shows that amplification of radiation of the third continua is practically impossible [78]. Therefore, only the second continua are considered here.

8.2.1.3 Bandwidth

In the absence of photodissociation, the gain is

$$\kappa = \sigma_{\text{phd}}[R_2^*]. \tag{8.4}$$

The effective bandwidth $\Delta\omega$ can be estimated on the assumption that the ''walls'' of a potential well confine the vibration motion of the nuclei. Projection of the turning points onto the repulsive (dissociating) term and then onto the energy axis (Figure 8.1) gives the width $\hbar\Delta\omega$ of the energy interval in which a photodissociative transition can take place.

The actual distribution of the probability $p(r)$ of finding atoms in a given nuclear separation r is governed by quantum-mechanical laws. However, for the zeroth vibrational level, which is most heavily populated in a dense gas, the width of the distribution $p(r)$ is slightly less than the separation between the turning points of classical motion, which makes this estimate relatively reliable.

The bandwidth $\Delta\omega$ of a photodissociative transition ($\sim 10^{15}$ s^{-1}) is several orders of magnitude greater than the corresponding bandwidth of atomic and ionic lines ($\Delta\omega \sim 10^{10}$–$10^{12}$ s^{-1}).

8.2.1.4 Threshold Characteristics

The large spectral width of the photodissociative transitions and the correspondingly small phototransition cross section (Table 8.2) together with the required low value of the gas temperature are responsible for a number of important features of excimer lasers: high threshold pump power density w_{th}, a high saturation intensity of the active transition I_{sat}, and stringent requirements with respect to gas purity.

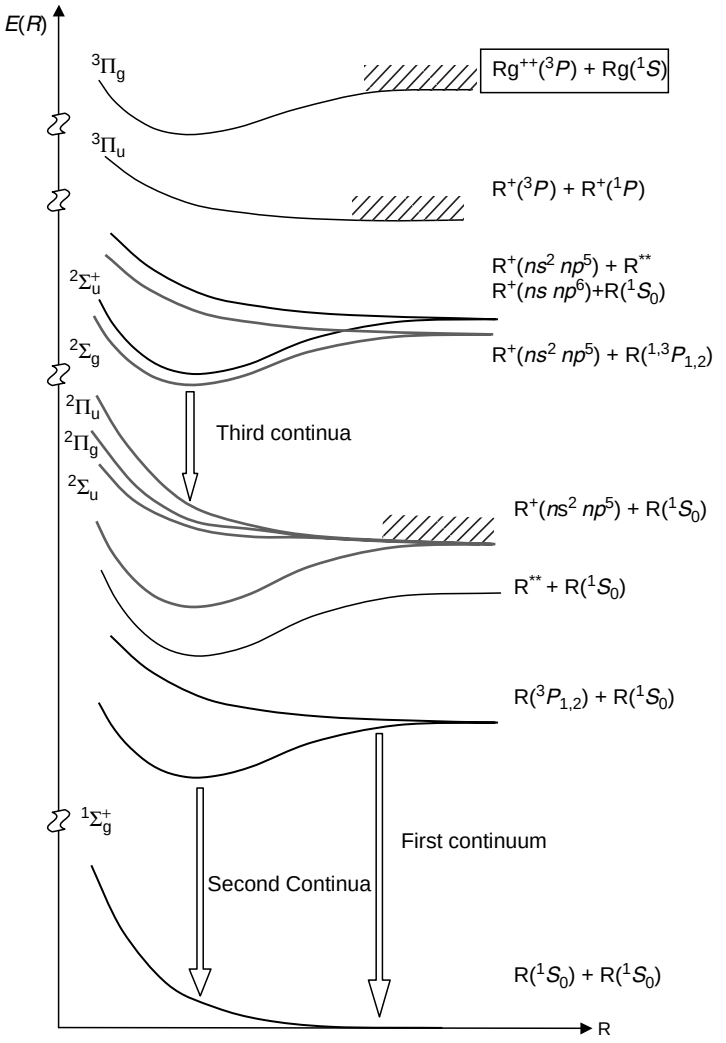

FIGURE 8.2 The term scheme of an R_2 dimer explaining the nature of the first, second, and third continua. (From Boichenko, A.M., Tarasenko, V.F., and Yakovlenko, S.I., *Laser Phys.*, 10(6), 1159–1187, 2000. With permission.)

TABLE 8.2
Cross Sections for Stimulated Photodissociative Emission of R_2^*

σ (cm^2)	Helium	Neon	Argon	Krypton	Xenon
$^3\Sigma_u^+$	$2.7 \cdot 10^{-22}$	$1.4 \cdot 10^{-21}$	$1.6 \cdot 10^{-20}$	$9.8 \cdot 10^{-20}$	$1 \cdot 10^{-18}$
$^1\Sigma_u^+$	$1.3 \cdot 10^{-18}$	$6.0 \cdot 10^{-18}$	$1.2 \cdot 10^{-17}$	$1.1 \cdot 10^{-17}$	$1.6 \cdot 10^{-17}$

Source: From Jacob, J.H., Hsia, J.H., Mangano, J.A., and Rokni, M., *J. Appl. Phys.*, 50(8), 5130–5134, 1979.

We shall now obtain some estimates by taking the xenon dimer as an example ($A \approx 2 \cdot 10^7$ s^{-1}, $\Delta\omega \approx 0.7$ eV, $\sigma_{phd} \approx 2 \cdot 10^{-18}$ cm^2). If the threshold gain is $\kappa_{th} \approx 0.01$ cm^{-1}, then the threshold excimer population needed for lasing is

$$[R_2^*]_{th} = \kappa_{th}/\sigma_{phd} \approx 0.5 \cdot 10^{16} \text{ cm}^{-3}.$$

The corresponding threshold density of the input energy is

$$W_{th} = J[R_2^*]_{th} \approx 10^{-2} \text{ J/cm}^3$$

($J = 12$ eV is the ionization energy of xenon); the threshold pump power density is

$$w_{th} = AW_{th} \approx 200 \text{ kW cm}^{-3};$$

and the saturation intensity of the active transition amounts to

$$I_{sat} \geq \hbar\omega A/\sigma_{phd} \approx 10 \text{ MW/cm}^2.$$

The requirements with respect to gas purity arise because the photodissociative transitions of rare-gas dimers lie in the vacuum ultraviolet (VUV) range and the photon energy is sufficient to ionize atoms and molecules of many impurities. The following condition must be satisfied to ensure that the absorption coefficient of impurities (parasitic absorption) is less than the gain:

$$N_{imp} < [R_2^*]\sigma_{th}/\sigma_{imp}. \tag{8.5}$$

Here, N_{imp} is the density of an impurity and σ_{imp} is its photoionization cross section. As the photoionization and photoexcitation cross sections of an impurity are usually of the same order as the photodissociation cross section of the active molecule, the impurity concentration should be less than the dimer concentration ($N_{imp} < 10^{16}$ cm^{-3}). On the other hand, a high-pump power density requires the use of dense gases ($N \sim 10^{20}$–10^{21} cm^{-3}). This leads to the requirement that purification should achieve $N_{imp}/N = 10^{-4}$–10^{-5}.

Fundamental limits on the output power of rare-gas dimer lasers are imposed by the photoionization of a dimer caused by the emitted radiation:

$$R_2^* + \hbar\omega \rightarrow \begin{cases} R_2^+ + e \\ R^+ + R + e \end{cases}. \tag{8.6}$$

If the photoionization cross section σ_{phi} is larger than the photodissociation cross section σ_{phd}, no amplification is possible. Although it is usual to find that $\sigma_{phd} > \sigma_{phi}$, the photoionization reaction (8.6) limits the length of the active medium that can be rationally utilized and, therefore, it limits the volume of the active medium of an efficient rare-gas dimer laser.

Although rare-gas dimer lasers have a number of shortcomings, it is of interest to analyze these lasers in detail because such an analysis makes it possible to understand many aspects of the physics of other exciplex lasers.

8.2.1.5 Simplest Model of the Active Medium

Relaxation of electrons between excited states of atoms and molecules in a dense ($N > 10^{19}$ cm^{-3}) gas is a very complex process. The process of populating excited electronic states is

influenced significantly not only by electron collisions and radiative transitions, but also by various plasma-chemical reactions, which can dominate various relaxation channels. However, plasma of a pure rare gas in all the channels "lead" to the upper active state where electrons are accumulated [61,69,73,74].

The most powerful channel of electron relaxation between excited levels is as follows. Ionization by fast and secondary electrons generated by an ionization cascade gives rise to atomic R^+ ions. Triple collisions convert these ions to molecular states R_2^+, which recombine dissociatively forming atoms in the ground (R) and excited (R^{**}) states. The excited R^{**} atoms then collide with neutral R atoms and electrons and "drop down" to the first excited state R*. The subsequent collisional transition to the ground atomic state is hindered because of the large energy of this transition and the radiative transition results in reabsorption. It follows that relaxation "deviates" to the formation of molecules: an excited R* atom colliding with two rare-gas molecules forms an active R_2^* dimer (Figure 8.3).

It follows that the R_2^* state is the "bottleneck" where electrons are accumulated. The R_2^* dimer state usually decays by spontaneous photodissociative transition (it is desirable that this transition should predominate) and also as a result of collisions of the excited R_2^* molecules with one another, accompanied by the Penning ionization process. So, the densities of dimers $[R_2^*]$ and electrons N_e can be calculated on the basis of the following simple relaxation model:

$$dN_e/dt = -N_e/\tau_{rec} + q[R_2^*]^2 + \nu_i N,$$
$$d[R_2^*]/dt = N_e/\tau_{rec} - 2q[R_2^*]^2 - A[R_2^*] + \nu_{ex} N. \tag{8.7}$$

Here, τ_{rec} is the characteristic electron recombination time; $q = <\sigma v>$ is the Penning ionization rate when two excited molecules collide; ν_i and ν_{ex} are, respectively, the frequencies of ionization and excitation by beam electrons and by the electrons of an ionization cascade generated by a beam (for details, see References [73,74]).

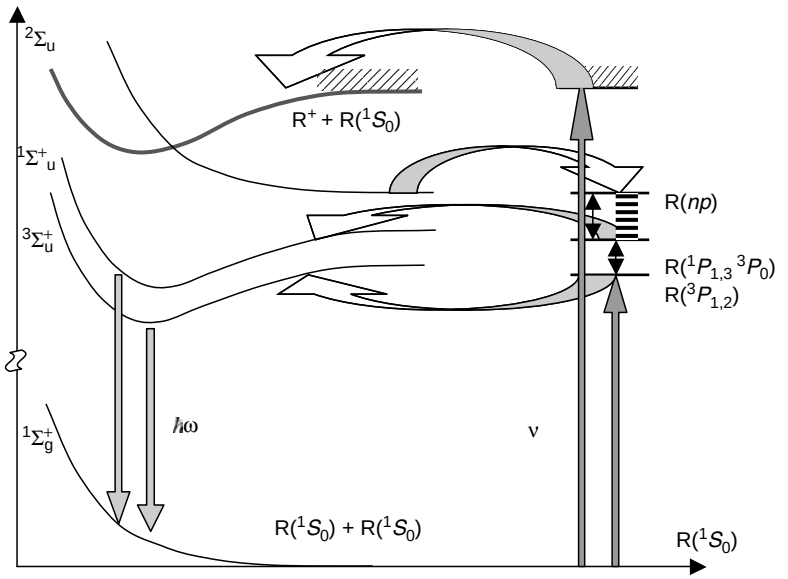

FIGURE 8.3 The basic processes that participate in populating dimer R_2^*.

8.2.1.6 Quasi-Steady Regime and Afterglow

The system of Equations (8.7) can be solved in two limiting cases: under steady-state conditions ($\nu_i = \text{const}$, $\nu_{ex} = \text{const}$) and during the afterglow ($\nu_i = \nu_{ex} = 0$).

If we assume that $dN_e/dt = d[R_2^*]/dt = 0$ under steady-state conditions, we find that the dimer concentration is described by

$$[R_2^*] = \frac{A}{2q}\left(\sqrt{1 + 4\nu Nq/A^2} - 1\right) = \begin{cases} \nu N/A, & \text{if } 4\nu N \ll A^2/q; \\ \sqrt{\nu N/q}, & \text{if } 4\nu N \gg A^2/q, \end{cases} \tag{8.8}$$

where $\nu = \nu_i + \nu_{ex}$.

It is convenient to introduce some parameters for which the rate of spontaneous decay of a dimer becomes equal to the rate of decay as a result of the Penning reactions: $[R_2^*]_{bd} = A/2q$, $w_{bd} = \varepsilon_p \nu_{bd} N \approx \varepsilon_{bd} A[R_2^*]$ ($\varepsilon_p \approx 2J$ is the energy needed to form an electron–ion pair), $\kappa_{bd} = \sigma_{phd}[R_2^*]$. For xenon dimers, we have $[R_2^*]_{bd} \approx 10^{17}$ cm^{-3}, $w_{bd} \approx 7$ MW cm^{-2} (for $\varepsilon_p \approx 22$ eV), and $\kappa_{bd} \approx 0.1$ cm^{-1}.

Since in the case of Xe_2^* the threshold pump power is considerably less than the limiting power at which Penning reactions begin to play a role ($w_{th} \ll w_{bd}$), lasing of Xe_2^* dimers becomes possible when the Penning reactions are insignificant. Each ionization and excitation event then creates a photon as a result of active transition.

When estimates are based on expression (8.8), we are not dealing with steady-state conditions, but with a quasi-steady regime because in the time $\tau T \sim T_{cr}/(\nu J)$, the active medium is heated to a temperature T_{cr} at which lasing is quenched. The quasi-steady approach is justified because when the degree of ionization is sufficiently low, the time in which the electron temperature (and, consequently, the pumping regime) becomes steady is much shorter than the time in which the gas becomes heated.

During afterglow, the accumulation of electrons occurs mainly in the active state R_2^*, because this state is the relaxation bottleneck, that is, $[R_2^*] > N_e$. In this regime, if $dN_e/dt = 0$, then

$$d[R_2^*]/dt = -A[R_2^*] - q[R_2^*]^2, \quad q[R_2^*]^2 = N_e/\tau_{pek}. \tag{8.9}$$

The solution of the previous equations is

$$\frac{[R_2^*](t)}{[R_2^*](t=0)} = \frac{e^{-At}}{1 + \eta_0(1 - e^{-At})}. \tag{8.10}$$

Here, $[R_2^*]$ $(t = 0)$ is the dimer population at some initial moment at which the adopted approximation is already valid; $[R_2^*](t = 0)q/A$ is the ratio of the initial population to the limiting value, which can be regarded as a fitting parameter when comparisons are made with the experimental results.

8.2.2 Experiments

8.2.2.1 Experiments on Liquid Xenon

Basov et al. investigated the emission spectra of rare gases in the liquid state [9–11] and observed a high rate of transfer of excitation from light to heavy rare gases, when the latter were added as impurities. They observed stimulated emission accompanied by narrowing of the emission spectrum of xenon dimers. The electron-beam current density reached 300 A cm^{-2}, the electron energy was 1 MeV, and the duration of the beam current pulses was 10 ns.

When the electron current density exceeded 100 A cm^{-2}, a bright spot appeared on a luminescent screen. The divergence of the radiation, determined from the size of the spot on the screen when a cavity was used, was approximately 7°.

For a long time, the attempts to reproduce the experiments on lasing in liquid xenon were unsuccessful. Lasing in mixtures of liquid rare gases containing xenon is reported in Reference [79]. However, the transitions in xenon and krypton resulted in lasing only when argon, which was the main component of the liquid mixture, contained a small amount of a heavy rare gas. May be lasing in References [9–11] took place in gas layer, not in liquid [61]. As pointed out earlier, the work of Basov et al. stimulated the experiments (described later) involving electron-beam pumping of high-pressure rare gases.

8.2.2.2 Principal Conditions in Experiments on High-Pressure Gases

The high-threshold pump power density means that it is necessary to use a dense gas so that the usual working pressure in the excimer lasers exceeds 5 bars. For example, the lasing process in xenon is maximal at 15 bars. Since in the course of strong pumping the gas should remain cold, the most acceptable solution is to use a "hard" ionize, which may be a high-current electron or ion beam, a powerful beam of short-wavelength photons, and so on. Under laboratory conditions it is usual to pump rare-gas dimer lasers by high-current (~100 A cm^{-2}) electron beams. In view of the high gas density, the pump beam is perpendicular to the direction of amplification of the radiation (transverse pumping). As mentioned earlier, the gas purity must be high.

We shall now consider the main experimental results in light of the physics of relaxation of plasmas of rare-gas dimers. We shall concentrate our attention on the Xe_2 laser (for details, see References [61,73,74]).

8.2.2.3 Factors Causing Suppression of Lasing

The suppression of lasing during a pump pulse can be explained by overheating of the gas, that is, by the fact that the gas temperature exceeds the critical value $T_{cr} \approx 0.1$ eV at which the photodissociative absorption coefficient begins to approach the photodissociative gain.

It is significant that when a dense (up to 25 bar) gas is ionized by an electron beam of current density $j = 200$–300 A cm^{-2}, the resultant medium begins to amplify light just before the end of the beam pulse [15,17]. Lasing is strongest during afterglow. An increase in the beam current density up to 800 A cm^{-2} changes drastically the time dependence of the laser radiation intensity: lasing suppression begins when the beam current is still rising [16]. When the energy of the beam electrons is of the order of 700 keV and the current density is $j \approx 3$ kA cm^{-2}, lasing suppression occurs again when the beam current is still rising (not later than 10 ns) [21]. If the beam current density is reduced to 300 A cm^{-2}, the duration of lasing in the same set-up increases to 90 ns [23]. These observations fit well the hypothesis of overheating of the gas by stronger pumping and are in agreement with the results of a numerical simulation.

Very powerful pumping quenches not only the population inversion but also the spontaneous luminescence [20]. Numerical calculations [52] show that the quenching of the luminescence is because of an increase in the electron concentration. This activates the channel of ionization deactivation of the excited states by the plasma electrons. Moreover, an increase in the gas temperature reduces the rate of the associative formation of dimers.

8.2.2.4 Afterglow

A peak of dimers' spontaneous emission, which becomes narrower with increase in the pressure, was observed during the afterglow stage following a short ($\tau \approx 1.6$ ns) electron-

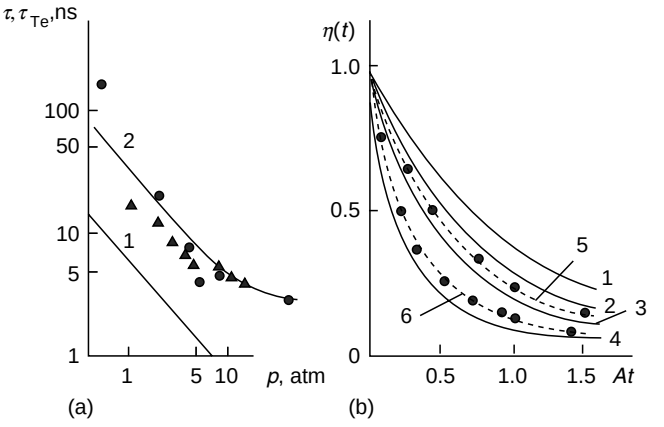

FIGURE 8.4 Comparison of the experimental results with calculations of relaxation behavior of the Xe_2 dimer during afterglow of pulsed electron-beam pumping. (a) Pressure dependences of the delay time τ of a lasing peak found experimentally. (From Koehler, H.A., et al., *Appl. Phys. Lett.*, 21(5) 198, 1972.)(-) and (From Koehler, H.A., et al., *Phys. Rev. A.*, 9, 768, 1974.) (•) Of the characteristic electron cooling time τ_{Te}, and of the results of numerical calculation. (From Gudzenko, L.I., et al., *Tr. Fiz. Inst. Akad. Nauk SSSR*, 120, 43, 1980.) (b) Time dependences of the intensity of the spontaneous radiation emitted by dimers investigated experimentally. (From Koehler, H.A., et al. *Phys. Rev. A.*, 9, 768, 1974.) (Points) Of the intensity calculated on the basis of formula (8.10). (Curves) Plotted for 1—$\eta_0 = 0$, 2—$\eta_0 = 0.65$, 3—$\eta_0 = 1.7$, 4—$\eta_0 = 5$, 5—$\eta_0 = 0.9$, 6—$\eta_0 = 3.5$.

beam pump pulse [12,22]. The delay time of the radiation pulse peak relative to the pump pulse matched approximately the cooling time τ_{Te} of free electrons (Figure 8.4) and, consequently, it was inversely proportional to the gas pressure. Numerical calculations [80] were also in good agreement with the experimental results.

The time dependence of the radiation intensity is described well (Figure 8.4b) by formula (8.10), which contains one fitting parameter.

8.2.2.5 Lasing in a Discharge

For a long time, there were no reports on successful pumping of dimer lasers in a discharge. Rather recently the lasing on Kr_2^* [81] and amplification on Ar_2^* [82] in a discharge have been reported. These experiments are not reproduced in other groups.

Lasing in discharge basically is possible if a fast uniform ionization of a dense gas without the gas heating is obtained. According to the recent researches [83,84], the nanosecond pulse with a subnanosecond front can provide the uniform dense gas ionization. In this case the ionization is because of multiplication of a small amount of background electrons. These conditions are rather different from conditions in References [81,82].

8.3 EXCIPLEX LASERS

8.3.1 The General Properties

8.3.1.1 Start of Rare-Halide Lasers

Lasers using rare-halide exciplex molecules are currently the most powerful lasers in the UV spectral range. The properties of KrF (248 nm), XeCl (308 nm), ArF (193 nm), and XeF (351

and 353 nm) lasers are well understood, and the highest energies and efficiencies are achieved for these lasers.

The total pressure of the medium in these experiments ranged from 0.5 up to several atmospheres. A detailed review of the first starts and the initial phase of the development of such lasers can be found in References [62,63]. The schemes of pumping and design of exciplex lasers often used in recent experiments are described in Reference [68].

The output energy per unit volume for the most efficient KrF laser may be as high as several tens of joules per liter, while the efficiency in energy deposited in the active medium may reach 10%. Laser radiation is usually emitted in such a laser through the excitation of ternary mixtures consisting of atoms of a buffer rare gas R′, working rare gas R, and halogen-containing molecules M(X) with a typical composition R′:R:M(X) ~ 1000:100:(1–10). Binary and quaternary R–M(X) and R_1–R_2–R–M(X) mixtures are also used in some cases. Exciplex lasers are widely employed for fundamental and applied research. The work is currently in progress on improving amplifying stages of KrF lasers designed for laser thermonuclear fusion. The brightness of radiation in the order of 10^{20} W/(cm^2 sr) has been achieved with these lasers [85,86]. The field of such radiation may be several tens of times higher than the Coulomb field acting on an electron in a hydrogen atom. Commercial modifications of these lasers have been also created and are permanently developed now [87].

8.3.1.2 The Structure of Potential Curves

The diagrams of potential curves for all the halides of rare gases are similar to each other (except XeF; Figure 8.5). The ground states of exciplex molecules consist of $^2\Sigma^+$ and $^2\Pi$ terms, which are often denoted also as X and A. At large distances, two components of $^2\Pi$ terms correlate with ^2P states of halogen atoms. The lower excited states have an ionic structure, correlating at large distances with $R^+(^2P) + X^-(^1S)$ ionic states, where X stands for a halogen atom. As the fine-structure splitting in $R^+(^2F)$ ions for Ar, Kr, and Xe is large (this quantity ranges from 1400 cm^{-1} for Ar up to 10,000 cm^{-1} for Xe), the c-type Hund coupling is typically observed for these species, and the corresponding ionic states are denoted as $B(1/2)$, $C(3/2)$, and $D(1/2)$. The lowest bound Rydberg state is denoted as E. This term is similar to the ground state of the relevant RX^+ion (or the ground state of an analogous isoelectronic X_1X halogen molecule) [65]. The results of theoretical analysis of potential curves are summarized in References [57,58].

In accordance with selection rules, spontaneous emission may arise only for $B \rightarrow X$, $C \rightarrow A$, and D–X transitions. The $B \rightarrow X$ transitions are especially strong (radiative lifetimes of the B and C states differ from each other by approximately an order of magnitude; see Table 8.3). Lasing has been mainly observed for these transitions (Table 8.4). Lasing usually starts at the lower vibrational level with $v = 0$ of the B state (four lower vibrational levels are involved in lasing in the case of a KrF laser). Lasing through the C–A transitions has been observed only for XeF molecules thus far.

The B and C states are very close to each other. As the depths of the B and C states are large (~5 eV, and each state involves about 100 vibrational levels) and lasing starts at lower vibrational levels of the B state, the understanding of mechanisms behind the population of the B and C states and the kinetics of these processes is very important for the modeling of lasing. The C state was initially believed to have a higher energy than the B state. However, the results of recent studies indicate that the C state lies lower than the B state. According to the data of various studies, the difference between the energies of these levels may vary by several times. However, this difference always remains small, never exceeding several hundreds of inverse centimeters.

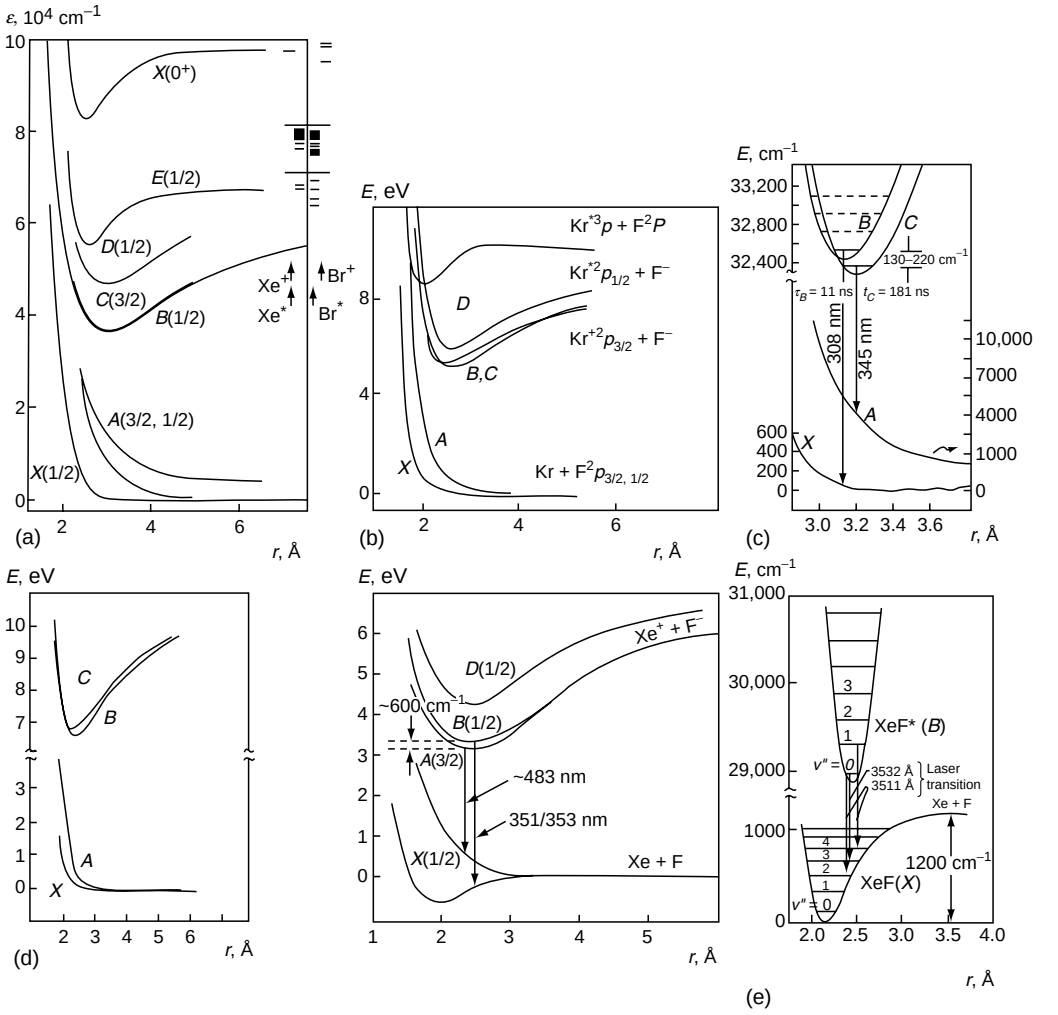

FIGURE 8.5 Diagrams of potential curves for exciplex molecules: (a) XeBr (from *Gas Lasers*, McDaniel, E.W. and Nighan, W.L., Eds., New York: Academic); (b) KrF (from *Gas Lasers*, McDaniel, E.W. and Nighan, W.L., Eds., New York: Academic); (c) XeCl (from Boichenko, A.M., Tarasenko, V.F., and Yakovlenko, S.I., Exciplex rare-halide lasers. *Laser Phys.*, 10(6), 1159–1187, 2000); (d) ArF (From Dunning, T.H., Jr. and Hay, P.J., The covalent and ionic states of the rare gas monofluorides, *J. Chem. Phys.*, 69(1), 134–149, 1978); and (e) XeF (from *Gas Lasers*, McDaniel, E.W. and Nighan, W.L., Eds., New York: Academic.).

8.3.1.3 Lasing Threshold

The lasing threshold of exciplex lasers is lower than the lasing threshold of excimer lasers. As mentioned in Section 8.3.1.1, the upper radiation-emitting *B* state of exciplex molecules is of ionic nature. The binding energy of ionic states (~5 eV) is much higher than the binding energy of covalent levels in the upper working states of excimers (~0.5 eV). So, the laser radiation of exciplex has a longer wavelength λ. In contrast to excimers, exciplexes feature transitions only to the lower term (*X*), which is either a weakly bound state or a sufficiently gently sloping term for molecular distances corresponding to the minimum of the upper

TABLE 8.3
Radiation Lifetimes (Nanosecond) for Transitions $B \rightarrow X$ and $C \rightarrow A$ in Rare-Halide Exciplexes

Molecule	$B \rightarrow X$	$C \rightarrow A$
NeF	2.6	38
ArF	4.2	48
KrF	9	63
XeF	13–19	100–150
XeCl	11	120
XeBr	12	120
XeI	12	110

Source: From Boichenko, A.M., Tarasenko, V.F., and Yakovlenko, S.I., *Laser Phys.*, 10(6), 1159–1187, 2000.

potential curve (B). Therefore, the spectral bandwidth $\Delta\omega$ of exciplex transitions is much less than the spectral bandwidth of excimer transitions. As a result, the cross section of photodissociation (stimulated emission) for RX* exciplexes σ_{phd} is nearly two orders of magnitude greater than the relevant cross section of R_2^* dimers.

Because of all these circumstances, the threshold pump powers are lower in the case under consideration. For example, in the case of KrF*, we have $\lambda \sim 250$ nm, $A \sim 10^8$ s^{-1}, and $\sigma_{\text{phd}} \sim 2.5 \cdot 10^{-15}$ cm^2. Assuming that the threshold gain is $\kappa_{\text{th}} \sim 10^{-2}$ cm^{-1}, we find that $[\text{KrF}^*]_{\text{th}} = \kappa_{\text{th}}/\sigma_{\text{phd}} \sim 4 \cdot 10^{13}$ cm^{-3}, the threshold energy deposition is $w_{\text{th}} = J[\text{KrF}^*]_{\text{th}} \sim 10^{-4}$ J cm^{-3} ($J \sim 14$ eV), the threshold pump power is $W_{\text{th}} = w_{\text{th}}A \sim 10$ kW cm^{-3}, and the saturation intensity is $I_{\text{sat}} \sim h\nu A/\sigma_{\text{phd}} \sim 1$ MW cm^{-2}. The results of calculations for the efficiency of radiation emission of exciplex lasers as a function of the power of energy deposition around the threshold are presented in Figure 8.6 [66,88–90]. An XeF laser is

TABLE 8.4
The Wavelengths (λ, nm) and Experimental Values of the Probability of Radiative Decay (A, s^{-1}) and Cross Sections of Stimulated Emission (σ, cm^2) for $B \rightarrow X$ Transitions in the Existing Exciplex Rare-Halide Lasers

Molecule	λ (nm)	A (s^{-1})	σ (cm^2)
KrF	248–249	$(1–1.5) \cdot 10^8$	$(0.6–2.7) \cdot 10^{-16}$
XeCl	307–308	$9 \cdot 10^7$	$4.5 \cdot 10^{-16}$
ArF	193	$(1–2) \cdot 10^8$	$2.9 \cdot 10^{-16}$
XeF	351, 353	$(5–7) \cdot 10^7$	$(2–5) \cdot 10^{-16}$
	470–480 (C → A)	$(0.6–1) \cdot 10^7$	$5 \cdot 10^{-18}$
KrCl	222	$4.5 \cdot 10^7$	$1.5 \cdot 10^{-16}$
ArCl	175	—	—
XeBr	282	$(5.7–8.3) \cdot 10^7$	$(1.5–2.2) \cdot 10^{-16}$
KrBr	206	—	—
XeI	253	$8.3 \cdot 10^7$	$1.4 \cdot 10^{-16}$
KrI	185	—	—
ArBr	161	—	—

Source: From Boichenko, A.M., Tarasenko, V.F., and Yakovlenko, S.I., *Laser Phys.*, 10(6), 1159—1187, 2000.

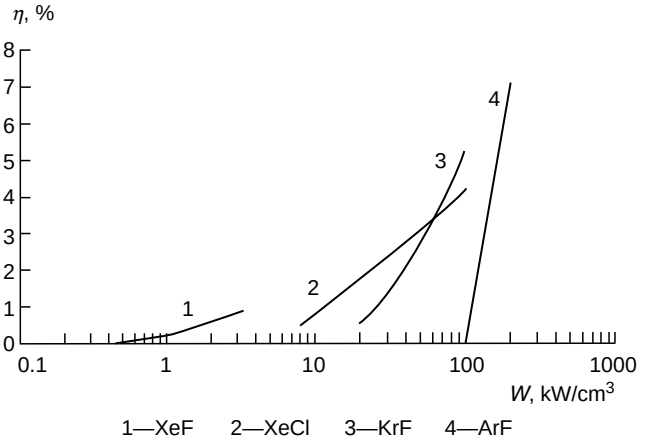

FIGURE 8.6 The efficiency (%) of radiation emission in XeF (from Boichenko, A.M., et al., *Quant. Electron*., 25(6), 521–524, 1995), XeCl (from Stielow, G., et al., *Appl. Phys. B*., 47(4), 333–342, 1988), KrF (from Plazmennye Lazery Vidimogo i Blizhnego UF Diapazonov (Visible and Near-UV Plasma Lasers) Tr. Inst. Obshch. Fiz. Akad. Nauka 21, 1989, Yakovlenko, S.I., Ed. [whole volume]), and ArF (from Boichenko, A.M., et al., *Laser Phys*., 2(3), 210–220, 1992) lasers calculated as a function of the pump power (kW/cm) around the threshold. Optimization with respect to the concentrations of reagents in the mixture and cavity parameters was performed for a fixed energy deposition (ionization frequency).

characterized by the minimum threshold. This value of the threshold power allows lasers of this type to be employed with nuclear pumping [90] under conditions characteristic of the available nuclear reactors and nuclear reactors that are designed.

8.3.2 On the Modeling of the Active Medium

The active medium can be excited either by a hard ionizer (e.g., an electron or ion beam, short-wavelength radiation, and so on) or a discharge. These methods of excitation are often combined. In particular, a discharge controlled with an electron beam can be used. Excitation of an active medium by a hard ionizer and a discharge usually leads to different results, giving rise to different nonequilibrium states of the medium with respect to the ionization degree (recombination and ionization nonequilibrium states, respectively [61,66,67]). Electron distribution functions $f(\mathbf{v})$ in velocities $\mathbf{v}$ also differ for different regimes of pumping. If the distribution function depends on the modulus of the velocity, an electron energy distribution function (EEDF) is often introduced. A considerable part of the reactions in kinetic models describing a laser active medium involves electrons. These reactions enter into kinetic equations through reaction rates $k = \int \sigma(v)\, vf(\mathbf{v})\, dv_x\, dv_y\, dv_z$ using EEDF and the cross sections $\sigma(v)$ of the relevant reactions, where v is the modulus of the electron velocity, $\varepsilon = m_e v^2/2$ is the electron energy.

8.3.2.1 Pumping with a Hard Ionizer

When a fast particle of a beam (e.g., an electron) propagates through a medium, it ionizes and excites atoms and molecules in this medium. The energy of many electrons emerging from this ionization process (electrons of the ionization cascade) is sufficient for the ionization and excitation of particles in the medium. The energy of electrons giving rise to such cascades is mainly spent on inelastic collisions. When this energy becomes insufficient for ionization and

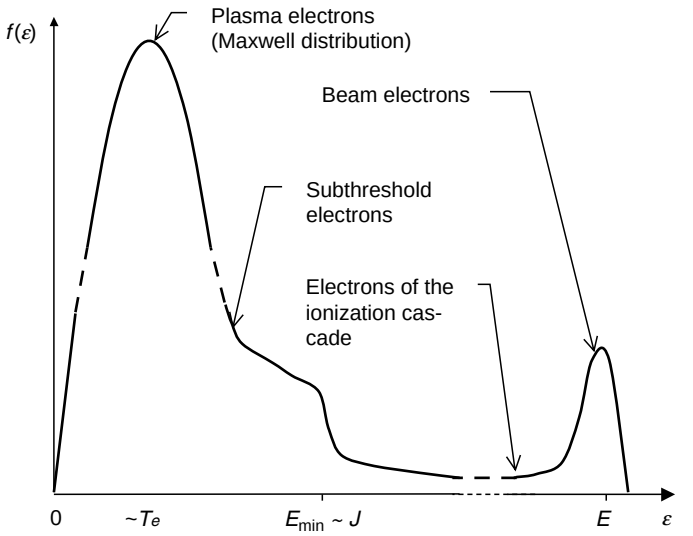

FIGURE 8.7 Characteristic energy distribution function of electrons in plasma produced by an electron beam. E is the e-beam energy and J is the energy of ionization of gas atoms.

excitation, further decrease of this energy is decelerated and occurs after that through elastic collisions with cold heavy gas species. A characteristic distribution of electrons in plasma produced by an electron beam is shown in Figure 8.7. Electrons whose energy is lower than the first excitation potential $E_{\min}$ are called subthreshold (or slow) electrons. Coulomb collisions play an important role in the case of electrons cooled down to energies much lower than $E_{\min}$ (the so-called plasma electrons). Coulomb collisions give rise to the formation of a Maxwell distribution. The characteristic electron temperature in active media of exciplex lasers pumped by a hard ionizer is approximately equal to 1 eV. The results of simulations show that the calculated lasing parameters and densities of different reagents change only slightly if the deviation of the EEDF from the Maxwell distribution for energies lower than and in the order of $E_{\min}$ is not included in the model and the time required for the establishment of this distribution is ignored with an assumption that the Maxwellian EEDF arises instantaneously at low energies. Calculating the rates of some important reactions that have a considerable influence on the operation of exciplex lasers, such as the attachment of electrons to halogen-containing molecules or excitation of these molecules by electron impact, one can assume that the EEDF is Maxwellian within the entire definition range of this function, as the cross sections of these reactions reach their maxima at energies not higher than several electronvolts.

When an active medium is pumped by a hard ionizer (e.g., an electron beam), the specific pump power can be conveniently characterized in terms of the ionization frequency of the medium, $\nu = \xi \frac{\sigma(E) j}{e}$, where $\sigma(E)$ is the ionization cross section of atoms (molecules) for ionizing particles with an energy E, j is the current density of these particles, e is the electron charge, and ξ is the factor that includes the influence of the ionization cascade ($\xi \approx 2$). Generally, the ionization frequency can be found from the relationship $\nu N E_{\text{pair}} = W$, where W is the specific power of energy deposition, N is the concentration of atoms (molecules) in the medium, and E_{pair} is the energy spent on the formation of an electron–ion pair in the case when a beam particle moves in the medium until it completely stops. When determining E_{pair}, one has to take into consideration all the ionization events, including primary ionization events, which occur in collisions with a fast particle, and secondary events, which are because

TABLE 8.5
The Energy Spent on the Production of an Electron–Ion Pair E_{pair} during the Propagation of a Beam Particle through Different Gases

Gas	He	Ne	Ar	Kr	Xe	H_2	N_2	O_2	Air
E_{pair} (eV)	46	37	26	24	22	36	37	33	36

Source: From Muller-Horsche, E., Oesterling, P., and Basting, D., *Proc. SPIE Int. Soc. Opt. Eng.*, 1225, 142–145, 1990.

of collisions with electrons emerging from primary ionization events. Some results of such calculations can be seen in Table 8.5. The qualitative estimation is $E_{pair} \approx 2J$.

8.3.2.2 Discharge Pumping

Modeling the regime of discharge pumping, we cannot employ a Maxwellian EEDF, as it is usually done in simulations of active media pumped by a hard ionizer (see the previous section). In the presence of an electric field in plasma, the electron distribution function depends not only on the modulus of the electron velocity (the electron energy), as in the case of the zero field, but also on the vector of the electron velocity. As the direction of the electric field is distinguished in this case, the electron distribution function is usually represented as an expansion in Legendre polynomials involving the cosine of the angle measured from the direction of the field. If the electron-free path length between collisions is small as compared with the sizes of the active area (this assumption is usually justified for active media of exciplex lasers with a large safety margin), then the velocity electron distribution function is virtually independent of the velocity direction because of a considerable bending of electron trajectories caused by collisions with heavy particles. This expansion usually includes only polynomials of the zeroth and first orders (correspondingly, this approach is called a nearly isotropic approximation).

8.3.2.3 Description of the Kinetics of the Active Medium

Although the analysis of kinetic equations is usually aimed at the investigation of populations of working levels, tens of equations describing hundreds of chemical reactions are often included in specific models of laser active media. Population and depopulation of working states in dense plasma often involve different relaxation channels. The role of some specific channel under these conditions considerably depends on the electron and gas temperatures, which may vary in the course of relaxation. Models of such processes should include collisions with electrons; spontaneous radiative transitions; excitation transfer; and various plasma-chemical reactions, such as three-body and dissociative recombination, Penning reactions, association of atoms into a molecule through three-body collisions, and so on.

Equations governing the balance of the densities [Y(m)] of particles of the sort Y in the state m can be formally written jointly with thermal balance equations for the electron and gas temperatures T_e and T_g:

$$\frac{d[\mathrm{Y}(m)]}{dt} = F_{\mathrm{Y}(m)}(\mathrm{Y}(m),\, T_e,\, T_g,\, I,\, r,\, t), \quad m = 1, 2, \ldots, m_1;$$

$$\frac{dT_{e,g}}{dt} = F_{e,g}(\mathrm{Y}(m),\, T_e,\, T_g,\, I,\, \vec{r},\, t).$$

Here, Y takes the values of all the chemical elements included in the model (e.g., Y = Ar, Ar_2^+, F_2, F, F^- and so on); m takes the values of all the electronic states of atoms and molecules included in the model (e.g., $m = 3s_j$ for an excited neon atom), and F are nonlinear functions or functionals whose specific form is determined by plasma-chemical reactions included in the model. The quantity F usually explicitly depends on the coordinate $\mathbf{r}$ and time t usually in those cases when the pump is nonuniform and nonstationary.

Such a formulation of the kinetic problem involves some simplifications oriented at the analysis of afterglow or pumping with a hard ionizer. In the case of discharge pumping, kinetic equations for the electron distribution function and equations for the electric circuit characterizing the power-supply source should be analyzed.

A zero-dimensional approximation is often employed for the consideration of the lasing properties of an active medium. In this approximation, the equation for the intensity averaged over the volume,

$$\frac{1}{c}\frac{dI}{dt} = (\kappa - \kappa^- - \gamma)I + \frac{Q}{4\pi}$$

is included in the set of kinetic equations. Here, I is the radiation intensity, c is the speed of light, κ and κ^- are the gain and the absorption coefficients of the medium, Q is the term that describes the contribution of spontaneous emission to the build-up of lasing, and the factor γ describes laser radiation coupled out of the cavity (the inverse lifetime of a photon in the cavity) in the zero-dimensional approximation of the radiation transfer equation,

$$\gamma = \frac{c}{2l}\ln\frac{1}{R_1 R_2}$$

where l is the length of the excited area and R_1 and R_2 are the reflection coefficients of cavity mirrors.

Performing a numerical simulation of the kinetics of active media, one has to take into account that characteristic times of different relaxation processes may differ by several orders of magnitude. Such sets of differential equations are called rigid sets in mathematics. Special methods based on implicit difference schemes have been developed for the solution of such equations. The Geer method is the most popular among them.

A PLASER software package has been developed at General Physics Institute, Russian Academy of Sciences, under the supervision of Yakovlenko for the convenience of modeling of laser active media [66,70]. This package uses the initial list of reagents and characteristics of elementary events to generate balance equations for the components of the active medium and equations of thermal balance for electrons and heavy particles, or equation for electron distribution function. A zero-dimensional approximation is employed to model emission of laser radiation. Methods of solution of three-dimensional problems can be applied to model the divergence of laser radiation [66,91,92]. This software package was used to model a large number of active media using atomic, molecular, and ionic transitions.

As a large set of physical parameters, such as the pump pulse duration, the power of energy deposition, and so on is fixed for each system, it is much easier to describe the experimental data with the use of an appropriate model in this case. However, when this model is employed to describe the results of other experiments, considerable discrepancies between the results of calculations and experimental data may arise. A model is especially useful when it can describe a broad class of experiments. Models of XeCl [93,94], ArF [88], and XeF [95] are examples of such forms.

The overwhelming majority of models are based on these mechanisms of laser operation. Although we believe that we understand, in general, the kinetics of active media employed in exciplex lasers, some difficulties arise in certain cases when new experimental information has to be interpreted. Different authors propose different ways of solving this problem. The difference in these approaches often gives rise to differences in the existing models. Problems of modeling are described in References [66,70].

8.3.3 Specific Features of the Kinetics of Exciplex Lasers

The design and creation of high-power laser systems would be impossible (especially in the case of KrF lasers) without a method of predicting radiative characteristics of these lasers as functions of different parameters with allowance for various factors influencing the lasing process. Such a prediction can be based on numerical simulations. The studies of kinetic processes in active media of lasers have started immediately after the detection of lasing. These studies resulted in the development of, first, elementary and then more and more sophisticated models.

Because of the results of a comprehensive theoretical analysis, the up-to-date modifications of such models include hundreds of plasma-chemical reactions. Next, we will consider the main reactions determining the operation of exciplex lasers. The main reactions are not several in number. Our experience shows that the modeling of lasers cannot be reduced to the inclusion of the main reactions. If we limit the ranges of parameters (e.g., the pump pulse duration, the pump power, and so on) where modeling is performed, then the kinetic model can be considerably simplified. However, predictions of such simplified models are often inconsistent with the results of observations made for other parameters or experimental conditions.

The highest lasing efficiencies were achieved with laser active media pumped by a hard ionizer. A powerful channel of population of excited exciplex molecules involving three-body reactions of ion–ion recombination of positively charged rare-gas ions with negatively charged halogen atomic ions can be efficiently employed in this regime. In the case when a hard ionizer is used for pumping, positive ions are produced when a particle beam passes through a medium. In the regime of discharge pumping, a medium is excited through reactions of step excitation of rare-gas atoms by electrons with subsequent generation of rare-gas positive ions through the ionization of these excited states by electrons. As a result, the efficiency of generation of rare-gas positive ions in the case of discharge pumping is much lower than in the case when a hard ionizer is employed for pumping. In the latter case, not less than 20%–30% of the pump flux can be usually used for the formation of working states of exciplex molecules.

8.3.3.1 A KrF Laser (248 nm)

Lasing in a KrF laser was obtained for the first time in References [38–41] for the case of electron-beam pumping and in References [46–50] for the regime of discharge pumping. The highest energies of laser radiation and the highest lasing efficiencies were experimentally achieved for a KrF laser. The specific output energy was as high as 64 J L^{-1} in the regime of electron-beam pumping [96] and 40 J L^{-1} in the case of proton-beam pumping [97,98]. The efficiency for this laser may reach 9%–10% [97–102]. Because of its high output energy, a KrF laser with electron-beam pumping soon became the main candidate for the role of a driver in laser-fusion problems [85,103–113]. Successful experiments on the interaction of laser radiation with plasma [114,115] stimulated further studies in this direction, which resulted in the creation of high-power laser systems (Table 8.6).

TABLE 8.6
Energy Parameters of Existing KrF and KrF Lasers Designed for Controlled Nuclear Fusion

Laser System	In Operation Since	Radiation Energy, kJ	Radiation Power, W
Rapier (Linl)	1982	0.8	10^{10}
SPRITE (Rutherford)	1983	0.2	$3 \cdot 10^9$
Euro-Laser (Rutherford)	1996	100	Variable
AURORA (Los Alamos)	1985	10	$2 \cdot 10^{10}$
	1988	1	$2 \cdot 10^{11}$
	1989	4	10^{12}
Nike (NRL)	1989	0.01	—
	1993	2	—
Rapier B (Un. of Alberta)	1988	0.01	—
		1	—
Ashura	1988	0.5	$2 \cdot 10^9$
(Electro-Technical Lab., Japan)		1	$2 \cdot 10^{11}$
Harpoon (Russia)	1991	0.06	$2 \cdot 10^9$

Source: From Boichenko, A.M., Tarasenko, V.F., and Yakovlenko, S.I., *Laser Phys.*, 10(6), 1159–1187, 2000.

As mentioned in Section 8.1, ternary mixtures are the first choice as active media. In the case of KrF lasers, Ar–Kr–F_2, Ne–Kr–F_2, and He–Kr–F_2 mixtures are usually employed. A Kr–F_2 binary mixture is also used in certain cases.

8.3.3.1.1 Kinetics of a KrF Laser

Let us consider the main reactions determining the operation of exciplex KrF lasers. The papers [64–66,96–98,100–103,116–142], devoted to the theoretical analysis of a KrF laser, may serve to illustrate the development of models of this laser.

A pump source produces ions and excited states of Ar^+, Kr^+, Ar*, and Kr*. As the ionization potential of krypton is lower than the ionization potential of argon, relaxation processes result in the efficient accumulation of Kr^+ and Kr_2^+ ions. Ar_2^+ ions are transformed into molecular Ar^+ ions through conversion reactions:

$$Ar^+ + 2Ar \rightarrow Ar_2^+ + Ar, \quad k = 2.5 \cdot 10^{-31} \text{ cm}^6/\text{s}.$$

Then, molecular argon ions are recharged through reactions involving krypton atoms,

$$Ar_2^+ + Kr \rightarrow Kr^+ + 2Ar, \quad k = 7.5 \cdot 10^{-10} \text{ cm}^3/\text{s}.$$

The attachment of electrons to F_2 molecules, in its turn, results in the accumulation of F^- ions in the active medium:

$$F_2 + e \rightarrow F^- + F.$$

The rate of this reaction varies from 10^{-8} to 10^{-9} $\text{cm}^3\ \text{s}^{-1}$ within the range of electron temperatures of 0–5 eV.

NF_3 molecules can be also employed as fluorine donors for lasing in XeF lasers (see Section 8.3.3.4). In contrast to F_2, NF_3 molecules do not absorb radiation emitted by KrF^*.

However, the highest lasing efficiencies were achieved in mixtures with F_2, rather than in mixtures with NF_3. This is because of the fact that NF_3 molecules can be efficiently recharged in reactions involving Kr^+ ions, resulting in the formation of NF_3^+ ions [65].

Radiation-emitting states of KrF* are populated through three-body reactions of ion–ion recombination,

$$Kr^+ + F^- + M \rightarrow KrF^* + M,$$

where M = Ar, Kr. The rates of reactions

$$R^+ + X^- + M \rightarrow RX^* + M,$$

where M is a rare-gas atom, depending on the gas pressure and temperature [65,143–145] and can be estimated in their order of magnitude as $(1–2) \cdot 10^{-6}$ cm^3 s^{-1} if normalization is made for effective two-body reactions

$$R^+ + X^- \rightarrow RX^*$$

at the pressure of the medium $p \sim 1–5$ atm. Ion–ion recombination of Kr_2^+ and $ArKr^+$ ions with F^- also results in the formation of KrF* molecules [144,146–148],

$$Kr_2^+ + F^- + M \rightarrow KrF^* + Kr + M$$

$$ArKr^+ + F^- + M \rightarrow KrF^* + Ar + M$$

with approximately the same reaction rates. Positively charged molecular ions are produced as a result of conversion reactions

$$Kr^+ + Kr + M \rightarrow Kr_2^+ + M, \quad k \sim 10^{-31} \text{ cm}^6/\text{s},$$

$$Kr^+ + Ar + M \rightarrow ArKr^+ + M, \quad k \sim 10^{-31} \text{ cm}^6/\text{s},$$

where M = Kr, Ar. In the case of He–Kr–F_2 and Ne–Kr–F_2 mixtures, Kr^+ ions are produced through Penning reactions

$$He^*(Ne^*) + Kr \rightarrow Kr^+ + He(Ne), \; k \sim 10^{-10} \text{ cm}^3/\text{s}.$$

Reactions of ion–ion recombination provide a dominant contribution to the population of KrF* molecules in the case when a hard ionizer is used for pumping [66,96–98,149, 150,151].

KrF^* molecules are also produced through harpoon-type reactions:

$$Kr^* + F_2 \rightarrow KrF^* + F, \quad k = 8.1 \cdot 10^{-10} \text{ cm}^3/\text{s},$$

$$Kr_2^* + F2 \rightarrow KrF^* + Kr + F, \quad k = 3 \cdot 10^{-10} \text{ cm}^3/\text{s},$$

$$Kr_2^* + F \rightarrow KrF^* + Kr, \quad k = 3 \cdot 10^{-10} \text{ cm}^3/\text{s},$$

In the case when a hard ionizer is used for pumping, reactions of dissociative recombination

$$Kr_2^+ + e \rightarrow Kr^* + Kr, \quad k \sim 10^{-7}\ cm^3/s$$

may also give rise to Kr* states along with direct excitation of these species by beam particles.

In the regime of discharge pumping, excited states of krypton may also arise through the reactions of direct excitation of krypton atoms by discharge electrons,

$$Kr + e \rightarrow Kr^* + e.$$

Molecular excited states of Kr_2^* are produced from Kr* states through association reactions

$$Kr^* + Kr + M \rightarrow Kr_2^* + M, \quad k \sim 10^{-31}\ cm^6/s,$$

M = Kr, Ar. In the case of discharge pumping, harpoon reactions and ion–ion recombination reactions may provide comparable contributions [64,149].

KrF^* molecules can also be populated through substitution reactions,

$$ArF^* + Kr \rightarrow KrF^* + Ar, \quad k = 3 \cdot 10^{-10}\ cm^3/s,$$

where ArF^* molecules emerge from reactions of ion–ion recombination of Ar^+ and Ar_2 with F^- and harpoon reactions of excited states of argon with fluorine. Apparently, substitution reactions do not occur in reactions with He and Ne buffer gases. HeF molecules were not observed under these conditions, while NeF molecules rapidly decay through the predissociation reaction.

We have considered the main channels of the formation of the working lasing states (Figures 8.8). Each of the considered excited or ionized states may enter into numerous reactions, giving rise to various molecular or atomic neutral or ionized states. As a result, the number of reactions in a real simulation model is much larger than the small number of

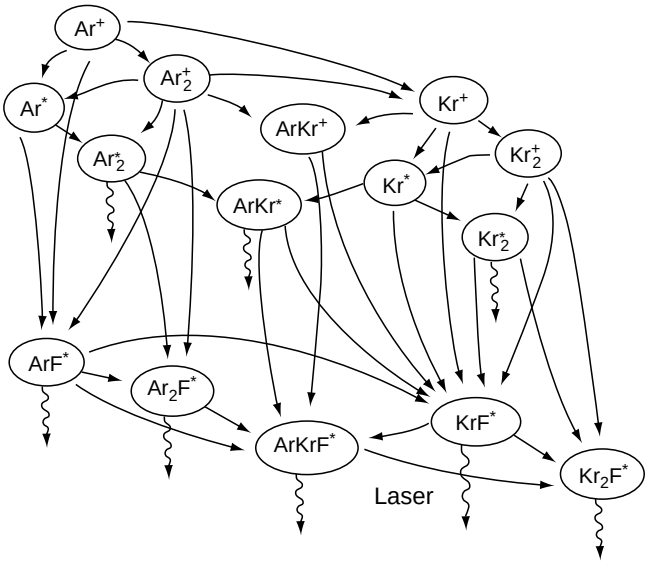

FIGURE 8.8 Diagram of relaxation channels in an Ar–Kr–F_2 plasma pumped by an electron beam. (From *Plazmennye Lazery Vidimogo i Blizhnego UF Diapazonov* (Visible and Near-UV Plasma Lasers) Tr. Inst. Obshch. Fiz. Akad. Nauka 21, 1989, Yakovlenko, S.I., Ed. [whole volume].)

reactions discussed here. In particular, one has to take into consideration reactions decreasing the population of KrF* states, including two-body quenching,

$$KrF^* + M \rightarrow Kr + F + M,$$

where M = e, Kr, Ar, F_2, and three-body quenching,

$$KrF^* + M_1 + M_2 \rightarrow Kr + F + M_1 + M_2,$$

where M_1, M_2 = Kr, Ar. In addition, KrF* states may also decay through a radiative process,

$$KrF^* \rightarrow Kr + F + h\nu \text{ (248 nm)}.$$

One has to also take into account absorption of radiation emitted by different components of the mixture. Especially strong absorption under optimal conditions of lasing arises because of F^- ions and F_2 molecules.

Reactions producing trimer exciplex states,

$$KrF^* + Kr + M \rightarrow Kr_2F^* + M, \quad k \sim 6 \cdot 10^{-31} \text{ cm}^6/\text{s},$$

where M = Kr, Ar, play an important role among reactions decreasing the populations of KrF* states. Lasing was observed for Kr_2F^* and Xe_2Cl^* molecules [152,153].

8.3.3.1.2 Wide-Aperture Systems

The work on the creation of wide-aperture exciplex lasers with radiation energy exceeding 1 kJ is done within the framework of the laser-fusion program and strategic defense initiative (SDI). Realization of both programs requires lasers not only ensuring high radiation powers and energies, but also producing a laser beam with a divergence close to the diffraction limit. In addition, these lasers should operate in the pulse-periodic regime. Currently, there are no lasers capable of solving the problems of controlled laser nuclear fusion and SDI, and the possibility of solving these problems by means of exciplex lasers has not been proved yet. Nevertheless, the work on laser nuclear fusion and SDI is in progress, and the creation of exciplex lasers with a radiation energy exceeding 1 kJ has been recently reported. As KrF molecules permit the highest radiation energies and lasing efficiencies to be achieved for exciplex lasers at comparatively short radiation wavelength of 248 nm, the main emphasis in the activity aimed at the creation of wide-aperture systems is placed on KrF lasers (see Table 8.6). The highest radiation energy of about 10 kJ in pulses with duration in the order of 500 ns has been achieved with an Aurora system in Los Alamos [109]. Reference [66] summarizes the results of calculations for the output characteristics of a KrF laser as functions of the pump power for the parameters of this system. The behavior of the laser emission efficiency around the threshold at $p = 1.75$ atm is shown in Figure 8.6. The creation of wide-aperture systems with a radiation energy exceeding 10 kJ is usually oriented at the generation of radiation with an energy density in the order of 10 J dm^{-3} with an efficiency of ~10%. The active volume of a laser in this case should not exceed 10^3 dm^3.

8.3.3.2 An XeCl Laser (308 nm)

Lasing for XeCl molecules was first observed in Reference [38]. The active medium was pumped by an electron beam in these experiments. A Cl_2 molecule was employed as a donor of chlorine in the first studies. It was found later that mixtures containing HCl ensure better

characteristics of laser radiation. Currently, HCl molecules are mainly used in laser mixtures. The use of CCl_4 molecules is much less frequent, while Cl_2 molecules are used only in very rare cases. In the case when a self-sustained discharge is used for pumping, sufficiently high energies of laser radiation can be achieved with BCl_3 and F_2Cl_2 halogen-containing molecules. Ar, Ne, and He are usually employed as buffer gases.

8.3.3.2.1 Kinetics of an XeCl Laser

The papers [154–183] may serve to illustrate the development of models of anXeCl laser. Next, we will discuss some specific features of the mechanisms behind the population of XeCl* states as compared with the mechanisms responsible for the population of KrF* states (Figure 8.9).

The generation of Xe^+ ions in XeCl lasers occurs through three-body recharging reactions,

$$Ar_2^+ + Xe + Ar \rightarrow Xe^+ + 3Ar, \quad k \sim 10^{-29}\ cm^6/s$$

rather than through two-body reactions.

The rate of the two-body recharging reaction

$$Ar_2^+ + Xe \rightarrow Xe^+ + 2Ar, \quad k = 7.2 \cdot 10^{-11}\ cm^3/s$$

is low, and it is difficult to explain the experimental data without invoking the three-body recharging reaction [66].

The lowest excited state of Xe* xenon, Xe(6*s*), cannot ensure the population of XeCl* through harpoon reactions with HCl molecules in the ground vibrational state. The population of XeCl* through harpoon reactions can now be described in the following way:

$$Xe^* + HCl\ (v > 0) \rightarrow XeCl^* + H,$$

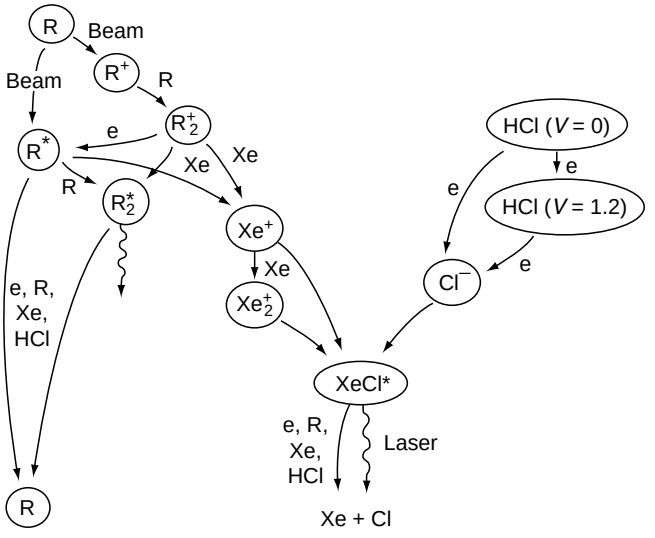

FIGURE 8.9 The main channels of relaxation in the active medium of an XeCl laser; R stands for an atom of a buffer gas (He, Ne, Ar). (From *Plazmennye Lazery Vidimogo i Blizhnego UF Diapazonov* (Visible and Near-UV Plasma Lasers) Tr. Inst. Obshch. Fiz. Akad. Nauka 21, 1989, Yakovlenko S.I., Ed. [whole volume]; Boichenko, A.M., Tarasenko, V.F., and Yakovlenko, S.I., *Laser Phys.*, 10(6), 1159–1187, 2000.)

$$k = (2.8-5.6)\cdot 10^{-10}\ \mathrm{cm^3/s},$$

$$\mathrm{Xe^{**}} + \mathrm{HCl}\ (v > 0) \rightarrow \mathrm{XeCl^*} + \mathrm{H},$$

Here, Xe^{**} stands for excited states of Xe atoms that lie higher than Xe* and v is the number of the vibrational level of a ground-state HCl molecule.

Dissociative attachment of electrons to an HCl molecule in the ground vibrational state with $v = 0$ is weak. The generation of Cl^- ions predominantly occurs through the attachment of electrons to vibrationally excited HCl molecules. Electrons first excite vibrational levels of the ground electronic state of an HCl molecule [184–187]:

$$\mathrm{HCl}\ (v = 0) + \mathrm{e} \rightarrow \mathrm{HCl}\ (v = 1, 2) + \mathrm{e},$$

$$\mathrm{HCl}\ (v = 1, 2) + \mathrm{e} \rightarrow \mathrm{Cl^-} + \mathrm{H},$$

The cross sections of attachment of electrons to HCl ($v = 1$) and HCl ($v = 2$) molecules are approximately 38 and 880 times greater than in the case of an HC1 ($v = 0$) molecule [188–190]. Then, the attachment cross sections display saturation. Thus, a model adequately describing the accumulation of negative Cl^- ions should include at least three vibrational levels of the ground electronic state of HCl molecules ($v = 0, 1, 2$). Some models include up to six vibrational levels.

These low lasing abilities of mixtures containing Cl_2 molecules are not only because of the fact that these molecules absorb the working emission. Apparently, even more serious problems arise because of the fact that, within the range of energies corresponding to the mean electron temperatures in active media (~1 eV), the cross section of attachment of electrons to a Cl_2 molecule is very small (it is much less than the electron attachment cross section for an F_2 molecule, which is employed as a halogen-containing molecule for a KrF laser). Theoretical analysis of an Ar–Xe–CCl_4 mixture [174] has shown that the efficiency of this mixture is not less than the efficiencies of mixtures containing HCl.

Many models do not include the substitution reaction

$$\mathrm{ArCl^*} + \mathrm{Xe} \rightarrow \mathrm{XeCl^*} + \mathrm{Ar}.$$

Ion–ion recombination reactions provide the main channels leading to the population of XeCl molecules both in the case when a hard ionizer is employed for pumping and in the case of discharge pumping [66,155–158,164–166].

The depth of the lower X state of an XeCl molecule is very small (−0.025 eV). However, this circumstance has virtually no influence on the operation of an XeCl laser. Many kinetic models even describe this state as a repulsive term.

8.3.3.2.2 Lasing Characteristics

The efficiency of XeCl lasers is lower than the efficiency of KrF lasers. Investigations performed within the range of pump power densities up to several hundreds of kilowatts per cubic centimeter and pressures of several atmospheres have demonstrated that, apparently, the maximum efficiency of an XeCl laser should not exceed 5%. Thus, the efficiency of an XeCl laser is approximately two times less than the efficiency of an KrF laser.

Systematizing the data available on the mixtures employed in XeCl lasers, we arrive at the following conclusions:

1. HCl halogen-containing molecules are especially promising for practical applications. Dissociation of these molecules does not yield solid compounds, which may be

deposited on optical elements and the inner surface of the laser chamber. These molecules can be recovered in the process of laser operation, especially in the case when the standard mixture contains small amounts (~0.1%) of hydrogen.

2. Energy parameters of laser radiation produced with CCl_4 and HCl mixtures are approximately the same. A considerable advantage of CCl_4 is associated with its lower activity. However, mixtures containing HCl allow a volume discharge to be produced in a simpler way in systems pumped with a self-sustained discharge and in the case of hybrid pumping.
3. Helium, neon, argon, and krypton can be employed as buffer gases in working mixtures of XeCl lasers. Lasing was also implemented in binary Xe–CCl_4 mixtures. However, the best parameters of lasing were achieved for mixtures with argon and neon.

8.3.3.3 An ArF Laser (193 nm)

Lasing of an ArF system was first observed in Reference [41] in the case of electron-beam pumping and in Reference [52] in the case of discharge pumping. Usually, Ne–Ar–F_2 and He–Ar–F_2 mixtures are employed to generate laser radiation. An Ar–F_2 binary mixture can be also used in the case of electron-beam pumping.

The number of papers devoted to the modeling of an ArF laser is not so large as the number of studies devoted to the modeling of KrF and XeCl lasers [88,191–196]. This may be because of the fact that emission characteristics of these lasers and especially the lasing efficiency achieved in first experiments with ArF lasers were not as good as characteristics of other lasers. Therefore, the main emphasis in modeling was placed on lasers of other types. In addition, an ArF laser generates radiation within the VUV range, which gives rise to additional difficulties associated with the fabrication of optical elements and the detection of laser radiation. Finally, radiation produced by an ArF laser is strongly absorbed under normal atmospheric conditions. However, theoretical modeling [88,196] shows that, once if these problems are solved, an ArF laser with a high-pump power may ensure better radiation characteristics than a KrF laser. In particular, the efficiency of an ArF laser may be as high as 20%.

8.3.3.3.1 Specific Features of the Kinetics of an ArF Laser

The main channels leading to the population of the working state of ArF molecules are essentially the same as in the case of KrF, XeCl, and XeF lasers. A pump pulse generates atomic and molecular ions of argon and electrons. The attachment of electrons to F_2 molecules results in the formation of F^- ions, which, in their turn, produce ArF* molecules through the processes of three-body ion–ion recombination with Ar^+ and Ar_2^+ ions. These molecules can also be produced because of harpoon reactions. A schematic diagram of plasma-chemical reactions occurring in an Ne–Ar–F_2 mixture is presented in Figure 8.10. The main channels responsible for the population of upper laser levels both in the case when a hard ionizer is employed for pumping and in the case of discharge pumping are associated with ion–ion recombination [88]. In accordance with Reference [193], ion–ion recombination and the harpoon channel provide comparable contributions in the case of discharge pumping.

Note that the cross section of attachment of electrons to vibrationally excited F_2 molecules ($v \neq 0$) is larger than the cross section of attachment of electrons to a molecule in the ground vibrational state. The increase in the cross section in this case is not so large as in the case of an HCl molecule. The attachment rate calculated with a Maxwellian EEDF for levels with $v = 1$–5 is not more than five times higher than the cross section for $v = 0$ [197]. This circumstance is often ignored in theoretical analysis (among all the papers devoted to the modeling of an ArF laser, this factor was taken into consideration only in References [88,196]). Usually, modeling includes only the ground vibrational state of an F_2 molecule.

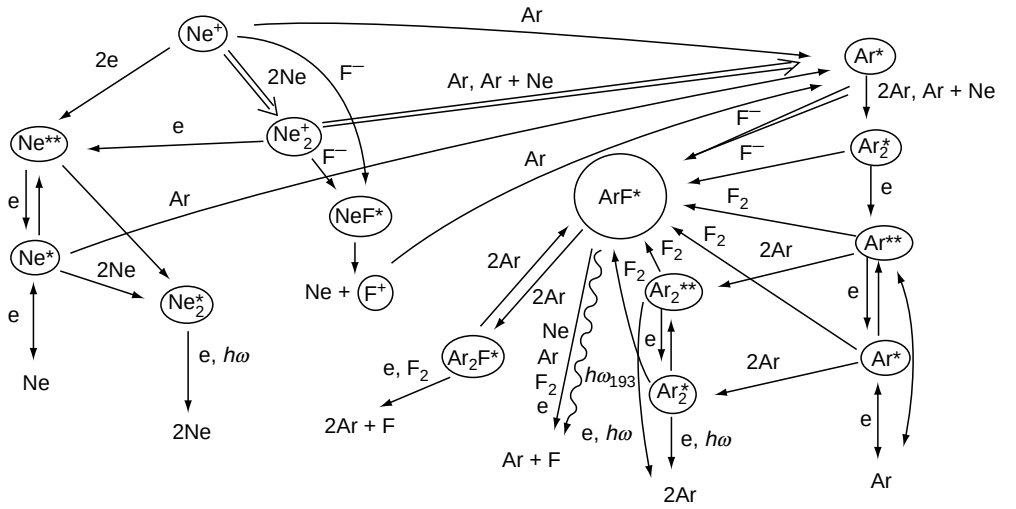

FIGURE 8.10 The main channels of relaxation in the active medium of an ArF laser. (From Boichenko, A.M., Derzhiev, V.I., and Yakovlenko, S.I., *Laser Phys.*, 2(3), 210–220, 1992.)

Another specific feature of the kinetics of the active medium in an ArF laser is associated with a small cross section of stimulated emission and a low spurious absorption. Lasing in this case occurs through $B \rightarrow X$ transitions, which has a cross section of stimulated emission equal to $3 \cdot 10^{-16}$ cm^2. This is the minimum value of this cross section for these (KrF, XeCl, ArF, and XeF) lasers. According to recent studies, the electronic C term lies lower than the B term. As a result, the population coming to the B level is equal to approximately one-third of the total population of the B and C terms, which is another factor limiting the gain. The lasing threshold under these conditions is sufficiently high (around 100 kW cm^{-2}, see Figure 8.6), and the lasing energy is highly sensitive to the presence of impurities in a mixture and losses in cavity windows and mirrors at moderate pump powers $W < 1$ MW/(cm^3 atm). On the other hand, virtually no absorption of radiation arises because of F_2 molecules and Ar_2^+ and Ne_2^+ molecular ions, which give rise to a strong absorption in KrF and XeCl lasers. Therefore, high specific characteristics of radiation emission can be achieved in the case under study with high-pump powers.

8.3.3.3.2 The Results of Modeling

Next, we discuss the properties of ArF lasers operating with various mixtures in different regimes of pumping. The threshold energy deposition (power of energy deposition) is one of the important laser parameters. This quantity is defined as the minimum value of energy deposition that allows the operation of a laser system. An ArF laser is characterized by a maximum threshold because of the specific features of its kinetics. This situation is illustrated by Figure 8.6, which compares the efficiency of an ArF laser in the near-threshold range as a function of the power of energy deposition with similar dependences for XeF, KrF, and XeCl lasers. These calculations were performed for a binary Ar–F_2 mixture with a total pressure of 0.5–1.5 atm and the half-maximum pump pulse duration of 80 ns. Note that, since the absorption of radiation emitted by the active medium is weak, the optimal efficiencies of an ArF laser in the near-threshold range are achieved when the reflection coefficients of cavity mirrors are higher than standard reflection coefficients (>60%), reaching $R \sim 90\%$.

The efficiency of an electron-beam-pumped ArF laser is higher than the efficiency of this laser in the case of discharge pumping. If an electron beam is used to pump this laser,

the highest efficiency is achieved with an $Ar–F_2$ mixture. We shall start our consideration of the properties of an ArF laser with the analysis of the regime of discharge pumping [70].

Theoretically, if there were no difficulties with discharge initiation in an $Ar–F_2$ mixture, this mixture would have been optimal for attaining high efficiencies of lasing in the case of discharge pumping also. However, because of several factors (e.g., discharge contraction), one has to employ mixtures with less heavy components ($He–Ar–F_2$ or $Ne–Ar–F_2$).

In the case of discharge pumping, a two-contour discharge circuit is often employed. An initial voltage $V_1 = U$ is applied to a capacitor C_1; whereupon the circuit is closed and the automatic preionization of the working mixture is switched on. A mixture containing neon as a buffer gas is more efficient than a mixture containing helium. Although the radiation energy grows with the increase in the initial voltage for $U \sim 40$ kV, the laser efficiency ceases to grow with a further increase in U. The optimal values of U for an $Ne–Ar–F_2$ mixture fall within the range of 35–40 kV. Here, one can observe some general features of discharge pumping, which is less efficient than beam pumping. For the values of U that are of particular interest for our analysis (that correspond to maximum efficiencies), the radiation energy grows virtually linearly as a function of U, although the initial energy coupled into the electric circuit is quadratic in U ($E = C_1 U^2/2$).

This effect is because of several factors, including the inefficient energy transfer from the master capacitor to the discharge mixture and a breakdown of the mixture. Each medium possesses some characteristic breakdown voltage, which is not very sensitive to the external conditions. When a voltage that is several times higher than the breakdown voltage is applied to a working mixture, a considerable increase in the radiation energy and efficiency cannot be achieved. A breakdown results in a fast generation of electrons, which leads to the formation of radiation-emitting molecules. Lasing builds up with a high rate under these conditions, and a laser pulse is emitted. After this stage, the residual potential difference is spent inefficiently. Because of the fast decrease in the current in the circuit after the emission of a laser pulse, the energy coupled into the gas medium ($E_g = \int U_D I_2 \, dt$) becomes lower. The ratios of the breakdown voltages to the initial voltage, U_{br}/U decrease virtually linearly with the increase in U. The efficiency of energy deposition in the medium, $\eta_{in} = E_L/E_g$ also decreases virtually linearly with the increase in U for an $Ne–Ar–F_2$ mixture, reaching its maximum around $U \sim 40$ kV for an $He–Ar–F_2$ mixture. Thus, because of the lower efficiency of energy deposition in the active mixture, the efficiency of lasers with discharge pumping is lower than the efficiency of lasers pumped by an electron beam. In accordance with the results of the calculations, the efficiency in the case of discharge pumping corresponds to approximately 4% of the energy deposited in the medium.

In the case when an electron beam is employed for pumping, the efficiency of energy deposition in the medium increases, improving energy parameters of a laser. The efficiency achieved in the first experiments with an ArF laser pumped by an electron beam ($W \sim 0.5$ MW cm^{-3}) was equal to 3%–4%. Experiments were performed with systems similar to those employed for the investigation of other (KrF, XeCl, and XeF) lasers. A gas mixture was prepared in a separate cell, which was then placed between cavity mirrors. Special care should be taken when such a procedure is used, as the output laser characteristics are highly sensitive to absorption for such levels of energy deposition. Experiments [198] provide an instructive example illustrating this statement. Mirrors in these experiments were inserted into the cell with a mixture, which allowed an efficiency of 7.7% to be achieved. The calculated efficiencies corresponded to 10%. However, the efficiencies attainable with an $Ne–Ar–F_2$ mixture are lower than the efficiencies that can be achieved with an $Ar–F_2$ mixture. In addition, neon-containing mixtures are characterized by a threshold in pressure (1–2 atm). Lasing is strongly suppressed below this threshold.

TABLE 8.7
The Results of Optimization Simulations for E-Beam Pumped Ar–F_2 Mixture. Half-Height Pumping Duration Is 65 ns

	Laser Energy, J/L	Efficiency, %	[Ar], cm^{-3}	[F_2], cm^{-3}	Deposition Power MW/cm^3
Optimum on laser energy	95.3	12.5	$11.5 \cdot 10^{19}$	$5 \cdot 10^{17}$	12
Optimum on laser efficiency	34.9	22.9	$2.3 \cdot 10^{19}$	$7.5 \cdot 10^{16}$	2.4

Source: From Boichenko, A.M., Derzhiev, V.I., and Yakovlenko, S.I., *Laser Phys.*, 2(3), 210–220, 1992.

The highest efficiency can be achieved with an Ar–F_2 mixture pumped by an electron beam. As the absorption of light in an Ar–F_2 medium is weak, sufficiently high efficiencies exceeding the maximum efficiency of KrF lasers can be achieved starting with the pump power $W \sim 1$ MW cm^{-3} at the mixture pressure $P = 1$ atm. In any case, it is clear already at this point that ArF lasers are competitive in their properties with KrF lasers.

The output characteristics of an Ar–F_2 mixture were experimentally studied in the amplification regime for $W \sim 1$ MW cm^{-3} [199]. With such a pump, the influence of absorption in a medium is not very strong. Several theoretical calculations [88,194,196] corresponding to different absorption coefficients in the medium (the real absorption corresponds to $\kappa^- = 3 \cdot 10^{-3}$ cm^{-1}) illustrate this tendency. When the pump power is increased up to $W \sim 2$ MW cm^{-3}, the output parameters of the system become even less sensitive to the absorption.

According to the results of the calculations, these levels of the pump power ($W > 2$ MW cm^{-3}) allow the maximum efficiencies to be achieved. The results of optimization performed for an ArF laser show that efficiencies as high as 20% in the energy deposited in the medium can be achieved in this case (see Table 8.7).

8.3.3.4 An XeF Laser (351, 353 nm)

Lasing in an XeF laser was first observed in References [34,36,42,43] with electron-beam pumping and in References [109–112] with discharge pumping. Lasing through *C–A* transitions (490 nm) has also been observed in addition to lasing through *B–X* transitions [200–203]. Ternary mixtures with xenon are usually employed for radiation generation; in this case, Ar, Ne, and He are usually employed as buffer gases, and F_2 or NF_3 molecules serve as halogen-containing components.

Studies [204–216] are devoted to the development and analysis of models of XeF (*B–X*). Kinetic models describing lasing through *B–X* and *C–A* transitions have much in common. The lower *X* state of XeF molecules has the largest depth among the *X* states of exciplex molecules. This circumstance determines the specific features of lasers using *B–X* transitions, which are mainly manifested in temperature dependences of lasing parameters (see the discussion that follows). The overwhelming majority of these studies ignore these specific features (e.g., *B–X* transitions are effectively considered as bound-repulsive transitions). Therefore, the difference between the models of lasers using *B–X* and *C–A* transitions is reduced in this case to the use of different cross sections of stimulated emission and different sets of absorption cross sections at different radiation wavelengths. However, with such an approach, one loses the features characteristic of *B–X* laser transitions. These key features of the relevant temperature dependences were quantitatively described in paper [214] (see also References [215,216]), where a nonstationary kinetic model including the emission of an XeF

laser at two wavelengths (351 and 353 nm) was developed. This model takes into account the influence of the finite depth of the well corresponding to the X state and the gas temperature on the kinetics of this laser and allows the temperature dependences of the main characteristics of the laser, including its energy, efficiency, the moment when the lasing frequency is switched from 353 to 351 nm, and so on, to be adequately described. The results of simulations performed with this model were compared in Reference [214] with extensive data of experiments where a hard ionizer was used for pumping. In what follows, we will employ the results of this paper in our analysis.

8.3.3.4.1 Specific Features of the Kinetics of an XeF Laser

The main reactions determining the operation of an XeF laser are similar to the reactions considered earlier.

XeF molecules are produced through reactions of ion–ion recombination,

$$\mathrm{Xe^+ + F^- + M \rightarrow XeF^* + M},$$

$$\mathrm{Xe_2^+ + F^- + M \rightarrow XeF^* + Xe + M},$$

$$\mathrm{RXe^+ + F^- + M \rightarrow XeF^* + R + M},$$

and harpoon reactions

$$\mathrm{Xe^* + F_2(NF}_i\mathrm{) \rightarrow XeF^* + F(}NF_{i-1}\mathrm{)}, \quad i = 1\text{–}3$$

$$\mathrm{Xe_2^* + F_2(NF}_i\mathrm{) \rightarrow XeF^* + }F\mathrm{(NF}_{i-1}\mathrm{)}, \quad i = 1\text{–}3$$

$$\mathrm{Xe_2^* + F \rightarrow XeF^* + Xe}.$$

In the case when NF_i molecules are used, negative F^- ions are produced through the attachment of electrons,

$$\mathrm{NF}_i + \mathrm{e} \rightarrow \mathrm{F^-} + \mathrm{NF}_{i-1}, \quad i = 1\text{–}3.$$

The cross section and the rate of this reaction calculated with a Maxwellian EEDF are presented in Reference [65]. Xe^+ ions are generated through the reactions:

$$\mathrm{He^*(Ne^*) + Xe \rightarrow Xe^+ + He(Ne) + e},$$

$$\mathrm{Ar_2^+(Ne_2^+) + Xe^+Ar(Xe) \rightarrow Xe^+ + 2Ar(Ne) + Ar(Xe)}.$$

When a hard ionizer is used for pumping, ion–ion recombination reactions provide a dominant contribution to the formation of working exciplex molecules [214]. In the case of discharge pumping, harpoon reactions may give a comparable contribution [65].

The specific features of an XeF laser are associated with the fact that lasing in this system occurs not only through $B \rightarrow X$ transitions (see Figure 8.5), but also through $C \rightarrow A$ transitions. In addition, the lower working level X is a bound state with a maximum depth of the well (~0.15 eV) among the X states of analogous rare-halide molecules. The presence of a sufficiently deep bound state gives rise to additional problems associated with the necessity of efficient depopulation of this state. Because of this circumstance, the efficiency of lasers of this type is not very high, and their lasing characteristics are highly sensitive to temperature.

8.3.3.4.2 Lasing Characteristics

The efficiency of an XeF laser is not very high (~3%). However, this laser attracts a considerable interest as it has the lowest pump threshold among the available exciplex lasers. In this context, the possibility of implementing a nuclear pumping of such a laser is under discussion now. However, a detailed computer simulation should be performed before nuclear-pumping experiments. Model experiments with microsecond electron beams are also desirable.

Radiation is emitted through $B \rightarrow X$ transitions at two wavelengths, 351 and 353 nm (Figure 8.5e). These wavelengths mainly correspond to ($0 \rightarrow 2$ and $1 \rightarrow 4$) and ($0 \rightarrow 3$) transitions (where the first number is the number of a vibrational level in the B state, while the second number is the number of a vibrational level in the X state). This temperature dependence of lasing characteristics is mainly determined by the influence of the temperature on the populations of vibrational levels in the upper and lower working states. The assumption that the populations of vibrational levels are characterized by the Boltzmann distribution at each moment of time allows temperature dependences of lasing parameters of the system to be described in an adequate way. The moments when lasing is switched from one wavelength to another are also satisfactorily described within the framework of this model. Note that the behavior of lasing as a function of temperature predicted by the considered model is more abrupt than the experimental dependence. When the gains were determined at the wavelengths specified here, the total populations of the B and X states were multiplied by a Boltzmann factor of the vibrational level involved in the amplification or absorption of radiation.

According to the results of the calculations, an XeF laser should have the lowest lasing threshold among all the rare-halide lasers. Because of this property, XeF lasers seem to offer much promise for implementing lasing with nuclear pumping, when the energy of fragments of nuclear reactions is directly coupled into a laser active medium without any intermediate conversion stages. A global optimization of laser parameters with respect to the initial contents of mixture components and cavity parameters at a mixture pressure of 1 atm and pump pulse durations up to 1 ms (these parameters are characteristic of the available nuclear-reactor systems and nuclear-reactor systems that are designed) was performed to determine the lasing threshold for the considered laser [215]. Such large durations of pump pulses are sufficient to substantially heat the gas. Therefore, the use of a kinetic model allowing the influence of the gas temperature to be included is of fundamental importance in this case. The threshold calculated with this approach is 400–500 W cm^{-3}. The results of the calculations for the emitted energy around the threshold for a pump pulse duration equal to 0.1 ms are presented in Figure 8.6.

If we consider pumping with a running ionization wave from a nuclear explosion, then both the experimental results and the results of calculations performed in Reference [216] allow us to conclude that radiation with a power of several hundreds of gigawatts can be emitted under these conditions.

8.3.3.5 Other Types of Exciplex Lasers Using Halides of Rare Gases

Let us briefly consider the specific features of lasing for other exciplex molecules.

8.3.3.5.1 A KrCl Laser (222 nm)

Lasing of a KrCl laser was observed for the first time in Reference [45] in the regime of electron-beam pumping. Pump power densities required to implement lasing in this system are higher than the pump power densities required for radiation generation in the case of other exciplex lasers using halides of rare gases. It is apparently because of this circumstance

that not so much attention has been focused on a KrCl laser. In particular, no studies on KrCl lasers with hybrid pumping have ever been reported. In the regime of pumping with a self-sustained discharge with high densities of energy deposition (~2 MW cm^{-3}) and a high uniformity degree of pump radiation, the radiation energy and the efficiency of lasers of this type are only two times lower than in the case of an XeCl laser. Similar to an XeCl laser, HCl molecules serve as a halogen-containing component in a KrCl laser, which ensures a rather large service lifetime of the working mixture. The main channel leading to the formation of KrCl molecules is associated with ion–ion recombination.

*8.3.3.5.2 An XeBr Laser (*282 nm)

Lasing of XeBr* molecules was observed in one of the first experiments devoted to exciplex lasers using halides of rare gases [37]. However, the energy parameters of laser radiation in this system were rather low. An appropriate choice of the halogen-containing component has allowed the efficiency and the energy of lasing to be substantially increased in subsequent experiments performed with both electron-beam and self-sustained-discharge pumping. In contrast to other exciplex lasers, the radiation energy of a XeBr laser considerably depends on the density of deposited energy. A radiation energy density of -1.5 $mJcm^{-3}$ with an efficiency of -1.5% was achieved at 282 nm. The main channel leading to the formation of XeBr* molecules is associated with the harpoon reaction.

*8.3.3.5.3 XeJ (*253 *nm), KrBr (*206.5 nm), and ArCl (175 *nm) Lasers*

XeJ, KrBr, and ArCl lasers are not very actively studied at the moment. It is also known that lasing can be implemented with ArCl [217], KrBr [218], and XeJ [219] molecules. For all these molecules, lasing was obtained only in the case when self-sustained discharge was used for pumping.

*An NeF Laser (*108 *nm)*. Emission through $B \rightarrow X$ transitions of NeF was predicted in Reference [220] and was observed in Reference [221] under conditions when an Ne–F_2 mixture was pumped by an electron beam. It is difficult to implement an NeF laser as the upper working B state crosses a Rydberg 4π state. The crossing point of the working and decay terms lies relatively far from the bottom of the well ($R_{cr} = 2.6$ Å, $R_{eq} = 1.93$ Å, and the difference between the energy corresponding to the bottom of the well and the energy of the crossing point is $\Delta E = 1.1$ eV). Therefore, several vibrational levels of the upper state are not subject to predissociation, and deactivation to these levels may be accompanied by subsequent radiation emission. However, the rate of NeF predissociation is rather high ($2 \cdot 10^9$ s^{-1}) [222], considerably exceeding the rate of radiative decay ($4.2 \cdot 10^8$ s^{-1}). As a result, a high specific pump power is required, which does not exclude the possibility of implementing the lasing effect, though [66]. Lasing may occur for ionization rates $\nu = 10^4$–10^5 s^{-1}, which corresponds to a deposited energy $E = 0.5$–5 kJ L^{-1}. The efficiency with respect to the deposited energy may reach 7%–15% under these conditions.

8.3.3.5.4 Lasing of Xe_2Cl and Kr_2F* Molecules*

An interest in studying complex molecules of halides of rare gases (R_2X^* and $RR'X^*$) is associated with the possibility of creating lasers emitting radiation within a broad spectral range. The first attempts of achieving a gain for molecules of this type were unsuccessful. In particular, absorption rather than gain was observed in the studies performed at a wavelength of 441.6 nm within the emission band of Kr_2F^* and ArXeF* molecules. Until now, lasing has been implemented with Xe_2Cl^* and Kr_2F^* molecules [152,153]. For the first time, lasing was obtained with Xe_2Cl^* molecules (520 nm) in the case when the conditions of pumping and the composition of the working mixture were optimized. An electron beam employed for pumping in these experiments had a duration of about 10 ns and a current density in the order of 0.8 kA cm^{-2}. Absorption was observed in an Ar–Xe–CCl_4 mixture during the action of an

electron beam, and a gain of ~6% per single pass was detected in the afterglow. When CCl_4 was replaced by HCl, no gain was observed, and the intensity of spontaneous emission of Xe_2Cl molecules was lower. The lasing line reached its maximum at 518 nm. Its spectral half-width was ~30 nm, and the peak emission power was 2 kW. Lasing in an Ar–Kr–NF_3 mixture was observed within the range from 380 to 480 nm. The maximum emission power in this case was 5 kW.

The results of studies devoted to the lasing of complex molecules of halides of rare gases indicate a low efficiency of such lasers, a high lasing threshold, and high working pressures. At the same time, lasers using RX* molecules allow the highest emission power and the highest lasing efficiency to be achieved in the UV spectral range.

8.4 PULSE REPETITION DISCHARGE EXCIPLEX LASERS

In electrodischarge exciplex lasers there are no such negative factors, as heating of a foil, pinch effect of a beam, or necessity of biological protection. The basic difficulties in creation of pulse repetition lasers are connected to creation of the uniform volumetric discharge. The experience of creation of the volumetric discharge in big (~10 L) volumes at pressure 1–10 atm for CO_2-lasers was used in the construction of exciplex lasers.

Uniformity of a current between extended electrodes is characterized by conditions of preionization, a mode of input of energy in the discharge, geometry of active volume and type of electrodes (metal, plasma). Additional complexities arise at creation of lasers with the high average power (~1 kW) and high repetition frequency of pulses. Difficulties of the uniform volumetric discharge creation are connected to acoustic fluctuations of the gas density that have a place at the beginning of the next discharge pulse.

8.4.1 KrF, ArF Lasers

For ArF, KrF lasers the highest efficiencies were achieved at cross section of the discharge 25 mm × 8 mm at its length of 750 mm. The pulse energy of lasing on KrF* was 500 mJ at lasing efficiency $\eta = 3.9\%$ in the pulse-periodic laser with such a cross section of the discharge and for lasing on ArF* it was 270 mJ and $\eta = 2.1\%$ [223].

For the first time high average power (210 Вт) in KrF laser with energy in a pulse 0.21 J at pulse frequency $f \approx 1$ kHz is obtained in Reference [224]. Detailed research of the KrF laser at high pulse frequencies $f = 800$ Hz was carried out in Reference [225] where average radiation power up to 300 W was realized. At present, the highest average power for the given types of KrF lasers, that is, 620 W was obtained in Reference [226] at an efficiency of ≈2.6% and energy in pulse ≈1 J. Record at the present average power of generation on ArF* obtained on the same laser is 300 W.

The most powerful commercial KrF, ArF lasers are produced now by corporation Lambda Physik AG. Average stabilized powers of KrF laser is 200 W and of ArF laser is 100 W at pulse frequency 300 Hz. The laser chamber includes only metal and ceramic details and so the guaranteed resource of the laser work for one gas mixture volume is very high —20–30 million pulses. These lasers also are characterized by good stability of lasing energy from pulse to pulse (<1.5%) and high reliability in a long-term operating mode.

8.4.2 XeCl Lasers

For the first time generation of XeCl molecules during excitation of the active medium by the independent discharge obtained in 1976 [227]. In 1984, XeCl laser with average power of 400W was created [228], and in 1990 with average power of 750 W [229].

The mode of lasing during many hours with constant average radiation power is necessary for technological applications [87]. Practically, the unique powerful comercial laser now is XeCl laser, which is released by Lambda Physik AG (Lambda STEEL 1000). This laser is capable of generating energy of radiation 1 J with pulse frequency 300 Hz, that is, 300 W average power without falling energy of generation and without change of a gas mixture during 30–50 million pulses. Maintenance of average power 300 W during many hours is provided with injection of small amounts of HCl and automatic increase of charge voltage.

The prototype of the following generation of commercial XeCl laser with an average power of 500 W for industrial applications is developed [223,228]. The compact high-aperture discharge system with UV preionization by radiation of the sliding discharge is applied for laser excitation. Compact gas-dynamic contour has allowed creating a gas stream with speed $\approx$30 m/s and uniform within 10% distribution of flux speed in all longitudinal sections of the discharge. It has enabled to provide the maximal pulse frequency of $\approx$300 Hz and stabilized average power of $\approx$500 W. The level of average power of 500 W was supported for 16 h without change of gas mixture. High stability of energy of generation from pulse to pulse ($\approx$1%) is achieved [228].

The review of development of key component and technologies for a high repetition rate and high-power excimer laser can be found in Reference [87].

8.5 CONCLUSION

The main advantages of exciplex lasers over solid-state and liquid lasers are manifested in problems requiring laser radiation with a high mean power or a high pulse energy, as well as radiation of UV and VUV ranges. Exciplex lasers cannot compete with diode lasers in creation of small-scale systems with a moderate power. Industrial applications of high-power exciplex lasers are impeded by the lack of technological development.

Some objective difficulties of the industrial production of exciplex lasers are associated with the fact that the generation of a large amount of high-quality light energy requires the use of high-quality energy for pumping. In particular, an electron beam or special types of high-power discharges are used for this purpose.

High-power excimer lasers are complex devices. Industrial production of such lasers requires the solution of technological problems of ensuring the purity of initial gases, chemical inertness of construction elements coming in contact with the working mixture, the precision of fabrication and alignment of separate elements, and so on. Only some parts of these problems have been solved thus far, and much time may be necessary for the development of the existing components and creation of new elements.

Because of a large demand for industrial exciplex lasers in various areas of science and technology, we can expect a considerable progress in laser instrument making in advanced countries in the nearest years.

REFERENCES

1. Birks, J.B., *The Exciplex*, New York, San-Francisco; London: Academic Press, 1975, pp. 39–74.
2. Finkelburg, W., *Kontinierlichche Spectren*. Berlin: Verlag von J. Springer, 1938, p. 368.
3. Houtermans, F.G., Uber Maser Wirkung im optischen Spektralgebiet und die Moglichkeit absolut negativer Absorption fur einige Falle von Molekulspektren (Licht-Lawine), *Helv. Phys. Acta*, 33(8), 933–940, 1960.
4. Leonard, D.A., Keck, J.C., and Litvak, M.M., Population inversion between bound and repulsive molecular electronic states by two-temperature equilibrium, *Proc. IEEE.*, 51(12), 1785–1786, 1963.

5. Leonard, D.A., Keck, J.C., and Litvak, M.M., Population inversion between bound and repulsive molecular electronic states, *Bull. Am. Phys. Soc. Series II*., 8(7), 530–530, 1963.
6. Carbone, R.J. and Litvak, M.M., Intense mercury-vapor green-band emission, *J. Appl. Phys*., 39(5), 2413–2416, 1968.
7. Palmer, A.J., Stimulated emission of the H_2 continuum, *J. Appl. Phys*., 41(1), 438–439, 1970.
8. Heer, C.V., A broadband ultraviolet molecular hydrogen laser, *Phys. Lett. A*, 31, 160–161, 1970.
9. Basov, N.G., Balashov, E.M., Bogdankevich, O.V., Danilychev, V.A., Kashnikov, G.N., Lantzov, N.P., and Khodkevich, D.D., Luminescence of condensed Xe, Kr, Ar and their mixtures in vacuum region of spectrum under excitation by fast electrons, *J. Luminescence*, 1–2(3), 834–841, 1970.
10. Basov, N.G., Danilychev, V.A., Popov Yu.M., and Khodkevich, D.D., The quantum generator in vacuum area of a spectrum at excitation liquid xenon by electronic beam, *Pis'ma Zh. Eksp. Tear. Fiz*., 12(10), 473–474, 1970 (*JETP Lett*., 12, 329, 1970).
11. Basov, N.G., Danilychev, V.A., and Popov, Yu.M., Stimulated emission in the vacuum ultraviolet region, *Sov. J. Quant. Electron*., 1(1), 18–22, 1971.
12. Koehler, H.A., Ferderber, L.J., Redhead, D.L., and Ebert, P.J., Stimulated VUV emission in high-pressure xenon excited by high-current relativistic electron beams, *Appl. Phys. Lett*., 21(5), 198–200, 1972.
13. Gerardo, J.B. and Johnson, A.W., 1730-A radiation dominated by stimulated emission from high-pressure xenon, *J. Appl. Phys*., 44(9), 4120–4124, 1973.
14. Wallace, S.C., Hodgson, R.T., and Dreyfus, R.W., Excitation of vacuum ultraviolet emission from high-pressure xenon by relativistic electron beam, *Appl. Phys. Lett*., 23(1), 22–24, 1973.
15. Hoff, P.W., Swingle, J.C., and Rhodes, C.K., Observation of stimulated emission from high pressure krypton and argon/xenon mixtures, *Appl. Phys. Lett*., 23(5), 245–246, 1973.
16. Hoff, P.W., Swingle, J.C., and Rhodes, C.K., Demonstration of the temporal coherence, spatial coherence, and threshold effects in the molecular xenon laser, *Opt. Commun*., 8(2), 128–131, 1973.
17. Hughes, W.M., Shannon, J., Kolb, A., Ault, E., and Blaumik, M., High-power ultraviolet laser radiation from molecular xenon, *Appl. Phys. Lett*., 23(7), 385–387, 1973.
18. Gerardo, J.B. and Johnson, A.W., High-pressure xenon laser at 1730 A, *IEEE J. Quant. Electron*, QE-9(7), 748–755, 1973.
19. Ault, E.R., Bhaumik, M.L., Hughes, W.M., Jensen, R.J., Robinson, C.P., Kolb, A.C., and Shannon, J., Xenon molecular laser in the vacuum ultraviolet, *IEEE J. Quant. Electron*., QE-9(10), 1031–1032, 1973.
20. Wallace, S.C., Hodgson, R.T., and Dreyfus, R.W., Short-pulse excitation of a xenon molecular dissociation laser at 172.9 nm by relativistic electrons, *Appl. Phys. Lett*., 23(12), 672–674, 1973.
21. Novaro, M. and Lagarde, F.G.C.R., Academ. Sci. Ser. B., *Optique Quantique*, 277(22), 671–673, 1973.
22. Koehler, H.A., Ferderber, L.J., Redhead, D.L., and Ebert, P.J., Vacuum-ultraviolet emission from high-pressure xenon and argon excited by high-current relativistic electron beams, *Phys. Rev. A*., 9(2), 768–781, 1974.
23. Ebert, P.J., Ferderber, L.J., Koehler, H.A., Kuckuck, R.W., and Redhead, D.L., Amplified spontaneous emission in xenon pumped by gamma rays, *IEEE J. Quant. Electron*., QE-10(9), 736–736, 1974.
24. Johnson, W.A. and Gerardo, J.B., Diluent cooling of a vacuum ultraviolet high pressure xenon laser, *J. Appl. Phys*., 45(2), 867–872, 1974.
25. Hughes, W.M., Shannon, J., and Hunter, R., 126.1 nm molecular argon laser, *Appl. Phys. Lett*., 24(10), 488–490, 1974.
26. Hughes, W.M., Shannon, J., and Hunter, R., Efficient high-energy-density molecular xenon laser, *Appl. Phys. Lett*., 25(1), 85–87, 1974.
27. Wallace, S.C. and Dreyfus, R.W., Continuously tunable xenon laser at 1720 A, *Appl. Phys. Lett*., 25(9), 498–500, 1974.
28. Koehler, H.A., Ferderber, L.J., Redhead, D.L., and Ebert, P.J., Vacuum-ultraviolet emission from high-pressure krypton, *Phys. Rev. A*., 12(3), 968–973, 1975.
29. Wrobel, W.-G., Rohr, H., and Steuer K.-H., Tunable vacuum ultraviolet laser action by argon excimers, *Appl. Phys. Lett*., 36(2), 113–115, 1980.

30. Kuznetsova, A.A., Kuzyakov, Yu.A., Shpanskii, V.A., and Khutaretskii, V.M., Emission spectra of XeF and XeF_2 molecule, *Vestnik MGU, Ser. II, Khimia* (Bulletin of Moscow Gov. University, Ser. II Chemistry), 3, 19–21, 1964.
31. Golde, M.F. and Thrush, B.A., Vacuum UV emission from reactions of metastable inert gas atoms: chemiluminescence of ArO and ArCl, *Chem. Phys. Lett*., 29(4), 486–490, 1974.
32. Golde, M.F., Interpretation of the oscillatory spectra of the inert-gas halides, *J. Mol. Spectrosc*., 58(2), 261–273, 1975.
33. Velazco, J.E. and Setser, D.W., Bound-free emission spectra of diatomic xenon halides, *J. Chem. Phys*., 62(5), 1990–1991, 1975.
34. Ewing, J.J. and Brau, C.A., Emission spectrum of XeI* in electron-beam-excited Xe/I_2 mixtures, *Phys. Rev. A*., 12(1), 129–132, 1975.
35. Velazco, J.E. and Setser, D.W., WA2. Quenching studies of $Xe(^3P_2)$ metastable atoms, *IEEE J. Quant. Electr*., QE-11(8), 708–709, 1975.
36. Brau, C.A. and Ewing, J.J., Emission spectra of XeBr, XeCl, XeF, and KrF, *J. Chem. Phys*., 63(11), 4640–4647, 1975.
37. Searles, S.K. and Hart, G.A., Stimulated emission at 218.8 nm from XeBr, *Appl. Phys. Lett*., 27(4), 243–245, 1975.
38. Ewing, J.J. and Brau, C.A., Laser action on the $^2\Sigma_{1/2}{}^+ \rightarrow {}^2\Sigma_{1/2}{}^+$ bands of KrF and XeCl, *Appl. Phys. Lett*., 27(6), 350–352, 1975.
39. Tisone, G.C., Hays, A.K., and Hoffman, J.H., 100 MW, 248.2 nm, KrF laser excited by an electron beam, *Opt. Commun*., 15(2), 188–189, 1975.
40. Bhaumik, M.L., Bradford, R.S., Jr., and Ault, E.R., High-efficiency KrF excimer laser, *Appl. Phys. Lett*., 28(1), 23–24, 1975.
41. Hoffman, J.M., Hays, A.K., and Tisone, G.C., High power UV noble gas halide lasers, *Appl. Phys. Lett*., 28(9), 538–539, 1976.
42. Tellinghuisen, J., Hoffman, J.M., Tisone, G.C., and Hays, A.K., Spectroscopic studies of diatomic noble gas halides: Analysis of spontaneous and stimulated emission from XeCl, *J. Chem. Phys*., 64(6), 2484–2490, 1976.
43. Ault, E.R., Bradford, R.S., Jr., and Bhaumik, M.L., High power xenon fluoride laser, *Appl. Phys. Lett*., 27(7), 413–415, 1975.
44. Brau, C.A. and Ewing, J.J., 354-nm laser action on XeF, *Appl. Phys. Lett*., 27(8), 435–437, 1975.
45. Murray, J.R. and Powell, H.T., KrCl laser oscillation at 222 nm, *Appl. Phys. Lett*., 29(4), 252–253, 1976.
46. Mangano, J.A. and Jacob, J.H., Electron-beam-controlled discharge pumping of KrF laser, *Appl. Phys. Lett*., 27(9), 495–498, 1975.
47. Bradford, R.S., Jr., Lacina, W.R., Ault, E.R., and Bhaumik, M.L., High efficiency discharge excitation of the KrF laser, *Opt. Commun*., 18(2), 210–211, 1976.
48. Sutton, D.G., Suchard, S.H., Gibb, O.L., and Wang, C.P., Fast-discharge-initiated KrF laser, *Appl. Phys. Lett*., 28(9), 522–523, 1976.
49. Burnham, R., Powell, F.X., and Djeu, N., Efficient electric discharge lasers in XeF and KrF, *Appl. Phys. Lett*., 29(1), 30–32, 1976.
50. Wang, C.P., Performance of XeF/KrF lasers pumped by fast discharges, *Appl. Phys. Lett*., 29(2), 103–105, 1976.
51. Ischenko, V.N., Lisitsin, V.N., and Razhev, A.M., Powerful superluminosity of excimers ArF, KrF, XeF in the electric discharge, *Pis'ma Zh. Tehn. Fiz*., 2(18), 839–842, 1976.
52. Burnham, R. and Djeu, N., Ultraviolet preionized discharge pumped lasers in XeF, KrF, and ArF, *Appl. Phys. Lett*., 29(11), 707–709, 1976.
53. Burnham, R., Harris, N.W., and Djeu, N., Xenon fluoride laser excitation by transverse electric discharge, *Appl. Phys. Lett*., 28(2), 86–87, 1976.
54. Wang, C.P., Mirels, H., Sutton, D.G., and Suchard, S.N., Fast-discharge initiated XeF laser, *Appl. Phys. Lett*., 28(6), 326–328, 1976.
55. Mangano, J.A., Jacob, J.H., and Dodge, J.B., Electron-beam-controlled discharge pumping of XeF laser, *Appl. Phys. Lett*., 29(7), 426–428, 1976.

56. Hay, P.J. and Dunning, T.H., Jr., The electronic states of KrF. *J. Chem. Phys*., 66, 1306–1316, 1977.
57. Dunning, T.H., Jr. and Hay, P.J., The covalent and ionic states of the rare gas monofluorides, *J. Chem. Phys*., 69(1), 134–149, 1978.
58. Hay, P.J. and Dunning, T.H., Jr., The covalent and ionic states of the xenon halides, *J. Chem. Phys*., 69(5), 2209–2220, 1978.
59. Gudzenko, L.I., Shelepin, L.A, and Yakovlenko, S.I., Gain in recombining plasma: plasma lasers, *Usp. Fiz. Nauk,* 114(3), 457–485, 1974. (*Sov. Phys. Usp*., 17, 848, 1975.)
60. Rhodes, C.K., Review of ultraviolet laser physics. *IEEE J. Quant. Electron*., QE-10, 153–174, 1974.
61. Gudzenko, L.I. and Yakovlenko, S.I., *Plazmennye Lazery* (*Plasma Lasers*), Atomizdat, Moscow, 1978, in Russian.
62. Brau, C.A., Rare gas halogen excimers. *Top. Appl. Phys*., 30, 87–133, 1979.
63. Lakoba, I.S. and Yakovlenko, S.I., Active media of exciplex lasers, *Kvantovaya Elektron* (*Moscow*), 8(4), 677–719, 1980. (*Sov. J. Quant. Electron,*, 10, 389, 1980.)
64. Brau, Ch. A., Gallagher, A., Hoff, P.W., Krauss, M., McCusker, M.V., Mies, F.H., and Rhodes, Ch. K., Excimer Lasers, Springer-Verlag, Berlin, 1979, pp. 272.
65. *Gas Lasers*, McDaniel, E.W. and Nighan, W.L., Eds., New York: Academic Press.
66. Plazmennye Lazery Vidimogo i Blizhnego UF Diapazonov (Visible and Near-UV Plasma Lasers) Tr. Inst. Obshch. Fiz. Akad. Nauka 21, 1989, Yakovlenko, S.I., Ed. [whole volume].
67. Yakovlenko, S.I., Plasma lasers, *Laser Phys*., 1(6), 565–589, 1991.
68. Mesyats, G.A., Osipov, V.V., and Tarasenko, V.F., *Pulsed Gas Lasers*, SPIE, Bellingham, 1995.
69. Tarasenko, V.F, Yakovlenko, S.I., Rare-gas dimer and halide lasers, *Quant. Electron*., 27(12), 1111–1118, 1997.
70. Boichenko, A.M., Tarasenko, V.F., and Yakovlenko, S.I., Exciplex rare-halide lasers, *Laser Phys*., 10(6), 1159–1187, 2000.
71. Yakovlenko, S.I., O vozmozhnosty usileniya na fotodissotsiativnih perehodah (On opportunity of lasing on photodissociative transitions) Preprint No. 2174, Institute of Atomic Energy, Moscow, 1972, pp. 20.
72. Gudzenko, L.M. and Yakovlenko, S.I., Plasma laser on electronic transitions of molecules, *Dokl. Akad. Nauk SSSR,* 207, 1085–1087, 1972. (Sov. *Phys. Dokl*., 17, 1172 , 1973.)
73. Gudzenko, L.I., Lakoba, I.S., and Yakovlenko, S.I., Plasma laser on molecules transitions to repulsive states, *Zh. Eksp. Tear. Fiz.,* 67, 2022–2034, 1974. (*Sov. Phys. JETP*, 40, 1005, 1975.)
74. Gudzenko, L.I., Lakoba, S.I., and Yakovlenko, S.I., Plasma lasers on transitions of diatomic molecules, *Tr. Fiz. Inst. Akad. Nauk SSSR*, 90, 61–90, 1976.
75. Yakovlenko, S.I., *Radiatsionno-Stolknovitel'nye Yavleniya* (*Radiative Collisional Phenomena*), Energoatomizdat, Moscow, 1984.
76. Boichenko, A.M., Tarasenko, V.F., Fomin, E.A., and Yakovlenko, S.I., Broadband emission continua in rare gases and in mixtures of rare gases with halides, *Quant. Electron*., 23(1) 3–25, 1993.
77. Boichenko, A.M., Tarasenko, V.F., and Yakovlenko, S.I., The nature of third continua in rare gases, *Laser Phys*., 9(5), 1004–1020, 1999.
78. Boichenko, A.M. and Yakovlenko, S.I., Analysis of the possibility of lasing on the third continuum in argon, *Quant. Electron*., 30(7), 567–572, 2000.
79. Loree, T.R., Showalter, R.R., Johnson, T.M., Birmingham, B.S., and Hughes, W.H., *Proceedings of International Conference on Lasers'88, Lake Tahoe, NV, 1988*, McLean: STS Press:, 1989, 253.
80. Gudzenko, L.I., Lakoba, S.I., Petrushchenko, G.Yu., Syts'ko, Yu.I., and Yakovlenko, S.I., Kinetic models in laser physics and the theory of oscillation, *Tr. Fiz. Inst. Akad. Nauk SSSR*, 120, 30–43, 1980.
81. Sasaki, W., Shirai, T., Kubodera, S., Kawanaka, J., and Igarashi, T. Observation of vacuum-ultraviolet Kr_2^* laser oscillation pumped by a compact discharge device, *Opt. Lett*., 26(8), 503–505, 2001.
82. Nakamura, K., Ooguchi, Y., Umegaki, N., Goto, T., Jitsuno, T., Kitamura, T., Takasaki, M., and Horiguchi, S., Gain measurements of Ar_2 excimer formed by high-pressure homogeneous discharge using plasma electrode, International Conference on Atomic and Molecular Lasers IV, 10–14

September 2001, Tomsk, Russia, *SPIE*, 4747, Tarasenko, V.F., Mayer, G.V., and Petrash, G.G., Eds., pp. 286–293.
83. Tarasenko, V.F. and Yakovlenko, S.I., The electron runaway mechanism in dense gases and the production of high-power subnanosecond electron beams, *Physics-Uspekhy*, 47(9), 953–971, 2004.
84. Tkachev, A.N. and Yakovlenko, S.I., Runaway of electrons in dense gases and mechanism of generation of high-power subnanosecond beams, *Cent. Eur. J. Phys. (CEJP)*, 2(4), 579–635, 2004 (www.cesj.com/physics.html).
85. Angood, S. et al., Specification for the TITANIA KrF laser system RAL-94-014, Rutherford Appleton Laboratory, Science and Engineering Research Council, 1994.
86. Inertial confinement fusion at Los Alamos, Progress in inertial confinement fusion since 1985, Comp. Cartwright, D.C., Los Alamos, 1, 262, 1989.
87. Goto, T., Takagi, S., Kakizaki, K., Saton, S., Kasugi, S., Ohishi, T., Kanawa, Y., Ishii, A., Teranishi, T., Yasuoka, K., Shinohe, T., Ohashi, H., Endo, F., and Okamura, K., Development of key component and technologies for a high repetition rate and high power excimer laser, *Rev. Sci. Instr.*, 69(1), 1–9, 1998.
88. Boichenko, A.M., Derzhiev, V.I., and Yakovlenko, S.I., Kinetic models for active media of an ArF laser, *Laser Phys.*, 2(3), 210–220, 1992.
89. Boichenko, A.M., Karelin, A.V., Sereda, O.V., and Yakovlenko, S.I., Kinetics of the active media of nuclear-pumped lasers, *Laser Particle Beams*, 11(4), 655–661, 1993.
90. Boichenko, A.M., Karelin, A.V., and Yakovlenko, S.I., Calculation of the threshold characteristics of a nuclear-pumped Ne–Xe–NF_3 laser, *Quant. Electron.*, 25(6), 521–524, 1995.
91. Golyatina, R.I. and Yakovlenko, S.I., Formation of the angular divergence in the superradiance regime, *Laser Phys.*, 11(9), 994–999, 2001.
92. Golyatina, R.I., Simakova, O.V., and Yakovlenko, S.I., Simulation of angular divergence in the plane-parallel resonator, *Laser Phys.*, 13(11), 1411–1421, 2003.
93. Johnson, T.H., Cartland, H.E., Genori, T.C., and Hunter, A.M., A comprehensive kinetic model of the electron-beam-excited xenon chloride laser, *J. Appl. Phys.*, 66(12), 5707–5725, 1989.
94. Kannari, F., Kimura, W.D., and Ewing, J.J., Comparison of model prediction with detailed species kinetic measurements of XeCl laser mixtures, *J. Appl. Phys.*, 68(6), 2615–2631, 1990.
95. Boichenko, A.M., Karelin, A.V., and Yakovlenko, S.I., A kinetic model of the XeF laser, *Laser Phys.*, 5(1), 80–93, 1995.
96. Peters, P.J.M., Bastiaens, H.M.J., Witteman, W.J., and Gerber, T.A., Study of the electron quenching of excimers in a KrF laser excited by a coaxial electron beam, *Appl. Phys. B*, 43, 253–261, 1987.
97. Arteev, M.S., Bunkin, F.V., Derzhiev, V.I., Sulakshin, S.S., Syts'ko, Yu.I., Yurovskii, V.A., and Yakovlenko, S.I., Lasing in He:Kr:F_2 mixture at ion beam pumping, *Izv. Akad. Nauk SSSR, Ser. Fiz.*, 48(12), 2321–2324, 1984.
98. Arteev, M.S., Bunkin, F.V., Derzhiev, V.I., Didenko, A.N., Kozhevnikov, A.V., Sulakshin, S.S., Syts'ko, Yu.I., Yurovskii, V.A., Yakovlenko, S.I., Exciplex KrF-laser pumped by ion beam, *Kvantovaya Elektron.*, 13(11), 2191–2202, 1986.
99. Jacob, J.H., Hsia, J.H., Mangano, J.A., and Rokni, M., Pulse shape and laser-energy extraction from e-beam-pumped KrF*, *J. Appl. Phys.*, 50(8), 5130–5134, 1979.
100. Rice, J.K., Tisone, G.C., and Patterson, P.L., Oscillator performance and energy extraction from a KrF laser pumped by a high-intensity relativistic electron beam, *IEEE J. Quant. Electron.*, 16(12), 1315–1326, 1980.
101. Edwards, C.B., O'Neil, F., and Shaw, M.J., 60-ns e-beam excitation of rare gas halide lasers, *Appl. Phys. Lett.*, 36(8), 617–620, 1980.
102. Swingle, J.C., Schlitt, L.G., Rapoport, W.R., Goldhar, J., and Ewing, J.J., Efficient narrowband electron beam pumped KrF laser for pulse-compression studies, *J. Appl. Phys.*, 52(1), 91–96, 1981.
103. Lowenthal, D.D., Ewing, J.J., Center, R.E., Mumola, P.B., Grossman, W.M., Olsen, N.T., and Shannon, J.P., Conceptual design of an angular multiplexed 50 kJ KrF amplifier for ICF, *IEEE J. Quant. Electron.*, QE-17(9), 1861–1870, 1981.
104. Parks, J.H., Angular multiplex laser fusion drivers, International Conference on High Power Lasers and Applications, *Proc. SPIE*, Tang, C.C., Ed., 270, 81–92, 1981.

105. Nuckolls, J.H., The feasibility of inertial-confinement fusion, *Phys. Today*, 35(9), 24–31, 1982.
106. Owadano, Y., Okuda, I., Tanimoto, M., Matsumoto, Y., Kasai, T., and Yano, M., Development of a 1-kJ KrF laser system for laser fusion research, *Fusion Technol.*, 11(3), 486–491, 1987.
107. Sullivan, J.A., Design of a 100 kJ KrF power amplifier module, *Fusion Technol.*, 11(3), 684–704, 1987.
108. Rosocha, L.A., Hanlon, J.A., McLeod, J., Kang, M., Kortegaard, L., Burrows, M.D., and Bowling, P.S., Aurora multikilojoule KrF laser system for inertial confinement fusion, *Fusion Technol.*, 11(3), 497–531, 1987.
109. Rosocha, L.A., Bowling, P.S., Burrows, M.D., Kang, M., Hanlon, J., McLeod, J., and York, G.W., Jr., An overview of Aurora: a multikilojoule KrF laser system for inertial confinement fusion, *Laser Particle Beams*, 4(1), 55–70, 1986.
110. Ueda, K.-I., Present status and prospect of KrF laser physics and technology large volume excitation and VUV optics, *Laser Particle Beams*, 7(3), 375–382, 1989.
111. Owadano, Y., Okuda, I., Matsumoto, Y., Tanimoto, M., Tomie, T., Koyama, K., and Yano, M., Development of a high-power KrF laser system, ASURA, *Laser Particle Beams*, 7(3), 383–392, 1989.
112. Inertial confinement fusion at Los Alamos, Progress in inertial confinement fusion since 1985, Comp. Cartwright, D.C., Los Alamos, 1, 262, 1989.
113. Basov, N.G., Bakaev, V.G., Grigoryants, E.A. et al., High aperture e-beam pumped excimer KrF laser, *Kvantovaya Elektron.*, 18(8), 902–904, 1991.
114. Holzricher, J.F., CLEO '83, *Conference on Lasers and Electro-Optics*, Baltimore, MD, May, 1983, pp. 17–20.
115. Ng, A., Pasini, D., Celliers, P., Parfeniuk, D., Da Silva, L., and Kwan, J., Ablation scaling in steady-state ablation dominated by inverse-bremsstrahlung absorption, *Appl. Phys. Lett.*, 45(10), 1046–1048, 1984.
116. Daugherty, J.D., Mangano, J.A., and Jacob, J.H., Attachment-dominated electron-beam-ionized discharges, *Appl. Phys. Lett.*, 28(10), 581–583, 1976.
117. Jacob, J.H. and Mangano, J.A., Modeling of the KrF laser discharge, *Appl. Phys. Lett.*, 28(12), 724–726, 1976.
118. Long, W.H., Jr., Electron kinetics in the KrF laser, *Appl. Phys. Lett.*, 31(6), 391–394, 1977.
119. Rokni, M., Mangano, J.A., Jacob, J.H., and Hsia, J.C., Rare gas fluoride lasers, *IEEE J. Quant. Electron.*, QE-14(7), 464–481, 1978.
120. Nighan, W.L., Plasma processes in electron-beam controlled rare-gas halide lasers, *IEEE J. Quant. Electron.*, 14(10), 714–726, 1978.
121. Lacina, W.B. and Cohn, D.B., Theoretical analysis of the electrically excited KrF laser, *Appl. Phys. Lett.,* 32(2), 106–108, 1978.
122. Nighan, W.L., Influence of electron–F_2 collisions in rare gas-halide laser discharges, *Appl. Phys. Lett.*, 32(5), 297–300, 1978.
123. Brown, R.T. and Nighan, W.L., Instability onset in electron-beam-sustained KrF* laser discharges, *Appl. Phys. Lett.*, 32(11), 730–733, 1978.
124. Greene, A.E. and Brau, C.A., Theoretical studies of UV-preionized transverse discharge KrF and ArF lasers, *IEEE J. Quant. Electron.*, QE-14(12), 951–957, 1978.
125. Long, W.H., Jr., Discharge stability in e-beam-sustained rare-gas halide lasers, *J. Appl. Phys.*, 50(1), 168–172, 1979.
126. Brown, R.T. and Nighan, W.L. Stability enhancement in electron-beam-sustained excimer laser discharges, *Appl. Phys. Lett.*, 35(2), 142–144, 1979.
127. Jacob, J.H., Hsia, J.H., Mangano, J.A., and Rokni, M., Pulse shape and laser-energy extraction from e-beam-pumped KrF*, *J. Appl. Phys.*, 50(8), 5130–5134, 1979.
128. Johnson, T.H. and Hunter, A.M. II., Physics of the krypton fluoride laser, *J. Appl. Phys.*, 51(5), 2406–2420, 1980.
129. Klimek, D.E., Hsia, J.H., Jacob, J.H., Trainor, D.W., Duzy, C., and Hyman, H.A., Kinetic issues for short pulse KrF laser operation, *IEEE J. Quant. Electron.*, QE-17(9), 1847–1855, 1981.
130. Kannari, F., Obara, M., and Fujioka, T., Theoretical study of output performance dependence on excitation rate for electron beam-excited KrF laser, *J. Appl. Phys.*, 53(1), 135–142, 1982.

131. Morgan, W.L., Winter, N.W., and Kulander, K.C., Vibrational relaxation and laser extraction in rare-gas halide excimers, *J. Appl. Phys*., 54(8), 4275–4279, 1983.
132. Edwards, C.B. and O'Neil, F., Computer modeling of e-beam-pumped KrF laser, *Laser Particle Beams*, 1(1), 81–95, 1983.
133. Witteman, W.J. and Kleikamp, B.M., On the electron-beam KrF laser, *J. Appl. Phys*., 55(5), 1299–1307, 1984.
134. Mandl, A., Klimek, D., and Parks, J.H., KrF laser kinetic studies, *J. Appl. Phys*., 55(11), 3940–3949, 1984.
135. Kannari, F., Obara, M., and Fujioka, T., An advanced kinetic model of electron beam KrF lasers including the vibrational relaxation in KrF(*B*) and collisional mixing of KrF(*B*, *C*), *J. Appl. Phys*., 57(9), 4309–4322, 1985.
136. Salesky, E.T. and Kimura, W.D., Electron-beam pumped KrF laser extraction measurements for high Kr concentration gas mixtures, *IEEE J. Quant. Electron*., QE-21(11), 1761–1765, 1985.
137. Coutts, J. and Webb, C.E., Stability of transverse self-sustained discharge-excited long-pulse XeCl lasers, *J. Appl. Phys*., 59(3), 704–710, 1986.
138. Kushner, M.J. and Pindroh, A.L., Discharge constriction, photodetachment, and ionization instabilities in electron-beam sustained discharge excimer lasers, *J. Appl. Phys*., 60(3), 904–914, 1986.
139. Molchanov, A.G., Theory of active media of excimer lasers, *Trudy FIAN*, 171, 54–127, 1986.
140. Kannari, F., Shaw, M.J., and O'Neil, F. Parametric study of an electron-beam-pumped krypton-rich KrF laser, *J. Appl. Phys*., 61(2), 476–488, 1987.
141. Czuchlewski, S.J., Hanson, D.E., Krohn, R.J., Larson, A.R., and Salesky, E.T., KrF laser optimization, *Fusion Technol*., 11(3), 560–575, 1987.
142. Kushner, M.J., Return current in large aperture electron-beam excited KrF laser, *IEEE J. Quant. Electron*., QE-26(9), 1546–1554, 1990.
143. Flannery, M.R. and Yang, T.P., Ionic recombination of rare gas atomic ions X_2^+ with F^- in a dense gas X, *Appl. Phys. Lett*., 32(5), 327–329, 1978.
144. Flannery, M.R. and Yang, T.P., Ionic recombination of rare gas molecular ions X^+ with F^- in a dense gas X, *Appl. Phys. Lett.,* 32(6), 356–357, 1978.
145. Lakoba, I.S., Suchkova, E.D., and Syts'ko, Yu.I., Calculation of ion-ionic recombination coefficients with temperature dependence, *Preprint Lebedev Phys. Inst., USSR Acad. Sci*., 8, Moscow, USSR, 1981.
146. Wadt, W.R. and Hay, P.J., The low-lying electronic states of Ar_2F, *Appl. Phys. Lett*., 30(11), 573–575, 1977.
147. Rokni, M., Jacob, J.H., and Mangano, J.A., Dominant formation and quenching processes in E beam pumped ArF* and KrF* lasers, *Phys. Rev. A*, 16, 2216–2224, 1977.
148. Morgan, W.R., Whitten, B.L., and Bardsley, J.N., Plasma shielding effects on ionic recombination, *Phys. Rev. Lett*., 45(28), 2021–2024, 1980.
149. Burtsev, V.A., Ermolaev, Yu.L., Kalinin, N.V., and Petrov, I.B., *Zh. Tekh. Fiz*., 64, 79, 1994.
150. Lee, Y.-W., Kannari, F., and Obara, M., Power extraction of an e-beam-pumped atmospheric pressure, Kr-rich KrF laser amplifier, *J. Appl. Phys*., 65(12), 4532–4541, 1989.
151. Lee, Y.-W. and Endoh, A., Kinetic study of a short pulse electron-beam pumped Kr/F_2 laser amplifier medium at very low pressure operation, *Appl. Phys. B*, 52(5), 245–250, 1991.
152. Tittel, F.K., Wilson, W.L., Stickel, R.E. et al., A triatomic Xe_2Cl excimer laser in the visible, *Appl. Phys. Lett*., 36(6), 405–407, 1980.
153. Tittel, F.K., Smayling, M., Wilson, W.L., and Marowsky, G., Blue laser action by the rare-gas halide trimers Kr_2F, *Appl. Phys. Lett*., 37(10), 862–864, 1980.
154. Levin, L.A., Moody, S.E., Klosterman, L., Center, R.E., and Ewing, J.J., Kinetic model for long pulse XeCl laser performance, *IEEE J. Quant. Electron*., QE-17(12), 2282–2289, 1981.
155. Maeda, M., Takahashi, A., Mizunami, T., and Miyazoe, Y., Kinetic model for self-sustained discharge XeCl lasers, *Jpn. J. Appl. Phys*., pt. 1., 21(8), 1161–1169, 1982.
156. Kannari, F., Suda, A., Obara, M., and Fujioka, T., Theoretical analysis of electron beam excited KrF laser performance: new F_2 concentration optimization, *IEEE. J. Quant. Electron*., QE-19(2), 232–242, 1983.

157. Kannari, F., Suda, A., Obara, M., and Fujioka, T., Theoretical simulation of electron beam excited xenon chloride (XeCl) lasers, *IEEE. J. Quant. Electron*., QE-19(10), 1587–1600, 1983.
158. Long, W.H., Jr., Plummer, M.J., and Stappaerts, E.A., Efficient discharge pumping of an XeCl laser using high voltage prepulse, *Appl. Phys. Lett*., 43, 735, 1983.
159. Hokazono, H., Midorikawa, K., Obara, M., and Fujioka, T., Theoretical analysis a self sustained discharge pumped XeCl laser, *J. Appl. Phys*., 56(3), 680–690, 1984.
160. Bruzzese, R., Comparison between experimental and theoretical results on discharge constriction in XeCl* lasers, *Lett. Nuovo Cimento*., 40(2), 45–52, 1984.
161. Miilda, P.Kh., Peat, V.E., Sorkina, R.A., Tamme, E.E., Treschalov, A.B., and Sharman, A.V., Theoretical and experimental investigation of gas discharge plasma of XeCl laser, *Kvantovaya Elektron*, 13(11), 2191–2202, 1986.
162. Kushner, M.J. and Pindroh, A.L., Discharge constriction, photodetachment, and ionization instabilities in electron-beam sustained discharge excimer lasers, *J. Appl. Phys*., 60(3), 904–914, 1986.
163. Baginskii, V.M., Golovinckii, P.M., and Shchedrin, A.I., Influence of halogenide concentration on discharge stability and power characteristics of lasers on mix He/Xe/HCl. Numerical modeling, *Zh. Tekh. Fiz*., 56(12), 2340–2345, 1986.
164. Kushner, M.J. and Pindroh, A.L., Discharge constriction, photodetachment, and ionization instabilities in electron-beam sustained discharge excimer lasers, *J. Appl. Phys*. 60(3), 904–914, 1986.
165. Fisher, C.H., Kushner, M.J., DeHart, T.E., McDaniel, J.P., Petr, R.A., and Ewing, J.J., High efficiency XeCl laser with spiker and magnetic isolation, *Appl. Phys. Lett*., 48(23), 1574–1576, 1986.
166. Ohwa, M. and Obara, M., Theoretical analysis of efficiency scaling laws for a self-sustained discharge pumped XeCl laser, *J. Appl. Phys*., 59(1), 32–41, 1986.
167. Mihkelsoo, V., Miidla, P., Peet, V., Sherman, A., Sorkina, R., Tamme, E., and Treshchalov, A., Theoretical simulation of physical processes in a discharge XeCl laser, *J. Phys. B*, 22(9), 1489–1504, 1989.
168. Dem'yanov, A.V., Kochetov, I.V., Napartovich, A.P., Starostin, A.N., and Taran, M.D., Mathematical model of XeCl-laser, *Kvantovaya Elektron*., 12(8), 1737–1740, 1985.
169. Baginskii, V.M., Golovinskii, P.M., Razhev, A.M., and Shchedrin, A.I., Dependence of plasma parameters and generation energy of excimer lasers on Xe percentage in He-Xe-HCl mixture, *Kvantovaya Elektron.,* 15(11), 2309–2317, 1988.
170. Stielow, G., Hammer, Th., and Botticher, W., Verification of a XeCl* laser model by measurement of the plasma conductivity, *Appl. Phys. B*., 47(4), 333–342, 1988.
171. Boichenko, A.M., Derzhiev, V.I., Zhidkov, A.G., and Yakovlenko, S.I., Kinetic model of the active medium of an XeCl laser pumped by an electron beam, *Sov. J. Quant. Electron*., 19(2), 182–184, 1989.
172. Ishihara, T. and Lin, S.-C., Theoretical modeling of microwave-pumped high-pressure gas laser, *Appl. Phys. B*, 48(4), 315–326, 1989.
173. Johnson, T.H., Cartland, H.E., Genori, T.C., and Hunter, A.M., A comprehensive kinetic model of the electron-beam-excited xenon chloride laser, *J. Appl. Phys*., 66(12), 5707–5725, 1989.
174. Mihkelsoo, V., Miidla, P., Peet, V., Sherman, A., Sorkina, R., Tamme, E., and Treshchalov, A., Theoretical simulation of physical processes in a discharge XeCl laser, *J. Phys. B*., 22(9), 1489–1504, 1989.
175. Boichenko, A.M., Derzhiev, V.I., Zhidkov, A.G., and Yakovlenko, S.I., Kinetic model of XeCl laser in mix Ar–Xe–CCl4, *Kratk. Soobshch. Fiz*., 9, 9–11, 1990, in Russian.
176. Kannari, F., Kimura, W.D., and Ewing, J.J., Comparison of model prediction with detailed species kinetic measurements of XeCl laser mixtures, *J. Appl. Phys*., 68(6), 2615–2631, 1990.
177. Sorkina, R., Theoretical simulation of spatial-time characteristics of a discharge XeCl excimer laser active medium, *J. Phys. D*, 23(7), 806–812, 1990.
178. Adamovich, V.A., Dem'yanov, A.V., Kochetov, I.V. et al., Modeling of excimer XeCl laser excited by e-beam, *Kvantovaya Elektron*., 17(11), 1395–1401, 1990.
179. Turner, M.M. and Smith, P.W., Modeling of the self-sustained, discharge-excited xenon-chloride laser, *IEEE Trans. Plasma Sci*., 19(2), 350–360, 1991.
180. Letardi, T., Fang, H., and Fu, S., Theoretical modeling of an X-ray preionized self-sustained XeCl laser, *IEEE J. Quant. Electron*., 28(7), 1647–1652, 1992.

181. Boichenko, A.M., Karelin, A.V., Sereda, O.V., and Yakovlenko, S.I., Kinetics of the active media of nuclear-pumped lasers, *Laser Particle Beams*, 11(4), 655–661, 1993.
182. Luck, H., Loffhagen, D., and Botticher, W., Experimental verification of a zero-dimensional model of the ionization kinetics of XeCl discharges, *Appl. Phys. B*, 58(2), 123–132, 1994.
183. Schwabedissen, A., Loffhagen, D., Hammer, T., and Botticher, W., Experimental verification of zero-dimensional model of the kinetics of XeCl* discharges by Xe*, Cl*, Ne*, and H* density measurements, *Appl. Phys. B*, 58(6), 471–481, 1994.
184. Schwabedissen, A., Loffhagen, D., Hammer, T., and Botticher, W., Experimental verification of zero-dimensional model of the kinetics of XeCl* discharges by XeCl* (*B*), (*C*) and Xe_2Cl density measurements, *Appl. Phys. B*, 61(2), 175–186, 1995.
185. Rohr, K. and Linder, F., Vibrational excitation of polar molecules by electron impact. I. Threshold resonances in HF and HCl, *J. Phys. B*, 9(14), 2521–2537, 1976.
186. Knoth, G., Radle, M., Gote, M., Ehrhardt, H., and Jung, K., Near-threshold electron impact rovibrational excitation of HCl and HF, *J. Phys. B*, 22(2), 299–326, 1989.
187. Radle, M., Knoth, G., Jung, K., and Ehrhardt, H., Rotational and rovibrational excitation of HCl and HF by low-energy electron impact, *J. Phys. B*, 22(9), 1455–1476, 1989.
188. Domcke, W. and Mundel, C., Calculation of cross sections for vibrational excitation and dissociative attachment in HCl and DCl beyond the local-complex-potential approximation, *J. Phys. B.*, 18(22), 4491–4509, 1985.
189. Allan, M. and Wong, S.F., Dissociative attachment from vibrationally and rotationally excited HCl and HF, *J. Chem. Phys.*, 74(3), 1687–1691, 1981.
190. Azria, R., Roussier, L., Paineau, R., and Tronnc, M., *Rev. Phys., Appl.*, 9, 469, 1974.
191. Petrovic, Z.Lj., Wang, W.C., and Lee, L.C., Attachment of low-energy electrons to HCl, *J. Appl. Phys.*, 64(4), 1625–1631, 1988.
192. Greene, A.E. and Brau, C.A., Theoretical studies of UV-preionized transverse discharge KrF and ArF lasers, *IEEE J. Quant. Electron.*, QE-14(12), 951–957, 1978.
193. Voitik, M.G. and Molchanov, A.G., Maximal efficiency of excimer lasers on Ar/F_2 mixes excited by an electronic beam, *Pis'ma Zh. Tekh. Fiz.*, 5(18), 1092–1097, 1979.
194. Ohwa, M. and Obara, M., Theoretical evaluation of the buffer gas effects for a self sustained discharge ArF laser, *J. Appl. Phys.*, 63(5), 1306–1312, 1988.
195. Boichenko, A.M., Derzhiev, V.I., Zhidkov, A.G., Sulakshin, S.S., and Yakovlenko S.I., *Kratk. Soobshch. Fiz.*, 5, 28–30, 1989, in Russian.
196. Lee, Y.M., Matsui, E., Kannari, F., and Obara, M., Theoretical high efficiency extraction study of a short pulse electron beam pumped KrF laser amplifier with atmospheric pressure Ar-rich mixtures, *IEEE J. Quant. Electron.*, 25, 2053–2065, 1989.
197. Boichenko, A.M., Derzhiev, V.I., Zhidkov, A.G., and Yakovlenko, S.I., Kinetic model of an ArF laser, *Sov. J. Quant. Electron.*, 22(5), 444–449, 1992.
198. Hall, R.J., Dissociative attachment and vibrational excitation of F_2 by slow electrons, *J. Chem. Phys.*, 68(4), 1803–1807, 1978.
199. Mandl, A., ArF short-pulse extraction studies, *J. Appl. Phys.*, 59(5), 1435–1445, 1986.
200. Lee, Y.-M., Kumagai, H., Ashidate, S., and Obara, M., High efficiency extraction study of an electron beam pumped ArF laser amplifier with an atmosphere pressure Ar-rich mixture, *Appl. Phys. Lett.*, 52(16), 1294–1296, 1988.
201. Bishel, W.K. et al., *International Conference on Lasers'78*, Orlando, FL, 1978.
202. Bishel, W.K., Nakano, H.H., Eckstrom, D.J., Hill, R.M., Huestis, D.L., and Lorents, D.C., A new blue–green excimer laser in XeF, *Appl. Phys. Lett.*, 34(9), 565–567, 1979.
203. Bason, N.G., Zuyev, V.S., Kanayev, A.V., Mikheev, L.D., and Stavrovskii, D.B., Lasing on Bound-free Transition $C(3/2)\sqrt{A(3/2)}$ of XeF under Photoionization of XeF_2 6(5), 1074, 1986.
204. Powell, H.T. and Wilder, R.E., *Topical Conference on Excimer Lasers*, Charleston, SC, 1979.
205. Finn, T.G., Palumbo, L.J., and Champagne, L.F., A kinetic scheme for XeF laser, *Appl. Phys. Lett.*, 33(2), 148–151, 1978.
206. Johnson, T.J., Palumbo, L.J., and Hunter, A.M., II, Kinetics simulation on high-power gas lasers, *IEEE J. Quant. Electron.*, 15(5), 289–301, 1979.

207. Mkrchyan, M.M., and Platonenko, V.T., Gas discharge kinetics of XeF laser, *Kvantovaya Elektron*, 6(8), 1639–1647, 1979.
208. Blauer, J.A., Yang, T.T., Turner, C.E., and Copeland, D.A., Excimer kinetics and multiline model for the electron beam pumped XeF ($B \rightarrow X$) laser, *Appl. Opt*., 23(23), 4352–4367, 1984.
209. Blauer, J.A., Yang, T.T., Turner, C.E., Jr., and Copeland, D.A., Multiline model for e-beam pumped XeF ($B \rightarrow X$) laser, *AIAA J*., 23(5), 741–748, 1985.
210. Moratz, T.J., Saunders, T.D., and Kushner, M.J., Heavy-ion versus electron-beam excitation of an excimer laser, *J. Appl. Phys*., 64(8), 3799–3810, 1988.
211. Moratz, T.J., Saunders, T.D., and Kushner, M.J., High temperature kinetics in He and Ne buffered XeF lasers: the effect of absorption, *Appl. Phys. Lett*., 54(2), 102–104, 1989.
212. Nishida, N., Takashima, T., Tittel, F.K., Kannari, F., and Obara, M., Theoretical evaluation of a short-pulse electron-beam-excited XeF ($B \rightarrow X$) laser using low-pressure, room-temperature $Ar/Xe/F_2$ gas mixture, *J. Appl. Phys*., 67(9), 3932–3940, 1990.
213. Abarenov, A.V., Persiantsev, I.G., Rakhimov, A.T., Rebric, S.P., Shugai, Ju.S., and Suetin, N.V., Computer model of the electron-beam excited XeF (B–X) laser, *IEEE J. Quant. Electron*., 27(7), 1946–1953, 1991.
214. Dem'yanov, A.V., Dyatko, N.A., Kochetov, I.V., et al., *Proc. Conf. Phys. Nuclear-Excited Plasma Problems Nuclear-Pumped Lasers*, 1, 252, 1992.
215. Boichenko, A.M., Karelin, A.V., and Yakovlenko, S.I., A kinetic model of the XeF laser, *Laser Phys*., 5(1), 80–93, 1995.
216. Boichenko, A.M., Bonyushkin, E.K., Karelin, A.V., Lazhintsev, B.V., Lakhtikov, A.E., Morovov, A.P., and Yakovlenko, S.I., Investigation of an XeF laser pumped by gamma radiation from a nuclear explosion, *J. Quant. Electron*., 26(5), 410–412, 1996.
217. Waynant, R.W., *Appl. Phys. Lett*., 30, 234, 1977.
218. Waynant, R.W., *Kvantovaya Elektron*., 5, 1767, 1978.
219. Lisitsin, V.N., Razhev, A.M., and Chernenko, A.A., *Kvantovaya Elektron*., 5, 424, 1978.
220. Winter, N.W., Bender, C.F., and Rescigno, T.N., *J. Chem. Phys*., 67, 3122, 1977.
221. Rice, J.K., Hays, A.K., and Woodworth, J.K., *Appl. Phys. Lett*., 31, 31, 1977.
222. McDaniel, E.W., Flannery, M.R., Thomas, E.W. et al., Rep. H-78–1-Alabama, pp. 2187, 1978.
223. Borisov, V.M., Khristoforov, O.B., Kiryukhin, Yu.B. et al., High average power excimer lasers, *Proc. SPIE Int. Soc. Opt. Eng*., 3574, 56–66, 1998.
224. Fahlen, T.S., 200 W KrF gas transport laser, *IEEE J. Quant. Electron*., QE-16, 1260–1262, 1980.
225. Bergman, H.M. and Swart, P.H., High repetition rate excimer and CO_2 TEA lasers, *Proceedings of International Conference on Lasers'89*, McLean: STS Press, 80–89, 1990.
226. Borisov, V.M., Vinokhodov, A.Yu., Vodchits, V.A., Demin, A.I., El'tsov, A.V., Basting, D., Stamm, U., and Voss F., Compact 600-W KrF laser, *Quant. Electron*., 28(2), 119–122, 1998.
227. Ishchenko, V.N., Lisitsyn, V.N., and Razhev, A.M., Efficient discharge pumping XeCl laser, *Opt. Commun*., 21, 30–33, 1977
228. Borisov, V.M., Khristoforov, O.B., Kiryukhin, Yu.B. et al., Theoretical and experimental investigations of the 1 kW XeCl laser with UV preionization, *Proc. SPIE Int. Soc. Opt. Eng*., 2987, 94–105, 1997.
229. Muller-Horsche, E., Oesterling, P., and Basting, D., Highest power excimer lasers, *Proc. SPIE Int. Soc. Opt. Eng*., 1225, 142–145, 1990.

9 Atomic Iodine Lasers

Steven J. Davis, William E. McDermott, and Michael C. Heaven

CONTENTS

9.1 INTRODUCTION

9.1.1 Overview of Iodine Lasers

In this chapter, we review laser systems based on the atomic iodine $5^2P_{1/2} \rightarrow 5^2P_{3/2}$ transition that produces output in the near-infrared near 1.315 μm. To present a cogent and complete discussion of this topic within the bounds of this chapter is a challenge considering the unique features, numerous excitation methods, and many applications of atomic iodine lasers. These systems have been the focus of intense research for over 40 years. Several excitation methods have been successful in producing laser oscillation. Indeed, selective photolysis of iodine-containing compounds and energy transfer pumping from chemically and electrically produced metastable species have been successfully applied to produce high-power, high-energy laser output. The energy transfer method includes both COIL (chemical oxygen iodine

laser) [1] and AGIL (all gas-phase iodine laser) [2]. Very recently, energy transfer from electrically excited metastable oxygen has also produced positive gain [3–6] and laser [7] oscillation on the $5^2P_{1/2} \rightarrow 5^2P_{3/2}$ system, laying the groundwork for a new class of iodine lasers. These are so new that several names have been used: Electric-COIL (E-COIL), discharge oxygen iodine laser (DOIL), or electric oxygen iodine laser (EOIL). Because of the pleasing symmetry with COIL, we will use EOIL for the remainder of this chapter.

This diversity of excitation sources is unique among gas-phase atomic lasers and serves as an example of the nearly perfect radiative properties of the atomic iodine system for both pulsed and continuous wave (CW) laser applications. For example, chemical excitation within a supersonic mixing flow and pulsed photolysis has been used to produce high-power laser output.

The literature on atomic iodine lasers is rich and continues to grow especially in the case of COIL-type systems. In this chapter, we are able to provide only a relatively brief summary of some topics: historical perspective, theory of operation, excitation schemes, and some applications. Because of its rapidly growing position as a high-power gas-phase laser, we focus on the COIL system, but provide brief descriptions both of photolysis lasers and AGIL. We also present some recent important developments in the EOIL concept. These new devices may offer distinct operational advantages when fully developed.

Kasper and Pimentel [8], who reported the first observations of lasing in 1964 using a pulsed flashlamp to selectively photodissociate alkyl-iodide molecules to the $I^2P_{1/2}$ state, suggested that this photodissociation was in fact a chemical laser.

Relatively soon, in a seminal series of flow tube chemiluminescence studies, Derwent et al. [9–13] determined that atomic iodine would be an excellent candidate system for energy transfer pumping from the highly metastable singlet molecular oxygen molecule, $O_2(a^1\Delta)$. In late 1977, McDermott et al. [1] demonstrated COIL using this energy transfer scheme and state-selective chemistry to produce singlet oxygen. This was a truly significant result as it demonstrated the first short-wavelength chemical laser. Before this, the hydrogen fluoride (HF) laser that operated on multiple rovibrational lines near 2.7 μm was the shortest wavelength chemical laser. The COIL device operates on a single line at 1.3152 μm, less than half the wavelength of HF. This has many important operational advantages for high-power applications such as smaller optics to obtain comparable spot size in the far field. As we describe here, the COIL system traditionally uses two-phase (liquid/gas) chemistry to produce the singlet oxygen, and this presents some limitations both in applications and size of the COIL system.

Manke et al. [2] produced the first AGIL chemical iodine laser that uses only gaseous reactants to produce $NCl(a^1\Delta)$ that subsequently excited $I^2P_{1/2}$ via energy transfer similar to COIL. This important development may offer some additional applications for iodine lasers. Recently, Carroll et al. [3–5] and Rawlins et al. [6] have demonstrated positive small signal gain using electric discharges to produce singlet oxygen, thus eliminating the chemical generator. Most recently, Carroll et al. [7] extended their work and have demonstrated the first electrically pumped oxygen iodine laser.

In the following sections, we provide a brief review of these developments and include a touch of the history of COIL. We have attempted to strike a balance between sufficient detail about the physics and kinetics of several types of iodine lasers and a broad view of some of the applications of this important system. We begin with a review of atomic iodine laser physics followed by a discussion of the photolysis iodine lasers. Next, we discuss the COIL system in some detail as it is by far the most important class of iodine lasers. We follow with descriptions of some of the newer classes of iodine lasers, AGIL and EOIL. Finally, we present some potential and actual applications of iodine lasers.

9.2 BASIC PHYSICS OF ATOMIC IODINE LASERS

The iodine laser involves two spin orbit terms of the ground-state configuration of atomic iodine: $5^2P_{1/2}$ and $5^2P_{3/2}$. As these terms arise from the same electronic configuration, the optical transitions between them are forbidden, and the radiative lifetime of the upper level ($5^2P_{1/2}$) is about 125 ms. Because the nuclear spin of ^{127}I is 5/2, the two spin orbit terms also display hyperfine structure with the quantum states designated by F. The $^2P_{1/2}$ state has two levels: $F' = 3$ and 4 while the $^2P_{3/2}$ state has $F'' = 2$, 3, and 4. This produces six closely spaced transitions shown in Figure 9.1. Also shown in Figure 9.1 is an absorption spectrum of the six hyperfine transitions obtained with a tunable diode laser. Table 9.1 summarizes the energy levels, transition frequencies, and radiative rates for all six transitions. The $F' = 3 \rightarrow F'' = 4$ transition has the largest transition moment with a radiative rate of 5.4 s^{-1}. In COIL and AGIL, the laser output is confined to this single line, making these chemically pumped devices spectrally very pure in contrast to vibrational lasers such as HF and DF.

The small signal gain for the $(F' = 3) \rightarrow (F'' = 4)$ transition is calculable from spectroscopic constants with an appreciation of the relevant degeneracies and statistical weights of the sublevels. Figure 9.1 shows the hyperfine levels associated with the $^2P_{1/2}$ and $^2P_{3/2}$ states. Each hyperfine subcomponent is degenerate in the absence of an external magnetic field with the degeneracy given by $g = 2F + 1$. Thus, the degeneracy of the $F' = 3$ is seven and that for $F' = 4$ is nine. In general, the small signal gain $g(\nu)$ is given by the following equation:

$$g(\nu) = \sigma(\nu)[N_u - (g_u/g_l)N_l], \tag{9.1}$$

where $\sigma(\nu)$ is the stimulated emission cross section, N_u the population density of the upper laser level, N_l the population density of the lower level and g_u and g_l are the degeneracies of the upper and lower levels, respectively. We must also recognize that the populations of the $F' = 3$ and $F' = 4$ sublevels are further subdivided by the fractional populations of these two levels with respect to the rest of the hyperfine sublevels. For most applications, especially in COIL and AGIL, we consider that these levels are populated according to their statistical weights. This is a reasonable assumption considering that the energy differences are negligible

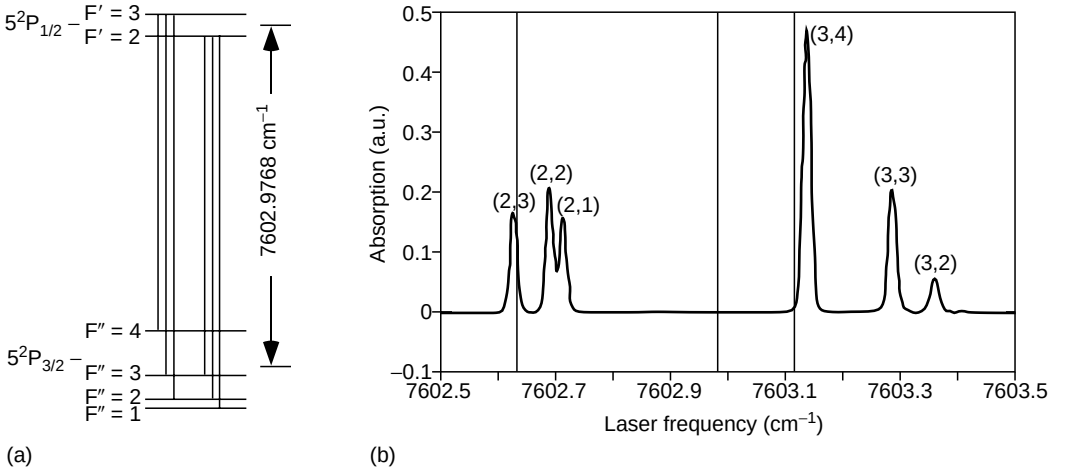

FIGURE 9.1 (a) Hyperfine transitions of atomic iodine. (b) Diode laser absorption spectrum of all six hyperfine lines in I atom $5^2P_{1/2} \leftarrow 5^2P_{3/2}$ transition.

TABLE 9.1
Hyperfine Transitions, Frequencies, and A-Coefficients for the I Atom $^2P_{1/2} \rightarrow {}^2P_{3/2}$ Transition

		Einstein A Coefficient (s^{-1})
(2,3)	7602.6201	2.4
(2,2)	7603.6858	3.0
(2,1)	7603.7104	2.3
(3,4)	7603.1385	5.0
(3,3)	7603.2793	2.1
(3,2)	7603.3449	0.6

under COIL conditions. Thus, the population density for the $F' = 3$ level is $N_u = 7/12\ [I(^2P_{1/2})]$ and that for the lower laser level $F' = 4$ is $N_l = 9/24[^2P_{3/2}]$.

For laser researchers and developers, the small signal gain at line center, $g(\nu_0)$, is a key parameter. In COIL, the laser cavity typically is at low pressure (a few Torr) and the absorption lineshape can be approximated as a Doppler-broadened (Gaussian) lineshape. The small signal gain at line center is therefore given by the following equation:

$$g(\nu_0) = 7/12(\lambda^2 A_{ul}/8\pi)(7.16 \times 10^{-7}\nu_0)(T/M)^{0.5} \times ([I^2P_{1/2}] - 0.5[^2P_{3/2}]). \tag{9.2}$$

The stimulated emission cross section at line center is defined by the term

$$\sigma(0) = 7/12(\lambda^2 A_{ul}/8\pi)(7.16 \times 10^{-7})(\nu_0)(T/M)^{0.5}. \tag{9.3}$$

At $T = 300$, the line center cross section has the value 7.5×10^{-18} cm^2. We conclude that the optical gain in COIL is relatively small. For example, the typical inversion density is $\sim 10^{15}$ cm^{-3} implying a small signal gain in the order of 1% cm^{-1}, and amplified spontaneous emission is not an issue. In contrast, photolytically pumped iodine lasers produce much higher inversion densities and one must control the amplified spontaneous emission. The low small gain of chemically pumped and electrically pumped iodine lasers proved to be a significant challenge in laser development as described below.

9.3 PHOTOLYTIC IODINE LASERS

Kasper and Pimentel [8] were the first to demonstrate an atomic iodine laser. Using a pulsed flashlamp with output covering 268 ± 50 nm to photolyze CF_3I and CH_3I, they observed single line emission at 7603 cm^{-1} from the $^2P_{1/2} \rightarrow {}^2P_{3/2}$ transition of atomic iodine. They also soon reported on follow-up kinetics experiments that demonstrated that I_2 was a significant quencher of I*, and they suggested that chemical lasers would be an interesting avenue of research for free radical reaction chemistry [14]. These observations, especially those concerning I_2 would also be relevant to the development of COIL.

In 1971, Gensel et al. [15] published an important paper on the energy storage in a photolytic iodine laser. Recognizing the long radiative lifetime of the $^2P_{1/2}$ state, they used a variable delay Q-switch to monitor the output pulse energy. They also applied an inhomogeneous magnetic field to reduce the gain and control the oscillation relaxation and amplified spontaneous emission. This work established the foundation for high-power photolytic iodine lasers.

The major processes in photolytic iodine lasers are summarized in the following equations:

$$RI + h\upsilon_{pump} \rightarrow I^* + R; \tag{9.4}$$

$$I^* \rightarrow I + h\upsilon_{laser}; \tag{9.5}$$

$$R + I + M \rightarrow RI + M; \tag{9.6}$$

$$R + R + M \rightarrow 2R + M; \tag{9.7}$$

$$I + I + M \rightarrow I_2 + M, \tag{9.8}$$

where M is a third-body collision partner, typically a noble gas.

Reaction 9.4 represents the photolytic pumping and reaction 9.5 accounts for the atomic iodine radiative emission. Reaction 9.6 through reaction 9.8 account for kinetic processes that affect the efficiency of the laser.

The earliest photolytic iodine lasers used alkyl-iodides as the fuel, and for these compounds, excitation in the ultraviolet (UV) spectral region of approximately 250–280 nm atomic iodine was produced with high yield in the $^2P_{1/2}$ state. A variety of iodine-containing compounds have been used since this first demonstration including CF_3I, CH_3I, C_3F_7I, and I_2. The molecular iodine case is distinct in that it requires pump radiation in the visible part of the spectrum (493–498 nm). In each case, quantum mechanical selection rules for radiative absorption and the correlations to the dissociation products produce $[I^*]/[I] > 0.5$, the condition for inversion.

Efficient pumping of the alkyl-iodides requires flashlamps with high blackbody plasma temperatures in the order of 20,000 K. Even then, the spectral overlap with the absorption spectra accesses may only be about 10% of the lamp energy. For a 20% efficient flashlamp, this translates to an upper limit of 2% for a photolysis iodine laser. Nevertheless, impressive power scaling has been demonstrated following the pioneering work of Kompa et al. [15] who recognized that the photolytic iodine laser had potential for producing Q-switched (~ns), high-energy pulses. A succinct review of these high-power photolytic iodine lasers is provided by Fill [16].

Collisional quenching of the $^2P_{1/2}$ level reduces the overall efficiency of the laser system, and laser developers have used bath gases that are weak quenchers such as rare gases. Fortunately, the parent iodide molecules and photo fragments are not severe quenchers. However, I_2 which can form from three-body recombination of two iodine atoms, is a very significant quencher, and removal of molecular iodine from the laser fuel especially after photolysis is required to prevent its buildup and the concomitant reduction in output energy of the laser.

The photolysis of alkyl-iodides such as CF_3I produces up to 90% of the atomic iodine products in the excited $^2P_{1/2}$ state and amplified spontaneous emission can become an issue. Collisional broadening of the I atom laser transition occurs from collisions with the bath gas. This is particularly relevant in high-power photolysis laser applications, where a master oscillator and several stages of power amplifiers are used. Typically, the oscillator is operated as a mode-locked train of pulses and one pulse is selected for amplification. Padrick and Palmer [17] provided early measurement of collisional broadening of the atomic iodine laser.

Collisional relaxation among the hyperfine levels is also important in order that all the energy can be extracted. Under the high-pressure conditions of the power amplifier, the severe broadening allows the single (3,4) laser emission from the oscillator to access the populations of all F′ levels. Relaxation among these sublevels in both the $^2P_{1/2}$ and the $^2P_{3/2}$ states is an important kinetic process in short pulse operations. These rates are not accurately known, but

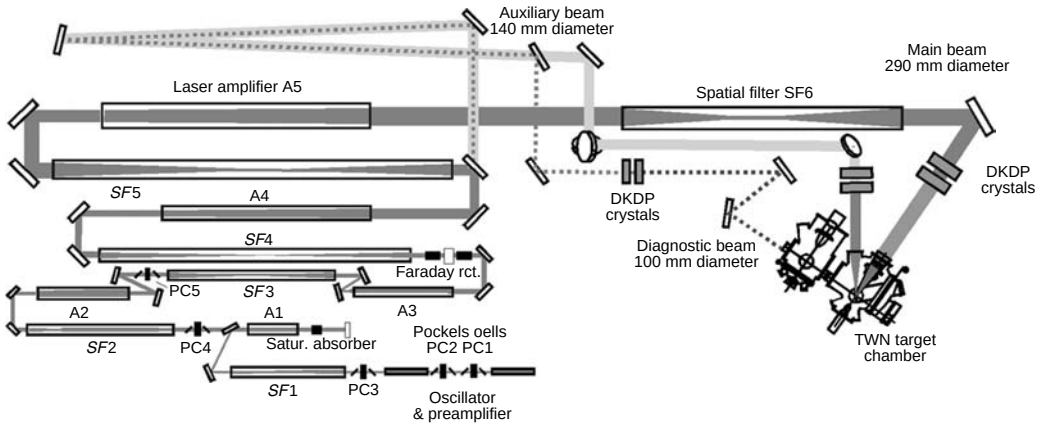

FIGURE 9.2 Block diagram of the Prague Asterix Laser System (PALS). (Courtesy of Dr. Jiri Ullschmied, PALS Deputy Director, Institute of Plasma Physics, Academy of Sciences, Czech Republic. With permission.)

theoretical calculations indicate that relaxation times among the F′ levels may be in the order of 100 ns and somewhat faster for the F″ levels.

The Asterix III laser developed at Garching, Germany, was the first truly high-power iodine laser [16]. The oscillator used 100 Torr of C_3F_7I and 400 Torr of Ar. The final power amplifier contained only 6 Torr of C_3F_7I and 3000 Torr of Ar. The Ar not only broadens the radiative transitions, but also reduces the gain at line center. A pressure of 3000 Torr of Ar will broaden each hyperfine transition to approximately 15 GHz, effectively making the system homogeneously broadened under these conditions. This reduces the peak gain by over an order of magnitude from the collision-free value of the (3,4) transition, and helps control the gain in the final amplifier and suppress amplified spontaneous emission. Asterix III produced 500 J in a pulse of approximately 1 ns. This system was further developed as Asterix IV.

Through an international agreement, the Physics Institute of the Czech Republic Academy of Sciences purchased Asterix IV. The system is now operational in Prague, and is known as the Prague Asterix Laser System (PALS). It is used for a number of experiments including XUV sources, laser ion sources, and laser-induced shock waves. Figure 9.2 shows the main elements of this system. Figure 9.3 shows a photograph of this system.

In an interesting variant of the pulsed photolysis iodine lasers, Schlie and Rathge [18] developed flowing gas systems that use CW lamps to produce continuous laser output on the (3,4) transition. These devices were developed to serve as gain probes for COIL described in a following section.

Finally, we mention another photolysis iodine laser that used I_2 as the laser fuel. Similar to the work of Schlie and Rathge [18], this was motivated by the need for a simple gain probe for the early COIL system. The I_2(B-X) absorption system correlates at infinite I atom separation to I* + I. Photodissociation of I_2(B) occurs for excitation wavelengths shorter than approximately 500 nm. Note that this satisfies the criterion for inversion in the I atom manifold $[I^*]/[I] > 0.5$. Using a pulsed dye laser to pump a sealed cell of I_2, Davis [19] observed I atom lasing for 493 nm $< \lambda_{ex} <$ 498 nm excitation. No degradation of laser output power was observed even for several thousand consecutive pulses as the I atoms recombined to form the stable I_2. While initially attractive, the efficiency was low because of unavoidable coincident absorption of pump photons to the repulsive $^1\pi_u$ that produces two ground-state iodine atoms. Indeed, this system barely reaches threshold and offers little hope for scaling to higher powers.

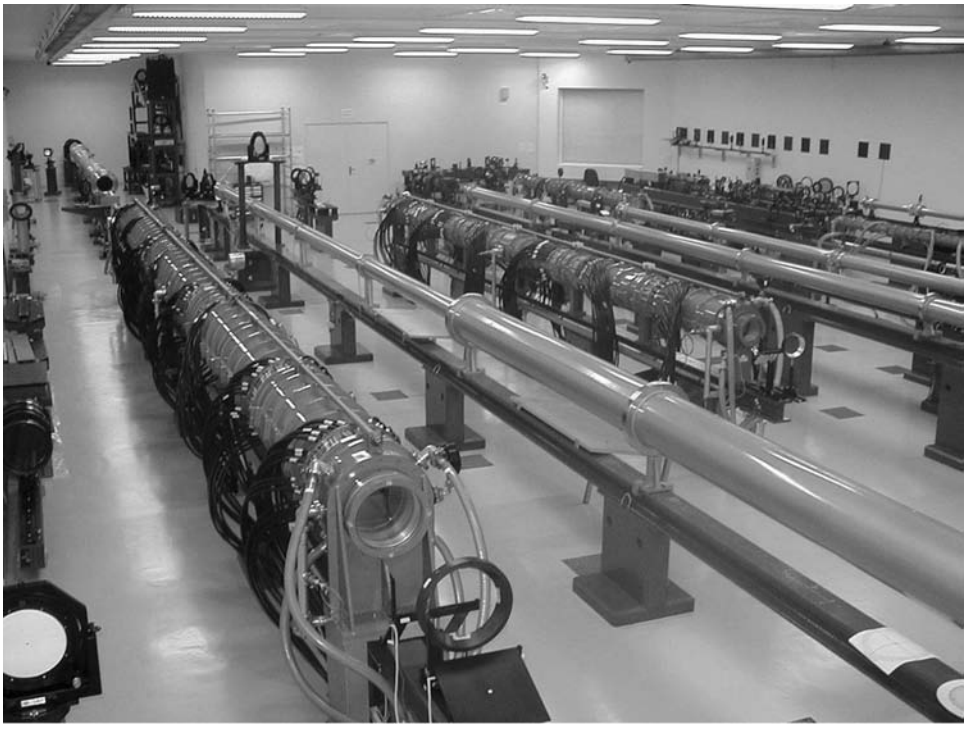

FIGURE 9.3 Photograph of Prague Asterix Laser System (PALS). (Courtesy of Dr. Jiri Ullschmied, PALS Deputy Director, Instiute of Plasma Physics, Academy of Sciences, Czech Republic. With permission.)

9.4 CHEMICAL OXYGEN IODINE LASERS

9.4.1 Introduction

Soon after the invention of photolysis laser, chemical HF lasers were demonstrated [20–24]. These are considered by many to be the first true chemical lasers. State-selective chemistry provides a path to partial inversions among the rovibrational levels within the HF(v,J) manifold.

With the success of the HF model, there was intense interest and research in the 1970s to develop an electronic transition chemical laser that operated at much shorter wavelengths than the HF system. The goal was to use state-selective chemistry to populate electronically excited product species. The seminal paper by Shuler [25] on adiabatic selection rules provides an excellent introduction to this subject. Considerable early work in this area focused on metal oxides such as BaO. In flow tube reactor work, Jones and Broida [26] observed that the $Ba + N_2O$ reaction produced strong emission from electronically excited BaO in the 500 nm spectral region. However, later detailed single-collision molecular beam studies [27,28] showed that in some sense the HF model was too accurate: the direct product was highly excited BaO(X,v), which subsequently excited BaO(A,A′) by collisional transfer through bath gas collisions with the highly excited, ground-state vibrational levels [28].

Indeed, relatively few reactions have been shown to efficiently partition energy into excited electronic states. High yields via chemical pumping have been demonstrated only for the species $O_2(a^1\Delta)$, $NF(a^1\Delta)$, and $NCl(a^1\Delta)$. Each of these isoelectronic states is metastable and strictly forbidden with respect to radiative emission to the ground $X^3\Sigma$ state because of two selection rules ($\Delta\Lambda = 0, \pm 1$ and $\Delta S = 0$).

The work of Derwent et al. [9–13] demonstrated an alternate route for producing an electronic transition chemical laser via energy transfer from a chemically excited product. Before discussing chemical production of singlet oxygen and the salient details of COIL, we discuss the basics of this unique transfer laser system. The energy levels of the lower lying levels of molecular oxygen and those of the I atom are shown in Figure 9.4. The T_0 for $O_2(a)$ lies 7882 cm^{-1} above that for the $O_2(X)$ state and is nearly resonant with the energy difference between I and I*. Indeed, I, I*, $O_2(X)$, and $O_2(a)$ rapidly establish an equilibrium

$$\begin{aligned} &O_2(a) + I \underset{k_r}{\overset{k_f}{\leftrightarrow}} O_2(X) + I^* + \Delta E \\ &\Delta E = 279\,cm^{-1}, \end{aligned} \tag{9.9}$$

where k_f and k_r are the pumping and reverse reactions, respectively.

At equilibrium, we can write

$$\begin{aligned} k_f[O_2(a)][I] &= k_r[O_2][I^*] \\ K_{eq} &= [I^*][O_2(X)]/[I][O_2(a)]. \end{aligned} \tag{9.10}$$

Rearranging this equation leads to the key expression for the ratio of excited iodine to ground-state iodine:

$$[I^*]/[I] = K_{eq}[O_2(a)]/[O_2(X)]. \tag{9.11}$$

From thermodynamic considerations, we also note that $K_{eq} = 0.75 \exp(402/T)$. Combining these two equations and invoking the $[I^*]/[I] > 0.5$ inversion requirement provides the key equation for the required singlet oxygen yield. At $T = 300$ K, $[O_2(a)]/[O_2(X)] > 0.15$. McDermott et al. [1] were the first to achieve lasing on atomic iodine using this concept. However, the story of how this success was attained involves many research groups. We provide here a short history of this work. For a more complete history of COIL including important developments worldwide, the reader is referred to Reference [29].

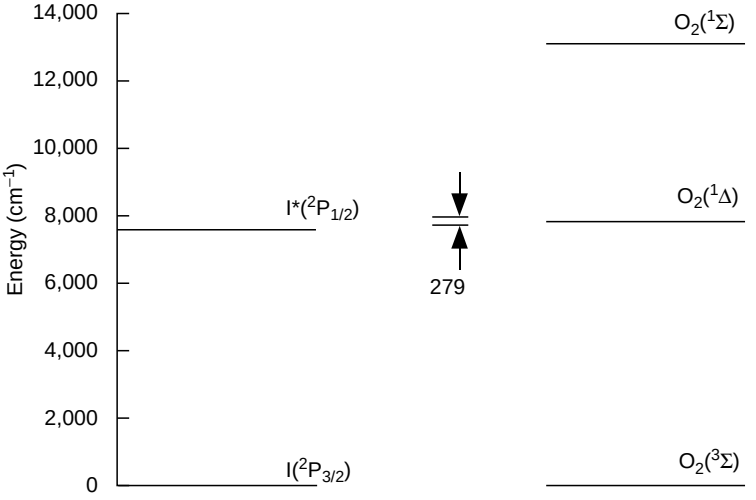

FIGURE 9.4 Energy levels of I atom and lower states of O_2.

9.4.2 History

COIL was the first electronic transition chemical laser and was initially demonstrated at the Air Force Weapons Laboratory (now the Air Force Research Laboratory) [1] in 1977. Since the energy for the laser is contained in the $O_2(a^1\Delta_g)$ and the gain in the $I(^2P_{1/2})$, scaling the laser to higher energies is simple as increased energy does not necessarily result in increased gain. In fact, megawatt-scale COILs are now tested [30]. COIL depends first on the production of $O_2(^1\Delta_g)$ in high yield.

Chemical sources of $O_2(^1\Delta_g)$ have been known for many years. Mallet [31] first reported a red glow obtained when hypochlorite solution and hydrogen peroxide were mixed. Groh [32] mentions the red chemiluminescence obtained when gaseous chlorine or bromine is added to basic hydrogen peroxide. Later, Groh and Kirriman [33] mixed gaseous chlorine with KOH and hydrogen peroxide and proposed that the red glow is from the collision of two $O_2(^1\Delta_g)$ molecules. Seigler [34] published the spectra of the hypochlorite–peroxide reaction in red at 634 nm. The spectrum of excited oxygen from the reaction of chlorine gas with basic hydrogen peroxide was published by Khan and Kasha [35].

Even though the chemical process that produced $O_2(^1\Delta_g)$ was known, the combination of oxygen and iodine came in discharge studies. The reaction of iodine and discharged oxygen was first reported by Ogryzlo et al. [36]. They observed that when iodine was added to excited oxygen, a bright yellow glow was seen. This was recognized as $I_2(B)$ state emission. They also observed a strong emission at 1.315 μm, the iodine atom $^2P_{1/2} \rightarrow {}^2P_{3/2}$ transition. The excitation of iodine was attributed to the near-resonant pumping by $O_2(^1\Delta_g)$. The iodine atoms were thought to be formed by the dissociation of molecular iodine by $O_2(^1\Sigma_u)$. As mentioned previously, Derwent et al. generated several papers [9–13]. They suggested that an inversion could be achieved on the iodine atom $^2P_{1/2} \rightarrow {}^2P_{3/2}$ transition if a sufficient $O_2(^1\Delta_g)$ fraction could be produced. Using the equilibrium constant for the energy pumping reaction, they showed that a flow containing about 15% $O_2(^1\Delta_g)$ could produce an inversion on the iodine $^2P_{1/2} \rightarrow {}^2P_{3/2}$ transition. This laser uses a pumping process that is at equilibrium and excites a two-level system terminating in the ground state as described by Equation 9.9 through Equation 9.11.

The achievement of lasing in the COIL system depended on two things: (1) the production of high amounts of $O_2(^1\Delta_g)$ and (2) the ability of $O_2(^1\Delta_g)$ to dissociate molecular iodine into iodine atoms.

9.4.3 Chemistry of Singlet Oxygen Production

The production of high amounts of $O_2(^1\Delta_g)$ was first achieved by reacting chlorine gas with a solution of H_2O_2 and a base such as NaOH. The chlorine gas diffuses into the liquid and reacts rapidly with the HO_2^- ion producing essentially 100% $O_2(^1\Delta_g)$ [37]. As the diffusion process is slow, this reaction occurs near the gas–liquid boundary allowing the $O_2(^1\Delta_g)$ to diffuse back into the gas phase. This is important since the lifetime of $O_2(^1\Delta_g)$ in water is in the order of microseconds. The overall stoichiometry of the process where M is an alkali metal ion is

$$Cl_2 + 2MOH + H_2O_2 \rightarrow O_2(a^1\Delta) + 2MCl + 2H_2O. \tag{9.12}$$

At high $O_2(^1\Delta_g)$ concentrations in the gas phase, the dominant loss is through the energy-pooling process.

$$O_2(a^1\Delta_g) + O_2(a^1\Delta_g) \rightarrow O_2(b^1\Sigma_u) + O_2(X^3\Sigma). \tag{9.13}$$

Thus, the flow from the gas–liquid generator to the laser nozzle must be rapid.

The chemical generator that produces the $O_2(^1\Delta_g)$ has taken many forms. Initial studies used a rotating wetted wall generator [38], which formed the basis for the first scalable generator, the rotating disk generator developed by Harpole et al. [39]. Although the first COIL and subsequent larger devices were powered by sparger generators, better control of the gas–liquid separation area led to the development of the jet generator by Zagidullin et al. [40]. The chemical engineering of the reaction between hydrogen peroxide and chlorine is discussed in several references [41–44]. The BHP (basic hydrogen peroxide) is usually run at temperatures near the freezing point of the mixture (−20°C) to reduce water and peroxide vapor in the effluent from the generator. Both species are known to quench $I(^2P_{1/2})$ although the observed quenching rates are too low to produce the observed power decreases in working lasers [45]. The laser can tolerate a relatively high water vapor content. The first operation of a COIL without a water vapor trap was reported by Kikuchi et al. [46] following a suggestion by Zagidullin et al. [47]. Actually, the cold traps used in the initial laser experiments [1,48] were quite inefficient and removed little of the water vapor in the flow stream.

9.4.4 Theory and Modeling of $O_2(^1\Delta_G)$ Generators

It turns out that an excellent parametric form for the generator utilization, the fraction of chlorine absorbed in the generator, is given by the kinetic rate-limited model with no depletion of the base at the gas–liquid interface. This well-stirred limit assumes that the exposure time of the liquid to the chlorine gas is short compared with the diffusion time of hydroperoxy ions to the surface of the liquid. In this case, the utilization is given by

$$\eta = 1 - e^{\frac{t}{\tau_g}}, \tag{9.14}$$

where η is the utilization, t the residence time in generator(s), and τ_g is the generator e-folding time(s).

The characteristic e-folding time of the generator is given by

$$\tau_g = \frac{1}{K_c a}, \tag{9.15}$$

where K_c is the mass transfer coefficient (cm/s) and a is the specific surface area (cm^{-1}).

The mass transfer coefficient can be decomposed into a gas-side resistance and a chemical resistance.

$$\frac{1}{K_c} = \frac{1}{k_g} + \frac{m_H}{k_c}, \tag{9.16}$$

where k_g is the gas-phase resistance and k_c is the chemical (reaction rate) resistance.

The gas-phase resistance, a measure of how fast the chlorine can diffuse from the bulk flow to the liquid surface, is a function only of pressure (and geometry). Thus, the gas-phase contribution can be evaluated by plotting the overall resistance versus pressure:

$$\begin{aligned} k_g &= \text{gas-phase resistance} \\ &= \frac{D_h}{S_h}\,\frac{1}{D_g^0 P}, \end{aligned} \tag{9.17}$$

where $\frac{D_h}{S_h}$ is the hydraulic diameter/Sherwood Number, D_g^0 is the diffusivity of Cl_2 at 1 Torr, and P is the total pressure (Torr).

Likewise, the chemical resistance depends only on the liquid-side properties.

$$k_c = \text{chemical (reaction rate) resistance} = \sqrt{k_1 \left[HO_2^-\right] D_{HO_2^-}}, \tag{9.18}$$

where k_1 is the rate of the reaction of Cl_2 with HO_2^-, $[HO_2^-]$ is the concentration of the base, $D_{HO_2^-}$ is the diffusion coefficient of HO_2^- in BHP, and m_H is the dimensionless Henry's Law coefficient.

In a typical jet generator, the overall mass transfer coefficient is about 50 cm/s. The chemical resistance is about 80 cm/s and the gas-side transfer contributes about 130 cm/s. By convention, the specific surface area (liquid surface area per unit gas volume) is taken as the geometric surface area per unit volume and depends on the spacing and diameter of the liquid phase. Jet generators have specific surface areas from 5 to 10 cm^{-1}. The higher the product $K_c a$, the shorter is the time that chlorine has to remain in the generator to reach a given utilization.

Of course, any desired utilization could be obtained whatever the $^1\Delta_g$ of the generator simply by letting the residence time increase. Unfortunately, $O_2(^1\Delta_g)$ is quenched in the generator; primarily through the pooling reaction 9.13.

Thus, construction of an efficient generator is a balance between efficient chlorine utilization and short residence times. For $O_2(^1\Delta_g)$ decay in a well-stirred reactor, Copeland [49] has shown that the yield (the ratio of $O_2(^1\Delta_g)$ to total oxygen) can be related to the utilization and the pooling rate k_p by

$$\frac{1}{Y} = \frac{1}{Y_0} + f(\eta) k_p p_{O_2} t, \tag{9.19}$$

where Y is the yield exiting the generator, Y_0 is the "detachment" yield (yield exiting the solution), p_{O_2} is the partial pressure of oxygen (Torr), t is the residence time in the generator (s), k_p is the pooling rate ($Torr^{-1}\ s^{-1}$), $f(\eta) = \frac{1}{\eta^2} + \frac{\left(1+\frac{\eta}{2}\right)}{(\eta \mathrm{Ln}(1-\eta))}$, and η is the chlorine utilization.

The longer the gas stays in the generator, the greater the loss of $O_2(^1\Delta_g)$. The performance of a chemical generator increases as τ_g increases. This expression can be used to calculate the optimum generator residence time for a particular generator (characterized by its experimental τ_g). A number of effects have not been included in the simple analysis given here, such as the behavior at low base concentrations and the effect of base depletion at the gas–liquid interface. The first can be evaluated experimentally by running the generator at a number of initial concentrations. The second effect is more subtle and depends on the relative velocity vectors of the gas and liquid streams. Without going into detail, it can be shown that base depletion effects are greatest for cross-flow devices, less for coflow, and least for counterflow devices.

The transport of oxygen from the generator is governed by the loss of $O_2(^1\Delta_g)$ because of the pooling reaction 9.13. The decrease in yield is given by Equation 9.19 with $f(\eta) = 1$. It is this process that results in the increase of the laser power with decrease in the pressure–residence time product.

9.4.5 Iodine Dissociation Kinetics

After nearly 30 years of study, a great deal is known about the kinetics that occur within COIL systems [50–65]. However, the mechanism by which I_2 is dissociated by $O_2(a^1\Delta)$ remains poorly understood [66–74]. This represents an important gap in our knowledge as

the dissociation process significantly affects the efficiency of the laser. There are two mechanisms by which this occurs. First, it is known from empirical studies that an average of four to six $O_2(a^1\Delta)$ molecules are needed to dissociate one I_2 molecule [61,75]. Hence, the dissociation process consumes a significant amount of energy [76–80]. Second, the time-scale of the dissociation process influences energy extraction as it determines the downstream position at which the maximum concentration of I* occurs. The rate of dissociation depends on concentration ratios, mixing dynamics, and total pressure. For example, it was recently discovered (by empirical experimentation) that increasing the number density of I_2 at the point of injection improves the overall efficiency of the laser. Rybalkin et al. [81] reported an increase in the efficiency of their COIL system from 30% to 40% when the I_2 density was increased by using lower injection temperatures. At present, our ability to design new types of mixing nozzles and develop systems that operate at higher pressures is limited, in part, by our incomplete knowledge of the dissociation kinetics.

The standard model for the dissociation of I_2 by $O_2(a)$ involves a short sequence of energy transfer reactions [58–60]. The process is initiated by the slow reaction

$$O_2(a) + I_2 \rightarrow O_2(X) + I_2^{\dagger}, \tag{9.20}$$

where $I_2^{\dagger}$ is assumed to be highly vibrationally excited $I_2(X)$ ($v > 23$). A second collision with $O_2(a)$ dissociates $I_2^{\dagger}$,

$$O_2(a) + I_2^{\dagger} \rightarrow O_2(X) + 2I. \tag{9.21}$$

Excitation of I* via the reaction $O_2(a) + I \rightarrow O_2(X) + I^*$ then acts as a chain-branching step [62]. I* rapidly transfers its energy to I_2

$$I^* + I_2 \rightarrow I + I_2^{\dagger}, \tag{9.22}$$

which greatly accelerates the dissociation process [65]. In this model, the number of $O_2(a)$ molecules required to dissociate one I_2 molecule depends on the competition between excitation and physical quenching of $I_2^{\dagger}$. The primary quenching agents are H_2O and $O_2(X)$ [62].

Kinetic measurements performed in recent years have revealed serious problems with this mechanism. The assumption that $I_2^{\dagger}$ is vibrationally excited $I_2(X)$ was examined in a series of state-resolved energy transfer measurements [69,82]. It was found that the rate constants for vibrational relaxation of I_2 by H_2O, O_2, and Ar were all quite similar, and that the rate constant for H_2O was a factor 60 times smaller than the accepted rate constant for the deactivation of $I_2^{\dagger}$ by H_2O. The initiation reaction is also in question. A rate constant for $O_2(a) + I_2 \rightarrow O_2(X) + I_2^{\dagger}$ of $k_1 = 5 \times 10^{-15}$ cm^3 s^{-1} had been estimated from modeling of I_2 dissociation rates measured in flow tube experiments [62]. Recently, Han et al. [71] attempted a direct measurement of the rate constant for the quenching of $O_2(a)$ by I_2 using a pulsed laser excitation technique. The quenching process was undetectably slow, establishing an upper bound for the rate constant of $< 5 \times 10^{-16}$ cm^3 s^{-1}. This is much too slow for reaction 9.20 to be viable as the initiation step.

Derwent and Thrush [52,53] advanced the first quantitative model of the dissociation process. They suggested that the key reaction was

$$O_2(b) + I_2 \rightarrow O_2(X) + 2I, \tag{9.23}$$

with $O_2(b)$ generated by the pooling processes

$$O_2(a) + O_2(a) \rightarrow O_2(b) + O_2(X) \tag{9.24}$$

and

$$O_2(a) + I^* \rightarrow O_2(b) + I. \tag{9.25}$$

This mechanism could reproduce the dissociation kinetics provided that the rate constant for reaction 9.23 was high (around 2×10^{-10} cm^3 s^{-1}). However, the model was dismissed when Houston et al. [63,64] found that the rate constant for quenching of $O_2(b)$ by I_2 was no greater than 7×10^{-11} cm^3 s^{-1}. Two values for this parameter were obtained, and it was argued that the lower value (4×10^{-11} cm^3 s^{-1}) was the more reliable. Muller et al. [64] examined the branching fraction for dissociation of I_2 by $O_2(b)$. An upper bound of <0.2 was estimated, yielding a rate constant for reaction 9.23 of $<8 \times 10^{-12}$ cm^3 s^{-1}.

Although it is clear that $O_2(b)$ is not the primary dissociation agent, a reinvestigation of reaction 9.23 was prompted by the discovery that reaction 9.20 is not fast enough to be the initiation step [71]. This raised the question of whether $O_2(b) + I_2$ could perform this function. Additional motivation for revisiting reaction 9.23 was provided by the fact that nonchemical singlet oxygen generators (those using discharge and optical excitation) provide higher yields of $O_2(b)$. Han et al. [71] remeasured the rate constant for quenching of $O_2(b)$ by I_2 and determined the branching fraction for the channel

$$O_2(b) + I_2 \rightarrow O_2(a) + I_2. \tag{9.26}$$

They obtained a rate constant of 5.8×10^{-11} cm^3 s^{-1} (closer to the higher value of Houston et al. [63,64]) and a branching fraction of 0.4. Transient absorption spectroscopy of ground-state I atoms was used to investigate the branching fraction for reaction 9.23 [70]. A value in excess of 0.5 was obtained, indicating that the rate constant is approximately 3×10^{-11} cm^3 s^{-1}. In principle, this is fast enough for $O_2(b)$ to be significant in the dissociation process. However, recent experiments by Azyazov and Heaven [83] reasserts that $O_2(b)$ is not important in conventional COIL systems. The rate for I_2 dissociation was observed in flows of singlet oxygen obtained from a chemical generator. N_2 and CO_2 were used alternately as the carrier gas. This provided a simple way of modulating the $O_2(b)$ concentration as CO_2 is a relatively fast quencher ($k = 3 \times 10^{-13}$ cm^3 s^{-1}) whereas quenching by N_2 is negligible. Comparing data for the two carrier flows, it was found that reducing the $O_2(b)$ concentration by almost an order of magnitude had a minimal effect on the I_2 dissociation rate.

In parallel with the efforts to evaluate the standard dissociation model, there have been investigations of alternative mechanisms. The most promising assume that $I_2^\dagger$ is electronically excited I_2 [54,66,67,72,74,84]. This possibility was originally suggested by Arnold et al. [50] who were the first to observe dissociation of I_2 by $O_2(a)$. The problem with this assignment is that the lowest energy excited state of I_2, $A'^3\Pi(2u)$, lies 10042 cm^{-1} above the ground state. Consequently, it cannot be excited by energy transfer from $O_2(a)$ or I*. Bacis et al. [66–68] considered models where vibrationally excited I_2 was promoted to the $A'^3\Pi(2u)$ and $A^3\Pi(1u)$ states by collisions with $O_2(a)$. This scheme was suggested by the results from spectroscopic studies of flowing $O_2(a)/I_2$ mixtures. $I_2(A'/A)$ was detected in these flows and the $I_2(X)$ vibrational distribution was consistent with population loss from $\nu'' > 10$ levels because of near-resonant excitation to A'/A. Tellinghuisen and Phillips [85] and Komissarov et al. [84] measured quenching rate constants for $I_2(A')$. These were

found to be in better agreement with the trends for $I_2^{\dagger}$ deactivation than the $I_2(X)$ vibrational relaxation rate constants.

Lilenfeld [54] noted that vibrationally excited $O_2(a)$ could excite $I_2(X, \nu = 0)$ to the A′ state. Using electron spin resonance (ESR) detection, he was able to show that vibrationally excited $O_2(X)$ was present in $O_2(a)/I_2$ flows, and he argued that vibrational energy would be readily transferred from $O_2(X)$ to $O_2(a)$. More recently, Azyazov et al. [72–74,86] have shown that chemical singlet oxygen generators produce appreciable concentrations of vibrationally excited O_2. From a quantitative analysis of the dimole emission spectrum, they were able to show that approximately 2% of the $O_2(a)$ was vibrationally excited. Azyazov et al. [73] traced the vibrational excitation back to the $O_2(a)$ energy-pooling process (reaction 9.24), which has a branching fraction of 64% for production of $O_2(b, \nu = 2)$. Vibrational excitation is then transferred to $O_2(a)$ and $O_2(X)$ via collisional exchange. The yield of vibrationally excited O_2 was dramatically increased when I_2 was added to the flow [74]. Because of rapid vibrational exchange, it is likely that this population distribution is also valid for a and X states. Azyazov and Heaven [83] has subsequently developed a kinetic model for the dissociation that is centered on the excitation of $I_2(A'/A)$ by vibrationally excited $O_2(a)$.

It has been estimated that the power of COIL systems could be increased by as much as 25% if the loss of energy in the I_2 dissociation process were avoided [78,87,88]. This could be achieved by dissociating the I_2 before mixing with the singlet oxygen. Two methods for injecting atomic iodine are currently being investigated. The first involves using electrical or microwave discharges to dissociate the I_2. Wakazono et al. [76] reported that the power from their subsonic COIL was increased by a factor of two when a discharge was used for dissociation. However, Endo et al. [87] found that the advantages of I atom injection were more difficult to realize in a supersonic device. Injection in the subsonic region of the flow actually reduced the efficiency of the laser. This occurred because the I atoms facilitated quenching of $O_2(a)$ by H_2O. A 9% power increase was seen with transsonic injection. Problems with heat transfer and mixing limited the enhancement [87]. Recombination of the I atoms is another problem that is difficult to avoid in discharge systems. The second scheme for injecting I atoms uses chemical production [78–80,88–91]. To date the reactions

$$F + HI \rightarrow HF + I \tag{9.27}$$

and

$$Cl + HI \rightarrow HCl + I \tag{9.28}$$

have been examined. The F or Cl atoms were derived from the reactions

$$F_2 + NO \rightarrow F + FNO \tag{9.29}$$

and

$$ClO_2 + 2NO \rightarrow Cl + 2NO. \tag{9.30}$$

While chemical generation of I atoms by both schemes has been demonstrated, a kinetic modeling study indicated that the Cl atom system would be more favorable [78]. Spalek et al. [88] have operated a COIL system using reaction 9.28 as the source of I atoms. They achieved a chemical efficiency of 12.7%, which is encouraging. Efforts to optimize the chemistry are in progress.

9.4.6 Laser Power

Dependence of laser power on the various input parameters are generally tracked using the "heuristic" equation originally proposed by Hon et al. [92]. The formulation by Copeland et al. [49] is the most straightforward.

$$P(\text{kW}) = 91.0\dot{m}_{\text{Cl}_2}\eta\delta_{\text{geo}}\delta_{\text{m}}(Y_{\text{NIP}} - Y_{\text{d}} - Y_{\text{s}}), \tag{9.31}$$

where P(kW) is the power in kW, $\dot{m}_{\text{Cl}_2}$ is the chlorine flow rate (moles/s), η is the chlorine utilization, δ_{geo} is the geometric loss, δ_{m} is the resonator loss $= \frac{T}{\text{Ln}(R)}$, Y_{NIP} is the yield at nozzle inlet, Y_{d} is the yield loss to dissociation of I_2, and Y_{s} is the yield at end of the mode.

The leading term, $91.0\dot{m}_{\text{Cl}_2}\eta$, is the maximum amount of power that could be extracted from the laser flow. The ratio of the laser power divided by $91.0\dot{m}_{\text{Cl}_2}\eta$ is called the chemical efficiency and is the yield of $O_2(^1\Delta)$ converted into (iodine) laser photons. Geometric losses account for the fraction of the flow not interrogated by the resonator. The yield loss to dissociation is often written as

$$Y_{\text{d}} = N\frac{x_{\text{I}_2}}{x_{\text{O}_2}}, \tag{9.32}$$

where x_{I_2} is the mole fraction of iodine and x_{O_2} is that of oxygen.

The parameter N is the number of $O_2(^1\Delta)$ molecules required to dissociate and iodine molecular ranges between 5 and 10. This is a relatively small loss as the iodine to oxygen ratio in most COILs is in the order of 1%. The yield at the end of the mode accounts for the saturation efficiency of the resonator. The equilibrium constant in reaction 9.33 is for the pumping reaction 9.11

$$Y_{\text{s}} = \frac{(\xi + 1)}{[(1 - K(T)) + \xi(1 + 2K(T))]}, \tag{9.33}$$

where Y_{s} is the yield at end of mode, $K(T)$ is the equilibrium constant, $\xi = \frac{g_0}{g_{\text{thr}}}$ is the ratio of unsaturated gain to threshold gain, $g_0 = \sigma N_{\text{I}_2}$, σ is the gain cross section (cm^2), and N_{I_2} is the iodine density in cavity (cm^{-3}). A more detailed description of the extraction efficiency in COIL is given by Barmashenko and Rosenwaks [93].

9.4.7 Novel COIL Devices

There are numerous COIL devices described in the literature. Figure 9.5 shows the elements of a typical supersonic COIL: SOG, transition regime, I_2 injection, and cavity. A photo of the first COIL device is shown in Figure 9.6. The SOG for this device is shown in Figure 9.7.

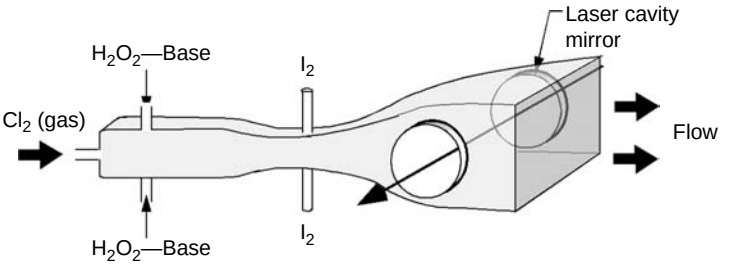

FIGURE 9.5 Elements of a typical chemical oxygen iodine laser (COIL) device.

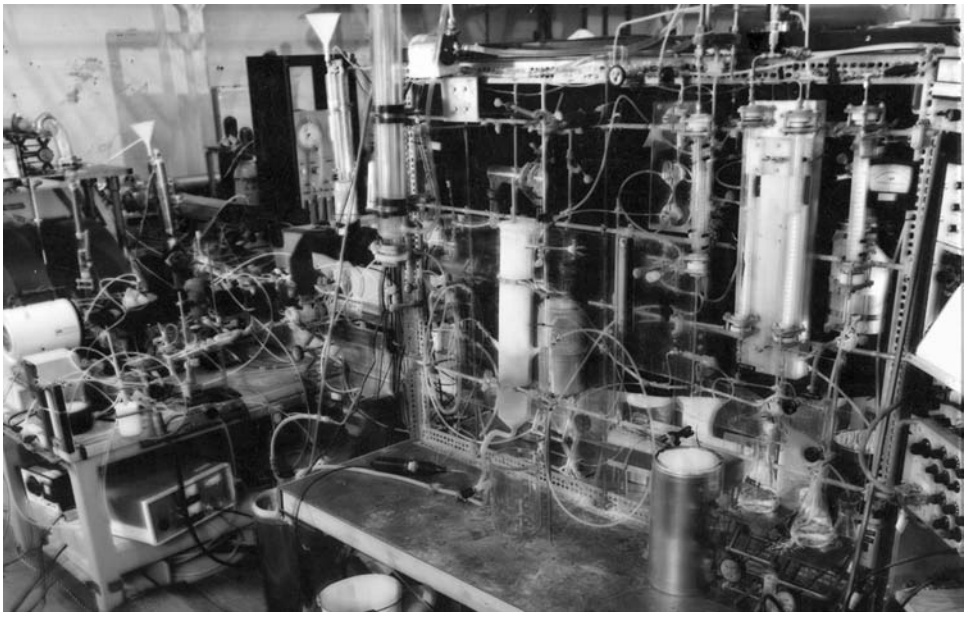

FIGURE 9.6 Photograph of world's first chemical oxygen iodine laser (COIL) device.

Tabulations of device performance can be found in References [94,95]. The development of higher-efficiency COIL devices has been an active area of research. Endo et al. [96] at Tokai University reported an efficiency of 32.9% using a novel "x-wing" nozzle to produce vortices and enhance mixing in the supersonic flow. They also precooled nitrogen to assist the gas-

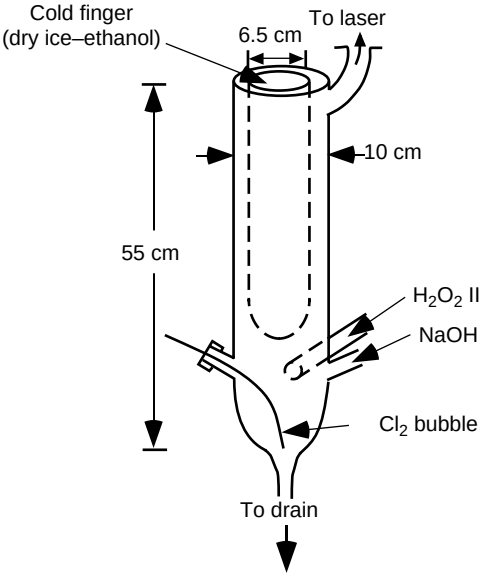

FIGURE 9.7 The first oxygen generator to power a laser. (Reproduced with permission of the American Institute of Physics.)

dynamic cooling through the nozzle. Rybalkin et al. [97] at Ben Gurion University used supersonic I_2 injection in a small-scale COIL system and measured a maximum efficiency of 32.7%. Most recently, the Ben Gurion group [98] has reported efficiencies as high as 40% obtained by decreasing the temperature of the secondary flow. They argue that this reduced the mass flow of the molecular iodine injected into the cavity and requires less singlet molecular oxygen to dissociate the I_2, leaving more singlet oxygen for laser power. It is fair to assume that production of higher-efficiency COILs will remain an active area of research because of the obvious advantages in system weight that may result. Chemical efficiencies as high as 41% have been reported by Yoshida et al. [99,100] for a subsonic device at low power and 30% for a supersonic laser at the 20 kW level by McDermott et al. [42]. A compact 2 kW laser operating at 27% efficiency was demonstrated by Helms et al. [101]. Subsonic devices at high power have been recently reinvestigated as a way to reduce pumping requirements [102].

Several investigators have produced pulsed COILs. At the Air Force Research Laboratory, the system was switched on and off with a magnetic field [103,104]. They used a high magnetic field (~1 kG) to split the magnetic sublevels of the hyperfine structure in the iodine atom manifold. With an external magnetic field, one can "tune" the gain of the hyperfine levels so that the (3,4) transition is not the strongest line.

The use of molecular iodine as the fuel in COIL presents some additional practical difficulties and constraints. The dissociation begins promptly on adding I_2 to a flow of singlet molecular oxygen, and as soon as atomic iodine is produced, the pumping and the reverse reactions begin. Any quenching of the atomic iodine leads to depletion of singlet oxygen through the forward pumping reaction. This makes it impractical to inject the molecular iodine into the subsonic flow very far upstream of the supersonic region because of excess consumption of singlet oxygen. A typical COIL nozzle element is shown in Figure 9.8. To produce a spatially uniform gain medium, a requirement for a good output beam profile, the iodine must be rapidly and efficiently mixed into the transsonic or supersonic regions of

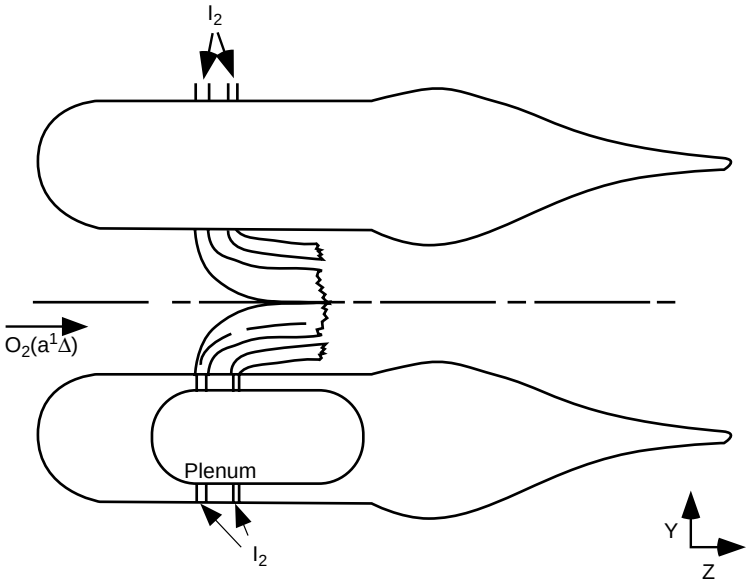

FIGURE 9.8 Typical chemical oxygen iodine laser (COIL) nozzle. Subsonic I_2 injection is shown.

the flow. This has forced COIL researchers to develop small-scale mixing nozzles to inject the I_2 into either the transsonic or supersonic flow.

It would be more advantageous if the iodine fuel could be premixed into the singlet oxygen stream. Yuryshev et al. [105–112] have demonstrated an interesting hybrid iodine laser that uses both photolysis of CF_3I and chemically produced singlet molecular oxygen to pump the photolysis I atom product. They have studied this system as a surrogate, laboratory bench device for a high-energy COIL. The CF_3I and $O_2(a)$ can be premixed, then the mixture photolyzed with a high-energy flashlamp. They have obtained over 2 J output with a peak power of 250 kW.

Humphreys et al. [113] at the Air Force Research Laboratory have demonstrated some interesting variations of COIL technology. For example, they used a KTP crystal to perform extracavity frequency doubling of a CW COIL, and produced over 600 W output at a radiation of 657.5 nm. This demonstrated a method for producing visible output from a chemical laser. Baba et al. [114] have demonstrated intracavity doubling of a COIL.

9.5 COIL DIAGNOSTICS

There has been a parallel development of COIL and diagnostics to probe key species and parameters. Indeed, the search for electronic transition chemical lasers including COIL benefited from the nearly simultaneous development of sensitive optical diagnostics that targeted important species and parameters. Chemiluminescence methods were among the first diagnostics for COIL and were skillfully applied by Derwent et al. [9–13] in their pioneering work that led to the prediction that a COIL could be developed. Later, chemiluminescence methods were used to monitor the number densities of both $O_2(a)$ and $I^2P_{1/2}$ in early laser development research. Indeed, the first successful COIL demonstration used the ratio of the chemiluminescence intensity emitted along the optical axis to that emitted from the side as a monitor for stimulated emission and this led to adjusting conditions for laser oscillation.

Tunable, room temperature diode laser–based diagnostics have been developed for most of the important species in COIL and also for translational temperature and small signal gain. In Table 9.2, we indicate target species or parameters, spectral features, and relevant wavelengths for these diagnostics.

Typically, fiber optic cables are used to couple the probe laser to the laser device at selected locations. Small, solid-state detectors are used to collect the transmitted diode laser beam. By scanning the narrowband diode laser over an entire absorption line, one can record line shapes and calculate the number density of the absorbing species.

The absorption line shapes can also be used to determine the temperature of the medium along the line of sight of the measurement by determining the Gaussian component of the

TABLE 9.2
Characteristics of Diode Laser–Based Chemical Oxygen Iodine Laser (COIL) Diagnostics

Species or Parameter	Spectral Feature	Wavelength (μm)
Water vapor	Combination band	1.39
Oxygen (singlet oxygen yield)	O_2(b-X) system	0.76
Atomic iodine	$^2P_{1/2} \leftarrow {}^2P_{3/2}$ transition	1.31
Temperature	Doppler width of I atom absorption line	1.31

total line shape. Typically, absorption line shapes are described by a Voigt profile that is a convolution of a Gaussian (Doppler broadening) and a Lorentzian (Collisional broadening).

A fit to a Voigt profile provides the Gaussian linewidth ($\Delta\nu_G$) from which the temperature can be determined using the following equation:

$$T = 1.95 \times 10^{12} (\Delta\nu_G)^2 M/\nu_0^2, \tag{9.34}$$

where M is the mass of the species and ν_0 is the center line frequency of the transition. Knowledge of the collisional broadening coefficients for the various gas phase species in COIL is valuable for extracting more accurate temperatures as one can restrict the two-parameter Voigt fit to only determining the Gaussian component. Davis et al. [115,116] have previously published broadening coefficients for most of the major components in COIL systems for all three sensors: oxygen, water vapor, and atomic iodine. Consequently, one can use the recorded line shapes to determine the translational temperature in either the SOG or the laser cavity.

Figure 9.1 illustrates the excellent spectral resolution provided by these diagnostic systems. The spectrum shows an absorption spectrum from the atomic iodine $^2P_{1/2} \rightarrow {}^2P_{3/2}$ transition obtained in a heated cell containing I and I_2. All six hyperfine components are clearly resolved. Spatial profiles of the small signal gain provide key insight into iodine injector performance. These diagnostics have also recently been used to guide the development of new iodine lasers: AGIL and EOIL.

9.6 SINGLET OXYGEN YIELD

The yield of singlet oxygen is the key parameter in assessing any SOG. Chemiluminescence methods can determine this parameter using sensitive near-infrared (IR) detectors to measure the intensity of the $O_2(a \rightarrow X)$ system near 1.27 μm. However, absolute radiometric calibrations are difficult for this weak emitter, especially for the relatively large volumes of most COIL devices. Allen et al. [117] developed a diode laser–based system that used 762 nm radiation to probe the $O_2(b - X)$ system and determine the concentration of the ground state of O_2 produced by a SOG. Simultaneous measurement of the chlorine flow rate entering the SOG and assuming that each chlorine molecule produces one oxygen molecule (either an $O_2(a)$ or an $O_2(X)$) allows one to measure the yield. This method has been successfully applied to a variety of SOGs including both disk and jet generators. One can also infer "*n*," the number of singlet oxygen molecules consumed in dissociating the molecular iodine.

Several other methods also have been used to determine the yield. Lilenfeld et al. [118] used ESR to determine the yield of both a microwave source and a chemical generator. While quite accurate, ESR is not a practical diagnostic for COIL. Gylys and Rubin [119] used pulsed Raman Scattering to determine the populations of both $O_2(a)$ and $O_2(X)$ in a chemical generator, and this method is also further developed. Rawlins et al. [120–122] have also recently described a novel method that measures [I*]/[I] and temperature. The yield is then calculated from the equilibrium (Equation 9.11). Williams et al. [123] have used intracavity methods and a diode laser to measure the absorption spectrum of the molecular oxygen Noxon bands ($O_2(b) \leftarrow O_2(a)$). The absorption line strength of this transition has not been measured, but has been calculated by Yarkony et al. [123]. This method may also hold promise as an alternate singlet oxygen diagnostic. Frolov et al. [124] have also recently reported a similar Noxon band approach for measuring $[(O_2^1\Delta)]$.

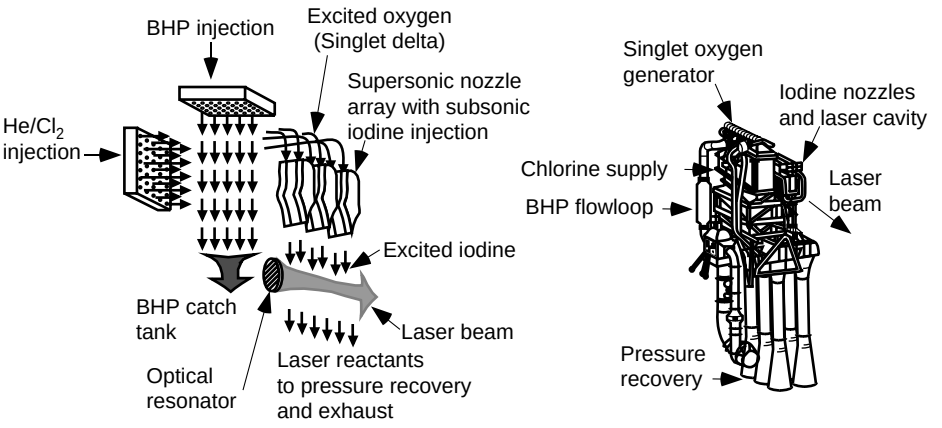

FIGURE 9.9 Schematic of AirBorne Laser (ABL) chemical oxygen iodine laser (COIL) module. (Reproduced with permission of the International Society of Optical Engineering.)

9.6.1 Applications

COILs have been proposed for use in material processing [125–160], for decommissioning of nuclear reactors [161–168], as a laser fusion driver [169–173], and for various defense applications [30,174]. As COIL has demonstrated spectrally pure, high-power output with good beam quality, it offers advantages for several military and commercial applications. COIL was selected as the high-power laser for the AirBorne Laser (ABL) system that is developed by the US Missile Defense Agency. A schematic of the ABL COIL is shown in Figure 9.9.

The COIL system also has been developed for use in materials processing, such as welding and cutting. Japanese researchers have led these efforts and have aggressively developed COIL to mature systems. Figure 9.10 shows a 1 kW COIL welder developed by Kawasaki Heavy Industry. Other potential applications include decommissioning and dismantlement of nuclear power reactors and a laser fusion driver. There has also been interest in using a portable COIL for hole drilling for mining applications.

9.7 THE ALL GAS-PHASE IODINE LASER

9.7.1 Introduction

The attributes of high output power and excellent beam quality have made COIL one of the most important high-energy laser systems. While COIL offers many advantages, the chemical production of the singlet oxygen requires two-phase (liquid and gas) chemistry.

As we described earlier, the NCl(a) state can also be produced chemically, and it provides an alternate source for an atomic iodine transfer laser. The energy level diagram for the NCl(a)/I system is shown in Figure 9.11. The energy of NCl(a) is approximately 1600 cm^{-1} higher that that for $O_2(a)$. Consequently, there is no backward reaction and the population ratio [I*]/[I] is governed by the pumping rate and the quenching rates of the reactants in the system. This is distinct from COIL where the [I*]/[I] ratio is driven by the ratio of $[O_2(a)]/[O_2(X)]$. One practical result of this difference is that in AGIL, the laser is less sensitive to temperature.

FIGURE 9.10 Photo of Kawasaki Heavy Industry's chemical oxygen iodine laser (COIL) welder. (Courtesy of Dr. Fumio Wani, Kawasaki Heavy Industry, Gifu, Japan. With permission.)

9.7.2 Demonstration of I Atom Inversion and Laser Oscillation

In 1992, Yang et al. [175] produced the first definitive evidence for the potential of an atomic iodine laser transfer laser pumped by NCl(a). The NCl(a) was produced by the reaction sequence listed in Equation 9.36 through Equation 9.40:

$$F_2/He \xrightarrow{\text{discharge}} F,F_2, \tag{9.35}$$

$$F + DCl \rightarrow DF + Cl, \tag{9.36}$$

$$Cl + ICl \rightarrow Cl_2 + I, \tag{9.37}$$

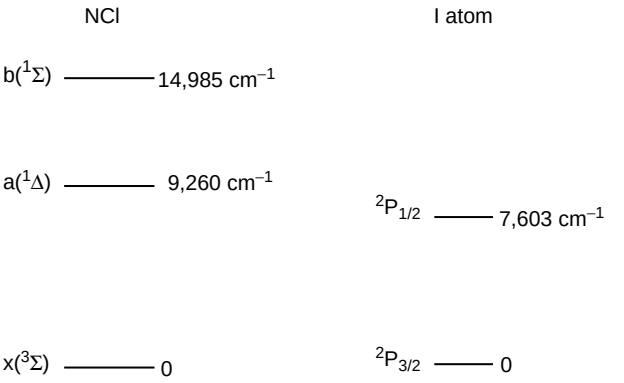

FIGURE 9.11 Energy level diagram for NCl(a) → I atom transfer laser.

$$Cl + HN_3 \rightarrow HCl + N_3, \tag{9.38}$$

$$Cl + N_3 \rightarrow NCl(a) + N_2, \tag{9.39}$$

$$NCl(a) + I \rightarrow I^* + NCl(X). \tag{9.40}$$

Ray and Coombe [176] demonstrated the first NCl/I laser using photolytic production of NCl(a) and I. While photolytic production of NCl(a) is not practical as a laser system, these results proved the NCl(a)/I laser concept.

Subsequent to these promising results, researchers at the Air Force Research Laboratory, Kirtland AFB [177] measured small signal gain on the $F' = 3 \rightarrow F'' = 4$ line of the atomic iodine $^2P_{1/2} \rightarrow {}^2P_{3/2}$ transition at 1.3152 μm with the chemistry of reaction 9.36 through reaction 9.40, but with HI as the iodine source. They used a tunable diode laser to probe this transition directly. In follow-up experiments, they demonstrated laser oscillation and recently reported output powers exceeding 10 W [178]. These important results indicate that a scalable AGIL device may be possible.

As an alternate NCl(a) source, Coombe et al. [179] developed an amine-based chemistry for producing NCl(a) that may offer some advantages over the azide-based process described earlier.

$$NCl_3 + H \rightarrow NCl_2 + HCl, \tag{9.41}$$

$$NCl_2 + H \rightarrow NCl(a) + HCl. \tag{9.42}$$

This reaction sequence is similar to the $NF_2 + H$ chemistry that has been previously shown to produce high concentrations of NF(a). McDermott et al. [180] and Hunter et al. [181] have both developed flow reactors and both groups are attempting to demonstrate positive gain on this system as of this writing.

From the perspective of chemical kinetics, the key issues for AGIL are associated with the energy storage capabilities of NCl(a). As compared with $O_2(a)$, this metastable has a far shorter radiative lifetime [182–184] (2 s versus 74 min) and is more prone to quenching by both physical and chemical processes [185–193]. Hence, transport loss is a more severe problem for NCl(a)-driven lasers. Good progress has been made in characterizing the kinetics of the system that uses HN_3 as a primary fuel [194], but much remains to be done. In acquiring the kinetic data required to build quantitative models of AGIL it will be essential to identify the critical rate constants and characterize their temperature dependencies. This is necessary because the generation of F atoms, NCl(a), and energy transfer from NCl(a) to I are all exothermic steps. Consequently, elevated temperatures (400–725 K) [195] are present in a subsonic system and the plenum of a supersonic device. In the initial stages of the chemistry, the elevated temperature is beneficial. The production of N_3 by reaction 9.38 is too slow to be of use at room temperature, but the rate constant increases from 1.3×10^{-12} to 1×10^{-11} $cm^3\ s^{-1}$ as the temperature is increased to 468 K [2]. The temperature dependence of reaction 9.39 is not known, but at room temperature the rate constant for the reaction of Cl with N_3 is rapid (2×10^{-11} $cm^3\ s^{-1}$) with a branching fraction for the production of NCl(a) estimated to be in excess of 0.5 [184]. The temperature dependence of reaction 9.40 is also relevant. Henshaw et al. [188] reported that this rate constant increased slightly (from 2.1×10^{-11} to 3.6×10^{-11} $cm^3\ s^{-1}$) over the temperature range from 298 to 482 K.

Quenching of NCl(a) by a wide variety of collision partners has been investigated at room temperature. For these measurements, NCl(a) was generated by reaction 9.39 (flow tube studies) [184,185,196,197] or by pulsed photolysis of ClN_3 [187,189,192,193]. Rate constants for most of the species that are present in AGIL were found to be small, typically of the order

of 10^{-15}–10^{-14} cm^3 s^{-1}. Quenching by Cl_2 is relatively fast (4×10^{-13} cm^3 s^{-1} at 298 K) [185,189] as this proceeds via the reaction [197]

$$NCl(a) + Cl_2 \rightarrow NCl_2 + Cl. \tag{9.43}$$

The temperature dependencies for quenching by H_2, HCl, Cl_2, and O_2 have been investigated over the temperature range 295–460 K [192]. Weak positive trends were observed for the HCl and Cl_2 rate constants. Quenching by O_2 appeared to be independent of temperature, while quenching by H_2 over the temperature range examined was too slow to be characterized by the measurement technique used ($<10^{-15}$ cm^3 s^{-1}).

The scalability of AGIL is critically dependent on the rate constant for NCl(a) self-annihilation [195],

$$NCl(a) + NCl(a) \rightarrow \text{products}. \tag{9.44}$$

This is a difficult property to determine as the absolute concentration of NCl(a) must be known. Two attempts to characterize the self-annihilation rate constant have been made using photolysis of ClN_3 to generate high concentrations of NCl(a) [187,189]. Conflicting values for the rate constant of 7.2×10^{-12} and 7.0×10^{-13} cm^3 s^{-1} were reported. The lower value is more consistent with the performance of AGIL devices [195]. However, it was recently discovered that studies of the self-annihilation kinetics that utilize ClN_3 photolysis are compromised because the NCl(a) is formed by a secondary photochemical reaction [192]. A lower bound for the self-annihilation rate constant was established by Manke and Setser [184] who obtained a rate constant of 1.5×10^{-13} cm^3 s^{-1} for the energy-pooling process

$$NCl(a) + NCl(a) \rightarrow NCl(b) + NCl(X). \tag{9.45}$$

Accurate determination of the full self-annihilation rate constant remains as a high priority requirement. The energy-pooling process

$$NCl(a) + I^* \rightarrow NCl(b) + I \tag{9.46}$$

is another possible energy loss mechanism. Production of NCl(b) by this process has been observed [177], but the rate constant has not yet been determined.

Self-removal of ground-state NCl occurs via the reaction [191,196],

$$NCl(X) + NCl(X) \rightarrow N_2 + 2Cl \tag{9.47}$$

with a rate constant of 8×10^{-12} cm^3 s^{-1}. The primary significance of this reaction is that it liberates Cl atoms that are known to be effective quenchers of I* [198]. It is therefore essential to run the laser under conditions where the Cl atoms are rapidly scavenged.

Madden et al. [195] have explored the sensitivity of a computational AGIL model to the rate constants for a mechanism that includes 65 elementary reactions. They noted the greatest sensitivities for the rate constants for the reactions 9.36, 9.38, 9.39, 9.44, and 9.43 (decreasing order). Two coupled reactions involving residual F_2 from the Cl atom generation process were also seen to be important. These were

$$I + F_2 \rightarrow IF + F \tag{9.48}$$

and

$$NCl(a) + IF \rightarrow NCl(X) + IF. \tag{9.49}$$

The temperature dependence of the rate constant for reaction 9.48 is unknown and the rate constant for reaction 9.49 has not been measured directly at any temperature. Clearly many more kinetic measurements will be needed to establish the temperature-dependent kinetic database required for computational optimization of AGIL system hardware.

9.8 ELECTRIC OXYGEN IODINE LASERS

There has been considerable interest in developing an electrically pumped atomic iodine transfer laser since the pioneering work of Derwent et al. [9–13]. As described earlier, they used a small microwave discharge of oxygen to produce $O_2(a)$ and subsequent energy transfer to I atoms. Early work by MacKnight and Modreski [199] at the Air Force Weapons Laboratory attempted to produce an iodine laser using six microwave discharge units. However, radiometric and ESR measurements demonstrated that the microwave discharges produced only 8%–10% singlet oxygen in a pure oxygen flow. In later work, Benard and Pchelkin [200] measured a singlet oxygen yield of 11% using a 2450 MHz microwave discharge of oxygen at low pressures (~0.5 Torr). Subsequent work by several groups has used a variety of discharge techniques to produce singlet oxygen. Pigache et al. [201] used an e-beam and an e-beam-sustained discharge at atmospheric pressure to produce singlet oxygen yields of about 2.5%. More recent results by Ionin et al. [202] using e-beam discharges also indicated singlet oxygen yields in the order of 7%. Hill [203] used an avalanche-controlled discharge in oxygen and reported a yield of 16%. The highest yields have involved low-pressure r-f or microwave discharges. Fujii [204] used an r-f generator and reported a 17% yield. Schmiedberger et al. [205,206] also used a low-pressure r-f source and reported yields from 20% to 32%. Itami et al. [207] used a low-pressure microwave discharge to produce a reported yield of 21%.

Quite recently, Carroll et al. [3–5] used a capacitive r-f discharge operating at 13.56 MHz to produce ~16% singlet oxygen in a low-pressure discharge. Rawlins et al. [6] have also recently employed a low-pressure flow reactor and a 2450 MHz microwave discharge to excite $O_2(a)$ in a dilute mixture of O_2 in Ar. They measured singlet oxygen yields as high as 25% at 340 K.

The chemical kinetic issues for EOIL devices are somewhat different from those of a conventional COIL. The differences stem from the fact that discharges produce high yields of atomic O [208,209] and there is no H_2O present. Because of the latter, much higher yields of $O_2(b^1\Sigma^+)$ are observed (as compared with a chemical SOG) and quenching of I* by H_2O is not a concern. One of the key problems in developing EOIL has been the difficulty in achieving threshold yields of $O_2(a)$. Increasing the energy deposited in the discharge can increase the yield but it also increases the temperature [208,210]. This in turn raises the threshold yield (Equation 9.11). In their preliminary analysis of EOIL, Carroll and Solomon [209] concluded that the energy loss in the I_2 dissociation process would be very detrimental, such that injection of predissociated I_2 would be needed to achieve efficient lasing. This conclusion was based on the standard I_2 dissociation mechanism in COIL. It was subsequently recognized that O atoms from the discharge would have the beneficial effect of dissociating the I_2 via the sequence

$$O + I_2 \rightarrow IO + I, \tag{9.50}$$

$$O + IO \rightarrow +O_2 + I. \tag{9.51}$$

These reactions proceed with near gas kinetic rate constants ($k_1 = 1.4 \times 10^{-10}$, $k_2 = 1.5 \times 10^{-10}$ cm^3 s^{-1}) [211]. As the flow of injected I_2 is small compared with the O atom flow, the dissociation process does not significantly reduce the O atom concentration. Consequently, the effect of the O atoms on the lasing kinetics is a matter for concern. Han et al. [212,213] speculated that O atoms may quench I* via transient formation of IO (a standard Landau-Zener curve-crossing mechanism).

$$I^* + O \rightarrow I + O. \tag{9.52}$$

Most recently Rawlins et al. and Azyazov et al. have examined reaction 9.52 using continuous flow and pulsed photolysis techniques. They obtained a consistent value for the rate constant of 1×10^{-11}cm^{3}s^{-1}.

As mentioned, Carroll et al. [3–5] developed r-f discharges that produced yields of O_2(a) in excess of 15%. Addition of NO to the He/O_2 discharge was found to be helpful as this facilitates operation of the discharge by lowering the effective ionization potential. Despite the high yield of O_2(a), the I* population was not inverted when I_2 alone was added to the products from the discharge. It was noted that the introduction of a very small quantity of I_2 dramatically decreased the O_2(a) present in the flow. They assumed that reaction 9.52 was responsible for this effect as O atoms could quench O_2(a) indirectly by perturbing the $I + O_2(a) \leftrightarrow I^* + O_2(X)$ equilibrium. NO_2 was added to the postdischarge flow to scavenge the O atoms by the reaction

$$O + NO_2 \rightarrow O_2 + NO. \tag{9.53}$$

This was successful and the O_2(a) concentration recovered as the NO_2 flow was increased. With this approach, Carroll et al. [3–5] demonstrated gain on the I atom ($F' = 3 \rightarrow F'' = 4$) hyperfine transition using a tunable diode laser gain diagnostic.

Similar to the observations of Carroll et al. [3–5], Rawlins et al. [6] noted that the addition of NO_2 that chemically removes O atoms caused the singlet oxygen concentration to recover and the iodine atoms transitioned from an absorptive to an amplifying medium. Using a similar small signal gain diagnostic, Rawlins et al. [6] measured a small signal gain of 8×10^{-7} cm^{-1} in a subsonic flow at 350 K, the first such measurement in a subsonic flow.

Most recently lasing on the EOIL, discharge-driven system has been reported by Carroll et al. [7]. This is an exciting development that poses new questions concerning the kinetics of the device. Carroll et al. [4] simulated their results using the assumption that reaction 9.52 was the cause of the deleterious effect of the O atoms. However, the dependence of I* yield on the NO_2 flow rate suggests that there are additional factors influencing I* that are more complex than just the quenching by O atoms. Both Carroll et al. [4] and Rawlins et al. [6] found that there are optimum flow rate for NO_2 was equal or greater than that needed to remove all of the O atoms. The efficient generation of I* under these conditions is surprising as there should not be any O atoms left for dissociation of I_2 by reactions 9.50 and 9.51. Conceivably, dissociation of I_2 by O_2(b) could be of importance when the O atoms are removed. In this context, it is of interest to note that fluorescence for O_2(b) was greatly enhanced when NO_2 was added to the system [4]. Clearly, further kinetic studies will be needed to identify and characterize the critical reactions of EOIL. The work of Carroll et al. [3–5,7] and Rawlins et al. [6] have demonstrated that, in principle, an EOIL device may be a viable, scalable system.

The next steps to scaling EOIL will require both higher power discharge SOGs and a better understanding of key kinetic processes. Several groups are currently active in this area as mentioned. Both self-sustained [214,215] and non-self-sustained [216] discharge sources are being investigated currently and show promise. For example, Rawlins et al. [216] have reported singlet oxygen yields of greater than 25% from a 1 kW microwave discharge. If the EOIL concept can be scaled to relevant power levels, there should be numerous important applications.

9.9 SUMMARY

In this rather brief description of iodine lasers, we have tried to stress important developments in this important and unique class of lasers. The fact that iodine lasers can be pumped both photolytically and by energy transfer from metastable species is unique for an atomic laser. The single line emission and high-power operation at 1.3 μ are advantageous for propagation through the atmosphere and through optical fibers, making iodine very attractive for a variety of important applications. The developments associated with atomic iodine lasers over the last 40 years have been quite remarkable, and there is reason to believe that further exciting advances will occur in the future.

ACKNOWLEDGMENTS

The authors would like to acknowledge Dr. Jiri Ullschmied, Institute of Physics, Prague, Czech Republic, and Dr. Fumio Wani, Kawasaki Heavy Engineering Gifu, Japan, for kindly providing the photos of the PALS and the KWI laser welder. They also thank the American Institute of Physics for permission to use Figure 9.7 and Dr. Steve Lamberson and the International Society of Optical Engineering for permission to use Figure 9.9. They would also like to acknowledge their many colleagues with whom they have had the pleasure of collaboration and innumerable discussions in this fascinating field of iodine lasers. S.J. Davis would like to thank Janet H. Davis for her helpful and insightful editorial comments. Finally, they owe a debt of gratitude to Ms. Karen Trevette of PSI for her skillful typing of this chapter. Her patience with all of the many drafts and edits is deeply appreciated. Some recent results described in this chapter were obtained under the support of the Air Force Office of Scientific Research, Multi-Disciplinary Research Grants (Grant numbers F49620-02-1-0331 and F49620-01-1-0357), Dr. Michael Berman, contract monitor. We are very grateful for this support.

REFERENCES

1. McDermott, W.E., Pchelkin, D., Benard, D.J., and Bousek, R.R., An electronic transition chemical laser, *Appl. Phys. Lett*., 32, 469, 1978.
2. Manke, G.C., Henshaw, T.L., Madden, T.J., and Hager, G.D., Temperature dependence of the $Cl+HN_3$ reaction from 300 to 480 K, *Chem. Phys. Lett*. 310, 111, 1999.
3. Carroll, D.L., Verdeyen, J.T., King, D.M., Zimmerman, J.W., Laystrom, J.K., Woodard, B.S., Richardson, N., Kittell, K., Kushner, M.J., and Solomon, W.C., Measurement of positive gain on the 1315 nm transition of atomic iodine pumped by $O_2(^1\Delta)$ produced in an electric discharge, *Applied Physics Letters*, 85(8), 1320, 2004.
4. Carroll, D.L., Verdeyen, J.T., King, D.M., Zimmerman, J.W., Laystrom, J.K., Woodard, B.S., Benavides, G.F., Kittell, K., and Solomon, W.C., XV International Symposium on Gas Flow and Chemical Lasers and High Power Laser Conference, Prague, 2004, SPIE 5777, 2005.

5. Carroll, D.L., Verdeyen, J.T., King, D.M., Zimmerman, J.W., Laystrom, J.K., Woodard, B.S., Benavides, G.F., Kittell, K.W., and Solomon, W.C., Path to the measurement of positive gain on the 1315-nm transition of atomic iodine pumped by $O_2(a^1\Delta)$ produced in an electric discharge, *IEEE J. of Quantum Electronics*, 41(2), 213–223, 2005.
6. Rawlins, W.T., Lee, S., Kessler, W.J., and Davis, S.J., Observations of gain on the $I(^2P_{1/2} \rightarrow {}^2P_{3/2})$ transition by energy transfer from $O_2(a^1\Delta_g)$ generated by a microwave discharge in a subsonic flow reactor, *Applied Physics Letters,* 86, 05 1105, 2005.
7. Carroll, D.L., Verdeyen, J.T., King, D.M., Zimmerman, J.W., and Laystrom, J.K., Continuous-wave laser oscillation on the 1315 nm transition of atomic iodine pumped by $O_2(a^1\Delta)$ produced in an electric discharge, *Appl. Phys. Lett*., 86, 111104, 2005.
8. Kasper, J.V.V. and Pimentel, G.C., Atomic iodine photodissociation laser, *Appl. Phys. Lett*, 5, 231, 1964.
9. Derwent, R.G., Kearns, D.R., and Thrush, B.A., The excitation of iodine by singlet molecular oxygen, *Chem. Phys. Lett*., 6(2), 115, 1970.
10. Derwent, R.G. and Thrush, B.A., Measurements of $O_2(^1\Delta)$ and $O_2(^1\Sigma)$ in discharge flow systems, *Trans. Faraday Soc*., 67, 2036, 1971.
11. Derwent, R.G. and Thrush, B.A., The radiative lifetime of the metastable iodine atom $I(5^2P_{1/2})$, *Chem. Phys. Lett*., 9(6), 591, 1971.
12. Derwent, R.G. and Thrush, B.A., Excitation of iodine by singlet molecular oxygen part 1-mechanism of the I_2 chemiluminescence, *Journal of the Chemical Society,* Faraday Discussions II, 68, 720, 1972.
13. Derwent, R.G. and Thrush, B.A., Excitation of iodine by singlet molecular oxygen part 2 - kinetics of the excitation of the iodine atoms, *Chemical Soc*., Faraday Discussions, 53, 162, 1972.
14. Kasper, J.V.V. and Pimentel, G.C., Iodine-Atom Laser Emission in Alkyl Iodide Photolysis, *J. Chem. Phys*., 43, 1827, 1965.
15. Gensel, P. Hohla, K., and Kompa, K.L., Energy Storage of CF_3I Photodissociation Laser, *Appl. Phys. Lett*., 18, 48, 1971.
16. Fill, E.E., The high-power iodine laser, in Developments in High-Power Lasers and Their Applications, 1981, LXXIV Corso, Soc. Italiana di Fisica, Bologna, Italy.
17. Padrick, T.D. and Palmer, R.E., Pressure broadening of the atomic iodine $5^2P_{1/2}$–$5^2P_{3/2}$ transition, *J. Chem. Phys*., 62, 3350, 1975.
18. Schlie, L.A. and Rathge, R.D., Closed-cycle gaseous alkyl-iodide (C_3F_7I) supply system, *Rev. Sci. Instrum*., 55(4), 482–485, 1984.
19. Davis, S.J., Dye laser pumped atomic iodine laser, *Appl. Phys. Lett*, 32, 656, 1978.
20. Spinnler, J.F. and Kittle, P.A., Hydrogen fluoride chemical laser – a demonstration of pure chemical pumping, presented at Second Conference on Chemical and Molecular Lasers, St. Louis, May 22–24, 1969.
21. Gross, R.W.F., Giedt, R.R., and Jacobs, T.A., Stimulated emission behind overdriven detonation waves in F_2O-H_2 mixtures, *J. Chem. Phys*., 51, 1250, 1969.
22. Bowen, J.R. and Overholtser, K.A., An appraisal of the continuous explosion laser (Continuous explosion laser study of stationary detonation waves to determine conditions leading to partial population inversion and critical population density), *Astronautica Acta*, 14, 475, 1969.
23. Spencer, D.J., Jacobs, T.A., Mirels, H., and Gross, R.W.F., Preliminary performance of a CW chemical laser, *Int. J. Chem. Kinet*., 1, 493, 1969.
24. Cool, T.A., Stephens, R.R., and Falk, T.J., DF-CO_2 and HF-CO_2 continuous-wave chemical lasers, *Int. J. Chem. Kinet*., 1, 295, 1970.
25. Shuler, K.E., Adiabatic Correlation Rules for Reactions Involving Polyatomic Intermediate Complexes and their Application to the Formation of $OH(^2\Sigma^+)$ in the H_2O_2 Flame, *J. Chem. Phys*., 21, 624, 1953.
26. Jones, C.R. and Broida, H.P., Gas-phase reaction of Ba with N_2O. I. Measurement of production efficiency of excited states, *J. Chem. Phys*., 60, 4369, 1974.
27. Dickson, C.R., George, S.M., and Zare, R.N., Determination of absolute photon yields under single-collision conditions, *J. Chem. Phys*., 67, 1024, 1977.

28. Hsu, Y.C. and Pruett, J.G., Nascent metastable products in the reactions Ba+NO_2 and Ba+N_2O, *J. Chem. Phys.*, 76, 5849, 1982.
29. McDermott, W.E., Historical perspective of COIL (Keynote Paper), in *Proceedings of SPIE*, 2002, 4631 (Gas and Chemical Lasers and Intense Beam Applications III), p. 1.
30. Lamberson, S., The airborne laser, in *Proceedings of SPIE-The International Society for Optical Engineering*, 1996, 2702 (Gas and Chemical Lasers), p. 208–213.
31. Mallet, I., unable to find title, *Compt. Rend.*, 185, 352ff, 1927.
32. Groh, M.P., Presentation de reactions accompagnees de luminescence rouge, *Bulletin De La Societe Chimique De France*, 5, 12, 1938.
33. Groh, M.P. and Kirriman, A.K., Etude spectrale d'une reaction luminescente, *Compt. Rend. Acad. Sci.*, 215, 275ff, 1942.
34. Seigler, H.H., unable to find title, *Anal. Biochem.*, 1, 60ff, 1960.
35. Khan, A.U. and Kasha, M.J., Red chemiluminescence of molecular oxygen in aqueous solution, *J. Chem. Phys.*, 39, 2105, 1963.
36. Arnold, S.J., Finlayson, N., and Ogryzlo, E.A., Some novel energy-pooling processes involving $O_2(^1\Delta_g)$, *J. Chem. Phys.*, 44, 2529ff, 1966.
37. Held, A.M., Halko, D.J., and Hurst, J.K., Mechanisms of chlorine oxidation of hydrogen peroxide. *Journal of the American Chemical Society*, 100(18), 5732, 1978.
38. McDermott, W.E. et al., New gas lasers, Frank J. Seiler Res. Lab., U.S. Air Force Acad., Colorado Springs, CO, USA. pp. 26, 1976.
39. Harpole, G.M. et al., Rotating disk oxygen generator, presented at AIAA 23rd Plasmadynamics and Lasers Conference, Nashville, TN, 1992.
40. Zagidullin, M.V., et al., Possible use of a sprayer unit in a chemical generator of singlet oxygen for an oxygen-iodine laser, *Kvantovaya Elektron.* (Moscow), 10(4), 797, 1983.
41. McDermott, W.E., The generation of singlet delta oxygen a technology overview, in *Proceedings of SPIE-The International Society for Optical Engineering*, 1871 (Intense Laser Beams and Applications), 135–47, 1993.
42. McDermott, W.E., et al., Operating experience with a high throughput jet generator, in *Proceedings of SPIE-The International Society for Optical Engineering*, 2987 (Gas and Chemical Lasers and Applications II), 146–156, 1997.
43. Aharon, O., et al., Oxygen $O_2(^1D)$ generation in a bubble column reactor for chemically pumped iodine lasers: experiment and modeling, *Journal of Applied Physics*, 70(10, Pt. 1), 5211, 1991.
44. Thayer, W.J., III, Cousins, A.K., and Romea, R.D., Modeling of uniform droplet singlet oxygen generators, in *Proceedings of SPIE-The International Society for Optical Engineering,* 1994, 2117 (Modeling and Simulation of Laser Systems III), p. 71–100.
45. Bonnet, J., et al., Experimental analysis of a chemical oxygen-iodine laser, *Applied Physics Letters*, 45(10), 1009, 1984.
46. Kikuchi, T., Tsuruyama, T., and Uchiyama, T., Performance characteristics of a chemical oxygen-iodine laser without a water vapor trap, *Journal of Applied Physics*, 64(6), 2873, 1988.
47. Zagidullin, M.V., et al., Operation of a COIL laser without a cold trap, *Kvantovaya Elektronika* (Moscow), 13, 75, 1983.
48. Benard, D.J., et al., Efficient operation of a 100 W transverse-flow oxygen-iodine chemical laser, *Applied Physics Letters*, 34(1), 40, 1979.
49. Copeland, D.A. et al., Exact and approximate solutions of the utilization and yield equations for $O_2(^1D)$ generators, in *Proceedings of SPIE-The International Society for Optical Engineering*, 1994, 2119 (Intense Beams and Applications: Lasers, Ions, and Microwaves), p. 27–41.
50. Lilenfeld, H.V., Oxygen-iodine laser kinetics, McDonnell-Douglas Research Laboratories, Technical Report, AFWL-TR-83-1, 1983.
51. Lilenfeld, H.V., Carr, P.A.G., and Hovis, F.E., Energy pooling reactions in the oxygen-iodine system, *J. Chem. Phys.*, 81, 5730, 1984.
52. Van Benthem, M.H. and Davis, S.J., Detection of vibrationally excited I_2 in the iodine dissociation region of chemical oxygen-iodine lasers, *J. Phys. Chem.*, 90, 902, 1986.

53. Copeland, D.A. and Bauer, A.H., Optical saturation and extraction from the chemical oxygen-iodine laser medium, *IEEE J. Quantum Electron*., 29, 2525, 1993.
54. Perram, G.P. and Hager, G.D., Standard chemical oxygen-iodine laser kinetics package, Air Force Weapons Lab., Kirkland AFB, NM, 1988.
55. Perram, G.P. and Hager, G.D. Standard chemical oxygen-iodine laser kinetics package, Revision, Air Force Weapons Lab., Kirkland AFB, NM, 1988.
56. Perram, G.P., Approximate analytical solution for the dissociation of molecular iodine in the presence of singlet oxygen, *Int. J. Chem. Kinet*., 27, 817, 1995.
57. Barmashenko, B.D. and Rosenwaks, S., Power dependence of chemical oxygen-iodine lasers on iodine dissociation, *AIAA J*., 34, 2569, 1996.
58. Heidner, R.F., III, Gardner, C.E., Segal, G.I., and El-Sayed, T.M., Chain reaction mechanism for I_2 dissociation in the $O_2(^1\Delta)$ I-atom laser, *J. Phys. Chem*., 87, 2348, 1983.
59. Aviles, R.G., Muller, D.F., and Houston, P.L., Quenching of laser-excited $O_2(b^1\Sigma_g^+)$ by CO_2, H_2O, and I_2, *Appl. Phys. Lett*., 37, 358, 1980.
60. Muller, D.F., Young, R.H., Houston, P.L., and Wiesenfeld, J.R., Direct observation of I_2 Collisional Dissociation by $O_2(b^1\Sigma_g^+)$, *Appl. Phys. Lett*., 38, 404, 1981.
61. Hall, G.E., Marinelli, W.J., and Houston, P.L., Electronic to vibrational transfer from $I^*(5^2P_{1/2})$ to I_2 ($25<V<43$), *J. Phys. Chem*., 87, 2153, 1983.
62. Cerny, D., Bacis, R., Bouvier, A.J., Poulat, S., Topouzkhanian, A., and Verges, J., The dissociation of molecular iodine by metastable oxygen—I. Populations of A 1 μ and B 0_u^+ iodine states through Fourier transform spectrometry analysis, *J. Quant. Spectrosc. Radiat. Transfer*, 47, 9, 1992.
63. Bouvier, A.J., Bacis, R., Bouvier, A., Cerny, D., Churassy, S., Crozet, P., and Nota, M., The dissociation of molecular iodine by metastable oxygen—II. Populations of reservoir states through laser excitation spectra, *J. Quant. Spectrosc. Radiat. Transfer*, 49, 311, 1993.
64. Barnault, B., Bouvier, A.J., Pigache, D., and Bacis, R., Absolute measurement of the I_2 high vibrational levels in the oxygen-iodine reaction, *Journal de Physique IV (Colloque)*, 1, C7/647-C7/650, 1991.
65. Heaven, M.C., Chemical Dynamics in Chemical Laser Media, in *Chemical Dynamics in Extreme Environments, Advanced Series in Physical Chemistry*, Editors, C.-Y. Ng and R.A. Dressler, World Scientific, Invited Chapter, p. 138–205 (2001).
66. Heaven, M.C., Han, J., Davis, S.J., and Lee, S., in *Proceedings of SPIE-The International Society for Optical Engineering*, 2004, 5334, p. 53–59.
67. Han, J., Komissarov, A.V., Tinney, S.P., and Heaven, M.C., *Proceedings of SPIE-The International Society for Optical Engineering*, 2003, 4971, p. 45–56.
68. Azyazov, V.N., Safonov, V.S., and Ufimtsev, N.I., Dissociation of I_2 and the vibrational kinetics in oxygen-iodine medium, *Quantum Electronics*, 30, 687, 2000.
69. Antonov, I.O., Azyazov, V.N., Pichugin, S.Y., and Ufimtsev, N.I., Detection of vibrationally-excited O_2 in O_2 ($a^1\Delta g$)-I mixture, *Chemical Physics Letters*, 376, 168, 2003.
70. Antonov, I.O., Azyazov, V.N., and Ufimtsev, N.I., Experimental and theoretical study of distribution of O_2 molecules over vibrational levels in O_2 ($a^1\Delta g$)-I mixture, *J. Chem. Phys*., 119, 10638, 2003.
71. Alsing, P.M., Davis, S.J., and Simmons, G.L., Observations concerning the efficiency of the I_2 Dissociation by $O_2(^1\Delta)$, in Laser Digest – Spring 1982, P.V. Avizonis, Ed., Air Force Weapons Laboratory Final Report, AFWL-TR-82-88. December 1982.
72. Wakazono, T., Hashimoto, K., Takemoto, T., Uchiyama, T., and Muro, M., in. *Proc. SPIE-Int. Soc. Opt. Eng*., 1998, 3574, p. 290.
73. Endo, M., Sugimoto, D., Okamoto, H., Nanri, K., Uchiyama, T., Takeda, S., and Fujioka, T., Output power enhancement of a chemical oxygen-iodine laser by predissociated iodine injection, *Jpn. J. Appl. Phys., Part 1,* 39, 468, 2000.
74. Jirasek, V., Spalek, O., Kodymova, J., and Censky, M., Chemical generation of atomic iodine for chemical oxygen-iodine laser: Modeling of reaction systems, *Chemical Physics*, 269, 167, 2001.
75. Censky, M., Spalek, O., Jirasek, V., Kodymova, J., and Jakubec, I., in *Proceedings of SPIE-The International Society for Optical Engineering*, 2004, 5334, p. 60.

76. Spalek, O., Jirasek, V., Censky, M., Kodymova, J., Jakubec, I., and Hager, G.D., in *Proceedings of SPIE-The International Society for Optical Engineering*, 2003, 5120, p. 350–356.
77. Rosenwaks, S.; Rybalkin, V.; Katz, A.; Barmashenko, B.D., XV International Symposium on Gas Flow and Chemical Lasers, Prague, 2004, p. S6–7.
78. Lawrence, W.G., Van Marter, T.A., Nowlin, M.L., and Heaven, M.C., *Journal of Chemical Physics*, 106, 127, 1997.
79. Azyazov, V.N. (private communication)
80. Komissarov, A.V., Goncharov, V., and Heaven, M.C., in *Proceedings of SPIE-The International Society for Optical Engineering*, 2001, 4184, p. 7–12.
81. Tellinghuisen, J. and Phillips, L.F., *J. Phys. Chem.*, 90, 5108, 1986.
82. Azyazov, V.N., Pichyugin, S.Y., Safonov, V.S., and Ufimtsev, N.I., *Quantum Electronics*, 31, 794, 2001.
83. Endo, M., Kawakami, M., Takeda, S., Wani, F., and Fujioka, T., in *Proc. SPIE-Int. Soc. Opt. Eng.*, 1999, 3612, p. 56–61.
84. Spalek, O., Censky, M., Jirasek, V., Kodymova, J., Jakubec, I., and Hager, G.D., *IEEE Journal of Quantum Electronics*, 40, 564, 2004.
85. Jirasek, V., Spalek, O., Kodymova, J., and Censky, M., in *Proceedings of SPIE-The International Society for Optical Engineering*, 2002, 4631, p. 43–52.
86. Spalek, O., Jirasek, V., Kodymova, J., Censky, M., and Jakubec, I., in *Proceedings of SPIE-The International Society for Optical Engineering*, 2002, 4631, p. 34–42.
87. Spalek, O., Jirasek, V., Censky, M., Kodymova, J., Jakubec, I., and Hager, G.D., *Chemical Physics*, 282, 147, 2002.
88. Hon, J., et al., Heuristic method for evaluating coil performance, *AIAA Journal*, 34(8), 1595, 1996.
89. Barmashenko, B.D. and Rosenwaks, S., Analysis of the optical extraction efficiency in gas-flow lasers with different types of resonator, Applied Optics, 35(36), 7091, 1996.
90. Truesdell, K.A., Helms, C.A., and Hager, G.D., A history of COIL development in the USA, in *Proceedings of SPIE-The International Society for Optical Engineering*, 1995, 2502: p. 217–37.
91. McDermott, W.E., Historical perspective of COIL, in *Proceedings of SPIE-The International Society for Optical Engineering*, 2002, 4631(Gas and Chemical Lasers and Intense Beam Applications III): p. 1–12.
92. Endo, M., Osaka, T., and Takeda, S., High-efficiency chemical oxygen-iodine laser using a streamwise vortex generator, *Appl. Phys. Lett.*, 84(16), 2983–2985, 2004.
93. Rybalkin, V., Katz, A., Barmashenko, B.D., and Rosenwaks, S., Nearly attaining the theoretical efficiency of supersonic chemical oxygen-iodine lasers, *Appl. Phys. Lett.,* 85(25), 5851–5853, 2004.
94. Rybalkin, V., Katz, A., Barmashenko, B.D., and Rosenwaks, S., A 33% efficient chemical oxygen-iodine laser with supersonic mixing of iodine and oxygen, *American Institute of Physics*, 82(22), 3838–3840, 2003.
95. Yoshida, S. et al., Highly efficient chemically pumped oxygen iodine laser, in *Proceedings of the International Conference on Lasers*, 1988, p. 223–9.
96. Yoshida, S., et al., Chemical oxygen iodine laser of extremely high efficiency, *Journal of Applied Physics*, 65(2), 870, 1989.
97. Rittenhouse, T.L., Phipps, S.P., and Helms, C.A., Performance of a high-efficiency 5-cm gain length supersonic chemical oxygen-iodine laser, *IEEE Journal of Quantum Electronics,* 35(6), 857, 1999.
98. Wani, F., Endo, M., and Fujioka, T., High-pressure subsonic mode operation of chemical oxygen-iodine laser, *Applied Physics B: Lasers and Optics*, 70(2), 225, 2000.
99. Hager, G.D., et al., Demonstration of a repetitively pulsed magnetically gain-switched chemical oxygen iodine laser, *Chemical Physics Letters*, 204(5–6), 420, 1993.
100. Hager, G.D. et al., Demonstration of a repetitively pulsed magnetically gain switched chemical oxygen iodine laser, in P*roceedings of SPIE-The International Society for Optical Engineering*, 1993, 1810 (Ninth International Symposium on Gas Flow and Chemical Lasers, 1992), p. 509–12.
101. Vagin, N.P., et al., Efficiency of a pulsed chemical oxygen-iodine laser, *Kratkie Soobshcheniya po Fizike*, 5, 47, 1987.

102. Vagin, N.P., et al., Effect of water vapor on the energy of the pulsed oxygen-iodine laser, *Kvantovaya Elektronika* (Moscow), 13(5), 1068, 1986.
103. Basov, N.G., Kryukov, P.G., and Yuryshev, N.N., Pulse-repetition operation of a chemical oxygen-iodine laser, *Kvantovaya Elektronika* (Moscow), 14(5), 924, 1987.
104. Basov, N.G. et al., Pulse operation of a chemical oxygen iodine laser, in P*roceedings of the International Conference on Lasers*, 1988, p. 230–3.
105. Vagin, N.P. and Yuryshev, N.N., A pulsed oxygen-iodine chemical laser excited by a longitudinal electric discharge, *Quantum Electronics*, 32(7), 609, 2002.
106. Vagin, N.P. and Yuryshev, N.N., Pulsed chemical oxygen-iodine laser initiated by a transverse electric discharge, *Quantum Electronics*, 31(2), 127, 2001.
107. Vagin, N.P., Pazyuk, V.S., and Yuryshev, N.N., Pulsed chemical oxygen-iodine laser with bulk formation of iodine atoms in an electric discharge, *Kvantovaya Elektronika* (Moscow), 22(8), 776, 1995.
108. Vagin, N.P., et al., Effect of molecular chlorine on the output energy of a pulsed chemical oxygen-iodine laser, *Kvantovaya Elektronika* (Moscow), 18(7), 840, 1991.
109. Humphreys, R.H. et al., Frequency doubling at 1.315 micrometers, Air Force Weapons Lab., Kirkland AFB, NM, USA, FIELD URL, 1988, p. 26 pp.
110. Baba, T. et al., Intracavity second-harmonic generation of chemical oxygen-iodine laser emission using a LBO crystal, *Applied Physics B: Lasers and Optics*, B60(4), 369, 1995.
111. Davis, S.J., Kessler, W.J., Bachmann, M., and Mulhall, P.A., Collisional broadening coefficients for oxygen and water absorption lines used in COIL diagnostics, presented at Gas and Chemical Lasers and Intense Beam Applications, SPIE Paper 3268–80, San Jose, CA, 1998.
112. Davis, S.J., Kessler, W.J., and Bachmann, M., Collisional broadening of absorption lines in water vapor and atomic iodine relevant to COIL diagnostics, The International Society for Optical Engineering, SPIE Paper No. 3612–25, San Jose CA, 1999.
113. Allen, M.G., Carleton, K.L., Davis, S.J. Kessler, W.J., and McManus, K.R., AIAA 25th Plasmadynamics and Lasers Conference, Colorado Springs, CO, June 1994.
114. Lilenfeld, H.V., Richardson, R.J., and Hovis, F.E., The electron spin resonance spectrum of the $^2P_{1/2}$ state of atomic iodine, *J. Chem. Phys*., 74, 2129, 1981.
115. Gylys, V.T. and Rubin, L.F., Direct measurement of $O_2(a^1\Delta)$ and $O_2(X^3\Sigma)$ in chemical oxygen iodine lasers with use of spontaneous Raman imaging, *Appl. Opt*., 37, 1026, 1998.
116. Rawlins, W.T., Davis, S.J., Lee, S., Silva, M.L., Kessler, W.J., and Piper, L.G., Optical diagnostics and kinetics of discharge-initiated oxygen-iodine energy transfer, presented at 34th AIAA Plasmadynamics and Lasers Conference, Orlando, FL, 23–26 June 2003.
117. Rawlins, W.T., Lee, S., Kessler, W.J., Oakes, D.B., Piper, L.G., and Davis, S.J., Spectroscopic studies of a prototype electrically pumped COIL system, presented at SPIE Photonics West 2004, SPIE Paper No. 5334–12, 2004.
118. Davis, S.J., Rawlins, W.T., Kessler, W.J., Lee, S., Hunter, A.J.R., and Silva, M., Next generation diagnostics for COIL: new approaches for measuring critical parameters, presented at XV International Symposium on Gas Flow and Chemical Lasers and High Power Lasers Conference, SPIE Paper No. S12–6, Prague, Czech Republic, 2004.
119. Williams, S., Gupta, M., Owano, T., Baer, D.S., O'Keefe, A., Yarkony, D.R., and Matsika, S., Quantitative detection of a singlet O_2 by cavity-enhanced absorption, *Optics Letters*, 29(10), 2004.
120. Frolov, M.P., Ionin, A.A., Kochetov, I.V., Napartovich, A.P., Podmar'kov, Yu.P., Vagin, N.P., and Yuryshev, N.N., $O_2(a^1\Delta_g)$ concentration measuring by intracavity laser spectroscopy of $b^1\Sigma_g^+$ - $a^1\Delta_g$ transition, in *Proceedings of SPIE*, Jarmila Kodymová, Ed., 2005, 5777 (XV International Symposium on Gas Flow, Chemical Lasers, and High-Power Lasers).
121. Vetrovec, J., Prospects for an industrial chemical oxygen-iodine laser, in *Proceedings of SPIE-The International Society for Optical Engineering*, 1997, 3092 (XI International Symposium on Gas Flow and Chemical Lasers and High-Power Laser Conference, 1996), p. 723–726.
122. Vetrovec, J., Conceptual design of an industrial chemical oxygen-iodine laser, in *Proceedings of SPIE-The International Society for Optical Engineering*, 1998, 3574 (XII International Symposium on Gas Flow and Chemical Lasers and High-Power Laser Conference, 1998), p. 461–465.

123. Endo, M. et al., Advanced technologies in chemical oxygen-iodine laser for industrial applications, in *Proceedings of SPIE-The International Society for Optical Engineering*, 1998, 3268 (Gas and Chemical Lasers and Intense Beam Applications), p. 106–114.
124. Endo, M. et al., Industrial chemical oxygen/iodine laser at Tokai University, in *Proceedings of SPIE-The International Society for Optical Engineering*, 2000, 3889 (Advanced High-Power Lasers), p. 438–446.
125. Endo, M. et al., Development of industrial COIL, in *Proceedings of SPIE-The International Society for Optical Engineering*, 1998, 3574 (XII International Symposium on Gas Flow and Chemical Lasers and High-Power Laser Conference, 1998), p. 253–264.
126. Fujii, H. and T. Atsuta, Industrial chemical oxygen iodine laser, in *Proceedings of SPIE-The International Society for Optical Engineering*, 1997, 3092 (XI International Symposium on Gas Flow and Chemical Lasers and High-Power Laser Conference, 1996), p. 700–705.
127. Fujii, H. et al., Development of chemical oxygen-iodine laser for industrial application, in *Proceedings of SPIE-The International Society for Optical Engineering,* 1991, 1397 (Int. Symp. Gas Flow Chem. Lasers, 8th, 1990, Pt. 1), p. 213–20.
128. Fujii, H., et al., Long-term stability in the operation of a chemical oxygen-iodine laser for industrial use [Erratum to document cited in CA111(14):123233w], *Journal of Applied Physics*, 66(8), 3964, 1989.
129. Kar, A., et al., Cutting performance of a chemical oxygen-iodine laser on aerospace and industrial materials, *Journal of Laser Applications*, 11(3), 119, 1999.
130. Kar, A., Rothenflue, J., and Latham, W.P., Materials processing with chemical oxygen-iodine laser: ceramic cladding for stainless steel substrate, in *Proceedings of SPIE-The International Society for Optical Engineering*, 1997, 3092 (XI International Symposium on Gas Flow and Chemical Lasers and High-Power Laser Conference, 1996), p. 719–722.
131. Kar, A., Rothenflue, J.A., and Latham, W.P., Scaling laws for thick-section cutting with a chemical oxygen-iodine laser, *Journal of Laser Applications*, 9(6), 279, 1997.
132. Kar, A., Scott, J.E., and Latham, W.P., Theoretical and experimental studies of thick-section cutting with a chemical oxygen-iodine laser (COIL), *Journal of Laser Applications*, 8(3), 125, 1996.
133. Kutsuna, M., Research and development of laser materials processing using high power laser, *Reza Kenkyu*, 28(11), 736, 2000.
134. Latham, W.P. and Kar, A., A review of the simple model for metal cutting with the chemical oxygen-iodine laser, in *Proceedings of the Laser Materials Processing Conference, ICALEO'98*, Laser Institute of America [Publication], 1998, 85, p. B150–B155.
135. Latham, W.P. and Kar, A., Review of the simple model for metal cutting with the chemical oxygen-iodine laser, in *Proceedings of SPIE-The International Society for Optical Engineering*, 2000, 3887, p. 205–210.
136. Latham, W.P. et al., Cutting performance of a chemical oxygen-iodine laser on aerospace and industrial materials, in *Proceedings of SPIE-The International Society for Optical Engineering,* 2000, 3887, p. 200–204.
137. Latham, W.P. and Quillen, B., Applications of the chemical oxygen-iodine laser, in *Proceedings of the Laser Materials Processing Conference, ICALEO'98*, Laser Institute of America [Publication], 1998, 85, p. A187–A195.
138. Latham, W.P. et al., Cutting performance of a chemical oxygen-iodine laser, in *Proceedings of SPIE-The International Society for Optical Engineering*, 1998, 3268 (Gas and Chemical Lasers and Intense Beam Applications), p. 130–136.
139. Li, Y.G., Latham, W.P., and Kar, A., Lumped parameter model for multimode laser cutting, *Optics and Lasers in Engineering*, 35(6), 371, 2001.
140. Nakabayashi, T. and Muro, M., High-power chemical oxygen-iodine laser welding, in *Proceedings of SPIE-The International Society for Optical Engineering*, 2000, 3888 (High-Power Lasers in Manufacturing), p. 359–366.
141. Rothenflue, J.A. et al., Measurement of the cutting performance of a high beam quality chemical oxygen-iodine laser on aerospace and industrial materials, in *Proceedings of the Laser Materials Processing Conference, ICALEO'97*, Laser Institute of America [Publication], 1997, 83, p. B/54-B/62.

142. Sakurai, T. et al., Study on material processing and fiber transmittance of COIL, in *Proceedings of the Laser Materials Processing Conference, ICALEO'96*, Laser Institute of America [Publication], 1996, 81, p. E28–E37.
143. Scott, J.E., Latham, W.P., and Kar, A., High speed material processing of thick stainless steel with a chemical oxygen-iodine laser, in *Proceedings of the Laser Materials Processing Conference*, *ICALEO 95*, Laser Institute of America [Publication], 1995, 80, p. 118–127.
144. Scott, J.E. et al., The use of a chemical oxygen-iodine laser for high speed cutting of thick stainless steel, in *Proceedings of SPIE-The International Society for Optical Engineering*, 1996, 2702 (Gas and Chemical Lasers), p. 339–348.
145. Scott, J.E. and Truesdell, K.A., Industrialization of the chemical oxygen-iodine laser, in *Proceedings of SPIE-The International Society for Optical Engineering*, 1994, 2214 (Space Instrumentation and Dual-Use Technologies), p. 188–96.
146. Shariff, S.M., Sundararajan, G., and Joshi, S.V., Parametric influence on cut quality attributes and generation of processing maps for laser cutting, *Journal of Laser Applications,* 11(2), 54, 1999.
147. Solomon, W.C. et al., Commercial applications for COIL, in *Proceedings of SPIE-The International Society for Optical Engineering*, 2000, 3887, p. 137–151.
148. Takeda, S., Nanri, K., and Fujioka, T., Industrial and reverse-industrial applications of COIL, in *Proceedings of SPIE-The International Society for Optical Engineering,* 1996, 2702 (Gas and Chemical Lasers), p. 191–194.
149. Xie, J. and Kar, A., Melting and vaporization for large-area film removal with a chemical oxygen-iodine laser, *Journal of Applied Physics*, 82(10), 4744, 1997.
150. Xie, J. et al., Comparative studies of metal cutting with high power lasers, in *Proceedings of SPIE-The International Society for Optical Engineering*, 1997, 3092 (XI International Symposium on Gas Flow and Chemical Lasers and High-Power Laser Conference, 1996), p. 764–767.
151. Xie, J. et al., Temperature-dependent absorptivity and cutting capability of CO_2, Nd:YAG and chemical oxygen-iodine lasers, *Journal of Laser Applications*, 9(2), 77, 1997.
152. Yasuda, K. and Muro, M., Study on material processing of chemical oxygen iodine laser, *Reza Kenkyu*, 28(11), 755, 2000.
153. Yoshida, S. and Shimizu, K., High power chemical oxygen iodine laser for industrial applications, in *Proceedings of SPIE-The International Society for Optical Engineering*, 1990, 1225 (High-Power Gas Lasers), p. 478–85.
154. Yoshida, S. and Shimizu, K., High power chemical oxygen iodine lasers and applications, in *Proceedings of SPIE-The International Society for Optical Engineering*, 1991, 1397 (Int. Symp. Gas Flow Chem. Lasers, 8th, 1990, Pt. 1), p. 205–12.
155. Carroll, D.L. and Rothenflue, J.A., Experimental study of cutting thick aluminum and steel with a chemical oxygen-iodine laser using an N_2 or O_2 gas assist, *Journal of Laser Applications*, 9(3), 119, 1997.
156. Carroll, D.L. et al., Experimental analysis of the materials processing performance of a chemical oxygen-iodine laser (COIL), in *Proceedings of the Laser Materials Processing Conference, ICALEO'96*, Laser Institute of America [Publication], 1996, 81, p. E19–E27.
157. Adachi, J. et al., Application of chemical oxygen iodine laser (COIL) for dismantling of nuclear facilities. *Progress in Nuclear Energy*, 32(3/4), 517, 1998.
158. Endo, M. et al., Development of a prototype COIL for decommissioning and dismantlement, in *Proceedings of SPIE-The International Society for Optical Engineering*, 2001, 4184 (XIII International Symposium on Gas Flow and Chemical Lasers and High-Power Laser Conference, 2000), p. 23–26.
159. Li, L., The potential role of high-power lasers in nuclear decommissioning, IMechE Conference Transactions, 2001 (8, Nuclear Decom 2001), p. 103–121.
160. Li, L., The potential role of high-power lasers in nuclear decommissioning, *Nuclear Energy-Journal of the British Nuclear Energy Society*, 41(6), 397, 2002.
161. Nomoto, A. et al., Chemical oxygen-iodine laser for decommissioning and dismantlement of nuclear facilities, *Journal of Advanced Science*, 12 (1 and 2), 146, 2000.
162. Tsurumaki, K. et al., Development of remote dismantling of a nuclear reactor with laser radiation transmitted through an optical fiber, *Dekomisshoningu Giho*, 17, 8, 1997.

163. Hallada, M.R., Chemical oxygen-iodine laser (COIL) for decontamination and decommissioning (D&D) of nuclear facilities, Topical Meeting on Decommissioning, Decontamination, and Reutilization of Commercial and Government Facilities, 2nd, Knoxville, TN, United States, Sept. 12–16, 1999, 1999: p. 184–188.
164. Duo, L. and Yang, B., Small-signal gain and intracavity loss of a CW chemical oxygen-iodine laser, *Zhongguo Jiguang*, A20(10), 733, 1993.
165. Hays, G.N. and Fisk, G.A., Chemically pumped iodine laser as a fusion driver, *IEEE Journal of Quantum Electronics*, QE17(9), 1823, 1981.
166. Kryukoov, P.G., Feasibility of constructing a laser thermonuclear fusion driver based on an oxygen-iodine chemical laser, *Kvantovaya Elektronika* (Moscow), 22(1), 12, 1995.
167. Kryukov, P.G., A new approach to laser inertial fusion driver construction, *Kvantovaya Elektronika* (Moscow), 20(3), 271, 1993.
168. Kryukov, P.G., A novel approach to laser inertial fusion driver construction, in *Proceedings of SPIE-The International Society for Optical Engineering*, 1994, 2096 (Lasers in Optical Systems and Devices), p. 125–34.
169. Dudeja, J.P. and Kalsey, G.S., Shipborne laser beam weapon system for defence against cruise missiles, *Defence Science Journal*, 50(2), 231, 2000.
170. Yang, T.T., Gylys, V.T., Bower, R.D., and Rubin, L.F., Population inversion between $I(^2P_{1/2})$ and $I(^2P_{3/2})$ of atomic iodine generated by excitation transfer from $NCl(a^1\Delta)$ to $I(^2P_{3/2})$, *SPIE,* Vol. 1871, 1993.
171. Ray, A.J. and Coombe, R.D., An I^* laser pumped with $NCl(a^1\Delta)$, *J. Phys. Chem.*, 99, 7849, 1995.
172. Herbelin, J.M., Henshaw, T.L., Rafferty, B.D., Anderson, B.T., Tate, R.F., Madden, T.J., Manke, G.C., II, Hager, G.D., The measurement of gain on the 1.315 μm transition in atomic iodine in a subsonic flow of chemically generated $NCl(a^1\Delta)$, *Chem. Phys. Lett.*, 299, 583, 1999.
173. Manke, G.C., II, Cooper, C.B., Dass, S.C., Madden, T.J., and Hager, G.D., A multiwatt all gas-phase iodine laser (AGIL), I*EEE Journal of Quantum Electronics*, 39, 995, 2003.
174. Exton, D.B., Gilbert, J.V., and Coombe, R.D., Generation of excited NCl by the reaction of hydrogen atoms with NCl_3, *J. Phys. Chem.*, 91, 2692, 1991.
175. McDermott, W.E., Coombe, R.D., Gilbert, J., Lambert, Z., and Heldt, M., Flow tube studies of NCl_3 reactions, presented at Gas and Chemical Lasers, and Applications III, Proc. of SPIE, Paper No. 5334–02, San Jose, CA, 26–27 January 2004.
176. Hunter, A.J.R., Kessler, W.J., Lee, S., and Davis, S.J., Spectroscopic studies of the NCl_3 + H reaction sequence as a candidate laser system, presented at Gas and Chemical Lasers, and Applications III, Proc. of SPIE, Paper No. 5334–03, San Jose, CA, 26–27 January 2004.
177. Becker, A.C. and Schurath, U., Matrix-isolated NCl. Radiative rates for $B^1\Sigma^+$ to $A^1\Delta$, $B^1\Sigma^+$ to $X^3\Sigma^-$ and $A^1\Delta$ to $X^3\Sigma^-$ in solid argon, *Chem. Phys. Lett.*, 160, 586, 1989.
178. Yarkony, D.R., On the radiative lifetimes of the $B^1\Sigma^+$ and $A^1\Delta$ states in NCL, *J. Chem. Phys.*, 86, 1642, 1987.
179. Manke, G.C., II, Setser, D.W., Measuring gas-phase chlorine atom concentrations: rate constants for Cl plsu HN_3 CF_3I and C_2F_5I, *J. Phys. Chem. A*, 102, 7257, 1998.
180. Hewett, K.B., Manke, G.C., II, Setser, D.W., Brewood, G., Quenching Rate Constants of NCl(a[Image]) at Room Temperature, *Journal of Physical Chemistry A*, 104, 539, 2000.
181. Ray, A.J. and Coombe, R.D., Collisional Quenching of $NCl(a^1\Delta, v=0)$ and the Chain Decomposition of ClN_3, *J. Phys. Chem.,* 98, 8940, 1994.
182. Henshaw, T.L., Herrera, S.D., Haggquist, G.W., and Schlie, V.A., Kinetics of $NCl(a^1\Delta)$ via Photodissociation of ClN_3, *J. Phys. Chem. A*, 101, 4048, 1997.
183. Henshaw, T.L., Herrera, S.D., and Schlie, L.A., Temperature Dependence of the $NCl(a^1\Delta)$ + $I(^2P_{3/2})$ Reaction from 300 to 482 K, *J. Phys. Chem. A*, 102, 6239, 1998.
184. Komissarov, A.V., Manke, G.C., II, Davis, S.J., and Heaven, M.C., Rate constants for quenching and self-annihilation of $NCl(a^1\Delta)$, *J. Phys. Chem. A*, 106, 8427, 2002.
185. Tschumper, G.S., Heaven, M.C., and Morokuma, K., An ab initio excursion on the lowest 18 electronic surfaces of the NCl + NCl system: Some insight into the long-range self-quenching pathways of the first excited state of NCl, *J. Phys. Chem. A*, 106, 8453, 2002.

186. Tschumper, G.S., Heaven, M.C., and Morokuma, K., Concerning the stability of dichlorodiazene, *Chem. Phys. Lett*., 370, 418, 2003.
187. Tinney, S.P., Han, J., and Heaven, M.C., in *Proceedings of SPIE-The International Society for Optical Engineering*, 2004, 5334, p. 25–31.
188. Komissarov, A.V., Manke, G.C., II, Davis, S.J., and Heaven, M.C., in *Proceedings of SPIE-The International Society for Optical Engineering*, 2000, 3931, p. 138–148.
189. Madden, T.J., Manke, G.C., II, and Hager, G.D., 34th AIAA Plasmadynamics and Lasers Conference, AIAA-2003-4310, 2003.
190. Clyne, M.A.A. and MacRobert, A.J., Elementary reactions of the NCl radical. I. Rate constants for the reactions NCl + NCl to $N_2 + 2Cl$ and O + NCl to NO + Cl, *J. Chem. Soc., Faraday Trans. 2*, 79, 283, 1983.
191. Clyne, M.A.A., MacRobert, A.J., Brunning, J., and Cheah, C.T., Kinetics of metastable singlet NCl radicals, *J. Chem. Soc., Faraday Trans. 2*, 79, 1515, 1983.
192. Komissarov, A.V. and Heaven, M.C., Quenching of $I(^2P_{1/2})$ by Cl_2 and Cl atoms over the temperature range, 297–663 K, *J. Phys. Chem. A*, 107, 10527, 2003.
193. MacKnight, A.K. and Modreski, P.J., Laser Digest, Fall 1974, Air Force Weapons Laboratory Final Report, AFWL-TR-74-344, January 1975.
194. Benard, D.J. and Pchelkin, N.R., Measurement of $O_2(^1\Delta)$ content in the gaseous effluents of a chemical generator, *Rev. Sci. Instrum*., 49(6), 795, 1978.
195. Pigache, D., Bonnett, J., David, D., and Fournier, G., $^1\Delta$ oxygen production with e-beam and e-beam controlled discharge in view of a high pressure oxygen-iodine laser, presented at CLEO'82, Phoenix, AZ, April 14–16, 1982.
196. Ionin, A., Frolov, M., Hager, G., Klimachev, Yu., Kochetov, I., Kotkov, A., Napartovich, A., Podmar'kov, Yu., Seleznev, L., Sinitsyn, D., Vagin, N., and Yuryshev, N., Singlet delta oxygen production in e-beam sustained discharge, theory and experiment, in *Proceedings of SPIE*, Jarmila Kodymová, Ed., 2005, 5777 (XV International Symposium on Gas Flow, Chemical Lasers, and High-Power Lasers, 2005).
197. Hill, E.A., The next generation of controlled avalanche discharge lasers – including an extension to the electric oxygen iodine laser, in *Proc. Int. Conf. Lasers 2000*, McClean, VA, 2001, pp. 249–258.
198. Fujii, H., COIL in Japan, in AIAA, Colorado Springs, CO, June 1994, 94–2419.
199. Schmiedberger, J., Hirahara, S., Ichinoche, Y., Suzuki, M., Masuda, W., Kihara, Y., Yoshitani, E., and Fujii, H., RF plasma jet generator of singlet delta oxygen for oxygen-iodine laser, *SPIE*, Vol. 4184, 32, 2001.
200. Schmiedberger, J. and Fujii, H., RF plasma jet generator of singlet delta oxygen and RF discharge pre-dissociation of iodine for oxygen-iodine laser at lowered temperature, presented at XV International Symposium on Gas Flow and Chemical Lasers and High Power Laser Conference, Prague, Czech Republic, 2004.
201. Itami, S., Nakamura, Y., Nakamura, A., Shinagawa, K., Kihara, Y., Okamura, M., Yoshitani, E., and Fujii, H., The development of hybrid oxygen-iodine laser, *SPIE*, Vol. 3889, 503, 2000.
202. Stafford, D.S. and Kushner, M.J., *Journal of Applied Physics*, 96(5), 2451, 2004.
203. Carroll, D.L. and Solomon, W.C., in *Proceedings of SPIE-The International Society for Optical Engineering*, 2001, 4184 (XIII International Symposium on Gas Flow and Chemical Lasers and High-Power Laser Conference, 2000), p. 40.
204. Carroll, D.L., Verdeyen, J.T., King, D.M., Woodard, B., Skorski, L., Zimmerman, J., and Solomon, W.C., Recent Work on the Development of an Electric Discharge Oxygen Iodine Laser, in *Proceedings of SPIE-The International Society for Optical Engineering*, 2003, 5120 (XIV International Symposium on Gas Flow, Chemical Lasers, and High-Power Lasers, 2002), p. 316.
205. Atkinson, D.B., Hudgens, J.W., and Orr-Ewing, A.J., Kinetic Studies of Reactions of IO Radicals Determined by Cavity Ring-down Spectroscopy, *J. Phys. Chem*. A, 103, 6173, 1999.
206. Han, J., Komissarov, A.V., Tinney, S.P., and Heaven, M.C., in *Proceedings of SPIE-The International Society for Optical Engineering*, 2003, 4971 (Gas and Chemical Lasers and Intense Beam Applications IV), p. 45.
207. Han, J., Tinney, S.P., and Heaven, M.C., in *Proceedings of SPIE-The International Society for Optical Engineering*, 2004, 5448 (Pt. 1, High-Power Laser Ablation V), p. 261.

208. Hicks, A., Utkin, Y., Lempert, W.R., Rich. J.W., and Adamovich, I.V., Progress in Development of a Non-Self-Sustained Electric Discharge Pumped Oxygen-Iodine Laser, Paper AIAA-2006-1359, presented at 44th Aerospace Sciences Meeting and Exhibit, Reno, NV, 9–12 January 2006.
209. Ionin, A.A., Frolov, M.P., Lebedev, P.N., Kochetov, I.V., Napartovich, A.P., Ochkin, V.N., Podmar'kov, Y.P., Rulev, O.A., Savinov, S.Y., Seleznev, L.V., Sinitsyn, D.V., Vagin, N.P., and Yuryshev, N.N., Singlet delta oxygen production in self-sustained and non-self-sustained slab discharges, presented at Photonics West 2006, Paper 6101C-52, San Jose, CA, January 2006.
210. Rawlins, W.T., Lee, S., Kessler, W.J., Oakes, D.B., Piper, L.G., and Davis, S.J., The electric oxygen-iodine laser: chemical kinetics of $O_2(a^1\Delta)$ production and $I(^2P_{1/2})$ excitation in microwave discharge systems, presented at Photonics West 2006, Paper 6101C-51, San Jose, CA, January 2006.

10 Metal Vapor Lasers

Nikola V. Sabotinov

CONTENTS

10.1 INTRODUCTION

In the period 1965–1980, metal vapor lasers (MVL) that later formed an individual class of gas lasers aroused a significant scientific interest in the field of quantum electronics. The active media of these lasers consist of chemical element vapor that does not exist in the gas state under normal conditions. The atomic vapor of metallic elements belongs to them and also all other elements that have no typical metallic properties. This laser class has made rapid strides because of the possibilities to attain laser generation of many spectral lines of different active chemical elements and the wide spectral range of their location: from the deep ultraviolet (UV) to the infrared (IR) region. MVLs oscillate on transitions between energy levels of atoms and ions as their output radiation beam has the properties typical of gas lasers, such as high levels of monochromaticity and coherence and low beam divergence.

Laser action in metal vapor was attained for the first time in cesium vapor with optical pumping, as with gas-discharge excitation laser oscillation was achieved for the first time in mercury (Hg) vapor. Subsequently, gas-discharge has proved to be the most proper medium for the operation of MVLs.

The use of metal vapor as the active medium in gas lasers has led to intensive scientific studies resulting in laser generation on 700 atomic and ion spectral lines, belonging to a total

of 42 elements. The different laser transitions are excited under different discharge conditions and have different regimes of laser generation. Some emit only in the pulsed regime, while others can oscillate in both pulsed and continuous regimes, respectively.

Despite the great spectral abilities of these lasers, they have advanced relatively slowly because of the need to overcome numerous difficulties of technical nature, related to their realization as practically operating devices. A primary problem in them is the creation of an active medium on the basis of metal atoms. The maintenance of a homogenous metal atom density requires a stable temperature regime in the discharge zone. A particularly serious problem is to keep the cleanliness of the optical surfaces of the windows in the active zone and their protection from metal deposition. Operational lifetime also has appeared to be a difficult problem to solve for these lasers.

Regardless of the existing difficulties, some MVLs have reached the stage of commercial development and different companies have adopted technologies for their production.

The most familiar and widespread MVL is the self-terminating copper laser. It generates two spectral lines, green and yellow, and is distinguished as the most powerful laser with the highest efficiency in the visible spectrum. Today two versions of copper laser are on the laser market: the copper vapor laser and the copper bromide vapor laser.

The helium–cadmium laser (He–Cd) is also another well-developed laser source of this class. It oscillates largely in the continuous-wave (CW) regime and produces output powers of some tens of milliwatts. This laser has two variants: the cataphoretic He–Cd laser and the hollow cathode (HC) He–Cd laser. The cataphoretic He–Cd laser generates CW output on one blue line and on one UV line. The HC He-Cd laser emits simultaneously blue, green, and red laser lines and in practice appears to be a "white-light" laser.

The He–Se laser has also reached some commercial level. This laser generates a very rich spectral band in the visible region: 47 lines, which can lase in the CW regime simultaneously with a total power of some tens of milliwatts.

Copper and silver ion HC lasers emitting in the deep UV spectrum in CW and pulsed regimes have also been developed. Their output powers are in the milliwatt range. MVLs have undergone the increasing competition of solid-state and semiconductor lasers. Copper lasers are continuously replaced by solid-state Nd:YAG lasers generating on second harmonic frequency in the green spectral region. At present, copper lasers keep good positions and most of all, thanks to their abilities to generate easily high average output powers from tens to some hundreds of watts, and their high beam quality (BQ) and comparatively lower costs. Metal vapor ion lasers emitting in the visible spectrum are replaced gradually by semiconductor lasers that have recently occupied the entire visible spectrum. At present, the high monochromaticity and coherence of MVLs make them unique for numerous applications and they have their good positions.

10.2 MVLs, General Points

10.2.1 History of the Development of MVLs

Laser oscillation in metal vapor was attained for the first time in 1961. In the work by Jacobs et al. [1] laser action in atomic cesium at the IR wavelength 7.2 μm was reported. In 1962, Rabinowitz et al. [2] obtained laser oscillation on a second IR line in the cesium atom at a wavelength of 3.2 μm. In both works cesium atoms were excited optically by a helium lamp. In 1963, Rigden and White [3] and Paanen et al. [4] attained for the first time with gas-discharge excitation pulsed laser oscillation in Hg atom vapor at a wavelength of 1.52 μm. In 1964, Bell [5] achieved pulsed laser oscillation in Hg ion vapor at a wavelength of 0.63 μm. In 1965, Foweles and Silfvast [6] reported laser oscillation on two ion lines in Cd and on two

ion lines in zinc. In 1966, Silfvast [7] attained pulsed laser oscillation on 12 ion lines in Cd, Zn, Ge, Sn, Pb, and In. In 1967, Foweles and Hopkins [8] reported on quasi-CW laser oscillation on the Cd ion line at 441.6 nm in the positive column (PC) He–Cd discharge. In the same year, Silfvast achieved CW laser action on the same line. The period 1968–1969 was characterized by a high advance in the development of the He–Cd laser as it was the object of a great interest as a source of blue laser light: Sosnowski [9], Goldsborough and Hodges [10], Fendley et al. [11].

The HC discharge was used for laser generation in metal vapor in 1965 for the first time. Byeret et al. [12] achieved lasing in Hg ions excited by a HC discharge. Laser oscillation in Cd^+ ions excited by a HC discharge was obtained by Asami et al. [13], Schuebel [14] and Sem et al. [15] in the period 1968–1969. Laser action in Cd^+ and Zn^+ ions under the conditions of HC sputtering was achieved by Karabut et al. [16] in 1965.

Laser oscillation in Cu^+ ions in a HC discharge with sputtered copper atoms was attained by Csillag et al. [17] in 1974. This has set the start of creating copper, silver and gold ion lasers generating in the deep UV region as shown by Mc Neil et al [18].

Intensive development of pulsed MVLs oscillating on transitions between resonance and metastable levels of atoms and ions has started since the 1960s in parallel with the development of metal and ion lasers oscillating in the pulsed, quasi-CW and CW regimes. The beginning was in 1965 when Foweles and Silfvast [19] obtained laser oscillation in lead vapor on the atomic lead line at a wavelength of 722.9 nm. The same year, Piltch et al. [20] and Silfvast and Foweles [21] simultaneously attained laser oscillation on atomic self-terminating transitions in manganese. A little later, still in 1965, laser oscillation on both self-terminating transitions at wavelengths of 511 and 578 nm in the copper atom was achieved by Walter et al. [22] and thus the most powerful visible laser was created. In 1968, Walter attained laser oscillation on the self-terminating transition at a wavelength of 627.8 nm in the gold atom [23].

An essential advance in the development of high-temperature MVLs was promoted by the work by Petrash [24], in which discharge heating for the laser active medium was suggested for the first time. This work has contributed to the development of practical applications for self-terminating MVLs.

Pulsed laser oscillation on ion transitions in strontium and calcium, under the conditions of recombination plasma, was obtained for the first time by Latush and Sem [25] in 1972. After these initial steps, intensive scientific research was started that resulted in rapid progress for the MVLs as a class of gas lasers.

10.2.2 Methods for Obtaining Metal Atoms in the Gas Phase

The most essential feature of MVLs is the need to maintain continuously the metal atoms in a gas phase. This special requirement makes them different from the other gas lasers and at the same time, makes them much more difficult for technical realization as reliable devices for practical use. There are various methods for generating metal vapor. The three methods that are the most widely employed in the MVLs will be described here.

10.2.2.1 Vaporization

The classical method to attain the metal atom density that is necessary for laser oscillation in the laser tube is heating the metal up to vaporization. The metal vapor pressure is controlled by temperature selection. The laser tube is filled with a buffer gas whose pressure is much higher than that of the metal component. The ratio between the two gases is determined by the conditions under which the given metal vapor is generated. The buffer gas limits diffusion

of metal vapor to the optical windows of the laser tube. The classical way for heating the active zone of the laser tube is by an external oven. The laser tube can be made of glass, quartz glass or ceramics depending on the metal used and the temperature required for maintaining the necessary metal vapor partial pressure. This method of using external heating for the laser tube is especially difficult when using metals with high temperatures of vaporization, such as over 1800°C, for example.

A great development in the method of metal vaporization has been achieved since one began to heat the metal with the heat released by the gas-discharge itself in the laser tube [24]. With a suitable thermal insulation for the tube, this method for self-heating of the active zone has proved to be very successful. It is easy for technical realization and its introduction has made MVLs to use metals with high temperatures of vaporization convenient for practical applications.

10.2.2.2 Dissociation of Metal Chemical Compounds

Besides direct vaporization, metal atoms can be generated in the active medium by molecular dissociation of metal chemical compounds. In this case, easily vaporizable metal compounds are used, thus the temperature regime of laser operation is facilitated. Dissociation of the metal compound molecules takes place by collisions with electrons in the discharge zone of the laser tube. Metal halides (MX) have proved to be very suitable for this method:

$$\mathrm{MX} + \mathrm{e} \rightarrow \mathrm{M} + \mathrm{X} + \mathrm{e} \tag{10.1}$$

Metal atoms resulted from the dissociation, play the same role as the vaporized metal atoms. The main difference is that in the latter case a halogen element participates besides the metal. This element exerts influence on the processes in the laser medium and its role is not positive in most cases.

10.2.2.3 Cathode Sputtering

Cathode sputtering enables to create a comparatively low metal atom density in the discharge region. The metal, of which the gas-discharge tube cathode is made, is subject to intensive bombardment by heavy positive ions. As a result of these impacts, the metal sputters as metal atoms and particles are released from its surface. Sputtered metal atoms entering the gas-discharge can take part in the process of laser generation. Efficient sputtering occurs in a HC discharge. This method of production of metal atom is in particular appropriate when working with metals that vaporize at very high temperatures and at the same time sputter very well. Different metals have different degrees of sputtering. For example, Ag sputters best and Al sputters worst among the metals Ag, Au, Cu, Pt, Ni, Fe, and Al. This method of cathode sputtering is widely employed in metal vapor ion lasers.

10.2.3 Electric Gas-Discharges Used for Excitation in MVLs

The most widely used means of excitation for the laser active medium in MVLs is the gas-discharge plasma. The major types of gas-discharge employed in MVLs are described here quite briefly. Information about the glow discharge and its versions was used from the works [26–28]. In the gas-discharge, many elementary processes take place that result in a population inversion between atomic and ion levels of metals and chemical elements allied to them.

Generally, the gas medium where lasing processes occur is a mixture of noble gas and vapors of chemical elements. Noble gases in this case are often called "buffer gases." In many cases, the buffer gas participates effectively in the excitation of metal laser levels. In other

cases, the buffer gas does not participate directly in the generation of metal ions, but enables to maintain the gas-discharge; reduces the diffusion of metal to the optical windows of the laser tube; promotes the homogenous distribution of metal atoms at the expense of the cataphoretic effect; and keeps cathode sputtering in cases when it is used for production of metal atoms in the discharge region.

The metal atom partial pressure in the gas mixture varies from 0.01 to 0.5 Torr for the different types of MVLs. The buffer gas pressure is generally within 10–100 Torr. This difference in the pressures of the two main gas components is because of the difference in their ionization potentials. Metal atoms have an ionization potential of over two times lower than that of the buffer gas. The buffer gas pressure is much higher in order to maintain a higher electron temperature needed for the efficient excitation of laser levels.

The gas-discharge is characterized by the following parameters: J—current density, E—electric field strength, p—gas or gas mixture pressure, and d—discharge zone diameter. The values of these parameters determine the type of discharge and the physical processes that take place in the gas-discharge plasma. A variety of gas plasma discharges are used. The following discharges are employed in MVLs: a stationary PC discharge, a pulsed PC discharge, a HC discharge, and a transverse RF discharge.

10.2.3.1 Stationary PC Discharges

The glow discharge arises in a gas-discharge tube with cold electrodes at a relatively low gas pressure and by limiting the electric current through the discharge tube by external resistance. The glow discharge region of distribution in a gas-discharge tube with a glow discharge (Figure 10.1) is well known. It is explained by the potential distribution between the cathode and anode in the discharge tube. The PC is the dominating zone in the glow discharge. The PC is the most employed means for excitation in MVLs. The PC gas-discharge plasma is characterized by equal radial densities of the positive and negative charges and by a constant longitudinal electric field. The current densities are 10^{-5}–10^{-1} Acm^{-2} for the PC. The length of the PC can be made as large as is needed, only if the applied voltage between the electrodes is high enough to keep the discharge. The discharge tube bore influences very strongly the processes occurring in the PC. The gas temperature in the PC is not very high and the temperature of the discharge tube wall is in the range of 80°C–300°C depending on current density. The electron density typical of this type of discharge is about 10^{12} cm^{-3}.

A schematic diagram of the general construction of a PC gas-discharge tube for a MVL is shown in Figure 10.2. The discharge zone is located in a ceramic tube, surrounded by a fused silica envelope. Two electrodes confine the discharge zone. Two windows are set at both ends of the discharge tube. Pieces of lasant metal are placed along the ceramic tube.

10.2.3.2 Pulsed PC Discharges

The pulsed PC discharge arises in a laser tube with a construction as is given schematically in Figure 10.2. The discharge channel has commonly a diameter from 0.3 to 4 cm; the gas

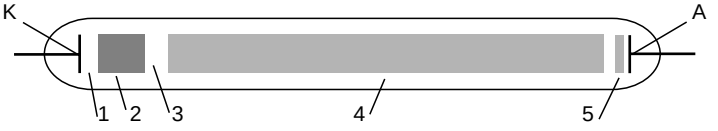

FIGURE 10.1 Main regions of the glow discharge. 1—Cathode dark space, 2—negative glow, 3—Faraday dark space, 4—positive column, 5—anode glow, K—cathode, A—anode. (From Raizer, Yu.P., *Gas-Discharge Physics,* Springer-Verlag, Berlin, 1991. With permission.)

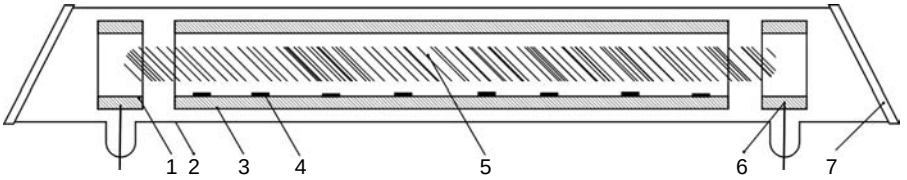

FIGURE 10.2 Schematic diagram of a positive column discharge tube. 1—Electrode, 2—fused silica tube, 3—ceramic tube, 4—lasant metal, 5—positive column discharge, 6—electrode, 7—window. (From Little, C.E., *Metal Vapour Lasers Physics, Engineering and Applications*, John Wiley & Sons Ltd, Baffins Lane, Chichester, West Sussex P019 IUD, England, 1999. With permission.)

pressure is in the range of 10–200 Torr, the discharge current can reach 10^3 A and the applied electric field intensity is 300 Vcm^{-1}. Under these conditions, the electron density is 10^{15} cm^{-3}. The current pulse duration is 0.1–10 μs depending on the lasant metal. The shape of the current pulse going through the active medium is very significant. Some MVLs that oscillate on transitions between resonance and metastable levels need fast excitation processes. The pulses in them have an abrupt leading edge. Other types of MVL, where a population inversion arises under the conditions of rapidly decaying plasma, operate during the lagging edge of the pulse. Here fast recombination processes take place.

10.2.3.3 Hollow Cathode Discharges

The negative glow (NG) discharge is characterized by a large density of high-energy electrons whose energy results from the strong potential gradient in the dark cathode space (DCS) (Figure 10.1). The cathode voltage fall is some hundreds of volts. If the cathode is a hollow cylinder and the anode is close to it, the positive column shortens so much that all the NG becomes concentrated in the HC (Figure 10.3). The HC discharge covers the NG. High-energy electrons in the NG excite very efficiently the ion upper energy levels. For this reason, the HC discharge is used to excite MVLs oscillating on ion transitions. There are two main types of HC tubes (Figure 10.4). The first type of HC discharge tube is for a longitudinal HC discharge. In it, the NG axis coincides with the cathode fall direction (Figure 10.4a). The second type of HC discharge tube is for a transverse HC discharge as the axis of the NG is

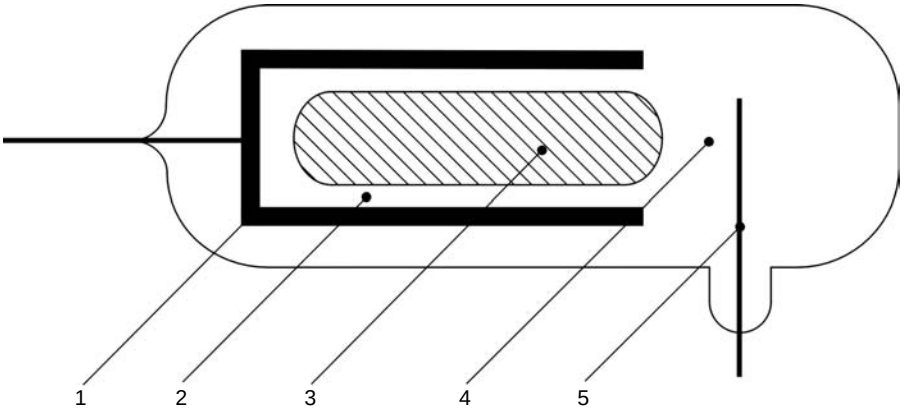

FIGURE 10.3 Schematic diagram of a hollow cathode discharge tube. 1—cathode, 2—cathode dark space, 3—negative glow, 4—Faraday dark space, 5—anode. (From Raizer, Yu.P., *Gas-Discharge Physics,* Springer-Verlag, Berlin, 1991. With permission.)

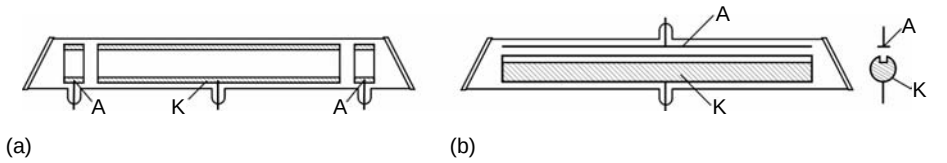

FIGURE 10.4 Types of hollow cathodes: (a) longitudinal hollow cathode; (b) transverse hollow cathode. (From Little, P.F. and Engel, A. von, *Proc. R. Soc. London A*, 224, 209, 1954. With permission.)

perpendicular to the cathode fall (Figure 10.4b). Each of these two types of HC discharge tubes has its varieties that are used in different cases of gas-discharge MVLs.

10.2.3.4 Transverse RF Discharges

The RF discharge has found wide applications in different types of gas lasers. The use of the RF discharge has resulted in many cases of significant improvement of laser output parameters. The differences between the RF discharge and the DC discharges or the pulsed current discharges can be maintained without electrodes located inside the gas-discharge tube. The electric field exciting the discharge changes its direction very quickly, so that the discharge cannot reach the electrodes or the discharge tube wall. The RF discharge parameters such as charged particle density, electron energy, gas temperature, and electric breakdown voltage depend on the kind of gas, gas operating pressure, field frequency, and discharge tube dimensions.

The RF discharges can be divided into two types: capacitive RF discharge and inductive RF discharge. The capacitive RF discharge is maintained in a discharge tube located between the plates of a capacitor included in a RF circuit. The inductive RF discharge tube is placed in the solenoid of an inductive circuit.

The capacitive RF discharge is the most appropriate one for use in the MVLs. Electron energy in the transverse RF discharge is significantly higher than that in the PC and is close to the electron energy in the NG in a HC discharge. Because of this, the discharge of high-energy electrons effectively produces ions and metastable excited states of the buffer gas that are needed for pumping of ion energy levels of some MVLs. A principle construction of a laser gas-discharge tube with capacitive RF excitation is shown schematically in Figure 10.5.

10.2.4 Main Excitation Processes in the Plasma of MVLs

The main elementary processes taking place in the gas-discharges and leading to the establishment of population inversions between energy levels of metal atoms and ions are described here. In the gas-discharge plasma, there are particles that take part in the physical processes in different degrees resulting in lasing action. Such particles are: neutral nonexcited atoms and

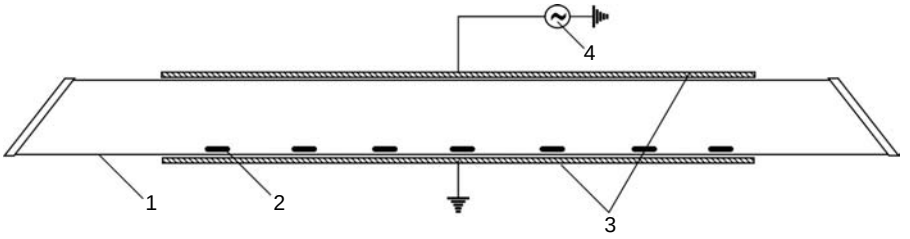

FIGURE 10.5 Schematic diagram of a transverse RF laser tube. 1—Fused silica tube, 2—lasant metal, 3—electrodes, 4—RF generator. (From Reich, N., Mentel, J., and Mizeraczyk, J., *IEEE J. Quant. Electron.*, QE-31(11), 1902, 1995. With permission.)

molecules of the buffer gas (A) and of the metal (M), excited atoms of the noble gas (A*) and of the metal (M*), nonexcited ions of the buffer gas (A^+) and the metal (M^+), excited ions of the buffer gas (A^+*) and the metal (M^+*), electrons (e).

All the particles have definite densities (n) that depend on the discharge conditions and the partial pressures of the buffer gas and metal. Under the discharge conditions, the particles move chaotically similar to the performance of the charged particles and a drift movement to the electrodes or the discharge tube wall under the influence of the applied electric field takes place. The energy of particles moving in the plasma is characterized by their temperature although not always very correctly. The electron temperature exceeds highly the ion temperature of the buffer gas and the metal ($T_e \gg T_i$), and the ion temperature is higher than that of the atoms ($T_i > T_a$).

All the processes of interaction between particles can be divided into two groups: elastic and inelastic ones. Elastic interactions are when the sum of the kinetic energies of particles, which collide with each other, remains constant. Inelastic interactions are when the sum of the kinetic energies of the interacting particles has changed as a result of changes in their internal energy in the process of collisions. Inelastic interactions lead to excitation of the metal and buffer gas atoms and ions.

There is a big diversity of elastic and inelastic interactions in the gas medium. Some main interactions that are especially important for attaining laser oscillation in the MVLs are described in the following.

10.2.4.1 Electron Collisions

Electron collisions are the basis of all the gas-discharge processes leading to population inversions in the MVLs. In some cases, they are the main pumping mechanisms and in other cases, they play an indirect role in obtaining a population inversion. If a fast electron interacts with a ground-state atom, it can transfer part of its kinetic energy to the atom or ion and thus can bring the atom to an excited state. This process is called "direct electron impact excitation":

$$e + M \rightarrow e + M^*, \tag{10.2}$$

$$e + M^+ \rightarrow e + M^{+*}. \tag{10.3}$$

This process is the primary one in the pulsed MVLs oscillating on self-terminated atomic and ion transitions.

By direct collisions with electrons the buffer gas and metal atoms are ionized:

$$e + A \rightarrow A^+ + 2e, \tag{10.4}$$

$$e + M \rightarrow M^+ + 2e. \tag{10.5}$$

Subsequently, the obtained ground-state buffer gas ions take part in the excitation of metal atoms and ions. These processes appear to be the main source of charged particles in the plasma of MVLs.

10.2.4.2 Charge Transfer and Penning Ionization

The charge transfer and Penning ionization are heavy-body impact interactions. They are basic mechanisms in the creation of population inversions in the ion MVLs. Penning ionization occurs when buffer gas atoms excited to a metastable state, transfer their internal energy to metal atoms and excite them to an ion excited state:

$$A^M + M \rightarrow A + M^{+*} + e. \tag{10.6}$$

This process needs the metastable state energy of the buffer gas atom to be relatively close to that of the metal ion excited state. A difference of about 1 eV in energy levels is still allowable as the cross section for interaction is of the order of 10^{-15} cm^2. In this process, the energy that is released can be removed by the liberated electron. The Penning excitation mechanism is applied in the ion MVLs.

Another process playing an important role in the creation of population inversions in MVLs is the Duffendack charge transfer. In the Duffendack charge transfer, the buffer gas ions upon collision with ground-state metal atoms bring them to an ion excited state:

$$A^+ + M \rightarrow A + M^{+*} + \Delta E. \tag{10.7}$$

The charge transfer process has a strong resonant character and the probability of its occurrence is large when $\Delta E \sim kT$, where T is the gas temperature in the active medium plasma. The cross section for excitation of upper laser levels in the charge transfer collisions is large and reaches up to 10^{-15} cm^2. The process is very efficient at $\Delta E = 0.1 - 0.5$ eV. Charge transfer collisions are responsible for excitation of the upper laser levels in most metal vapor ion lasers.

10.2.4.3 Recombination of Doubly Charged Ions

Pulsed laser action in metal vapor can arise in the afterglow of a pulsed discharge as a result of collisional recombination of doubly ionized metal ions. This recombination includes two processes. The first process occurs during the current pulse. Then doubly ionized metal atoms are produced in collisions between metal atoms and buffer gas ions:

$$A^+ + M \rightarrow M^{++} + A + e. \tag{10.8}$$

The second process is developing the afterglow when the plasma produced begins to decay. Then fast recombination of doubly charged metal ions begins as different energy levels of singly ionized metal ions are populated. The recombination process results from collisions of doubly ionized metal ions with slow electrons:

$$M^{++} + e + e \rightarrow M^{+*} + e. \tag{10.9}$$

An inversion population can arise on some of the singly ionized metal ion energy levels that are optically connected and have different radiative lifetimes. The conditions for such a population in many cases are improved owing to the depopulation of lower laser levels of the metal ion in further collisions with slow electrons. As a result of the so-created population inversion, recombination generation of some metal ions can be observed with typical representatives such as strontium and calcium ions, on the basis of which powerful recombination lasers emitting in the blue and UV spectrums have been created.

10.3 TYPES OF MVLs

10.3.1 MVLs on Self-Terminating Atomic and Ion Transitions

Scientific studies in the area of gas lasers since their creation have been directed mainly to the achievement of powerful laser output with high efficiency. This is valid in particular for the gas lasers generating in the short-wave spectral range. In most cases of CW gas lasers, the

upper laser level in this spectral range has energies as high as 15–30 eV. These levels are not readily populated as the main part of the energy introduced into the gas-discharge plasma is lost for population of the lower atomic levels and for ionization; therefore, the excitation efficiency for the upper laser levels is low. Thus the efficiency of the CW gas laser in the short-wave range is usually 10^{-3} to 10^{-4}. For the atomic systems, in most cases, the main part of the energy in the discharge goes for excitation of the first resonance level. The first resonance level, as a rule, has the most efficient cross section for excitation by direct electron impacts, so it is very desirable that the first resonance level be used as an upper laser level. In such cases, the lower laser level can be only a metastable level. Thus it may be expected that on transitions from a resonance level to a metastable level an inversion population can be established. The pulsed oscillation on transitions terminating in metastable levels is called "self-terminating" or "oscillation on self-terminating transitions" bearing in mind that the duration of oscillation is determined by properties of the transition itself. The stimulated emission occurs until the populations of the operating levels become equal.

Using the first resonance atomic level as an upper laser level suggests a high efficiency. The real efficiency of generation of transitions from a resonance level to a metastable level has been estimated to be about 10%. This implies that using transitions from a resonance level to a metastable level would enable to attain high efficiencies in the pulsed regime. Energy level structures of some metal atoms have proved to be very suitable for the attainment of laser oscillation on self-terminating transitions. Metal ions have similar energy level structures. So, there exist appropriate conditions for them also in order to achieve laser oscillation with pulsed gas-discharge excitation.

Pulsed gas-discharge MVLs oscillating on transitions from a resonance level to a metastable level are a typical example of three-energy-level systems in which a nonsteady-state inversion population is established (Figure 10.6). In a fast pulsed discharge, an inversion

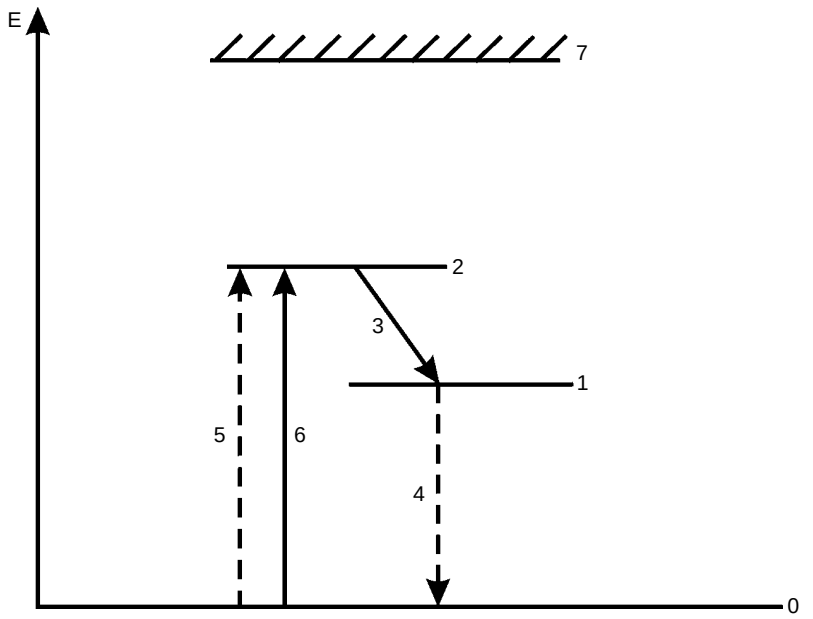

FIGURE 10.6 Energy level structure of an "ideal" self-terminating laser. 0—Ground-state level, 1—metastable level, 2—resonance level, 7—basic ion level, 3—laser transition, 5—resonance radiative trapping, 4—electron impact de-excitation. (From Walter, W.T., Piltch, M., Solimene, N., and Gould, G., *Bull. Am. Phys. Soc.*, 11(1), 113, 1966. With permissison.)

population is established for a short time between the first resonance level (2) and that lying below the metastable level (1) at the expense of differences in the rates of population of these levels at the beginning of the discharge. All atoms are in the ground state (0) until the beginning of the discharge current pulse. After the switch-on of the pulsed discharge and the appearance of high-energy ions in the plasma, population of upper energy levels begins by electron impacts. The rate of excitation by direct electron impacts as a rule is the highest for the first resonance level and significantly exceeds the excitation rate for all other levels, including the metastable ones. In the beginning of the discharge, the processes of excitation from the ground state play the main role, while the other secondary processes have not developed yet:

$$M^0 + e \rightarrow M^2 + e. \tag{10.10}$$

Under these conditions, a population inversion is established on the transition from a resonance level to a metastable level and laser oscillation can be achieved:

$$M^2 \rightarrow h\nu_L + M^1. \tag{10.11}$$

Because the lower laser level is a metastable one, its rate of decay is generally much low, its population increases with time and the population inversion disappears. At low electron densities, the time of existence of a population inversion is of the order of the lifetime of the upper laser level. At higher electron densities, the population inversion time of existence shortens, first of all, as a result of collisions with electrons. Under such conditions, the oscillation duration has proved to be considerably smaller than the radiative lifetime of the upper laser level and has values from units to some tens of nanoseconds. The de-excitation of the lower level in such systems occurs in the time between two excitation pulses. The maximum possible laser pulse recurrence frequency is determined by the decay time of the metastable level. The metastable level decay is promoted by collisions with electrons,

$$M^1 + e \rightarrow M^0 + e, \tag{10.12}$$

as well as by atom–atom collisions and collisions with the discharge channel wall.

Walter et al. [22] have defined five basic criteria for efficient laser oscillation in the self-terminating MVLs:

1. The upper laser level should be a resonant one, that is, should be strongly connected optically to the ground state.
2. The lower laser level should be a metastable one, that is, it should be slightly connected optically to the ground state.
3. The presence of competitive transitions from the upper laser level is not desirable. A strong radiation trapping should be available for the resonant emission to the ground state that is attained at active metal atom densities larger than 10^{13} cm^{-3}.
4. The coefficient of Einstein for the laser transition should be smaller than that for the excitation transition but larger than that for relaxation of the metastable level to the ground state by electron collisions.
5. The lower laser level should be located at 0.7–2.2 eV above the ground state in order to prevent its equilibrium-thermal population at the operating temperatures of the metal active medium.

The self-terminating MVLs possess numerous features making them very important for practical applications. First of all, they are characterized by high efficiencies that may reach 5%–10% in the visible, near infrared (NIR) and UV spectral regions under real conditions.

These lasers are of great interest for achieving high peak powers that may reach up to 10^4 Wcm^{-3}; at such a peak power an energy yield of 10^{-2} Jcm^{-3} can be attained. At pulse durations of 20–40 ns, the highest energy is achieved with the self-terminating lasers. This laser class is characterized by high-pulse recurrence frequencies that can reach up to 100 kHz and more. The high-pulse recurrence frequencies of laser pulses and the high peak powers provide another valuable feature of the MVLs, namely, they are sources of high and medium output powers that can reach up to hundreds of watts.

At present, pulsed laser oscillation on transitions from a resonance level to a metastable level in atoms and ions of 12 metals has been achieved. Table 10.1 gives the laser transitions for different kinds of metal atoms and Table 10.2 shows the self-terminating transitions of the different metal ions that have been made to lase. In the tables are given the kinds of atoms or ions, the wavelengths generated, the lifetimes of upper and lower laser levels and the active medium temperature at which optimum laser action has been achieved. Laser generation of average output powers higher than 1 W has been achieved to date in seven self-terminating MVL sources: Cu, Pb, Mn, Ba, Eu, Au, and Sr. The copper vapor laser (CVL) has proved to have the best parameters and the greatest capabilities for practical applications. The CVL will be described in more detail in an individual section of this chapter.

10.3.2 CW Metal Vapor Ion Lasers

In these lasers, the conditions for laser action are created in a constant discharge, where as a result of collisions between atoms of the vaporized metal and excited atoms or ions of a noble gas, a population inversion is established between energy levels of metal ions. In these lasers, three main types of discharges are used: the PC discharge, the HC discharge and the RF discharge. These lasers are featured with that laser lines can be generated besides in the CW

TABLE 10.1
Self-Terminating Laser Lines in Neutral Metal Atoms

Element	Operating Temperature, °C	Wavelength
Au	1600	312.2 nm
		627.8 nm
Ba	720	1.130 μm
		1.500 μm
		1.820 μm
		1.902 μm
		2.157 μm
		2.326 μm
		2.476 μm
		2.552 μm
		2.923 μm
		3.959 μm
		4.008 μm
		4.329 μm
		4.670 μm
		4.717 μm
		4.718 μm
		5.032 μm
		5.480 μm

continued

TABLE 10.1 (continued)
Self-Terminating Laser Lines in Neutral Metal Atoms

Element	Operating Temperature, °C	Wavelength
		5.564 μm
		5.890 μm
Bi	700	472.2 nm
Ca	600	5.547 μm
Cu	1500	303.6 nm
		306.3 nm
		510.6 nm
		570.0 nm
		578.2 nm
Eu	600	1.665 μm
		1.760 μm
		2.582 μm
		2.718 μm
		4.321 μm
		4.695 μm
		5.066 μm
		5.283 μm
		5.431 μm
		5.772 μm
		5.950 μm
		6.059 μm
Fe	1680	452.9 nm
Mn	1200	534.1 nm
		542.0 nm
		547.1 nm
		548.1 nm
		551.7 nm
		553.8 nm
		1.290 μm
		1.329 μm
		1.332 μm
		1.363 μm
		1.386 μm
		1.400 μm
Pb	1000	363.9 nm
		405.7 nm
		406.2 nm
		722.9 nm
Sm		1.912 μm
		2.048 μm
		2.701 μm
		2.966 μm
		3.465 μm
		3.536 μm
		4.137 μm
		4.866 μm
Sn		657.9 nm
		1.924 μm

continued

TABLE 10.1 (continued)
Self-Terminating Laser Lines in Neutral Metal Atoms

Element	Operating Temperature, °C	Wavelength
Sr	600	1.771 μm
		1.976 μm
		2.088 μm
		2.706 μm
		3.012 μm
		3.067 μm
		3.232 μm
		3.493 μm
		3.608 μm
		3.742 μm
		4.027 μm
		5.430 μm
		6.457 μm
Tl	800	535.0 nm
Tm	800	589.9 nm
		1.069 μm
		1.304 μm
		1.310 μm
		1.338 μm
		1.434 μm
		1.449 μm
		1.453 μm
		1.460 μm
		1.500 μm
		1.638 μm
		1.676 μm
		1.732 μm
		1.959 μm
		1.972 μm
		1.995 μm
		2.106 μm
		or
		2.113 μm
		2.385 μm
Yb	500	1.032 μm
		1.255 μm
		1.428 μm
		1.479 μm
		1.746 μm
		1.798 μm
		1.984 μm
		2.004 μm
		2.119 μm
		4.802 μm

Au – gold, Ba – barium, Bi – bismuth, Ca – calcium, Cu – copper, Eu – europium, Fe – iron, Mn – manganese, Pb – lead, Sm – samarium, Sn – tin, Sr – strontium, Tl – thallium, Tm – thulium, Yb – ytterbium.

Source: From Little, C.E., *Metal Vapour Lasers Physics, Engineering and Applications*, John Wiley & Sons Ltd, Baffins Lane, Chichester, West Sussex P019 IUD, England, 1999. With permission.

TABLE 10.2
Self-Terminating Laser Lines in Metal Ions

Element	Operating Temperature, °C	Wavelength
Ba^+	700	614.2 nm
		649.7 nm
		2.592 μm
		2.906 μm
Ca^+	700	854.2 nm
		866.2 nm
Eu^+	600	664.5 nm
		989.8 nm
		1.002 μm
		1.017 μm
		1.361 μm
		1.477 μm
Hg^+	70	398.4 nm
Pb^+	1000	1.159 μm
Sr^+	600	1.033 μm
		1.092 μm
Yb^+	500	1.271 μm
		1.345 μm
		1.650 μm
		1.806 μm
		2.148 μm
		2.438 μm

Source: From Little, C.E., *Metal Vapour Lasers Physics, Engineering and Applications*, John Wiley & Sons Ltd, Baffins Lane, Chichester, West Sussex P019 IUD, England, 1999. With permission.

regime, also in the pulsed regime, as the laser pulse duration is from some microseconds to some milliseconds.

The choice of a construction for the metal vapor ion laser is associated, first of all, with the efficiency of excitation of the corresponding laser levels during the electric discharge. The possibilities for excitation of laser transitions in metal ions are principally different in the PC glow discharge and in the NG discharge in a hollow cathode discharge tube. It has been proved that in the NG discharge in a HC tube, neutral and ionized atoms can be excited effectively while in the PC glow discharge the possibilities are more limited.

The causes for the different mechanisms of excitation of the laser levels in the two types of discharges should be searched in the electric characteristics of these discharges. One of these characteristics is the function of electron energy distribution. Electron energy distribution functions enable to define a general principle of the efficiency of excitation for the laser levels in both types of electric discharges. In the PC glow discharge, there are better conditions for excitation of the levels of lower energy potentials. In the NG discharge, in a HC tube and in the RF discharge, the energy levels of higher potentials are easier to be excited. It should be noted that lower energy levels can also be excited effectively in the HC tube discharge.

The necessary metal atom density and metal ion density are generated mainly in two ways. The first one and the most widely used way is direct metal thermal vaporization. Usually, easily vaporizable metals are used with this method. The more hardly vaporizable metals impose the use of special constructions and materials. Another way for producing metal

atoms and ions is sputtering where the sputtered metal is released from the gas-discharge tube cathode as a result of ion bombardment.

Three different processes for excitation of metal ions in a gas-discharge are used mainly in the CW MVLs oscillating on ion transitions. The first process is the Penning collision that takes place between the metal atoms M in the ground sate and the noble gas atoms (He, Ne, Ar) excited to metastable states A^m:

$$A^m + M \rightarrow M^{+*} + A + e. \tag{10.13}$$

This mechanism of excitation of metal ions takes place mainly in the PC gas-discharge. Another mechanism of excitation of ion laser levels are the charge transfer collisions. These collisions occur between noble gas ions A^+ in the ground state and ground state metal atoms M:

$$A^+ + M \rightarrow M^+ + A + \Delta E. \tag{10.14}$$

Charge transfer collisions take place mainly in the HC discharge and the RF discharge. In some cases, the excitation of metal ion laser levels occurs by direct electron impacts:

$$e + M \rightarrow M^{+*} + 2e. \tag{10.15}$$

To date, laser oscillation has been obtained on 483 ion lines of totally 34 elements. Among them, the ions of 22 elements can lase in the continuous regime and in the quasi-continuous regime [29]. Table 10.3 lists all the metals and chemical elements from which CW laser output

TABLE 10.3
Continuous Wave (CW) and Quasi-CW Metal Vapor Lasing

Element	Number of Lines	Spectral Range, nm
Be	2	467–1203
Cu	52	248–2000
Zn	15	491–5084
Se	49	447–1259
As	8	538–710
Ag	33	224–2080
Cd	24	325–3288
Te	35	484–938
I	30	448–888
Au	24	226–887
Hg	3	615–1555
Tl	13	474–1175
Mg	2	922–924
Al	5	358–747
Ga	2	633–720
Sn	2	1062–1074
Pb	3	537–1322
Ca	2	1183–1195
Sr	4	1087–1245

Source: From Ivanov, I.G., Latush, E.L., and Sem, M.F., in *Metal Vapour Ion Lasers—Kinetic Processes and Gas-Discharges*, John Wiley, Chichester, 1996. With permission.

has been obtained. Each metal has its own specific conditions under which it lases, which determines the relevant construction for the laser source. Usually, the construction is determined by the type of gas-discharge tube that is used by the corresponding electronic power supply block, which ensures the specific electric excitation for the discharge in the active laser tube.

From all CW metal vapor ion lasers, the greatest advance has been attained by the He–Cd laser oscillating in the PC discharge and in the HC discharge.

10.3.3 Recombination MVLs

Pulsed laser oscillation in the discharge afterglow has been obtained in the ions of Be, Mg, Al, Ca, Zn, Sr, Cd, Su, Ba, Hg, Tl and Pb. The conditions, under which metal ions lase in this regime, are described in detail in Reference [29].

Table 10.4 gives the metal ions and wavelengths for which laser oscillation has been achieved in the recombination regime. From all these metals, the recombination lasers with strontium and calcium vapors [30] have the best characteristics. The mechanism of attaining laser action in the ions of these metals is almost the same. In order to describe the principle of operation for recombination MVLs, it is very convenient to use the energy level diagram for the strontium atom as shown in Figure 10.7. An inversion population is established in the

TABLE 10.4
Metal Vapor Recombination Lasers

Elements	Laser Lines, nm	Elements	Laser Lines, nm
Be II	527.2	Cd II	533.7
Mg II	924.4		537.8
	921.8	Sn II	558.9
Al II	622.8		579.9
	623.3		1062.0
	624.3		1074.0
	683.0	Ba II	677.1
	747.1		687.6
	835.4		1109.2
	836.1		1158.1
	836.5		1193.5
	1063.3		1247.8
	1063.6	Hg II*	567.7
	1063.9	Tl II	473.7
Ca II	370.6		498.1
	373.7		507.9
	994.0		515.2
Zn II	491.2	Pb II	537.2
	492.4		1162.8
Sr II	416.2		1322.1
	430.5		
	870.0		
	1087.0		
	1123.0		

Source: From Ivanov, I.G., Latush, E.L., and Sem, M.F., in *Metal Vapour Ion Lasers—Kinetic Processes and Gas-Discharges*, John Wiley, Chichester, 1996. With permission.

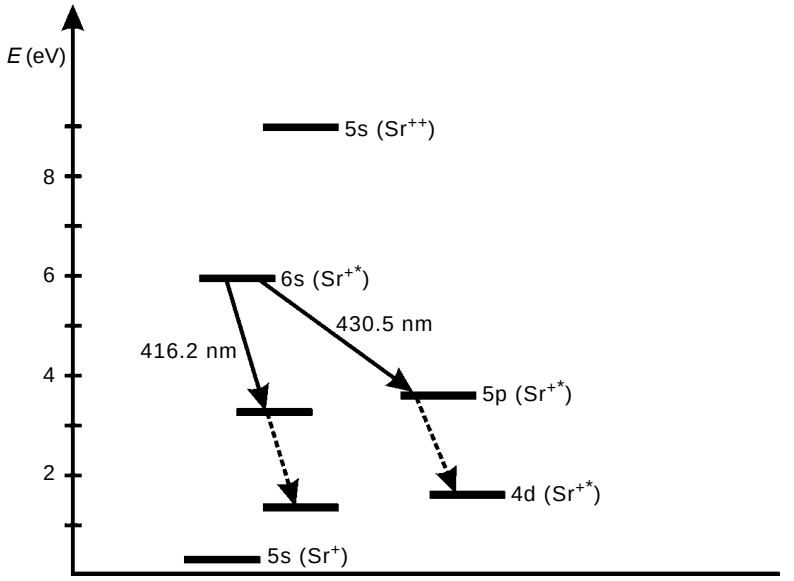

FIGURE 10.7 Energy level diagram of strontium ion showing the levels of the recombination transitions. (From Latush, E.L. and Sem, M.F., *Sov. Phys. JETP*, 37(6), 1017, 1973. With permission.)

pulsed discharge afterglow in the process of collision recombination of doubly ionized strontium. Ionization of strontium occurs during the excitation pulse. Because the first and second ionization potentials of strontium are lower than the helium ionization potential in the discharge in a helium–strontium mixture, doubly ionized metal ions are generated as a result of collisions between helium and strontium atoms:

$$He^{+} + Sr \rightarrow Sr^{++} + He + e. \tag{10.16}$$

After termination of the discharge pulse, recombination of doubly charged strontium ions occurs in the afterglow:

$$Sr^{++} \rightarrow Sr^{+*}(6s) + e. \tag{10.17}$$

As a result of these recombination processes, the upper laser levels 6s of the strontium laser are populated. Under the same conditions of afterglow, the lower levels 5p of the strontium ion are also populated. They are de-excited very quickly by collisions with slow electrons:

$$Sr^{+*}(5p) + e \rightarrow Sr^{+*}(4d) + e. \tag{10.18}$$

Because of the difference in lifetimes of the strontium ion levels 6s and 5p, an inversion population is established between them as conditions for laser oscillation arise. The recombination strontium ion laser oscillates on two lines:

$$430.5\ \text{nm}(6s^2S_{1/2} - 5p^2P_{3/2}) \text{ and } 416.2\ \text{nm}(6s^2S_{1/2} - 5p^2P_{1/2}). \tag{10.19}$$

Laser oscillation on the recombination calcium ion transitions takes place in the same way:

$$373.7\ \text{nm}(5s^2S_{1/2} - 4p^2P_{3/2}) \text{ and } 370.6\ \text{nm}\ (5s^2S_{1/2} - 4p^2P_{1/2}). \tag{10.20}$$

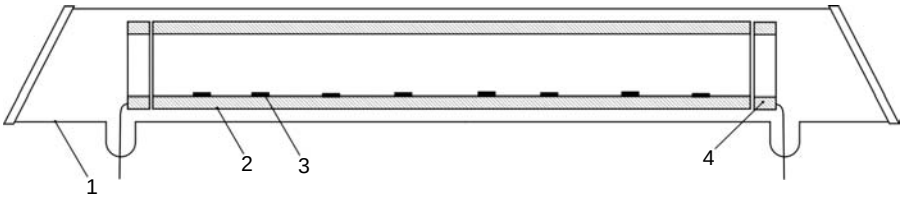

FIGURE 10.8 Schematic diagram of the laser tube of a strontium recombination laser. 1—Quartz tube, 2—ceramic tube, 3—Sr pieces, 4—electrode. (From Latush, E.L. and Sem, M.F., *Sov. Phys. JETP*, 37(6), 1017, 1973. With permission.)

An essential role in obtaining inversion populations is played by the slow electrons, whose density should be considerable. Slow electrons, resulting from collisions with helium, promote the fast cooling of electrons in the afterglow. In this connection, the optimum helium pressure for these lasers is as high as some hundreds of Torrcelli.

A laser tube construction typical of the strontium recombination laser is shown schematically in Figure 10.8. It consists of a quartz envelope in which a ceramic tube is inserted. Because strontium is a highly aggressive chemical element, the best ceramic material has proved to be beryllium oxide. Materials, resistive to corrosion, such as nickel or tantalum, are usually applied for electrodes. The operating temperature of the active discharge zone is in the range of 550°C–700°C. The laser is operated largely in the self-heating regime. The metallic strontium should be not held in the air; its replenishment in the tube should be made in an inert gas as the tube should be cleaned well before the replenishment. The strontium recombination laser appears to be one of the most powerful laser radiation sources in the blue–violet spectral range. A maximum power of 3.9 W at a wavelength of 430.5 nm was attained [31]. In this case, the laser tube active zone had a diameter of 11 mm and a length of 30 cm. The laser peak power was 0.65 kW, the laser pulse energy was 0.13 mJ as an efficiency of 0.075% was attained. The laser pulse repetition frequency was 29 kHz and the helium pressure was 500 Torr. At the optimum temperature of 600°C, the strontium vapor partial pressure was about 0.1 Torr. The gain in the active medium was about 5% cm^{-1}, which is much less than in lasers oscillating on self-terminating transitions of metal atoms and ions, but is high compared with that in many other gas lasers generating in the visible spectrum.

The strontium laser resonator includes usually one high reflective mirror, with a reflectivity of 99.5%, and one transmitting mirror of 70%–80% reflectivity depending on the active medium length.

The laser oscillation pulse arises in the afterglow with a delay of about 0.5 μs after the current pulse maximum and is about 1 μs in duration. These values vary depending on the discharge conditions and laser tube geometry. The power supply for the strontium recombination laser requires high-voltage (15–30 kV) pulses, the value of which is determined by the helium buffer gas pressure and the discharge active zone length. The current pulse has amplitude of some hundreds of amperes and duration of 100–300 n (FWHM).

Because the strontium and calcium lasers are powerful lasers, oscillating in the blue–UV spectrum, they are very suitable for application in the Raman and fluorescence spectroscopies. Other possible applications are in medicine for fluorescent diagnostics, photodynamic therapy, sterilization of medical tools and so on. These lasers are applied in the photolithography in microelectronics and in stereo polymerization for making prototypes.

Commercial production of strontium and calcium lasers has been implemented mainly by Russian manufacturing companies [32].

10.4 COPPER LASERS

10.4.1 Introduction

The copper laser emitting in the visible spectrum oscillates in the pulsed regime on two self-terminating transitions at wavelengths of 510.6 and 578.2 nm. That laser is one of the most widely spread laser sources used in practice. The copper laser is the most powerful laser source in the visible spectrum and has the highest efficiency reaching up to 3.8%.

The copper laser is of great interest because of its ability to generate short laser pulses, 20–50 ns, with high peak powers reaching up to megawatts. The energy yield of the copper active medium is the highest one for gas lasers generating in the visible spectral region and reaches up to 5.10^{-4} Jcm^{-3}. The laser output pulse repetition frequency is an essential parameter characterizing the copper laser and is determined by the lifetime of the metastable level. The highest laser pulse repetition frequency attained for the copper laser was 300 kHz. The high laser pulse recurrence frequency (PRF) enables to obtain laser output of high average power. The maximum average output power achieved with a copper laser of one active element was 750 W [33].

The self-terminating copper laser is suitable for various practical applications owing to its especially valuable performance parameters, such as short laser oscillation pulses, high average and peak output powers, high laser PRF and visible laser output.

For the first time, Walter [22] in 1965 observed laser oscillation on copper atomic lines in a mixture of copper vapor with a noble gas excited by a pulsed discharge.

10.4.2 Principle of Operation

In the copper laser, laser action occurs between the low-lying energy levels of the copper atom for which the energy level diagram is shown in Figure 10.9.

The copper atom ground state $^2S_{1/2}$ is formed by the electron configuration $3d^{10}4s$. During energy transfer to the outer 4s electron by electron impact, it lifts to higher orbits and forms the configurations $3d^{10}4p$, $3d^{10}5p$ and so on. Thus is formed a series of resonance ^2P levels connected with the ground state via strong resonant transitions at wavelengths of 324.8 and 327.4 nm. In the copper atoms, there is an electronic configuration $3d^94s^2$ of lower energy, only 1.5 eV above the ground state. This configuration constitutes the energy levels $^2D_{3/2}$ and $^2D_{5/2}$, which are metastable levels as radiative transitions from them to the ground state $^2S_{1/2}$ are strictly forbidden by the rules for selection of electron dipole radiation. Copper atoms can relax rapidly from the resonance levels ^2P to the ground state $^2S_{1/2}$ as their radioactive decay is $1.4 \times 10^8 s^{-1}$. At a high copper atom density of over 10^{14} cm^{-3}, when laser oscillation takes place, the radiative decay from the upper laser levels ^2P directly to the ground state brings about nonessential losses of copper atoms that are on the levels ^2P as the optical resonant transitions at 324.8 and 327.4 nm are subject to strong trapping of radiation. Under these conditions, the only way for decay of the resonance levels ^2P is via the laser transitions 510.6 and 573.2 nm to the metastable lower laser levels ^2D, which have rates of radiative emission of 2×10^6 and 1.6×10^6 s^{-1}, respectively. If under these conditions, a current pulse with quickly increasing amplitude is applied to the copper atom system, then excitation of the described copper atom energy levels begins by direct electron impact:

$$Cu(^2S_{1/2}) + e \rightarrow Cu^*(^2P_{1/2},^2P_{3/2}) + e. \tag{10.21}$$

In this process, the levels of the $3d^{10}4s^2$ configuration are very likely to be excited. As a result of this, the temperature of electron energy distribution exceeds 1 eV, the levels ^2P are populated much faster than the levels ^2D. Thus, between the levels ^2P and ^2D a high inversion

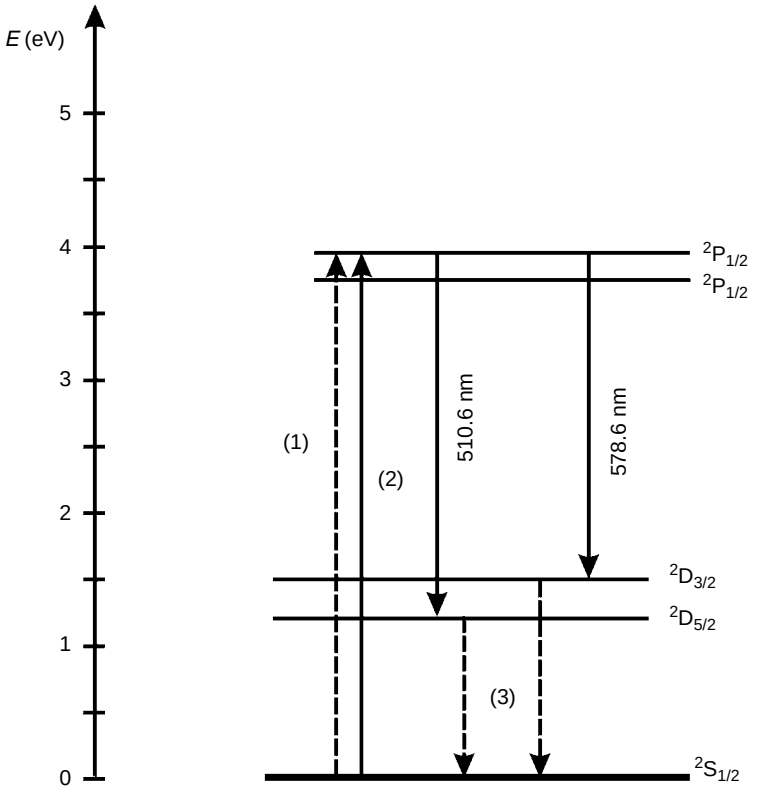

FIGURE 10.9 Energy level diagram for the self-terminating copper laser. $^2S_{1/2}$—Ground-state level of the copper atom; $^2D_{3/2}$, $^2D_{5/2}$—metastable levels of the copper atom; $^2P_{3/2}$, $^2P_{1/2}$—resonance levels of the copper atom; (1)—direct electron impacts, (2)—radiation trapping, (3)—electron de-excitation of metastable levels. (From Walter, W.T., Piltch, M., Solimene, N., and Gould, G., *Bull. Am. Phys. Soc.*, 11(1), 113, 1966. With permission.)

population is established in a short time. The rate of excitation for the ^2P levels by inelastic atom–electron collisions between copper atoms in the ground state $^2S_{1/2}$ with electrons at electron temperatures in the range 4–6 eV, is of the order of 10^{-7} cm^3s^{-1}. This process of excitation dominates over other processes and results in that most electrons transfer their energy to excite the ^2P levels. This explains the high efficiencies of the copper laser.

The population of the lower laser level increases owing to the laser emission becoming equal to the ^2P level population; then the inversion destroys and oscillation terminates. Sometimes, an average of 40–150 μs is needed for the metastable level population to fall to a low value: about 10^{13} cm^{-3} for $^2D_{5/2}$ and 10^{12} cm^{-3} for $^2D_{3/2}$. Then, the process described here can be repeated as an excitation pulse is delivered again to the active medium containing copper atoms with a density of about 10^{15} cm^{-3}. Thus a cyclic oscillation process on self-terminating transitions takes place in the active medium with copper atoms.

10.4.3 Types of Copper Lasers

There are four types of copper lasers divided according to the method for producing copper atoms and the active medium composition: the CVL, the copper bromide vapor laser (CuBrVL), the hybrid copper laser (CuHyBrID) and the kinetically enhanced copper vapor laser (KE-CVL).

10.4.3.1 The CVL

For the first time laser generation on self-terminating transitions between resonance and metastable levels of the copper atom was achieved in a mixture of copper vapor and noble gas excited by a pulsed discharge [22]. The needed copper atom density was obtained at 1500°C temperature of the active medium. The laser tube made of high-temperature ceramics was heated by an external source. Such a method of heating makes the copper laser very difficult for technical realization and for practical applications. A significant advance in the development of the CVL had been made by Petrash [24] who was the first to show that the active medium of the CVL can be heated up to 1500°C by powerful discharge current pulses with a recurrence frequency of some kilohertz. This result has led to fast technological development of the copper laser and to its wide practical applications. The CVL thus has become the main classical variant of the copper laser and is the most used today. Some companies produce it as CVLs of average output powers from some watts to 100 W at optimum laser PRFs of 5–10 kHz.

10.4.3.2 The CuBrVL

The use of copper chemical compounds as sources of copper atoms was suggested by Walter [22] as a solution for the main flaw of the CVL: the high operating temperature. Some copper compounds have temperatures of vaporization much lower than 1500°C and their molecules dissociate easily in a gas-discharge as copper atoms are released. In 1973, Liu et al. [34] was the first to report on laser generation on self-terminating transitions of copper in copper iodide. In the same year, Chen et al. [35] reported on laser generation in copper chloride vapor. In 1974, laser oscillation in copper bromide vapor was attained by Sabotinov et al. The first publications on the copper bromide laser appeared in 1975 [36–38].

Subsequent intensive studies of different copper halides as sources of the lasing medium for laser oscillation on copper self-terminating transitions have shown that the most suitable active medium consists of copper bromide [39]. As a result of investigations of CuBrVLs in the sealed-off regime, a lifetime of 1000 h for the laser tube has been achieved at 10-W average laser output power and a laser output stability of up to 1%. In 1985, Astadjov et al. [40] found a strong effect of hydrogen in the CuBrVL. Small additives of hydrogen added to the neon buffer gas lead to a double increase in the output power and efficiency of the laser emission. The hydrogen partial pressure is about 0.3 Torr and in practice, remains constant, independent of the discharge conditions and active medium geometry. The discovery of the strong effect of hydrogen in the CuBrVL has led to a new stage in the development of copper lasers. By the use of the strong hydrogen effect in the sealed-off CuBrVL, maximum output power of 120 W and 3.8% efficiency have been attained as the latter is the highest efficiency for copper lasers at all. By adding hydrogen to the active lasing medium, the record high specific output power of 1.4 Wcm^{-3} has been obtained from a small-bore laser tube [41].

10.4.3.3 The CuHyBrID

Good results obtained with the CuBrVL and the strong hydrogen effect found in this laser have served as the basis for the creation of a new type of copper laser: the CuHyBrID laser, by Maitland et al. [42]. This laser is a combination of the CVL and the CuBrVL. Through the laser tube with the construction of high-temperature copper laser, where copper metal pieces are placed at equal distances of some centimeters along the tube, vapors of the Ne+HBr mixture flows. Bromine interacts with copper and as a result copper bromide molecules are produced. These molecules dissociate as copper atoms are released. Their density is sufficient to obtain powerful laser generation. This is the principle of operation of the hybrid copper

laser. It is like the operation of the CuBrVL at a low (600°C) temperature of the active medium. High output powers and high efficiencies of up to 3.8% characterize the CuHyBrID laser [43]. That is explained with the great homogeneity of the active medium resulting from the laser operation in the gas flow regime. Moreover, under these conditions, a significantly larger copper atom density can be attained as a result of the chemical reaction between metallic copper and HBr. The maximum output power achieved from a CuHyBrID laser was 280 W. From a small-bore laser tube, a 2 W cm^{-3} specific output power has been attained, which is the highest for copper lasers [44].

10.4.3.4 The KE-CVL

KE-CVL was proposed for the first time by Piper [45] as a result of the development of CVLs and the CuHyBrID laser. The KE-CVL operates at 1500°C temperature of the active medium as the excitation discharge is generated in a mixture of copper vapor and Ne-HBr-H_2 and/or Ne-Cl-H_2. In practice, this laser includes the same gas mixture as the CuHyBrID laser as the main difference is in the high temperature of the laser tube wall in the KE-CVL. Because of the high operating temperature, the metallic copper is in a liquid phase as copper dendrites that reduce the laser tube lifetime as in CuHyBrID laser, are not observed. The active medium of the KE-CVL provides significantly better parameters than in the CVL. For example, the average output power of the KE-CVL is about 2.5 times higher; the laser beam quality is closer to the diffraction limit; the laser pulse duration is about two times larger; and the efficiency is 1.5 times higher. From such a KE-CVL, a maximum output power of 320 W has been attained [46].

From these details about the four types of copper lasers, we can conclude that the CVL and KE-CVL belong to the high-temperature copper lasers (1500°C). They have longer warm-up times and have maximum efficiencies of up to 2%. The CuBr vapor and CuHyBrID lasers operate at relatively lower temperatures of the active medium (500°C–600°C). In them higher efficiencies are attained (up to 3.8%) and they have short startup times. Table 10.5 [75] summarizes

TABLE 10.5
General Parameters for the Main Types of Copper Lasers

	Types of Copper Lasers			
Parameters	**CVL**	**CuBrVL**	**CuHyBrID**	**KE-CVL**
Average output power (W)	550	125	280	150
Pulse energy (mJ)	138	6.9	15.5	8
Specific average power, (W/cm^3)	1	1.4	2	
Pulse recurrence frequency (kHz)	5–10	15–25	15–25	15–25
Operating temperature (°C)	1500	500	600	1500
Operating regime	Sealed-off flow	Sealed-off	Flow	Flow
Start-up time (min)	30–60	10–15	15–30	30–60
Construction features	Quartz + ceramics	Quartz	Quartz + ceramics	Quartz + ceramics
Efficiency (%)	1.5	3.5	3.8	2
Commercial availability	Yes	Yes	None	Yes

Note: CVL, copper vapor laser; CuBrVL, copper bromide vapor laser; CuHyBrID, hybrid copper laser; KE-CVL, kinetically enhanced copper vapor laser.
Source: From Sabotinov, N.V., *Proc. SPIE, Vol. 5120*, XIV International Symposium on Gas Flow, Chemical Lasers, and High-Power Lasers, SPIE, Bellingham, 30, 2003. With permission.

some parameters of the four main types of copper lasers. Maximum average output powers, listed in the table, were obtained at different sizes of the active medium. The best developments with commercial realization and wide practical applications have the CVLs and the CuBrVLs. For this reason, they will be described in more detail.

10.4.4 The CVL

The development of the copper laser has been related with the solution of two complicated technical problems. The first one concerns the laser active element: the gas-discharge tube. As was said, a copper atom density of 10^{15}cm^{-3} is needed to attain laser action. To obtain such a density, the metallic copper is to be heated up to 1500°C. That implies that the creation of an active element for the elemental CVL is related to the adoption of a high-temperature gas-discharge technique. The second problem refers to the system for excitation of the copper laser.

From this, it can be seen that an inversion population is established for a short time during the leading edge of the excitation pulse. Therefore, the electric power supply for the copper laser has to provide high-voltage pulses that excite a pulsed discharge current with a rise time of some tens of nanoseconds in the laser tube. Usually, the total duration of the current pulse is 150–200 ns. The peak value of current can reach up to some hundreds of amperes. The pulse recurrence frequency can be from some kilohertz value to some tens of kilohertz depending on the active element features. All these requirements with respect to the power supply constitute a complicated task to solve bearing in mind that the load, that is, the laser tube during the discharge pulse alters its active resistance from infinitely large to some ohms. This makes quite difficult the matching of the active element with the power supply pulse generator.

10.4.4.1 Gas-Discharge Tubes for the Copper Laser

In the gas-discharge tube the active medium of the copper laser is created. It should have high temperature properties, that is, it should provide for a long time the conditions for laser action at an operating temperature of about 1500°C. Moreover, it should possess high-vacuum qualities and maintain a clean gas mixture. This imposes certain requirements with respect to the materials used in the laser tube. They should have low electric conductivity at high temperatures, low vapor pressure for the material of the tube at the operating temperatures of the active medium in order to prevent contaminations, vacuum-tightness and stability at the operating temperature. The best materials for the gas-discharge channel are the ceramics Al_2O_3, BeO.

The first type of gas-discharge tube for CVL was heated by an external own [22]. Before 1971, this type of laser tube had been used largely for scientific research. A schematic diagram of the tube is shown in Figure 10.10. The discharge channel is built by a ceramic tube 3 along which are placed copper pieces 4. The discharge channel is located inside a vacuum-tight ceramic tube 5, which ends with metallic flanges 8. Glass end-fittings 1 are attached to the

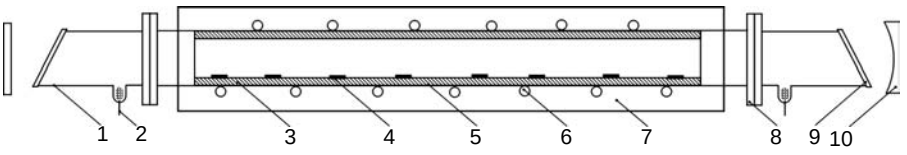

FIGURE 10.10 Schematic diagram of a copper vapor laser with external heating. (From Walter, W.T., *IEEE J. Quant. Electron.*, QE-4(5), 355, 1968. With permission.)

metallic flanges. Electrodes 2 are mounted across the glass fittings. For the electrodes, usually high melting point metals such as the refractories wolfram, molybdenum and the like are used. The glass fittings are cut at 5–6° and on the cuts optical windows 9 are affixed. In the copper laser, the output windows are not set at the Brewster angle because the losses due to reflection are much smaller compared with the high coefficient of gain for the active medium. The ceramic tube 5 is placed in an oven or onto itself a heater 6 is wound. The heater has a good thermal insulation 7 and hence with not much losses to keep a temperature of about 1500°C on the internal wall of the ceramic tube 3. The high temperature laser tube is placed in an optical resonator comprising of two mirrors 10, one of which is with a high reflectivity of 99.8% for both laser output wavelengths 510.6 and 578.2 nm; the other is a usual plane parallel quartz plate with a reflectivity of 8%. The described laser tube with external heating can be used mainly for laboratory investigations. It is not convenient for using out of a laboratory; therefore the copper laser has not found practical applications for a long time. This type of laser tube is used mainly in the regime of single pulse excitation or at low laser pulse recurrence frequencies.

The second type of gas-discharge tube is operated in the self-heated regime. It was suggested in 1972 [24]. In this type of laser tube, the operating temperature of the active volume is established at the expense of the heat released during the flow of the discharge current. The temperature value can be regulated by changing the average input power introduced into the discharge. To obtain a discharge needed for heating the tube, and also for reducing the losses of operating substance from the hot zone, a buffer gas: neon, helium, or argon is used. In this type of tube, the pulsed discharge is of high frequency, usually between 10 and 20 kHz. A typical example of self-heated laser tube is shown schematically in Figure 10.11. Usually, it comprises of a vacuum quartz envelope 4 along the axis of which is placed a ceramic tube 5. Between tubes 4 and 5 there is high-temperature insulation 6 (ceramic wadding). Along the ceramic tube, small pieces of elemental metallic copper 7 are placed. At both ends of the ceramic tube there are metal electrodes 3. Aside the metal electrodes are attached glass end-fittings 2, which end with optical windows 1. This construction of the tube requires thorough degassing. Both the types of gas-discharge tubes for the elemental CVL are operated under very heavy conditions defined mainly by the high operating temperature. The fast temperature changes affect badly the ceramic discharge channels. They often lead to cracking the ceramic tube, which is why its forced heating or cooling is not allowed. For this reason, the elemental CVL has a long warm-up time and slow start of oscillation, usually between 30 and 60 min. Moreover, the operation at high temperatures creates conditions for gradual contamination of the buffer gas with additives of H_2, O_2, N_2, CO, CO_2, thus making difficult the discharge regime. The operational lifetime for such a type of sealed-off tube is usually about 300 h. The longest lifetime, 4000 h, for such tubes has been achieved in Reference [47]. Their preparation needs a special technology. They are suitable for obtaining

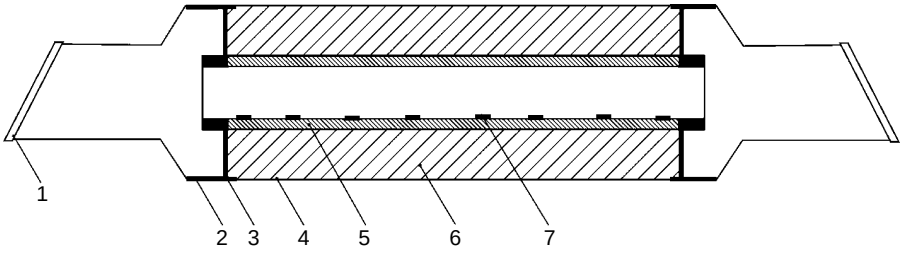

FIGURE 10.11 Schematic diagram of the gas-discharge tube for a self-heated copper vapor laser. (From Burmakin, V.A., Evtyunin, D.N., Lesnoi, M.A., and Bylkin, V.I., *Sov. J. Quant. Electron.*, 8(5), 574, 1978. With permission.)

low average output powers of about 4 W. For more powerful lasers (above 10 W), usually a regime of a continuous gas flow through the active zone is recommended. The high temperature of the active zone is the cause for the copper to move toward the cold zone, thus contributing to the reduction in lifetime for the sealed-off laser tube.

In order to reduce losses of copper, the neon buffer gas has a pressure as high as 400 HPa. In CVLs generating high output powers, discharge channels of above 30 mm in diameters are used. In them, the tube construction is usually dismountable in order to allow replenishment with pure metallic copper after 200 h of operation. Dismountable constructions also enable a fast clean of the optical windows of the laser tube. They cannot be operated in the sealed-off regime. This type of laser tube operates in the regime of a gas flow consisting usually of neon or neon plus hydrogen mixture. In such lasers, a pump to provide circulation of the gas through the laser tube and a cylinder containing neon or neon–hydrogen mixture will be needed as some complication for the lasers results .

10.4.4.2 Electric Power Supply Schemas for CVLs

A significant advance has been attained in CVLs by using the self-heated regime of operation. The essence of the self-heated regime is that the pulse discharge power used for pumping the active medium to establish a population inversion there is used also for self-heating of the gas-discharge tube, that is, for creating the active medium itself. The two roles played by the discharge, first, to prepare the active medium and second, to excite it, impose hard requirements to the power supply block and its matching with the gas-discharge tube. A typical requirement of the power supply is to provide a fast increase for the pulse voltage in about 40 ns and a rise in the pulse current up to 10^3 A. Also, it is necessary that the pulse recurrence frequency is high enough: from 5 to 20 kHz. The total average power, consumed by the power supply block can be different as it reaches up to 10 kW in high-power laser systems.

The principal schema for the electric discharge circuit used in the copper laser comprises a high voltage source (5–10 kV), which charges the pulse capacitor. With the aid of the commutator, the capacitor discharges through the laser tube. The low laser discharge impedance imposes heavy requirements to the commutator. It must commutate currents of large amplitudes and with high recurrence frequencies.

The first commutators to be used have been the spark gaps. They have a simple principle of operation, low impedances and abilities for fast start-up. The ark charger usually has been designed for work at a certain voltage and the pulse recurrence frequency is determined by the capacity and resistivity included in the discharge circuit. One of the chief flaws for this type of commutator is the instability in PRF, which results from noncontrollable conditions of breakdown in the discharger.

The most widely spread is the electric circuit using hydrogen thyratron as a commutator. This commutator has proven to be the most convenient one for excitation of a nanosecond discharge with a high PRF to ensure a high average power needed to maintain about 1500°C in the laser tube. A schematic diagram of the principal circuit for excitation is shown in Figure 10.12. The working capacitor C_0 is charged by the high-voltage rectifier through the charge inductances L_1 and L_2 and the charge diode D. The charging time for the capacitor should be less than the periods following of the excitation pulses. The diode D obstructs discharging C_0 through the rectifier until the thyratron is not triggered. The inductance L_2 besides charging C_0 serves also to switch on the discharge tube as a load of the thyratron generator. The value of L_2 is selected such that the voltage fall in it during charging C_0 is small enough so that no current flows through the gas-discharge tube. On the other hand, during the thyratron

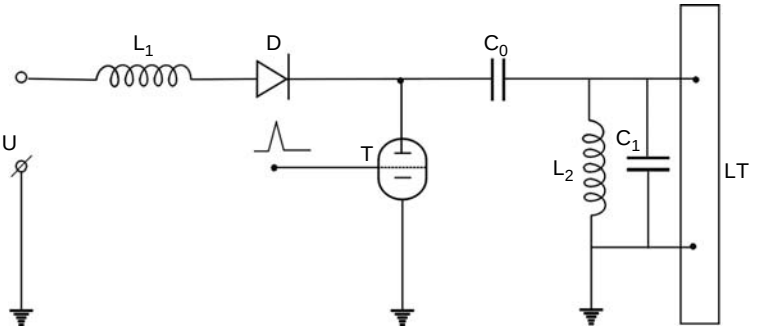

FIGURE 10.12 A principle scheme of the power supply for a copper vapor laser. (From Little, C.E., *Metal Vapour Lasers Physics, Engineering and Applications*, John Wiley & Sons Ltd, Baffins Lane, Chichester, West Sussex, P019 IUD, England, 1999. With permission.)

commutation, the inductive resistance ωL_2 must be large enough to prevent both shunting of the gas-discharge tube and decreasing the excitation pulse energy.

The laser pulse energy strongly depends on the fast rise of the current pulse. For this reason, in the CVL, the efforts are directed toward reducing the discharge circuit inductance. This is achieved by means of the discharge capacitor C_1. This capacitor removes the influence of the thyratron and the electric circuit connecting it with the tube. The discharge circuit now switches on the discharge tube and the capacitor C_1 is in close proximity. Thus, the initial rise of the current through the tube becomes faster. This leads to an increase in the laser power: by an average of 20%. Because of the role played, the capacitor C is called ''peaking'' capacitor.

That classical schema of excitation has been developed over time depending on the laser construction, output power and pulse recurrence frequency. Solid-state commutators such as field transistors or thyristors have been successfully used recently. Also, additional saturating inductances can be used that lead to a shift between the high-voltage pulse and the current pulse in the commutator. This leads to reduction of electric losses in the commutator and improves its regime of commutating.

10.4.5 The CuBrVL

The CuBrVL is a different and very promising alternative to the CVL. The CuBrVL operates at a relatively low temperature, 500°C, and hence many difficulties related to the laser tube construction are removed. The laser tube is made only of quartz glass that makes its preparation easy.

10.4.5.1 Physical Processes in the CuBrVL

The processes leading to an inversion population are considerably more complicated in the CuBrVL than for the CVL. Besides the important process of excitation of copper atoms, the dissociation of copper bromide molecules in the discharge zone is also essential. The active medium of the CuBrVL in the operating regime consists of copper bromide molecules and buffer gas atoms. The copper bromide at room temperature goes from a solid to a gaseous phase as a result of thermal heating. In the active medium of the CuBrVL, five main processes take place: (1) dissociation of copper bromide molecules (10.22); (2) excitation of the liberated copper atoms and population of the upper laser level (10.23); (3) laser oscillation (10.24); (4) decay of metastable levels (10.25); and (5) recombination of copper and bromine atoms, so that copper bromide molecules are produced (10.26). The dissociation of copper bromide

molecules occurs by electron collisions. The energy of dissociation for the copper bromide molecule is about 3.4 eV. The process of dissociation takes place during the discharge pulse. At a high-pulse recurrence frequency, during each successive pulse, copper atoms are liberated in a sufficiently high density that can take part in the process of laser action. The processes participating in laser oscillation are:

$$\mathrm{CuBr} + \mathrm{e} \rightarrow \mathrm{Cu} + \mathrm{Br} + \mathrm{e}, \tag{10.22}$$

$$\mathrm{Cu} + \mathrm{e} \rightarrow \mathrm{Cu}^{*} + \mathrm{e}, \tag{10.23}$$

$$\mathrm{Cu}^{*} \rightarrow \mathrm{Cu}^{\mathrm{M}} + h\nu(511\,\mathrm{nm},\ 578\,\mathrm{nm}), \tag{10.24}$$

$$\mathrm{Cu}^{\mathrm{M}} + \mathrm{e} \rightarrow \mathrm{Cu} + \mathrm{e}, \tag{10.25}$$

$$\mathrm{Cu} + \mathrm{Br} \rightarrow \mathrm{CuBr}. \tag{10.26}$$

Processes (2), (3) and (4) are the same ones that occur in the CVL. New processes in the CuBrVL are (1) and (5). The presence of an electronegative halogen element, bromine, leads to serious changes in the plasma of the laser active medium. These changes influence the laser output parameters.

10.4.5.2 CuBrVL Gas-Discharge Tubes

There are different construction decisions with respect to gas-discharge tubes for the CuBrVLs depending on the generated output power, the laser pulse recurrence frequency, the operating regime of the laser tube (sealed-off or gas flow) and the method for heating the copper bromide and so on. The common aspect among all them is that the laser tube is made of fused silica.

Figure 10.13 shows one of the widely used constructions of the CuBrVL tube [48]. In the active zone of the tube, there are quartz diaphragms to confine the discharge 1, which remove the discharge from the laser tube wall. In the active zone of the laser tube there are reservoirs 2, which contain copper bromide and each of them is heated by a temperature-stabilized external oven. The optimal temperature for heating these reservoirs is about 500°C. The wall of the hot discharge zone is maintained at about 550°C temperature in order to prevent deposition of copper bromide on it. The electrodes 3 of the laser tube are made of porous copper. The construction of these electrodes allows keeping a low bromine partial pressure in the laser tube. At both ends of the laser tube are set quartz optical windows at some distance from the hot zone, and between the electrodes and the windows there are quartz diaphragms to reduce diffusion of copper bromide into the windows, thus preventing them from contamination. The zone between the discharge region confined by the quartz diaphragms and the tube wall plays an important role in the CuBrVL. In this zone there are copper bromide molecules in a large concentration that enter continuously the discharge

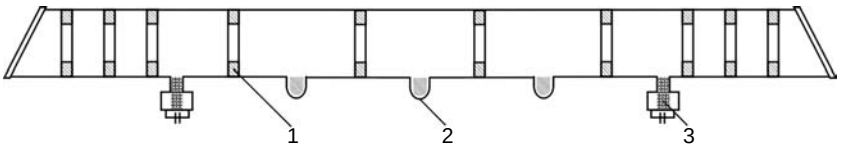

FIGURE 10.13 Schematic diagram of the laser tube construction for a copper bromide vapor laser. (From Sabotinov, N.V., *Pulsed Metal Vapour Lasers—Physics and Emerging Applications in Industry, Medicine and Science*, Kluwer Academic Publishers, Dordrecht, 113, 1996. With permission.)

region and dissociate. The cold zones of the tube between the electrodes and the optical windows have a temperature in the range from 35°C to 40°C. They also have an important role in the operating regime of the laser tube as conditions for trapping the free bromine are created in them and so its accumulation in the tube during the operation is prevented. For stable laser operation, the bromine partial pressure in the laser tube should not exceed 1 Torr. The laser tube is filled with a gaseous mixture of the buffer neon gas of about 20–25 Torr of pressure and hydrogen of 0.3–0.5 Torr of partial pressure. The active zone of the laser tube has a length of 50 cm and a diameter of 20 mm. With this tube, a total average power of 20 W can be generated for both lines. The laser consumption from the power supply unit is an average electric power of 1.5 kV. The lifetime for such a laser tube operated in the sealed-off regime is about 1000 h.

The electric pulse supply unit and schema of excitation are not very different from those described for the CVL. The only difference is that a possibility should be available for operation at a higher PRF, reaching up to 20 kHz.

10.4.5.3 Main Features of the CuBrVL

The most important quality of the CuBrVL is the low temperature, 500°C, of its active medium. This determines some significant excellences for the CuBrVL.

First, the CuBrVL has a short start-up time, from 5 to 15 min depending on the discharge tube sizes. This makes the CuBrVL convenient for practical applications.

The presence of electronegative chemical elements in the active zone (bromine and hydrogen) leads to a change in the plasma parameters, as the conditions for laser action are changed. As a result, the laser pulse duration increases up to 40–50 ns, while under similar conditions in the CVL it is 20–30 ns. The longer laser pulse duration increases the number of roundtrips of the optical radiation in the resonator during one pulse. This leads to a significant improvement in the beam quality that can reach close to the diffraction limit.

Another new quality of the CuBrVL is its higher laser pulse recurrence frequency, 15–20 kHz, while for the CVL under the same geometrical conditions it is 5–8 kHz.

The electric resistance of the active discharge zone in the CuBrVL is larger than for the CVL; therefore, the matching between the laser tube and the pulse power supply is better. The operating regime for the commutating element, the thyratron, is improved significantly, thus its lifetime increases.

The low-temperature operating regime of the CuBrVL and the changed conditions in the gas-discharge plasma as a result of the presence of a halogen element and hydrogen lead to significantly better laser output generation reaching up to 3.8% efficiency. For the CVL, the maximum efficiency is up to 1.5%.

In CuBrVL, the sealed-off operating regime is easily applicable to the laser tube as the lifetime can reach over 1000 h. At low-output powers, 2–3 W, the laser tube lifetime reaches 2000 h.

The main requirements of the CuBrVL are related to the stabilization of the tube's thermal regime. This is the most important condition to be observed, otherwise, the laser output power will be unstable and the laser tube lifetime will be reduced. There is a well-developed electronic technique for stabilizing the thermal regime of the laser operation.

10.4.6 Applications of Copper Lasers

Copper lasers offer great possibilities for practical applications because of their unique characteristics, such as powerful laser output in the visible spectral region, generation of nanosecond laser pulses with high PRFs, high BQ, high gain of the active medium, narrow

laser line spectrum, and laser generation in the deep UV spectrum as a result of nonlinear conversion of the laser radiation. The main areas where this laser has found applications are: industry, mainly for precision processing of different materials technology, for separation of different kinds of isotope; medicine, mainly in dermatology, surgery and photodynamic therapy; navigation; lidar technique; high-speed photography; astronomy, for correction of optical telescopes; laser displays; laser projection microscopy; entertainment business, light illuminations and show effects. These applications could be attained with all main types of copper lasers described so far.

10.4.6.1 Precision Processing of Materials

Over the last years, the use of copper lasers for precision materials processing was highly developed. The ability for generation of high output power in the short-wave visible spectrum, provides possibilities for applications mainly for focusing the laser beam in a small-size spot, of the order of some microns. The good focusing in the copper laser is also a result of its high BQ with divergence close to the diffraction limit.

Major technological operations that can be performed with the copper laser are drilling precise microholes of some tens of micrometers (Figure 10.14), making microcuts and marking different details.

The copper laser is convenient for processing of different metals, ceramics, semiconductors, plastics and the like. It is particularly suitable for processing of copper and aluminum because of their great absorption of laser radiation in the visible spectral region. For these metals, the use of powerful IR lasers (Nd:YAG lasers and CO_2 lasers) is problematic. In the focal spot of copper lasers peak power concentrations of 1–10 $GWcm^{-2}$ can be achieved. For example, in a laser of 45 W average output power, a PRF of 5 kHz and a focus spot size of 50 μm, a temperature of the order of 12,000°C may be attained. Even with a low-power CVL generating 2.5 W output and with a divergence of about 100 μrad, marking operations can be performed [49].

For some special applications in precision materials processing, powerful laser systems, including a leading oscillator and an amplifier stage (MOPA), fitted with computer control and positioning systems have been developed, such as a CuBrVL MOPA system generating 100 W of average output power [50].

10.4.6.2 Laser Isotope Separation

The CVL is of particular interest with respect to building powerful systems for separation of isotopes of different chemical elements. The principle of operation of such a system is based on the possibility of effective pumping of a re-tunable DYE laser, generating at a high PRF. The radiation from the DYE laser is re-tuned precisely at different wavelengths, which are

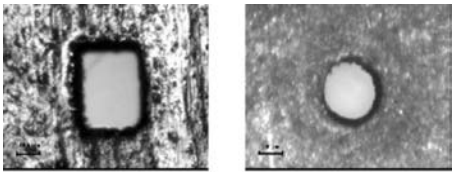

(a) (b)

FIGURE 10.14 Drilling holes of small diameters: (a) Brass, rectangular 230 μm × 280 μm, 578 nm, 5 W. (b) Brass, hole diameter 200 μm, 511 nm, 3.5 W. (From *Laboratory of Metal Vapor Lasers,* Institute of Solid-State Physics, BAS. With permission.)

absorbed selectively by the different isotopes. Thus, some of the isotopes can be ionized and in a strong electric field they can be separated from the isotope mixture. This process is very important in uranium enrichment. For this reason, many countries had organized special programs for the development of this technology and powerful copper lasers were developed. In particular, these programs included the development of multichannel MOPA systems, comprising several amplifier stages [51].

10.4.6.3 Medical Applications

One of the most widespread medical applications of the copper laser is in healing port-wine stains. In this trouble, certain areas of the skin are lavishly supplied by blood as a result of abnormal capillary broadening. By laser irradiation, photocoagulation of these capillaries takes place as the normal blood supply to the skin is restored. Particularly suitable for this method is the yellow line of 578.2 nm, generated by the copper laser. This method has found wide use in cosmetic surgery.

The photodynamic therapy also has been developed as a method for destroying cancers. In this method, cancer cells that have preliminary absorbed chemical substances absorb strongly a determined wavelength of laser radiation and thus they can be destroyed without damaging the sound tissue around them. The copper laser in this case is suitable as a pumping source for a re-tunable DYE laser generating in the red spectral region at a wavelength of 628 nm. For such an application, another self-terminating laser, the gold vapor laser, can be used directly.

10.4.6.4 Laser Projection Microscope

The use of the copper laser as a laser projection microscope is based on the high gain of its active medium. The copper laser tube may be used as an amplifier of brightness in amplifying the optical signal reflected by the object and by an optical system to project it on a big screen (Figure 10.15). By this method, microstructures can be observed on a big screen; also corrections can be made if needed, for example, as in microelectronics [52].

10.4.6.5 Companies Producing Copper Lasers

At present, because of the strong competition between copper lasers and the solid-state Nd:YAG laser generating second harmonics in the visible spectral region, the number of companies producing copper lasers is very reduced. Many of the copper laser applications have been accepted by the solid-state laser generation in the green spectral range.

At present, one of the most active companies—producers of CVLs is the British firm, Oxford-Laser, produces lasers with output powers of some watts to hundreds of watts, suitable for various applications. This company has established its activity on the basis of the scientific studies and original constructions developed by Prof. Dr. Colin Webb and his team.

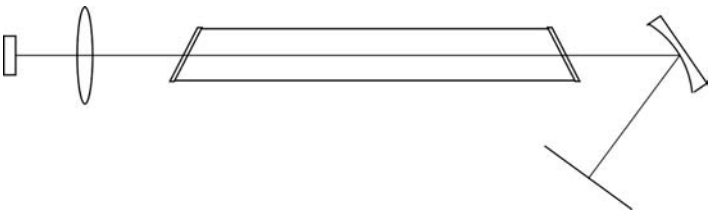

FIGURE 10.15 Schematic diagram of a laser projection microscope. (From Zemskov, K.I., Isaev, A.A., Kazaryan, M.A., and Petrash, G.G., *Sov. J. Quant. Electron.*, 4(1), 5, 1974. With permission.)

Another company producing CVLs is Laser Consult Inc., U.S.A., established in 1968 and guided by the inventor of the CVL, Prof. Dr. W.Walter. The company Vosstok, Russia, produces CVL with sealed-off tubes, generating output powers from 1 to 35 W and with laser tube lifetimes of over 1000 h. This firm employs the rich scientific experience of the team guided by Prof. Dr. Petrash. Other Russian companies, manufacturing CVLs are Copris & M, Lamet, Evrica and Zond.

The CuBrVL is produced by the companies stated in the following. The company Norseld, Australia, produces lasers that are used mainly in medicine and cosmetics and also in industry for precision materials processing [53]. The company was the first to implement in practice the CuBrVL, patented by the group of Prof. Dr. Sabotinov [54].

The firm Pulslight, Bulgaria, produces CuBrVLs for the entertainment business, industry (precision materials processing) and medicine. This company takes part in numerous scientific research projects in cooperation with the team of Prof. Dr. Sabotinov [55].

10.5 THE HE–CD LASER

10.5.1 Laser Action with Cadmium Ions

10.5.1.1 Historical Information about the He–Cd Laser

The He–Cd laser is the main representative of the class of CW MVLs. It is the first laser system of this type in which laser action has been obtained. As in most CW MVLs, in the He-Cd laser, in the beginning, pulsed laser action has been obtained. First in 1965, pulsed lasing was achieved on the lines of 533.7 and 537.8 nm. In 1966, pulsed laser oscillation on the 441.6 nm line was attained [7]. For the first time, CW lasing in a He–Cd discharge on the cadmium ion line of 441.6 nm was obtained in 1968. The laser transition for the 441.6 nm line occurs between the upper ion level $5s^2\ ^2D_{5/2}$ and the lower ion laser level $5p^2P_{3/2}$. A little later, UV laser generation was achieved on the line at 325.0 nm wavelength. In 1970, CW lasing on the cadmium ion lines of 533.7, 537.8, 635.5, 636.0, 723.7, and 728.4 nm was achieved in the NG discharge in a HC. To date, 11 CW laser lines in the single ionized cadmium ion have been known.

10.5.1.2 Energy Level Diagram for the Cadmium Ion

The energy level diagram with laser lines for the single ionized cadmium ion is shown schematically in Figure 10.16. In this figure, all the upper and lower laser levels for the 11 laser lines are denoted and also, are given the metastable state energy levels, $2s^3S_1$ and $2s^1S_0$, for the helium atom, and also the ground level, $1s^2S_{1/2}$, for the helium ion. Laser action on the 11 lines of the cadmium ion is obtained under different discharge conditions. For some lasing lines most suitable is the PC of a glow discharge, while for others, it is the NG discharge in a HC. The cadmium–ion laser lines generated in the He–Cd discharge can be divided by lasing mechanism in three main groups. These groups include: laser lines excited largely by Penning collisions with helium metastable atoms; laser lines excited by charge transfer collisions with helium ions; and laser lines excited by a combination of charge-transfer collisions, cascade processes from upper levels and direct electron impacts.

10.5.2 The Cataphoretic He–Cd Laser

The CW cataphoretic He–Cd laser is the best known and widely used MVL. It emits the 441.6 nm violet line and the 325. 0 nm UV line. The He–Cd laser oscillates in the PC of a DC discharge like the He–Ne laser. The use of the cataphoretic effect in the laser tube [57] is

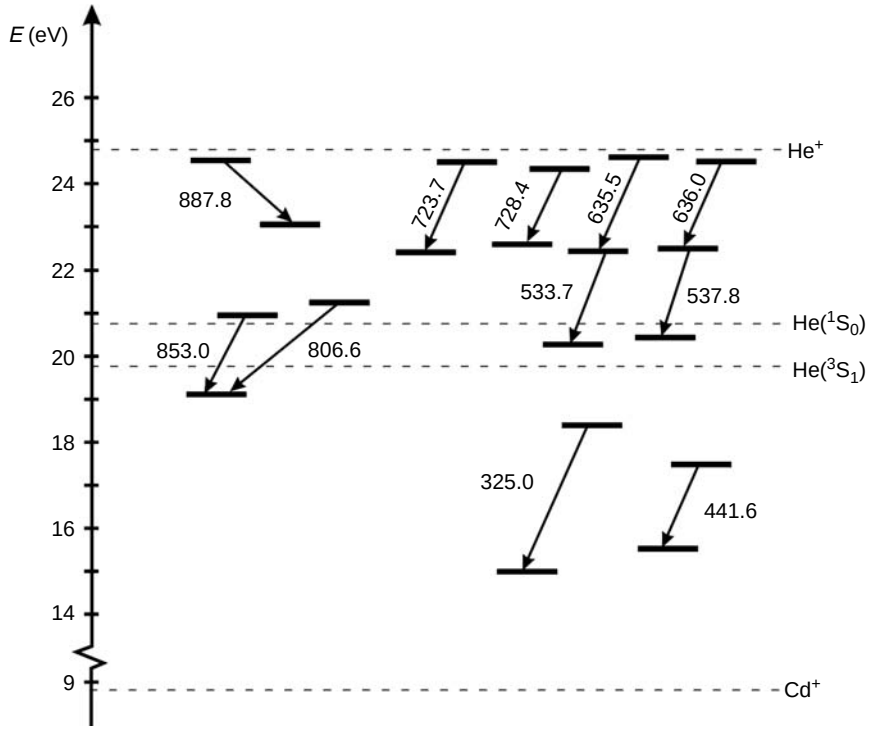

FIGURE 10.16 Laser energy level diagram for the cadmium ion. Wavelengths are in nm. (From Ivanov, I.G., Latush, E.L., and Sem, M.F., in *Metal Vapour Ion Lasers—Kinetic Processes and Gas-Discharges*, John Wiley, Chichester, 1996. With permission.)

very useful in the creation of suitable constructions for the He–Cd laser. The cataphoretic effect allows maintaining the cadmium vapor density constant along the discharge tube. Cadmium vapor, which has come in the helium discharge, is excited by electron collisions and collisions with excited helium atoms. Thus the produced positively charged cadmium ions begin to move toward the negative cathode end of the laser tube. At appropriate discharge tube bores, optimal conditions for cataphoretic transportation of cadmium vapor are found. The use of the cataphoretic technique in the He–Cd laser aids in establishing favorable conditions for the confinement of cadmium vapor into a certain section of the laser tube. This leads to reducing the danger of contamination of the Brewster windows by cadmium deposition onto them. The cadmium is placed in a reservoir near to the tube anode end and is heated by a small oven. The oven sets the required temperature by which it controls the cadmium vapor pressure independently of the discharge current through the laser tube. This method allows building of He–Cd lasers of a very simple design that is very close to that of the He–Ne laser.

The lasing regime in the He–Cd laser depends on some parameters, which are mutually related. Cadmium vapor pressure, P_{Cd}, determines availability of lasant particles in the laser. The helium atom density in the discharge ensures the transfer of energy needed for excitation of cadmium ions to the upper laser level. Atoms and ions in the discharge are excited by collisions with electrons. The probability that these collisions take place depends on the electron density. The populations of given excited energy levels of atoms and ions are determined mainly by the electron energy. Thus, another essential parameter is the density of the discharge electric current through the active part of the laser tube. The optimal

operating conditions for the laser at fixed geometry of the discharge tube and resonator parameters, are determined by the cadmium vapor P_{Cd}, helium pressure P_{He} and the discharge electric current.

10.5.2.1 Lasing Mechanisms for the 441.6 and 325.0 nm Lines

The cadmium ion laser lines at wavelengths of 441.6 and 325.0 nm have upper levels with the electronic configuration $4d^9 5s^2$. The 441.6 nm line includes the upper laser level $5s^2\ ^2D_{5/2}$ and the lower laser level $5p^2P^0_{3/2}$. The 441.6 nm line is the only optical transition starting from $5s^2\ ^2D_{5/2}$ that aids its experimental study very much. The 325.0 nm UV line is between the upper laser level $5s^2\ ^2D_{3/2}$ and the lower level $5p^2\ ^2D_{1/2}$. The upper laser energy levels are the most close to the helium metastable level $2s^3S_1$ as their energy is about 2.5 eV lower than that of the helium metastable level. The most favorable mechanism for excitation of these levels is the Penning collisions between helium metastable atoms and ground state cadmium atoms:

$$He(2s^3S_1) + Cd \rightarrow (Cd^+)^* + He + e. \tag{10.27}$$

These collisions do not have a strong resonant character as the energy difference between the helium metastable level and the cadmium ion excited level is removed by the liberated electron. The cross section for the Penning process leading to population of the level $5s^2\ ^2D_{5/2}$ is 4.5×10^{-15} cm^2.

Besides the Penning process, the upper laser levels are also populated by direct electron impacts:

$$Cd + e \rightarrow (Cd^+)^* + 2e. \tag{10.28}$$

The cross section for this process is 0.3×10^{-16} cm^2.

There is another process, photoionization, contributing to the upper laser level population. This process is not as essential as the first two ones. The upper laser levels of the lines 441.6 and 325.0 nm can be populated also by photoionization, which is caused by UV emission from helium atoms in the deep UV region. Both laser transitions have Doppler broadening of the lines. Because the laser generation is obtained by using mainly metallic cadmium that is a mixture of eight isotopes, the total width of laser generation lines is the sum of the Doppler widths of all the isotopes. Each isotope has a line width from 1.0 to 1.5 GHz. The total spectral width of the 441.6 nm laser line for the natural mixture of isotopes is about 9.5 GHz. The greatest contributions to the He–Cd laser generation on the 441.6 nm line has the isotopes Cd^{112} and Cd^{114}. If the He–Cd laser is made on the basis of only isotope Cd^{114}, it has a narrow laser spectral line of about 2 GHz and a high coefficient of gain attaining 20%/m, as the laser output power is significantly higher. With the use of a natural isotope mixture, the maximum gain coefficient for the active medium reaches up to 5%/m.

The laser line 441.6 nm has 1.4×10^6 s^{-1} probability of transition, as the upper laser lifetime is 7.1×10^{-7} s. The laser line at 325.0 nm wavelength has a probability of transition of $7.8 \times 10^5 s^{-1}$ as the lifetime of the upper laser levels is 1.1×10^{-6} s. Under the conditions that are typical for laser generation, the population inversion density is 4×10^{16} m^{-3} [56].

10.5.2.2 Designs of the He–Cd Cataphoretic Laser

The simplest design of the cataphoretic He–Cd laser is shown schematically in Figure 10.17. The principle of operation is described by Goldsborow in Reference [56]. The tube is made of glass. The glass should be of high quality and should withstand high temperatures and abrupt temperature changes because the operating temperature of the laser is about 350°C.

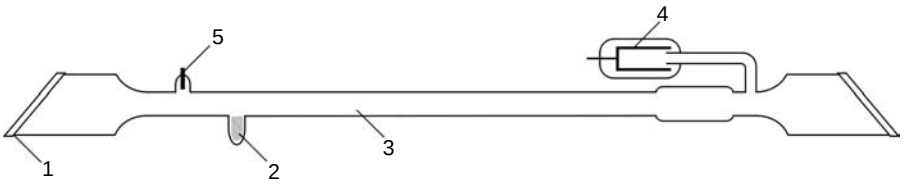

FIGURE 10.17 Schematic diagram of the tube of a He–Cd^+ cataphoretic laser. 1—Brewster windows, 2—reservoir with cadmium, 3—discharge channel, 4—cold hollow cathode, 5—anode. (From Goldsborough, J.P., *Appl. Phys. Lett.*, 15(6), 159, 1969. With permission.)

The active part of the laser tube can be from 1 to 2.5 mm in bore as the length ranges from 25 to 80 cm depending on the output power for which the laser has been designed to emit. Usually a cold cathode is used. The superiority of the cold cathode includes mainly its long lifeterm and an operating regime, which is easier, compared with the hot cathodes. The cathode material can be aluminum, molybdenum, and wolfram, impregnated with beryllium. The cathode has usually the form of a hollow cylinder. The use of the cathode of a larger active surface facilitates its operating regime and reduces the harmful effects of sputtering resulting from bombardment by heavy positive ions. The laser tube anode is not burdened in the gas-discharge; therefore; molybdenum or wolfram rod can be used as anode. Near the anode, at the end of the active zone of the laser tube, there is a glass reservoir containing metallic cadmium. The glass reservoir is placed in a cylindrical oven, which can be heated to 300°C. At both ends of the active zone of the laser tube, there are widenings that serve as traps for cadmium vapor. The cold zones of the laser tube end with plane parallel Brewster windows. They are made usually of fused silica and their surface is well processed. The tube is filled with helium buffer gas that has a pressure between 5 and 10 Torr. The ratio between the helium pressure and the cadmium vapor partial pressure is usually 100:1. Under the optimum conditions for laser generation, the operating temperature of the discharge channel is 350°C and of the cadmium in the reservoir is 260°C. The discharge current flowing through the active zone of the laser tube ranges from 50 to 120 mA as is determined by the discharge channel diameter.

During the operation of the cadmium laser, active capture of the helium buffer gas is observed during condensation of the cadmium in the cold zones of the tube; as a result, the helium pressure falls gradually. These losses of helium are compensated by means of a reservoir for helium attached to the laser tube, which by electrical control can deliver helium to the active zone of the laser tube. Another problem, also associated with the lifetime of the laser tube, is the loss of metallic cadmium. This problem is usually solved by making a diffusion channel to the tube to carry the cadmium from the cathode zone back to the anode zone in the cadmium reservoir. Different constructions are available and are used by manufacturing companies to solve this problem of back diffusion.

The lifetime of the laser tubes in He–Cd cataphoretic lasers usually exceeds 5000 h. The He–Cd laser output power depends on the geometry of the laser tube and the discharge current through it. For laser tubes of 20–40 cm lengths, the maximum output power can reach up to 60 mW for the line 441.6 nm. With laser tubes of 60–70 cm active lengths, maximum output powers of 200 mW can be achieved for the line 441.6 nm, and 100 mW for the line at 325 nm wavelength. In the cataphoretic He–Cd laser, the input power supply is a high-voltage rectifier with maximum voltage of up to 10 kV and a current from 100 to 200 mA. The voltage fall at the discharge tube is 5–6 kV as the rest of the voltage is distributed at the ballast resistance, which can be up to 100 kΩ. The particular feature in the power supply for this laser is that the discharge resistance varies. Initially, it is relatively large as the discharge arises in

clean helium without the presence of metal vapor. During the entry of the cadmium vapor into the discharge zone, the discharge voltage falls as the discharge current rises. This feature of the He–Cd discharge tube to change its resistance requires the provision of a stabilized current flow by the high-voltage rectifier. For this purpose, feedback is used to maintain the initially set discharge current constant independently of the change in the gas-discharge tube resistance.

10.5.3 The Hollow Cathode He–Cd Ion Laser

The NG discharge in a HC has proved to be very suitable for excitation of metal ion energy levels by charge transfer collisions. This is explained with the increased density of high-energy electrons in the NG discharge in a HC. For this reason, in a HC discharge with a mixture of helium and cadmium vapors, the processes of charge transfer excitation of high-lying cadmium ion energy levels that take part in the laser oscillation occur very efficiently. Under such conditions, the known cadmium ion lines are excited, including those lasing in the PC of the glow discharge and pumped by Penning ionization and direct electron impacts.

The possibility of simultaneous generation of two red lines, two green lines and one blue line makes the HC He–Cd laser an efficient laser source of "white" laser light. This is why, the laser is still called "the He–Cd white-light laser."

The HC He–Cd laser oscillates on all cadmium ions' laser lines and in this respect excels the cataphoretic He–Cd laser. Two problems, however, obstruct the development of the HC He–Cd laser. The first problem is the relatively short lifetime of the laser tube. The second problem is the uncontrollable conversion of the glow discharge into an arc discharge as then the laser generation terminates. These are the main causes making difficult the commercial development of the HC He–Cd laser.

For the first time, pulsed laser oscillation in a HC was obtained by Sem and Michailevski [58] on lines at wavelengths of 441.6, 533.7, and 537.8 nm. In the period 1969–1970, a HC of flute-type was used for laser action in cadmium [59,60]. These studies provide the basis for the development of the CW HC He–Cd laser.

The most serious advance in this field was made by Fujii, who created the first HC white-light laser oscillating simultaneously on the lines 441.6, 533.7, 537.8, 636.0, and 635.5 nm. The laser created by him oscillated in a HC of flute-type. The pressure of the helium buffer gas in the laser tube was 9–14 Torr and the discharge current flowing through it was 0.5 A, as the laser action was obtained with excitation by pulses with a PRF of 50 Hz. A cylindrical HC of an active length of 80 cm and a bore of 4 mm was used, as the total laser output power reached up to 10 mW.

10.5.3.1 Mechanism of Laser Oscillation on the Cadmium Ion Lines in a Hollow Cathode

All upper laser levels of the cadmium ion that energetically lie higher than the helium metastable level 2^1S_0 (20.96 eV), Figure 10.16, are excited mainly by charge transfer collisions between ground-state helium ions and ground-state cadmium atoms:

$$He^+ + Cd \rightarrow (Cd^+)^* + He. \tag{10.29}$$

These laser lines depending on oscillation mechanism are divided into two groups. The first group of lines: 635.5, 636.0, 723.7, 728.4 and 887.8 nm have upper levels spaced at about 0.3 eV near to the helium ion ground-state level. These lines are excited by direct charge transfer collisions. The difference between the energy levels of these lines and the helium ion ground-state level is small enough that the resonance charge transfer process is very likely to take place.

The other group of the lines 533.7, 537.8, 806.7, and 853.1 nm are at about 1.9 eV apart from the helium ion ground state.

The laser lines 806.7 and 853.1 nm have other mechanisms of excitation. Their upper levels are populated by charge transfer collisions and by cascade processes from upper excited levels of the cadmium ion.

Both green laser lines of the cadmium ion 533.7 ($4f^2F^0_{5/2}$–$5d^2D_{3/2}$) and 537.0 m ($4f^2F^0_{7/2}$–$5d^2D_{5/2}$) have a more interesting mechanism of excitation. These laser lines have three population mechanisms for the upper laser levels: charge transfer collisions with helium ions, cascade transitions from upper levels and electron impacts. Besides them, population of these levels occurs also by de-excitation collisions between cadmium ions excited into higher levels and slow electrons. Laser oscillation on the described lines is obtained only in the NG discharge in a HC. This is explained with the large number of fast electrons available in the HC discharge. At the same time, in this discharge, the process of excitation of the cadmium ion lines of 441.6 and 325.0 nm excited by Penning collisions as was described for the cataphoretic He-Cd laser take place efficiently.

10.5.3.2 Constructive Features of the HC He–Cd Laser

In the HC He–Cd laser, different constructions of gas-discharge tube are used. They can be divided into two types according to the electric field direction with respect to the HC axis: discharge tubes with a transverse discharge and discharge tubes with a longitudinal discharge. Moreover, the HC laser tubes depending on the discharge voltage between the anode and cathode, can be low-voltage ones of up to 200–400 V and high-voltage ones of above 500 V. Depending on the HC geometry, the laser tubes can be with a cylindrical cathode or with a HC that has usually a rectangular slot [61,62].

One of the most commonly used constructions of HC laser tube is that of the ''flute''-type (Figure 10.18). It belongs to the low-voltage construction with a HC transverse discharge. The laser tube is made of glass; HC 3 is mounted in it. The HC is prepared from a copper cylindrical tube as oxygen-free copper is usually used. The tube has 4 mm inner diameter, 8 mm outer diameter and 60 cm length. Along the cathode length, seven equally spaced apertures of 3 mm diameter are made. Opposite to them, also equidistantly along the HC, six apertures of 4 mm in diameter are made. Seven anodes 6 of molybdenum or wolfram of 2 mm diameter are placed opposite to the first row of apertures. Opposite to the second row of apertures of 4 mm diameter, there are six glass reservoirs containing the metallic cadmium 2. Each reservoir is heated by an oven 1. At both sides of the cathode, lateral anodes are placed at 10 mm distances from the cathode. Both ends of the tube are cut at the Brewster angle and fused silica optical windows 4 are affixed to them. The anodes are connected with the power supply current rectifier by ballast resistances 7 of about 1 kΩ. They promote the discharge to be stable and make difficult for arc to rise in different sections of the discharge tube.

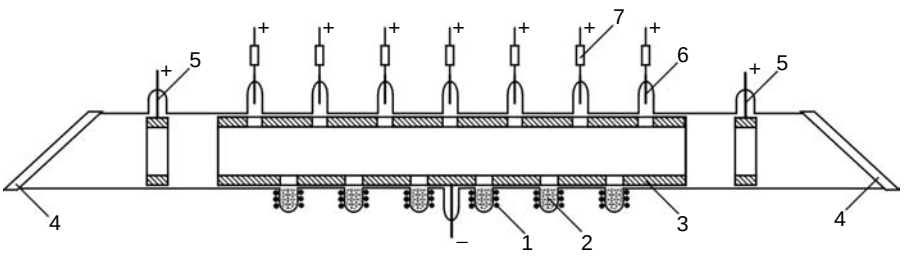

FIGURE 10.18 Schematic diagram of a flute hollow cathode laser tube. (From Fujii, K., *Trans. Inst. Electron. Eng. Jpn.*, in Japanese, 93-C(1), 1, 1973. With permission.)

The laser tube is filled with helium of 6–8 Torr of pressure. The NG gas-discharge is initially in the helium and fills the cylindrical HC. From the reservoirs heated up to 280°C, cadmium vapor comes into the discharge zone. Thus in the He–Cd discharge, the processes of excitation of cadmium ions take place. The lateral anodes prevent cadmium from spreading to the discharge zone and contaminating the Brewster windows. In this case, the cataphoretic effect is used to repulse positive cadmium ions to the cathode. The laser resonator includes one high-reflectivity broadband (420–680 nm) mirror. The output coupler is a mirror with a transmissivity of 1%–1.5%. The gains for different lines under the discharge conditions typical of "white"-light generation are: 441.6 nm—12% m^{-1}, 537.8 nm—15% m^{-1}, 533.7 nm—11% m^{-1}, and 636.0 nm—5% m^{-1} [63]. In order to equalize the intensities of different laser lines, a radiation maximum close to the "white" light needs to be obtained and the output mirror should provide reflectivities for different wavelengths. The losses are for both the blue and green lines rise while the red lines lase under the most optimal conditions. From the laser tube with a construction as illustrated in Figure 10.18, maximum output powers were obtained as follows: about 90 mW for 441.6 nm, 60 mW for both laser lines 533.7 and 537.8 nm and about 40 mW for the lines 635.7 and 636.0 nm.

10.5.3.3 The RF "White" He–Cd Laser

The HC He–Cd laser is faced with numerous problems concerning the discharge stability in the laser tube. Also, the metal deposition changes the electrode configuration and reduces the tube lifetime. A solution of the problem is to use a RF discharge for excitation of cadmium ion lines. The RF discharge can be created by means of external electrodes on the basis of capacitive coupling. Thus the tube has a very simplified construction and the main problem is the reduction of the matched introduction of RF electric power into the laser tube. In a RF discharge through a He–Cd gas mixture, the same lines of laser generation are excited as in the HC NG discharge. It has turned out that the RF plasma parameters are the same as those for the HC discharge; thus, the use of a RF discharge is a good alternative to the HC discharge. The transverse RF He–Cd discharge has been well studied as output powers of some tens of milliwatts have been obtained for each individual line [64]. The principle of operation of the RF He–Cd laser is illustrated in Figure 10.19. The laser tube is made of quartz glass. A ceramic tube of 4 mm inner diameter and 40 cm length are inserted into it. The external electrodes are made of nickel or other suitable metals, which does not change its qualities during long operation. The cadmium is placed in a quartz reservoir, which is situated in the central zone of the laser tube and is heated by a temperature-adjustable oven. Cadmium vapor enters the active discharge zone through an opening of 3 mm diameter made in the ceramic tube and is spread by diffusion to the cold zones of the tube. At both ends of the active zone of the tube before the Brewster windows, there are widenings where cadmium condenses. At both ends of the laser tube there are quartz windows set at the Brewster angle.

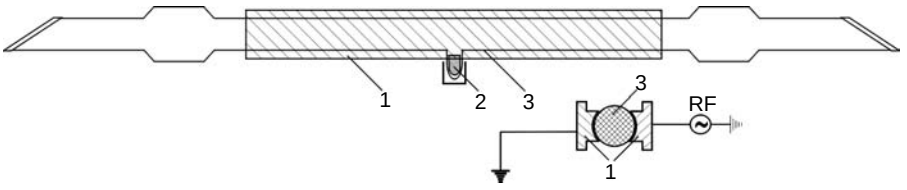

FIGURE 10.19 Schematic diagram of an RF-excited He–Cd laser. 1—External electrodes, 2—reservoir with cadmium, 3—quartz tube. (From Reich, N., Mentel, J., and Mizeraczyk, J., *IEEE J. Quant. Electron.*, QE-31(11), 1902, 1995. With permission.)

The helium pressure is about 10 Torr. The high-frequency generator, which supplies the tube, operates at 27 MHz frequency. Between the tube and the power supply generator there is a matching unit that enables the introduction of electric power in the gas medium with minimum losses.

10.5.4 Applications of the He–Cd Lasers and Company Producers

10.5.4.1 Applications of the He–Cd Cataphoretic Laser

The He–Cd laser, generating the lines 441.6 and 325.0 nm, has been still of interest for numerous applications in spite of the great competition by the diode lasers that emit in the blue spectral range and the Nd:YAG laser generating third harmonics in the UV spectral range. The He–Cd laser because of its high coherence is very valuable in holography, where it is used for making different holographic markers in credit cards, security markers, trade marks, holographic images of marks and the like. By the use of the He–Cd laser with a $LiNbO_3$ crystal, vast bulks of holographic information can be stored.

Because of the great sensitivity of photoresists in the spectral band of the He–Cd laser, it is used in photolithography and also in the production of compact disks, CD-ROMs, laser video-disks, holographic diffraction gratings and the like.

The He–Cd laser is also used for detection and diagnostics of cancers with combined usage of medical preparations, which are accumulated in the cells and fluoresce when irradiated at 441.6 nm wavelength. The wavelength 325.0 nm is used in the fluorescence microscopy in biomedicine. By this method, small admixtures of fluorescencing molecules can be detected with high sensitivity. The photonic energy on the 325 nm line is suitable for stimulating photochemical reactions that are particularly important in biochemistry. In medicine, the 325 nm wavelength is applied for fast cell analysis.

The He–Cd laser is widely used in scientific studies. It is an important light source in the Raman spectroscopy. The He–Cd laser is used for control of different deformations by interferential diagnostics methods [65].

10.5.4.2 Applications of the "White" He–Cd Laser

The most important applications of the "white" He–Cd laser are in the color holography, color television image, different types of medical diagnostics, where several wavelengths are used simultaneously. The "white" He–Cd laser is used in the color laser microscopy. This laser has found very successful applications in color printing. In connection with this application, the development of this laser has began, as great efforts have been focused in the creation of long-lived He–Cd laser tubes of flute-type with lifetimes of over 1500 h. This laser is used in the multiwave metrology and in the maintenance of color standards.

10.5.4.3 Companies Producing He–Cd Lasers

At present, two companies produce cataphoretic He–Cd lasers and have stable positions in the market. The firm Kimmon is the biggest producer of these lasers. It has begun to produce He–Cd lasers since 1971. The company makes various models of He–Cd lasers, generating different output powers at both wavelengths. The highest power for the line 441.6 nm offered by the company, is 180 mW emitted in the single-mode regime. Kimmon produces He–Cd lasers of 50 mW output power at 325.0 nm wavelength in the single-mode regime, and 100 mW output power in the multimode regime. The lifetime of the sealed-off laser tubes made by the company is over 6000 h. The coherence length of the lasers is from 10 to 30 cm. To date, the company has sold above 25,000 lasers.

Another company, also well known, that produces He-Cd lasers is Melles Griot. It offers different laser models generating different output powers. The most powerful laser, made by this company emits 135 mW output at 441.6 nm wavelength. The highest output power for the 325 nm UV line is 55 mW.

10.6 UV COPPER ION LASERS

10.6.1 Introduction

MVLs are of great interest because of their ability to oscillate in the deep UV spectral region. Laser action in the deep UV takes place in ions of copper, gold and silver, excited by a HC discharge. The deep UV transitions can occur in a pulsed regime as in a continuous regime. Usually, the atoms of copper, gold and silver are obtained by sputtering of the HC, which is made of these metals or is covered by a layer of them.

The laser action in a HC where metal atoms result from sputtering has become intensively studied because of the possibility of realizing relatively simple and reliable laser devices. HC laser oscillation in copper ions was achieved by Csillag et al. [66] in 1974 on the IR copper ion line at a wavelength of 708.8 nm. Copper atoms are produced by sputtering of the copper HC. This result was soon followed and developed by Collins et al. [67] who obtained laser oscillation on many transitions in copper, gold and silver ions, in a broad spectral range from the deep UV to the IR spectral region.

10.6.2 Laser Oscillation on Ion Transitions in Copper, Gold, and Silver

Laser oscillation on copper ion transitions in the NG discharge has been obtained to date on 54 laser lines in the spectral range of 248.6 nm–2001 μm. The lasing process for different laser lines occurs with excitation by atom–ion charge transfer collisions between metal atoms and helium or neon ions. In the deep UV range, 248.6–274 nm, the copper ion generates totally 12 laser lines. These lines are excited by charge transfer collisions of copper atoms with neon ions [68]. Laser action in gold ions has been obtained on totally 24 laser transitions in the spectral range of 226.4–886.8 nm. Ten of these lines are in the deep UV spectral region, 226.4–295.8 nm. The excitation of gold ion lines oscillating in the deep UV is promoted by charge transfer collisions with ground- state helium ions [68]. Silver is the third metal whose ions generate 33 laser lines. Lying in the spectral range of 224.3 nm–2.080 μm. In the deep UV, there is laser generation on three lines in the range of 224.3–318.1 nm [68]. Laser action in the ions of copper, gold and silver is the most successful in three types of HC. The first type of HC is a slot made on a metal rod. This slot can be with a rectangular section or can be fitted with a cylindrical opening, Figure 10.20. In the hollowness of the cathode or of the cylindrical opening, the NG discharge is formed as the metal atoms sputtered from the cathode surface occupy the opening. This type of HC operates in a transverse low-voltage discharge [69].

The second type of HC is called "high-voltage HC" and has a construction as is shown schematically in Figure 10.20 [70]. It is a cylindrical cathode inside which near the cylinder wall, a set of anodes are situated in a circle. In the central zone, bounded by anode rods, a negative discharge glow with a large density of high-energy electrons is obtained and the process of excitation of metal ion lines takes place effectively. This HC has a high-discharge voltage (~1 kV), because of which it is called "high-voltage cathode."

The third type of HC has a helical configuration, as shown in Figure 10.21 [71]. This type of cathode is characterized by high-discharge voltage, which is directly proportional to the helical step. This type of HC is featured besides by the high-electron energy, also by the efficient metal sputtering, as a result of which are obtained good conditions for laser action in sputtered metal ions.

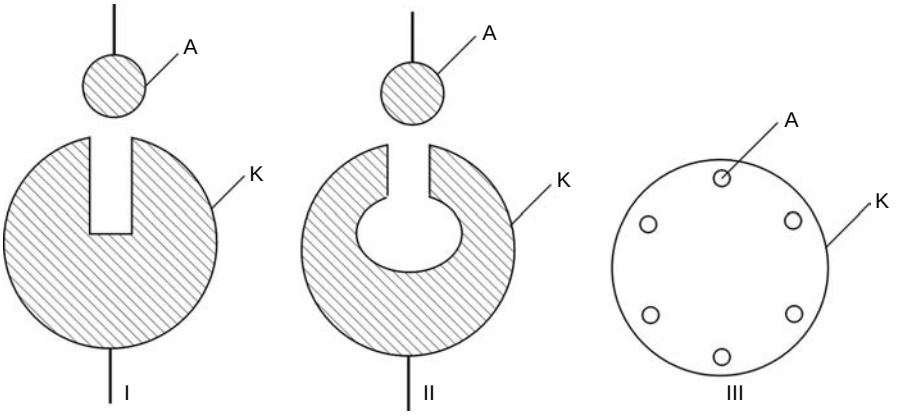

FIGURE 10.20 Cross sections of a hollow cathode with a rectangular slot (I), with a cylindrical slot (II); a high-voltage hollow cathode (III). (From Little, C.E., *Metal Vapour Lasers Physics, Engineering and Applications*, John Wiley & Sons Ltd, Baffins Lane, Chichester, West Sussex, P019 IUD, England, 1999. With permission.)

10.6.3 The Copper Ion Laser

10.6.3.1 Principles of Laser Generation

Laser oscillation on UV copper ion laser transitions occurs between the upper laser levels with the electronic configuration $3d^9 5s$ and the lower laser levels $3d^9 4p$. The electron energy level structure is shown schematically in Figure 10.22. Upper laser levels of the copper ion are pumped by charge transfer collisions:

$$Cu + Ne^+ \rightarrow Cu^{+*}(3d^9 5s) + Ne. \tag{10.30}$$

In the copper ion UV laser, the processes influencing the population of the lower laser level are of great significance. There are three important processes, which lead to population of the lower laser level, and they influence essentially the laser generation regime. Because the lower laser level lies energetically near the metastable level of neon, it is excited very efficiently by a Penning ionization process:

$$Cu + Ne^m \rightarrow Cu^{+*}(3d^9 4p) + Ne + e. \tag{10.31}$$

The second process, which also has an effect on the lower laser level populations, is excitation by direct electron impacts from the levels $3d^9 4s$:

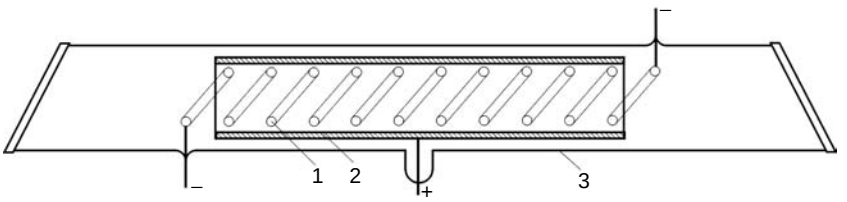

FIGURE 10.21 Schematic diagram of a laser tube with a helical hollow cathode. 1—Hollow cathode, 2—cylindrical anode, 3—glass tube. (From Grozeva, M. and Sabotinov, N., *Opt. Commun.*, 41(1), 57, 1982. With permission.)

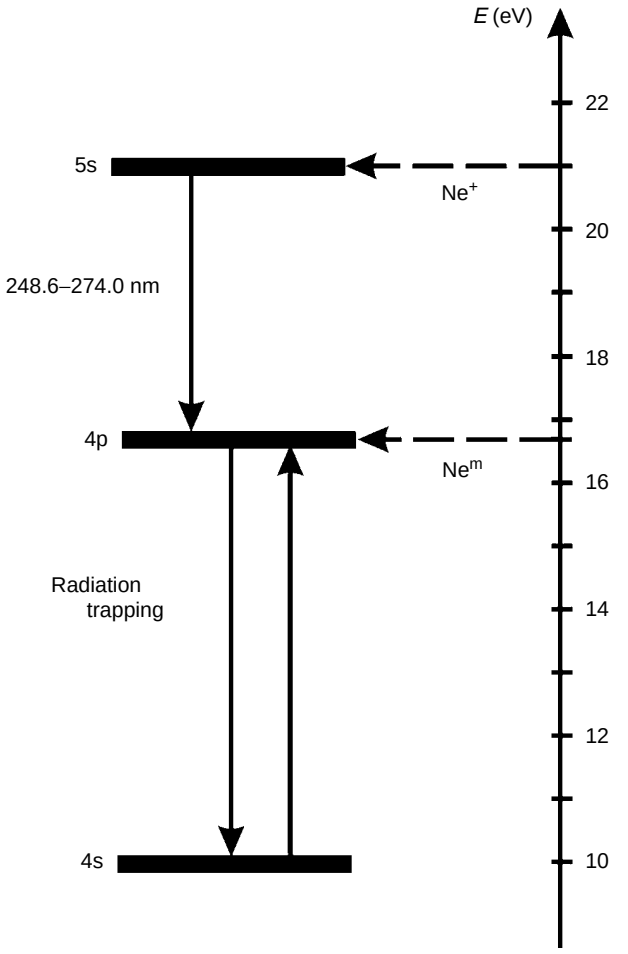

FIGURE 10.22 Energy level diagram of copper ion laser lines in the deep ultraviolet spectral region. (From McNeil, J.R., Collins, G.J., Persson, K.B., and Franzen, D.L., *Appl. Phys. Lett.*, 27(11), 595, 1975. With permission.)

$$Cu^{+}*(3d^{9}4s) + e \rightarrow Cu^{+}*(3d^{9}4p) + e. \tag{10.32}$$

The third mechanism to populate the lower laser levels is radiation trapping of a transition from the metastable levels $3d^{9}4s$. In order to obtain intensive laser generation, it is important to reduce maximally the efficiency of the population process for the lower laser levels in collisions with metastable neon atoms. This may be achieved with the aid of some additives in the gas mixture that disrupts the "harmful" metastable neon level, thus the lower laser level population is reduced and the laser generation intensity is enhanced, as a result.

10.6.3.2 Copper Ion Laser with a Slotted HC

Stable laser oscillation on the copper ion transitions is obtained in a slotted HC discharge. The most used HC is made of copper and has a rectangular slot of 6 mm depth and 2 mm width. Good results have been attained at HC lengths from 25 to 120 cm. Optimal conditions

for laser oscillation on UV laser lines are achieved at a current density of 0.65 Acm^{-2}, which corresponds to a discharge voltage of 260 V. The laser operates very stably in a quasi-continuous regime. At a slotted HC length of 120 cm, the maximum peak output power of 900 mW was obtained for the most intensive UV line of 248.6 nm. Intensities of the strongest lines 248.6, 259.1, 260.0 and 270.3 nm correlate as 14:38:30:18. The highest gain coefficient for the line 248.6 nm is 9% m^{-1} [72]. The laser resonator comprises a dense mirror of high reflectivity for the spectral range, in which the lines lase and an output mirror of a transmissivity of 1%–2%. There are different construction solutions for making the laser resonator. In some cases, internal laser mirrors are used. In other cases, the mirrors are external and Brewster windows of optical quartz, introducing small losses in the generated UV spectral output, are affixed to the laser tube.

10.6.3.3 Other Discharge Solutions for Generation of UV Copper Ion Laser Lines

Besides the HC discharge, still two ways are known to obtain laser oscillation on the copper ion transitions in the UV spectrum. The first way is to use a transverse RF discharge with external electrodes and capacitive coupling to the discharge tube. A similar construction of laser tube was described for a RF He–Cd ion laser [73]. The source of copper atoms is the compound copper bromide whose molecules dissociate after entering the discharge zone. The liberated copper atoms take part in the laser generation process like the sputtered copper atoms in a HC discharge.

Particularly good results have been obtained recently for lasing on copper ion laser transitions in the deep UV spectrum with excitation in the PC of a pulsed longitudinal discharge in a mixture of copper bromide vapor and neon [74]. A total maximum average output power of 1.3 W was obtained for the most intensive four copper ion laser lines 248.6, 259.1, 260.0, 270.3 nm, as for the most intensive UV laser line of 248.6 nm, a maximum average output power of 0.85 W was achieved. The active length of the discharge zone was 60 cm, the diameter was 6 mm and the laser pulse recurrence frequency was between 15 and 20 kHz.

10.6.4 Applications and Production of Metal Vapor Ion Lasers Generating in the Deep UV

Metal vapor ion lasers generating in the deep UV spectrum are applied mainly in medicine, scientific studies in biology, and in the development of spectral methods based on the Raman spectroscopy. On the basis of these lasers, systems have been developed for examination of water contamination and also for liquid chromatography, mini-Raman microscope, and apparatus based on the UV fluorescence.

Only one company is known at present to produce deep UV lasers oscillating on ion transitions in copper and silver. This is Photon Systems established in the U.S.A. in 1997. It produces He–Ag ion lasers oscillating on the line at 224 nm wavelength and Ne–Cu ion lasers oscillating on the four lines 248, 259, 260, and 270 nm. The copper ion laser emits the maximum peak power of up to 500 mW for a wavelength of 248.6 nm. It operates in the pulsed regime as the maximum laser PRF can reach up to 300 kHz. The average output power for this laser is 1 mW. During a short time, the laser may emit a maximum average output power of 200 mW. The laser BQ is 10, at which value a focal spot of a minimal size down to 3 μm may be obtained. Unique devices, such as the UV Raman spectroscope have been developed on the basis of this laser. This laser is of great importance in finding small admixtures of elements, and in ecology.

REFERENCES

1. Rabinowitz, P., Jacobs, S., and Gould, G., Continuous optically pumped Cs lasers, *Appl. Opt*., 1(4), 513, 1962.
2. Rabinowitz, P., Jacobs, S., The optically pumped cesium laser, *Quant. Electron*., III(4), 489, 1964.
3. Rigden, J.D. and White, A.D., Optical laser action in iodine and mercury discharges, *Nature,* 198, 774, 1963.
4. Paananen, R.A., Tang, C.L., Horrigan, F.A., and Statz, H., Optical laser action in He–Hg RF discharges, *J. Appl. Phys*., 34, 3148, 1963.
5. Bell, W.E., Visible laser transitions in Hg^+, *Appl. Phys. Lett*., 4(2), 34, 1964.
6. Fowles, G.R. and Silfvast, W.T., Laser action in the ionic spectra of zinc and cadmium, *IEEE J. Quant. Electron*., QE-1(6), 1965.
7. Silfvast, W.T., Fowles, G.R., and Hopkins, B.D., Laser action in singly ionized Ge, Sn, Pb, In, Cd and Zn, *Appl. Phys. Lett*., 8(12), 318, 1966.
8. Fowles, G.R. and Hopkins, B.D., CW laser oscillation at 4416 A in cadmium, *IEEE J. Quant. Electron*., QE-3(10), 419, 1967.
9. Sosnowski, T.P., Cataphoresis in the helium–cadmium laser discharge tube, *J. Appl. Phys*., 40(13), 5138, 1969.
10. Goldsborough, J.P. and Hodges, E.B., Stable long life operation of He–Cd lasers at 4416 A and 3250 A, CLEA'69, *IEEE J. Quant. Electron*., QE-5(6), 361, 1969.
11. Fendley, J.R., Gorog, I., Hernqvist, K.G., and C. Sun, Characteristics of a sealed-off He–^{114}Cd laser, *RCA Rev*., 30(3), 422, 1969.
12. Byer, R.L., Bell, W.E., Hodges, E., and Bloom, A.L., Laser emission in ionized mercury: isotope shift, line width and precise wavelength, *J. Opt. Soc. Am*., 55(12), 1598, 1965.
13. Asami, Y., Sugawara, Y., Tokiwa, Y., and Iijima, T., Laser oscillation due to hollow cathode discharge, Preprints, in *1969 Meeting Inst. Electron. Commun. Eng. Jpn., Quantum Electronics*, in Japanese, 600, 1969.
14. Schuebel, W.K., New CW Cd-vapor laser transitions in a hollow-cathode structure, *Appl. Phys. Lett*., 16(11), 470, 1970.
15. Sem, M.F. and Mikhalevskii, V.S., Pulsed oscillation in zinc and cadmium vapours, *Zh. Prikl. Spektrosk*., in Russian, 6(5), 668, 1967.
16. Karabut, E.K., Mikhalevskii, V.S., Papakin, V.F., and Sem, M.F., Continuous generation of coherent radiation in a discharge in Zn and Cd vapor, *Sov. Phys. Tech. Phys*., 14(10), 1447, 1970.
17. Csillag, L., Janossy, M., Rozsa, K., and Salamon, T., Near infrared CW laser oscillation in Cu II, *Phys. Lett*., A 50(1), 13, 1974.
18. McNeil, J.R., Collins, G.J., Persson, K.B., and Franzen, D.L., CW laser oscillation in Cu II, *Appl. Phys. Lett*., 27(11), 595, 1975.
19. Fowles, G.R. and Silfvast, W.T., High-gain laser transitions in lead vapor, *Appl. Phys. Lett*., 6(12), 236, 1965.
20. Piltch, M., Waler, W.T., Solimene, N., Gould, G., and Bennett Jr W.R., Pulsed laser transitions in manganese vapor, *Appl. Phys. Lett*., 7(11), 309, 1965.
21. Silfvast, W.T. and Fowles, G.R., Laser action on several hyperfine transitions in Mn I, *J. Opt. Soc. Am*., 56(6), 832, 1966.
22. Walter, W.T., Piltch, M., Solimene, N., and Gould, G., Pulsed laser action in atomic copper vapor, *Bull. Am. Phys. Soc*., 11(1), 113, 1966.
23. Walter, W.T., Metal vapor lasers, 1968 Int. Quantum Electron. Conf., *IEEE J. Quant. Electron*., QE-4(5), 355, 1968.
24. Petrash, G.G., Pulsed gas-discharge lasers, *Sov. Phys. Usp*., 14, 747, 1972.
25. Latush, E.L. and Sem, M.F., Stimulated emission due to transitions in alkaline-earth metal ions, *Sov. J. Quant. Electron*., 3(3), 216, 1973.
26. Engel, A. von and Steenbeck, M., Elektrische Gasentladungen, *Ihre Physik und Technik*, 2(83), 1932.
27. Little, P.F. and Engel, A. von, The hollow-cathode effect and the theory of glow discharges, *Proc. R. Soc. London A*, 224, 209, 1954.
28. Raizer, Yu.P., *Gas-Discharge Physics,* Springer-Verlag, Berlin, 1991.

29. Ivanov, I.G., Latush, E.L., and Sem, M.F., in *Metal Vapour Ion Lasers Kinetic Processes and Gas-Discharges*, Little, C.E., Ed., John Wiley, Chichester, 1996.
30. Latush, E.L. and Sem, M.F., Laser recombination transitions in Ca II and Sr II, *Sov. Phys. JETP*, 37(6), 1017, 1973.
31. Bukshpun, L.M., Latush, E.L., and Sem, M.F., Influence of the temperature of the active medium on the stimulated emission characteristics of an Sr–He recombination laser, *Sov. J. Quant. Electron.*, 18(9), 1098, 1988.
32. Bukshpun, L.M., Latush, E.L., Sebast'yanov, B.Ya., and Sem, M.F., Active elements for pulsed recombination lasers using vapors of strontium and calcium, *Prib. Tekh. Eksp.*, 2, 235, in Russian, 1991.
33. Hackel, R.P. and Warner, B.E., Copper-pumped dye laser system at Lawrence Livermore National Laboratory, in *Proc. SPIE 1859*, Laser Isotope Separation, ed. Paisner, J.A., 120, 1993.
34. Liu, C.S., Sucov, E.W., and Weaver, L.A., Copper superradiant emission from pulsed discharges in copper iodide vapor, *Appl. Phys. Lett.*, 23(2), 92, 1973.
35. Chen, C.J., Nerheim, N.M., and Russell, G.R., Double-discharge copper vapor laser with copper chloride as a lasant, *Appl. Phys. Lett.*, 23(9), 514, 1973.
36. Sabotinov, N.V., Telbizov, P.K., and Kalchev, S.D., Bulgarian patent N 28674, 1975.
37. Shukhtin, A.M., Mishakov, V.G., Fedotov, G.A., and Ganeev, A.A., Interference method for observing the dissociation of copper halide molecules in a pulsed discharge, *Opt. Spectrosc.*, 39(4), 444, 1975.
38. Akirtava, O.S., Dzhikiya, V.L., and Oleinik, Yu. M., Laser utilizing Cu I. transitions in copper halide vapors, *Sov. J. Quant. Electron.*, 5(8), 1001, 1975.
39. Gabay, S., Smilanski, I., Levin, L.A., and Erez, G., Comparison of CuCl, CuBr and CuI as lasants for copper-vapor lasers, *IEEE J. Quant. Electron.*, QE-13(5), 364, 1977.
40. Astadjov, D.N., Sabotinov, N.V., and Vuchkov, N.K., Effect of hydrogen on CuBr laser power and efficiency, *Opt. Commun.*, 56(4), 279, 1985.
41. Astadjov, D.N., Dimitrov, K.D., Little, C.E., Sabotinov, N.V., and Vuchkov, N.K., A CuBr laser with 1.4 W/cm^3 average output power, *IEEE J. Quant. Electron.*, QE-30(6), 1358, 1994.
42. Maitland, A., Livingstone, E.S., and Little, C.E., Metal vapour laser apparatus, EEV Ltd, U.K., application no. 9225084.4, Dec. 1, 1992.
43. LeGuyade, E., Coutance, P., Bertrand, G., and Peltier, C., A 280-W average power Cu-Ne-HBr laser amplifier, *IEEE J. Quant. Electron.*, 35(11), 1616, 1999.
44. Sabotinov, N.V., Jones, D.R., Akerboom, F., Maitland, A., and Little, C.E., 9.5-W copper HyBrID laser with a specific average output power of 2.0 W/cm^3, in *CLEO'94, Tech. Dig.*, Optical Society of America, Washington DC, 402, 1994.
45. Withford, M.J., Brown, D.J., Carman, R.J., and Piper, J.A., Kinetic enhancement in copper vapour lasers using halogen donor gas additives, in *IQEC'96, Tech. Dig.*, Opt. Soc. Am., Washington, DC, 238, 1996.
46. LeGuyades, E., Nouvel, P., and Regnard, P., A high average power copper vapour and HCl–H_2 laser, in *GCL/HPL 2004 Book of Abstracts,* P1–47, 135, XV International Symposium on Gas Flow and Chemical Lasers & High Power Laser Conference, GCL/HPL 2004, Prague, Czech Republic.
47. Burmakin, V.A., Evtyunin, D.N., Lesnoi, M.A., and Bylkin, V.I., Long-life sealed copper vapour laser, *Sov. J. Quant. Electron.*, 8(5), 574, 1978.
48. Sabotinov, N.V., Copper bromide lasers, in *Pulsed Metal Vapour Lasers-Physics and Emerging Applications in Industry, Medicine and Science*, Little, C.E. and Sabotinov, N.V., Eds., Kluwer Academic Publishers, Dordrecht, 113, 1996.
49. Warner, B.E., Boley, C.D., Chang, J.J., Dragon, E.P., Havstad, M.D., Martinez, M., and Mclean II, W., Industrial applications of high-power copper vapor lasers, in *Pulsed Metal Vapour Lasers-Physics and Emerging Applications in Industry, Medicine and Science,* Little, C.E. and Sabotinov, N.V., Eds., Kluwer Academic Publishers, Dordrecht, 331, 1996.
50. Salimbeni, R., Bergmann, H., Sabotinov, N., Mizeraczyk, J., and Kostadinov, I., Project NATO SfP 972685, "NATO SfP-Copper Bromide Laser."
51. Warner, B.E., Status of copper vapor laser technology at Lawrence Livermore National Laboratory, in *CLEO'91 Tech. Dig.*, Opt. Soc. Am., Washington, DC, 516, 1991.

52. Zemskov, K.I., Isaev, A.A., Kazaryan, M.A., and Petrash, G.G., Laser projection microscope, *Sov. J. Quant. Electron*., 4(1), 5, 1974.
53. www.norseld.com.
54. Sabotinov, N.V., Telbizov, P.K., and Kalchev, S.D., Bulgarian patent N 28674, 1975.
55. Sabotinov, N.V., Kostadinov, I., Bergman, H., Salimbeni, R., and Mizeraczyk, J., A 50-W CuBr laser, XIII International Symposium of Gas Flow and Chemical Lasers and High Power Laser Conference, in *Proc. SPIE*, 4184, 203, 2001.
56. Goldsborough, J.P., Stable, long life CW excitation of helium–cadmium lasers by DC cataphoresis, *Appl. Phys. Lett*., 15(6), 159, 1969.
57. Mizeraczyk, J.K., On saturation mechanisms in PC He–Cd^+ lasers, *IEEE J. Quant. Electron*., QE-11(5), 218, 1975.
58. Sem, M.F. and Mikhalevskii, V.S., Pulsed oscillation in zinc and cadmium vapours, *Zh. Prikl. Spektrosk*., in Russian, 6(5), 668, 1967.
59. Asami, Y., Fujii, K., and Takahashi, T., Hollow cathode type He–Cd^+ laser as a source of white light, *Trans. Inst. Telev. Eng. Jpn*., in Japanese, 27(8), 617, 1973.
60. Fujii, K., Characteristics of negative glow type He–Cd II laser tube and fundamental studies on its designing, *Trans. Inst. Electron. Eng. Jpn*., in Japanese, 93-C(1), 1, 1973.
61. Sugawara, Y., Tokiwa, Y., and Iijima, T., Excitation mechanisms of CW laser oscillations in Zn II and Cd II in hollow cathode discharges, in *Proc. Sixth Int. Quant. Electron. Conf*., Kyoto, 320, 1970.
62. Fujii, K., Recent developments and applications of white-light lasers, in *Proc. Int. Conf. Lasers '87*, STS Press, McLean, 285, 1988.
63. Mizeraczyk, J., Mentel, J., Schmidt, E., Reich, N., Carlsson, C., and Hard, S., A hollow-cathode discharge CW multicolour He–Cd^+ laser module, *Meas. Sci. Technol*., 5 936, 1994.
64. Reich, N., Mentel, J., and Mizeraczyk, J., CW radio-frequency excited white-light He–Cd^+ laser, *IEEE J. Quant. Electron*., QE-31(11), 1902, 1995.
65. Tompkins, J.D., The commercial helium–cadmium laser, *Laser Focus*, 5(8), 32, 1969.
66. Csillag, L., Janossy, M., Rozsa, K., and Salamon, T., Near infrared CW laser oscillation in Cu II, *Phys. Lett. A*, 50(1), 13, 1974.
67. McNeil, J.R., Collins, G.J., Persson, K.B., and Franzen, D.L., CW laser oscillation in Cu II, *Appl. Phys. Lett*., 27(11), 595, 1975.
68. Little, C.E., *Metal Vapour Lasers Physics, Engineering and Applications*, John Wiley & Sons Ltd, Baffins Lane, Chichester, West Sussex, P019 IUD, England, 1999.
69. Schuebel, W.K., Transverse-discharge slotted hollow-cathode laser, *IEEE J. Quant. Electron*., QE-6(9), 574, 1970.
70. Peard, K.A., Tobin, R.C., Rozsa, K., and Donko, Z., A high-voltage hollow-cathode Au-II 282 nm laser, *IEEE J. Quant. Electron*., QE-30(5), 1181, 1994.
71. Grozeva, M. and Sabotinov, N., Coil hollow cathode for metal vapor lasers, *Opt. Commun*., 41(1), 57, 1982.
72. Eichler, H.J., Koch, H., Molt, R., Qiu, J.L., and Martin, W., Optimization of the UV Cu II laser, *Appl. Phys. B*, 26, 49, 1981.
73. Schulze, J., Lucking, C., Reich, N., Turner, D., Mentel, J., Grozeva, M., and Mizeraczyk, J., CCRF excited copper–ion-laser, *Gas Lasers Recent developments and Future Prospects*, Witterman, W.J. and Ochkin, V.N., Eds., Kluwer Academic Publishers, Dordrecht, 221, 1996.
74. Vuchkov, N., Temelkov, K., and Sabotinov, N., UV Lasing on Cu^+ in a Ne–CuBr pulsed longitudinal discharge, *IEEE J. Quant. Electron*., 35(12), 1799, 1999.
75. Sabotinov, N.V., Recent progress in copper vapor lasers, in *Proc. SPIE, Vol. 5120*, XIV International Symposium on Gas Flow, Chemical Lasers, and High-Power Lasers, Krysztof M. Abramski, Edward F. Plinski, and Wieslaw Wolinski, Eds., SPIE, Bellingham, 30, 2003.

11 Other Gas Lasers

Krzysztof M. Abramski and Edward F. Plinski

CONTENTS

11.1 INTRODUCTION

This chapter deals with gas lasers other than those discussed earlier in this book, which also play an important role in physics and technology, but are not in the forefront of scientific and commercial development now.

In most cases, the reason is simple—their technology had been developed in the past and it reached a level where these lasers are mainly developed commercially (like helium–neon, argon–krypton ion lasers). The development of some other gas lasers has stopped after some period of their intense investigations (FIR, HCN, xenon, nitrogen lasers). This chapter reviews six types of lasers:

Atomic lasers (helium–neon, He–Ne)—Section 11.2.

Probably the most popular gas lasers with the best-established technology. They are very well known to all students in academic laboratories using visible (red, green, yellow, infrared) radiation in elementary experiments with a coherent light.

Ion lasers (argon ion)—Section 11.3.

These are quite useful lasers operating in the green–blue and ultraviolet (UV) regions as well. These lasers, with relatively high power in a visible region, are particularly popular in light-show enterprises and holography or medicine as well.

FIR lasers (far infrared radiation)—Section 11.4.

These are lasers operating in millimeter and submillimeter wavelengths joining two electromagnetic opto- and radioregions. They are based on optically pumped multiatom molecular gas media. The FIR lasers still wait for their undoubtedly great future.

Submillimeter hydrogen cyanide (HCN) lasers—Section 11.5.

These are the submillimeter lasers that are not pumped optically. They are pumped by discharge like many gas lasers. We introduce them rather like an exotic laser that was invented in the past.

IR xenon (Xe) lasers—Section 11.6.

Xe as a high gain medium can be applied as an ion laser but it is probably more popular as an atomic laser giving radiation in the IR region. Different excitation techniques (DC, pulsed, RF, e-beam, x-ray, nuclear) can be demonstrated with this laser medium.

Molecular UV (nitrogen [N_2] lasers)—Section 11.7.

It used to be quite an exciting "Do It Yourself" device for amateurs. The air, rich in N_2, can be easily applied to the laser medium without any vacuum technology. Hence, many ideas and constructions have been presented for pulsed lasing in the past and present (see web sites).

This is not the end of the list and some future development of the gas lasers can be expected.

11.2 HE–NE LASERS

He–Ne lasers are probably the most popular gas lasers in many university laboratories. Most students passing elementary courses in physics, optics, photonics, or optoelectronics are quite familiar with these lasers. Their nice red, green, orange, yellow beams (or some IR, as well) are applied to many elementary experiments—interferometers, modulators, holograms, scanners, and the like.

11.2.1 Constructions and Technology

We will start from the description of the He–Ne laser constructions and technology. Taking into account the contemporary worldwide laser market, it is difficult to imagine today that each laboratory designs and elaborates He–Ne lasers, as it happened 30 to 40 years ago in most laboratories. The technology of a He–Ne laser has become perfect during the last four decades. Many He–Ne lasers have operated for over 20 to 30 years without any visible degradation. Their practical lifetime overcomes that of the laser diodes. Development of technology of He–Ne lasers has established two basic constructions of laser tubes presented in Figure 11.1.

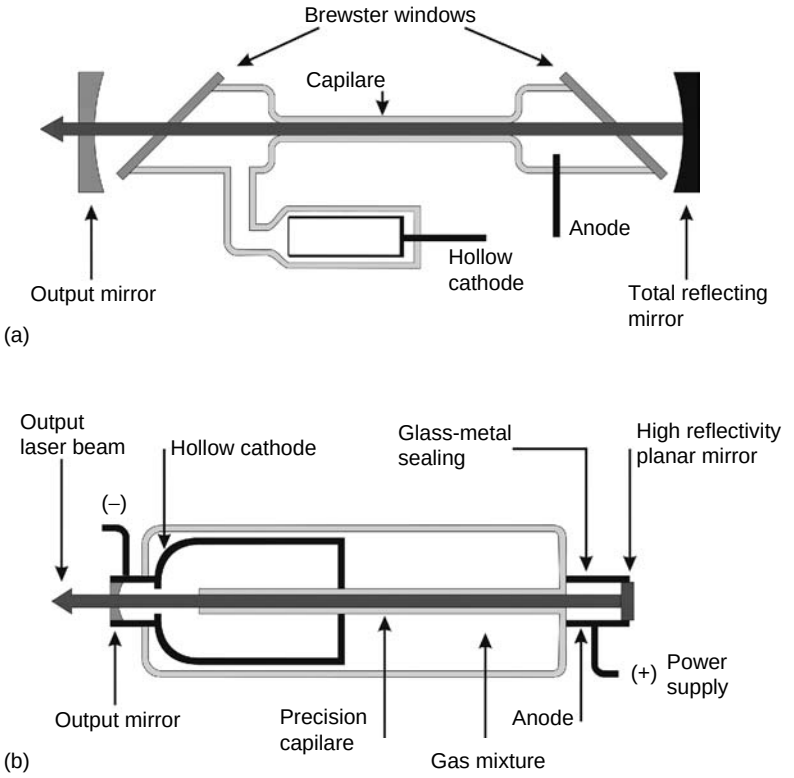

FIGURE 11.1 Typical structures of helium–neon discharge tubes and resonators: (a) with Brewster windows and external mirrors; (b) compact with internal mirrors.

In both cases, the main element of the laser tube is a capillary in which the laser plasma is formed. The internal diameter of the capillary is determined by two conditions:

- It should select the basic TEM_{00} mode and it should damp the higher-order transverse modes.
- It should be thin enough to depopulate lower laser levels because of extra collisions of excited Ne atoms with the capillary walls (see next chapter).

These two conditions establish a typical internal diameter of capillary at $d \cong 1$–2 mm. It also fulfills important practical condition for optimal pressure–diameter product [1,2]:

$$pd \cong 3.6\ [\text{Torr} \cdot \text{cm}] \tag{11.1}$$

The laser tube is filled with the mixture of the He and Ne in a typical proportion of about 10:1, respectively, at the total pressure $p = 2$–5 Torr. The typical value of electric field–pressure ratio in the laser tube is:

$$\frac{E}{p} \cong 2.8\left[\frac{\text{V}}{\text{cm Torr}}\right] \tag{11.2}$$

where electrons reach the temperature $T_e \approx 80{,}000$ K in the discharge.

The plasma in the capillary is obtained mostly by DC discharge (3–15 mA), although the first He–Ne laser was excited by the inductively coupled RF discharge [3]. The highly developed high-vacuum technology applied in the process of the laser tube manufacturing is the main factor that established high-quality long-life laser discharge tubes. The laser tube presented in Figure 11.1b shows a typical cross section of the laser with internal mirrors. The central part of the laser is formed with a capillary, and the discharge current passes through its internal part. Both the electrodes, aluminum cathodes and anode are naturally composed of Kovar (nickel–iron–cobalt alloy) tubes, which form high-quality hard glass metal seals. It is known that Kovar alloy and some special glasses (borosilicate) have similar thermal expansion. Hence, such metal glass seals accept great changes of temperature very well without damaging stresses. The external glass tube forms the reservoir for a gas mixture sufficiently increasing the total ratio of mixture volume to plasma volume. A specially inserted getter can neutralize some impurities, which can appear during discharge.

Considering the power supplies, it has to be mentioned that supply technology has also reached the perfect level. Very efficient, small dimension power supplies are available for all types of discharge tubes. Their operation is based on the converter, where DC voltage is transported into the required high operation voltage. The starting voltage needed to switch on the discharge (which depends mainly on the length of the tube and pressure) can reach the value from 8 to 15 kV. After switching the discharge on, the voltage drops to the operation value. The operation voltage depends on the tube parameters. Shorter tubes (20 cm long) have a typical operation voltage $U_{op} = 1000$–1500 V, when longer tubes (60 cm) need operation voltage of $U_{op} = 4000$–6000 V. Well-designed supply has a current ripple at the level below 0.3%. As usual, the ballast resistor (100–200 kΩ) has to be connected in series with the tube to stabilize the discharge.

11.2.2 Physics of He–Ne Lasers

The diagram of energy levels significant to the laser actions in He–Ne mixture is presented in Figure 11.2. Laser actions are obtained from transitions of the Ne atoms. The He atoms play an important role in transferring pumping energy. There are two excited levels of He (2^3S and 2^1S around 20 eV) shown, which deliver energy to the upper laser level of Ne atom (3s and 2s levels). The s-levels of Ne atoms are around the energies of 19.8 and 20.6 eV, respectively. The He atom excited to levels 2^3S or 2^1S is not able to decay spontaneously back to the ground state (forbidden radiation transitions). These levels have quite long lifetimes (a few seconds).

Free electrons appear as a result of the ionization process of atoms. They are accelerated in the DC electrical field. The free electrons that have high kinetic energy collide with He atoms in the ground state and excite them to the metastable levels according to the equations:

$$e_{\text{kinetics energy}} + He_{\text{ground level}} \rightarrow He(2^1S) + e_{\text{kinetic energy}} - 20.6\ \text{eV}, \tag{11.3}$$

$$e_{\text{kinetics energy}} + He_{\text{ground level}} \rightarrow He(2^3S) + \text{elastic energy}. \tag{11.4}$$

Because He atoms dominate in the mixture, there is a high probability of their collisions with neutral Ne atoms. Energetic coincidence of metastable levels with 3s and 2s levels of Ne allows transferring energy from excited He atom to the Ne atoms as the effect of elastic collisions. The upper levels (excited in transfer process) form the population inversion.

There are many lasing transitions that can be forced to operate when an optical resonator with dielectric selective mirrors is applied. The He–Ne laser can operate at many wavelengths in the visible and infrared range. Many of these wavelengths are well established

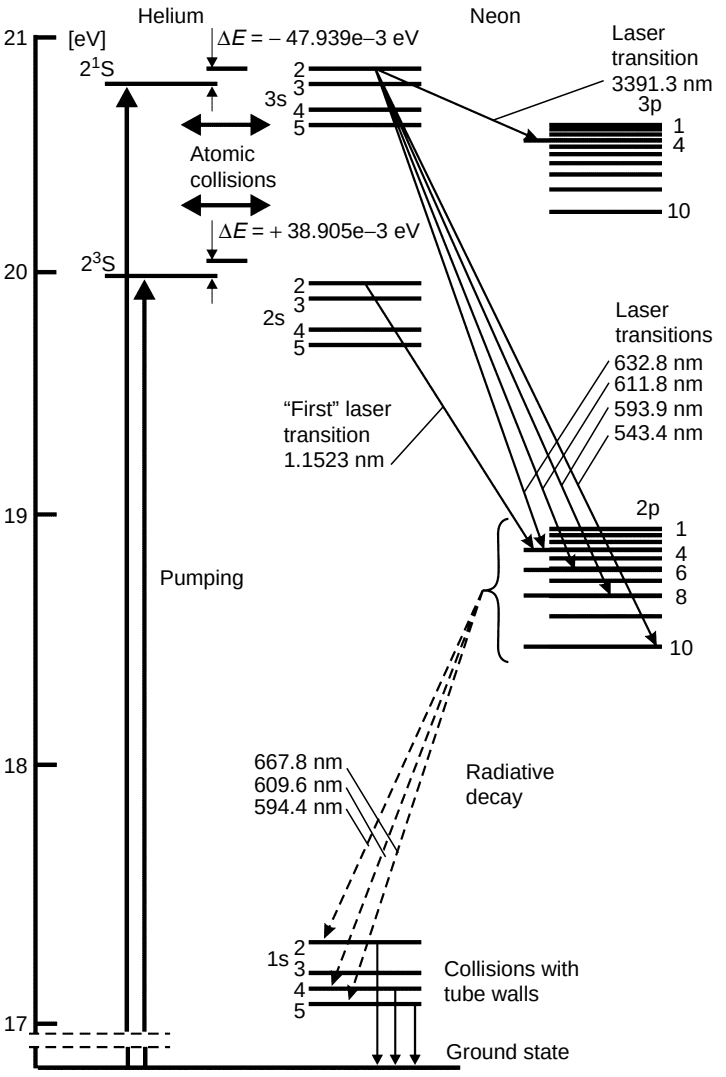

FIGURE 11.2 The helium–neon energy level diagram.

commercially. Table 11.1 lists most of the lasing transitions. The bold ones indicate lines that are commercially developed and available [2].

As indicated in Figure 11.2, the lower levels have to be fast depopulated in order to keep population inversion. Fortunately, decay times of 2p levels are short enough, and these levels are depopulated by spontaneous emission to 1s levels. (This spontaneous emission determines orange–red color of the discharge observed in the tube.) Depopulation of 1s levels is caused by collisions with the glass walls of the discharge tube. That is why a discharge tube should be thin enough to assure high probability of collision depopulation.

11.2.3 Resonators in He–Ne Lasers: Mode Structure and Spectrum of Radiation

The small gain of most He–Ne laser transitions determines particularly high-quality, low-loss optics and a Gaussian configuration of optical resonators. Very high selectivity and

TABLE 11.1
Helium–Neon Laser Transitions (Bold Terms—Commercially Available and Most Applicable)

Transition	Wavelength	Relative Intensity	Comments
$3s_2 \rightarrow 2p_1$	730.49 nm	0.1	
$3s_2 \rightarrow 2p_2$	640.11 nm	0.3	
$3s_2 \rightarrow 2p_3$	635.19 nm	0.3	
$3s_2 \rightarrow 2p_4$	**632.82 nm**	**1.0**	**Red**
$3s_2 \rightarrow 2p_5$	629.38 nm	0.3	
$3s_2 \rightarrow 2p_6$	**611.80 nm**	**0.3**	**Orange**
$3s_2 \rightarrow 2p_7$	604.61 nm	0.15	
$3s_2 \rightarrow 2p_8$	**593.93 nm**	**0.15**	**Yellow**
$3s_2 \rightarrow 2p_{10}$	**543.36 nm**	**0.8**	**Green**
$3s_2 \rightarrow 3p_4$	**3.3913 μm**	**0.1**	**Mid-infrared (very high gain)**
$2s_2 \rightarrow 2p_1$	**1.5231 μm**	**0.3**	**Infrared (telecomm. window)**
$2s_2 \rightarrow 2p_4$	**1.1523 μm**	**0.2**	**Infrared ("first" gas laser action)**

low-loss mirrors have to be used in a laser resonator to choose the required wavelength of radiation. Small gains (a few percentage per pass) of most transitions also determine high reflectivity of the outcoupling mirror (usually below or around 1%).

Selective properties of the mirrors are reached by using dielectric multilayer coatings. The He–Ne discharge tube, determined with Brewster windows and equipped with a pair of external selective mirrors, can give lasing at different lines (from red, via yellow to green). However, considering the gain, there is one exception. That is the 3.39 μm radiation ($3s_2 \rightarrow 3p_4$), which has a huge differential small gain signal (about 6000 m^{-1}), which is fourfold higher when compared with other lines (much below 0.3 m^{-1}). Such a huge gain of a transition of 3.39 μm allows lasing even on polished aluminum plates. This laser also accepts high internal losses. The 3.39 μm radiation competes for the oscillating radiation, and it "steals" the population of $3s_2$, which is the common level for most visible transitions (Figure 11.2). It then operates as parasitic oscillations. To avoid this competition, it is necessary to use internal optics such as Brewster windows, made of nontransparent glasses, for 3.39 μm (most optical glasses, not fused silica).

Commercially available lasers are designed in a way that selects only a basic Gaussian mode, TEM_{00}. When the internal diameter of the discharge tube is large enough, the laser can operate in higher transverse modes. It gives nice patterns of mode structures, as shown in Figure 11.3 [4].

The width of an inhomogeneously broadened gain curve is mainly proportional to the central frequency ν_0 of a laser line according to formula (1.49). For the typical red radiation (632.8 nm), a Doppler-broadened linewidth is about $\Delta\nu_0 = 1500$ MHz. The length of a laser resonator and the level of internal losses determine the number of axial (longitudinal) modes oscillating in the laser resonator as shown symbolically in Figure 11.4.

For the He–Ne laser with internal Brewster windows all axial modes are linearly polarized (as in Figure 11.4c). However, when there is any polarizing element inserted in the laser resonator, the axial modes are still linearly polarized, but they are alternatively orthogonal as shown in Figure 11.4d. This effect is caused by the competition between neighboring modes that arrange their polarization to get the maximum gain. The longer laser resonators stimulate larger number of axial modes with closer frequency separation $\Delta\nu_{FSR}$. As a consequence, the output power of the laser with a larger discharge tube is higher. For example, a typical

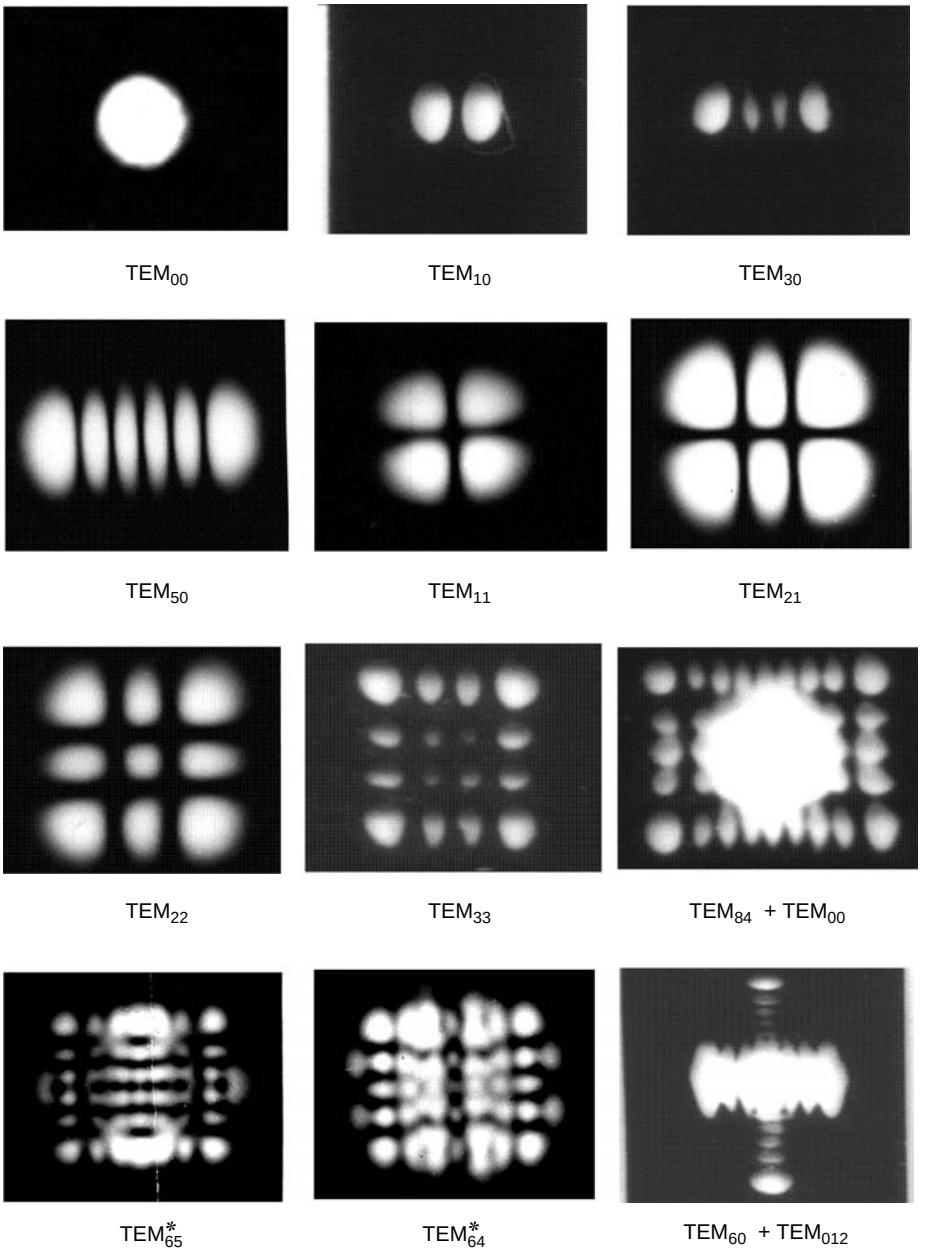

FIGURE 11.3 Mode patterns of helium–neon 1.15 μm laser (*—plus other higher modes).

20 cm long He–Ne 632.8 nm laser emits the output power at the level of 2–3 mW. The 1 m long laser has the output at the level of 30–40 mW. However, a larger number of axial modes significantly decrease the coherence length of laser radiation. The single-frequency operation can be obtained for two cases:

when the laser is short enough to fulfill condition:

$$\Delta\nu_{\mathrm{FSR}} = \frac{c}{2L} > \Delta\nu_{\mathrm{D}}. \tag{11.5}$$

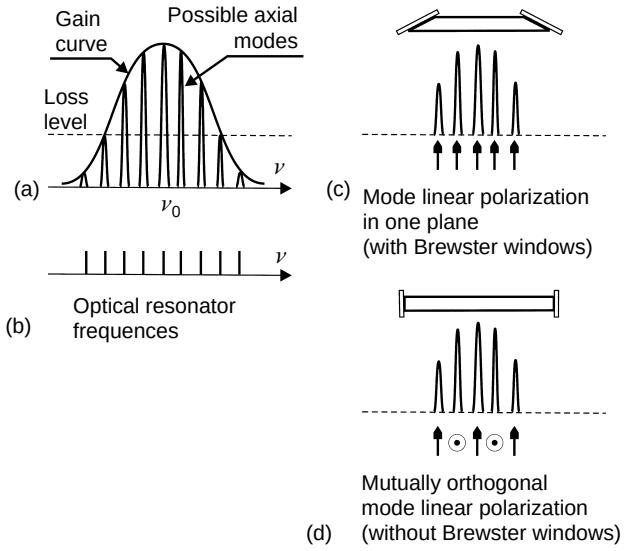

FIGURE 11.4 The idea of multimode operation of helium–neon lasers: (a) gain curve with axial modes; (b) resonances of a passive laser cavity, (c) linearly polarized modes; and (d) mutually orthogonal axial modes.

In practice, it means that single-frequency operation is assured when only one longitudinal mode covers a Doppler emission line.

The second case, much more academic and not very practical, lies in increasing the internal losses to a level where only one axial mode is able to oscillate (Figure 11.4a—"loss level"). Assuming that the practical linewidth of laser radiation of a separate longitudinal mode is about $\Delta\nu_i \cong 10$ kHz, the coherent length L_c can be calculated according to the formula:

$$L_c = \frac{c}{\Delta\nu_i} = 30 \text{ km}. \tag{11.6}$$

However, for multimode operation (assuming that the combination of many modes gives 1.5 GHz gain curve envelope) the coherence length, L_c, drastically decreases to a value of 20 cm.

11.2.4 Frequency Stabilization of He–Ne Lasers

The frequency of a single axial mode of free-running He–Ne lasers fluctuates because of environmental perturbations, which are many orders of magnitude larger than intrinsic quantum linewidth (see Section 1.6, formula (1.70)). Temporal variations $\Delta\nu(t)$ of the frequency ν_q of the cavity mode are caused by geometrical length fluctuations $\Delta L(t)$ (the resonator length fluctuations) and refractive index fluctuations $\Delta n(t)$ according to the formula:

$$\Delta\nu(t) = -\frac{\nu_q}{nL_0}[n_0\Delta L(t) + \Delta n(t)L], \tag{11.7}$$

where L_0 is the optical length of the laser resonator.

Acoustical and mechanical vibrations, power supply instabilities, variations of pressure, and temperature cause the fluctuations of the refractive index and resonator length. All these fluctuations are called environmental fluctuations.

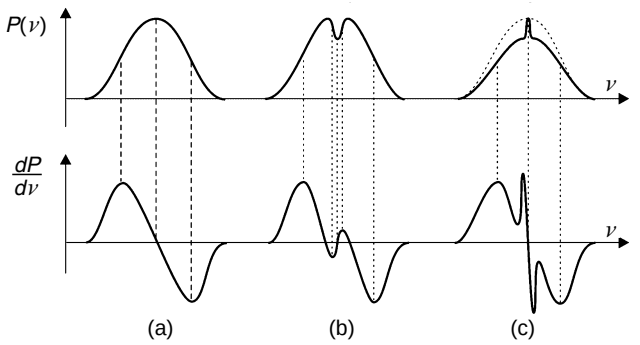

FIGURE 11.5 Helium–neon laser gain curves and their first derivatives (discriminant shapes) applied for frequency stabilization: (a) Gaussian shape of the laser gain curve (stabilization to the center of the shape), (b) a gain curve with a burned "Lamb dip," and (c) a gain curve with an "absorption peak."

Let us consider some examples. The change of discharge current introduces the change of an average refractive index: the 1 mA current change introduces the frequency tuning of a few megahertz; the 1 nm displacement of the mirror in a 10 cm long resonator (according to Equation 11.7) gives about 5-MHz frequency deviation of the laser radiation. It is also interesting to notice that switching on the laser with internal mirrors causes a fast thermal frequency drift because of glass heating by the discharge. This drift usually takes 10–20 min for a free-running laser.

The single-frequency He–Ne lasers are particularly good objects as frequency standards. Many methods have been developed for active stabilization of the laser oscillation frequency. A stable reference frequency that overlaps the bandwidth of the laser gain may be an "absolute" reference point such as atomic or molecular spectral resonances [5].

Representative examples of the reference points are presented in Figure 11.5:

– The center of the laser gain curve
– Lamb dip in the gain curve
– Inverted Lamb dip of the absorption line overlapping the gain curve

As seen, the laser is stabilized to the center of the chosen spectral features—the center of the laser gain curve, Lamb dip, or absorption peak (in some cases, the absorption peak can be at the slope of the gain curve). An electronic servo-loop has to be applied to control and tune the laser toward the center of the specific spectral point—reference frequency.

To obtain an efficient stabilization, the servo-loop electronics has to produce the so-called discriminant shape of the error signal for feedback control. In practice, the discriminant shape is obtained by electronic differentiation of the output power profile $dP/d\nu$. Figure 11.5 presents references and their first derivatives. These discriminating shapes may be obtained using the synchronous detection technique. The precision with which the frequency is stabilized depends on the slope $dP/d\nu$ around the zero crossing regions. In practice, the slope corresponding to a narrower resonance feature increases the stability of the laser, because of larger signal-to-noise ratio in the feedback loop system. Hence, stable, narrow, and high-contrast spectral resonances overlapping the laser gain curve are the best candidates for reference frequencies in active stabilization.

The setup of the classic servo-loop for frequency stabilization of the He–Ne laser, in which the laser frequency is locked to the center of the laser gain curve (corresponding to the first case presented in Figure 11.5a) is shown in Figure 11.6.

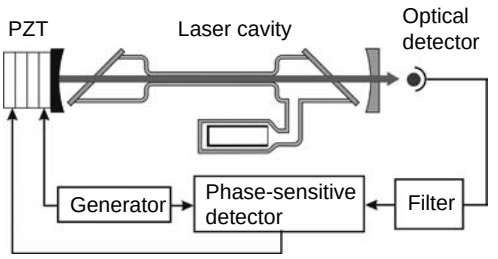

FIGURE 11.6 An electronic servo-loop for stabilization of the laser to the center of the gain curve.

A low-frequency modulation signal (a ''dither'' signal) between a few hundred hertz and a few kilohertz is applied to drive a piezoelectric transducer (PZT), to which one of the resonator mirrors is mounted. The PZT modulation causes laser frequency modulation and output power modulation, as well. The magnitude of power modulation and the phase relative to the modulation drive signal depend on the operation point on the frequency scale. The power modulation is monitored with a photodetector, and it is amplified, filtered, and synchronously detected in a phase-sensitive detector (like a popular lock-in amplifier) providing an error signal. The filtered and amplified error signal is put to the PZT. The low-pass filter protects the loop against its self-oscillations. The typical frequency stability is defined as:

$$S(\tau) = \frac{\sigma[\Delta\nu(\tau)]}{\nu_0}, \tag{11.8}$$

where $\sigma[\Delta\nu(\tau)]$ is the standard deviation of frequency averaged over time τ [5], for described center gain curve stabilization is 10^{-8}–10^{-9} for 1 s averaging time. This value of stability can be improved by approximately an order of magnitude when the Lamb dip is applied as the reference.

The best absolute frequency stability has been obtained for He–Ne lasers with intracavity saturable absorbers (Figure 11.5c). The best candidate as a frequency standard is the 3.39 μm He–Ne laser line stabilized at the absorption peak in methane—CH_4. One of the absorption lines of the CH_4 almost exactly coincides with the Ne^{22} isotope, and gives a relatively high contrast peak (a few percentage on the line background).

The laser setup with an internal methane cell (He–Ne/CH_4 3.39 μm laser) is shown in Figure 11.7. The absorption peak can be as narrow as a few kilohertz. The frequency stability of this kind of a laser can reach the value $S(\tau) = 10^{-15}$ over an averaging time of 1 s.

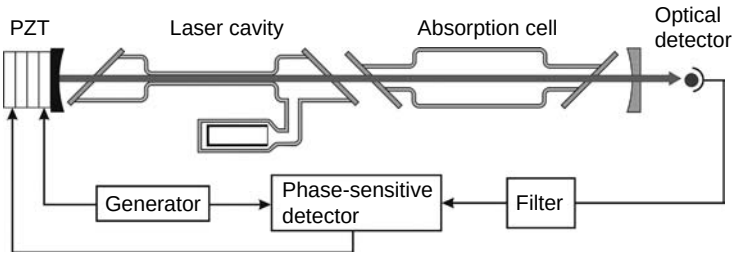

FIGURE 11.7 Frequency stabilization servo-loop with an internal absorption cell.

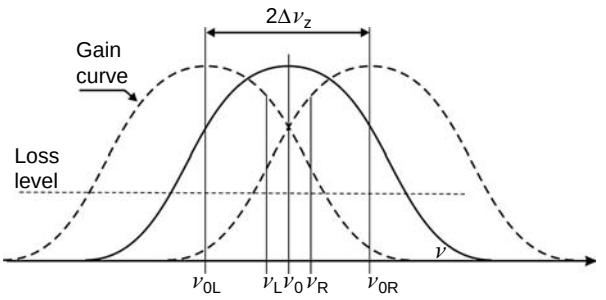

FIGURE 11.8 Zeeman Effect. The main line ν_0 is split into two lines, ν_{0L} and ν_{0R}.

The single-frequency He–Ne 632.8 nm laser with an intracavity iodine absorption cell (hyperfine absorption components in I^{127}) has narrow inverted Lamb dips in its tunable profile. The stabilization electronics, similar to that described here, gives stability on the level $S(\tau) = 10^{-11}-10^{-12}$ over an averaging time of 1 s.

All these techniques have one serious disadvantage. Applied "dither" harmonic modulation introduces FM optical radiation, which is a source of additional laser frequency instabilities. This problem is avoided in a popular technique of frequency stabilization of a He–Ne 632.8 nm laser, based on Zeeman Effect. When the laser is inserted in the axial magnetic field (about $5{\cdot}10^{-2}$ T), the laser gain line is split into two, shifted in frequency ($\Delta\nu_z = \nu_R - \nu_L$) lines according to the Zeeman Effect (see Figure 11.8). The single-frequency He–Ne 632.8 nm laser in such a magnetic field is split into two circular frequencies (left-handed ν_L and right-handed ν_R). The frequency offset between these two circulations is about $\nu_R - \nu_L \cong 1$–2 MHz.

When the laser is tuned, the intensities of both circulations change. At the center of the line, both circulations are equal. Separating both circulations in the setup presented in Figure 11.9, the discriminant shape for the effective stabilization can be obtained. The frequency stabilization of such a laser can get a value of $10^{-8}-10^{-9}$. Although this value is not very high, the He–Ne laser stabilized by means of a Zeeman Effect is quite a popular device. These lasers are useful sources for many interferometric applications.

11.3 ION LASERS

Laser transitions in atomic lasers, as He–Ne lasers described in Section 11.1, occur between levels of atoms. There is another class of lasers, in which lasing exists between excited levels of ions. These lasers are called ion lasers [6,7].

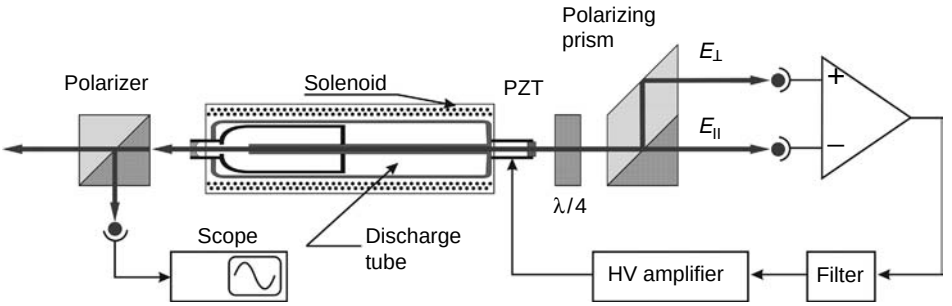

FIGURE 11.9 A helium–neon 632.8 nm laser frequency stabilization setup using Zeeman Effect.

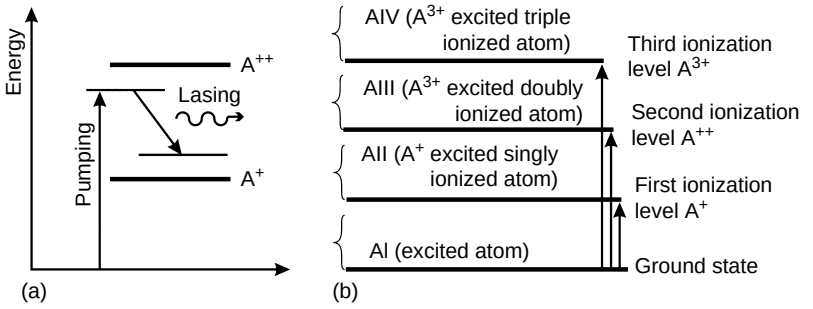

FIGURE 11.10 (a) The basic spectral diagram of ion laser action. (b) Illustration of ionization levels in atoms.

The ion lasers operate on many high-power transitions (compared with the output power of He–Ne lasers) discretely covering the spectrum from UV, through visible, to NIR. Two of the most representative ion laser media are based on heavy rare gases—argon (Ar) and krypton (Kr). In practice, all commercially available ion lasers are Ar, Kr, or their mixtures. The ion laser is still an atom laser but it differs significantly in physics and technology. The main idea of ion lasers is shown in Figure 11.10a.

Generally, the laser transitions can occur between levels of single or multiple ionized atoms. Figure 11.10b gives a terminology of spectral ranges of excited atoms (AI), singly (AII or A^{+}), doubly (AIII or A^{++}), or triply (AIV or A^{3+}) ionized atoms. To obtain a large number of excited ions, most of the atoms have to be ionized. Hence, the high current of the discharge has to flow over the medium to get population inversion, and gain conditions in an ion laser. Next, we present a typical construction, supply conditions, and physics of Ar ion lasers with some parallel information about other ion lasers.

11.3.1 Construction and Supply System of Ion Lasers

The ion laser is mainly DC supplied, although the pulsed operation [8–10] was developed. An RF excitation [11,12] and microwave [13] were investigated, as well. The qualitative difference between an atom and ion lasers is current density. Ion lasers operate at current densities up to 10 A/mm^2 compared with a current density of 10 mA/mm^2 for He–Ne lasers. Hence, the temperature conditions make the construction of the ion laser tube with DC discharge much more complicated.

The view of a typical ion laser discharge tube is shown in Figure 11.11. The discharge is maintained between electrodes, where the cathode has to be additionally heated (because of high discharge current). Therefore, it requires effective cooling of the plasma discharge. An extra ceramic or glass tube forms the space for water-cooling through an external chiller. The construction has an additional concentric structure of magnets or solenoids as a source of axial magnetic field. The high current discharge is developed between electrodes along bored disks. The space in a line array of metal disks (copper–tungsten or in the past—graphite) is centered coaxially to a ceramic tube (beryllium or alumina) as shown in Figure 11.11b. The copper–tungsten disks form the main cooling structure. These are electrically isolated from each other and inserted into a ceramic tube. Because of high current flow, the electrons push neutral atoms along the tube toward the anode. The average velocity of the main stream of discharge inside the tube can reach a value of couple of tens of centimeters per second. The consequence of this is gas separation to the opposite ends of the tube. It causes a pressure

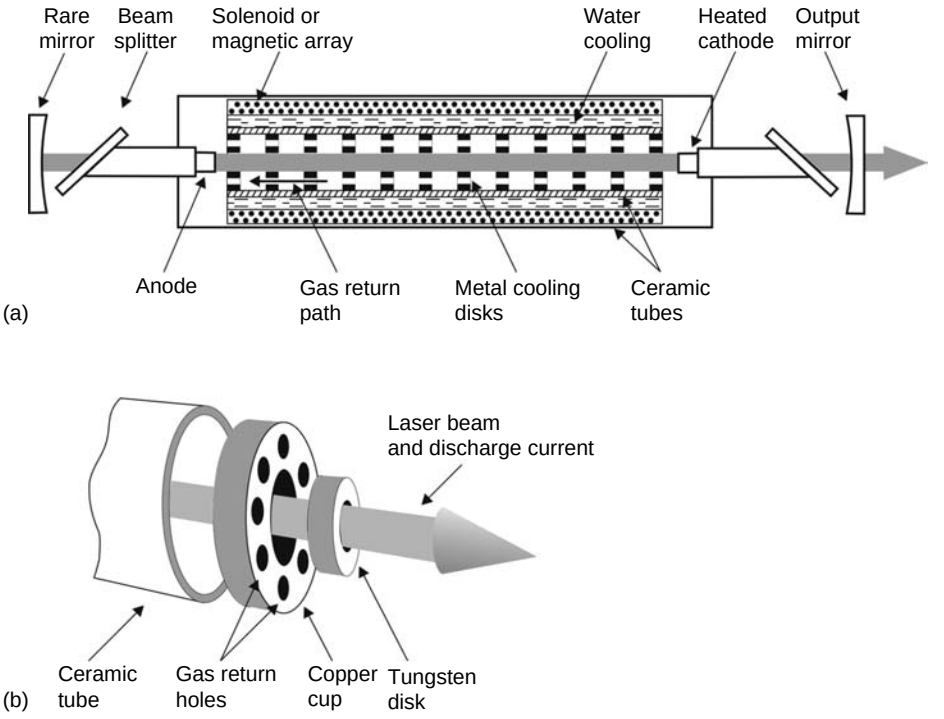

FIGURE 11.11 (a) Cross section of a typical ion laser discharge tube. (b) Details of the disks that cool the gas medium and give pressure balance in the tube.

gradient along the tube, and it is a source of plasma instabilities. To avoid this problem, the gradient pressure is balanced by gas-return holes in the cooling copper disks (Figure 11.11b). In this way, the bypass flow equalizes the pressure along the tube. The dimensions of the disks, holes in disks, space between disks, and their mutual positions are very important subjects for optimization conditions. The structure has to give homogeneous and stable discharge without its jumping from one disk to another. The ratio of the central hole diameter to disk thickness should be large enough for efficient gas-return circulation [14].

There are four candidates as ion media: Ne, Ar, Kr, and Xe. However, a commercial level has been obtained only by Ar and Kr, and their mixtures. There is no need to use extra buffer gases in ion lasers because of the direct excitation of upper lasing levels by an impact electron effect. The laser tube is filled with relatively low gas pressure. Typical pressures for ion lasers are around or below 1 Torr, usually a few hundred of mTorrs. High current flow (tens of amperes), pressure, and the length of the discharge in the tube determine the voltage applied between electrodes. For example, a typical voltage of 200–300 V applied to a 50 cm long tube causes a flow of 20–30 A current. Hence, the power delivered into discharge reaches a value of 5–10 kW. The discharge resistance (see Section 1.8.1) is quite low and a tube has to be connected with a ballast resistor of a few ohms in order to obtain stable operation. The efficiency of the ion laser increases when a magnetic field is applied along the axis of a tube. The construction has an additional external composition of solid magnets or solenoids as a source of an axial magnetic field. Because of a magnetic field, the trajectory of ion beams spirals, this mechanism prevents ions to contact metal disks. The axial magnetic field is optimized for operation conditions (pressure, discharge current) and its typical value is

below 0.1 T (Tesla). It is clear that DC power supplies, water cooling systems, and magnetic field supply make the ion laser a rather large device. It is particularly difficult to minimize dimensions of the power supply and cooling system.

11.3.2 Physics of Ion Lasers—Ar Ion Lasers

The main mechanism of the ion excitation in ion lasers is electron impact. The lasing species (in this case, an ion) is excited by direct collisions of neutral atoms with highly energetic electrons or by collisions of ions with energetic electrons. Following is the list of elementary mechanisms of Ar ion excitations (Figure 11.12). These mechanisms can be symbolically written as reactions that are shown as follows [14]:

One-step excitation process (Figure 11.12a):

$$\mathrm{Ar} + \mathrm{e} \Rightarrow \mathrm{Ar}_{\mathrm{u}}^{+*} + 2\mathrm{e} \tag{11.9}$$

where "u" means the upper level, "+" means the ion, and "+*" the excited ion.

Two-step excitation process (Figure 11.12b):

$$\begin{aligned} \mathrm{Ar} + \mathrm{e} &\Rightarrow \mathrm{Ar}^{+} + 2\mathrm{e} \\ \mathrm{Ar}^{+} + \mathrm{e} &\Rightarrow \mathrm{Ar}_{\mathrm{u}}^{+*} + \mathrm{e} \end{aligned} \tag{11.10}$$

Two-step excitation process with intermediate ion metastable level (Figure 11.12d):

$$\begin{aligned} \mathrm{Ar} + \mathrm{e} &\Rightarrow \mathrm{Ar}^{*} + \mathrm{e} \\ \mathrm{Ar}^{*} + \mathrm{e} &\Rightarrow \mathrm{Ar}_{\mathrm{u}}^{+*} + 2\mathrm{e} \end{aligned} \tag{11.11}$$

Two-step excitation process with atom excited level (Figure 11.12c):

$$\begin{aligned} \mathrm{Ar} + \mathrm{e} &\Rightarrow \mathrm{Ar}^{+*} + 2\mathrm{e} \\ \mathrm{Ar}^{+*} + \mathrm{e} &\Rightarrow \mathrm{Ar}_{\mathrm{u}}^{+*} + \mathrm{e} \end{aligned} \tag{11.12}$$

Cascade excitation process (Figure 11.12e):

$$\begin{aligned} \mathrm{Ar} + \mathrm{e} &\Rightarrow \mathrm{Ar}^{+} + 2\mathrm{e} \\ \mathrm{Ar}^{+} + \mathrm{e} &\Rightarrow \mathrm{Ar}^{+*} + \mathrm{e} \\ \mathrm{Ar}^{+*} + \mathrm{e} &\Rightarrow \mathrm{Ar}_{\mathrm{u}}^{+*} + h\nu \end{aligned} \tag{11.13}$$

The candidates for gas ion lasers are usually noble gases. Lasing from ionized oxygen and N_2 atoms have been also observed [10,11]. Table 11.2 lists these atoms, their ionization energies, and some representative transitions obtained in two main excitation regimes: pulsed and continuous wave (CW) [14–16]. The pulse operation is usually an easier way to obtain laser radiation for multiply ionized atoms. The reason is that higher ionized atoms can be obtained only for high current densities in the level of tens and more amperes per square millimeter.

Figure 11.13 illustrates the energy level diagram for the Ar laser with the main visible transitions of singly ionized Ar. Apart from this, UV transitions (351.1 and 363.8 nm) of doubly excited Ar III ion are symbolically indicated. The group of laser IR transitions of

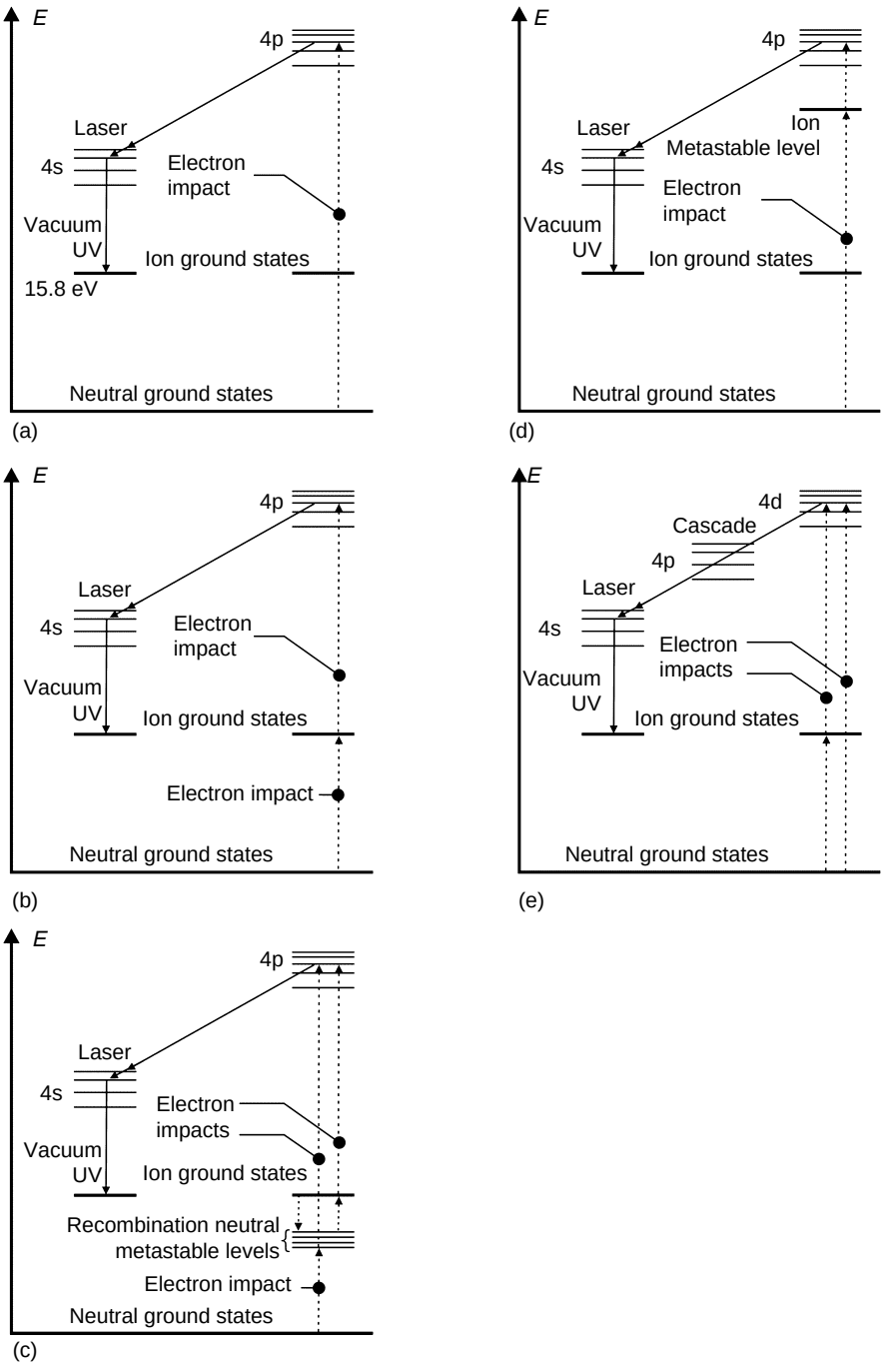

FIGURE 11.12 (a) One-step excitation; (b) two-step excitation; (c) two-step excitation via metastable atom level; (d) two-step excitation with metastable ion level; and (e) cascade excitation. (From Cottrell, T.H.E., *IEEE J. Quant. Electron.*, QE-4(4), 435–441, 1968. With permission.)

TABLE 11.2
Ionization Energies of Ion Laser Gases (the Rule for Noble Gases Is Simple: Heavier Atom, Lower Ionization Energy), and Some Representative Transitions Distinguished for Pulsed and Continuous Wave (CW) Operations

		Wavelength (nm)			Wavelength (nm)			Wavelength (nm)		
	A^{+} (eV)	Pulsed	CW	A^{++} (eV)	Pulsed	CW	A^{3+} (eV)	Pulsed Only	A^{4+} (eV)	Atomic Mass
Neon	21.56	332.4	332.4	62.52	247.33		125.96		223.09	20.18
			337.8							
		337.8	339.3							
Argon	15.76	457.9	457.9	43.39	351.1	351.1	84.13	211.4	143.94	39.95
		465.8	465.8		363.8	363.8		275.4		
			472.7							
		472.7	476.5							
			488.0							
		476.5	496.5							
			501.7							
			514.5							
		488.0	528.7							
		496.5								
		501.7								
		514.5								
		528.7								
Krypton	14.00	743.6	350.74	38.36	350.7		75.31	219.2	127.81	83.80
			356.4					225.5		

			406.7							
			476.2							
			482.5							
			520.8							
			530.9							
			568.2							
			647.1							
			676.4							
			752.5							
Xenon	12.13			33.34		374.6	65.46	231.5	—	131.29
						388.1		324.7		
								364.5		
								430.6		
								495.4		
								500.8		
								515.9		
								526.0		
								535.3		
								539.5		
Oxygen	13.62	374.9		48.74	376.0		103.67		181.10	16.00
					559.2					
Nitrogen	14.53			44.13	409.7		91.58	347.9	169.06	14.09

Source: From Davies, C.C., *Lasers and Electrooptics. Fundamentals and Engineering*, Cambridge University Press, Cambridge, 1996, chapter 9; Tio, T.K., Luo, H.H., and Lin, S.-C., *Appl. Phys. Lett.,* 29(12), 795–797, 1976; Davies, C.C. and King, T.A., Gaseous ion lasers, in *Advances in Quantum Electronics*, Vol. 3, Goodwin, D.W., Ed., Academic Press, London, 1975. With permission.

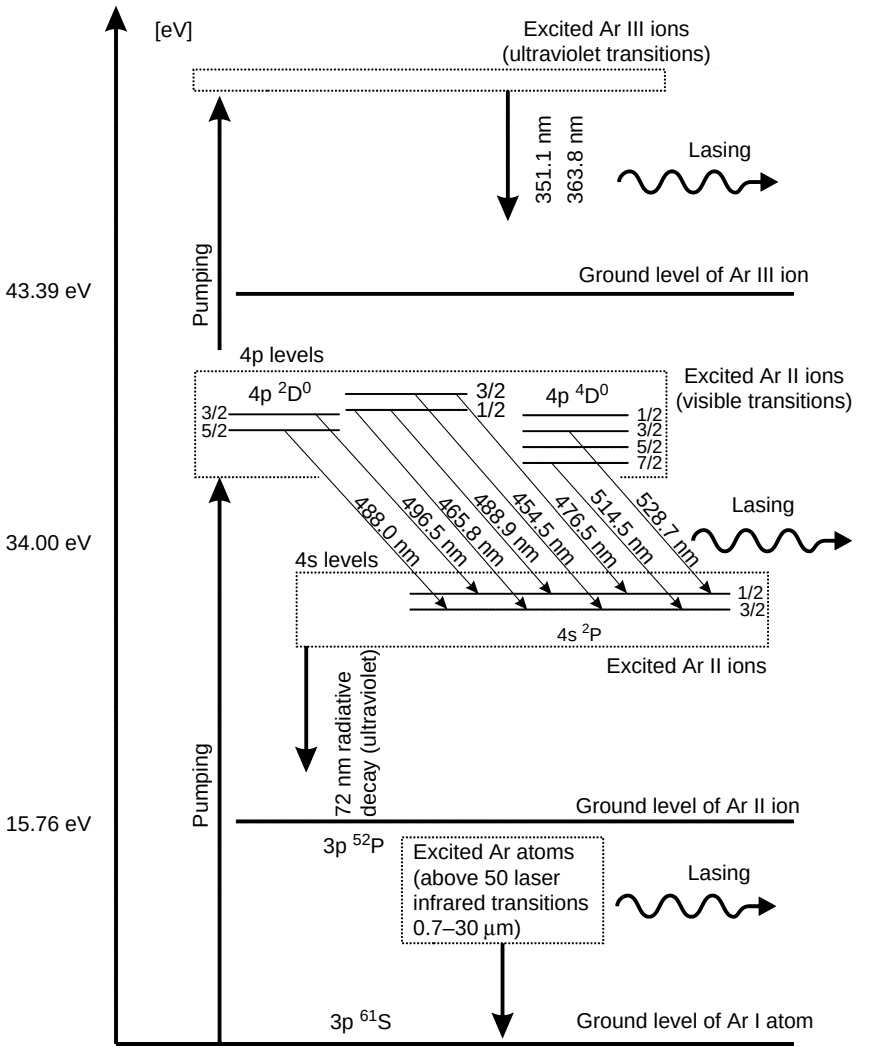

FIGURE 11.13 Argon laser energy diagram.

excited Ar atom (Ar I, atomic gas laser) is included in the diagram as well. The reader can find different symbols indicating ions in a literature. The suitable relations are presented in the following:

$$\mathrm{Ar_{neutral}} \Rightarrow \mathrm{Ar} \Rightarrow \mathrm{ArI}$$

$$\mathrm{Ar_{singly\ ionized}} \Rightarrow \mathrm{Ar^{+}} \Rightarrow \mathrm{ArII}$$

$$\mathrm{Ar_{excited\ singly\ ionized}} \Rightarrow \mathrm{Ar^{+*}} \Rightarrow \mathrm{Ar^{*}II}$$

$$\mathrm{Ar_{doubly\ ionized}} \Rightarrow \mathrm{Ar^{++}} \Rightarrow \mathrm{Ar^{2+}} \Rightarrow \mathrm{Ar\ III}$$

$$\mathrm{Ar_{triple\ ionized}} \Rightarrow \mathrm{Ar^{3+}} \Rightarrow \mathrm{Ar\ IV} \tag{11.14}$$

Similar relation can be generalized for other atoms. The Ar ion laser can operate in two basic configurations—multiline and single line. These configurations are shown schematically in

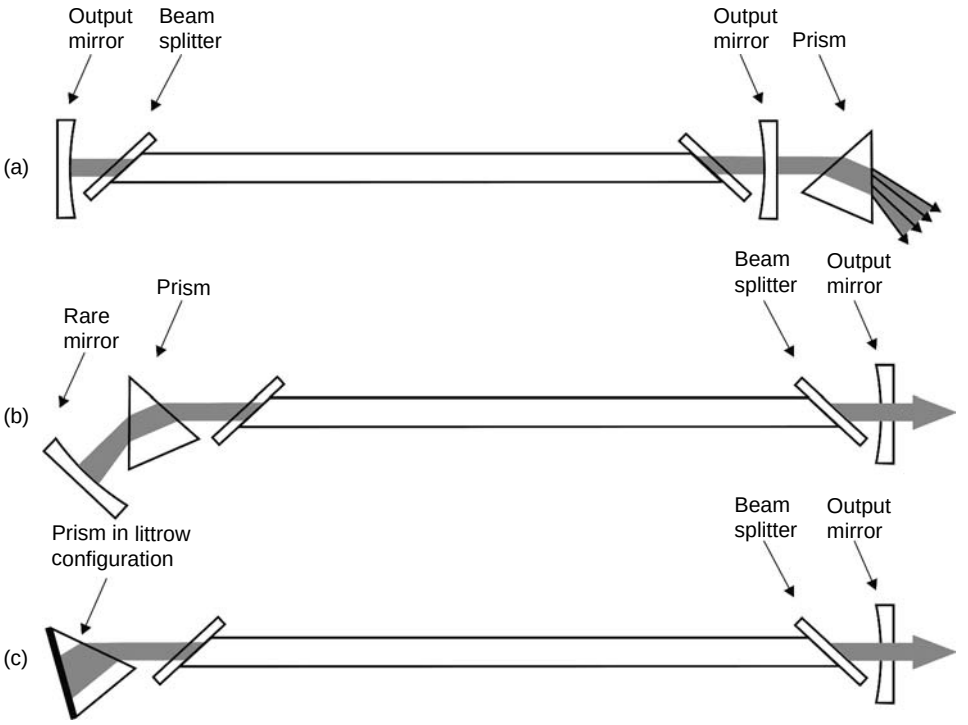

FIGURE 11.14 Typical structures of argon lasers: (a) multiwave operation; (b,c) single-line operation.

Figure 11.14. Multiline operation (Figure 11.14a) allows to simultaneously lase several wavelengths that are only limited by gain–loss conditions. A typical spectrum of lasing emission lines includes about ten lines in a visible region. The approximate relative power distribution and maximum powers for multiline operations are presented in the first and second columns, respectively (Table 11.3).

TABLE 11.3
Representative Wavelengths of an Argon Ion Laser in the Visible Region

Wavelength (nm)	Multiline Operation (Relative Power)	Single-Line Operation (W)
528.7	0.07	1.8
514.5	0.40	10.0
501.7	0.07	1.8
496.5	0.12	3.0
488.0	0.32	8.0
476.5	0.12	3.0
472.7	0.05	1.3
465.8	0.03	0.8
457.9	0.06	1.5
454.6	0.03	0.8

For special constructions with strongly ionized high-current regime, the UV lines can be obtained, mostly from:

- Doubly ionized Ar (Ar III)—363.8, 351.4, 351.1, 334.0, 305.5, 302.4, and 300.3 nm
- Also, triple ionized Ar (Ar IV)—275.4 and 211.4 nm

Multiline operation requires a set of broadband mirrors with reflectivities designed to achieve laser generation for all desired spectral lines.

Single-wavelength operation (Figure 11.14b,c) can be obtained in two different ways:

- Using special selective optics, which selects only the required wavelength (no popular method)
- By inserting an intracavity prism between a Brewster window and fully reflected mirror or prism in a Littrow configuration with fully reflected mirror at the rare surface (Figure 11.14c). The prism mounted on the vertical micrometer adjustments changes the angle of the prism and selects the wavelength of the laser operation

A typical multiline operation of commercial Ar ion laser gives the output power of 5–30 W. The output power drops significantly (in practice to 30%) when the laser is set by an internal prism on the strongest 514.5 or 488.0 nm lines. Figure 11.15 shows the spectra of the multiline operation for an Ar ion laser with qualitative power distribution.

The width of the emission laser lines of an Ar ion laser is dominated by Doppler broadening. In accordance with expressions (1.48) and (1.49), their widths are determined by three main factors—the absolute frequency of the transition, temperature, and atomic mass. For the strongest 514.5 nm line, the spectral width of a Doppler-broadened line is about $\Delta\nu_D \approx 3.5$ GHz. All visible lines have their linewidth within 3–5 GHz. The UV transitions have twice as short wavelengths and much higher temperatures of gas, because they are highly excited to obtain doubly or triple ionized Ar. Their Doppler linewidths are $\Delta\nu_D \approx 5$–12 GHz. For the typical 0.75 m long resonator, the Ar laser operates with 100-MHz spaced longitudinal modes ($\Delta\nu_{FSR} = c/2L$). It can reach a large number (a few tens) of longitudinal frequencies at the output.

11.3.3 Kr Ion Lasers

In addition to Ar ion lasers, another noble gas—Kr—has found practical applications [17,18]. The construction of an Ar ion laser can be easily adapted by the Kr medium. In practice, a Kr laser needs larger holes in metal cooling disks to get faster gas-return effect. Relative and absolute output powers of Kr laser transitions are shown in Table 11.4.

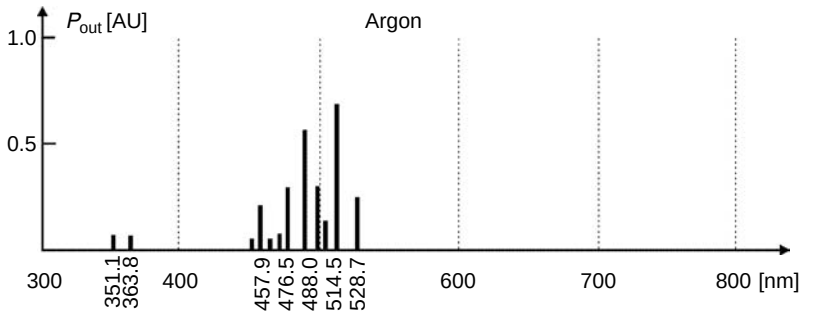

FIGURE 11.15 Argon ion laser spectrum.

TABLE 11.4
Representative Wavelengths of a Krypton Ion Laser in the Visible Region

Wavelength (nm)	Multiline Operation (Relative Power)	Single-Line Operation (W)
676.4	0.05	1.2
647.1	0.14	3.5
568.2	0.04	1.1
530.9	0.06	1.5
520.8	0.28	0.7
482.5	0.02	0.4
476.2	0.02	0.4
468.2	0.02	0.5
415.4	0.07	0.28
413.1	0.04	1.8
406.7		0.9

For highly ionized high-current regime, the UV lines can be obtained from doubly ionized Kr (Kr^{++}): 356.4, 350.7, and 337.4 nm. The spectrum of typical Kr ion laser lines is given in Figure 11.16. In practice, the Kr-based plasma is more unstable. The total power in multiline regime is three or four times lower than for an Ar ion laser. The large attraction of a Kr laser is a strongest, red 647-nm line with 2 W output. This feature can find an interesting application, as described in the following.

11.3.4 White Ar–Kr Ion Lasers

The similar physical properties of Ar and Kr discharges gave the inspiration to put both noble gases together into a common laser structure. Comparing the Ar and Kr ion spectral features (Figure 11.17), one can see that the spectra cover three basic colors—blue, green, and red. Mixing two gas media in a laser discharge cavity can give surprisingly good results—the "white" laser output beam.

The white light is obtained by playing with combinations of Ar–Kr lines. Usually the combination of red, blue, and green at the output power ratio of red:blue:green = 3:1:1 (60% + 20% + 20%) gives the impression of whiteness. To obtain pure "white" light, it is

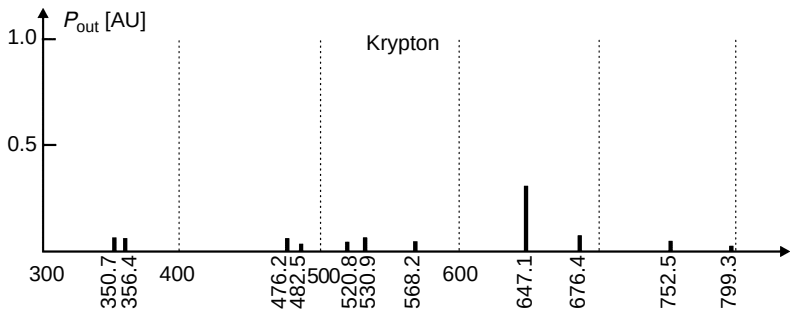

FIGURE 11.16 Krypton ion laser spectrum.

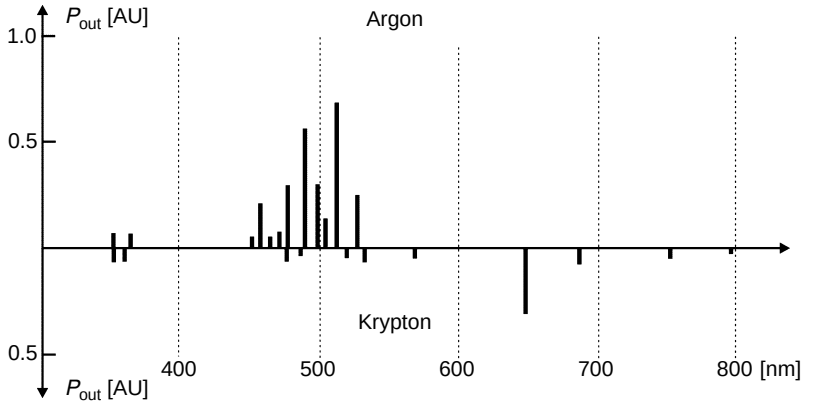

FIGURE 11.17 Idea of a "white" laser argon and krypton spectra.

necessary to balance the Ar–Kr mixture discharge current, pressure, and spectral characteristics of laser optics. It is a tricky balancing problem, which has been commercially overcome.

11.3.5 Applications of Ion Lasers

The ion lasers play an important role in many sophisticated applications. The Ar lasers found many applications in optical metrology because of relatively high power and good beam quality (TEM_{00}). They can be effective sources for:

- Doppler velocimetry
- Doppler anemometry
- Particle sizing devices
- Laser interferometry

The Ar ion laser is the basic coherent source for holography. Recently, it has been used as a source for forming Bragg gratings in fibers. The UV lines of Ar laser are used for illumination of lithographic masks.

The Ar and Kr lasers work as pumps for other lasers such as:

- Dye laser
- CW Ti:sapphire lasers (green lines of Ar laser)

Easily coupled to a fiber, Ar laser beam is applied in the microtechnological and microsurgical experiments and for stimulation of molecules to fluorescence.

Stimulated by Ar laser, fluorescence of oils in human fingerprints can be applied for the forensic analysis.

The fluorescence stimulated by Ar laser lines is a powerful mechanism for self-structure and DNA study.

Simultaneous acquisition of the temporal and spatial distributions of the fluorescence intensity (because of picosecond mode-locked Ar and Kr lasers) yields lifetime and amplitude maps of biological media in real time.

Ar and Kr lasers found many medical applications in:

- Ophthalmology
- Cytometric analysis (counting and sorting particles)

– Dermatology
– Otolaryngology, and so on

The selected lines of Ar or Kr lasers are very good coherent sources for Raman spectroscopy experiments.

The Ar and particularly mixed Ar–Kr lasers are very popular devices in all kinds of illumination performances, where visible laser beams can be scanned making patterns and pictures at discos and entertainment and advertising events.

11.4 FIR LASERS

The main excitation technique of gas lasers, plasma discharge, has a broad energy distribution, which fails to get an effective population when the levels are separated by tens of meV. It is not selective enough to excite only the upper level without excitation of lower levels. There is no doubt that only selective optical pumping is the best way of getting the population inversion in a gas medium with a small level of separation. The upper level can be populated via absorption of the coherent radiation from the ground level (or some higher level). This idea was successfully applied to pump dye lasers via coherent radiation of Ar ion laser or solid-state lasers optically pumped by semiconductor laser arrays [19].

The idea of optical pumping was also well developed for FIR lasers. They are also called submillimeter-wave or terahertz lasers, and they establish a spectacular branch of molecular lasers. These lasers were intensively investigated in the seventies and eighties of the previous century [20–22]. The attractiveness of optical pumping is that it is very selective, intense, and nondestructive. There are a lot of optically pumped molecules, which are candidates for FIR lasing, but there are only a few winners (CH_3OH, CH_3F, HCOOH, NH_3, D_2O) that have large gains, relatively high power and relevant wavelengths. After about two decades of investigations, the recent works concentrated on development of technology and applications of these lasers.

The FIR laser spectra are discrete, but they cover the wavelength range from about 20 μm to about 3 mm. FIR lasers cover a part of the middle IR region (till 30 μm) and FIR where we can distinguish submillimeter band (below 1 mm) and millimeter (between 1 and 10 mm). It is difficult to define the strict border of each region, because the regions are defined much more by the technology used than by formal definitions.

11.4.1 FIR Molecules

In the world of molecules, despite the two-atom ones, there are huge numbers of multiatom molecules. Each molecule is characterized by the so-called degrees of freedom. It is the total number N of vibration modes in a molecule:

$$N = 3n - 6 \text{ vibration modes, for nonlinear molecules,} \tag{11.15}$$

$$N = 3n - 5 \text{ vibration modes, for linear molecules,} \tag{11.16}$$

where n is the number of atoms in a molecule.

Assuming that each vibrational level is quantized in a large number of rotational levels, the quantum structure of a multiatom molecule can be quite complex (see Section 1.3.2). Most of the multiatom molecules have one common feature—they have quite a large electrical dipole momentum μ_e caused by an asymmetric structure of the molecule. Because of a permanent dipole momentum of the molecule, radiation transitions between neighboring rotational

levels of the same vibrational state are allowed, according to the quantum selection rule (see Equation 1.39):

$$\Delta v = 0, \quad \Delta J = \pm 1, \tag{11.17}$$

where v is a vibrational quantum number and J is a rotational quantum number.

In reality, the spectroscopy of such molecules is much more complicated. Let us consider the very popular molecule, methanol (CH_3OH), as an FIR medium. It is the so-called top molecule (see Figure 11.18a) with 12 vibrational modes ($3n - 6 = 12$, nonlinear molecule)—11 normal vibrational modes and 1 so-called torsional-vibrational mode (a torsion motion of OH group with respect to the CH_3 group, as seen in Figure 11.18a). The frequency for this torsional–vibrational mode is $v = 31 \cdot 10^{12}$ Hz = 31 THz, and it is well covered with a P-branch of 9.6 μm rotational band of the CO_2 laser.

The CH_3OH molecule can be treated as one two-atomic molecule, particularly when light hydrogen atoms are ignored. It reminds a CO molecule with its main vibrational mode ν_5 (Figure 11.18b). The quantum states of a simple two-atom molecule consist of vibrational (v) and a ladder of rotational levels (see Section 1.3). However, the CH_3OH molecule does not behave as a classic diatomic molecule. This situation is presented in Figure 11.18a, where additional quantized motions are shown in a demonstrative way. Three hydrogen atoms in CH_3 are responsible for the torsional (quantum number N) movement [23–25].

This quite complicated kinematics of the CH_3OH molecule causes the molecule to experience extra external rotations and it splits into three different ladders of rotational levels $K = \pm 1, 0$ (Figure 11.19). Quantum number K is associated with the projection of the total angular momentum vector onto the molecular axis of symmetry [23,25]. This figure also

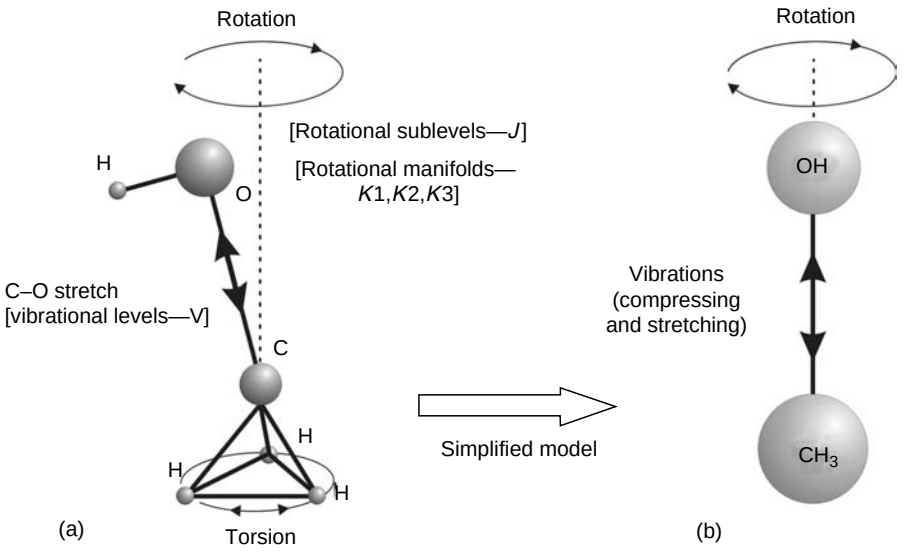

FIGURE 11.18 (a) Weakly asymmetric methanol molecule and its simplified two-atom version. C–O stretch is shown (responsible for vibrational levels v), and a torsional motion of the OH group with respect to the CH_3 group (or vice versa). Frequency for the C–O stretch is 31.01 THz. This is why a CO_2 laser line matches the vibrational transition of methanol (CH_3OH). (b) Simplified diatomic model of CH_3OH molecule.

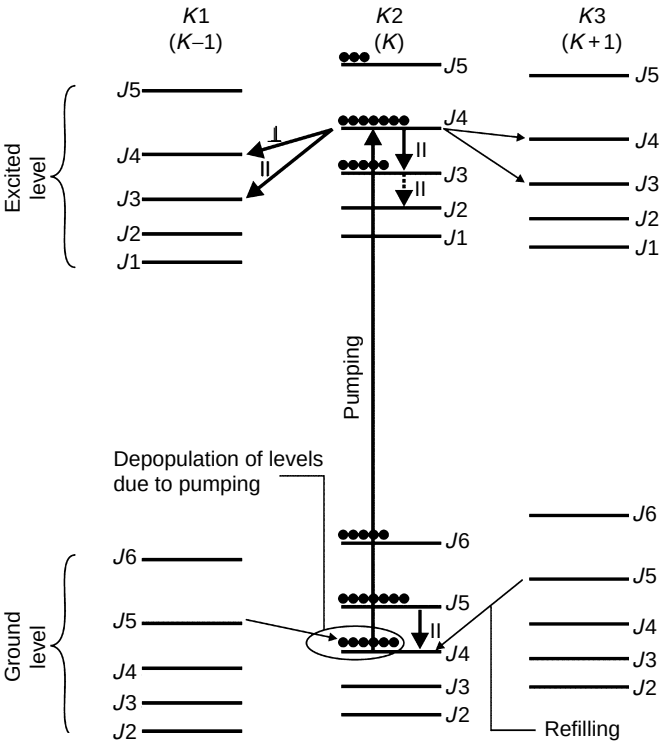

FIGURE 11.19 Three possible mechanisms of lasing because of optical pumping in a methanol molecule: direct—solid thick lines (top), cascade—dashed thick line (top), in the ground state—solid thick line (bottom). Other possible collisions and refilling are indicated with solid thin lines. The polarization related to the pumping laser beam is also shown.

illustrates the mechanism of pumping CH_3OH molecule to obtain effective population inversion in the medium. If the IR lines of a CO_2 laser pump the medium, a few mechanisms of FIR laser transitions are possible. They are:

$\Delta K = 0$, $\Delta J = 1$, with parallel polarization ($\|$),
$\Delta K = 1$, $\Delta J = 0$, with perpendicular polarization ($\perp$),
$\Delta K = 1$, $\Delta J = 1$, with parallel polarization ($\|$),

with respect to a linear polarization of a pumping CO_2 laser beam (as is indicated in Figure 11.19). The polarization of the FIR radiation is relative to the linear polarization of the pumping beam. The spectra of these lasing transitions are in the FIR region (from 19 μm to over 3 mm) and more than 2000 discrete FIR laser lines have been reported [26–28].

It is necessary to emphasize the other paths of upper laser level excitation. The population inversion can be obtained by direct pumping from the vibrational fundamental band (C–O stretch) with three possible techniques: pumping the excited level by absorption or pumping the ground level by refilling (see Figure 11.20a); direct pumping of the first hot band from excited state to the higher excited state (Figure 11.20b); and pumping by two or more pumping wavelengths (Figure 11.20c,d).

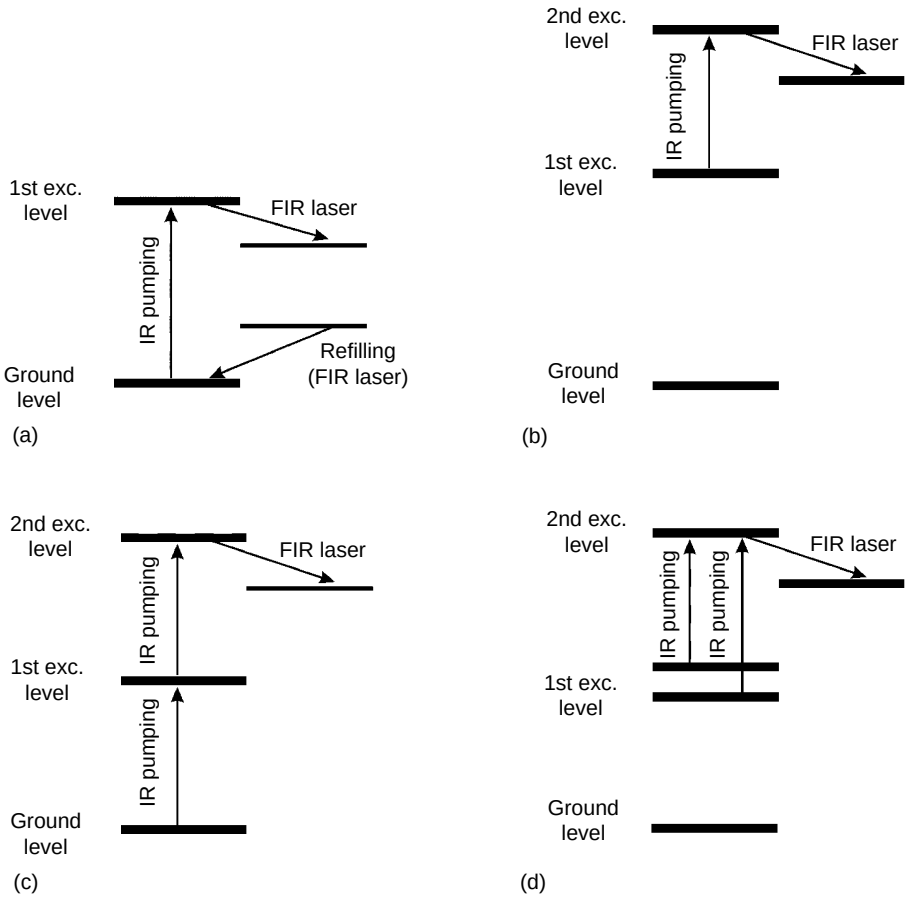

FIGURE 11.20 Possible mechanisms of the FIR upper laser level population: (a) directly from the ground to upper laser level; (b) from the first excitation FIR molecule level to the second excitation level; (c) double pumping, indirectly via the first excited level; and (d) double pumping from two different first excited levels.

11.4.2 Line Assignment

The spectral width of the absorption lines for pumping transitions are determined by Doppler broadening (see Section 1.4, Equation 1.49) and they are comparable with the emission linewidth of CW low-pressure (10–20 Torr) CO_2 laser ($\Delta\nu_D \approx 60$ MHz). The lines of a CO_2 laser are spectrally quite narrow (tens of megahertz) compared with the spectral offsets between them (30–60 Hz). Hence, it is not too easy to overlap a chosen absorption line of the FIR medium by the pumping radiation of a CO_2 laser. For example, only a few lines of a CO_2 laser can cover some absorption lines of CH_3OH. They are usually not covered centrally [29].

This rather random coincidence of a few pumping lines of a CO_2 laser and absorption lines of FIR media forces development of line matching techniques [30–32]. There are two matching techniques: the emission lines can be spectrally broadened or shifted. The first method requires higher CO_2 pressure causing pressure broadening of the laser emission line (according to considerations in Section 1.4.3). The line of high-pressure lasers (like transverse electrical atmospheric [TEA] or RF-excited waveguide CO_2 lasers) can be broadened quite

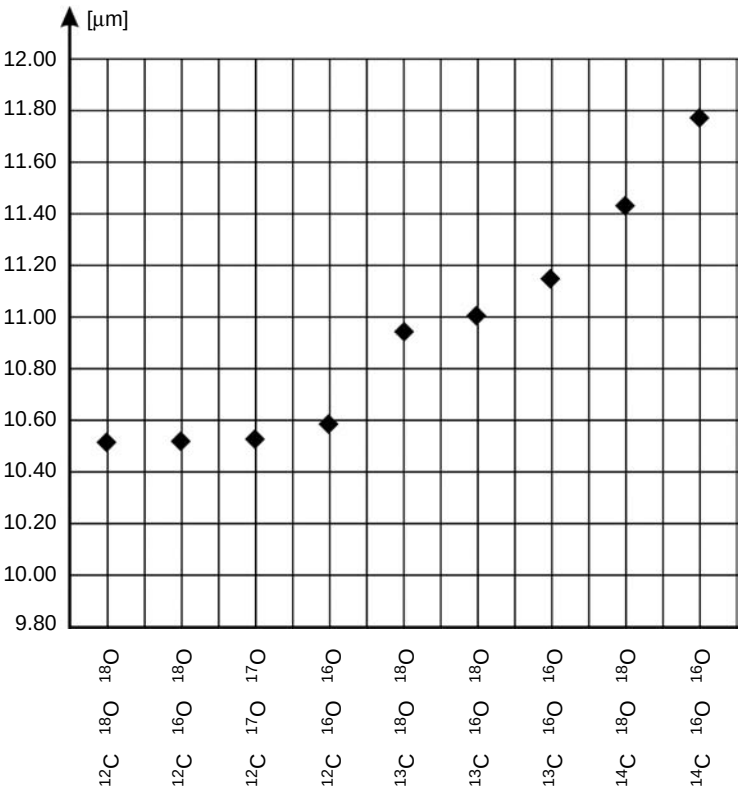

FIGURE 11.21 Relative displacement of the central band frequencies of the CO_2 molecule for different isotopes of C and O.

significantly by pressure broadening (5 MHz/Torr). However, TEA CO_2 lasers can operate only in a pulsing regime.

Another much popular procedure to overlap pumping and absorption lines is shifting the pumping line by using different isotopomers of a CO_2 molecule [33]. Figure 11.21 qualitatively illustrates the isotopic frequency shift of CO_2 isotopomers.

There is still the possibility to shift the pumping line of a CO_2 laser by using its radiation from the so-called hot bands or sequence bands, which increases the variety of possible laser transitions. The idea of lasing from hot or sequence bands is presented in Figure 11.22. The lines of hot or sequence bands are displaced relatively to the regular band and they increase the possibility of access of FIR levels. Figure 11.23 schematically shows the shapes of the hot and sequence bands with respect to the shape of a regular band of a CO_2 molecule as a reference.

Another method of line overlapping is using isotopomers of the FIR medium [34]. As an example, the family of P, Q, and R branches of absorption bands of a CH_3OH molecule and its isotopomers ($^{13}CH_3OH$, $CH_3{}^{18}OH$, CD_3OH, $^{13}CH_3OH$) relative to the 10.6 and 9.6 μm bands of CO_2 emission lines are shown in Figure 11.24.

Most of the FIR lasers are pumped by CO_2 lasers. Hence, one can say that all FIR technology is fated to the CO_2 laser pumping, and only limited numbers of FIR lines of molecules are attainable in practice. There is no doubt that a tunable, narrow line and relatively high-power coherent sources (tens of watts) would be the fullness of spectroscopic requirements allowing insight into the FIR molecular world. In our opinion, the recently fast

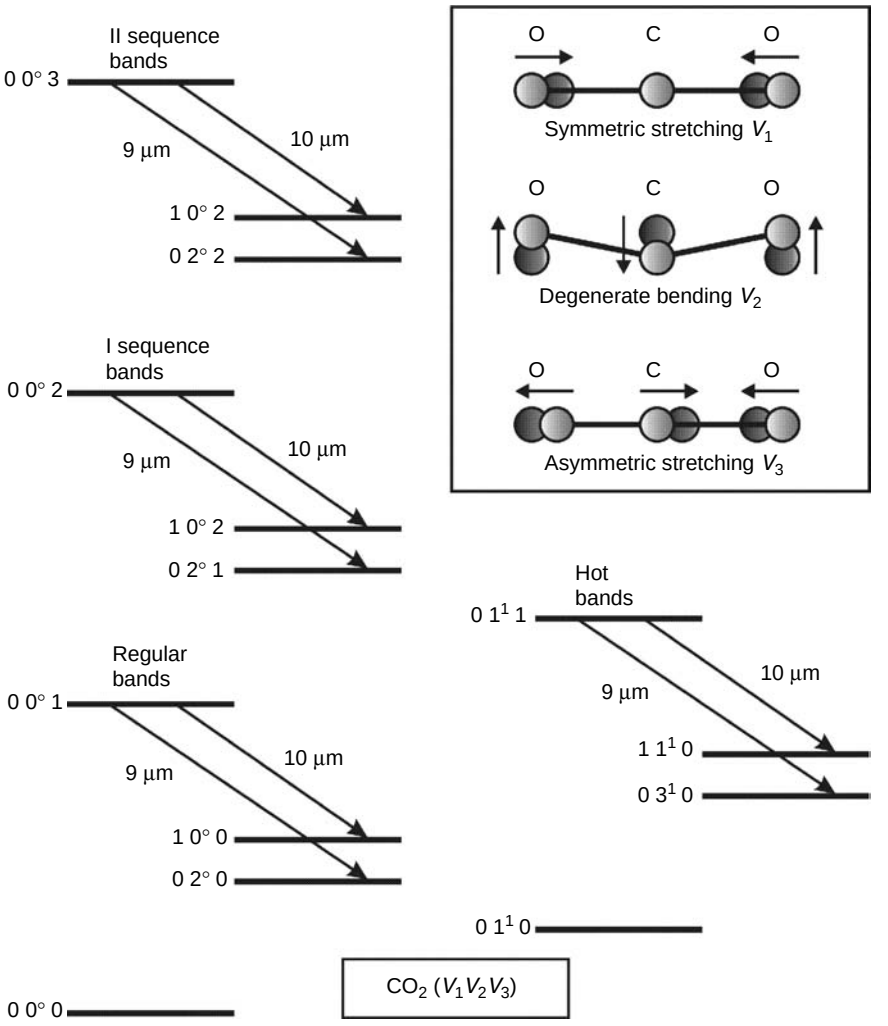

FIGURE 11.22 Regular, hot, and sequence transitions in a CO_2 laser. Possible vibrations of the CO_2 molecule are shown (described by quantum numbers v_1, v_2, and v_3).

developing new technology of semiconductor lasers, the so-called quantum cascade lasers (QCL), gives a chance to fulfill these expectations.

The QCL is tunable and its linewidth of radiation is about 1 MHz. The array technique and further development toward the higher output lasers (now their output is in the level of a few milliwatts) would make them ideal pumps for FIR lasers. Maybe in the future we will witness new hybrid FIR lasers pumped by QCL [35].

11.4.3 FIR Laser Radiation

Because of Doppler inhomogeneous broadening of the absorption line of the FIR medium (when it is pumped coherently), only part of the molecules will be pumped. The homogeneous lines of interaction are shown in Figure 11.25 as two saturation shapes (one coherent radiation interacts with Doppler shifted two groups of molecules). They burn two dips in the absorption profile of the FIR molecule. The upper line of IR pumping radiation also plays

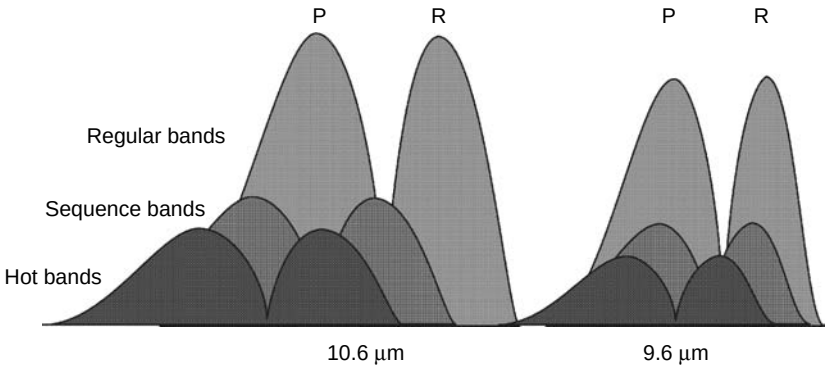

FIGURE 11.23 Relative displacement of the hot and sequence bands of a CO_2 molecule with respect to regular bands 10.6 and 9.6 μm. (From Telles, E.M., Odashima, H., Zink, L.R., and Evenson, K.M., *J. Mol. Spectrosc.*, 195, 360, 1999. With permission.)

a role of the upper line of FIR radiation. In practice, the frequency ν_{FIR} of FIR radiation is much lower than the frequency of pumping

$$\nu_{FIR} \ll \nu_{pump}. \tag{11.18}$$

That is why the Doppler broadening for an FIR transition is weak compared with IR transition, and it is of ν_{FIR}/ν_{pump} smaller. For example, when $\lambda_{FIR} = 570$ μm (CH_3OH molecule), the Doppler broadening is given as: $\Delta\nu_D = 1.15$ MHz.

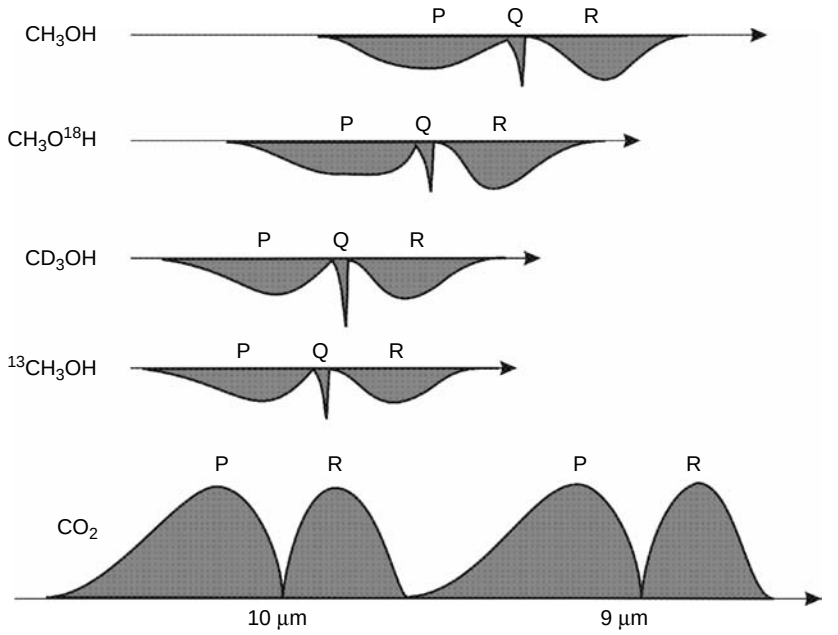

FIGURE 11.24 Relative displacement of the rotational–vibrational bands of methanol (CH_3OH) and their isotopomers: $^{13}CH_3OH$, $CH_3{}^{18}OH$, CD_3OH, $^{13}CH_3OH$. Other mutations are also possible, such as $^{13}CD_3OH$, CD_3OD, $^{13}CD_3OD$, CH_3OD, CH_2DOH, CH_2DOD, and CHD_2OH. They can give hundreds of the far infrared laser lines. (From Xu, L.-H., Lees, R.M., Vasconcellos, E.C.C., Zerbetto, S.C., Zink, L.R., and Evenson, K.M., *IEEE J. Quant. Electron.*, 32, 392–399, 1996. With permission.)

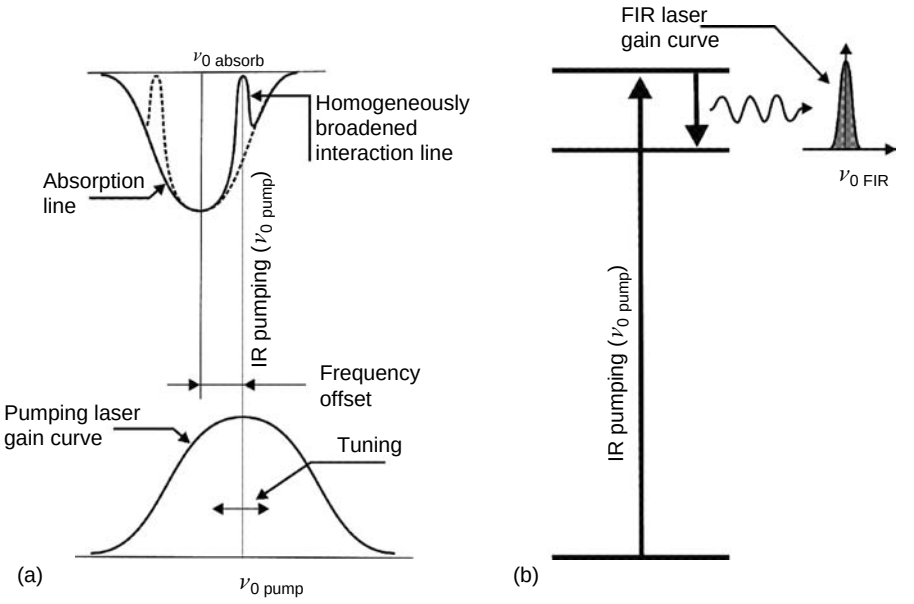

FIGURE 11.25 (a) Mechanism of the optically pumped far infrared (FIR) laser interaction of the Doppler-broadened (50 MHz) pumping laser gain curve and Doppler-broadened (~40–60 MHz) absorption line of the FIR medium. (b) Saturation effect in the absorption line is indicated. The laser frequency $\nu_{0\ pump}$ is set with some frequency offset with respect to the central frequency of the absorption line, and can be tuned toward $\nu_{0\ absorb}$ for efficient pumping. The pumping intervibration transition, FIR interrotational lasing, and profile of the FIR emission gain curve (1–5 MHz) are shown.

The collisional (pressure) broadening—38 MHz/Torr has a much larger contribution to the line broadening. For analyzed line $\lambda_{FIR} = 570$ μm, both Doppler and pressure broadenings become equal at pressures of about 30 mTorr [36]. The FIR molecular gas is usually filled with the pressure from tens of mTorr to about 1 Torr. That is why we can say that, in practice, the emission lines of FIR radiation are homogeneously broadened, as shown in Figure 11.25.

The pressure of an FIR medium usually does not exceed 1 Torr. The slow vibrational relaxations cause a large accumulation in the excited vibrational state (Figure 11.26). On the other hand, increasing the pressure means increasing rotational relaxation inside the excited vibrational manifold equalizing the population distribution among rotational levels and reducing significantly the population inversion between upper and lower FIR transition levels. Hence, in practice, the optional pressure in FIR media is usually below 1 Torr [37].

11.4.4 Representative FIR Transitions

FIR laser action by optical pumping with a CO_2 laser was presented for the first time by Chang and Bridges in CH_3F gas [20]. Their paper had initiated rapid development of FIR lasers based on many similar organic molecules. The most popular FIR medium is CH_3OH with its deuterated and isotopic varieties. A molecule has to fulfill two main conditions for producing efficient FIR laser action:

It has to have a large permanent electrical dipole moment $\mu_e \approx 1$ Debye (1 Debye = $3.3356 \cdot 10^{-30}$ cm).

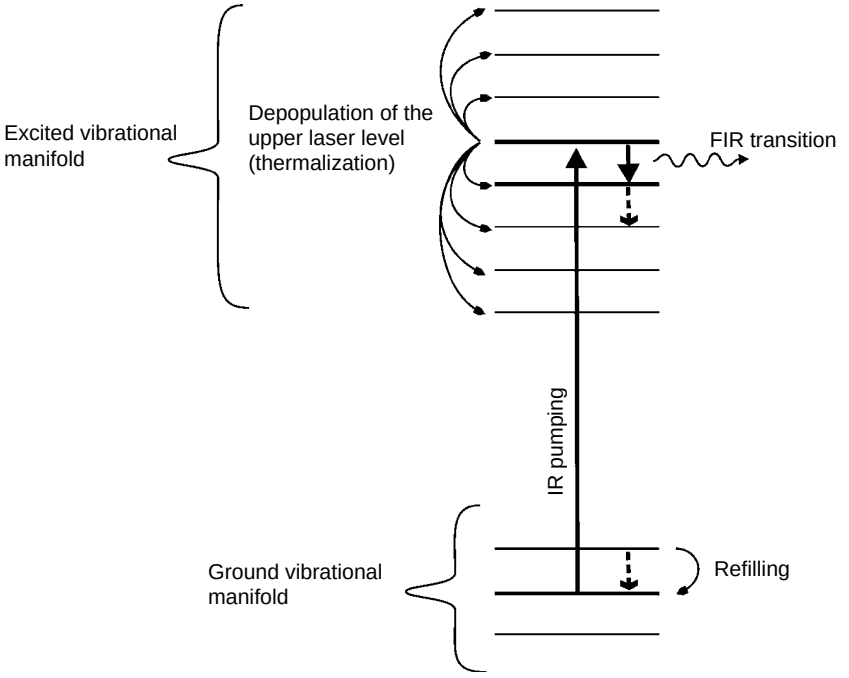

FIGURE 11.26 Mechanism of simultaneous depopulation and population of higher and lower far infrared (FIR) laser levels, respectively. IR laser intervibrational pumping and FIR lasing are indicated. Possible laser transitions are also marked with dashed lines (top: "cascade," and bottom: ground-state FIR lasing).

It has to have a vibrational–rotational absorption line in coincidence with the available pumping source emission line. In practice, the frequency offset between the centers of a pump line and absorption FIR line should be less than ± 60 MHz (Figure 11.25).

The CO_2 laser source limits the pumping availability. That is why most of the research activity on FIR lasers has been concentrated on searching molecules with intervibrational transitions matching the CO_2 laser radiation. Table 11.5 lists some chosen representative FIR molecules and transitions with wavelengths, pumping lines, and input and output powers.

11.4.5 FIR Laser Constructions

The seventies and eighties of the twentieth century are the main period of intense investigation and development of physics and technology of terahertz or submillimeter lasers—synonyms of an FIR laser. Pumping configuration, types of resonators with outcoupling of submillimeter radiation are the most important problems, which have to be solved during designing the total construction of an FIR laser. The IR and FIR radiations require different materials for optical elements. The FIR laser construction consists mainly of two parts: the pump laser and the FIR cavity. As a pump, usually a DC CO_2 laser equipped with a diffraction grating (allows establishing a chosen transition line) and a PZT (allows tuning and stabilizing the frequency of a CO_2 laser) is used. The recent development of the RF-transversely excited CO_2 waveguide and slab-waveguide lasers allows using them as more powerful pumps with a bit larger tunability. The FIR part of the system consists of a relatively long chamber (tens of centimeters to a few meters) equipped with special internal optics forming the FIR resonator.

TABLE 11.5
Some Far Infrared (FIR) Molecules' Transitions

Molecule	λ[μm] Wavelength	CO_2 Pumping Line	P_{in} (W) Pumping Power	P_{out} (mW) Output Power
Methyl fluoride	192.78	10R32	55	4.7
CH_3F	372.68	9P50	14	5.8
$C^{13}H_3F$	1221.79	9P32	58	2.4
Methylacetylene	647.89	10P14	100	3.3
CH_3CCH	1174.87	10P44	35	2.7
Methanol	41.7	9P32	3.7	4.0
CH_3OH	118.8	9P36	20	3.0
Cyanomethane	570.5	9P16	20	3.0
CH_3CN	372.87	10P20	84	3.5
Chloromethane	713.72	10P32	44	0.7
CH_3Cl	1814.37	10P46	48	0.3
Bromomethane	275.00	9R14	44	1.7
CH_3Br	870.80	9P52	16	1.3
Iodomethane	943.97	9R12	45	13.0
CH_3I	1886.87	9P26	57	1.6
Formic acid	264.05	10R10	73	5.3
HCOOH	380.02	10R18	83	7.0
Difluoroethene	414.98	10R2	46	17.0
CH_2CF_2	531.06	10P24	108	5.5
Ethanediol	545.21	10P38	39	8.8
$C_2H_4(OH)_2$	545.39	10R32	63	10.0
Ethyl alcohol	660.70	10R20	68	15.0
C_2H_5OH	925.52	10R46	33	14.0
	1310.38	10R4	90	5.3
	377.45	9R16	47	5.1
	1063.29	10P38	71	6.5
	1253.67	10P32	98	13.0
	309.00	10R42	100	5.0
	388.00	9R16	100	10.0
	393.62	9R18	150	100.0
	428.00	9R20	100	10.0
	512.00	9R28	100	10.0
	554.40	10P14	10	3.0
	884.00	10P12	5	1.0
	70.10	9P34	100	10
	396.00	9P32	20	0.01

Source: From Rosenbluh, M., Temkin, R.J., and Button, K.J., *Appl. Opt.,* 15(11), 2635, 1976. With permission.

Two main concepts of FIR cavities can be distinguished as follows:

The Fabry–Perot open Gaussian resonator (in a wide tube)
The waveguide construction (cylindrical or rectangular symmetry) with plane–plane resonator mirrors

Each research group usually develops its own CO_2–FIR configuration. Some of the most representative structures are shown in Figure 11.27. As seen, two pumping techniques can be distinguished—coaxial pumping technique and zig-zag pumping.

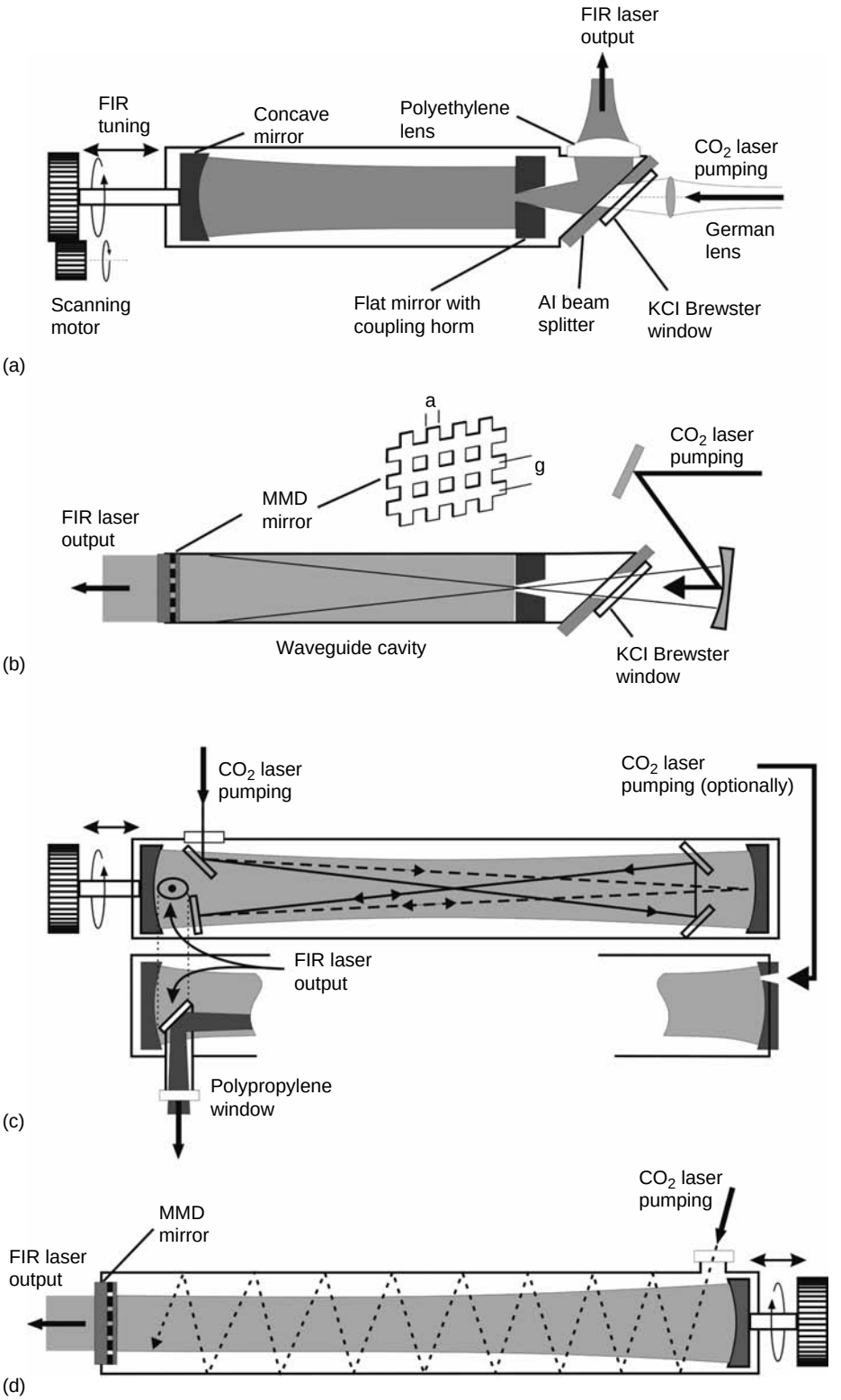

FIGURE 11.27 Some typical structures of far infrared (FIR) lasers: (a) historical Chang's structure; (b) waveguide with metal-mesh-dielectric (MMD) mirror; (c) X–V structure; and (d) zig-zag structure.

Because the pump wavelengths differ significantly from FIR laser wavelengths, there is a problem with common optics. Apart from fully reflecting metal optics, which can be common for IR and FIR radiations, the transparent optical elements (windows, mirrors, and lenses) are made of different materials [38]. Hence, many tricks are used to outcouple the submillimeter radiation from the laser cavity.

Figure 11.27 reviews same basic configurations of FIR lasers. The classical Fabry–Perot Gaussian resonator scheme is shown in Figure 11.27a. The FIR part of the laser consists of a relatively long chamber. The pumping beam is injected through the ZnSe Brewster window into a medium (a few hundreds of mTorr pressure) through the hole in the metal mirror. The outcoupling of the FIR radiation goes through the same hole and it is directed via transparent organic (polyethylene) lens [20,21].

The alternative solution for an open Gaussian resonator is the waveguide configuration (Figure 11.27b). The pumping beam is injected via the hole into a waveguide resonator with an internally polished cylindrical tube of diameters of 10–30 mm and plane–plane resonator. The special output coupling mirrors (called metal-mesh-dielectric [MMD]) have been developed to obtain much higher efficiency of FIR lasers [39,40]. The mesh mirror consists of silicon substrate with dielectric coating for IR radiation (very high reflection for IR), which is covered with the metal mesh structure that is transparent for FIR radiation. By varying the mesh spacing a (a few μm), and mesh strip width g (tens of μm)—see Figure 11.27b—the power reflectance from 0 to 100% can be achieved.

Figure 11.27c,d demonstrates nonaxial pumping geometries, so-called X–V [41,42], and zigzag shapes [43], respectively.

The important element of each FIR laser is a precise mechanical setup for tuning its resonator length. The passive resonance of an FIR resonator (free spectral range for 1 m long resonator is 150 MHz) has to overlap the FIR emission line (the width of a few megahertz) to reach the FIR lasing. This can be obtained by a scanning motor, which can tune the mirror over $\lambda_{FIR}/2$ distance. By larger tuning of the FIR resonator, say, by ten or more half-wavelengths, an averaged FIR wavelength can be determined to an uncertainty of approximately 0.5 μm [41,42]. A much more sophisticated method—the use a heterodyne technique—is necessary for precise wavelength measurements [44].

Figure 11.28 presents a futuristic idea, which in our opinion would be an ideal FIR laser solution. The efficient pumping with an array of QCL is proposed. Relatively easy tunability and quite narrow spectral width (about 1 MHz) of output radiation of the QCL can be a huge

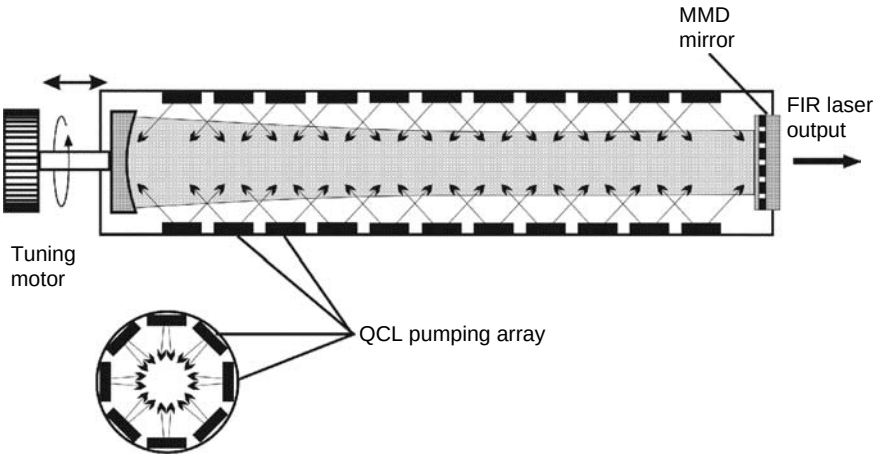

FIGURE 11.28 The far infrared (FIR) laser structure combining an FIR laser cavity, and arrays of quantum cascade lasers distributed along the FIR cavity.

advantage of a QCL–FIR hybrid system. Precise tunability allows matching any absorption transition of the FIR media without complicated procedures of fitting lines as in the case of a CO_2 pumping laser. However, relatively low output (a few milliwatts)—not enough for pumping FIR media—is still a weak point of the QCL [45]. Sooner or later, one can expect an increase in both an output power, and developing array technology of the QCL. It should open the door to design simple and compact FIR laser devices. It has significant meaning in penetration of the space, and investigations of the interstellar gas, where weight of the scientific apparatus on the board of the satellites is of great importance.

The optical efficiency P_{out}/P_{pump} of an FIR laser is quite low, unfortunately. A typical output of a few milliwatts is achievable for a few tens of watts of pumping power. It corresponds to an efficiency of about 0.1%. However, there are some exceptions—the maximum output power over 1 W at the efficiency of 1% for both 119 μm wavelength of a CH_3OH molecule and for 57 μm wavelength of a CH_3OD molecule have been obtained [46].

11.4.6 Applications of FIR Lasers

The FIR micromillimeter wave's region (approximate spectral range of 30 μm–3 mm) can be treated as a bridge between micromillimeter waves and optical regions. This is the spectral region of high interest of many fields: spectroscopy of heavy molecules, laser magnetic resonance spectroscopy, laser sideband spectroscopy, plasma diagnostic, wide variety of solid-state physics studies, and potentially—telecommunications. Many molecules in the interstellar space have radiation spectra in the millimeter and submillimeter regions. FIR lasers are ideal sources for molecular line astronomy and they are used as diagnostic tools for investigations of interstellar gases (density, temperature, and velocity) [47]. More than 120 multiatomic molecules (from diatomic to 13 atoms) have been recognized in the interstellar space. The hot (with temperature up to 5000 K) and dense molecules give a lot of information about media and some answers on key processes like star formation and evolution. The rich spectrum in IR and FIR regions provides data for investigations of the space physics. The frequency stabilization of FIR lasers is particularly an attractive branch of metrology for setting the absolute measurements of transition frequencies in the FIR region. Frequency-stabilized FIR lasers are used as intermediate frequency links in experiments comparing frequency stability of laser standards from different optical regions. Special heterodyne setups of mixing three laser beams (two different CO_2 lasers operating on different lines and an FIR laser) for the measurement of FIR laser frequency were developed [44].

The FIR radiation, if put into some plasma absorber, is particularly sensitive for changes of plasma density. Hence, special FIR interferometers are quite often used for measuring the electron density profiles in different plasma experiments.

There is no doubt that millimeter and submillimeter wave radiations are getting rapidly to be extremely attractive spectral regions for interplanetary telecommunications. Stable FIR lasers with narrow line radiation are attractive carrier sources with potential application to free-space optical FM telecommunications.

11.5 THE SUBMILLIMETER HCN LASER

HCN is a linear molecule with three fundamental vibrational modes (ν_1, ν_2, ν_3). The operation of an HCN gas laser was first announced by Gabbie et al. in *Nature* in 1964 [48] and its physics and constructions have been investigated by various groups in the seventies and eighties [49–66] of the twentieth century. The HCN laser is an example of submillimeter laser successfully excited by discharge.

The laser action can be obtained between rotational levels ($J = 10$ to $J = 9$) of different vibrational levels (010) and (040) corresponding to the wavelength $\lambda = 337$ μm (891 GHz).

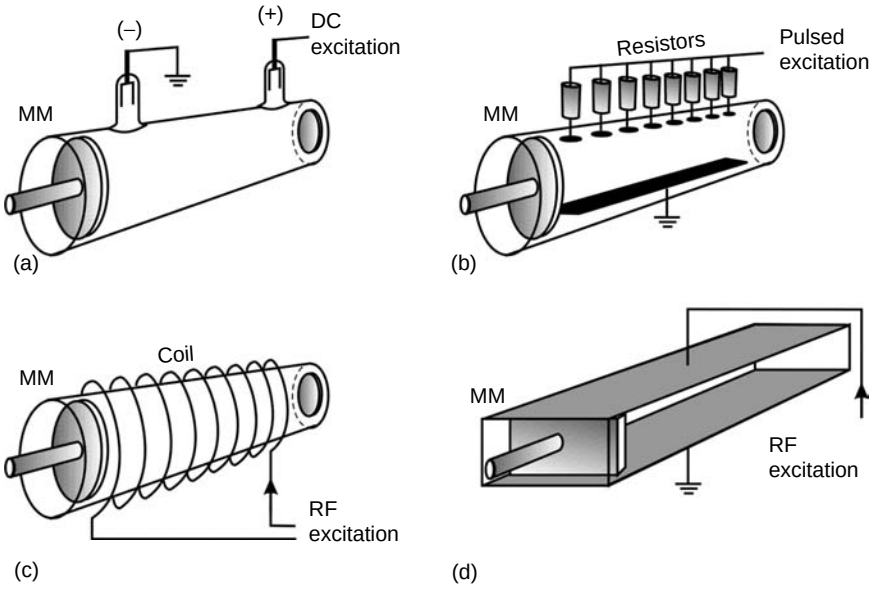

FIGURE 11.29 Four typical techniques of plasma excitation in hydrogen cyanide lasers: (a) DC electrical discharge; (b) transverse electrical pulse discharge; (c) inductive RF-excitation; and (d) capacitive RF-excitation. MM: movable mirror.

It can also oscillate between rotational levels ($J = 9$ to $J = 8$) within the same vibrational state (040) at the wavelength $\lambda = 373$ μm (805 GHz) [67].

This medium experienced all kinds of discharge excitation—electrical longitudinal DC, transverse pulsed, RF-inductively coupled, RF-capacitively coupled, and pulsed operation with the so-called auxiliary DC discharge. Figure 11.29 shows all four techniques of excitation.

HCN lasers are not commercially available. Different constructions can be met depending on the experience and needs of research group.

There are many ways to obtain stable and stationary conditions of excited HCN molecules. To avoid chemical degradation of molecules caused by strong discharge impact, a laser volume is usually filled with different mixtures, which, in the process of discharge, give HCN molecules as a product. A few such typical gas mixtures are listed here:

CH_4—N_2 (1:2),
CH_4—N_2—He (1:1:2), and
CH_3CN—He, CN_2—H_2, HCN—CH_4—He, CH_4—NH_3.

Typical pressure of the gas mixture is around 0.5–3 Torr. To maintain stable conditions of the gain medium, slow flow of gas is usually applied at the level of 10 Torr L/min. Optical components forming a laser resonator are very similar to FIR lasers described in Section 11.3.

Two resonators can be applied—Gaussian Fabry–Perot (not very often) or mainly waveguide resonators (circular or rectangular geometry). The laser beam is outcoupled via mesh mirror or mirror with a hole. The waveguide structure (the rectangular waveguide Figure 11.29d) is particularly attractive. It determines the mode structure as in CO_2 waveguide lasers (see Chapter 6A). Two main wavelengths can lase from an HCN laser—337 μm (891 GHz) and $\lambda = 373$ μm (805 GHz).

The length of the laser tube is usually 1–3 m long. In the case of DC discharge, the discharge current is at the level of 1 A and the walls of the discharge have to be thermocooled

by a water jacket. The optical power efficiency of the HCN laser is much below 1%. The output power depends on the length of the resonators and it ranges from tens to hundreds of milliwatts. In the case of pulse operation (the laser supplied by pulsed Marx generators), the output energy of a few millijoules with 1 μs pulse duration can be obtained (output power at the level of 1 kW).

The isotopic mutations of HCN laser is the DCN laser, which, in its technology and physics, differs only in the wavelength emitted by the laser. The DCN laser operates at two lines—190 and 195 μm at the CW operation with a few milliwatts of output [68].

The Doppler broadening effect is negligible because of quite a low frequency of the laser transitions compared with the Doppler width of transitions in the visible range. It is comparable with homogenously broadened vibrational–rotational transitions. This laser is a very good candidate as a frequency standard [55]. The linewidth of the laser radiations can be as low as 1 kHz.

Two main areas of applications of HCN lasers can be distinguished. These lasers have found applications in plasma diagnostic of electron densities n_e, at the level $n_e \sim 10^{14}$ cm^{-3}, typical for TOKAMAKs [69]. HCN is one of the most representative interstellar molecules. Hence, the coherent radiation from HCN lasers can be used as the probing frequencies of rotational–vibrational excitation of molecular clouds, in particular in the star-forming regions [70].

11.6 XE LASER

The Xe laser was discovered in 1962 [71], quite shortly after the first laser. It was excited by inductively coupled RF discharge operation in the pure Xe at a pressure of 20 mTorr. The first oscillating wavelength was 2026 nm with an output of 5 mW. The noble gas Xe had demonstrated very high gain. It reminds the transition $3s_2$–$3p_4$ in He–Ne laser at 3.39 μm line (see Figure 11.2 and Table 11.1), which also has a high gain. Quite soon, the lasing for 3508 nm line was reported at the small signal gain to be as high as 50 dB/m (10^5/m). The first constructions were performed in classical Pyrex glass tubes with fused quartz Brewster windows (fused quartz is transparent for near IR) in a mixture of Xe and He, with typical ratio 1:100 (p_{Xe} about 20–40 mTorr). For the next few years, there was great interest in Xe lasers, because of their extremely high gain and their potential applications in the middle IR range [72–74] and the new laser lines were discovered in the range of 2–13 μm.

The low-pressure Xe lasers are usually DC excited, and there are some commercial He–Xe lasers operating in single-line regime, tuned by diffraction gratings in the range of 2.5–3.5 μm with an output power of a few tens of milliwatts [75]. Typical wavelengths obtained at lower currents are 1.73 and 2.485 μm. For higher currents, usually only 2.026 μm wavelength is observed. The range of available wavelengths can be enlarged when He–Xe laser is excited by high current pulses. Higher discharge current allows lasing more lines.

Figure 11.30 shows energy level diagram of Xe atom emphasizing the strongest laser transitions.

The Xe lasers also have the possibility to lase in much higher pressure regime (100–300 Torr). Because of the application of different pulse configurations to He–Xe mixtures, new lines were discovered. Many pulse excitation techniques have been investigated in the past for searching new lines and higher energies. These techniques remind very much of the TEA configuration with transverse pulse excitation and UV preionizaton circuits with the achievements of tens of millijoules in the pulse [76]. When the pulse repetition is higher, it is necessary to apply fast flow system [77] with the maximum pulse repetition frequency of 20 Hz. Newman and DeTemple [78] applied electron beam-sustained discharge to excite atomic Xe.

Probably the most promising results were obtained by an RF excitation configuration of Xe laser, which was first demonstrated by Christensen et al. [79] with the symbolic

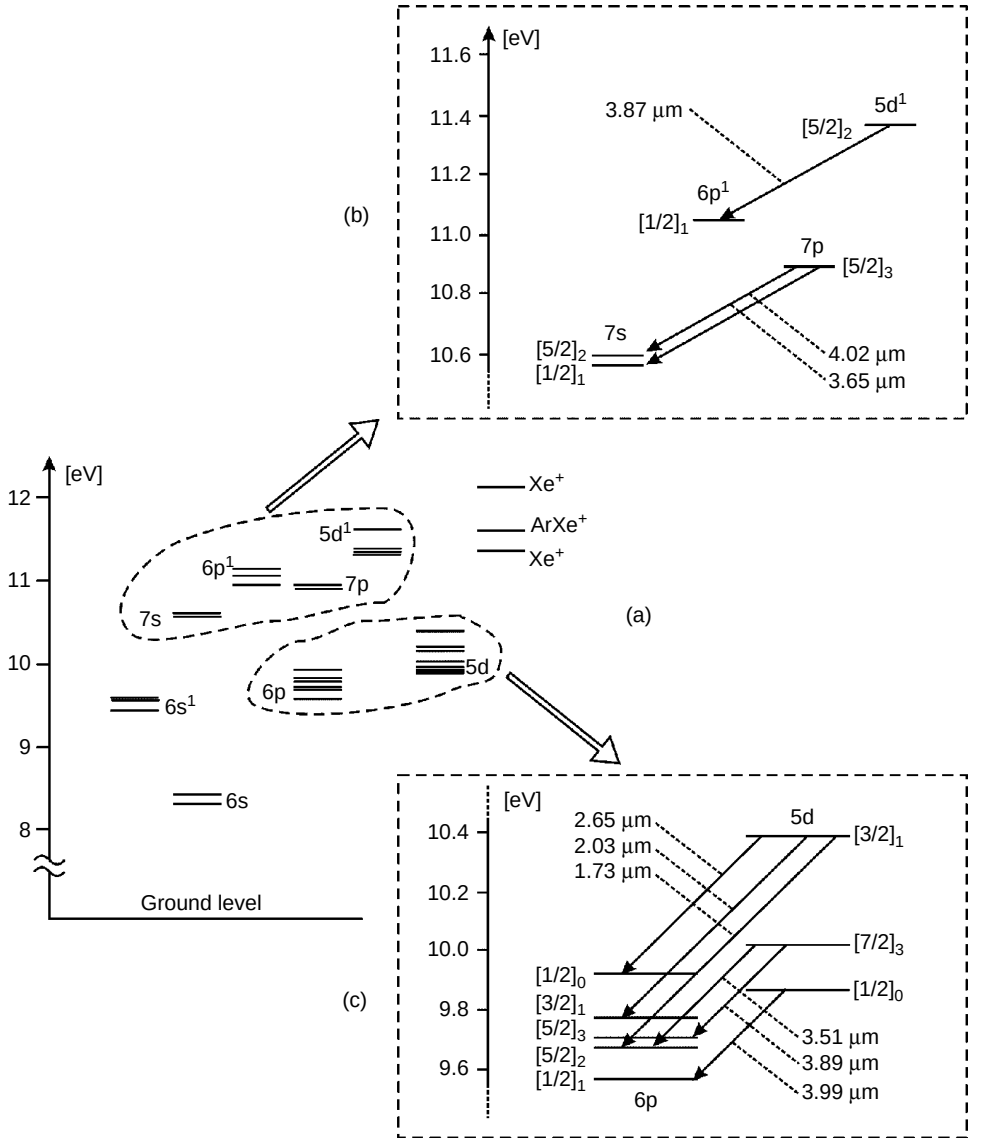

FIGURE 11.30 (a) Energy level diagram of xenon; strongest laser transitions are shown in detail in (b) and (c).

output power 30 mW. The real breakthrough was introduced by Udalov et al. [80] with the output power more than 300 mW and 0.2% efficiency, operating at 2.03, 2.65, 3.37, and 3.51 μm lines. The same group later obtained 1.5 W output power [81]. The RF excited Xe laser, with RF-excited of the slab resonator operating with the output power of 6.5 W, was demonstrated by Wendland et al. [82]. Wavelength selection of coating mirrors allowed selecting other lines from 3.5 to 4.0 μm range (3.51, 3.65, 3.87 and 3.89 μm) [82].

Typical gas mixture consists of Xe (0.1–1%) and He (0–99%) or Xe/Ar/He mixture (0.25:60:40) at pressures of about 100 Torr. The RF slab laser with unstable resonator concept was adapted from RF-excited CO_2 lasers (see Chapter 6A) and its typical scheme is shown in Figure 11.31. The efficiency of RF-excited Xe laser is below 1% for multiline operation.

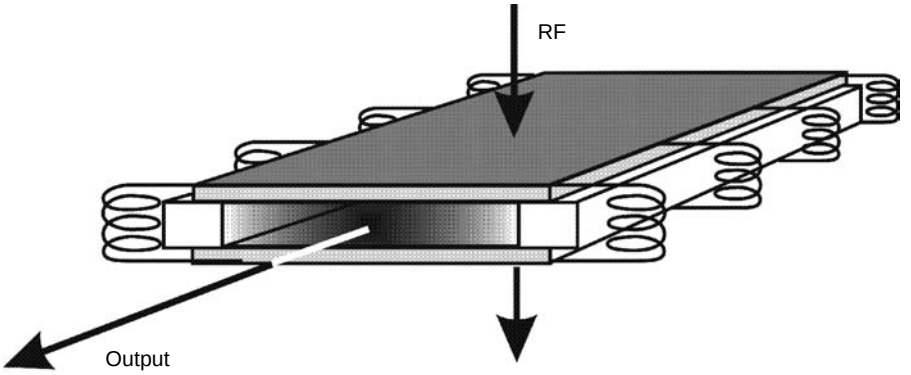

FIGURE 11.31 RF-excited slab xenon laser. Top and bottom Al electrodes are separated with ceramic bars. Shunt inductors along the structure are visible.

11.7 THE N_2 LASER

The N_2 laser action was first demonstrated in 1963 by Heard [83]. The N_2 laser is a molecular laser but it differs substantially from other known molecular lasers like CO_2 or CO, which operate in the middle IR region. It behaves much more like excimer laser. The N_2 molecule reminds an excited excimer (see Chapter 8) and the population inversion is obtained between its two different electronic states. The energy states of N_2 molecule are shown in Figure 11.32, where four basic electronic states taking part in laser actions are drowned—the ground level state forms vibration potential $X^1\Sigma_q^+$ and the excited electric states $A^3\Sigma_u^+$, $B^3\Pi_g$, and $C^3\Pi_u$.

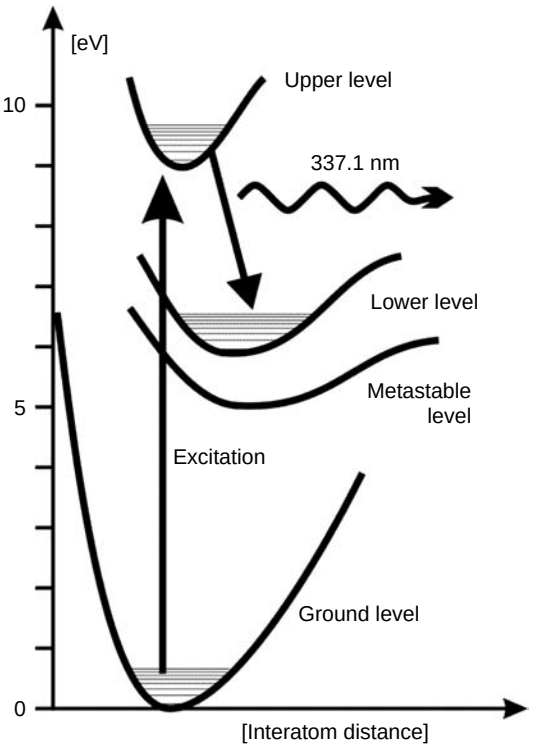

FIGURE 11.32 Important energy states of nitrogen molecule.

Energetic distances are separated by a few electron volts and all these levels are spread between 0 and 13 eV. Some vibrational low levels are also emphasized. The main laser action occurs between $C^3\Pi_u$ ($\nu = 0$, J) and $B^3\Pi_g$ ($\nu = 0$, $J \pm 1$), which gives the wavelength $\lambda = 337.1$ nm with transition linewidth $\Delta\nu \cong 250$ THz ($\Delta\lambda \cong 0.1$ nm). Weaker laser oscillations can take place between oscillation $\nu = 1$ and $\nu = 0$ ($\lambda = 357.7$ nm) or $\nu = 0$ and $\nu = 1$ ($\lambda = 315.9$ nm) of this electronic transition.

For some special conditions, the laser action can also be obtained between electronic lines $B^3\Pi_g$ and $A^3\Sigma_u^+$ in the NIR region (0.74–1.2 μm) [84]. The potential minimum of B state is shifted relatively to the ground state. According to the ideal situation, the lifetime of the upper laser level should be much longer compared with the lifetime of the lower laser state. In N_2 molecule, the situation is reverse. The lifetime of $C^3\Pi_u$ state is 40 ns and the lifetime of $B^3\Pi_g$ is 10 μs. This is the reason N_2 laser can only operate in the pulse manner.

However, the electrical pulse width has to be very narrow, because lasing starts immediately when population inversion appears. For efficient pumping, all the energy has to be delivered to the laser medium in a time that is shorter than the optical pulse width, it means shorter than 10 ns. To form such short pulses, a low-inductance configuration of a laser head is required. It is the same problem of pulse discharge energy delivering like in excimer lasers. There are many electrical short-pulse supply systems, which fulfill these requirements. The circuits usually consist of high-voltage supply, high-voltage capacitors, charging resistors, charging inductors, spark gaps or thyratrons [85,86], or even ultrafast magnetic pulse compression circuits [87].

Typical configuration of the N_2 laser head of the low inductance is shown in Figure 11.33 and it reminds of transverse excitation configuration applied to excimer lasers (see Chapter 3).

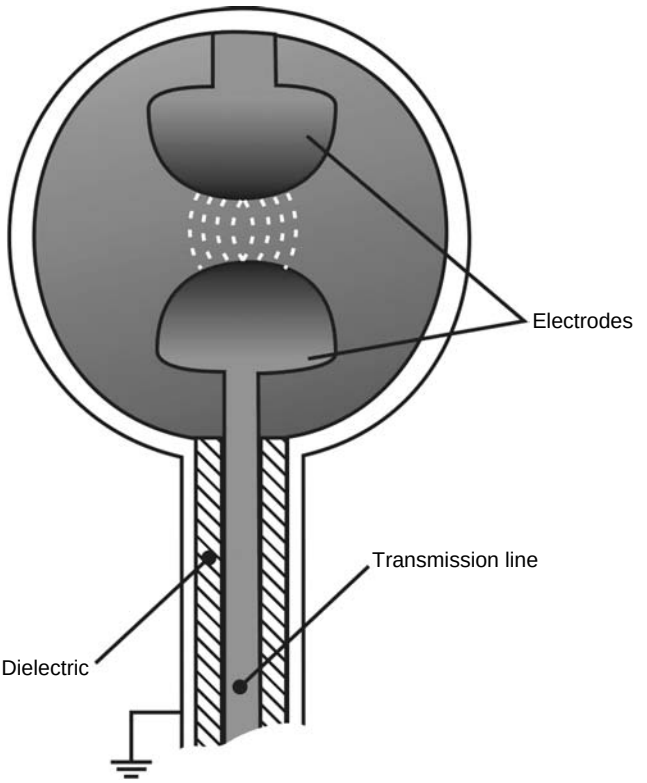

FIGURE 11.33 Cross section of a low-inductance nitrogen laser head.

Typical gas pressure of N_2 laser is about a few tens of mTorr of N_2 and it is usually filled up with He to quasi-atmospheric pressure. To get efficient and homogenous discharge, it is necessary to apply an electric field of about $E = 10–15$ kV/cm between electrodes. The length of N_2 laser is usually about tens of centimeters. Typical parameters obtained from such lasers are:

– The pulse energy—from few tens of microjoules to tens of millijoules
– Pulse width—a few nanoseconds (3–5 ns)
– Repetition rate—up to 200 pps (pulses per second)
– The power of single pulse—tens of kilowatts to megawatts

The N_2 lasers found applications as dye pumping sources, in lidar investigations (remote sensing), in atomic and lifetime spectroscopy, and in medicine and biology research.

REFERENCES

1. Labuda, E.F. and Gordon, E.I., Microwave determination of average electron energy and density in He–Ne discharges, *J. Appl. Phys.*, 35, 1647–1651, 1964.
2. Verdeyen, J.T., *Laser Electronics*, Prentice Hall, Englewood Cliffs, New Jersey, 1995.
3. Javan, A., Bennet, W.R., and Herriott, D.R., Population inversion and continuous optical maser oscillations in a gas discharge containing He–Ne mixtures, *Phys. Rev.*, 6, 106, 1961.
4. Godziński, Z., *First Wrocław Laser*, Private archive, Wrocław Technical University, Wrocław, 1965.
5. Abramski, K.M. and Hall, D.R., Frequency stabilization of lasers, in *The Physics and Technology of Laser Resonators*, Hall, D.R. and Jackson, P.E., Eds., Adam Hilger, Bristol, 1989.
6. Gordon, E.I., Labuda, E.F., and Bridges, W.B., Continuous visible laser action in singly ionized Argon, Krypton and Xenon, *Appl. Phys. Lett.*, 4(10), 178–180, 1964.
7. Labuda, E.F., Gordon, E.I., and Miller, R.C., Continuous-duty Argon ion lasers, *IEEE J. Quant. Electron.*, QE-1(6), 273–279,1965.
8. Ahmed, S.A., Faith, T.J., and Hoffman, G.W., Effects of magnetic fields on pulse and CW operation of the large bore ionized gas laser, *Proc. IEEE*, 55, 691–692, 1967.
9. Cottrell, T.H.E., Output power characteristics of the pulsed argon ion laser, *IEEE J. Quant. Electron.*, QE-4, 435–441, 1968.
10. Marling, J.B., Ultraviolet ion laser performance and spectroscopy—Part I: new strong noble gas transitions below 2500 Å, *IEEE J. Quant. Electron.*, QE-11, 822–834, 1975.
11. Goldslorough, J.P., Hodges, E.M., and Bell, W.E., RF induction excitation of CW visible laser transitions in ionized gases, *Appl. Phys. Lett.*, 8, 137–139, 1966.
12. Ahmed, S.A., Campillo, A.J., and Cody, P., RF inductively excited ion laser with aperture magnetic confinement, *IEEE J. Quant. Electron.*, QE-6, 267–271, 1969.
13. Paik, S.F. and Credon, J.E., Microwave excited ionized Argon laser, *Proc. IEEE*, 56, 2086–2087, 1968.
14. Davies, C.C., Gas lasers. *Lasers and Electrooptics. Fundamentals and Engineering*, Cambridge University Press, Cambridge, 1996, chapter 9.
15. Tio, T.K., Luo, H.H., and Lin, S.-C., High CW power ultraviolet generation from wall-confined noble gas ion lasers, *Appl. Phys. Lett.*, 29(12), 795–797, 1976.
16. Davies, C.C. and King, T.A., Gaseous Ion Lasers, in *Advances in Quantum Electronics*, Vol. 3, Goodwin, D.W., Ed., Academic Press, London, 1975.
17. Bridges, W.B., Ionized gas lasers, in *Handbook of Laser Science and Technology*, Vol. 2, Weber, M.J., Ed., Gas Lasers, CRC Press, Boca Raton, 1982.
18. Bridges, W.B., Ion lasers—the early years, *IEEE J. Selec. Topics Quant. Electron.*, 6(6), 885–898, 2000.
19. Swelto, O., *Principles of Lasers*, Plenum Press, New York, 1998.
20. Chang, T.Y. and Bridges, T.J., Laser action at 482, 496, and 541 μm in optically pumped CH_3F, *Opt. Commun.*, 1, 423–426, 1970.
21. Chang, T.Y., Optically pumped submillimeter-wave sources, *IEEE J. Trans. Micro. Theory Techn.*, 22(12), 983–988, 1974.

22. Hennigsen, J.O., New FIR laser lines from optically pumped CH_3OH: measurements and assignments, *IEEE J. Quant. Electron.*, 14, 958–961, 1978.
23. Lees, R.M. and Baker, J.G., Torsion-vibration-rotation interactions in methanol. I. Millimeter wave spectrum, *J. Chem. Phys.*, 48, 5299–5318, 1968.
24. Danielewicz, E.J. and Coleman, P.D., Assignments of the high power optically pumped CW laser lines of CH_3OH, *IEEE J. Quant. Electron.*, QE-13(6), 495–490, 1977.
25. Drozdowicz, Z., Temkin, R.J., and Lax, B., Laser pumped molecular lasers—Part I: theory, *IEEE J. Quant. Electron.*, QE-15(3), 170–177, 1979.
26. Rosenbluh, M., Temkin, R.J., and Button, K.J., Submillimeter laser wavelength tables, *Appl. Opt.*, 15(11), 2635–2644, 1976.
27. Mueller, E., Submillimeter wave lasers, in *Willey Encyclopedia of Electrical and Electronics Engineering*, Webster, J.G., Ed., John Willey & Sons, Inc., 20, 597–615, 1989.
28. Jacobson, S., Review—optically pumped far infrared lasers, *Infrared Phys.*, 29, 853–874, 1989.
29. Telles, E.M., Odashima, H., Zink, L.R. and Evenson, K.M., Optically pumped FIR laser lines from CH_3OH: new laser lines, frequency measurements, and assignments, *J. Mol. Spectrosc.*, 195, 360–366, 1999.
30. Hodges, D.T., A review of advances in optically pumped far-infrared lasers, *Infrared Phys.*, 18, 375–384, 1978.
31. Danielewicz, E.J. and Weiss, C.O., New efficient CW far-infrared optically pumped CH_2F_2 laser, *IEEE J. Quant. Electron.*, 14(10), 705–707, 1978.
32. Xu, L.-H., Lees, R.M., Evenson, K.M., Chou, C.C., Shy, J.T., Vasconcellos, E.C.C., Spectroscopy of new CH_3OH FIR laser lines pumped by new CO_2 laser lines, *Can. J. Phys.*, 72, 1155–1164, 1994.
33. Witteman, W.J., *The CO_2 Laser*, Springer-Verlag, Berlin, 1987.
34. Xu, L.-H., Lees, R.M., Vasconcellos, E.C.C., Zerbetto, S.C., Zink, L.R., and Evenson, K.M., Methanol and the optically pumped far-infrared laser, *IEEE J. Quant. Electron.*, 32, 392–399, 1996.
35. Faist, J. and Capasso, F., Quantum cascade, in *McGraw Hill Yearbook of Science and Technology*, 265–267, 1997.
36. Hennigsen, J.O. and Jansen, H.G., The optically pumped far-infrared laser: rate equations and diagnostic experiments, *IEEE J. Quant. Electron.*, 11(6), 248–252, 1975.
37. Tucker, J.R., Absorption saturation and gain in pulsed CH_3F lasers, *Opt. Commun.*, 16(2), 209–212, 1976.
38. Plant, T.K., Coleman, P.D., and DeTemple, T.A., New optically pumped far-infrared lasers, *IEEE J. Quant. Electron.*, 9, 962–963, 1973.
39. Danielewicz, E.J. and Coleman, P.D., Hybrid metal-mesh dielectric mirrors for optically pumped far infrared lasers, *Appl. Opt.*, 15(3), 761–767, 1976.
40. DeTemple, T.A. and Danielewicz, E.J., Continuous-wave CH_3F waveguide laser at 496 μm: theory and experiment, *IEEE J. Quant. Electron.*, 12(1), 40–47, 1976.
41. Vasconcellos, E.C.C., Zerbetto, S.C., Holecek, J.C., and Evenson, K.M., Short-wavelength far-infrared laser cavity yielding new lines in methanol, *Opt. Lett.*, 20(12), 1392–1393, 1995.
42. Jackson, M., Hockel, H., Lauters, M., Vasconcellos, E.C.C., Allen, M.D., and Evenson, K.M., New short-wavelength laser emissions from optically pumped $^{13}CD_3OD$, *IEEE J. Quant. Electron.*, 38, 429–431, 2002.
43. Coleman, P.D., Present and future problems concerning lasers in the far-infrared region, *J. Opt. Soc. Am.*, 67(7), 894–901, 1977.
44. Peterson, F.R., Evenson, K.M., Jennings, D.A., Wells, J.S., Goto, K., and Jimenez, J.J., Far infrared frequency synthesis with stabilized CO_2 lasers: accurate measurements of the water vapor and methyl alcohol laser frequencies, *IEEE J. Quant. Electron.*, 11(10), 838–843, 1975.
45. Gagliardi, G., Viciani, S., Inguscio, M., DeNatale, P., Gmachl, C., Capasso, F., Sivco, D.L., Baillargeon, J.N., Hutchinson, A.L., and Cho, A.Y., Generation of tunable far-infrared radiation with a quantum cascade laser, *Opt. Lett.*, 27(7), 521–523, 2002.
46. Farhoomand, J. and Picket, H.M., Stable 1.25-W CW methanol laser, *Appl. Opt.*, 28(15), 3255, 1989.
47. Roser, H.P. and Shultz, G.V., Development of an optically pumped molecular lasers, *Infrared Phys.*, 17, 531–536, 1977.

48. Gabbie, A., Stone, N.W.B., and Findly, F.D., A simulated emission source at 0.34 millimeter wavelength, *Nature*, 16, 685, 1964.
49. Turner, R. and Poehler, T.O., Characteristics of the HCN laser radiation at high-excitation currents, *J. Appl. Phys*., 42, 3819–3826, 1971.
50. Yamanaka, M., Yamauchi, T., and Yoshinaga, H., Time behavior of pulsed gain at 337 micrometers of HCN laser, *Jpn. J. Appl. Phys*., 10, 1601–1603, 1971.
51. Wells, J.S., A stabilized HCN laser for infrared frequency synthesis, *IEEE Trans. Instrum. Meas*., IM-22, 113–118, 1973.
52. Lam, M.F., Jassby, D.L., and Casperson, L.W., Transverse-excitation pulsed HCN laser, *IEEE J. Quant. Electron*., QE-9, 851–852, 1973.
53. Birch, J.R. and Bradley, C.C., A variable loss determination of HCN laser gain, *Infrared Phys*., 13, 99–108, 1973.
54. Belland, P. and Veron, D., A compact CW HCN laser with high stability and power output, *Opt. Commun*., 9, 146–148, 1973.
55. Belland, P., Ciura, A.I., and Whitbourn, L.B., Gain saturation and oscillation linewidth of a CW 337 μm HCN laser, *Opt. Commun*., 11, 21–26, 1974.
56. Yoshihiro, K. and Yamanouchi, C., A stable CW HCN laser, *Rev. Sci. Instrum*., 45, 767–768, 1974.
57. Mizuno, K., Kuwahara, R., Shimoe, O., and Ono, S., Correlation between the 337- and 311-mm line in a CW HCN laser, *J. Appl. Phys*., 45, 5464–5465, 1974.
58. Lourtioz, J.M. and Adde, R., Design of a stable CW HCN laser for far infrared frequency synthesis, *Rev. Phys. Appl*., 11, 533–540, 1976.
59. Robinson, D.W., Chemical pumping of the far infrared HCN laser, *Opt. Commun*., 27, 281–286, 1978.
60. Burneau, J.L., Belland, P., Lebertre, T., and Veron, D., CW HCN laser gain in a hollow dielectric rectangular cross-section discharge tube, *Appl. Phys*., 19, 359–361, 1979.
61. Sturzenegger, Ch., Vetsch, H., and Kneubuhl, F., Transversely excited double-discharge HCN laser, *Infrared Phys*., 19, 277–296, 1979.
62. Makiuchi, M., Kawamura, M., and Itoh, H., An increase in output power of a compact CW HCN laser by RF-excited discharge, *Trans. Inst. Electron. Commun. Eng. Jpn., Section e (English)*, E64, 451, 1981.
63. Makiuchi, M. and Kawamura, M., CW-HCN laser output characteristics based on temperature properties of electrons and gases, *Trans. Inst. Electron. Commun. Eng. Jpn., Section e (English)*, E65, 294, 1982.
64. Hutchinson, I.H., A heterodyne plasma interferometer based on polarisation modulation of a HCN laser, *J. Phys. E—Sci. Instrum*., 15, 903–905, 1982.
65. Ute, H., Fukuyama, T., Okabayashi, I., Makiuchi, M., and Kawamura, M., Operational characteristics of an RF-excited CW-HCN laser, *Trans. Inst. Electron. Commun. Eng. Jpn*., Part C, J66C, 725–731, 1983.
66. Kawamura, M., Okabayashi, I., and Fukuyama, T., A capacitively coupled RF-excited CW-HCN laser, *IEEE J. Quant. Electron*., QE-21, 1833–1837, 1985.
67. Schilke, P. and Menten, K.M., Detection of a second, strong submillimeter HCN laser line toward carbon stars, *Astrophys. J*., 583, 446–450, 2003.
68. Bruneau, J.L., Belland, P., and Veron, D., A CW DCN waveguide laser of high volumetric efficiency, *Opt. Commun*., 24, 259–264, 1978.
69. Jie, Y.X., Gao, X., Cheng, Y.F., Yang, K., and Tong, X.D., Multi-channel FIR HCN laser interferometer on HT-7 tokamak, *Int. J. Infrared Millimeter Waves*, 21, 1375–1380, 2000.
70. Zelinger, Z., Amano, T., Ahrens, V., Brunken, S., Lewen, F., Muller, H.S.P., and Winnewisser, G., Submillimeter-wave spectroscopy of HCN in excited vibrational states, *J. Mol. Spectrosc*., 220, 223–233, 2003.
71. Patel, C.K.N., Bennet Jr. W.R., Faust, W.L., and McFarlane, R.A., Infrared spectroscopy using stimulated emission technique, *Phys. Rev. Lett*., 9, 102, 1962.
72. Patel, C.K.N., Faust, W.L., and McFarlane, R.A., High gain gaseous (Xe–Ne) optical masers, *Appl. Phys. Lett*., 1, 84, 1962.
73. Walter, E.T. and Jarret, S.M., Strong 3.27 μm laser oscillation in Xenon, *Appl. Opt*., 3, 789, 1964.
74. Clark, P.O., Investigation of the operating characteristics of the 3.5 μm Xenon laser, *IEEE J. Quant. Electron*., 1, 109, 1965.

75. Photonics spectra, *Edinburgh Instruments—Helium–Xenon Laser*, 150, 1995.
76. Collier, F., Labastie, P., Maillet, M., and Michon, M., High-efficiency infrared Xenon laser excited by a UV preionized discharge, *IEEE Quant. Electron*., 19, 1129, 1983.
77. Orchard, D.A. and Hollins, R.C., A high pulse repetition rate Helium–Xenon laser, GCL/HPL'96, *SPIE* 3092, 82, 1996.
78. Newman, L.A. and DeTemple, T.A., High-pressure infrared Ar–Xe laser system: ionizer–sustainer mode of excitation, *Appl. Phys. Lett*., 27, 678, 1975.
79. Christensen, C.P., Powell, F.X., and Djeu, N., Transverse electrodeless RF discharge excitation of high-pressure laser gas mixtures, *IEEE J. Quant. Electron*., 16, 949, 1980.
80. Udalov, Y.B., Peters, P.J.M., Heeman-Ilieva, M.B., Ernst, E.H.J., Ochkin, V.N., and Witteman, W.J., New continuous wave infrared Ar–Xe laser at intermediate gas pressure pumped by a transverse radio frequency discharge, *Appl. Phys. Lett*., 63, 721, 1993.
81. Tshei, S.N., Udalov, Y.B., Peters, P.J.M., and Witteman, W.J., Continuous wave near-infrared atomic Xe laser excited by a radio frequency discharge in a slab geometry, *Appl. Phys. Lett*., 66, 801, 1993.
82. Wendland, J.J., Morley, R.J., Baker, H.J., and Hall, D.R., High power mid-infrared operation of the atomic Xenon laser, *Appl. Phys. Lett*., 72, 1436, 1998.
83. Heard, H., Ultraviolet gas laser at room temperature, *Nature*, 200, 667–676, 1963.
84. Svelto, O., *Principle of Lasers*, Plenum Press, New York, 1989.
85. Bosting, D., Schafer, F.P., and Steyer, A.B., *Simple, High Power Nitrogen Laser, Optoelectronics*, Kluwer Academic Publishers, 1972, 43–49.
86. Levatter, J.I. and Lin, S.-C., High power generation from a parallel-plates-driven pulsed nitrogen laser, *Appl. Phys. Lett*., 25(12), 703–705, 1974.
87. Seki, H., Takamori, S., and Sato, T., Development of a high efficient nitrogen laser using an ultra-fast magnetic pulse compression circuit, *IEEE J. Select. Topics Quant. Electron*., 1, 825–829, 1995.

Index

D

E

F

G

H

I

K

L

M

N

O

P

Q

R

S

T

U

V

W

X

Z

Electrical Engineering

Gas Lasers

Lasers with a gaseous active medium offer high flexibility, wide tunability, and advantages in cost, beam quality, and power scalability. **Gas lasers** have tended to become overshadowed by the recent popularity and proliferation of semiconductor lasers. An unfortunate result of this shift in focus has been that details on gas lasers have become difficult to find. In addition, different types of gas lasers have unique properties that are not well described in other references. Collecting expert contributions from authorities dealing with specific types of lasers, **Gas Lasers** examines the fundamentals, current research, and applications of this important class of lasers.

It is important to understand all types of lasers, from solid-state to gaseous, before making a decision for any application. This book fills in the gaps by discussing the definition and properties of gaseous media along with its fluid dynamics, electric excitation circuits, and optical resonators. From this foundation, the discussion launches into the basic physics, characteristics, applications, and current research efforts for specific types of gas lasers: CO lasers, CO_2 lasers, HF/DF lasers, excimer lasers, iodine lasers, and metal vapor lasers. The final chapter discusses miscellaneous lasers not covered in the previous chapters.

A single source of broad yet thorough information, this book…

- Discusses the basics, capabilities, applications, and research initiatives for a wide variety of gas lasers
- Provides depth of coverage that is comparable to monographs on specific lasers
- Presents state-of-the-art discussions contributed by experts on each type of gas laser
- Offers unique data on less common lasers, some of which appear here for the first time in print
- Covers the chemical Oxygen–Iodine laser along with other novel iodine lasers

Collecting hard-to-find material into a single, convenient source, **Gas Lasers** offers an encyclopedic survey that helps you approach new applications with a more complete inventory of laser options.

DK553X

ISBN 0-8493-3553-1

90000

9 780849 335532

CRC Press
Taylor & Francis Group
an informa business
www.taylorandfrancisgroup.com

6000 Broken Sound Parkway, NW
Suite 300, Boca Raton, FL 33487
270 Madison Avenue
New York, NY 10016
2 Park Square, Milton Park
Abingdon, Oxon OX14 4RN, UK

www.crcpress.com